

Copyright

by

Jorge de Novais Telles de Faria Correa Bastos

1987

To my parents, Manuela and Joaquim, and to my brother Paulo that, although on the other side of the Atlantic Ocean, were always on my mind.

To the great Portuguese navigator D. Vasco da Gama, who was 29 years old when he first reached India.

AN APPRAISAL OF REINFORCED CONCRETE SLAB-BEAM-COLUMN JOINT TESTS

by

JORGE DE NOVAIS TELLES DE FARIA CORREA BASTOS, ENGENHEIRO CIVIL

DISSERTATION

Presented to the Faculty of the Graduate School of

The University of Texas at Austin

in Partial Fulfillment

of the Requirements

for the Degree of

DOCTOR OF PHILOSOPHY

THE UNIVERSITY OF TEXAS AT AUSTIN

May 1987

ACKNOWLEDGEMENTS

The author of this research study is deeply indebted to Professor James O. Jirsa who supervised the work throughout the past four years. His huge amount of patience and willingness to spend his time and impart his knowledge are greatly appreciated.

The author also acknowledges the guidance of the other members of his supervisory committee - Professors N. H. Burns, D. W. Fowler, R. E. Klingner, C. H. Yew, and J. A. Yura for their advice, help, and valuable suggestions in this work.

Special thanks are also endorsed by the author to Professor Joaquim R. Sarmento (Universidade do Porto - Portugal) who lectured on structural concrete during undergraduate work, showing its potential as a construction material.

The continuous help of the Fullbright-Hays exchange program, the INVOTAN Fellowship Scientific Program, the Department of Architecture - U.T.L., and The University of Texas at Austin are gratefully acknowledged. The facilities of both The Ferguson Structural Engineering Laboratory and The Department of Civil Engineering (U.T. Austin) were used.

This study was conducted under the U.S.-Japan Joint Technical Cooperative Program on Large Scale Testing. The National Science Foundation support under grants PFR-8009039 and CEE-8320586 is also gratefully acknowledged.

The cooperation of The University of Michigan at Ann Arbor through Professor J. K. Wight and V. Sattary was indispensable in making available the data from the BRI building test. Professors K. Krawinkler (Stanford University), B. Wallace (The University of Oklahoma) were also very helpful in providing the author with the data from their component tests. The energy studies on component tests would not be complete without the help and advice of Professors Jose M. Roesset (The University of Texas at Austin), and M. Seckin (Royal Military College of Canada). Drs. Patricia Baker and Phil Kelton (Department of Astronomy - The University of Texas at Austin) proved to be a superteam in helping the author in recovering the lost data from FSEL-UTA tests.

During all the years that this work was carried on, the suggestions, critiques, and encouragement from mainly three of my colleagues proved to be very helpful - C. Michael Donoghue (Austin, Texas), Jens Dossing (Copenhagen, Denmark), and Yuki Kurose (Tokyo, Japan). Particularly, the help provided by Yuki Kurose in giving the best insight of the currently used Japanese design code provisions is gratefully acknowledged.

The friendly cooperation of Sharon Cunningham in typing the complete manuscript and her assistance is sincerely appreciated.

J. N. B.

Austin, Texas - Christmas 1986

AN APPRAISAL OF REINFORCED CONCRETE
SLAB-BEAM-COLUMN JOINT TESTS

Publication No. _____

Jorge de Novais Telles de Faria Correa Bastos, Ph.D.
The University of Texas at Austin, 1987

Supervising Professor: James O. Jirsa

The satisfactory response of well-detailed and carefully built reinforced concrete ductile moment resisting frames (DMRF) during recent earthquakes has shown that these structural systems are efficient for providing seismic resistance. However, poor performance of the critical region where the beam, the column and the slab join may limit the satisfactory performance of the structure. Consequently, intense research has been conducted on components that model this critical region in order to assess this response under simulated earthquake loads. The research results have been incorporated into design recommendations which are intended to improve the safety of such structures.

The US-Japan Joint Technical Cooperative Program on Large Scale Testing provided a unique opportunity to carry out

correlation studies on data gathered in experimental test programs. Different test conditions, specimen sizes, load histories, and reinforcement detailing were studied and require careful interpretation. The main objective of the work reported herein is to compare the response of critical regions in a full-scale seven-story building tested at the Building Research Institute (BRI), Tsukuba, Japan with the response of component tests of different scale representing these regions. Comparisons between the BRI building and components were made using equivalent drift levels. The components failure modes were clearly identified through energy absorption, dissipation characteristics and levels of equivalent hysteretic damping.

Current design methodologies continually must be modified and improved as new data becomes available. The component tests were used to evaluate joint shear stress and reinforcement bond performance in comparison with current design standards. Finally, the ultimate strength of the BRI building was evaluated by a Limit Analysis in which the strength of the building members was calculated using the results of the component tests. The ultimate strength evaluation gave results which were nearly equal to the experimental values and provide a clear indication of the importance of the floor slab in determining overall building lateral capacity.

TABLE OF CONTENTS

Chapter		Page
I	INTRODUCTION	1
	1.1 General	1
	1.2 Cooperative Research Program	2
	1.3 Objective of this Study	3
	1.4 Structure of this Report	5
II	CURRENT CONCEPTS IN FRAME SEISMIC DESIGN	9
	2.1 Introduction	9
	2.2 The Current Design Approach	11
	2.2.1 Initial Comments	11
	2.2.2 The Definition of Loads	12
	2.2.3 The Total Reliability of Structural Systems	14
	2.2.4 Working Stress Method vs. Ultimate Strength Design	17
	2.2.5 The Limit States Design Method in Earthquake Design	20
	2.3 The Ductile Reinforced Concrete Structural System	23
	2.3.1 Basic Requirements in Seismic Design	23
	2.3.2 Different Types of R/C Structural Systems	26
	2.3.3 The Desirable Failure Mode in a DMRF	29
	2.3.4 The Desired Failure Mode in a Shear-Wall	31
	2.3.5 The Frame-Shear Wall (Dual) System	31
	2.4 The Ductile Moment Resisting Frame	32
	2.4.1 The Search for Ductility	32
	2.4.2 Critical Regions in a DMRF	36
	2.4.3 The Beam Member in a DMRF	39
	2.4.4 The Column Member in a DMRF	43
	2.5 The Beam-Column Joint in DMRF	50
	2.5.1 The Position of the Problem	50
	2.5.2 Knee Joints	56

TABLE OF CONTENTS (continued)

Chapter		Page
	2.5.3 Exterior Joints	57
	2.5.3.1 Types of exterior joints	58
	2.5.3.2 Resistance mechanisms in inelastic exterior joints	58
	2.5.3.3 Exterior joints in spatial DMRF	64
	2.5.4 Interior Joints	65
	2.5.4.1 Resistance mechanisms in interior joints	66
	2.5.4.2 Interior joints in spatial DMRF	77
	2.5.5 Slab Participation in R/C Connections	81
	2.5.5.1 Statement of the problem	81
	2.5.5.2 Shear-lag in wide flanged beams	85
	2.5.5.3 Wide flange R/C beam response	97
	2.5.6 Transverse Beam Participation ...	100
	2.5.7 Suggestions for Improved Performance	105
	2.6 Design Code Optimization	107
	2.7 References	109
III	THE US-JAPAN COOPERATIVE EARTHQUAKE ENGINEERING PROGRAM	118
	3.1 The Cooperative Research Program	118
	3.1.1 Introduction	118
	3.1.2 Objectives of the Cooperative Research Program	119
	3.1.3 Tests of Reinforced Concrete Structures	120

TABLE OF CONTENTS (continued)

Chapter		Page
3.2	The Japanese Participation	121
3.2.1	The Full-Scale Building	121
3.2.1.1	The specimen geometry ..	123
3.2.1.2	The material properties.	125
3.2.1.3	The loading program	128
3.2.1.4	Instrumentation	129
3.2.2	One-Half Scale Subassemblage Tests	136
3.2.2.1	Geometry	136
3.2.2.2	Material properties	137
3.2.2.3	Loading program	142
3.2.2.4	Instrumentation	144
3.3	U.S. Participation	147
3.3.1	Full-Scale Joint Tests - Univer- sity of Texas at Austin	147
3.3.1.1	Specimen geometry	147
3.3.1.2	Material properties	153
3.3.1.3	Loading program	154
3.3.1.4	Instrumentation	156
3.3.2	The Stanford University Small- Scale Tests	164
3.3.2.1	The geometry of the specimens	168
3.3.2.2	Material properties	169
3.3.2.3	Loading program	171
3.3.2.4	Instrumentation	171
3.3	Other U.S. Tests	173
3.3.1	The U.C.B. 1:5 Tests	173
3.3.2	P.C.A. 1:3.5 Tests	177
3.3.3	The University of Illinois 1:10 Tests	179
3.4	References	181
IV	BASIS FOR COMPARISON IN RESPONSE OF DIFFERENT TESTS	183
4.1	Introduction	183
4.2	Performance Criteria	183
4.3	Test Specimens	184

TABLE OF CONTENTS (continued)

Chapter	Page
4.4	Levels of Comparison 185
4.5	Equivalent Drift Ratio 187
4.6	Other Deformation Response Variables ... 195
4.7	The P-Delta Effect on Component Test Results 197
4.8	References 200
V	TOTAL SPECIMEN RESPONSE 203
5.1	Interpretation of Test Results 203
5.2	Cracking Patterns 205
5.2.1	BRI Building 205
5.2.2	Component Tests vs. BRI Building. 206
5.2.3	Exterior Component Tests with Slab 212
5.2.4	Exterior Joint Region - Building vs. Components 217
5.2.5	The Interior Component Tests with Slab 218
5.2.6	Interior Joint Region - Building vs. Components 222
5.2.7	Exterior vs. Interior Component Crack Response 222
5.3	Stiffness and Strength Degradation 225
5.3.1	BRI Building 225
5.3.2	The Exterior Component Tests 229
5.3.2.1	Strength character- istics 229
5.3.2.2	Stiffness character- istics 235
5.3.3	Interior Component Tests 240
5.3.3.1	Strength character- istics 240
5.3.3.2	Stiffness character- istics 245
5.3.4	Exterior vs. Interior Component Response 248
5.4	Final Observations 252
5.5	References 254

TABLE OF CONTENTS (continued)

Chapter		Page
VI	ASPECTS OF LOCAL RESPONSE	256
	6.1 Introduction	256
	6.2 Longitudinal Beam Rotation	256
	6.2.1 Exterior Joint Beam Rotation	257
	6.2.2 Interior Joint Beam Rotation	260
	6.3 Beam Strength in Components	266
	6.3.1 Exterior Components	266
	6.3.2 Interior Components	269
	6.4 Longitudinal Beam Stiffness	272
	6.4.1 Exterior Components	273
	6.4.2 Interior Components	278
	6.4.3 Exterior vs. Interior Component Beam Stiffness	285
	6.5 Longitudinal Beam	290
	6.5.1 BRI Building	290
	6.5.2 UTA Tests	292
	6.6 Slab Participation in Longitudinal Beam Response	297
	6.6.1 Exterior Joints	297
	6.6.2 Interior Joints	303
	6.6.3 Effective Slab Width	308
	6.7 Joint Region Performance	312
	6.7.1 Joint Core Reinforcement Reponse.	313
	6.7.2 Joint Core Distortion	319
	6.8 Transverse Beam Participation	321
	6.8.1 Transverse Beam Deformation	321
	6.8.2 Transverse Beam Stiffness Response	331
	6.8.3 Transverse Beam Yielding	337
	6.9 Final Comments	340
	6.10 References	348
VII	ENERGY ASSESSMENT IN TEST RESPONSE	349
	7.1 Introduction	349
	7.2 The Energy of Deformation	351
	7.3 Energy Assumptions in Component Tests ..	356
	7.3.1 Total Input Energy	358
	7.3.2 Longitudinal Beam Dissipated Energy	358

TABLE OF CONTENTS (continued)

Chapter		Page
	7.3.3 Joint Core Dissipated Energy	361
	7.3.4 Transverse Beam Dissipated Energy	363
	7.3.5 Design Code Torsional Stiffness .	365
	7.3.6 Damping and Energy Dissipation Mechanisms	366
	7.3.7 Other Aspects of Component Energy Response	373
7.4	Evaluation of Component Energy Response	375
	7.4.1 Exterior Components	375
	7.4.2 Interior Components	380
	7.4.3 Exterior vs. Interior Components	386
	7.4.4 Joint Core Participation	388
	7.4.5 Estimated Total Component Energy Response	392
7.5	Hysteretic Damping Response	394
	7.5.1 BRI Building	395
	7.5.2 Exterior Component Tests with a Slab	398
	7.5.3 Interior Components with a Slab .	404
	7.5.4 Response of Components Without a Slab	407
7.6	Hysteretic Damping in Components	412
	7.6.1 Exterior Components	414
	7.6.2 Interior Components	420
7.7	Hysteretic Damping in Component Elements	422
	7.7.1 Exterior Joint Longitudinal Beam	426
	7.7.2 Interior Joint Longitudinal Beam	431
	7.7.2.1 West Beam	431
	7.7.2.2 East Beam	431
	7.7.3 Exterior vs. Interior Joint Longitudinal Beam	434
7.8	Conclusions	439
7.9	References	442
VIII	EVALUATION OF DESIGN CODE REQUIREMENTS	445
	8.1 Introduction	445
	8.2 Horizontal Joint Shear	445
	8.2.1 Initial Remarks	445
	8.2.2 Exterior Joint Shear Stress	450

TABLE OF CONTENTS (continued)

Chapter		Page
	8.2.3 Interior Joint Shear Stress	453
8.3	Normalized Joint Shear Stress	453
	8.3.1 Gross Joint Core Area	455
	8.3.2 Reduced Joint Core Area	455
8.4	Component Tests-Bond Response	458
	8.4.1 Development Length	461
	8.4.1.1 Exterior Joints	461
	8.4.1.2 Interior Joints	463
	8.4.2 Beam Bar Bond Index	463
	8.4.3 Bond and Hysteretic Response	467
8.5	BRI Building - Ultimate Strength Evaluation	469
	8.5.1 Background	469
	8.5.2 Experimental Evidence	470
	8.5.2.1 Spread of Yielding	470
	8.5.2.2 Beam Member Rotation ...	472
	8.5.2.3 Shear Wall Deformation .	474
	8.5.3 BRI Building Ultimate Strength ..	476
	8.5.4 Comments on the Assumed Failure Mechanism	488
8.6	Final Observations	489
8.7	References	492
IX	SUMMARY AND CONCLUSIONS	496
	9.1 Objective	496
	9.2 Scope	497
	9.3 Summary of Behavior - Strength and Stiffness	498
	9.4 Summary of Behavior - Energy Considerations	500
	9.5 Design Implications and Conclusions	501
	9.5.1 Slab Participation	501
	9.5.2 Shear	502
	9.5.3 Bond	502
	9.5.4 Ultimate Strength	502
	9.6 An Overview of the Research Program	503
	APPENDIX A	505
	APPENDIX B	536
	APPENDIX C	617

LIST OF TABLES

Table		Page
2.1	Research programs on R/C joints	52
2.2	Effective breadth ratios [Moffat and Dowling (53)]	89
2.3	Effective width code requirements (1964) in symmetrical beams without fillets [Brendel (16)]	99
2.4	Summary of torsion tests [Tassios (82)]	102
3.1	Initial US-Japan cooperative research program	122
3.2	Actual US-Japan cooperative research program	122
3.3	Building concrete characteristics	127
3.4	Building steel properties	127
3.5	Building loading program	130
3.6	Targeted vs. actual results	130
3.7	General properties of half-scale components .	139
3.8	Material properties for UTA tests	155
3.9	UTA tests - available data	157
3.10	Stanford University material properties	170
3.11	Stanford University component data	170
3.12	Material Properties (Aktan et al(3))	176
4.1	Comparison studies in component tests	186
7.1	Transverse Beam Torsional Stiffness	364
8.1	Design Code Horizontal Shear Strength	448

LIST OF TABLES (continued)

Table		Page
8.2	Joint Shear Stress - Kamimura Equation	449
8.3	Experimental vs. Code Ultimate Joint Shear Stress	451
8.4	Code Development Length	462
8.5	Required Top Beam Development Length	462
8.6	Experimental vs. Nominal Bond Index Ratio	466
8.7	Plastic Hinge Length and Curvatures	485
8.8	Virtual Work Computation	487
8.9	Effect of Considering Different Beam Hinge Locations	487
8.10	Member Participation in Ultimate Strength	487

LIST OF FIGURES

Figure		Page
2.1	Risks of death of various activities	15
2.2	RC materials response	18
2.3	RC material stress/unit weight vs. strain response, [Bertero and Bresler (9)]	18
2.4	Current types of planar RC structural systems	28
2.5	DMRF failure modes [Park (57), Park and Paulay (62)]	28
2.6	Cantilever shear wall failure modes [Paulay and Williams (66)]	28
2.7	Frame-shear wall response [Park and Paulay (60)]	33
2.8	A model of the cage - "A gaiola" [Tobriner (84)]	33
2.9	SDOF system response to ground excitation [Park and Paulay (60)]	33
2.10	SDOF oscillator ductility evaluation [Park and Paulay (60)]	33
2.11	RC member hysteretic behavior [Park and Paulay (60)]	37
2.12	DMRF critical regions and models [Bertero and Popov (10)]	37
2.13	RC members hysteretic response [Leonhardt (43)]	37
2.14	Column interaction curve [Blume et al. (13)]..	44

LIST OF FIGURES (continued)

Figure		Page
2.15	General RC column performance [Ferguson (28)]	44
2.16	Column biaxial response, after Furlong [Ferguson (28)]	48
2.17	Elastic stress distribution in a knee joint [Leonhardt and Monnig (45); Nilsson and Losberg (56)]	48
2.18	Types of RC Beam-Column Joints	53
2.19	Possible component failure modes [Meinheit and Jirsa (48)]	55
2.20	Knee joints under load reversals [Park and Paulay (60)]	55
2.21	Exterior joint in a planar frame [Jirsa (34)]	59
2.22	Exterior component forces [Paulay and Park (64)]	59
2.23	Exterior joint performance [Paulay and Park (64)]	62
2.24	Exterior joint model[Fenwick and Nguyen (27)]	62
2.25	Interior joint force distribution [Jirsa (34)]	67
2.26	Interior joint region [Paulay and Park (64)].	67
2.27	Interior joint response [Paulay and Park (64)]	71

LIST OF FIGURES (continued)

Figure		Page
2.28	Inelastic response of an interior joint [Tassios (82)]	71
2.29	Interior joint stress load history [Paulay and Park (64)]	71
2.30	Principal stress distribution on deformed bars [Leonhardt and Monnig (45)]	76
2.31	Rupture of a concrete teeth and confinement action [Tassios (81)]	76
2.32	Effect of concurrent beam hinging on columns and joints [Armstrong (4)]	76
2.33	Space frame interior joint	79
2.34	Spatial diagonal compression strut response [Leon (43)]	79
2.35	Interior joint spatial failure plane [Beckingsdale (5)]	79
2.36	Joint shear capacity under different codes [Jirsa (34)]	82
2.37	UTA member strength with different slab widths	82
2.38	Plate-bar interaction for different plate stiffnesses [Kuhn (41)]	86
2.39	T-beam web-flange junction shear flow [Brendel (15)]	86
2.40	Plate-girder performance [Schade (72)]	89
2.41	Shear lag variation along the span [Leonhardt and Monnig (45)]	89

LIST OF FIGURES (continued)

Figure		Page
2.42	Effective breadth in infinitely large T-beams, after Chwalla [Brendel (15)]	92
2.43	Simple supported box girder [Lamas (42)]	92
2.44	Maximum effective breadth ratio [Lamas (42)].	96
2.45	Wide flange beam collapse modes [Lamas (42)].	96
2.46	Effective breadth for different flange/thickness ratios [Lamas (42)]	96
2.47	T-beam participation in different regions [Joglekar (37)]	99
2.48	Comparison between cyclic and monotonic skeleton curves	102
2.49	Typical torsion hysteresis loops [Jakobsen (33)]	102
2.50	Development of secant stiffness [Jakobsen (33)]	104
2.51	Energy dissipation history [Jakobsen (33)] ..	104
2.52	History of equivalent viscous damping, ξ [Jakobsen (33)]	104
2.53	Transverse beam torsional response [Joglekar (37)]	106
2.54	Improved interior joint details	106
2.55	Design process in a modern code [Bosshard (14)]	108
3.1	Full-scale seven-story building	124

LIST OF FIGURES (continued)

Figure		Page
3.2	Building geometric characteristics	124
3.3	Building cross section details	126
3.4	Displacement transducer location	132
3.5	Building beam end rotation measurements	133
3.6	Building instrumented joint regions at level Z2	133
3.7	Strain gauge locations in the Level Z2 joint regions	135
3.8	Strain gauges in slab bars (Level Z2)	138
3.9	Component locations in the frame	139
3.10	Japanese half-scale interior tests	140
3.11	Japanese half-scale exterior tests	141
3.12	Japanese half scale exterior tests	141
3.13	Steel properties in half-scale tests	143
3.14	Cross section details	143
3.15	Component loading program	143
3.16	Loading apparatus for Japanese tests	145
3.17	Displacement transducers in half-scale tests.	145
3.18	Strain gauge locations in I-series tests	146
3.19	Beam strain gauge identification	146

LIST OF FIGURES (continued)

Figure		Page
3.20	UTA component geometry	149
3.21	UTA tests reinforcement details	151
3.22	UTA - USJ-4 - Exterior modified joint detail.	155
3.23	UTA loading apparatus	155
3.24	UTA support conditions	157
3.25	UTA - Interior component load cells	159
3.26	USJ-1,3 - Displacement transducers	159
3.27	USJ-1,3 - Beam rotation and twist	159
3.28	UTA - Joint panel distortion	160
3.29	USJ-1,3 - Bar slippage detail	160
3.30	Interior component beam strain gauges	162
3.31	Interior joint region strain gauges	163
3.32	UTA interior component slab strain gauges ...	163
3.33	Exterior test load cell	165
3.34	USJ-2,4 - Displacement transducers	165
3.35	Exterior test beam rotation	165
3.36	USJ-2,4 - Bar slippage	165
3.37	UTA Exterior Test Beam Strain Gauges	166
3.38	UTA Exterior Test Slab Strain Gauges	166

LIST OF FIGURES (continued)

Figure		Page
3.39	Stanford University Tests	167
3.40	Material stress-strain curves	167
3.41	Stanford Univ. test setup	172
3.42	Exterior joint instrumentation	172
3.43	Interior joint instrumentation	172
3.44	UCB 1:5 model	174
3.45	UCB model instrumentation	174
3.46	Wall participation in the total structure ...	174
3.47	Outrigging effect on Shearwall-Frame System, [Aktan et al. (3)]	178
3.48	PCA medium-scale tests	180
3.49	University of Illinois small-scale tests	180
4.1	BRI building and component tests	189
4.2	Column moment variation in ductile frames under lateral loads [Paulay (3)]	190
4.3	Equivalent drift assumption	191
4.4	Equivalent drift for different tests	192
4.5	BRI building - load-deformation response	194
4.6	Story shear and horizontal joint shear force.	198
4.7	Variable axial column load exterior test [Inada and Kurose (1)]	201

LIST OF FIGURES (continued)

Figure		Page
5.1	Interior joint region resisting elements	204
5.2	Spatial load-deflection planes and hysteretic response	204
5.3	BRI Building - cracking patterns (end of PSD 4)	207
5.4	Cracking patterns in exterior tests	213
5.5	Cracking patterns in building and exterior tests	215
5.6	Cracking patterns in interior tests	219
5.7	Cracking Patterns in Building and Components.	221
5.8	Cracking Around Load Point	224
5.9	Japanese Tests - Slab Effect [Nakata et al. (3)]	224
5.10	BRI Building Load - Deflection Response	226
5.11	BRI Building - Total Base Shear vs. Roof Displacement	227
5.12	BRI Building - Enlarged Response at Level Z2.	227
5.13	BRI Building - Peak Secant Stiffness History.	228
5.14	BRI Building Response at Peak Displacements .	230
5.15	UTA and SU Exterior Components	231
5.16	Japanese Exterior Tests with a Slab	232
5.17	Japanes and SU Tests without a Slab	233

LIST OF FIGURES (continued)

Figure		Page
5.18	UTA - Story Shear Secant Stiffness History ..	236
5.19	SU - Story Shear Secant Stiffness History ...	237
5.20	Japanese Tests - Story Shear Secant Stiffness History	238
5.21	Exterior Components - Story Shear Secant Stiffness History	239
5.22	UTA and SU Interior Prototype Response	241
5.23	Japanese Interior Prototype Response	242
5.24	Japanese and SU Interior Joints without a Slab	243
5.25	UTA - Interior Joint Secant Stiffness History	246
5.26	SU - Interior Joint Secant Stiffness History.	247
5.27	Japanese Interior Joints Stiffness Degradation	249
5.28	Interior Tests Peak Secant Stiffness History.	250
5.29	UTA - Modified Tests Response	251
6.1	Exterior Joint Longitudinal Beam Rotation ...	258
6.2	Exterior Joint Longitudinal Beam Rotation History	259
6.3	Span 6.0 m - Interior Joint Beam Rotation Near Column Face	261
6.4	Span 5.0 m - Interior Joint Beam Rotation Near Column Face	262

LIST OF FIGURES (continued)

Figure		Page
6.5	Interior Joint Beam Rotation (enlarged scale plot)	263
6.6	UTA - Longitudinal Beam Rotation	264
6.7	SU Longitudinal Beam Rotation	265
6.8	Exterior Prototype Tests Beam Strength	267
6.9	Other Exterior Tests Beam Strength	268
6.10	Interior Tests West Beam Strength	270
6.11	Interior Tests East Beam Strength	271
6.12	UTA Exterior Tests Beam Stiffness Degradation	274
6.13	SU Exterior Tests Beam Stiffness Degradation.	275
6.14	Beam Stiffness Degradation in Japanese Tests with a Slab	276
6.15	Beam Stiffness Degradation in Japanese Tests without a Slab	277
6.16	First Peak Drift Stiffness Response in Japanese Exterior Tests	277
6.17	Exterior Tests - Beam Secant Stiffness at First Peak Drifts	279
6.18	UTA - USJ-1 - Beam Secant Stiffness	280
6.19	UTA - USJ-3 - Beam Secant Stiffness	281
6.20	SU - IS - Beam Secant Stiffness	283
6.21	SU - IJ - Beam Secant Stiffness	284

LIST OF FIGURES (continued)

Figure		Page
6.22	Interior Test (W-beam) Secant Stiffness	286
6.23	Interior Test (E-beam) Secant Stiffness	287
6.24	UTA Beam Secant Stiffness Response at First Peak Drifts	288
6.25	SU Beam Secant Stiffness Response at First Peak Drifts	289
6.26	Exterior joint - top and bottom beam bars (BRI)	291
6.27	Interior joint - tip and bottom beam bars (BRI)	291
6.28	UTA - Exterior Test Beam Bar Strains	293
6.29	UTA - Interior Test Beam Bar Strains	294
6.30	UTA Longitudinal Beam Top Bar Slip	296
6.31	Equivalent Drift Histories	298
6.32	Exterior Joint Slab Steel Yielding	299
6.33	Exterior Joint Slab Steel Yielding (enlarged)	300
6.34	Japanese Exterior Test Slab Strains	302
6.35	UTA - USJ-4 - Exterior Test Slab Strains	304
6.36	Interior Tests Slab Yielding	305
6.37	Interior Tests Slab Yielding (enlarged plot).	306
6.38	Japanese Interior Tests Slab Strains	307

LIST OF FIGURES (continued)

Figure		Page
6.39	UTA - USJ-3 - Interior Test Slab Strains	309
6.40	Design Code Effective Slab Width	310
6.41	Component Tests Effective Slab Width Ratio ..	311
6.42	BRI Building - Exterior Joint Column Bars Strains	314
6.43	UTA - Exterior Tests Column and Core Bar Strains	316
6.44	BRI Building - Interior Test Column Bar Strains	317
6.45	UTA - Interior Tests Column and Core Bar Strains	318
6.46	UTA Tests Joint Core Distortion	320
6.47	BRI Building - Interior Joint Beam Rotation History	322
6.48	BRI Building - Transverse Beam Rotation	324
6.49	BRI Building - Exterior Joint Beam Rotation History	324
6.50	BRI Building - Beam Rotation at Level Z2	325
6.51	UTA Exterior Tests Beam Twist History	327
6.52	UTA Interior Tests Beam Twist History	328
6.53	UTA Prototype Transverse Beam Response at First Peak Drifts	329
6.54	UTA Modified Transverse Beam Response at First Peak Drifts	330

LIST OF FIGURES (continued)

Figure		Page
6.55	UTA Tests Transverse Beam Twist Response at First Peak Drifts	333
6.56	Approximate Transverse Beam Secant Stiffness.	334
6.57	UTA Transverse Beam secant Stiffness History.	335
6.59	Transverse Beam Secant Stiffness at First Peak Drifts	336
6.60	BRI Building Transverse Slab Yielding in Level Z2	338
6.61	BRI Building - Transverse Slab Yielding in Level Z2	339
6.62	UTA - USJ-2 - Transverse Beam Strains	341
6.63	UTA - USJ-4 - Transverse Beam Strains	342
6.64	UTA - USJ-1 - Transverse Beam Strains	343
6.65	UTA - USJ-3 - Transverse Beam Strains	344
7.1	Earthquake Magnitude Interpretation	350
7.2	Building Seismic Excitation	352
7.3	Bar Element	352
7.4	Energy Expenditure in Bank of New Zealand Building	355
7.5	Interior Component Potential Plastic Hinge Locations	355
7.6	Component Deformation Mechanisms	357
7.7	Hysteresis Cycles at Different Response Stages	357
7.8	Beam Tip Inputed Energy	359

LIST OF FIGURES (continued)

Figure		Page
7.9	Beam Flexural Deformation	359
7.10	Joint Core Participation in Interior Test ...	362
7.11	Panel Orientation fo K_t	364
7.12	Space Truss Model for Torsion	367
7.13	Energy Dissipation and Equivalent Viscous Damping	370
7.14	T-Beam Effect in Component Response	372
7.15	Hysteretic Modelling in RC Systems, after Umemura and Takizawa (17)	374
7.16	Hysteretic Response in a Symmetric Section ..	376
7.17	Exterior Tests - Total Inputed Energy	377
7.18	Exterior Tests - Beam Dissipated Energy	379
7.19	Interior Tests - Beam Inputed Energy	381
7.20	Interior Tests - Total Inputed Energy	382
7.21	Interior Tests - Beam Dissipated Energy	384
7.22	Interior Tests - Total Dissipated Energy	385
7.23	Input vs. Interior Beam Dissipated Energy	387
7.24	Input vs. Exterior Beam Dissipated Energy	387
7.25	UTA - Net Twist History	389
7.26	UTA - New Twist at First Peak Drifts	391
7.27	UTA - Total Component Dissipated Energy	393
7.28	BRI Building - Hysteretic Damping History	396

LIST OF FIGURES (continued)

Figure		Page
7.29	BRI Building - Hysteretic Damping at First Peak Displacements	397
7.30	USJ-2 - Exterior Test Damping History	399
7.31	USJ-4 - Exterior Test Damping History	400
7.32	ES - Exterior Test Damping History	402
7.33	E-1, E-2 - Exterior Tests Damping Histories ..	403
7.34	USF-1 - Interior Test Damping History	405
7.35	USJ-3 - Interior Test Damping History	406
7.36	SU-IS - Interior Test Damping History	408
7.37	I-1, I-2 - Interior Test Damping History	409
7.38	EJ - Exterior Test Damping History	410
7.39	IJ - Interior Test Damping History	411
7.40	E-3, I-3 Japanese Tests Damping History	413
7.41	US - Exterior Tests Damping at Peak Drifts ..	415
7.42	Japanese Exterior Tests Damping at Peak Drifts	416
7.43	Exterior Prototype Tests Damping	418
7.44	Other Exterior Tests Damping	419
7.45	US Interior Tests Damping Ratio	421
7.46	Japanese Interior Tests Damping Ratio	423
7.47	Interior Prototype Tests Damping Ratio	424
7.48	Other Interior Tests Damping Ratio	425

LIST OF FIGURES (continued)

Figure		Page
7.49	US West Beam Exterior Tests Damping	427
7.50	Japanese West Beam Exterior Tests Damping	428
7.51	Exterior Prototype West Beam Damping	429
7.52	Other Exterior Tests West Beam Damping	430
7.53	US Interior Tests West Beam Dumping	432
7.54	US Interior Tests East Beam Dumping	433
7.55	West Beam Damping in Interior Prototypes	435
7.56	East Beam Damping in Interior Prototypes	436
7.57	West Beam Damping in Other Interior Tests	437
7.58	East Beam Damping in Other Interior Tests	438
8.1	Joint Shear Stress Area	446
8.2	Component Test Joint Shear Stress	446
8.3	Joint Shear Stress - Kamimura Equation	449
8.4	UTA Exterior Joint Shear Stress	452
8.5	UTA Interior Joint Shear Stress	454
8.6	Gross Area Exterior Joint Multiplier	456
8.7	Gross Area Interior Joint Multiplier	457
8.8	Reduced Area Exterior Joint Multiplier	459
8.9	Reduced Area Interior Joint Multiplier	460
8.10	Column Ratio vs. Top Beam Bar Sizes	464
8.11	Interior Joint Bond Index Ratio	466

LIST OF FIGURES (continued)

Figure		Page
8.12	EHD vs. Beam Bar Bond Index Ratio	466
8.13	US Interior Tests Bond Index Ratio Response ...	468
8.14	BRI Building at the End of Test PSD-4	471
8.15	BRI Building Experimental Member Rotation	473
8.16	First Floor Shear Wall Deformation	475
8.18	Effective Slab Width	477
8.19	Shear Wall Moment Curvature	479
8.20	Column Moment Curvature	480
8.21	Longitudinal Beam Moment Curvature	481
8.22	Transverse Beam Moment Curvature	482
8.23	Shear Wall Interaction Diagram	484
8.24	Gravity Loads in Vertical Members	485
8.25	Plastic Hinge in Cantilever Wall	485
8.26	End Wall Restraint	490
8.27	Failure Mechanism Considering the Whole Slab Width a Effective	490

CHAPTER I
INTRODUCTION

1.1 General

Analytical methods used to evaluate the inelastic response of reinforced concrete structures under reversed cyclic loads are difficult to apply when large deformation levels are considered. Experimental results are needed to solve complex problems and to test newly devised analytical methods. Experimental methods often are considered to be too expensive and time consuming but they provide the cornerstone for the scientific process, i.e. verification of the formulated hypothesis. Testing programs are used in fundamental structural research to: (1) verify and target current design code criteria; (2) test analytical models proposed for materials, elements, components, and other structural systems under different response conditions; (3) investigate possible critical loading conditions derived from unevenly occurring events (cyclonic winds, earthquakes, waves); and, (4) perform parametric studies on one or more particular aspects of response.

The occurrence of severe events such as the Japanese 1968 Tokachi-Okii and the California 1971 San Fernando earthquakes alerted the general public and the authorities to the urgent problem of achieving safe and sound structural design in

important facilities (schools, hospitals). The multitude of problems and questions raised by the 1968 and 1971 earthquakes led to the development of a US-Japan Cooperative Program where structural design problems were reviewed in joint seminars. The US-Japan Cooperative Research Program on Earthquake Engineering with Emphasis on the Safety of School Buildings started in 1973. By the end of 1975, Japanese and US investigators reached an agreement towards the organization and implementation of a research program involving large-scale testing. In 1977, the US-Japan Cooperative Research Program Utilizing Large-Scale Testing Facilities was initiated.

1.2 Cooperative Research Program

The main objectives of the US-Japan Cooperative Earthquake Research Program were: (1) to improve the scientific knowledge and engineering practices adopted in the design of seismic-resistant structures in both countries; (2) to correlate test results from components, shaking-table, and small-to-medium scale experiments with the behavior of a prototype, full-scale structure subjected to severe loadings; and, (3) to design, build, and test a full-scale 7-story reinforced concrete building structure in Japan and compare its response with supporting tests to be carried out both in the US and Japan.

These experiments were devised to provide information on force-deformation relationships, energy absorption/dissipation response, cracking patterns, spread of yielding, and identification of resisting mechanisms and their participation in the damage/failure modes.

The information gathered on the component tests with similar boundary and loading constraints to the real structure was used to evaluate: (1) the full-scale prototype vs. component tests response; (2) the reliability and applicability of detailing requirements in US and Japanese Design Codes; and, (3) the feasibility and limitations of reduced scale model tests for determining structural response.

1.3 Objective of this Study

As stated in the previous section, the ultimate objective of the US-Japan Cooperative Research Program was to compare the response of the full-scale Building Research Institute (BRI) building critical regions with the supporting tests to be carried out both in the US and Japan.

The BRI structure was built in 1980 and tested in 1981. The first floor (Level Z2) was thoroughly instrumented with strain gauges and displacement transducers. Two exterior joints and two interior joints were instrumented for beam rotations. The strain gauges were placed on four exterior joint and four

interior joint regions. The slab rebars were instrumented at Level Z2 along the interior and exterior frame boundaries, as well as along two transverse frame directions. There were over 1200 data points recorded per channel and there were about 200 channels of data at Level Z2.

The BRI beam-column component test data was not readily available and the load-deformation response was digitized based on the available reports. The load-deformation files included 75 to 120 data points per specimen.

The four University of Texas at Austin component tests were performed from July 1981 (USJ-1) until February 1983 (USJ-4). Much of the recorded data was discarded and not analyzed before this work was initiated. However, through the efforts of researchers in the Department of Astronomy at The University of Texas at Austin and the author's skill and endeavor, a computer program was developed, all the available information retrieved and carefully interpreted over approximately a one-year period. For each specimen nearly 125 channels of data were recorded with 400 to 700 data points. All recovered data is reported in Appendix B.

The Stanford University models consisted of four beam-column joints tested during 1982-83. In the two exterior tests, 5 to 6 channels of information with 7,800 to 11,200 data points

were analyzed. In the interior tests, 13 to 17 channels of information with 7,800 to 8,400 data points were recorded.

Most of this information has been reported throughout the Cooperative Program through technical presentations and individual project reports and articles. However, no in-depth evaluation or correlation studies of the response of the BRI building critical regions and the components have been reported. The objective of this study was to unify the information so that comparisons could be made using common units from which the response of the various components could be interpreted and design recommendations examined or proposed.

1.4 Structure of this Report

Design codes are revised on a regular basis to reflect results from previous research and from damage observations following earthquakes or other events leading to failures or inadequate performance. However, different solutions may be obtained using different codes or design recommendations. Such differences lead to doubts in the designer's mind about the validity of the proposed rules. For the design of structures in earthquake zones, it is recognized that a performance criteria stated explicitly or included implicitly, underlies the Code and links the structural system strength/stiffness with energy absorption/dissipation characteristics (ductility).

Although the idea of inelastic response is not new, the designer may not always associate design requirements with ductility demands. One of the eminent structural designers to recognize the limitations of the Theory of Structures was the Italian engineer Pier Luigi Nervi in his book, "Construire Correttamente" (Hoepli Ed., Bologna 1955) where he stated:

"The fundamental assumption of the Theory of Structures is that structural materials are isotropic and perfectly elastic. But the most commonly used materials are far from being isotropic and elastic.

Theory of Structures considers our buildings as being out of time, in a kind of eternal stability and invariability. But the simple and commonplace fact is that all structures decay and, after shorter or longer periods of time, become unstable or at least show excessive displacements and amounts of damage. Thus, this second assumption is also unrealistic.

No soil is perfectly stable nor settles uniformly as time goes by. All building materials, and particularly masonry and concrete, flow viscously. The daily and seasonal temperature variations are irregularly distributed in the structure and, because of prevented displacements, create stresses of unforeseeable magnitude and direction. Cements and limes keep hardening for decades and even centuries. All materials are slowly being transformed. Every building has a physical and chemical inner life whose existence is clearly shown by the sudden failures of even very old structures. In other words, the theory of structures may be compared to the physiology of perfect organisms, which are permanently youthful and untouched by disease or functional deficiencies. This kind of physiology is certainly indispensable in a school of medicine, but such a school would graduate very poor doctors if it did not take into account the difference between this ideal conception and physiological reality."

The approach followed in this report was to study structural response from a traditional approach (load-deflection, bar strains, cracking) and a more realistic view where the reversed cyclic loading effects are recognized. This reversed cyclic loading assessment includes strength/stiffness envelope evaluations under increased deflections, the energy absorption/dissipation progression with the computation of hysteretic damping ratios, bond deterioration, and ultimate capacity analysis.

The earthquake mechanism is a process where large amounts of stored strain energy are released over a short time interval. Therefore, the energy evaluation provides fertile data for the design/research team.

This report is organized into eight main chapters as follows: (a) Chapter II - a literature survey was done to place into perspective the US-Japan Joint Research Program in current earthquake reinforced concrete design practice. The importance of the beam-column-slab connection in moment resisting frames is emphasized. The active role of the slab in component and frame response are also discussed; (b) Chapter III - the different test components used both in US and Japan and the full-scale BRI building are described. Reinforcement details and materials properties are provided for the different specimens; (c) Chapter IV - the recognition of different response stages under

increased deformation levels is developed using a common parameter for comparison of all tests - the equivalent drift ratio; (d) Chapter V - the complete specimen response based on the available loads, and deformations is provided with identification of possible sources of distress and failure mechanisms. Deterioration of specimen response throughout the loading program and at selected deformation peaks is shown; (e) Chapter VI - localized aspects of response in the different critical region components are described for the longitudinal beam, transverse beam, slab and joint core region. Particular emphasis is given to the role of the slab in the overall resisting mechanism; (f) Chapter VII - the important features of energy dissipation in the BRI building and component tests are studied. Ductility is assessed in the tests using a hysteretic damping ratio. The energy dissipated by a major resisting element - the longitudinal beam - is studied. Sources of energy dissipation that may pass unnoticed, e.g., the joint core region, are clearly identified; (g) Chapter VIII - the ultimate capacity of the BRI building is evaluated at a selected drift level. In addition, test results are important variables examined against current design code recommendations for joint shear constant, and limiting bar diameter to joint dimension ratio; and (h) Chapter IX - conclusions and design recommendations are developed.

C H A P T E R I I

CURRENT CONCEPTS IN FRAME SEISMIC DESIGN

2.1 Introduction

The information gathered on some recent devastating earthquakes, e.g., 1968 Caracas, 1971 San Fernando, 1972 Managua, 1976 Tangshan, has shown that well-detailed and carefully built reinforced concrete (R/C) structural systems performed well under severe conditions.

Among this general group of R/C structural systems there is a particular one that has been the focus of attention in Earthquake Resistant Design because of the many advantages it offers - the Ductile Moment Resisting Frame (DMRF). Unfortunately, some "modern" DMRF systems have performed poorly under severe conditions. As an example, the Olive Mountain View Hospital - a high importance level facility - was the scenario of some dramatic structural and non-structural failures during the 1971 San Fernando, California earthquake, [Housner and Jennings (32)].

Poor performance of DMRF can be attributed to a multitude of reasons such as: (1) ill-conceived detailing of reinforcement detailing; (2) lack of data and test results on DMRF behavior; (3) lack of knowledge on soil-structure interaction; (4) the traditional designer's routine in devoting

much of his attention to frame members (columns, slabs, beams, footings) and by neglecting the frame critical regions in the large lateral displacements. One of the most important critical regions is the connection where the beam, column and slab join. The extensive damage observed in this type of structures has shown the importance of ductile vs. brittle structural behavior under large drifts. The beam-column-slab connection must perform without brittle failure or excessive loss of stiffness throughout large inelastic deformations of the structure. In addition, local loss of stiffness and failure must be examined in the light of the overall response of the structure. Some of the dramatic failures observed in previous earthquakes has spurred research programs (mainly in those countries afflicted by the problem e.g., U.S.A., New Zealand, Japan, China, U.S.S.R.) with strong emphasis on improving existing R/C structural systems and developing new ones.

Research programs have been carried on during the past two decades to study the behavior of frame components under reversed cyclic loads. The main categories of investigations reported are [Jirsa (34)]: (1) studies of material properties; (2) isolation of one aspect of member response; (3) behavior of frame subassemblages consisting of multiple members and the connections between them; and, (4) studies of complete structures.

The current trend followed in research programs is not directed to the "gestalt" DMRF rather, by studying the response of frame components or subassemblages, there is a generalized concern about the validity of these results as compared to an actual full-scale structure. Many R/C structures have been designed using procedures based on reported results of subassemblage tests. However, there is always a question in the designer's mind about the assumptions and extrapolations made vis a vis the actual engineered structure. Considerable ingenuity and compromise is needed to accomplish a safe, reliable design by today's standards.

2.2 The Current Design Approach

2.2.1 Initial Comments. The design of any type of structure involves a structural safety process, involving equilibrium between the applied forces - actions and the response within the body continuum - reactions is involved. The applied loads create stresses and strains in the structure. They may result from the direct action of imposed generalized forces or displacements, and from indirect actions due to restraint of deformations.

In structural design the most important factors to be taken into account are: (1) the definition of applied loads; (2) the properties of the materials; and (3) the choice of a

suitable structural system. However, the ultimate objective is to achieve an optimum design, where the total capitalized cost of the structure is minimized, including initial cost, maintenance costs and insurance against failure [von Neumann and Morgenstern (54)].

2.2.2 The Definition of Loads. Numerically, two types of loads are usually considered: (1) dead loads and, (2) live loads. Whereas dead loads are usually well defined the same cannot be said about live loads due to natural actions or intentionally developed by the use of structure. The broad group of live loads encompasses wind forces, wave forces, occupancy loads in buildings, bridge loads and earthquake loads. The amount of data on earthquake loads is scarce due to the self nature of the phenomena and it has been studied more extensively during recent years. Earthquake motion computer simulation has been used initially by considering a stationary random process and, lately, as a non-stationary random process. Bayesian Probability Theory has also been used to predict the probability of earthquake occurrence based on the available historical records.

In reality, many structures experience some type of dynamic loads and this structural response is given in the form of time-dependent dynamic generalized displacements and generalized forces. To find the response of the structure under dynamic loading, the designer is left with two possible

approaches [Clough and Penzien (21)]: (1) Deterministic - the time variation of the load is completely known, even if it is highly irregular, the loading can be dynamically prescribed; and (2) Probabilistic - the load is considered as a random function of time, and it can only be described in a statistical sense, e.g., by a stochastic (random) process.

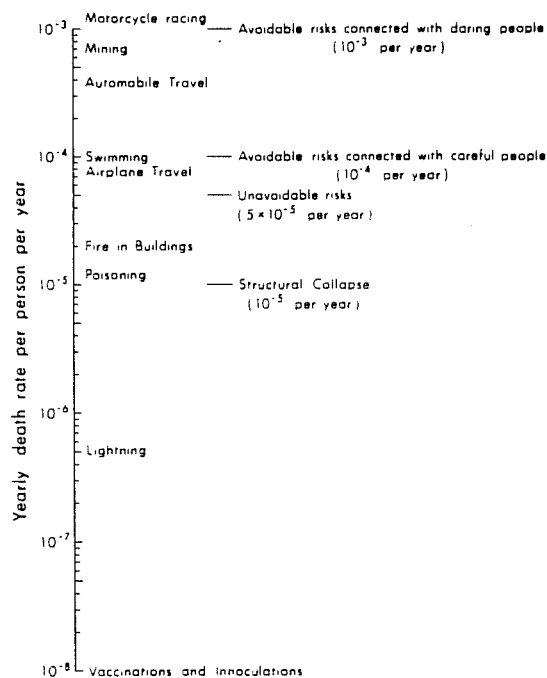
Usually displacements are the recorded variables of the dynamic response of the structure. If the deterministic approach is followed, the prescribed load history is then used to get the displacement history directly. With the displacement computed, stresses, strains, shears and moments can be found. Alternatively, if the probabilistic approach is used, displacements are statistical in nature, and probabilistic analysis must be used to evaluate the stress and strain distributions, [Clough and Penzien (21)]. Consequently, depending on the type of materials and structure chosen by the designer, two types of responses can be obtained under a random vibration excitation. The first one may use the principle of superposition of effects of forces if the dynamic behavior of the structural system is considered linear, elastic, and time invariant. The second one considers a non-linear structure under a random vibrating load and a frequency domain analysis with numerical integration is used. However, it is a cumbersome process and the usual approach is by

an equivalent linearization procedure that may not account for the non-linear aspects of the problem.

2.2.3 The Total Reliability of Structural Systems. All human activities are performed with risks and structural design is no exception, Fig. 2.1 [MacGregor (46)]. During the life of a structure different types of hazards can trigger failure [Bosshard (14)]: (1) Man-made hazards - errors in the planning, design, construction phases, overloads, fire, vehicular collisions, fatigue, deterioration due to lack of maintenance; (2) Natural hazards - wind, earthquake, snow, landslides. These hazards can be handled by: (1) avoiding them - with changes in overall design or structure location; (2) controlled - with adequate planned measures; (3) overpowered - with provisions in structural design and robustness; and (d) accepted as inevitable.

The probability of failure is currently evaluated based on assumed distribution functions of resistance, R and load, S . However, it is very sensitive to the fit of these distributions and an adjustable design safety factor concept was developed [MacGregor (46)].

Structural design is achieved by creating a balance between human safety, serviceability requirements and economic considerations. The current procedure of assessing safety is to evaluate the rates of failure of actual structures under use, but they are difficult to define as they depend upon different vari-



a. Risks of Death For Various Activities.

Activity	Yearly death rate per person per year	
	For those concerned	For the total population
Motorcycle racing	5×10^{-4}	
Mountain climbing	5×10^{-3}	
Mining	7×10^{-4}	
Swimming	1×10^{-4}	2×10^{-5}
Automobile travel		3.6×10^{-4}
Airplane travel	1×10^{-4}	
Fire in buildings		2×10^{-5}
Poisoning		1.1×10^{-5}
Lightning		5×10^{-7}
Vaccinations and innoculations		1×10^{-8}
Structural collapse		
During construction	3×10^{-5}	
All others		2×10^{-7}

*Data from Allen (1968), Otway *et al.* (1970), and Rüsck and Rackwitz (1972).

b. Estimated Involved Risks.

Fig. 2.1 - Risks of Death of Various Activities, [MacGregor (46)].

ables: (1) workmanship; (2) competent structural engineering; and, (3) the use of safety and serviceability criteria in design computations, [Allen (3)]. A safety index, β , has been developed and it is very useful when comparing design rules for different load combinations, materials, types of failure.

On the other hand, the importance of gross errors, mostly human errors in structural design, should be noted. The design factors for loads and resistances, ϕ -factor [ACI Code (2)], γ -factor [CEB-FiP Model Code (19)], are adjusted to take such errors into account.

The usual models of structural behavior studied are: (1) Weakest link - usually found in isostatic systems; (2) Alternate load paths such as hyperstatic systems with both brittle and/or ductile elements; and, (3) Fail-safe - collapse-type of design.

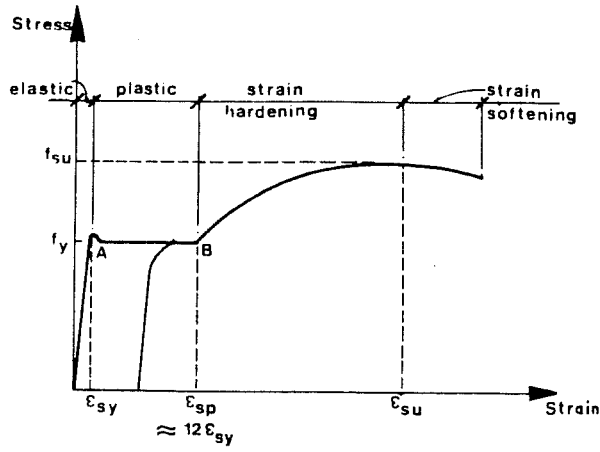
In most cases the simple concept of one-strength and one-load (R-S) random variable is used in reliability analysis. In hyperstatic systems complex models are more suitable to study the structure with its multi-load random variables and multi-operational failure modes.

In isostatic or hyperstatic systems with brittle elements a weakest-link type behavior is usually found where the failure of a single element can trigger a chain-failure reaction. The presence of ductile elements in the structural system allows

an easier approach with a collapse-type formulation than with the alternate load path method where following all the possible failure paths may become extremely cumbersome.

The collapse formulation or limit failure of structural systems is complex and approximate solutions were developed similar to the ones to be found in limit or plastic analysis.

2.2.4 Working Stress Method vs. Ultimate Strength Design. Although the early developments of R/C theories were based on ultimate strength analysis (such as Ritter - Parabolic Stress Distribution Theory (1899)), the elastic theory based on admissible (working) stresses became preponderant because it was common practice with other types of construction materials (masonry, iron, steel). With carefully chosen admissible stresses it was possible to obtain satisfactory performance under service load conditions as well as acceptable safety margins against collapse. Using the Working Stress Method (W.S.M.) a predetermined safety factor cannot be imposed in the design of a structural member because stress values are used to proportion cross sections under service conditions, assuming that the structure remains elastic. Actually, it is known that steel reinforcement behaves elastically only in a limited strain range ($\epsilon_{\text{elast}} \approx 0.002$) and concrete behaves inelastically even at low stresses, Figs. 2.2(a) and (b). On the other hand, most



\overline{OA} = Elastic zone,
 $\epsilon_{sy} \approx 0.1-0.2\%$

\overline{AB} = Yield plateau,
 $\epsilon_{sp} \approx 10-20 \epsilon_{sy}$

\overline{BC} = Strain hardening,
 $\epsilon_{su} \approx 8-10 \epsilon_{sp}$

a. Mild Steel Uniaxial Test Response, [Dowrick (25)].

b. Uniaxial Concrete Test Response, [Park & Paulay (60)].

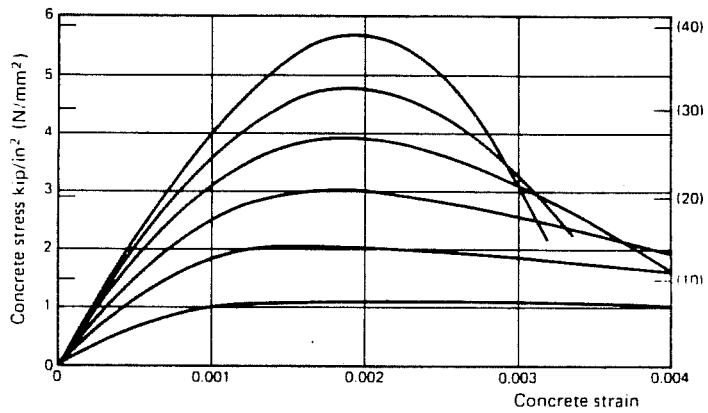


Fig. 2.2 - RC Materials Response.

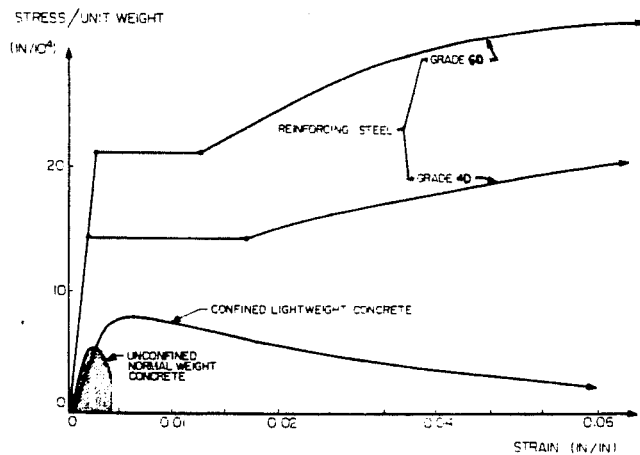


Fig. 2.3 - RC Material Stress/Unit Weight vs. Strain Response, [Bertero & Bresler (9)].

structures are built hyperstatically, in which case force redistribution can be observed and advantageously used. In R/C structures inelastic deformation is possible if minimum confinement requirements are met. These facts were long ago intuitively perceived by structural engineers by considering that the load carrying capacity of a ductile-type structure is not exhausted as long as the distribution of internal stresses can be found in equilibrium with the external loads and without exceeding the yield limit anywhere along the structure. Consequently, by the W.S.M., few structures would survive to extreme load conditions because failure would arise as soon as the yielding limit would occur at any point of the structure, [Koiter (40)]. Although inelastic structural behavior was recognized long ago, the first collapse theorem was clearly stated only 70 years ago by Kazinczy (1914) and independently by Kist (1917) [Koiter (40)]. The elastoplastic behavior of R/C is more extensively analyzed with the pioneering work of Loleit, Steuermann and Gvozdev (URSS 1933-36), Jensen and Evans (USA 1943), Saliger and Gebner (Austria 1947) in the Ultimate Design Method. With this method, the sections in the members of the structures are designed using the inelastic stress-strain relationships for the materials (assuming that concrete is at maximum (ultimate) strength and steel is yielding) when an ultimate load (resultant of the product of service loads by load

factors) is applied to the structure. Linear-elastic behavior is assumed in computing the generalized resisting forces in the members of the hyperstatic structure, but some redistribution is allowed in order to account for the inelastic behavior near ultimate. The ultimate strength theories advantageously use the following aspects [Park and Paulay (60)]: (1) inelastic behavior of R/C section at higher load stages - concrete shows a non-linear stress-strain curve at any instant of deformation and time dependent (creep strains) behavior allows stress redistribution; (2) economic benefits which may arise with the best use of high-strength steels and other types of concrete (high-strength, lightweight); and, (3) ductility of the structure within the inelastic range - its full use can be made when designing for dynamic-type loads.

2.2.5 The Limit States Design Method in Earthquake Design. The Ultimate Strength Method led to the development of the Limit States Design Method because of cracking and excessive deflections observed in structures designed with the former method.

A Limit State is defined as, [CEB-FIP (19)]:

"A structure, or a part of a structure, is considered to become unfit for its intended purpose when it reaches a particular state, called limit state, in which one of the criteria relating to its load bearing capacity or its conditions of service is infringed."

The Limit States can be divided into two categories: (1) ultimate Limit States - which correspond to the maximum load-bearing capacity of the structure; loss of static equilibrium, resistance; instability; fatigue and resonance; and, (2) serviceability Limit States - control of excessive cracking, deformation, vibration.

Based on this design philosophy design codes for concrete practice have been implemented in different countries. Although design codes try to cover extensively all possible situations, only recently have particular sections with recommendations for earthquake design been implemented as guidelines. This may derive from the lack of knowledge in this new area of study, from the scarcity of meaningful test data, and from a missing guideline in the Limit States Design Method for Earthquake Design.

Based on the past experience of structures that underwent severe load conditions with real earthquakes, and from test data reported in research programs, a "Damageability Limit State" (D.L.S.) procedure has been proposed [Bertero (6, 7), Bertero and Bresler (9)]. Considering that ductility is deemed necessary for an energy absorption-dissipation mechanism within the structure, the performance may be unsatisfactory because of large permanent deformations, instability, low-cycle fatigue, degradation of stiffness and strength. It has been observed that although good

design practices have been used in modern engineered R/C structures that experienced strong ground motions, some of them had to be razed because of large permanent deformations and extensive structural and non-structural damage. Therefore, the main objective in Earthquake Structural Design is not only to build into the structure strength and ductility but also an effective control of deformations. Several deformation indices have been proposed such as, interstory drift, drift ductility factors, and tangential story drift; some of these are being incorporated into Codes of Practice - maximum allowed story drift.

The D.L.S. is a design method based on limit control of the maximum deformations (story drift) to be experienced in a structural system. The damageability criteria differentiates three general types of damage: local, global, and cumulative, [Bertero and Bresler (9)]. The proposed reformulation of the Limit State R/C earthquake design philosophy is as follows: (1) Serviceability Limit State - an acceptable and reliable method for specifying design earthquakes is used, e.g., the linear elastic design response spectra with low values of damping. It should represent earthquakes with return periods of 5 to 10 years and with maximum accelerations of 0.05 to 0.10 g. The interstory drift should be limited to $3/1000$; (2) Damageability Limit State

- some yielding occurs and higher percentage of damping, e.g. 5 to 7% is used to compute the still elastic response of the structure. Maximum ground accelerations to be used will correspond to a moderate intensity earthquake in the range of 0.15 - 0.20 g. Careful construction detailing must be enforced with the use of "non-structural" elements. Such elements can also be isolated from the structure; and, (3) Collapse Ultimate State - under maximum ground acceleration in the order of 0.40 to 0.50 g, large in-elastic deformations are likely to occur in the structure's critical regions, followed by extensive structural and non-structural damage. Non-linear methods of analysis or an approximate corrected elastic analysis should be used.

The failure mechanism for the structure must allow an "intelligent" - type of failure, i.e., the generation of a large number of plastic hinges - "energy dissipation devices" - preferably in the beams, rather than in the columns. Overall displacement ductilities in the order of $\mu(\Delta) \approx 5$ should be provided and limiting the story drifts up to 1/100 - 1/50 are necessary to control possible further development of secondary (P- Δ) effects.

2.3. The Ductile Reinforced Concrete Structural System

2.3.1 Basic Requirements in Seismic Design. In seismic design, the R/C structure must perform satisfactorily under se-

vere load conditions. A reinforced concrete structure that is designed as a ductile, monolithic and continuous structural system, with adequate energy absorption - dissipation characteristics may achieve these objectives. Structural concrete can be used to provide a flexible or a stiff structure by carefully detailing its structural components. Several factors influence the choice of a flexible vs a stiff structure [Dowrick (25)]: (1) substructure foundation requirements; (2) detailing requirements; (3) analytical facilities available; (d) contractor capabilities; and, (e) local preferences. Under earthquake loads the R/C structure must be able to sustain its load carrying capacities when it experiences large inelastic excursions. Ductility should be provided and it can be related to the structural material, the structural member, or the structure itself. Four main types of ductility can be identified [Popov (70)]: (1) Material Ductility - $\mu_{mat.}$ - (a) for monotonically applied loads is computed as a ratio of the absolute maximum strain, $\epsilon_{u_{max}}$, to the strain at yield; (2) for reversed cyclic loadings, $\epsilon_{u_{max}}$, can be defined as the maximum strain developed from the initially unstrained material, or, more correctly, as the strain from the beginning of a new cycle until it reaches its maximum. Plain concrete under rapid loadings has brittle characteristics as compared to steel reinforcement, Fig. 2.3, but ductility in concrete can be enhanced by providing carefully

detailed confinement; (2) Section Ductility $-\mu_\phi-$ (a) for monotonically loaded R/C cross sections is defined as the ratio (b) for reverse cyclic loadings, two curvature ductilities may be derived for unequally reinforced cross sections; (3) Member Ductility $-\mu_\theta-$ is obtained by integrating the cross-section ductility over a given length; (a) for monotonic loadings is computed as the ratio of $\theta_{u_{max}}$ (member ultimate rotation capacity) to θ_y (member rotation at first yield); (b) for reversed cyclic, the curvature ductility, μ_θ , can have different values in opposite directions but $\theta_{u_{max}}$ can be used as the total value for each inelastic half-cycle excursion; and, (4) Structural Ductility $-\mu_\Delta-$ it can be defined as the ratio of the ultimate maximum horizontal deflection, $\Delta_{u_{max}}$, in a given story of the structure, to the deflection at first yield, Δ_y . Although, the horizontal displacements are relevant in the response of DMRF, the value of Δ_y may be difficult to define precisely and it is usually determined by the point at which the force-displacement curve of the whole structure starts to deviate considerably from linear elastic behavior. This index gives an estimate of the overall inelastic deformation capacity.

A global relationship between all these ductility factors may be established:

$$\mu_{mat} > \mu_\phi > \mu_\theta > \mu_\Delta \quad (2.1)$$

However, it is possible in some cases that sections or members in a structure exhibit lower ductility levels than the whole structure. If the structure has available built-in ductility, allowance in the overall deformation without reduction in the level of applied forces, is very likely to occur. On the other hand, under reversed load cycles loss of stiffness and progressive structural degradation may arise if consistent bond action is not maintained. Large amounts of slip due to deficient interaction between steel and concrete are likely to occur with the consequent development of permanent member deflections and full-depth cracks along the cross section. Full depth cracking will adversely affect the mechanism of shear transfer in the member. All these factors detrimentally affect the structure's available ductility. An increase in the available member curvature ductility is possible by [Park and Paulay (60)]: (1) reducing the area of tension steel or the rebar strength; (2) increasing in the area of compression steel; (3) increasing the concrete ultimate strength; and, (d) increasing the concrete ultimate strain, if adequate lateral confinement is provided.

2.3.2 Different Types of R/C Structural Systems. It is commonly accepted that it is uneconomical to design R/C structures for the greatest possible earthquake ground motion without damage. Accepting this premise, the next logical step is to guarantee that for a major earthquake action a collapse state

is not reached, even though some extensive damage may occur. In order to assure the structural survival, ductility must be provided. A general guideline has been proposed by Park (58, 59) and Paulay (61, 62) in the "Capacity Design Philosophy":

In the capacity design of earthquake-resistant structures, elements of primary lateral load resisting systems are chosen, suitably designed and detailed for energy dissipation under severe deformations. All other structural elements are then provided with sufficient reserve strength capacity so that the chosen mechanisms for energy dissipation may function throughout the possible reversals of inelastic deformations.

Three main types of basic structural concrete systems are used in earthquake-resistant design, Fig. 2.4 (1) the Ductile Moment Resisting Frame (DMRF); (2) the Shear Wall - cantilever or coupled-type; and, (3) the Frame-Shear Wall (Dual System). These systems are identified in a 2-D plane, although actual cast in-situ R/C structures are monolithically built in a 3-D layout. Also, it is very often found that the actual built structure results from the association of two or more of the above plane systems. However, for an easier assessment of the desired failure mode, only a 2-D structural system is considered herein.

The consideration of a failure mode in a collapse or limit-type of analysis gives a good insight into the problem, as well as a more realistic portrait of the ultimate behavior of the structure.

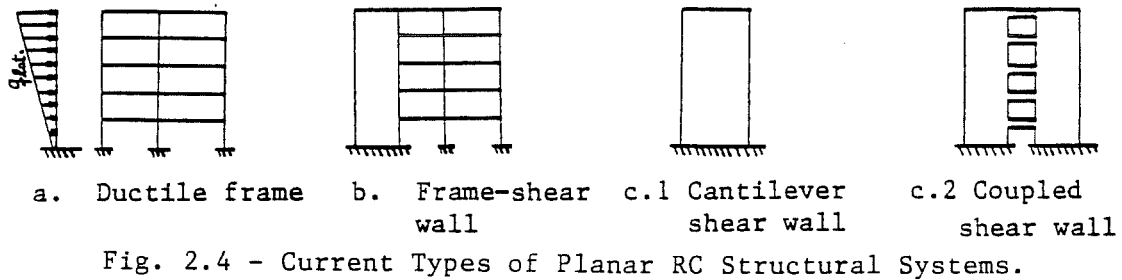
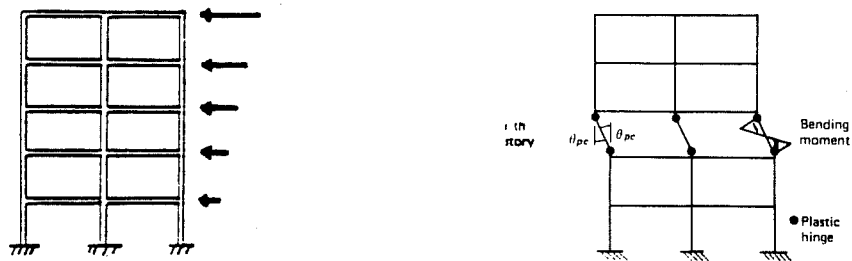
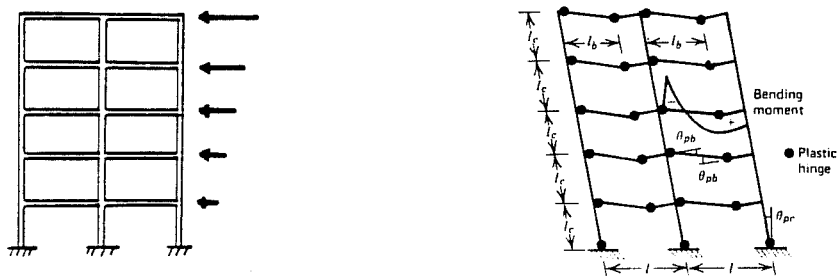


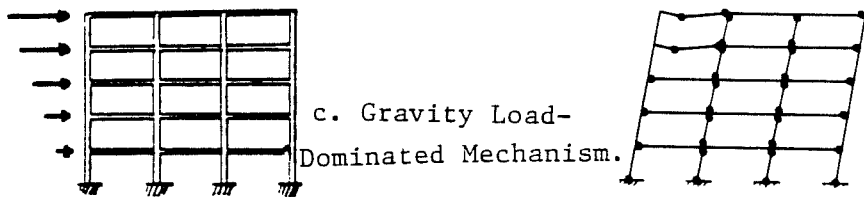
Fig. 2.4 - Current Types of Planar RC Structural Systems.



a. Column Sidesway Mechanism.



b. Beam Sidesway Mechanism.



c. Gravity Load-Dominated Mechanism.

Fig. 2.5 - DMRF Failure Modes, [Park (57) , Park & Paulay (62)].

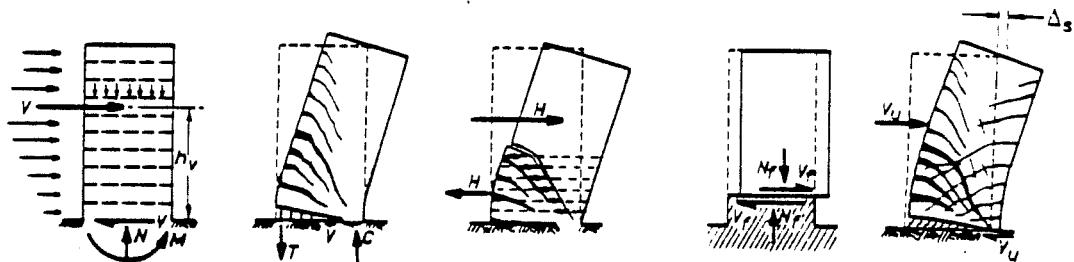


Fig. 2.6 - Cantilever Shearwall Failure Modes, [Paulay & Williams (66)].

2.3.3 The Desirable Failure Mode in a DMRF The procedure used by the DMRF to dissipate the large amounts of input seismic energy is usually done by the formation of plastic hinges throughout the overstressed regions in the frame. Although, the random formation of plastic hinges is possible, the designer has the tools to provide a controllable plastic hinge formation process. This process requires the formulation of a basic design criteria which assumes the existence of a "hierarchy" in the formation of plastic hinges, as well as a minimum level of gravity load carrying capacity, [Paulay (62)]. Three possible solutions exist in formalizing this plastic hinging hierarchy level in DMRF, by designing for: (1) Column Sidesway Mechanism - this characterized by the development of yielding at the column critical sections before the adjacent beams reach the yield curvature level, Fig. 2.5(a). This type of failure mechanism requires that all the input energy be dissipated at both ends of columns in a given story level. This is highly undesirable because large amounts of curvature ductility at the column plastic hinges in a certain frame story level are required and may be not feasible [Park (57)]; (2) Beam Sidesway Mechanism - it occurs when yielding begins at the critical sections of the beams before the columns yield, Fig. 2.5(b). This type of failure mechanism allows a more rational, uniform spreading of energy dissipation by plastic hinging, from the base

to the top of the frame. Besides, it only requires moderate ductility demands on the individual plastic hinges, [Park (57)]. As a consequence, columns should be made stronger than the beams, particularly at the beam-column connections. In a deterministic design code approach, this is done by allocating certain strength levels to these members, such as columns, that need protection from yielding, and by allowing other members, such as beams, to undergo large plastic deformations with the development of plastic hinge mechanisms [Paulay (62)]. Plastic hinges will form at the foundation level of each column, but the remaining column levels will be elastic. This type of failure mechanism may lead to serious problems with detailing in the connection region if adequate measures are not taken; and, (3) Gravity Load-dominated Frame Mechanism - it has been found that in low rise buildings with long spans and located in low to moderate risk seismic zones, gravity load controls design. Therefore, if the previously discussed beam sidesway mechanism is chosen for design, stronger columns than required may result, and, at a given interior beam-column joint, the combined flexural strength of two adjacent beams developed by the lateral sway mechanism may be in excess of that required. This later type of failure mechanism allows the interior columns to have column hinges on both sides, but the exterior columns must have some reserve strength in order

to avoid yielding while plastic hinges in the beams and in the interior columns are being developed, Fig. 2.5(c), [Paulay (62)].

2.3.4. The Desired Failure Mode in a Shear-Wall. The term shear wall is currently employed in a misleading sense because in most cases it is used in high-rise buildings where deformations and strength are mainly controlled by flexure, $H/W > 2.0$ (H =height; W =width). On the other hand, for low-rise buildings, where shear walls have an $H/W < 2.0$, the deformations and strength are mainly controlled by shear. The main objective is to obtain a ductile shear wall which shows good energy dissipation characteristics under reversed cyclic loads. If ductility and strength are not provided by careful detailing, some other less desirable failure modes may occur cantilever shear wall, Fig. 2.6, [Paulay and Williams (66)]. Different types of shear walls can be also classified by shape: (1) rectangular wall; (2) flanged wall; (c) core (tubular) wall; (d) coupled wall; (e) framed wall; and, (f) infilled frame.

2.3.5 The Frame-Shear Wall (Dual) System. The excessive lateral displacements found in some R/C D.M.R.F. that experienced severe ground motions produced extensive non-structural damage, even though the structural components performed reasonably well. A possible solution to limit these displacements is by using a stiffening element, e.g. shear wall, hybridized with the frame. It is obvious that several advantages may arise [Dowrick (25)]:

(1) reduction in lateral drift; (2) suppression of some connection detail problems; (c) insurance of uniform spreading of plastic hinges along the height of the structure; and (d) prevention of column failure in a sway mode due to the P- Δ effects. However, some problems may arise because of the distinct nature of the response of each system under lateral loads. The wall will respond mainly in flexure, whereas the frame will deflect mainly in shear (if we neglect the axial deformation in the columns is neglected). Consequently, the lower levels in this dual system will have compatible deflections and they will act together in resisting the lateral load. At the upper levels the behavior will be more likely in opposition as the deformations will become incompatible and the shear wall will be "negatively" loaded, Fig. 2.7, [Park and Paulay (60)].

2.4 The Ductile Moment Resisting Frame

2.4.1 The Search for Ductility. It has been reported that in order to achieve a successful design with a R/C structure two basic features should be input to the system: (1) ductility; (2) good energy absorption and dissipation characteristics. The quest for ductility and its enforcement into Codes of Practice has been done repeatedly over the last couple hundred years. The first recorded method of providing ductility and structural integrity into a brittle material (masonry) occurred in Portugal

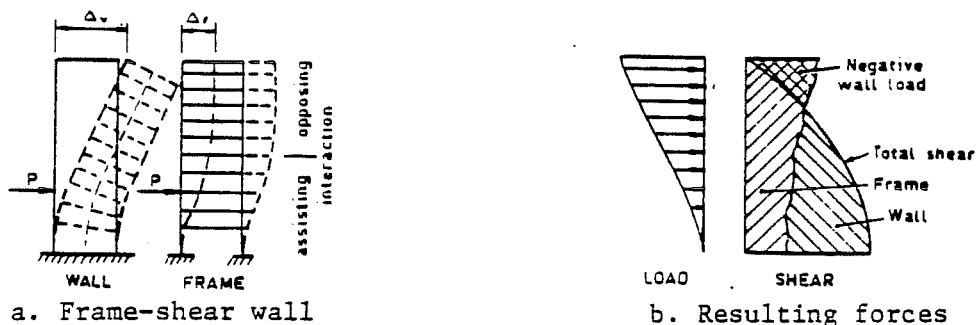


Fig. 2.7 - Frame-Shearwall Response, [Park & Paulay (60)].

Fig. 2.8 - A Model of the Cage-
"A Gaiola", [Tobriner (84)].

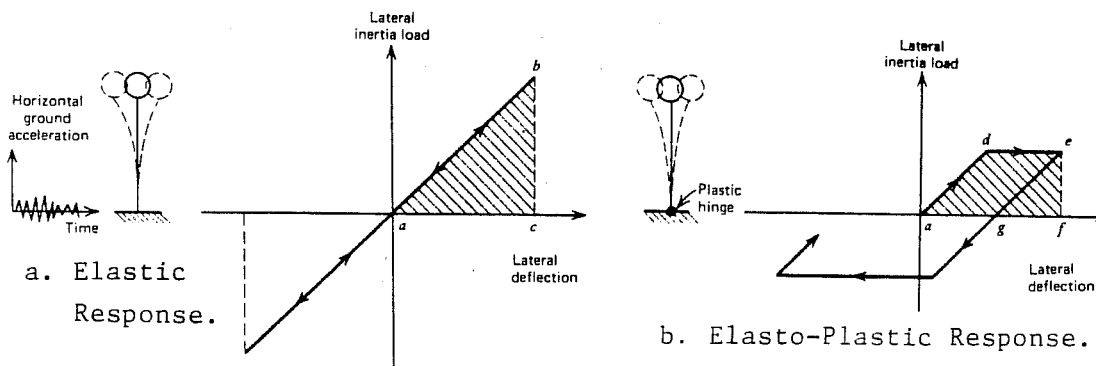
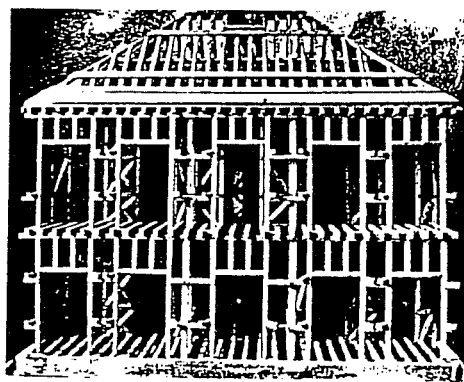


Fig. 2.9 - SDOF System Response to Ground Excitation,
[Park & Paulay (60)].

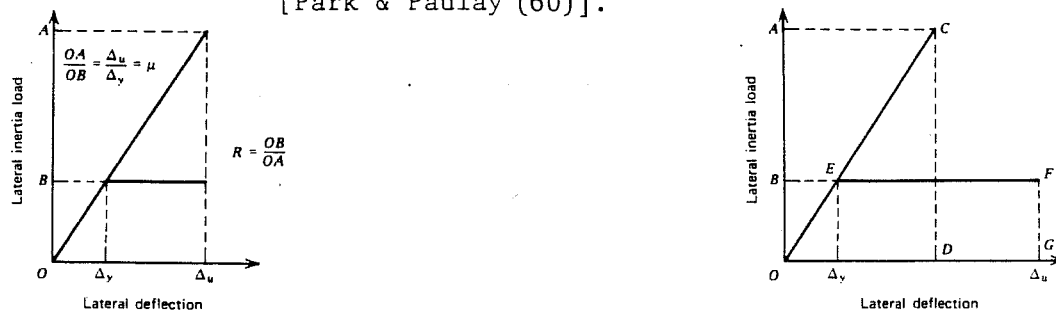


Fig. 2.10 - SDOF Oscillator Ductility Evaluation,
[Park & Paulay (60)].

after the November 1, 1755, Lisbon earthquake [S. Tobrinner (84)]. Under the directives of the Marquis de Pombal, military engineers devised a self-supporting X-braced interior wooden cage, "a gaiola", that would confine and provide the necessary lateral resisting effect to the brittle walls, Fig. 2.8. Other earthquake safety measures like height limitations and increased street widths were also enforced, [Tobrinner (84)].

The current SEAOC Seismic Design Code philosophy requires that the structure must resist [SEAOC (74)]: (1) minor intensity earthquakes - without damage, which often implies that the structure should remain in the elastic range; (2) moderate intensity earthquakes - with minor structural damage and some non-structural damage; and (3) major catastrophic earthquakes - without collapse.

Although the degree of intensity of the earthquake, the probabilities of occurrence, the type of ground motion, and the range of frequencies to be used are difficult to choose because of the randomness involved with this type of phenomena and structure, it is clearly recognized that ductility must be provided [Park and Paulay (60)]. The need for ductility is obvious because along with the formation of stable plastic hinges large amounts of energy may be absorbed and dissipated. On the other hand, the lateral inertia force acting upon the system is sub-

stantially reduced as shown in the SDOF system example, Figs. 2.9 and 2.10.

The behavior of a structural concrete frame is strongly dependent on the behavior of its components: beams, columns, beam-column connections, slabs. Therefore, there is a profound interest in assessing the available ductility level in each of this components.

The current available technique used to evaluate the behavior of structural concrete members establishes a relationship between: (1) moment-curvature; (2) moment-rotation; (3) shear-rotation; (4) shear-shear distortion; or, (5) load-displacement of the whole element. However, for linear elements the most common procedure is to use the moment-curvature ($M-\phi$) diagram for the critical section. The $M-\phi$ relationship is derived based on the following assumptions: (1) plane sections remain plane (Bernoulli-Navier hypothesis); (2) material behavior is described by uniaxial stress-strain curves; (3) concrete does not resist tensile stresses; (4) force equilibrium; and, (5) strain compatibility.

Different types of moment-curvature ($M-\phi$) relationships may be obtained depending on the type of loading. Usually, three major groups of loading (low-cycle level) are currently identified: (1) Monotonically Applied Loads - the velocity of loading does not depend on the material or member response; (2)

Repeated Loads - it has been observed that the monotonic load response curve acts as the envelope for repeated loadings of the same sign; (3) Reversed Cyclic Loads - reversed sign loadings occur which affect member performance. It has been shown that the response of a R/C member strongly depends on the reinforcement stress-strain curve. Under strong reversed cyclic loads, full-depth cracks will develop throughout the member's cross section along with residual strains in the compression steel reinforcement. This creates a potentially dangerous situation where buckling of the longitudinal bars may occur at very low load levels due to strain-softening of steel at early load stages, i.e., the Bauschinger effect (Fig. 2.11).

The current technique used to minimize losses in member ductility is by careful detailing. This requires the use of closely spaced closed ties, longitudinal compression reinforcement, sound concrete and ductile (mild) steel. The practical effect of strain hardening is to increase the ultimate moment capacity that was initially computed without taking into account strain hardening effects. Current earthquake design code provisions assess this problem by specifying a strain hardening factor as a function of the class of steel.

2.4.2 Critical Regions in a DMRF. The earthquake attack has a complete random feature and the structure's response is no

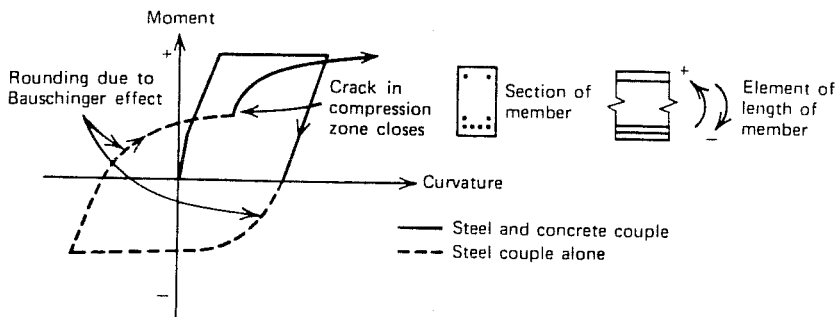


Fig. 2.11 - RC Member Hysteretic Behavior, [Park & Paulay (60)].

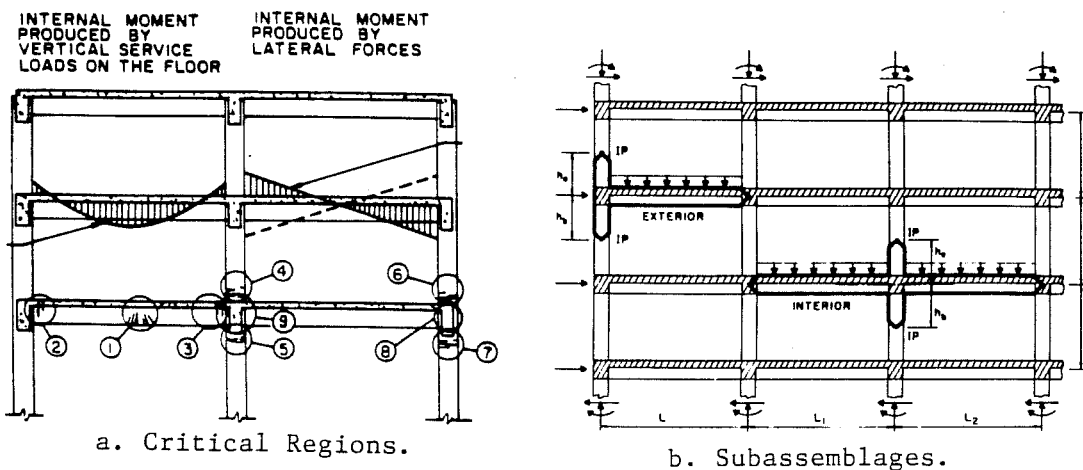


Fig. 2.12 - DMRF Critical Regions and Models, [Bertero & Popov (10)].

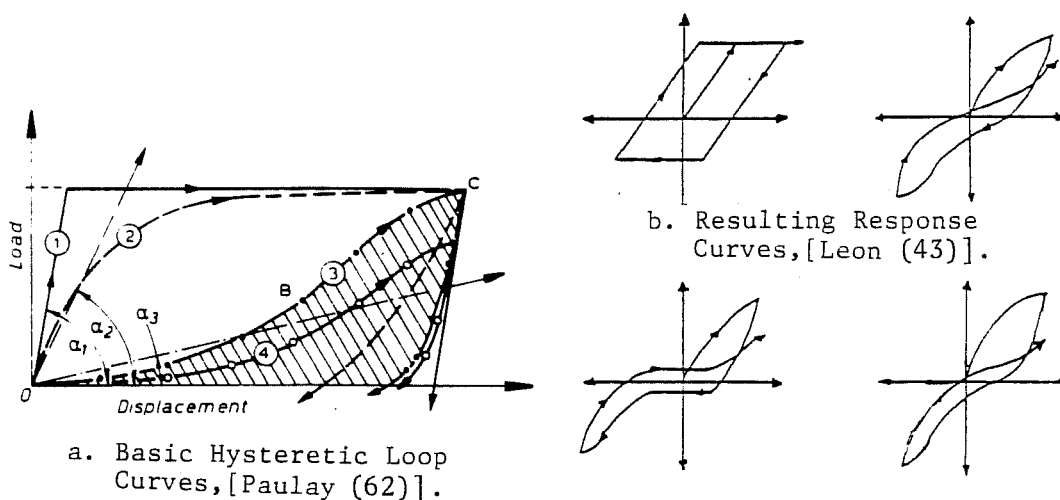


Fig. 2.13 - RC Members Hysteretic Response.

exception. Under two horizontal and one vertical acceleration components it is expected that the structure would respond in a 3-D fashion. Although, spatial frame monolithism is always implicit in cast-in-place R/C construction due to the inherent advantages of hyperstatism this is not currently enforced at a design level for several reasons. First, little data is available on load history effects in biaxial loading, torsional actions in members, skew deflections in plan which are recognized to become critical under severe loading conditions. Secondly, the material and member response, the nature of actual loading conditions, the soil-structure interaction are quite hard to assess for a planar DMRF and eventually they will become extremely cumbersome to evaluate for a spatial DMRF. Therefore, planar behavior is assumed throughout this report and spatial (3-D) behavior is discussed wherever deemed necessary.

The data obtained from earthquake failures observed in R/C structures that experienced strong ground motions has shown more severe degradation of strength, ductility, and energy absorption-dissipation characteristics than those experienced under monotonically applied loads. In great part these large degradations arise at localized concentrated areas in the DMRF - the critical regions, Fig. 2.12(a) [Bertero and Popov (10)]. The critical regions in a R/C frame are overstressed zones where large inelastic deformations occur with consequent increase

demands in ductility. The identification of these critical regions under lateral loads has lead researchers to study their response by isolating representative test specimens - the subassemblages, Fig. 2.12(b) [Bertero and Popov (10)]. The main components of a subassemblage are: (1) the beams (longitudinal and transverse); (2) the column; (3) the joint; and, (4) the slab. The critical region behavior has been extensively studied and can be identified by their states of response stress: (1) flexural critical stress in the response: regions - where bending controls the response; (2) flexural critical regions with high shear - where bending associated with large shear forces controls the inelastic behavior; and, (3) high axial and shear force - bending plays a less important role in the inelastic response.

2.4.3 The Beam Member in a DMRF. It was shown previously that the designer should aim at a beam sidesway mechanism when developing the DMRF layout. Current design codes specify ductility levels for the structure in the order of 4 to 6 based on the work of Blume et al. (13). Consequently, the potential critical regions (plastic hinges) where large stress concentrations are expected to occur accompanied by increasingly higher ductility demands should be detailed accordingly. The behavior of the critical regions in beams is usually flexurally dominated with two possible variations [Bertero (8)]: (1) low shear stresses,

($v \leq \sqrt{3}f'_c$ (psi)); and, (2) high shear stresses, ($v > \sqrt{3}f'_c$ (psi)). Cross section ductility is a function of several parameters and it may: (1) increase - by increasing the compression steel content, ρ or the ultimate concrete strain ϵ_{cu} ; (2) decrease - by increasing the tension steel content, ρ , or by increasing the steel yield stress.

Increased member ductility can be obtained without significant variations in strength. The current design approach is to fully exploiting the confined concrete ultimate strength. Confinement is provided by using closely spaced closed ties that restrain lateral expansion of highly compressed concrete in the plastic hinge regions bringing it to a near volumetric incompressibility level. At this stage the material strength is kept nearly constant, while a large deformation process followed by an energy absorption-dissipation mechanism is under way. Usual values taken for the plastic hinge lengths (L_p) in rectangular cross section beams range from $L_p \cong d/2$ (cantilever beams) to $L_p \cong d - 2d$ (interior beam hinges), where d = cross section depth.

Reasonable curvature ductilities ($\mu_\phi \sim 10$) for the R/C beam member may be obtained by adopting different measures [Paulay (61, 62)]: (1) Limit the amount of longitudinal reinforcement - a reinforcement ratio, ρ , shall be in the order of $\rho = 0.5$ to $0.75 \rho_{bal}$; (2) At the support locations - the

positive moment (M_S^+) should be closely related to the negative moment (M_S^-) in the order of $M_S^+/M_S^- = 0.50 - 0.75$; (3) Moment redistribution in beams has several advantages such as: (1) more uniform strength distribution if the maximum moment at the supports (critical regions) is reduced with subsequent increase in positive moment at midspan (non-critical region); (b) with the reduction of beam moment input into the columns by equalizing the moments at both sides of interior columns, bar congestion and anchorage problems are reduced in the joint region; and, (c) with positive-negative moment equalization an increase in steel costs may arise but this may be offset by ease of fabrication and workmanship and improved dynamic behavior resulting from the absence of curtailed bars; and, (4) Well-detailed transverse reinforcement is extremely effective for: (1) concrete confinement - large ultimate concrete strains (deformability), increase in strength and improved bond performance; (b) restraint of longitudinal highly-compressed bars (buckling resistance); (c) resistance to shear forces and sliding shear in concrete; and, (d) correct positioning of the rebar steel cage during concreting by providing a global stiffening effect. Closed ties at small spacings (s) should be used - $s < 4-8d_b$, $h_{beam} / 4$ or 0.10 m, where d_b = longitudinal bar diameter.

The existence of high nominal unit shear stresses ($v > 3 \sqrt{f'_c}$ (psi)) in a flexural critical region is a common fact and its

detrimental effects may be observed in the member's hysteretic behavior under reversed cyclic loads, Fig. 2.13(a). Far from the ideal situation of an elastic-perfect plastic behavior - curve 1, or the initial stable response of an integral material - curve 2, the existence of shear leads to a rapid material deterioration (brittle behavior) with extensive diagonal cracking under reversed cyclic loads. The resulting hysteresis curves clearly show a significant reduction of the load absorption-dissipation loops where a "pinching" effect is apparent, - curves 3 and 4. On the other hand, the occurrence of a single phenomenon like high shear is accompanied by bar slippage, Fig. 2.13(b).

The R/C beam member response in a spatial DMRF has not been studied extensively because the existence of skew bending is constrained by the interaction between beam and slab which provides extra strength and a stabilizing effect. However, the existence of a torsional-bending moment combination tends to create unstable behavior that requires the verification of section compactness. Compact sections are desirable so that the risk of failure by lateral torsional buckling of plastified sections under extreme ductility demands is avoided.

As a final remark we can see that a flexural member plays a very important role in DMRF as one of the main sources of energy-absorption-dissipation through the plastic hinge

mechanism's (critical regions). Consequently, in the global DMRF layout minimum requirements should be met. First, the beam sidesway mechanism where beams fail before columns is the desired failure mode. Second, failure should be reached by flexure (ductile) rather than in shear (brittle). Failure at the connections should be delayed and, if possible avoided, until the moment that the beam plastic hinging capacity is exhausted.

2.4.4 The Column Member in a DMRF. The DMRF design aims toward a beam sidesway mechanism which implies that the columns should not develop an inelastic mechanism in a severe earthquake. Beam plastic hinging should occur and spread over the DMRF. Column plastic hinging is also expected only at the foundation level, Fig. 2.5(b), and at the top of low-rise multi-story buildings, Fig. 2.5(c).

The plastic hinges formed in R/C column members can be associated at: (1) low axial force levels with flexural dominated behavior or flexural behavior with high shear forces; and, (2) high axial force levels with flexural dominated behavior and high shear forces [Bertero (8)].

An examination of a typical interaction diagram (P-M- ϕ) is most helpful to visualize current code limitations and observed column failures under strong ground motions, Fig. 2.14. It can be observed that if the total axial load (P) falls within the range between zero and balance load (P_b) moderate curvature

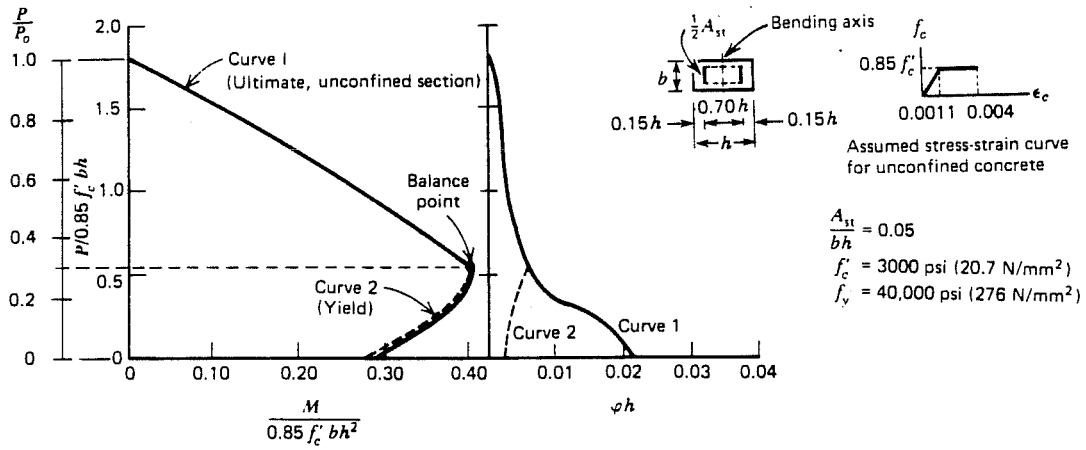
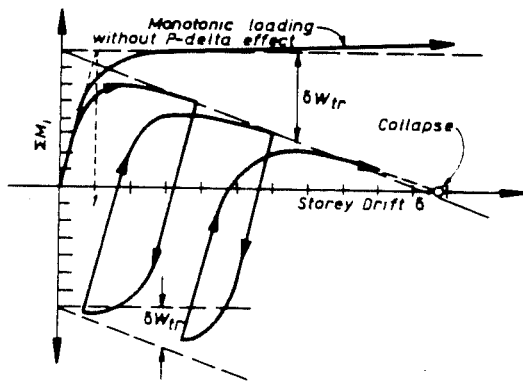
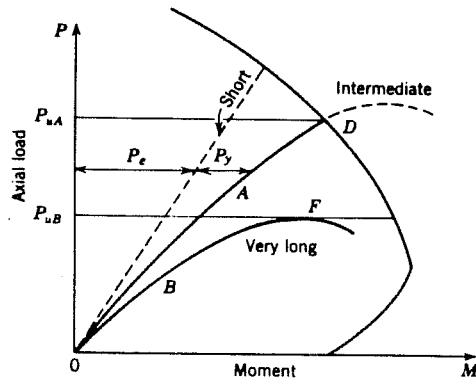


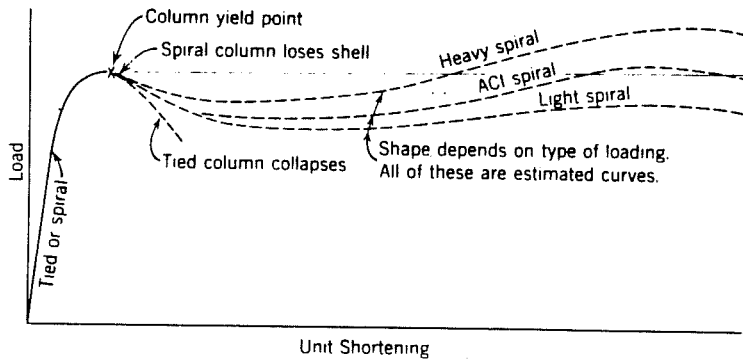
Fig. 2.14 - Column Interaction Curve, [Blume et al. (13)].



a. "Crawling" due to Biased Story Drift, [Paulay (2)].



b. Short vs. Long Column Behavior, [Ferguson (28)].



c. Ductility in Unconfined & Confined Columns, [Ferguson (28)].

Fig. 2.15 - General RC Column Performance.

ductility demands are imposed into the member. If the total axial load falls into the tension range ($P > 0$) extremely large curvature demands are made to the member that heavily penalize its behavior. On the other hand, large axial loads above balance load combined with flexural moments and high shears may develop an easily attained failure condition stage. Ductility is insured in a column member by designing for load combinations which fall in a flexurally dominated region. Some design codes allow column design as a flexural member if the maximum factored load is below a given level [ACI 318 (2)]:

$$P_e < \phi * 0.40 * P_b \quad (2.2)$$

where: ϕ = strength reduction factor and it varies from 0.70 (column dominated behavior) up to 0.90 (beam dominated behavior); P_b = nominal axial load at balance strain conditions.

However, from studies of R/C structures subjected to very large earthquake ground motions, e.g., Tokachi-Oki 1968 [(Hisada et al. (31)], San Fernando 1971 [Housner and Jennings (32)] earthquakes, it was observed that columns were the most damaged structural members. This may derive from unfavorable stress conditions created at the plastic hinge critical regions due to the simultaneous combination of several effects such as: (1) high shear forces-column lengths are usually shorter (3 - 4.5m) than beam lengths (6 - 9m); (2) overturning moments due to lateral loads that create very high compression forces or even

more serious tension forces; (3) the often neglected vertical component of acceleration that creates axial load fluctuations from tension into compression and vice-versa with the correspondent large ductility demands; and, (4) biaxial effects and 3-D loading in spatial frames.

In long columns, failure may occur by instability or lateral buckling long before column materials reach their ultimate strength. This derives from the existence of a P- Δ effect which is very important in seismic design because P- Δ moments are associated with loss of energy dissipation which can lead to a biased story drift with a "crawling" type of response and eventual incremental collapse, Fig. 2.15-a, [Paulay (62)]. Full inelastic time history computer studies have been used to represent the inelastic lateral displacement, secondary effects due to overturning moments and the P- Δ phenomena. Results from these studies have shown that instability conditions resulting from P- Δ effects are seldom critical for frames with six stories or less. Large ductility demands were found when the number of stories exceeded twelve where unstable effects became critical. In earthquake design of DMRF the story drift index (R) may be considered as a ductility index for the whole structure. An effective control of the story drift due to inelastic P- Δ ef-

fects may be achieved by providing an increase in strength instead of stiffness, [Paulay (62)].

In column plastic hinge regions, two major stages of behavior arise: (1) the initial integral column - where the entire section participates in resisting the external applied loads; and, (2) the confined core - where at higher loading stages, the concrete cover spalls off and load carrying capacity is left to the confined concrete core (often extensively cracked) with the longitudinal reinforcement carrying all the applied load, Fig. 2.15(b),(c) [Ferguson (28)].

Observations made on earthquake damaged structures show that biaxial loading effects on columns are larger than values predicted by standard 1-D analysis [Takiguchi et al. (78), Takizawa (79), Takizawa et al. (80)]. Pecknold et al. (67) found that under 2-D excitation, member ductilities twice as large as for 1-D members are required, at 1-D ductility levels of 5 or more. Furthermore, a period shift is created that will lead to a larger displacement response. Therefore, it is recommended that sufficient ductility levels be provided to reduce the possibility of developing permanent yield strains for a satisfactory response under earthquake loads. The interaction curve for biaxially loaded R/C cross-sections can be based on the Soviet Code (NyTu 123-55) design equation, Fig. 2.16 [Bresler (17), Furlong (29)]:

$$1/P_u = 1/P_{ux} + 1/P_{uy} - 1/P_{uo} \quad (2.3)$$

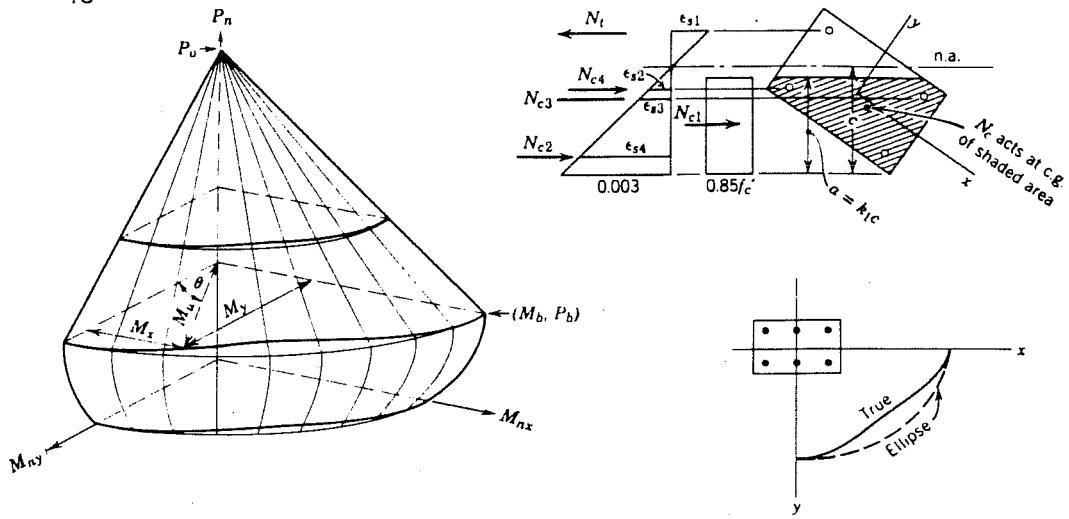
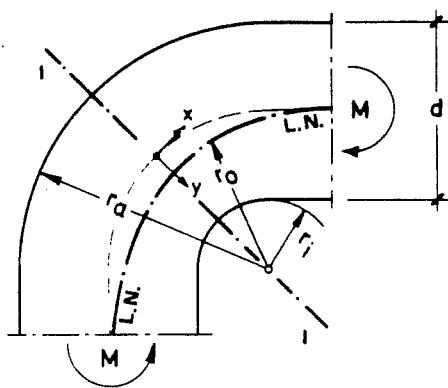
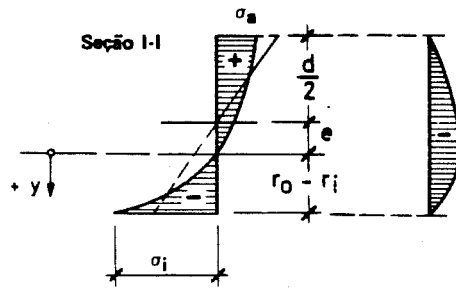


Fig. 2.16 - Column Biaxial Response, after Furlong, [Ferguson (28)].



a. Closing Loads.



$$\sigma_x = \frac{M \cdot y}{b \cdot d \cdot e \cdot (r_o - y)} \quad \text{com } r_o = \frac{d}{\ln \frac{r_a}{r_i}}$$

b. Opening Loads.

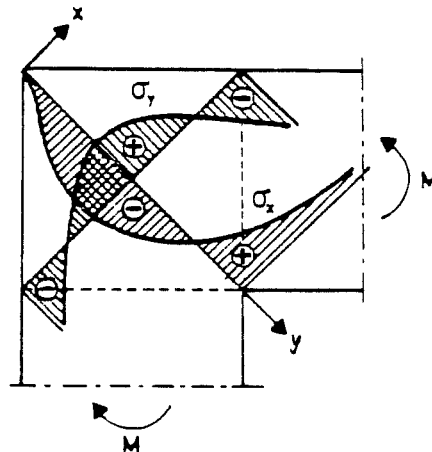


Fig. 2.17 - Elastic Stress Distribution in a Knee Joint, [Leonhardt & Monnig (45)]; [Nilsson & Losberg (56)].

where: P_{u0} = theoretical axial load design strength with $e_x = e_y = 0$; P_{ux} = design strength for the same column under the same eccentricity ($e_x, 0$); P_{uy} = same as P_{ux} but under an eccentricity ($0, e_y$).

Recent tests conducted at the University of Texas at Austin by Jirsa et al. (36) provided new valuable information about column behavior under reversed cyclic 3-D loading including shear and variable axial load. Based on the available data some conclusions for 3-D column behavior were drawn: (1) constant compressive loads have reduced influence on column performance; (2) constant tension loads have a greater detrimental influence on columns subjected to biaxial bending as compared with simple biaxial bending without axial load; (3) under reversed cyclic biaxial bending, compressive loads increase column shear capacity slightly, whereas at low level tensile loads, the column stiffness and shear capacity are reduced drastically. Near tensile yielding of the longitudinal column reinforcement, the strong influence of the previous loading history on response resulted in severely reduced load-carrying capacity. This happened due to prior or simultaneously loading in the orthogonal directions.

On the other hand, axial loads only affect performance while the applied load is on the structure and they do not influence further response. It has also been found that lateral loads when applied unidirectionally in a two-way frame system

will influence subsequent response in the orthogonal direction [Bertero (7), Bertero et al. (8)].

2.5 The Beam-Column Joint in DMRF.

2.5.1 The Position of the Problem. Well-detailed DMRF of modern design have shown poor performance under strong ground motions, due in some cases to ill-conceived reinforcement detailing, particularly at the beam-column joint critical regions. After the recent 1980 El-Asnam earthquake numerous structures showed beam-column joint failures, [Bertero and Shah (11)]. On the other hand, the designer's assumption of an rigid joint region in conjunction with the excessive attention paid to the design of other frame members such as columns, beams, slabs may lead to incorrect and inadequate connection detailing.

Although the beam-column joint problem seems to be a new one in structural concrete design, the earliest reported work in this area was done by E. Winkler in 1858, [Leonhardt and Monnig (45)]. By using the Theory of Elasticity he was able to derive the elastic stress distribution in a prismatic beam of strong curvature, Fig. 2.17(a), and he demonstrated that the stress distribution along the cross section is not linear but rather hyperbolic. Recent tests conducted in Sweden by Nilsson and Losberg (56) confirmed this stress concentration at a sharp angle for knee joints, Fig. 2.17-b.

During the past twenty five years intensive research has been conducted in this area. Subassemblage specimens have been subjected to different types of loading programs. Table 2.1 contains a summary of some of the research done with different joint types, Fig. 2.18.

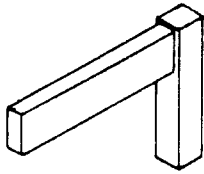
There are important differences in recorded test data due to variations in the parameters being considered relevant (load histories, specimen's geometries, reinforcing percentages) and different performance criteria. In spite of the large amount of available test data, a large set of design recommendations have been proposed by different groups (ACI, NZS, ACI-ASCE Committee 352). Consequently, the designer may be confused when he tries to use different recommendations. A performance criteria must be established which should relate the capacity of the structural system to its energy absorption-dissipation aptitude, that is, the ductility [Paulay and Park (64)].

The initial laboratory specimens to be tested were simpler so that basic parameters of response could be identified. In a planar DMRF system several different types of connections were analyzed: (1) exterior; (2) interior; (3) corner; and, (4) knee joints. Different types of loading histories were also applied: (1) monotonic; (2) repeated; and, (3) reversed cyclic loads. The current trend in the 1980's points toward more elaborate specimens where the spatial frame is modeled.

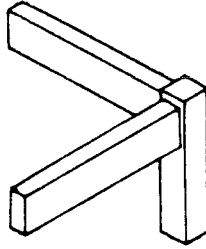
TABLE 2.1 - RESEARCH PROGRAMS ON R/C JOINTS.

YEAR REPORTED	INVESTIGATOR(S)	LOCATION	NO. OF TESTS	JOINT TYPES
1965	Higashi	AIJ (Kanto)	16	9, 10
1967	Hanson & Conner	PCA	7	4, 5
1969	Higashi & Ohwada	Tokyo Metrop. U.	13	9, 10
1971	Hanson	PCA	5	4, 9, 10
	Megget	U. Canterbury (NZ)	3	4
	Bychenkov et al.	U.S.S.R.	19	9
1972	Hanson & Conner	PCA	4	4, 9, 10
	Pattor	U. Canterbury	3	4
	Renton	U. Canterbury	4	4
	Smith	U. Canterbury	3	4
	Townsend & Hanson	U. Michigan	22	4
	Kordina & Schaaff	Braunschweig U.	5	4
1973	Megget	U. Canterbury	2	4, 6
1974	Thompson & Park	U. Canterbury	7	9
	Seckin & Uzumeri	U. Toronto	8	4, 5
	Kokusho et al.	AIJ	6	9
1975	Priestley et al.	Min. of Works (NZ)	2	9
1976	Gulkan	Ankara, Turkey	2	9
	Lee & Wight	U. Michigan	8	9
	Chwada	AIJ	9	4,6,9,10
	Tada et al.	AIJ (Kanto)	5	9
	Yamaguchi et al.	Takenaka Tech. Res.	6	6
	wang et al.	U. Calif. Berkeley	4	9
1977	Fenwick & Irvine	U. Auckland (NZ)	4	9
	Meinheit & Jirsa	U. Texas @ Austin	14	9, 10
	Ogura et al.	AIJ	4	4
	Nakada et al.	U. Tokyo	2	9
	Ishibashi et al.	U. Tokyo	4	9
	Galunic et al.	U. Calif. Berkeley	2	9
	Blakely et al.	U. Canterbury	3	9
1978	Keong & Park	U. Canterbury	3	9
	Birss et al.	U. Canterbury	2	9
	Beckingsdale	U. Canterbury	3	9, 10
	Hamada & Kamimura	AIJ	3	9
	Ogura et al.	AIJ	4	9
	Yamaguchi et al.	AIJ	5	6
1979	Soleimani et al.	U. Calif. Berkeley	2	9
	Forzani et al.	U. Calif. Berkeley	2	9
	Res. Group China	China	10	4
	Sekine & Ogura	AIJ	5	4, 6
	Bessho et al.	AIJ	3	9, 10
	Scribner & Wight	U. Michigan	12	4, 9
	Viwathanatepa	U. Calif. Berkeley	3	9
	Gravilovic et al.	Skopje, Yugoslavia	3	4
	Vasilescu	IASI, Romania	3	9
	Carvalho	LNEC, Portugal	4	4
1980	Fenwick & Nguyen	U. Auckland		
	Nakata et al.	BRI, Japan	8	3, 6, 10
1981	Scarpas et al.	U. Canterbury		
	Gaerty et al.	U. Canterbury	1	9
1982	Ehsani & Wight	U. Michigan	12	4, 6
	Durrani & Wight	U. Michigan		
	Thurston	U. Canterbury	3	9
	Milburn & Park	U. Canterbury	4	4, 9
1983	Leon & Jirsa	U. Texas @ Austin	14	6, 10
	Meli et al.	UNAM, Mexico	7	6
1984	Milind et al.	U. Texas @ Austin	4	6, 10
	Suzuki et al.	Kajima Co., Tokyo	2	10
	Otani et al.	U. Tokyo	12	9
1985	Inada & Kurose	Shimizu Co., Japan	2	6, 10
	Otani et al.	U. Tokyo	3	9
	Aoyama et al.	U. Tokyo	2	10

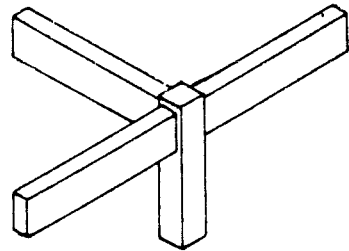
1. Exterior Joints .



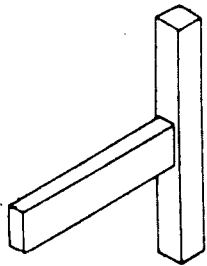
(1)



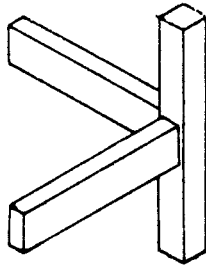
(2)



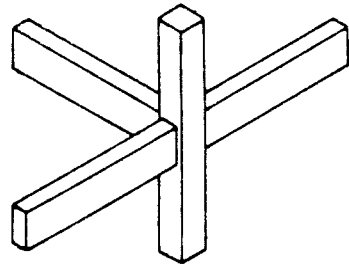
(3)



(4)

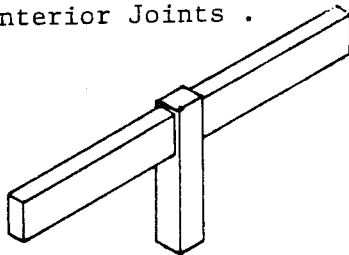


(5)

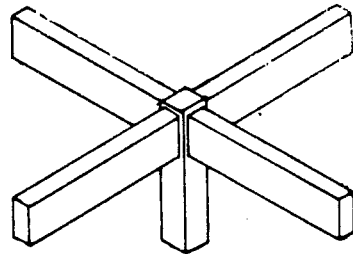


(6)

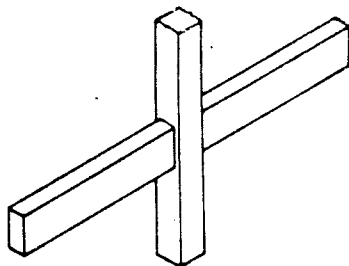
2. Interior Joints .



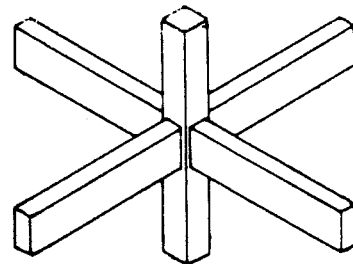
(7)



(8)



(9)



(10)

Note : Slab not shown
for clarity.

Fig. 2.18 - Types of RC Beam-Column Joints.

For example, the transverse beam provides lateral confinement but also produces torsion which is transferred through the joint. The cast-in-situ slab results in higher flexural capacity of the floor system. Biaxial loading patterns produce substantially different distress in joint region.

From the available test data several critical features of behavior may be identified when large shearing forces are introduced into the joint region due to the development of beam plastic hinges at the column faces, Fig. 2.19, [Jirsa (34), Meinheit and Jirsa (48)]: (1) Shear in the joint - reversed cyclic hysteresis loops show "pinching" of the interaction curves near the origin with reduced stiffness and fairly rapid strength deterioration. To provide joint integrity under large deformations, well detailed reinforcement (horizontal and vertical) is required; (2) Anchorage failure - very large stress gradients are introduced by the rebars into the joint core and, under load reversals, bond deterioration accompanied by yield penetration into the joint core arises. A reduction of stiffness and energy absorption-dissipation in the hysteresis loops is expected near the origin; (3) Beam or column hinging - if the connection capacity is larger than the adjoining members, concentrated inelastic deformations will occur by hinging in the beam or in the column; (4) Compressive failures through the joint - were not observed in experimental tests, but they are

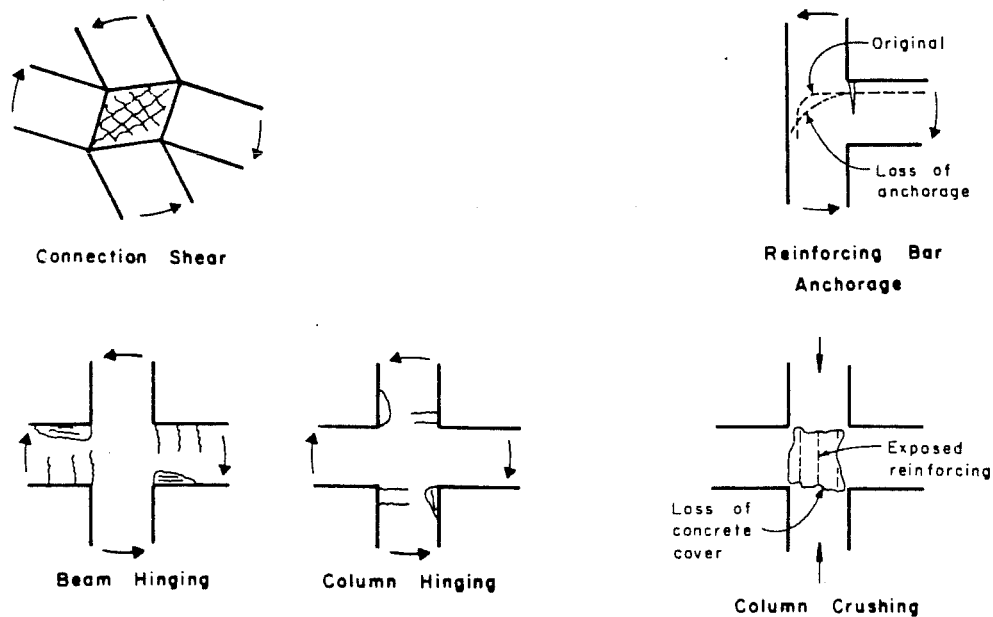
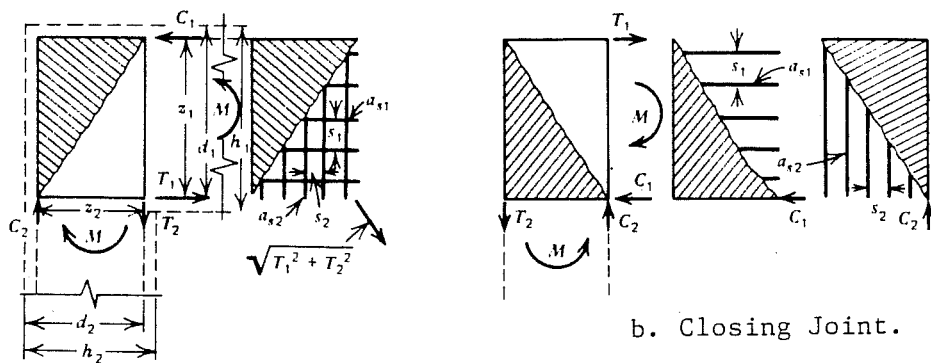


Fig. 2.19 - Possible Component Failure Modes, [Meinheit & Jirsa (48)].



a. Opening Joint.

b. Closing Joint.

c. Reinforcement Detail.

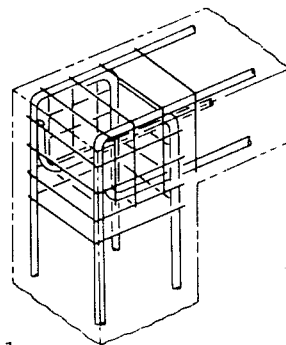


Fig. 2.20 - Knee Joints under Load Reversals, [Park & Paulay (60)].

likely to occur in members with reduced lateral confinement, ex: exterior beam-column joints, corner joints.

The current New Zealand design criteria for beam-column joints [Paulay (61, 62)] requires that: (1) the joint strength should not be less than the maximum strength of the weakest member it connects; (2) the joint should not be the main source of energy dissipation; (3) under moderate earthquake loading, it is desirable that the joint remain in the elastic range; (4) under large earthquake loadings, joint degradation due to inelastic frame displacements should not affect the column load carrying capacity. The joint must be considered as an integral part of the column; and, (5) good detailing should be enforced in joint design so that acceptable workmanship standard would be reached, e.g., easy detailing, fabrication and concrete placement procedures.

2.5.2 Knee Joints. These joints are expected to be found at the top levels of DMRF where very low-axial and shear forces are introduced into the joint core. With low-level forces present smaller cross-section size members are used. However, large stresses may arise due to the presence of shear forces and diagonal tension cracks in the joint that can jeopardize the load carrying capacity of framing members.

Three types of joint loading conditions are dominant: (1) closing loads; (2) opening loads; and, (3) reversed cyclic loads.

The existence of external reversed cyclic loads leads to an orthogonal cracking pattern throughout the joint panel with bond deterioration and yield penetration into the joint core, Fig. 2.20. Several measures may be adopted to guarantee effective bar anchorage under progressive bond deterioration [Park and Paulay (60)]: (1) limit beam steel content and bar size; (2) use mechanical anchorage; (3) change member sizes; (4) design a beam stub for bar anchorage; and, (5) relocate the beam plastic hinge far from the column face.

The common observed failures in knee joints may be derived from [Nilsson and Losberg (56)]: (1) diagonal tension cracking; (2) splitting; (3) yielding of reinforcement; (4) anchorage failure; and, (5) crushing of concrete.

2.5.3 Exterior Joints. Exterior joints can be found either in planar or two-way DMRF. The externally applied lateral loads in a R/C DMRF results in a complex interplay of forces transmitted by the beam-slab member through the joint region into the column. Failure mechanisms controlling joint performance include: (1) shear in joint panel region; (2) anchorage deterioration along beam or column bars through the joint; and, (3) compression failure of the concrete in the joint.

2.5.3.1 Types of exterior joints. Based on the premise that a beam sidesway mechanism will develop, two main types of joint response have been defined [Paulay and Park (64)]: (1) Elastic joint - when the members (beam, slab, column) converging to the connection remain elastic throughout seismic loading. It is characterized by the absence of yield penetration of the rebars (beam, slab, column) passing through the core, the absence of diagonal cracking in the concrete joint panel, a more uniform distribution of both bond stresses and shear flow around all faces of the joint core. This type of joint may be obtained either by providing very large members or by relocating the potential beam plastic hinges away from the column faces by using extra flexural steel, haunched girders; (2) Inelastic joint - characterized by the formation of beam plastic hinges near column faces with consequent yield penetration and loss of bond of reinforcement passing through the joint.

2.5.3.2 Resistance mechanisms in inelastic exterior joints. With plastic hinges forming near the joint core a set of tension (T_1, T_3, T_4) and compression (C_{S1}, C_{S3}, C_{S4}) forces will be input by the steel reinforcement to the joint core, Fig. 2.21(b). A set of beam concrete compression resultant forces (C_{C1}, C_{C3}, C_{C4}) is needed to equilibrate the tension forces. "Neglecting" the existence of the slab, a beam shear force, V_1 , and a column shear force, V_{C01} are also introduced into the connection, Fig.

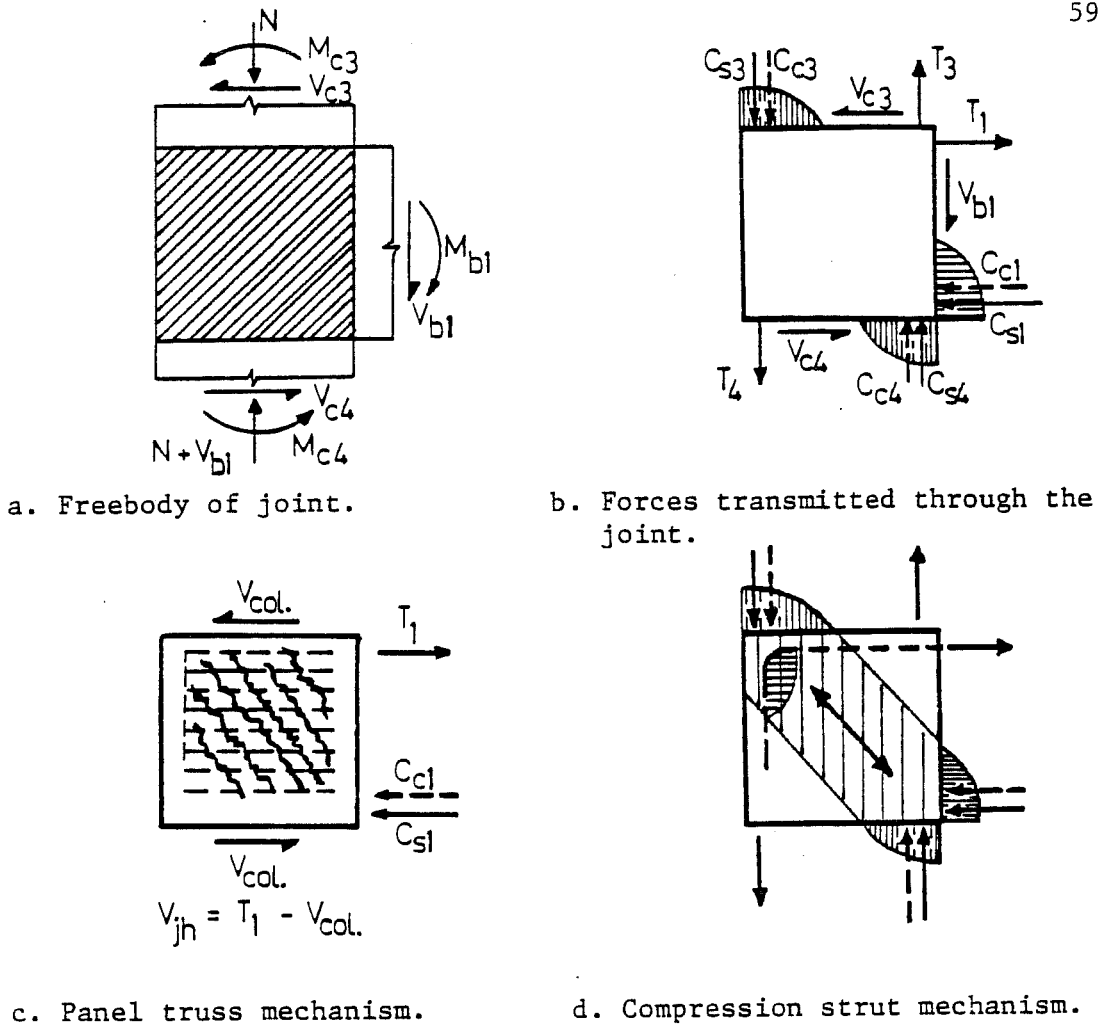
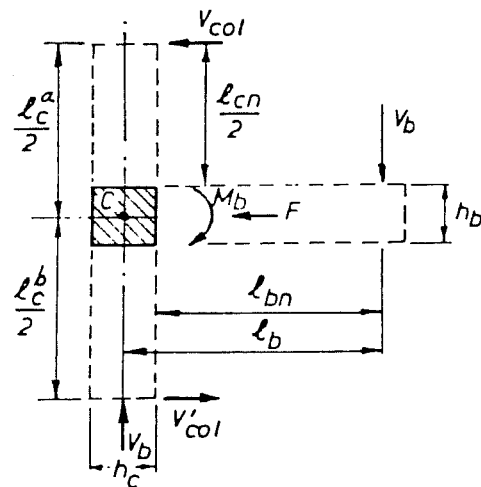


Fig. 2.21 - Exterior Joint in a Planar Frame, [Jirsa (34)].

Fig. 2.22 - Exterior Component Forces, [Paulay & Park (64)].



2.22. Assuming that inflection points will develop at mid-length of columns and beams under low-level axial compression loads (unfavorable in most cases), we will have from statics, [Paulay and Park (64)]:

1. Average Column Shear, V_{col} :

$$V_{col} = (2M_b + h_c V_b) / (l_c^a + l_c^b) \quad (2.4)$$

where: M_b = beam moment; h_c = depth of column at joint panel; h_b = height of beam at joint panel; l_c^a = column length above; l_c^b = column length below; and, V_b = beam shear;

2. Total Joint Shear Force:

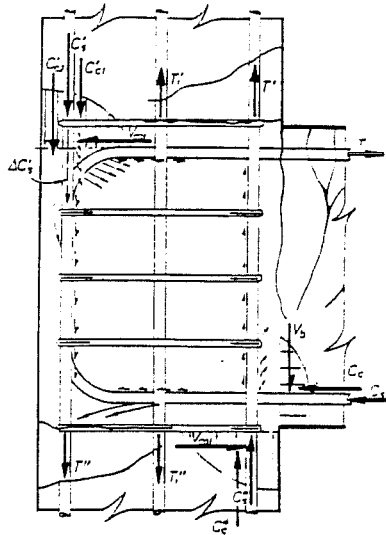
- (a) horizontal, V_{jh} $V_{jh} = T_1 - V_{col}$ (2.5)

- (b) vertical, V_{jv} $V_{jv} = T_4 + (C_{c3} + C_{s3})$ (2.6)

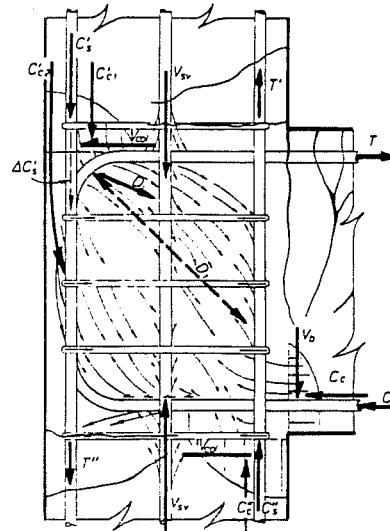
These forces create a complex stress field in the joint region which is difficult to assess mathematically. Further complications may arise at later loading stages when in the inelastic loading range, extensive cracking and steel yielding occurs throughout the core.

Two major loading-response stages may be identified, [Paulay and Scarpas (63)]: (1) At first loading of the beam - when the external load is monotonically applied through the beam-slab to the joint core. A concrete strut mechanism dominates the transfer of shear forces because of good bond conditions around

beam bars and the large concrete compression stresses at the beam anchorage, Fig. 2.23(a). By increasing the applied load, transverse tensile stress fields may create splitting cracks at early loading stages with consequent loss of bond and yield penetration in the beam rebars. This would modify the stress transfer mechanism from bond to bearing against the bend in the anchorage detail. At this instant it can be assumed that relatively good bond conditions exist around the compression beam flexural steel inside the joint core. Yielding of the column rebars is assumed not to have taken place up to this moment; (2) Inelastic beam reversed cyclic loading - large residual inelastic strains in the flexural bars would occur. Under reversed cyclic loading the top beam bars would eventually experience further decay in bond resistance and extensive yield penetration into the joint core. Although an initial good response may be expected from the bottom beam bars, the ultimate performance tends to worsen more rapidly as compared to the top beam rebars. This results from shorter anchorage straight lengths with serious bond deterioration particularly in shallow columns. The outer column bars are also under severe bond conditions because a very large force must be developed over a relatively short anchorage length. Vertical splitting cracks will generate at large load reversals and may connect with others formed in the previous load cycles.



a. Joint Core Internal Forces.



b. Compression Stress Trajectories.

c. Diagonal Compression Strut Mechanism.

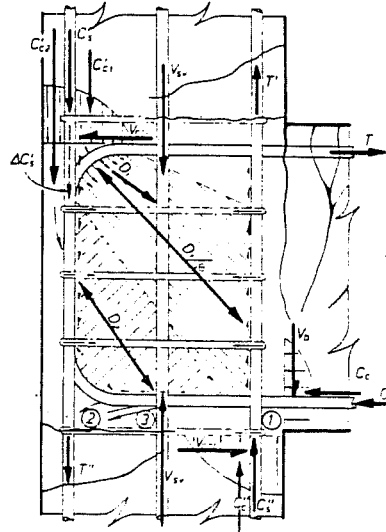


Fig. 2.23 - Exterior Joint Performance, [Park & Paulay (64)].

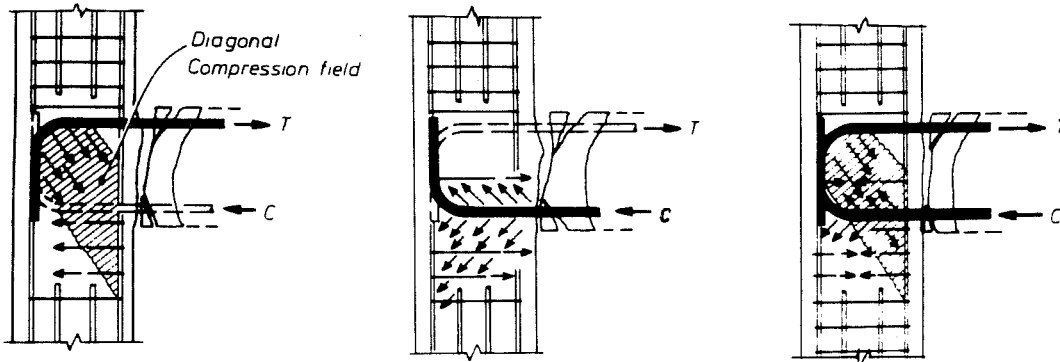


Fig. 2.24 - Exterior Joint Model, [Fenwick & Nguyen (27)].

The top beam bars will "kickout" and the concrete shell in the back of the column will spall off, with serious consequences in bond action for the outer column bars. Transverse tensile cracks will develop decreasing the load-carrying capacity of the diagonal compression strut mechanism. Consequently, most of the horizontal shear force is transferred through a panel truss mechanism with reduced participation of the diagonal compression strut mechanism, Fig. 2.23(b),(c). It has been found that strong bond degradation starts when the steel yield strain is exceeded. Also, when the concrete in the joint is extensively cracked strength and stiffness are greatly affected. Soleimani et al. (77) found that bond deterioration due to plastic strains in a rebar embedded in a joint core can contribute up to the 50% of the overall beam-column subassemblage deflections. On the other hand, near ultimate strength, the volumetric increase of the joint core may be observed and it can be considered as a warning of the imminence of failure.

The exact amount that each of the resistance mechanisms (diagonal compression strut vs. panel truss) allocated to the joint is strongly dependent on the load history, geometry, reinforcement properties, and detailing of the subassemblage. However, some recent research has shown that the diagonal compression strut mechanism has not a "static" feature and it may be mobilized up to very late load stages, [Fenwick and Nguyen (27)].

Under the concept of the diagonal compression field theory [Mitchell and Collins (51), Thürlimann (83)], a more complete interpretation of the exterior beam-column joint response is proposed, based on test results. These tests have shown that large column confinement with closely spaced column ties in the immediate vicinity of the joint core had remarkable performance, Fig. 2.24. Although the reversed load cycles would lead to concrete spalling, spread of yielding in the beam rebars, yielding in column rebars, the concrete compression strut mechanism would still be present. This results from the "migration" of the resisting compression strut from a "disaster" area to a more sound region by developing a steeper diagonal strut, Fig. 2.23. This steeper and more efficient diagonal compression strut requires that sufficient closely spaced column ties be present near the joint core. Reported test data showed an increase in joint shear strength of 75 to 100% [Fenwick and Nguyen (27)].

2.5.3.3 Exterior Joints in Spatial DMRF. The current design approach assumes a plane frame in each orthogonal direction and earthquake loading is applied accordingly. However, under large inelastic load reversals the effects of concurrent hinging of all beams framing into the joint may be detrimental to its performance by: (1) creating a possible column hinge sway

mechanism instead of the beam one; (2) unexpectedly amplifying the shears and moments over the columns and joints; and, (3) increasing the axial overturning forces in the exterior and corner columns.

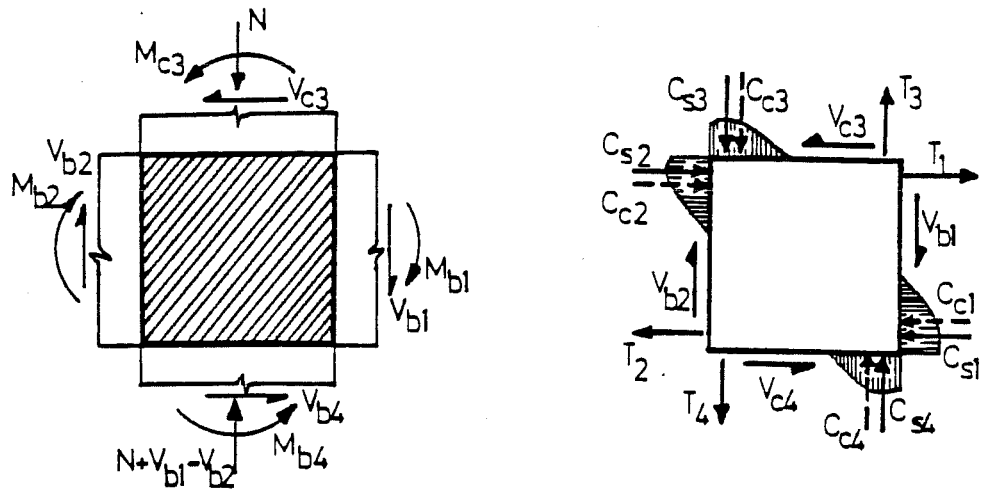
Some advantages may result from "spatial" framing by providing lateral confinement with the lateral transverse beams and the cast-in-situ slab for the joint core, [Megget (47), Seckin and Uzumeri (75), Uzumeri (86)]. Although the slab would provide extra lateral confinement, it may very well be able to create larger shear forces and torsional moments that are difficult to account for in design [Jirsa (34), Park (58)].

2.5.4 Interior Joints. Interior joint performance is discussed first for the plane frame and then, for the two-way spatial frame system. A major aspect must be considered under a given design criteria: (1) the joint is going to remain elastic throughout all the inelastic loading process; and, (2) the joint responds inelastically when plastic hinges develop in the immediate vicinity of the joint core. Whereas the latter aspect is commonly observed in most joints, the first one results from the relocation of the beam plastic hinge mechanism either by haunching the beam or by providing a particular arrangement of reinforcement detailing, Fig. 2.5(d).

Similar to an exterior joint all the generalized forces developed by the end zones of the beams and columns need to be

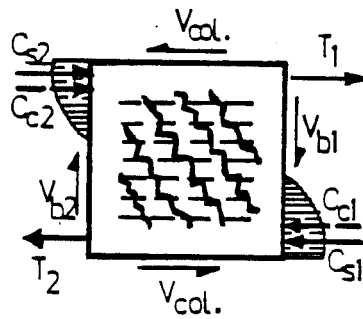
adequately resisted by the joint core. The critical aspects in the interior joint response are: (a) shear resistance; (b) anchorage mechanisms; and, (c) confinement action. Although these variables are the same as for an exterior joint one can infer that major differences may arise. First, the anchorage length under reversed cyclic loads needs to be carefully reviewed. As soon as a beam plastic hinge forms adjacent to the joint core, spalling of the beam concrete shell is expected to occur, with progressive bond destruction, yield penetration and internal cracking into the connection. Second, the horizontal joint shear forces can become twice as large as in the similar exterior joints near ultimate load. This can be found in span-drel beams designed under gravity loads with top and bottom reinforcement areas about the same, [Paulay and Park (74)]. In exterior joints, the bend in the beam rebars provides a last resource for stress transfer (steel concrete) when bond is destroyed with extensive yield penetration into the core.

2.5.4.1 Resistance mechanisms in interior joints. If we initially assume a plane from where a beam sidesway mechanism develops near an ultimate lateral loading condition, the resulting critical moments introduced into the joint by the converging beams would cause rotations in the same sense. The resulting axial forces, shears and moments applied to the joint are shown in Fig. 2.25(a,b). The beam and column bars passing



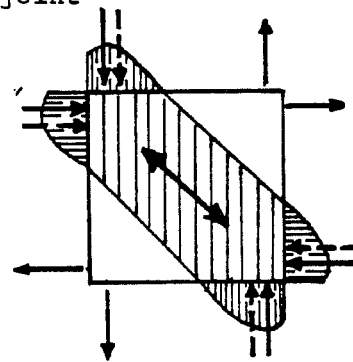
a. Joint freebody.

b. Forces transmitted through the joint



$$V_{jh} = T_1 + (C_{s2} + C_{c2}) - V_{col.}$$

c. Panel truss mechanism.



d. Compression strut mechanism.

Fig. 2.25 - Interior Joint Force Distribution, [Jirsa (34)].

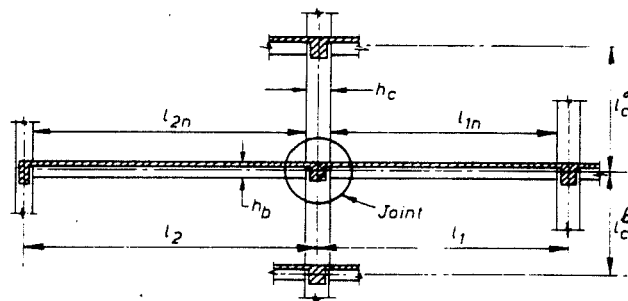


Fig. 2.26 - Interior Joint Region, [Paulay & Park (64)].

through the core develop tension (T_1, T_2, T_3, T_4) and compression ($C_{s1}, C_{s2}, C_{s3}, C_{s4}$) forces whereas the resultants of the concrete compression stresses of the members are represented by $C_{c1}, C_{c2}, C_{c3}, C_{c4}$. Assuming the unfavorable condition in the connection of a low level column axial load, only the beam (V_{b1}, V_{b2}) and the column (V_{c3}, V_{c4}) shear forces need to be analyzed. Considering that inflection points will develop at midlength of columns and beams Fig. 2.26, we will have from statics [Paulay and Park (64)]:

1. Average Column Shear, V_{col} :

$$V_{col} = 2 \cdot (M_{1,0} + M_{2,0}) / (l_c^a + l_c^b) \quad (2.7)$$

2. Maximum Horizontal Joint Shear Force, V_{jh} :

$$V_{jh} = T_1 + (C_{s2} + C_{c2}) - V_{col} \quad (2.8)$$

where: $V_{col} = V_{c3} = V_{c4}$ and it is usually equal to 10-20% of V_{jh} . This equation can be simplified if $T_2 = C_{s2} + C_{c2}$ which is valid in most cases. Then:

$$V_{jh} = T_1 + T_2 - V_{col} \quad (2.9)$$

3. Maximum Vertical Joint Shear Force, V_{jv} :

$$V_{jv} = T_4 + (C_{s3} + C_{c3}) - V_{b2} \quad (2.10)$$

However, if multiple-layers of column reinforcement are present the computation of the stress resultants may become very cumbersome. An approximate equation may be used instead:

$$V_{jv} = (h_b/h_c) \cdot V_{jh} \quad (2.11)$$

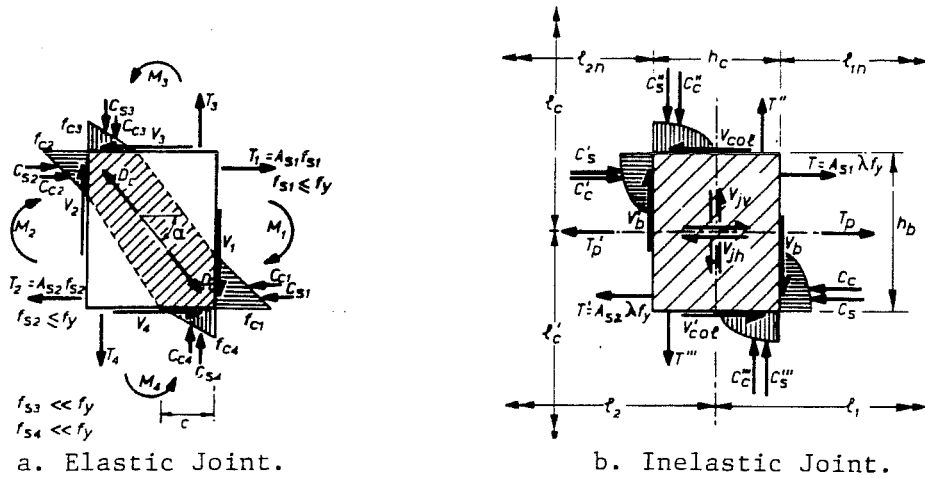
where: h_b = beam height and h_c = column height, both determined at the joint core faces.

Comparing the equations found for the shear force in exterior joints (4, 5) with the ones for interior joints (6 to 10) we can infer that the horizontal and vertical shear forces may become much larger for the latter joints near ultimate conditions.

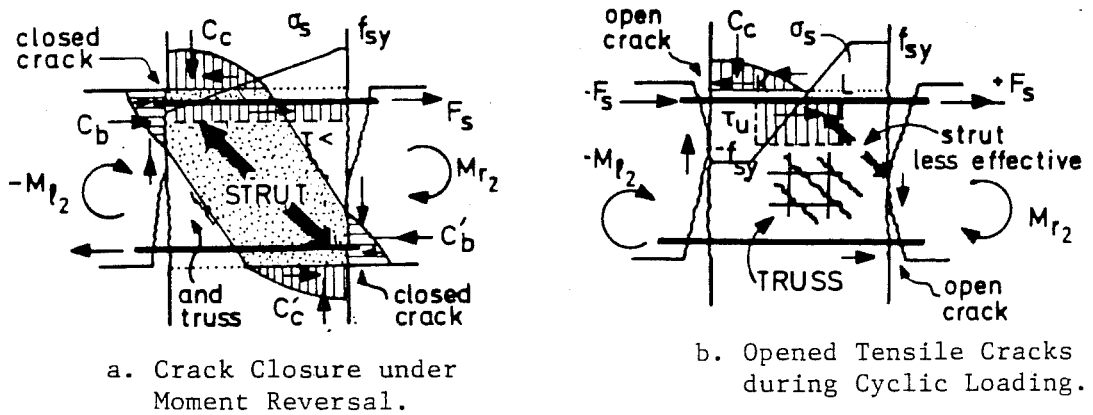
The joint resistance mechanisms are strongly time-dependent and function of the applied load history. Considering that the bending moments are about the same near the connection, the resulting shear force would lead to "growing" cracks throughout the joint core. This shear force needs to be effectively opposed and different types of resisting mechanisms have been identified, [Fenwick and Irvine (26)]: (1) shear resisted by concrete; (2) diagonal compression strut action (similar to arch action in beams); and, (3) panel truss action (similar to the web reinforcement action in beams - Morsch Theory).

The participation of each mechanism in the joint shear evolves with time: (1) Elastic initial loading - under

monotonic quasi-static loads will have a large contribution of concrete to joint shear resistance. From the previous equation (2.8) we see that the magnitude of the horizontal shear force is strongly dependent on the magnitude of the tensile forces T_1 , T_2 . At initial loading stages good bond conditions exist around the beam rebars and the transmission of compression forces applied at the joint core boundaries is made through a nearly integral diagonal concrete compression strut and the joint concrete, Fig. 2.27(a). Meanwhile, as the applied external loads increase, large tension forces associated with high shears will lead to the first joint cracking with consequent bond degradation. At this stage that marks the onset of inelastic behavior within the concrete core, joint integrity needs to be safeguarded and effective lateral confinement is necessary. The use of horizontal multi-legged joint ties is required in order to: (a) keep joint integrity and preserve the diagonal concrete compression strut as an effective load carrying mechanism; and, (b) lateral bracing to the vertical column bars under compression loads. On the other hand, some participation in the total joint strength results from the panel truss mechanism, Fig. 2.25(e) and 2.28(b). Based on the participation of these two mechanisms the elastic joint shear strength can be computed based on the old German Code "rule of addition of resistances" with:



a. Elastic Joint. b. Inelastic Joint.
 Fig. 2.27 - Interior Joint Response, [Paulay & Park (64)].



a. Crack Closure under Moment Reversal. b. Opened Tensile Cracks during Cyclic Loading.
 Fig. 2.28 - Inelastic Response of an Interior Joint, [Tassios (82)].

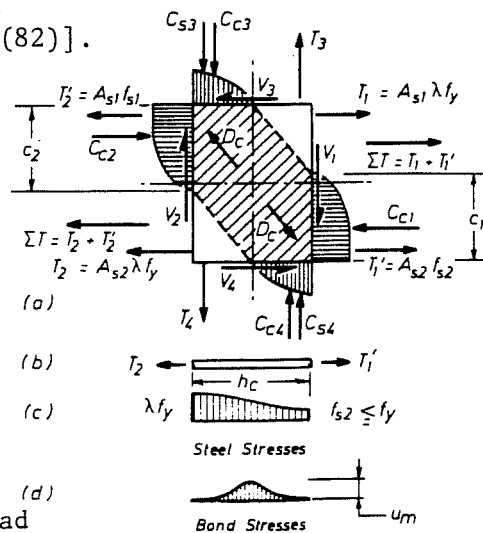


Fig. 2.29 - Interior Joint Stress Load History, [Paulay & Park (64)].

$$V_{jh} = V_{ch} + V_{sh} \quad (2.12)$$

$$V_{jv} = V_{cv} + V_{sv} \quad (2.13)$$

where the total shear force is resisted by the contribution of steel reinforcement, (V_s) plus the concrete, (V_c). Although, vertical joint shear needs to be computed as well as the horizontal one, experimental testing programs have shown that regularly distributed column bars along the joint core cross section strongly enhances its performance, [Paulay and Park (74)]. Therefore, in some design codes the participation of the diagonal concrete compression strut in vertical joint shear is increased by 20%. The participation of axial load in joint shear resistance is very favorable if it is of the compressive type. This can be easily understood since the presence of a large axial compressive load would make the diagonal concrete compression strut much steeper. Then the participation of concrete core in joint shear would increase, with the consequent decrease in the required joint shear reinforcement. The confinement requirements of the column end regions would become the design criteria and it will govern the necessary amount of horizontal joint shear reinforcement. On the other hand, the presence of tensile axial loads in the columns is detrimental to joint performance. Therefore, in most situations it is conservatively assumed that the level of axial load in the column is close to zero; and (2)

Inelastic joint under repeated load reversals - result from the formation of plastic hinges in the vicinity of the joint core when the beams introduce large inelastic deformations. After the first inelastic half-cycle loading, the top beam steel on one side of the joint core has yielded permanently with residual plastic deformations. When the load reverses, the previously yielded bars first need to yield in compression before the flexural cracks in the beam close. New cracks will form at the tension zone with the possible interconnection with other cracks formed during the previous load cycles. At a certain instant, only a top steel - bottom steel couple would be resisting the external applied loads and very large bond forces must be transferred over the exiguous embedment length available in the joint core, Figs. 2.28(a) and 2.29(a). The formation of beam plastic hinges adjacent to the joint, the opening of debris-infilled cracks, the spalling of concrete and the bond destruction around rebars only tends to worsen the joint response. With the continued application of large load cycles, yield penetration through the joint core with bar slippage and large diagonal cracking will be a sign of the imminence of joint shear failure, Fig. 2.28(b). The mechanism of joint resistance within the joint core results from the contribution of the diagonal compression strut and the panel truss actions each one varying with the amount of damage accumulated throughout the

history of applied loads. Although flexural bar slippage during the initial loading cycles does not affect the diagonal compression strut mechanism, the alternate opening and closing of wide diagonal joint cracks continuously reduces joint stiffness. In experimental subassemblage tests, bar slippage results when yield penetration along beam bars becomes excessive. Bond breakdown arises because bond stresses cannot be maintained and a dramatic redistribution of internal forces in the adjacent beam sections is necessary, Fig. 2.29(b), [Paulay and Park (74)]. When bond breakdown occurs all the beam bars at a given stage of the reversed loading cycle will be in tension due to the large inelastic displacements previously experienced. Therefore, the top and bottom beam bars in tension over the full width of the joint need to be equilibrated by an equal concrete compression force with a greatly increased neutral axis depth. These horizontal beam forces will be available with a reduced internal lever arm. As a consequence of bond breakdown along beam rebars, a reduction in joint stiffness and energy absorption-dissipation in the frame would result. Beam members may also experience flexural failure due to concrete crushing at the critical plastic hinge regions, [Paulay and Park (74)]. Bond strength and bond-slip are very hard to simulate mathematically and experimentally. However, it has been observed that bond deterioration starts when

the yield strain in steel is exceeded at the given section. For bars anchored in a joint core, bond deterioration resulting from spreading of yielding may account for up to 50% of the total subassembly deflection. On the other hand, if the joint core concrete remains uncracked (elastic joint), larger bond stresses may be reached without a detrimental effect on joint response. Bond action results from the steel-concrete transfer of tangential and radial stresses, Fig. 2.30 [Leonhardt and Monnig (45)]. Consequently, bond action in a connection can be enhanced with: (a) deformed rebars, Fig. 2.31; (b) effective confinement (ties, axial load, prestress force); (c) by limiting bar sizes as a function of the length of the joint; (d) an adequate clear distance between rebars; (e) high strength, well-compacted concrete; and, (f) by limiting the depth of the concrete layer being placed (sedimentation, laitance reduces bond). Near failure, the volumetric core expansion drastically reduces the diagonal compression strut strength. Although this type of resistance mechanism theoretically does not need stirrups for shear resistance, some transverse steel is necessary to control crack growth and the splitting force normal to the compression strut, [Fenwick and Irvine (26)]. The existence of an axial compression force (large column axial loads, prestressing forces) enhances the compression strut mechanism because of the resultant steeper diagonal compression strut. Consequently, less

•

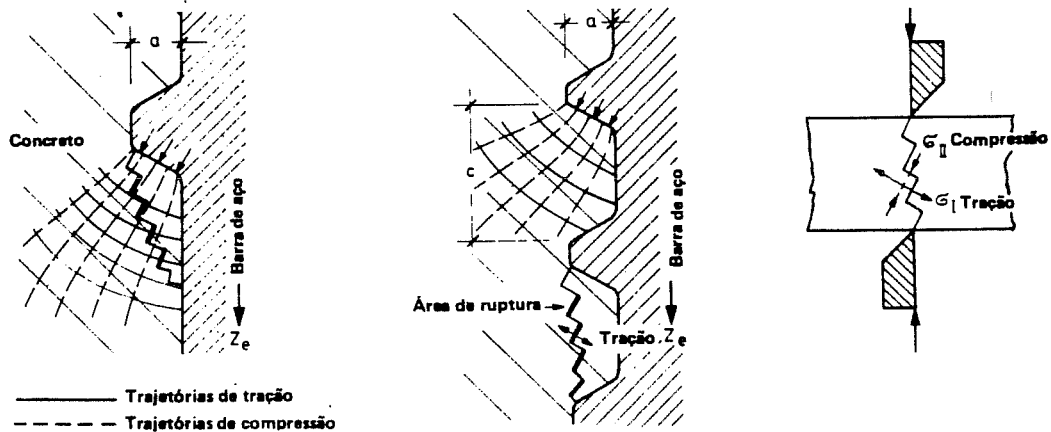


Fig. 2.30 - Principal Stress Distribution on Deformed Bars,

[Leonhardt & Monnig (45)].

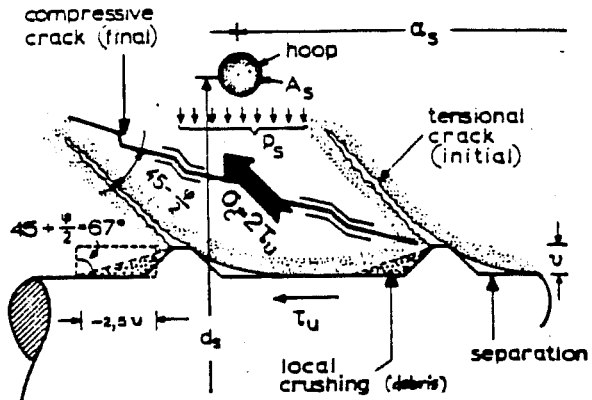
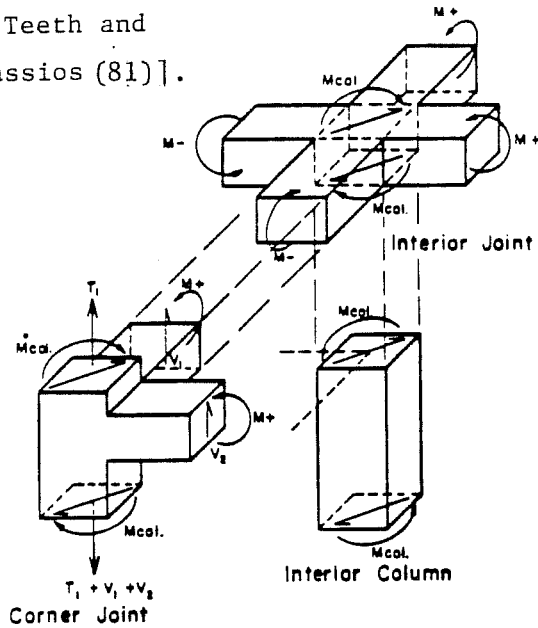


Fig. 2.31 - Rupture of a Concrete Teeth and Confinement Action, [Tassios (81)].

Fig. 2.32 - Effect of Concurrent Beam Hinging on Columns and Joints, [Armstrong (4)].



transverse steel is needed with the resulting ease of fabrication and concrete placement. Large compression stresses applied by column members will also improve bond action around beam bars. On the other hand, the participation of the panel truss mechanism in the joint shear resistance tends to increase towards ultimate. As the amount of internal damage accumulates in the joint core by extensive cracking, the shear force transfer needs to be transmitted through horizontal and vertical stirrups. If the placement of horizontal stirrups is an arduous task, the provision of vertical stirrups is almost impossible. Therefore, in current design practice, the vertical column bars regularly spaced around the joint core ($s > 4-6$ in.) are assigned to carry the vertical joint shear [Paulay and Scarpas (65)].

2.5.4.2 Interior joints in spatial DMRF. The space frame design is currently approached by substructuring the system into plane frames with the earthquake loading being separately applied along each of the orthogonal principal directions. Earthquake attack does not choose any particular direction when applied to the structure and it is very likely that skew loading would be the most common situation, Fig. 2.32. Under large inelastic displacements, it is possible that plastic hinges will develop simultaneously in the beams at all four faces of the connection. This extreme loading condition resulting from skew bending where the full strength of all interior joint four beams

is mobilized, will deteriorate the joint region and severely impair frame response. The mechanism of shear resistance in a spatial joint is complex because the orientation of the critical failure planes is harder to understand than in a planar frame. Under orthogonal beam loading conditions six compression stress blocks would form around the six faces of the joint core, Fig. 2.33, [Beckingsdale (5)]. At early loading stages, a spatial diagonal compression strut mechanism will develop along the concrete core. This diagonal strut would span from corner to corner in the joint, if wide beams are provided because of lateral confinement at the ends of the strut, Fig. 2.34(a). However, if narrow beams are used instead, it is more likely that two crossing compression struts would form due to lack of confinement at the strut ends, Fig. 2.33-b [Leon (43), Zhang and Jirsa (91)]. At later load stages, the reduced amount of joint reinforcement may lead to the destruction of compression strut with the development of a diagonal failure plane, Fig. 2.35 [Beckingsdale (5)]. If the beams in the two orthogonal directions have similar strengths and yield simultaneously, it can be proved that spatial biaxial shear in the joint would require twice the amount of reinforcement as compared to uniaxial shear design in planar DMRF, Fig. 2.35. This results from the increase of the theoretical horizontal shear force along the joint cross section

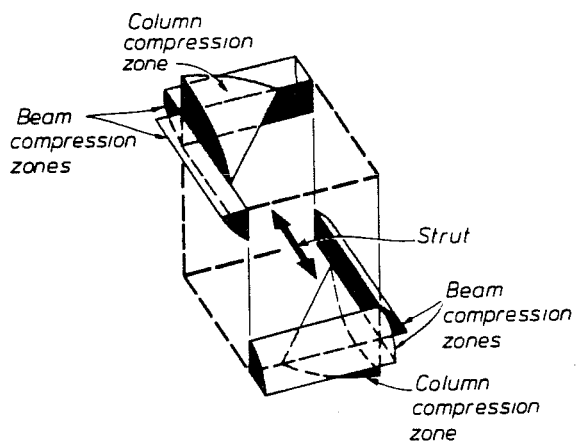


Fig. 2.33 - Space Frame Interior Joint, [Beckingsdale (5)].

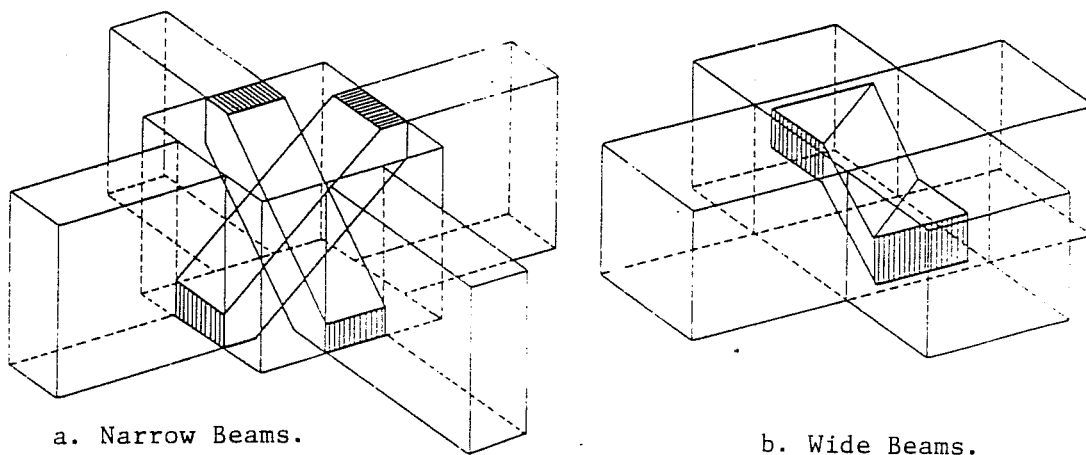
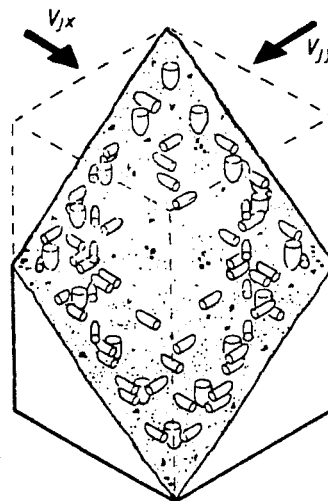


Fig. 2.34 - Spatial Diagonal Compression Strut Response, [Leon (43)].

Fig. 2.35 - Interior Joint Spatial Failure Plane, [Beckingsdale(5)].



diagonal by $\sqrt{2}$ uniaxial shear force and, the decrease of joint steel bars effective area by $1/\sqrt{2}$ (uniaxial shear value) when the diagonal tension crack plane intersects the same amount of bars as for uniaxial shear [Beckingsdale (5)].

Some recent subassemblage tests performed at The University of Texas at Austin where unidirectional vs. simultaneous bidirectional or alternate bidirectional behavior was studied show that [Burguières, Longwell, and Jirsa (18), Leon (43)]: (1) interior beam-column joints have very high shear resistance, but after the first load cycle at a certain deformation level, rapid strength and stiffness degradation may occur; (2) load history strongly affects bond action and shear resistance. "Pinching" effects on load-deflection hysteresis curves result from shear distress and, concrete spalling may also be observed in the joint vicinity; and, (3) the behavior under skew loading was similar as for unidirectional loading. In the earlier series of tests conducted by [Meinheit and Jirsa (48)] other factors affecting the capacity of interior beam-column joints were also investigated. It was observed that: (1) although lateral beams introduced critical shear stresses into the joint core, lateral beam confinement would allow an increase in the allowable joint shear stress of 50%; (2) unloaded transverse beams would allow an increase in stress by 20%; (3) minimum lateral beam confinement requires that beams must be more than

half as wide as the column and more than three-fourths as deep as the deepest beam framing into all the four sides of the column; (4) horizontal joint shear reinforcement would improve joint shear capacity but not under the same ratio as the addition rule $V_c + V_s$; (5) under monotonic loadings, joint shear strength could reach a unit shear stress of $20 \sqrt{f'_c} - 30 \sqrt{f'_c}$ (psi); and, (6) under reversed cyclic loads, a satisfactory performance level would result for a unit shear stress of $12 \sqrt{f'_c}$ (psi), Fig. 2.36. These results have been introduced into the recent ACI-ASCE Committee 352 design recommendations for beam-column joints in monolithic R/C structures [ACI Comm. 318 (2), ACI-ASCE Comm. 352 (35, 69)]. Other than joint shears, the "secondary" torsional effects that arise when the axis of beam and column members do not coincide or because of spatial behavior (transverse beams) were also responsible for some important structural failures in the 1968 Tokachi-Oki earthquake [Higashi and Ohwada (30)].

The introduction of torsional effects into the joint core through transverse beam - slab action is also not well understood and it may have detrimental effects in joint response.

2.5.5 Slab Participation in R/C Connections

2.5.5.1 Statement of the problem. The behavior of a R/C DMRF system under lateral loads (earthquake, wind) is strongly dependent on the active participation of the slab cast monolithi-

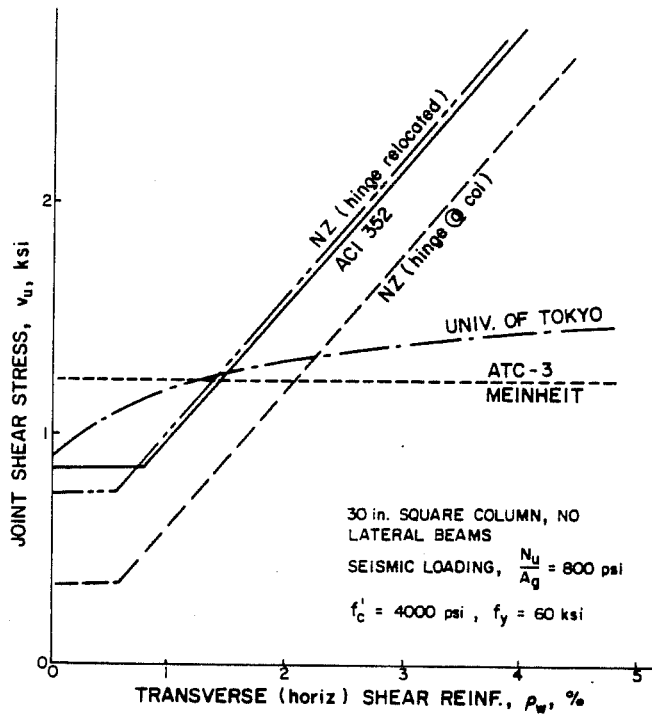
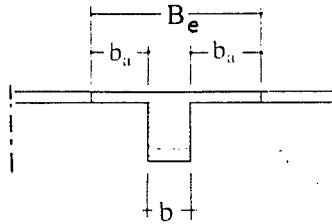


Fig. 2.36 - Joint Shear Capacity under Different Codes, [Jirsa (34)].



* Flexural Member's Strength *

		Beam only	ACI slab width	Full slab width		Balanced Moment	Zero axial Load (N=0)
M^+	Beam (k-in)	1635	2485	4380	Column (k-in)	6300	3345
M^-		1200	1810	2220			

* Joint Strength Ratio * $\Sigma M_{col} / \Sigma M_{bm}$

Balance condit.	4.44	2.93	1.91
N = 0	2.36	1.58	1.01

Note : 1. B_e (ACI) = 1.5 m
2. B_e (UTA) = 4.0 m

Fig. 2.37 - UTA Member Strength with Different Slab Widths.

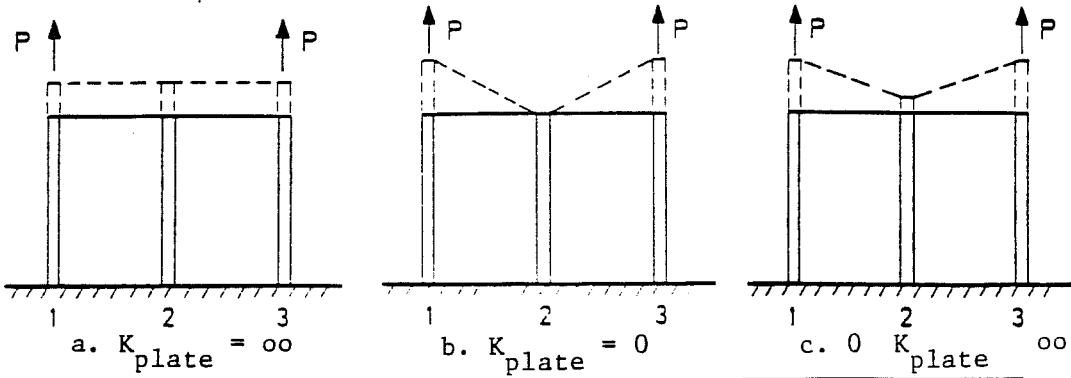
cally with the column, beam and joint in resisting the applied loads. Although this has been recognized, slab action with the interior joint has received little attention and even been ignored in most research programs. However, it is known that not only shear forces can be introduced into the joint core under large deformations but it is also assumed that increased core confinement by the slab may provide extra shear strength [Jirsa (34)].

The current design methodology simplifies the three-dimensional spatial frame into a planar frame system, for example by the use of the ACI "Equivalent Frame Method." Although the beam and column usually have similar widths, the slab is usually 10-20 times wider than the beam or columns. Consequently, the effective slab width needs to be carefully defined. In two-way systems the slab will frame into a transverse beam which will introduce torsional moments into the joint core. All of these factors need to be considered in design at a service and at a ultimate strength level [Joglekar (37)]: (1) the lateral drift of the structure must be evaluated for serviceability reasons; and, (2) at ultimate, the forces introduced into the columns by the floor elements due to large imposed lateral deformations need to be carefully assessed in order to prevent a column sideways mechanism.

On the other hand, the simplified approach of considering only the bare frame by ignoring the existence of the slab is conservative for gravity load design but it may become inadequate for lateral load design. This may be less obvious when an assumed design code slab width is considered, as in the "Equivalent Frame Method." The stiffness coefficients were derived based on experimental results and elastic analyses on structures under gravity loading conditions only. Consequently, the extension of the method to lateral loading design needs careful consideration. Particular care must be taken to avoid the formation of an highly ductility demanding column sidesway mechanism and the slab participation becomes a critical aspect. The earthquake-resistant design approach requires that the sum of the column moments divided by the sum of the beam moments in an interior joint (planar frame) be larger than 1.15 - 1.2, [ACI 318 (2), NZS 3108 (55), Pinto [CEB](68)]. Although column capacity is not hard to evaluate the same cannot be said about the beam-slab strength where design codes omit the required slab width that must be considered in seismic design. In its absence, an easy solution is to consider an effective slab width equal to 6-8 times the slab thickness for both cases of positive (top slab in compression) and negative (top slab in tension) moments. For large spanning slabs the latter case may become critical in a lateral load resisting system, Fig. 2.37, [Joglekar (37)]. As we

can see the consideration of a full slab width can lead to reduced moment ratios as compared with the flexural capacity of a rectangular beam. The situation becomes more dramatic when the absence of a compressive axial load is considered in the evaluation of the column flexural capacity which may lead to moment ratios below 1.0 (column sidesway mechanism).

2.5.5.2 Shear-lag in wide flanged beams. The Bernoulli-Navier hypothesis of plane sections remaining plane before and after deformation is generally assumed for flexure. However, in a wide-flanged beam this hypothesis does not hold due to the action of in-plane shear strains in the flanges. This results in a linear 2nd-order effect that alters the stress distribution in the beam flange where initially infinite shear stiffness was assumed in the derivation of the Flexural Theory equations. The example shown in Fig. 2.38 illustrates the consequences of neglecting or taking into account the shear stiffness of a stiffened steel plate [Kuhn (41)]. Consequently, it can be seen that the longitudinal displacements in flange zones far from the webs lag behind those near the webs. The phenomenon of shear lag arises when both the deflections and longitudinal stresses at the web-flange beam junctions are larger than those found in Flexural Theory, Figs. 2.39(a,b), [Brendel (15, 16), Leonhardt and Monnig (45)]. Design pragmatism with wide-flanged beams requires the



BAR STRESSES	BAR 1	BAR 2	BAR 3
1 st case	$\frac{2P}{3A}$	$\frac{2P}{3A}$	$\frac{2P}{3A}$
2 nd case	$\frac{P}{A}$	0	$\frac{P}{A}$
3 rd case	$\frac{2P}{3A} < \sigma < \frac{P}{A}$	$0 < \sigma < \frac{2P}{3A}$	$\frac{2P}{3A} < \sigma < \frac{P}{A}$

Fig. 2.38 - Plate-Bar Interaction for Different Plate Stiffnesses, [Kuhn(41)].

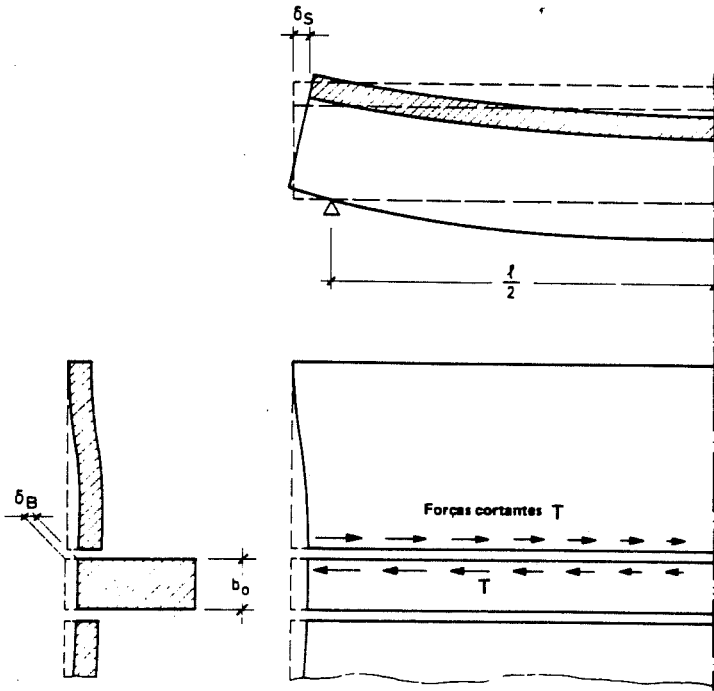


Fig. 2.39 - T-Beam Web-Flange Junction Shear Flow, [Brendel (15)].

replacement of the actual breadth, B , of each flange by a reduced effective breadth, B_e , such that the application of Flexural Theory to the transformed beam cross section yields correct results for the maximum deflection or longitudinal stress. In the elastic range the effective breadth is given by:

$$B_e = (\int \sigma_{11} \cdot dA) / (\sigma_{\max} \cdot t) \quad (2.14)$$

or,

$$B_e = \sigma_{\text{avg}} / \sigma_{\max} \quad (2.15)$$

and,

$$\psi = B_e / B \quad (2.16)$$

where, ψ = effective breadth coefficient, σ_{\max} , σ_{avg} = maximum, average values of the longitudinal stress distribution. As far as deflection criteria are concerned another type of effective breadth needs to be considered for the resulting finite flange shear stiffness.

Historically, the shear lag problem was first studied by von Kármán (39) in the 1920's and thereafter, by Chwalla (20), Metzger (49), and Dischinger (24). The numerous applications range from aeronautics [Kuhn (41) and Williams (88)] to naval architecture and civil engineering [Schade (72, 73), Youille (90), Winter (89), Abdel-Sayed (1)]. Although the terms

"effective breadth" and "effective width" can be used, Comm. Schade makes a clear distinction between both, Fig. 2.40: (1) Effective width - the flange is subjected to inplane compressive loading parallel to its stiffening members. It is inferred that the load creates buckling of the plate between stiffeners resulting in non-uniform stressing; and, (2) Effective breadth - it results from the lateral loading of an assemblage (plate and stiffeners) bending out of the original plane with either tension or compression stresses in the plane of the plate. The effective part of the plate associated with the stiffeners is the one that uniformly stressed would be compatible with the actual assemblage flexure. Whereas the effective width is associated with an instability phenomena, the effective breadth is linked to shear transmission that creates non-uniform stress distributions in a stiffened plate.

A systematic study of the parameters ruling the response of wide flange beams was only done recently by Moffatt and Dowling (52, 53). It was found that the effective breadth of a flange varies along the span and depends on the load distribution, cross-sectional properties, boundary conditions and plan dimensions of the slab-girder system. Although the study was associated with box girder bridges it provides useful information for the shear lag phenomena.

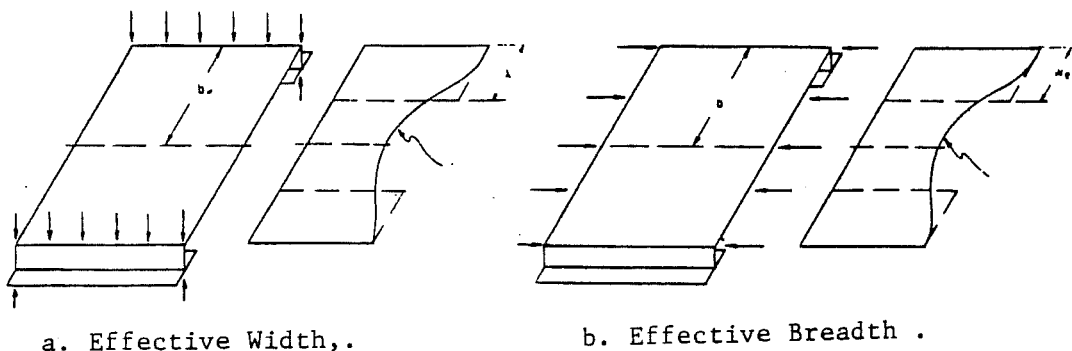


Fig. 2.40 - Plate-Girder Performance, [Schade (72)].

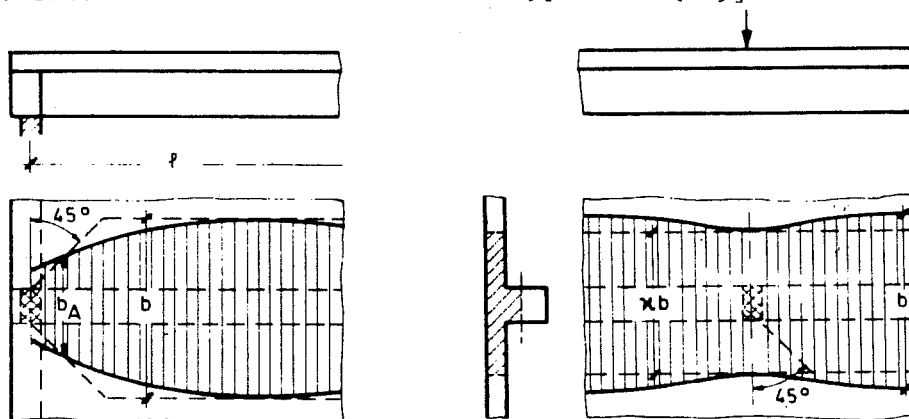


Fig. 2.41 - Shear-Lag Variation Along the Span, [Leonhardt & Monnig (2.45)].

TABLE 2.2 - EFFECTIVE BREADTH RATIOS, [Moffat & Dowling, (53)].

a. Uniformly Distributed Load. b. Concentrated Point Load at Midspan.

$\frac{B}{L}$	Stress effective breadth ratios			Deflexion effective breadth ratios			$\frac{B}{L}$	Stress effective breadth ratios			Deflexion effective breadth ratios		
	Mid-span	Quarter-span	Support	Mid-span	Quarter-span	Support		Mid-span	Quarter-span	Support	Mid-span	Quarter-span	Support
0	1.00	1.00	1.00	1.00	1.00	1.00	0	1.00	1.00	1.00	1.00	1.00	1.00
0.05	0.98	0.98	0.84	0.98	0.98	0.98	0.05	0.80	1.00	1.00	0.98	0.98	0.99
0.10	0.95	0.93	0.70	0.94	0.94	0.93	0.10	0.67	1.00	1.00	0.93	0.94	0.95
0.20	0.81	0.77	0.52	0.79	0.79	0.77	0.20	0.49	0.98	1.00	0.77	0.80	0.82
0.40	0.50	0.46	0.32	0.48	0.47	0.47	0.40	0.30	0.63	0.70	0.47	0.49	0.50
0.60	0.29	0.28	0.22	0.31	0.30	0.30	0.60	0.19	0.36	0.42	0.30	0.31	0.32
0.80	0.20	0.19	0.16	0.21	0.20	0.20	0.80	0.14	0.23	0.28	0.21	0.22	0.23
1.00	0.16	0.15	0.12	0.17	0.16	0.16	1.00	0.12	0.19	0.20	0.16	0.17	0.17

The two major parameters affecting shear lag are the: (1) breadth to length ratio of flange; and, (2) load distribution, which were already considered by Schade (72), Fig. 2.41. The type of load distribution has a strong influence particularly with concentrated loads where shear stresses show an high gradient. Compared with these two factors, the cross-sectional shape and the cross-sectional dimensions become secondary factors. However, stress effective breadths in the regions of point loads are dependent on geommetric cross section properties and several investigators proposed a non-dimensional parameter, β , to be used. The non-dimensional factor, β , is defined as the ratio of the cross-sectional area of the flange under consideration (A_f) to the cross-sectional area of the associated web (A_w). This results from the bending resistance of a fictitious T-beam being a function of its moment of inertia:

$$I_{T\text{-beam}} = I_w + I_f + [(A_w \cdot A_f)/(A_w + A_f)] \cdot e = I_w + I_f + [\beta/(1 + \beta)] \quad (2.17)$$

where: I_w, I_f = moment of inertia of the web and flange; e = vertical distance between the web and flange centroids. The first two terms represent the flexural resistance of the girder and the third term results from the shear resistant connection between web and flanges. For a simply supported beam uniformly loaded, the windspan effective breadth stress ratios are shown in

Table 2.2 and it can be shown that the ratio B_e/L remains approximately constant and equal to $1/6$. This is the value found in the German [DIN 1045 (23)] and Swiss [SIA 161 (76)] codes for the effective breadth ($B_e/L = 1/6$) under this type of loading. On the other hand, resulting from the type of loading being applied, the effective breadth will vary along the span of the beam. Consequently, the effective breadth to be considered needs to be adjusted not only for the transverse cross-section as well as for the longitudinal span length. The effective breadth variation along the span has first been shown by Chwalla (20) as the theoretical solution for the problem of a girder with a infinite flange width, Fig. 2.42, [Brendel (15, 17)]. A sharp reduction towards the beam ends is observed in simply supported beams because the normal stresses and shear stresses must vanish along the edges of the flanges at the ends of the beam. The French code assumes a straight line variation near the ends for the effective breadth under these circumstances.

Current trends in structural design call for an evaluation of the structure's ultimate capacity. In the particular case of a beam-slab connection, the stress concentration at the junction rapidly attains the elastic limit and an elastic design approach would not be economically feasible. A more realistic criteria involves the acceptance of a certain level of permanent plastic deformation with subsequent stress redistribution. The

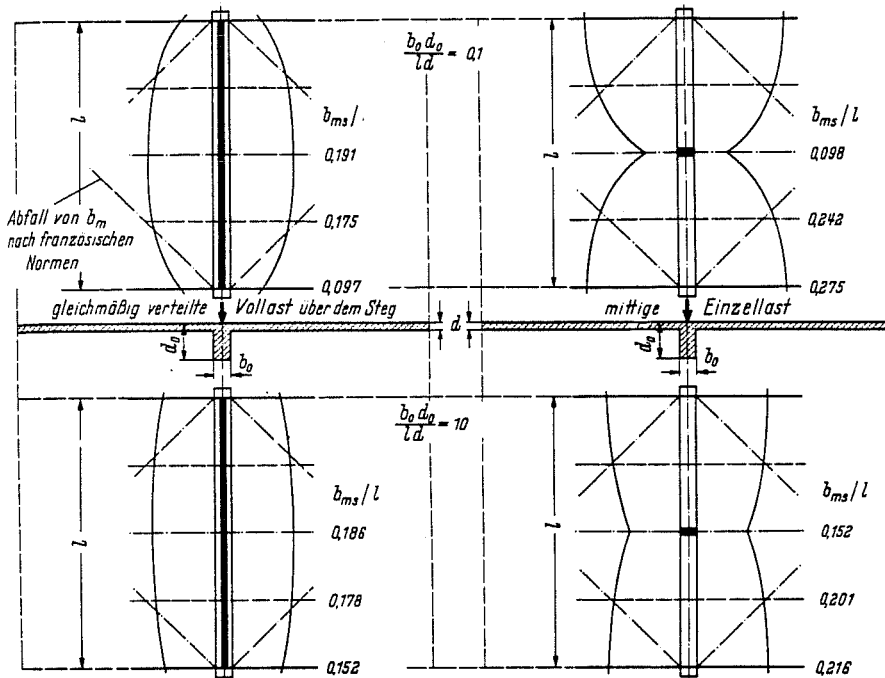


Fig. 2.42 - Effective Breadth in Infinitely Large T-Beams under Different Loading Conditions, after Chwalla, [Brendel (15)].

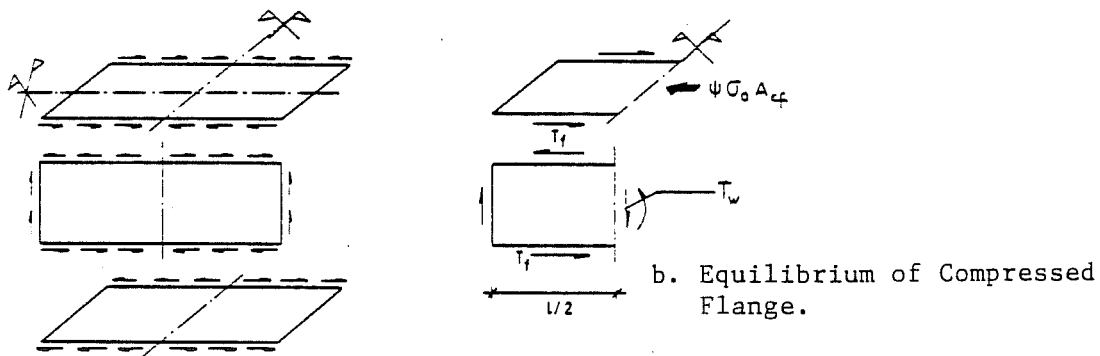
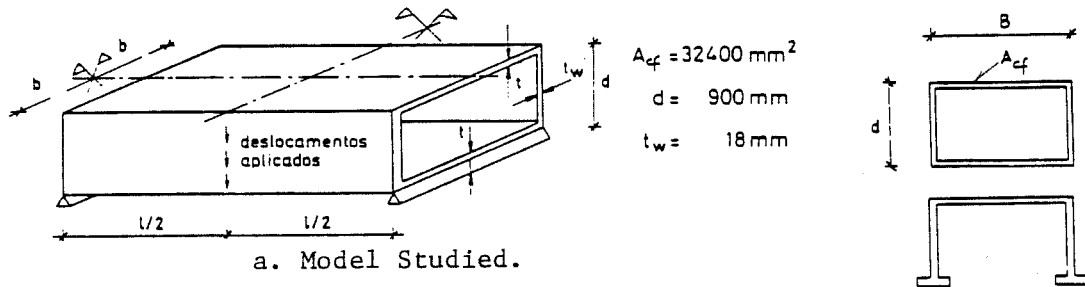


Fig. 2.43 - Simple Supported Box Girder, [Lamas (42)].

identification in wide flange boxed beams of the possible failure modes, the mechanisms of stress redistribution (spread of plasticification) was done recently by Lamas (42). The model used was a simple supported box beam with two webs linked to a top flange with or without a closing bottom tension flange, under a midspan concentrated load (Fig. 2.43). The redistribution of longitudinal stresses was observed mainly at midspan, with subsequent spread of yielding along the span under an increasing load.

The ultimate flange capacity can be evaluated also by using an extension of the effective breadth concept to ultimate conditions, ψ^u . Then:

$$\psi_u = B_e/B = \sigma_{avg}/\sigma_y \quad (2.18)$$

where: σ_y = material yield stress; ψ^u = elastoplastic effective breadth.

Three possible failure modes were identified for the compression flanges of girders under a concentrated load at midspan: (1) Flange capacity limited by web shear resistance - from Fig. 2.43(b), and admitting the same yield stress for the web and flange, equilibrium considerations require that:

$$2T_f = \psi^u \cdot \sigma_y \cdot A_c^f \quad (2.19)$$

where: T_f = shear stress resultant along the longitudinal edge;

A_C^f = flange compressed area; y = yield stress. Consequently, the flange capacity is bounded by the maximum shear flow, T_f , at the junction. On the other hand, T_f is also limited both by the maximum shear strength of the flange and of the web. Lamas (42), proved that although different stress components exist at the web-flange junction, after the onset of yielding, the elastoplastic stress flow under a constant equivalent stress leads to an increase in shear stresses with a decrease in longitudinal stresses. The upper boundary limit for T_f results from a pure shear stress yielding along the longitudinal junctions,

$$T_f \leq [(\sigma_y^{web})/\sqrt{3}] \cdot [(t_{web} \cdot \ell)/2] \quad (2.20)$$

or, for the compressed flange:

$$\psi \leq [(\sigma_y^{web})/\sqrt{3}] \cdot [(t_{web} \cdot \ell)/(\sigma_y^f \cdot A_C^f)] \quad (2.21)$$

The squash load in the flange (σ_y^f , A_C^f) can be related to the flange area (B.t) through the parameter B/l:

$$\psi = (1/\sqrt{3}) \cdot (t_{web}/t) \cdot [1/(B/\ell)] \quad (2.22)$$

(2) Flange capacity limited by its own shear resistance - where the yield stress under pure shear is reached in the web-slab junction:

$$T_f \leq (\sigma_y^f/\sqrt{3}) \cdot [(t^f \cdot \ell)/2] \quad (2.23)$$

and,

$$\psi \leq (\sigma_y^f / \sqrt{3}) \cdot [(t^f \cdot l) / (\sigma_y^f \cdot A_C^f)] \quad (2.24)$$

or,

$$\psi \leq [1/\sqrt{3}] \cdot [1/(B/l)] \quad (2.25)$$

and, (3) Flange capacity limited by its own squash capacity - the upper limit,

$$\psi < 1 \quad (2.26)$$

If we plot the above equations we can see that the maximum use of the material ($\psi = 1$) occurs for values of $B/l = 0.577$, Fig. 2.44.

Lamas (42) also showed that in the inelastic range, associated to the compression flange collapse mechanism is a different collapse mode. For the upper limit correspondent to the shear limit resistance of the web-flange junction a well-defined collapse mode arises - "shear-lag" collapse mode. For the ultimate flange capacity under a squash compression load - the "buckling" collapse mode occurs. Figures 2.45(a), and (b) show each collapse mode where an initial imperfection was assumed to exist. If the data is rearranged in function of ψ_{\max} and B/L , several curves are obtained for different B/t , Fig. 2.46. The set of curves under the hyperbolic range, $B/L > 1.0$ corresponds to the elasto-plastic "buckling" failure mode. A transi-

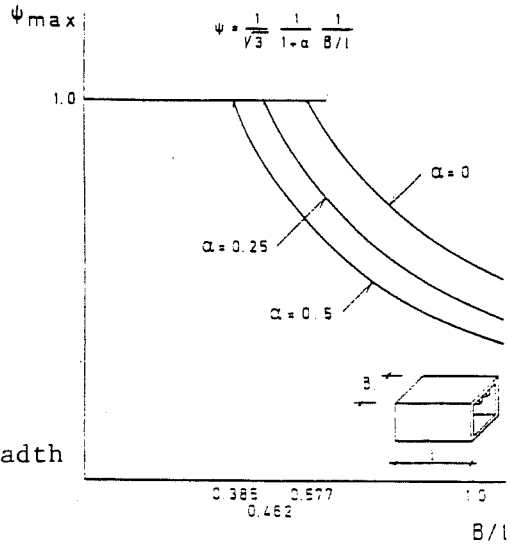


Fig. 2.44 - Maximum Effective Breadth Ratio, [Lamas (42)].

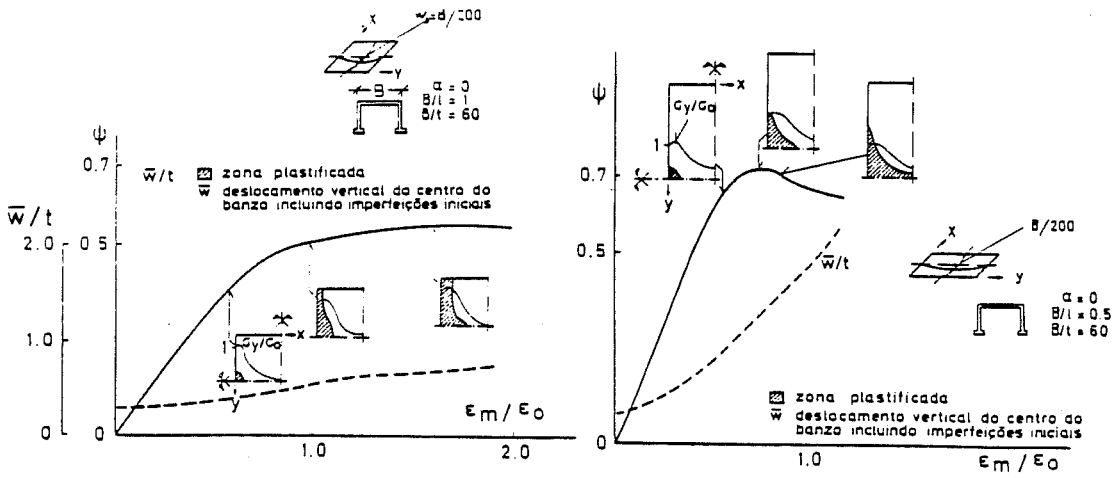


Fig. 2.45 - Wide Flange Beam Collapse Modes, [Lamas (42)].

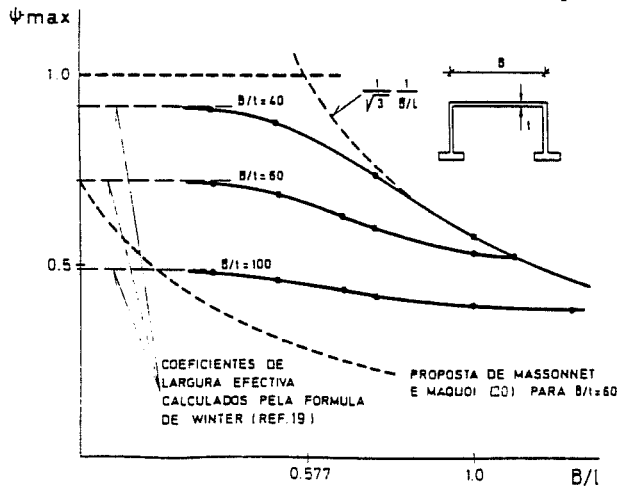


Fig. 2.46 - Effective Breadth for Different Flange/Thickness Ratios, [Lamas (42)].

tion range exists where elasto-plastic "buckling" is combined with the "shear-lag" failure mode for $1.0 > B/L > 0.6$. Finally, for smaller B/L (< 0.6) values, the "shear-lag" failure mode occurs with total stress redistribution in compression flanges. These last results agree quite well with the values proposed by Winter (89) for the effective width under uniform axial compression.

2.5.5.3 Wide Flange R/C Beam Response. The previous discussion was centered in the assumption of a continuous, homogeneous material with elasto-plastic behavior, most suitable for a steel wide flange beam.

In R/C the situation changes after the onset of cracking and the spread of yielding throughout the cross-section. In the particular case of a T-beam, spread of yielding becomes even more distinct as two major response modes need to be considered: (1) top flange in compression (positive bending moment); and, (2) top flange in tension (negative bending moment). Current design guidelines indistinctively consider an effective breadth of slab for both positive and negative bending moments as [ACI 318-83 2)]:

Clause 8.10.2 - "width of slab effective as a T-beam flange shall not exceed $1/4$ the span length of the beam, and the effective overhanging slab width on each side of the web shall not exceed:

- (a) 8 times the slab thickness, or
- (b) $1/2$ the clear distance between the web."

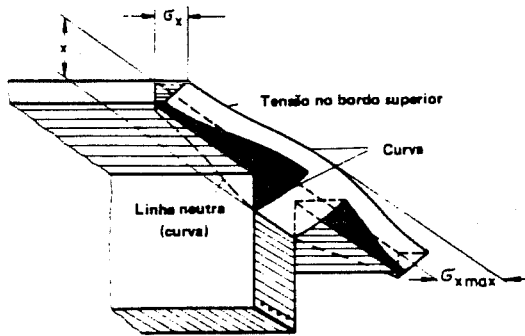
The CEB-FIP (19) Model Code reads:

Clause 8.6 - "Effective width of top compression slabs for T-Beams:

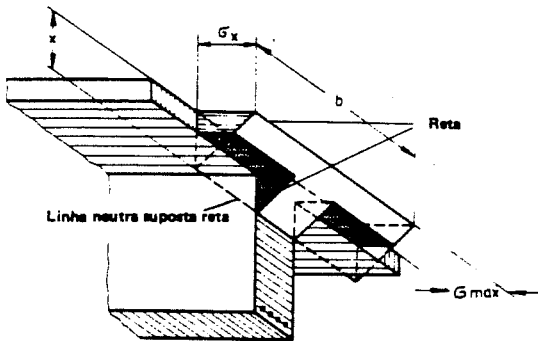
In the absence of a more accurate determination, the effective width to be used to obtain the load effects for a given span of a symmetrical T-beam, should be taken as being equal to the thickness of the web, plus 1/5th of the distance between points of zero moment but not exceeding the actual width of the top slab. The slab width should be taken as constant over the entire span, including the parts near the supports for intermediate beams."

The current design guidelines in the ACI 318-83 Code result from the work of the 1924 Joint Committee on Standard Specifications for Concrete and Reinforced Concrete (38). The set of empirical provisions were based on tests of T-beams where an elastic analysis and a shear lag approach were used. They have remained unchanged and are similar to the provisions used in some other countries, Table 2.3. These effective slab width requirements yield a conservative estimate of the positive moment capacity but were not developed for negative moment when cracking and yielding occur. In a recent testing program conducted at The University of Texas at Austin, Joglekar (37) found that the actual negative moment capacity of a wide flange T-beam was considerably larger than the one expected by using the design code effective slab width. It was observed that two main stages of response characterize the specimens behavior, Fig. 2.47: (1) At small deflection levels - the slab close to the beam acted

TABLE 2.3 - EFFECTIVE WIDTH CODE REQUIREMENTS (1964) IN SYMMETRICAL BEAMS WITHOUT FILLETS [Brendel(16)]



a. Observed Stress Distribution.



b. Effective Slab Width.

Country	b_e
Belgium	$6t$ or $L/6 - b_o/2$
Brazil	Same as Austria
Germany	$6t$ or $L/4 - b_o/2$
France	$L/6$ or distance from nearest support or point of contraflexure
Greece	Same as Germany
Great Britain	Same as Belgium
Italy	$5t$ or $L/12 - b_o/2$
Netherlands	$8t - b_o/2$ or $L/6 - b_o/2$
Austria	$b/\sqrt{1+100(b/L)^2}$
Poland	$5t$
Sweden	$6t$ or $L/8$
Switzerland	$8t$ or $L/8$
Soviet Union	Single beam, same as Belgium T-beam floors: Main girder $L/4 - b_o/2$ Secondary beam $s = b$
Spain	Same as Germany
Czechoslovakia	Same as Germany
United States	$8t$ or $L/8 - b_o/2$

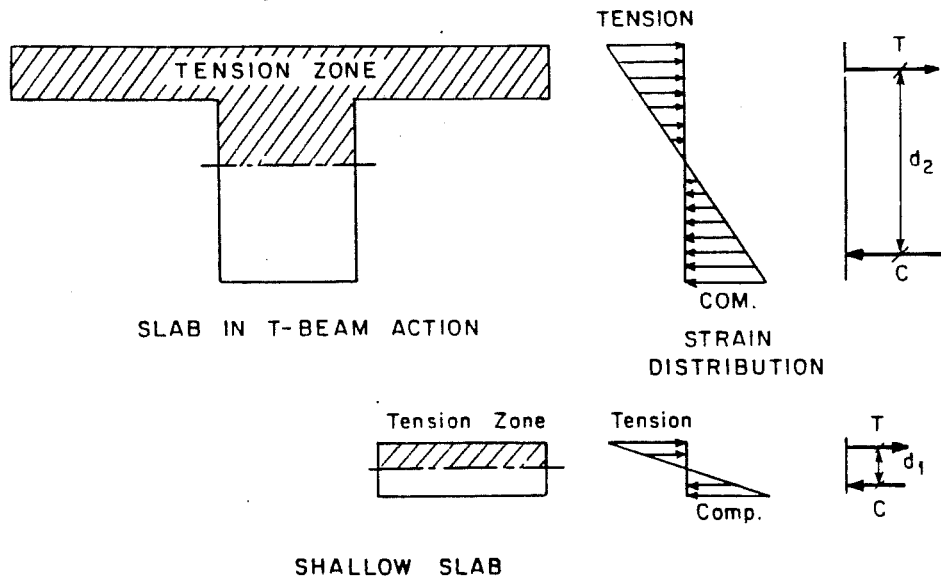


Fig. 2.47 - T-Beam Participation in Different Regions, [Joglekar (37)].

integrally with the beam. However, far from the beam the slab would act like a shallow flexural section. The observed strain decrease in slab bars far from the web may result from the shear deformations in the flange-shear lag; and (2) At large deformation levels - an increasing slab width is called on to participate as the tension flange of the T-beam. It was observed that an increasing amount of both top and bottom slab bars were in tension under negative bending moment as the spread of yielding propagated throughout the flange cross section. To equilibrate these large forces the bottom beam bars had to attain very large strains (possibly in the strain hardening region) with possible squashing of the compressed concrete block and longitudinal bar buckling.

2.5.6 Transverse Beam Participation. The monolithism created by the cast in-situ R/C slab in a beam-column-slab two-way frame connection requires the participation of the transverse beam to resist torsional forces that cannot be neglected. The resultant force and moment in a given member cross section can be decomposed in a cartesian reference frame into a set of forces (axial force, two orthogonal shear forces) and a set of moments (torsional moment, two orthogonal flexural moments). If the transverse beam is located orthogonally to the plane of flexural loading (longitudinal beam) and connectivity exists between both members (slab), the torsional moment becomes an important varia-

ble in design. The amount of data available in tested members under cyclic torsion is scarce, Table 2.4, [Tassios (82)]. Among all the different observations made in these tests, one that becomes relevant is that the amount of stiffness reduction after cracking is very high. Some codes recognize this drastic decrease of torsional stiffness by reducing the torsional moment in the uncracked state, C , function of the type of cracks, [CEB-FIP (19)]: (1) Stiffness in the uncracked state, K_I :

$$K_I = 0.30 E_c \cdot C / (1 + 1.0\psi) \quad (2.27)$$

(2) Stiffness in State II, bending cracks, K_{IIIm} :

$$K_{IIIm} = 0.10 E_c \cdot C / (1 + 0.3\psi) \quad (2.28)$$

and, (3) Stiffness in State III, shear and torsional cracks, K_{IIIt} :

$$K_{IIIt} = 0.05 E_c \cdot C / (1 + 0.3\psi) \quad (2.29)$$

where: ψ = long term creep coefficient; E_c = modulus of elasticity for concrete.

In the reported tests (22, 33), where the specimens were monotonically and cyclically loaded it was observed that the monotonic loading curve was the envelope for the hysteretic load cycles, Fig. 2.48. Also, the presence of axial load would increase the cracking torque and the tangential stiffness at low

TABLE 2.4 - SUMMARY OF TORSION TESTS [Tassios (82)].

Test	SPECIMEN				LOADING				MAIN PARAMETER
	No. of specimens	Outer dimensions, (mm)	Wall thickness, (mm)	Reinforcement ratio, %	Torque, M_T	Max. twist, angle	Axial force, N	$N/A_c \cdot f_c^2$	
Collins and Chockalingam, Ref. /4.5-1/	3	380 x 380	65	long: 1.95 stirrup: 1.08	Monotonic and Cyclic	$62 \cdot 10^{-3}$	No	-	- Type of torsional loading; monotonic, non-alternating and reversed cyclic
Yu and Whycong Ref. /4.5-2/	4	200 x 250	(solid)	long: 0.63 ₃ stirrup:	Monotonic and Cyclic	$60 \cdot 10^{-3}$	Yes and No	0.2	- Presence of axial load - Type of torsional loading; monotonic and reversed cyclic
Jakobsen, Ref. /4.5-3/	6	500 x 500	60	long: 0.89-1.48 stirrup: 0.87-1.74	Cyclic	$23 \cdot 10^{-3}$	Yes and No	0.08	- Presence of axial load - Reinforcement content

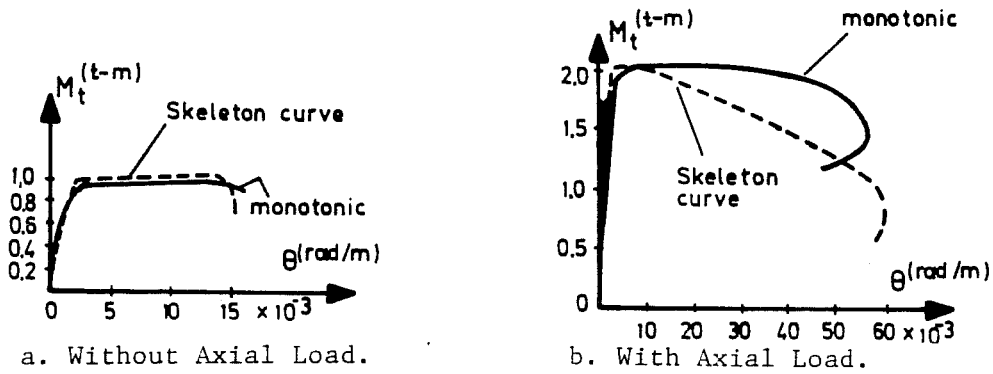


Fig. 2.48 - Comparison between Cyclic and Monotonic Skeleton.

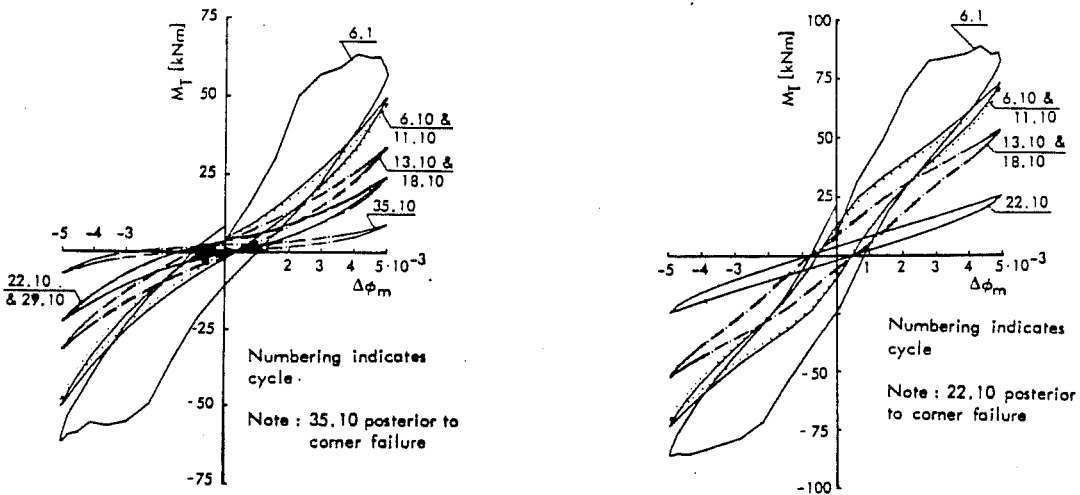


Fig. 2.49 - Typical Torsion Hysteresis Loops, [Jakobsen (33)].

load levels. Once cracking occurs, depending on the amount of axial load present, cracks will remain closed over a large range of load cycles. After cracking a large drop in the secant stiffness is observed, but then stabilization occurs up to failure (Fig. 2.49, 2.50). It also can be seen in this figure the good prediction made of the measured torque by the space truss analogy. An energy approach was used by Jakobsen (33) to evaluate the torsional response and it was found that energy dissipation increases significantly on each new "virgin" inelastic torsional incursion. This results from cracking, bond slip and yielding. However, cycling at the same level reduces the amount of dissipated energy (Fig. 2.51). It was also observed that independently of the level of twisting angle, axial load, the minimum value of the equivalent viscous damping ratio, ζ , was constant (Fig. 2.52). The equivalent viscous damping ratio is defined as:

$$\zeta = \Delta W / (4\pi W_{\text{sec}}) \quad (2.30)$$

where: ΔW = energy dissipated during each load cycle; W_{sec} = "elastically" stored energy corresponding to the current secant stiffness. Failure in thin-walled members occurred by spalling the concrete in the corners with some contribution of the axial load. It was also observed that the hysteresis curves are both strongly load and history dependent, and the presence of axial

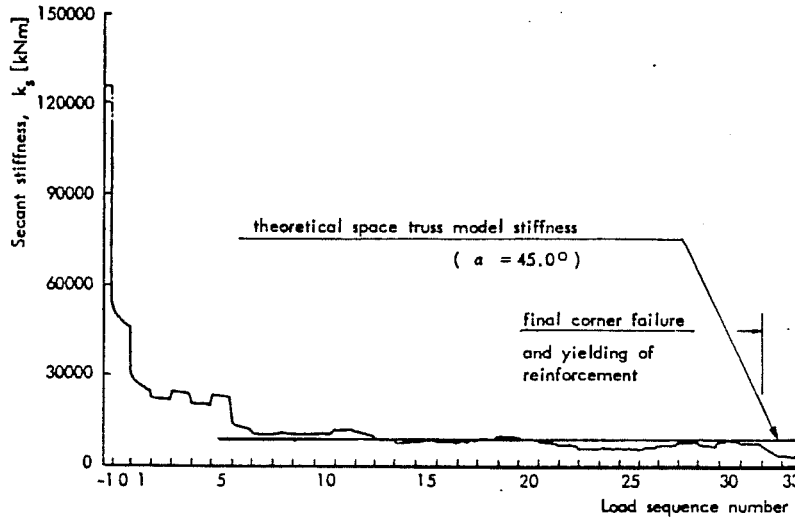


Fig. 2.50 - Development of Secant Stiffness, [Jakobsen (33)].

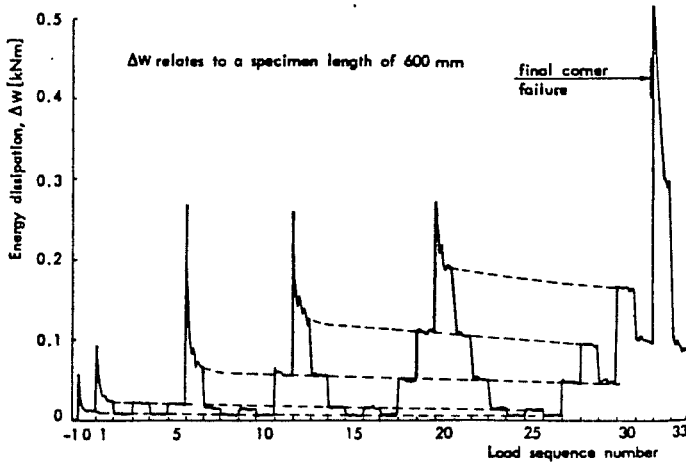
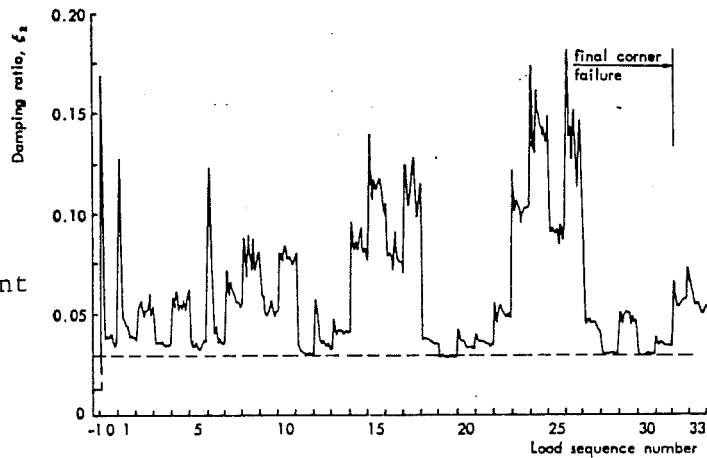


Fig. 2.51 - Energy Dissipation History, [Jakobsen (33)].

Fig. 2.52 - History of Equivalent Viscous Damping, [Jakobsen (33)].



load tends to decrease the amount of displayed ductility. In the referred tests performed by Joglekar (37), it was observed that the torsional rotation introduced by the slab into the transverse beam remains about the same along the span at all deflection levels (Fig. 2.53). However, after cracking the transverse beam loses most of its torsional stiffness and concentrated torsional plastification occurs adjacent to column faces.

2.5.7 Suggestions for Improved Performance. The critical parameters governing the R/C connection response were tentatively identified previously as: (1) Anchorage behavior - which depends on several variables: (a) load history; (b) stress level attained by the rebar in the previous load cycle; (c) lateral compression; (d) level of axial load in the column; and, (e) absolute size of the joint; (2) Shear resistance - which will depend on: (a) diagonal compression strut ultimate capacity; (b) yielding of transverse steel in the panel truss mechanism; and, (c) diagonal cracking in the joint core; and, (3) Confinement - effective confinement is reached with: (a) adequate percentage of horizontal transverse reinforcement; (b) regular column bar distribution around the joint core (vertical transverse reinforcement); and, (c) transverse beams with adequate cross section dimensions at the joint faces.

Although the level of forces present in an interior joint may be larger at ultimate than in an exterior joint similar

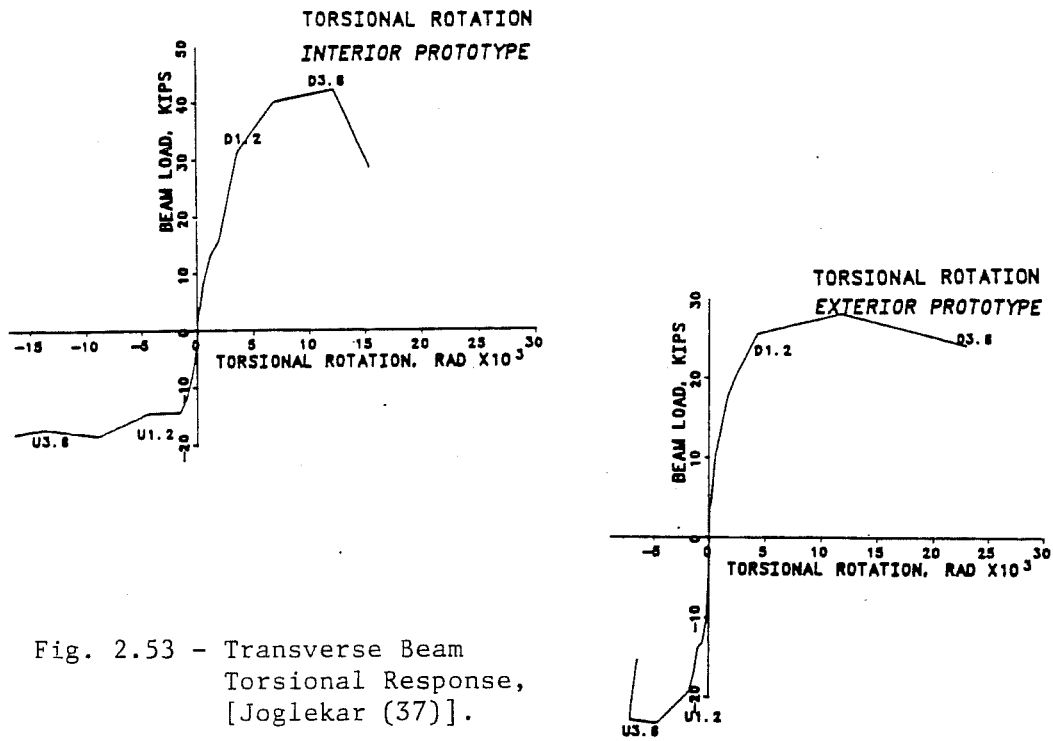


Fig. 2.53 - Transverse Beam Torsional Response, [Joglekar (37)].

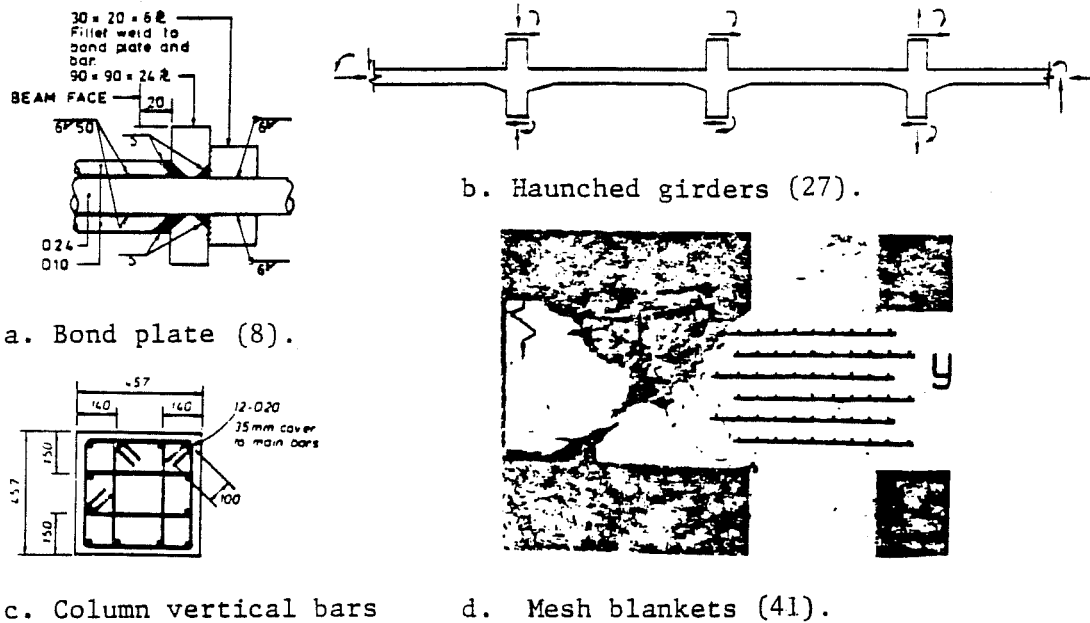


Fig. 2.54 - Improved Interior Joint Details.

response mechanisms are observed in both of them. Several different measures adopted in order to enhance joint response were proposed by investigators in testing programs. In regard to improve: (1) Anchorage behavior - (a) vary joint geometry by increasing column size; (b) limit longitudinal bar diameter passing through the core; (c) use bond plates; (d) use vertical, horizontal haunched girders; (2) Shear resistance - use in the joint core: (a) horizontal shear reinforcement; (b) well-distributed peripheral column bars; (c) rebar mesh blankets; (d) prestressing compression force; (e) fiber steel reinforced concrete (Fig. 2.54); (3) Confinement - use: (a) horizontal and transverse reinforcement; (b) prestressed transverse reinforcement; and, (c) transverse beams with effectively confining cross sections.

2.6 Design Code Optimization

From the conceptual stage of a structural system up to its implementation as a constructed facility a continuous "interactive feedback" must exist. Practical experience from a population of realized structures (laboratory test specimens, full-scale "real" structures) and the personal experience of different designers provide a fertile ground in the domain of design/decisions modeling of a hazard scenario. Continuous upgrading of information available in design codes results from

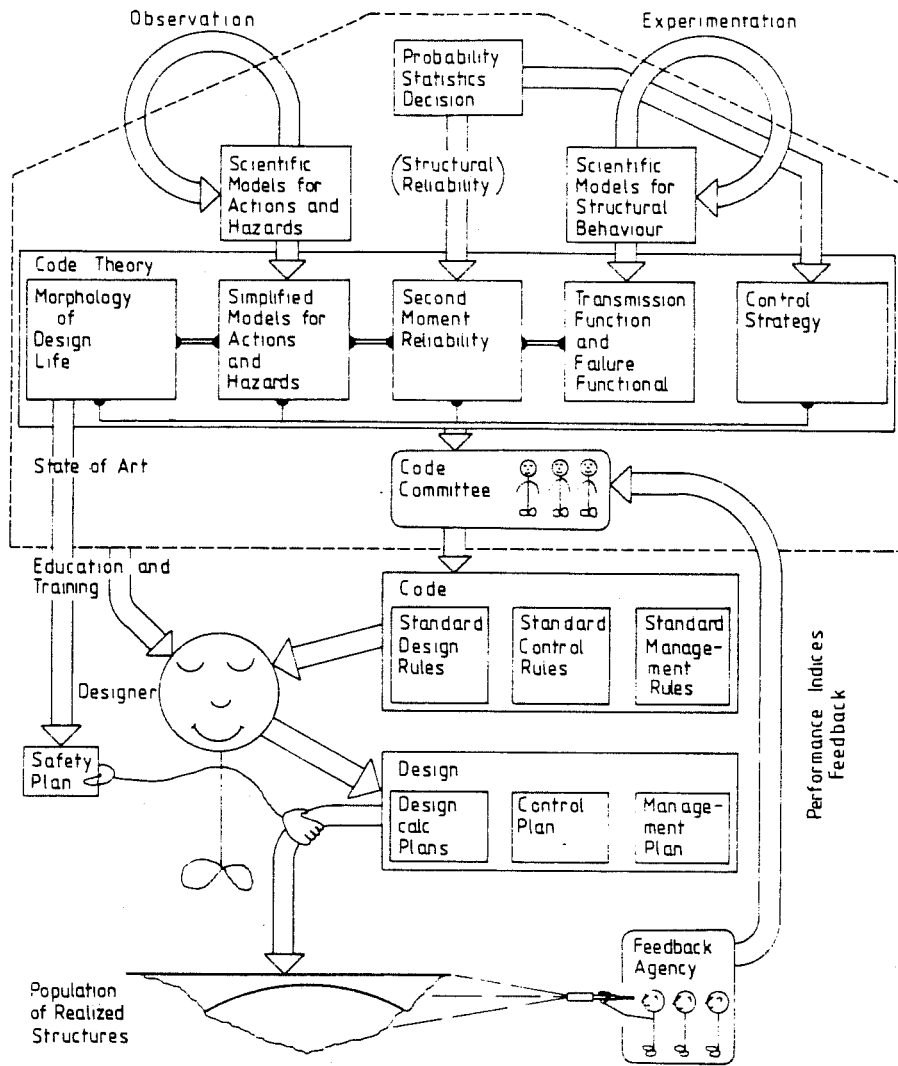


Fig. 2.55 - Design Process in a Modern Code, [Bosshard (14)].

this feedback which can be best represented in Fig. 2.55, [Bosshard (14)].

2.7 References

1. G. Abdel-Sayed - "Effective Width of Steel Deck-Plate in Bridges," Journal of the Structural Division, American Society of Civil Engineers (ASCE), vol. 95, July, 1969.
2. ACI Committee 318 - Building Code Requirements for Reinforced Concrete and Commentary. American Concrete Institute (ACI), Detroit, MI, 1983.
3. D. Allen - "Limit State Design - A Probabilistic Study," Canadian Journal of Civil Engineering, vol. 2, no. 1, March, 1975.
4. I. Armstrong - "Capacity Design of Reinforced Concrete Frames for Ductile Earthquake Performance," Bulletin of the New Zealand National Society for Earthquake Engineering (N.Z.N.S.E.E.), vol. 5, no. 4, December, 1972.
5. C. Beckingsdale - "Post-Elastic Behavior of Reinforced Concrete Beam-Column Joints," Research Report no. 80-20, Dept. of Civil Engineering, University of Canterbury, New Zealand, August, 1980.
6. V. Bertero - "Research Needs in Limit Design of Reinforced Concrete Structures, Earthquake Engineering Research Center (EERC), University of California, Berkeley, Report No. EERC 71-4, June 1971.
7. V. Bertero - "State-of-Art in Establishing Design Earthquakes," Proceedings of a Workshop on Earthquake Resistant Reinforced Concrete Building Construction (W.E.R.R.C.B.C.), University of California, Berkeley, 1978.
8. V. Bertero - "Seismic Behavior of Structural Concrete Linear Elements (Beams, Columns) and their Connections," Proceedings of the 25th AICAP-CEB Symposium, vol. 1, Rome, 1979; Comite Euro-International du Beton (CEB); Bulletin d'Information (B.I.), no. 131, Paris, 1979.

9. V. Bertero and B. Bresler - "Failure Criteria (Limit States)," vol. I, 6th World Conference on Earthquake Engineering (WCEE) New Delhi, India, 1977.
10. V. Bertero and E. Popov - "Seismic Behavior of Ductile Moment - Resisting Reinforced Concrete Frames," Reinforced Concrete in Seismic Zones, ACI Special Publication-53, Detroit, MI, 1977.
11. V. Bertero and H. Shah - "El-Asnam, Algeria Earthquake October 10, 1980," Earthquake Engineering Research Institute, (EERI) January, 1983.
12. R. Blakeley and R. Park - "Seismic Resistance of Prestressed Concrete Beam-Column Assemblies," Journal of the ACI, September, 1971.
13. J. Blume, N. Newmark and L. Corning - Design of Multistorey Reinforced Concrete Buildings for Earthquake Motions, Portland Cement Association, Skokie, IL, 1961.
14. W. Bosshard - "Structural Safety - A Matter of Decision and Control," International Association of Bridge and Structural Engineering (IABSE), Surveys - S9/79, Zurich, 1979.
15. G. Brendel - "Die 'mitwirkende Plattenbreite' nach Theorie und Versuch," Beton und Stahlbetonbau, 55 Jahrgang, Heft 8, August, 1960.
16. G. Brendel - "Strength of the Compression Slab of T-beams Subjected to Single Bending," Journal of the ACI, January, 1964.
17. B. Bresler - "Design Criteria for Reinforced Concrete Columns under Axial Load and Biaxial Bending," Journal of the ACI, vol. 57, 1960.
18. Burguières, J. Longwell and J. O. Jirsa - "The Behavior of Beam-Column Joints under Bidirectional Load Reversals," Proceedings of the 25th AICAP-CEB Symposium, vol. 2, Rome, 1979; CEB-FIP, B.I. no. 132, Paris, 1979.
19. CEB-FIP - International Recommendations (vol. I - Structural Concrete; vol. II - Concrete Structures), Comité Euro-Internationale du Béton - Fédération Internationale de La Précontrainte, Cement and Concrete Association Edition, London, 1978.

20. E. Chwalla - "Die Formeln zur Berechnung der 'voll mittragenden Breite' dünner Gurt - und Rippenplatten," *Der Stahlbau*, no. 10, 1936.
21. R. Clough and J. Penzien - Dynamics of Structures, McGraw-Hill, New York, 1975.
22. M. Collins and S. Chockalingam - "Reinforced Concrete Beams under Reversed Cyclic Torsional Loading," CEB, Bulletin d'Information no 132, vols. 2 and 3, Paris, April, 1979.
23. DIN 1045 - Beton - Kalendar 1984, DIN 1045 (Ausgabe 1978), Beton und Stahlbeton Bernennung und Ausföhrung, Wilhelm Ernst und Sohn Verlag, Berlin, 1984.
24. F. Dischinger - "Massivbau," in *Schleichem: Taschenbuch für Bauingenieure*, Berlin, 1943.
25. D. Dowrick - Earthquake Resistant Design, J. Wiley and Sons, Chichester, U.K., 1978.
26. R. Fenwick and H. Irvine - "Reinforced Concrete Beam-Column Joints for Seismic Loading," Part I - Theory (September 1977, and Part II - Experimental Results (December 1977); *Bulletin of the N.Z.N.S.E.E.*, vol. 10, nos. 3 and 4, 1977.
27. R. Fenwick and H. Nguyen - "Reinforced Concrete Beam-Column Joints for Seismic Loading," Report no. 220, Department of Civil Engineering, University of Auckland, New Zealand, January, 1981.
28. P.M. Ferguson - Reinforced Concrete Fundamentals, 4th ed., J. Wiley and Sons, New York, 1979.
29. R.W. Furlong - "Ultimate Strength of Square Columns under Biaxially Eccentric Loadings," *Journal of the ACI*, no. 9, March 1961.
30. Y. Higashi and Y. Ohwada - "Failing Behaviors of R/C Beam-Column Connections Subjected to Lateral Load," *Memoirs of the Faculty of Technology, Tokyo Metropolitan University*, Tokyo, Japan, 1969.

31. T. Hisada, N. Ohmori and S. Bessho - "Earthquake Design Considerations in Reinforced Concrete Columns," International Journal of Earthquake Engineering and Structural Dynamics (E.E.S.D), vol. 1, July-September, 1972.
32. G. Housner and P. Jennings - "The San Fernando California Earthquake," International Journal of Earthquake Engineering and Structural Dynamics (E.E.S.D.), vol. 1, no. 1, July-September, 1972.
33. B. Jacobsen - "Cyclic Torsion Tests of Concrete Box Columns," Report No. 80-2, Division of Structural Mechanics, The Norwegian Institute of Technology, The University of Trondheim, September, 1980.
34. J.O. Jirsa - "Beam-Column Joints: Irrational Solutions to a Rational Problem," Chester P. Siess Symposium, ACI SP-72, Detroit, MI, 1972.
35. J.O. Jirsa (Chr.), ACI-ASCE Committee 352 - "Recommendations for Design of Beam-Column Joints in Monolithic Reinforced Concrete Structures," Journal of the ACI, July, 1976.
36. J.O. Jirsa, K. Maruyama and H. Ramirez - "Reinforced Concrete under 3-D Loading Histories," Paper submitted at the ACI Convention, Houston, November, 1978.
37. M. Joglekar - "Behavior of Reinforced Concrete Floor Systems under Lateral Loads," Ph.D. Dissertation, The University of Texas at Austin, December, 1984.
38. The Joint Committee on Standard Specifications for Concrete, - "Report of the Joint Committee on Standard Specifications for Concrete and Reinforced Concrete," Proceedings of the ACI, vol. 21, 1928.
39. Theodore von Karman - "Die mittragende Breite," August Foppl - Festschrift, 1924.
40. W.T. Koiter - "General Theorems for Elasto-Plastic Solids," Chapter IV, Progress in Solid Mechanics, I.N. Sneddon and R. Hill, eds., vol. I, North Holland Publishing Co., Amsterdam, 1960.
41. P. Kuhn - Stresses in Aircraft and Shell Structures, McGraw-Hill Co., New York, 1956.

42. A. Lamas - "O Problema do 'Shear Lag' na Analise de Estruc-turas," Seminario 296, Laboratorio Nacional de Engenharia Civil, Lisboa, 1982.
43. R. Leon - "The Influence of Floor Members on the Behavior of Reinforced Concrete Beam-Column Joints Subjected to Severe Cyclic Loading," Ph.D. Dissertation, The University of Texas at Austin, December 1983.
44. F. Leonhardt - Construccoes em Concreto: vol. VI - (1979) - Principios Basicos da Construccao de Pontes de Concreto; Interciencia, Rio de Janeiro, 1979; (Portuguese Translation of: "Vorlesungen uber Massivbau - Sechster Teil. 1 Grundlagen des Massivbruckenbaues;" Springer-Verlag, Berlin/Heidelberg, 1979)
45. F. Leonhardt and E. Monnig - Construccoes de Concreto: vol. I - (1977) Principios Basicos de Dimensionamento de Estructuras de Concreto Armado; vol. III (1978) - Princi-pios Basicos sobre a Armacao de Estructuras de Concreto Armado; Interciencia, Rio de Janeiro, 1977, 1978; (Portu-guese Translation of: Vorlesungen uber Massivbau - Erster Teil: Grundlagen zur Bewassung in Stahlbeton; - Dritter Teil: Grundlagen zum Bewehren in Stahlbetonbau; Springer-Verlag, Berlin/Heidelberg, 1973, 1974, 1976, 1978).
46. J. MacGregor - "Safety and Limit States Design for Reinforced Concrete," Canadian Journal of Civil Engineering, vol. 3, no. 4, December, 1976.
47. L. Megget - "Cyclic Behavior of Exterior Reinforced Concrete Beam-Column Joints," Bulletin of the N.Z.N.S.E.E., vol. 7, no. 1, March, 1974.
48. D. Meinheit and J.O. Jirsa - "Shear Strength of R/C Beam-Column Connections," Journal of the Structural Division, ASCE, ST 11, November, 1982.
49. W. Metzger - Die mittragende Breite, Luftfahrtforschung, 1929.
50. V. Mikhailov - "Triaxially Prestressed Members," Proceedings of 6th Congress of the Federation Internationale de la Precontrainte, Prague, 1970.

51. D. Mitchell and M. Collins - "Diagonal Compression Field Theory - A Rational Method for Structural Concrete in Pure Torsion," Journal of the ACI, vol. 71, August, 1974.
52. K. Moffat and P. Dowling - "Steel Box Girders, Parametric Study on the Shear Lag Phenomenon in Steel Box Girder Bridges," CESLIC Report BG 17, Engineering Structures Laboratories; Imperial College of Science and Technology, London, 1972.
53. K. Moffat and P. Dowling - "Shear Lag in Steel Box Girder Bridges," The Structural Engineer, October, 1975, no. 10, vol. 53.
54. J. von Neumann and O. Morgenstern - Theory of Games and Economic Behavior, Princeton University Press, Princeton 1953.
55. New Zealand Standard - NZS: 3101 - The Design of Concrete Structures - Code of Practice and Commentary; Standards Association of New Zealand (SANZ), Wellington, 1982.
56. I. Nilsson and A. Losberg - "Reinforced Concrete Corners and Joints Subjected to Bending Moment," Journal of the Structural Division, ASCE, ST6, June, 1976.
57. R. Park - "Ductility of Reinforced Concrete Frames under Seismic Loading," New Zealand Engineering, November, 1968.
58. R. Park - "Accomplishments and Research and Development Needs in New Zealand," Proceedings of a W.E.R.R.C.B.C., vol. 2, University of California, Berkeley, June, 1978.
59. R. Park - "Review of Code Developments for Earthquake Resistant Design of Concrete Structures in New Zealand," Bulletin of the N.Z.N.S.E.E., vol. 14, no. 4, December, 1981.
60. R. Park and T. Paulay - Reinforced Concrete Structures, J. Wiley and Sons, New York, 1975.
61. T. Paulay - "Capacity Design of Reinforced Concrete Ductile Frames," Proceedings of a W.E.R.R.C.B.C., vol. 3, University of California, Berkeley, June, 1978.

62. T. Paulay - "Developments in the Seismic Design of Reinforced Concrete Frames in New Zealand," Canadian Journal of Civil Engineering, vol. 9, no. 2, June, 1981.
63. T. Paulay and A. Scarpas - "The Behavior of Exterior Beam-Column Joints," Bulletin of the N.Z.N.S.E.E., vol. 14, no. 3, September, 1981.
64. T. Paulay and R. Park - "Joints in Reinforced Concrete Frames Designed for Earthquake Resistance," Research Report R. 84-9, University of Canterbury, Christchurch, New Zealand, June, 1984.
65. T. Paulay and A. Scarpas - "The Behavior of Exterior Beam-Column Joints," Bulletin of the N.Z.N.S.E.E., vol. 14, no. 3, September, 1981.
66. T. Paulay and R. Williams - "Section B: The Analysis and Design of and the Evaluation of Design Actions for Reinforced Concrete Ductile Shear Wall Structures," Bulletin of the NZNSEE, vol. 13, no. 2, June 1980.
67. D. Pecknold and M. Siharwardy - "Effects of Two Dimensional Earthquake Motion on Response of R/C Columns," Proceedings of a W.E.R.R.C.B.C., University of California, Berkeley, June, 1978.
68. P. Pinto - CEB Task Group on Seismic Design - CEB Model Code for Seismic Design of Concrete Structures; CEB, Bulletin d'Information, no. 165, Paris, April, 1985.
69. C. Pinkham (Chr.), ACI-ASCE Committee 352 - "Recommendations for Design of Beam-Column Joints in Monolithic Reinforced Concrete Structures," Journal of the ACI, no. 3, Proc. vol. 82, May-June, 1985.
70. E. Popov - "Seismic Behavior of Structural Subassemblages," Journal of the Structural Division, ASCE, ST7, July, 1980.
71. E. Popov, V. Bertero, B. Galunic and G. Lantaff - "On Seismic Design of R/C Interior Beam-Column Joints of Frames," Proceedings of the 6th WCEE, New Delhi, India, 1977.
72. H. Schade - "The Effective Breadth of Stiffened Plating under Bending Loads," The Society of Naval Architects and Marine Engineers (N.A & M.E.), Transactions, vol. 59, New York, 1951.

73. H. Schade - "The Effective Breadth Concept in Ship-Structure Design," The Society of N.A. & M.E., Transactions, vol. 61, New York, 1953.
74. SEAOC - Recommended Lateral Force Requirements and Commentary, Seismology Committee, Structural Engineers Association of California (SEAOC), San Francisco, 1975.
75. M. Seckin and S. Uzumeri - "Behavior of Reinforced Concrete Beam-Column Joints Subjected to Slow Load Reversals," Publication 74-05, Department of Civil Engineering, University of Toronto, Canada, March, 1974.
76. S.I.A. - Normes Concernant les Constructions en Beton, en Beton Armeé et en Beton Precontraint. Normes Techniques S.I.A. n^o. 162, Societe Suisse des Ingenieurs et des Architectes, Zurich, 1956.
77. D. Soleimani, E. Popov and V. Bertero - "Hysteretic Behavior of Reinforced Concrete Beam-Column Subassemblages," Journal of the ACI, Vol. 76, no. 11, November, 1979.
78. K. Takiguchi, S. Kokusho and K. Ohada - "Analysis of Reinforced Concrete Sections Subjected to Biaxial Bending Moments," Transactions of the Architectural Institute of Japan (A.I.J.), no. 250, December, 1976.
79. H. Takizawa - Technical note on: "Biaxial Effects in Modeling Earthquake Response of R/C Structures," International Journal of the E.E. & S.D., vol. 4, no. 6, October-December, 1976.
80. H. Takizawa and H. Aoyama - "Biaxial Effects in Modeling Earthquake Response of Reinforced Concrete Structures," International Journal of the E.E. & S.D., vol. 4, no. 6, October-December, 1976.
81. T. Tassios - "Properties of Bond Between Concrete and Steel under Load Cycles Idealizing Seismic Actions," CEB-B.I. no. 131, Paris, 1979.
82. T. Tassios (Reporteur), "CEB General Task Group 10: Response of Structural Concrete Critical Regions under Large Amplitude Reversed Actions," C.E.B., Bulletin d'Information no. 161, Paris, August, 1983.

83. B. Thurlimann - "Plastic Analysis of Reinforced Concrete Beams," Introductory Report of I.A.B.S.E. Colloquium-Plasticity in Reinforced Concrete, Kopenhagen, 1979; IABSE, Zurich, 1979.
84. S. Tobrunner - "A History of Reinforced Masonry Construction Designed to Resist Earthquakes: 1755-1907," Earthquake Spectra, The Professional Journal of the E.E.R.I., vol. 1, no. 1, November, 1984.
85. H. Umemura and H. Takazawa - Dynamic Response of Reinforced Concrete Buildings, Structural Engineering Documents no. 2, I.A.B.S.E., Zurich, 1982.
86. S. Uzumeri - "Strength and Ductility of Cast-In-Place Beam-Column Joints," Paper no. 12, Reinforced Concrete Structures in Seismic Zones, ACI SP-35, August, 1977.
87. A. Vasiliev, Y. Bichenkov and N. Matrov - "Prefabricated Reinforced Concrete Multistorey Frame Buildings in the USSR," Proceedings of the International Conference on Planning and Design of Tall Buildings, vol. I-a - Systems and Concepts, ASCE-IABSE, Lehigh University, Pittsburgh, Pa, 1972.
88. D. Williams - Theory of Aircraft Structures, Edward Arnold Ltd., London, 1960.
89. G. Winter - "Strength of Thin Steel Compression Flanges," Cornell University, Engineering Experiment Station, Bulletin no. 35, Part 3, October, 1947.
90. I. Youille - "Shear Lag in Stiffened Plating," Transactions of the Society of N.A. & M.E., vol. 61, New York, 1953.
91. L. Zhang and J.O. Jirsa - "A Study of Shear Behavior of Reinforced Beam-Column Joints," Phil M. Ferguson Engineering Structural Laboratory, Report no. 82-1, The University of Texas at Austin, February, 1982.

CHAPTER III

THE US-JAPAN COOPERATIVE EARTHQUAKE ENGINEERING PROGRAM

3.1 The Cooperative Research Program

3.1.1 Introduction. In 1968, the Tokachi-Oki (Japan) and in 1971 the San Fernando (U.S.A.) earthquakes, caused extensive damage to modern reinforced concrete structures. Serious questions were raised regarding the validity of design provisions and recommendations. The urgent need to upgrade and implement sound design recommendations and expand the available scientific knowledge prompted a series of seminars between U.S. and Japanese engineers. The purpose of the seminars was: (1) to learn from the experience of the Tokachi-Oki and other earthquakes; (2) to review and/or change building codes; (3) to improve design and construction practices; and, (4) to initiate cooperative research programs.

The first 1968 Tokachi-Oki earthquake inflicted serious damages in school buildings, and led to the U.S.-Japan Joint Seminar on Earthquake Engineering with Emphasis on Safety of School Buildings held in 1970 in Sendai, Japan. The second 1971 San Fernando earthquake led to a U.S.-Japan Cooperative Science Program held in 1973 in Berkeley, California. Here, particular attention was given to means of upgrading the resistance of existing buildings and post-earthquake damage repair techniques.

The review of the School Buildings Safety research program in 1975 at the University of Hawaii meeting resulted in a broader U.S.-Japan Cooperative research program. The need for controlled dynamic testing of large scale building systems in the field, in the laboratory and on large-size shaking table was delineated. Such tests would provide valuable information on: (1) force-deformation characteristics; (2) energy-absorption; and (3) failure patterns. In 1977 funds were made available for the organization and planning of the US-Japan Cooperative Research Program Utilizing Large-Scale Testing Facilities under the auspices of the U.S.-Japan Panel on Wind and Seismic Effects, United States - Japan Natural Resources (U.J.N.R.) Program [Penzien and Umemura (11)].

3.1.2 Objectives of the Cooperative Research Program.

The two main objectives were:

1. Improve the scientific knowledge and engineering practices currently used in the design and construction of seismic-resistant structures; and,
2. Correlate the information (test results) obtained from the prototype, full-scale structure under seismic-type loading with small-to-medium scale and component tests. In parallel with experimental work analytical studies were to be used to verify the validity of the assumptions formulated, to forecast

the possible response of the test specimens and to ascertain the deviation in response of the analytical model from the test specimen. The priority in choosing the materials to be used in the test specimens was imposed as follows: (1) reinforced concrete; (2) structural steel; (3) precast prestressed concrete; (4) composite steel-reinforced concrete; (5) masonry; and, (6) timber.

3.1.3 Tests of Reinforced Concrete Structures. The reinforced concrete test series included the design, construction and testing of:

1. A full-scale seven story R/C building structure that reflected a compromise between current (1978) design and construction practices used in the U.S. and Japan. The structure was tested at the Building Research Institute (B.R.I.), Tsukuba Science City, Japan, in 1980-1981;
2. Supporting tests to be conducted in both the U.S. and Japan on subassemblage specimens (both full-scale and reduced scale), components, and scale models of the full-scale structure (static and dynamic tests).

The planned initial test series is shown in Table 3.1 [Penzien and Umemura (11)]. The actual tests performed were more limited due to time and budget constraints, Table 3.2 [Wight (14)].

The correlation study developed in this report involves a comparison of the response of critical regions in the full-scale building (level Z2) with subassemblage tests modelled after those regions. The subassemblage tests to be considered include the full-scale specimens (University of Texas at Austin), the 1:12.5-scale specimens (Stanford University) and the Japanese 1:2-scale specimens, representing both the exterior and the interior beam-column joint regions to be found at level Z2 of the full-scale building.

3.2 The Japanese Participation

3.2.1 The Full-Scale Building. The design and construction of the full-scale 7-story building tested at the B.R.I. (Japan) was an amalgam of engineering techniques used in both countries. Three construction techniques used deserve special mention. First, the gas pressure welding technique (effect of Joule) commonly used in Japan was initially planned to be applied in all the main longitudinal bars of beams and columns. However, pressure welds were used only on the foundation and the column splices. Lap splices were used for all

TABLE 3.1 - INITIAL US-JAPAN COOPERATIVE
RESEARCH PROGRAM.

<p>A. JAPAN</p> <p>1. FULL-SCALE BUILDING STRUCTURE - 1 specimen (7 storeys)</p> <p>2. ASSOCIATED TESTS -</p> <p>a. Joint Assemblies - quasi-static 1/2-scale tests</p> <p>1. Exterior beam-column - 3 specimens</p> <p>2. Interior beam-column - 4 specimens</p> <p>3. Top floor exterior beam-column - 2 specimens</p> <p>4. Wall-beam - 2 medium scale walls with 3 or 4 storeys.</p> <p>b. Planar Structures - quasi-static full-scale tests</p> <p>1. Wall-frame systems - 3 or 4 storeys</p> <p>2. Plane frame.</p> <p>c. Shaking-table tests - full-scale tests</p> <p>1. Frame model - 3 storeys.</p> <p>B. U.S.A.</p> <p>1. ASSOCIATED TESTS -</p> <p>a. Joint Assemblies - quasi-static tests</p> <p>1. Exterior beam-column - 3 specimens</p> <p>2. Interior beam-column - 2 specimens</p> <p>3. Wall-beam - 2 specimens</p> <p>b. Planar Structures - quasi-static tests</p> <p>1. Isolated wall - medium-scale</p> <p>2. Wall-frame</p> <p>3. Plane frame</p> <p>c. Shaking-table Tests - 1:10 scale models of B.R.I. structures</p> <p>1. "Bare" structures</p> <p>2. Bare structure and non-structural components</p> <p>3. Structure with non-structural features</p> <p>d. Shaking-table Tests - medium-scale [1:3] tests</p> <p>1. Test 1 - without non-structural components (free forced vibration)</p> <p>2. Test 2 - with non-structural components.</p>	
--	--

TABLE 3.2 - ACTUAL US-JAPAN COOPERATIVE
RESEARCH PROGRAM.

<p>A. JAPAN</p> <p>1. FULL-SCALE BUILDING STRUCTURE - BRI building [1 spec.]</p> <p>2. ASSOCIATED TESTS -</p> <p>a. Joint Assemblies - quasi-static 1/2-scale tests</p> <p>1. Exterior beam-column - 3 specimens</p> <p>2. Interior beam-column - 3 specimens</p> <p>3. Exterior beam-top column - 2 specimens</p> <p>4. Shear wall-to-beam - 2 specimens (3 storeys)</p> <p>b. Shaking-table Tests - 1/2-scale tests</p> <p>1. Two-storey frame - 2 specimens</p> <p>c. Pseudo-dynamic Tests</p> <p>1. Two-storey frame - 2 specimens</p> <p>B. U.S.A.</p> <p>1. ASSOCIATED TESTS -</p> <p>a. Joint Assemblies - quasi-static tests</p> <p>1. Full-scale Tests - University of Texas at Austin</p> <p>1.1. Interior beam-column - 2 specimens w/ slab</p> <p>1.2. Exterior beam-column - 2 specimens w/ slab</p> <p>2. Small-scale Tests - Stanford University</p> <p>2.1. Interior beam-column - 2 specimens w/ slab and 1 specimen w/o slab</p> <p>2.2. Exterior beam-column - 2 specimens w/ slab and 1 specimen w/o slab</p> <p>b. Planar Structures - quasi-static tests</p> <p>1. Medium-scale Tests - 1:3.5 at the P.C.A.</p> <p>1.1. Shear wall-frame - 1 specimen</p> <p>1.2. Cantilever wall - 1 specimen</p> <p>2. Small-scale Tests - 1:12.5 Stanford University</p> <p>2.1. Shear wall-frame - 1 specimen</p> <p>2.2. Cantilever wall - 1 specimen</p> <p>c. Shaking-table Tests -</p> <p>1. Medium-scale tests - 1:5 U. of California at Berkeley - 7 storey BRI bldg.</p> <p>2. Small-scale tests - 1:10 U. of Illinois at U.-C. - 2 frames and 1 shear wall tested simultaneously no slab coupling</p>	
---	--

the beams, slabs and shear walls. Second, the building was cast following the Japanese tradition of placing all the concrete for the walls and columns in a given floor level as well as the beams and slabs of the next floor level. In current U.S. practice, the walls and columns are cast first with a construction joint at the soffit and at the top of the floor system.

Finally, some concern on the strength of the reaction wall at the B.R.I. led to a reduction in reinforcement ratios of the structural members (beams, slabs, columns, walls). Consequently, a very ductile low-reinforcement ratio building was constructed which is also common practice in Japan, [Wight, Nakata and Kaminosono (15)]. The building structure was firmly anchored to the strong floor and the lateral load conditions are simulated by means of hydraulic rams reacting against a strong wall, Fig. 3.1.

3.2.1.1 The Specimen Geometry. The B.R.I. building consisted of three main longitudinal frames (A, B, C) aligned along the plane of loading (N-S direction). Furthermore, the intermediate frame B is of the dual-type, i.e., frame-shear wall, where the shear wall completely infills the central 5.00 m span with a nominal thickness of 0.20 m (8.0 in.), Fig. 3.2.

In the transverse direction, four frames (1, 2, 3, 4) and the cast-in place R/C transverse beams and slab connect the three longitudinal frames. The end transverse frames also had a

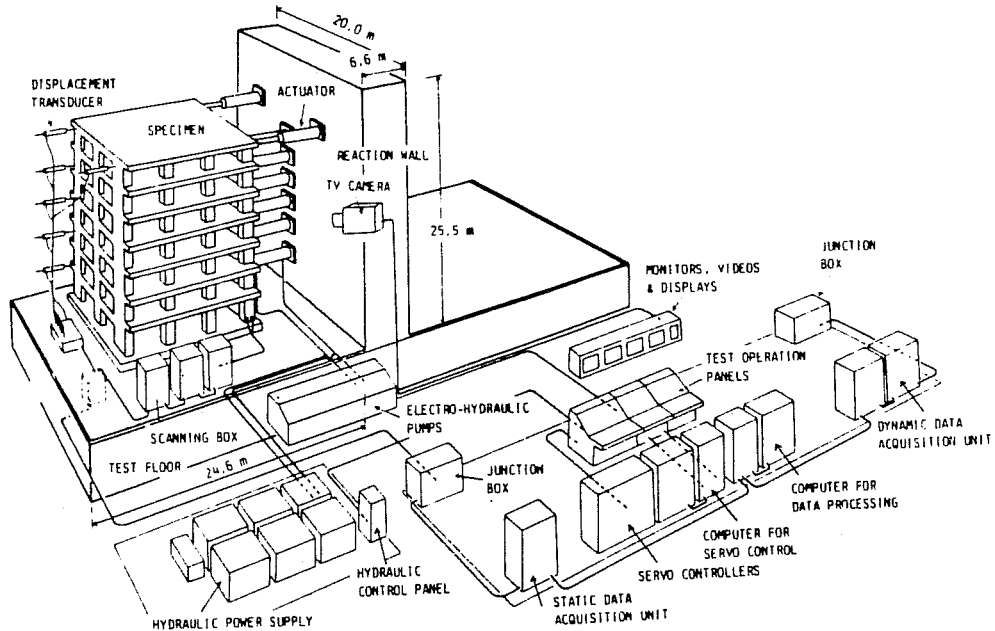


Fig. 3.1 - Full-Scale Seven-Story Building.

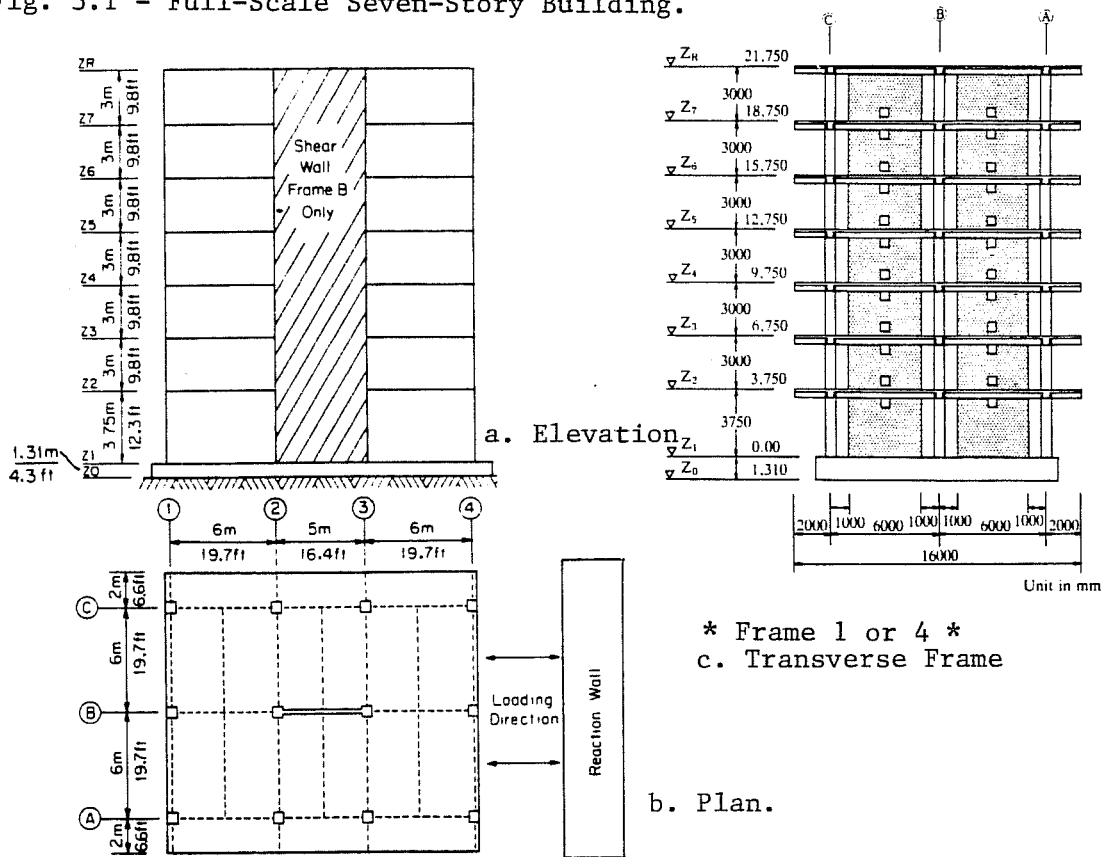
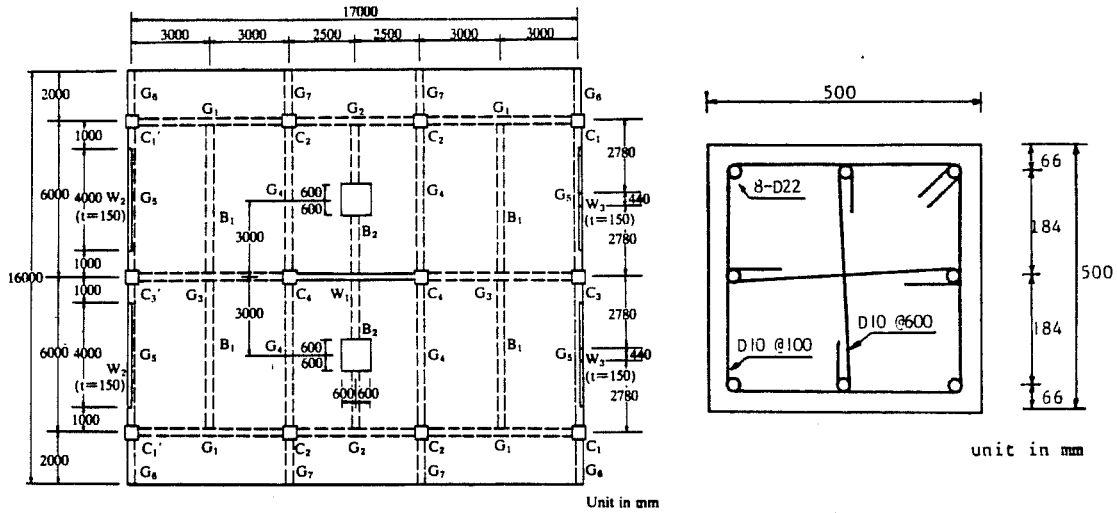


Fig. 3.2 Building Geometric Characteristics.

0.15 m (6.0 in.) thick shear walls (spandrel walls) in spans A-B and B-C. The spandrel walls did not frame into the columns. A 0.75 m (30.0 in.) gap between the spandrel wall and the column was needed for instrumentation beams supported by a frame on the extension of the test structure. The main objective of the spandrel walls was to limit lateral, out-of-plane displacements by increasing the torsional stiffness of the whole building, Fig. 3.2(c). The member cross-sections were kept constant throughout the height: (1) 0.50 m x 0.50 m (20-in. x 20-in.) columns; (2) 0.30m x 0.50m (12-in. x 20-in.) longitudinal beams; and, (3) 0.30m x 0.45m (12-in. x 18-in.) transverse beams, Fig. 3.3(a)(b), (c). The slab had the same thickness 0.12m (approx. 5.0 in.) in all seven floors, Fig. 3.3(e).

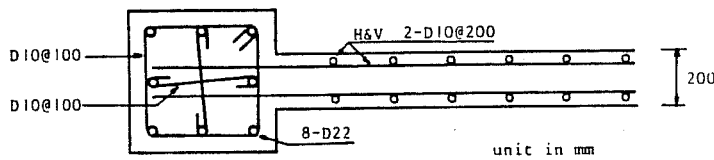
3.2.1.2 The Material Properties. The building was constructed with ready-mix concrete with a nominal strength of 270 Kgf/cm² (3840 psi) and a class SD 35 reinforcement (35 Kgf/mm²; Grade 50).

The observed concrete properties varied particularly, the sixth and seventh story compressive strengths obtained from field cured cylinders, which showed a significantly lower value than the specified strength, Table 3.3. However, complementary tests carried on standard cured cylinders and concrete cores extracted from the undamaged part of the structure after the test, did not show the above mentioned strength decrease.

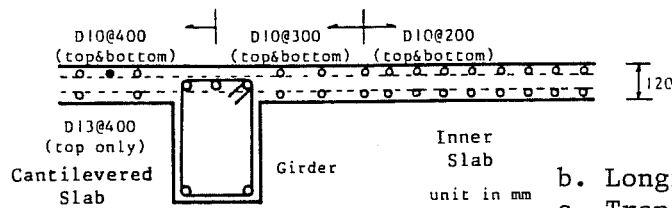


* Plan *

a. Column.



unit in mm



Inner Slab
unit in mm

b. Longitudinal Beam

c. Transverse Beam

d. Slab and Beam.

MARK	G ₁ , G ₃ (300 x 500)		G ₂ (300 x 500)	
	END	CENTER	END	CENTER
SECTION (STIRRUP)				
MARK	G ₄ (300 x 450)		G ₅ (300 x 450)	
POSITION	END	CENTER	END	CENTER
SECTION (STIRRUP)				

Fig. 3.3 - Building Cross Section Details.

TABLE 3.3 - BUILDING CONCRETE CHARACTERISTICS.

Story		1	2	3	4	5	6	7	Average
1. Four week Strength	Standard curing	F _c 311	—	303	343	351	305	332	324.17
	Field curing	F _c 253	259	237	241	250	—	—	248.00
2. Concrete cylinder test before the structural test March 20, 1981	F _c	289.38	291.63	274.00	290.38	294.50	143.88	188.88	253.24
	F _t	24.20	24.55	22.76	23.28	23.61	13.61	13.27	20.70
	E _t	2.72	2.91	2.79	2.92	3.08	1.92	2.15	2.64
	E _w	2.62	2.59	2.45	2.46	2.46	1.78	2.00	2.34
	E _d	3.64	3.60	3.42	3.51	3.62	2.66	3.05	3.36
3. Concrete cylinder test before the repair test July 14, 1981	F _c	283.75	270.25	260.67	289.00	291.50	152.75	196.63	249.22
	F _t	23.75	19.84	17.98	17.34	24.64	11.48	17.43	18.92
	E _t	2.22	2.45	2.31	2.19	2.29	2.64	2.26	2.19
	E _w	2.16	2.70	2.07	2.29	2.72	1.73	2.08	2.25
	E _d	2.80	2.82	2.57	2.69	2.84	2.06	2.70	2.64
4. Concrete cylinder test after the repair test January 27, 1982	F _c	286.38	288.50	267.25	290.63	312.50	160.95	208.95	259.27
	F _t	24.20	23.58	21.68	23.46	25.07	17.72	20.77	22.35
	E _d	2.30	2.27	1.94	2.05	2.35	1.63	1.80	2.05
	E _w	2.15	2.09	2.00	2.06	2.52	1.60	2.04	2.07
	E _d	2.95	3.02	2.98	2.93	3.31	2.38	2.69	2.89
5. Test of Concrete core, after the repair test February 18, 1982	F _c	429.18	398.14	359.81	410.68	439.90	368.90	376.10	397.53
	E _t	2.81	2.45	2.26	2.52	2.68	2.35	2.51	2.51
	E _d	2.46	2.54	2.54	2.29	2.37	2.24	2.37	2.40
6. Total Average from 2 to 5	F _c	289.82							
	E _t	2.35							
	E _d	2.82							

F_c : Compressive strength (kg/cm²)F_t : Tensile Strength (kg/cm²)E_t : 1/3 secant modulus of elasticity measured by displacement transducer (x100000 kg/cm²)E_w : 1/3 secant modulus of elasticity measured by wire strain gauge (x100000 kg/cm²)E_d : dynamic elasticity measured by super-sonic (x100000 kg/cm²)

TABLE 3.4 - BUILDING STEEL PROPERTIES.

Reinforcing bar	Number of test pieces	Yield stress (ton/cm ²)	Maximum Stress (ton/cm ²)	Yield strain (%)	Strain hardening strain (%)	Elongation (%)	Elastic modulus (x1000ton/cm ²)
D-10	12	3.700	5.585	0.1999	1.738	19.62	1.890
D-13	9	3.740	5.500	0.1966	2.017	19.20	1.901
D-16	3	3.847	5.722	0.2025	1.866	17.47	1.900
D-19	13	3.660	5.470	0.1933	1.284	21.96	1.903
D-22	13	3.780	5.960	0.1981	1.390	23.28	1.913
D-25	9	3.720	5.680	0.1917	1.653	24.81	1.949

Bar Diameter	$\frac{\sigma_u}{\sigma_y}$	$\frac{\epsilon_{sth}}{\epsilon_y}$	$\frac{\epsilon_u}{\epsilon_{sth}}$	$\frac{\epsilon_u}{\epsilon_y}$	Obs.
D - 10 (mm)	1	1.47	10.2	9.7	98.8
	2	1.475	8.8	10.4	91.3
	3	1.49	8.0	12.7	101.6
D - 13 (mm)	1	1.44	9.9	9.5	93.7
	2	—	—	—	—
	3	1.49	10.5	11.0	115.6
D - 16 (mm)	1	1.49	9.2	9.4	86.3
	2	—	—	—	—
	3	—	—	—	—
D - 19 (mm)	1	1.19*	7.7	11.3	86.8
	2	1.57	7.7	16.0	123.5
	3	1.60	5.2	22.9	119.9
D - 22 (mm)	1	1.54	8.0	9.0	72.5
	2	1.63	6.5	23.9	155.3
	3	1.57	6.6	17.6	115.8
D - 25 (mm)	1	1.5	11.0	9.2	102.0
	2	—	—	—	—
	3	1.54	7.7	18.7	143.5

* very low σ_u

The SD 35 reinforcement had reasonable ductility, i.e., large yield plateau, Table 3.4 Based on the available data a f_u^S/f_y^S ratio of ± 1.5 and an ultimate steel strain $\epsilon_s^u = 20\%$ was consistently observed.

3.2.1.3 The Loading Program. The complete test sequence that was applied to the building is shown in Table 3.5 Two major test sequences can be differentiated: first, the group of tests applied to the undamaged structure; and second, the after-repair test series. Only the first group is pertinent in the scope of this report and from this subset attention will be focused on the pseudo-dynamic test series (PSD1, PSD2, PSD3 and PSD4).

The pseudo-dynamic (PSD) testing method was used in the testing program after lengthy discussions in the first JTCC meeting where four requirements were agreed upon the testing methodology [Okamoto et al. (10)]:

1. A modified ground motion should be used so that the first vibrational mode of the model would dominate the response;
2. Shear reversal would not occur along the specimen height for the tests where the angle of building rotation was beyond 1/1000;

3. Three complete load reversal cycles at $1/400$ and $3/400$ angles of building rotation would be imposed; and,
4. In the complete test program the model should experience nine complete load reversals.

Based on the above premises, an on-line computer actuator system was used, where the MDOF system was reduced to a SDOF system with the external force distributed in an inverted triangular mode. The inverted triangular displacements were introduced to the specimen through eight hydraulic rams (actuators). At the roof level, two actuators with a capacity of ± 100 ton and a ± 1000 mm stroke each were used. In each of the other floor levels one actuator was used with a capacity of ± 100 ton load and a ± 500 mm stroke, Fig. 3.1 A comparison made between the targeted values and the actual values obtained in the PSD testing sequence is shown in Table 3.6

3.2.1.4 Instrumentation. Instrumentation for the full-scale structure consisted of: (a) displacement measuring devices; and, (b) strain gages [Sattary and Wight (12)].

The displacement measurements of the building and its structural components were made using 183 displacement transducers. The lateral building displacement was measured by an additional group of 8 Linear Voltage Differential Transducers (LVDT). The LVDT's numbered from JB1 to JB8 are shown in Fig.

TABLE 3.5 - BUILDING LOADING PROGRAM.

Test No.	Contents
VT 1	Free & forced vibration tests
FLL 1	Single load application tests
SL 1	Static tests under inverted triangular load distribution
PSD 1	$\delta_{max} = \pm 3mm$ (Rmax=1/7000) MIYAGIKENOKI TOHOKU U. NS Gmax=23.5ga1
PSD 2	$\delta_{max} = \pm 5mm$ (Rmax=1/400) MIYAGIKENOKI TOHOKU U. NS Gmax=105ga1
PSD 3	$\delta_{max} = \pm 163mm$ (Rmax=3/400) 1952 TAFT EW Gmax=320ga1
PSD 4	$\delta_{max} = \pm 290mm$ (Rmax=1/75) TOKACHIOKI HACHINOHE EW Gmax=350ga1
FLL 2	Single load application tests
VT 2	Free & forced vibration tests
Repairs by epoxy injection	
VT 3	Free & forced vibration tests
Arrangement of non-structural elements	
VT 3	Vibration tests
FLL 3	Single load application tests
SL 2	Static tests under inverted triangular load distribution
PSD 5-7	Pseudo-dynamic tests as SDOF system (1/7000 - 3/400)
SL 3	Static tests under uniform load distribution (Rmax=1/50)

TABLE 3.6 - TARGETED VS. ACTUAL RESULTS.

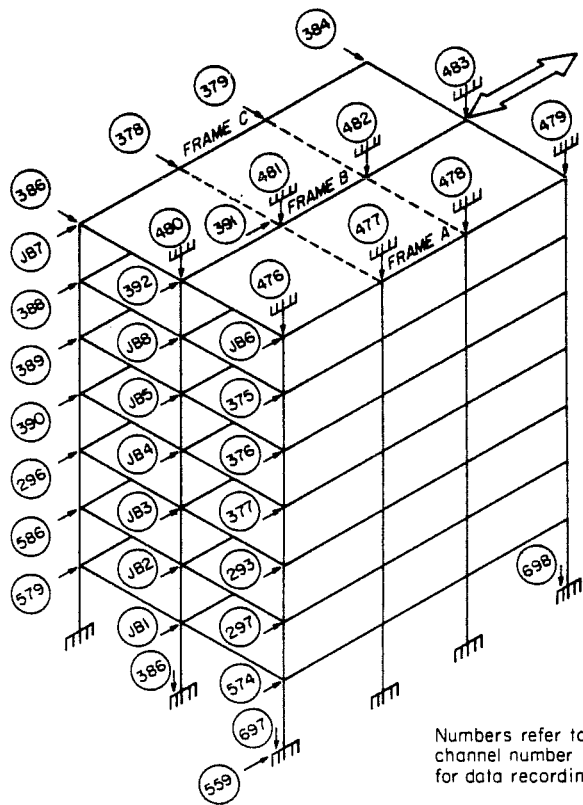
Test No.	Testing Condition	Test Results
PSD 1	TOHOKU-U-NS (Modified) Gmax. = 23.5 gal h = 0 % $\Delta t = 0.01$ sec $\delta_o = \pm 3$ mm R _o = $\pm 1/7000$	$\delta t = 2.5$ mm Rt = 1/8600 Qt = +31.5 ton -15.3 ton
PSD 2	TOHOKU-U-NS (Modified) Gmax. = 105 gal h = 0 % $\Delta t = 0.01$ sec $\delta_o = \pm 55$ mm R _o = $\pm 1/400$	$\delta t = +26$ mm -33 mm Rt = +1/836 Qt = +194.4 ton -224.0 ton
PSD 3	TAFT EW (Modified) Gmax. = 320 gal h = 0 % $\Delta t = 0.01$ sec $\delta_o = \pm 163$ mm R _o = $\pm 3/400$	$\delta t = +238$ mm -223 mm Rt = +1/91 Qt = -1/97 +414.3 ton -409.3 ton
PSD 4	HACHINOHE EW Gmax. = 350 gal h = 0 % $\Delta t = 0.01$ sec $\delta_o = \pm 290$ mm R _o = $\pm 1/75$	$\delta t = +342$ mm -321 mm Rt = +1/64 Qt = -1/68 +432.5 ton -439.0 ton

Gmax : The max. acceleration of input ground motion
h : Damping coefficient in pseudo-dynamic tests
 Δt : Time interval for numerical integration
 $\delta_o, \delta t$: The max. horizontal displacement at the roof floor
(o: Target, t: Realized)
R_o, Rt : The max. angle of rotation (δ / Total height)
Qt : Total shear force

3.4(a). The externally applied actuator loads and displacements, and the external building displacements recorded by the LVDT's had its information stored as channels -6 to -29, Fig. 3.4(b). The lateral displacement response at levels Z2, Z3 and ZR under tests PSD2 to PSD4 is shown in Appendix A.

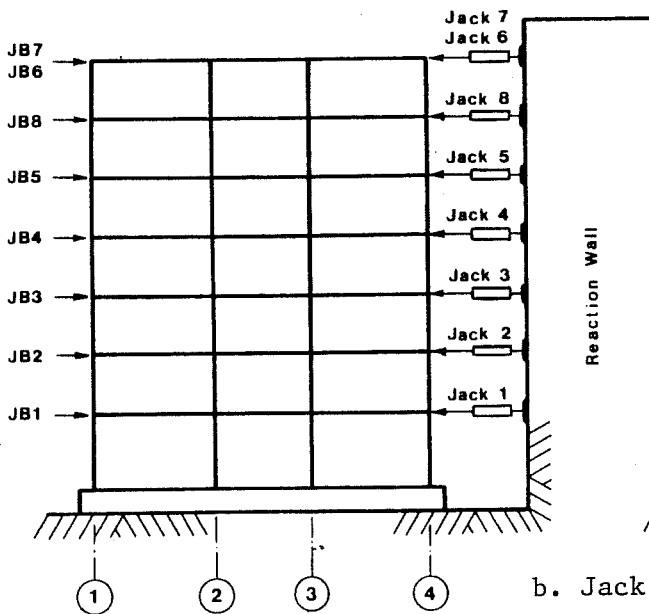
The foundation deformation throughout the PSD testing program was very small and complete rigidity of the base was attained with negligible influence on the building deformation.

The second group of recorded displacements that pertain to this study derive from the spring-loaded displacement transducers to be found at level Z2. Particularly important are the displacement transducers in Frames A and B and in transverse Frame 2, Fig. 3.5, which monitored the beam rotation response in the joint regions. The readings obtained from these instruments had a high noise level, and a low-pass digital filter was designed to eliminate the undesirable noise from the displacement records. This filtering process affects the characteristics of the main response, particularly when the noise frequency is of the same magnitude as the lower frequencies of building response and an error is expected to occur in the vicinity of peak displacements. High frequency random oscillations around the main response were also filtered out. Although this averaging technique becomes unreliable for biased noise cycles, it was



a. External LVDT's.

Numbers refer to channel number for data recording.



Floor Level	Jack	Channels:			
		L	DJ	DB	
Roof	East	6	-21	-22	-23
	West	7	-24	-25	-26
7	8	-27	-28	-29	
6	5	-18	-19	-20	
5	4	-15	-16	-17	
4	3	-12	-13	-14	
3	2	-9	-10	-11	
2	1	-6	-7	-8	

L : Jack Load, Ton
 DB: Building Displacement, mm
 DJ: Jack Displacement, mm

b. Jack Loads and Displacements.

Fig. 3.4 - Displacement Transducer Location.

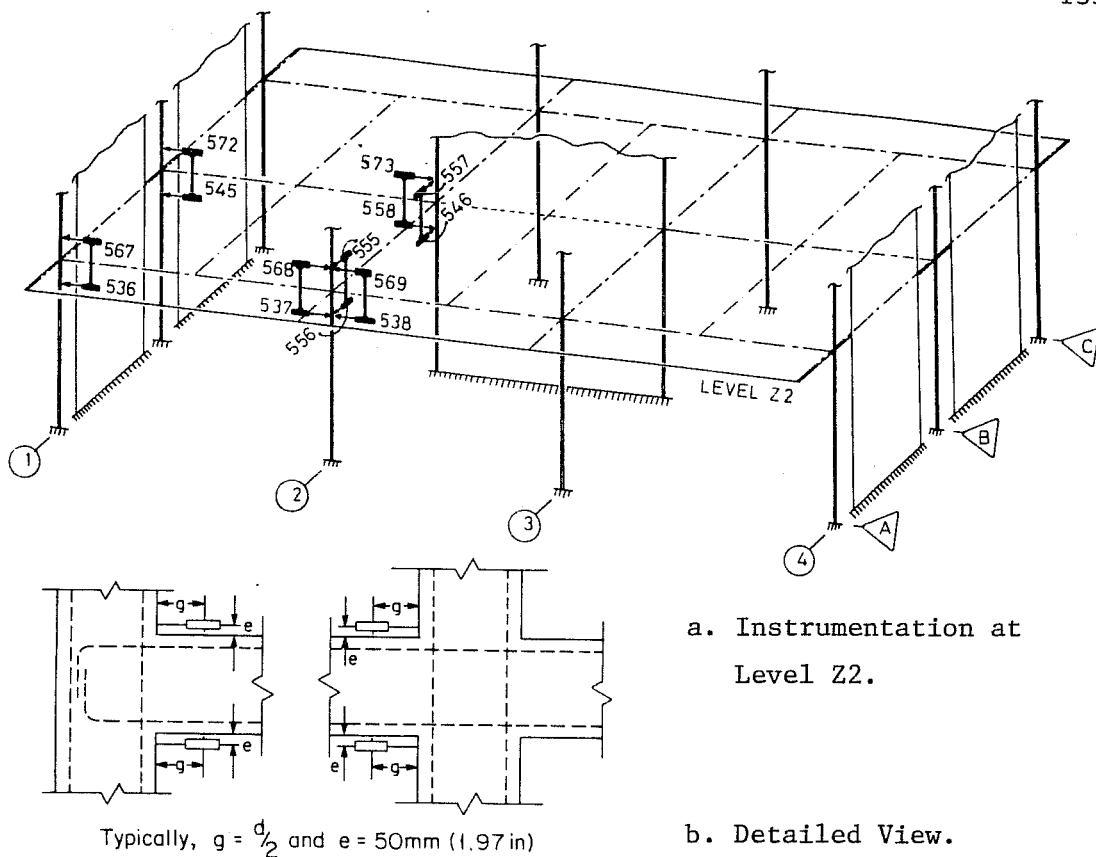


Fig. 3.5 - Building Beam End Rotation Measurements.

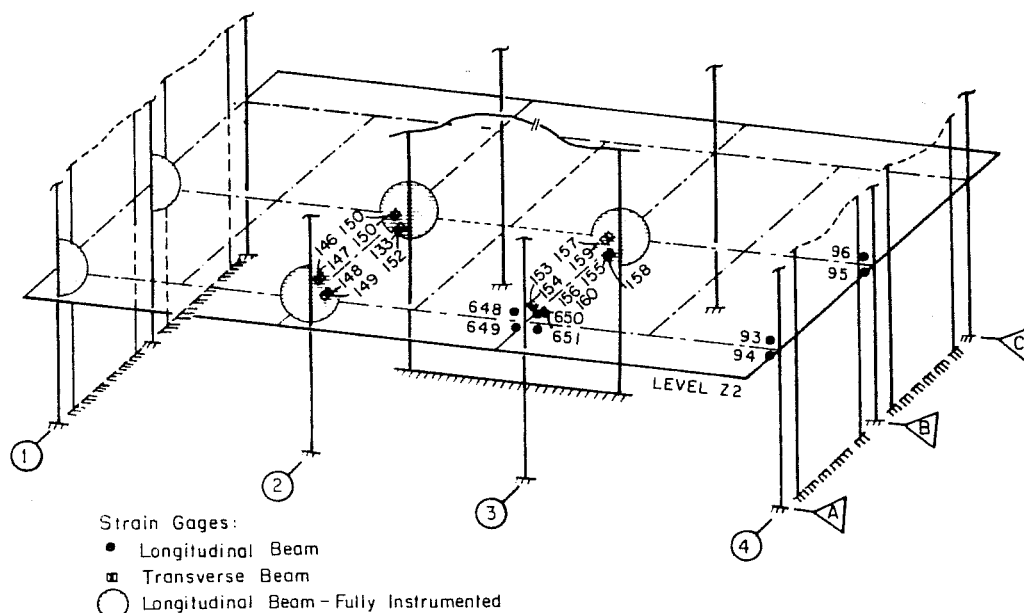
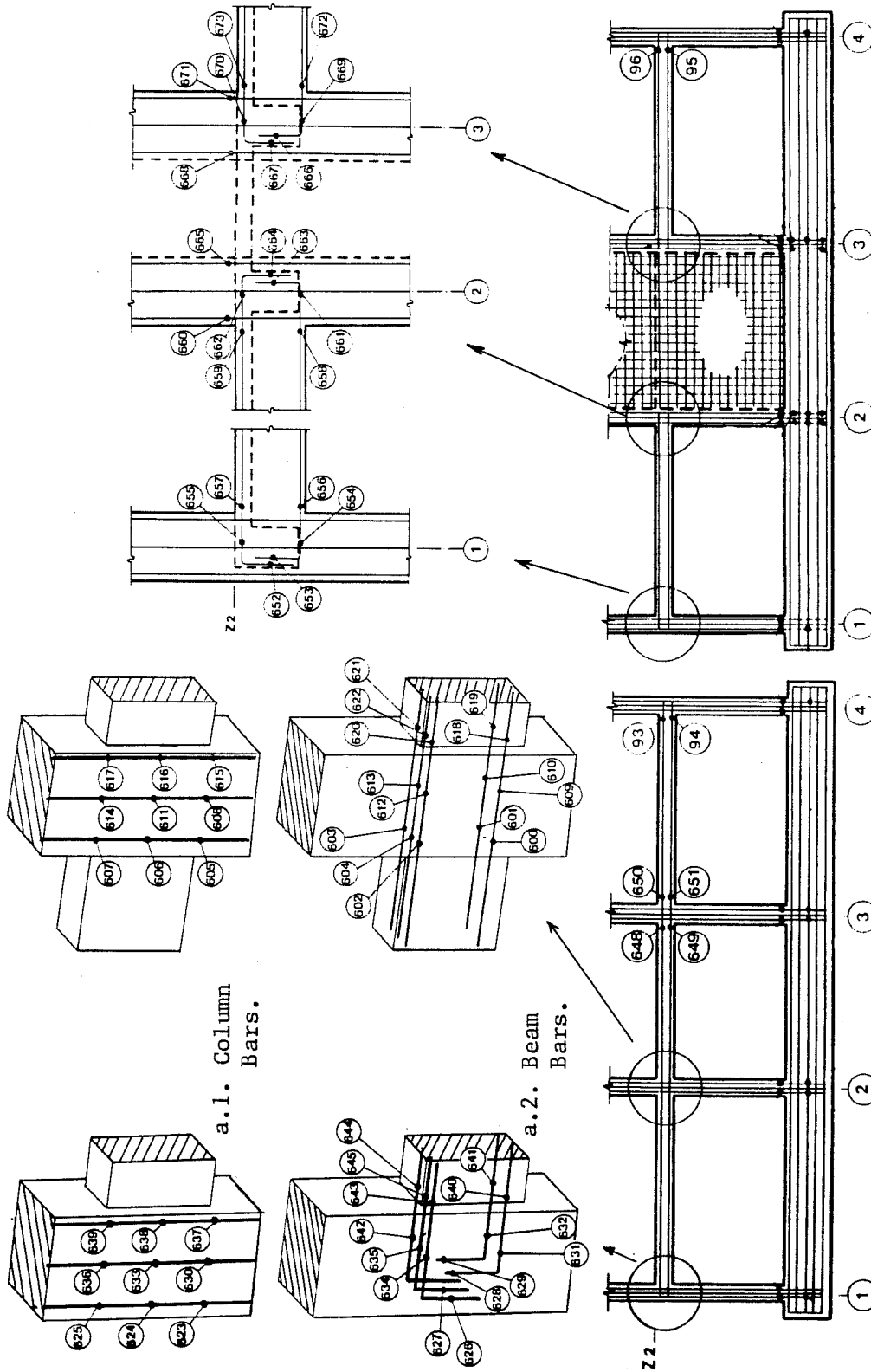


Fig. 3.6 - Building Instrumented Joint Regions at Level Z2.

considered the best solution to obtain the required data [Sattary and Wight (12)].

The beam end rotation was evaluated by assuming plastic hinge regions equal in length to half of the beam depth at both ends of the beam. The beam rotation at the hinge is obtained by dividing the difference between the top and the bottom transducer readings by their vertical separation, Fig. 3.5(b). In reality the plastic hinging develops over a variable length region depending on the loading conditions, interaction with the slab and column, and reinforcement arrangement. The resulting readings for the different locations are shown in Appendix A.

The total of 541 wire resistance strain gauges were mounted on the reinforcement and on the concrete surface. Only the strain gauges on longitudinal reinforcement at the beam-column connections and cast-in-situ floor slab at level Z2 are of interest, Fig. 3.6. Five main beam-column connections were extensively instrumented: A/1, A/2, B/1, B/2 and B/3 (Figs. 3.7(a)(b)). In the orthogonal direction, the transverse beams at the intersections of Frames 2 and 3 with Frames A and B were instrumented, Fig. 3.6. Other connection regions were also instrumented with a few strain gauges, Fig. 3.6. The readings were used to check the values obtained in the heavily instrumented connections. The recorded response for the tests



b. Frame B - Strain Gauges.

a. Frame A - Strain Gauges.

Fig. 3.7 - Strain Gauge Locations in Level Z2 Joint Regions.

PSD2 through PSD4 are shown in Appendix A, including crack patterns.

The strain measurements (Level Z2) of the connection region are incomplete without the slab bar strain readings. It is unfortunate that strain gauges were not mounted on slab bars adjacent to and in the same direction as the heavily instrumented joints. The location of slab bar gauges is shown in Fig. 3.8(a). Bottom slab reinforcement, Fig. 3.8(b) was heavily instrumented along support boundaries and is of little value without top bar instrumentation.

The recorded response of the slab strain gauges in Tests PSD2 - PSD4 is shown for Frame A and B alignments (bottom reinforcement only) in Appendix A. In the orthogonal direction, measurements were made on bottom slab bars along transverse Frames 3 and 4 and on top slab bars along Frame 4, as shown in Appendix A.

3.2.2 One-Half Scale Subassemblage Tests

3.2.2.1 Geometry. The one-half scale test specimens consisted of three major groups that were tested at the Aoyama Laboratories, University of Tokyo [Nakata et al. (9)]:

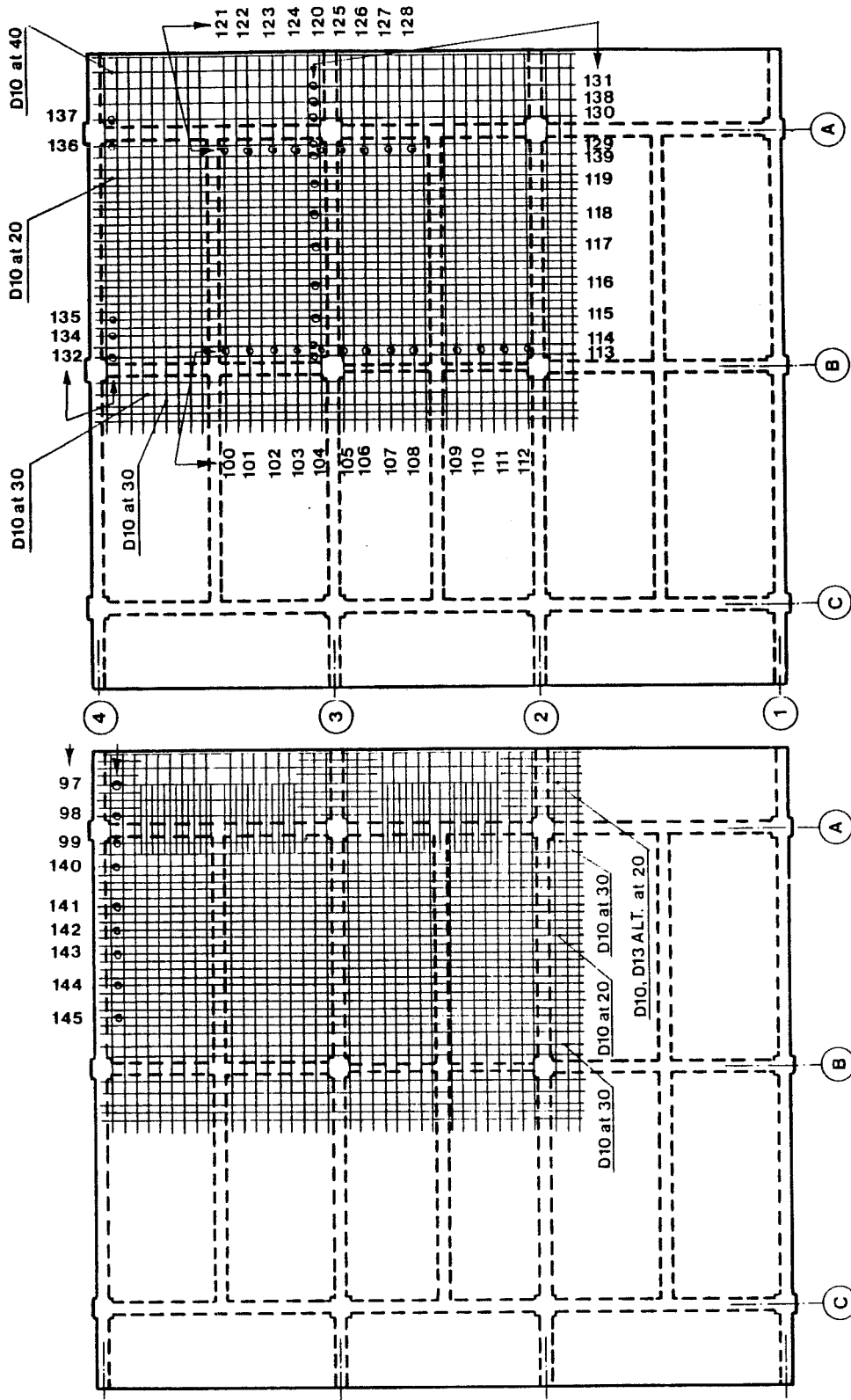
1. Interior beam-column assemblies (I-series);
2. Exterior beam-column assemblies ((E-series); and,
3. Exterior beam-top column assemblies (T-series).

The first two sets were modelled after the critical regions of Level Z2 in the full-scale building. Each set consisted of three subassemblages: one of them designed according to U.S. requirements with a cast-in situ slab and the other two designed by Japanese standards (one of them without the slab). The last set of tests consisted of only two specimens both with cast-in situ slab; one designed by U.S. and the other by Japanese standards, Table 3.7.

In the exterior joint design, the major differences between the U.S. and Japanese practices reside on the amount and arrangement of lateral reinforcement in the core region [Hiraishi et al. (5)]. It is common practice in Japan to bend the beam bottom reinforcement down into the exterior joint lower column (below the joint core) because concrete is cast from one slab face the slab face above.

By assuming inflection points at the mid-length of the members (beam, column) framing into the building critical regions, boundaries (Figs. 3.2 and 3.9) were defined for the half-scale subassemblage specimens, Figs. 3.10, 3.11 and 3.12.

3.2.2.2. Material Properties. High-early strength concrete was used in all the specimens. Each was cast in an upright position using one concrete batch. The average concrete strength was 340 Kgf/cm^2 (4800 psi) which is 20% greater than the 270 Kgf/cm^2 (3800 psi) ultimate concrete strength specified for



b. Bottom Slab Bars.

a. Top Slab Bars.

Fig. 3.8 - Strain Gauges in Slab Bars (Level Z2).

TABLE 3.7 - GENERAL PROPERTIES OF HALF-SCALE COMPONENTS.

Specimen	Slab	Design Code	Lateral Reinforcement	
			Column (%)	Beam (%)
I-1	Yes	Japan	0.290	0.238
I-2	Yes	U.S.A.	1.310	0.430
I-3	No	Japan	0.290	0.238
E-1	Yes	Japan	0.290	0.238
E-2	Yes	U.S.A.	1.310	0.430
E-3	No	Japan	0.290	0.238
T-1	Yes	Japan	0.290	0.238
T-2	Yes	U.S.A.	1.310	0.430

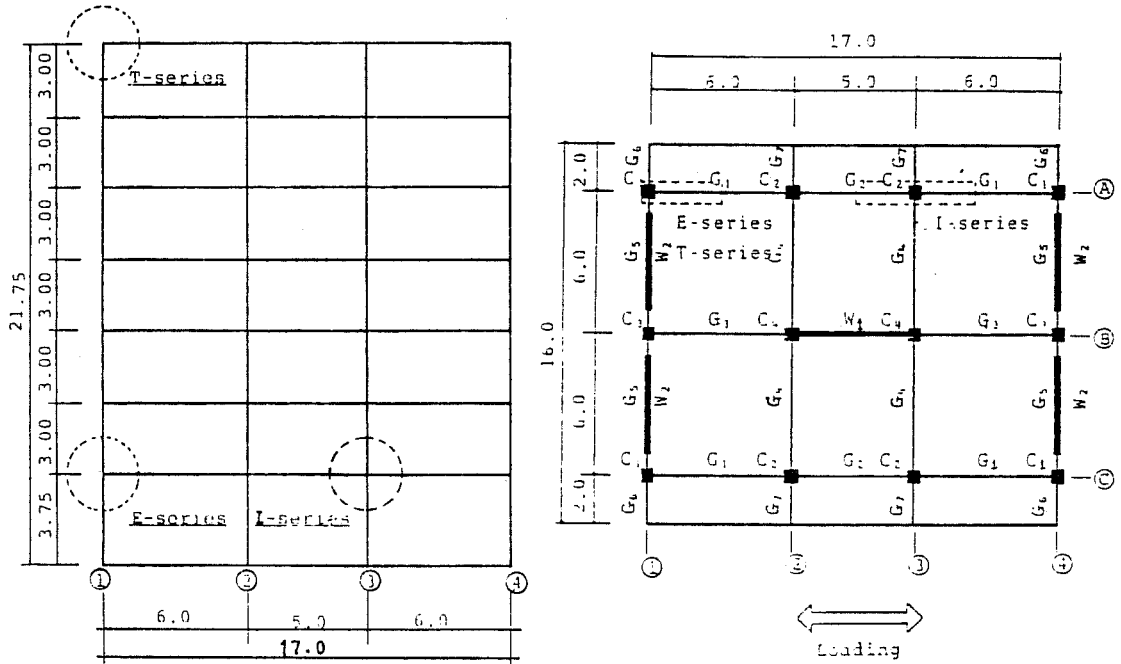
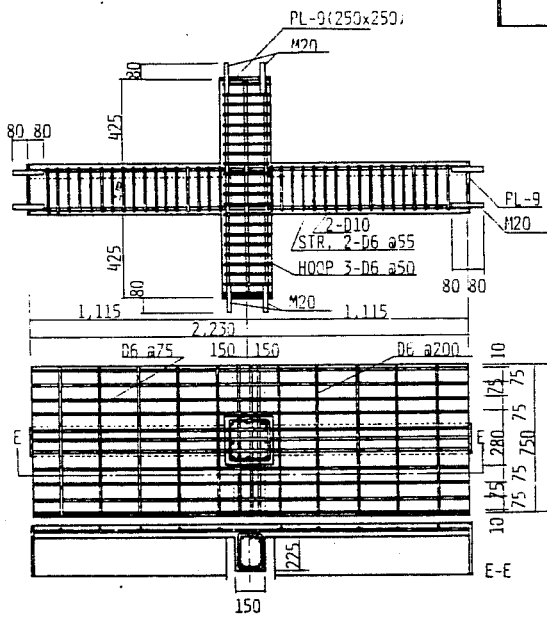
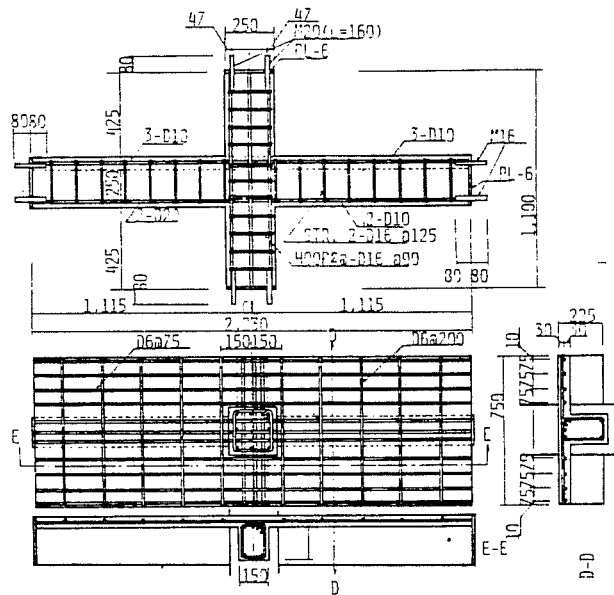
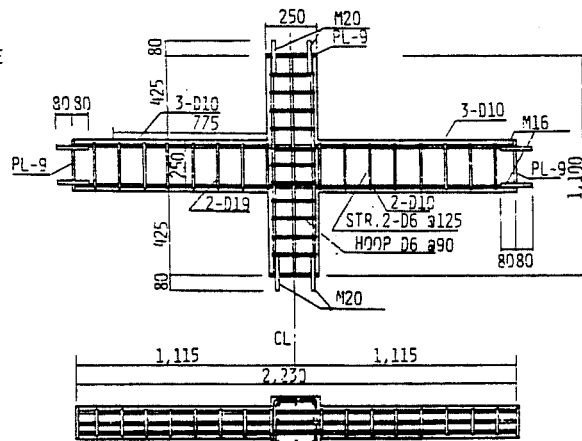


Fig. 3.9 - Component Locations in the Frame.

a. Japanese Detailing.

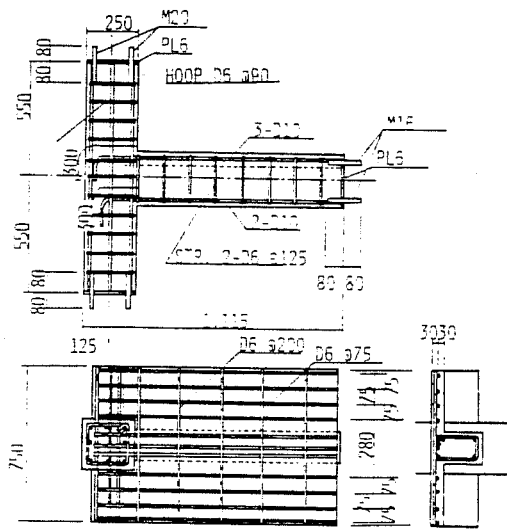


b. US Detailing.

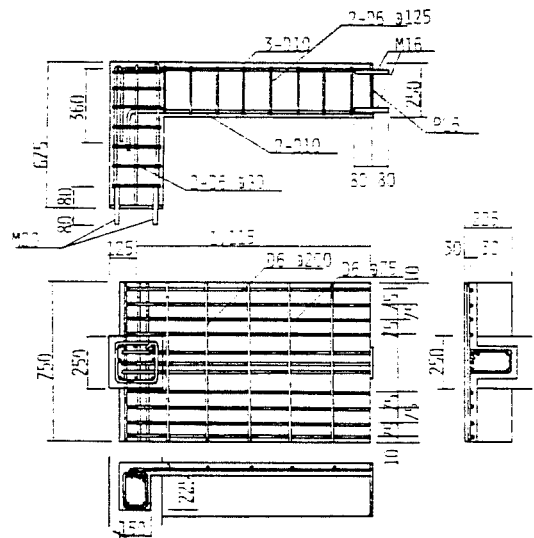


c. Japanese Detailing.

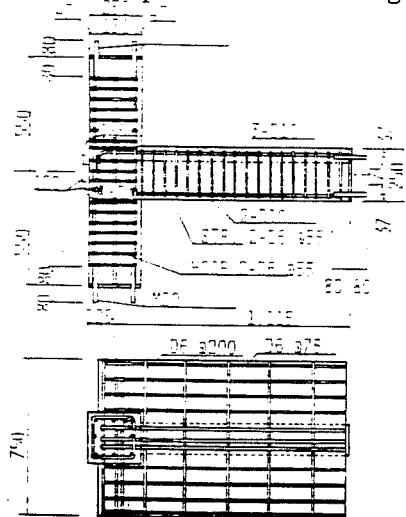
Fig. 3.10 - Japanese 1/2-scale Interior Tests.



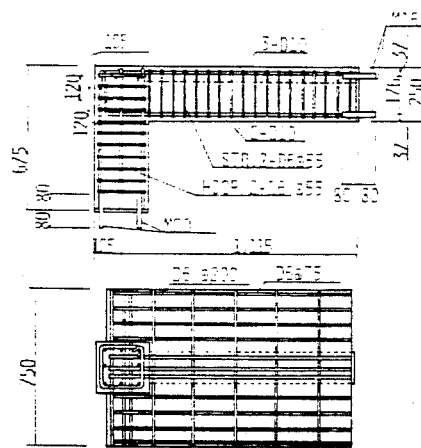
a. Japanese Detailing.



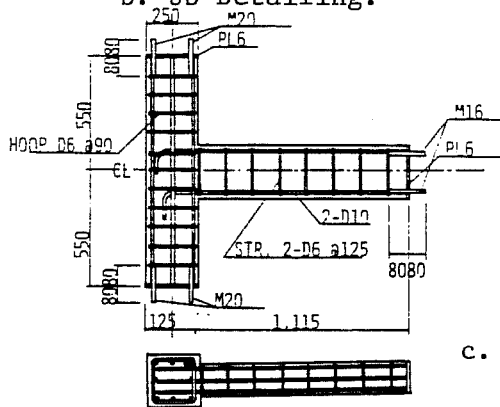
a. Japanese Detailing.



b. US Detailing.



b. US Detailing.



c. Japanese Detailing.

Fig. 3.11 - Japanese 1/2-scale Exterior Tests.

Fig. 3.12 - Japanese Top-Floor 1/2 - scale Exterior Tests.

the full-scale building. However, the measured values for the building and the subassemblage were similar.

The SD 35 (Grade 50) deformed reinforcement was also scaled by half. The small bars had yield and ultimate strengths about 10-15% larger than the class values, Fig. 3.13.

The reinforcement detail modelled the full-scale building critical regions. The interior joint, the exterior joint and the top floor joint details are shown in Fig. 3.14. The most conspicuous feature of the specimens with a slab is the single rebar layer and the relatively narrow slab width, 0.75 m (29.5 in). This resulted from application of the Architectural Institute of Japan (A.I.J.) Code effective width recommendations [A.I.J. (4)].

3.2.2.3 Loading Program. A deterministic loading program was imposed on all specimens. However, preliminary studies were performed on a computer with the 1978 Miyagi-Ken Oki earthquake used in the analysis. Two types of response corresponding to a medium intensity ($a_{\max} = 200 \text{ cm/s}^2$) and a maximum intensity ($a_{\max} = 450 \text{ cm/s}^2$) earthquakes were used by scaling the acceleration amplitude of the earthquake record. The studies indicated that the maximum beam rotation in the level Z2 would range from 1/200 rad. (medium intensity earthquake) up to 1/100 rad. (maximum intensity earthquake), if all the rotation were concentrated in a beam plastic hinge near the column face.

Fig. 3.13 - Steel Properties in Half-Scale Tests.

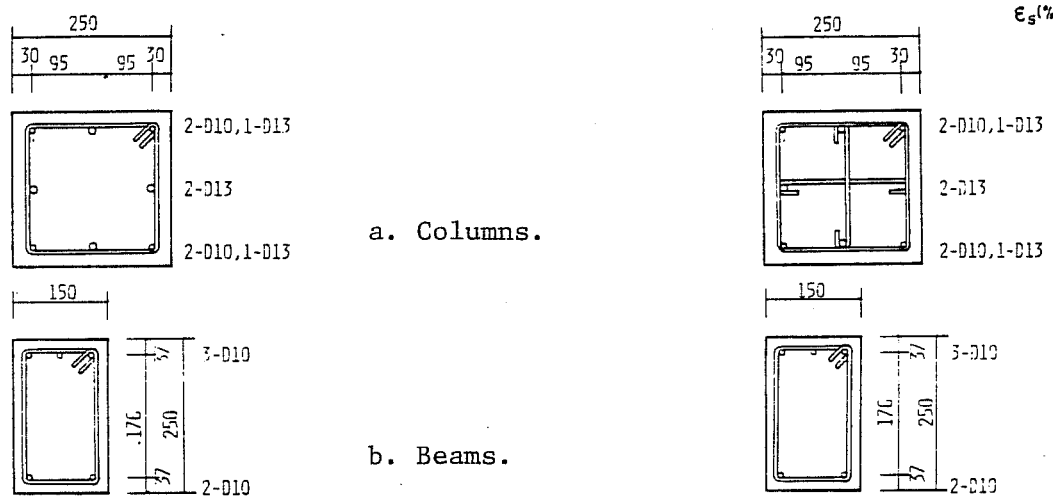
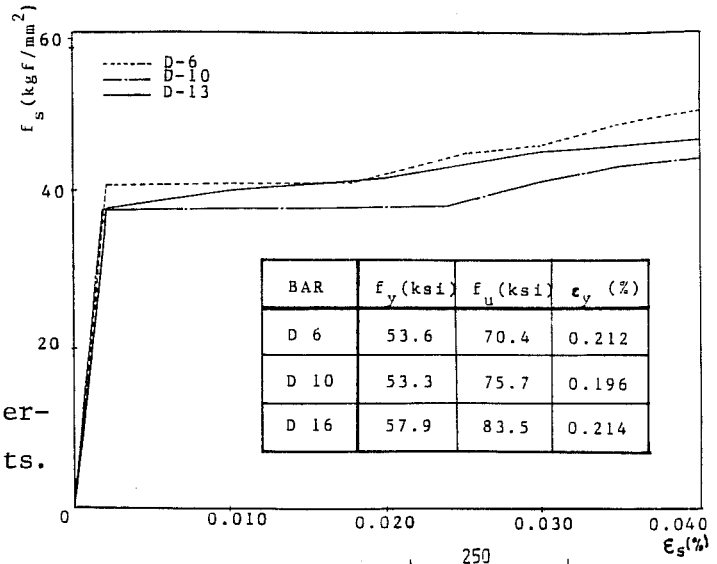


Fig. 3.14 - Cross-Section Details.

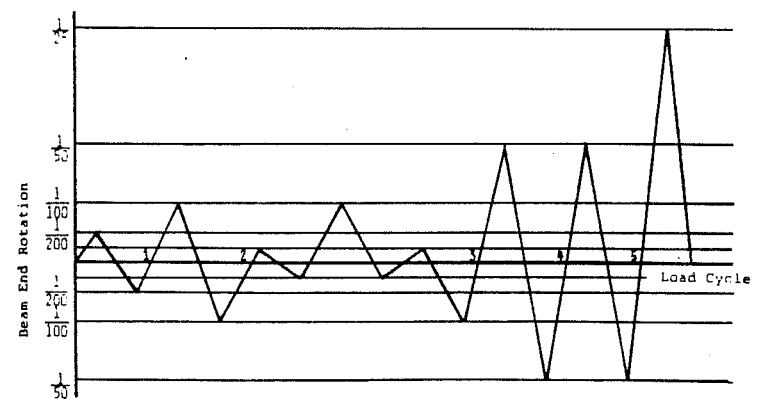


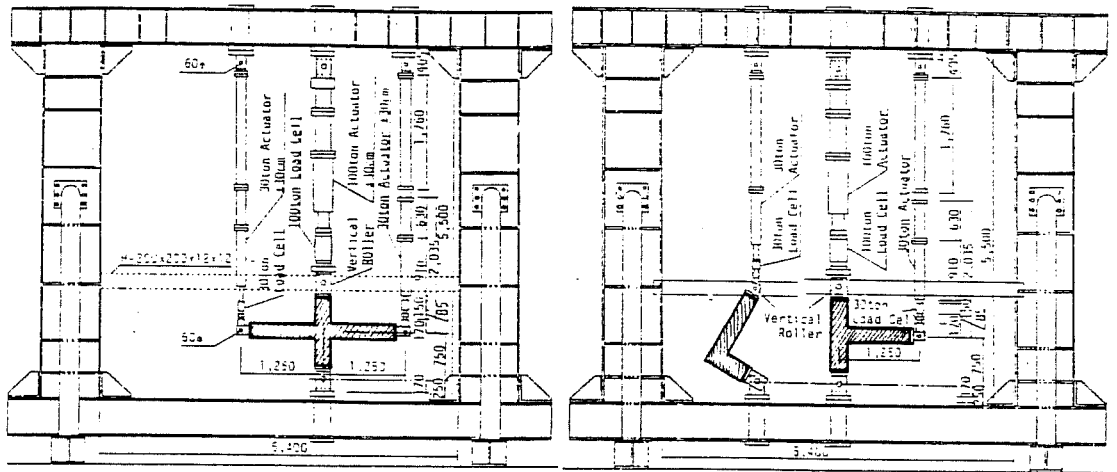
Fig. 3.15 - Component Loading Program.

The specimens ultimate capacity was further exploited by bringing the maximum beam rotation up to $1/50$ rad. with two successive complete reversed load cycles at the same deformation level. Finally, a $1/25$ rad. beam rotation was imposed, Fig. 3.15. In the interior specimen, the load reversals were applied in opposite direction on each beam.

The complete configuration of the reaction frame with the specimen under racking loads is shown for the interior joint (Fig. 3.16(a)) and exterior and top floor joints (Fig. 3.16(b)).

3.2.2.4 Instrumentation. The data channel records (strain gauges, displacement transducers) were not available for this study. However, based on the report of Nakata et al. (9), the locations of the measuring devices are available. The results are presented in terms of cracking patterns and force-deformation response at various deformation levels. The location and purpose of the displacement transducers in the three sets of specimens is shown in Fig. 3.17.

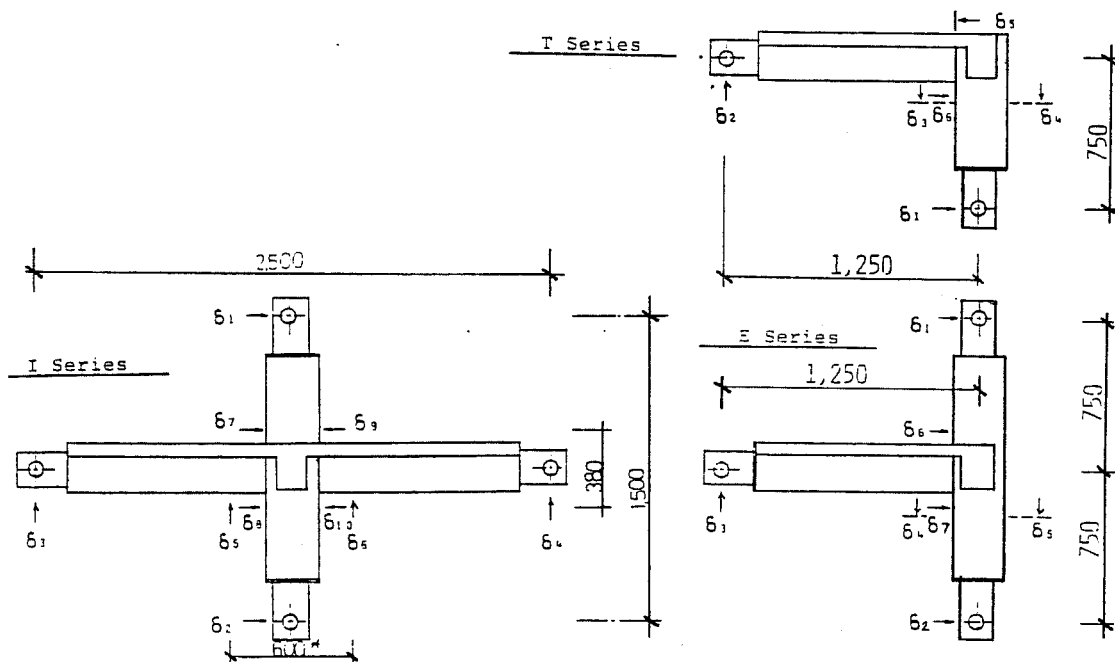
The response of the beam, column and slab bars were monitored with strain gauges throughout the loading program. In the column, strain gauges were placed at the beam top and bottom face levels. In the beam, strain gauges were placed at the column face and mid-joint length to study the spread of yielding and bond deterioration. Finally, strain gauges were placed in all slab bars at the column face, Fig. 3.18. The gauge numbering



a. Interior Tests.

b. Exterior Tests.

Fig. 3.16 - Loading Apparatus for Japanese Tests.



	Specimen I,	Specimen E,	Specimen T
Column Deformation	δ_1, δ_2	δ_1, δ_2	δ_1
Beam Deformation	δ_3, δ_4	δ_3	δ_2
Joint Panel Deformation	$\delta_5 - \delta_6$	$\delta_4 - \delta_5$	$\delta_3 - \delta_4$
Beam End Rotation	$\delta_7 - \delta_8, \delta_9 - \delta_{10}$	$\delta_6 - \delta_7$	$\delta_5 - \delta_6$

Fig. 3.17 - Displacement Transducers in 1/2-scale Tests.

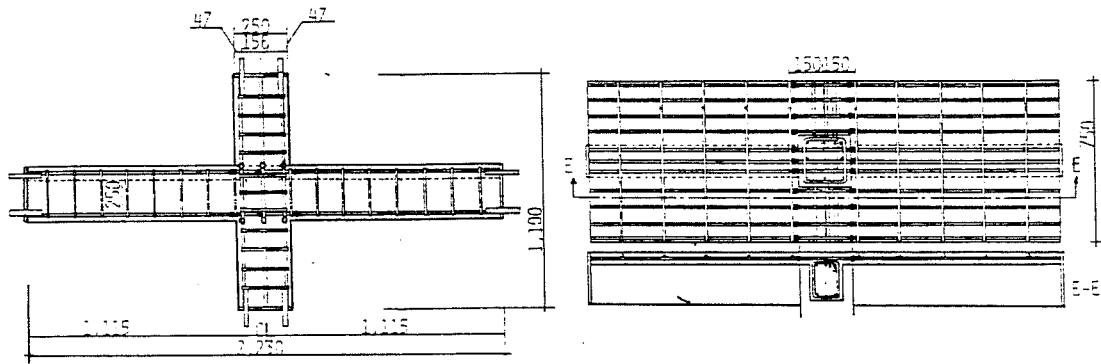


Fig. 3.18 - Strain Gauges Location in I-series Tests.

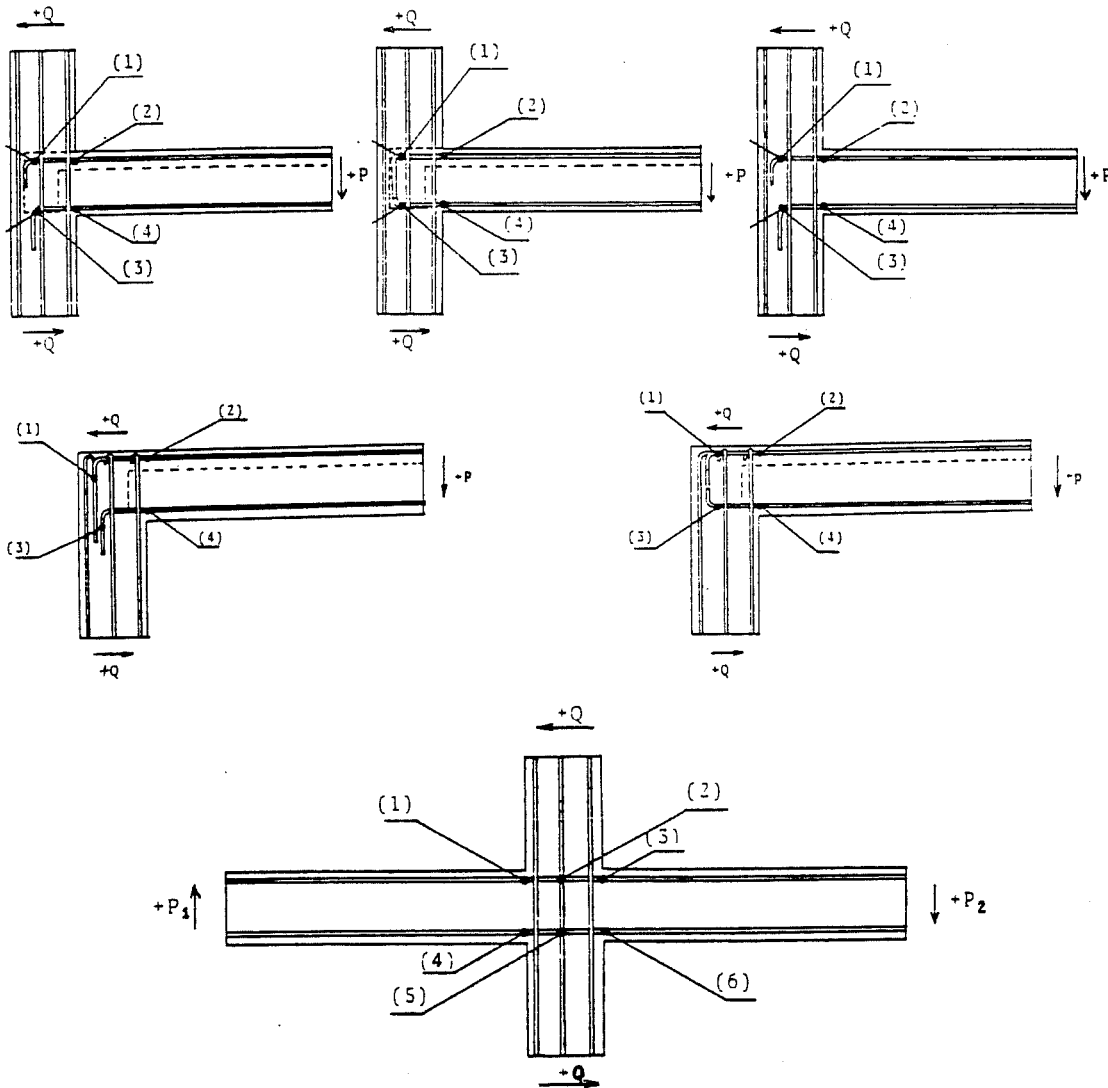


Fig. 3.19 - Beam Strain Gauge Identification.

for series I, E and T tests is shown in Fig. 3.19 for specimens of Japanese design (Type 1) and U.S. design (Type 2) only.

3.3 U.S. Participation

3.3.1 Full-Scale Joint Tests - University of Texas at Austin. Under the U.S.-Japan cooperative research program, four full-scale beam-column-slab subassemblies were tested at the Ferguson Structural Engineering Laboratory (F.S.E.L.) at the University of Texas at Austin. The set of specimens was modelled after the connection critical regions to be found at level Z2 of the B.R.I. building tested in Tsukuba, Japan. The initial part of the program consisted of testing two subassemblage specimens with the same reinforcement details as the B.R.I. building. The specimens ("prototype") represented an exterior and an interior connection region of the B.R.I. building, Fig. 3.2. The second subset of two tests were identical in dimensions (geometry) to the first one except that the specimens ("modified") had higher percentages of reinforcement. The applied load history was deterministic with increasingly larger displacement controlled reversed load cycles.

3.3.1.1 Specimen Geometry. The test specimen dimensions were based on the ideal conditions of zero-moment inflection points at the mid-length of the members (beams,

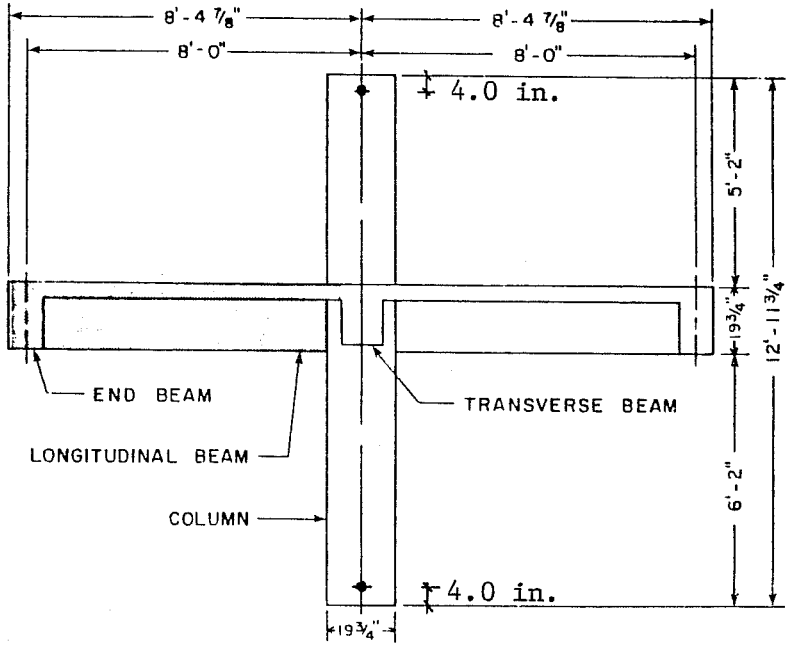
columns). However, due to the laboratory grid layout, some constraints had to be imposed to the specimen size, [Murray (8)].

The typical subassemblage specimen consisted of (Fig. 3.20): (1) longitudinal beam; (2) transverse beam; (3) end beam; (4) upper and lower column; and (5) cast-in situ slab.

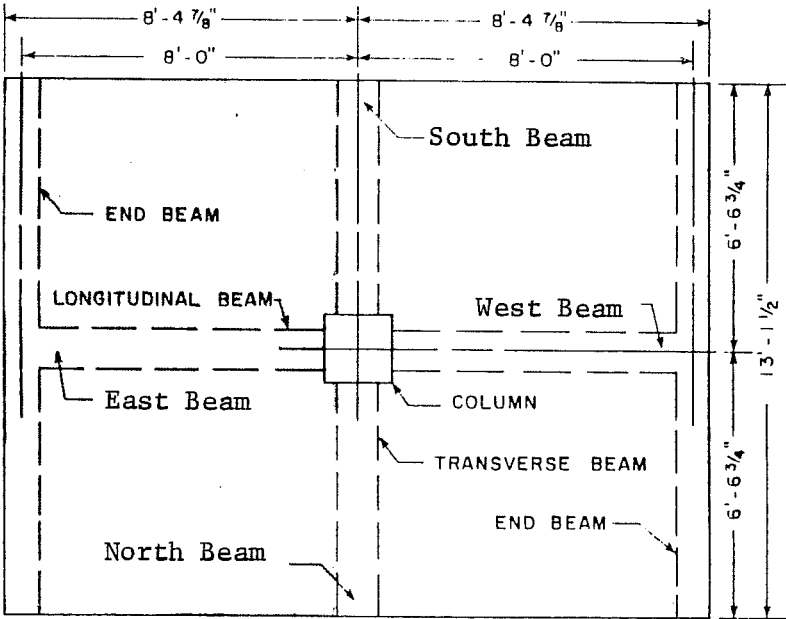
The longitudinal beam was parallel to the direction of loading (N-S direction in the B.R.I. building) and spanned in the long direction of the specimen, passing through the joint region. Racking loads were applied at the ends of the beam. The beam length to load point of 2.44 m (8.0 ft.) measured from the column centerline was close to half-span of the full-scale building middle bay of 2.50 m (8.2 ft.), Figs. 3.2 and 3.20. In the prototype the end bay half-span length of 3.00 m (9.85 ft.) was not duplicated to permit the construction of a symmetrical specimen which would fit the bolt grid layout on the test floor.

The transverse dimensions of the specimen were 2.00 m (6.56 ft.) from either side of the column centerline. On one side, this dimension duplicates that of the B.R.I. building but on the other side, it is 1.00 m (3.25 ft.) less than the actual half-span length between frames A and B, Fig. 3.2.

The transverse end beams at the end of the longitudinal beams represented the secondary beams at the midspan of all the bays in the B.R.I. building. The orientation (N, S, E, W) of the beam members is shown in Fig. 3.20.



a. Elevation.



b. Plan.

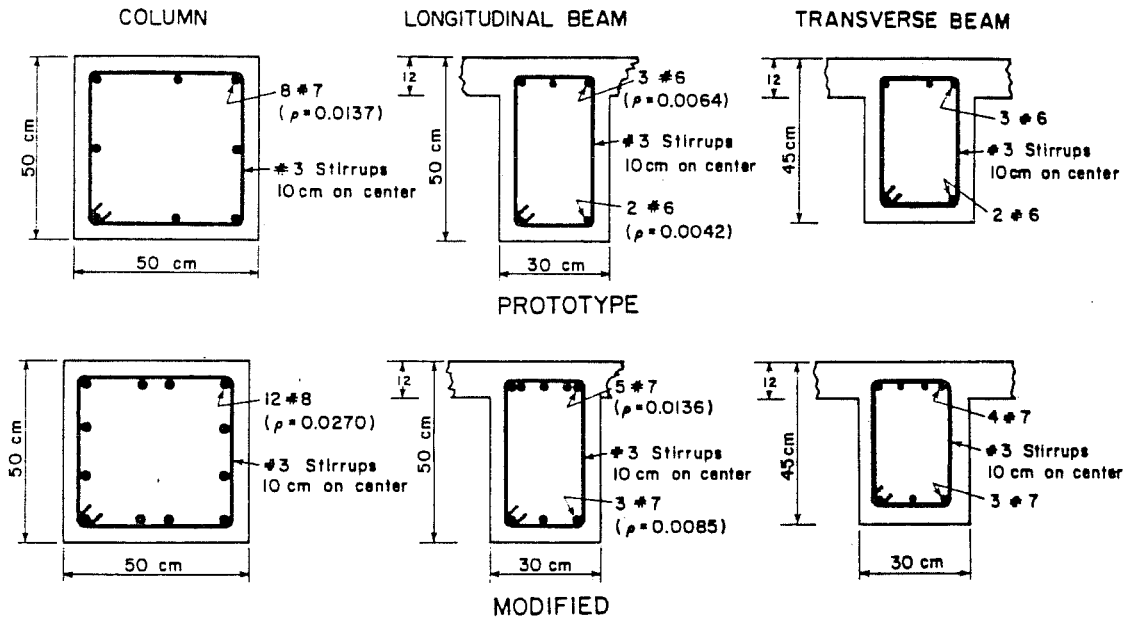
Fig. 3.20 - UTA Component Geometry.

Ideally, the column height should correspond to the distance between inflection points in the B.R.I. building, e.g., 1.50 m (4.92 ft.) for the height above the slab top face and 1.875 m (6.15 ft.) for the height below the same reference level. However, due to limitations on the existing casting bed and the loading actuator height in the planned test set-up, some modifications were required. Consequently, the lower column is 0.50 m (20 in.) longer than the corresponding zero moment inflection point in the original B.R.I. building, [Murray (8)].

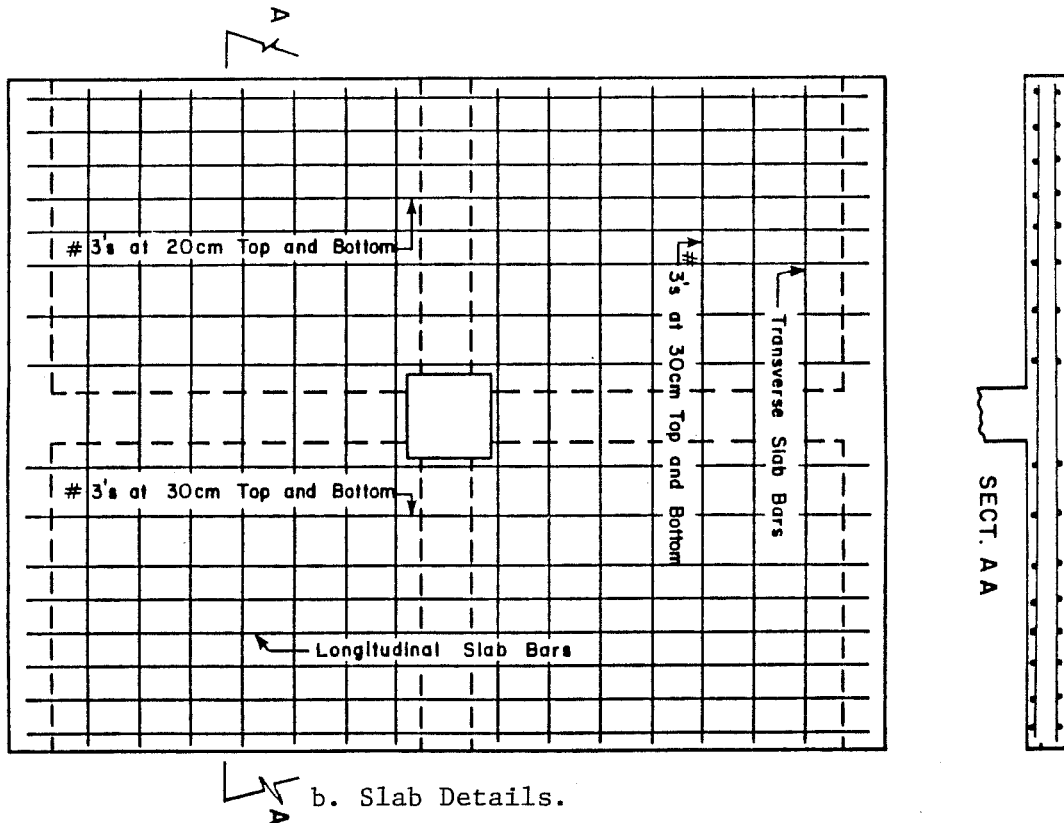
The geometry for the exterior beam-column-slab subassemblages is identical to the interior ones except for the exclusion of the east longitudinal beam, the end transverse beam and the cast-in situ slab, Fig. 3.20 (shaded regions).

The cross-section characteristics of the subassemblages are shown in Fig. 3.21(a) where the U.S. bar sizes are equivalent to the ones to be found in the B.R.I. building. The prototype specimens had lower reinforcement percentages than could be considered typical for U.S. construction practice. The ratios were close to the recommended minimum values using ACI 318-77 (1). However, they represented the values found in the B.R.I. building and common in Japanese practice.

In the exterior joints, the longitudinal beam top reinforcement was continuous under the transverse beam top rebars at the joint region and anchored with a standard 90°-hook at the end



a. Cross Section Details.



b. Slab Details.

Fig. 3.21 - UTA tests reinforcement details.

beam. In Japanese practice, the exterior joint longitudinal bars stop near the column center whereas in U.S. practice they are anchored at the far end of the column.

The longitudinal and transverse beam closed stirrups were made of #3 (10 mm) hoops at 0.10 m (4 in.) o.c. for the first 1.00 m (40 in.) from the column face. The first beam stirrup was at 0.05 m (2.0 in.) from the column face. Thereafter, the spacing was increased to 0.20 m (8.0 in.). In the beam and column stirrups the common A.I.J. (4) 6-bar diameter hook extension was used instead of the ACI. 318-83 - Appendix A (2) 10-bar diameter hook extension.

The slab reinforcement consisted of two mats of #3 (10 mm) bars with a 0.02 m (0.75 in) clear cover, Fig. 3.21(b) The longitudinal bar spacing varied from 0.30 m (12.0 in.) for the first 0.90 m (36.0 in) measured from the beam centerline to 0.20 m (8.00 in.) spacing thereafter. The longitudinal slab steel had a 180°-hook at the ends. The longitudinal top steel was placed above the transverse top steel whereas the longitudinal bottom steel was placed under the transverse bottom steel.

The modified subassemblage specimens differed from their geometrical identical prototype specimens by the reinforcement ratios in the beams and columns, Fig. 3.21(a), and by reinforcement details. The exterior prototype specimen showed premature anchorage failure during testing. Therefore, an improved design

was required for the modified specimen and additional cross-ties were used to improve the response, Fig. 3.22. The cross-ties were made of #3 (10 mm) bars with a 135° ACI standard hook at each end. Each of the four #3 (10 mm) joint core hoops had a cross-tie placed in the longitudinal direction.

In the modified specimen members (beams, columns), the amount of reinforcing steel was increased by nearly 100%, Fig. 3.21(a), in order to exploit the response of the joint under high shears introduced by stronger members. The beam stirrup and column tie spacing remain unchanged, [Joglekar et al. (6)].

The slab reinforcement was the same in all specimens. The longitudinal slab steel (bottom layer) was placed continuously over the transverse beam. This detail is not normally used in U.S. design practice for interior joints.

The two modified specimens had reinforcement ratios nearly the same as those of the reduced 1:3.5 scale frame tests performed at the Portland Cement Association [Morgan et al. (7)].

3.3.1.2 Material Properties. Grade 60 (42.2 Kgf/mm²) steel was used in the fabrication of all four specimens. The yield strength is higher than SD 35 (Grade 50) steel used in the B.R.I. building. Coupon tests performed on bar samples showed yield stresses 30% greater than the nominal values, Table 3.8.

Such overstrength should be considered in seismic-resistant design.

The ultimate concrete strength was determined using 6-in. x 12-in. (0.15 m x 0.30 m) cylinders cast during each operation and cured with the test specimens. The average strength is higher than the design values 270 Kg/cm^2 (3800 psi) used in the Japanese building. However, the prototype specimens showed very low ultimate values on the cast upper column, in particular the exterior subassemblage, Table. 3.8. This had little influence on the specimen behavior because the column did not participate in the failure.

3.3.1.3 Loading Program. The applied loading program on all four specimens was of the deterministic type. It was intended that the loading history on the specimens be displacement controlled. The reversed cyclic racking loads were applied at the cantilever beam tip through hydraulic rams, Fig. 3.23. The applied load and displacement were monitored throughout the experiment by a load cell attached to the ram and a displacement transducer at the beam tip.

In testing the first specimen - interior prototype, USJ-1 - the load-control was used by mistake. During the first two parts of the loading program, the error was unnoticed because small displacements were imposed. In the third part, a large beam displacement was inadvertently applied to the east beam with

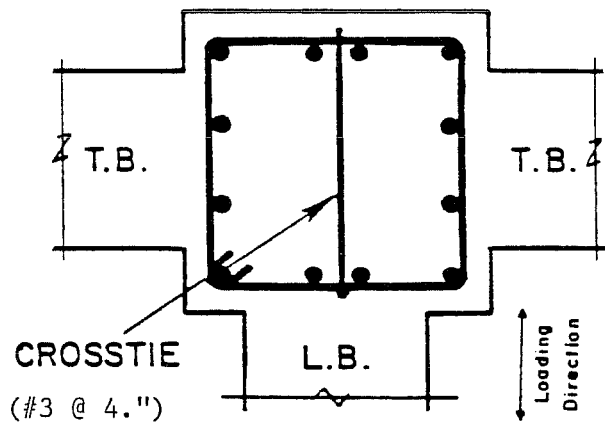


Fig. 3.22 - UTA(USJ-4)
Exterior Modified Joint
Detail.

TABLE 3.8 - MATERIAL PROPERTIES FOR UTA TESTS.

concrete Specimen Test Code	First. Cast Lower Column and Floor (psi)	Second Cast Upper Column (psi)	steel Location	Bar Size	Steel Strength	
					Yield (ksi)	Ultimate (ksi)
<u>Prototype Specimens</u>						
USJ - 1 Interior Prototype	4860	3430	Longitudinal Column Bars	#7 (22 mm)	79	116
			Longitudinal Beam Bars	#6 (20 mm)	61	93
USJ - 2 Exterior Prototype	4690	2340	Longitudinal Slab Bars	#3 (10 mm)	58	82
			Transverse Steel	#3 (10 mm)	60	87
<u>Modified Specimens</u>						
USJ - 3 Interior Modified	3950	4940	Longitudinal Column Bars	#8 (25 mm)	72	n/a
			Longitudinal Beam Bars	#7 (22 mm)	75	110
USJ - 4 Exterior Modified	4850	5010	Longitudinal Slab Bars	#3 (10 mm)	75	125
			Transverse Steel	#3 (10 mm)	67	n/a

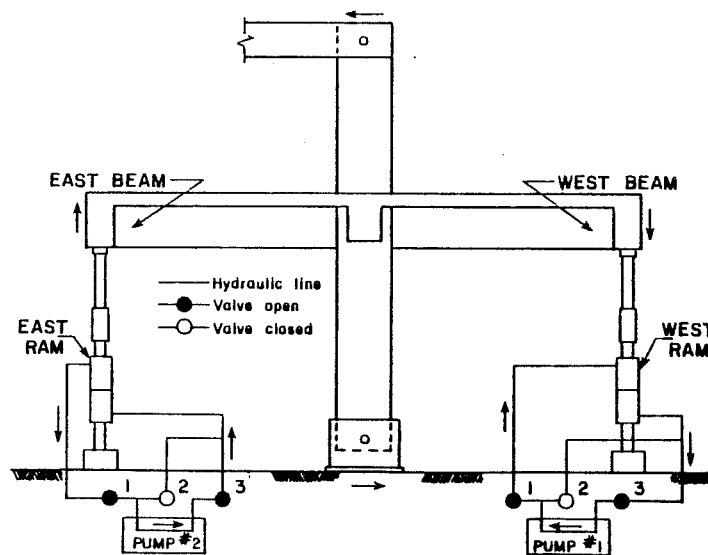


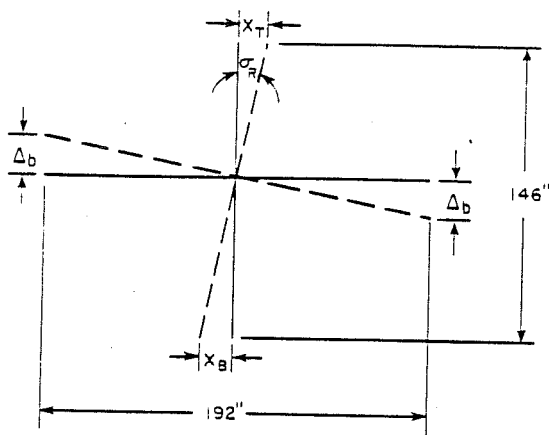
Fig. 3.23 - UTA Loading Apparatus.

an upward deflection (negative) of nearly 2.50 in (0.05 m). This led to the bottom reinforcement premature yielding under tension which propagated into the joint region, [Murray (8)].

A second problem during the USJ-1 test program developed from the slip or horizontal displacement of the lower and upper column pin connections. A correction to the measured beam displacements was required, particularly at small displacement levels where slip accounted for 15-25% of the total beam deflection, Fig. 3.24-a. In the subsequent tests (USJ-2, 3 and 4), the support slip was almost eliminated by using stiffened steel plates clamped on either side of the channels, at the top and bottom pin connections, Fig. 3.24-b High-strength bolts were tightly torqued to get the necessary clamping force that would ensure adequate response at all deflection levels.

The testing program for all the four specimens is shown in Table 3.9. The first interior prototype specimen (USJ-1), was subjected to an extensive cycling program but the other three were tested with a shorter loading program, [Joglekar et al. (6)].

3.3.1.4 Instrumentation. The four specimens were thoroughly instrumented to measure the external response (load cells, displacement transducers) and the internal response (strain gauges) during testing.



$$\sigma_R = \frac{X_T + X_B}{146}$$

$$\Delta_b = \frac{X_T + X_B}{146} (96) = 0.658(X_T + X_B)$$

X_T = measured slip at top, in.

X_B = measured slip at bottom, in.

σ_R = angle of rigid body rotation, rad.

Δ_b = correction for beam deflection, in.

a. Support Slip Correction.

b. Lower Column Pin-End Detail.

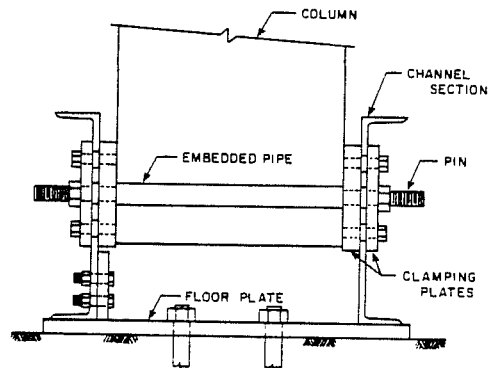


Fig. 3.24 - UTA Support Conditions.

TABLE 3.9 - UTA TESTS - AVAILABLE DATA.

TEST NAME	TEST RUN	DATE	NO. OF DATA POINTS	OBSERVATIONS
USJ - 1	0	17 Jul 81	100	Instr. check
Interior	1	1 Oct 81	122	Real test
Prototype	2	9 Oct 81	119	starts
	3	14 Oct 81	154	
	4	4 Nov 81	190	
USJ - 2	0	15 Jun 82	25	Instr. check
Exterior	1	16 Jun 82	40	Real test
Prototype	2	17 Jun 82	178	starts
	3	18 Jun 82	187	
USJ - 3	0	20 Dec 82	24	Instr. check
Interior	1	21 Dec 82	130	Real test
Modified	2	22 Dec 82	266	starts
USJ - 4	0	21 Jan 83	31	Instr. check
Exterior	1	1 Feb 83	202	Real test
Modified	2	3 Feb 83	208	starts

Records of loads and displacements were made on channels 200 to 229, whereas strains were recorded on channels 230 to 324. Several channels showed poor response at early load stages and others became inoperable during the experiment.

The interior specimens (USJ-1 and 3) were subjected to racking loads applied at the tip of the longitudinal cantilever beams, Fig. 3.25. Two double-rodDED hydraulic rams, each one with the capacity of 100,000 lbs (45.360 kgf) were used to load the specimen.

The specimen external response was monitored with LVDT's placed on the longitudinal beams and at the end of the columns, Fig. 3.26. The rotation of the longitudinal beams was computed by a set of LVDT's at 6.0 in. (0.15 m) and 24.0 in. (0.60 m) from the column face, Fig. 3.27(a). The torsional rotation of the transverse beams was computed by LVDT's mounted at 19.5 in. (0.50 m) and 63.5 in. (1.61 m) from the column face, Fig. 3.27 (b).

Two other external deformation measurements were also made: (a) joint panel distortion, Fig. 3.28; and (b) bar slip-page, Fig. 3.29. They are both important to evaluate the beam deflection and bond deterioration through the joint.

The internal response was obtained through strain gauges placed on the: (1) longitudinal beam bars; (2) transverse beam bars and stirrups; (3) column longitudinal bars and ties; and, (4) slab bars.

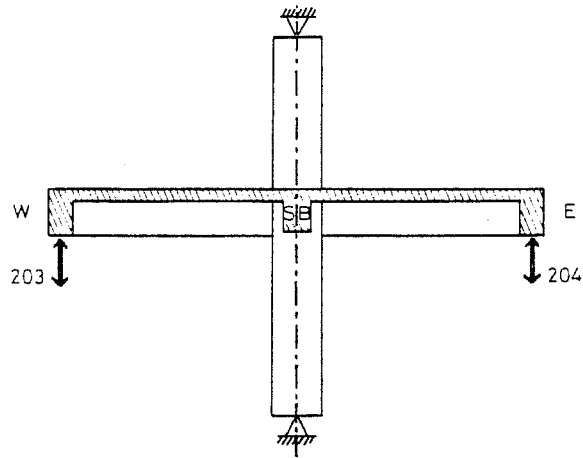


Fig. 3.25 - UTA Interior Component Load Cells.

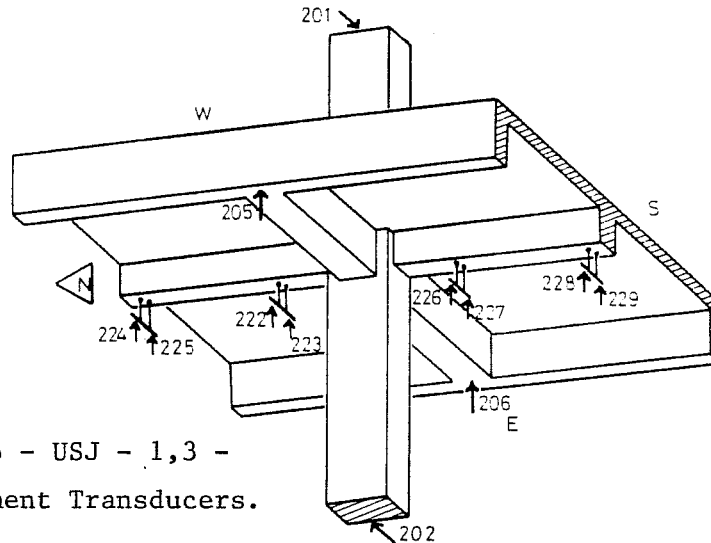
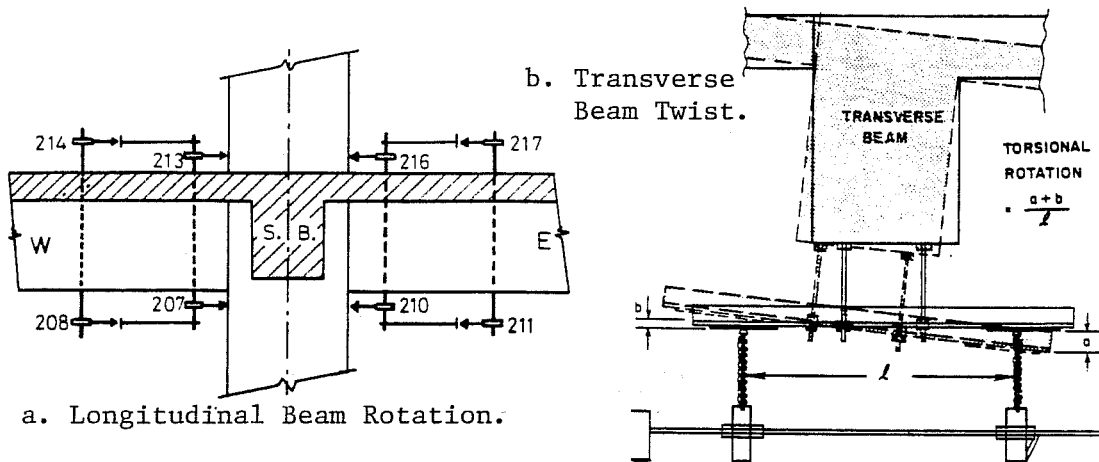


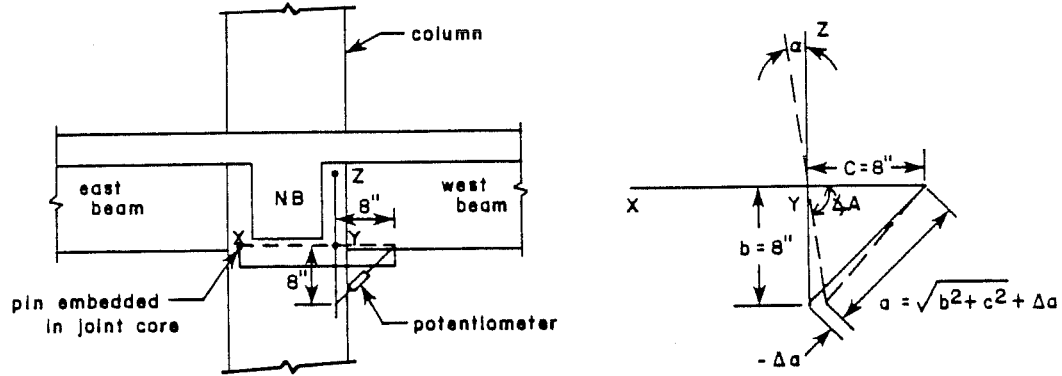
Fig. 3.26 - USJ - 1,3 - Displacement Transducers.



a. Longitudinal Beam Rotation.

b. Transverse Beam Twist.

Fig. 3.27 - USJ - 1,3 - Beam Rotation and Twist.



Law of cosines:

$$a^2 = b^2 + c^2 - 2bc \cos \Delta A$$

α = joint shear strain, rad.

Δa = potentiometer measurement, in.

$$\Delta A = \cos^{-1} \left(\frac{-a^2 + b^2 + c^2}{2bc} \right)$$

$$= \cos^{-1} \left(\frac{b^2 + c^2 - (\sqrt{b^2 + c^2 + \Delta a})^2}{2bc} \right)$$

$$\alpha = \Delta A - \frac{\pi}{2}$$

$$= \cos^{-1} \left(\frac{128 - (11.31 + \Delta a)^2}{128} \right)$$

Fig. 3.28 - UTA Joint Panel Distortion.

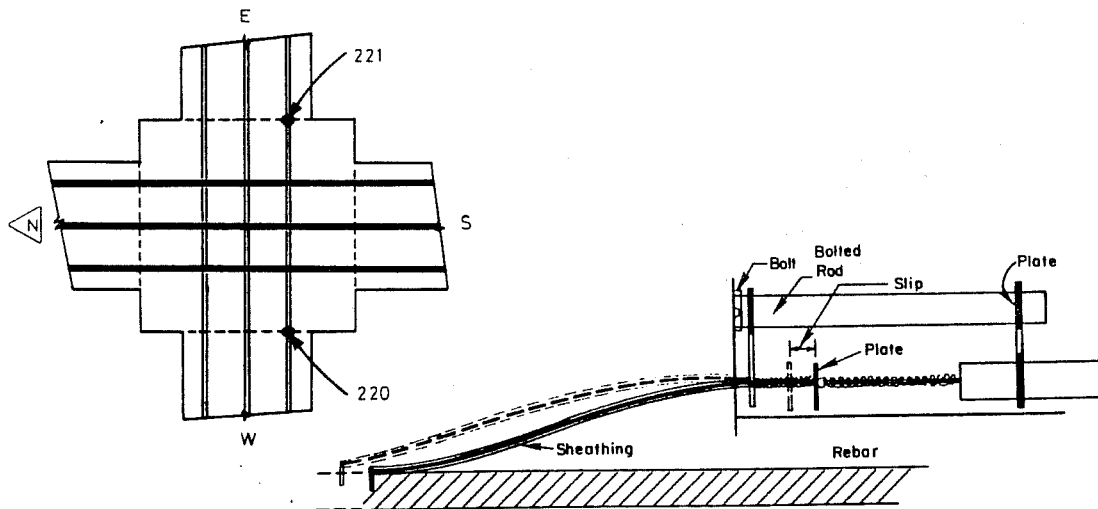


Fig. 3.29 - USJ - 1,3 - Bar Slippage Detail.

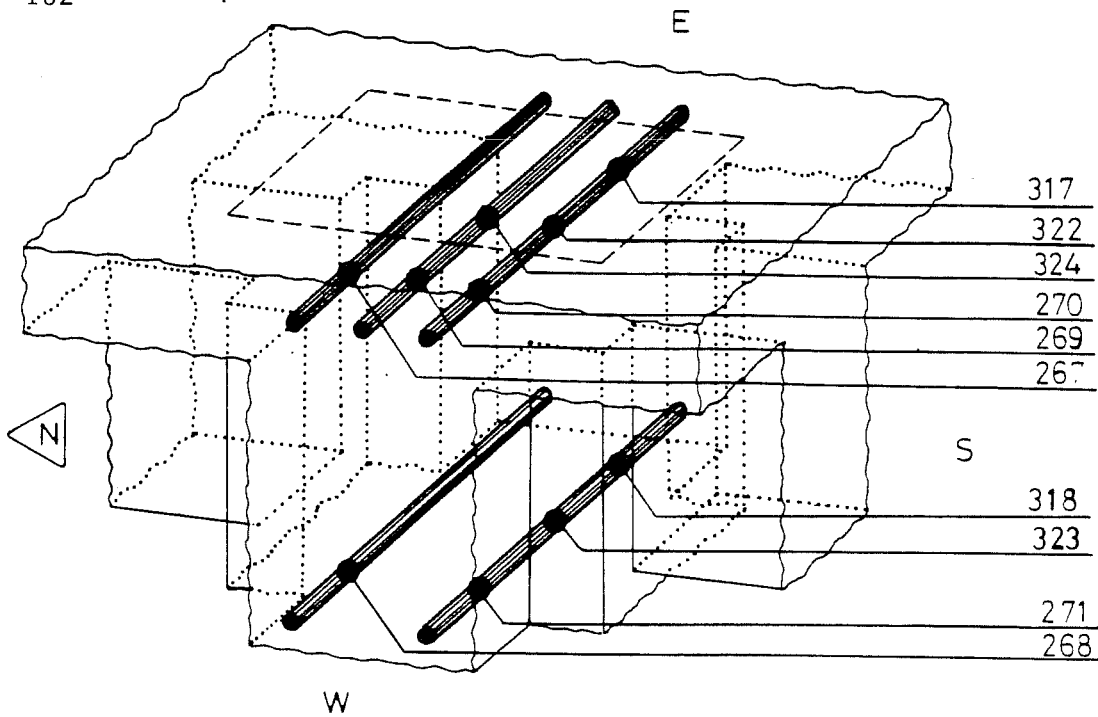
The longitudinal beam bars were not instrumented in as much detail as the equivalent B.R.I. building interior joint. Only one top and one bottom bar had three strain gauges placed on the bar to determine yield progression and bond deterioration in detail, Fig. 3.30(a).

The transverse beam bars were extensively instrumented with the particular objective of finding the transverse beam deformation role on the subassemblage response, Fig. 3.30(b).

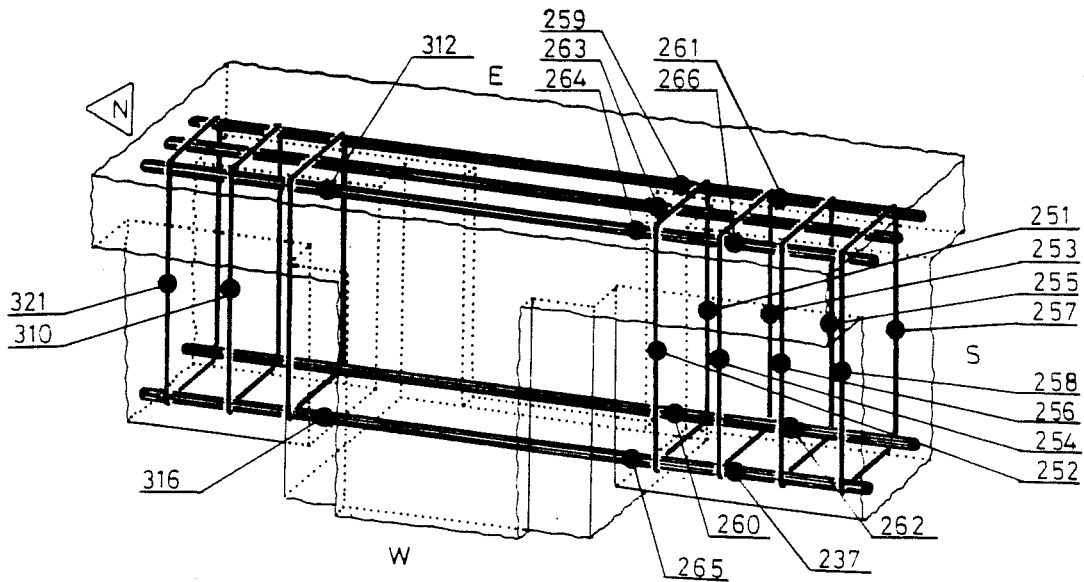
The longitudinal column bars were instrumented in more detail than the corresponding column bars in the B.R.I. building interior joint. The joint hoop had a large number of strain gages which are important in evaluating the amount of damage and the strain level in the joint core near ultimate, Fig. 3.31.

The top and bottom slab bars in the subassemblage specimens were also extensively instrumented, Fig. 3.32, in contrast with only the bottom slab bars in the B.R.I. building interior joint. By using symmetry, only the SW-quadrant was fully instrumented which reduced the total number of strain gauges in the slab bars. However, some extra strain gauges were placed in the remaining quadrants for checking readings on strain gauges.

The response of all channels during the applied loading program for the interior subassemblage specimens (USJ-1 and 3) is shown in Appendix B. Crack patterns for USJ-1 are also shown.

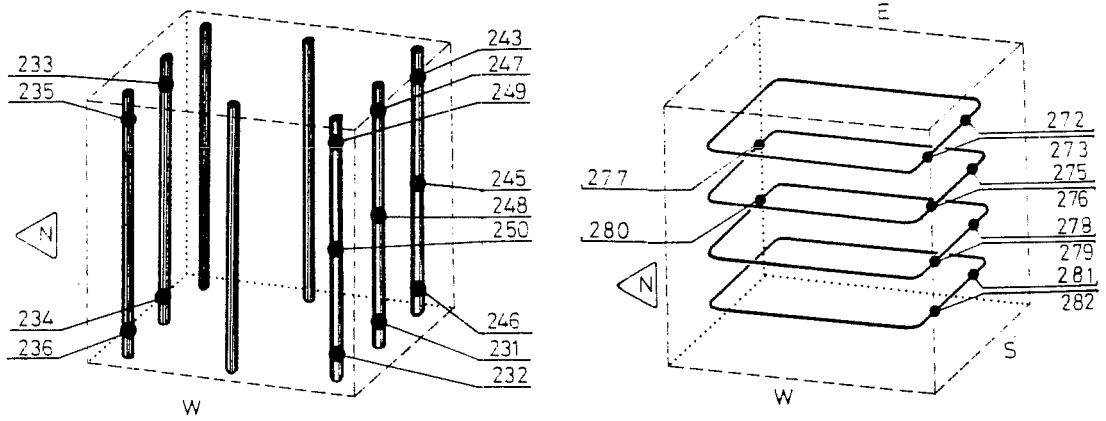


a. Longitudinal Beam Strain Gauge Location.



b. Transverse Beam Strain Gauge Location.

Fig. 3.30 - Interior Component Beam Strain Gauges.



a. Column Bars.

b. Joint Core Stirrups.

Fig. 3.31 - UTA Interior Joint Region Strain Gauges.

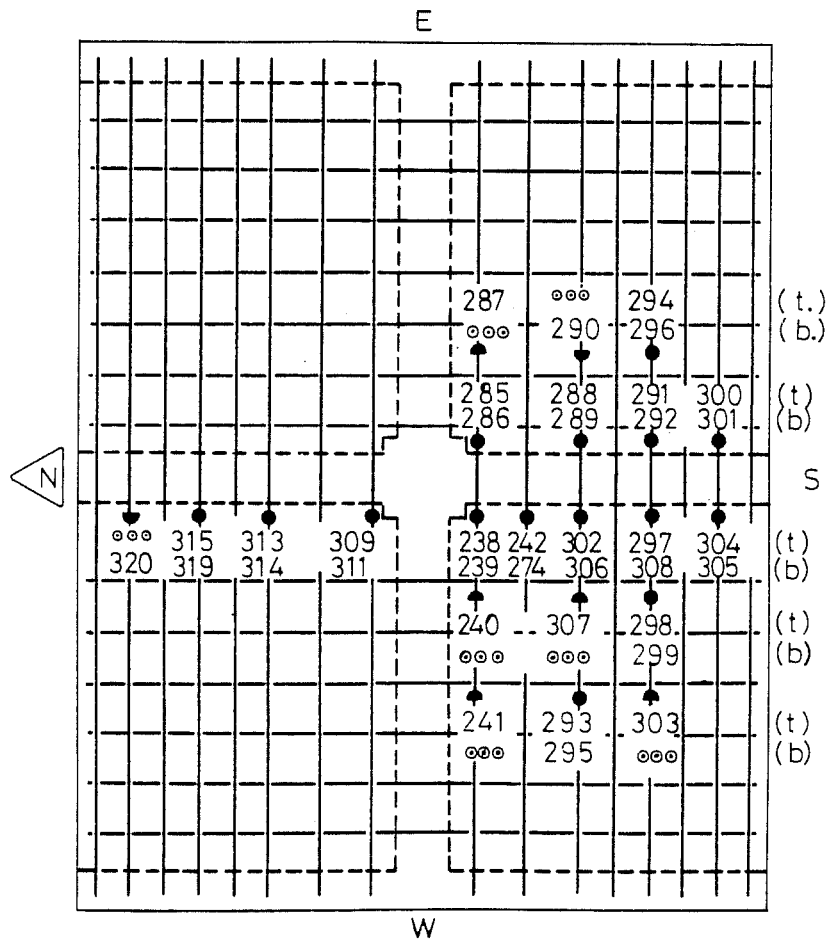


Fig. 3.32 - UTA Interior Test Slab Strain Gauges.

The exterior specimens USJ-2 (prototype) and USJ-4 (modified) were subjected to identical loading programs. The specimen response was monitored similarly to the interior subassembly by load cells, displacement transducers and strain gauges, Figs. 3.33 to 3.38.

In the exterior joints, increasingly severe strain gradients were introduced into the joint core by the 90° - hook anchorages when loading was incremented from the elastic range up to ultimate. The assessment of yield penetration, joint core volumetric expansion and bar slippage need to be monitored. Consequently, longitudinal beam bar anchorages were extensively instrumented, Fig. 3.37. Strain gauges were labeled as shown in Fig. 3.38.

The response of all channels during the imposed loading program for the exterior subassembly specimens (USJ-2 and 4) and crack patterns (USJ-2) are shown in Appendix B.

3.3.2 The Stanford University Small-Scale Tests. In the experimental program several small-scale (1:12.5) specimens were constructed and tested. Two beam-column-slab subassemblies modelled after the prototype specimens were tested as well as one exterior and one interior subassemblies without the cast-in situ slab. Other tests included an isolated shear wall and a shear wall-frame system, Fig. 3.39.

Fig. 3.33 - Exterior Test Load Cell.

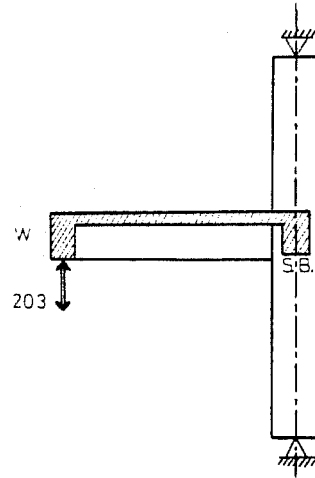
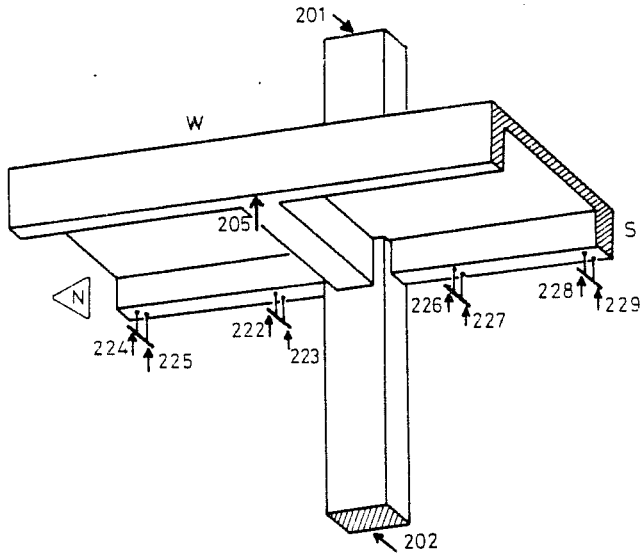


Fig. 3.34 - USJ - 2,4 - Displacement Transducers.

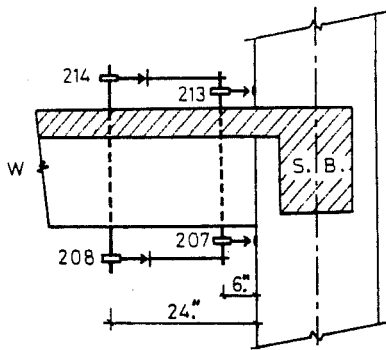


Fig. 3.35 - Exterior Test Beam Rotation.

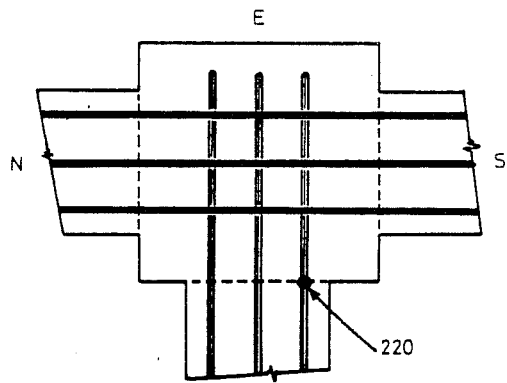
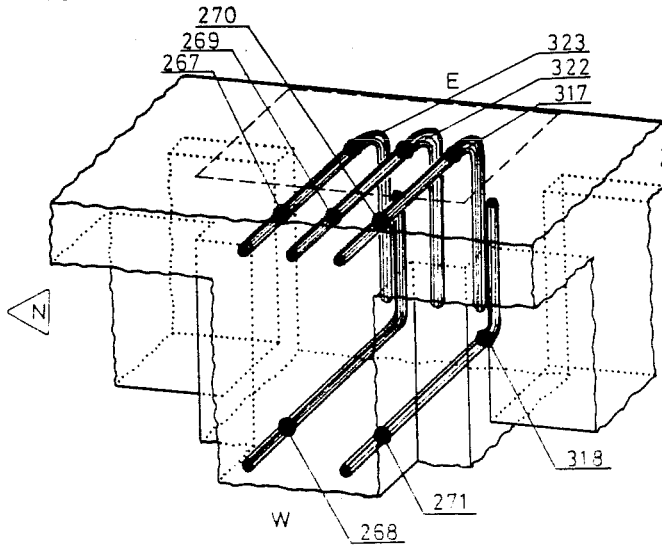
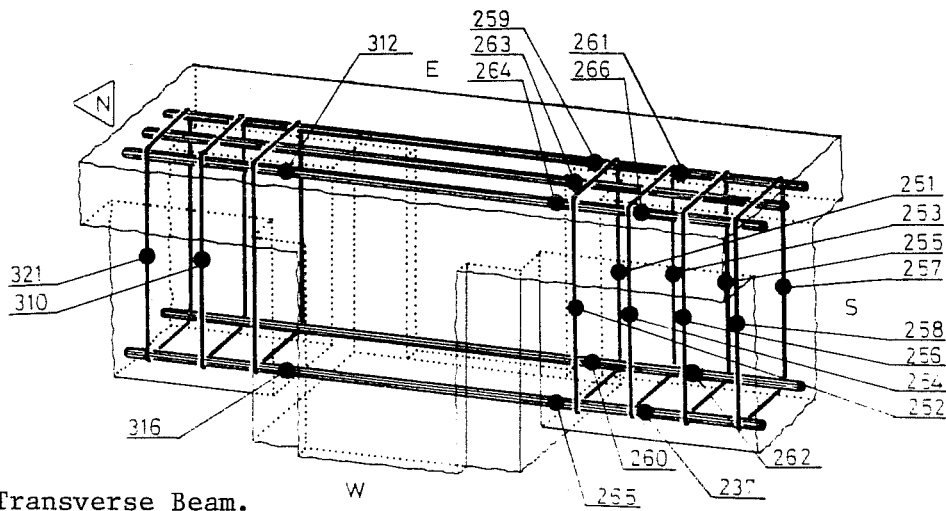


Fig. 3.36 - USJ - 2,4 - Bar Slippage.

166



a. Longitudinal Beam.



b. Transverse Beam.

Fig. 3.37 - UTA Exterior Test Beam Strain Gauges.

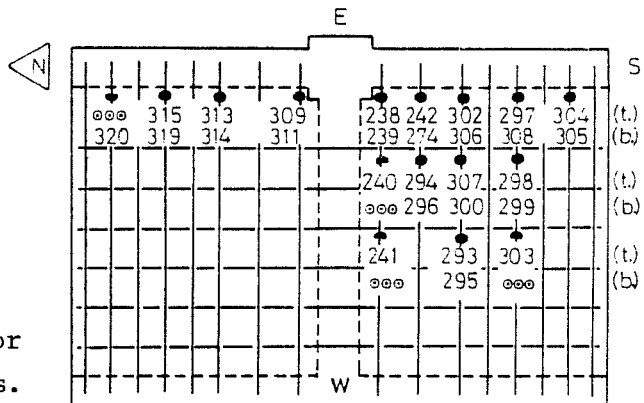


Fig. 3.38 - UTA Exterior Test Slab Strain Gauges.

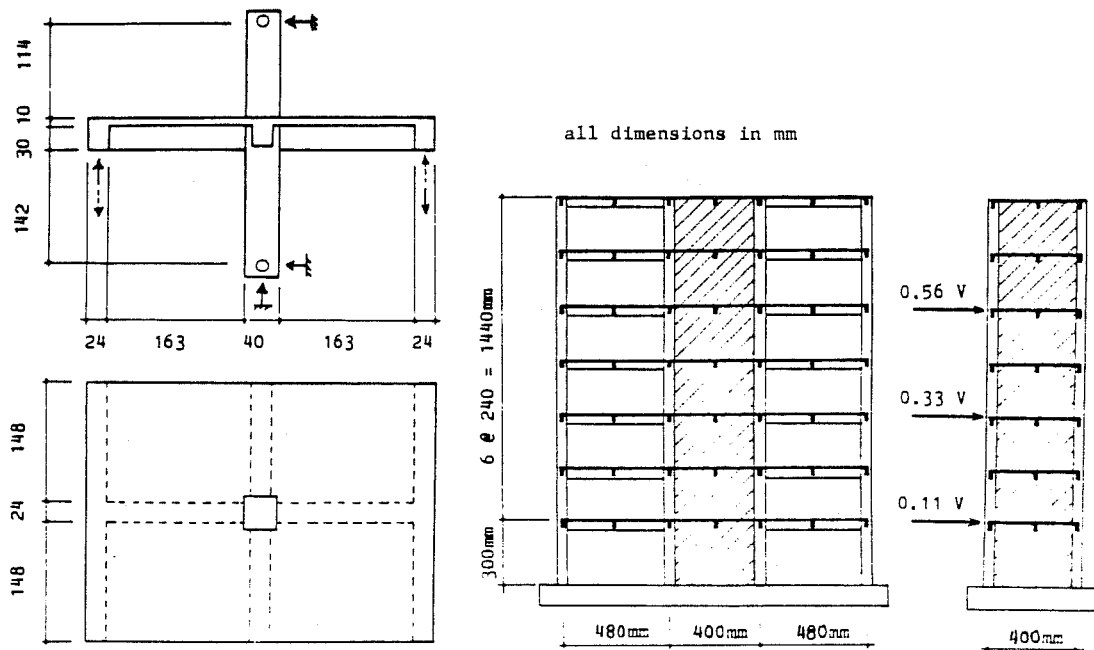


Fig. 3.39 - Stanford University Tests.

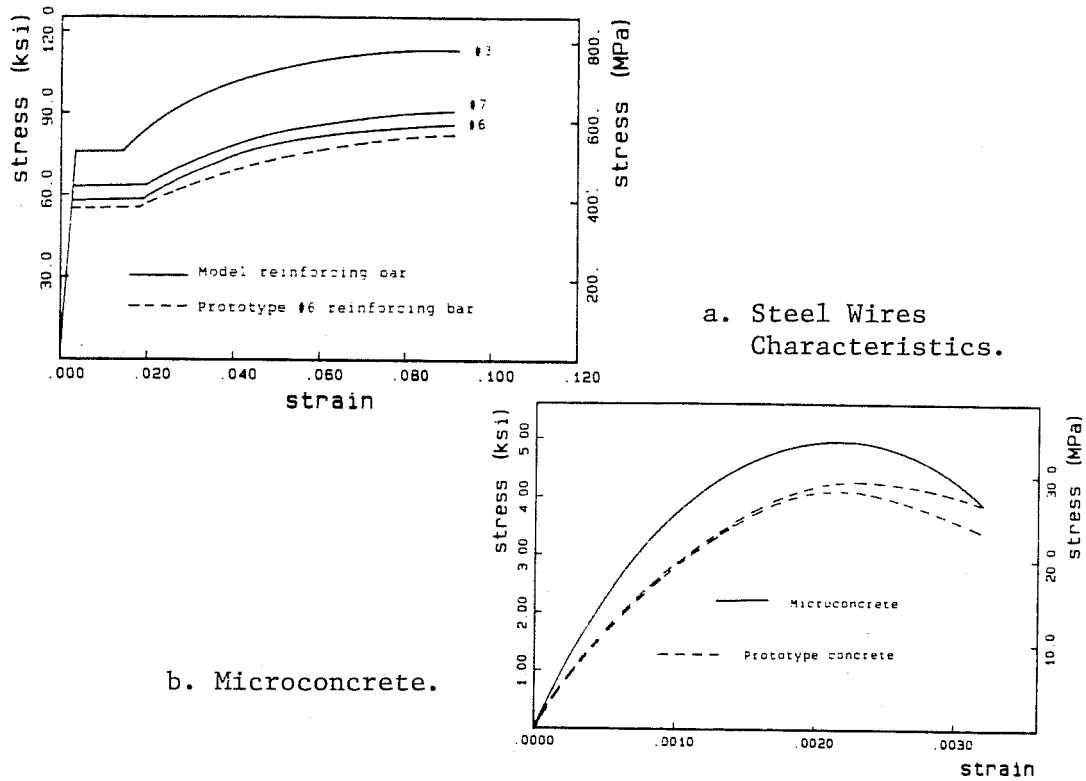


Fig. 3.40 - Material Stress-Strain Properties.

Several advantages arise from the use of reduced-scale models: reduction in costs (fabrication and testing), simpler and less costly set-ups, and the possibility of conducting dynamic tests using small shaking tables. However, there are also important limitations that cannot be ignored, such as localized effects, crack propagation patterns and crushing (failure modes). In this test series it was observed that the global response could be studied with confidence in small-scale R/C models, but after strength deterioration begins it is difficult to assess bond deterioration and localized effects [Wallace and Krawinkler (13)]. It should be noted that localized failure modes that induce strength deterioration within the specimen can be identified and studied in full-scale prototype specimens such as the full-scale subassemblage tests.

3.3.2.1 The Geometry of the Specimens. The four Stanford University components were modelled after the University of Texas full-scale prototype subassemblage tests. The geometric dimensions were reduced by a factor of 12.5 based on the prototype's subassemblage dimensions, Fig. 3.20. Each of the interior and exterior components was built with and without cast in-situ slab in order to study the slab participation effect.

The reinforcement steel was scaled down and wires were used to model the equivalent bars in the prototype specimens. To

model the #3 (10 mm), #5 (19 mm) and #7 (22 mm) bars, No. 22, 16 and 15 gauge wires were used respectively.

3.3.2.2 Material Properties. The reinforcement steel for the models was custom made in the laboratory to obtain a stress-strain diagram with a flat yield plateau and strain-hardening characteristics of full-size bars, Fig. 3.40(a). This scaling process was carried out by using AISI (0.6%) carbon wire with deformations machined by a pair of grooved rollers. After grooving, the wires were heated in an oven at 900°C for 30 minutes and then cooled slowly to restore the yield plateau and the stress-strain diagram [Wallace and Krawinkler (13)].

The microconcrete was made with high-early strength Type III Portland cement, water and washed sea sand in the proportions of 1.0:0.75:3.5. The microconcrete design mix was quality controlled by testing 50 mm x 100 mm (2.0 in x 4.0 in.) cylinders. The resulting stress-strain diagram showed a consistently higher response than the prototype concrete, Fig. 3.40(b). The casting procedure followed in the models was identical to the prototype specimens. First, all the forms were filled with microconcrete to the top of the slab and then, the upper column was cast. The reinforcement layout in the model components followed the size and spacing found in the prototypes. The material properties measured for different batches are shown in Table 3.10.

TABLE 3.10 - STANFORD UNIVERSITY MATERIAL PROPERTIES

		Concrete Properties		Reinforcing Properties							
				Beam Steel		Column Steel		Slab Steel		Wall Steel	
Specimen	Units	f'_c	f_t	f_y	f_u	f_y	f_u	f_y	f_u	f_y	f_u
Interior assembly with slab	MPa	39.4	—	389.	561.	427.	613.	513.	779.	—	—
	ksi	5.7	—	56.	81.	62.	89.	75.	113.	—	—
Interior assembly without slab	MPa	39.4	—	389.	561.	427.	613.	—	—	—	—
	ksi	5.7	—	56.	81.	62.	89.	—	—	—	—
Exterior assembly with slab	MPa	39.8	3.77	389.	561.	427.	613.	513.	779.	—	—
	ksi	5.8	0.55	56.	81.	62.	89.	75.	113.	—	—
Exterior assembly without slab	MPa	39.8	3.77	389.	561.	427.	613.	—	—	—	—
	ksi	5.8	0.55	56.	81.	62.	89.	—	—	—	—
Isolated Wall	MPa	30.9	2.71	--	--	415.	589.	—	—	475.	758.
	ksi	4.5	0.39	--	--	60.	86.	—	—	69.	110.
Shear wall —Frame	MPa	33.8	2.90	389.	561.	415.	589.	449.	668.	475.	758.
	ksi	4.9	0.42	56.	81.	60.	86.	65.	97.	69.	110.

TABLE 3.11 - STANFORD UNIVERSITY COMPONENT DATA.

Component	Exterior		Interior	
	EJ	ES	IJ	IS
Code Name	EJ	ES	IJ	IS
Slab	no	yes	no	yes
No. Data Points	7,826	11,271	7,810	8,451
Channel 1	W-beam load cell		W-beam load cell	
2	W-beam tip deflection		E-beam load cell	
3	W-beam rot. near col.		W-beam tip deflection	
4	W-bm. rot. far f. col.		E-beam tip deflection	
5	Joint shear distortion		W-bm. rot. far f. col.	
6	x	Tr.Bm.Twist	W-bm. rot. near col.	
7			E-bm. rot. near col.	
8			E-bm. rot. far f. col.	
9			Joint shear distortion	
10			S.G. Top W-beam (ext.)	
11			S.G. Bott. W-bm. (ext.)	
12			S.G. Top W-beam (int.)	
13			S.G. Bott. W-bm. (int.)	
14			x	S.G. top tie
15			x	S.G. bot. tie
16			x	S.G. slab #1
17			x	S.G. slab #2

3.3.2.3 Loading Program. The beam-column subassemblages were mounted in a test frame and loaded with weights to simulate dead load effects to be found in the prototype, Fig. 3.41. The applied displacement history was of the deterministic type where the beam tip displacements magnitude had the same scaled value as the displacement history used with the prototype specimens. The vertical loads were applied at the beam tip through hand operated screw jacks. The available recorded data is very extensive and is listed in Table 3.11. Selected portions of this data are used herein.

3.3.2.4 Instrumentation. The four specimens tested at Stanford were instrumented in a similar way but to a much lesser extent when compared with the prototype specimens. As seen previously, external (load cells, displacement transducers) and internal (strain gauges) measurements monitored the specimen response. The exterior subassemblages were instrumented as shown in Fig. 3.42, but without strain gauges. The recorded response for the exterior joint with slab (ES) and without slab (EJ) is shown in Appendix C. The instrumentation of the interior subassemblages is shown in Fig. 3.43, with the major difference of strain gauges being used. The response of the specimen with slab (IS) and without slab (IJ) is shown in Appendix C, as well as the crack failure pattern for IS.

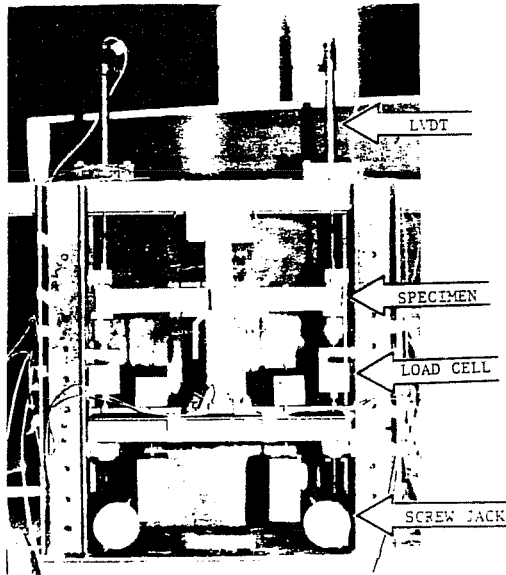


Fig. 3.41 - Stanford Univ. Test Set-up.

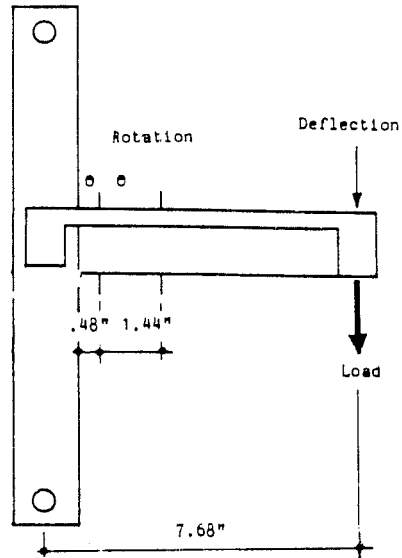
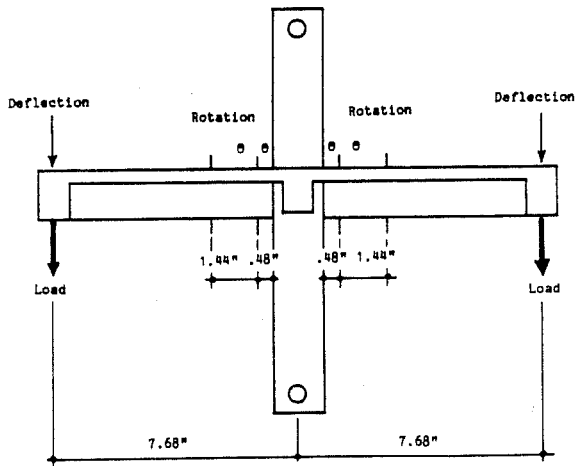
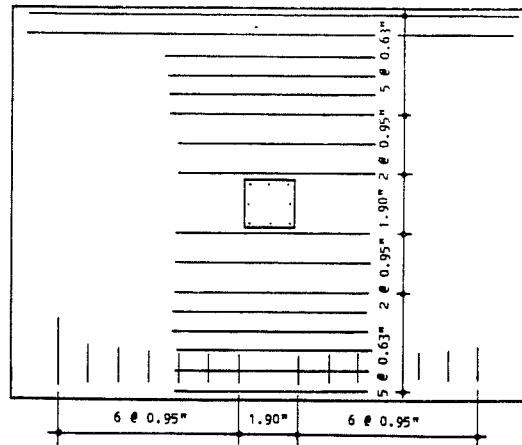


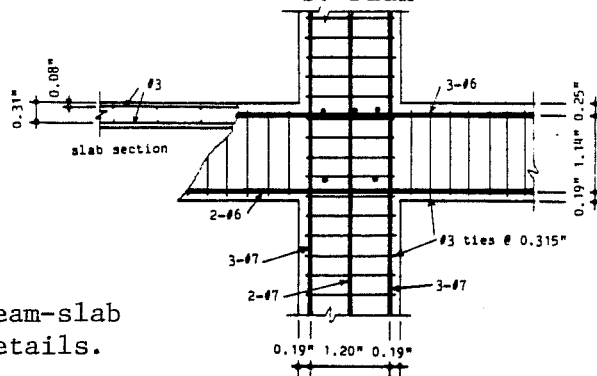
Fig. 3.42 - Exterior Joint Instrumentation.



a. Elevation.



b. Plan



c. Beam-slab Details.

Fig. 3.43 - Interior Joint Instrumentation.

3.3 Other U.S. Tests

The remaining reduced scale full-size tests performed in the U.S. under auspices of the U.S.-Japan Cooperative Research Program consisted of: (a) University of California - Berkeley (U.C.B.) 1:5 - medium-scale tests; (b) Portland Cement Association (P.C.A.) - 1:3.5 - medium-scale tests; and, (c) University of Illinois - Urbana - Champaign - 1:10 - small-scale tests.

Although there is no detailed information on the critical regions response at level Z2, there are strong similarities between the global response of the reduced scale models and the full-scale 7-story building which should be noted.

3.3.1 The U.C.B. 1:5 Tests. The reduced-scale building was designed and constructed based on the available data from the Japanese specimens also on the analytical correlation studies prior to the experimental testing program [Aktan et al. (3)].

The geometry of the tested specimen was identical to the B.R.I. specimen and was scaled by a factor of 5 to fit the shaking table grid, Fig. 3.44. The specimen was firmly attached through the base to the shaking table with prestressing cables in order to attain fixed-based conditions. The model reactive mass had to be corrected in order to reproduce gravity stresses of the B.R.I. building. Lead bricks were prestressed to the floor slabs. The added masses proved to be an important factor in the response [Aktan et al. (3)].

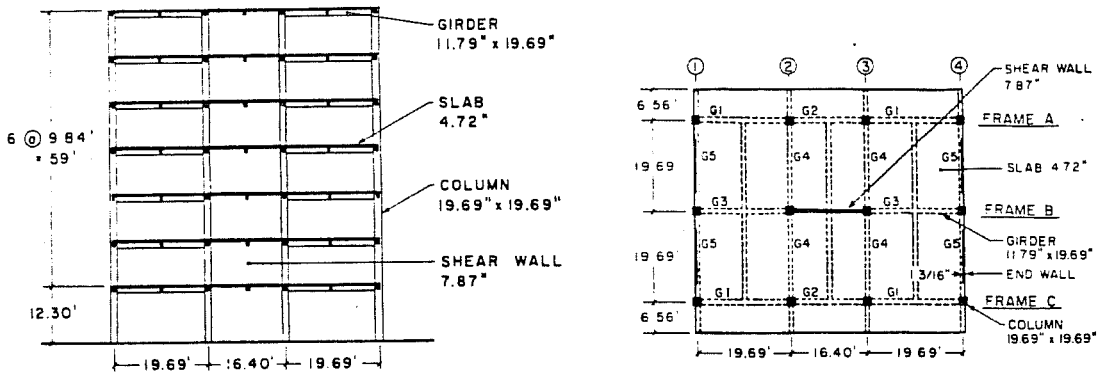


Fig. 3.44 - U.C.B. (1:5) Model [Aktan et al. (3)].

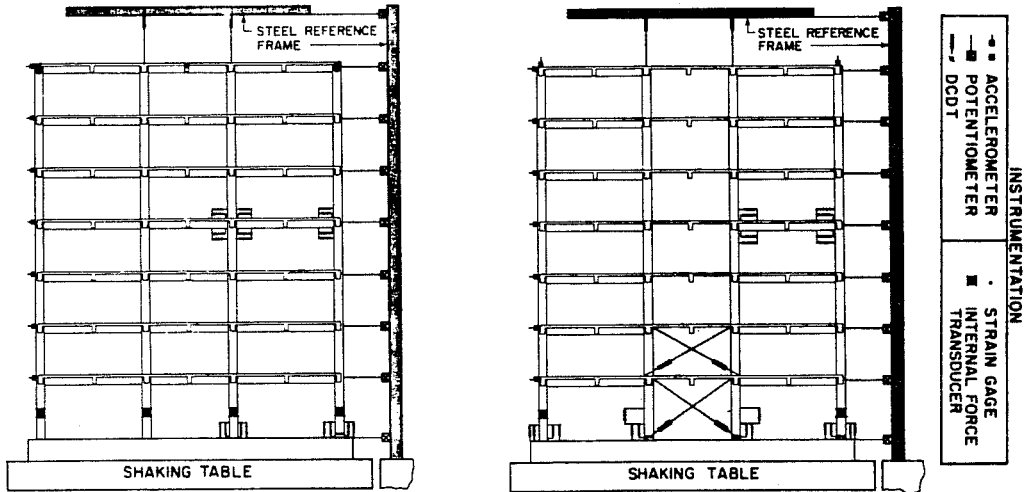


Fig. 3.45 - U.C.B. Model Instrumentation [Aktan et al. (3)].

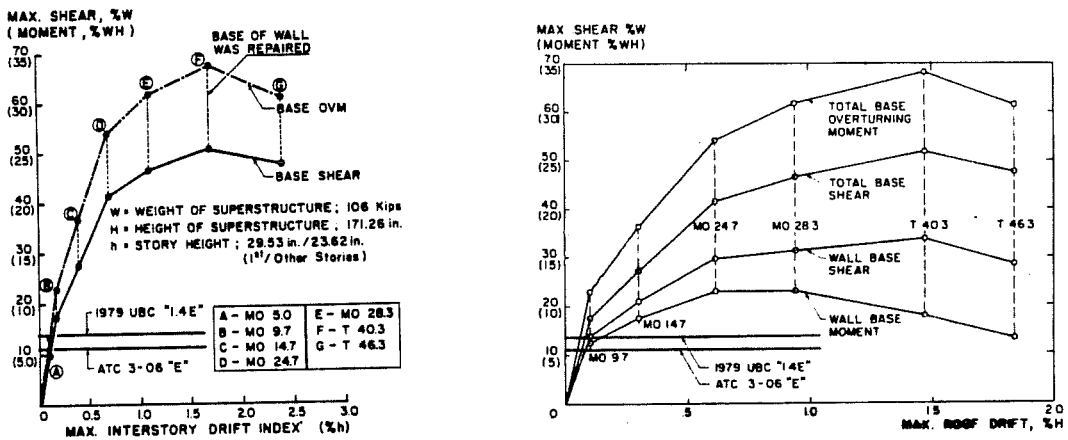


Fig. 3.46 - Wall Participation in the Total Structure.

Some problems arose as a result of scaling. First, the ultimate microconcrete strength was consistently higher than the target value, which was also observed with the Stanford University models. Consequently, some problems may have arisen in simulating the cracking limit state and ultimate strength. On the other hand, the use of small diameter bars (larger specific surface) proved to be beneficial in regard to bond action. Lower bond stresses at the interface steel-concrete are developed with consequent improved anchorage lengths. The material properties are shown in Table 3.12.

A similar loading program as the one used in the B.R.I. building was used. However, some important differences existed: (a) the shaking table introduced horizontal as well as small vertical and rotational motions at the base level; (b) the used excitation histories were of full duration with complete ground motion records.

This loading program is somewhat different from the B.R.I. structure where loads were introduced throughout the height at each floor level by on-line computer controlled hydraulic jacks. Also the P.S.D. loading method results in slower loading rates and different load histories due to the time spent in applying the displacements and the error accumulation with the iterative P.S.D. technique [Aktan et al. (3)]

TABLE 3.12 - MATERIAL PROPERTIES [Aktan et al.(3)].

Reinforcement	$\frac{E_m}{E_p}$	$\frac{F_{ym}}{F_{yp}}$	$\frac{\epsilon_{STH_m}}{\epsilon_{STH_p}}$	$\frac{E_{STH_m}}{E_{STH_p}}$	$\frac{F_{um}}{F_{up}}$	$\frac{\epsilon_{um}}{\epsilon_{up}}$
Columns	1.091	1.074	1.20	0.407	0.878	1.110
Beams	0.980	1.112	1.545	0.629	0.938	0.977
Walls/ Slabs	1.099	1.067	1.676	0.311	0.953	0.875

E_m, E_p = modulus of elasticity for model and prototype

F_{ym}, F_{yp} = yield force of model and prototype

$\epsilon_{STH_m}, \epsilon_{STH_p}$ = strain at onset of strain hardening of model and prototype

E_{STH_m}, E_{STH_p} = strain-hardening modulus for model and prototype

F_{um}, F_{up} = maximum tensile force for model and prototype

$\epsilon_{um}, \epsilon_{up}$ = ultimate strain for model and prototype

Location concrete	Age, days	Sample Size	$f_{c,max}$ ksi	$\sigma_{f_{c,max}}$ ksi	$\bar{\epsilon}_0$ in./in.	σ_{ϵ_0} in./in.	$\bar{E}_{0.45f_{c,max}}$ ksi	$\sigma_{E_{0.45f_{c,max}}}$ ksi
Footing	254	1	5.44	--	0.00340	--	2970	--
Column Stubs	254	1	6.51	--	0.00330	--	3490	--
First Floor	28	3	3.61	0.116	0.00250	0.000325	2800	123.94
	216	2	5.68	0.032	0.00350	0.000141	3160	183.85
	456	4	5.67	0.215	0.00380	0.000206	2940	61.22
Second Floor	28	3	4.18	0.141	0.00292	0.000157	2940	109.70
	208	2	5.66	--	0.00350	0.000283	3380	158.39
	446	3	5.70	0.026	0.00355	0.000132	2990	123.52
Third Floor	28	3	3.93	0.146	0.00282	0.000274	3340	63.17
	195	2	5.99	--	0.00350	--	3380	28.99
	434	4	5.59	0.465	0.00345	0.000208	3070	125.55
Fourth Floor	28	3	3.68	0.142	0.00261	0.000153	2930	85.91
	187	2	5.26	--	0.00320	--	3320	229.10
	425	4	5.54	0.156	0.00361	0.000189	2930	81.18
Fifth Floor	28	3	4.75	0.086	0.00283	0.000293	3080	61.65
	175	1	5.88	--	0.00320	--	3530	--
	413	2	5.50	0.110	0.00330	0.000141	3030	22.63
Sixth Floor	28	2	4.16	0.040	0.00288	0.000354	2880	11.31
	168	1	5.48	--	0.00350	--	3290	--
	408	3	5.45	0.263	0.00344	0.000351	2970	59.77
Seventh Floor	28	3	4.87	0.122	0.00284	0.000290	3060	93.40
	159	1	5.84	--	0.00290	--	3020	--
	399	4	5.80	0.421	0.00353	0.000340	3150	154.00

*As determined from load control tests of 3-in. x 6-in. field-cured cylinders.

$\bar{f}_{c,max}, \sigma_{f_{c,max}}$ = mean and standard deviation of maximum concrete compressive stress.

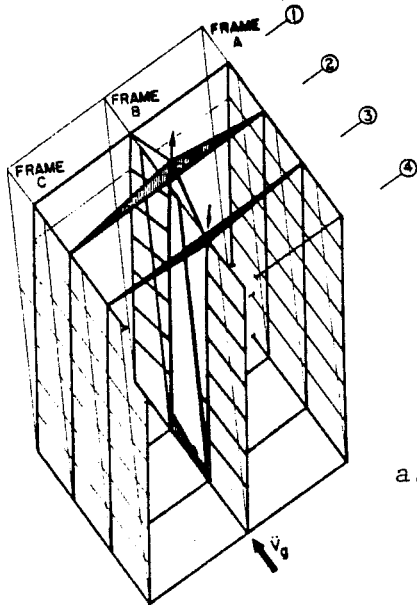
$\bar{\epsilon}_0, \sigma_{\epsilon_0}$ = mean and standard deviation of strain at maximum compressive concrete stress.

$\bar{E}_{0.45f_{c,max}}, \sigma_{E_{0.45f_{c,max}}}$ = mean and standard deviation of secant modulus at 45% of maximum compressive concrete stress. 1 in. = 25.4 mm ; 1 ksi = 6.89 MPa

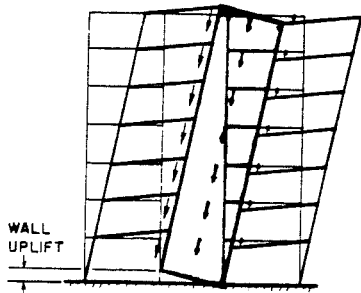
The specimen instrumentation consisted of Fig. (3.45) (a) internal force transducers (IFT) at mid-height of the first floor columns; (b) displacement transducers (L.P. and L.V.D.T.) at each floor level; (c) two accelerometers at different floor levels; and (d) strain gauges at the column base.

The response of the whole model varied throughout the test. The wall participated as the most important element in providing lateral stiffness and resistance. At an initial undamaged stage, 80% of the total shear resistance and 56% of the total overturning resistance were taken by the wall, Fig. 3.46. Towards the end of the test, as damage is built into the most strained elements were damaged and spread of plastification occurred, the above values decreased to 60% (-20%) and 22% (-38%), respectively. Also, due to 3-D action, the lateral frames through the transverse beams and cast in-situ slab restrained the wall of "expanding" because of unclosed cracks and built-in permanent steel yield strains. The outrigging frame action on the wall led to substantial increase in the axial compression level at the wall base, Fig. 3.47, [Aktan et al. (3)].

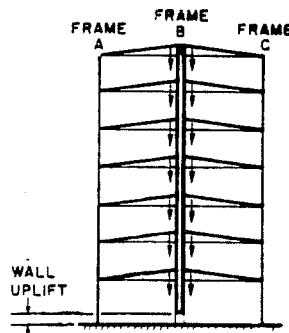
3.3.2 P.C.A. 1:3.5 Tests. The two medium-scale specimens tested at the P.C.A. laboratories modelled the cantilever wall and the frame-shear wall to be found in the B.R.I. building, Fig. 3.48(a,b). Although the analytically predicted strengths were close to the experimental values, they failed to reach the



a. U.C.B. Model - 3-D Perspective.



b. Wall Uplift - Inner Frame.



c. Transverse Frame.

d. Wall Interaction Curve.

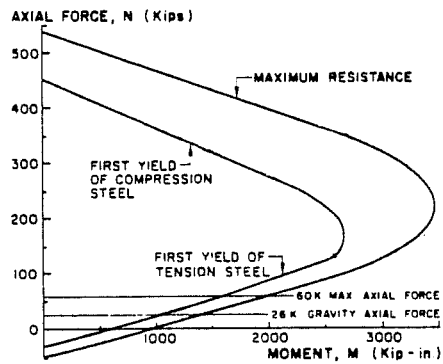


Fig. 3.47 - Outrigging Effect on Shearwall-Frame System, [Aktan et al.(3)].

observed B.R.I. building values. Corrections made to take into account 3-D effects resulted in the analyses which agreed well with the measured B.R.I. building strength, [Morgan et al. (7)]. The dual system slab participation was modelled with 13.0 in. (0.32 m) stubs on either side of the beam centerline.

3.3.3 The University of Illinois 1:10 Tests. The three small-scale (1:10) tests conducted at the earthquake simulator (U. of I.) were modelled after the B.R.I. building. The aim of this test program was to understand the role of small-scale models in portraying the dynamic behavior of full-scale buildings [Wolfgram et al. (16)].

Although good correlations were obtained in the overall response and ultimate strength, only planar behavior at low drift levels was successfully reproduced. This may derive from the absence of a cast in-situ slab that induces 3-D participation on all the concerned lateral resisting structural systems: external frames and central frame-shear wall, Fig. 3.49.

As observed with the previous small to medium-scale tests, localized behavior (bond anchorage and cracking patterns) could not be realistically portrayed.

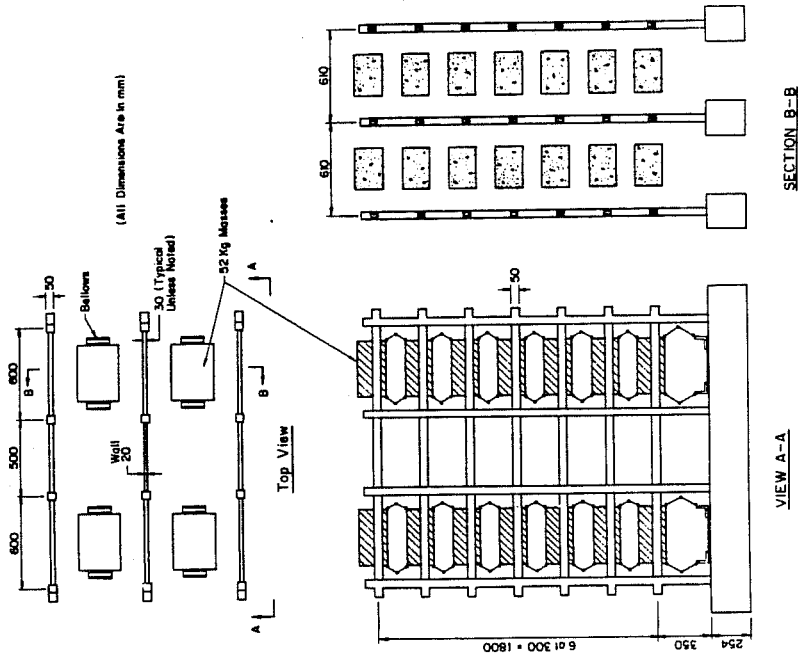
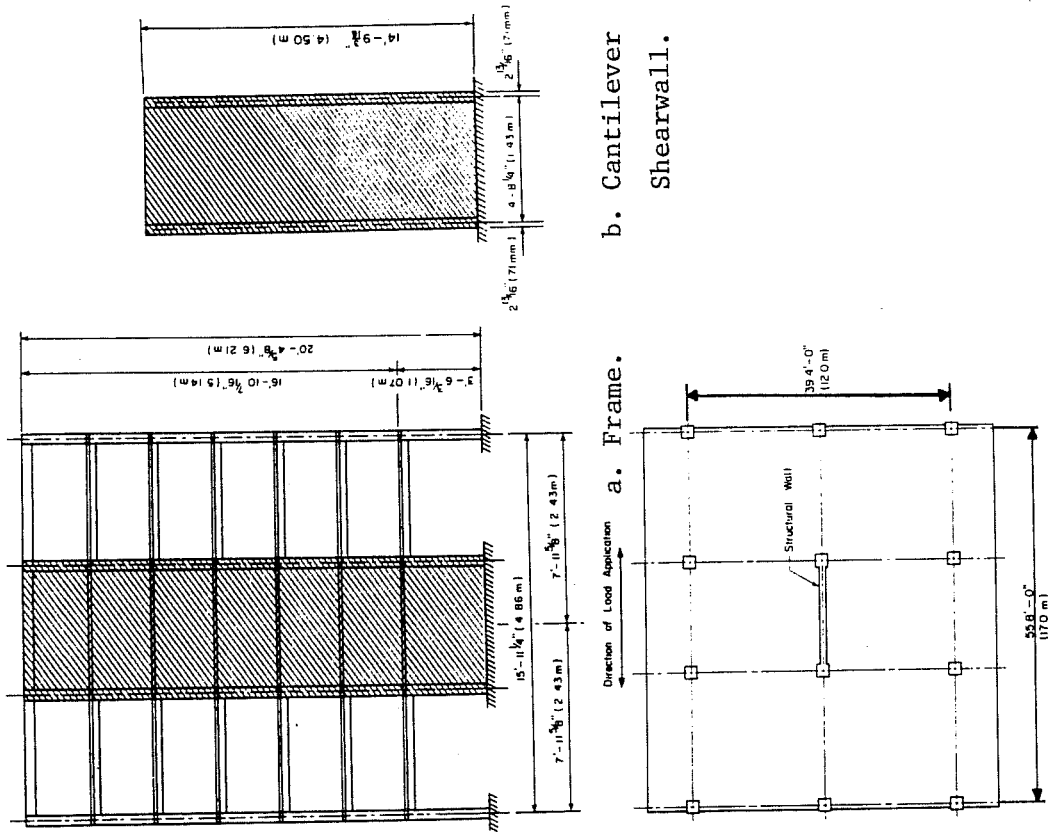


Fig. 3.48 - PCA Medium-scale Tests, [Morgan et al. (7)J].

Fig. 3.49 - University of Illinois Small-scale Tests, [Wolfram(16)J].

3.4 References

1. ACI Committee 318 - Building Code Requirements for Reinforced Concrete and Commentary, American Concrete Institute (ACI), Detroit, MI, 1977.
2. ACI Committee 318 - Building Code Requirements for Reinforced Concrete and Commentary, ACI, Detroit, MI, 1983.
3. A. Aktan, V. Bertero, F. Charney and R. Sause - "Earthquake Simulator Tests and Associated Experimental, Analytical, and Correlation Studies of One-Fifth Scale Model", ACI SP 84-13, ACI, Detroit, MI, 1985
4. A.I.J. - Architectural Institute of Japan Standard for Structural Calculation of Reinforced Concrete Structures, A.I.J., Tokyo, Japan, 1982.
5. H. Hiraishi, S. Nakata, Y. Kitagawa and T. Kaminosono - "Static Tests on Shear Walls and Beam-Column Assemblies and Study on Correlation Between Shaking Table Tests and Pseudo-Dynamic Tests", ACI SP 84-2, ACI, Detroit, MI, 1985.
6. M. Joglekar, P. Murray, J. Jirsa and R. Klingner - "Full-Scale Tests of Beam-Column Joints", ACI SP 84-10, ACI, Detroit, MI, 1985.
7. B. Morgan, H. Hiraishi, and W. Corley - "Medium Scale Wall Assemblies: Comparison of Analysis and Test Results", ACI SP 84-9, ACI, Detroit, MI, 1985.
8. P. Murray - "A Study of Beam-Column Joints under Seismic Loads: Component Tests vs. Building Response", unpublished Master's thesis, The University of Texas at Austin, August, 1982.
9. S. Nakata, S. Otani, T. Kabeyazawa, Y. Kai and S. Kimura - "Tests of Reinforced Concrete Beam-Column Assemblages," U.S.-Japan Cooperative Research Program - 1st Meeting, Joint Technical Coordinating Committee, B.R.I., Tsukuba, Japan, January 1981.
10. S. Okamoto, S. Nakata, M. Yoshimura and T. Kaminosono - "A Progress Report on the Full-Scale Seismic Experiment of a Seven-Story Reinforced Concrete Building - Part of the U.S.-

Japan Cooperative Research Program", Report No. 94, Building Research Institute, Ministry of Construction, Tokyo, Japan, March 1982.

11. J. Penzien and H. Umemura - "Recommendations for a U.S.-Japan Cooperative Research Program Utilizing Large-Scale Testing Facilities", Report No. UCB/EERC - 79/26, University of California, Berkeley, Earthquake Engineering Research Center, September, 1979.
12. V. Sattary and J. Wight - "U.S.-Japan Cooperative Research Program: Instrumentation of the Full-Scale Reinforced Concrete Test Structure", Report UMCE 85-5, Department of Civil Engineering, The University of Michigan, Ann Arbor, MI, April, 1985.
13. B. Wallace and H. Krawinkler - "Small Scale Model Tests of Structural Components and Assemblies", ACI SP 84-11, ACI, Detroit, MI, 1985.
14. J.K. Wight, Ed. - Earthquake Effects on Reinforced Concrete Structures, U.S.-Japan Research, American Concrete Institute Publication SP-84, Detroit, MI, 1985.
15. J. Wight, S. Nakata and T. Kaminosono - "Construction and Instrumentation of the Full Scale Specimen", ACI SP-84-3, Detroit, MI, 1985.
16. C. Wolfgram, D. Rothe, P. Wilson and M. Sozen - "Earthquake Simulation Tests of Three One-Tenth Scale Models", ACI SP-84-12, ACI, Detroit, MI, 1985.

CHAPTER IV

BASIS FOR COMPARISON IN RESPONSE OF DIFFERENT TESTS

4.1 Introduction

Monotonic or cyclic load tests of isolated structural members form the basis of many design requirements for seismic loading. To avoid the limitations inherent in such tests, current trends in assessing structural response include testing increasingly complex structural systems or subassemblies. Such systems have been analyzed and tested under a variety of seismic loadings.

Although the importance of the structure's seismic response has been recognized, different sets of tests and interpretations of those tests have led to divergent design rules among different professional groups. The differences in design recommendations may result from [Paulay and Park (4)]: (1) different performance criteria; (2) inadequate identification of the important parameters that affect the behavior; and, (3) significant variations in the interpretation of laboratory test results.

4.2 Performance Criteria

The design and construction of a DMRF subjected to severe loading conditions requires attention to detailing. It is

clearly recognized that particular care should be given to the design of joints between beams, columns or slab system.

The subassemblage seismic design criteria requires that the joint must have [Paulay (3)]: (1) larger strength capacity than the members it connects; (2) column load-carrying capacity cannot be jeopardized by strength degradation in the joint vicinity; (3) elastic behavior under moderate seismic disturbances (small story drifts); and (4) easy fabrication and assembly requirements.

Although design requirements can be readily met, degrading shear and bond strength and stiffness deterioration may render the structure unusable under severe seismic loadings. Consequently, a performance criteria must be developed in which stiffness and energy absorption-dissipation features are considered. The DMRF stiffness criteria can be defined in terms of the imposed deformation levels (interstory drifts). The energy criteria can be defined using ductility and energy dissipation characteristics through hysteretic damping in a load-displacement cycle.

4.3 Test Specimens

The availability of test data from a full-scale building and data from tests of components of the structure provide a rare opportunity to conduct a comparative study. It is recognized

that there are major differences between a total system and a component. Different boundary conditions and methods of applying loads lead to differences in observed response. However, within the scope of this work it is assumed that a comparative study illustrating similarities and differences among the different tests is valuable (Table 4.1). The available test results are used to target different criteria (stiffness, energy) under various deformation levels. Finally, design criteria are evaluated considering the results of tests on different specimens.

4.4 Levels of Comparison

In R/C structures three distinct stages of behavior can be identified: (1) initial elastic uncracked; (2) post-cracking, pre-yielding; and, (3) post-yielding phase, depending on the imposed deformation levels.

These stages can be observed in the B.R.I. building and in the component tests. Therefore, it is assumed that the test results can be correlated. The approach followed in this study covers two aspects: (1) direct comparisons between the B.R.I. building critical regions and correspondent components and/or, (2) direct comparisons between components. Reversed cyclic displacement-controlled loading was imposed on the test specimens where successively larger displacements were alternated with

TABLE 4.1 - COMPARISON STUDIES IN COMPONENT TESTS

LOCATION	Japan - BRI Tsukuba City	University of Texas Austin	Stanford University
Test Scale	1 : 1	1 : 1	1 : 12.5
Type of Tests	Seven - storey building	Subassemblage Beam - Column Tests	
		1. Interior 2. Exterior 3. Top corner	2. Modified a. Interior b. Exterior
		1. Prototype a. Interior b. Exterior	w/ slab : 1. Exterior 2. Interior
I. INPUT			
Load Histories	Horizontal Lateral Load	Vertical Beam Tip Load (displacement controlled)	
II. OUTPUT - MEASUREMENTS			
A. Direct :			
1. Bar Strains	Y	Y	Y
1.1 Beams	Y	Y	Y
1.2 Columns	Y	Y	Y
1.3 Slabs	Y	Y	Y
2. Displacements	Y	Y	Y
3. Load (Beam Tip, Storey sh.)	Y	Y	Y
B. Computed :			
1. Joint Distort.	N	Y	Y
2. Beam Rotation	Y	Y	Y
3. Trv. Bm. Twist	N	Y	Y
4. Equiv. Drift	Y	Y	Y
C. Macrodata			
1. Cracking Patt.	Y	Y	N/A

smaller ones. Depending on the deformation level and history of previous load cycles it is expected that increasing damage levels would be observed in the specimens.

The data obtained from the direct observations performed on the test specimens consists of three main groups: (1) bar strains; (2) LVDT displacements; and, (3) applied loads. Based on these elementary observations, more meaningful indications of structural response (derived data) can be computed, e.g., member rotations, twists, drifts, joint distortions.

The instrumentation used to measure displacements covers a wide range of possible deformation levels. Therefore, it is a convenient parameter to be used in comparisons with other data.

The most important variable in the set of "derived" data is the equivalent drift ratio, R , because it is not strongly affected by localized aspects of response (concrete spalling, cracking, bond deterioration) over a wide range of deformations.

4.5 Equivalent Drift Ratio

The seismically loaded DMRF transfers inertial forces from one floor to another through the columns. During this force transfer process, it is usually assumed in analysis that the columns in each floor level are under opposite and nearly equal horizontal shears and moments at both ends. Therefore, the point of counter-flexure for the column would be located near its

midheight, Fig. 4.1. However, it is recognized that under seismic actions, lower story drifts may become very large and the location of the plastic hinge can vary along the column's height, Fig. 4.2, [Paulay (3)]. On the other hand, it has been found that elastic analyses used to assess P- Δ demands during inelastic response leads to incorrect predictions of the inelastic distortions.

In order to meet compatibility requirements, it is necessary that not only the columns but also the beams framing into the joint be in reverse curvature. It is assumed that the inflection points are located at the beam's midspan, although it has been observed that the inflection point shifts during loading. By specifying the location of inflection points (zero moments) it is possible to define the subassemblage geometry, Fig. 4.1. Although joint behavior could be studied if the whole structural system would be tested in the laboratory, economic and physical constraints impose a limit on the specimen size.

The calculation of the equivalent drift ratio, R, (Fig. 4.3) is simply given by:

$$R = \frac{\Delta_n}{h_n} = \frac{\Delta_b}{l_b/2} \quad (4.1)$$

where: Δ_n = horizontal building deflection at level n;
 h_n = floor height at level n;

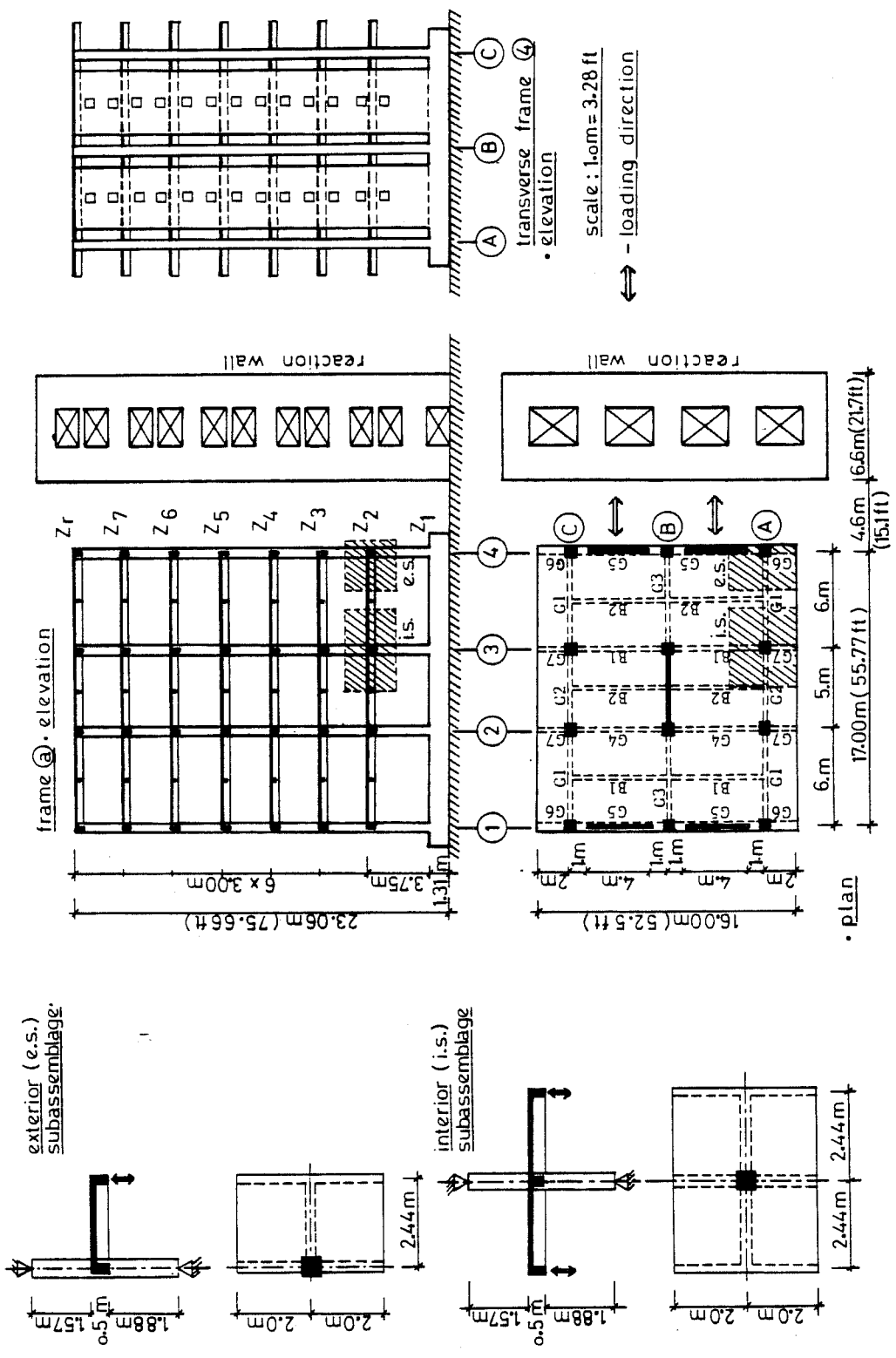
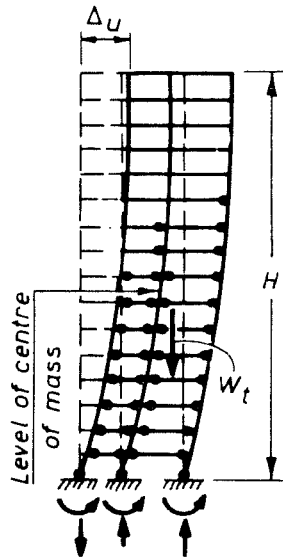
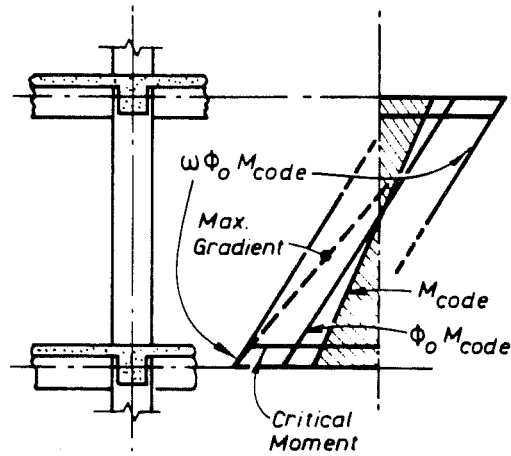


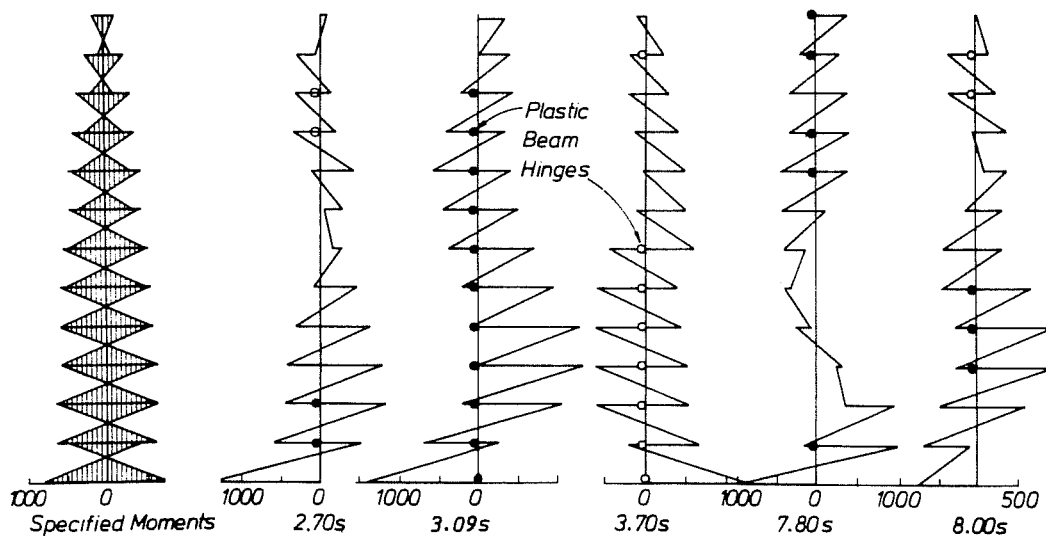
Fig. 4.1 - BRI Building and Component Tests.



a. Typical Configuration under Earthquake Attack.

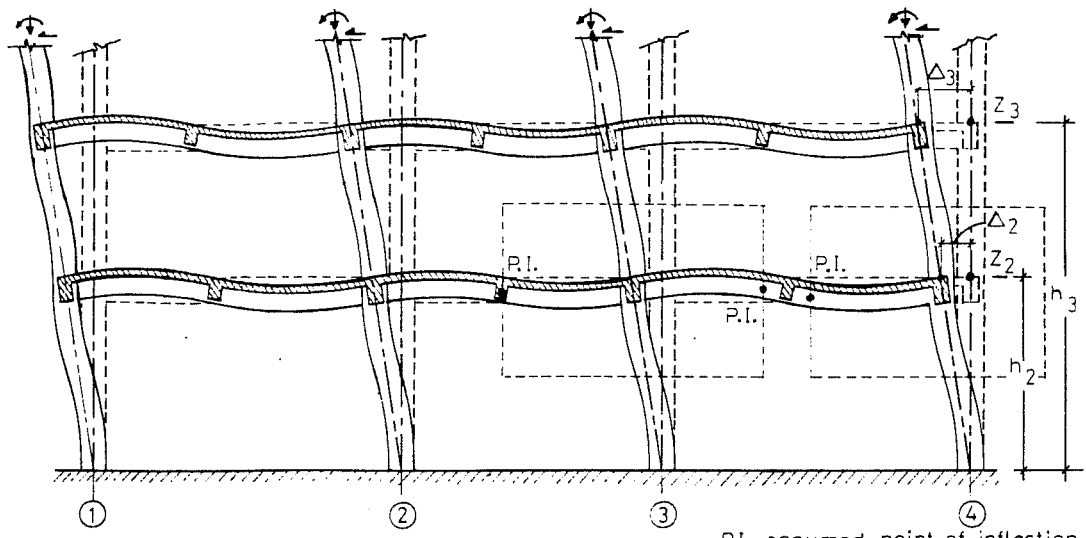


b. Column Design Moment Magnification.

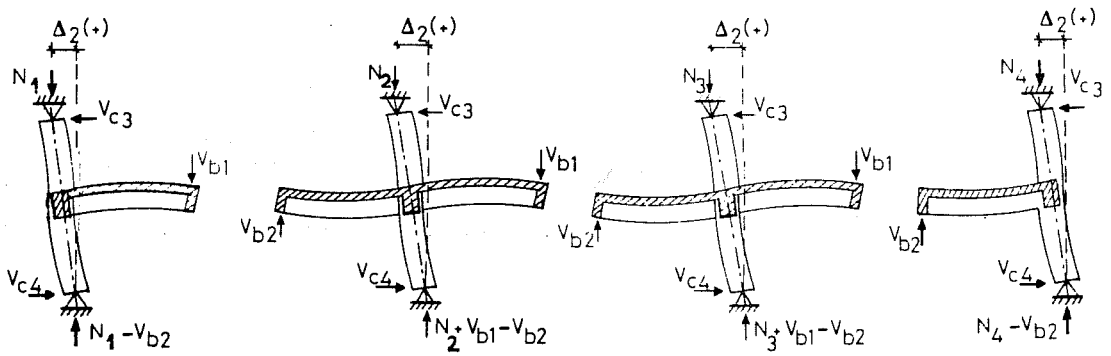


c. Exterior Column in a 12-story Frame - Bending Moment Patterns at Instants of Large Earthquake Motions.

Fig. 4.2 - Column Moment Variation in Ductile Frames under Lateral Loads, [Paulay (3)].

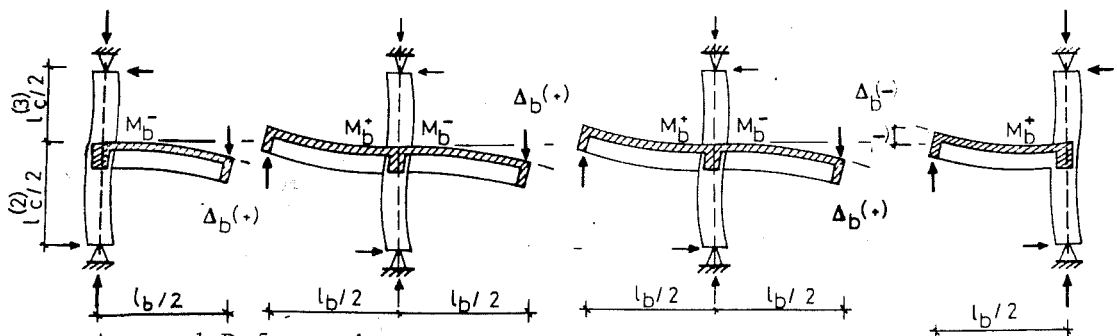


a. Deformed Frame.



b. Actual Deformation.

$$\text{Drift ratio } R = \frac{\Delta_2}{h_2} = \frac{\Delta_b}{l_b/2}$$



c. Assumed Deformation.

Fig. 4.3 - Equivalent Drift Assumption.

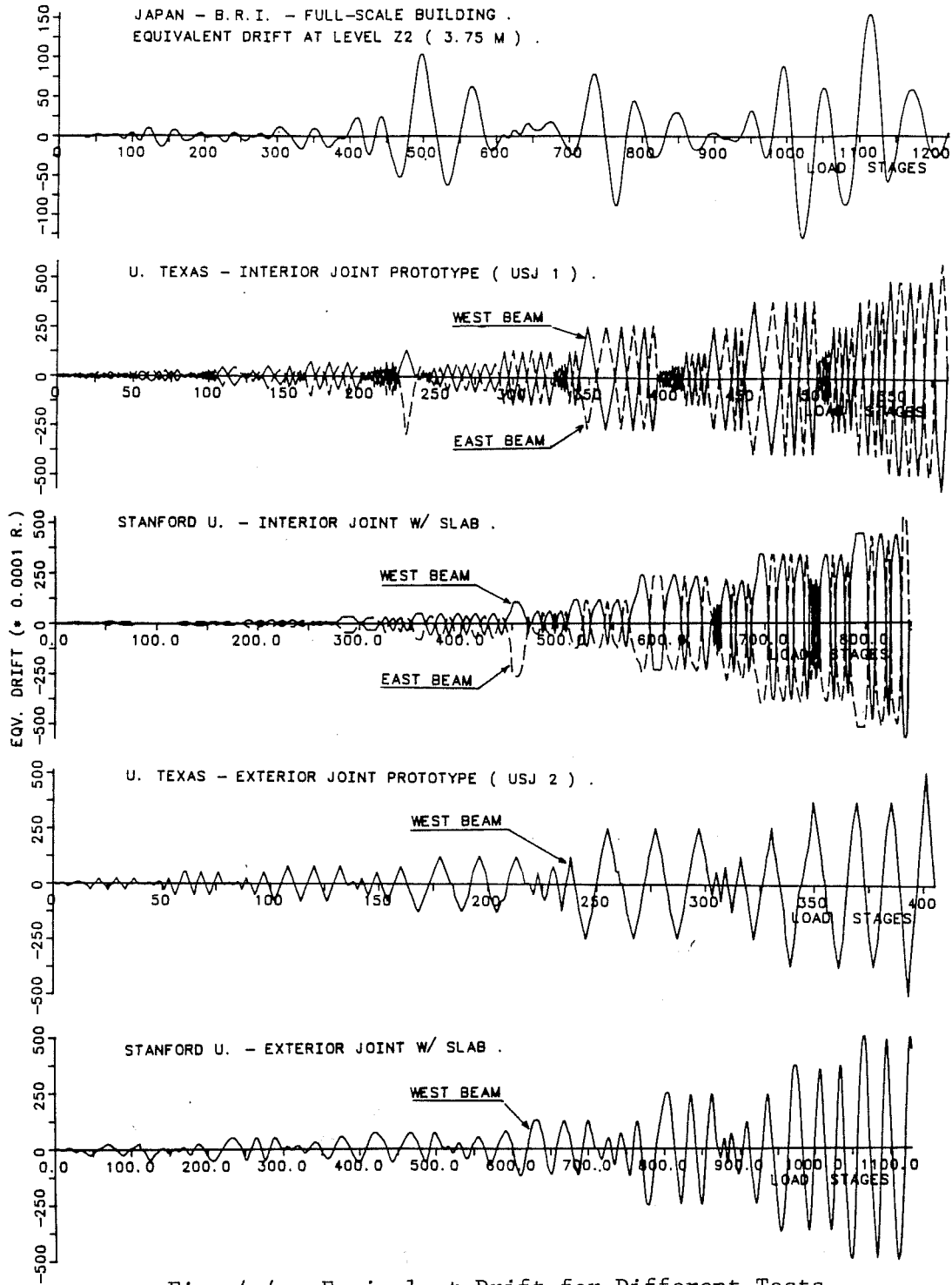


Fig. 4.4 - Equivalent Drift for Different Tests.

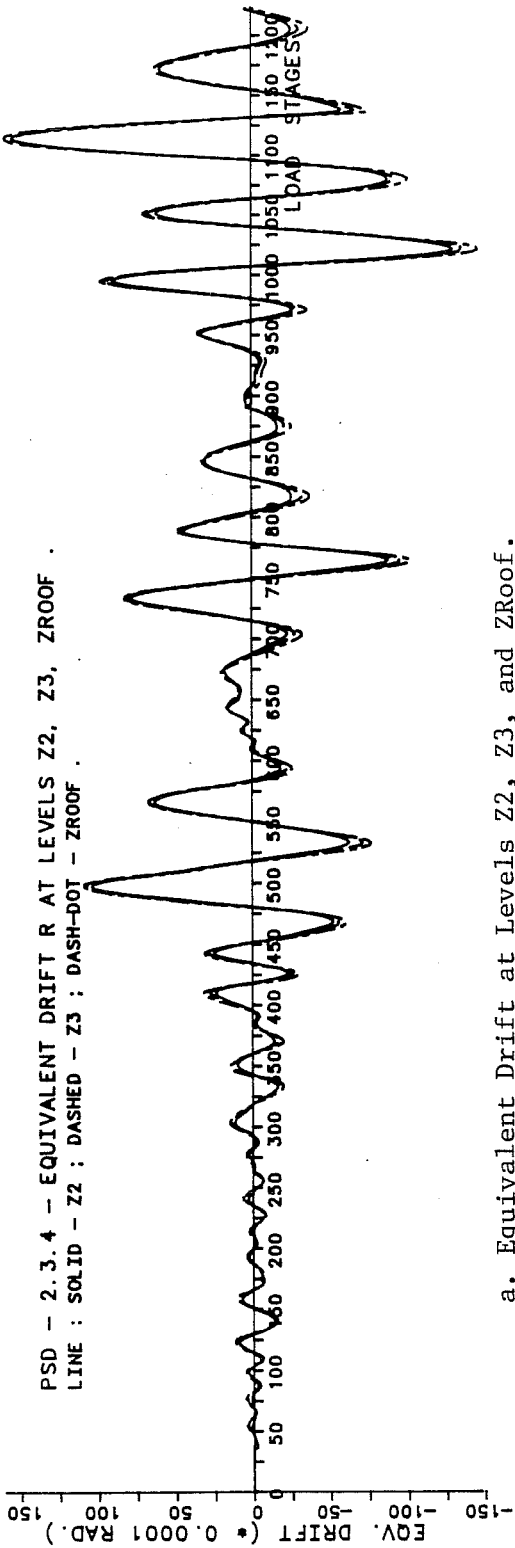
Δ_b = beam tip deflection; and

$l_b/2$ = beam cantilever length

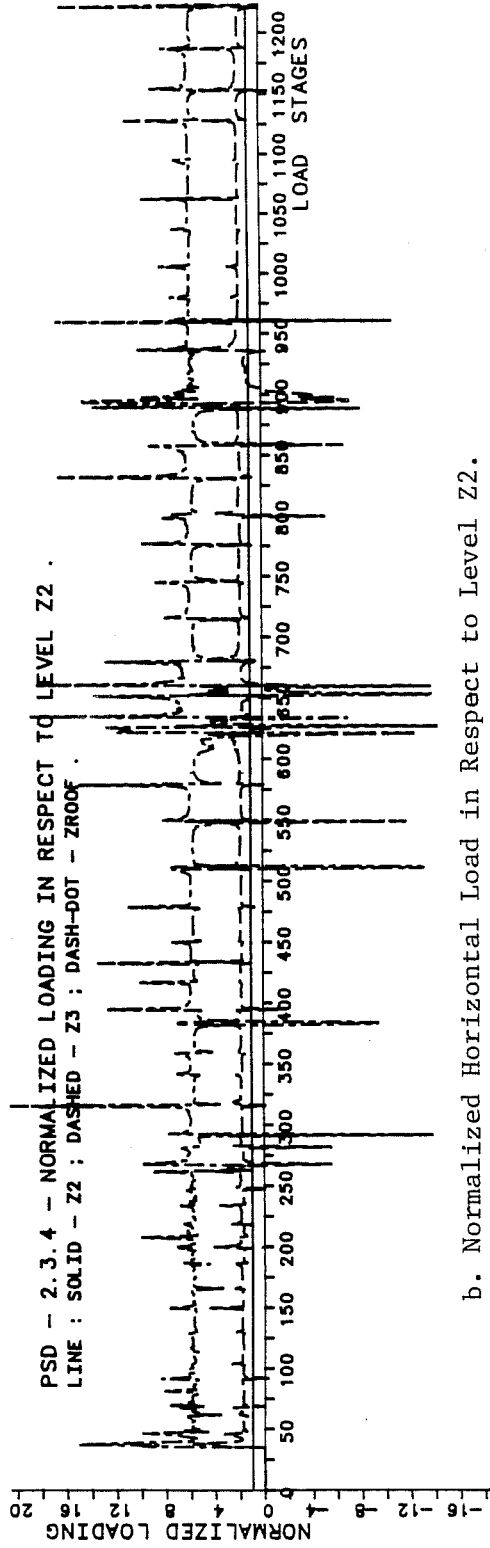
The equivalent drift history is shown in Fig. 4.4 for the various tests studied in detail. The equivalent drift can be readily verified with the results obtained in the B.R.I. building where the structure was laterally loaded with hydraulic actuators controlled by an on-line computer system. The loads were applied using an inverted triangular distribution. The verification of the equivalent drift ratio was made for levels Z2, Z3 and Zroof with their results normalized in regard to level Z2, Fig. 4.5-a. It can be seen that good agreement was obtained for the overall building rotation at each floor level based on equation 4.1.

The normalization of the applied horizontal loads at levels Z3 and Zroof with respect to the load at level Z2 also shows that they are approximately 1.80 and 5.80 times larger, Fig. 4.5-b. A story height ratio (Z_n/Z_2) confirms the inverted triangular loading pattern imposed on the structure.

It should be noted again that inverted triangular loading pattern primarily excited the first response mode and was considered for simplicity. It is recognized that under large inelastic pulses the contribution of higher modes can play a dominant role in the DMRF response.



a. Equivalent Drift at Levels Z2, Z3, and ZRoof.



b. Normalized Horizontal Load in Respect to Level Z2.

Fig. 4.5 - BRI Building - Load-Deformation Response.

4.6 Other Deformation Response Variables

The other important variables that characterize response include bar strains, beam rotations, beam twist, joint shear distortion, bar slip and cracking patterns.

Bar strains are important in characterizing early stages of deformation. However, under increasing displacements, yielding occurs in some bars. Once yielding occurs, it is difficult to estimate precisely the force in the bar due to the Bauschinger effect and the previous load history.

Beam plastic hinge rotations are derived based on a pair of top and bottom potentiometers installed on an embedded rod at the beam's critical cross section as shown in Fig. 3.5-b. The difference in the two readings in relation to the column is used to compute the amount of beam rotation from the column face to the cross section with the rod. The distance at which the rod was installed varied from 0.20 - 0.23 m (8.-9. in.) in the BRI building to 0.15m (6. in.) in the University of Texas and Stanford University components. In the components a second set of potentiometers were installed at 0.60 m (24 in.) from the column face. These secondary beam rotation measurements are important in order to verify if the assumption of a plastic hinge region development near the column is valid. It should be noted that the calculated rotations do not represent the actual beam rotations since no detailed corrections were made for joint

distortions and elastic flexural column rotations. However, in the BRI building, the Japanese (1/2-scale) components, and the U.S. components, the beam rotations were determined in the same way.

Transverse beam twist was only evaluated in the University of Texas and one exterior Stanford University specimens. Twists were computed at 0.50m (20 in.) and 1.61m (64 in.) from column face. The first value corresponds to d (beam depth) and the second one is near the end of the transverse beam. As the longitudinal beam was loaded, the action of the slab on the transverse beam resulted in beam twist with respect to the column. The amount of twist imposed pm the joint core is important for evaluating the extent of stiffness degradation.

Joint shear distortion is evaluated through the relationship shown in Fig. 3.28. The joint shear distortion was determined only in the U.S. tests and provided a measure of the total of shearing distortion strain imposed on the joint core.

Bar slip in conjunction with strain measurements at different sections throughout the joint core gives a good indication of bond performance during the test.

The cracking distribution gave a macroscopic image of response at different loading stages. Cracking indicated the regions where high stresses were occurring.

4.7 The P-Delta Effect on Component Test Results

The U.S. tests were performed on components where the column remained vertical throughout and no axial load was applied. The test setup is simpler if the racking loads are introduced by hydraulic actuators at the beam tip. The Japanese 1/2-scale tests represent a more realistic model, in which a constant axial load was present and the column end was free to displace vertically. Racking loads were applied at the beam ends based on a deterministic load history.

Although a more realistic test setup including P-delta effects could have been considered, the testing of components with a vertical column and the presence of axial load, requires that some corrections to the test data. The joint shear force, V_j , and the story shear, V_c , can be readily corrected Fig. 4.6 [Nakata et al. (2), Seckin (5)].

The required correction for the P-delta effect due to the specimen rotation under a given story drift can be derived by considering free body diagram. If the member weight is neglected, the corrected horizontal joint shear force, V_{jh} , is given by [Seckin (5)]:

1. Interior Joints

$$V_c = V_{ce} - \Delta V_c = V_{ce} - 2 \frac{\Delta_D}{l_D} \cdot [N - \alpha (V_{b2} - V_{b1})] \quad (4.2)$$

and,

$$V_{jh} = T_1 + T_2 - V_c \quad (4.3)$$

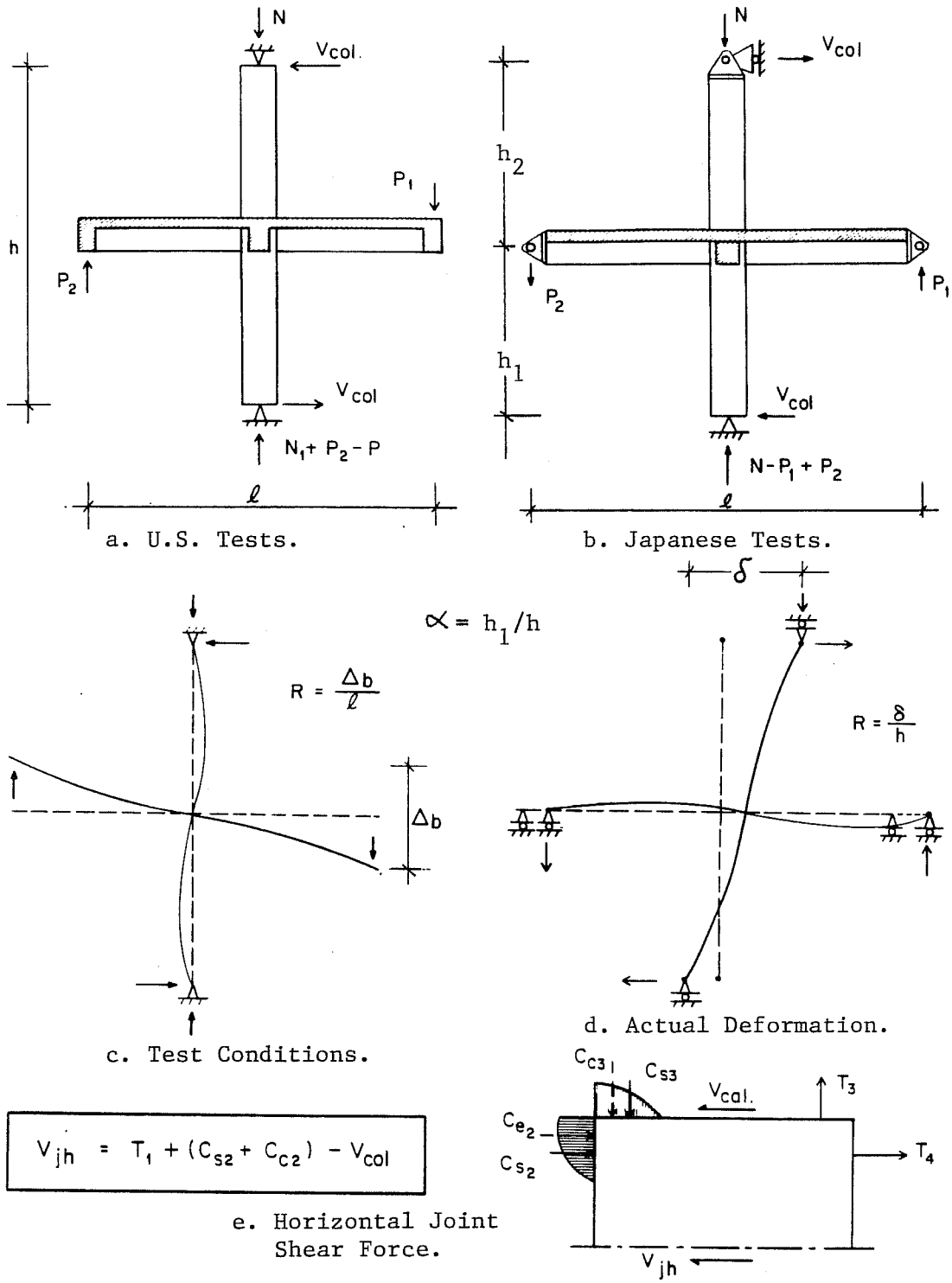


Fig. 4.6 - Story Shear and Horizontal Joint Shear Force.

2. Exterior Joints

$$V_c = V_{ce} - \Delta V_c = V_{ce} - 2 \frac{\Delta_b}{l_b} [N + \alpha V_{b1}] \quad (4.4)$$

and,

$$V_{jh} = T_1 - V_c \quad (4.5)$$

where: V_c = column shear force at the P.I. (actual configuration);

V_{ce} = column shear force at the P.I. (experimental configuration);

Δ_b = beam tip deflection (assumed equal for both beams of an interior joint);

V_{b1}, V_{b2} = beam tip load;

$l_b/2$ = cantilever beam length;

N = column axial load (compression is positive); and
 $\alpha = h_1/h$

T_1, T_2 = tensile forces in the beam bars at the column face

For the designer, the significant parameter is the actual column shear, V_c , rather than the experimental column shear, V_{ce} . The variation in column shear force at the joint region is given by ΔV .

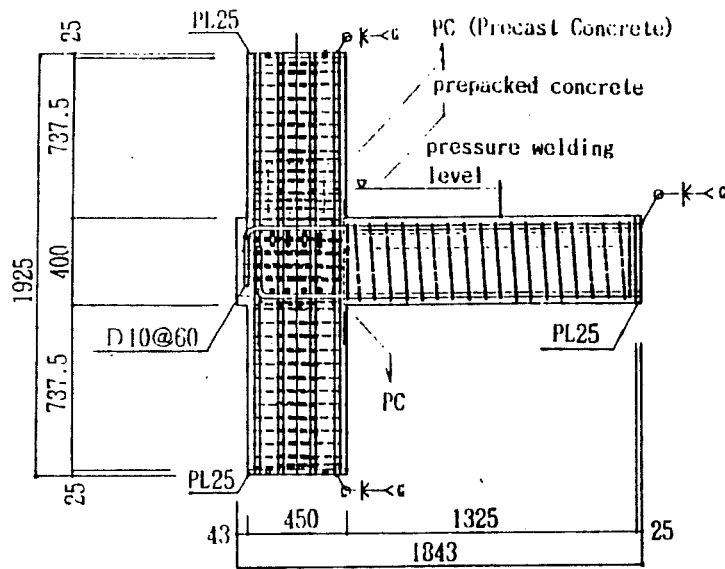
It can be shown that for an interior joint under reduced axial load ($N \sim 0$), the correction due to story drift is reduced as the terms in equation 4.2, V_{b2}, V_{b1} , can cancel each other and $\Delta_b/(l_b/2)$ reaches a maximum of approximately 1/20 in the

component tests. However, in the exterior joint, if more realistic axial load conditions were used, the correction term, ΔV , can play a more significant role. In the component tests, it was observed that the term, N , (axial load) was either constant (Japanese 1/2 - scale) or null (U.S. Tests).

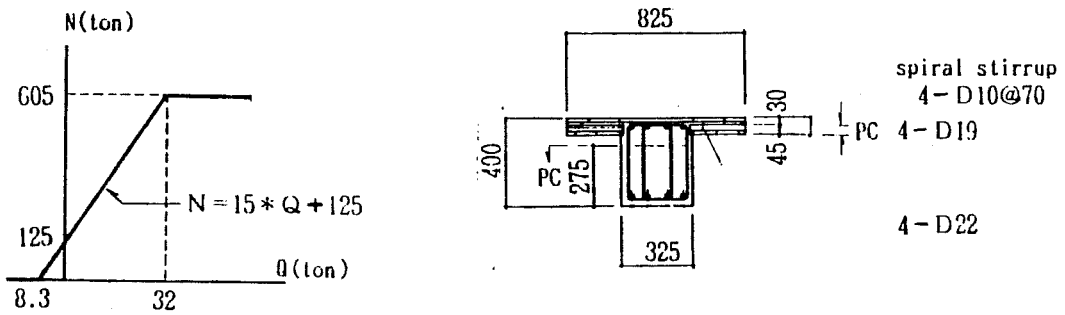
On the other hand, it is recognized that due to overturning moments in a complete frame under lateral loads, exterior joints are subjected to a load that may vary from tension to compression under different drift configurations. This loading scheme may prove to be more detrimental than a constant axial compressive load or a zero-load condition. Recent exterior component tests performed in Japan used variable compression loads depending on the level of story shear whereas for interior joints a constant compression load was applied, Fig. 4.7 [Inada and Kurose (1)].

4.8 References

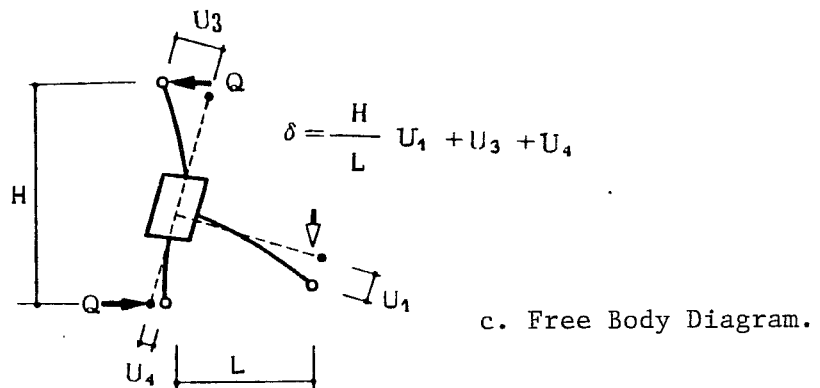
1. Y. Inada and Y. Kurose - Structural System for Reinforced Concrete High-Rise Building, Technical Report, Shimizu Construction Co. Ltd., Tokyo, Japan, May 1985.
2. S. Nakata, S. Otani, T. Kabeyazawa, Y. Kai and S. Kimura - Tests of Reinforced Concrete Beam-Column Assemblages - Technical Report - Joint Technical Coordinating Committee, U.S. - Japan Cooperative Research Program (1st Meeting), Tokyo, Japan, October 1980.



a. Exterior Component.



b. Relationship between N and Q.



c. Free Body Diagram.

Fig. 4.7 - Variable Axial Column Load Test, [Inada and Kurose (1)].

3. T. Paulay - "Developments in the Seismic Design of Reinforced Concrete Frames in New Zealand", pp. 91-112, Canadian Journal of Civil Engineering, Vol. 8, No. 2, June 1981.
4. T. Paulay and R. Park - "Joints in Reinforced Concrete Frames Designed for Earthquake Resistance", Research Report, No. 84-9, University of Canterbury, Christchurch, New Zealand, June, 1984.
5. M. Seckin - "Hysteretic Behavior of Cast-in-Place Exterior Beam-Column Sub-Assemblies", unpublished Ph.D. Thesis, Department of Civil Engineering, University of Toronto, Toronto, Canada, 1981.

CHAPTER V
TOTAL SPECIMEN RESPONSE

5.1 Interpretation of Test Results

It was shown before that the overall resistance in a DMRF under lateral loads is developed through the critical connection regions. Therefore, the results obtained within the US-Japan Joint Research Program which are related to joint response will be studied in detail. Each of the joint region constituents shown in Fig. 5.1 plays a critical role in the response.

Direct measurements include cracking patterns, bar strains, member displacements and applied external loads which provide the basic data for this study. From the direct measurements a more elaborate set of derived responses is also presented, e.g., longitudinal beam rotation, transverse beam twist, story shear and displacement (equivalent drift) and, energy absorbing characteristics. These derived aspects of joint response will be discussed in the next chapters.

The cracking patterns provide an excellent indication of performance because not only the amount of damage, but also the resistance mechanisms, and localized distress are easily perceived. No numerical interpretations are involved. The global aspect of response will be assessed by studying the cracking patterns at different deformation levels. Whenever

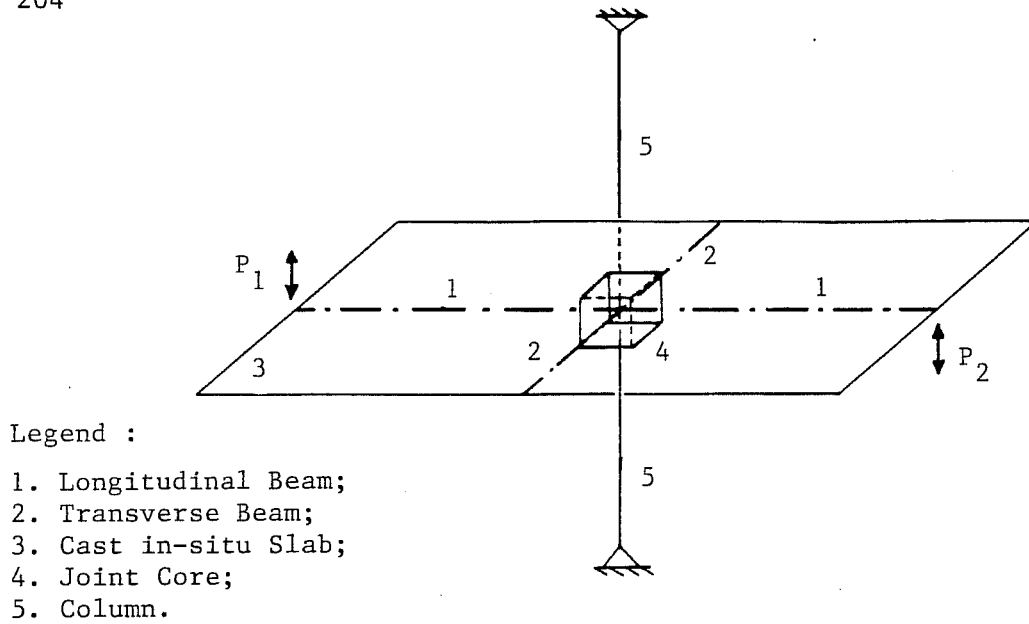


Fig. 5.1 - Interior Joint Region Resisting Elements .

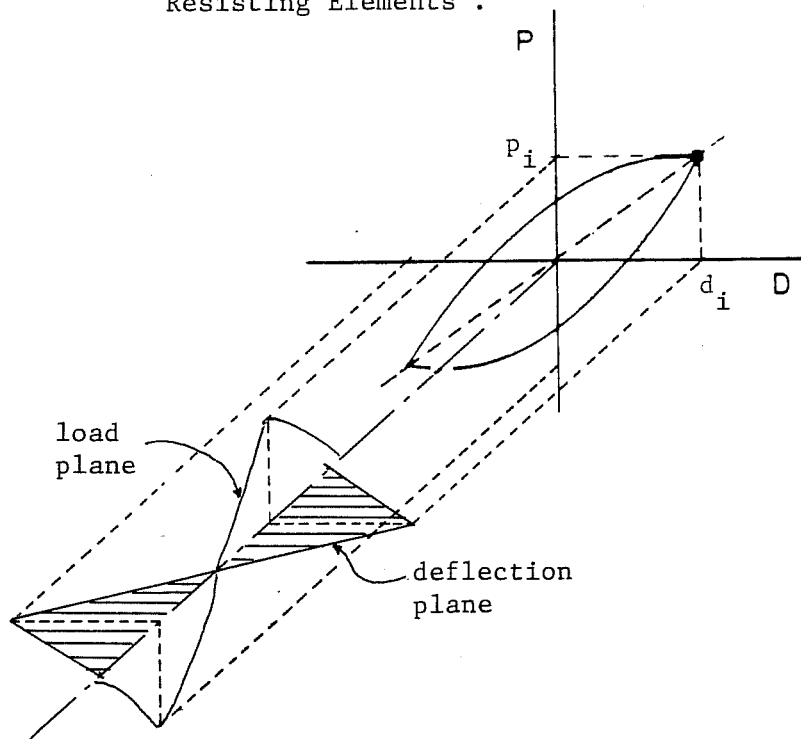


Fig. 5.2 - Spatial Load-Deflection Planes and Hysteretic Response.

possible, comparisons with equivalent BRI building regions will also be made at similar drift levels.

The important characteristics of stiffness degradation under reversed cyclic loads is studied by using the secant stiffness at peak load-displacement levels which showed more stable behavior. The secant stiffness is defined by the ratio between the applied load and induced displacement, Fig. 5.2. In this figure the spatial aspect of hysteretic behavior resulting from a lag in the deformation-time plane is also shown.

5.2 Cracking Patterns

5.2.1. BRI Building. In RC systems cracking patterns provide a fast visual means of observing the amount of damage as a result of the deformation applied to the structure. The recorded response during the four PSD tests applied before repair is shown in Appendix A. It was observed that after tests, [Okamoto et al., (4)]: (a) PSD1 ($R = + 1/8600$) - no cracks were observed and the structure remained within the elastic range; (b) PSD2 ($R = + 1/836; - 1/659$) - cracks developed in the shear wall lower region and in the beams and slabs adjacent to the shear wall; (c) PSD3 ($R = + 1/91; - 1/97$) - the existing cracks widened and new flexural and shear cracks were formed in the boundary columns and the shear wall panel. At the wall end of the beams, flexural cracks and concrete spalling was observed.

The shear wall uplift created cracks radiating from the shear wall edge boundary columns into the slab; and, (d) PSD4 ($R = +1/64$; $-1/68$) - no new cracks were observed but crack widths increased substantially. The cracking in the beams framing into the shear wall was more extensive than in beams framing into columns at the connection region. No severe damage was observed in the beam-column joints despite the low amount of shear reinforcement.

The cracking patterns at critical regions of Level Z2 of frames A, B, C and transverse frames 1, 2, 3, 4, show that at the end of test PSD4, several flexural cracks were present in the longitudinal and transverse beams, columns and slab at the interior joint regions, Fig. 5.3. The transverse beams were flexurally cracked due to the wall uplift. Also, cracks radiating from the loading points propagated in the slab and in the shear wall boundary columns.

In the exterior joint regions, the end walls substantially restrained the transversed spandrel beams and increased the torsional stiffness. Relatively large concentrated slab cracks (yield lines) developed at early load stages (ex: PSD2) close to the joint regions and they grew into a family of cracks along the spandrel transverse beams by the end of the PSD4 test, Fig. 5.3.

5.2.2 Component Tests vs. BRI Building. The Japanese half-scale tests (JPN) consisted of three interior (I-series),

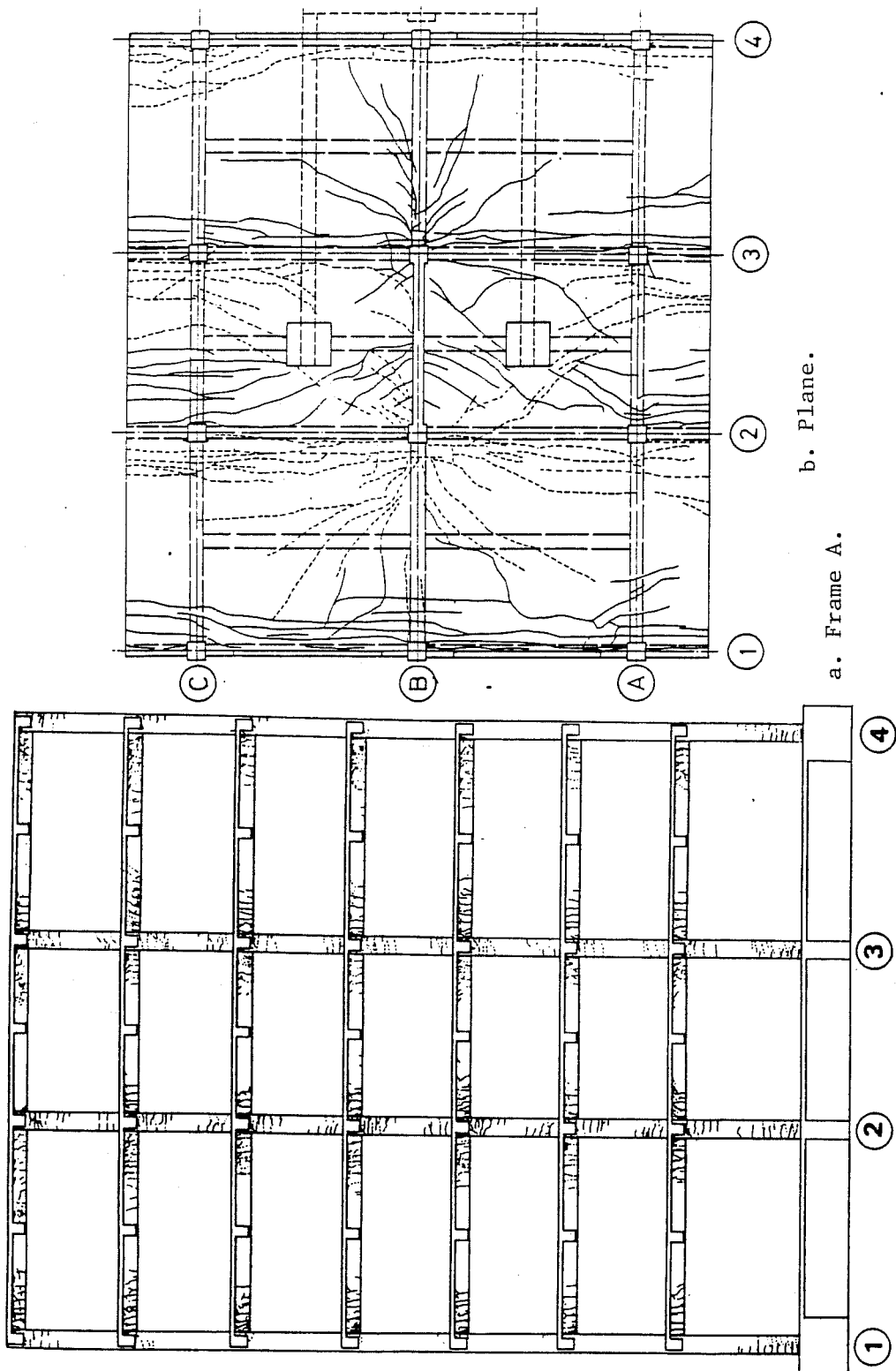
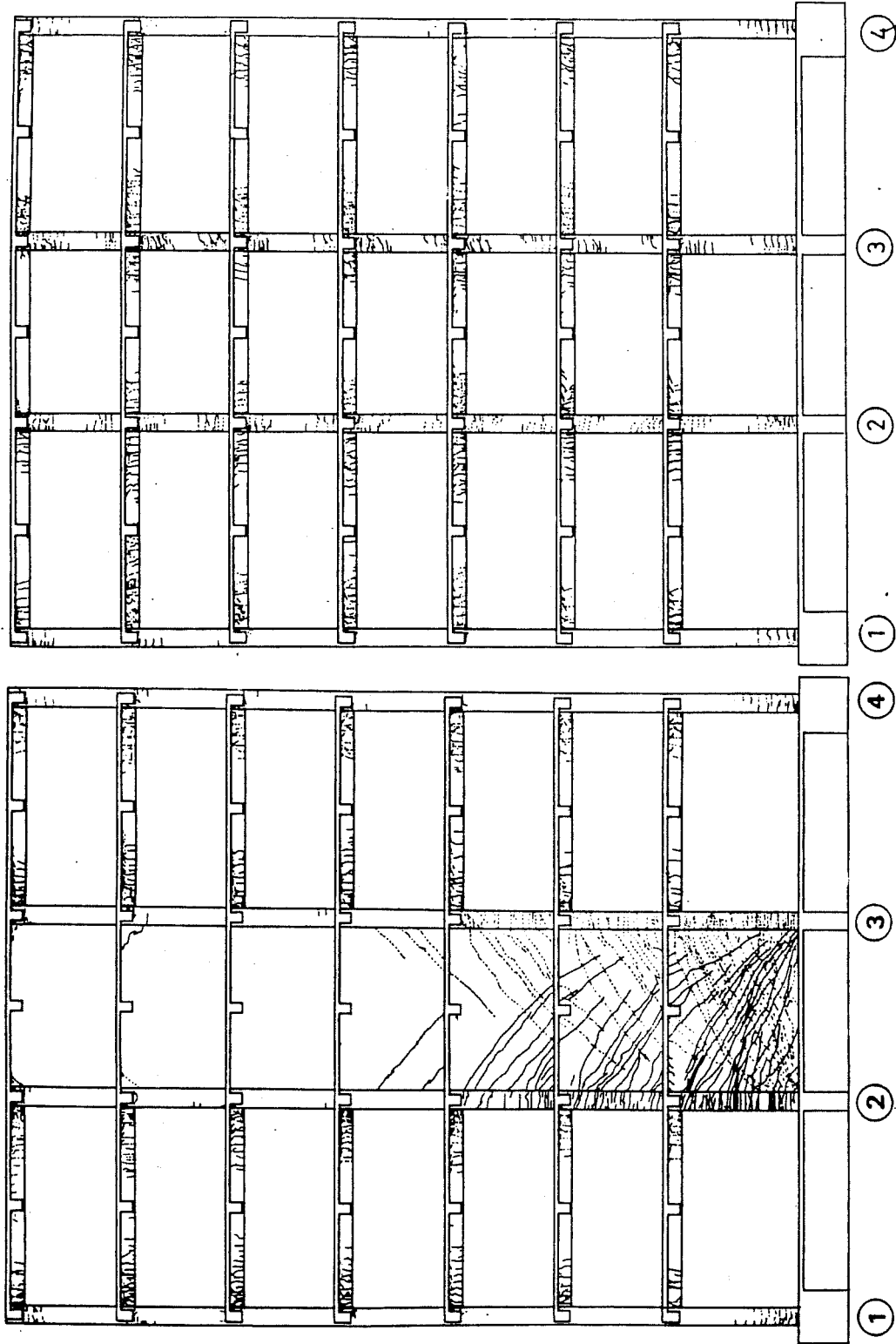
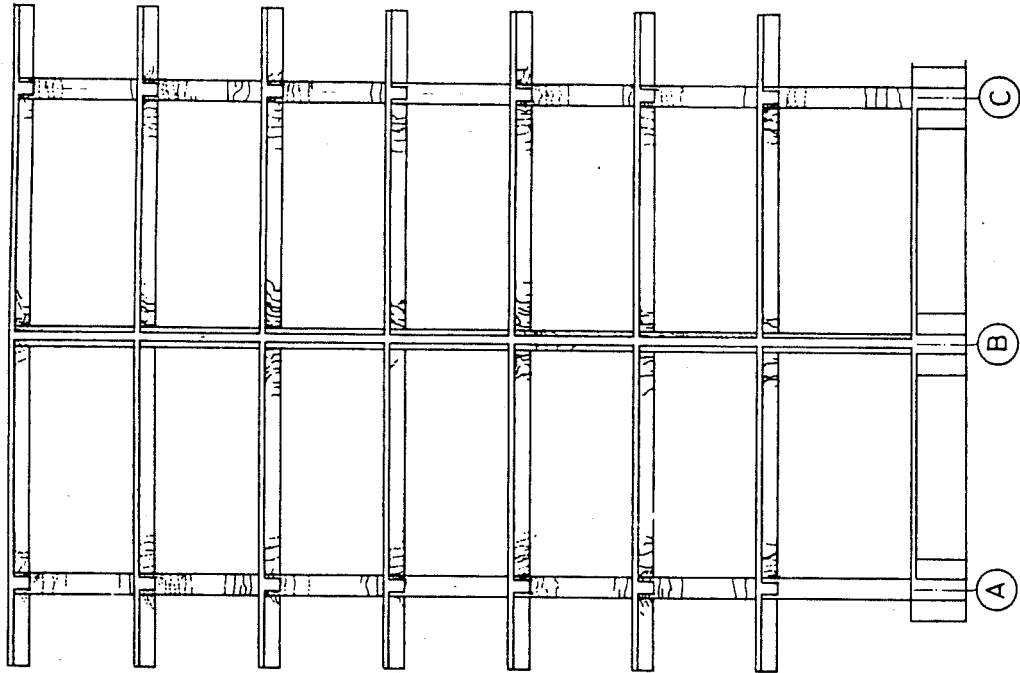


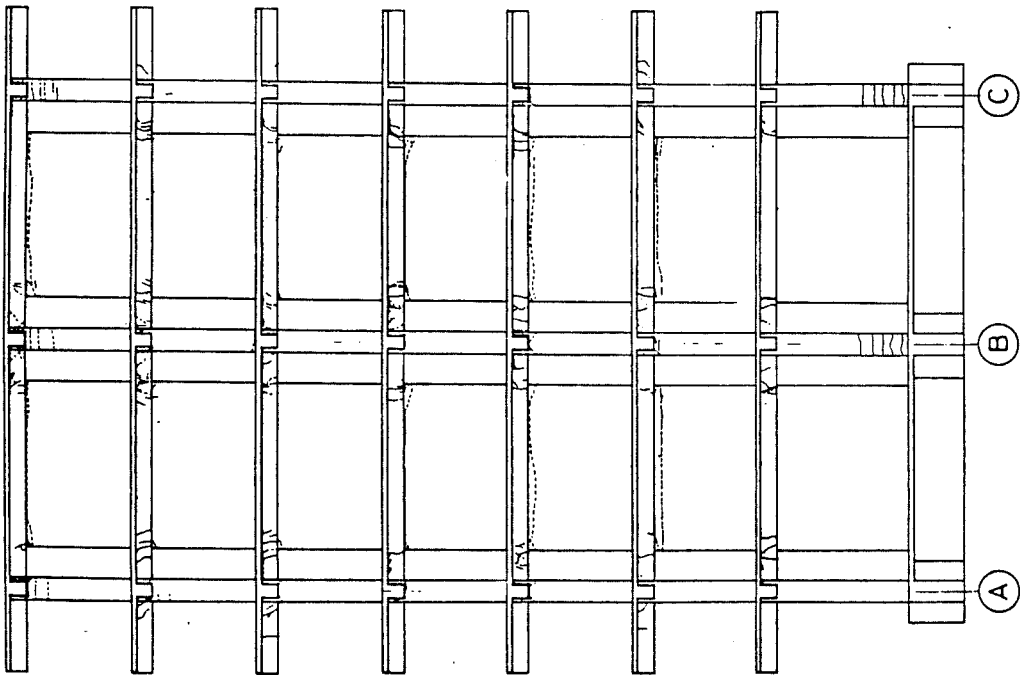
Fig. 5.3 - BRI Building - Cracking Patterns (end of PSD 4).



c. Frame B.
d. Frame C.
Fig. 5.3 (contd.) - BRI Building - Cracking Patterns (end of PSD 4).

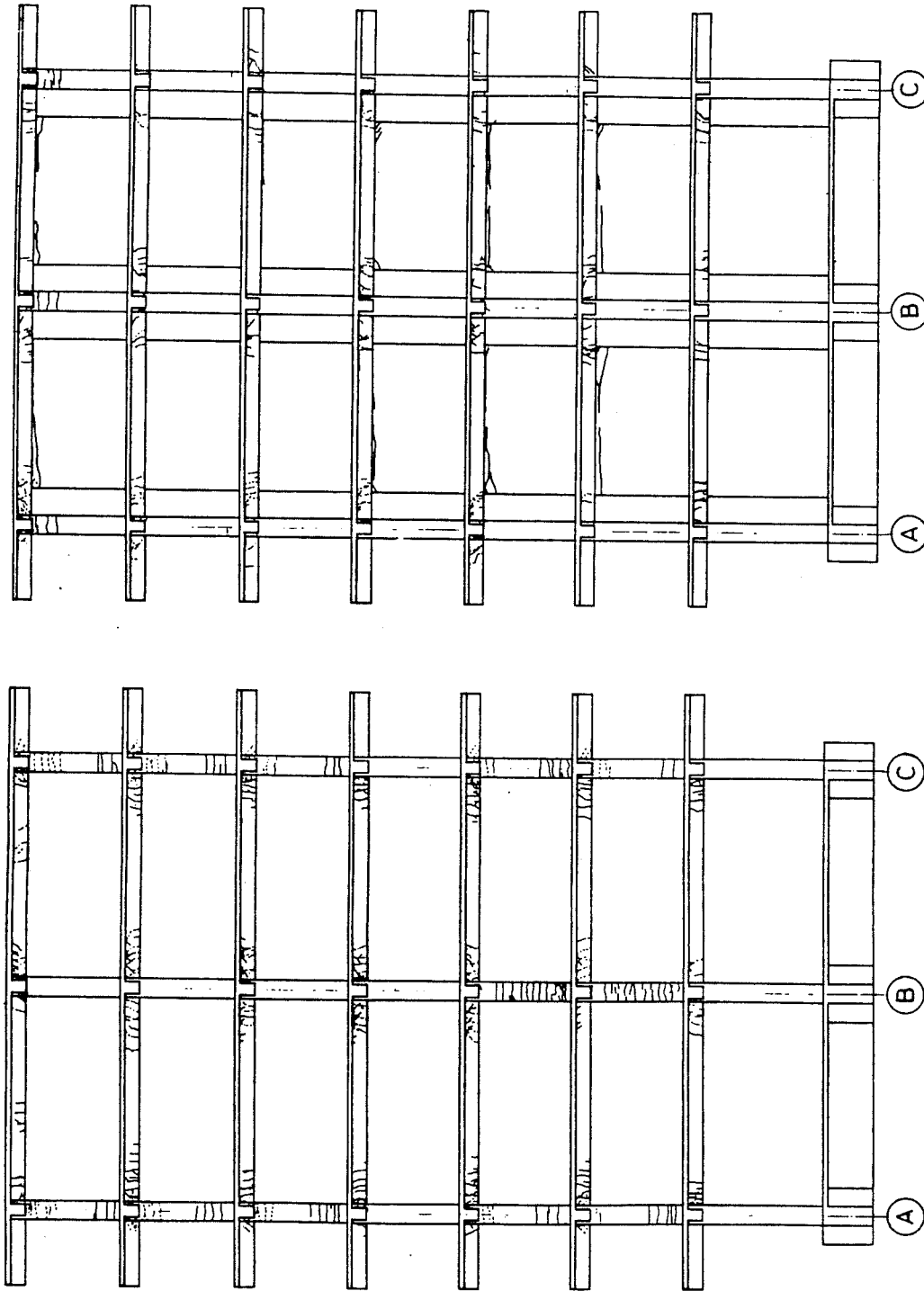


f. Frame 2.



e. Frame 1.

Fig. 5.3 (contd.) - BRI Building - Cracking Patterns (end of PSD 4).



g. Frame 3.
h. Frame 4.
Fig. 5.3 (concl.) - BRI Building - Cracking Patterns (end of PSD 4).

three exterior (E-series) and, two top exterior (T-series) components subjected to increasing story drifts (R) from 1/200 up to 1/50 drift cycles with a final half-cycle of 1/25. The cracking patterns for each of the two first test groups are shown in Appendix A. In each set of three tests, two had a 1.50 m (59 in.) wide cast in-situ slab and one had no slab. The major difference between the two specimens with slabs is the lateral reinforcement ratio in the beam and column: (a) Japanese design - low ratio; (b) US design - higher ratio. The third specimen was designed using Japanese practice lateral reinforcement ratios.

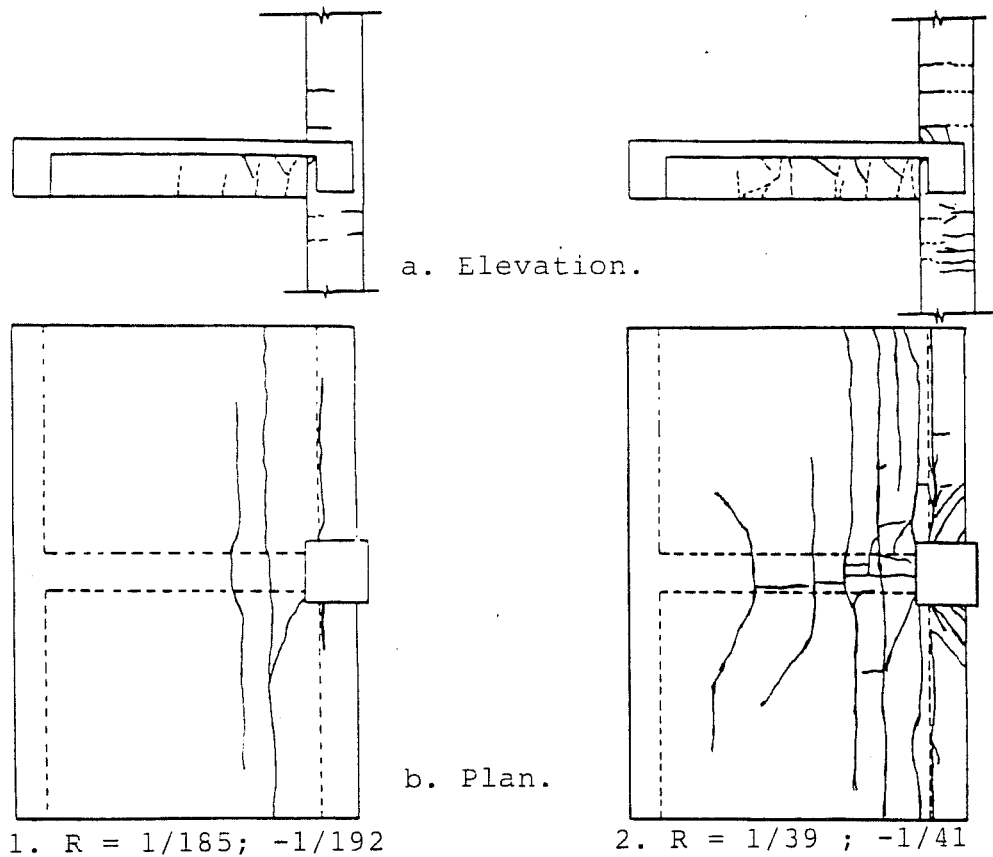
At the University of Texas at Austin (UTA), four full-scale components were tested: one exterior and one interior (prototype) designed similarly to the BRI building joints; and, one exterior and one interior (modified) designed in accordance to US practice. The cracking patterns for both prototype specimens are shown in Appendix B for various drift levels.

The four Stanford University (SU) specimens (two exterior and two interior) were small-scale models of the UTA full-scale prototypes. However, to study the slab participation influence, one exterior and one interior specimen was built without a slab. Only the interior joint with slab (IS) cracking pattern at the end of the testing program is available and is shown in Appendix C.

The component cracking patterns are analyzed by joint type (exterior vs. interior) and by the presence of a slab.

5.2.3 Exterior Component Tests with Slab. The presence of a cast in-situ slab had considerable influence on the specimen response which depended on whether the slab was in tension (negative moment) or in compression (positive moment).

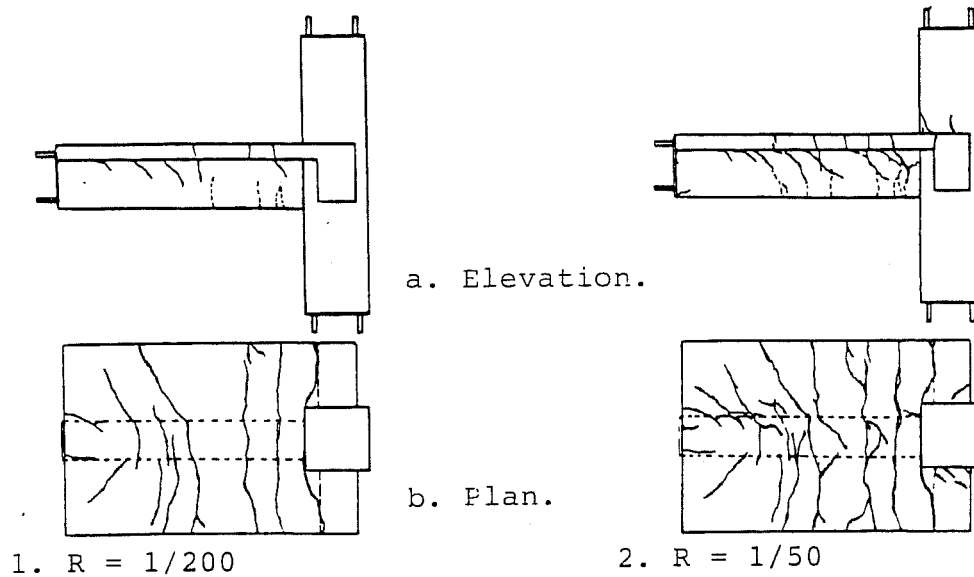
In the exterior JPN specimens, some difference in cracking patterns was observed between the specimens with Japanese (E-1) or US (E-2) lateral reinforcement detailing. Therefore, specimen E-2 is examined here because the reinforcement detailing ratio is similar to the BRI building. No crushing was observed in the column region. The observed slab cracking patterns vary depending on when the slab is in tension or compression. At early loading stages and small drift ratios ($R = 1/200$), flexural cracks extended at regular intervals through the entire width of the relatively narrow slab, Fig. 5.4. As the applied load increased, the slab flexural cracks (slab in tension) propagated into the beam at angles of 30-60° with the horizontal. When the slab was in compression, vertical, regularly spaced beam flexural cracks developed through about half the beam depth. The difference in crack orientation showed that higher shear forces were developed when the slab was in tension. Another crack pattern can be seen near the load point, Fig. 5.4. The semi-



1. $R = 1/185$; $-1/192$

2. $R = 1/39$; $-1/41$

a. UTA (USJ-2) - Exterior Prototype Test.



1. $R = 1/200$

2. $R = 1/50$

b. Japanese 1/2-scale Test (E-2).

Fig. 5.4 - Cracking Patterns in Exterior Tests.

circular pattern becomes linear near the transverse beam column face region. Slightly better response was also obtained with specimen E-2 as compared to E-1. At a large drift level (1/100 - 1/75) where wide shear cracks, crushing of concrete in the beam and column and longitudinal bar buckling started to occur, the larger amount of transverse reinforcement improved concrete confinement. In addition, column flexural cracking was restrained due to the constant level of axial compressive load of 219 kips (99.3 tf) which corresponded to a stress of 519 psi (36.5 kgf/cm²).

The UTA exterior prototype test exhibited very little flexural cracking in the slab and main beam but the spandrel beam showed early torsional distress, Figs. 5.4 and 5.5. Beam anchorage failure occurred at early loading stages. Consequently, the applied external load had to be transferred through the slab into the spandrel beam and then into the column. The top and end view show the diagonal torsional cracking patterns in the spandrel beam at the end of the test, Fig. 5.5. The observed torsional cracking in E-2 was small because of the narrow slab width. This may imply that the moments transferred from the slab into the spandrel (transverse) beam were lower, Figs. 5.4, 5.5. At early load stages (low drift levels), the UTA exterior prototype specimen showed a response similar to specimen E-2. When the slab was in tension, flexural slab cracks

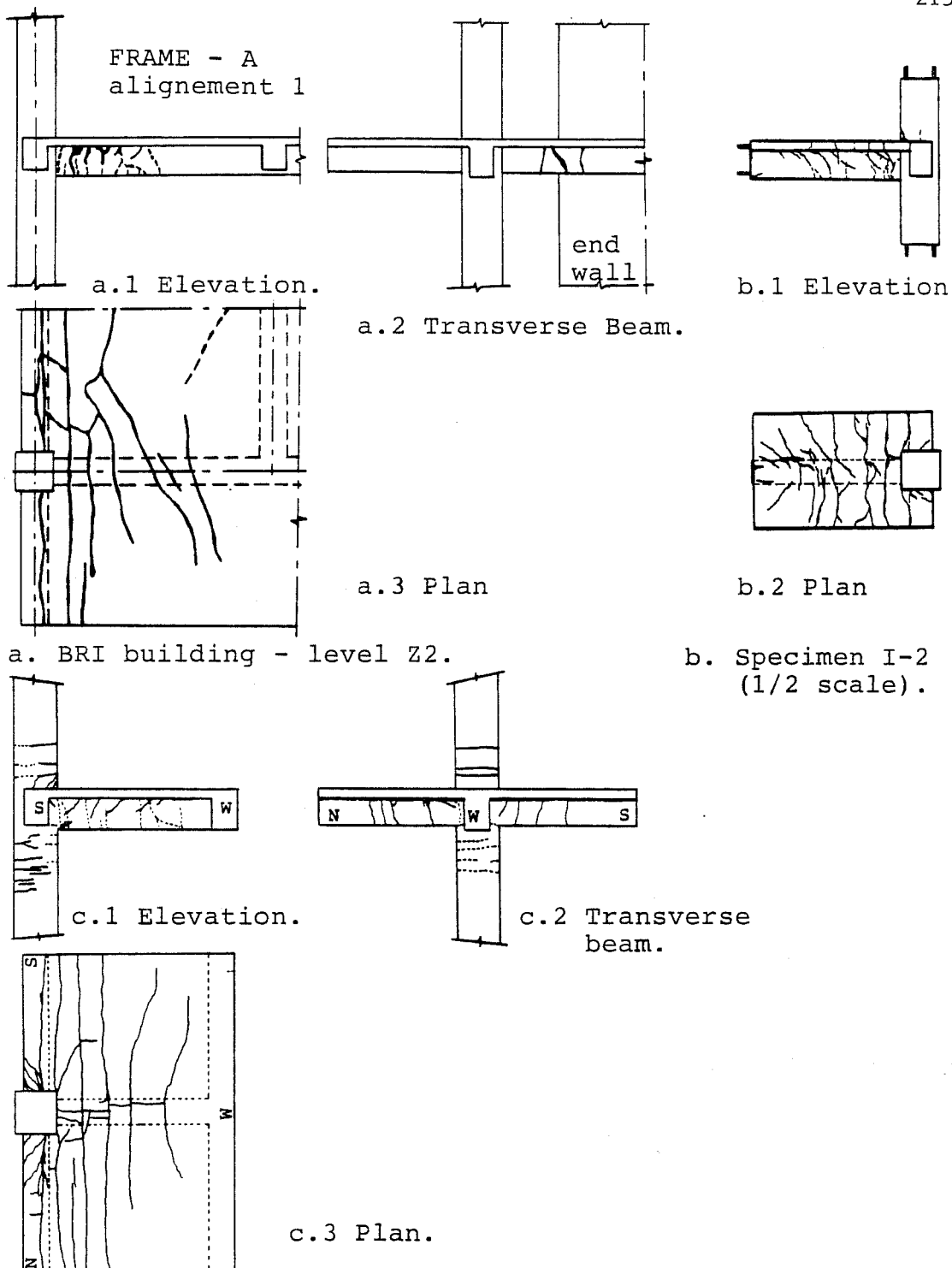


Fig. 5.5 - Cracking Patterns in Building and Exterior Tests.

propagated from the longitudinal beam towards the edges and parallel to the transverse beam. The top slab cracks were longer than the corresponding bottom slab cracks which extended into the longitudinal beam. Diagonal cracks formed at small distances from the column (8-10 in.) along the transverse beam. The bottom slab cracks propagated into the beam and inclined towards the column (shear cracks). When the slab was in compression, regularly spaced flexural cracks were observed along the longitudinal beam near the column. At large drift levels ($1/50 - 1/25$), a large separation crack formed between the longitudinal beam and the slab. Crushing and spalling was observed near the joint region in the longitudinal and transverse beams. At the end of the test that terminated with anchorage failure, the concrete cover at the back of the column was easily removed with a hammer. The wider slab width as compared with specimen E-2 showed that when the slab was in tension the flexural slab cracks gradually propagated towards the edge. Also, larger shear forces were applied to the beam as shown by the shallower beam shear cracks oriented towards the column. When the slab was in compression regularly spaced flexural beam cracks were observed near the joint region. Although similar cracking patterns were observed, the amount of diagonal torsional cracking in the transverse beam was greatly reduced in the UTA modified specimen because the anchorage detailing was improved.

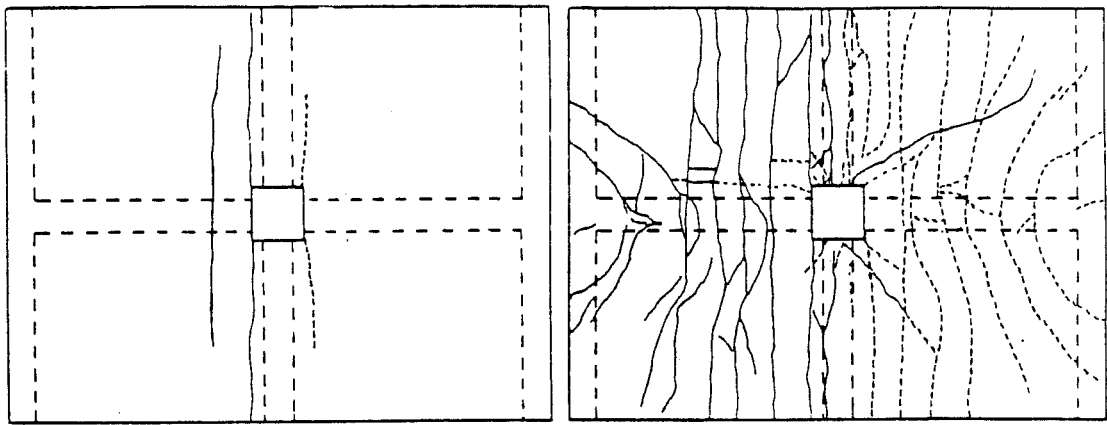
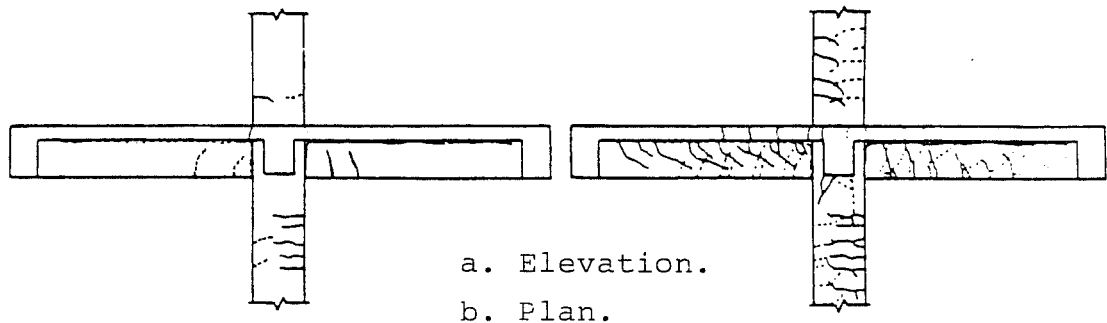
The SU exterior component showed that under negative bending moment (slab in tension) the transverse spandrel beams on both column sides experienced significant torsion [Wallace and Krawinkler, (5)]. Large torsional cracks occurred and a very large loss in the transverse beam torsional stiffness was observed. In this small-scale model, wide slab and beam cracks with large spacings were observed.

5.2.4 Exterior Joint Region - Building vs. Components.

The general crack pattern observed in the exterior joint region of the BRI building and cracking in the component tests is very similar, Fig. 5.5. The existence of an end wall cast with the transverse beam created a torsional restraint for the beam. This resulted in localized cracking at the discontinuity region in the transverse beam where the end wall terminated. Large torsional cracking was observed in the UTA specimen due to the longitudinal beam anchorage failure and the increasingly more important load carrying role played by the slab. A reduced number of torsional cracks were observed in specimen E-2 because of the smaller slab width. The most striking similarities were shown by the flexural slab cracks that were orthogonal to the loading plane and were concentrated near the joint region. The formation of flexural cracks in the longitudinal beam (slab in compression) as well as the transformation of flexural slab cracks into progressively

deeper beam shear cracks which pointed towards the column was remarkably similar to the UTA tests. Extensive column flexural cracking was observed in the UTA component column. The BRI building did not show extensive column cracking near the joint region. This response was the result of a more active load carrying role performed by the end walls, compression in the columns due to the dead load of the floors above and different boundary conditions.

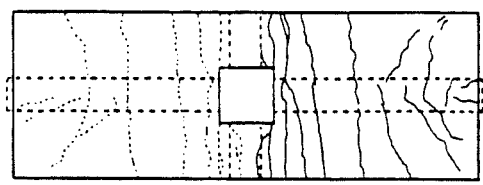
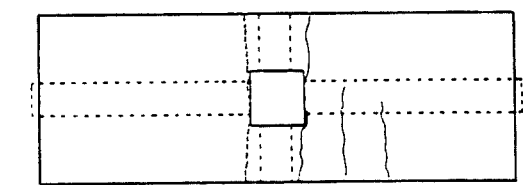
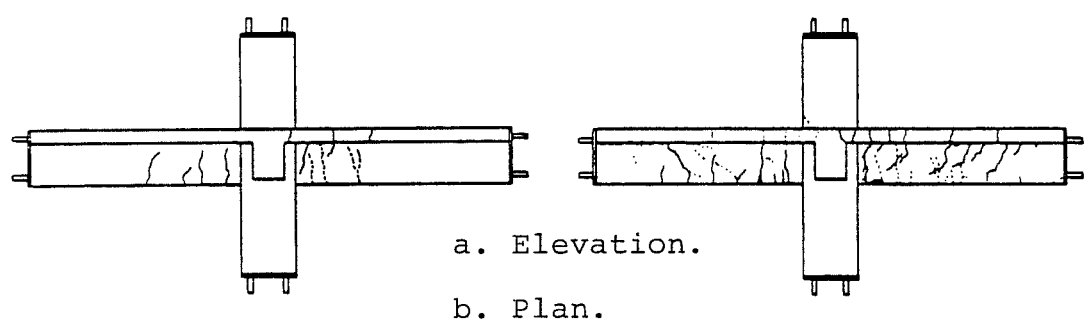
5.2.5 The Interior Component Tests with Slab. Flexural cracks were first observed in the beam and slab of the Japanese tests I-1, I-2. Due to the narrow slab width, slab cracks developed over the entire width at early load stages normal to the longitudinal beam, Fig. 5.6. At $R = 1/200$, diagonal shear cracks were observed in the beam region beneath the slab extending downward from the slab. The slab participation in tension increased the beam flexural capacity and created large shear forces that led to shear cracking. However, when the slab was in compression, bending capacity was not influenced significantly [Nakata et al. (3)]. At a deformation level of $R = 1/50$, several cracks developed at the beam - slab interface and wide beam flexural cracks were concentrated near the column. Small flexural cracks were observed in the columns near the beam faces. Concrete crushing was not observed in either the beams or columns. Substantially less flexural cracking occurred in the



1. $R = 1/217$; $-1/179$.

2. $R = 1/38$; $-1/38$.

a. UTA (USJ - 1) - Interior Prototype.



1. $R = 1/200$.

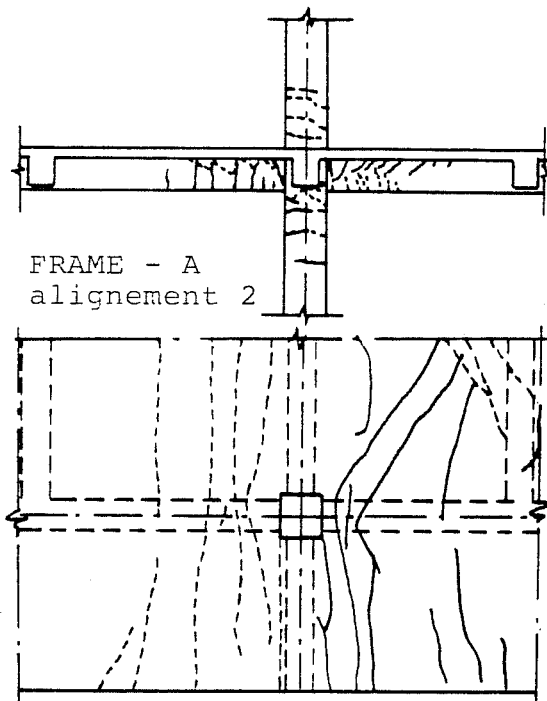
2. $R = 1/50$.

b. Japanese 1/2-scale Test (I-2).

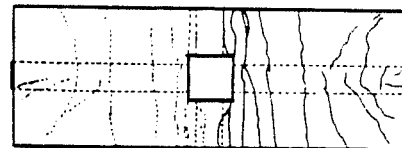
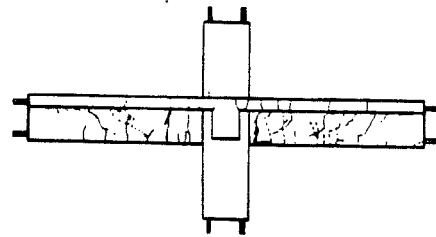
Fig. 5.6 - Cracking Patterns in Interior Tests.

column due to the presence of a constant compressive axial load of 230.4 kips (104.5tf) which corresponded to a stress of 546 psi (38.4 kgf/cm²). At larger drift levels, specimen I-2 performed better than I-1 due to the larger amount of transverse reinforcement in I-2.

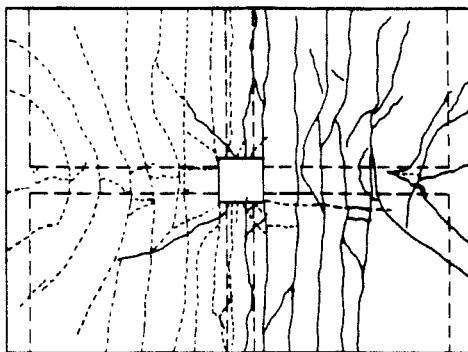
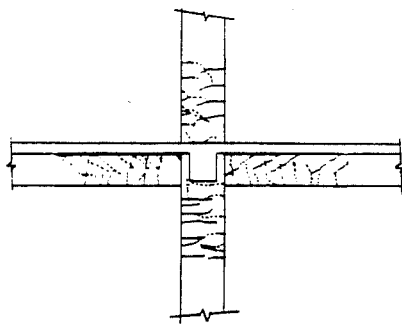
The UTA interior prototype exhibited cracking patterns (longitudinal beam, slab) similar to those of Japanese tests, Figs. 5.6, 5.7. When the slab was in tension, slab cracks formed normal to the longitudinal beam and propagated towards the free edge as the deformation level increased. Other flexural cracks developed at the bottom slab surface and extended toward the free edge but not at the same rate as the cracks on the top surface. These cracks also extended into the beam up to $2/3 - 3/4$ of the total depth and inclined towards the column. Torsional diagonal cracking was first observed at $R = 1/80$ with two parallel cracks inclined at a 30° angle with the horizontal and at 10 in. (0.25 m) from the column face. The steeper, closely spaced torsional cracks which formed near the column became flatter away from the column. The joint region showed little distress in terms of shear cracking or spalling. However, in the longitudinal beams near the end of the test ($R = 1/40$) some crushing and spalling occurred near the joint. Minor flexural cracking was observed in the columns, Fig. 5.6. The observed failure mode was flexurally dominated with the formation of longitudinal beam plastic



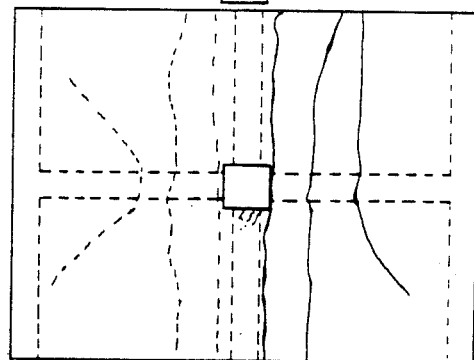
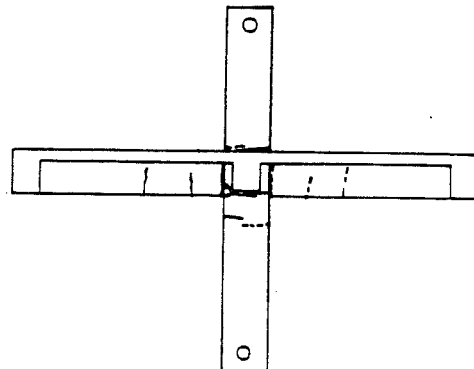
a. BRI building - level Z2.



b. Specimen I-2 (1/2 scale).



c. U. Texas - USJ-1.



d. Stanford U. - Test IS.

Fig. 5.7 - Cracking Patterns in Building and Components.

hinging. The overall cracking pattern for the UTA modified interior component was very similar to the prototype specimen cracking response previously described.

The SU interior model showed general cracking patterns similar to the full-scale UTA prototype component, but with fewer cracks, Fig. 5.7. This resulted from size effects and cannot be avoided in small models. Because the cracks were widely spaced, flexural stiffness increased [Wallace and Krawinkler (5)].

5.2.6 Interior Joint Region - Building vs. Components.

The cracking patterns observed in the BRI building interior joint regions were similar to the ones observed in the component tests, Fig. 5.7. The flexural cracking on the top slab surface was oriented normal to the loading plane with a large concentration of cracks near the column and parallel to the transverse beam, and around the loading point. Under increasing drift levels, the slab cracks propagated through most of the longitudinal beam and were inclined towards the column. When the slab was in compression, regularly spaced vertical cracks starting at the beam bottom face were observed in the joint vicinity. Column flexural cracks were observed in the BRI building and in the UTA component over 1-2 column depths from the joint region. Diagonal shear cracking is not as extensive as in exterior components.

5.2.7 Exterior vs. Interior Component Crack Response.

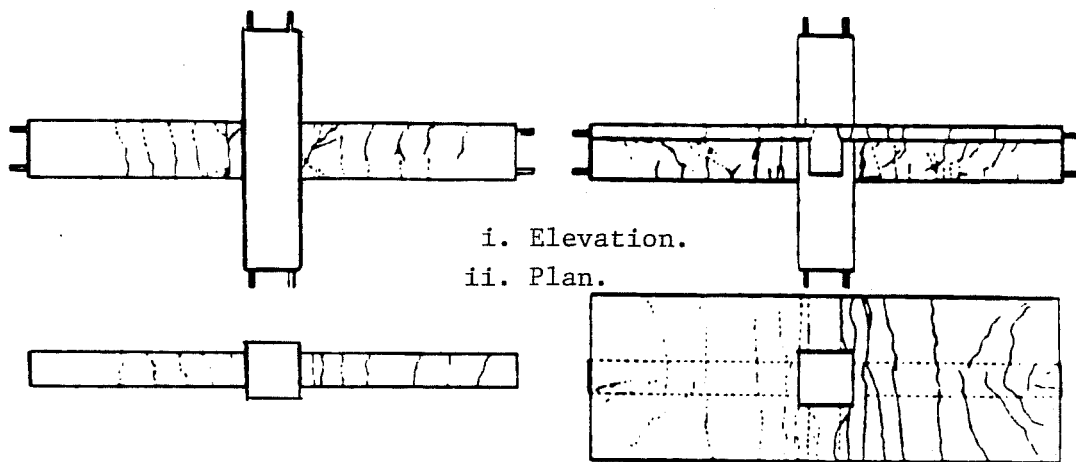
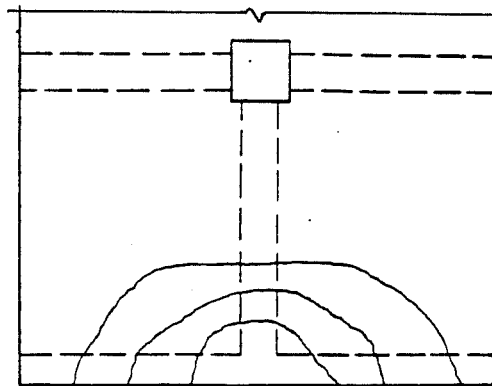
The global cracking response of an exterior vs. an interior joint

region depended to a large extent on the moment transfer mechanism around the connection and on the transverse beam torsional stiffness. Under increasing positive peak deflections (slab in tension) large demand was placed on the transverse beam torsional stiffness. Early cracking and deterioration at the slab-transverse beam junction resulted in poor response.

The applied concentrated load normal to the plane of a RC plate created a characteristic pattern observed in all components (both exterior and interior). At large load levels, a semi-circular cracking pattern developed, Fig. 5.8.

Finally, the existence or the absence of a cast in-situ slab had very important implications on component response. In both the interior and exterior 1/2 scale Japanese component tests without a slab, the shear force in the beams was limited because of the low flexural yielding capacity. Therefore, no diagonal shear cracks were observed and all the cracks were due to flexure [Nakata et al. (3)]. No shear cracks were observed in the joint panel nor flexural cracks in the column because of the presence of an axial compressive load, Fig. 5.9. The component tests without a slab showed that there was not a definite plastic hinge region. With a slab, a dramatic change in the stiffness around the connection region was created and with high shear forces, a well-defined plastic hinge formed, Fig. 5.9.

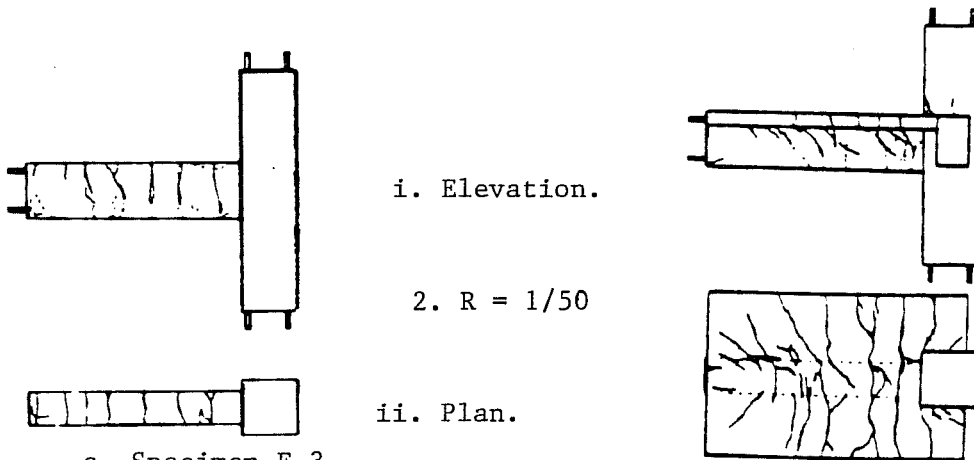
Fig. 5.8 - Cracking around Load Point.



a. Specimen I-3.

b. Specimen I-2.

1. $R = 1/50$



c. Specimen E-3.

d. Specimen E-2.

Fig. 5.9 - Japanese Tests - Slab Effect, [Nakata et al.(3)].

5.3 Stiffness and Strength Degradation

5.3.1 BRI Building. The BRI building test was conducted using an inverted triangular loading pattern applied on the structure. The response of levels Z2, Z3 and the roof is shown in Fig. 5.10. A relatively fat, stable hysteretic response is obtained even at later loading stages where a large lateral drift $R = +1/64; - 1/68$ was reached (test PSD4). The total base shear vs. horizontal roof displacement also showed the same hysteretic response even at large deformation levels, Fig. 5.11.

All plots in Fig. 5.10 were to the same scale. Because the resolution for level Z2 response is reduced, an enlarged scale plot is shown in Fig. 5.12.

It can be seen from Figs. 5.10 to 5.12 that a certain amount of stiffness degradation occurred throughout the test. A more quantitative evaluation of this stiffness degradation was considered of interest in the scope of this report. Secant stiffnesses generally provided a more consistent measure of response in tests performed under reversed cyclic loads. However, near zero load or zero displacement, localized instabilities occurred when the applied load was reversed. At peak displacements, stable peak secant stiffness values generally were obtained. The results in Fig. 5.13 showed the different stiffness values observed throughout the entire loading history compared with the equivalent drift history at level Z2. The peak

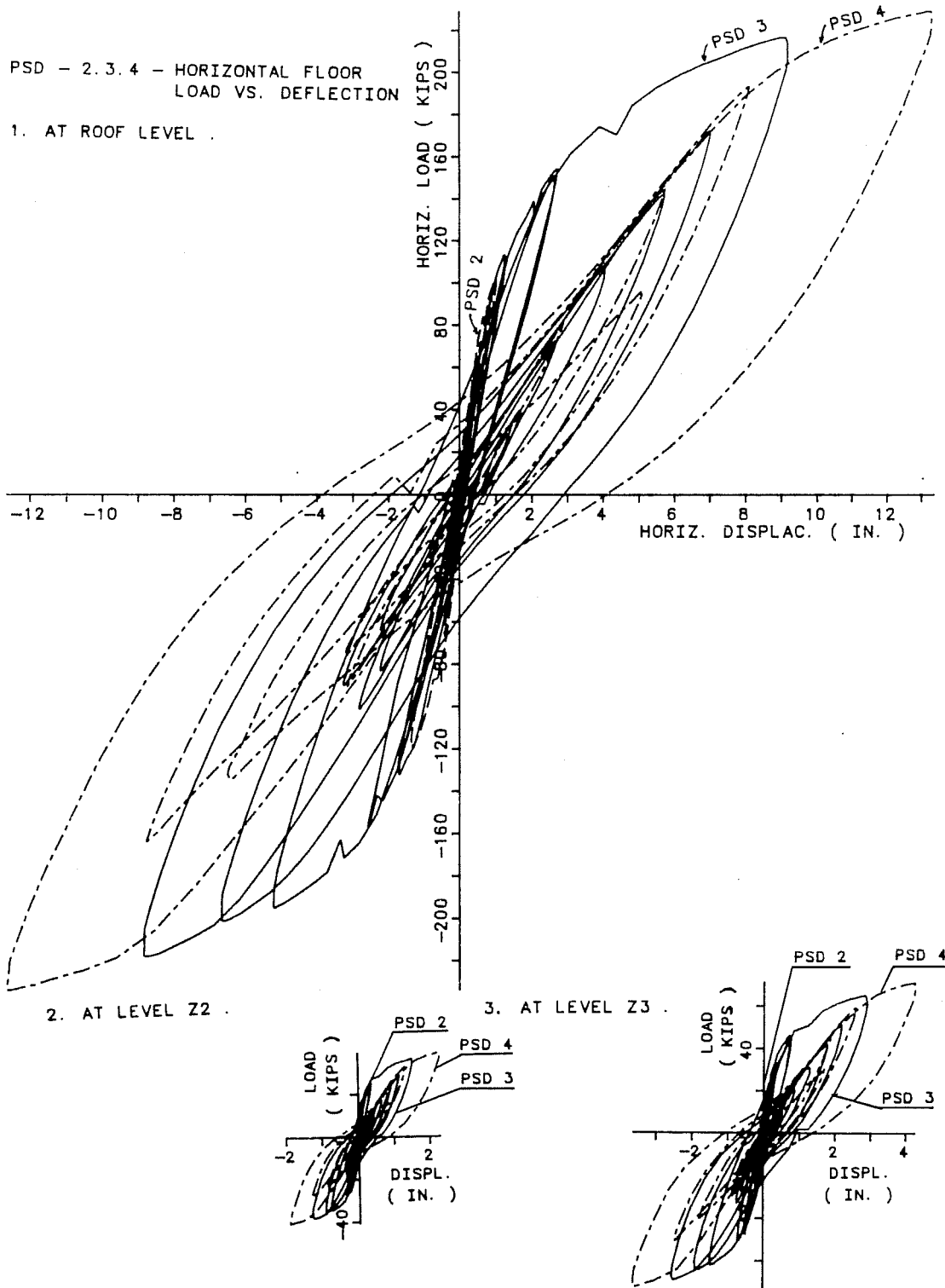


Fig. 5.10 - BRI Building Load-Deflection Response.

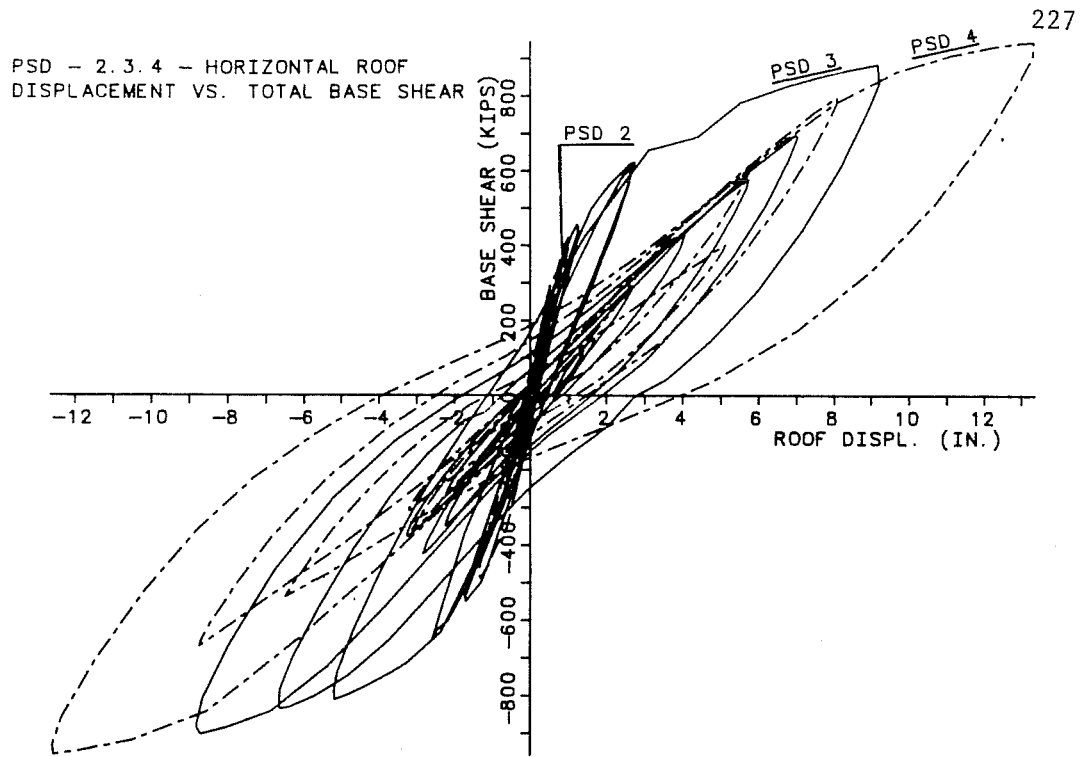


Fig. 5.11 - BRI Building - Total Base Shear vs. Roof Displacement.

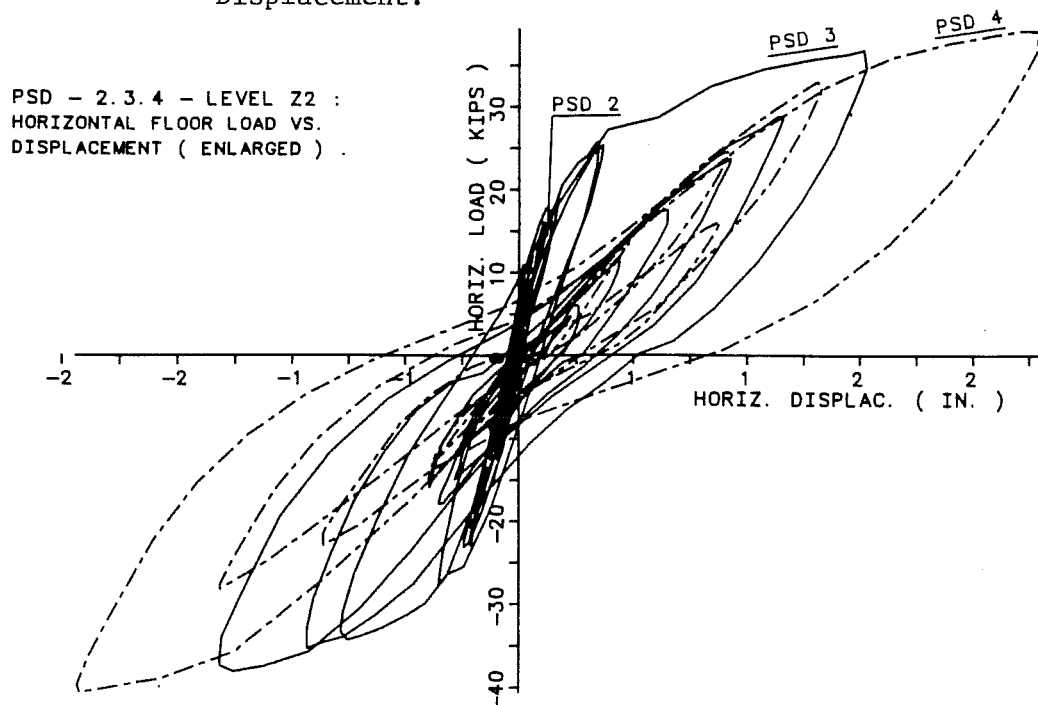


Fig. 5.12 - BRI Building - Enlarged Response at Level Z2.

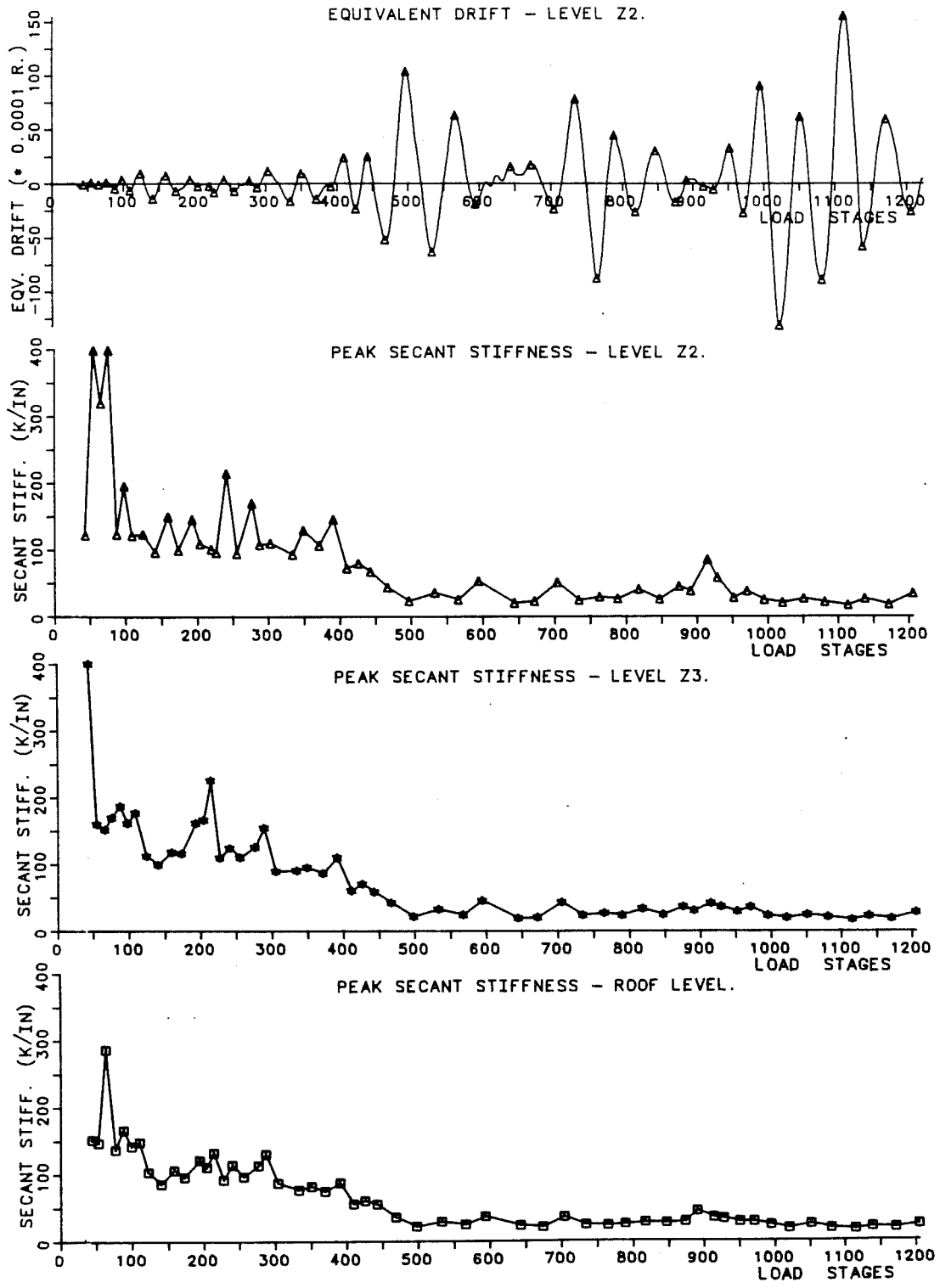


Fig. 5.13 - BRI Building - Peak Secant Stiffness History.

stiffness curve is given by solid lines uniting the different peak secant stiffness marks.

If level Z2 is used as a reference for the equivalent drift history at first peak displacements, the three different secant stiffness response curves can be plotted on one figure and compared, Fig. 5.14. Good agreement is obtained for all these levels and also at first peak drifts. The decaying curves shown in Fig. 5.14-c are far from the origin as well as symmetric about the vertical axis. This showed that the structure had the same secant stiffness at all three levels, symmetric response under positive or negative loading, and was able to maintain its integrity even under large displacement levels. From Fig. 5.14-c it can be seen that stiffness dropped steadily up to a 1/300 equivalent drift and tended to change very slowly thereafter.

5.3.2 The Exterior Component Tests.

5.3.2.1 Strength Characteristics. The exterior components response is shown in Figs. 5.15 to 5.17. The results are plotted using story shear, Q , defined in Chapter IV as V_{col} (column shear) vs. equivalent lateral drift, R .

The U.S. prototype tests showed that good correlation with respect to ultimate design code predicted load was observed between the 1:1 (UTA) and the 1:12.5 (SU) specimens, Fig. 5.15. However, some major differences can also be pointed out: (1) severe pinching in the UTA (USJ-2) hysteresis loop was observed

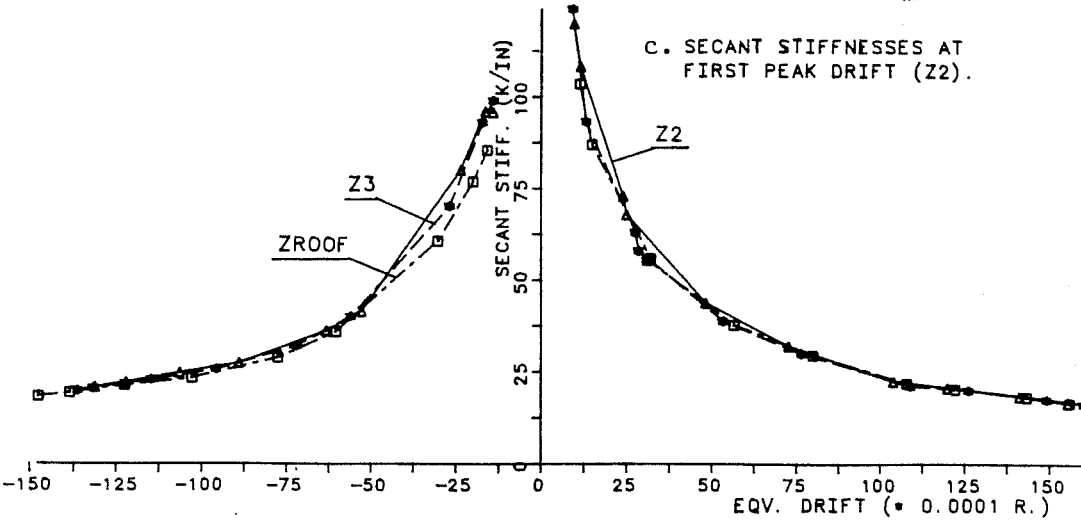
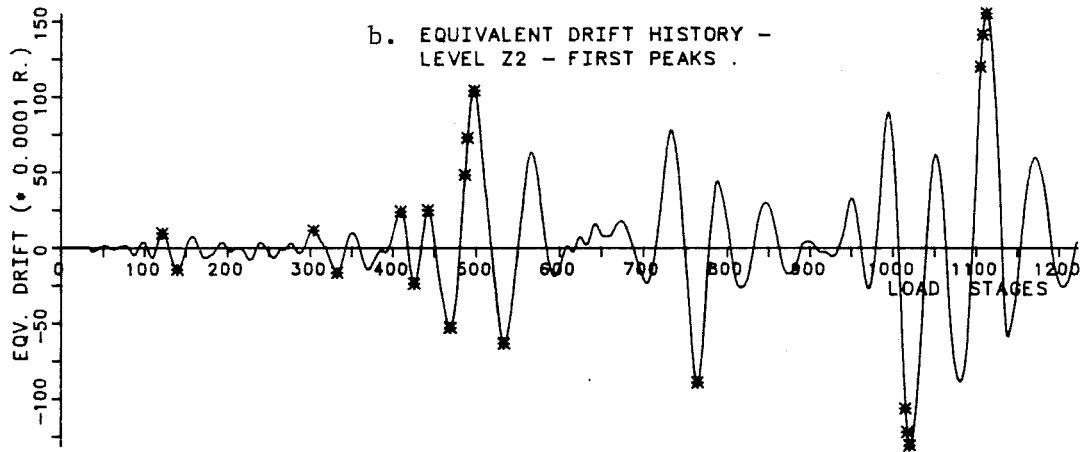
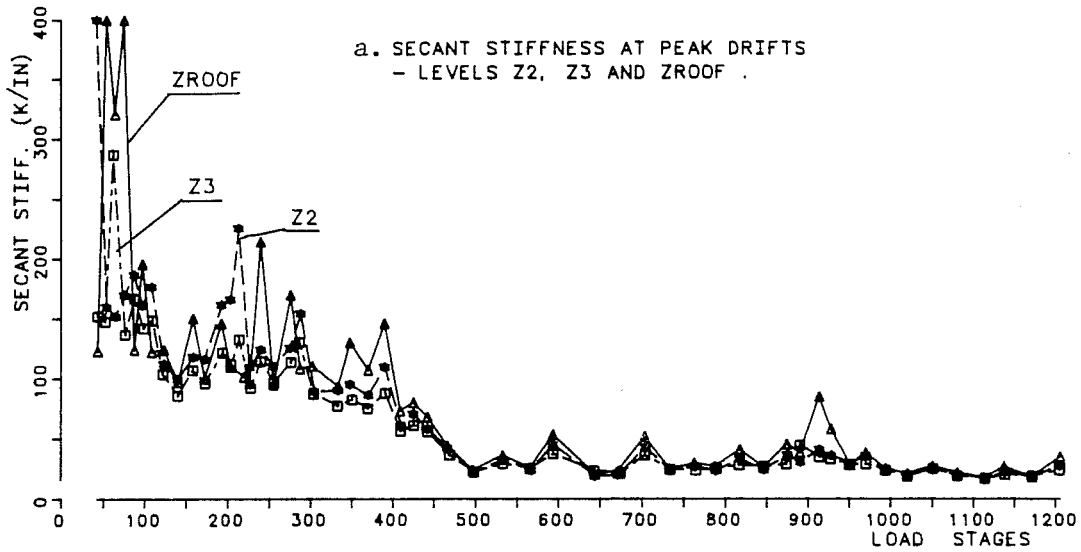


Fig. 5.14 - BRI Building Response at Peak Displacements.

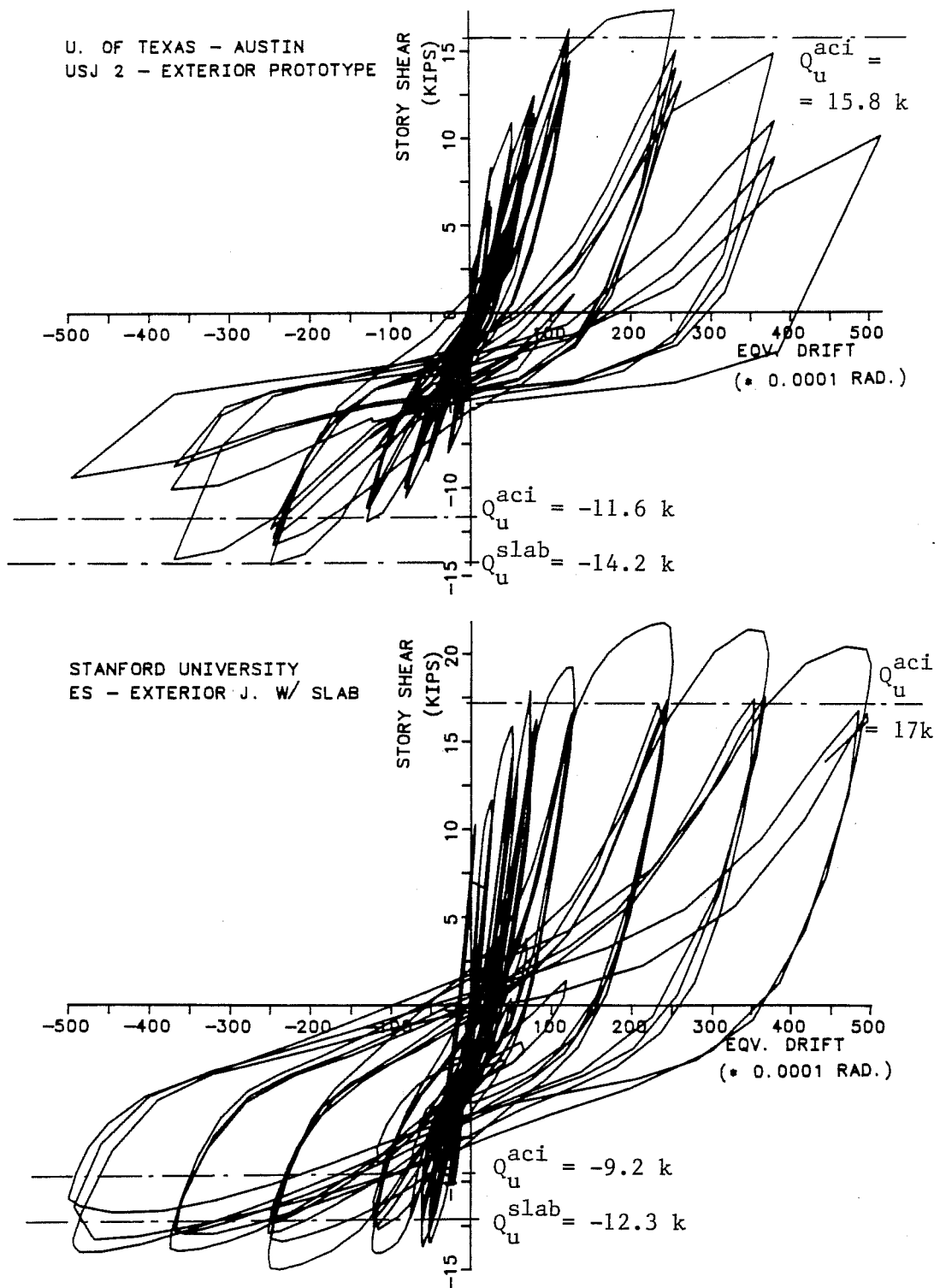
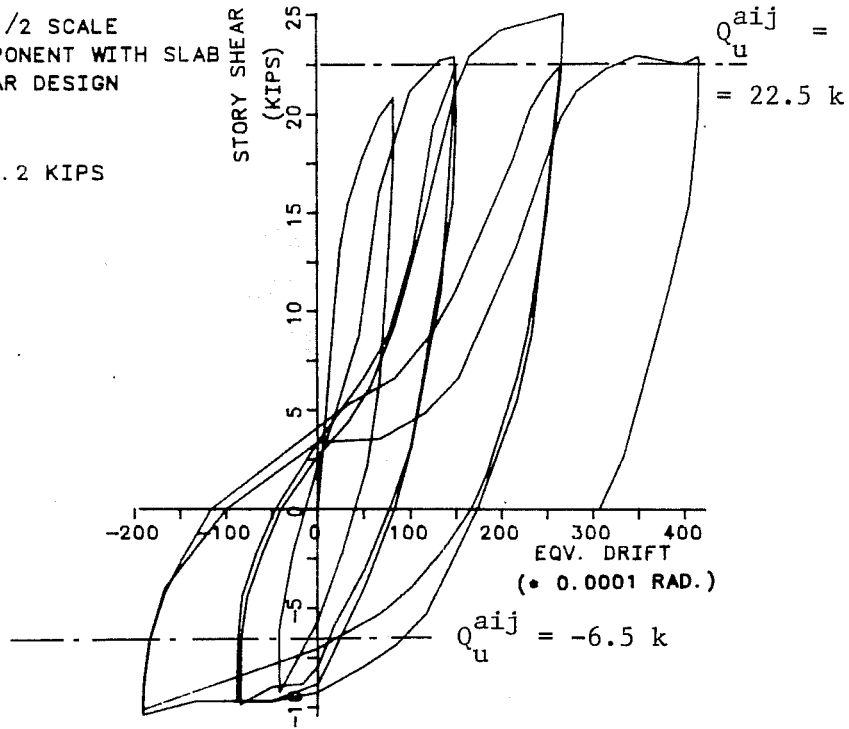


Fig. 5.15 - UTA and SU Exterior Components.

JAPAN - 1/2 SCALE
 E1 - COMPONENT WITH SLAB
 JPN. SHEAR DESIGN

$N_e = 219.2$ KIPS



JAPAN - 1/2 SCALE
 E2 - COMPONENT WITH SLAB
 U.S. SHEAR DESIGN

$N_e = 219.2$ KIPS

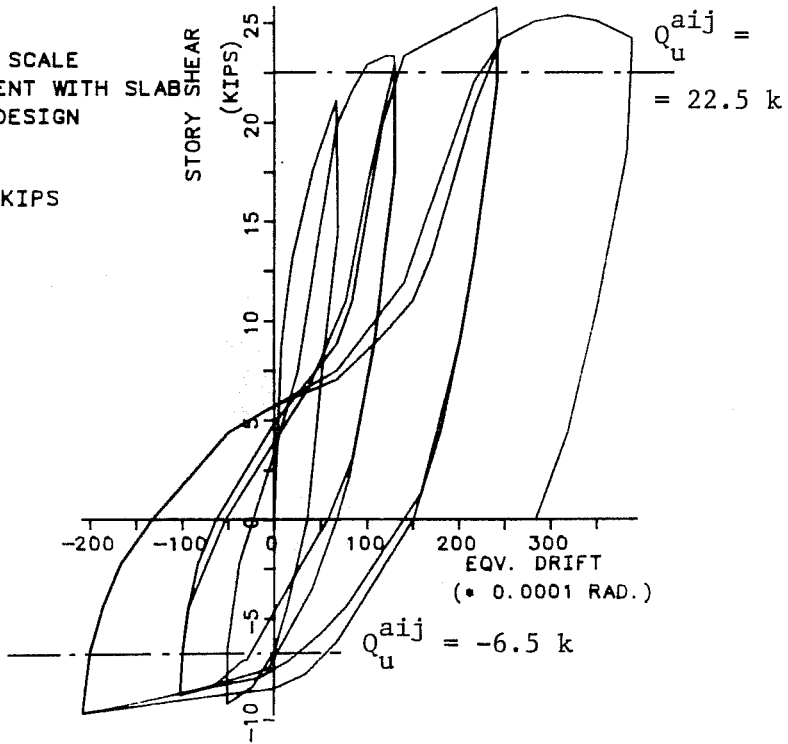
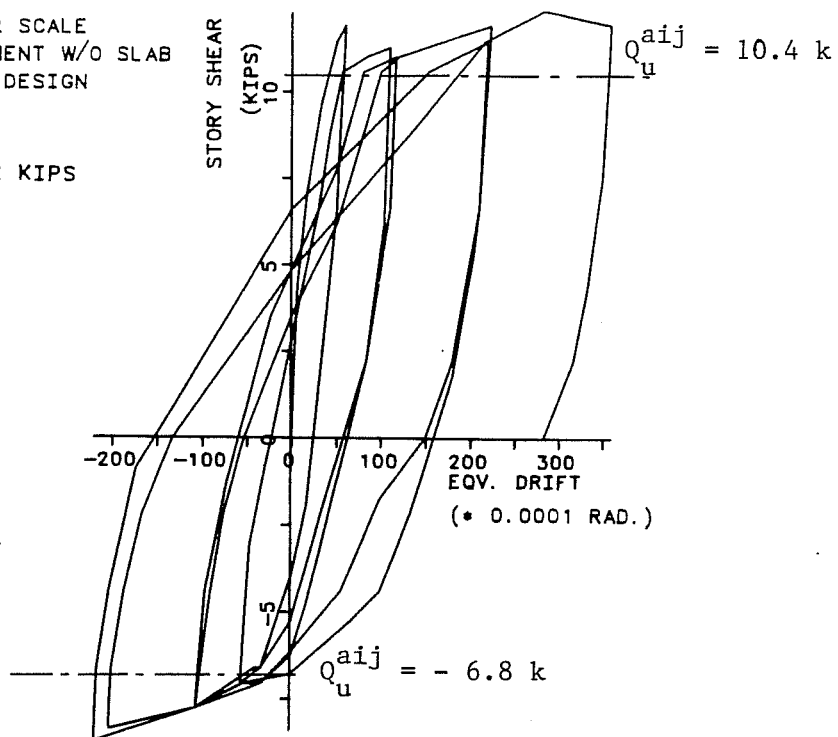


Fig. 5.16 - Japanese Exterior Tests with a Slab.

JAPAN - 1/2 SCALE
 E3 - COMPONENT W/O SLAB
 jpn. SHEAR DESIGN

$N_e = 219.2$ KIPS



STANFORD UNIVERSITY
 EJ - EXTERIOR J. W/O SLAB

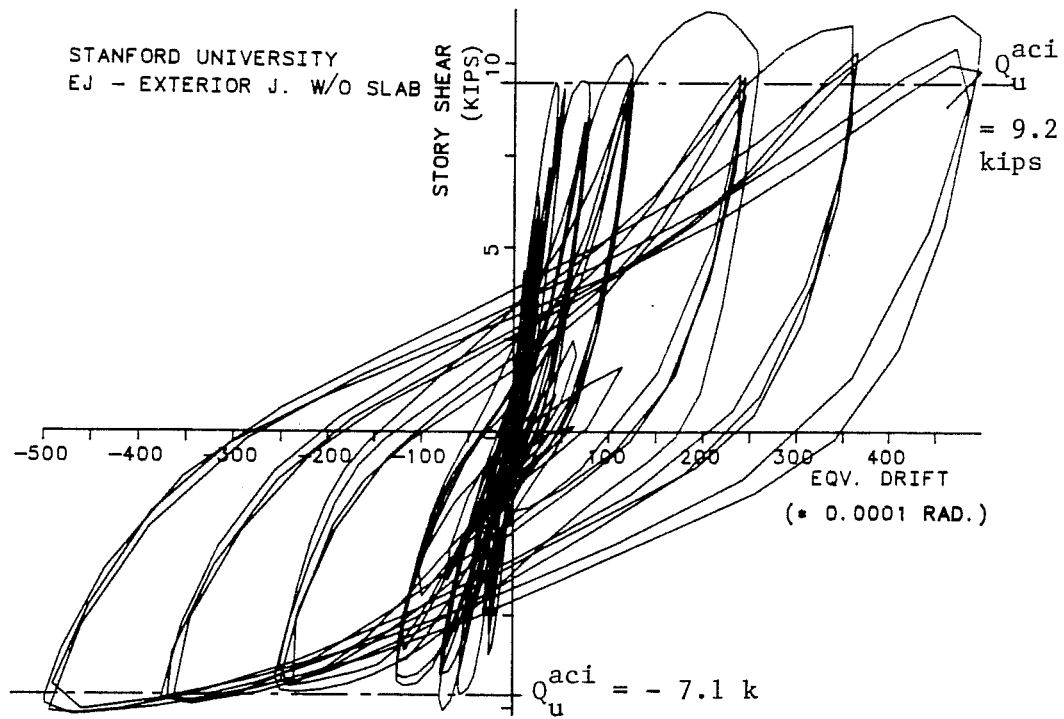


Fig. 5.17 - Japanese and SU Tests without a Slab.

near the origin; (2) the SU(ES) test showed consistently higher strength than the USJ-2 tests; and, (3) in both specimens, a larger ultimate load (slab in tension) as predicted using the 4.00 m (157.5 in.) ACI slab width was not reached. The explanations for each of these major differences will be elaborated further but it was observed that severe pinching resulted from beam bar anchorage failure of test USJ - 2. The increased strength of test SU(ES) resulted from the high slab steel yield strength [Wallace and Krawinkler (5)].

The 1/2-scale Japanese tests had an ultimate strength close to that predicted by the 1.50 m (59.0 in.) AIJ slab width (2). For specimens E-1, E-2, the computed AIJ strengths were 42% higher (slab in tension) and 56% lower (slab in compression) than equivalent UTA values, Figs. 5.15, 5.16. The Japanese exterior tests were conducted under an axial compression load of 219 kips ($= 0.14 P_{max}$) which fluctuated +10% during the test. The response for the Japanese and US design specimens is shown in Fig. 5.16 (with a slab) and Fig. 5.17 (without a slab).

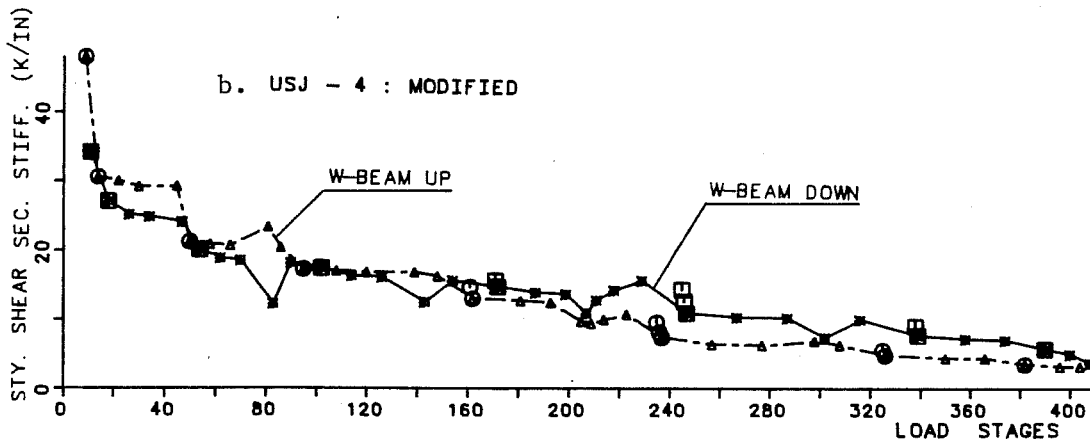
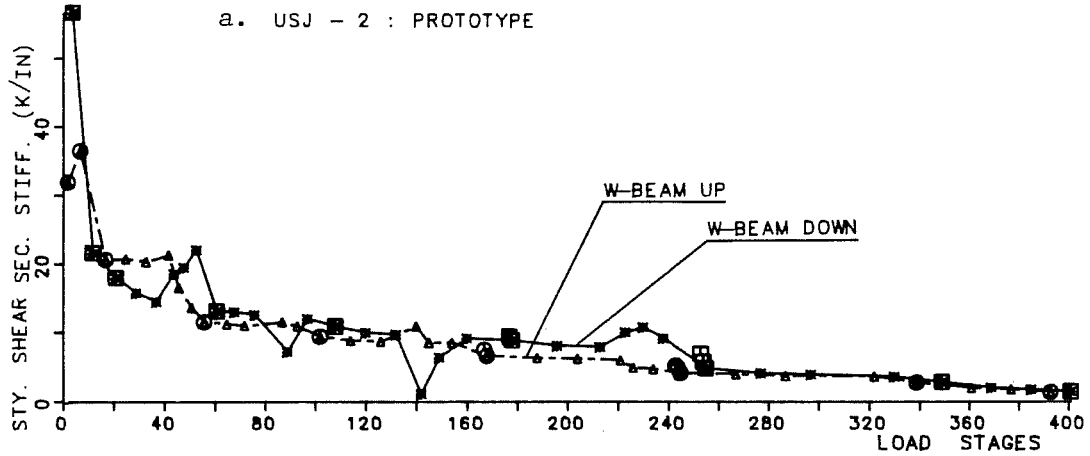
The large difference in strength for specimens with slab vanishes in tests without a slab. Nearly the same ultimate strength was observed in both the JPN (1:2) and SU (1:12.5) tests in spite of the different loading program, Fig. 5.17. Good hysteretic behavior was observed in both tests.

By comparing the specimens with and without a slab, it can be found that the presence of a slab increased the maximum by 85% (slab in tension) and 30% (slab in compression) over the estimated strength using the ACI, AIJ code, lab width. The SU specimen ultimate maximum load (slab in compression) increased even further (+73%), Figs. 5.15 and 5.17.

5.3.2.2 Stiffness Characteristics. The story shear secant stiffness obtained by dividing the story shear by the correspondent story deflection gives a measure of cumulative damage. Other peculiar aspects of response derived from the fact of using a T-beam are also shown by the difference in direction of loading response, Figs. 5.18 to 5.21.

When the slab was in tension, the secant stiffness was consistently higher in the exterior component tests. In Fig. 5.18 the modified specimen (USJ-4) exhibited higher secant stiffness than USJ-2 which had less beam reinforcement. In Fig. 5.19, the specimen without a slab showed significantly lower stiffness during the whole test. However, at very large drift levels (+1/20) the stiffnesses are almost equal. The difference in stiffness is more easily observed in specimen E-2, Fig. 5.20. When the beam is loaded downward, the slab cast monolithically with the beam greatly increases the stiffness. This can also be observed at first peak drifts where components without a slab had consistently lower stiffness. A comparison among all the

U. TEXAS AT AUSTIN - EXTERIOR JOINTS .
STOREY SHEAR SECANT STIFFNESS HISTORY .



SECANT STIFFNESS AT FIRST PEAK DRIFTS .

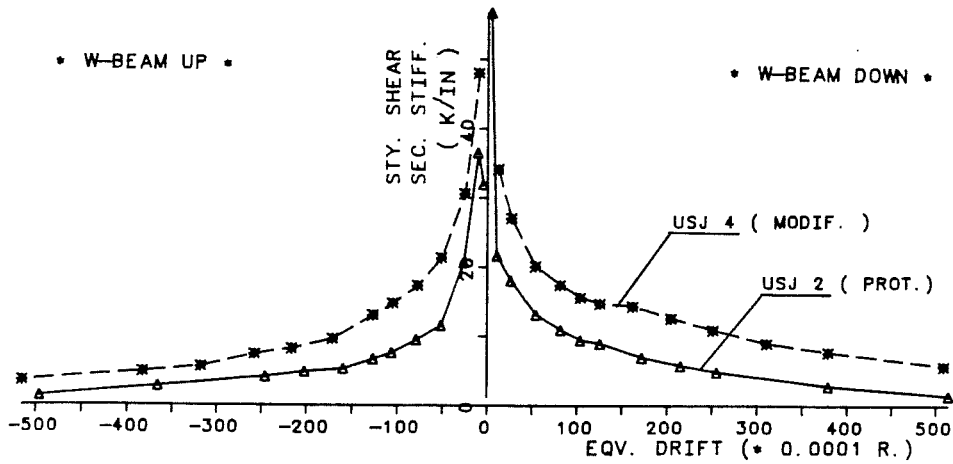
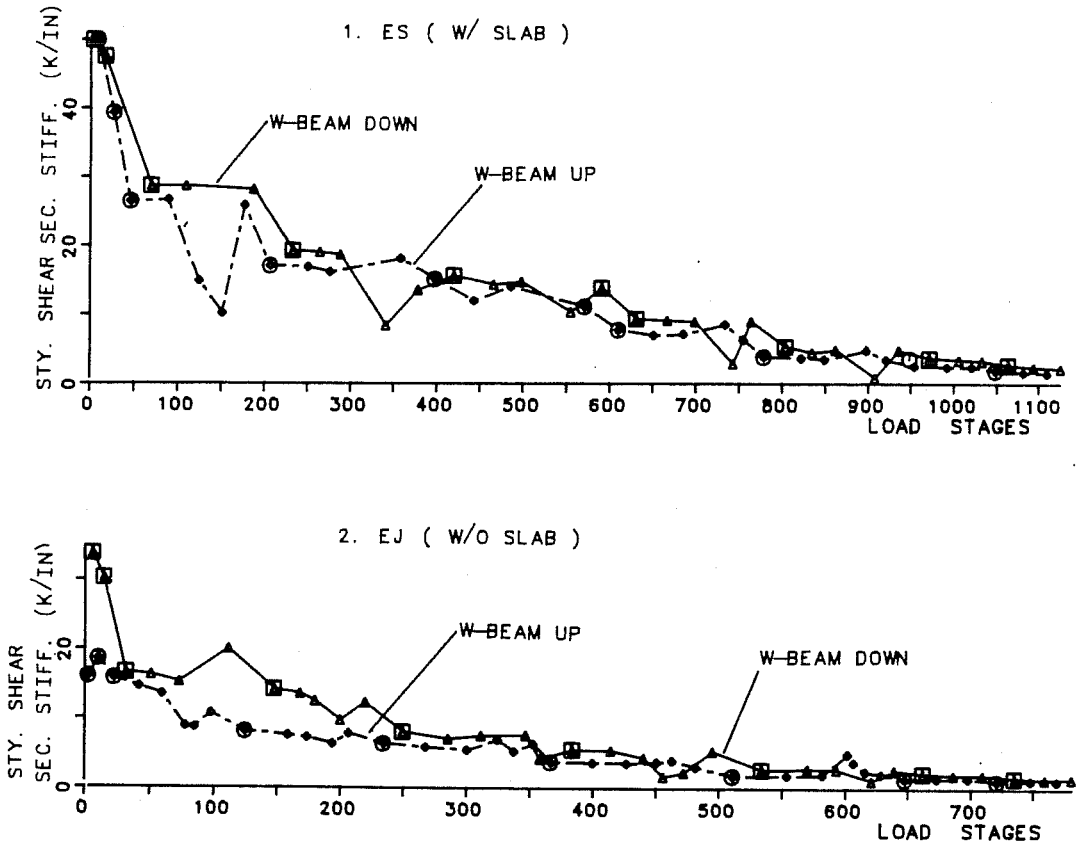


Fig. 5.18 - UTA - Story Shear Secant Stiffness History.

STANFORD U. - EXTERIOR JOINTS .
STOREY SHEAR SECANT STIFFNESS HISTORY .



SECANT STIFFNESS AT FIRST PEAK DRIFTS .

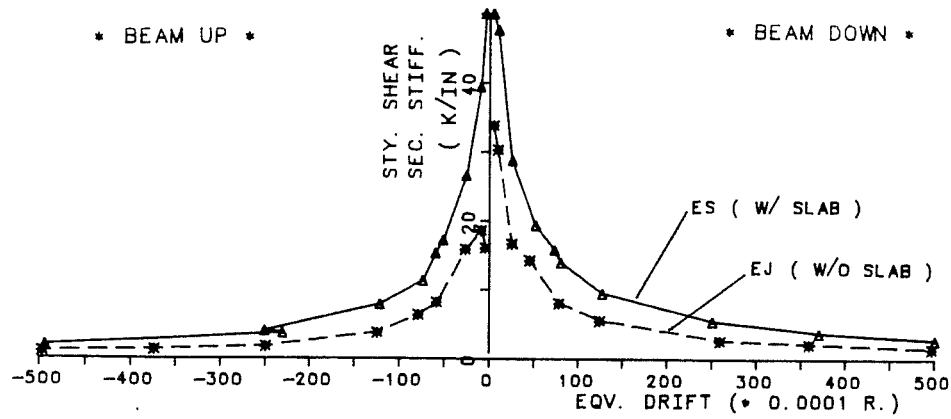
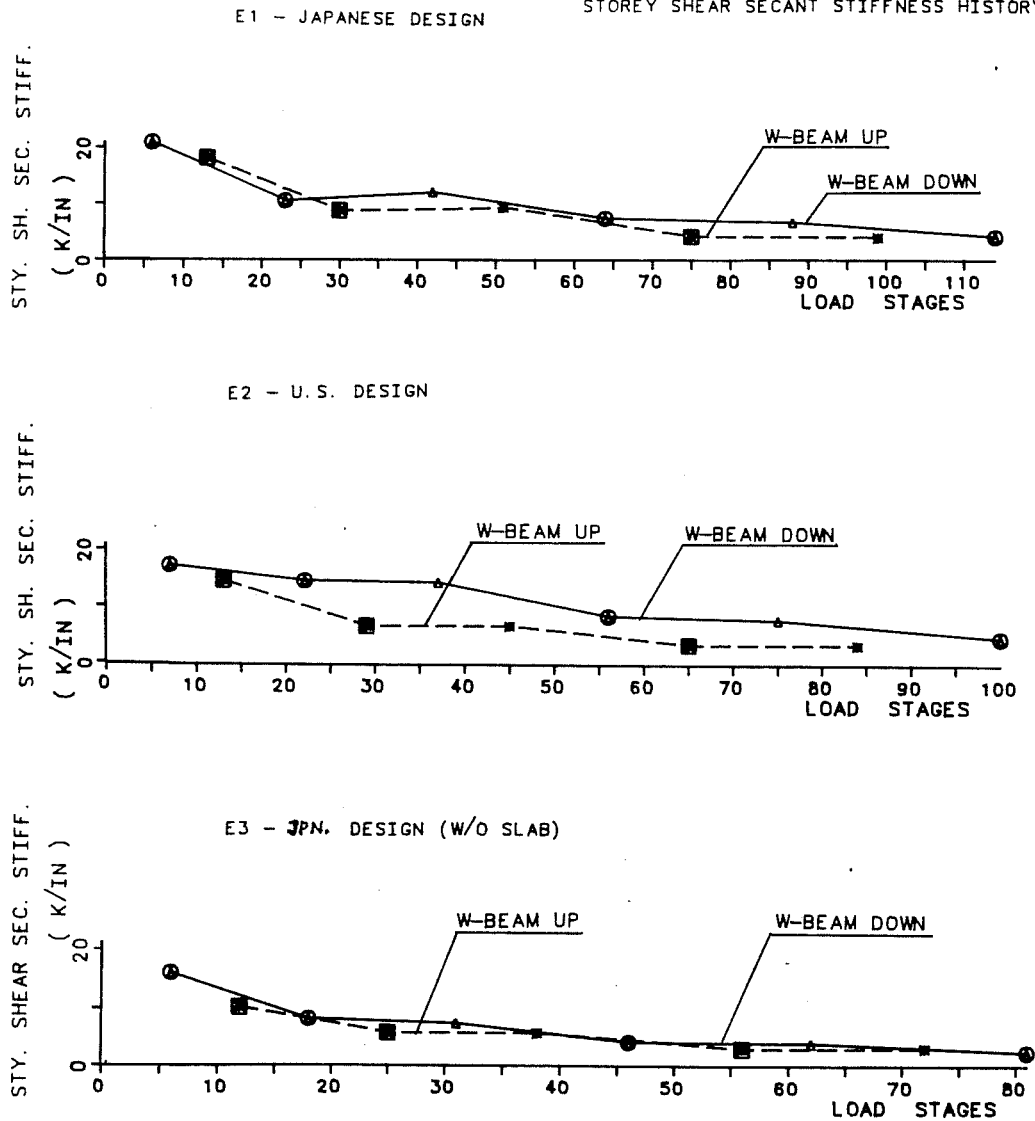


Fig. 5.19 - SU - Story Shear Secant Stiffness History.

JAPAN (1/2 SCALE) - EXT. JOINTS .
STOREY SHEAR SECANT STIFFNESS HISTORY .



SECANT STIFFNESS AT FIRST PEAK DRIFTS .

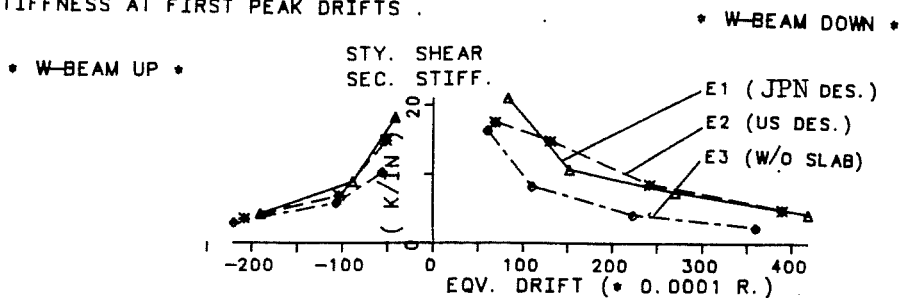


Fig. 5.20 - Japanese Tests- Story Shear Secant Stiffness History.

EXTERIOR JOINTS :
STOREY SHEAR SECANT STIFFNESS
AT FIRST PEAK DRIFTS .

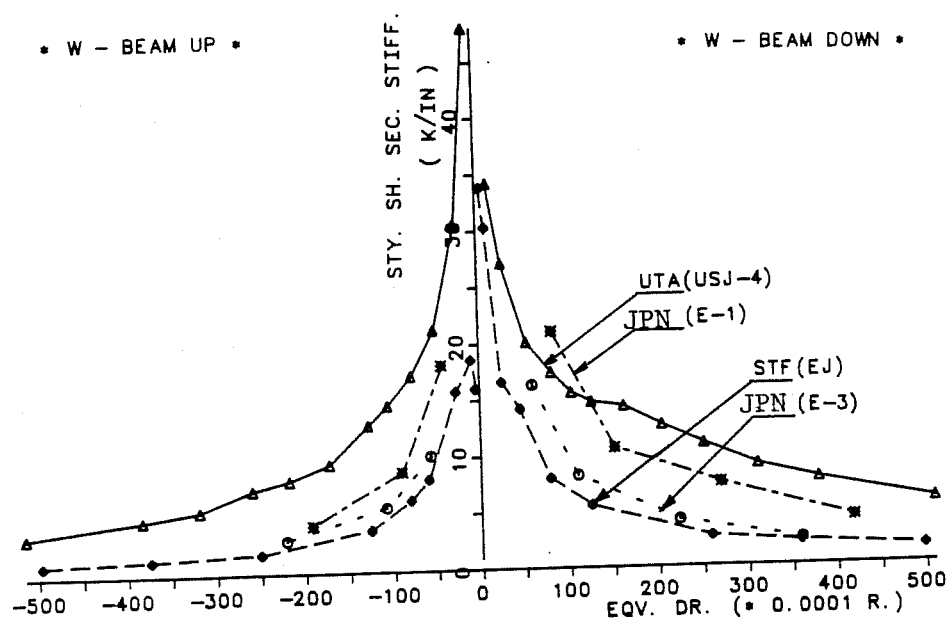
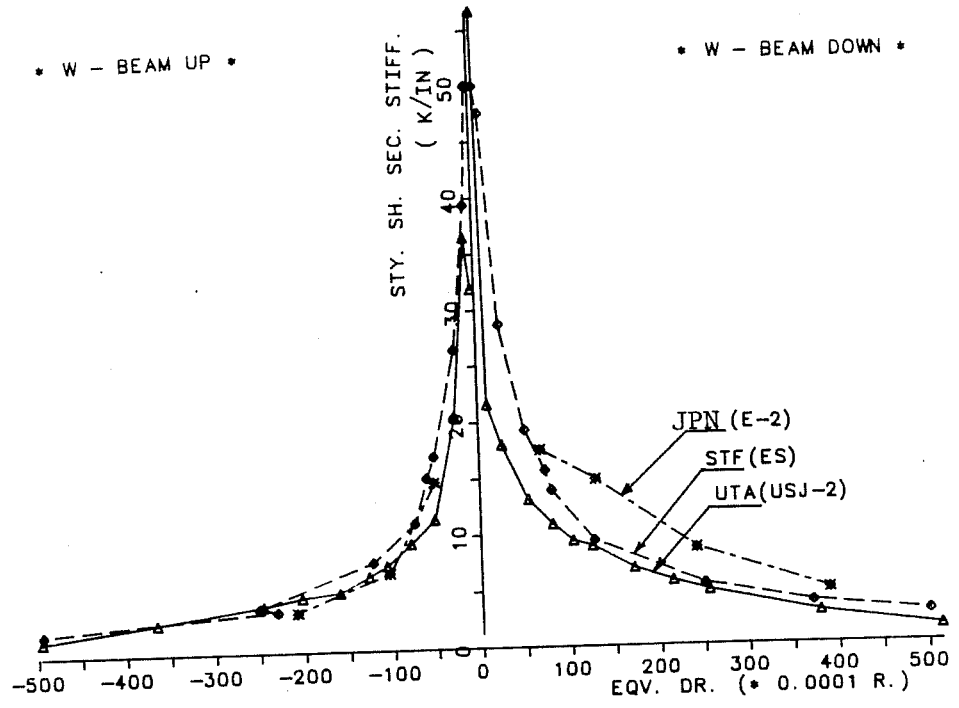


Fig. 5.21 - Exterior Components - Story Shear Secant Stiffness History.

exterior components, Fig. 5.21, showed that (1) a major drop in stiffness occurred for the prototype specimens (E-2, ES, USJ-2) up to 1/100 equivalent drift level; (2) the Japanese components reached nearly the same peak drifts, showed less stiffness deterioration due to the reduced number of loading cycles; (3) an increase in the beam reinforcement ratio by 100% (USJ-4) and improved anchorage details reduced stiffness deterioration both in the positive and negative loading cycles; and (4) specimens without a slab (EJ, E-3) had lower stiffness as compared with specimens with a slab, particularly when the slab was in tension.

5.3.3 Interior Component Tests

5.3.3.1 Strength Characteristics. The interior specimens response is characterized by curves which are similar in both directions of loading, Figs. 5.22 to 5.24. This is to be expected because the beams in both sides of the column are the same and there is always one beam loaded downward while the other is loaded upward regardless of the loading direction. Consequently, the asymmetry with loading directions observed in the exterior components is not seen when the total story shear is plotted for interior components.

The interior prototype specimens (USJ-1, IS) show that the maximum strength is reached at a peak drift of 1/50. The story shear at 2% drift was slightly below the value obtained if the whole slab width of 4.00 m (157.5 in.) is included in the

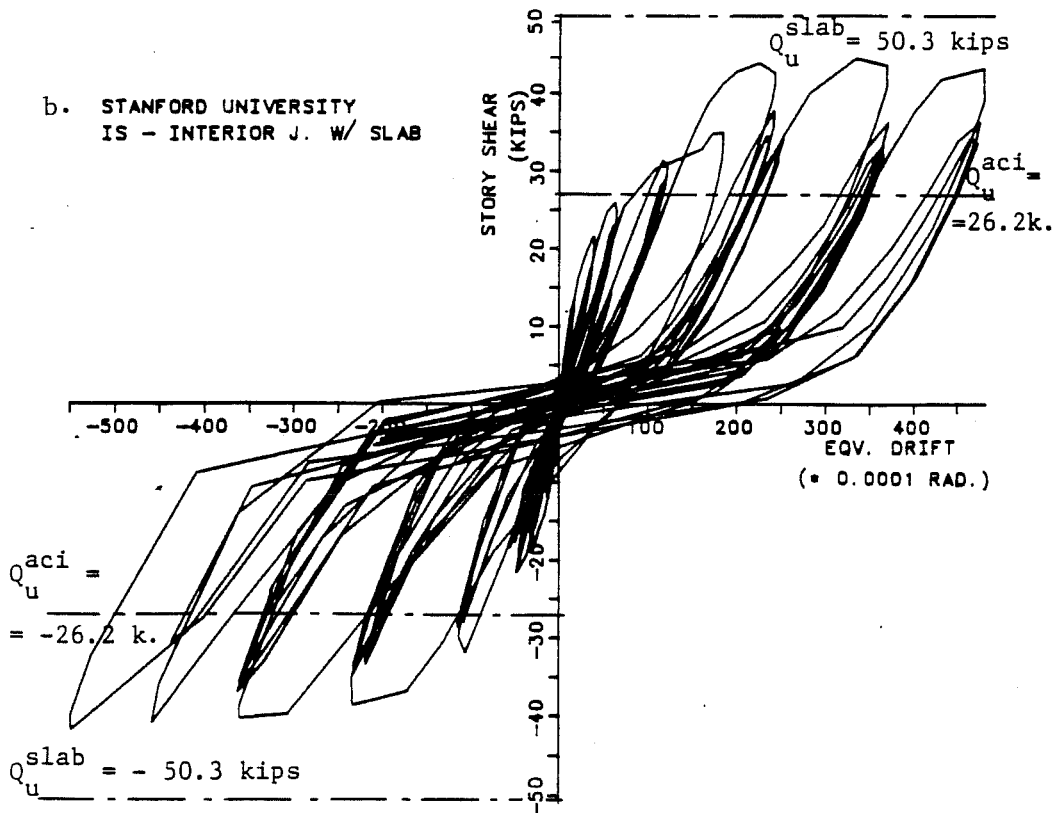
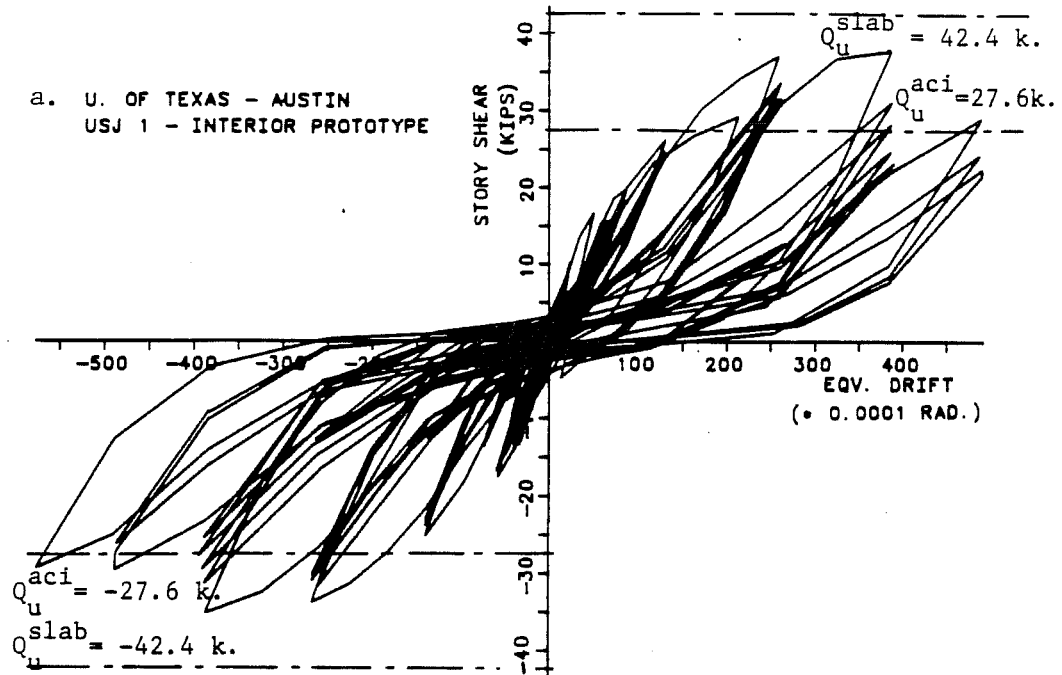


Fig. 5.22 - UTA and SU Interior Prototype Response.

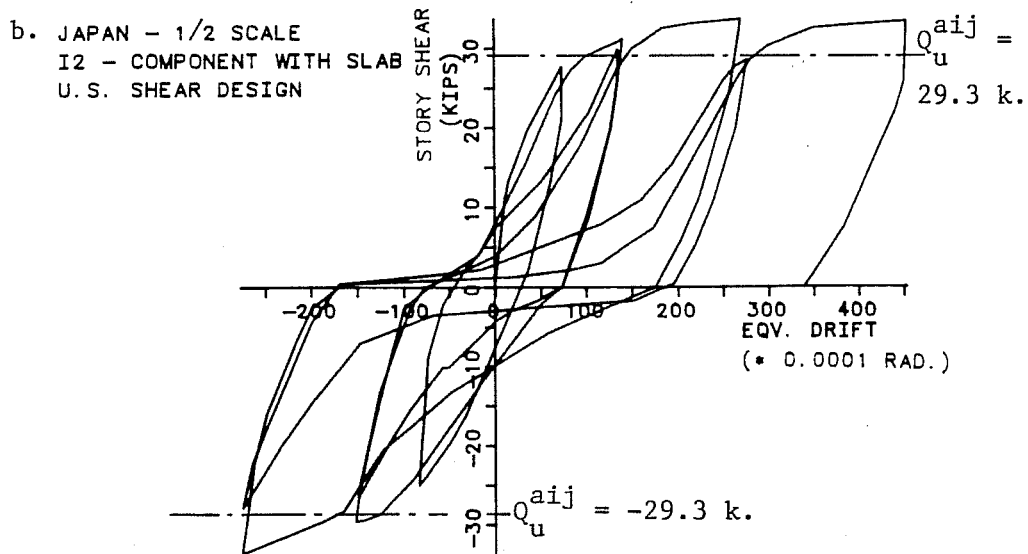
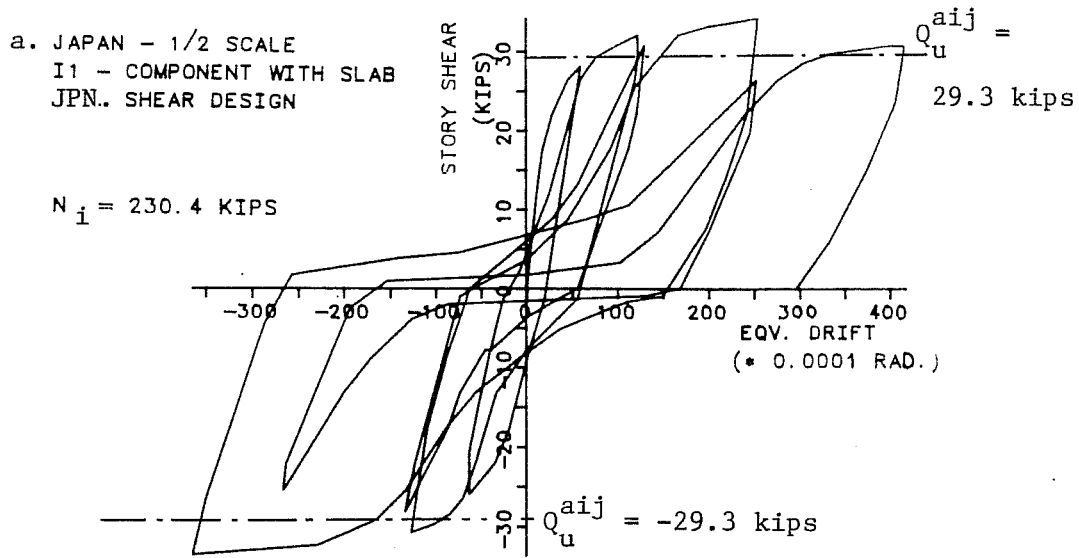
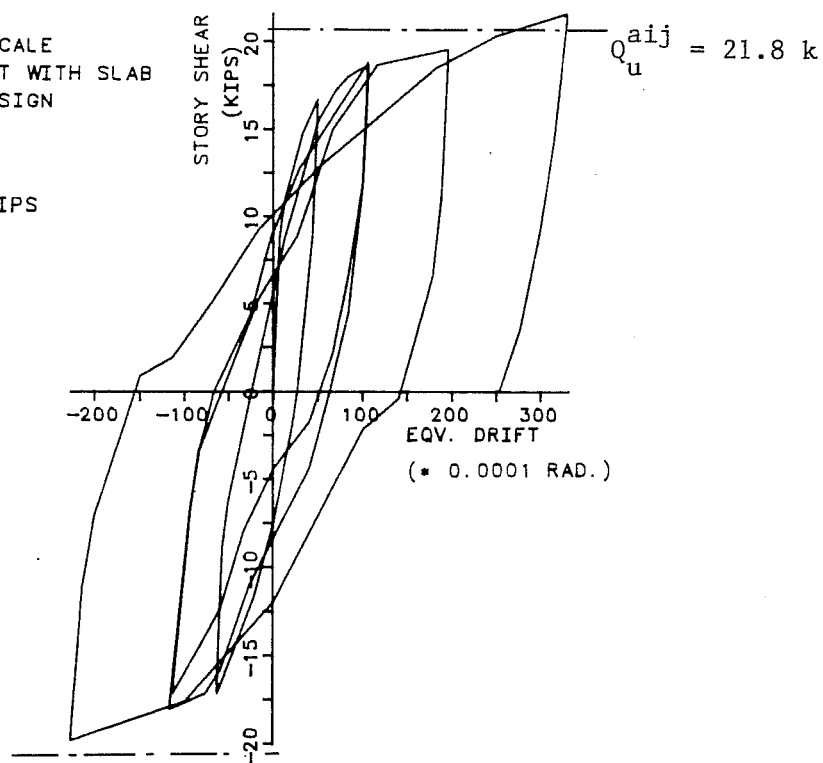


Fig. 5.23 - Japanese Interior Prototype Response.

a. JAPAN - 1/2 SCALE
 I3 - COMPONENT WITH SLAB
 JPN. SHEAR DESIGN

$N_i = 230.4$ KIPS



b. STANFORD UNIVERSITY
 IJ - INTERIOR J. W/O SLAB

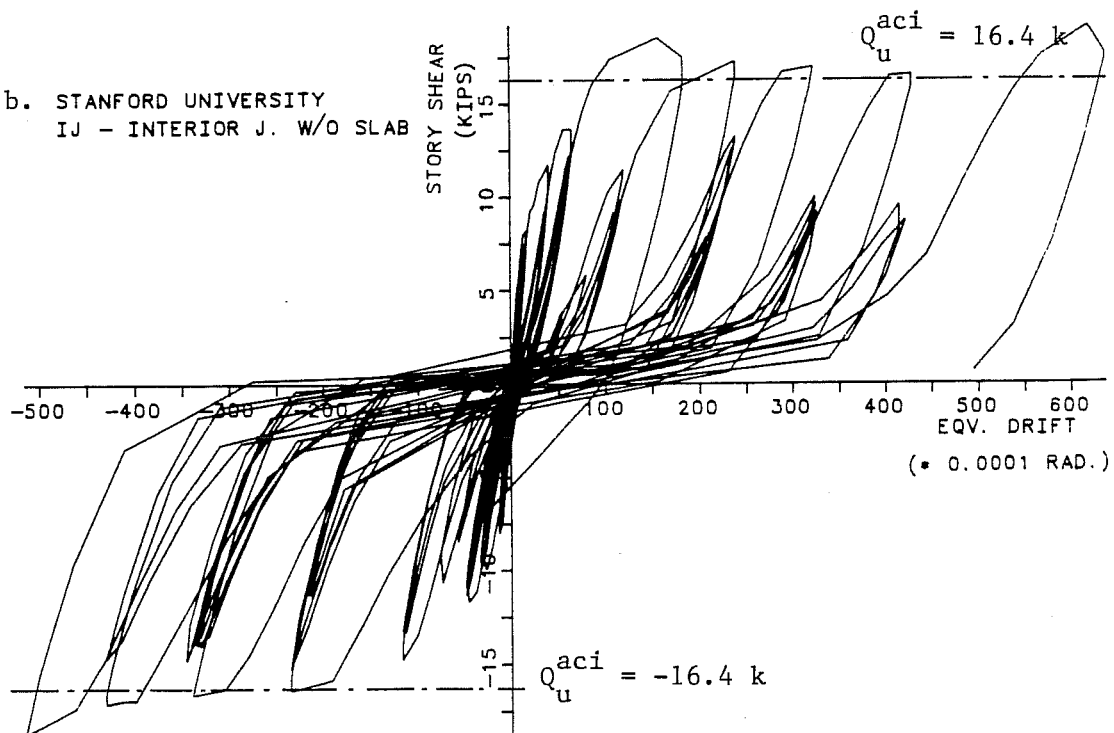


Fig. 5.24 - Japanese and SU Interior Joints without a Slab.

strength calculation (Q_u^{slab}) but well above the computed strength (Q_u^{ACI}) using ACI 318-83 (1). The values range from approximately +40% for USJ-1 to +65% for IS, Fig. 5.22. The observed values for IS is higher because steel with a higher ultimate strength was used in the slab but not considered in calculating the strength.

The Japanese 1/2-scale specimens, included a slab width equal to that considered effective in the AIJ standards of 1.50 m (59 in.). The recorded story shear agreed quite well with the AIJ design values. High strengths were achieved at a drift level of 1/100 and increased only slightly at 1/50 drift. Specimen I-2, designed for shear according to US standards exhibited better hysteretic response, Fig. 5.23-b. The components were tested under a compressive axial load of 230.4 kips which created a compressive stress of 546 psi in the column. The response is shown in Figs. 5.23 and 5.24.

The response of the components without a slab (I-3, IJ) showed good agreement with the predicted response level by both AIJ and ACI standards, Fig. 5.24. Although good agreement was observed, specimen I-3 was +33% stronger. Also, small and stable hysteresic loops were observed during the few cycles imposed on I-3. Specimen IJ showed severe pinching near the origin from excessive bar slippage and bond deterioration in the bottom beam bars. The poor performance of the bar anchorage was likely the

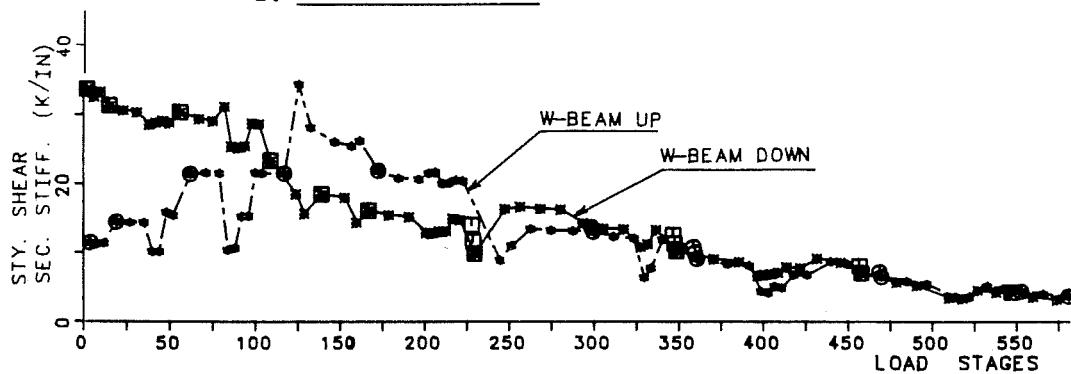
result of excessive vibration which segregated the microconcrete during the casting of the column lower part [Wallace and Krawinkler, (5)].

5.3.3.2 Stiffness Characteristics. The story shear secant stiffness was computed by dividing the story shear force (column shear) by the interstory displacement. Since the total beam shear was used, the particular effects of T-beam (slab participation) response were masked. However, in specimen USJ-1 (up to load stage (LDS) 240) a load-controlled program was used by mistake. The duality in peak secant stiffness is clearly shown in Fig. 5.25. On the other hand, USJ-3 was subjected to a displacement-controlled program and this dichotomy in response was no longer observed. The response at first peak drifts showed a clear difference in stiffness degradation between USJ-3 (which had twice the beam steel) and USJ-1, Fig. 5.25.

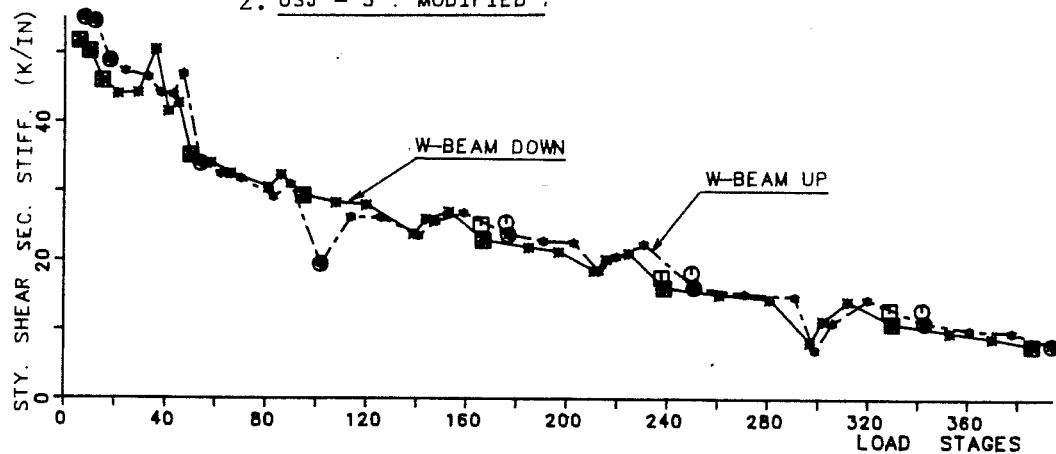
The SU specimens also showed the same difference in response as USJ-1 because the same loading program was used in both cases, Fig. 5.26. The stiffness degradation at first peak drift was very severe in the specimen without a slab (IJ) up to 1/100 drift. For the specimen with a slab, stiffness gradually decreased after reaching 1/70 - 1/50 drift, Fig. 5.26.

U. TEXAS AT AUSTIN - INTERIOR JOINTS
STOREY SHEAR SECANT STIFFNESS HISTORY

1. USJ - 1 : PROTOTYPE



2. USJ - 3 : MODIFIED



SECANT STIFFNESS AT FIRST PEAK DRIFTS

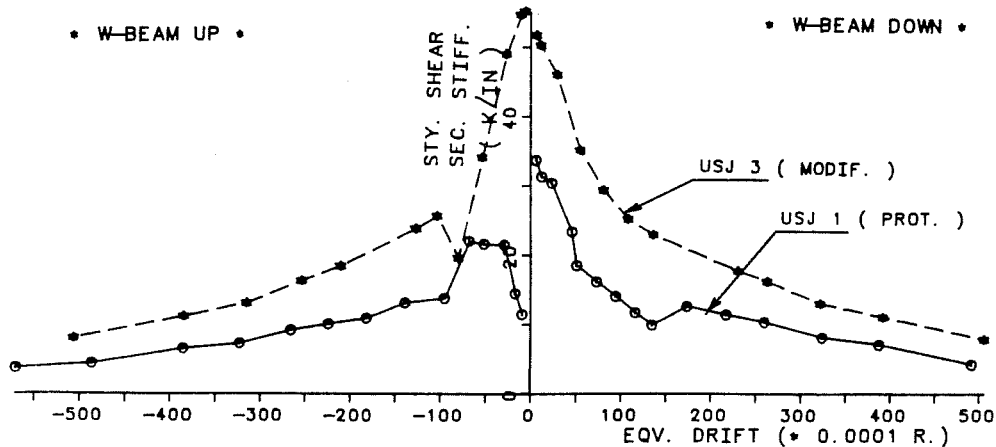
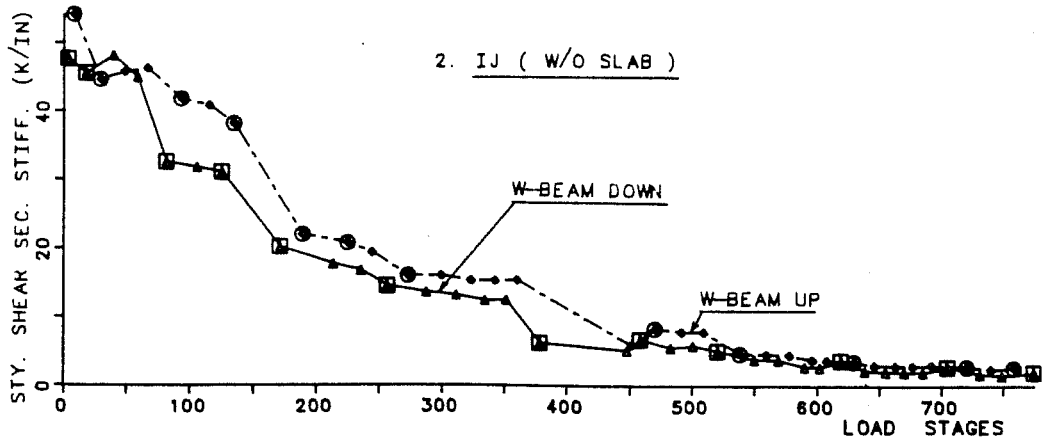
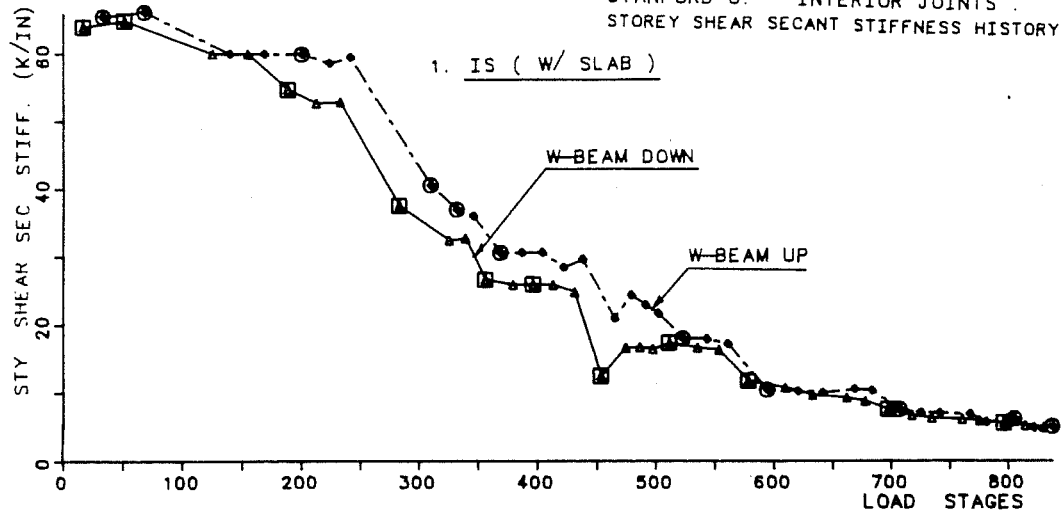


Fig. 5.25 - UTA - Interior Joint Secant Stiffness History.

STANFORD U. - INTERIOR JOINTS
STOREY SHEAR SECANT STIFFNESS HISTORY



SECANT STIFFNESS AT FIRST PEAK DRIFTS

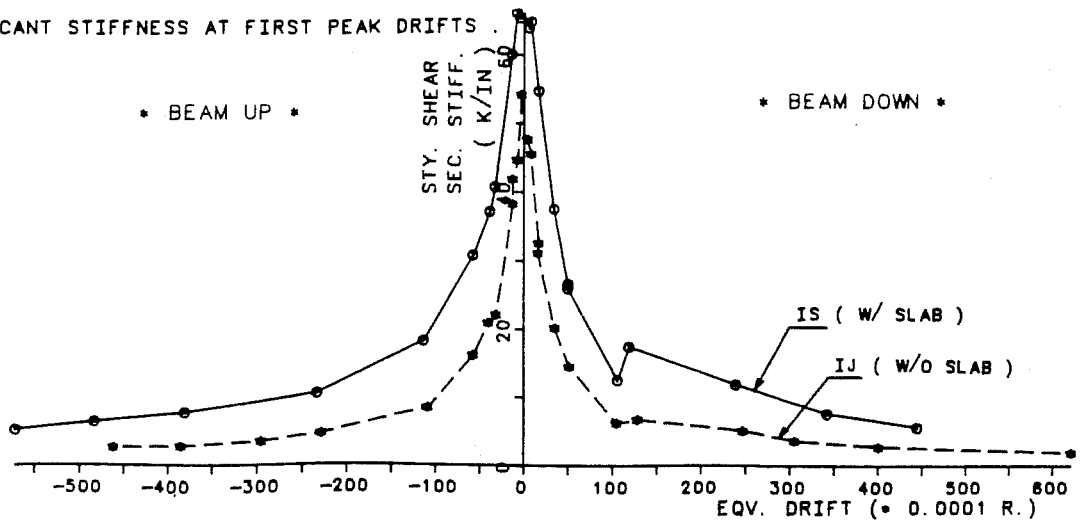


Fig. 5.26 - SU - Interior Joint Secant Stiffness History.

In the Japanese 1/2-scale tests, specimens with a 1.50 m (59 in.) width slab (I-1, I-2) showed a higher secant stiffness than the specimen without a slab (I-3), Fig. 5.27.

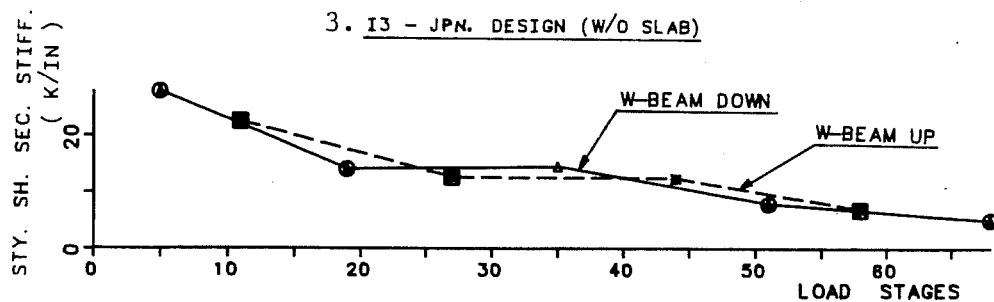
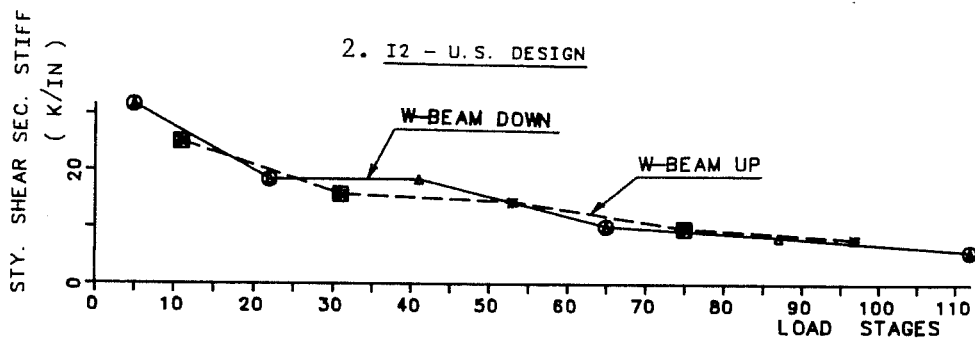
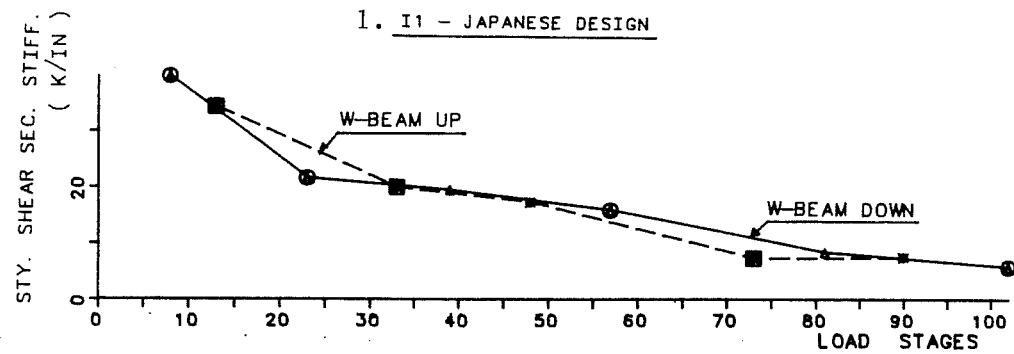
A comparison between all the interior specimens made by considering two groups: (a) components similar to the prototype - I-2, IS, USJ-2; and, (b) other components - I-1, I-3, IJ, USJ-4, where variables other than scale were considered (slab, beam reinforcement ratio).

The first group showed that good correlation can be obtained among the components in spite of scale effects, Fig. 5.28. Also a major drop in stiffness occurred up to 1/100 - 1/70 equivalent drift. Specimen USJ-1, initially subjected to a load - controlled test, showed lower initial stiffness values which may be due to the severity of the loading program.

The other group of tests showed that the specimens with a slab had a higher stiffness with a slower degradation rate than the specimens without a slab (IJ, I-3), Fig. 5.28. Also, in the components without a slab, major stiffness degradation occurred up to a peak drift of 1/100 - 1/70. Specimen IJ (casting problems) clearly had a lower secant stiffness as compared with I-3.

5.3.4 Exterior vs. Interior Component Response. Two UTA specimens are used to compare the attained strength under identical loading circumstances, Fig. 5.29. The interior joint

JAPAN (1/2 SCALE) - INT. JOINTS .
STOREY SHEAR SECANT STIFFNESS HISTORY .



SECANT STIFFNESS AT FIRST PEAK DRIFTS .

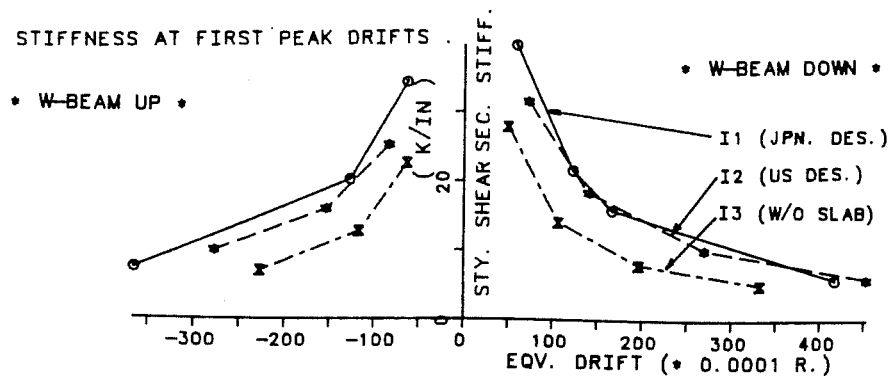
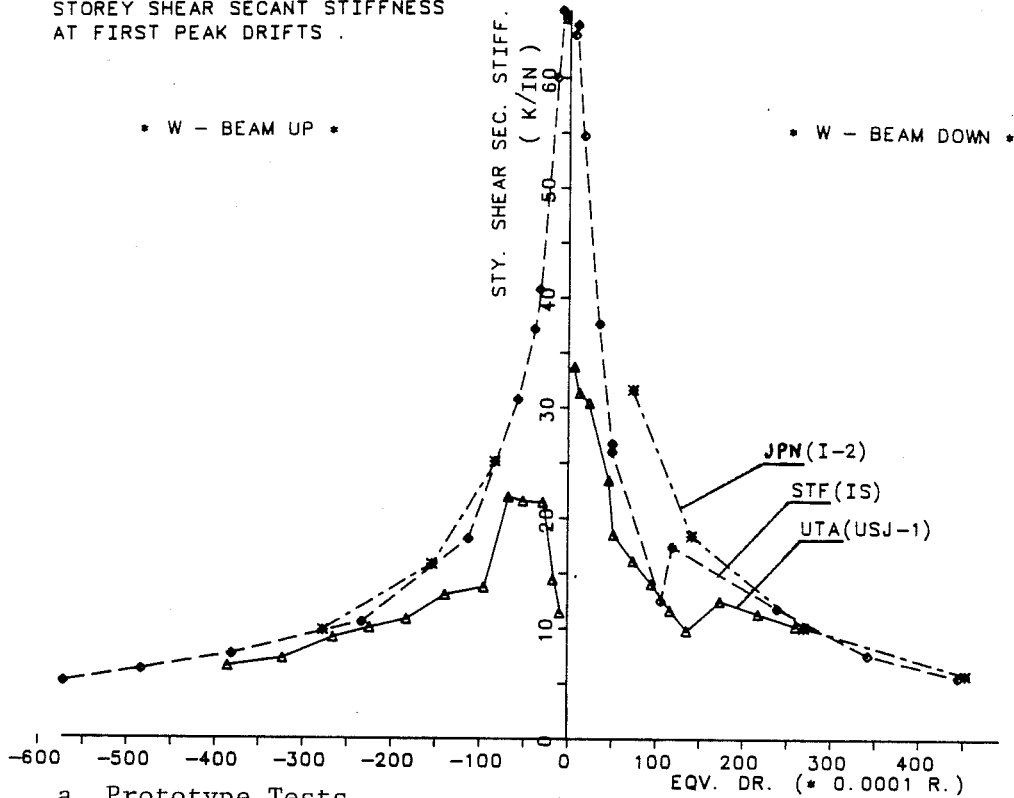
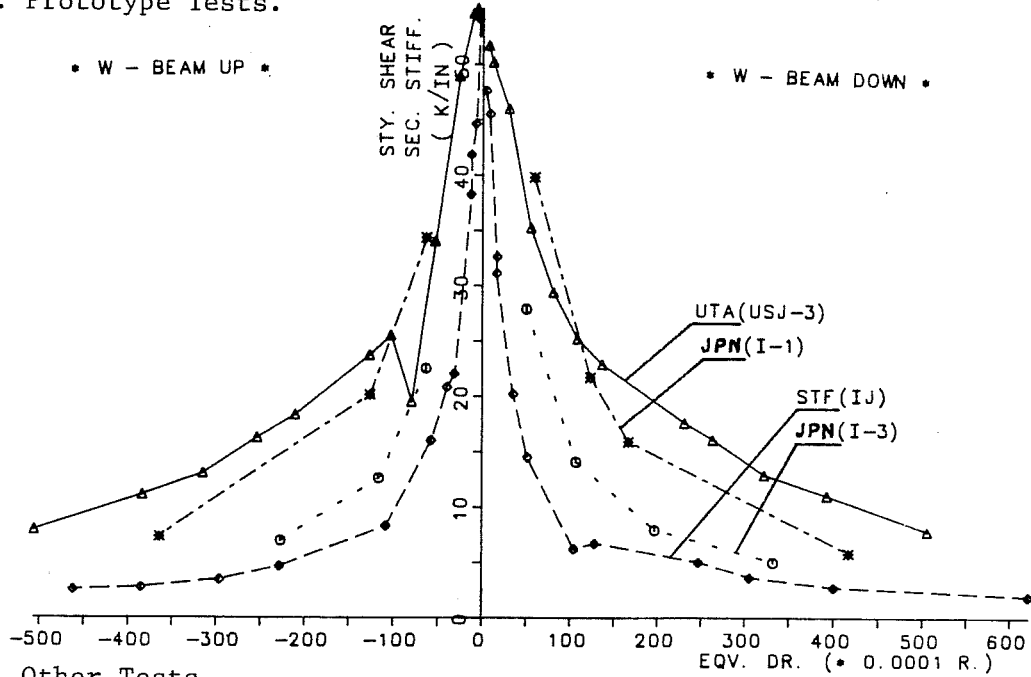


Fig. 5.27 - Japanese Interior Joints Stiffness Degradation.

INTERIOR JOINTS :
STOREY SHEAR SECANT STIFFNESS
AT FIRST PEAK DRIFTS .



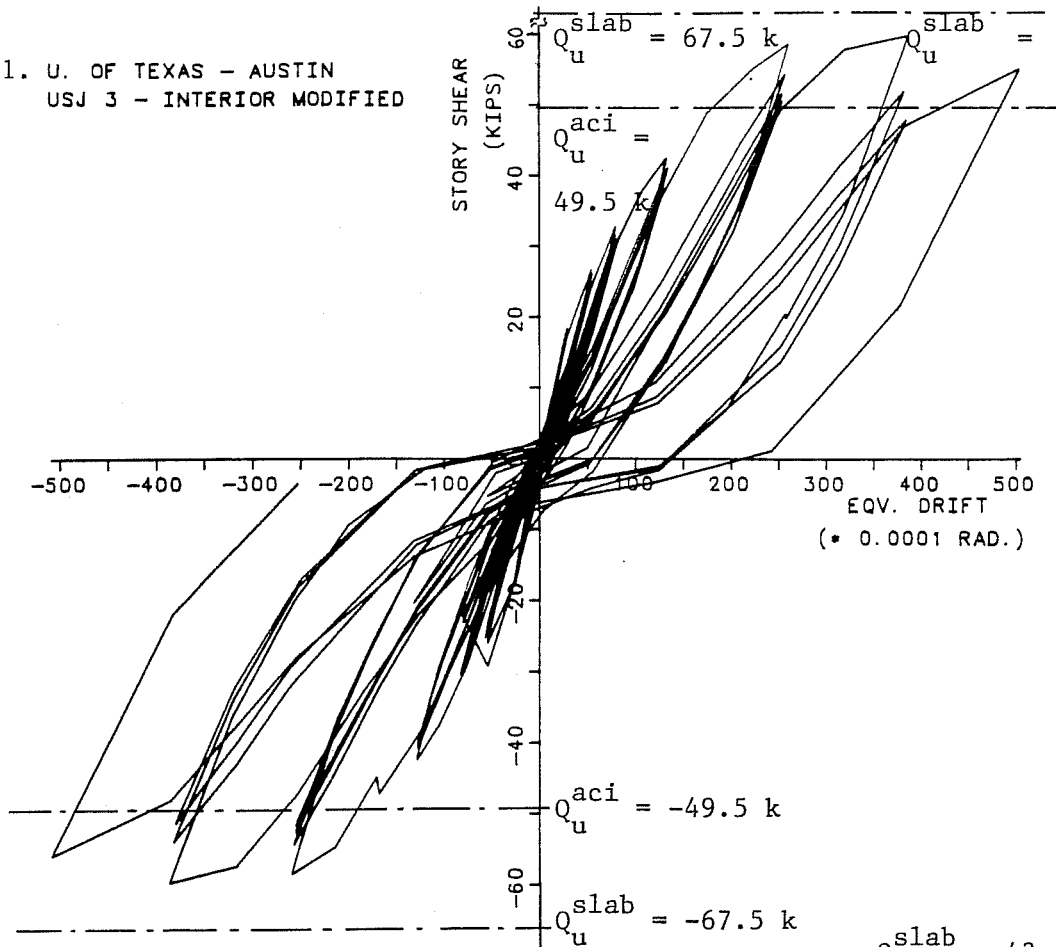
a. Prototype Tests.



b. Other Tests.

Fig. 5.28 - Interior Tests Peak Secant Stiffness History.

1. U. OF TEXAS - AUSTIN
USJ 3 - INTERIOR MODIFIED



2. U. OF TEXAS - AUSTIN
USJ 4 - EXTERIOR MODIFIED

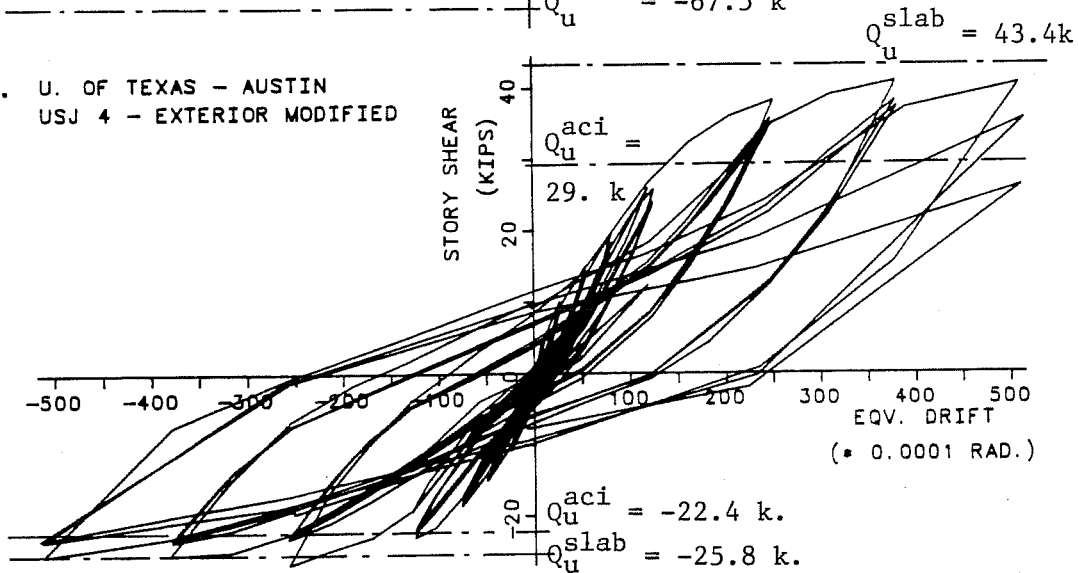


Fig. 5.29 - UTA - Modified Tests Response.

(USJ-3) does not show any difference under positive or negative drift. The observed maximum story shear occurred between 1/50 and 1/40 drift. The curves are bounded by the absolute maximum value considering a slab width of 4.00 m (157.5) and the lower value computed using the standard ACI code slab width of 1.50 m (59 in.).

The exterior specimen (USJ-4) had asymmetrical response derived from the effect of the slab in tension. The maximum story shear when the slab was in tension occurred between 1/50 - 1/33 story drift and was very close to the value obtained by considering the whole slab width of 4.00 m. The role of the slab was smaller (15%) when the slab was in compression. The maximum story shear strength was attained at 1/50 equivalent drift value, Fig. 5.29.

In the exterior component smaller shear forces were applied to the joint as compared with the interior component: (1) -35% for positive drift; and, (2) -60% for negative drift. These values were computed by considering the whole slab width as effective in the maximum story shear calculation, Fig. 5.29.

5.4 Final Observations

The available test data provided an excellent opportunity for comparing response of segments of a full-scale building and isolated components. First the external macroscopic response

aspects observed directly (cracking patterns, component forces and displacements) were compared. The cracking patterns observed both in the BRI building joint regions and in the component tests with a slab showed strong similarities. It was shown that the difference in cracking response between an interior and an exterior joint depended to a large extent on the moment transfer mechanism integrity around the joint region and on the transverse beam stiffness. Under negative bending at the column face, the slab acting in tension created large shears in the longitudinal beams and joint core, and torsional demands on the transverse beam. These large forces were accompanied by extensive cracking and evidence of detailing problems which resulted in an anchorage failure in USJ-2 exterior component. The components with a slab showed a characteristic semi-circular cracking pattern around the point of application of the large concentrated loads. The presence of a slab led to large ductility demands near the column region (localized plastic hinge) whereas in components without a slab ductility demands were more uniformly distributed throughout the longitudinal beam (diffused plastic hinge).

Stiffness and strength response were also analyzed for the BRI building and the components. The BRI building stiffness response showed that levels Z2, Z3 and Zr (roof) had the same floor lateral secant stiffness throughout the test. The exterior component ultimate strength with the slab in tension was close to

the value estimated by using the design code slab width of 1.50 m (59 in.). This was well below the value obtained by using the full-slab width of 4.00 m (157.5 in.) in the UTA and SU tests.

When the slab was in compression, the maximum story shear force agreed well with the value computed by using the entire slab width of 1.50 m (Japanese tests) or 4.00 m (US tests). The components stiffness deteriorated steadily up to an equivalent drift of 1/100 and remained fairly constant thereafter. The major feature of the interior components was the similarity of the response under either positive or negative drift. This was due to the contribution of the slab in tension to either E- or W-beams under racking loads. The maximum measured story shear never reached the value computed using the whole slab width in tension but it was greater than that obtained using the standard slab width of 1.50 m (59 in.).

5.5 References

1. ACI Committee 318 - Building Code Requirements for Reinforced Concrete and Commentary. American Concrete Institute (ACI), Detroit, MI, 1983.
2. AIJ - Standard for Structural Calculation of Reinforced Concrete Structures (English version), The Architectural Institute of Japan (AIJ), Tokyo, Japan, 1980.
3. S. Nakata, S. Otani, T. Kabeyazawa, Y. Kai and S. Kimura - "Tests of Reinforced Concrete Beam-Column Assemblages", Technical Report - Joint Technical Coordinating Committee, U.S. - Japan Cooperative Research Program (1st Meeting), Tokyo, Japan, October, 1980.

4. S. Okamoto, S. Nakata, M. Yoshimura, T. Kaminosono. "A Progress Report on the Full-Scale Seismic Experiment of a Seven Story Reinforced Concrete Building - Part of the U.S.-Japan Cooperative Program", Building Research Institute, Ministry of Construction, Tokyo, Japan, 1982.
5. B. Wallace and H. Krawinkler - "Small-Scale Model Experimentation on R/C Assemblies, U.S.-Japan Research Program", Report No. 74, J.A. Blume Earthquake Engineering Center, Stanford University, June 1985.

CHAPTER VI
ASPECTS OF LOCAL RESPONSE

6.1 Introduction

Examination of local (component) response provides a complement to the macroscopic behavior discussed in the previous chapter. The data on loads, displacements and strains is used to derive other quantities (rotations, twists, bar slippage) which are useful for identifying potential locations of component degradation in the BRI building and component tests. The longitudinal and transverse beams, the slab and the joint core responses are assessed using beam rotations and twists, bond degradation, and spread of yielding.

6.2 Longitudinal Beam Rotation

The longitudinal beams in the BRI frame and in the prototype components were instrumented to measure deformations at the top and bottom of the beams at selected distances from the column face. In the BRI building the transducers were placed at a distance $d/2$ (d = beam depth) from the column face. In the components, deformations were measured at a distance $0.3d$ and $1.2d$ from the column. The exterior spans in the BRI building are 6.00 m (236 in.) and the interior span is 5.00 m (197 in.) In the UTA and SU tests the beams were loaded at a point 8.0 ft (2.44 m) from the center of the column. These differences led to

some problems making comparisons between rotations in the BRI structure and the component tests.

6.2.1 Exterior Joint Beam Rotation. The plot in Fig. 6.1 shows that good agreement exists between the UTA (USJ-2) specimen and the BRI building exterior joint, both with the slab in tension (positive drift) and in compression (negative drift), up to drift levels of 1/100 to 1/64 which was the maximum value to the BRI building. The component tests were subjected to very large drifts of 1/20 to 1/16. Specimen USJ-2 also shows a marked increase in beam rotation at an equivalent drift of about +1/66 and a decrease (increase in stiffness) at about +1/40 drift.

Another important aspect of component response was the location and amount of damage in the longitudinal beam member. The use of two sets of LVDT's one at 6.0 in. (0.15 m) and other at 24.0 in. (0.60 m) from the column face was extremely useful for this purpose. In Fig. 6.2, it is clearly shown that for both UTA and SU exterior joints, the largest amount of plastic beam rotation occurs near the column face. The rotation near the column face was 2 to 7 times larger for the UTA specimens and 3 to 12 times larger for the SU tests. Furthermore, it can be observed that in the SU specimens most of the rotation occurred near the column face and almost none occurred between 0.3d and 1.2d from the column.

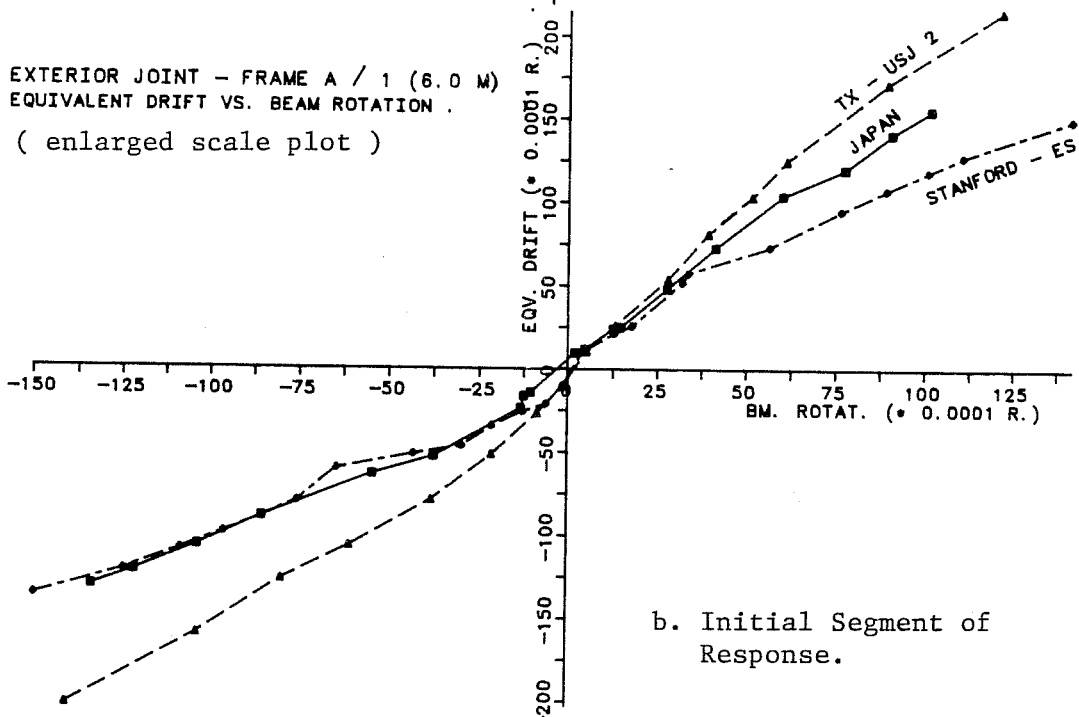
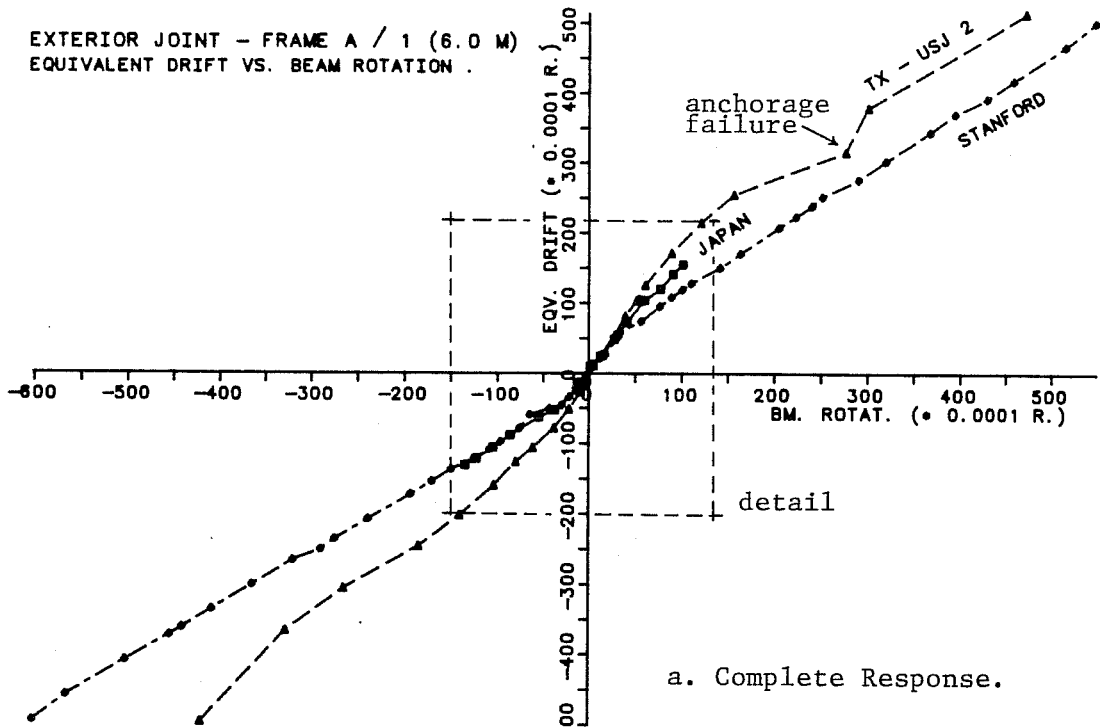


Fig. 6.1 - Exterior Joint Longitudinal Beam Rotation.

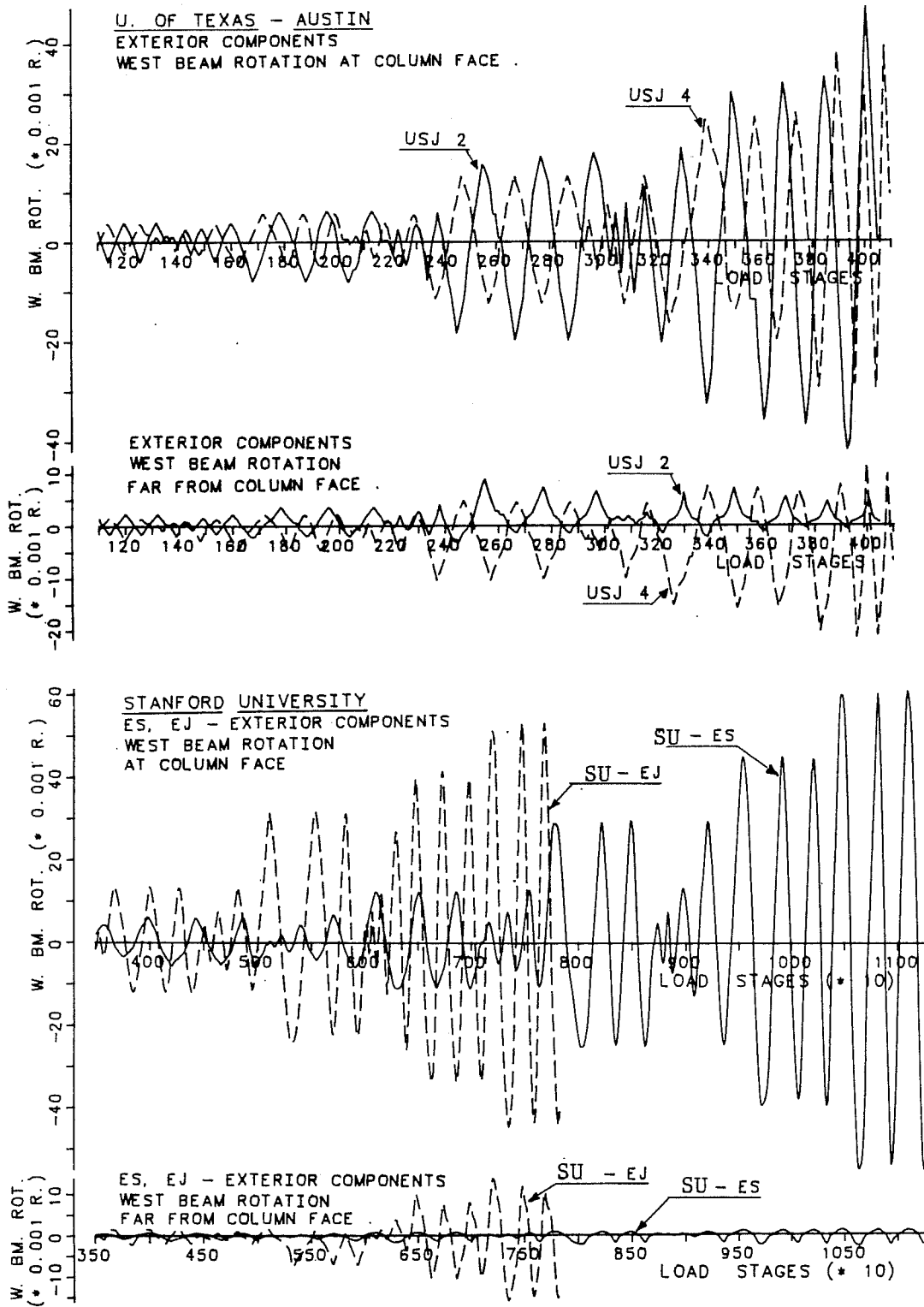


Fig. 6.2 - Exterior Joint Longitudinal Beam Rotation History.

6.2.2 Interior Joint Beam Rotation. The longitudinal beams in the BRI building interior joint had two different span (6.0 and 5.0 m) on each side of the joint. In the component tests, the east and west beams were damaged initially through the inadvertent use of load-control. Values were plotted for each beam span and compared with the prototype, Figs. 6.3, 6.4. It should be noted that the 6.0 m BRI beam was under negative rotation when the building experienced positive drift (pushed against the wall). Rotation-drift comparisons were then made by using alternatively the west and east component beams.

Several important observations arise from the curves shown: (1) good agreement was obtained with both BRI building spans and the components E- or W-beams; (2) the loading program used in the component tests was more severe than the one used in the BRI test; (3) the UTA specimen exhibited less beam rotation at equivalent drifts throughout the loading program than the SU specimen; and, (4) at very large displacement levels ($R = 1/20$), the beam rotation for both USJ-1 and IS were nearly the same. Also in Fig. 6.5-b it can be observed that in the BRI building, the beam rotations were larger than those in the component tests when the slab was in compression.

As in the exterior components, most beam plastic deformation was near the column face in both UTA and SU tests (Figs. 6.6, 6.7). The amount of beam rotation in the first 6 in.

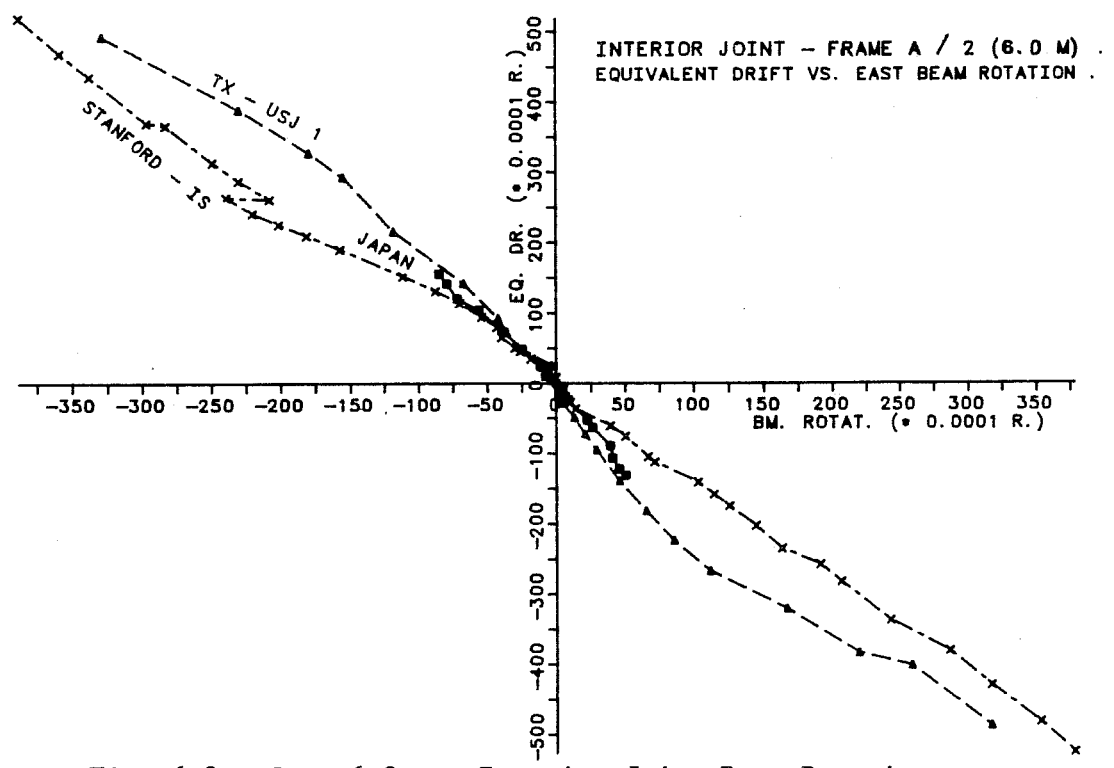
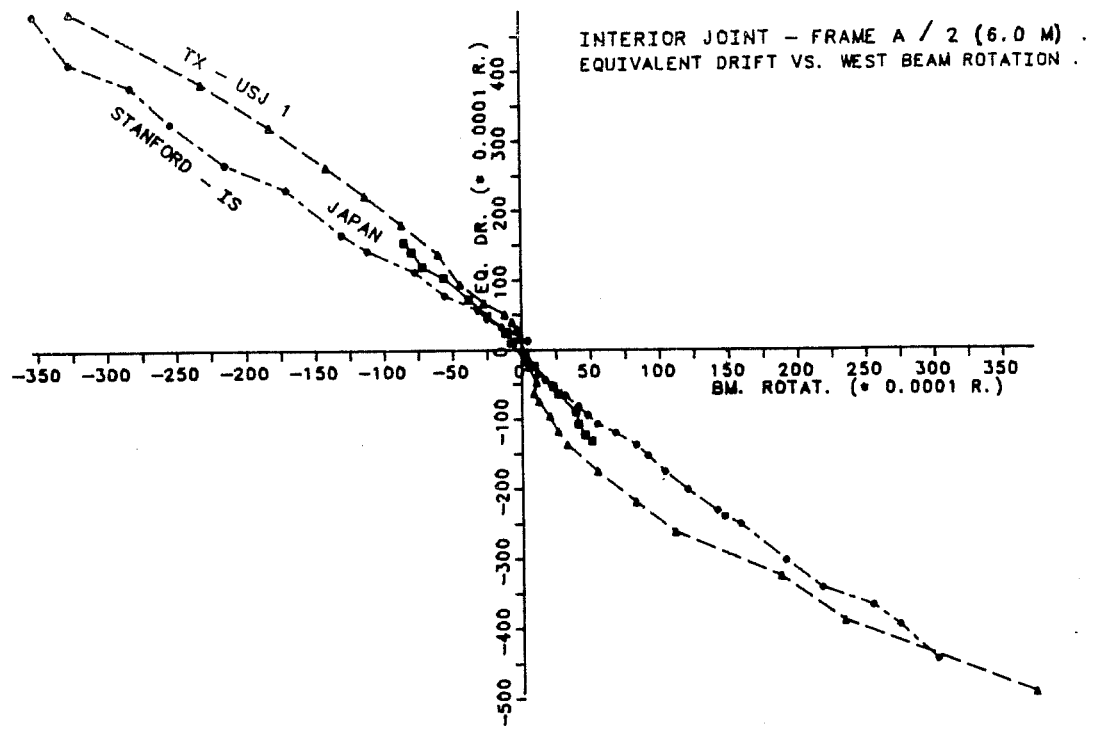
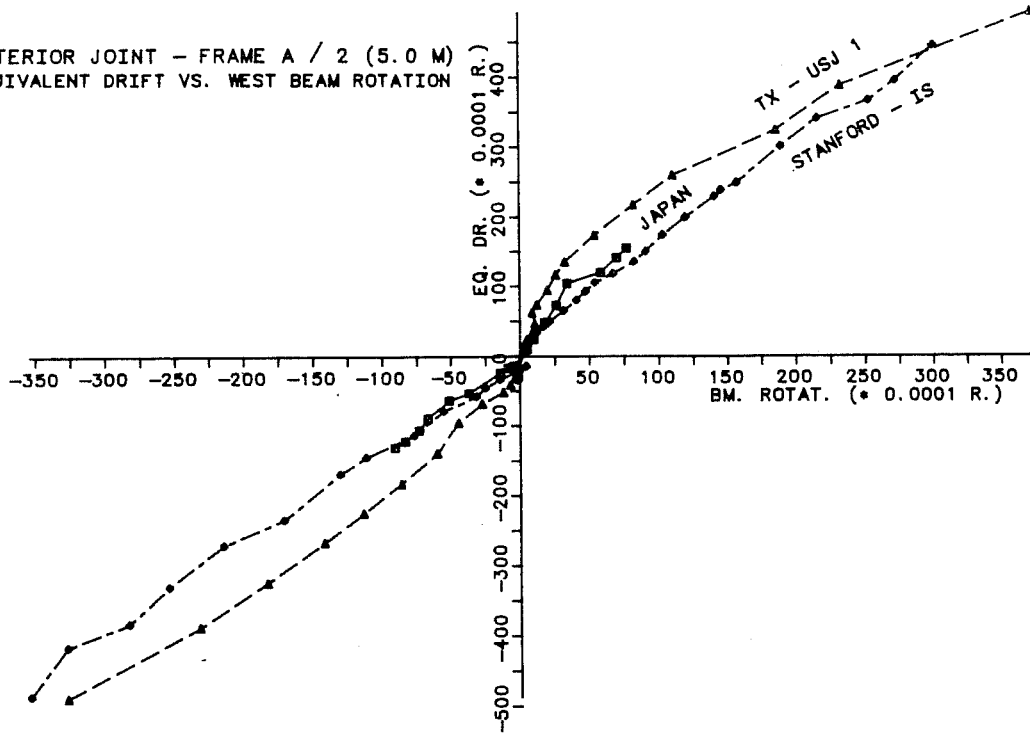


Fig. 6.3 - Span 6.0 m - Interior Joint Beam Rotation near Column Face.

INTERIOR JOINT - FRAME A / 2 (5.0 M)
EQUIVALENT DRIFT VS. WEST BEAM ROTATION



INTERIOR JOINT - FRAME A / 2 (5.0 M)
EQUIVALENT DRIFT VS. EAST BEAM ROTATION

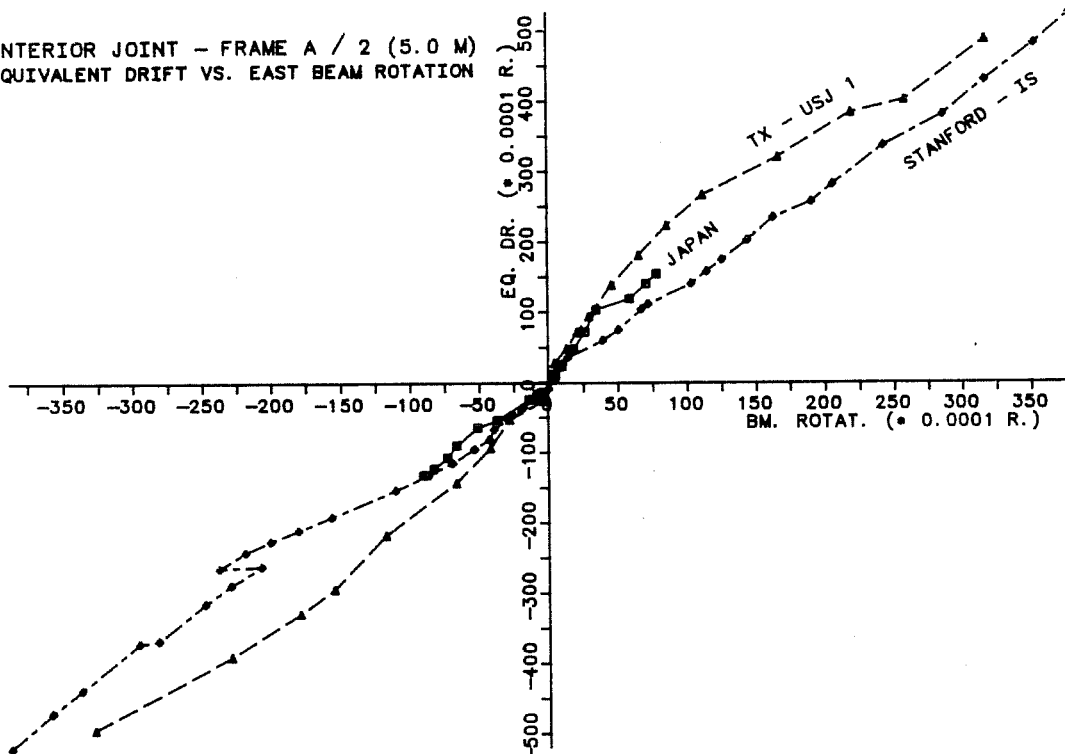
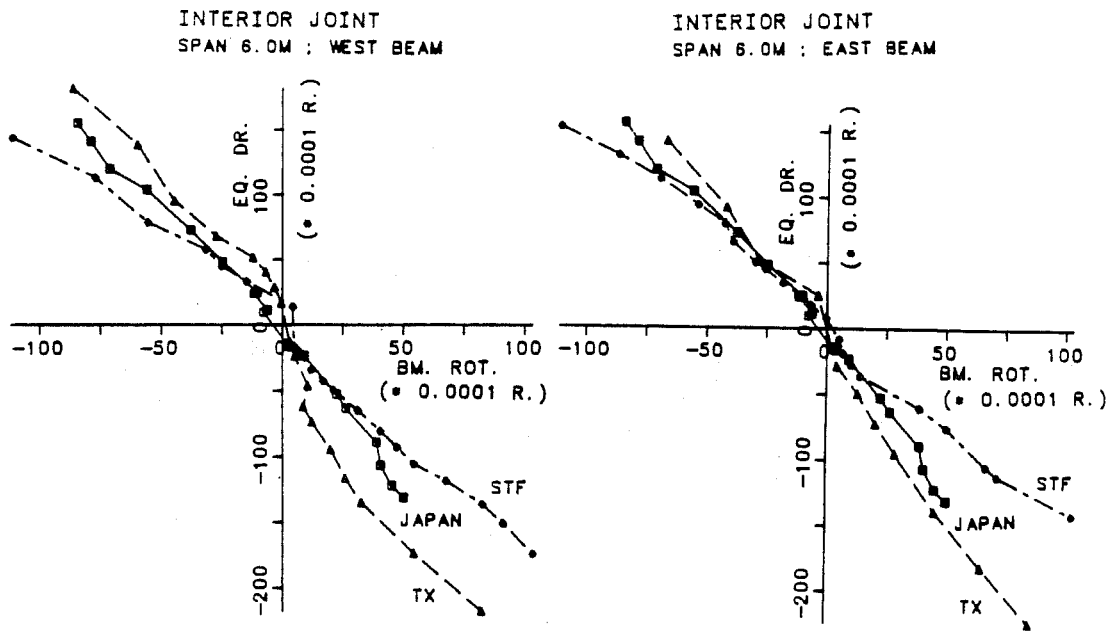
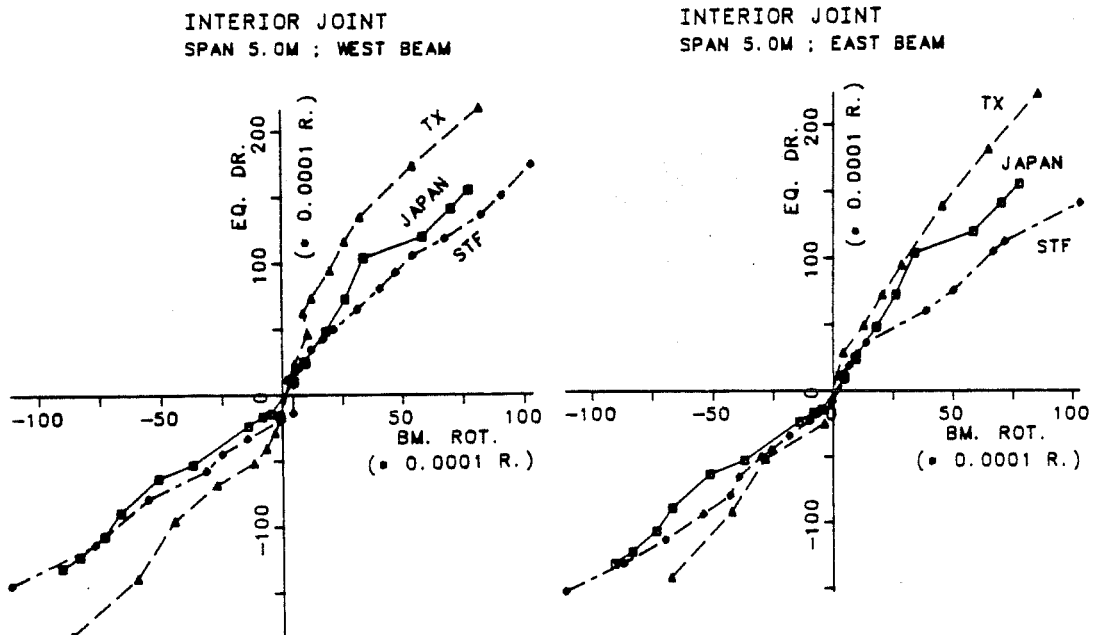


Fig. 6.4 - Span 5.0 m - Interior Joint Beam Rotation near Column Face.



a. Span 6.00 m - BRI alignment 21.



b. Span 5.00 m - BRI alignment 23.

Fig. 6.5 - Interior Joint Beam Rotation (enlarged scale plot).

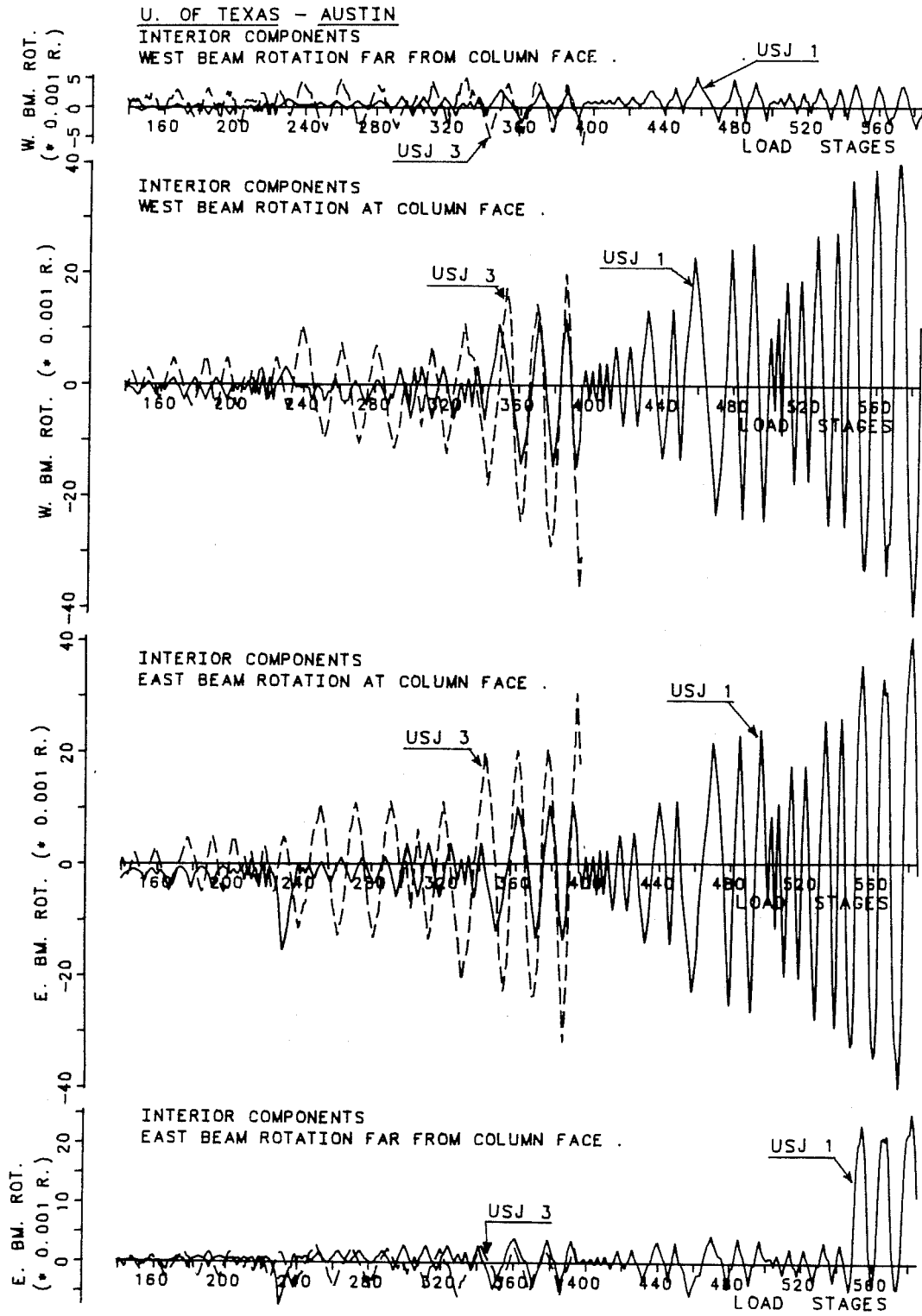


Fig. 6.6 - UTA - Longitudinal Beam Rotation.

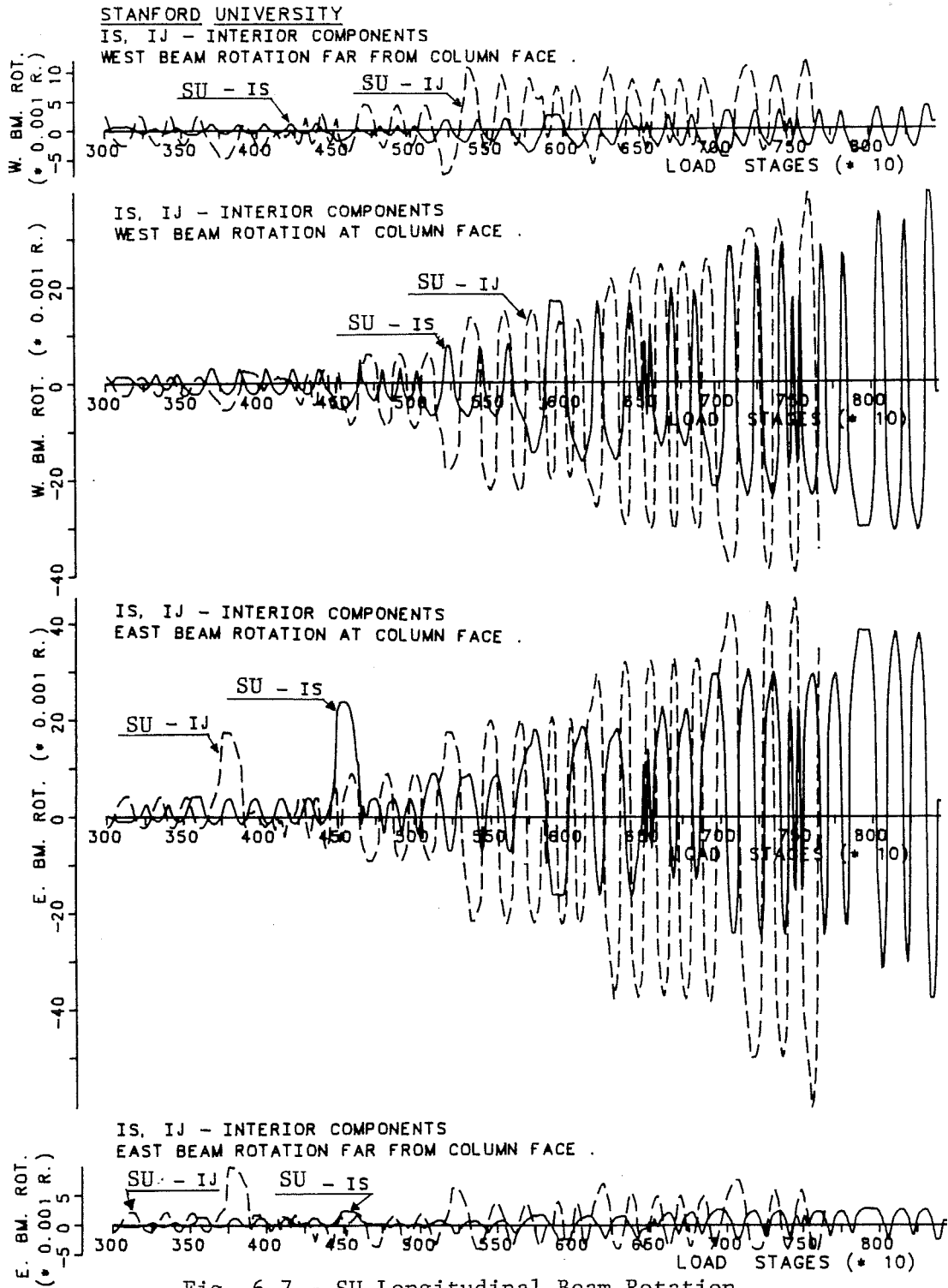


Fig. 6.7 - SU Longitudinal Beam Rotation.

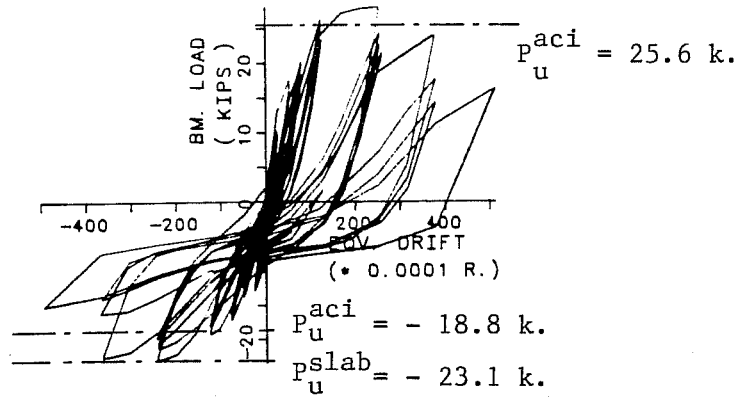
(0.15 m) of the beam was generally 8-12 times greater than at 24 in. (0.60 m) from the column face.

6.3 Beam Strength in Components

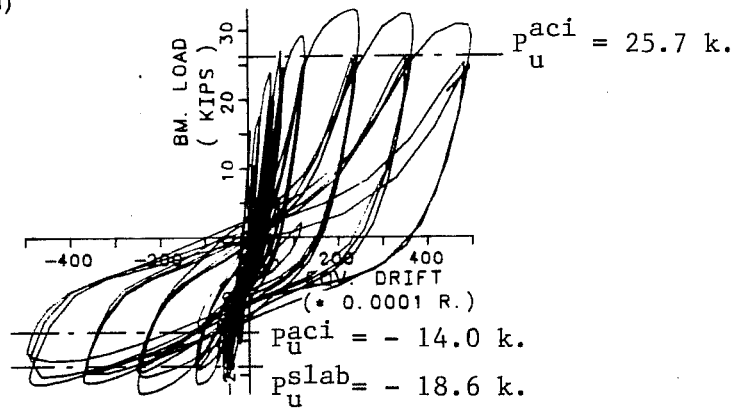
The load-deformation response of each component test shows the characteristic response of a T-beam. When the slab is in tension (positive load and equivalent drift) the resulting strength is much greater than when the slab is in compression. This can be shown using the data obtained for the specimens without a slab.

6.3.1 Exterior Components. The load-deflection response is shown in Figs. 6.8, 6.9. It can be observed that the predicted (design) beam load is easily attained at equivalent drifts of about 1/100 in both directions. However, a major aspect in response peculiar to the exterior joints with a slab can be observed. When the slab was in tension it was unable to reach the very large ultimate load corresponding to the full slab width calculations, Figs. 6.8, 6.9. This phenomena may result from two important aspects: (1) there was insufficient development length for both beam and slab bars; and, (2) without a slab and longitudinal beam on the opposite side of the column, the transverse beam had less lateral torsional restraint and it rotated more.

U.T.A. - EXT. JOINT
 USJ - 2 : WEST BEAM



S. U. - EXT. JOINT
 ES : W-BEAM (W/ SLAB)



JAPAN - 1/2 SC. TESTS
 E2 : EXT. JOINT - US DES.

$N_e = 219.2 \text{ kips}$

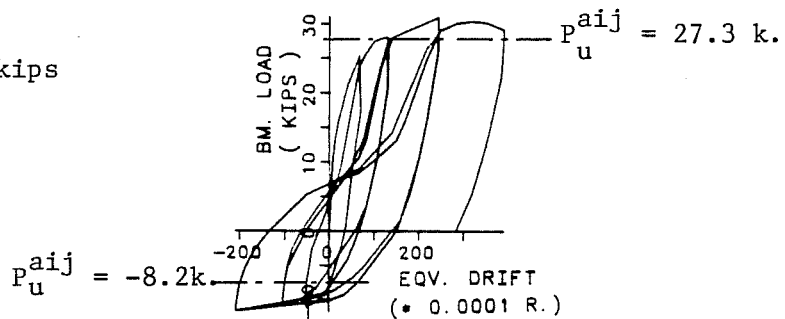
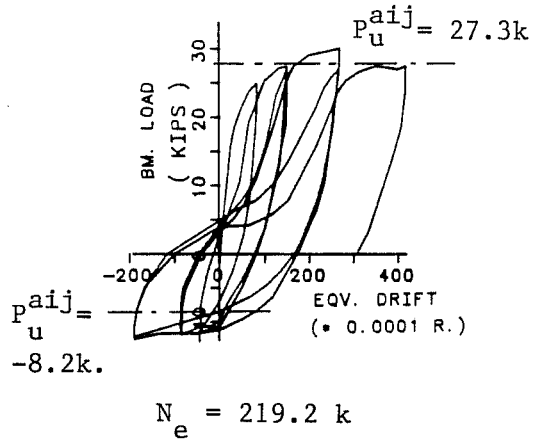
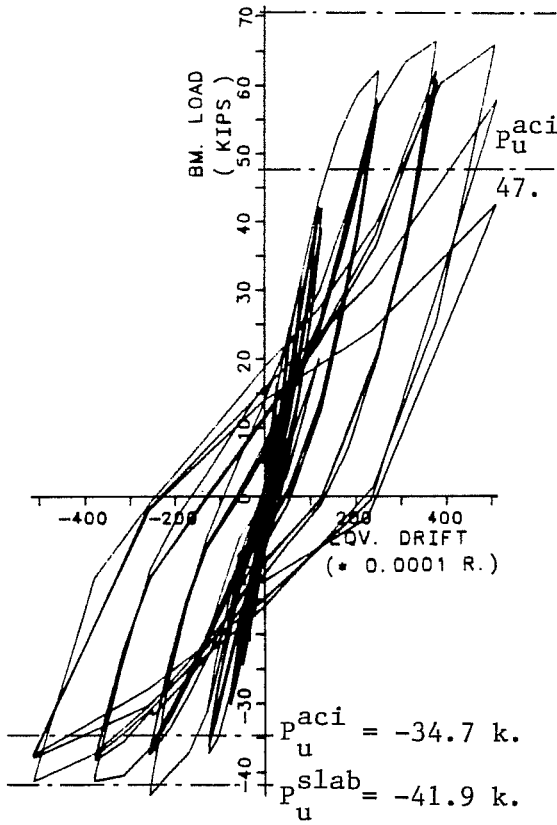


Fig. 6.8 - Exterior Prototype Tests Beam Strength.

U. T. A. - EXT. JOINT
 USJ - 4 : WEST BEAM

$$P_u^{slab} = 70.4 \text{ k.}$$



S. U. - EXT. JOINT
 EJ : W-BEAM (W/O SLAB)

JAPAN - 1/2 SC. TESTS
 E3 : EXT. JOINT (W/O SLAB)
 - JAPANESE DESIGN .

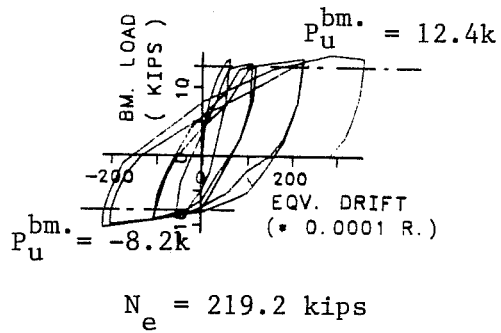
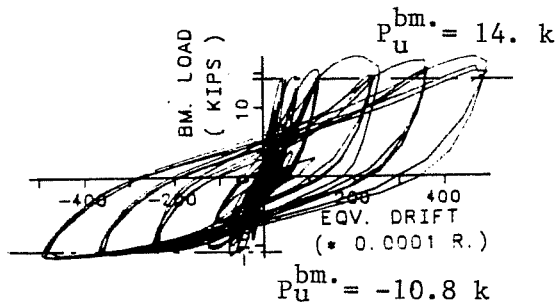


Fig. 6.9 - Other Exterior Tests Beam Strength.

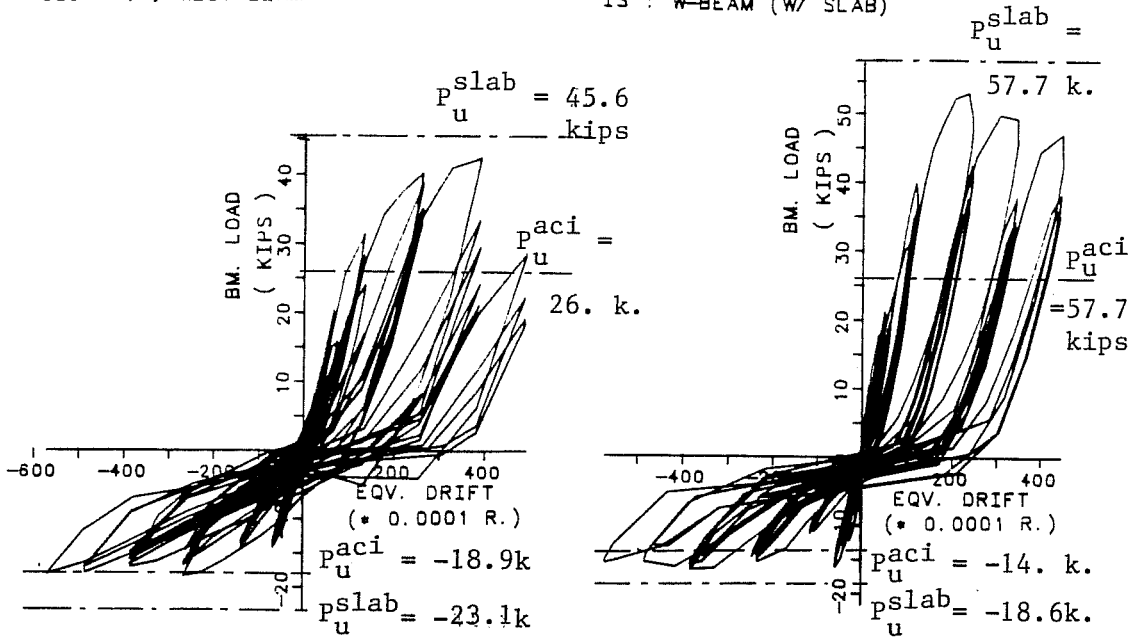
The loss of anchorage resistance in specimen USJ-2 translates into beam response by severe pinching near the origin, Fig. 6.8. The other SU and JPN specimens show relatively flat and stable hysteresis loops. An improvement in the anchorage detail resulted in better beam response in spite of higher shear loads as shown by the flat and stable USJ-4 hysteresis loops, Fig. 6.9. The 100% increase in top and bottom reinforcement lead to a nearly 100% increase in load-carrying capacity as compared with USJ-1.

The 1/2 scale (JPN) and 1:12.5 scale (SU) specimens without a slab had good hysteretic behavior and very similar patterns in spite of the different loading programs. The absence of a slab decreased beam load carrying capacity (positive load) by 40 to 50% than the tests with a slab.

6.3.2 Interior Components. The interior joints showed that the positively loaded beams were more likely to reach higher ultimate loads at large deformation levels than their exterior counterparts. In interior joints, the slab strength in tension was more fully developed during the loading process, Figs. 6.10, 6.11. The SU (IS) west beam showed severe pinching whereas the east beam had more stable hysteretic behavior. Specimen USJ-3 with larger beam reinforcement ratios was unable to reach the calculated value of $P_u = - 41.9 \text{ K (19.0 tf)}$ when the slab was in compression. When the slab was in tension the ultimate load $P_u =$

U. T. A. - INT. JOINT
USJ - 1 : WEST BEAM

S. U. - INT. JOINT
IS : W-BEAM (W/ SLAB)



U. T. A. - INT. JOINT
USJ - 3 : WEST BEAM

$p_u^{slab} = 67.6 \text{ k.}$

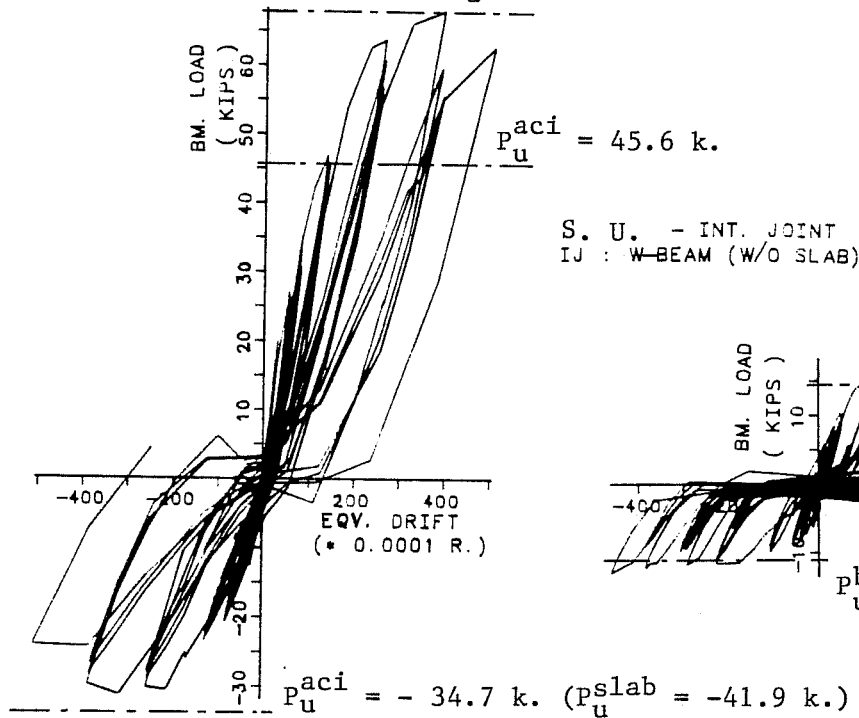
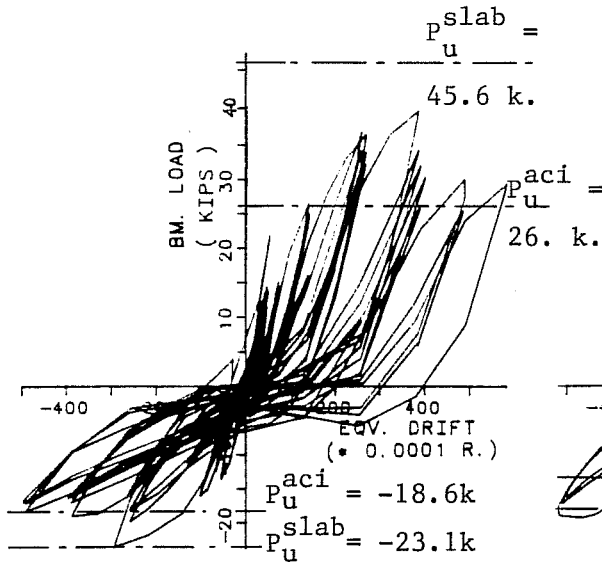
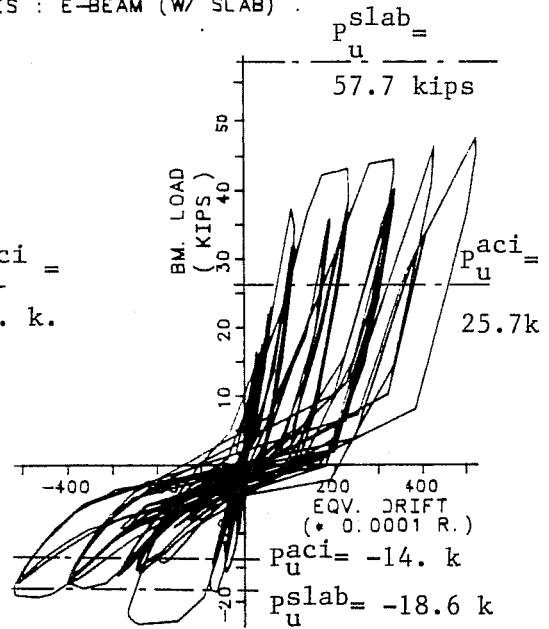


Fig. 6.10 - Interior Tests West Beam Strength.

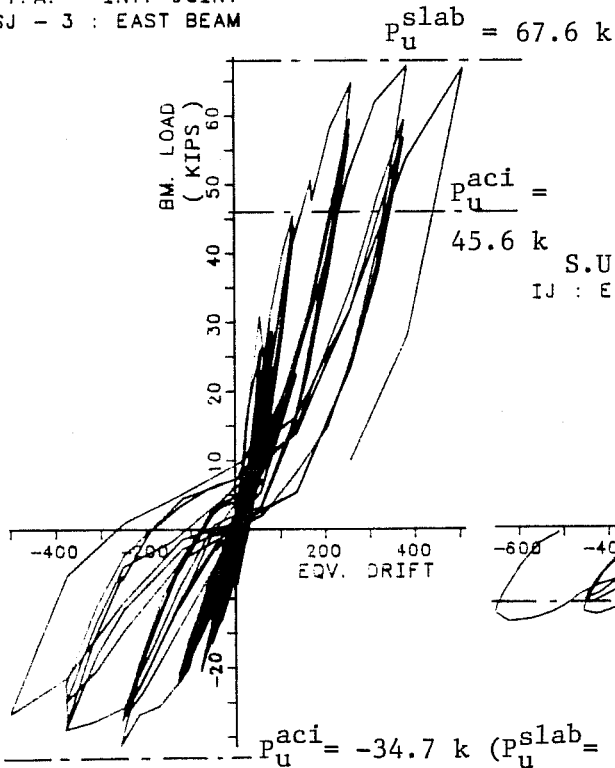
U.T.A. - INT. JOINT
USJ - 1 : EAST BEAM



S.U. - INT. JOINT
IS : E-BEAM (W/ SLAB)



U.T.A. - INT. JOINT
USJ - 3 : EAST BEAM



S.U. - INT. JOINT
IJ : E-BEAM (W/O SLAB)

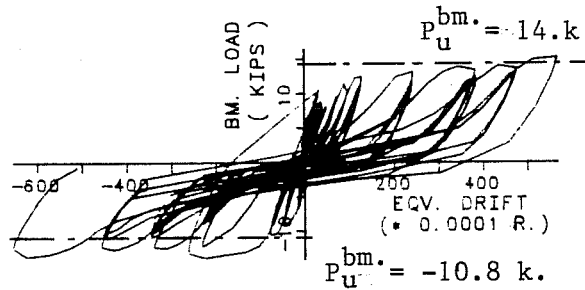


Fig. 6.11 - Interior Tests East Beam Strength.

+67.6 K (30.7 tf) was reached at large drift levels of 1/50 - 1/33.

In general, the full-scale and the small-scale interior joint tests had very similar longitudinal beam response characteristics. The slab influence on the beam load-carrying capacity was more drastic when the slab was in tension than in compression. This underscores the importance of considering the slab in strength calculations of monolithic systems.

6.4 Longitudinal Beam Stiffness

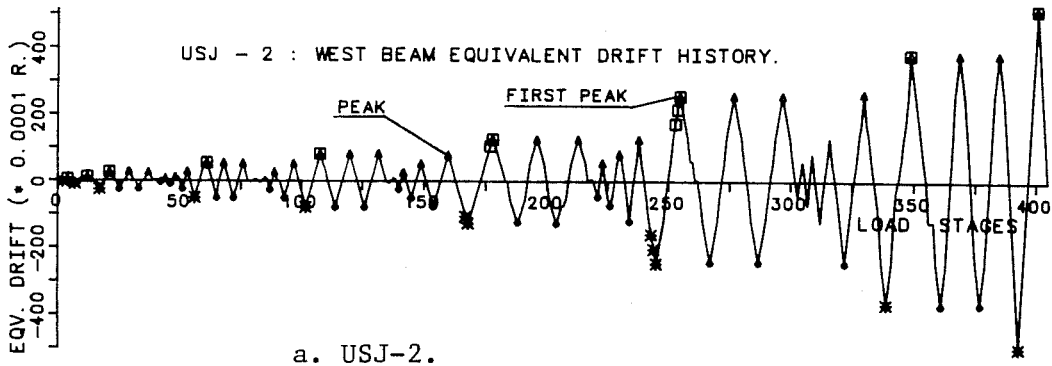
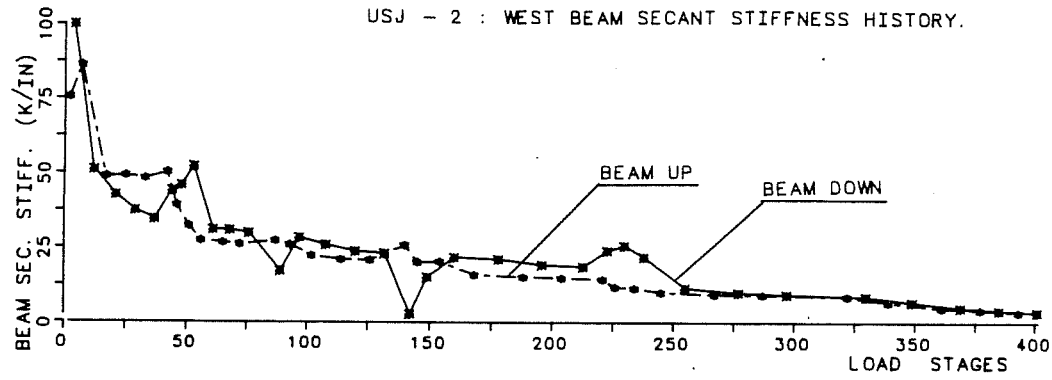
The longitudinal beam secant stiffness was derived directly from the load-deflection curves by dividing the total load applied at the beam tip by the correspondent tip deflection. It is recognized that not all the applied load is resisted by the T-beam and part will be resisted by the transverse beam and joint region. However, this method of determining stiffness provides valuable insight into beam response.

The response of the longitudinal beams in the interior tests conducted in Japan is not available because only the story shear was reported. However, the exterior joint tests provide comparable data. The stiffness response was based on the function of the slab in carrying compression or tension under flexural forces on the beam.

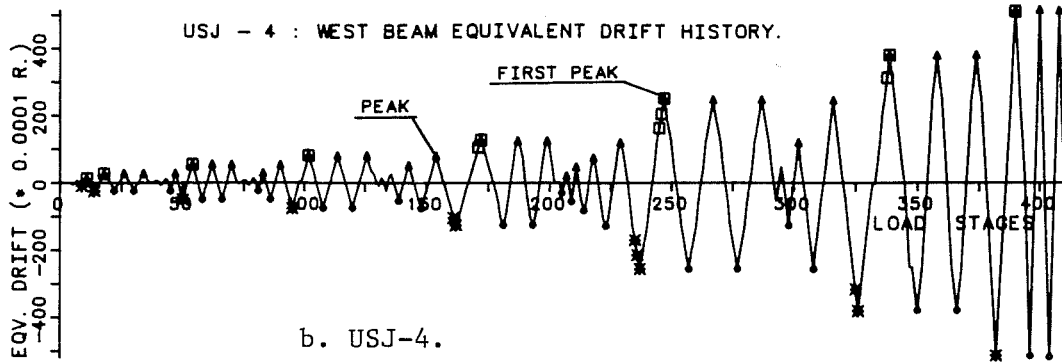
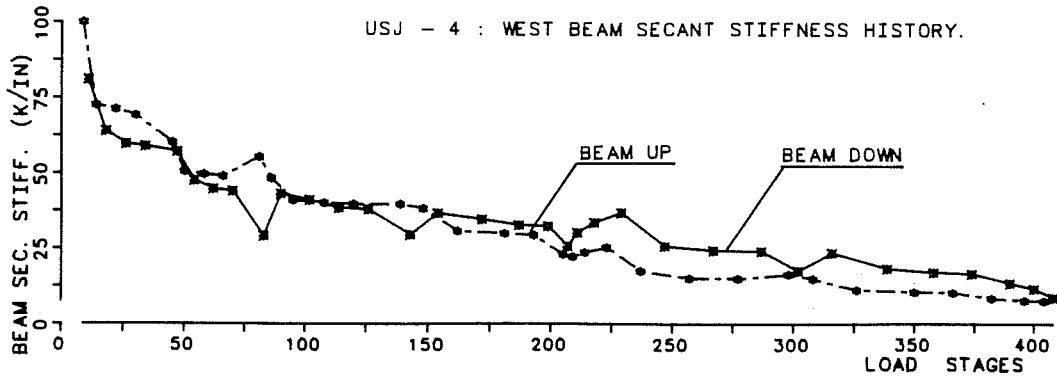
6.4.1 Exterior Components. The beam secant stiffness degradation history for all the exterior components is shown in Figs. 6.12 to 6.16. In the UTA (Figs. 6.12, 6.13) specimens, it can be seen that an additional deterioration in beam stiffness occurred at each new level of peak deformation. At early loading stages and for small drifts (less than $1/200 - 1/100$), the beam stiffness for the slab in compression is slightly higher than when the slab is in tension. With twice the amount of beam reinforcement (USJ-4), the stiffness does not degrade as rapidly, Fig. 6.12-b.

The SU (ES) specimen showed stiffness response comparable to USJ-2, Fig. 6.13-a. There was not a clear difference between stiffnesses at positive and negative peak drifts. However, it was observed that drops in stiffness occurred at each new peak drift. The SU (EJ) specimen without a slab, Fig. 6.13-b, had much lower stiffness values and quite rapid deterioration of stiffness in the early cycles as compared with specimen ES (with slab).

The 1/2-scale (JPN) specimen response is shown in Figs. 6.14 - 6.16. It can be observed that the influence of the 1.50 m (59 in.) slab on the response occurred at very early load stages. There is some difference in response for the slab when it was in tension or compression, Fig. 6.16. When the slab was in

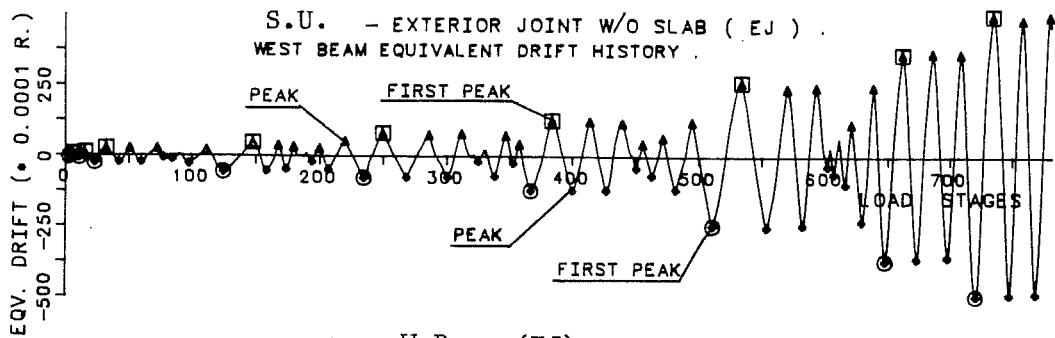
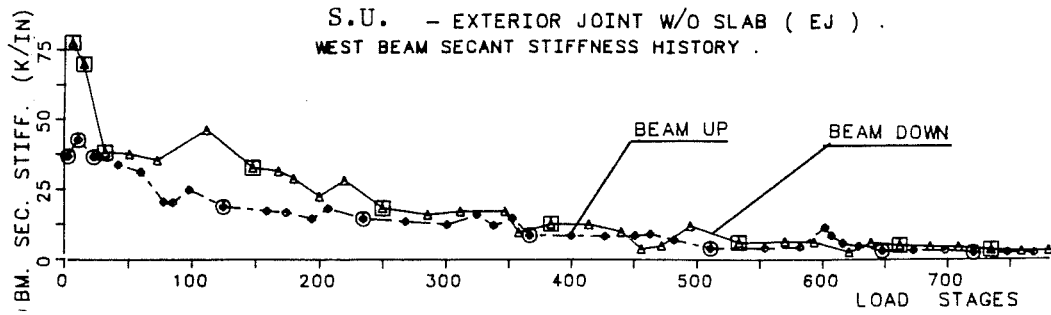


a. USJ-2.

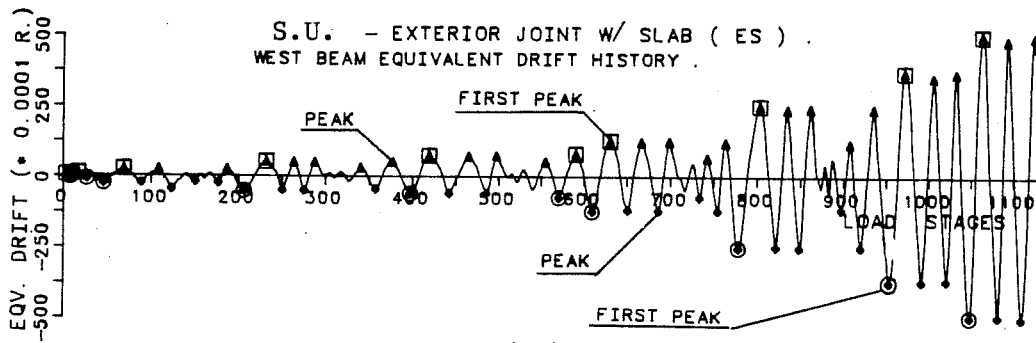
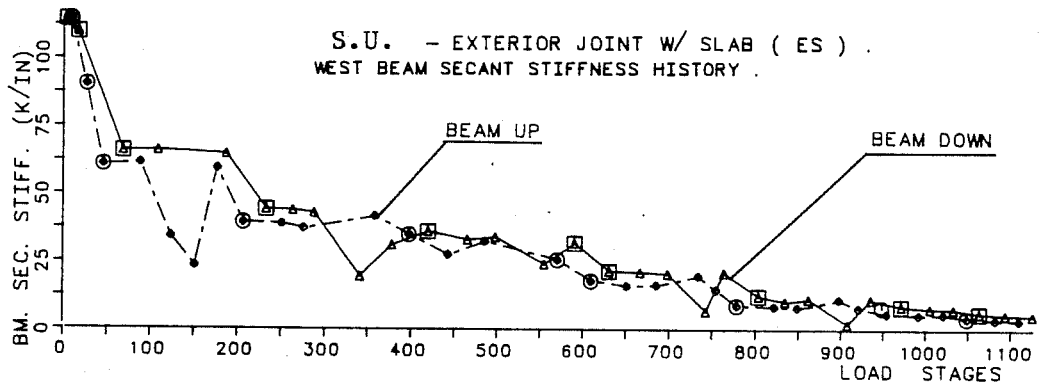


b. USJ-4.

Fig. 6.12 - UTA Exterior Tests Beam Stiffness Degradation.



a. W-Beam (EJ).



b. W-Beam (ES).

Fig. 6.13 - SU Exterior Tests Beam Stiffness Degradation.

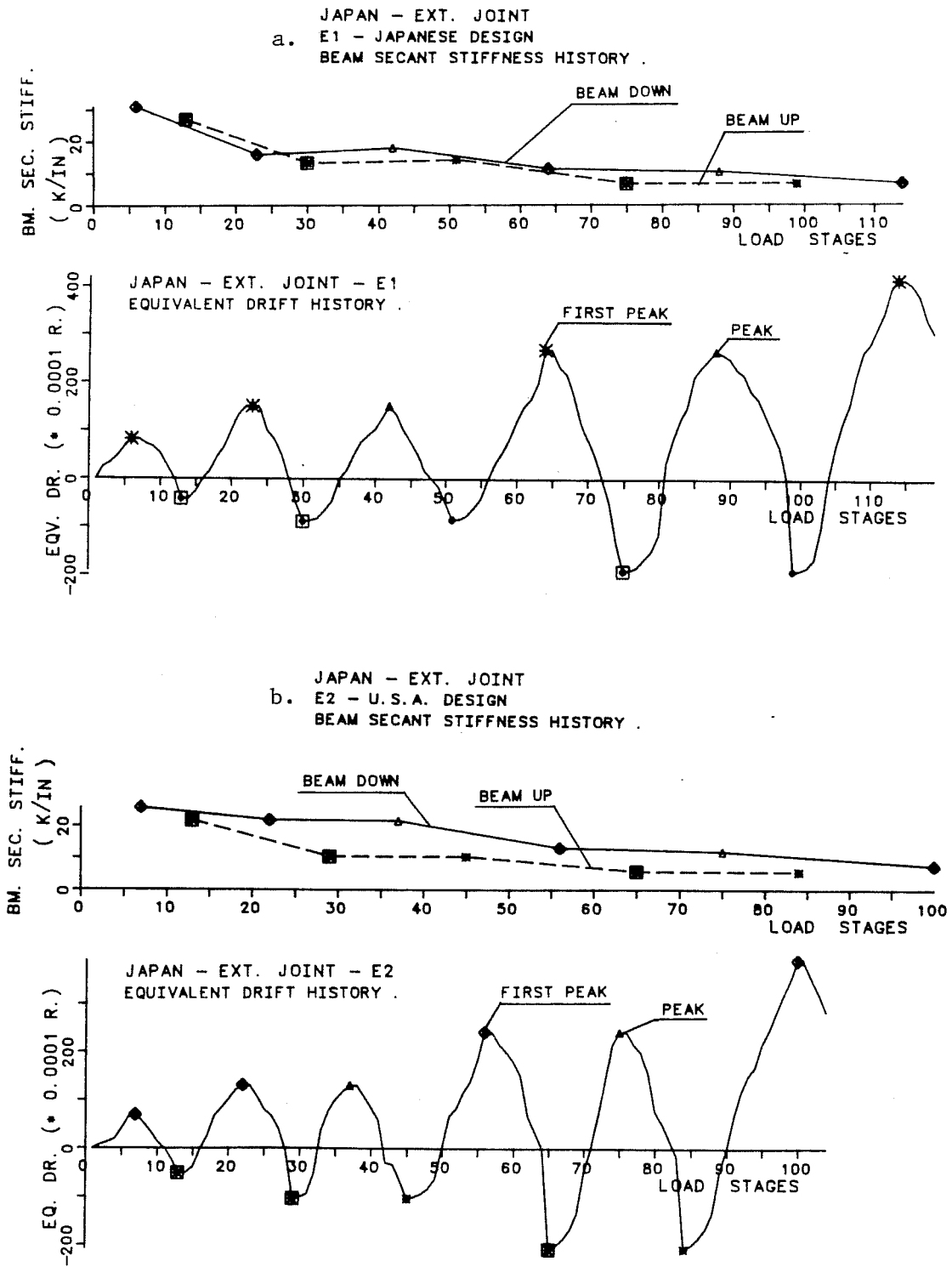


Fig. 6.14 - Beam Stiffness Degradation in Japanese Tests with a Slab.

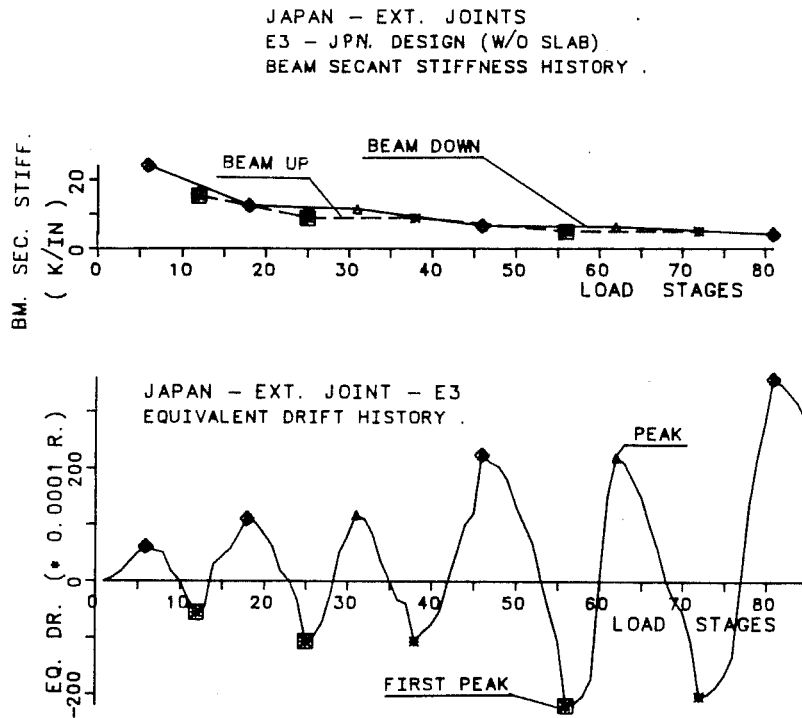


Fig. 6.15 - Beam Stiffness Degradation in Japanese Tests without a Slab.

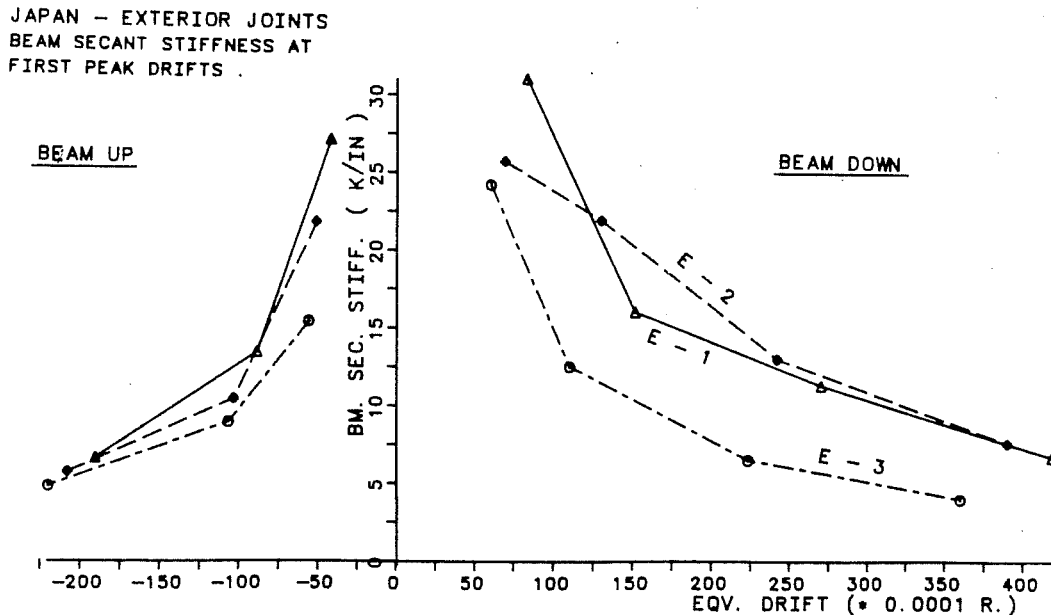


Fig. 6.16 - First Peak Drift Stiffness Response in Japanese Exterior Tests.

compression, the difference in response between specimens with a slab (E-1, E-2) and without a slab (E-3) was very small.

An overall comparison between the prototype specimens (USJ-2, ES, E-2) and other specimens (USJ-4, EJ, E-1, E-3) is shown in Fig. 6.17. Good agreement for both loading directions is obtained for the full-size and small-scale prototype components with a 4.00 m (157.5 in.) slab width. The specimen with 1.50 m (59 in.) slab width, E-2, shows a lower secant stiffness (slab in compression), Fig. 6.17. The group of tests without a slab (EJ, E-3) also show good agreement in response. The slab influence in tension is clearly shown by tests USJ-4 and E-1 vs. tests EJ and E-3. The influence of a larger beam reinforcement ratio is provided by test USJ-4, Fig. 6.17. For most specimens the largest drop in beam stiffness occurred for equivalent drifts of $1/133$ - $1/100$. The increase of beam steel content in test USJ-4 delayed pronounced stiffness deterioration up to an equivalent drift of $1/66$.

6.4.2 Interior Components. The UTA component beam stiffness response is shown in Figs. 6.18 and 6.19. The effects of using load-control in the initial portion of the testing program for USJ-1 up to LDS 240 is clearly evident in Fig. 6.18-a,b. For the east beam in USJ-1, the initial portion of response was controlled by yielding of the bottom beam reinforcement. A major drop in secant stiffness occurred after a new first peak

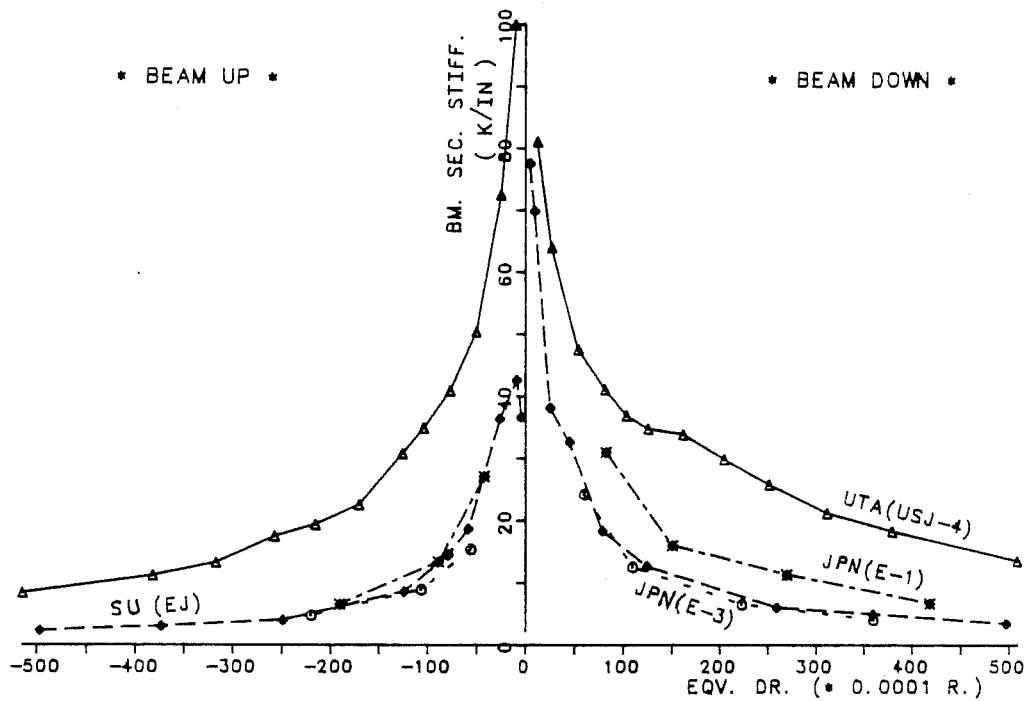
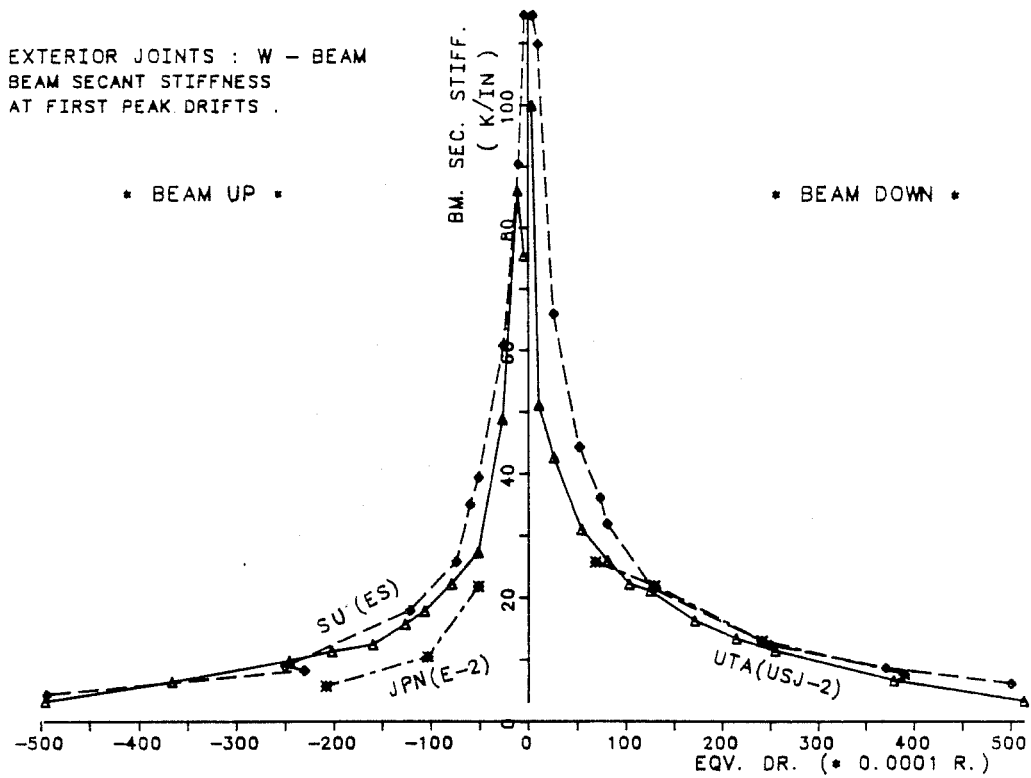
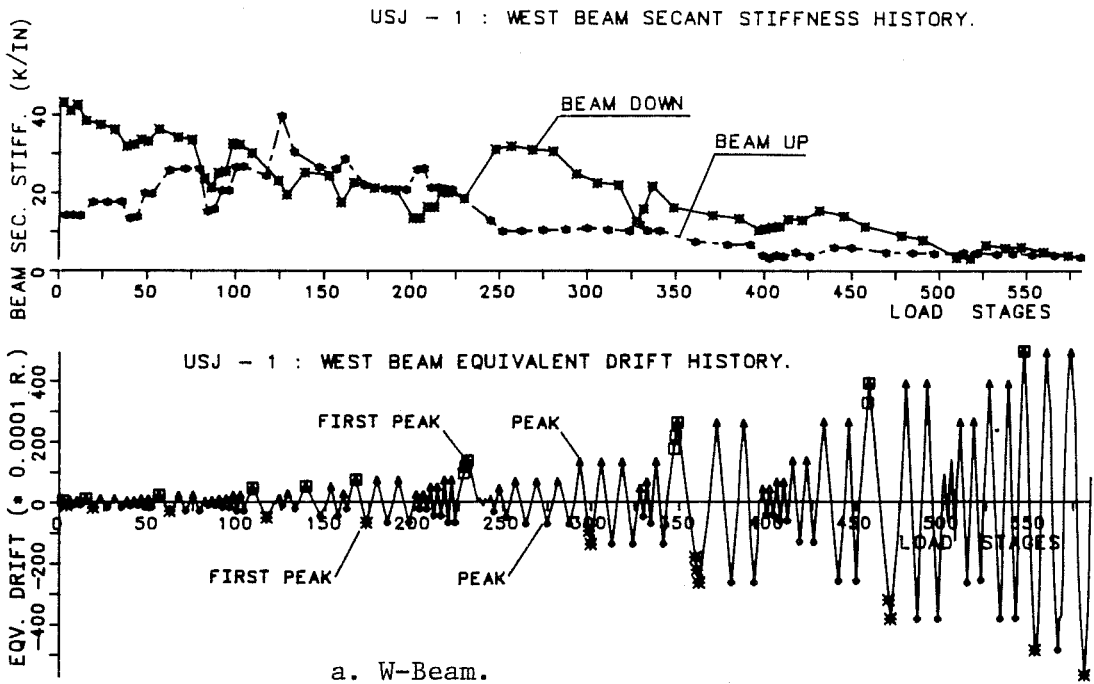
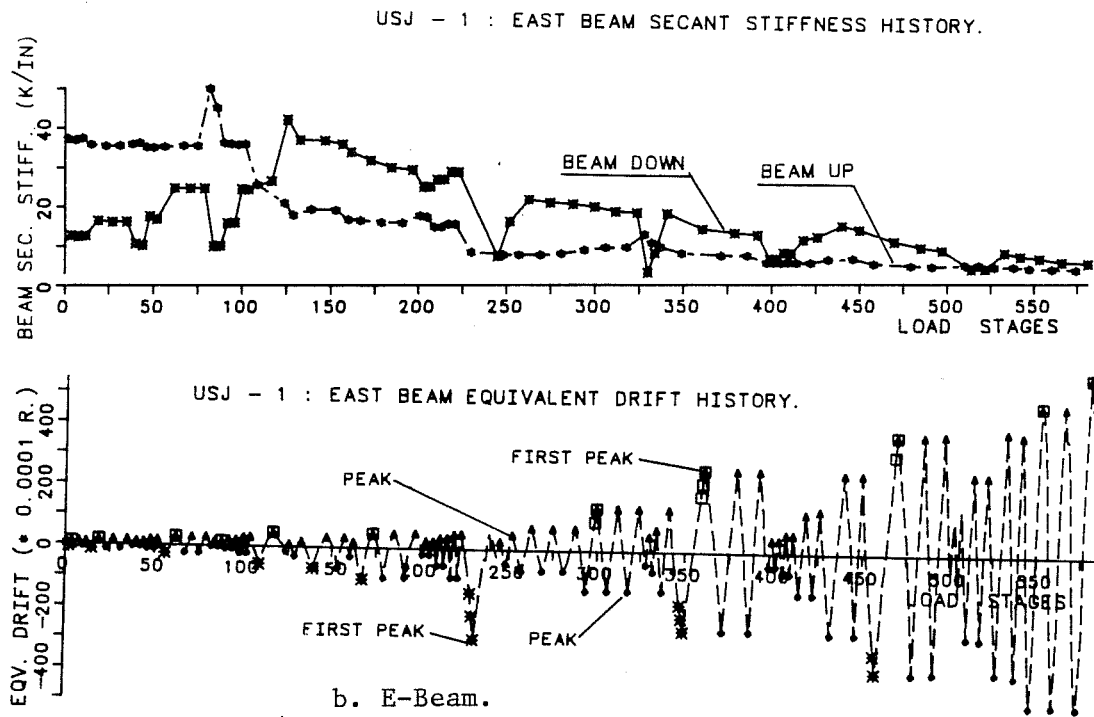


Fig. 6.17 - Exterior Tests - Beam Secant Stiffness at First Peak Drifts.

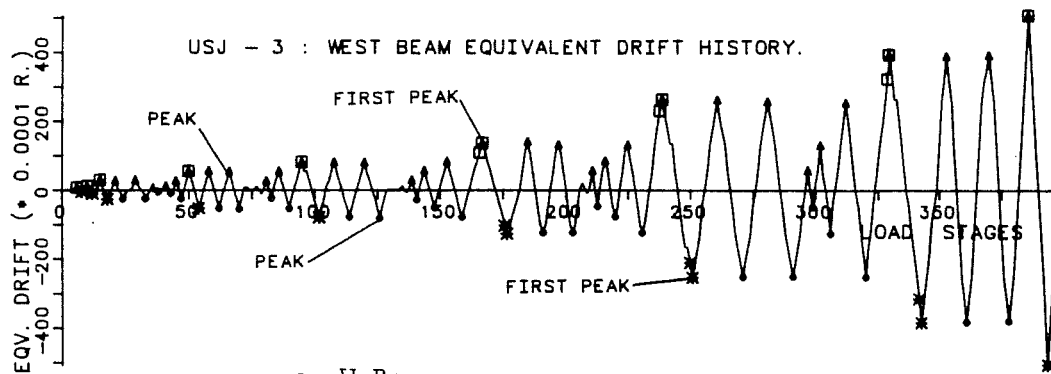
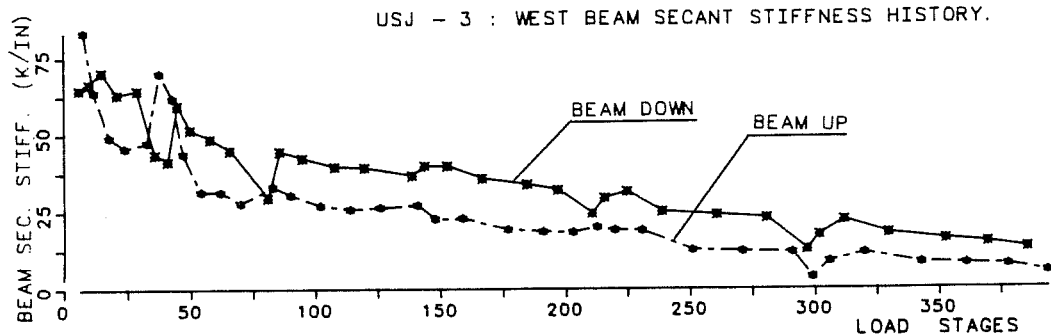


a. W-Beam.

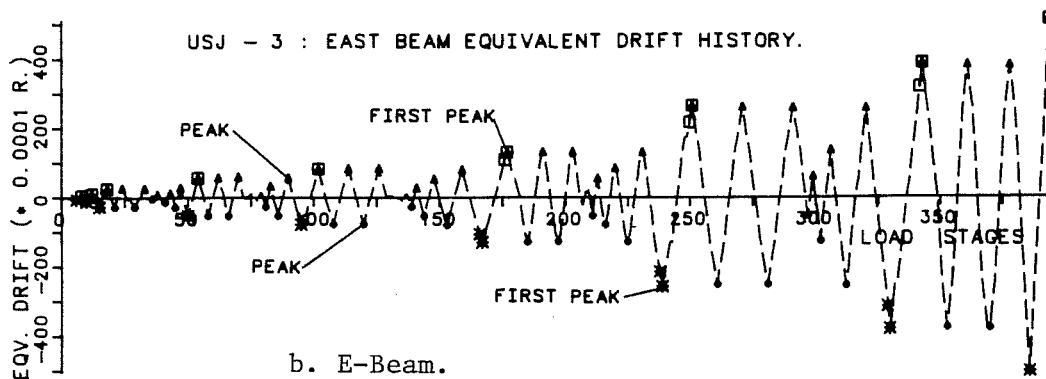
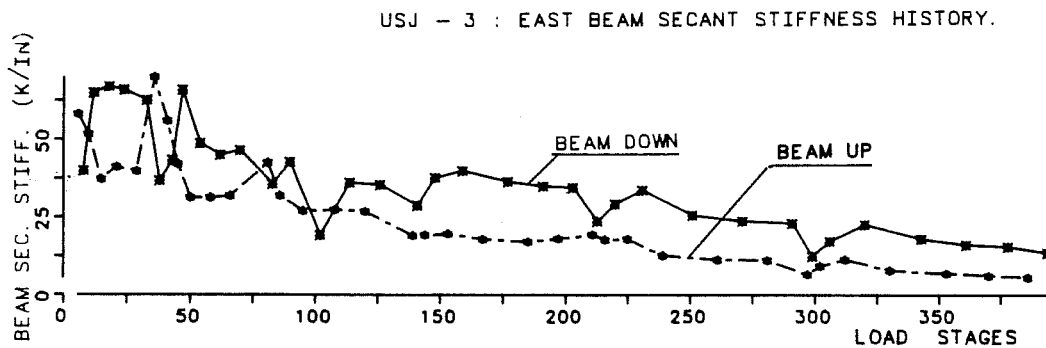


b. E-Beam.

Fig. 6.18 - UTA - USJ-1 - Beam Secant Stiffness.



a. W-Beam.



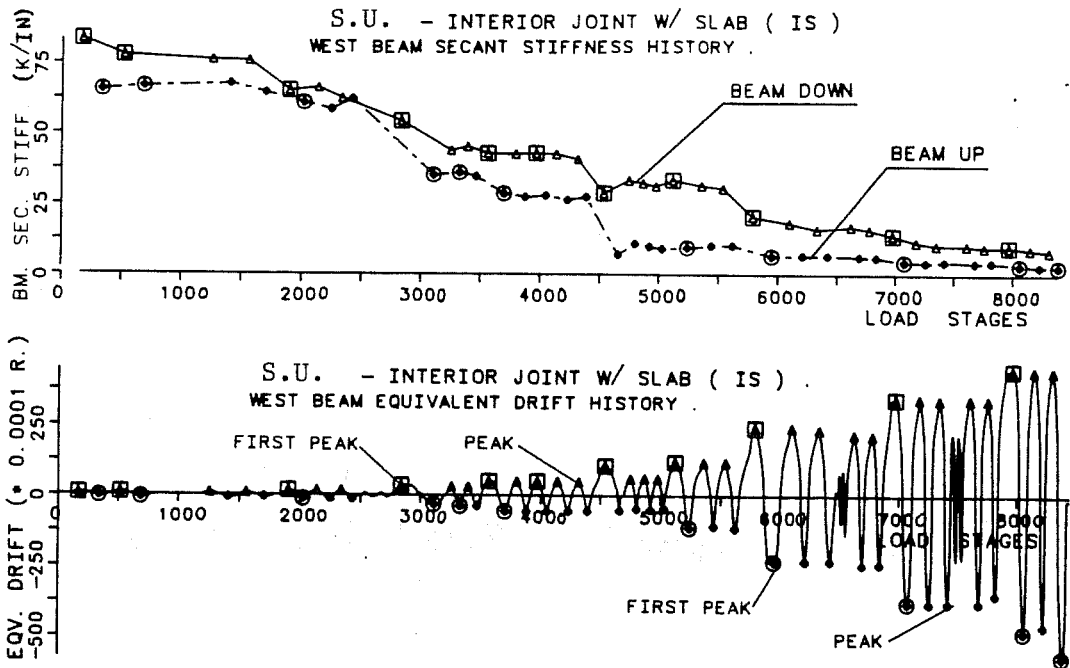
b. E-Beam.

Fig. 6.19 - UTA - USJ-3 - Beam Secant Stiffness.

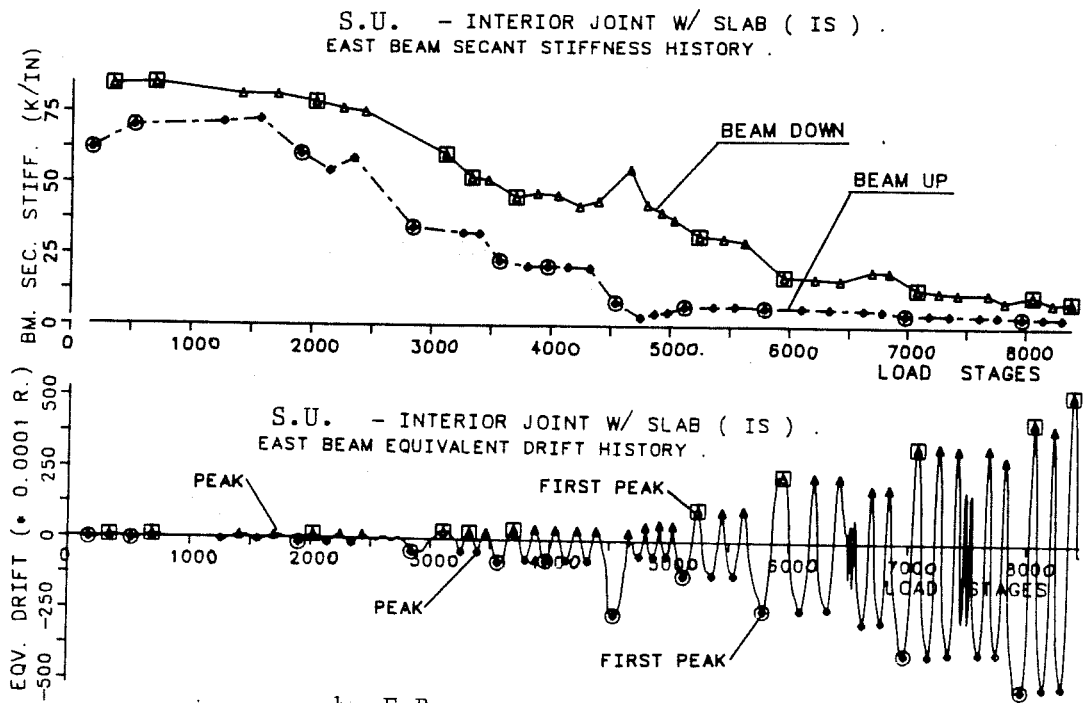
displacement was reached, particularly near LDS 240 ($R = 1/33$), Fig. 6.18-b. The active participation of the slab when the beam was displaced downwards clearly increased the beam stiffness at peak equivalent drifts, Figs. 6.18, 6.19. However, at very large deformation levels ($+1/20$) this difference in stiffness vanished with the same stiffness value observed in both directions.

In test USJ-3 conducted from the beginning on a displacement controlled basis, the stiffness with the slab in tension was consistently higher throughout the test, Fig. 6.19-a,b. Drops in secant stiffness occurred at the beginning of new first peak drifts. The stiffness at large deformations was higher than in test USJ-1.

The SU loading program (specimens IS, IJ) was identical to the UTA USJ-1 test. The beam stiffness in the SU interior components is shown in Figs. 6.20, 6.21. In the SU (IS) specimen with slab, clear separation between positive and negative bending can be seen. In the east beam of specimen IS, a large drop in beam stiffness occurred at $-1/33$ (LDS 4600), Fig. 6.20-b. The stiffness was higher than in USJ-1 throughout the loading history. The lower stiffness values obtained for IJ in both E- and W-beams (Fig. 6.21) demonstrate the effect of the slab. The difference between secant stiffnesses when the beam was either up or down and the stiffness at large drift values ($+1/20$) are both less than observed in specimen IS.

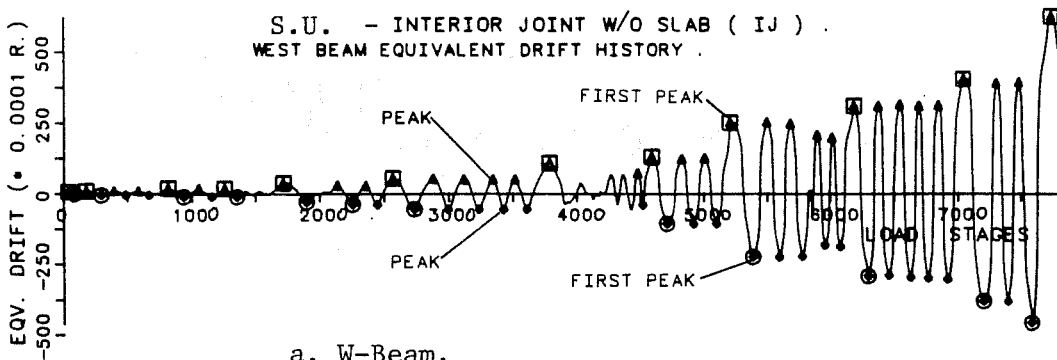
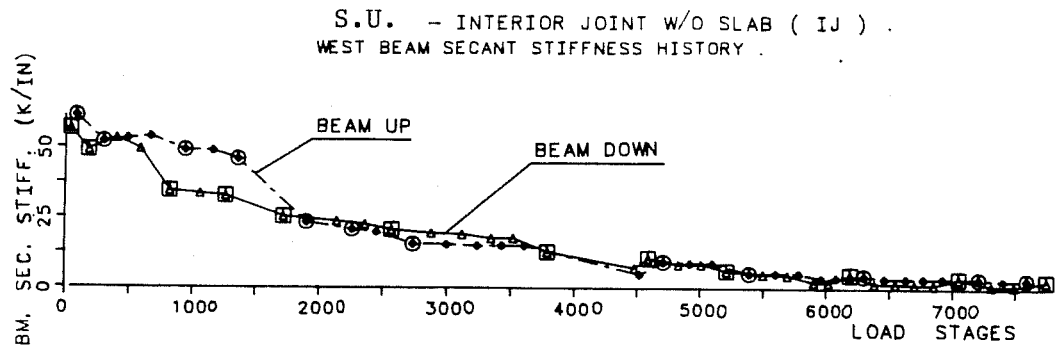


a. W-Beam.

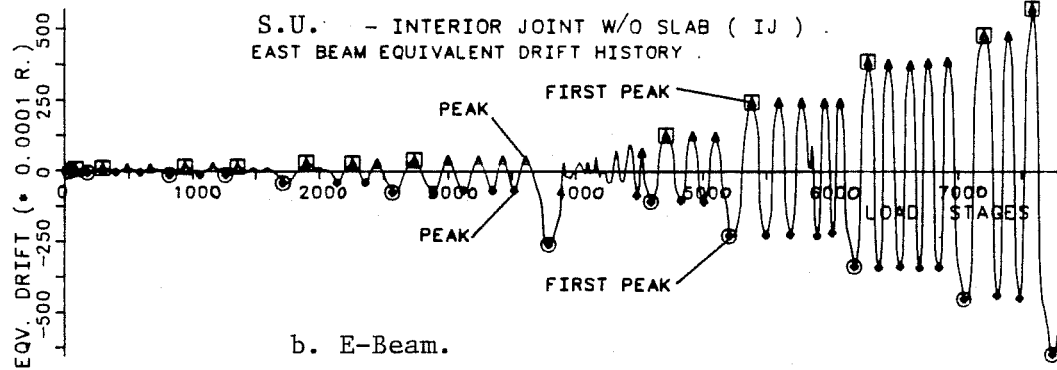
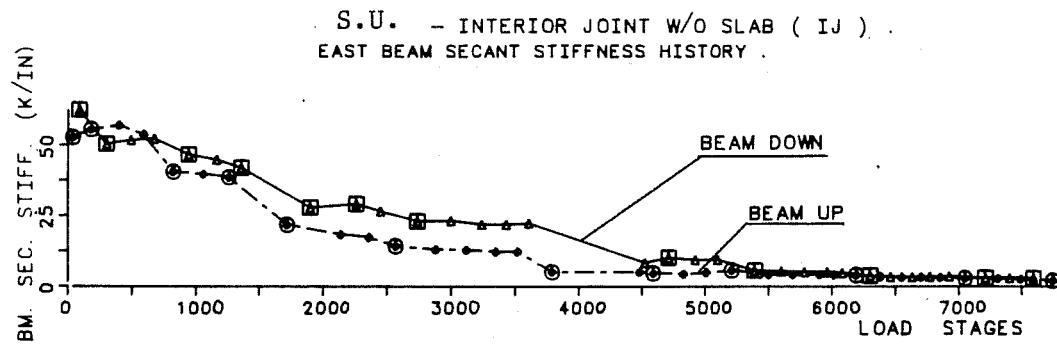


b. E-Beam.

Fig. 6.20 - SU - IS - Beam Secant Stiffness.



a. W-Beam.



b. E-Beam.

Fig. 6.21 - SU - IJ - Beam Secant Stiffness.

A more general comparison can be made by considering the response at first peak drifts, Figs. 6.22, 6.23. For specimens USJ-1 and IS major stiffness degradation occurred up to $1/100$ equivalent drift and specimen IS had slightly higher stiffness, Figs. 6.22-a, 6.23-a. The load-control program during the initial portion of the test resulted in the break in the curve at drifts of $1/50 - 1/33$ where a large displacement was inadvertently applied, Fig. 6.23-a.

Specimen USJ-3 with twice the beam reinforcement was stiffer up to large drifts and the difference in response when the slab was in tension becomes sharper compared with the slab in compression, Figs. 6.22-b, 6.23-b. Nearly symmetric response is observed for the SU (IJ) specimen without slab and a major stiffness drop occurred at $1/133 - 1/100$ drift level.

6.4.3. Exterior vs. Interior Component Beam Stiffness.

A comparison of the beam stiffness for the UTA program is given in Figs. 6.24 and 6.25. The stiffnesses match quite well throughout the loading program. The stiffness of USJ-4 with the slab in compression is higher than that of USJ-3, Fig. 6.24. The SU specimen shows the importance of slab participation in both exterior and interior component tests, Fig. 6.25.

INTERIOR JOINTS : W - BEAM
 BEAM SECANT STIFFNESS
 AT FIRST PEAK DRIFTS .

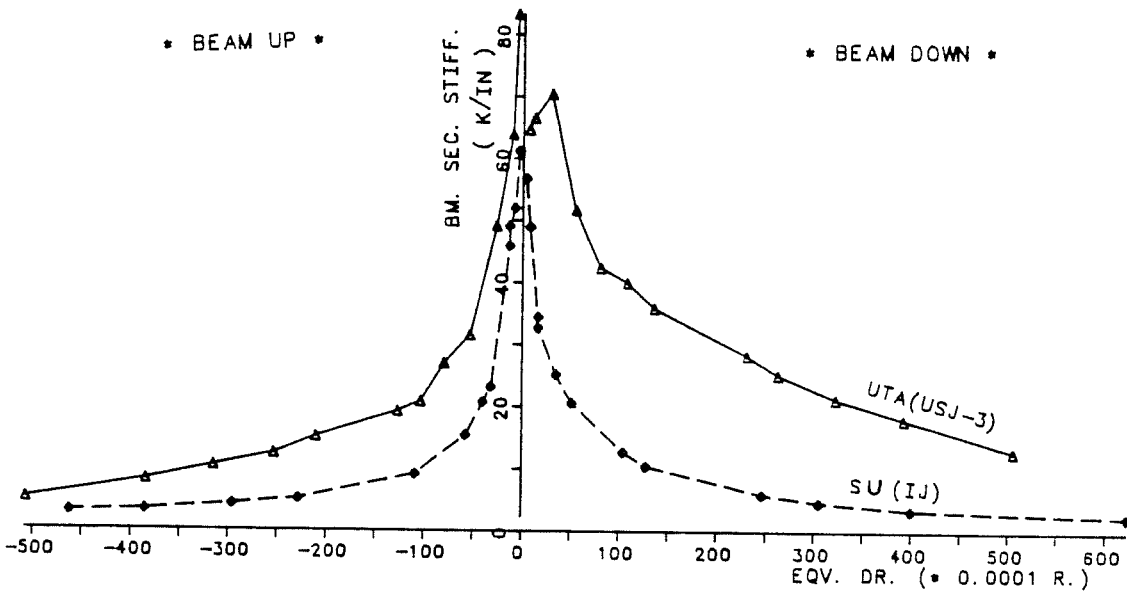
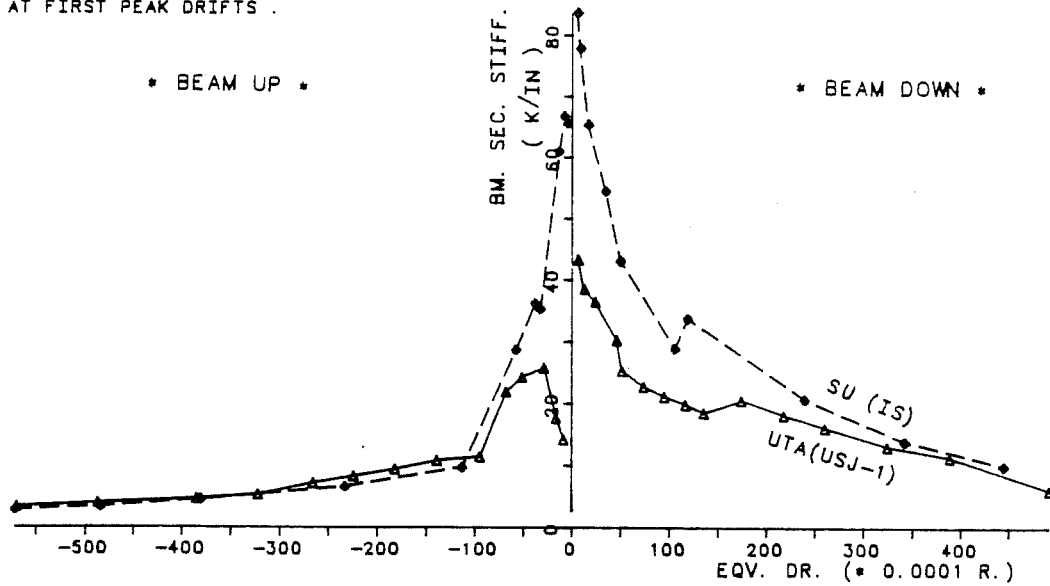
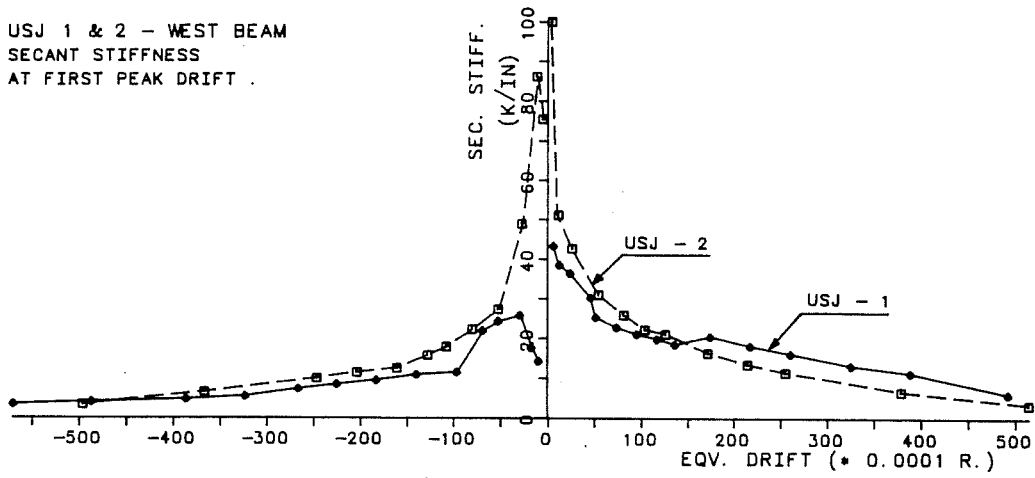
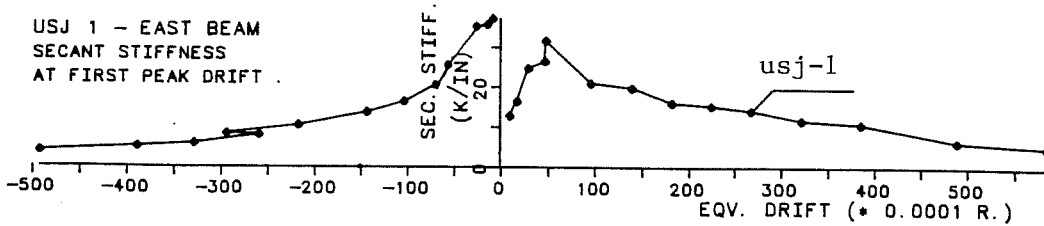


Fig. 6.22 - Interior Test (W-beam) Secant Stiffness.

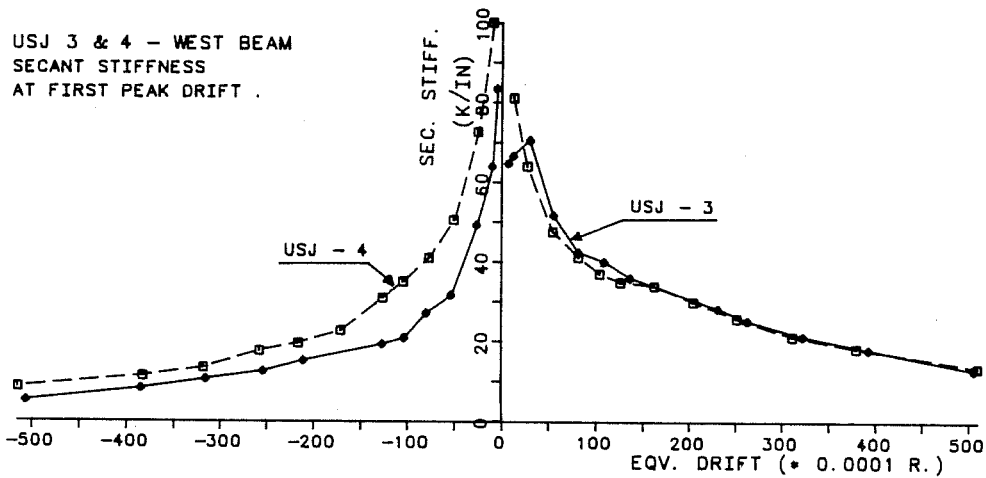
USJ 1 & 2 - WEST BEAM
SECANT STIFFNESS
AT FIRST PEAK DRIFT .



USJ 1 - EAST BEAM
SECANT STIFFNESS
AT FIRST PEAK DRIFT .



USJ 3 & 4 - WEST BEAM
SECANT STIFFNESS
AT FIRST PEAK DRIFT .



USJ 3 - EAST BEAM
SECANT STIFFNESS
AT FIRST PEAK DRIFT .

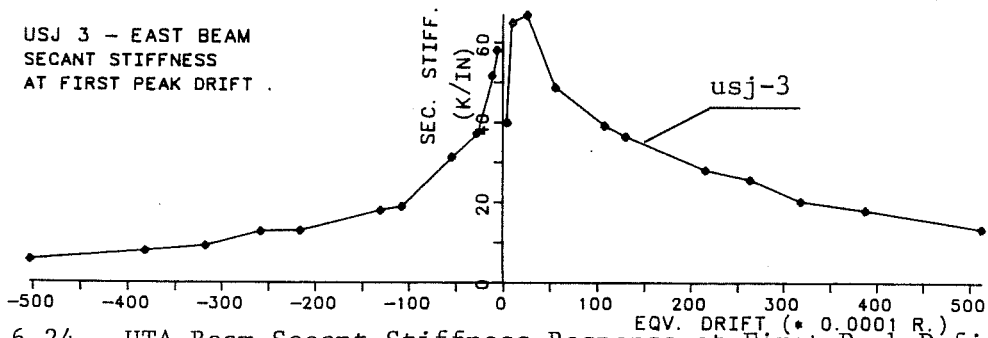
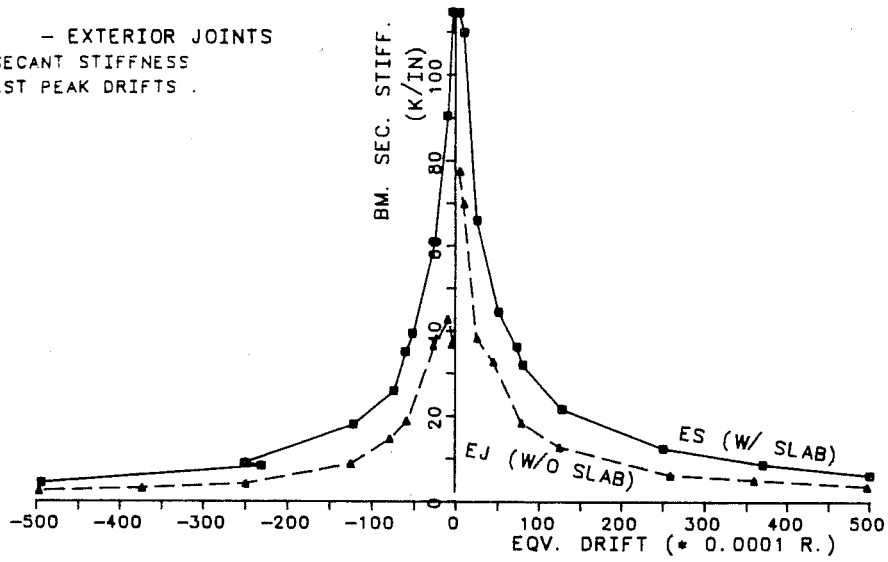
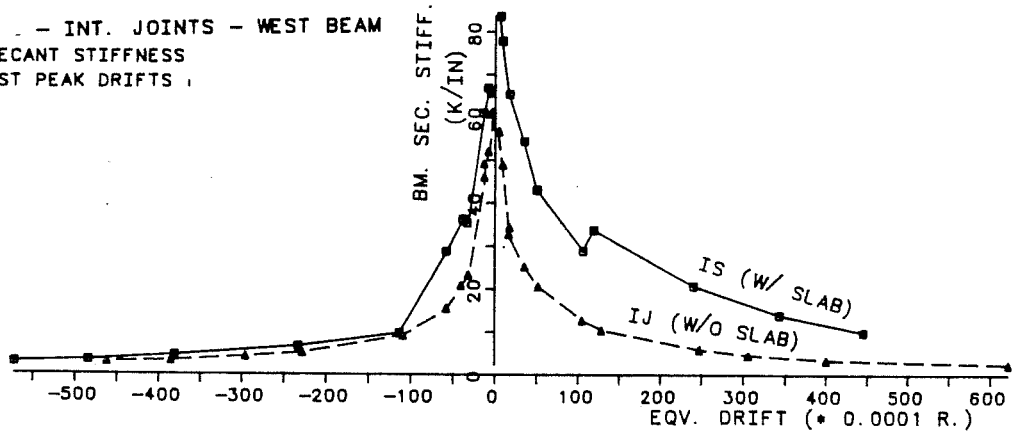


Fig. 6.24 - UTA Beam Secant Stiffness Response at First Peak Drifts.

S.U. - EXTERIOR JOINTS
 BEAM SECANT STIFFNESS
 AT FIRST PEAK DRIFTS .



S.U. - INT. JOINTS - WEST BEAM
 BEAM SECANT STIFFNESS
 AT FIRST PEAK DRIFTS .



S.U. - INT. JOINTS - EAST BEAM
 BEAM SECANT STIFFNESS
 AT FIRST PEAK DRIFTS .

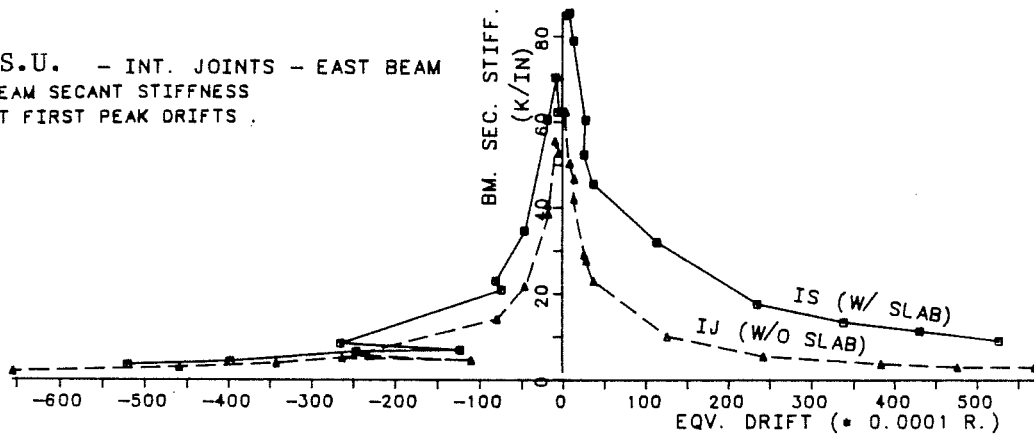


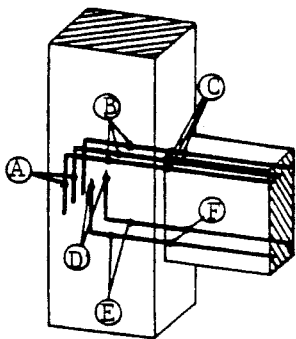
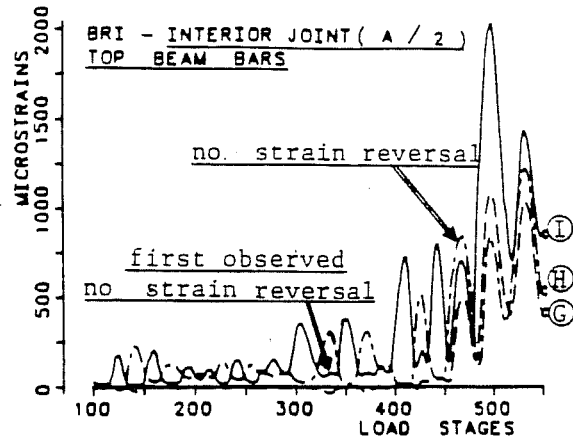
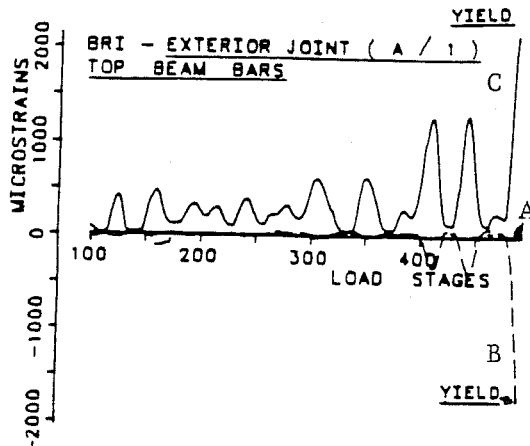
Fig. 6.25 - SU Beam Secant Stiffness Response at First Peak Drifts.

6.5 Longitudinal Beam

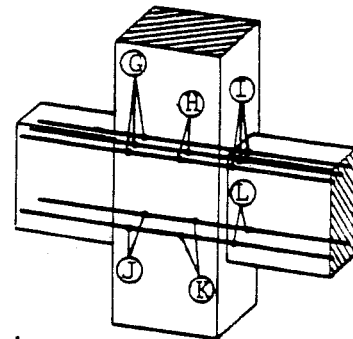
6.5.1 BRI Building. The occurrence of yielding in longitudinal beam bars can be studied by using the bar strain readings for both exterior and interior joints in Frame A at level Z2.

The first yielding in the exterior joint (A/1) top beam bars occurred at an equivalent drift of 1/155, (LDS 489) and the bottom beam bars yielded at LDS 462, ($R = 1/250$), Figs. 5.13 (drift history) and 6.26 (bar strains). A beam plastic hinge formed near the column face at relatively low deformation levels. It can also be observed in Fig. 6.26 that yield penetration through the top beam bars may have occurred at LDS 489 even though strain gauges at Section B showed yielding in compression (possibly because they were placed on the top surface of the bent bar).

The most important response feature in the interior joint (A/2) is the early loading bond destruction accompanied by top bar slippage. As early as LDS 333 ($R = 1/605$), the top beam bars showed signs of slippage and non-strain reversal, Fig. 6.27. This becomes more evident at LDS 469 ($R = -1/189$) with slip also occurring at a very low strain level of about 0.0007 in./in. well below the yield level of 0.002 in./in. The interior joint bottom beam bars yielded at a drift level of $R = 1/175$ (LDS 487) and the



Exterior Joint



Interior Joint

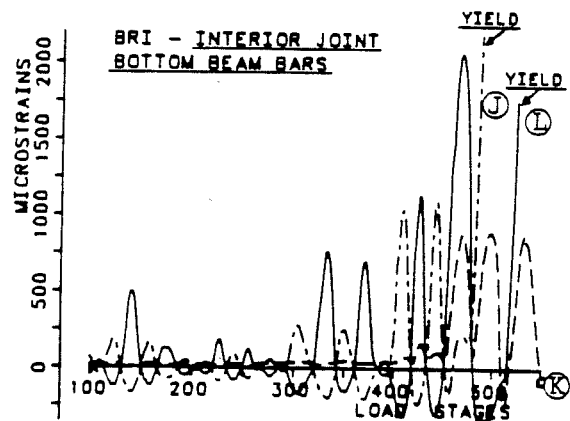
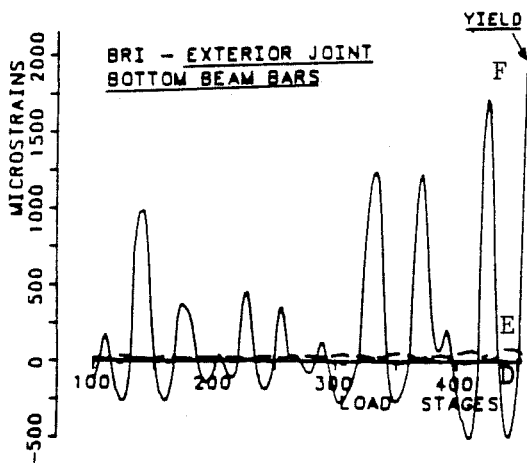


Fig.6.26-Exterior joint - top and bottom beam bars (BRI).

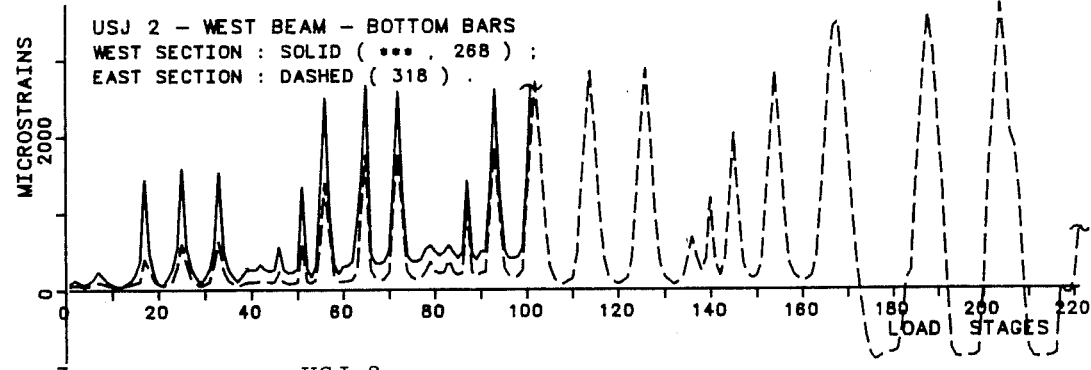
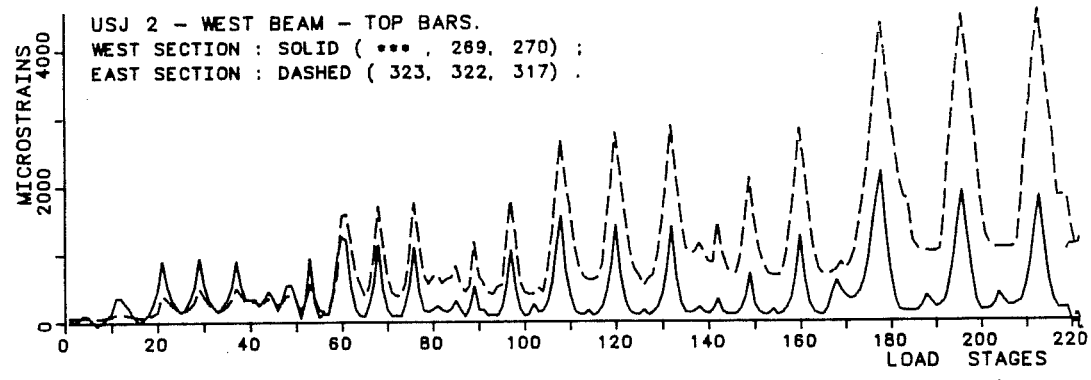
Fig.6.27-Interior joint - top and bottom beam bars (BRI).

bar exhibited no compression in the previous negative cycle at a peak equivalent drift of $R = -1/189$ (LDS 469).

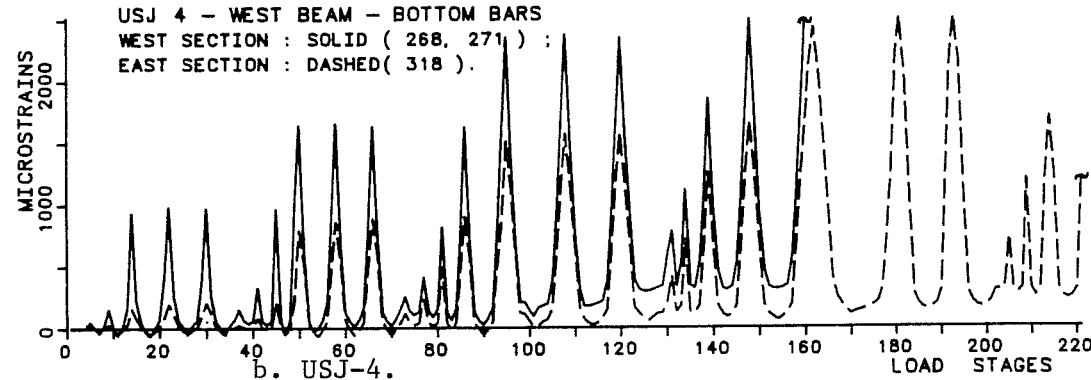
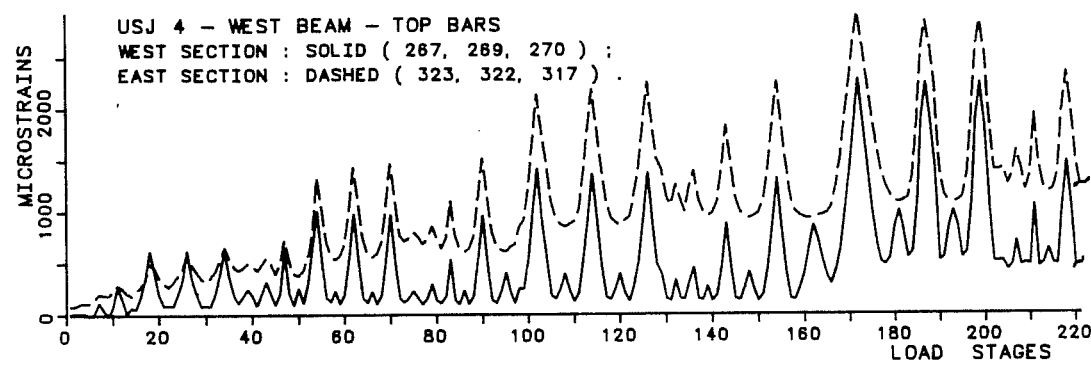
6.5.2 UTA Tests. The previously observed phenomena of early bond deterioration, progression of yield and non-strain reversal was also observed in the component tests. The exterior component USJ-2 shows no strain reversal when beam bars reached strains of 0.0005 to 0.0008. At LDS 21 ($R = 1/392$), the bars no longer exhibited compression and LDS 61 ($R = 1/185$) the top beam bars reached strains of 0.0010 to 0.0012 at both column faces, Figs. 6.28-a (bar strains) and 6.12-a (drift history). Bottom beam bars showed no strain reversal at LDS 17 ($R = -1/360$) at strains of 0.0010 - 0.0012. Bottom beam bar yielding occurred at LDS 102 ($R = -1/124$).

The exterior component USJ-4 also showed signs of no strain reversal at LDS 18 ($R = 1/371$) for the top bars and at LDS 14 ($R = -1/398$) for the bottom bars. Yielding at the column face occurred in the top bars for $R = 1/79$ (LDS 172) and for the bottom bars at $R = -1/79$ (LDS 162), Figs. 6.28-b and 6.12-b.

The interior component USJ-1 showed no strain reversal at LDS 109 ($R = 1/197$) and yielding at the west column face at LDS 439 ($R = 1/39$) for the top beam bars. The bottom beam bars showed no strain reversal at LDS 109 ($R = 1/197$) which became more obvious at LDS 172 ($R = -1/174$). Bottom bar yielding occurred at LDS 229 ($R = 1/39$), Figs. 6.29-a and 6.18-a.

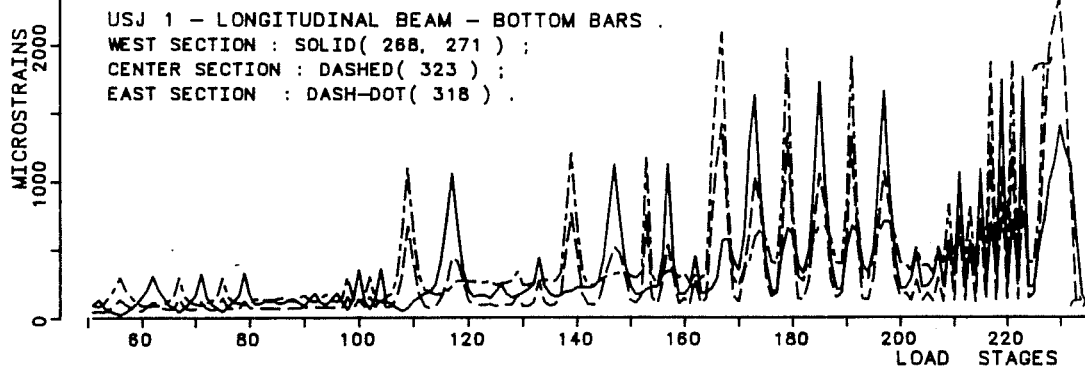
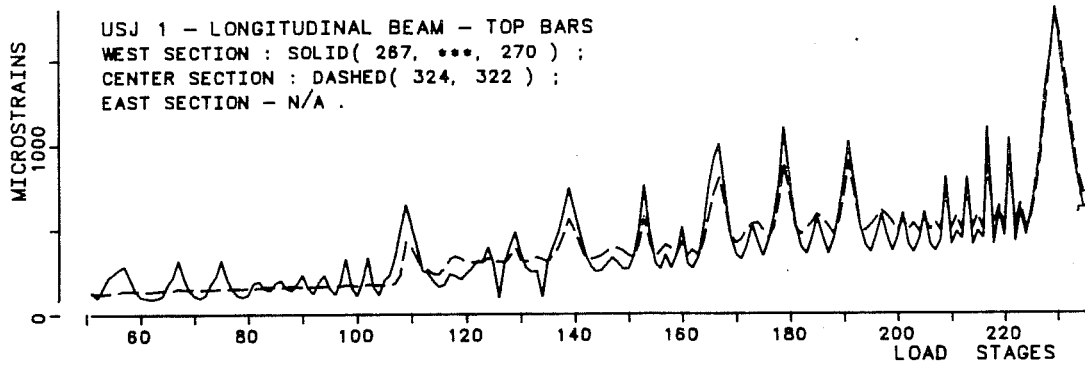


a. USJ-2.

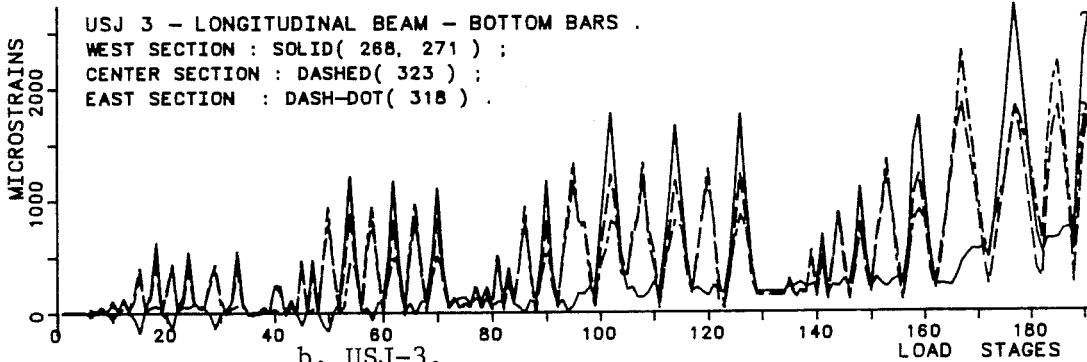
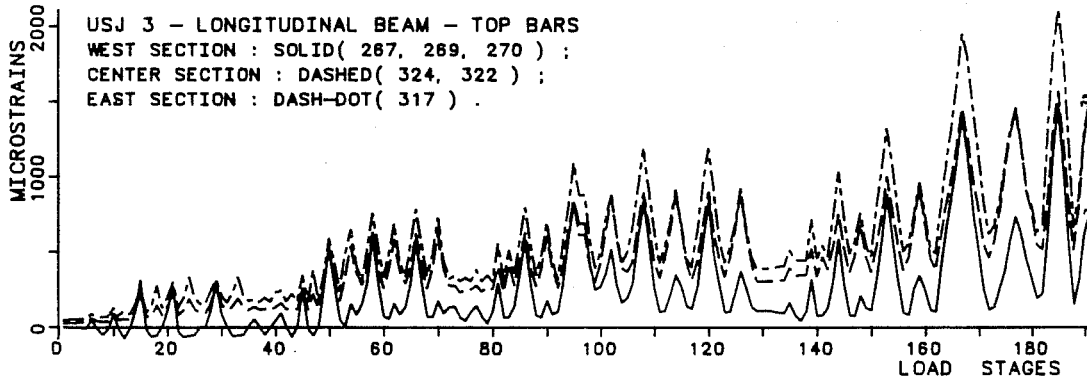


b. USJ-4.

Fig. 6.28 - UTA - Exterior Test Beam Bar Strains.



a. USJ-1.



b. USJ-3.

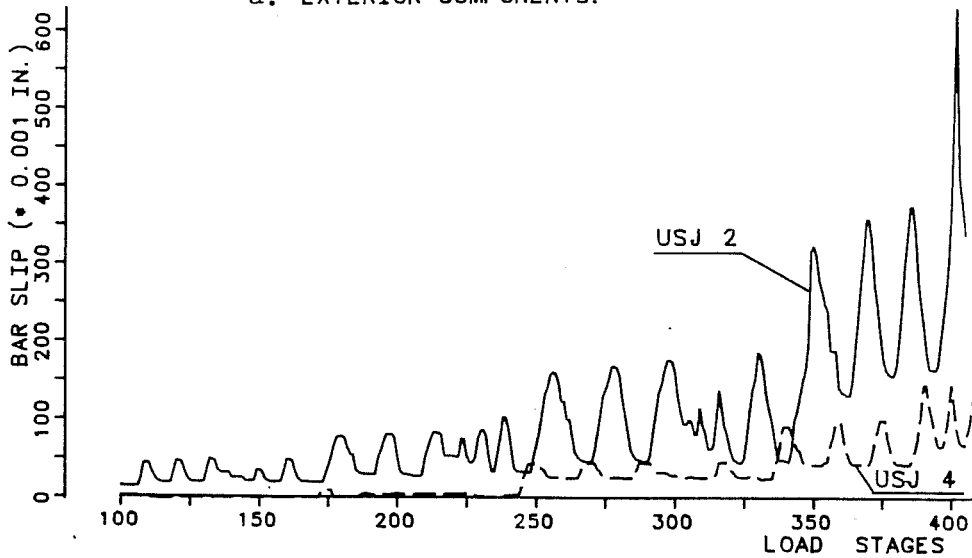
Fig. 6.29 - UTA - Interior Test Beam Bar Strains.

The interior component USJ-3 showed non-strain reversal at LDS 54 ($R = -1/184$) when bar strains of 0.0005 - 0.0012 were reached. For top bars, no strain reversal became more evident at LDS 95 ($R = 1/125$) and for the bottom bars at LDS 102 ($R = -1/124$). Yielding of top and bottom beam bars near the column face occurred at LDS 239 ($R = 1/38$), Figs. 6.29-b and 6.19-a.

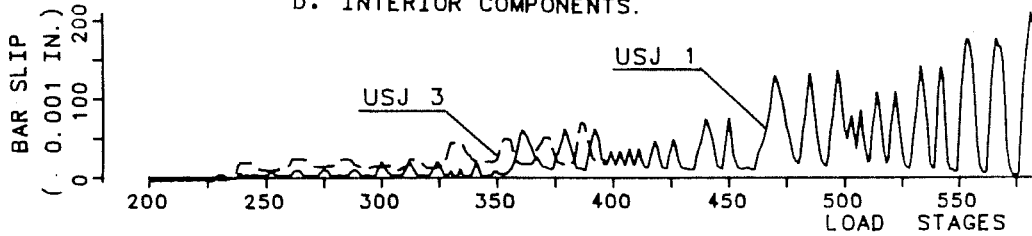
The destruction of bond and the progression of yield in the longitudinal beam top bars can be evaluated by the available bar slip data, Fig. 6.30. The exterior component USJ-2 clearly showed the effects of anchorage failure by exhibiting a slip of 0.62 in. (15.7 mm) near the end of the test. Bar slip with improved anchorage detail in USJ-4 test was much smaller 0.15 in. (3.8 mm) in spite of the larger bond forces being developed. The interior specimens USJ-1 and USJ-3 showed relatively small top bar slip values. Specimen USJ-1 was initially subjected to a load-control test and had a final bar slip value of 0.20 in. (5.1 mm) which is nearly 2.5 times larger than the maximum value of 0.08 in. (2.0 mm) for USJ-3, Fig. 6.30-b. In both exterior and interior components, the modified specimens (USJ-3, USJ-4) showed better bond performance as compared with the prototypes (USJ-4, USJ-2) due to more careful detailing and use of a deformation controlled loading program.

U. OF TEXAS : WEST BEAM - TOP BAR SLIP HISTORY (W-S).

a. EXTERIOR COMPONENTS.



b. INTERIOR COMPONENTS.



c. WEST BEAM TOP BAR SLIP AT FIRST PEAK DRIFTS .

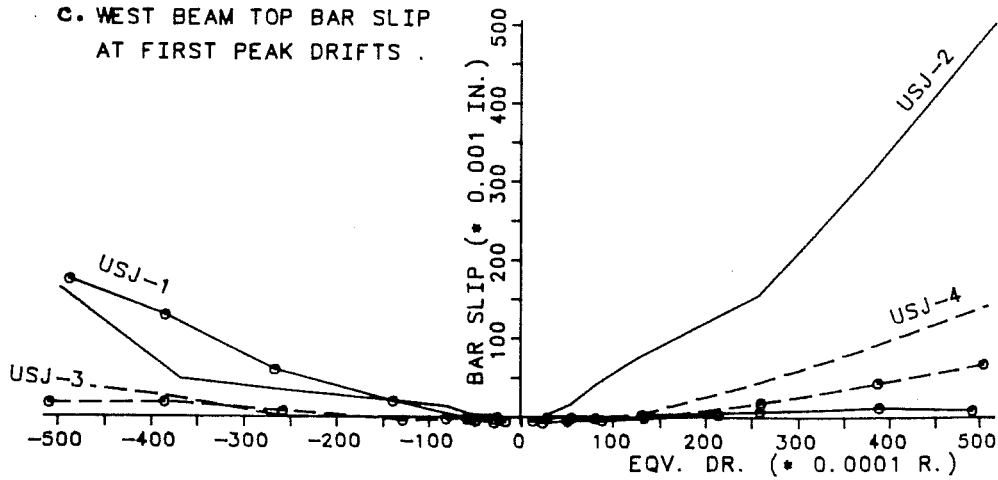


Fig. 6.30 - UTA Longitudinal Beam Top Bar Slip.

6.6 Slab Participation in Longitudinal Beam Response

The importance of the slab participation in the stiffness and strength resisting mechanisms was clearly shown in the previous sections by direct comparisons with specimens without a slab. The development of slab bar strains with increased deformation levels is particularly important in understanding ultimate collapse mechanisms. At selected equivalent drift levels the strains in the BRI building and in the isolated components are compared for the slab in tension (negative moment at the column face). The interior components response is compared with the BRI slab steel at level Z2 (Frame A/2) when the building is deflected away from the strong wall. The slab was in tension for the exterior joint region (Frame A/4) when the BRI building was deflected towards the strong wall. Consequently, comparisons are made for positive drift (BRI) with the interior components group and for negative drift (BRI) with the exterior group, Fig. 6.31. Strain distributions were plotted across the floor section to allow a better insight into the response at various displacement levels.

6.6.1 Exterior Joints. The observed strain distributions in the exterior joints show the importance of the BRI building end walls in increasing the torsional restraint of the transverse beam, Figs. 6.32 and 6.33. This torsional restraint resulted in a fairly uniform slab strain distribution

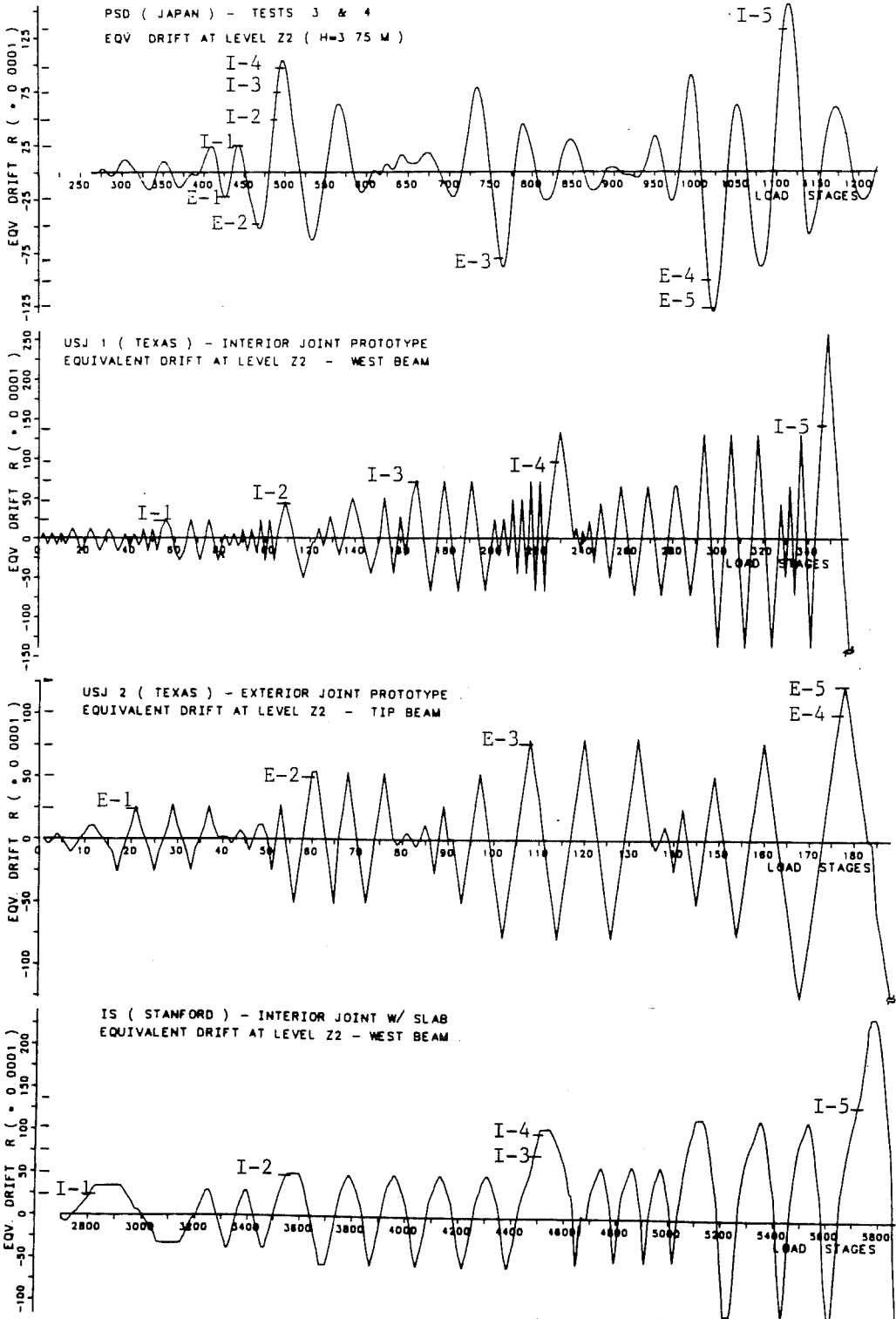
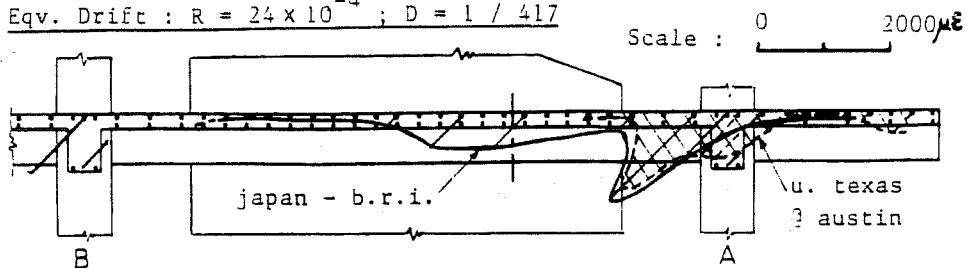
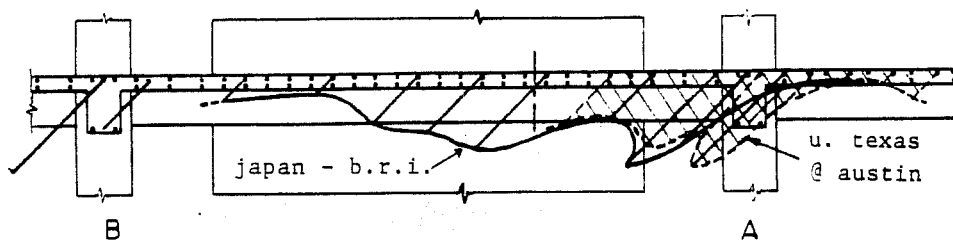


Fig. 6.31 - Equivalent Drift Histories.

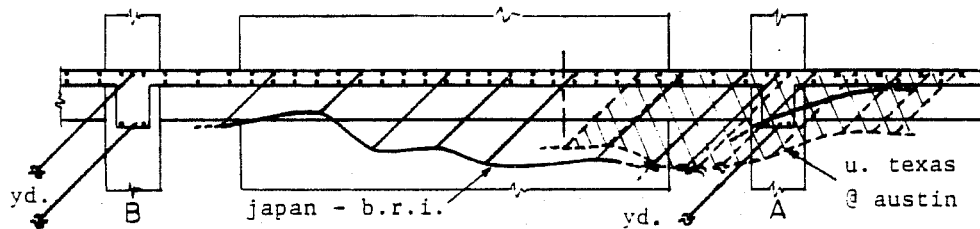
E-1. Eqv. Drift : $R = 24 \times 10^{-4}$; $D = 1 / 417$



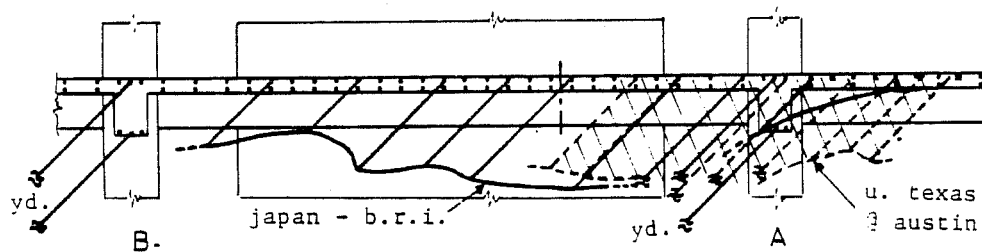
E-2. Eqv. Drift : $R = 48 \times 10^{-4}$; $D = 1 / 208$



E-3. Eqv. Drift : $R = 81 \times 10^{-4}$; $D = 1 / 123$



E-4. Eqv. Drift : $R = 103 \times 10^{-4}$; $D = 1 / 97$



E-5. Eqv. Drift : $R = 125 \times 10^{-4}$; $D = 1 / 80$

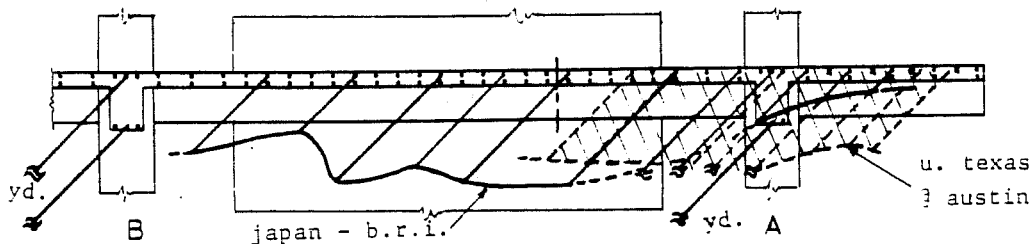
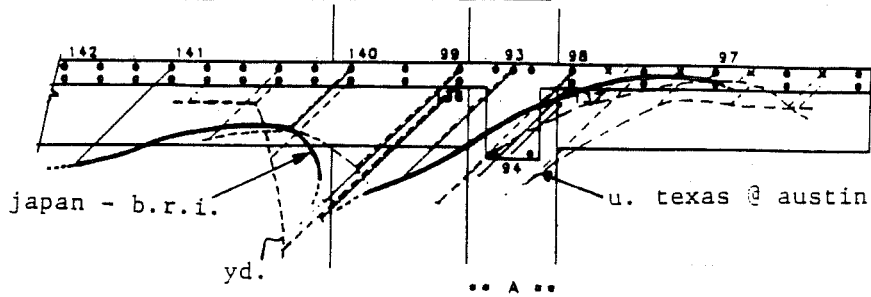
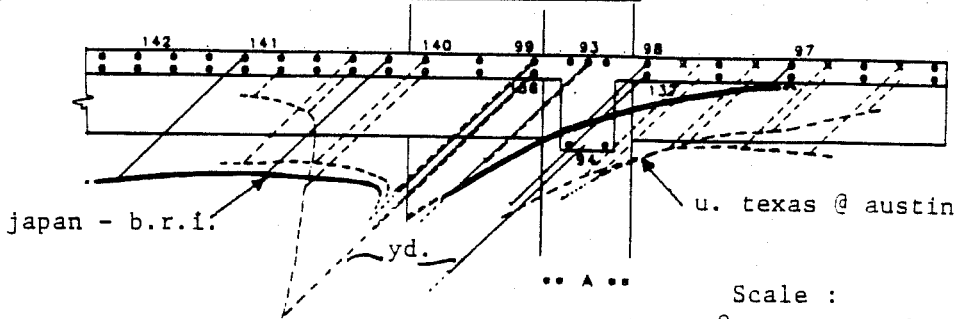


Fig. 6.32 - Exterior Joint Slab Steel Yielding.

E-2 : Eqv. Drift - $R = 48 \times 10^{-4}$; $D = 1/208$.

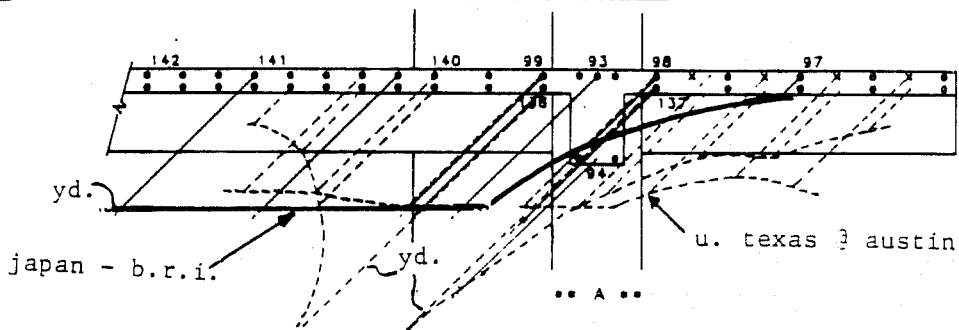


E-3 : Eqv. Drift - $R = 81 \times 10^{-4}$; $D = 1/123$.



Scale :
0 2000 ME

E-4 : Eqv. Drift - $R = 103 \times 10^{-4}$; $D = 1 / 97$.



E-5 : Eqv. Drift - $R = 125 \times 10^{-4}$; $D = 1 / 80$.

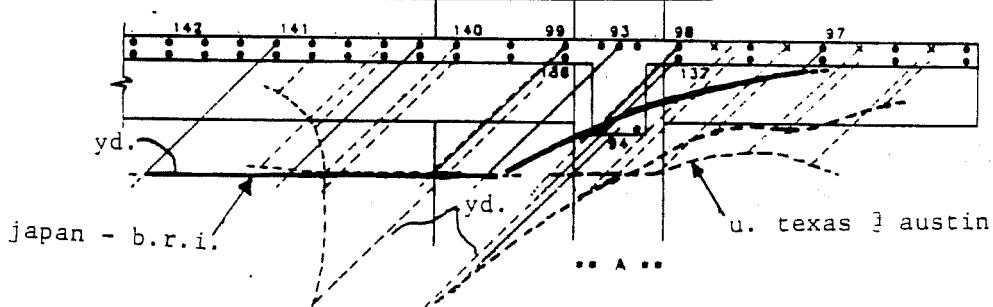
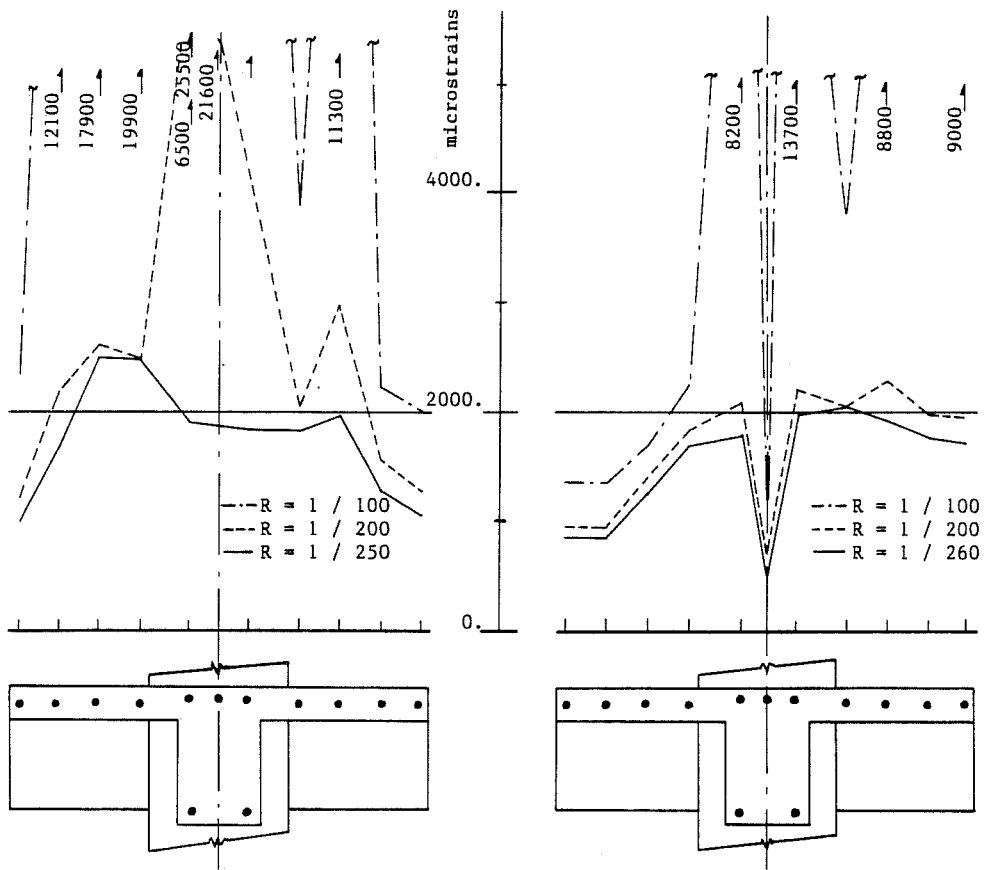


Fig. 6.33 - Exterior Joint Slab Steel Yielding (enlarged).

across the entire slab width at early loading stages. At a small drift level, $R = 1/417$, the slab region between the end wall and column A/4 had nearly yielded. As larger displacements were applied, a yield line developed along the transverse beam as indicated by the spread of high steel strains. Near ultimate, yielding occurred over a large portion of the slab section in the building and in the component tests. It also can be seen that the top slab bar strains in the building overhang section remained low even at large drifts. This is likely due to different applied loading or deformation to that portion of the structure and different boundary conditions between the components and the building structure, Figs. 6.32 and 6.33.

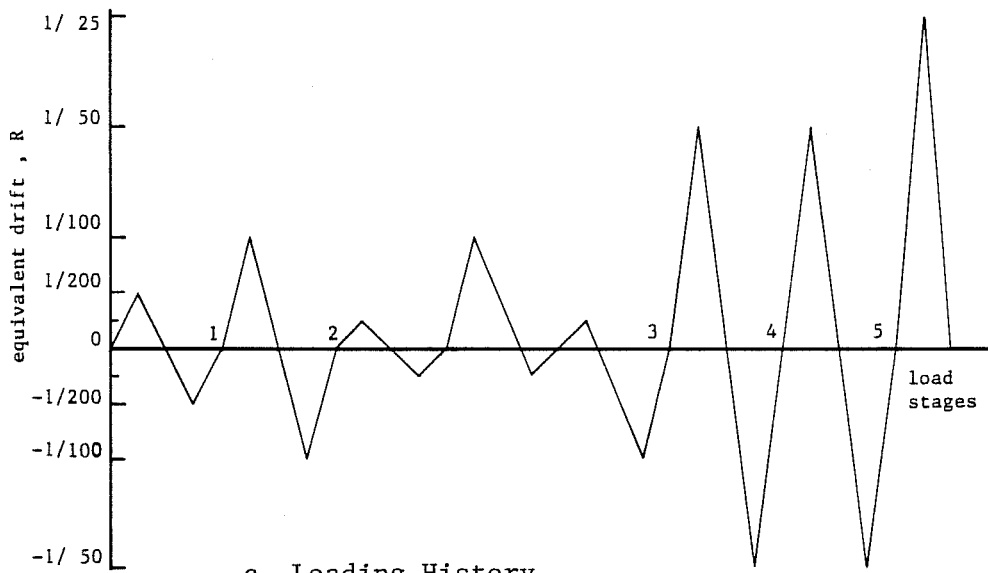
The Japanese exterior components with code-specified slab width (1.50 m, 59 in.) also showed spread of yielding under increased deformation levels, Fig. 6.34. However, complete yielding of the single layer of steel (placed at the slab mid-height) seemed to occur only at a relatively large drift, $R = 1/100$. This may be due to the fact that the slab steel was placed well below the top fiber as compared with the US tests.

The UTA (USJ-4) modified exterior component also showed yield spreading in the top slab bars at increased peak drifts. The top steel across the complete cross section yielded at a peak drift $R = 1/40$. The top beam bars showed lower strain levels because they were placed below the top slab steel. The lower



a. E-1 - Japanese Design.

b. E-2 - US Design.



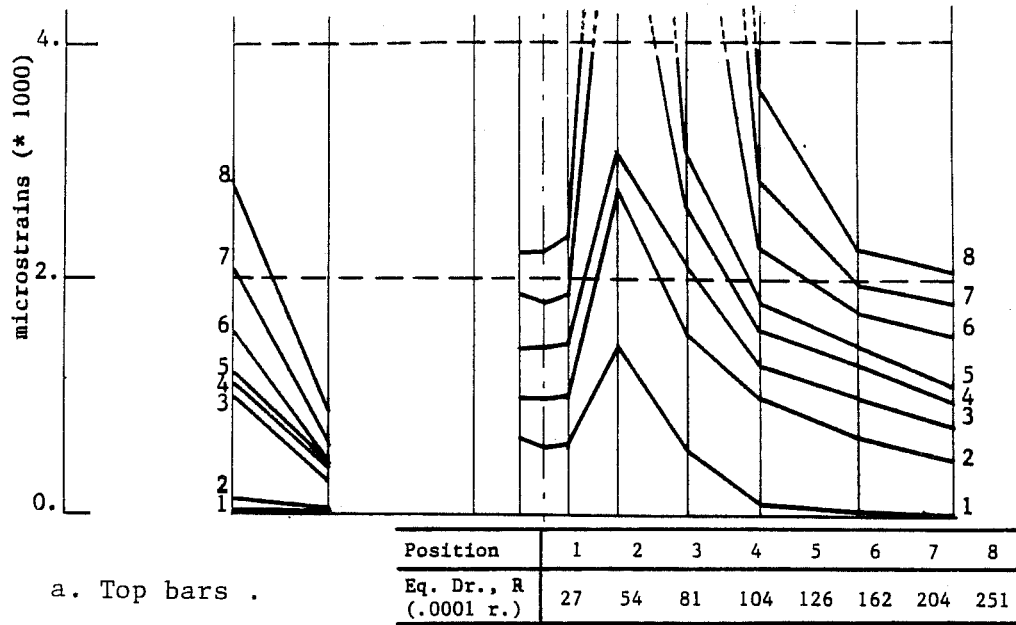
c. Loading History.

Fig. 6.34 - Japanese Exterior Tests Slab Strains.

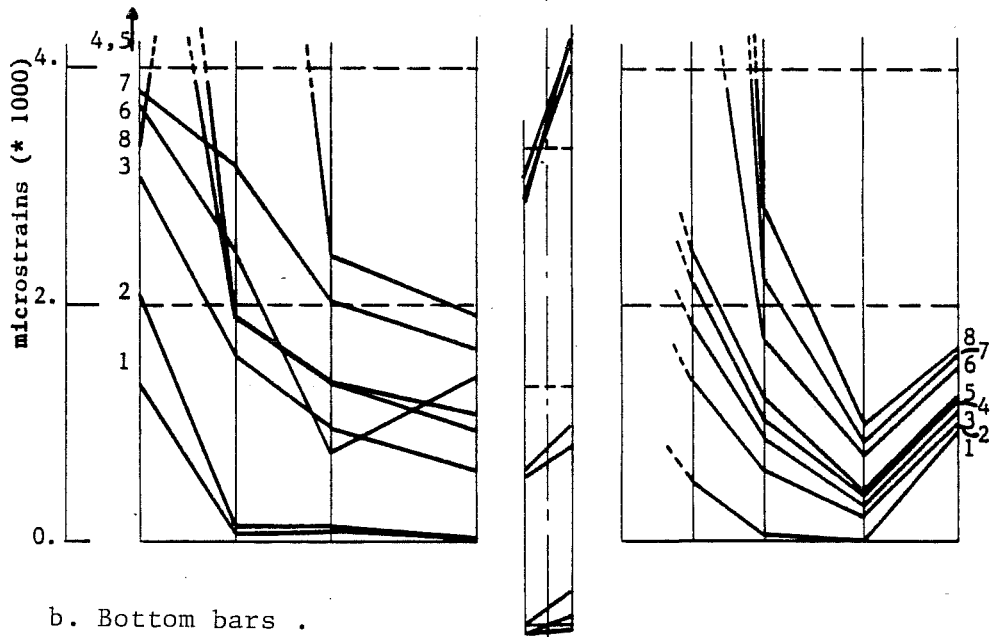
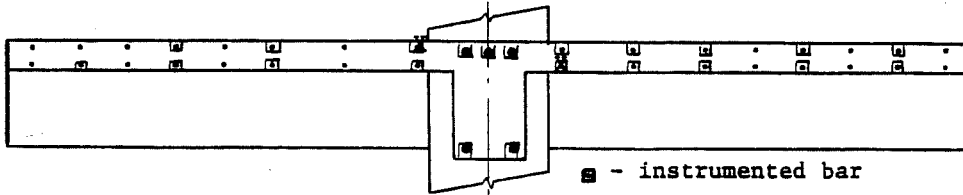
slab steel layer showed a more pronounced strain decay within a short distance from the beam (SW-quadrant), although the same could not be said about the NW-quadrant, Fig. 6.35. However, there were fewer functioning gauges at that location.

6.6.2 Interior Joints. The interior joint response (Frame A/3) in the BRI building is shown in Figs. 6.36 and 6.37. The data available refers only to the bottom slab bars and it can be observed that strains increased as lateral deformations increased. At large lateral displacements, yielding occurred at some considerable distance from the joint, implying that top slab steel also yielded under negative moment (slab in tension). Good agreement was observed at $R = 1/105$ although at a larger displacement level ($R = 1/77$) it seemed that the bottom slab steel in the components experienced larger strains, Fig. 6.37. As observed in the exterior joint, the measured bar strains in the overhanging section of the slab showed that this region was not as heavily stressed as the "continuous" section between columns.

The Japanese interior component tests showed that cross section yielding occurred at an approximate equivalent drift $R = 1/100$, Fig. 6.38. As for the exterior joint, a large deformation level was required to yield the slab steel and may result from the location of a single layer at mid-depth.



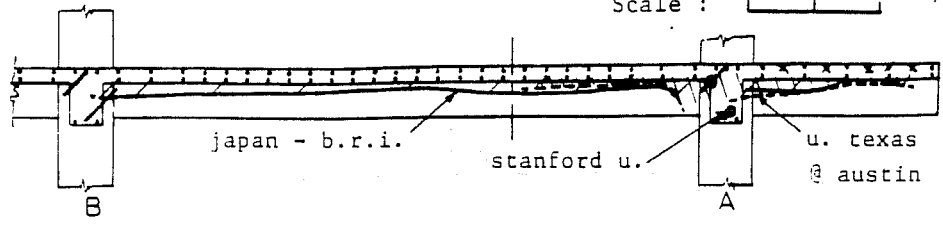
a. Top bars .



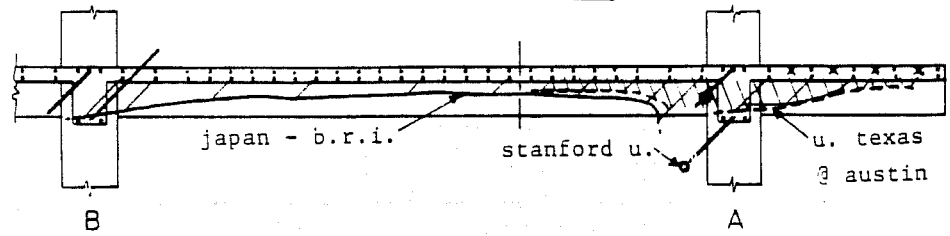
b. Bottom bars .

Fig. 6.35 - UTA - USJ-4 - Exterior Test Slab Strains.

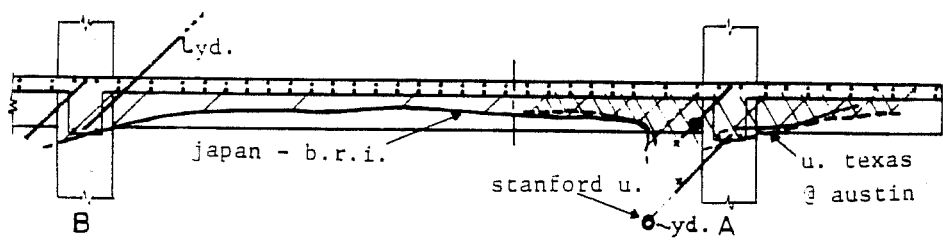
I-1. Eqv. Drift : $R = 23 \times 10^{-4}$; $D = 1 / 435$ Scale : 0 2000 $\mu\epsilon$



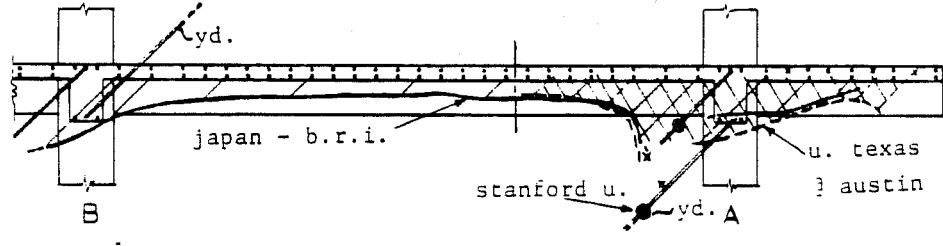
I-2. Eqv. Drift : $R = 48 \times 10^{-4}$; $D = 1 / 208$



I-3. Eqv. Drift : $R = 74 \times 10^{-4}$; $D = 1 / 135$



I-4. Eqv. Drift : $R = 95 \times 10^{-4}$; $D = 1 / 105$



I-5. Eqv. Drift : $R = 129 \times 10^{-4}$; $D = 1 / 77$

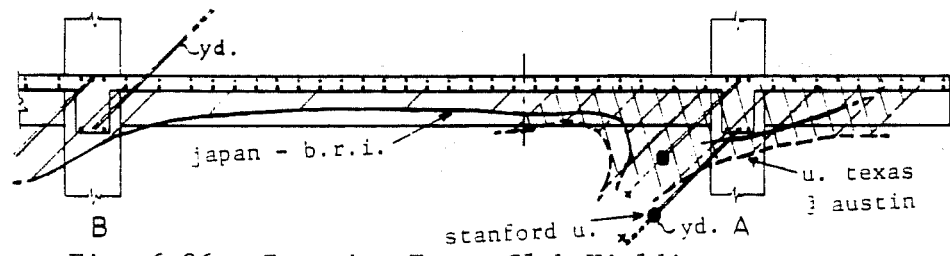
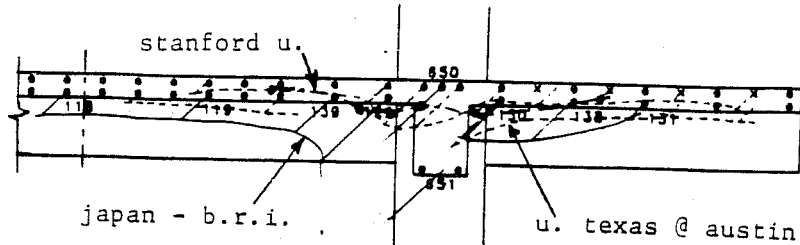


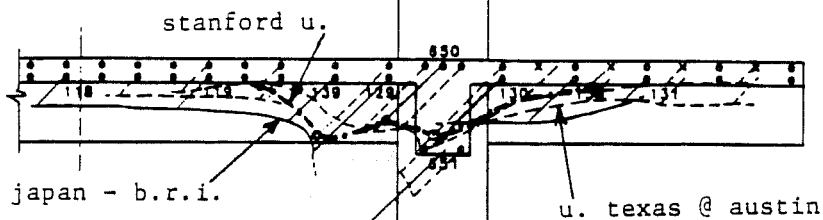
Fig. 6.36 - Interior Tests Slab Yielding.

I-2 : Eqv. Drift - $R = 48 \times 10^{-4}$; $D = 1 / 208$.

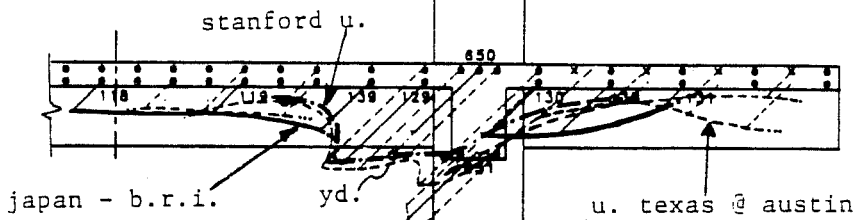
Scale : 0 2000 μE



I-3 : Eqv. Drift - $R = 74 \times 10^{-4}$; $D = 1 / 135$.



I-4 : Eqv. Drift - $R = 95 \times 10^{-4}$; $D = 1 / 105$.



I-5 : Eqv. Drift - $R = 129 \times 10^{-4}$; $D = 1 / 77$.

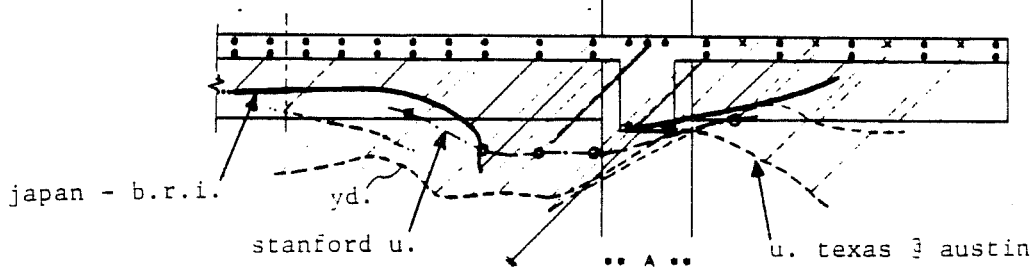
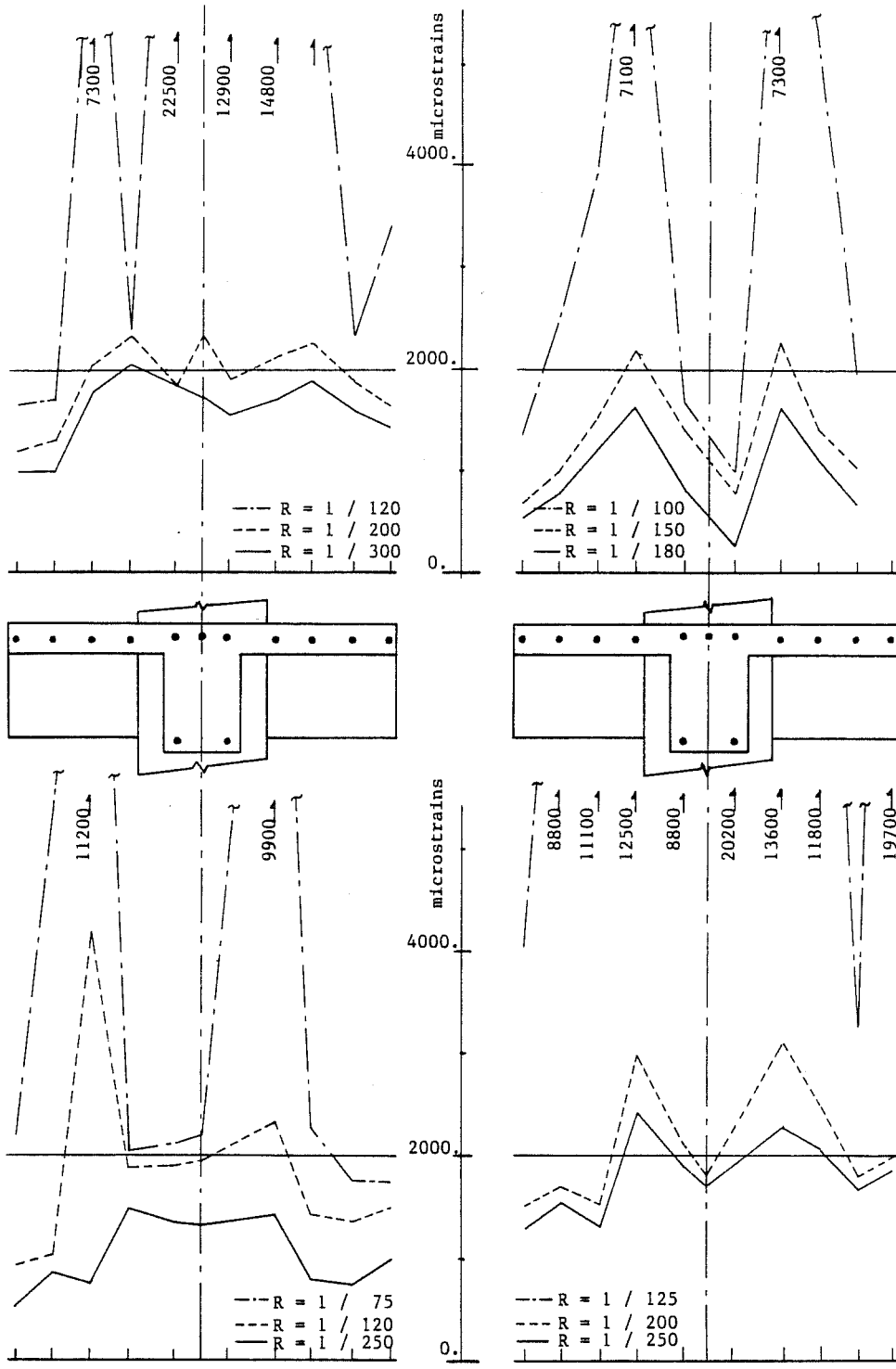


Fig. 6.37 - Interior Tests Slab Yielding (enlarged plot).



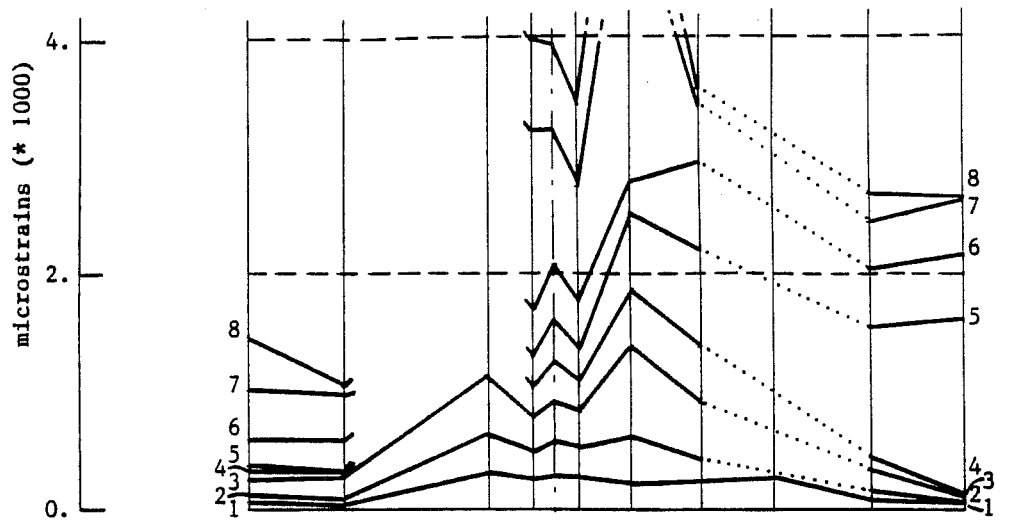
a. I-1 - Japanese Design.

b. I-2 - US Design.

Fig. 6.38 -Japanese Interior Tests Slab Strains.

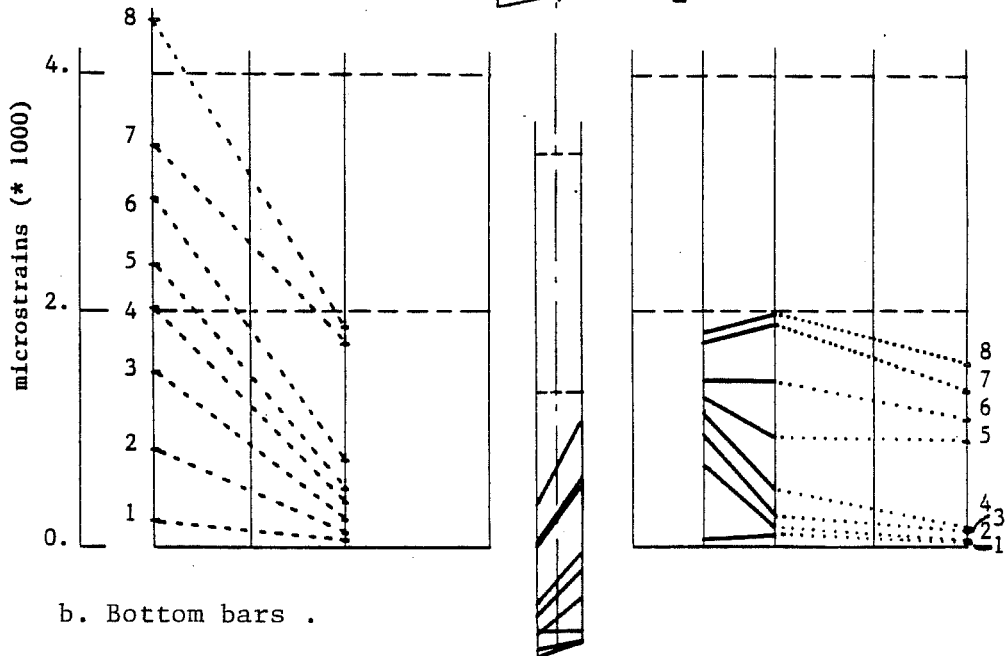
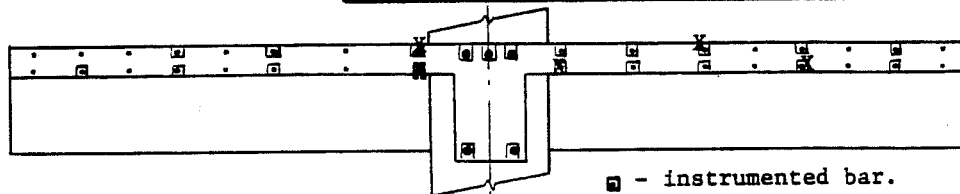
The UTA (USJ-3) Fig. 6.39 interior modified specimen showed similar slab yielding patterns at test USJ-4. In this test full top slab yielding was reached at a much lower equivalent drift of $R = 1/56$. It was also observed that the top beam steel strains lagged behind the top slab steel strains because the steel was placed 1.50 in. (3.8 cm) below the slab steel.

6.6.3 Effective Slab Width. A very important parameter for design purposes is the amount of slab effectively participating with the beam in T-beam action. Current code provisions for the evaluation of the effective slab width were developed based on tests with the slab in compression (positive moment). As the codes omit the provisions for the case of slab in tension (negative moment), designers have been using the positive moment effective slab width for both cases. On the other hand, two different codes [ACI 318 (1), AIJ (2)] coincide in the BRI frame case on the required value for the effective slab width, Fig. 6.40. It is considered that the 6.00 m span is the controlling case. Based on the measured slab strains an effective width ratio (non-dimensional) was devised. It represents the width of slab in which the bars yielded divided by the design code effective slab width defined for the tests which is $B_e = 1.50$ m (59 in.), Fig. 6.41.



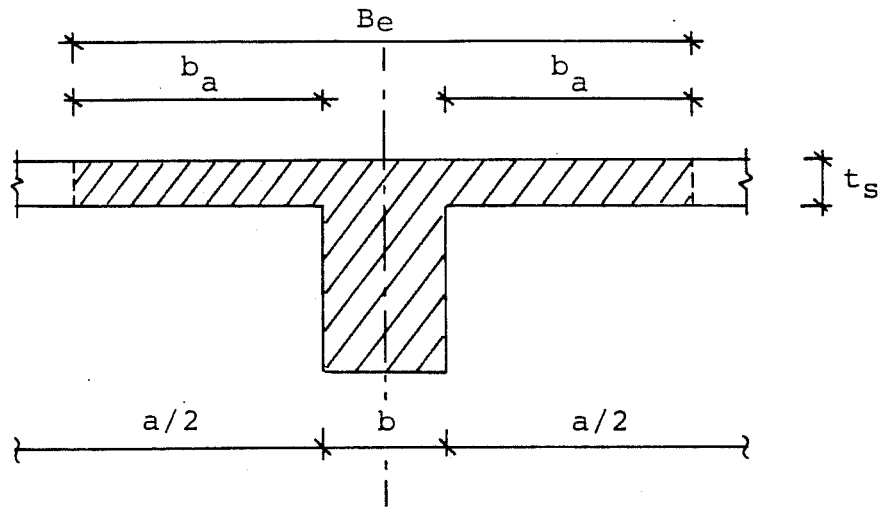
a. Top bars .

Position	1	2	3	4	5	6	7	8
Eq. Dr., R (.0001 r.)	28	55	81	108	136	179	231	263



b. Bottom bars .

Fig. 6.39 - UTA - USJ-3 - Interior Test Slab Strains.

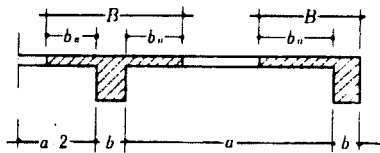
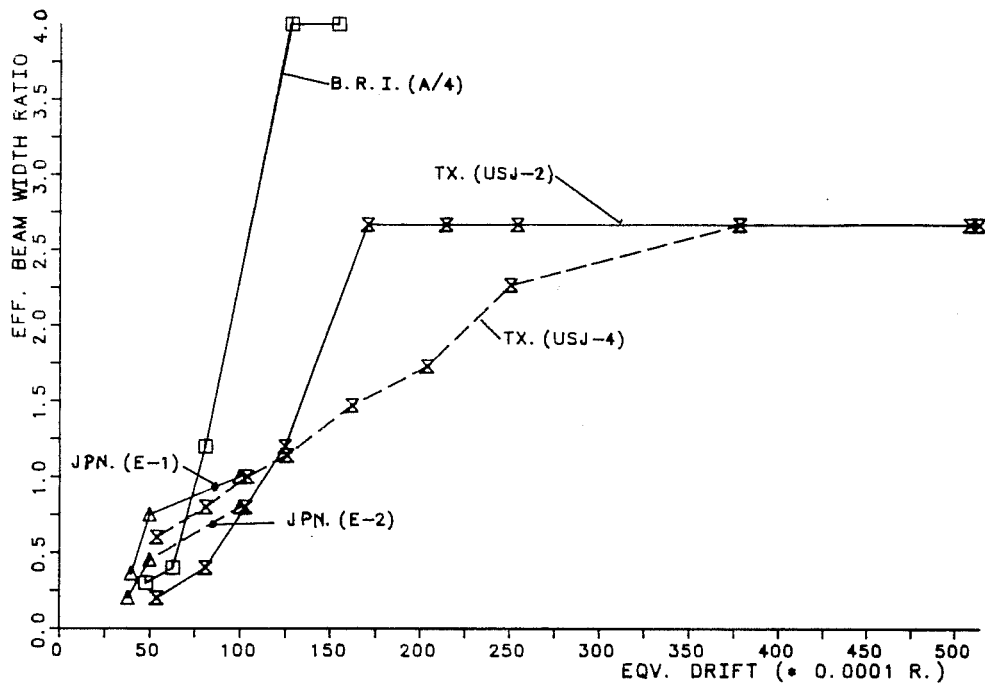


ACI 318-83 / 8.10.2	Span 6.00 m
1. $B_e \leq \frac{L_{bm}}{4}$	1.50 m
2. $B_e \leq b + 2 \times 8t_s$	2.22 m
3. $B_e \leq \frac{a}{2}$	3.00 m

AIJ - 82 / 8.(3)	Span 6.00 m
1. $b_a = \left(\frac{1}{2} - 0.6\frac{a}{l}\right)$ $a < 1/2$	$a > 1/2$ $\therefore b_a = 0.60 \text{ m}$
2. $b_a = 0.1 l$ $a \geq 1/2$	$B_e = 1.50 \text{ m}$

Fig. 6.40 Design Code Effective Slab Width.

a. EXTERIOR JOINTS - EFFECTIVE WIDTH RATIO



$$\text{EFF. BEAM WIDTH RATIO} = \frac{\text{WIDTH OF PLASTIC YIELDING}}{\text{DESIGN CODE EFFECTIVE WIDTH}}$$

(A.C.I. , A.I.J. : $B_E = 1.50 M$)

b. INTERIOR JOINTS - EFFECTIVE WIDTH RATIO

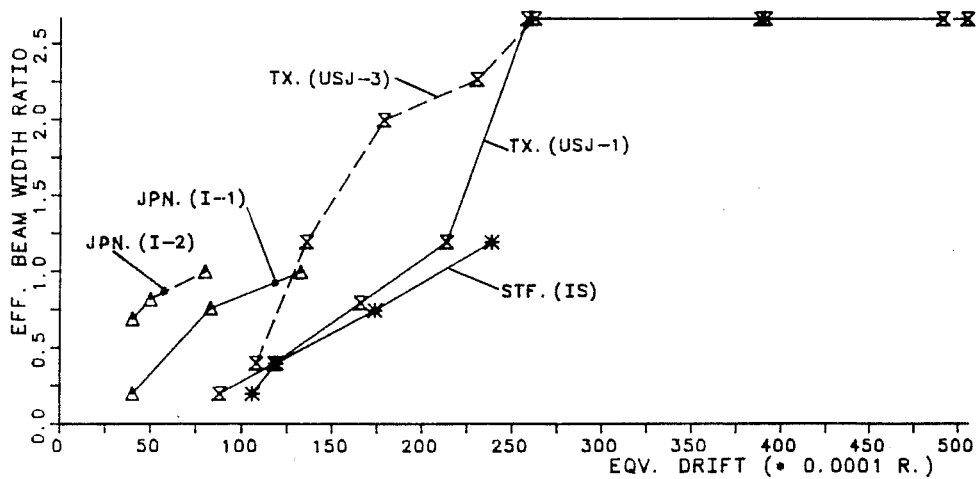


Fig. 6.41 - Component Tests Effective Slab Width Ratio.

For the exterior joints it can be seen that, Fig. 6.41-a: (1) the BRI exterior joint reached full width yielding at very low deformations, $R = 1/77$, due to the end wall restraint for the transverse beams; (2) USJ-2 slab effectiveness was altered due to the beam bar anchorage failure which transferred forces to the slab reinforcement; (3) only USJ-4 exhibited complete slab yielding at a very large equivalent drift, $R = 1/26$ because of the improved anchorage detailing and stiffer longitudinal beams; and, (4) the Japanese exterior components (E-1, E-2) reached nearly complete yielding at a deformation level $R = 1/100$.

Slab yielding at the interior joints was characterized by, Fig. 6.41-b; (1) complete top slab steel yielding at a drift level $R = 1/38$ for both prototype (USJ-1) and modified (USJ-3) specimens; (2) slab yielding of the SU (IS) interior specimen followed the USJ-1 trend for the data available; and, (3) slabs in the Japanese interior specimens yielded faster than the other specimens.

6.7 Joint Region Performance.

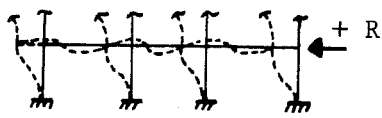
The response of the joint region was assessed by strain gauges (S.G.) placed on reinforcement and by the joint shear distortion recorded by displacement transducers. Small scale

tests (SU) and Japanese components are excluded from this study due to the lack of available data.

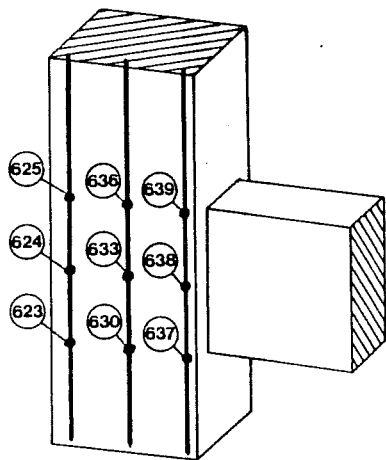
6.7.1 Joint Core Reinforcement Response. The recorded data for the BRI building exterior joint (Frame A/1) showed that the column bars did not yield under the applied loads, Fig. 6.42. Under the maximum positive equivalent drift, $R = +1/64$, the highest recorded strain of 0.0005 was well below yield. It is important to note that only one plane in the column bars was instrumented and the central bar (S.G. 636, 633, 630) exhibited almost zero strains throughout. The highest strains were reached in S.G. 625. Under a maximum negative drift of $R = -1/82$, the highest recorded strain reached nearly 0.0010 in S.G. 625.

The UTA exterior joint strains response under positive equivalent drifts (slab in tension) are shown in Fig. 6.43. Although some column bar strain gauges were inactive (S.G. 249, 248, 245), the interaction between longitudinal beam anchorage failure and joint core response can be seen, namely: (1) the column bars did not yield except at the very last load stage where $R = 1/19$; (2) the joint core hoops did not experience the yielding that occurred in Specimen USJ-4 at large deformation levels (volumetric core expansion); and, (3) the joint core hoops experienced a drop in strain at equivalent drifts $R = +1/26$, $+1/20$, after yielding was nearly reached at a lower equivalent drift $R = 1/40$.

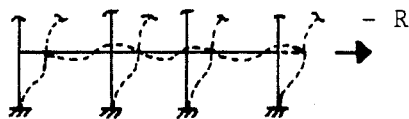
Position	Eq. Dr., R
1	25
2	45
3	75
4	104
5	120
6	155



a. Positive Drift.



Position	Eq. Dr., R
1	-24
2	-53
3	-76
4	-106
5	-122



b. Negative Drift.

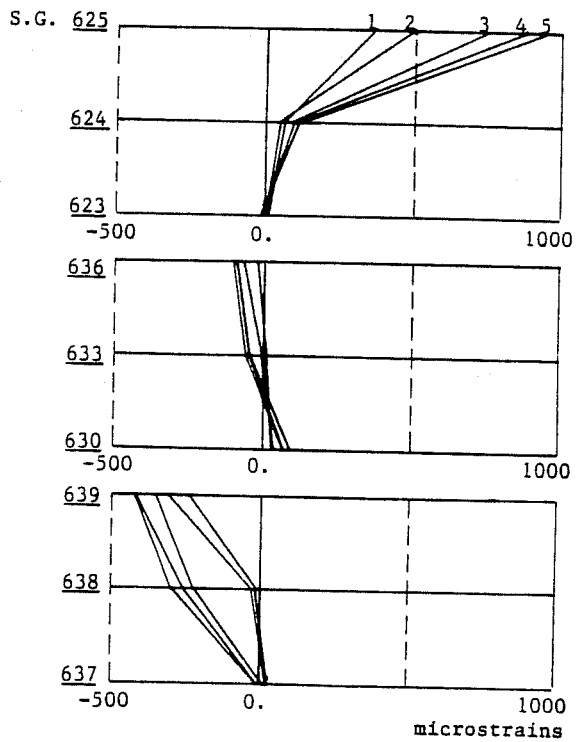
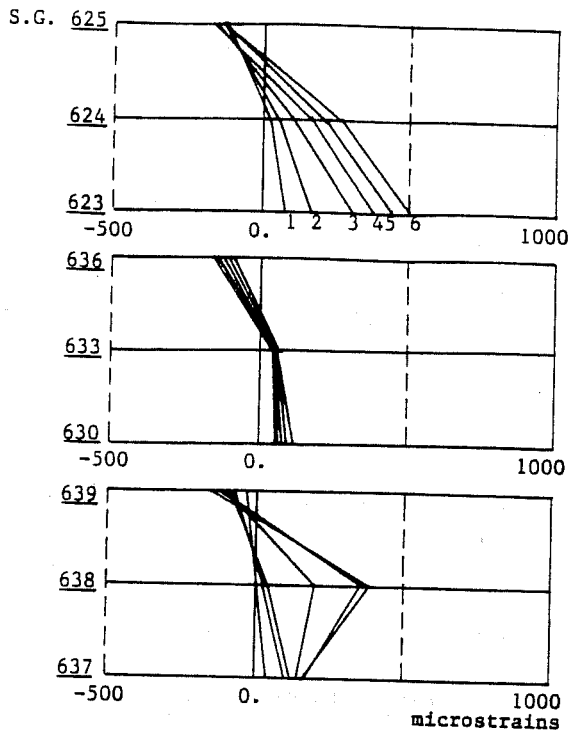


Fig. 6.42 - BRI Building - Exterior Joint Column Bars Strains.

On the contrary, the response of USJ-4 showed the results of the improved anchorage detail, Fig. 6.43-b: (1) the column bars showed increased strains at peak drifts; (2) a plastic hinge may have formed in the column above the joint at a peak drift $R = 1/62 - 1/40$; and, (3) the joint core hoops reached yielding at a peak drift $R = 1/62$. At this drift level the joint core started to experience high strains showed by the recordings in the joint hoops due to the large tensile forces in the top beam bars.

The BRI interior joint response is shown in Fig. 6.44. It is important to note that: (1) top level column bars yielded at a drift $R = +1/83$; (2) under a negative drift, $R = -1/94$ the lower column bar (S.G. 615) experienced yielding; and, (3) at mid-depth, the column bars experienced yielding at peak drifts $R = 1/97, 1/83$.

In the UTA interior joints, Fig. 6.45-a,b: (1) the column bars yielded in test USJ-1 at $R = +1/76$ although only two gauges were operating; (2) in specimen USJ-3, column bars showed yielding at $R = +1/38$; (3) in both specimens, joint core hoops yielded in the central tier at $R = 1/57 - 1/56$; and, (4) hoop yielding in the modified USJ-3 specimen reached larger values in the range $R = 1/37 - 1/19$ than the interior prototype (USJ-1) which remained at $0.002 - 0.004$ for the same drift range.

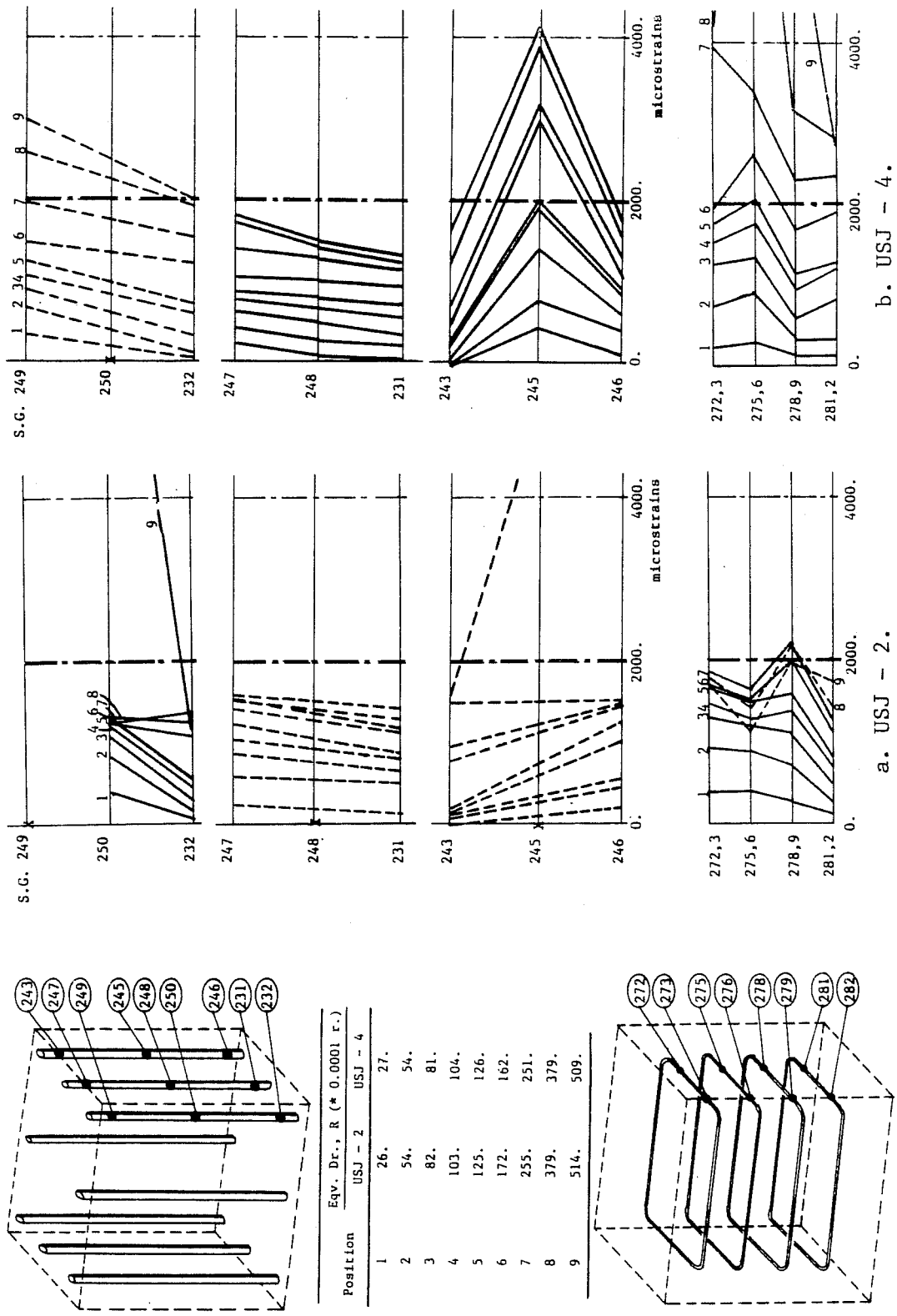
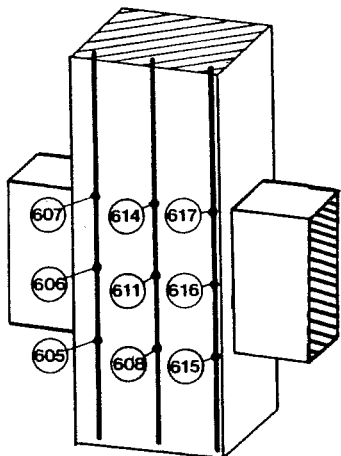
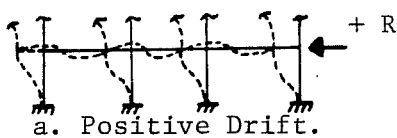


Fig. 6.43 - UTA - Exterior Tests Column and Core Bar Strains.

Position	Eq. Dr., R
1	25
2	45
3	75
4	104
5	120
6	155



Position	Eq. Dr., R
1	-24
2	-53
3	-76
4	-106
5	-122

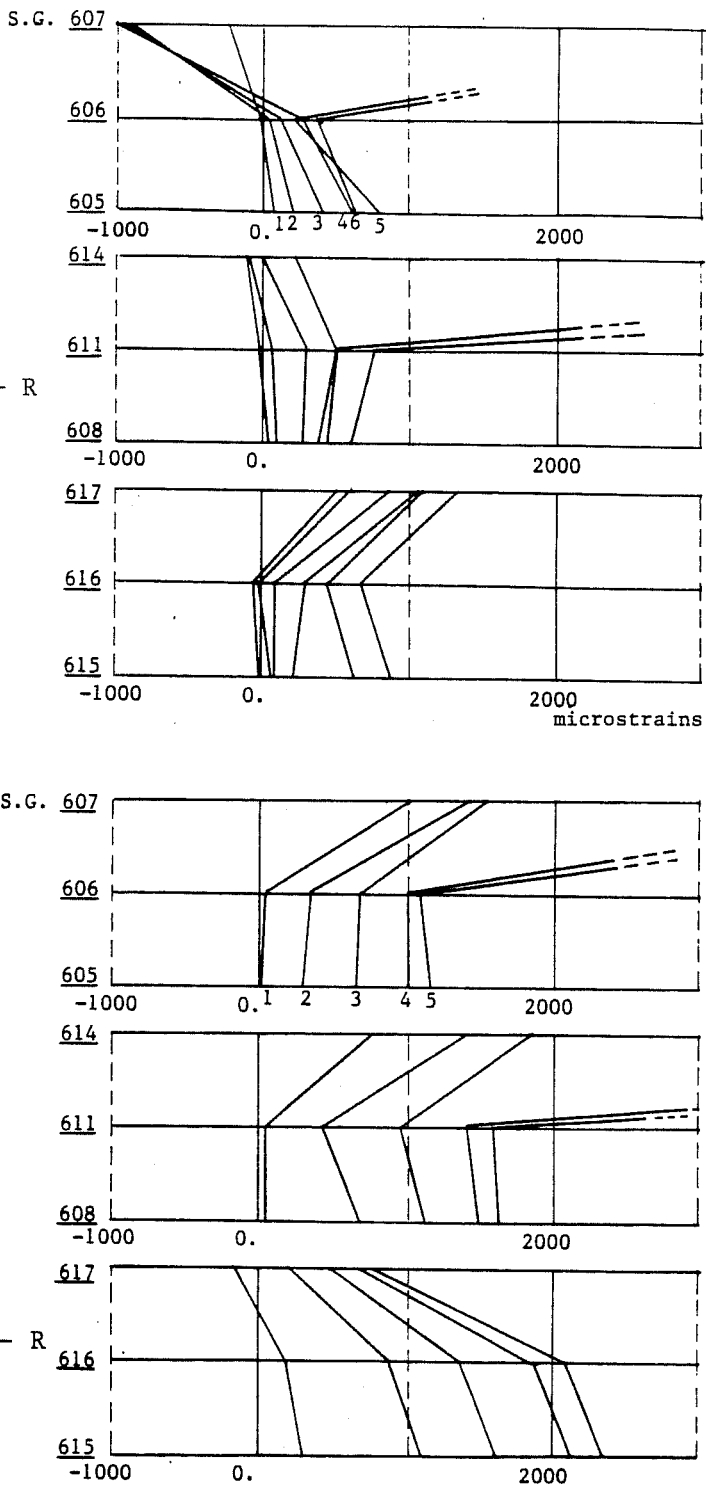
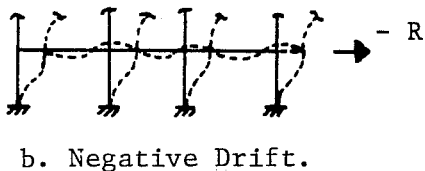


Fig. 6.44 - BRI Building - Interior Test Column Bar Strains.

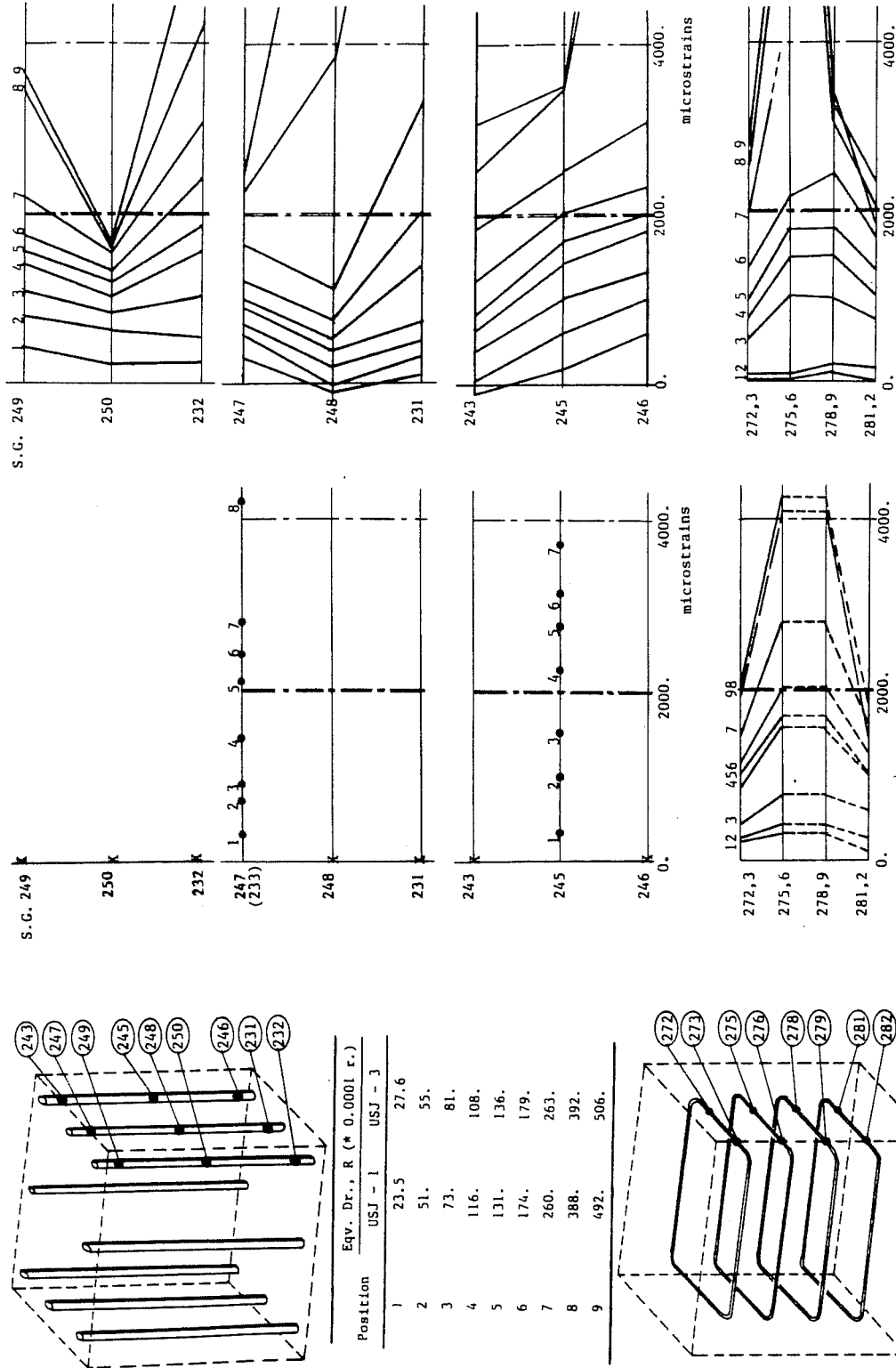


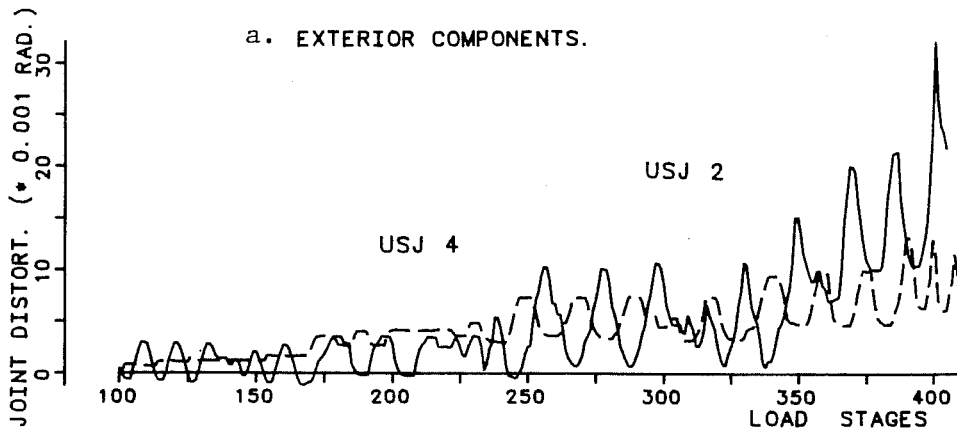
Fig. 6.45 - UTA - Interior Tests Column and Core Bar Strains. a. USJ - 1 . b. USJ - 3 .

Comparisons between the BRI building and the UTA component tests are also possible. For the exterior joint, column bar strains were below the yield level in both tests - Frame A/1 and USJ-2, for the maximum equivalent drift level of $R = +1/64$. For the interior joints, at a peak drift level $R = +1/64$ the column bars in USJ-1 reached yielding whereas in the BRI building (Frame A/2) they remained near 0.001. It must be noted that: (1) the BRI building joints at level Z2 had a certain amount of axial compression due to the dead load of the above floors; (2) USJ-2 suffered beam anchorage failure; and, (3) in specimen USJ-1 only a very few number of joint region strain gauges worked throughout the test.

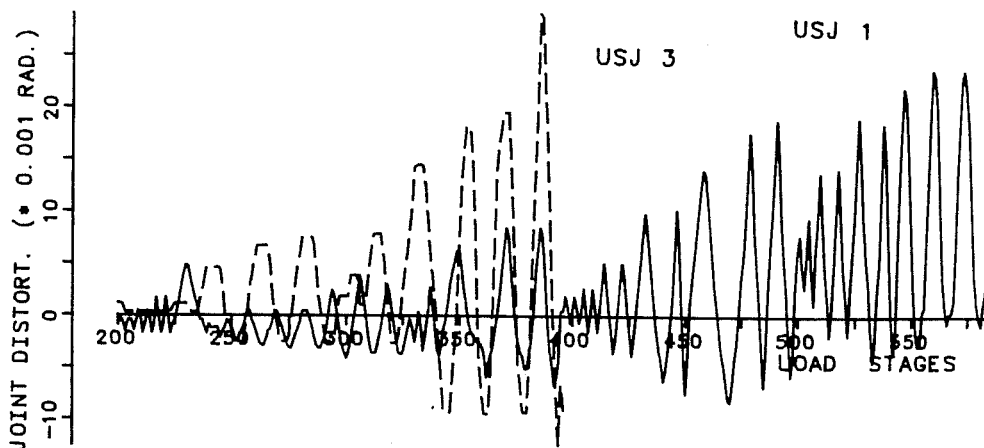
6.7.2 Joint Core Distortion. The distortion of the core due to joint shear is shown in Fig. 6.46. In the exterior specimens only positive distortion occurred because of the higher shear forces developed by the slab in tension. The maximum joint distortion was 0.00320 rad for USJ-2 (anchorage failure) and 0.00129 rad for USJ-4. The interior specimens showed both positive and negative joint distortions due to the alternate contribution of the E- and W-beams with the slab in tension. The specimen USJ-1 had a smaller response range of -0.0008 to +0.00240 rad as compared with USJ-3, -0.00125 to +0.00290 rad. This was to be expected since the beams were considerably stronger in USJ-3.

U. OF TEXAS : JOINT DISTORTION .

a. EXTERIOR COMPONENTS.



b. INTERIOR COMPONENTS .



c. JOINT DISTORTION AT FIRST PEAK DRIFTS .

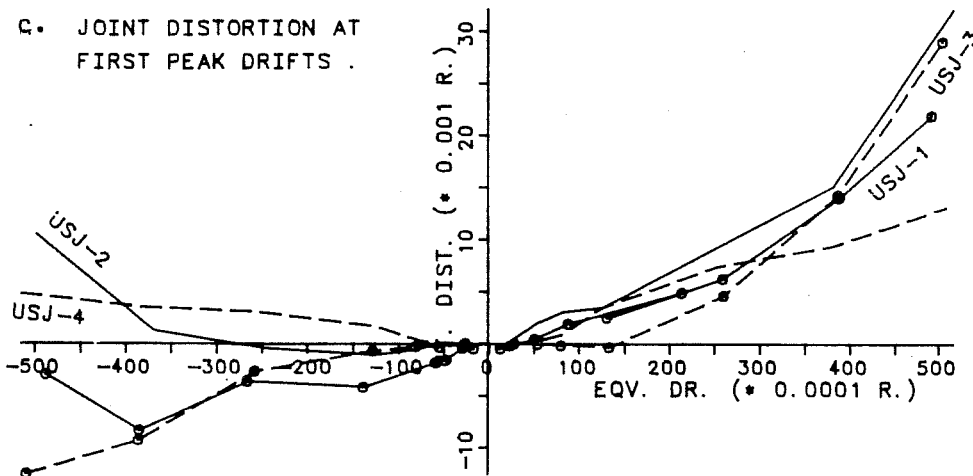


fig. 6.46 - UTA Tests Joint Core Distortion.

6.8 Transverse Beam Participation

The transverse beam plays an important role in the joint response. In order to study its role two major paths were followed: (1) evaluation of the beam twist and stiffness deterioration; and, (2) the spread of yielding throughout the transverse beam and slab cross section. With respect to the first point, it should be noted that the main deformation mode observed for the BRI building interior joint (transverse direction) was flexural instead of torsional. This resulted from the wall uplifting effect mentioned in the previous Chapters.

6.8.1 Transverse Beam Deformation. The BRI building had two interior and two exterior joints instrumented at level Z2, Fig. 3.5. The longitudinal beam rotation in frames A and B at transverse frame alignments 1 and 2 were instrumented with LVDT's placed at a distance $d/2$ from the column face. The transverse beam at the interior joint in frame A was also instrumented with LVDT's in span A-B near column A/2 and near column B/2 at a distance $d/2$ from the column face.

The interior joint beam rotation history is shown in Fig. 6.47. It can be seen that large changes occurred at LDS 450 and 1025 and may indicate a problem with the record for the 6.00m span, Fig. 6.47-a (longitudinal direction).

The transverse beam rotation near the interior joint at Frame A experienced flexural rotation. At the shear wall (Frame

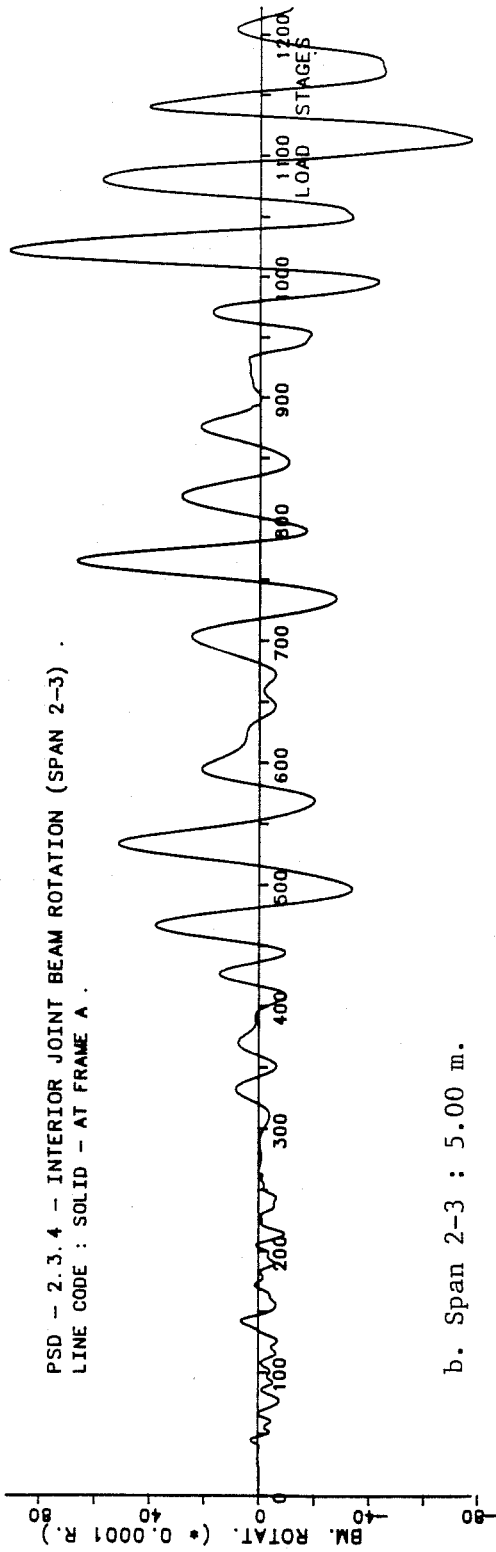
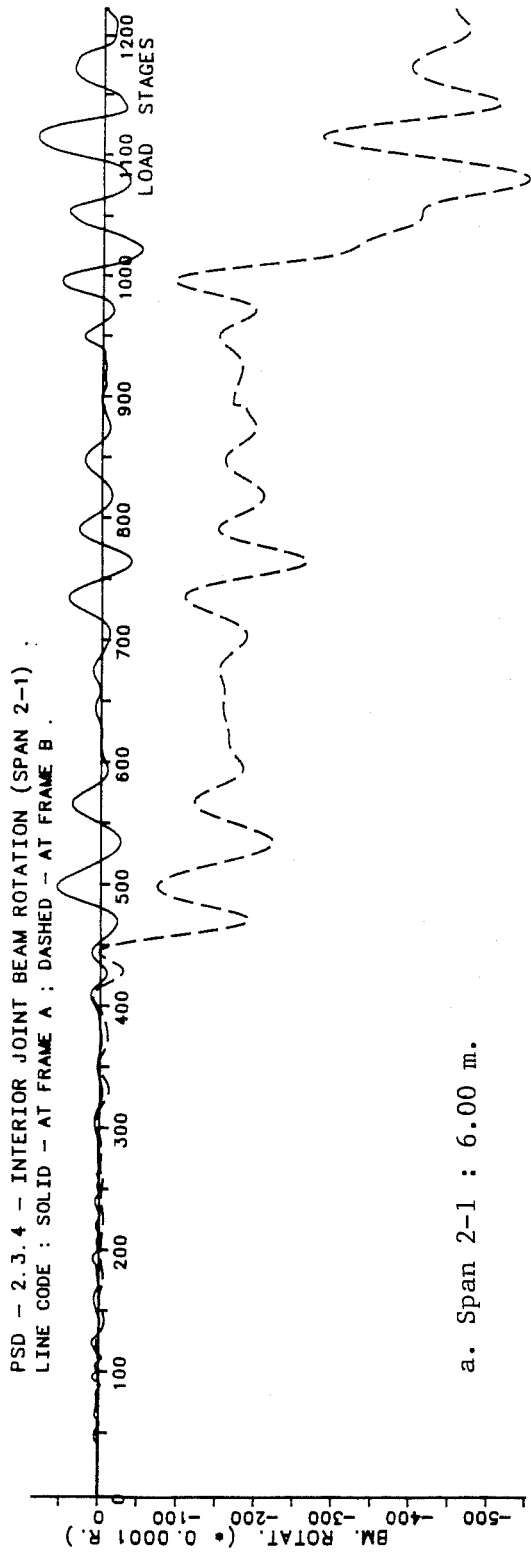


Fig. 6.47 - BRI Building - Interior Joint Beam Rotation History.

B) little rotation was observed, but axial compression or extension was noted, Fig. 6.48. This peculiar behavior may be due to the procedure used to measure deformation: the LVDT's were attached to reference rods inserted into the transverse beam instead of an independent external transverse frame to measure twist angles. The exterior beam rotation response is shown in Fig. 6.49. The observed beam rotations in Frame B (with shear wall) were larger than in the exterior joint of frame A.

A better understanding of the role played by rotations of the exterior and interior joints in both orthogonal directions is shown in Fig. 6.50. The exterior joint longitudinal beam rotation was nearly identical in both Frame A and B, at peak displacement drifts, Fig. 6.50-a. In this range, slightly larger rotations occurred in the frame B exterior joint. The interior joint beam rotation tended to be symmetrical about the vertical beam rotation axis in both span 2-1 (6.00 m) and span 2-3 (5.00 m) directions, Fig. 6.50-b. Another important aspect of transverse beam response was observed in the BRI building. Almost no beam rotation occurred at the transverse beam - shear wall connection (Frame B/2) when the building was pushed away from the strong wall (positive drift) because the shear wall boundary column was in compression, Fig. 6.50-c. However, when the same boundary column (Frame B/2) was subjected to tension, as the building was deflected towards the strong wall (negative

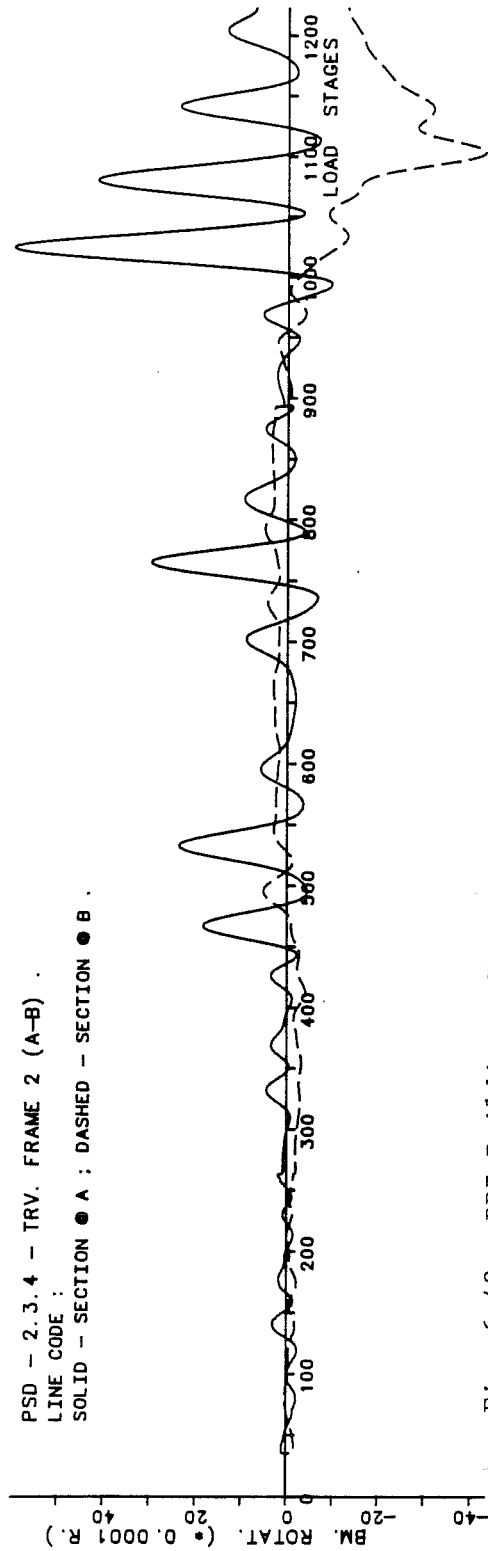


Fig. 6.48 - BRI Building - Transverse Beam Rotation.

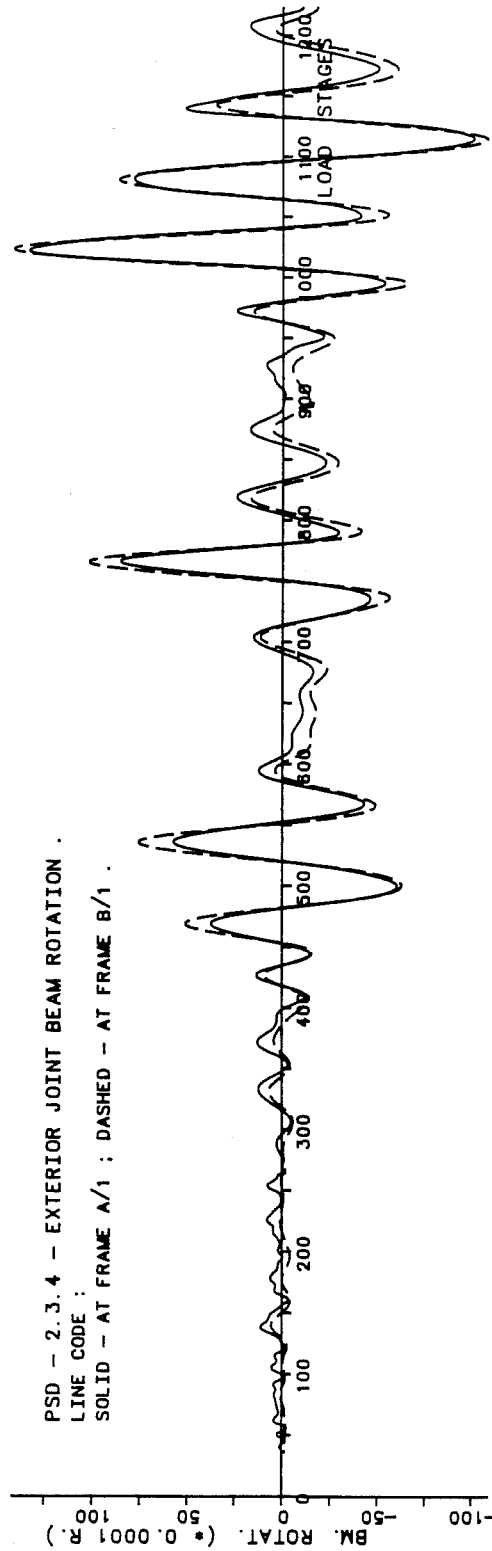
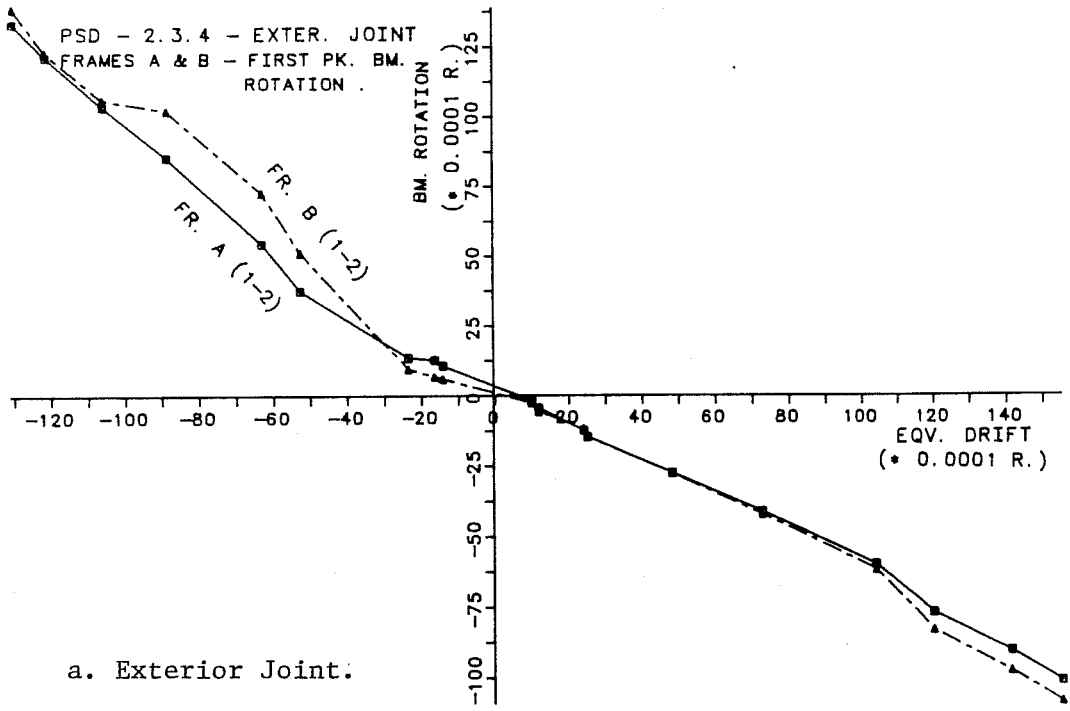
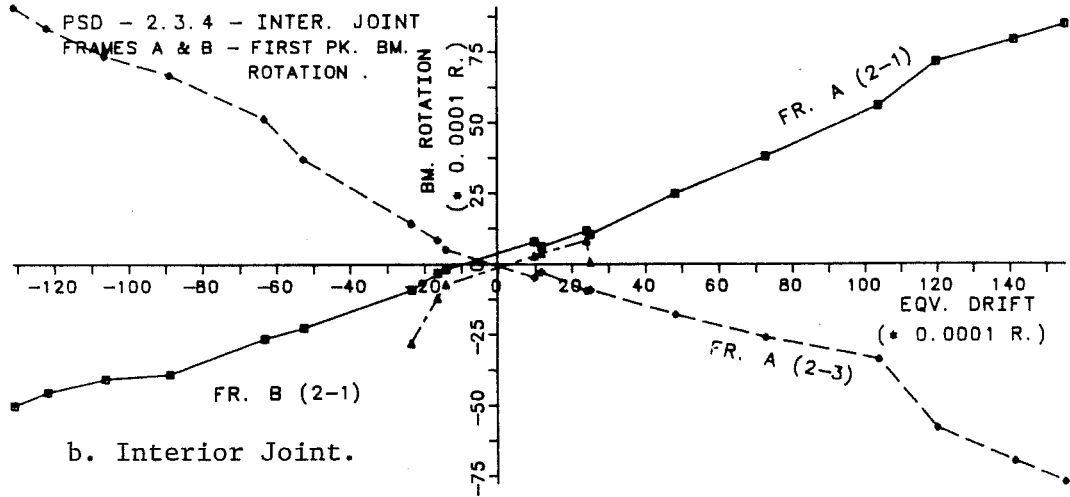


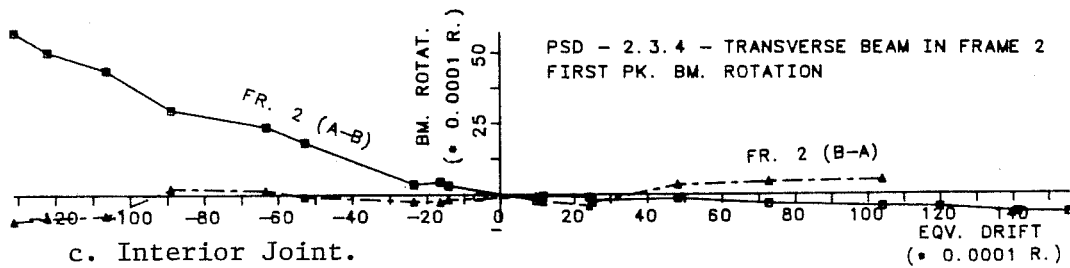
Fig. 6.49 - BRI Building - Exterior Joint Beam Rotation History.



a. Exterior Joint.



b. Interior Joint.



c. Interior Joint.

Fig. 6.50 - BRI Building - Beam Rotation at Level Z2.

drift), only the frame A/2 transverse beam joint region experienced rotation. The connection at the other end of the transverse beam (Frame B/2) didn't rotate within the distance $d/2$, Fig. 6.50-c, while the shear wall was uplifting.

The deformability of the transverse beams in the UTA components was assessed by the twist vs. equivalent drift. Two cross sections were instrumented to measure twist angles at 19.5 in. (0.50 m) and 63.5 in. (1.61 m) from the column face in order to determine the possible location of the torsional plastic hinge along the beam axis. It was observed that in both exterior, Fig. 6.51, and interior, Fig. 6.52, components, torsional plastic hinges may have formed in both transverse beams at a distance less than 0.50 m (19.7 in.) from the column face. This can be shown by the equal amount of twist observed near and far from the column face. The exterior joints also experienced "non-symmetric" twist depending on which direction the longitudinal beam was deformed and larger twists were observed in the south beam as compared with the north beam, Fig. 6.51. The interior specimens showed nearly symmetric twist behavior for both transverse beams, Fig. 6.52. The transverse beam rigid body twisting motion can be better shown in Figs. 6.53, 6.54. The symmetric response for the interior prototype and modified specimens at first peak drifts is shown in Figs. 6.53-a and 6.54-a, respectively. The exterior components showed different

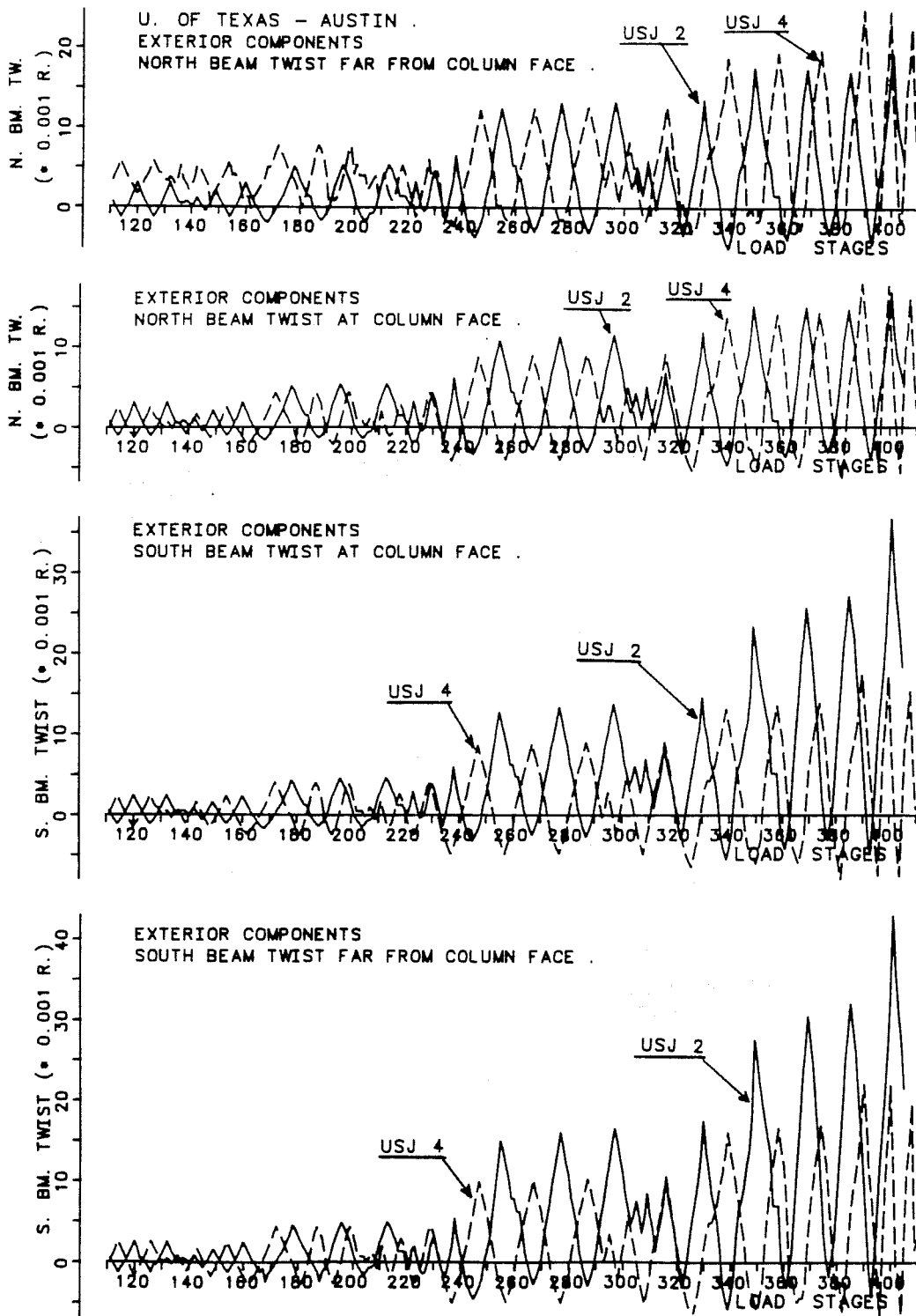


Fig. 6.51 - UTA Exterior Tests Beam Twist History.

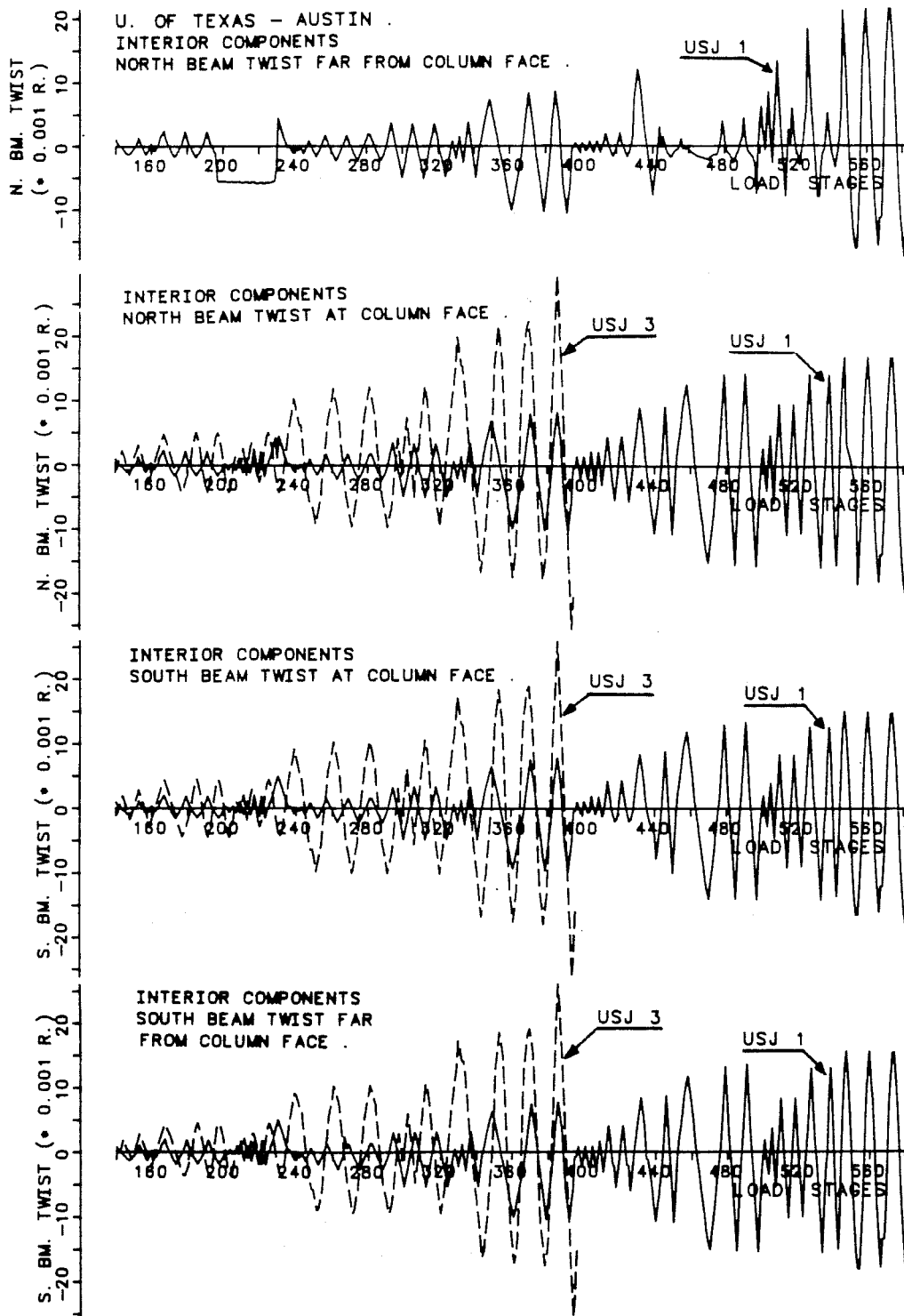


Fig. 6.52 - UTA Interior Tests Beam Twist History.

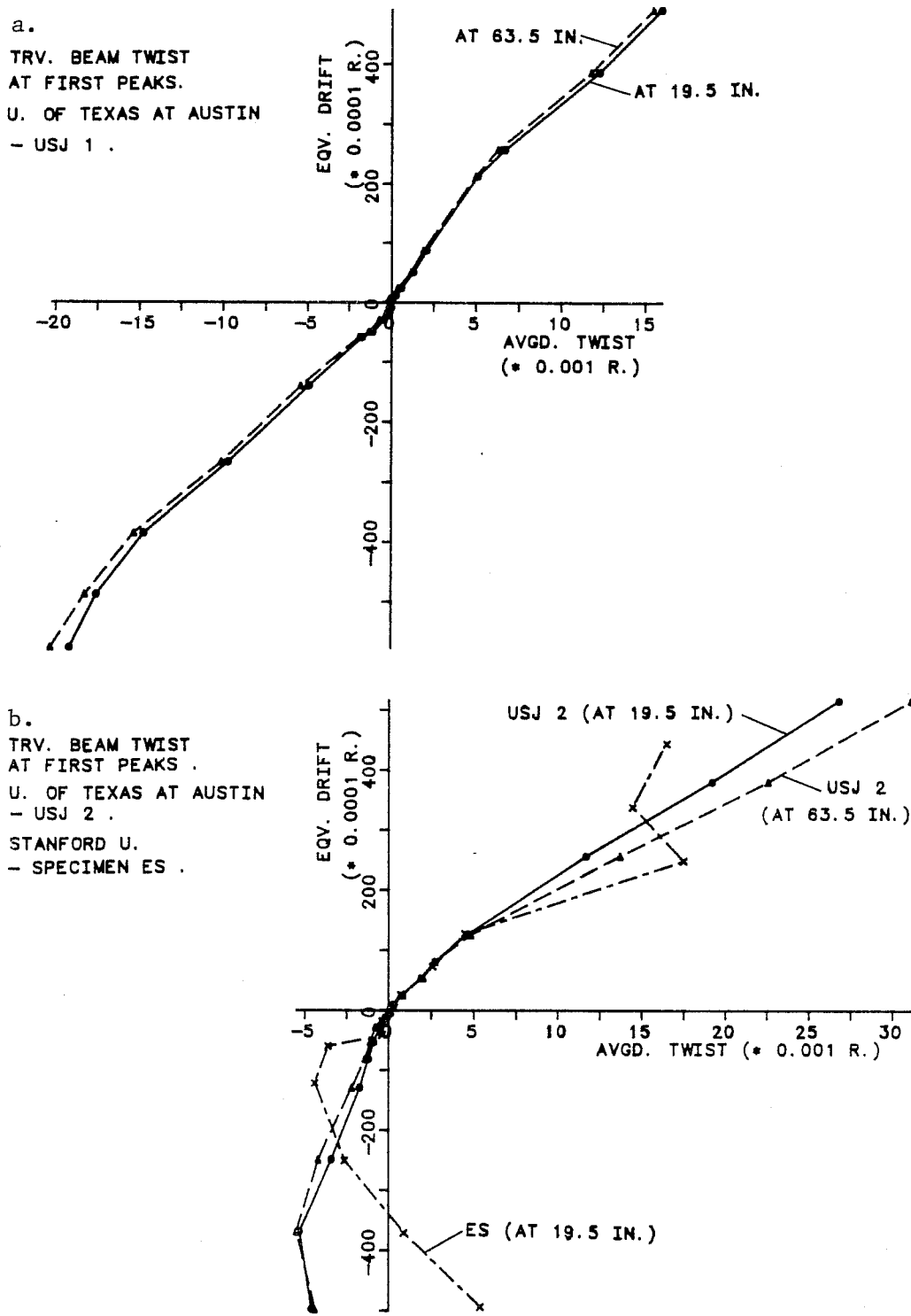
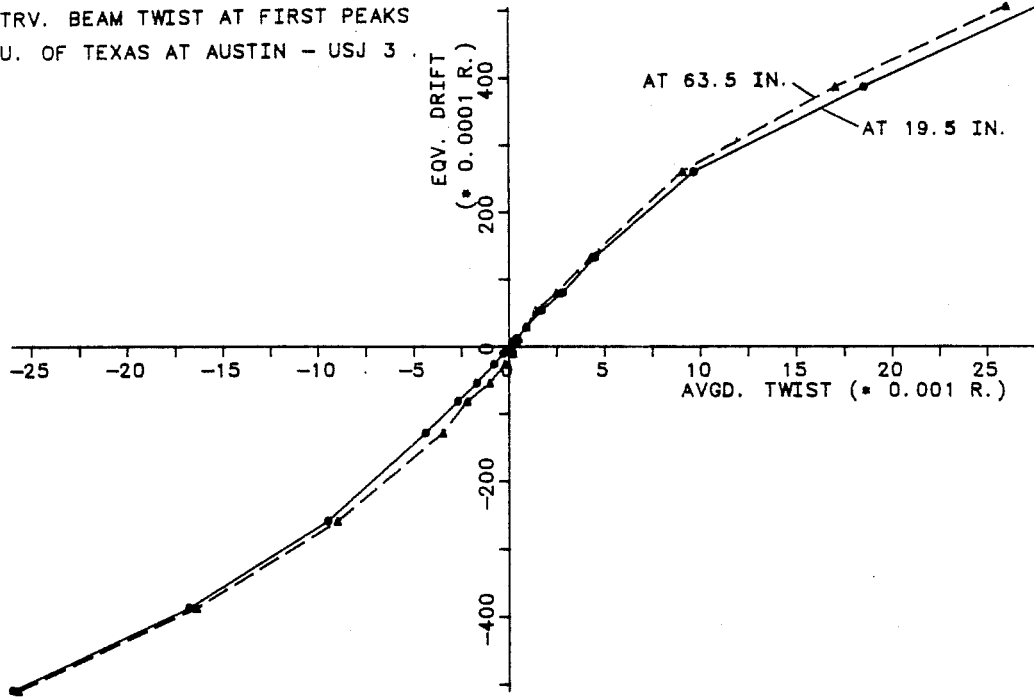


Fig. 6.53 - UTA Prototype Transverse Beam Response at First Peak Drifts.

a.
TRV. BEAM TWIST AT FIRST PEAKS
U. OF TEXAS AT AUSTIN - USJ 3 .



b.
TRV. BEAM TWIST AT FIRST PEAKS
U. OF TEXAS AT AUSTIN - USJ 4 .

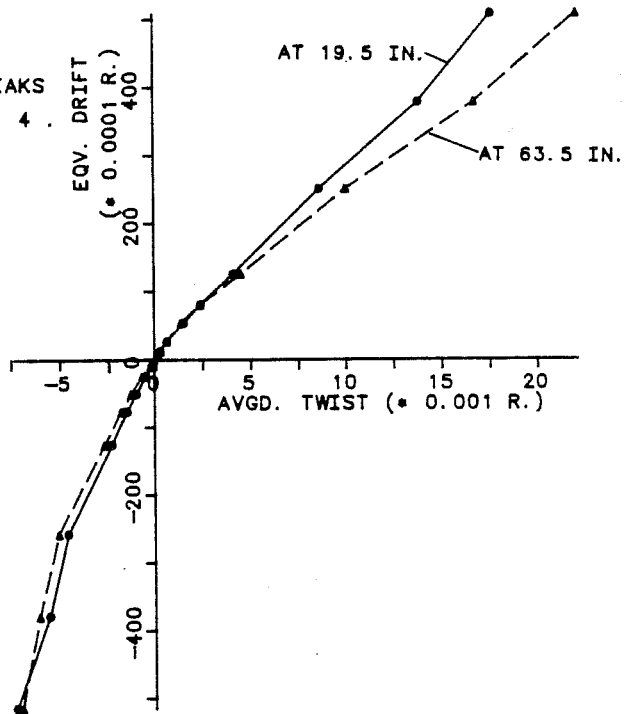


Fig. 6.54 - UTA Modified Transverse Beam Response at First Peak Drifts.

behavior when positive and negative drifts were applied. The amount of transverse beam twist was very large under positive drift (slab in tension) as compared when the slab was in compression (negative drift). The positive/negative twist ratio was 4:1 (USJ-2 prototype) and 6:1 (USJ-4 modified) when peak drifts reached $R = +1/20$, Figs. 6.53-b and 6.54-b. This phenomena was due to several factors: (1) larger beam loads were applied downwards (positive drift) than upwards; and, (2) the transverse beam stiffness was increased when the slab was pushed against the beam (L-beam action). However, it is possible that when a negative drift is applied some part of the force is used to close slab cracks and compress slab bars which have yielded in compression and consequently, the "start" of negative twist is delayed. This fact can be observed in the SU specimen (ES), Fig. 6.53-b, where permanent positive twist could not be overcome even at large negative peak drifts of $-1/25$, $-1/20$. This may result from bar sliding, bond destruction, microconcrete settling effect in the joint region of specimen ES.

A comparison among exterior and interior UTA specimens with the same transverse beam reinforcement detailing is given in Fig. 6.55. It can be seen that anchorage failure in USJ-2 led to a larger twist angle under positive drift.

6.8.2 Transverse Beam Stiffness Response. The transverse beam stiffness was computed for all the available

specimens by dividing half of the total moment applied to the joint by the twist angle at 19.7 in. (0.50m) from the column face, Fig. 6.56. It was assumed that: (1) the twist angles in both N- and S- sides near the column face were identical; (2) all the applied load was carried in torsion by the transverse beams; and, (3) the applied load was shared equally by the N- and S-transverse beams. Assumption (2) will be adjusted and discussed in the next Chapter. For the UTA specimens, the transverse beam stiffness history is shown in Fig. 6.57. The exterior component torsional stiffness was higher when the beam moved up than when the beam was loaded downwards. For the interior components the total twist moment was nearly constant during the test and there was no marked difference between positive and negative drift torsional stiffnesses during the test, Fig. 6.57.

The SU (ES) exterior component response was erratic during the initial portion of the test and consequently, it was truncated, Fig. 6.58.

A final summary for the different torsional stiffnesses at first peak drifts is shown in Fig. 6.59. It can be seen that: (1) a major drop in torsional stiffness occurred at early loading stages up to $R = 1/500 - 1/333$; (2) when the exterior component beam moved up (negative drift) the torsional stiffness matched

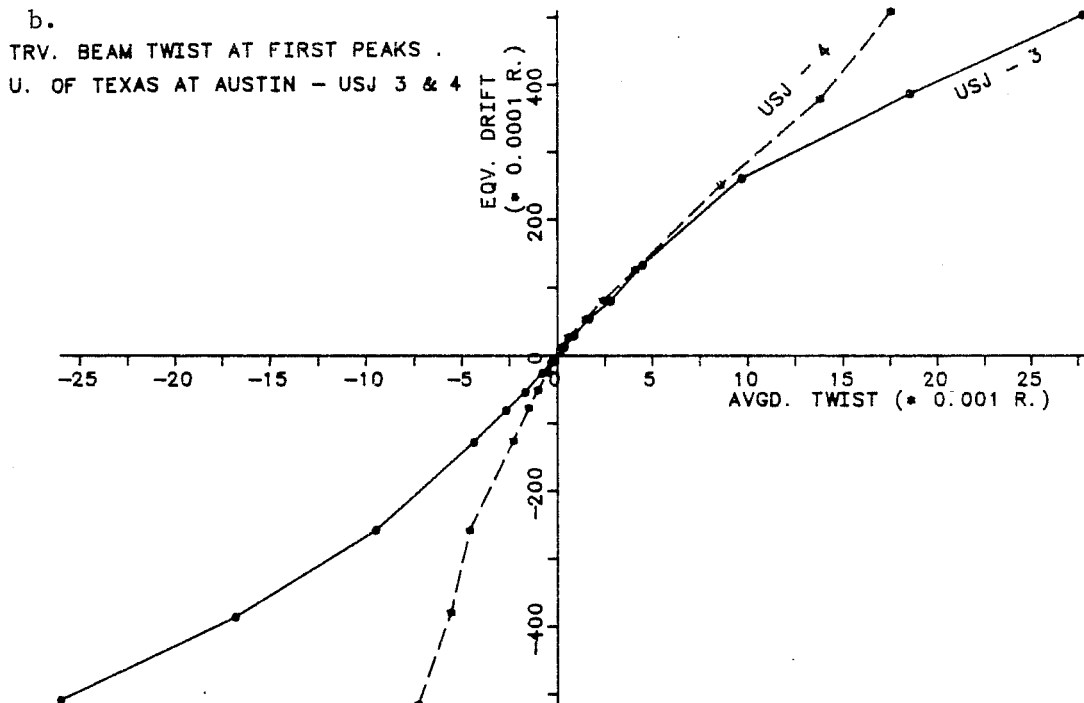
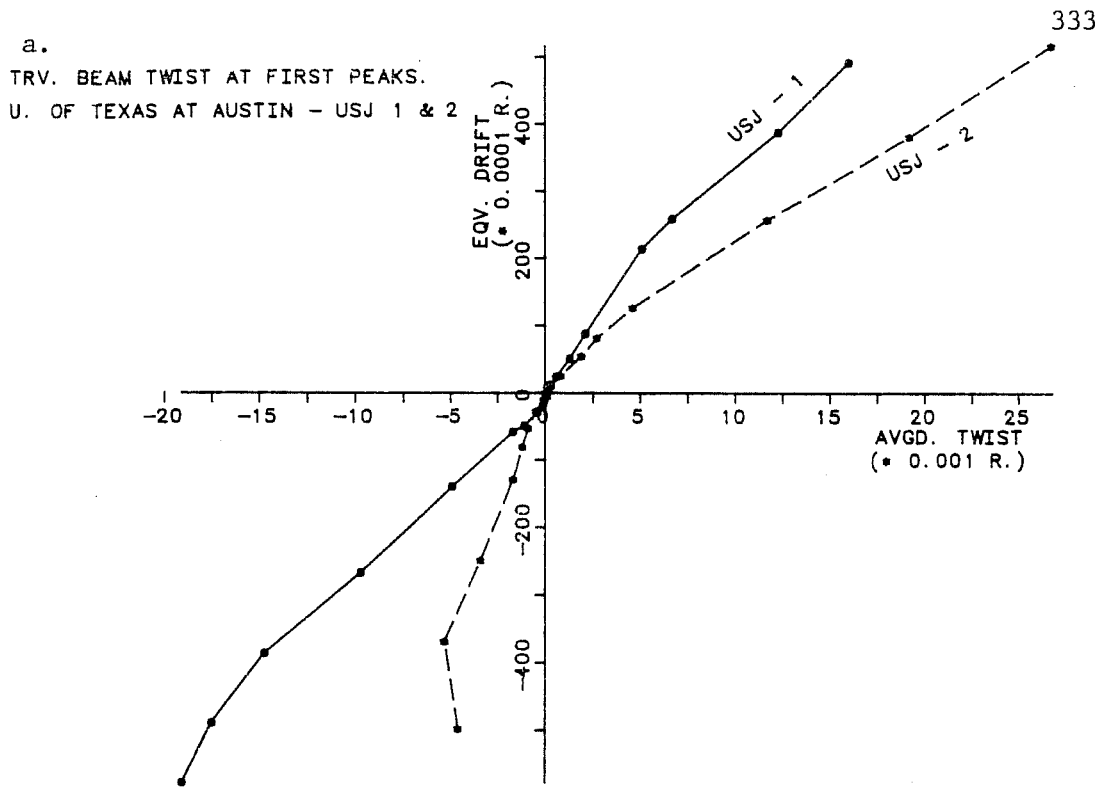
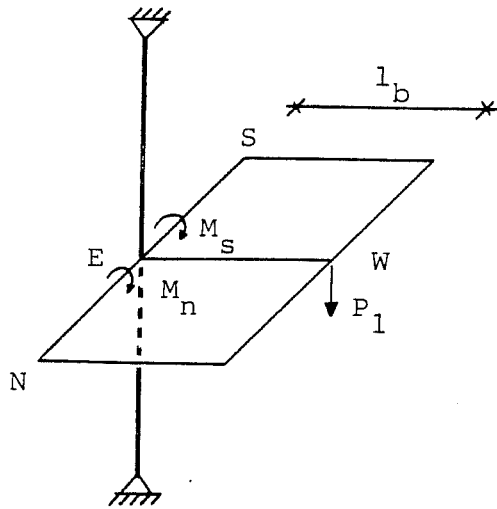


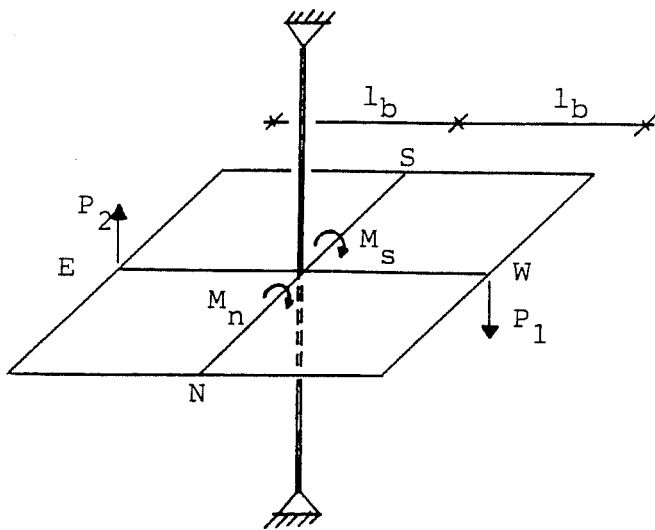
Fig. 6.55 - UTA Tests Transverse Beam Twist Response at First Peak Drifts.



$$M_n = M_s = M = \frac{P_1 \cdot l_b}{2}$$

$$K_{tors}^{sec} = \frac{M}{\phi_t}$$

a. Exterior Joint.



$$M_n = M_s = M^* = \frac{(P_1 + P_2) \cdot l_b}{2}$$

$$K_{tors}^{sec} = \frac{M^*}{\phi_t}$$

b. Interior Joint.

Fig. 6.56 Approximate Transverse Beam Secant Stiffness.

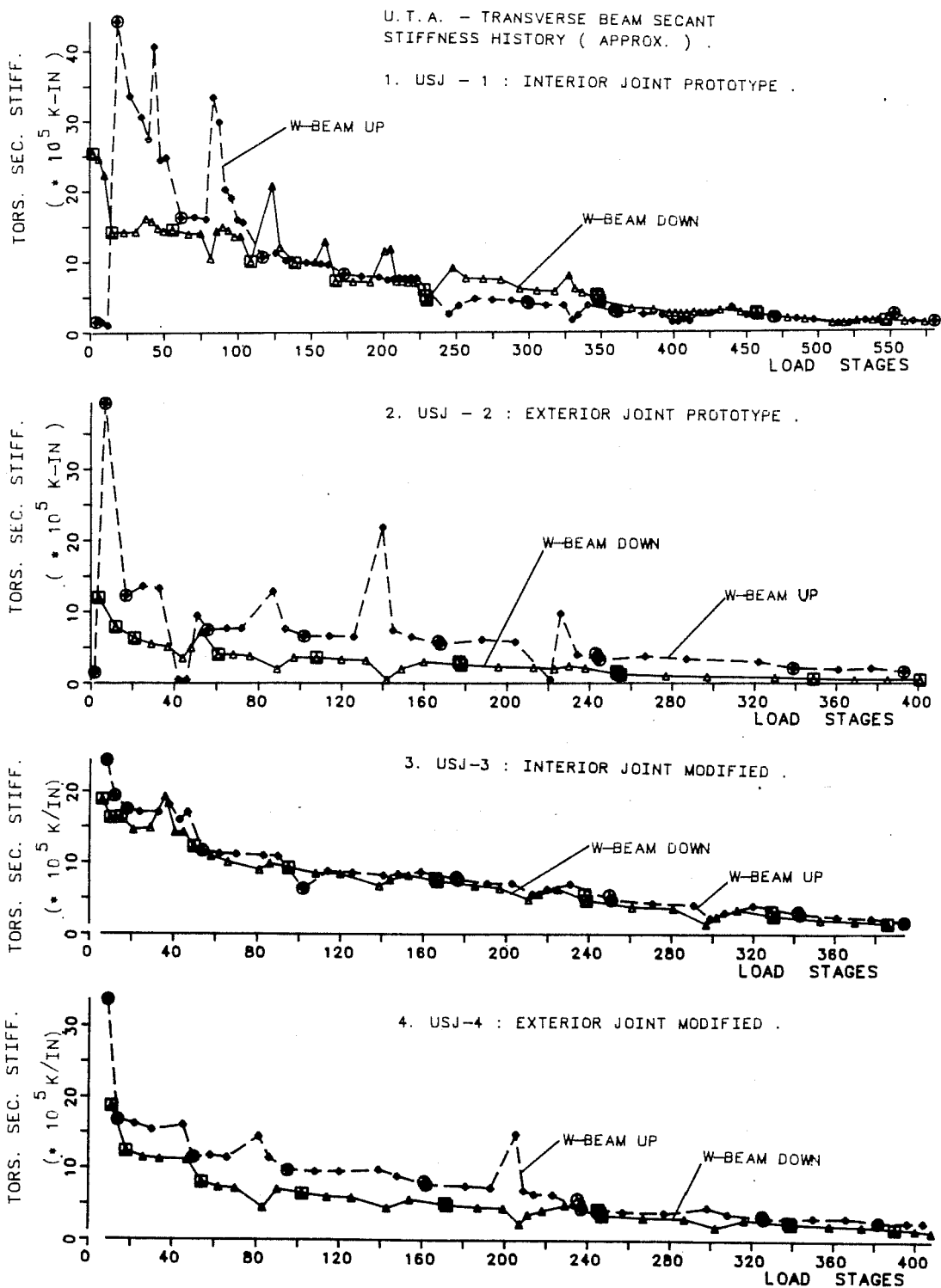


Fig. 6.57 - UTA Transverse Beam Secant Stiffness History.

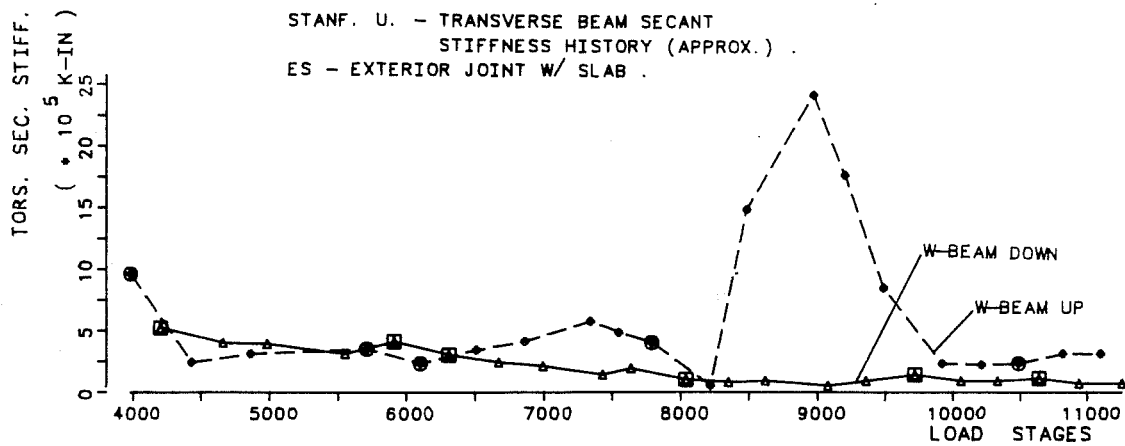


Fig. 6.58 - SU-ES - Transverse Beam Secant Stiffness History.

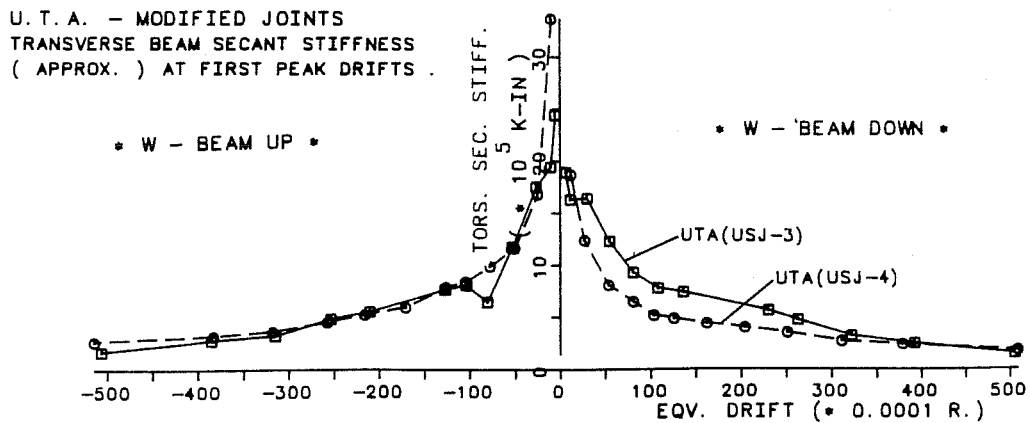
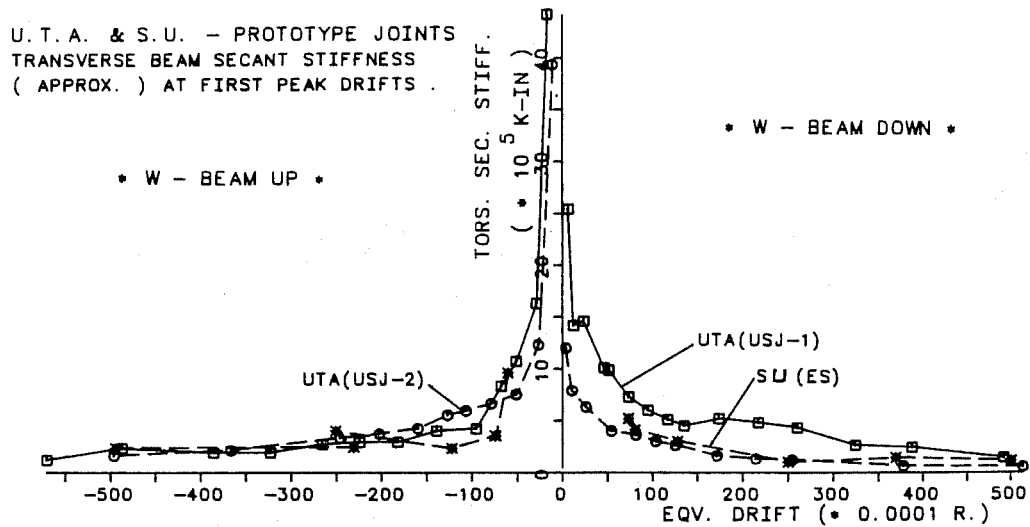


Fig. 6.59 - Transverse Beam Secant Stiffness at First Peak Drifts.

the interior component values quite well; (3) when the exterior component beam moved down (positive drift), the difference in torsional secant stiffnesses was evident up to equivalent drifts $R = 1/33 - 1/25$; (4) this difference became minimal for very large drifts ($R > 1/25$) in the interior components because of permanent damage (yield strains, cracking); and, (5) the modified components transverse beam stiffness was higher than in the prototypes because of the larger reinforcement ratios.

6.8.3 Transverse Beam Yielding. In the BRI building transverse direction (along the plane of loading), only the bottom slab bars in level Z2 were instrumented and the transverse beam bars framing into the wall. However, the alternating wall uplift effect can be seen in Figs. 6.60 and 6.61. Under positive drift, the bottom slab strains experienced a maximum peak strain of 0.002 (Frame B/3) at a peak drift $R = 1/64$. These bottom strains rapidly decreased along Frame B towards the midspan. Along Frame A, relatively large bottom strains of 0.001 occurred at the interior joint (column 3) and decreased towards the midspan along Frame A at the same peak drift $R = 1/64$, Fig. 6.60.

Under negative drifts, the shear wall uplifted in the region of Frame B/2. Transverse slab bar strains decreased near the regions of frame B/3 as well as the region of frame A/3. Transverse beam top bar strains in Frame A/2 showed small compression levels due to wall uplift, Fig. 6.61.

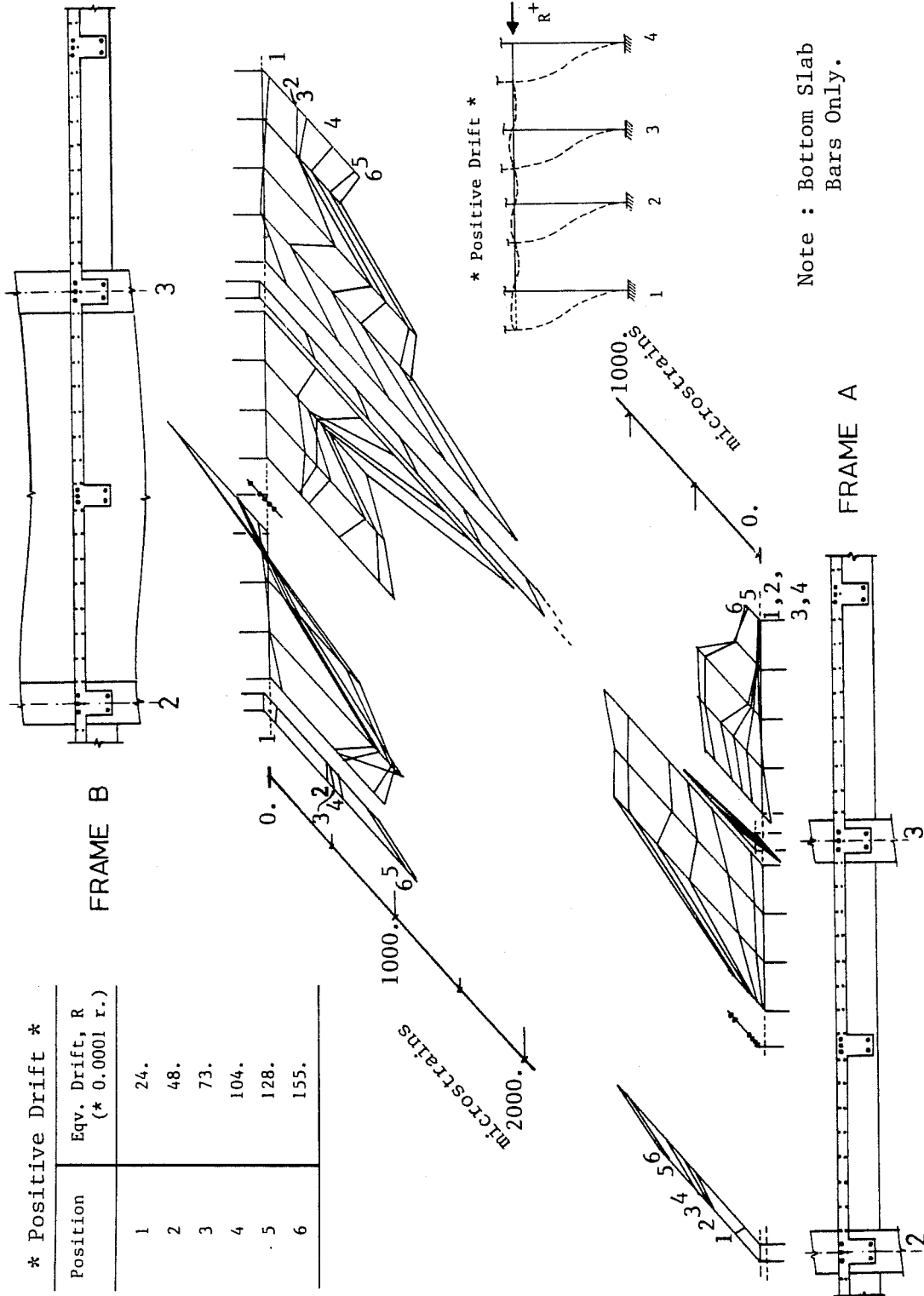


Fig. 6.60 - BRI Building Transverse Slab Yielding in Level Z2.

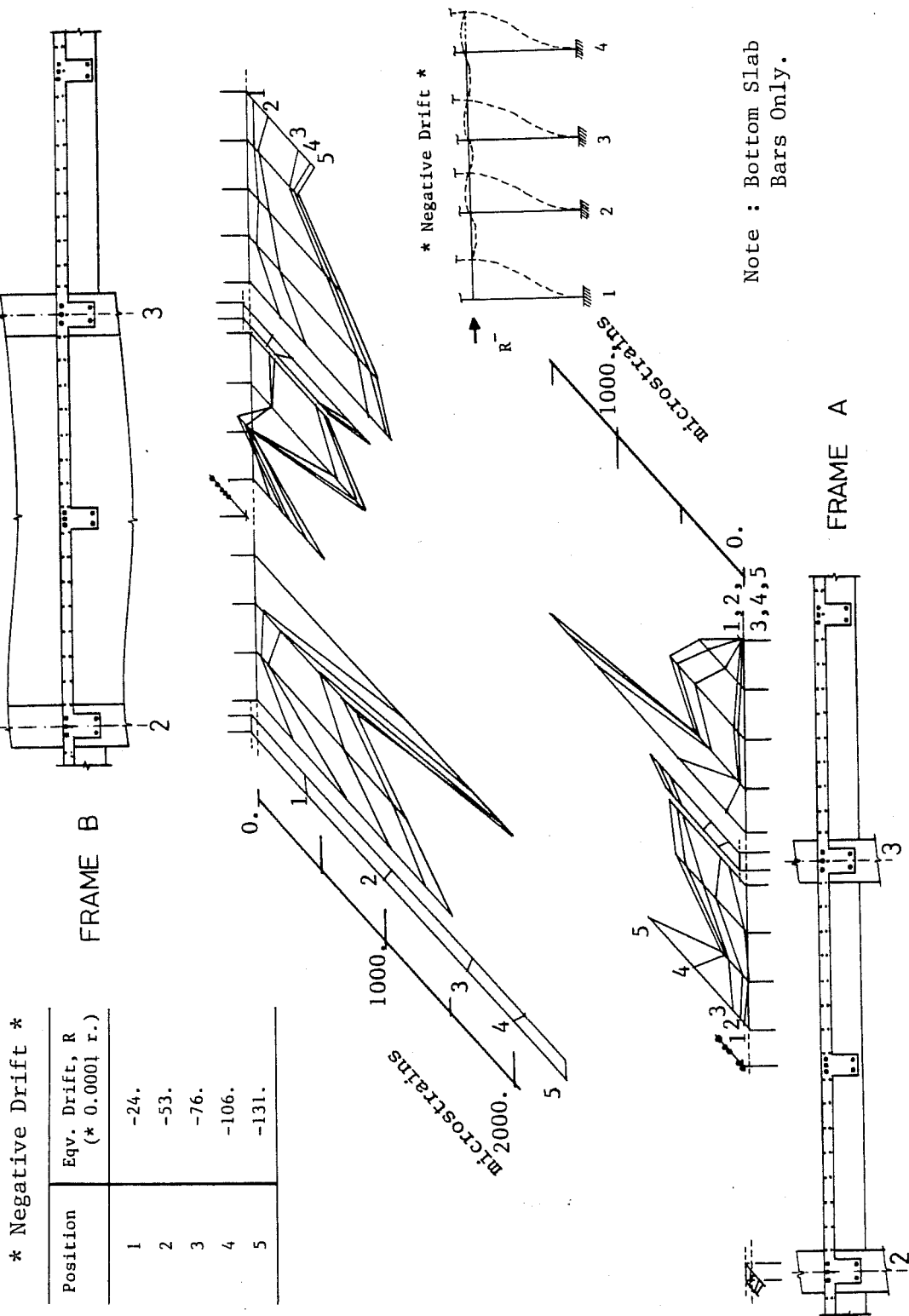


Fig. 6.61 - BRI Building - Transverse Slab Yielding in Level Z2.

The UTA component transverse beam bar strain distribution is plotted at two sections on the south side. The first section at 2.0 in. (0.05 m) and the second at 6.0 in. (0.15 m) from the column face.

The exterior components USJ-2, USJ-4 showed that beam bar yielding occurred only under positive drift (beam loaded down) at first peak drifts, $R = 1/59 - 1/40$. Under negative drift, bar strains remain quite low as smaller twists were applied in this direction, Figs. 6.51, 6.62 and 6.63. It also can be observed that bar strains were higher in the prototype than in the modified transverse beam (exterior component).

For the interior components, the observed bar strains remained about the same under either positive or negative peak drifts, Figs. 6.64 and 6.65. The transverse beam hoop bar strains were also generally higher in the interior as compared to the exterior components. This is likely due to the higher torsional moments produced by loading both beams instead of a single beam. In order to equilibrate these higher moments all the available reinforcement is mobilized into the resisting torsional mechanism.

6.9 Final Comments

The local response was evaluated through rotations, twists, strains and distortions in each of the component

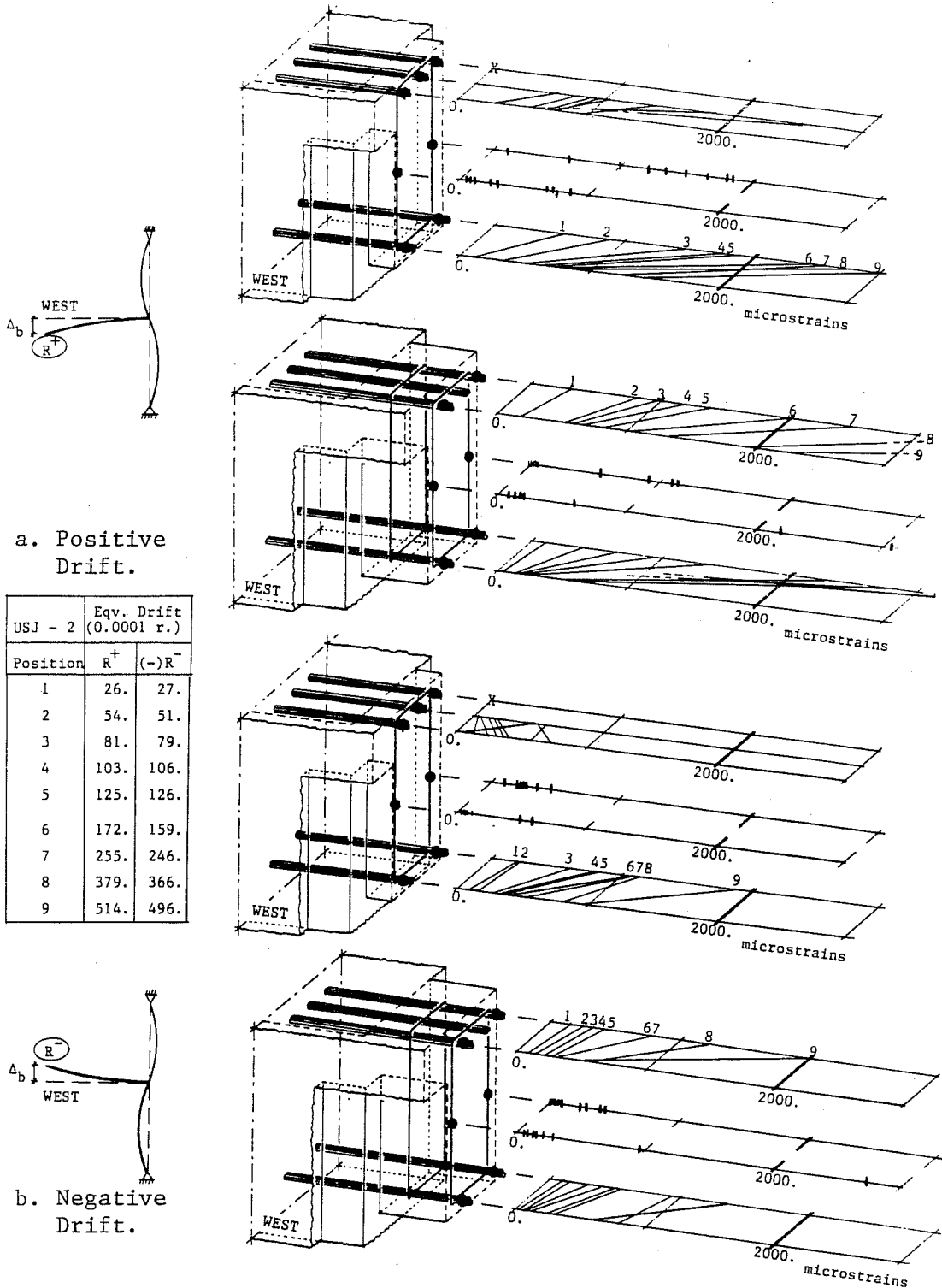


Fig. 6.62 - UTA - USJ-2 - Transverse Beam Strains.

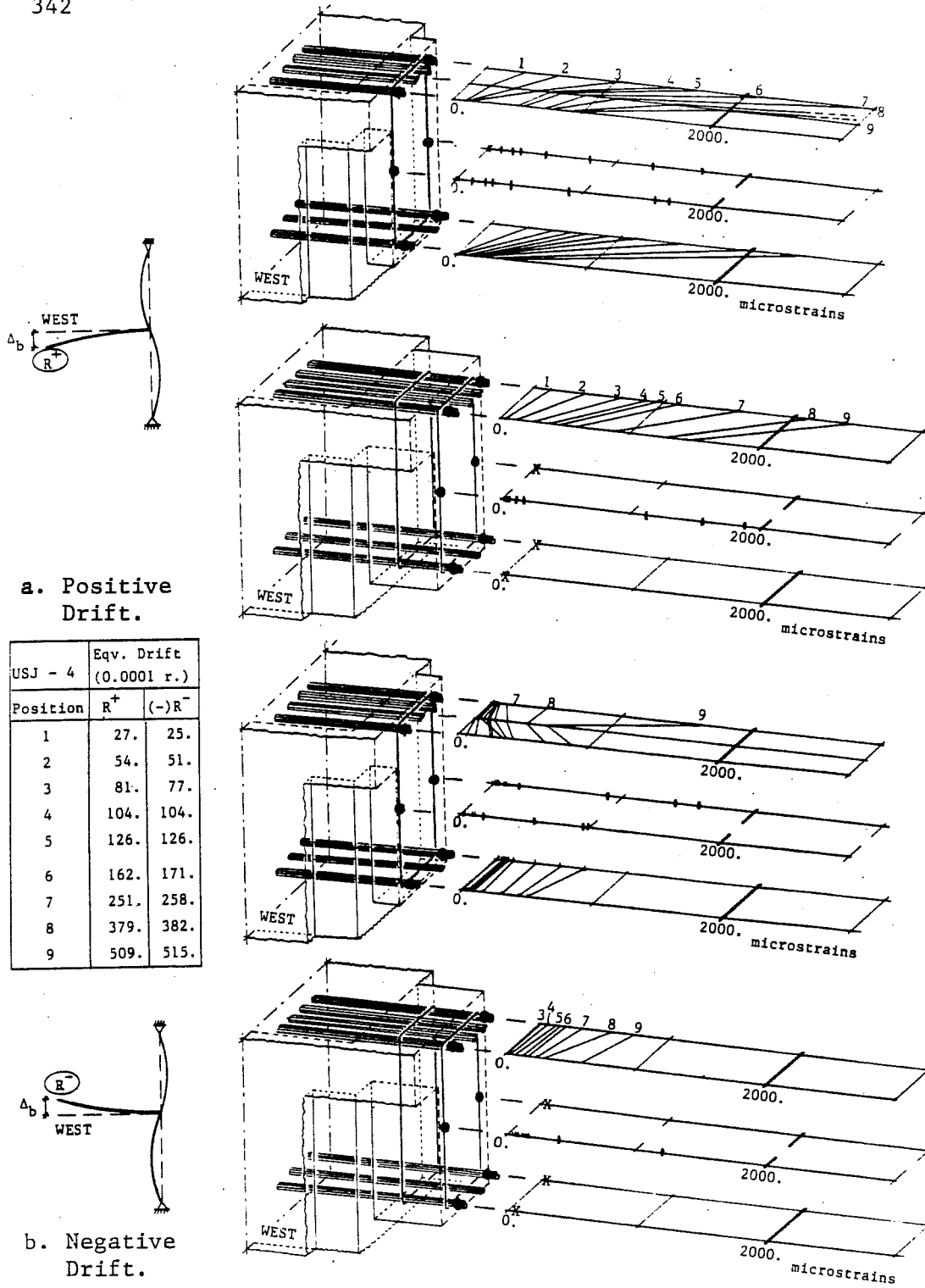


Fig. 6.63 - UTA - USJ-4 - Transverse Beam Strains.

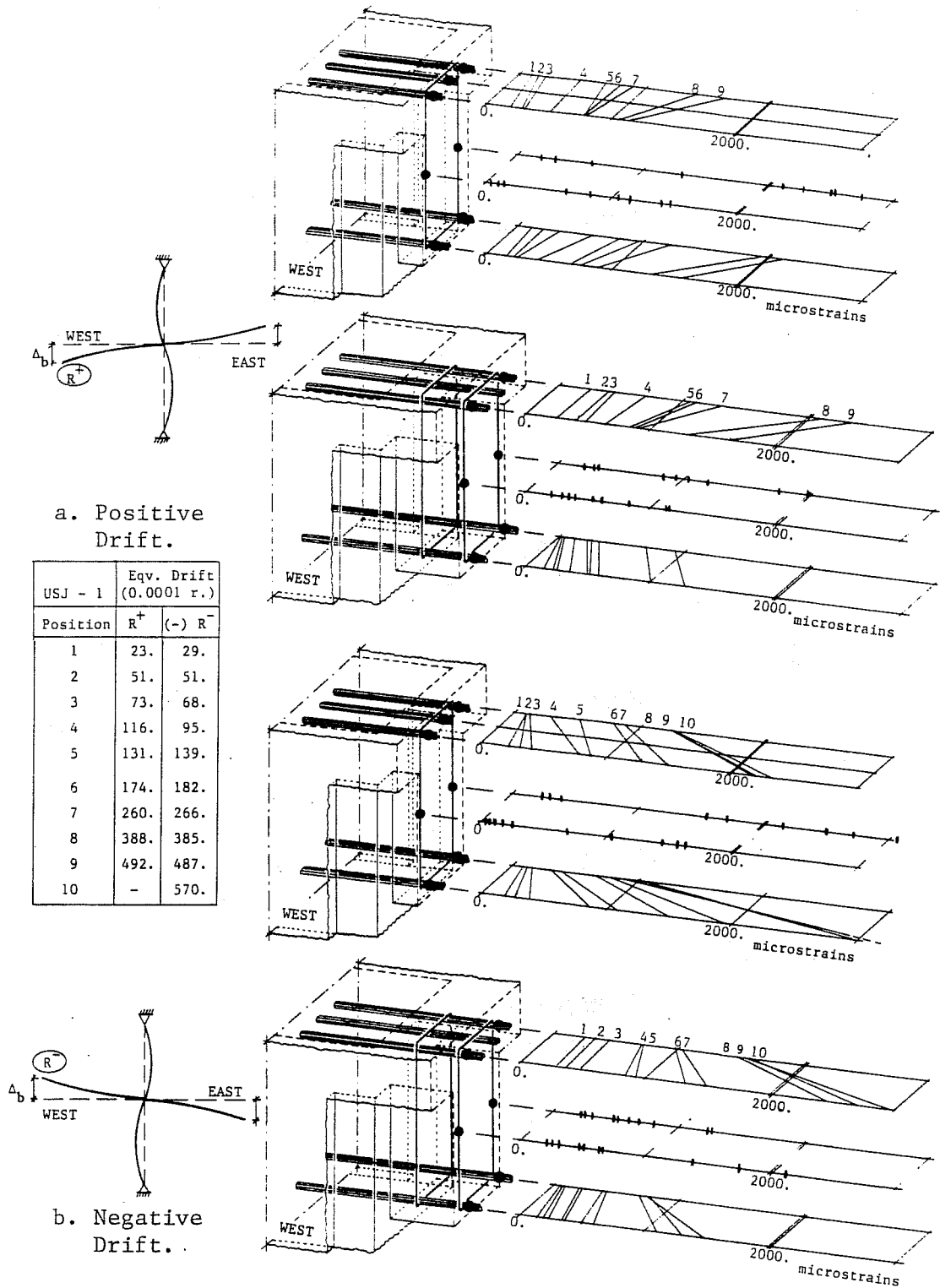


Fig. 6.64 - UTA - USJ-1 - Transverse Beam Strains.

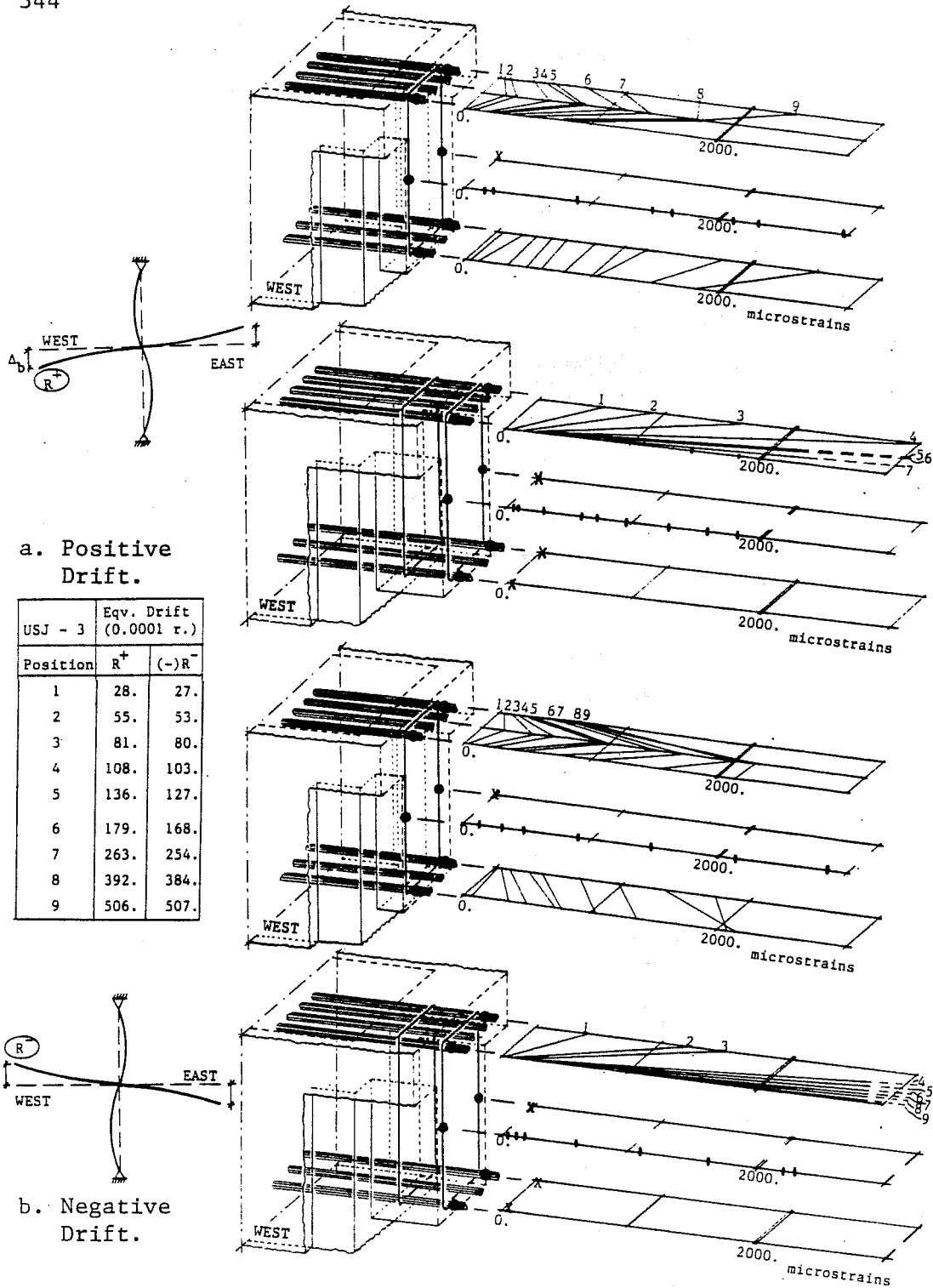


Fig. 6.65 - UTA - USJ-3 - Transverse Beam Strains.

elements. The important features in the exterior and interior component response are summarized below.

For the exterior components with a slab: (1) the maximum ultimate beam strength was reached at $R = 1/100 - 1/50$ when the slab was in tension and the strength agreed quite well with value computed using the code effective slab width; (2) the ultimate beam strength (slab in tension) would have been larger and nearly equal to the value computed by using the whole slab width (4.00 m) as effective, provided that anchorage details were satisfactory (ex: specimen USJ-4); (3) the maximum ultimate beam strength with the slab in compression was reached at $R = 1/100 - 1/50$; (4) the USJ-2 measured beam rotation agreed very well with measured rotations in the BRI building in the negative drift range (slab in compression) but the building was stiffer than the component when the slab was in tension; (5) the component beam rotation was concentrated within the first 6.0 in. (0.15 m) or $d/3$ length from the column face; (6) the beam secant stiffness response was stiffer when the slab was in tension than when the slab was in compression; (7) the component beam stiffness deteriorated up to drift values of about $R = +1/100$; (8) once the longitudinal beam bars reached tensile strains of 0.0005 - 0.0008, load reversals no longer produced compressive strains in the bars; (9) the spread of yielding across the slab was similar in the BRI building and in the component tests; (10)

the BRI building transverse beam restraint provided by the end walls was reflected by complete slab bar yielding at small deformation levels; (11) BRI column yielding in the joint region was not observed because of precompression from the dead load of the floors above; (12) the column bars and hoops in USJ-4 yielded at very large equivalent drifts of $R = 1/38$; (13) joint distortion in the exterior components was biased towards lateral deformations which placed the slab in tension (larger forces were applied in this direction); (14) transverse beam twist and plastic yielding were concentrated in a very small beam length d from the column face; (15) once cracking occurred, transverse beam secant stiffness dropped drastically after a few loading cycles; (16) the full-scale and small-scale transverse beam stiffness degradations were similar.

The interior components and BRI building interior joint region response was governed mainly by symmetry of dimensions and reinforcement about the column. The main features of response were: (1) the maximum ultimate beam strength was reached at a drift level $R = 1/50 - 1/33$, for the slab in tension and it was about equal to the value computed using the entire slab width instead of the design code effective width; (2) the small-scale SU component was nearly twice as flexible as the equivalent full-scale UTA component at a drift level $R = +1/100$; (3) most of the

component (UTA, SU) beam rotations were concentrated in a distance $d/3$ from the column face; (4) the beam secant stiffness was markedly higher when the slab was in tension than when the slab was in compression; (5) the beam bars did not exhibit compression under load reversal once tensile strains from 0.0005 to 0.0008 were reached; (6) beam bar slip in USJ-1 was 2-3 times less than in the USJ-3; (7) large strains were observed in the bottom slab bars near the column support at a drift level of $1/100 - 1/77$; (8) yielding of slab bars was observed in the interior component at a drift $R = 1/62$; (9) the UTA interior component joint core reinforcement showed yielding at a peak drift level of $1/57$; (10) the UTA interior component joint distortion was nearly symmetric in both displacement directions; (11) the BRI transverse beam plastic hinge rotation was developed over a distance greater than $d/3$ from the shear wall face and was only observed when the column was in tension due to shear wall uplift; (12) transverse beam torsional plastic yielding was observed over a distance $d/3$ from the column face; (13) transverse beam twist response was similar in both directions of loading; (14) a drastic reduction in torsional stiffness was noted in the $1/200 - 1/100$ drift range; (15) extensive slab yielding occurred in the BRI building near the shear wall under uplifting; and, (16) good correlation was obtained between the

full-scale and the small-scale transverse beam component response.

The 1/2-scale Japanese and the small-scale SU tests without a slab demonstrated the important role played by the slab when results were compared for similar specimens with a slab. Without a slab, smaller beam tip loads were developed in the component. Furthermore, the transverse beam was "inactive" because there was no continuity between the longitudinal beam and transverse beam in the absence of a linking slab.

The range of component scales from the full (1:1) to small-scale (1:12.5) proved to be very useful in studying local response. The tests showed satisfactory response when compared with the BRI building equivalent critical regions in spite of different boundary conditions, loading methods and geometric scaling.

6.10 References

1. ACI Committee 318 - Building Code Requirements for Reinforced Concrete and Commentary. American Concrete Institute (ACI), Detroit, MI, 1983.
2. AIJ - Standard for Structural Calculation of Reinforced Concrete Structures (English version). The Architectural Institute of Japan (AIJ), Tokyo, Japan, 1980.

CHAPTER VII

ENERGY ASSESSMENT IN TEST RESPONSE

7.1 Introduction

The earthquake phenomena involves the release over a short time interval of large amounts of strain energy stored in the tectonic plates. Part of the strain energy is liberated from the focal region as a seismic-wave motion. The remaining portion is transformed into potential energy that generates crustal deformation and energy absorption by rock destruction fault slippage [Wakabayashi (18)].

For shallow earthquakes, the energy E (in ergs) being released and the seismic magnitude, M , have been related empirically by Richter (14) as:

$$\ln E = 11.4 + 1.5 M \quad (7.1)$$

An analogy relating the different factors influencing seismic actions - magnitude, released energy, effect on constructions, comparisons with other energy events - is provided by Fig. 7.1 [Carvalho and Oliveira (4)].

The seismic action on a building has been identified as a two-phase process [Borg (3)]: (1) an initial transient-phase corresponding to a "shudder" going up through the construction; and, (2) the steady-state response phase where the building

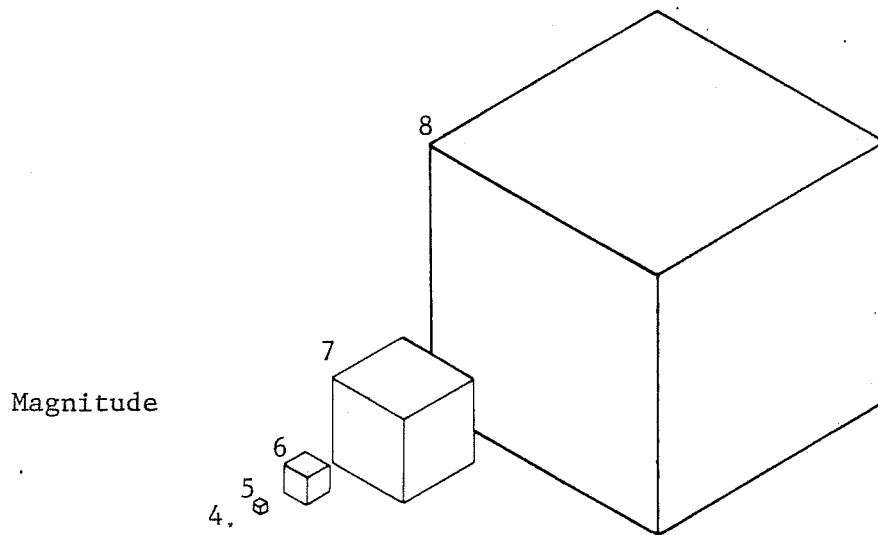
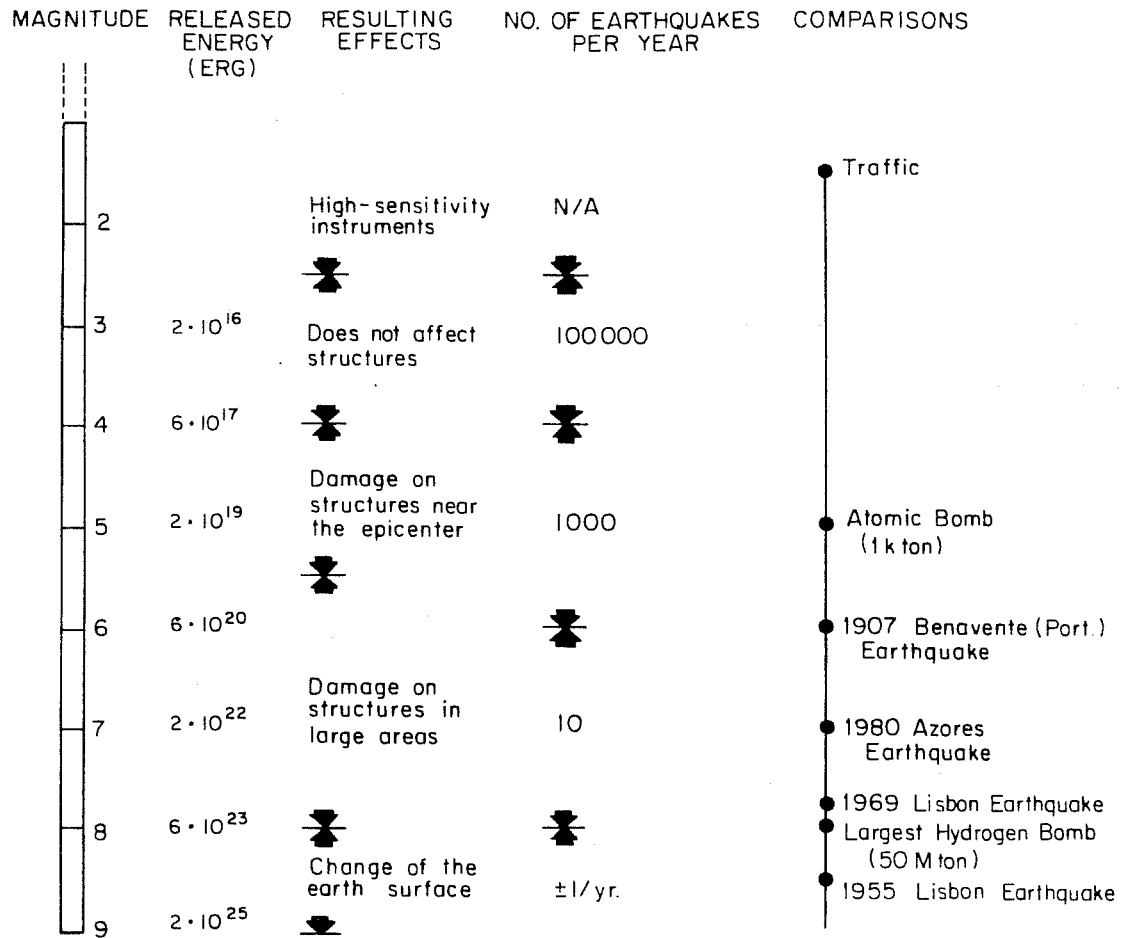


Fig. 7.1 - Earthquake Magnitude Interpretation.

begins to vibrate (sway). The initial excitation is due to the shear wave travelling up the building height which generates shear deflections and balances the inertial forces. During this period, bending moments are also introduced but bending deflections are not yet fully developed, Fig. 7.2. Following the transitory phase, fully developed bending moments are acting upon the structure and develop flexural stresses and deformations. These flexural deformations are responsible for most of the energy absorption - dissipation mechanisms. In a flexural system, the bending strain energy often processes most of the energy input to the structure. It can be uncoupled using symmetric and skew-symmetric components, Fig. 7.2.

The tests conducted on finite-bounded components provide a good opportunity to perform studies on the energy response of each element and to evaluate their role in global response of a structure.

7.2 The Energy of Deformation

Under a deformation process, the elastic body response is given by the total work of the applied forces, W :

$$W = U + K \quad (7.2)$$

where: U = potential energy of deformation (strain energy); and

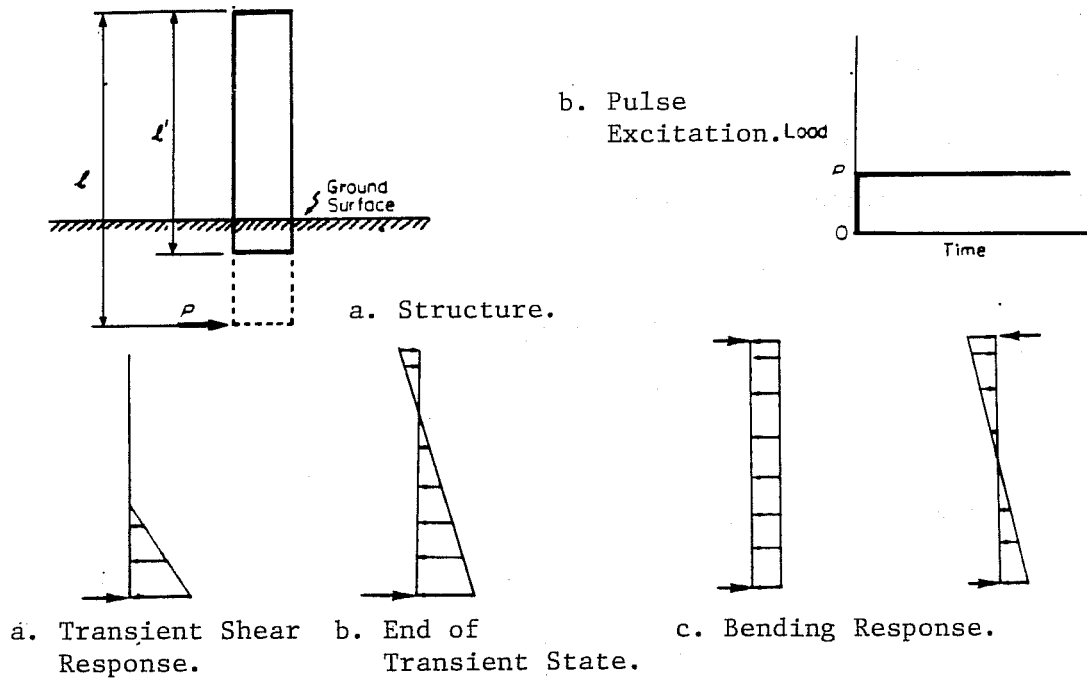
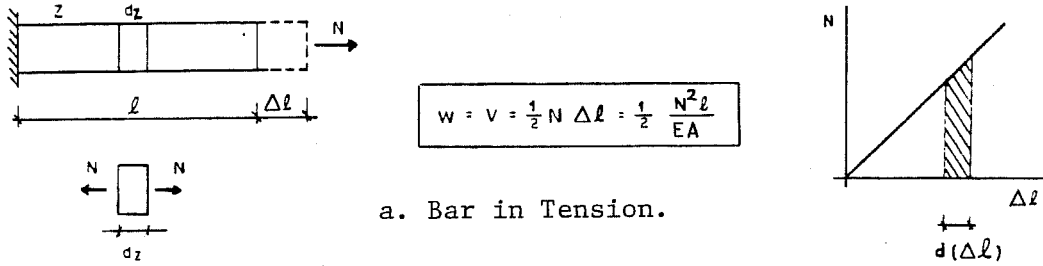
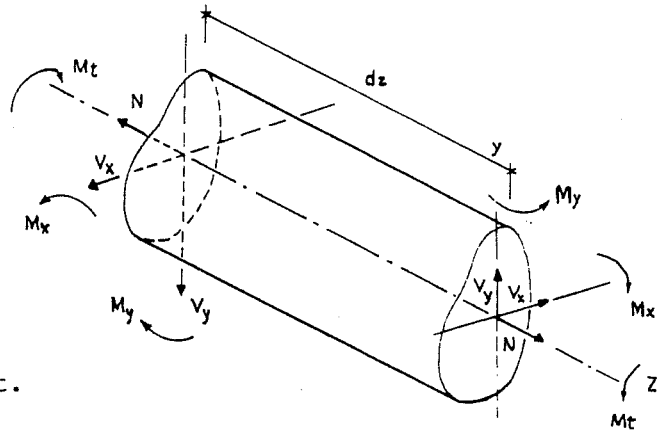


Fig. 7.2 - Building Seismic Excitation.



b. Spatial Beam.

Fig. 7.3 - Bar Element.



K = kinetic energy of the body mass under a certain velocity, v .

If the external forces are gently applied into the body, $K \rightarrow 0$, and all the external force work is converted into strain energy:

$$W = U \quad (7.3)$$

When the applied load is removed, work is produced by the stored strain energy, as shown for a bar element, Fig. 7.3-a.

The elementary strain energy in a space beam results from the algebraic sum of the work produced by each of the six independent generalized forces:

$$dU = dU(V_x) + dU(V_y) + dU(N) + dU(M_x) + dU(M_y) + dU(M_t) \quad (7.4)$$

where: N = axial force; V_x, V_y = shear forces along $\overline{OX}, \overline{OY}$;
 M_x, M_y = bending moments along $\overline{OX}, \overline{OY}$; and M_t = torsional moment.

Or for a beam element of length dz , Fig. 7.3-b:

$$dU = \frac{N^2}{2EA} dz + \frac{k_x V_x^2}{2GA} dz + \frac{k_y V_y^2}{2GA} dz + \frac{M_x^2}{2EI_x} dz + \frac{M_y^2}{2EI_y} dz + \frac{M_t^2}{2GJ} dz \quad (7.5)$$

where: A = cross section area; I_x, I_y = moment of inertia about $\overline{OX}, \overline{OY}$; J = torsional constant; E = Young

modulus; G = shear modulus; k_x, k_y = shear shape constants.

Considering only in-plane loading (plane YZ) on a beam element, the resultant strain energy (bending only) is:

$$dU = \frac{M^2}{2EI} dz \quad (7.6)$$

This equation requires that the loads are gradually applied, i.e., the beam will be in deflection equilibrium as well as static equilibrium at all times [Borg (3)]. However, for instantaneous loads the beam does not have enough time to deform in flexure, the strain energy is given by:

$$dU = \frac{M^2}{EI} dz \quad (7.7)$$

This is the strain energy introduced into the system (under constant loading) of which 1/2 is required for the quasi-static balancing of inertia loads and the other 1/2 is dissipated through vibratory energy (vibrating structure), Fig. 7.2-b.

Energy studies have been recognized as a useful tool to assess the total building energy response. An example is given in Figure 7.4 for an important facility under the first few seconds of the N-S El Centro 1940 earthquake component, Fig. 7.4, [Dowrick (8)]. The excitation has been amplified by a factor of 1.5.

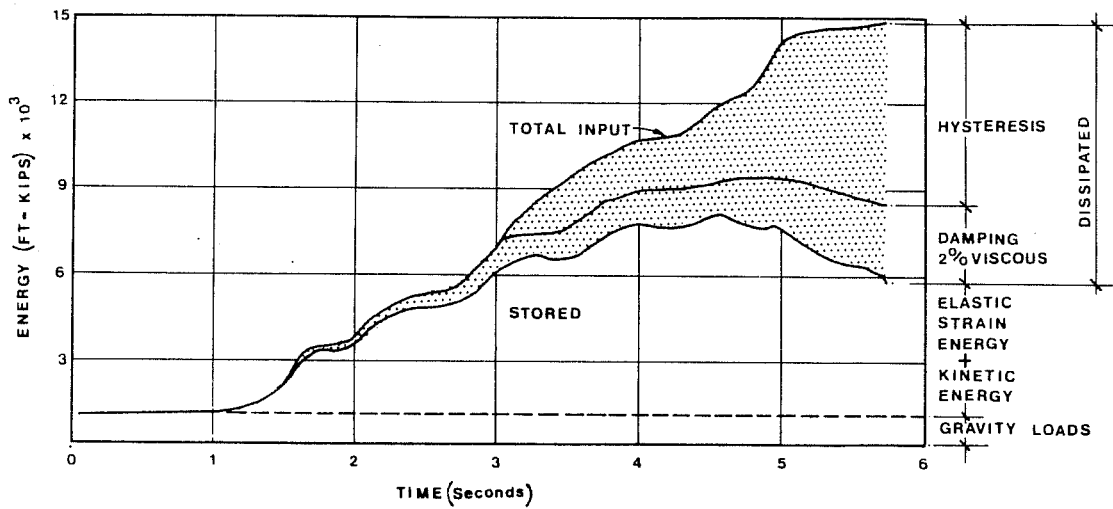


Fig. 7.4 - Energy Expenditure in Bank of New Zealand Building.

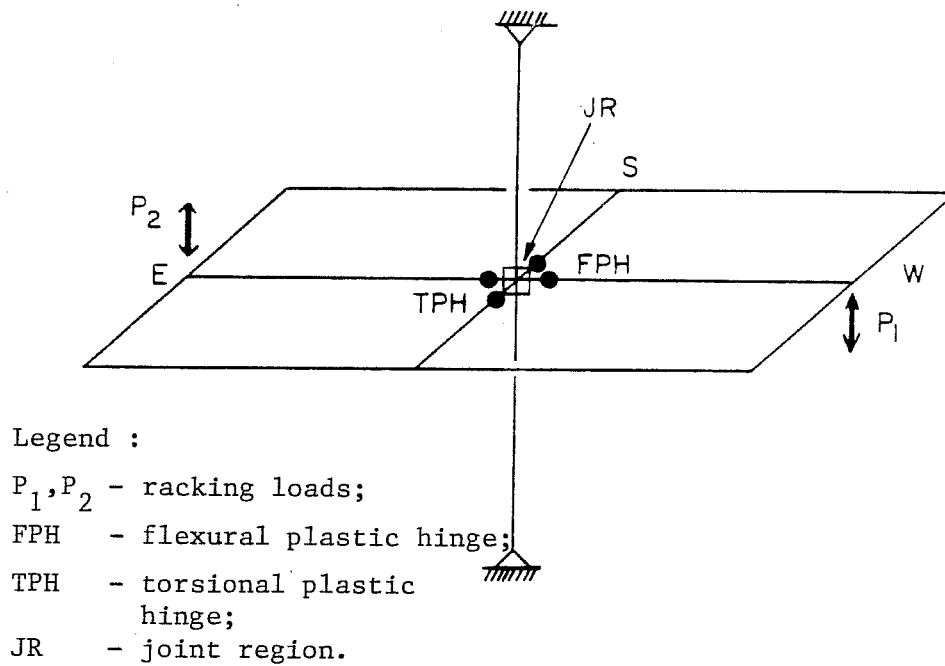


Fig. 7.5 - Interior Component Potential Plastic Hinge Locations.

The previously reported US-Japan component tests provided an excellent opportunity to perform some studies on the energy aspects of response for several reasons. First, the components had well-defined boundaries where the total amount of input energy was known. Second, the available data bank on strains, rotations, distortions, provided a useful tool to identify sources of energy dissipation. Finally, a qualitative evaluation of load-deflection curves may be too general to be useful, but energy evaluation of the response hysteresis loops may identify possible problems in energy absorption-dissipation zones of elements that appear to be sound in terms of strength and stiffness.

7.3 Energy Assumptions in Component Tests

In the US-Japan component tests, the external energy was input through beam tip loads, Fig. 7.5. This external work was dissipated internally through five main deformation mechanisms, Fig. 7.6: (1) beam and column elastic bending; (2) beam plastic bending; (3) joint distortion; (4) column plastic bending; and (5) transverse beam twist. Each one of these mechanisms plays an important role in the energy response. However, it was observed in the previous chapters that the undamaged elastic regions exhibited high secant stiffness but dissipated very little energy in a loading cycle. On the other hand, in regions where damage

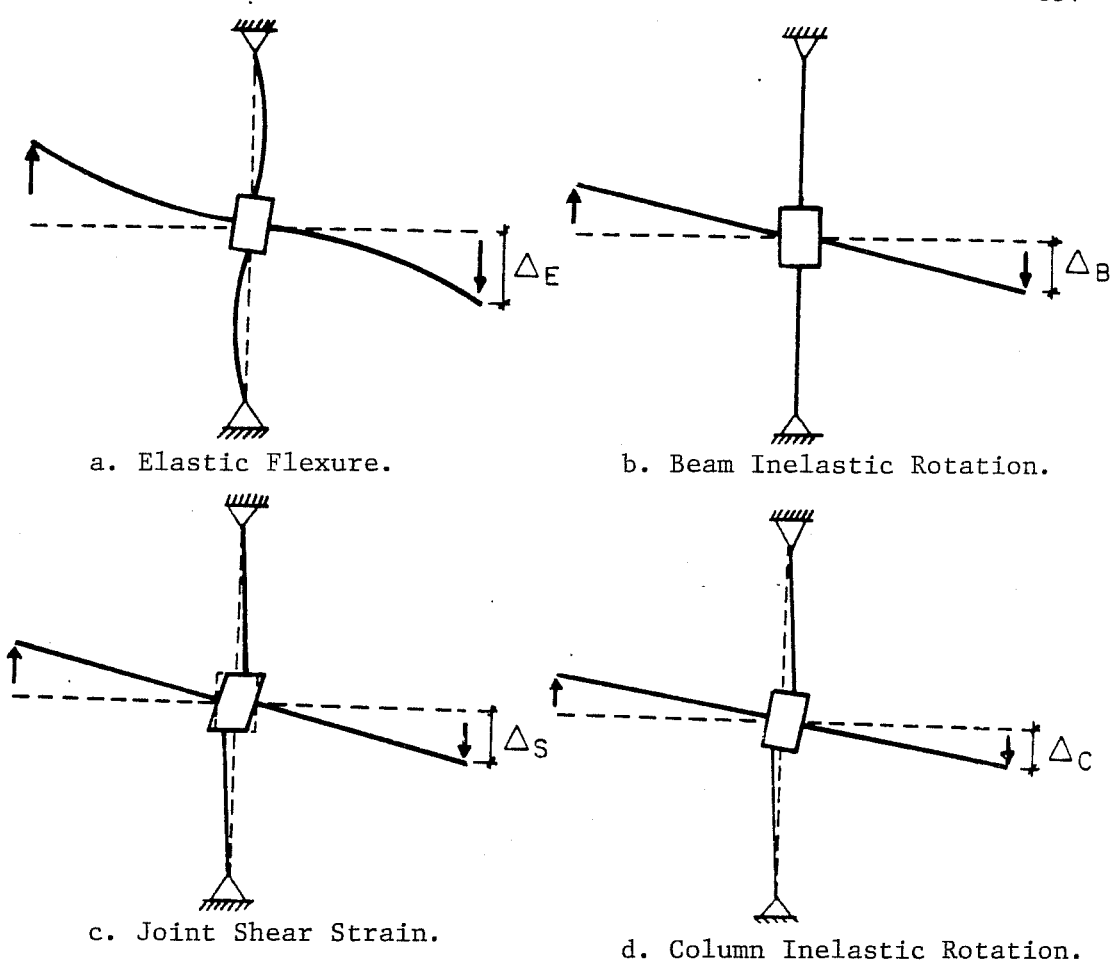


Fig. 7.6 - Component Deformation Mechanisms.

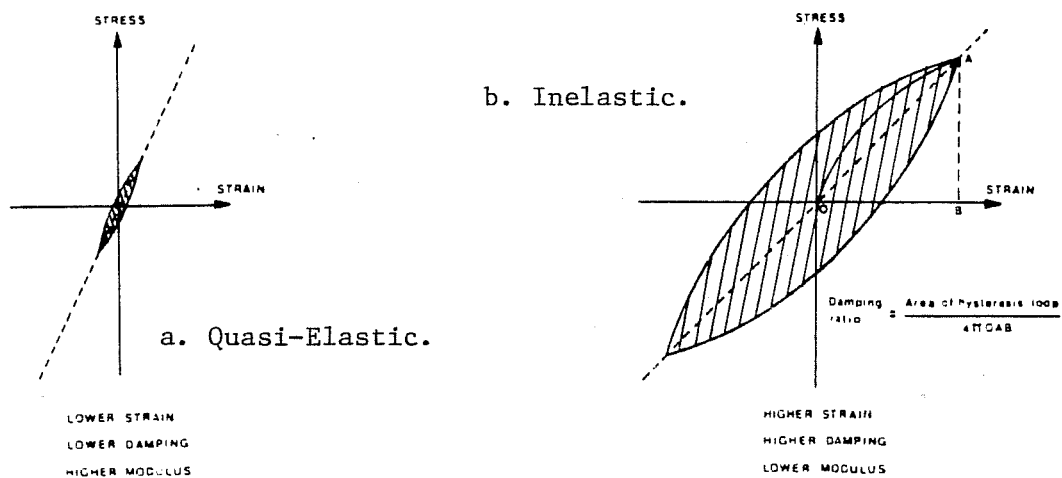


Fig. 7.7 - Hysteresis Cycles at Different Response Stages.

occurred, the secant stiffness was lower but the energy dissipated (the area within the hysteresis cycle) was much larger, Fig. 7.7. Therefore, the error involved by neglecting quasi-elastic hysteresis cycles (elastic members) was acceptable when compared with the large inelastic hysteresis cycles. In the UTA component tests, the specimens were designed so that the prime source of energy dissipation (hysteresis) would be located at the column face for both the longitudinal and the transverse beams or along the slab-transverse beam junction.

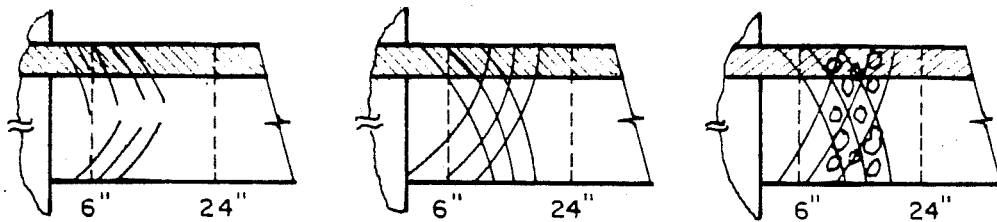
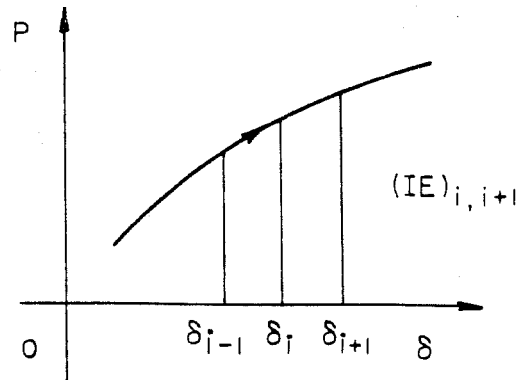
7.3.1 Total Input Energy. The load at the subassemblage beam tip produced a certain amount of work which was computed by considering the applied force and the induced displacement. Considering that the behavior of the structure remained linear between two successive load increments, the amount of energy input to the beam, IE, is given by, Fig. 7.8:

$$IE = 1/2 (P_{i+1} + P_i) \cdot (\delta_{i+1} - \delta_i) \quad (7.8)$$

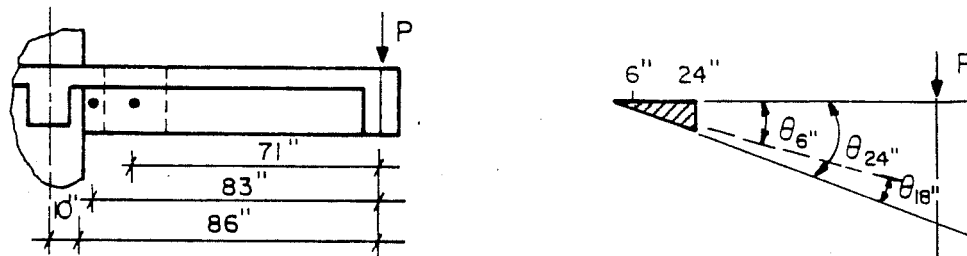
For an interior component the total input energy was equal to the sum of the work done by two beams between the same time intervals t_i and t_{i+1} .

7.3.2 Longitudinal Beam Dissipated Energy. In all specimens the longitudinal beams were instrumented with LVDT's to measure the average strain profile along the tension and the compression faces. These measurements were taken in the US

Fig. 7.8 - Beam Tip Inputed Energy.



a. Plastic hinge formation.



b. Assumed beam rotations (U.T.A., S.U.).

Dissipated energy :

$$DE_{i,i+1} = A_{\overline{AE}} - A_{\overline{BC}}$$

GL = gauge length

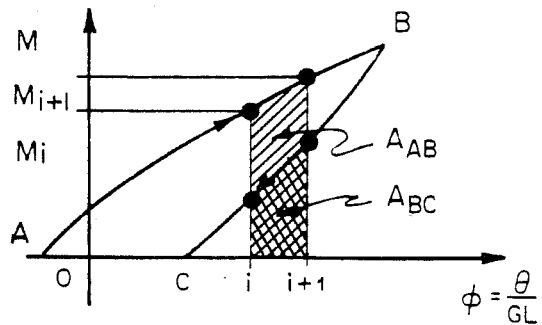


Fig. 7.9 - Beam Flexural Deformation.

specimens at 6 in. (0.15 m) and 24 in. (0.60 m) from the column face, Fig. 7.9-a. All the longitudinal beam dissipated energy was assumed to occur in the 6 in. (0.15 m) and 18 in. (0.45 m) discrete segments. This hypothesis was verified by examining the recorded data. Computation for the dissipated energy, DE, was based on the moment-curvature characteristics of these discrete segments located along the beam, Fig. 7.9-b. For each segment the applied moment and the beam rotations were computed at every load stage. The applied moment was calculated by the product of the beam force times the distance to the centroid of the segment. The beam rotations were computed from LVDT readings on top and bottom beam surfaces.

Similarly to the inputted energy, the amount of beam dissipated energy, DE_b , due to inelastic actions is given by:

$$DE_b = \sum_{i=1}^n 1/2 (M_{i+1} + M_i) \cdot (\phi_{i+1} - \phi_i) \cdot (\overline{GL}) \quad (7.9)$$

where: \overline{GL} = gauge length (ex: 6", 18");

n = number of discrete segments.

This equation is analogous to the strain energy equation given previously for a space beam under quasi-static loading:

$$U_b = \int_0^l \frac{MM}{2EI} dz \quad (7.10)$$

In components without slab the amount of total input energy is very close to the beam dissipated energy:

$$IE \approx DE_b \quad (7.11)$$

Some losses were expected to occur in the joint region and in the "elastic" columns. In components with slab some strain energy was also processed by the joint region and the transverse beams.

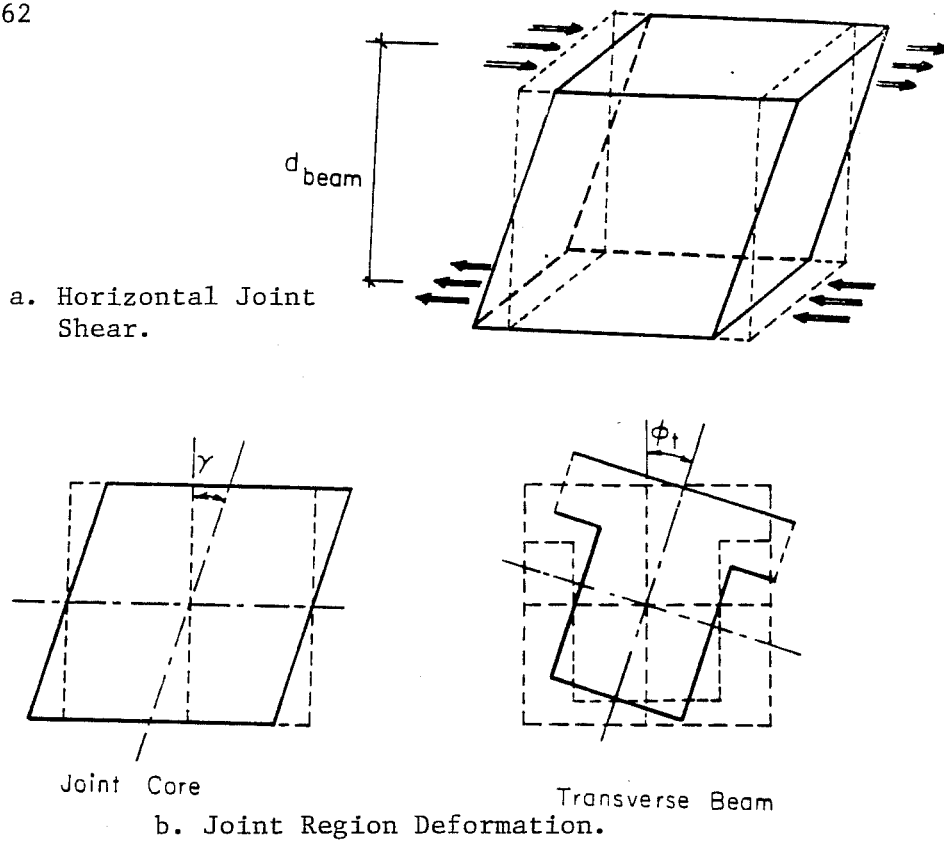
7.3.3 Joint Core Dissipated Energy. The obtained joint core distortion data for all the UTA components indicated that a strong possibility existed of large strain energies being dissipated by the joint panel under reversed cyclic actions. Consequently, it was assumed that the distortional angle experienced by the joint panel would lead to support rotation for the transverse beam. The strain energy being released by the joint core, DE_{jc} , was computed based on, Fig. 7.10, as:

$$DE_{jc} = \sum_{i=1}^n 1/2(V_{ji+1} + V_{ji}) \cdot (\gamma_{i+1} - \gamma_i) \cdot (\overline{GL})_{jc} \quad (7.12)$$

where: V_j = horizontal joint shear; γ = joint distortional angle; and $(\overline{GL})_{jc}$ = joint core gauge length.

This equation is similar to the shear strain energy term:

$$U_{sh} = \int_0^l k \frac{V_j \cdot V_j}{2GA} dz \quad (7.13)$$



* Net Twist * $\phi_{tn} = \phi_t - \gamma$

1. Shear from Beam Steel : $V_s = M / d$
2. Column Shear : $V_c = M / h$
3. Joint Shear : $V_j = V_s - V_c = M \cdot \left(\frac{1}{d} - \frac{1}{h} \right)$ or,
 $V_j = (P_1 - P_2) \cdot \left(\frac{1}{d} - \frac{1}{h} \right) \cdot L$
4. Energy Dissipated by Joint Core :

$$U_{jc} = \frac{1}{2} \cdot (V_{j,i+1} + V_{j,i}) \cdot (\gamma_{i+1} + \gamma_i) \cdot \overline{GL}$$

where : \overline{GL} = gauge length .

Fig. 7.10 - Joint Core Participation in Interior Test.

7.3.4 Transverse Beam Dissipated Energy. At each load stage of the UTA tests, the net twist angle (ϕ_{tn}) is given by subtracting the joint distortion angle (γ) from the measured absolute twist angle (ϕ_t). The transverse beam dissipated energy, DE_{tb} , can be calculated as:

$$DE_{tb} = \sum 1/2(M_{i+1}^{tn} + M_i^{tn}) \cdot (\phi_{i+1}^{tn} - \phi_i^{tn}) \cdot (\overline{GL})_t \quad (7.14)$$

where: M_{tn} = net plastic hinge torsional moment; ϕ_{tn} = net plastic hinge twist; and $(\overline{GL})_t$ = torsional element length.

This equation is analogous to the torsion strain energy equation term described before:

$$U_t = \int \frac{M_{tn} \cdot M_{tn}}{2GJ} dz \quad (7.15)$$

To take into account the new joint shear and transverse beam strain energy terms, equation (7.11) must be modified:

$$IE \tilde{>} DE_b + DE_{jc} + DE_{tb} \quad (7.16)$$

The data obtained from the LVDT's placed at a distance d and $3.2 d$ (d = beam depth) shows that the transverse beam rotated as a rigid body between a distance d (or less) from the column face and the free edge. This leads to the possibility of a plastic torsional hinge forming near the column where some amount

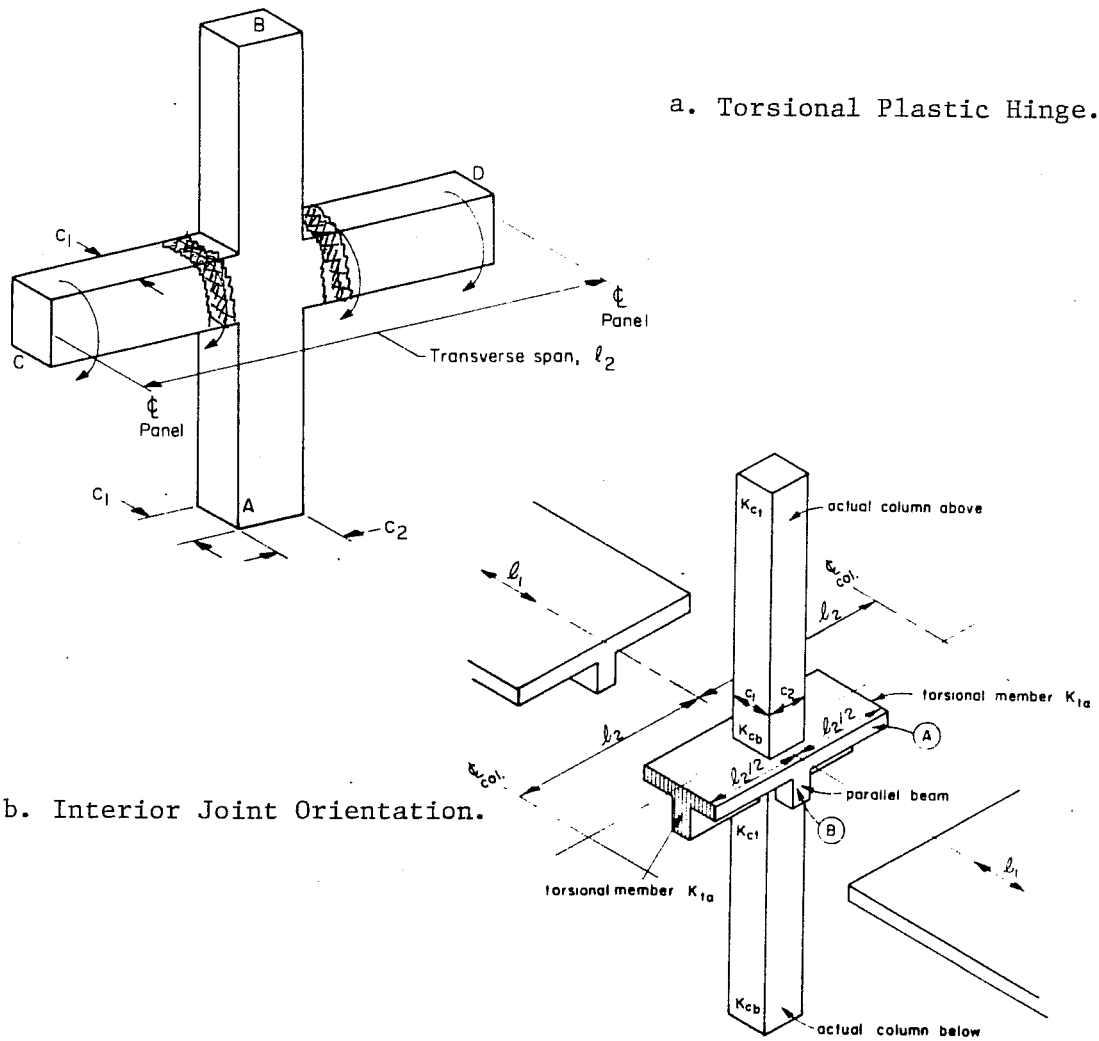


Fig. 7.11 - Panel Orientation for K_t .

TABLE 7.1 - TRANSVERSE BEAM TORSIONAL STIFFNESS.

Design Code (* 10^5 r/i)	Exterior Joints		Interior Joints	
	USJ - 2	USJ - 4	USJ - 1	USJ - 3
ACI 318-83	1.31	1.45	1.55	1.52
CEB-FiP $\psi = 0$ $\psi = 3$	2.38	2.54	2.46	2.33
	1.17	1.18	1.25	1.17
Park & Paulay	4.58	5.40	4.58	5.40

of energy would be dissipated, Fig. 7.11-a. The actual situation requires that part of the load is taken by the longitudinal beam and the other part by the joint core and the transverse beam.

The proposed method to evaluate a more correct torsional secant stiffness is by targeting the probable value of DE_{tb} in equation (7.16). The torsional secant stiffness computation has importance for the equivalent frame analysis method and in the computation of an equivalent column stiffness for design of two-way slabs.

7.3.5 Design Code Torsional Stiffness. Tests of torsional beams show that cracking occurs at very small deformation levels and once cracking has developed the correspondent torsional secant stiffness drops drastically. On the other hand, the junction between the slab flange and the transverse beam is also subjected to cracking. Therefore, the T-beam effect in a torsional beam under large reversed load cycles is disregarded. The torsional secant stiffness is conservatively estimated by design code calculations for a rectangular cross section [Park and Paulay (13)].

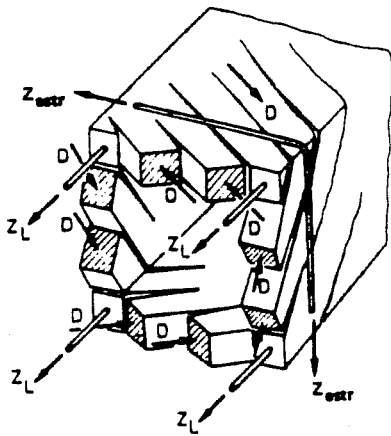
The ACI 318-83 (1) design code equations [13.6, 13.7] based on the work of Corley and Jirsa (7) were used to compute the values of K_t as shown in Table 7.1. Corrections for the ACI Code panel direction effect (Fig. 7.11-b) were also included.

The CEB-FIP Model Code (5) considers two equations to compute the torsional stiffness in the cracked state [8.8, 8.11]. The second equation is more accurate because it includes the effect of reinforcement. Two extreme values were found depending on the age of loading and creep effects of $\psi = 0$ and $\psi = 3$, Table 7.1.

The space truss model (Fig. 7.12-a) which is the background of the CEB recommendations is based on tests at the University of Stuttgart [Leonhardt (12)] and ETH Zurich [Lampert (10); Lampert and Thürlimann (11)]. It is found that in the UTA modified component tests the increase in longitudinal steel without the correspondent increase in transverse steel leads to stirrup premature yielding, (Fig. 7.12-b) [Hsu (9)]. The resulting shallower concrete compression strut has an angle $\alpha_c = 27^\circ$ which is below the minimum $\alpha_c = 31^\circ$ recommended by the CEB-FIP Model Code.

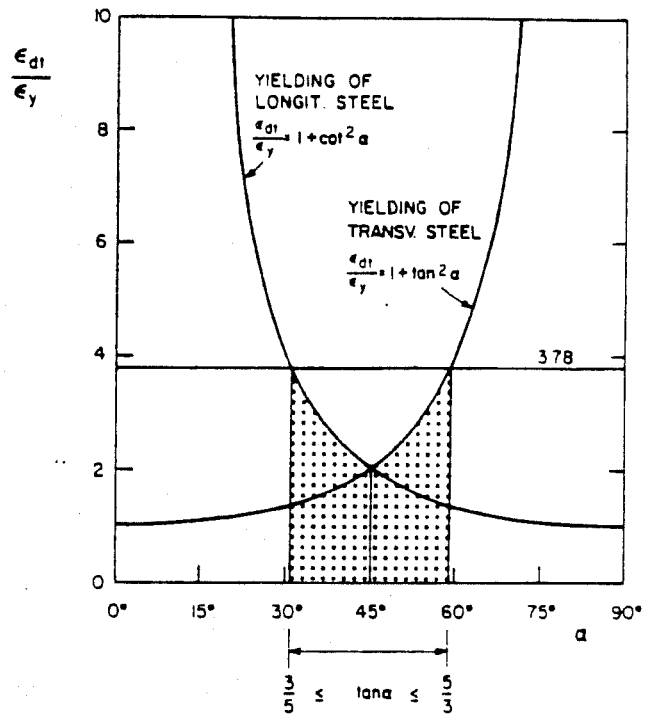
7.3.6 Damping and Energy Dissipation Mechanisms. The dynamic response of RC components is affected by stiffness, mass and damping properties of the components. Damping is one of the least studied parameters and yet, it is one of the most important factors influencing the ability of a structure to dissipate energy under dynamic excitation.

Two main phases in the dynamic response of RC members must be considered when studying energy dissipation [Tassios



a .Space Truss Model, after Leonhardt (12).

b. The α - angle, after Hsu (9).



c. UTA α - angles.

U T A Tests	A_s (in. ²)		A_{st} (stirrups)	α (angle)
	Top	Bottom		
USJ-1,2	1.32	0.88	.11@4."	35.6°
USJ-3,4	2.40	1.80	.11@4."	27.3°

Fig. 7.12 - Space Truss Model for Torsion.

(16)], (1) in the virgin linear elastic range, the dissipation results mainly from microscopic plastification and planar displacements, thermoelastic effects; and, (2) in the inelastic range, due to reinforcement yielding and triaxial concrete confinement (in compression), large plastic elongations can be attained in the reversed loading cycles.

Three major types of damping have been identified [Clough and Penzien (6)]:

1. Viscous damping (c)-simple mathematical models where the damping force is assumed to be proportional to the velocity ($f_{DV} = c \cdot \dot{x}$);
2. Coulomb damping (μ) - considered to be constant and in phase with velocity ($f_{DC} = \mu \cdot F_N \cdot \dot{x}/|\dot{x}|$); and
3. Hysteretic damping (ζ_H) - in this model, the damping force is in phase with velocity and proportional to the system restoring force ($f_{DH} = \zeta_H \cdot k \cdot |x| \cdot x/|x|$).

Given a linear elastic, viscously damped, SDOF system, Fig. 7.13, the critical damping coefficient, c_{crit} , is obtained as [Clough and Penzien (6)]:

$$c_{crit} = 2 \frac{\sqrt{k}}{\omega} = 2 \frac{k}{\omega} = 2m\omega \quad (7.17)$$

This value is used to normalize the system viscous damping and it gives the viscous damping ratio, ζ :

$$\zeta = \frac{c}{c_{\text{crit}}} \quad (7.18)$$

Consequently, damping characteristics can be evaluated either by using the damping coefficient, c , or the dimensionless damping ratio ζ .

The energy dissipated (DE) in a cycle by a linear viscously damped structure with amplitude d , ($x_{\text{max}} = d$) and circular frequency, ω is given by the area of an ellipse, Fig. 7.13.

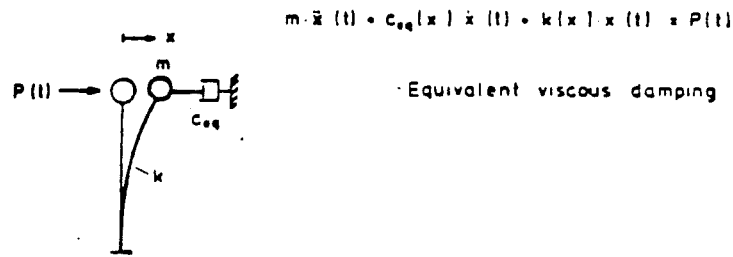
$$W_{\text{DE}} = \pi [c d \omega] d = \pi c \omega d^2 \quad (7.19)$$

or;

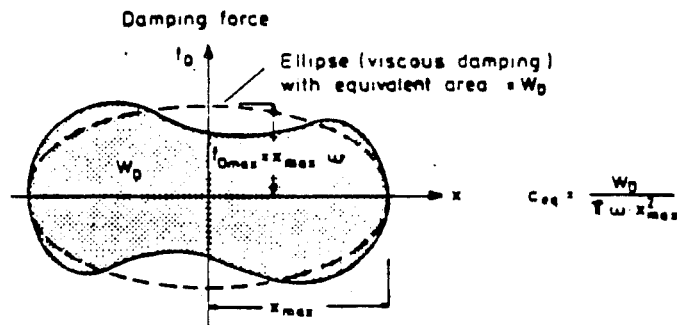
$$c = \frac{W_{\text{DE}}}{\pi \omega d^2} \quad (7.20)$$

In the case of nonlinear systems, a simple dynamic analysis is done by linearizing the response. The maximum strain energy per (1/2) cycle is, Fig. 7.13:

$$W_s = (1/2)k_{\text{eq}}d^2 = (1/2)c_{\text{crit}}(\omega/2)d^2 = (1/4)c_{\text{crit}}\omega d^2 \quad (7.21)$$



Equation of motion of a SDOF-System



observed and equivalent energy dissipation per cycle

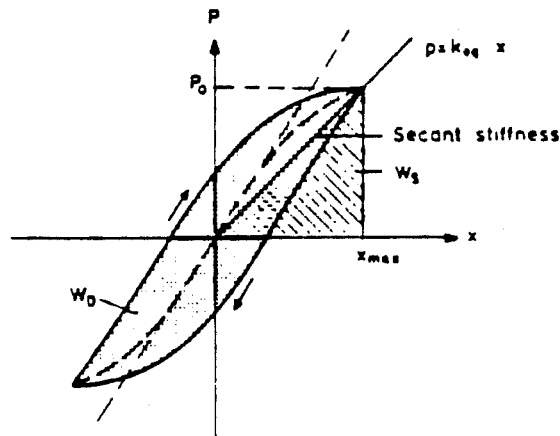


Fig. 7.13 - Energy Dissipation and Equivalent Viscous Damping.

The equivalent viscous damping, ξ , can be obtained by computing the ratio of dissipated energy to the strain energy of an equivalent linear system with stiffness k_{eq} divided by the constant, 4π , [Clough and Penzien (6)];

$$\xi = \frac{c}{c_{crit}} = \frac{W_{DE}}{4\pi \cdot W_{IE}} \quad (7.22)$$

The experimental results obtained in the component tests showed that some doubts may arise when assessing the energy absorbed/dissipated and the equivalent viscous damping value for the structure. First, one may study either the T-beam or the whole subassemblage. Second, differences exist between the exterior and the interior component responses. In the initial portion of this study T-beam response for positive moment (slab in compression), negative moment (slab in tension) and the complete load-deflection cycle throughout the test program was considered, Fig. 7.14. Then the equivalent viscous damping was evaluated for the complete subassemblage by considering the story shear - story displacement as characteristics of the component (exterior or interior). The BRI building viscous damping characteristics can also be evaluated for the different floors. Finally, comparisons are made among the available tests for the different equivalent peak drifts.

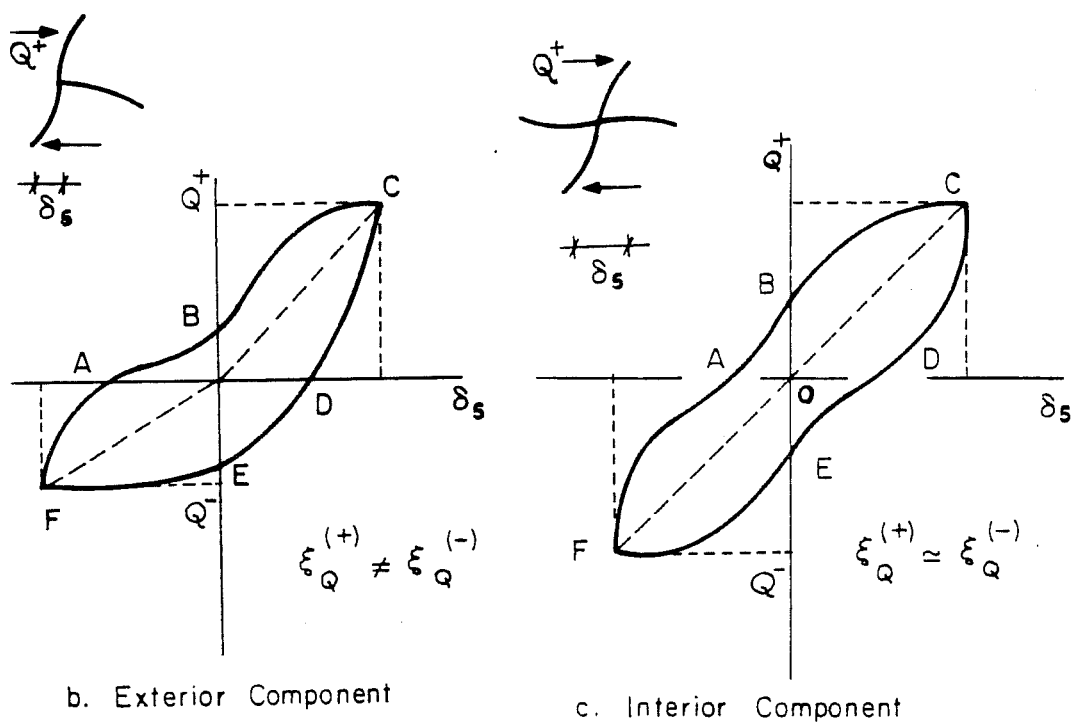
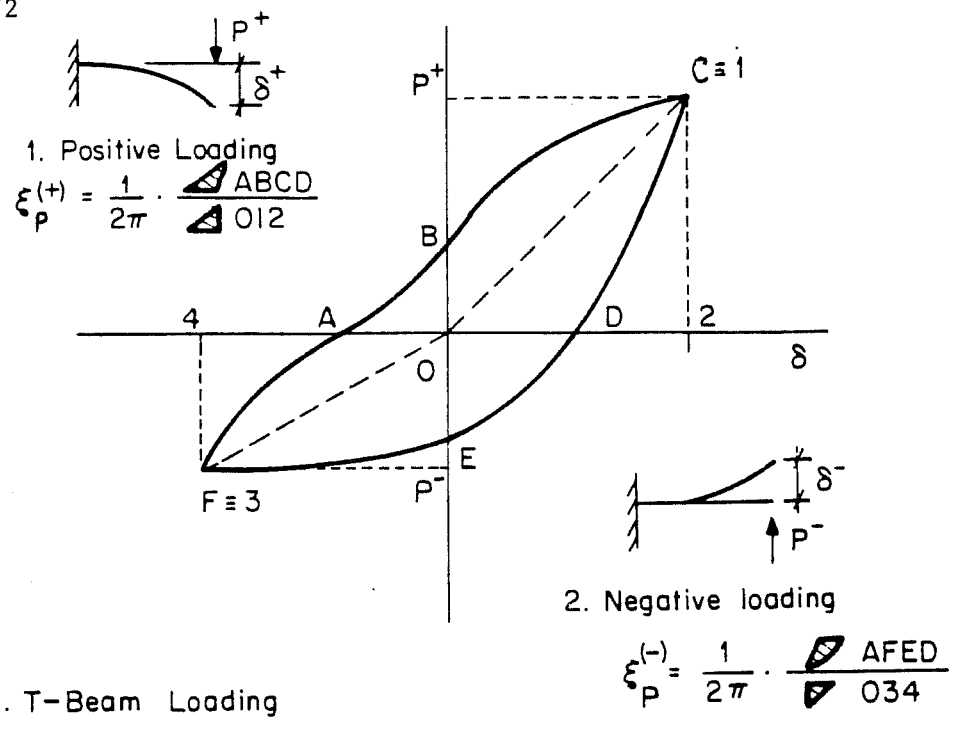
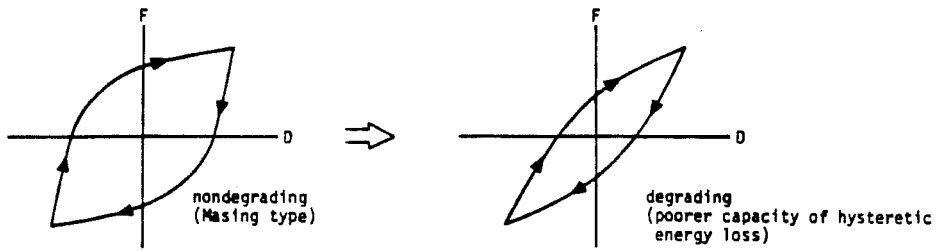


Fig. 7.14 - T-Beam Effect in Component Response.

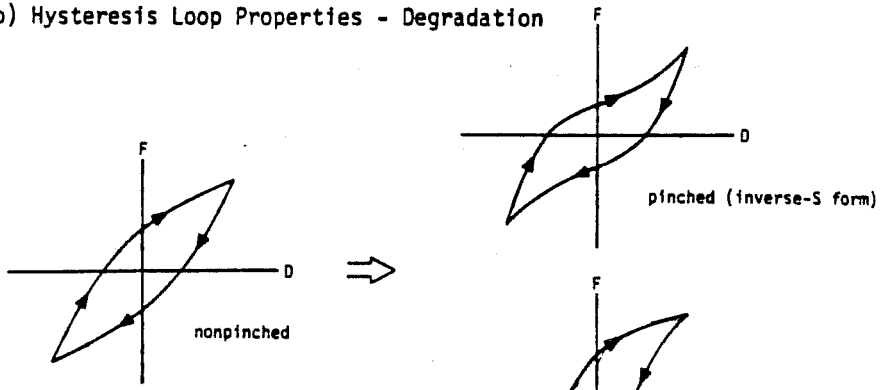
7.3.7 Other Aspects of Component Energy Response. A consistent feature in RC systems is the gradual decline of load-carrying capacity under reversed cyclic loadings with specified amplitudes of deformation. Relatively stable loops may be obtained if flexural failure dominates. On the other hand, unstable response results under a shear failure mechanism. A summary of the most important aspects in modeling RC restoring force relationships is shown in Fig. 7.15 [Umemura and Takizawa, (17)]. Most of the current idealizations used (left side) should be replaced by more realistic ones (right side). Depending on the amount of applied deformation, degradation, pinching and instability may be dominant in the component response.

Current test results described in the previous chapters show that a melange of hysteretic loop properties are observed where one or more of the possible degrading aspects may dominate.

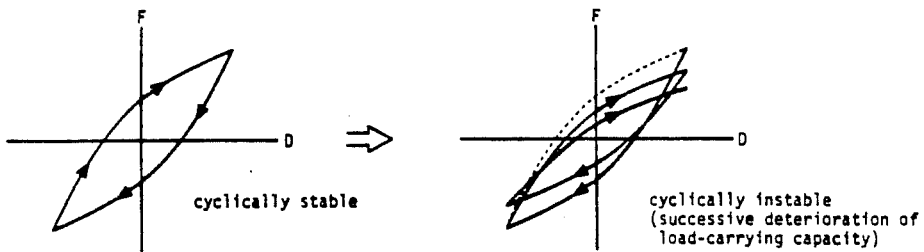
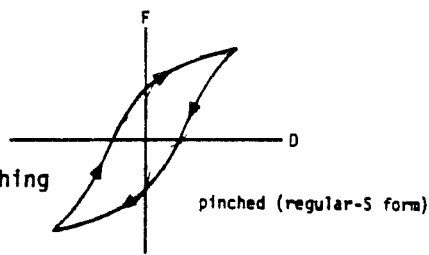
Based on the available test results, a more detailed interpretation of the hysteretic phenomena on component response is provided. The tests were conducted on a displacement-control basis with increasingly more severe peak displacements followed by other smaller peak cycles. Although some specimens were built similarly, geometry (existence of a slab) or local failures (excessive cracking, anchorage loss) resulted in different



(b) Hysteresis Loop Properties - Degradation



(c) Hysteresis Loop Properties - Pinching



(d) Hysteresis Loop Properties - Instability

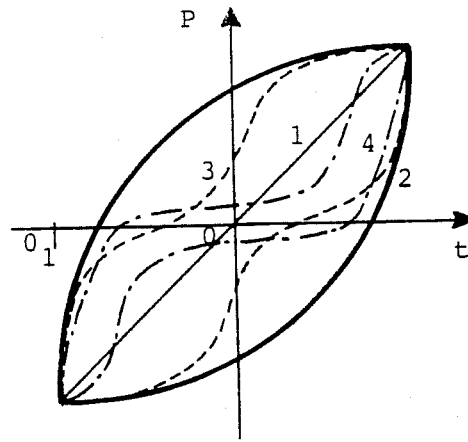
Fig. 7.15 - Hysteretic Modelling in RC Systems, after Umemura and Takizawa (17).

responses. An interpretation of the different hysteresis mechanisms is provided, Fig. 7.16.

First, a perfect elastic response without any hysteresis is obtained with the load-deflection planes in phase along the time axis (Curve 1) Fig. 7.16. The stable hysteresis loop, Curve 2, requires that the applied load during the loading phase be larger than in a linearly perfect elastic body reaching the same peak load and deflection. However, the recovery unloading is processed at a faster pace. Pinching in the hysteresis loops due to shear (Curve 3) or bar sliding (Curve 4) is reflected in Fig. 7.16 by similar behavior as Curve 2 near peak displacements with a marked reduction in the applied load or a sloped load plateau near the origin.

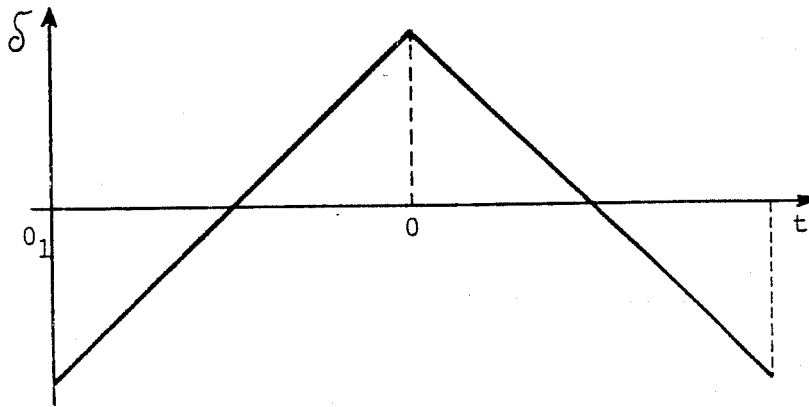
7.4 Evaluation of Component Energy Response

7.4.1 Exterior Components. The total input energy for each exterior component was computed by integrating the area under the beam tip load-deflection curve for each load stage (LDS), Fig. 7.17. The UTA component tests showed that a sharp rise in input energy occurred in test USJ - 4 after LDS 237 when an equivalent drift ratio $R = 1/39$ was attained. Specimen USJ-2 showed a much smaller increase after LDS 245 ($R = 1/40$) in part due to the beam anchorage failure. At the end of the test, the total input energy in specimen USJ - 4 was 3.75 times larger than

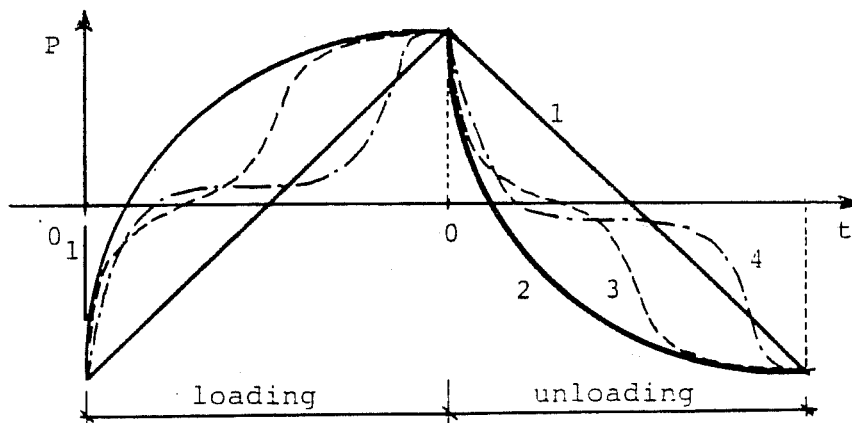


- 1. Elastic Response
- 2. Spindle Hysteresis
- 3. Pinched Response
- 4. Severe Pinched Response

a. Hysteresis Loops.



b. Displacement-control Cycle.



c. Resulting Load Cycle.

Fig. 7.16 - Hysteretic Response in a Symmetric Section.

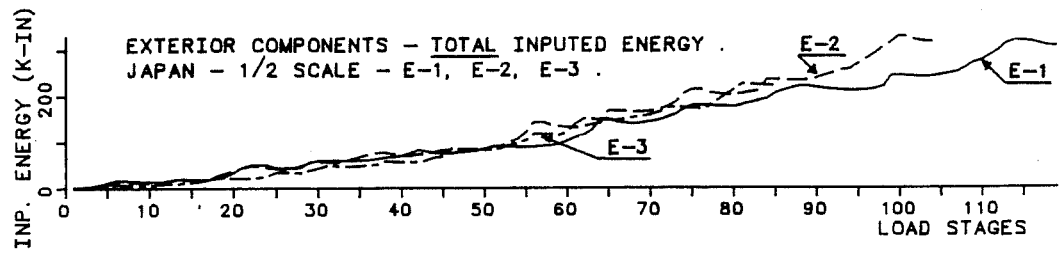
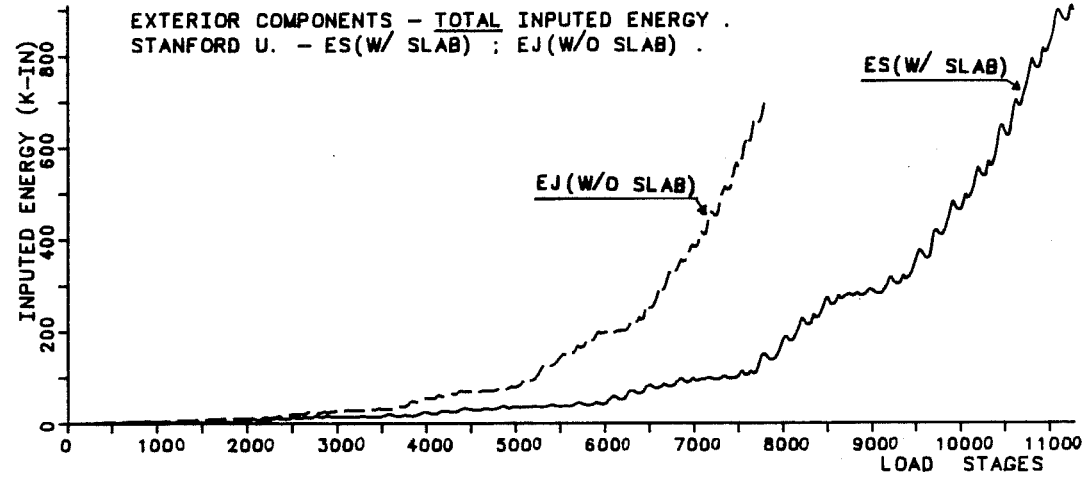
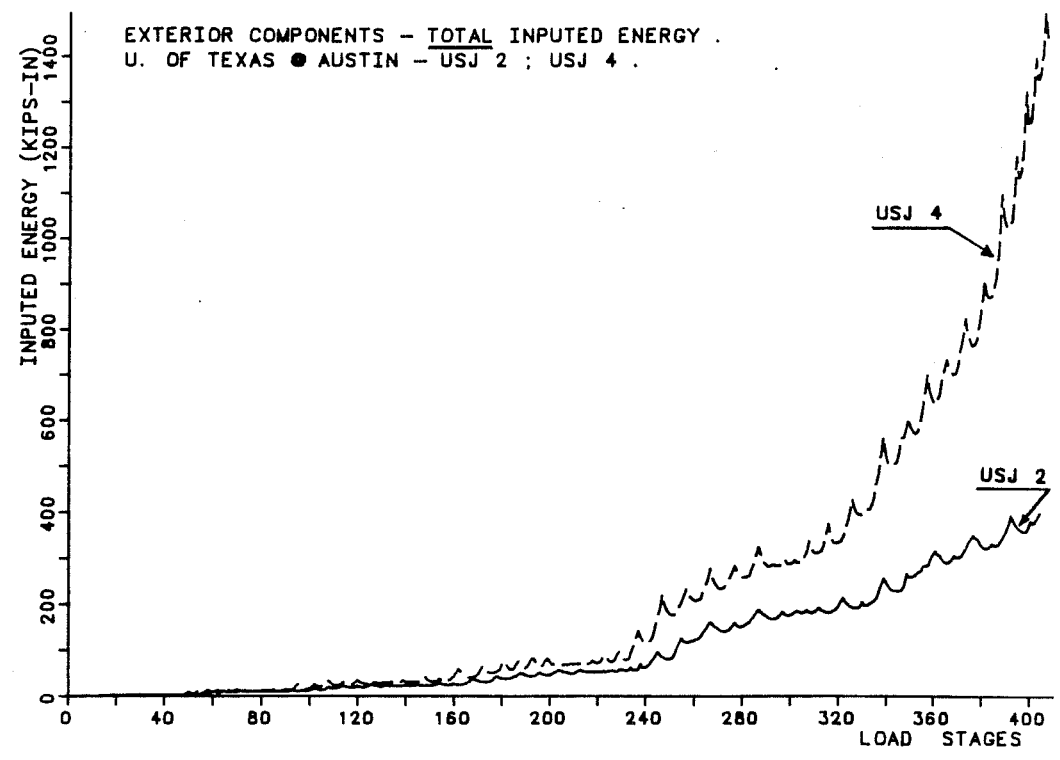


Fig. 7.17 - Exterior Tests - Total Inputed Energy.

the value in USJ - 2. The SU tests gave the opportunity of comparing components response with a slab (ES) vs. one without a slab (EJ). In test EJ, the amount of input energy increased substantially after LDS 5100 ($R = 1/40$) and in test ES after LDS 7700 ($R = 1/41$). The total amount of input energy was 20% higher in test ES as compared with EJ. The amount of input energy in the Japanese 1/2-scale tests was similar for Tests E-1 and E-2 whereas test E-3 (without a slab) had smaller input energy. The smaller Japanese tests were subjected to less severe input energy compared with the SU tests and the UTA USJ - 2 test because of the limited number of loading cycles applied.

The evaluation of beam dissipated energy was based on the assumptions in Sec. 7.3.2. Dissipated energy is plotted in Fig. 7.18. The US components showed that most of the energy was dissipated in the first 6.0 in. (0.15 m) from the column face. However, in the UTA USJ-4 test ($\rho_t = 1.36\%$; $\rho_b = 0.85\%$) which had twice as much beam longitudinal steel as USJ - 2, after LDS 237 ($R = 1/39$) an additional 18 in. beam length was also actively dissipating energy. In the SU - EJ tests, the additional 18.0 in. beam length started to dissipate energy after LDS 6400 ($R = 1/41$) which showed that larger rotational demands progressed throughout the beam under increasingly larger deflections. The total amount of beam dissipated energy was 30% higher in the SU - ES specimen as compared with the EJ test. The UTA tests showed

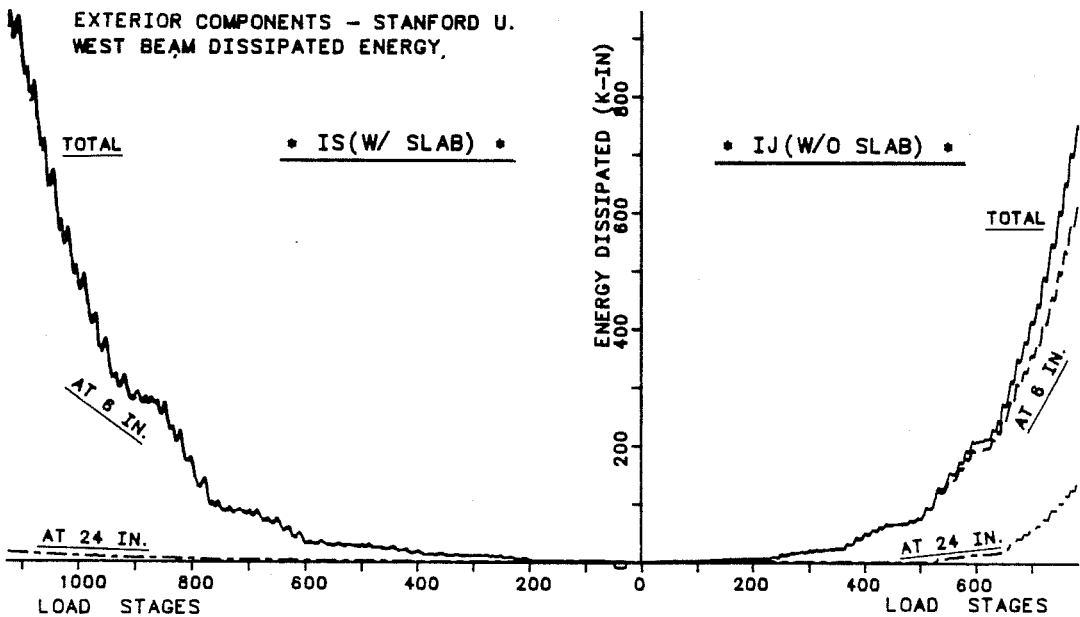
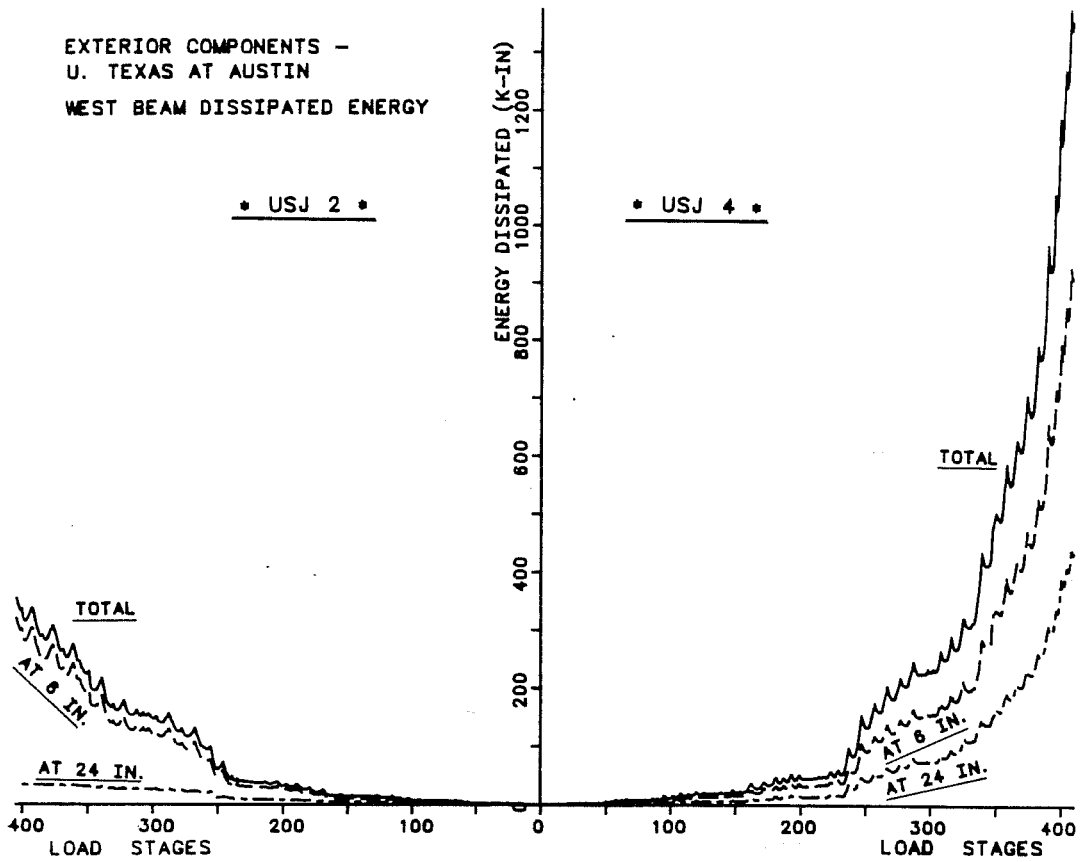


Fig. 7.18 - Exterior Tests - Beam Dissipated Energy.

the same difference in total beam dissipated energy as compared with the input energy.

7.4.2 Interior Components. The work done by the applied tip load on both East and West beams is shown in Figs. 7.19 and 7.20. In UTA USJ-1, larger energy inputs were applied from LDS 349 ($R = 1/39$) onwards. The initial load - control test applied to USJ - 1 up to LDS 240 did not create much work, except in the east beam where at LDS 230, a peak drift $R = 1/47$ was applied. USJ-3 showed a higher rate of work input from LDS 239 ($R = 1/38$) onwards, in both E- and W- beams. In test SU (IS), the E- and W-beams showed a growing energy response under increasing drifts, particularly after LDS 5780 ($R = 1/42$). On the other hand, test IJ without a slab showed a W-beam steady response as compared with a growing energy input on the E-beam. This phenomena may have resulted from the localized damage experienced by the E-beam during the initial load-control phase where a large peak load was applied. The W-beam was not subjected to localized damage and longer, intact beam sections resisted the load.

To characterize the components, the total amount of input energy (both E- and W-beams) was used, Fig. 7.20. It can be seen in the UTA tests that energy input to USJ - 1 and USJ - 3 components was nearly the same. The increase in input energy

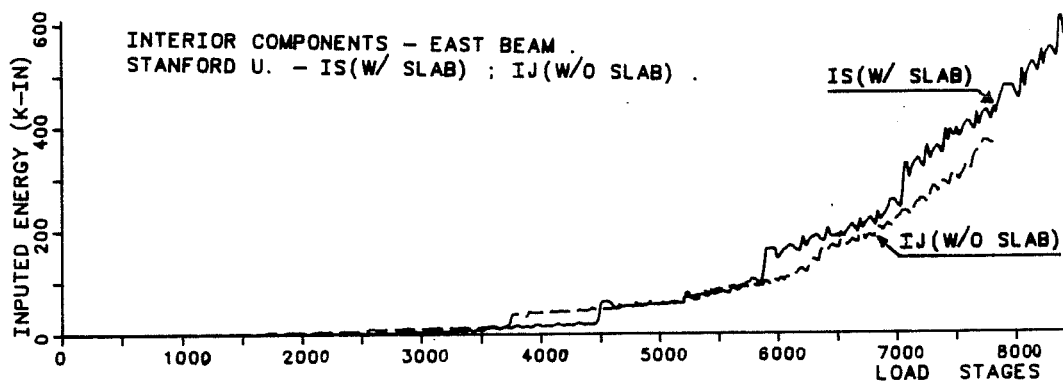
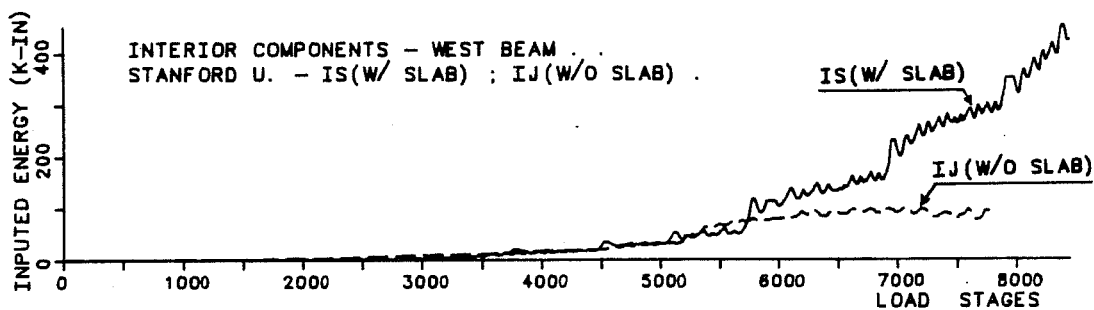
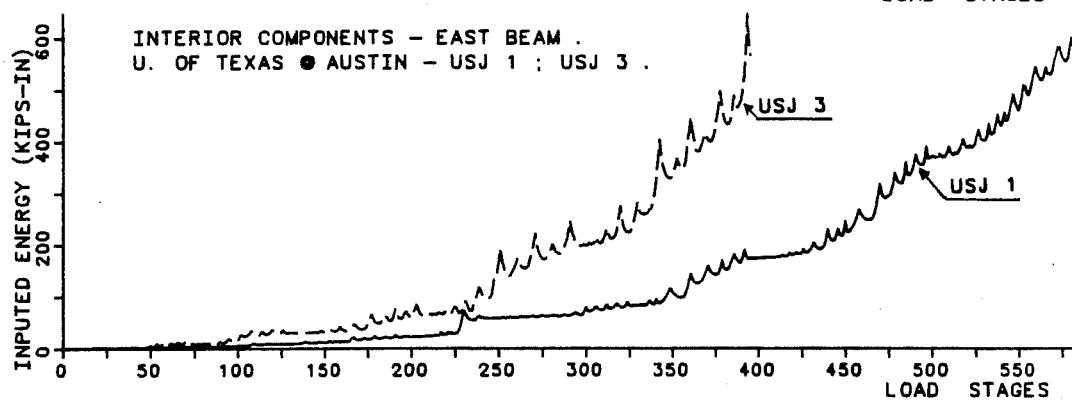
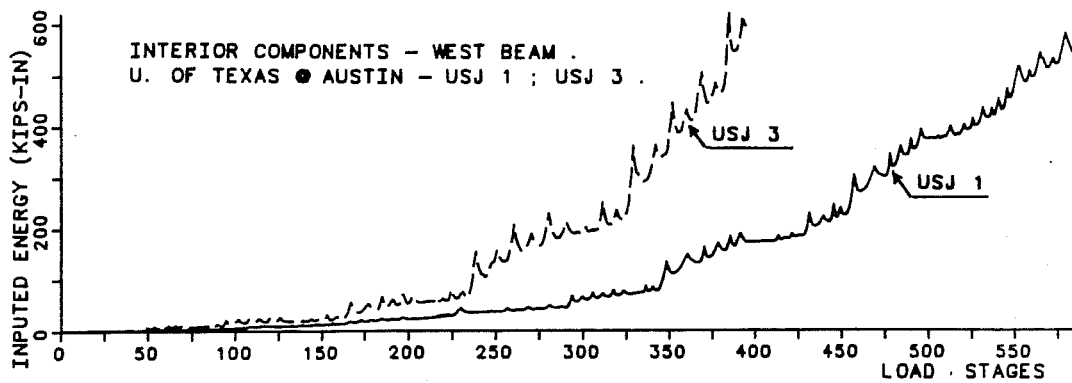


Fig. 7.19 - Interior Tests - Beam Inputed Energy.

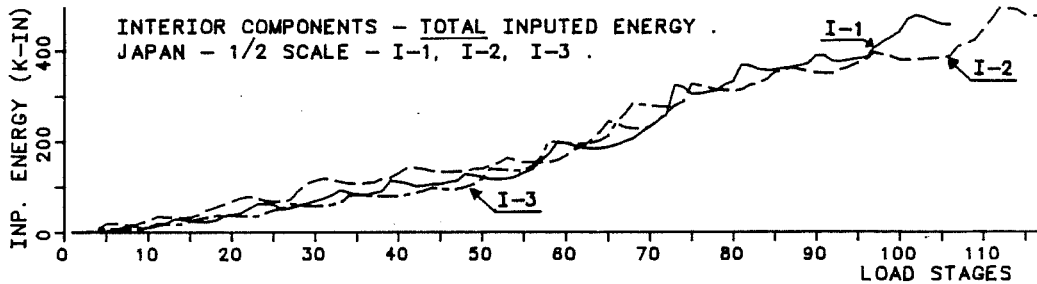
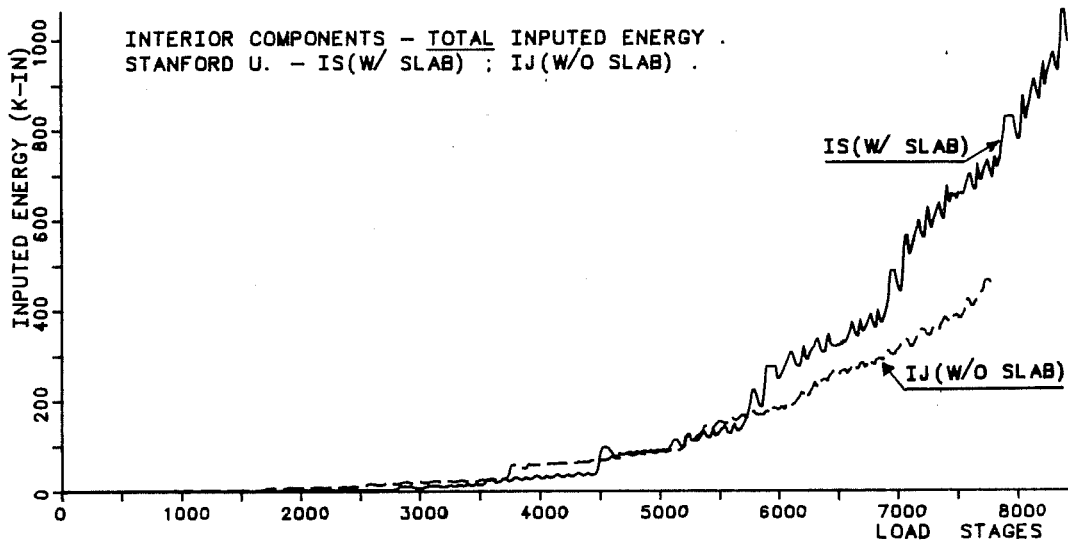
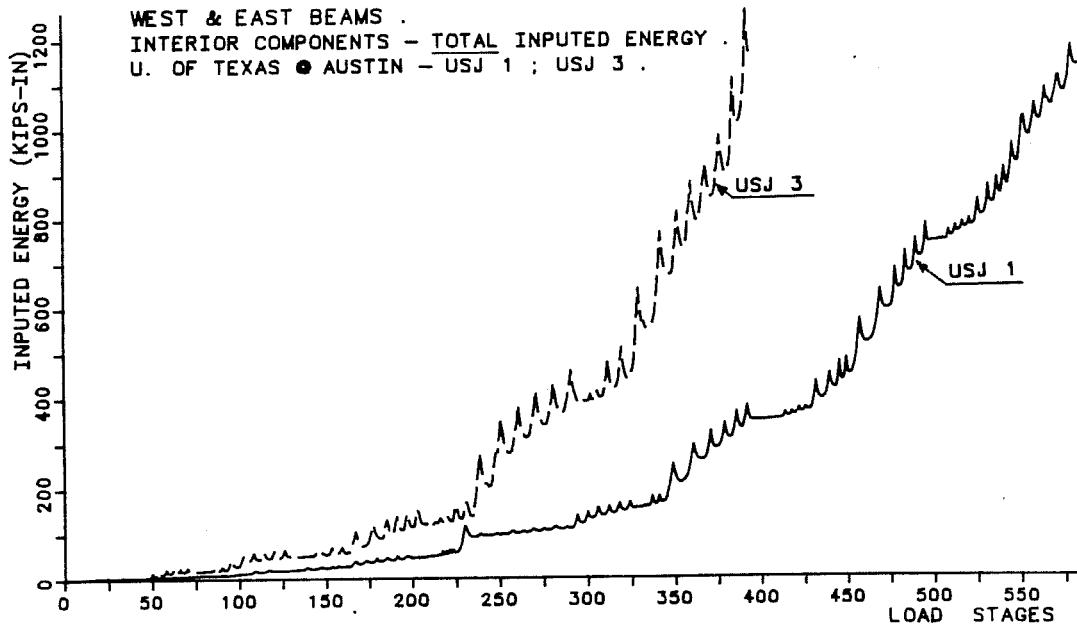


Fig. 7.20 - Interior Tests - Total Inputed Energy.

occurred in the components at the same LDS as for the individual beams. The SU components showed that the total input energy in a specimen with a slab was twice as much as in one without a slab for a similar loading program. The Japanese interior components were subjected to a more limited input energy. The component without a slab (I-3) was unable to reach the same energy levels as the specimens with a slab (I-1, I-2) which was consistent with the SU observations.

The energy dissipated in the interior components E- and W-beams is shown in Figs. 7.21 and 7.22. The UTA components showed that most of the beam dissipated energy was located within the first 6 in. from the column face. An exception is the USJ - 1 E-beam which was subjected to large deformations under an unintended load-control test. The SU-IS test had similar energy dissipation response as the UTA tests. In the specimen without a slab (IJ), the E-beam that was more damaged by the initial load-control program showed that most of the energy was being dissipated along the first 6 in. region from the column. Along the adjacent 18 in. region, about 1/3 of the total beam energy was being dissipated. In the W-beam most of the beam dissipated energy occurred in the 6 in. distance from the column face. In the SU tests, the beam dissipated energy was much less than in the W-beam region than in the E-beam. The difference in the UTA specimens was not markedly different between both E- and W-beams.

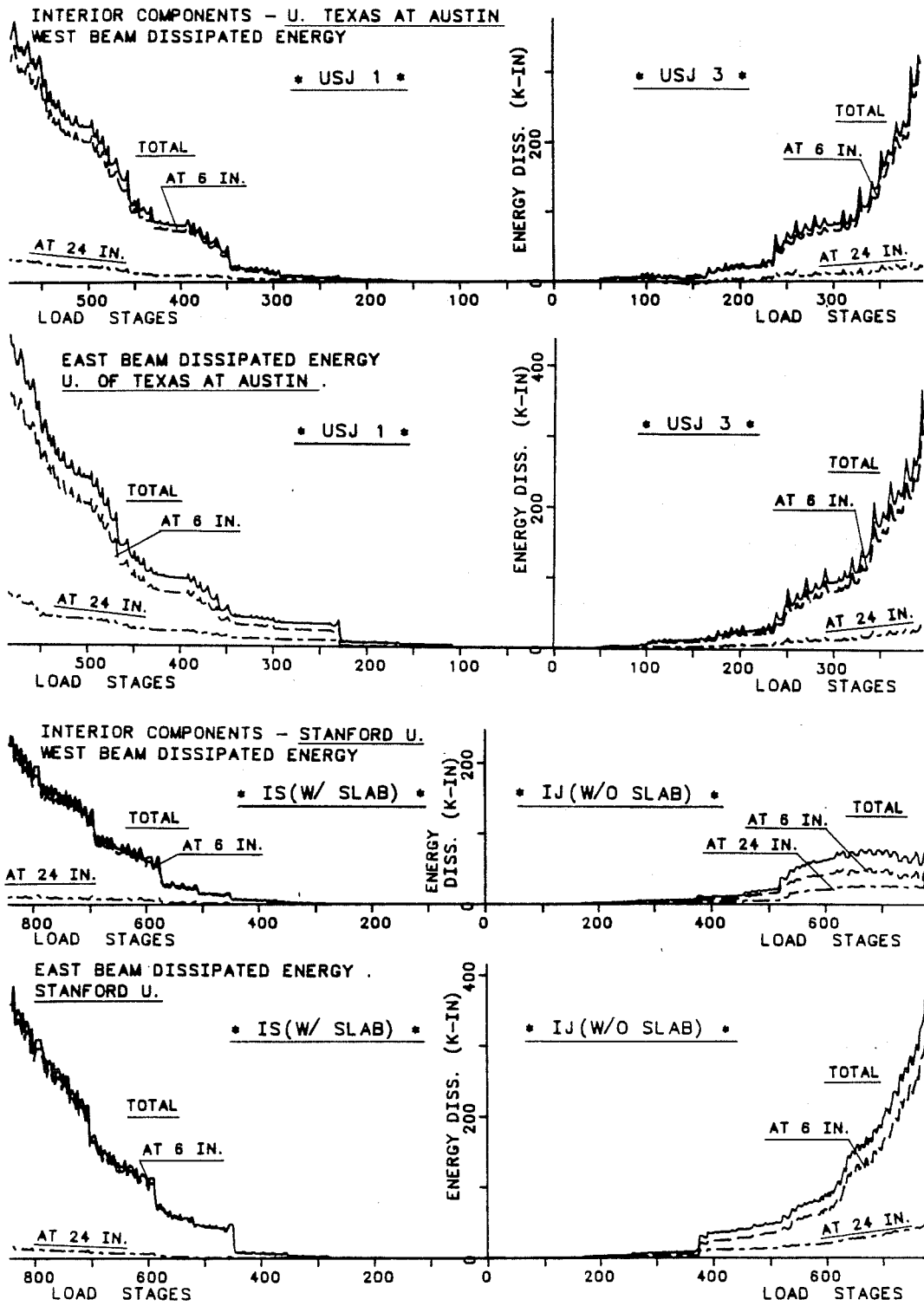


Fig. 7.21 - Interior Tests - Beam Dissipated Energy.

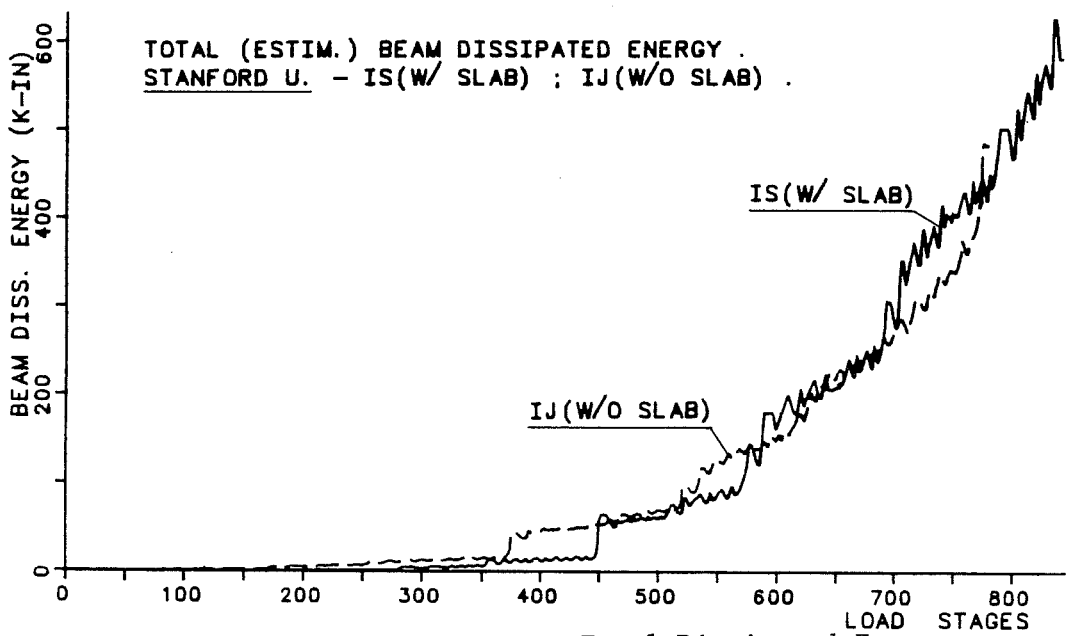
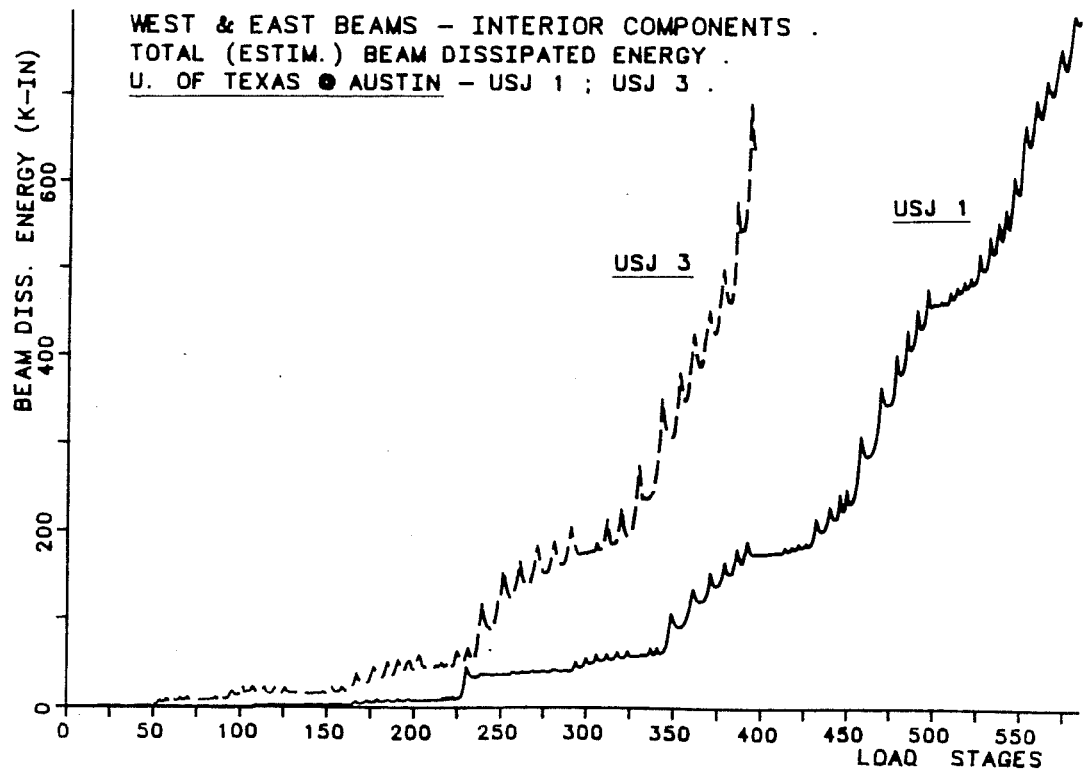


Fig. 7.22 - Interior Tests - Total Dissipated Energy.

The characterization of the components was done by evaluating the total beam energy being dissipated in both beams. The UTA components dissipated nearly 20% more energy at the end of testing (800 k-in.) than the SU tests under the same loading program (630 k-in.), Fig. 7.22. USJ - 1 had two major energy increments: the first at LDS 230 ($R = 1/47$) and, the second at LDS 349 ($R = 1/39$) whereas test USJ - 3 showed the start of increasing energy dissipation at LDS 239 ($R = 1/38$). The SU tests (IJ and IS) showed similar total beam energy dissipation. Major energy increases occurred in test IJ at LDS 3700 ($R = 1/96$) and in test IS at LDS 4500 ($R = 1/95$). The final total beam energy dissipated by test IS was larger than for test IJ under similar displacement histories.

7.4.3. Exterior vs. Interior Components. If the input energy was largely dissipated at the longitudinal beam locations near the column face and there was minimal energy dissipation elsewhere, the input vs. dissipated energy relationship would be a straight line with a 1:1 slope, Figs. 7.23 and 7.24. This can be seen in the SU tests without a slab (IJ, EJ) which fall very close to the 45° line. The other interior specimens with slab showed a response curve below the 45° line. Therefore, the energy deficit must have been dissipated at other locations such as joint core, transverse beams and columns. Test USJ - 3 showed that the longitudinal beams were dissipating less energy

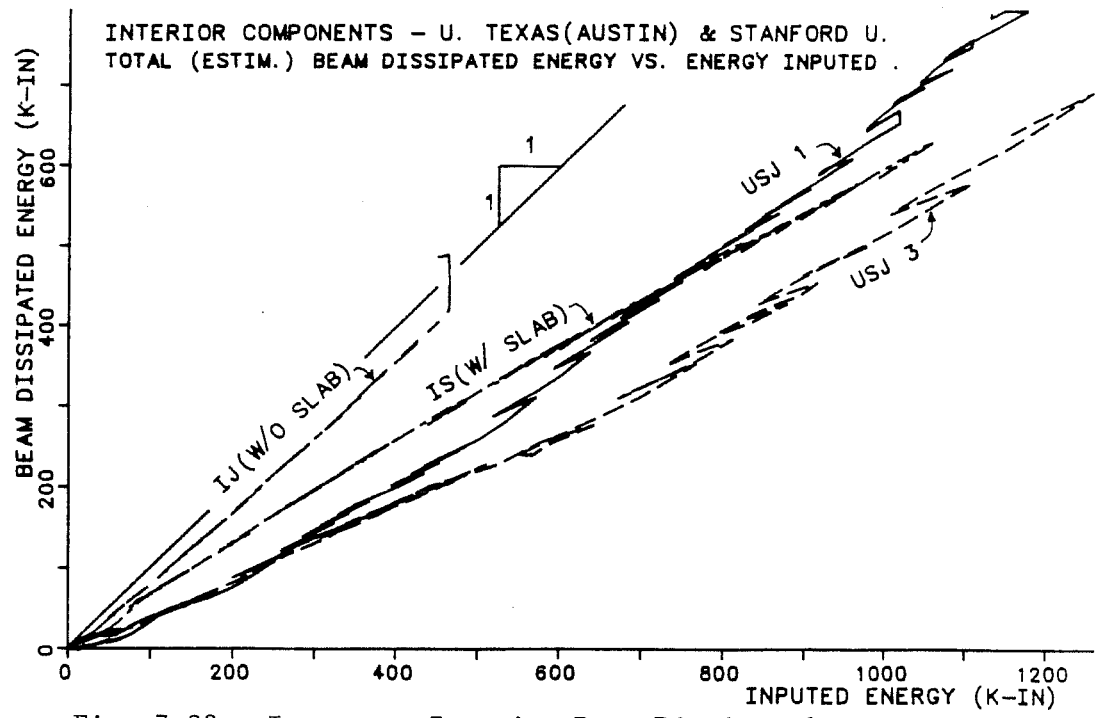


Fig. 7.23 - Input vs. Interior Beam Dissipated Energy.

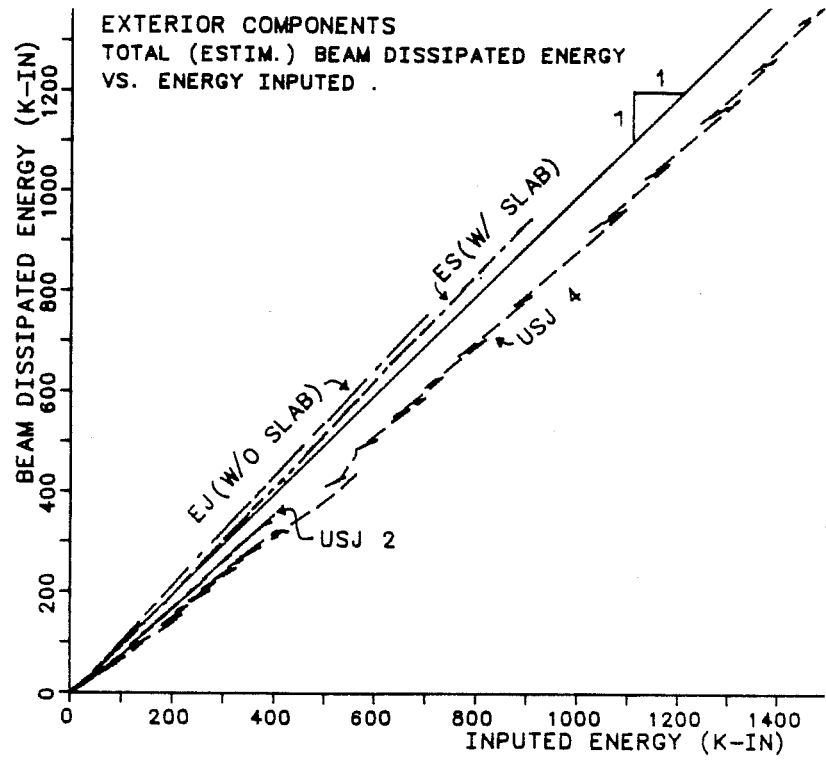


Fig. 7.24 - Input vs. Exterior Beam Dissipated Energy.

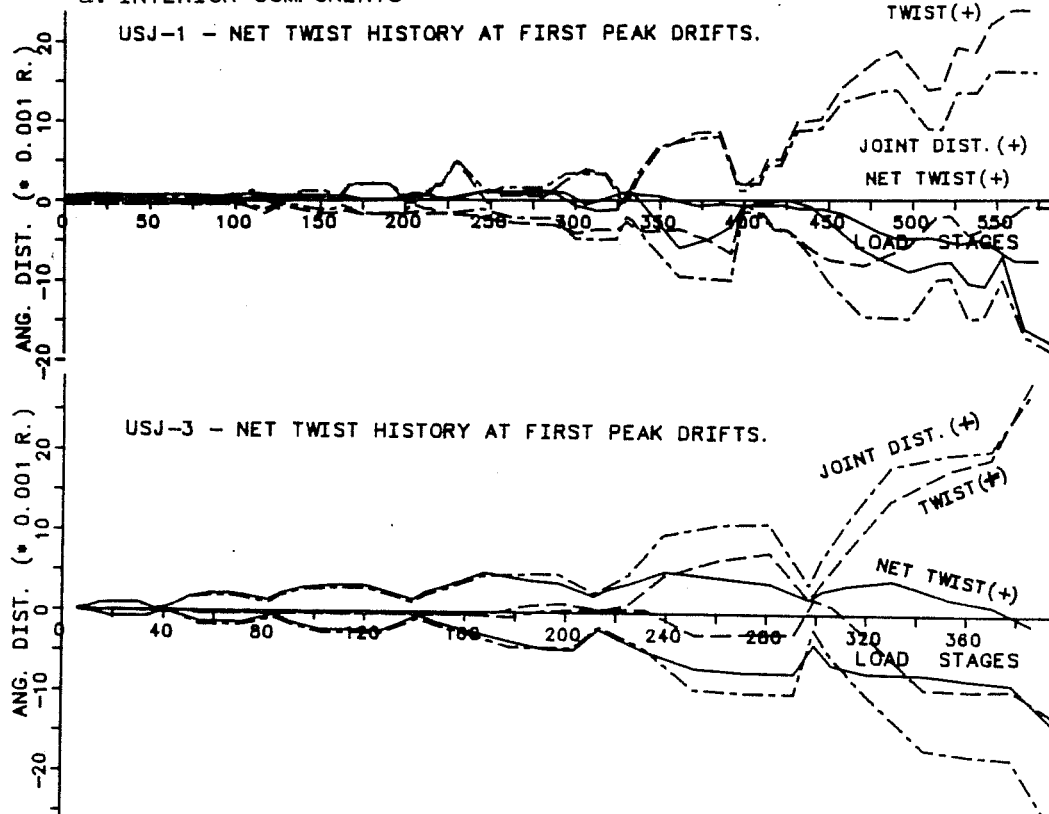
than in test USJ - 1 in spite of the larger beam reinforcement ratios. Consequently, it is plausible to assume that the joint and the transverse beams would dissipate energy and experience high strains at large deformation levels.

The exterior components with slab showed that most of the input energy was dissipated by the longitudinal beam, Fig. 7.24. Clear evidence of anchorage failure in USJ - 2 was provided by the energy response curve plotted in Fig. 7.24. Better energy response was obtained with the improved joint detailing in USJ - 4.

7.4.4 Joint Core Participation. The strain energy being released by the joint core was computed based on the assumptions shown in Fig. 7.10. The transverse beam contribution to work was not considered because: (1) the amount of beam tip load to be attributed to the torsional beam was not well known and it varied depending on sense of loading (positive or negative); and, (2) the net transverse beam twist was greatly reduced after considering the support - rotation.

The UTA interior components net twist history is depicted in Fig. 7.25-a. It can be seen in test USJ - 1 that up to LDS 470 ($R = \pm 1/26$) almost no net twist occurred in the transverse beam in the positive direction and in the negative direction was very small ($\phi_{tn} = 0.006$ rad/in.). The same phenomena was also observed in the other interior specimen

a. INTERIOR COMPONENTS



b. EXTERIOR COMPONENTS

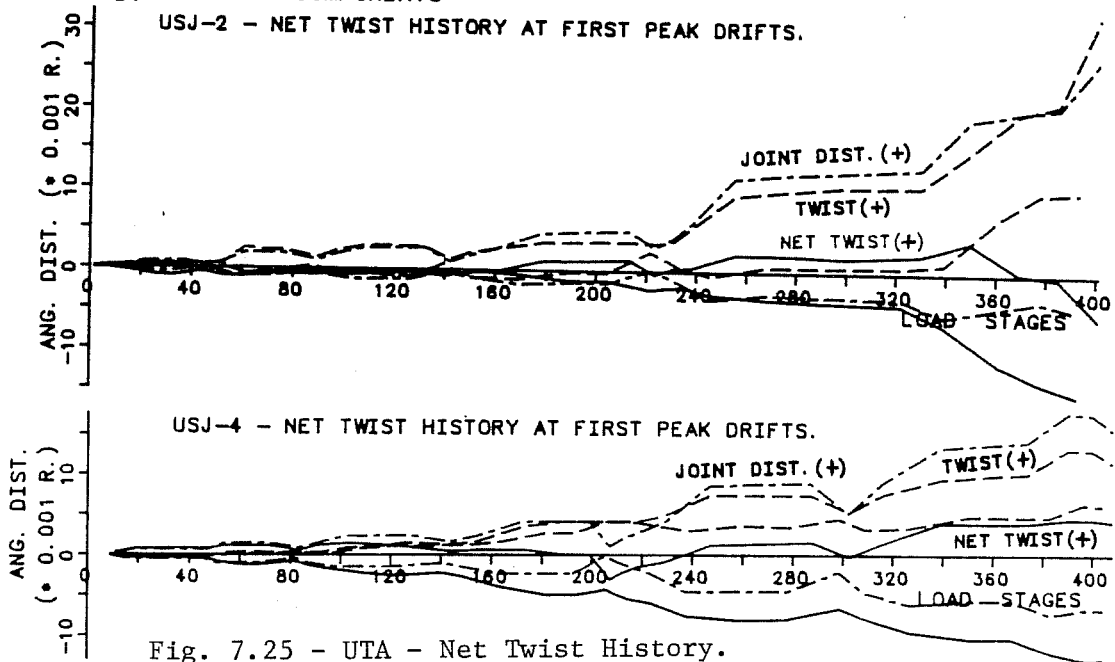


Fig. 7.25 - UTA - Net Twist History.

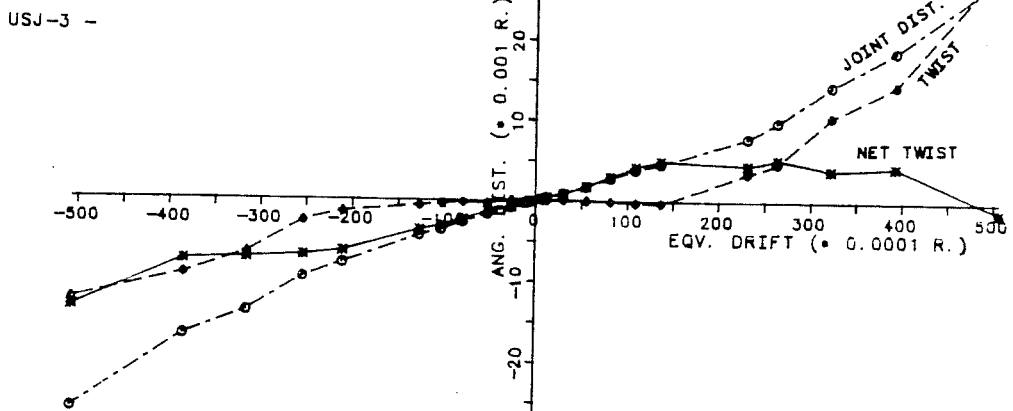
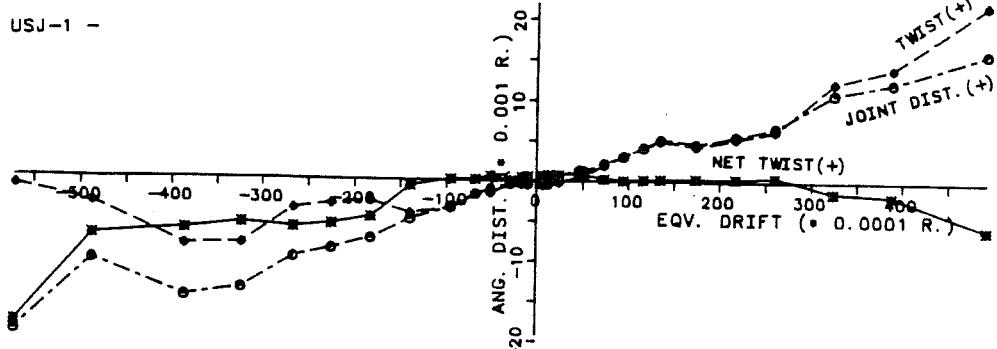
USJ - 3 where the progress of net twist throughout the test remained limited.

The UTA exterior components showed a net twist history that was marked by the duality in response depending on whether the beam was loaded downwards (positive angular distortion) or upwards, Fig. 7.25-b. In both tests USJ - 2 and USJ - 4 the net twist remained below 0.005 rad/in. when the beam moved downwards. In the other direction, the original twist deformation remained either close to zero or positive whereas the joint shear distortion was below -0.010 rad/in.

The net twist variation at first peak drifts was also plotted for both interior and exterior tests, Fig. 7.26-a,b. It can be seen that for both USJ - 1 and USJ - 3 (interior tests) the net twist angle remained in the ± 0.005 rad/in. up to an equivalent drift $R = \pm 1/25$, Fig. 7.26-a. In test USJ - 1, subjected to a load-control sequence, it can be observed that the joint distortion and original twist recorded values were almost identical in the $R = -1/70$ to $+1/38$ drift range which revealed the severity of the initial testing program. In test USJ - 3, the transverse beam started to rotate significantly outside the $R = \pm 1/40$ interval, Fig. 7.26-a.

In the exterior component tests USJ - 2 and USJ - 4, the transverse beam rotated together with the joint core in the positive direction (slab in tension) up to $R = \pm 1/26$,

a. NET TWIST AT FIRST PEAK DRIFTS.



b. NET TWIST AT FIRST PEAK DRIFTS

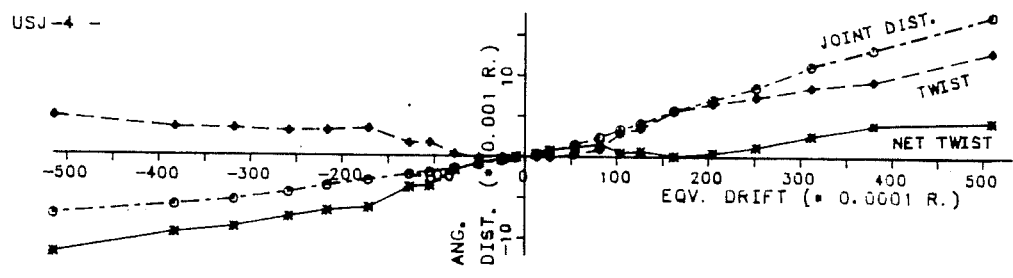
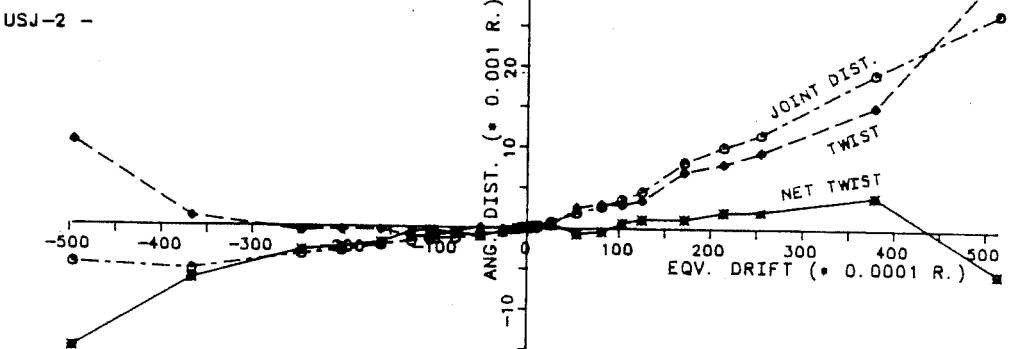


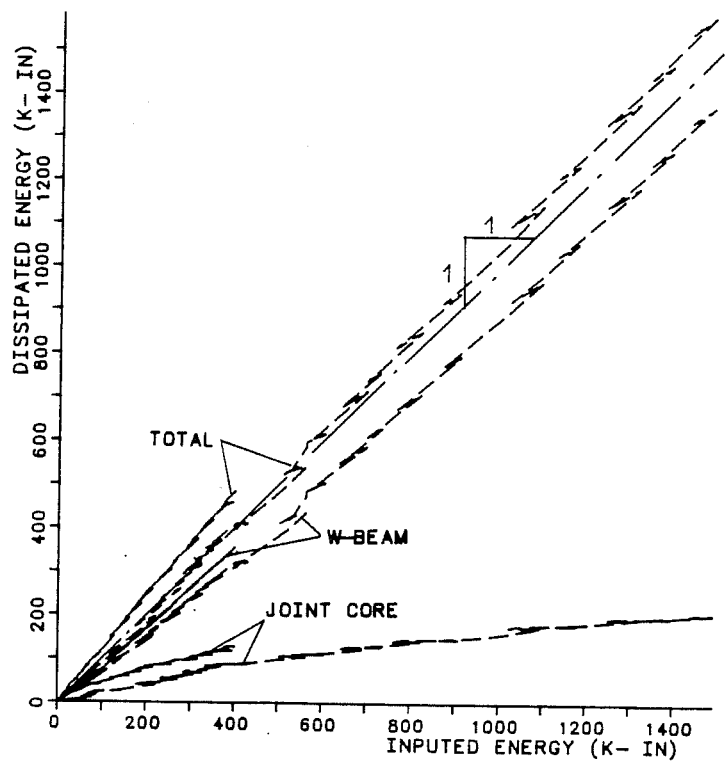
Fig. 7.26 - UTA - Net Twist at First Peak Drifts.

Fig. 7.26-b. However, in test USJ - 2 due to anchorage failure the original twist became larger than the joint distortion value beyond $R = +1/26$. In the negative direction (slab in compression) almost no twist occurred in the USJ - 2 test up to $R = -1/27$, and beyond this equivalent drift it remained positive due to the previous loading cycle. In test USJ - 4, the original transverse beam twist remained positive and small (less than 0.005 rad/in.) inside the $R = -1/100$ to $-1/19$ drift range.

7.4.5 Estimated Total Component Energy Response. The total component response was assessed using an energy approach based on the paragraph 7.3 assumptions. It can be seen that the major sources of energy absorption/dissipation were the longitudinal beam(s) and the joint core, Fig. 7.27. For the exterior components USJ - 2 and USJ - 4, the total energy input/dissipation curve is slightly above the 1:1 line which corresponds to a system where elastic energy losses are negligible. This verifies that transverse beam participation in energy response was not large. In the interior components USJ - 1 and USJ - 3, the total energy response curve remained below but close to the 45° line during the whole test for USJ - 1 and it crossed the USJ - 3 curve during the last loading cycles where $R = \pm 1/20$.

TOTAL (ESTIM.) COMPONENT DISSIPATED ENERGY
VS. INPUTED ENERGY .

UTA - EXTERIOR COMPONENTS



UTA - INTERIOR COMPONENTS

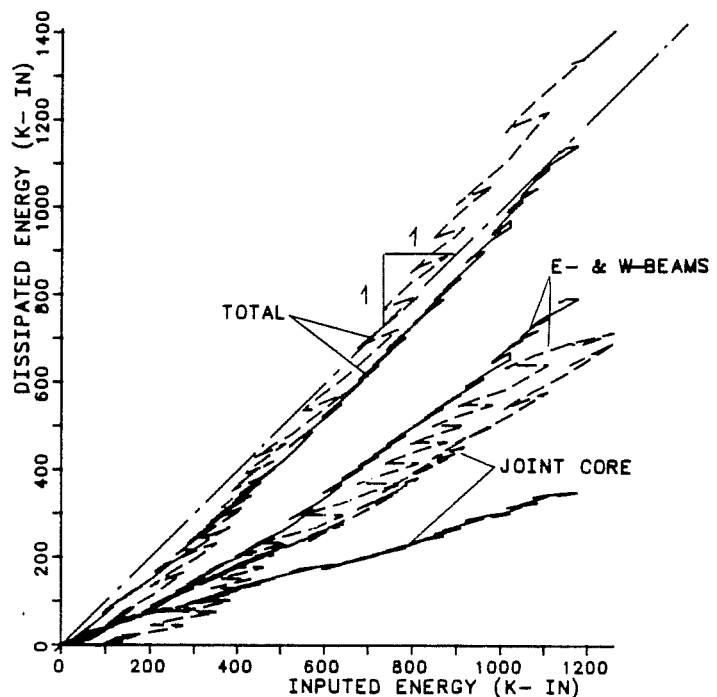


Fig. 7.27 - UTA - Total Component Dissipated Energy.

In general good agreement between the input/dissipated energy curves was obtained by considering only two sources of energy dissipation - longitudinal beam inelastic deformation and joint distortion.

7.5 Hysteretic Damping Response

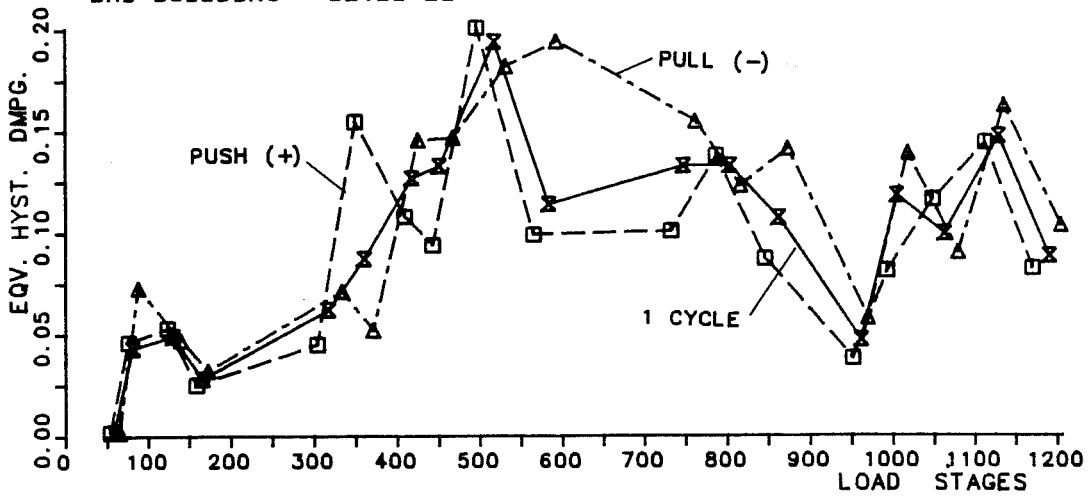
The dynamic response of the BRI building and component tests is assessed through equivalent hysteretic damping. Experimental tests have shown that hysteretic damping is independent of the test frequency as opposed to the frequency dependence of viscous damping. However, if the hysteretic energy loss is assumed to be modeled by an equivalent viscous damper, the equivalent viscous-damping ratio still is obtained by equation (7.20). This means that equation (7.20) can be used to compute the damping ratio of the structure independently of the internal energy-loss mechanisms [Clough and Penzien (6)]. Therefore, the experimentally correlated equivalent hysteretic damping (i.e., the damping force in phase with velocity and proportional to displacements) is described well by equation 7.20.

The US-Japan Test Program provided data which enabled computation of the equivalent hysteretic damping (EHD) for the BRI building and components. The EHD was considered to be an important parameter in characterizing the test response under

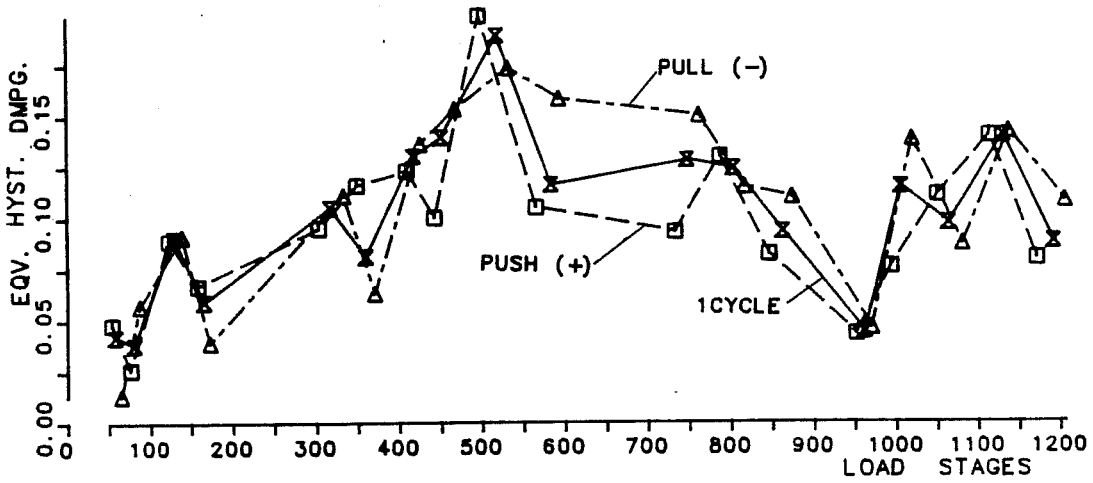
reversed cyclic loads. Evaluations of EHD histories for the BRI structure, components and component T-beams were performed. Correlations among the different tests were also made at first peak displacements.

7.5.1 BRI Building. The EHD response history for the different BRI levels (Z2, Z3, ZRoof) is shown in Fig. 7.28 for three different cases for each level: (1) positive half-cycle; (2) negative half-cycle; and, (3) one complete cycle. This approach was followed because of the non-symmetric load and displacement histories as depicted for level Z2 in Fig. 7.29. The EHD for each half-cycle was computed by integrating the energy dissipated between two zero load consecutive points. The resulting value was divided by 2π times the strain energy stored at the peak displacement obtained in the half-cycle. The EHD was computed for a complete cycle and the resulting value provided an average for two consecutive positive and negative half-cycles. The EHD history showed that large damping ratios were obtained when large displacements were input, Figs. 7.28, 7.29. It also can be observed that the damping ratio envelope had a nearly-symmetric pattern for both positive and negative drifts where a maximum $\xi = 20\%$ was attained at a $R = + 1.04\%$ (levels Z2, Z3) and for $R = - 0.65\%$, the maximum was $\xi = 17.5\%$, Fig. 7.29. The first peak drift - damping ratio envelopes also showed larger values for levels Z2 and Z3 throughout most of the test as compared with

EQUIVALENT HYST. DAMPING
BRI BUILDING - LEVEL Z2



BRI BUILDING - LEVEL Z3



BRI BUILDING - LEVEL ZROOF

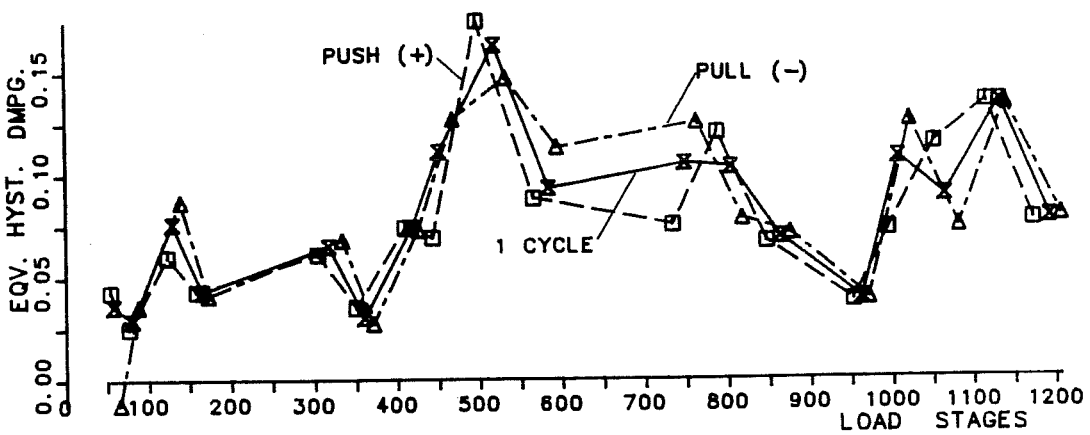


Fig. 7.28 - BRI Building - Hysteretic Damping History.

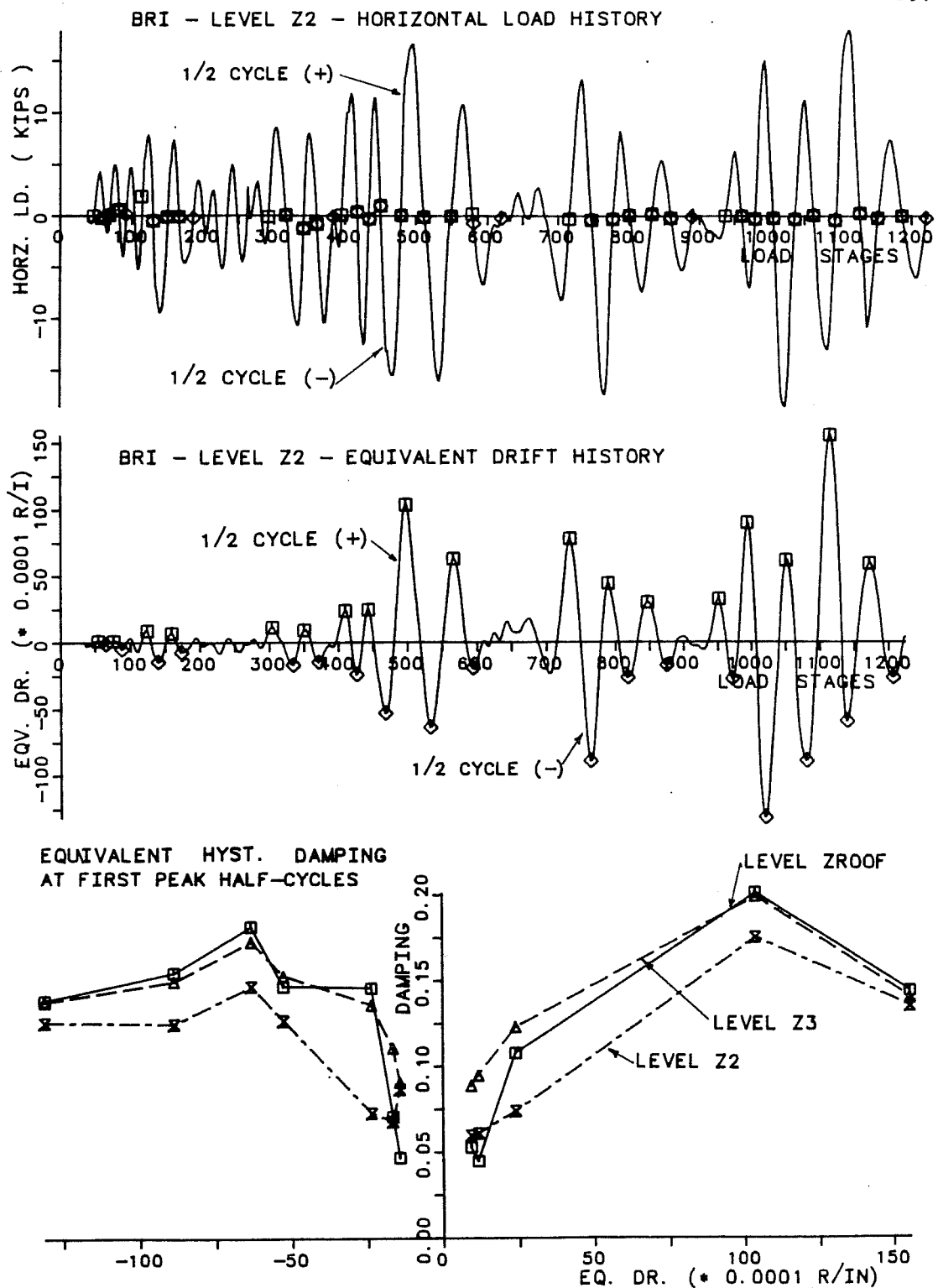


Fig. 7.29 - BRI Building - Hysteretic Damping at First Peak Displacements.

the roof level. This may result from the concentration of a shear wall plastic hinge at the lower story levels where most of the work of deformation with correspondent energy absorption/dissipation is processed.

7.5.2 Exterior Component Tests with a Slab. The EHD history for the components was studied based on the total story shear and displacement response.

The UTA exterior tests were subjected to identical story displacement histories but due to anchorage problems the maximum story shear in test USJ - 2 was well below that of specimen USJ - 4. Specimen USJ - 4 with twice the beam reinforcement ratios as USJ - 2 did not exhibit an increase in damping throughout the test, Figs. 7.30, 7.31. From these two tests it can be observed that the damping ratio when the slab was in tension (positive 1/2 cycle) was generally lower than when the slab was in compression (negative 1/2-cycle). The reduced compression zone in the beam, larger tension slab forces, large beam shear forces, top bar sliding and bond destruction and, bottom bar buckling (pinching effects) are possible sources for reduced damping ratios in the positive 1/2-cycle hysteresis loop.

The SU exterior component with a slab (ES) experienced a story displacement history similar to test USJ - 2. The maximum observed story shears were also in the same range as test USJ 2,

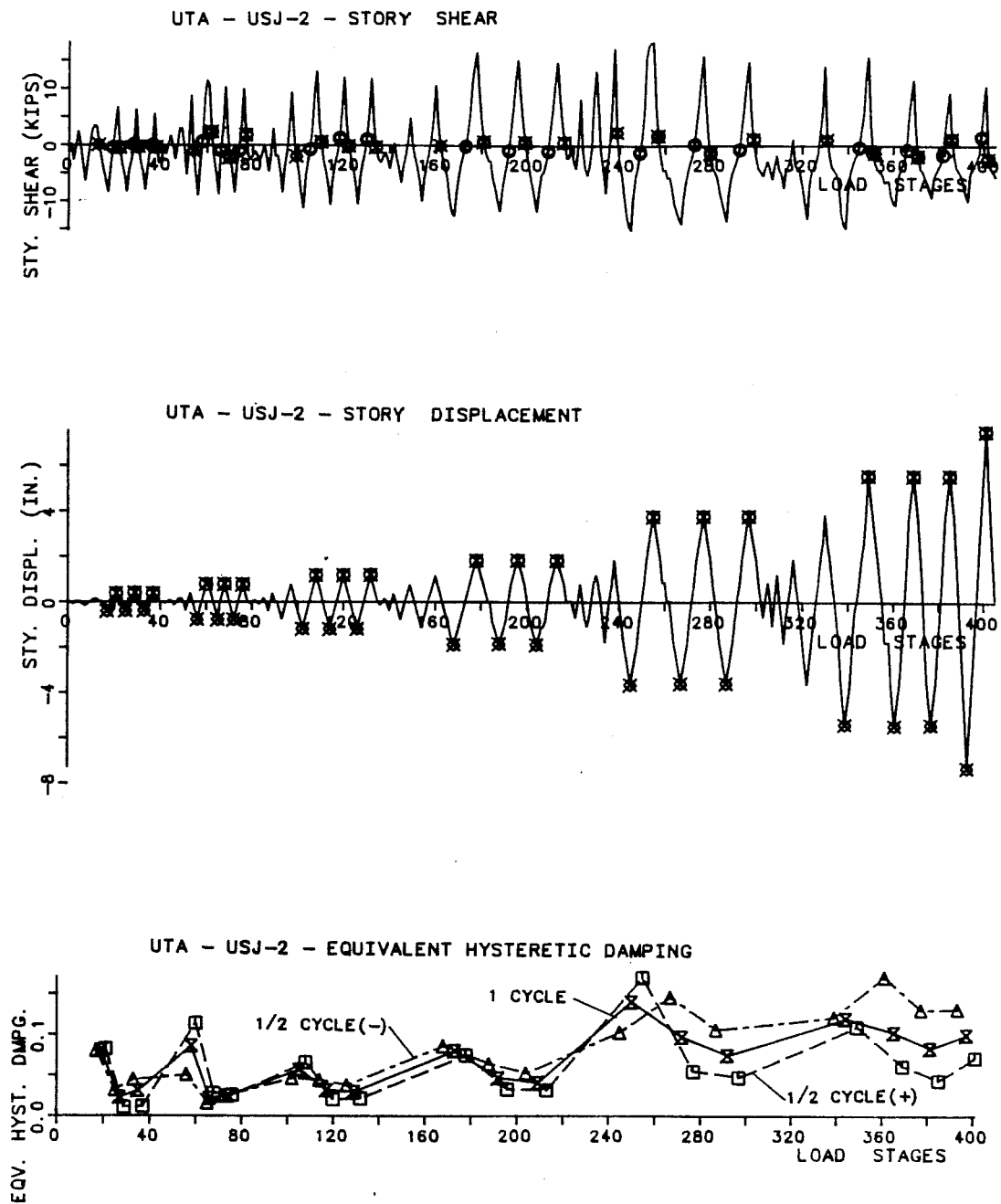


Fig. 7.30 - USJ-2 - Exterior Test Damping History.

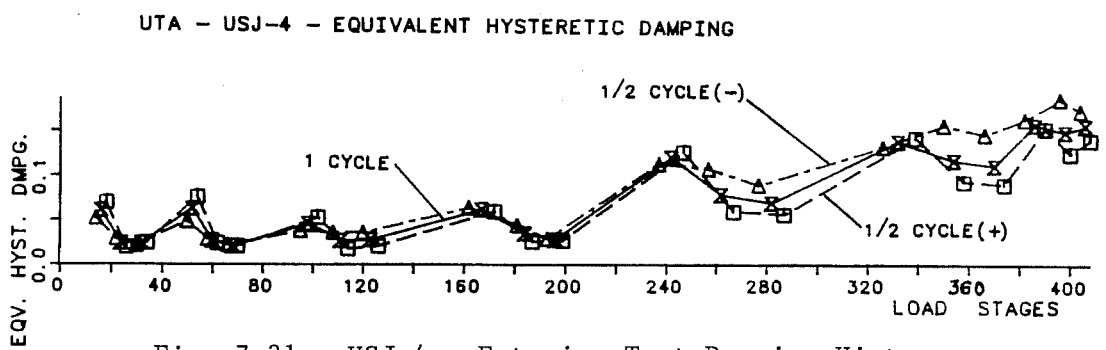
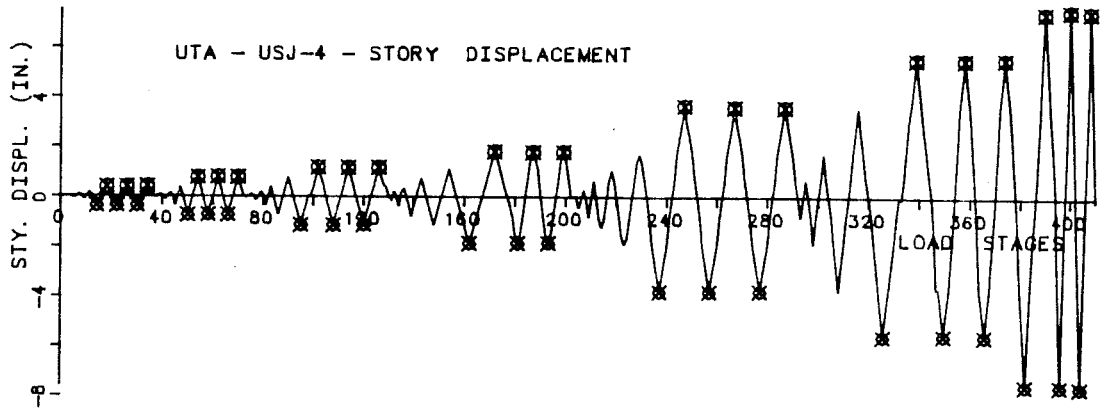
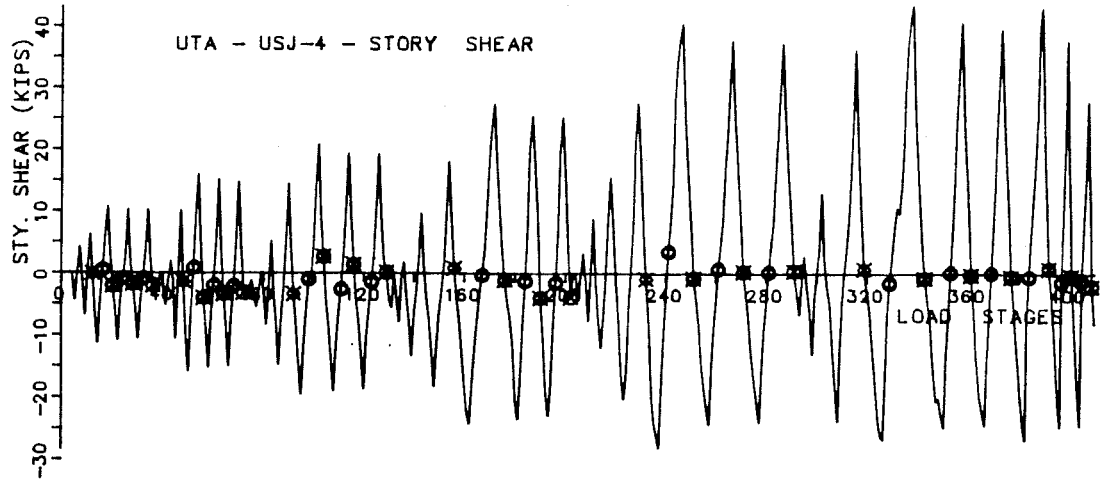


Fig. 7.31 - USJ-4 - Exterior Test Damping History.

Fig. 7.32. However, the EHD history yielded values twice as large as in test USJ - 2 with a more striking difference in response between positive and negative half-cycle values. The larger damping ratios of 25 to 33% in specimen ES may have resulted from bond deterioration in the joint region (casting problems) and localized cracking in the micro-concrete structure.

The Japanese 1/2-scale tests were subjected to a small number of displacement cycles of increasing amplitudes, Fig. 7.33. However, the observed story displacements were smaller as compared to the US specimens because of: (1) the smaller imposed drift rotations, and (2) the smaller height in Japanese specimens (3.00 m, 118.1-in) as compared to the US tests (3.75 m, 147.6 in.). Consequently, the resulting story displacements were 20% smaller at the same equivalent drift level. The observed story shear was higher than in the US tests with a strong strength difference when the slab was in tension vs. the compression. The observed damping ratios were well above the US tests mainly in the positive 1/2-cycles. This difference in response may result from the presence of a constant axial load of 219-kips (99.3 tf) applied throughout the whole test which may have precompressed the joint region. The fewer loading cycles with smaller amount of cumulative damage may also be responsible for larger damping ratios, Fig. 7.33.

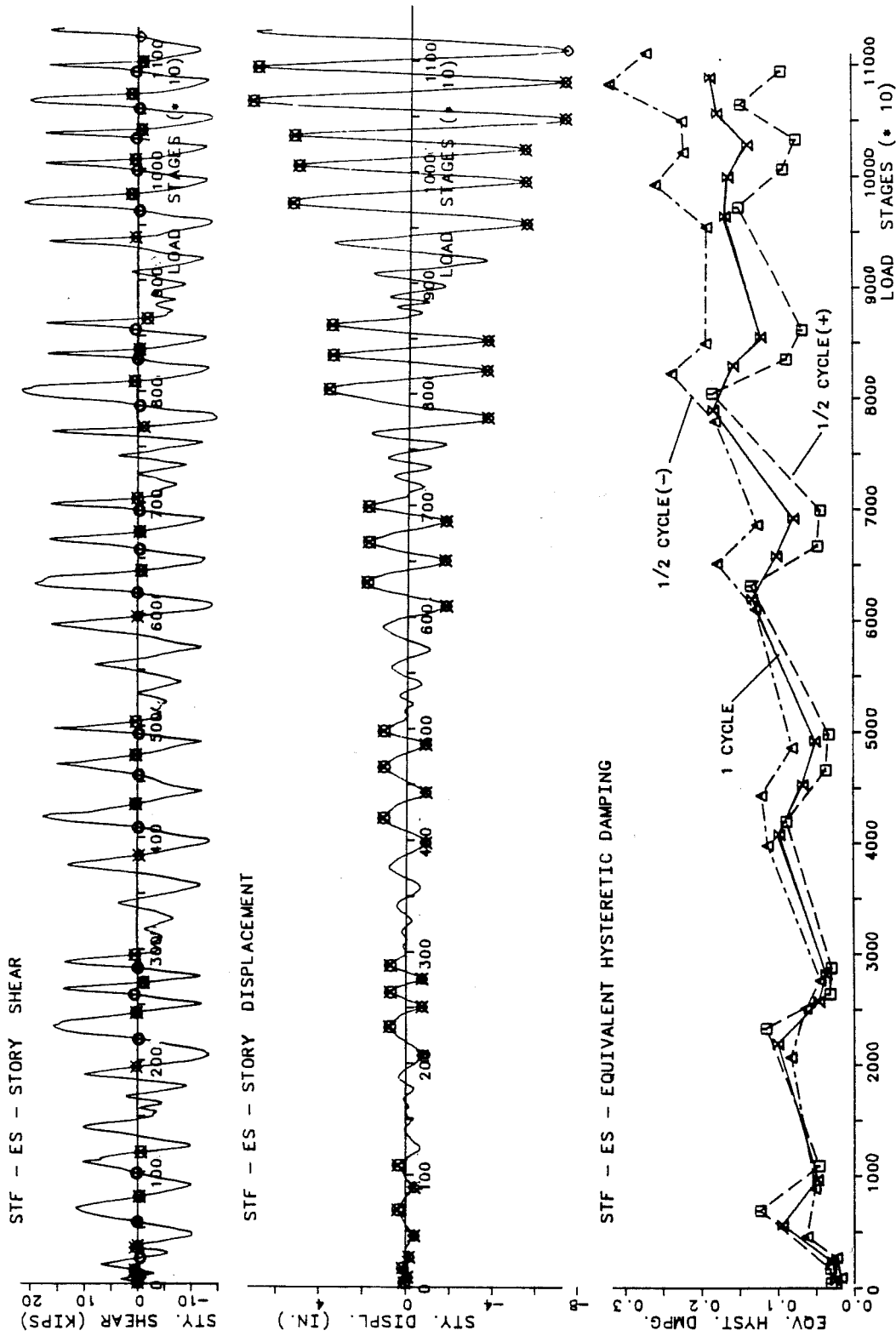
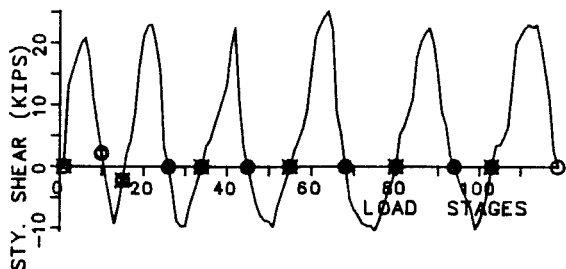
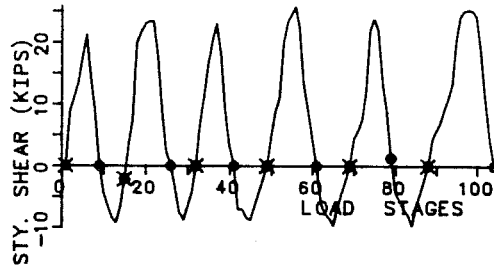


Fig. 7.32 - ES - Exterior Test Damping History.

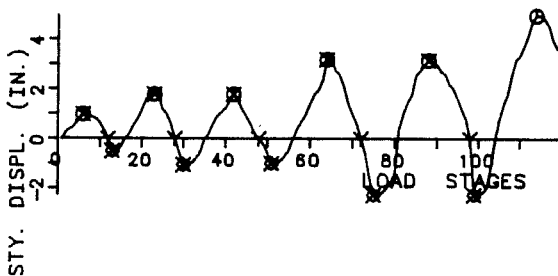
JPN - E-1 - STORY SHEAR



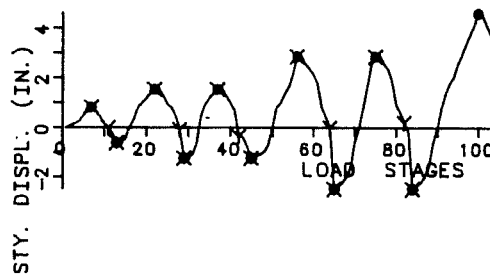
JPN - E-2 - STORY SHEAR



JPN - E-1 - STORY DISPLACEMENT

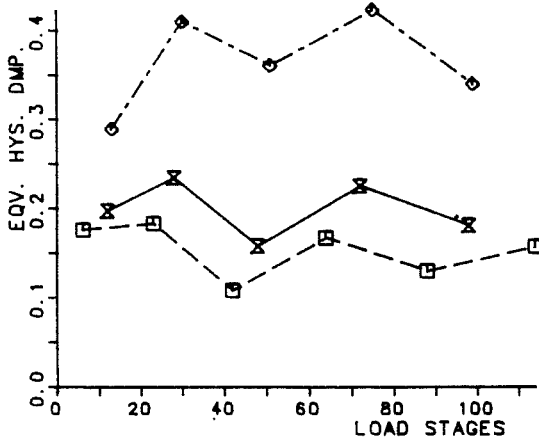


JPN - E-2 - STORY DISPLACEMENT



$N_e = 219.2$ Kips

EQUIVALENT HYSTERETIC DAMPING
JAPAN - E-1 (JP DESIGN)



EQUIVALENT HYSTERETIC DAMPING
JAPAN - E-2 (US DESIGN)

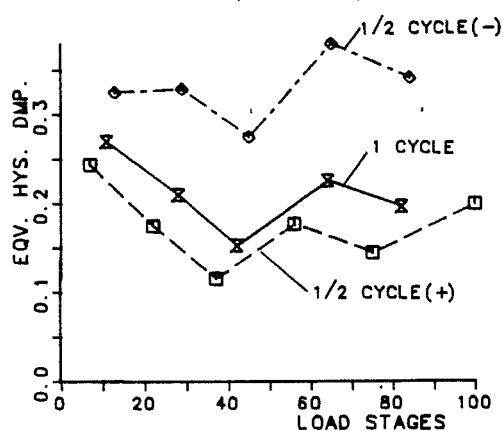


Fig. 7.33 - E-1, E-2 - Exterior Tests Damping Histories.

7.5.3 Interior Components with a Slab. The interior components response history was characterized by its symmetry along the time axis for the story shear and displacement and by similar hysteretic response under either positive or negative half-cycles. This resulted from the alternating contribution of the E- and W- beams to the global component response.

In the UTA specimens USJ - 1, USJ - 3, EHD ratios in the order of 10 to 15% were obtained, Figs. 7.34, 7.35. It can be noticed in test USJ - 1 conducted under a load-control program up to LDS 240 that larger initial damping demands were made during the beginning of the test as compared with the increasing pattern observed in test USJ - 3. It can also be observed that at the large applied displacement (LDS 230) greater damping demands had to be met as compared to the previous loading cycles. The observed phenomena that larger damping ratios are obtained during the first incursion into virgin displacement regions as compared with subsequent cycles at the same displacement level can be observed test USJ - 3, Fig. 7.35.

The SU (IS) test was subjected to a displacement history similar to UTA - USJ - 1 test where the same large peak displacement was imposed near LDS 4500, Fig. 7.36. The same results as for the UTA interior joint tests can be observed with this specimen, Fig. 7.36: (1) as the applied displacements increased, large damping ratios were also observed; and, (2) at

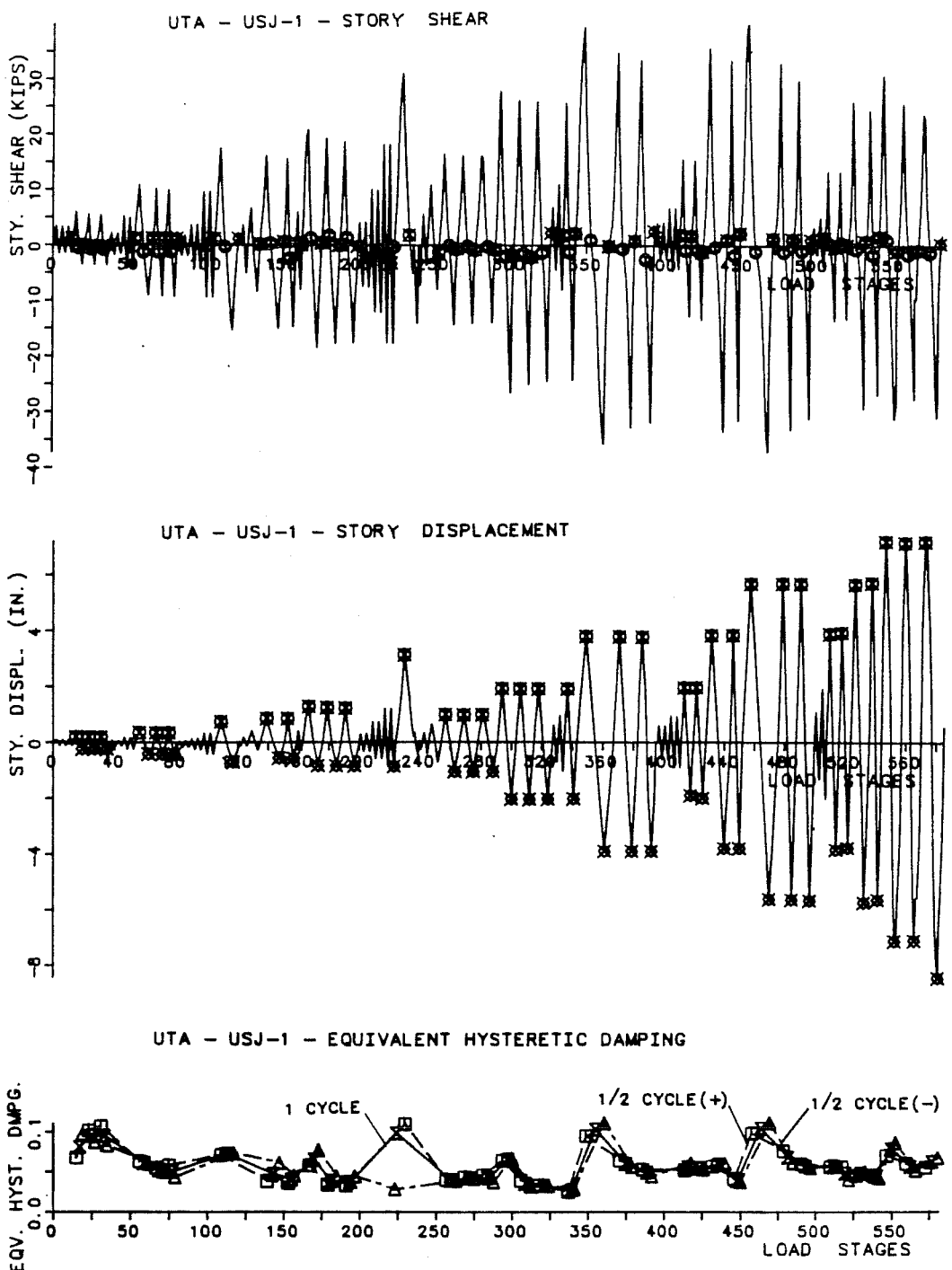


Fig. 7.34 - USJ-1 - Interior Test Damping History.

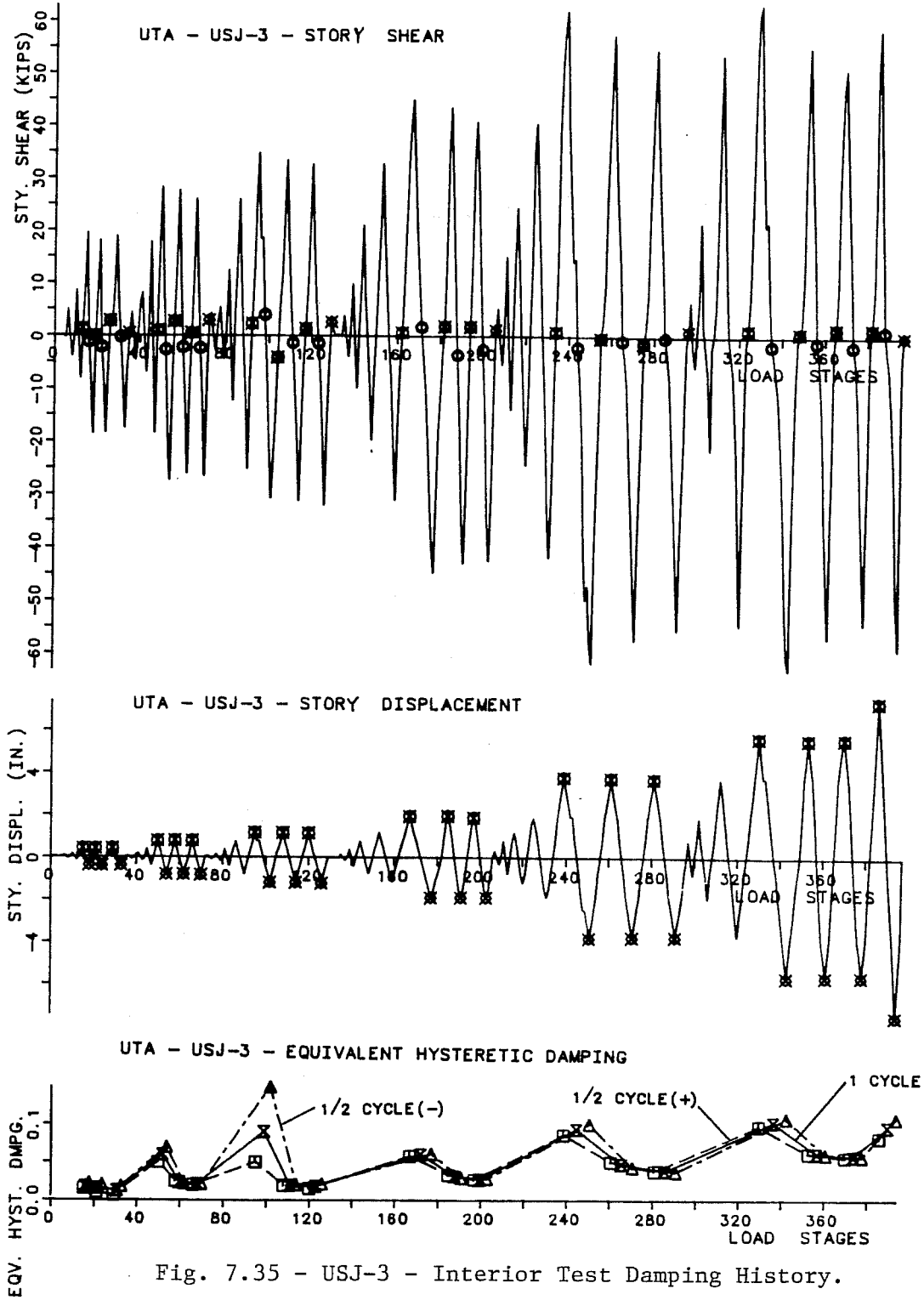


Fig. 7.35 - USJ-3 - Interior Test Damping History.

a given displacement level, the subsequent cycles to the first virgin loading in the same displacement range showed lower damping ratios.

The Japanese interior tests showed symmetric behavior around the time axis for both the story load and displacement histories, Fig. 7.37. The maximum story displacements were below the values attained for the US specimens by the same reasons stated for the exterior component tests. The interior Japanese tests damping ratio was in the 15 to 17% range which was well below the 15 to 40% range observed for the exterior components, Fig. 7.37. The interior tests were performed under a slightly larger axial compressive load of 230 kips (104.3 tf).

7.5.4 Response of Components Without a Slab. The response of components without a slab was characterized mainly by the much smaller story shear force under displacement histories identical to the components with a slab.

The observed damping ratio history showed that larger damping ratios were obtained when the top beam bars were in compression than in tension, Figs. 7.38, 7.39, although the difference was not as large as with the exterior components with a slab. The EJ exterior test reached larger hysteretic damping ratios of 25 to 30% towards the end of the test program as compared with the IJ interior component values of 10 to 20%. It was also observed that after the first incursion into virgin

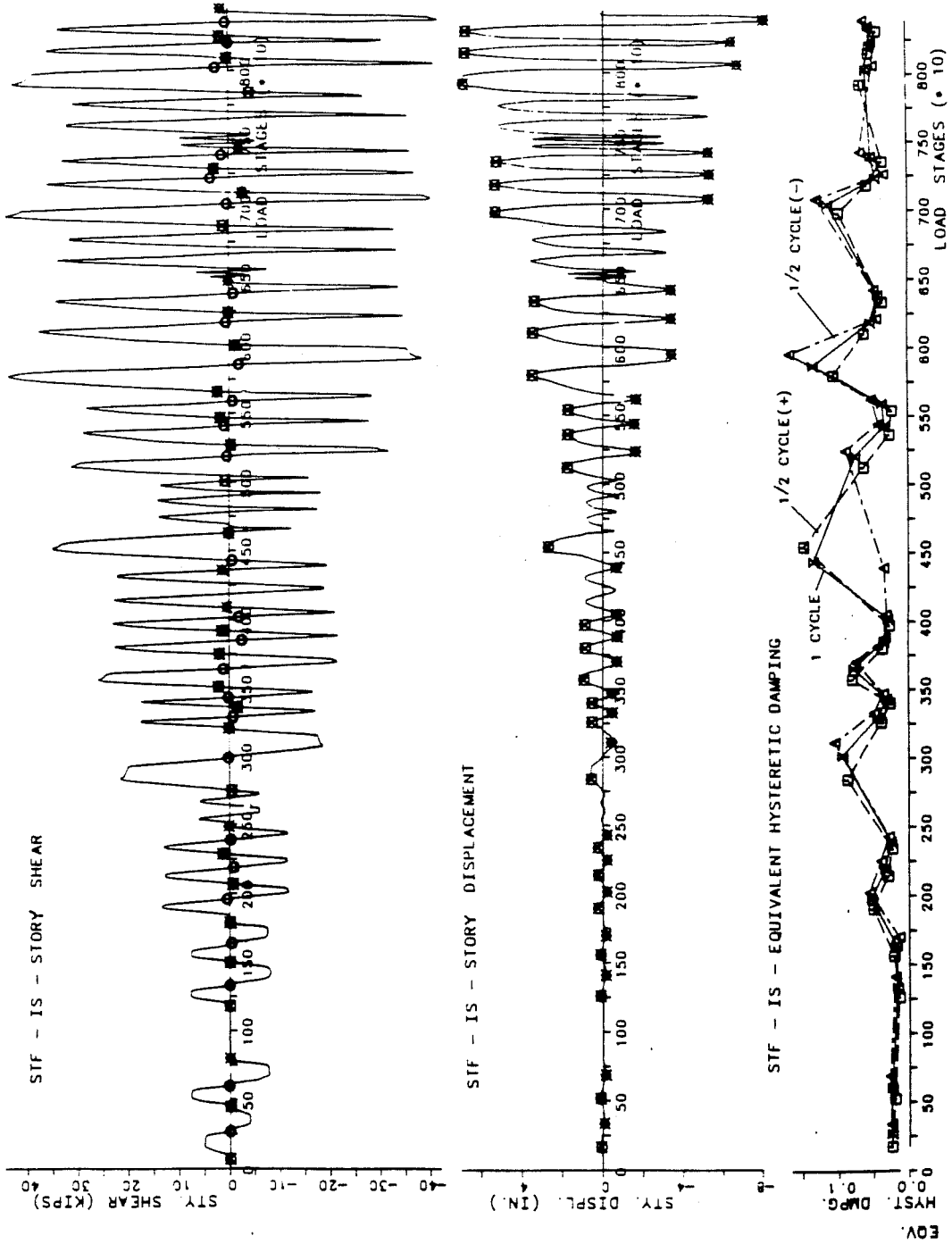


Fig. 7.36 - SU-IS - Interior Test Damping History.

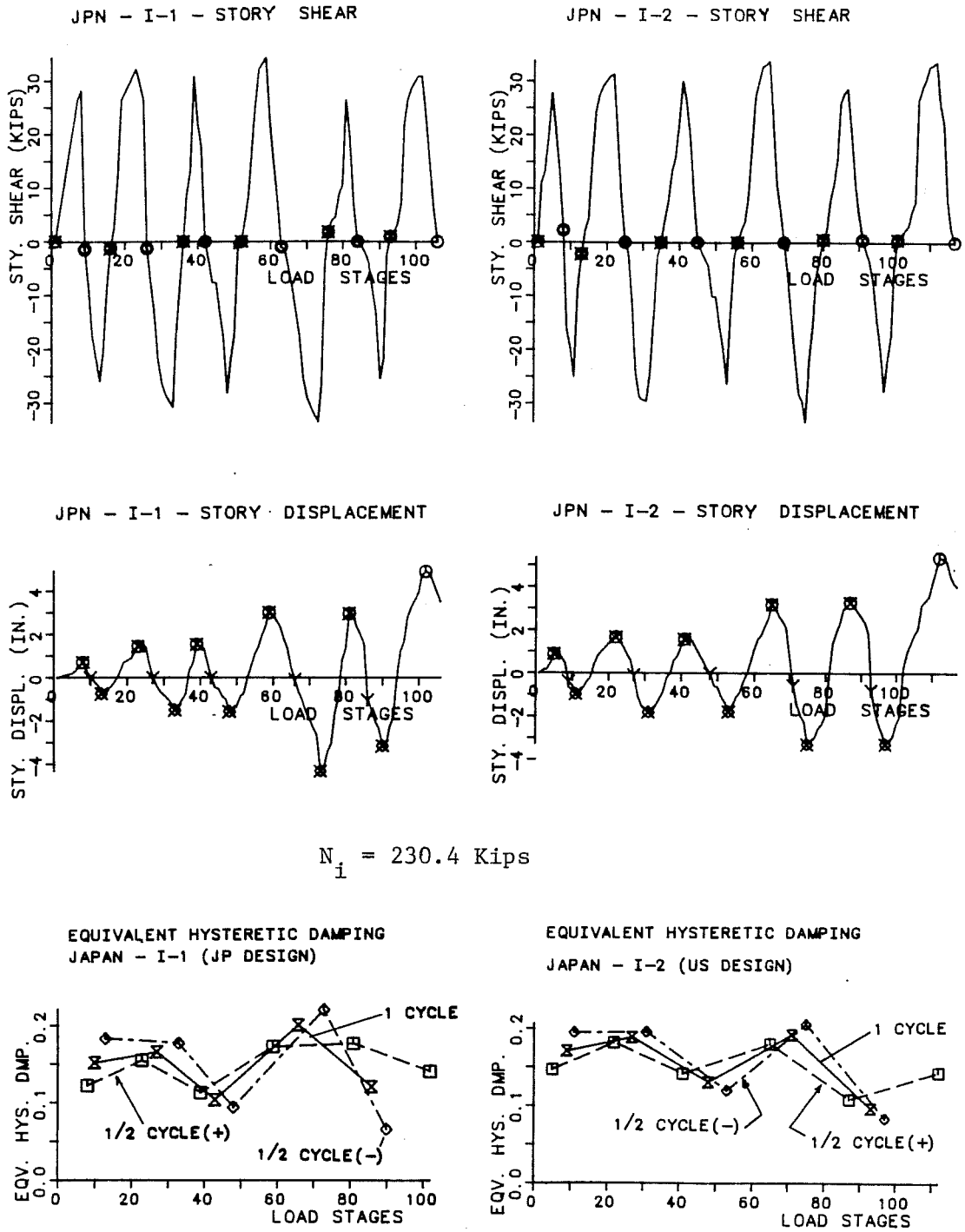


Fig. 7.37 - I-1, I-2 - Interior Test Damping History.

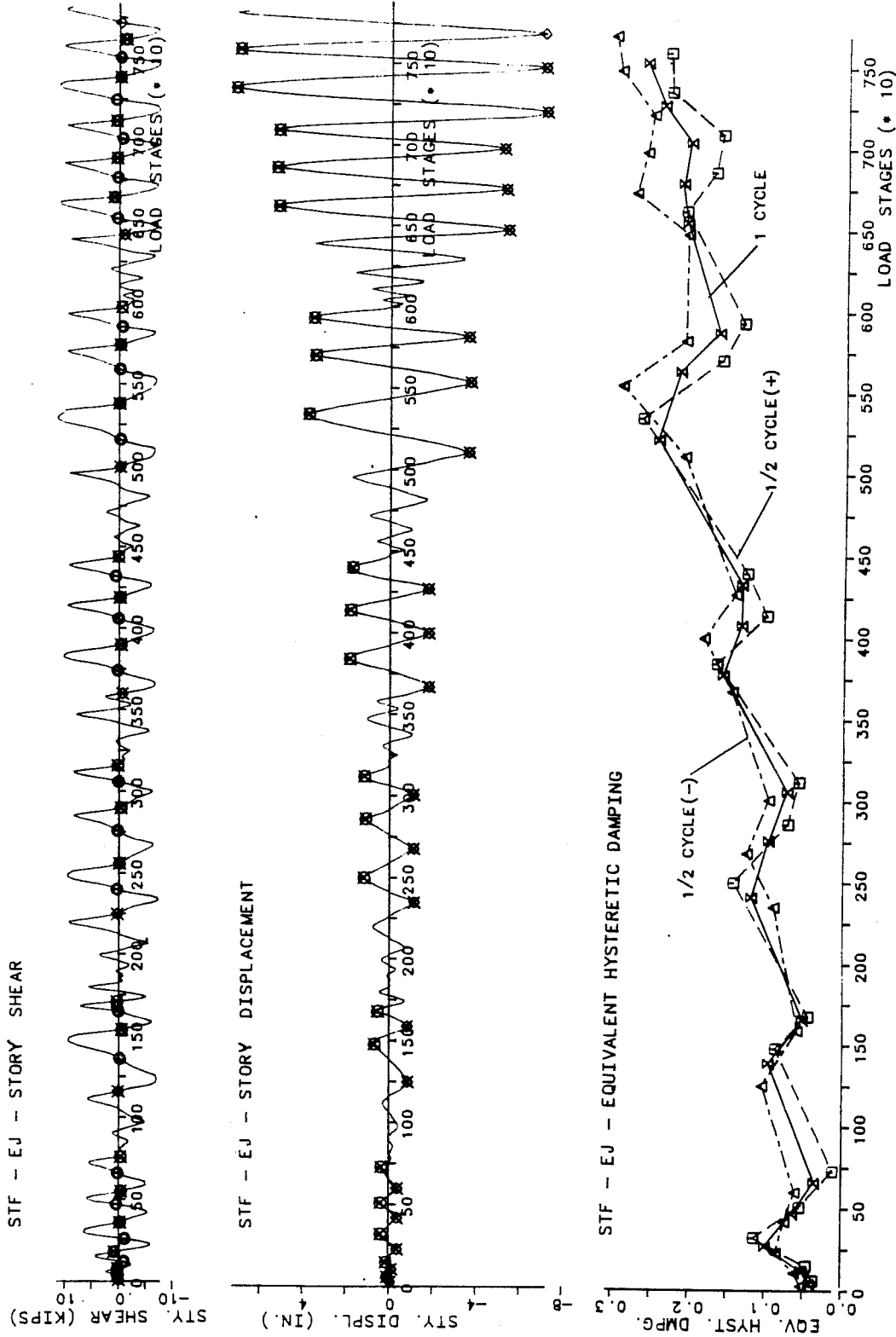


Fig. 7.38 - EJ - Exterior Test Damping History.

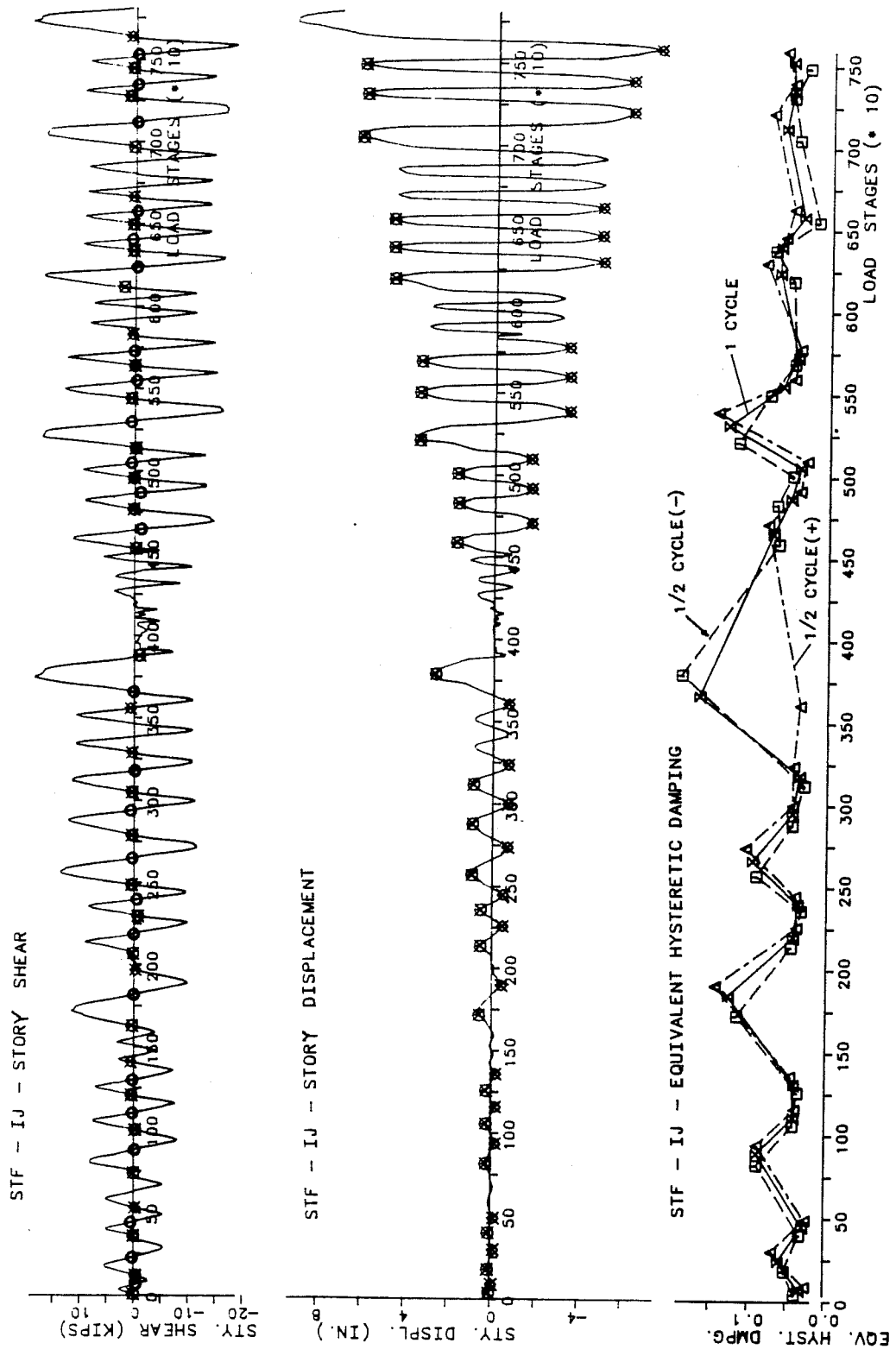


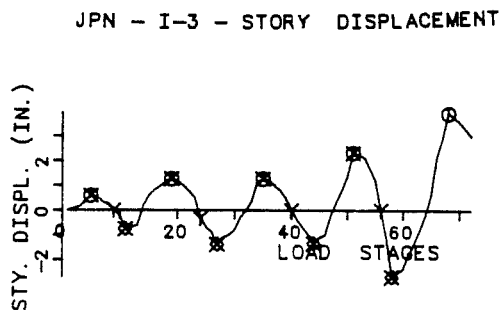
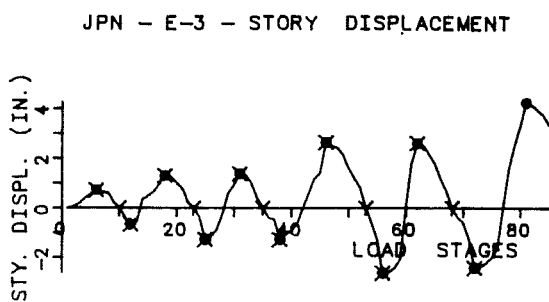
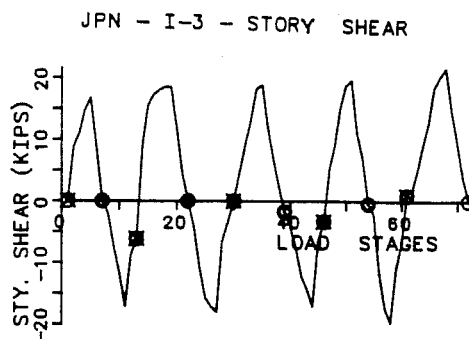
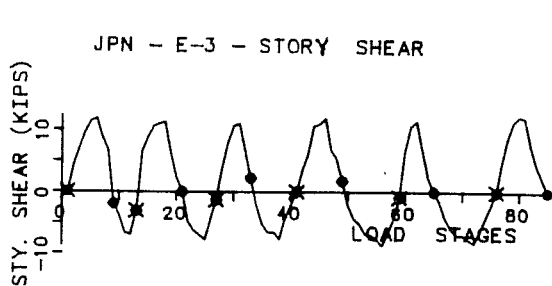
Fig. 7.39 - IJ - Interior Test Damping History.

displacements, the damping ratio was smaller in the next cycle at the same displacement level.

The Japanese 1/2-scale tests had similar response history as the US Stanford University tests without a slab, Fig. 7.40. The maximum exterior joint story shear was in the -10 to 10 kips range identical to the SU - EJ test, whereas for the interior joint, the -20 to 22 kips was similar to the SU-IJ test. The applied axial loads in both tests were equal to the values used for the same specimens with a slab roughly, $0.14 - 0.15 P_o$. The difference in the damping ratio response between the exterior and interior tests was analogous to the SU tests. The exterior joint damping ratios were generally higher than the interior joint with a larger value for the negative half-cycle in the exterior joint.

7.6 Hysteretic Damping in Components

The history of hysteretic damping response in the complete BRI floor system at level Z2 and in the component tests is studied. Two main sets are considered: (1) the exterior joints, and (2) the interior joints. Within each set, two subsets are analyzed: (a) the prototype joint tests, with reinforcement detailing and a cast-in-situ slab similar to the BRI building; (b) the "other" joint tests, which include



$N_e = 219.2$ Kips

$N_i = 230.4$ Kips

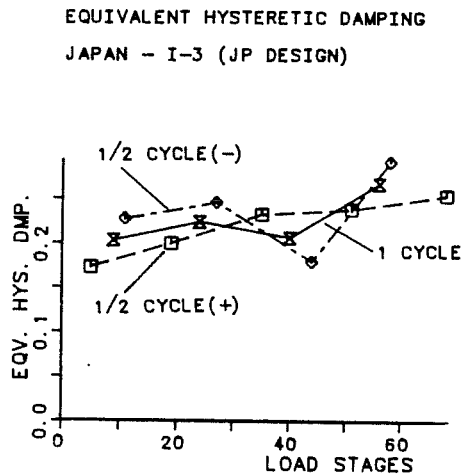
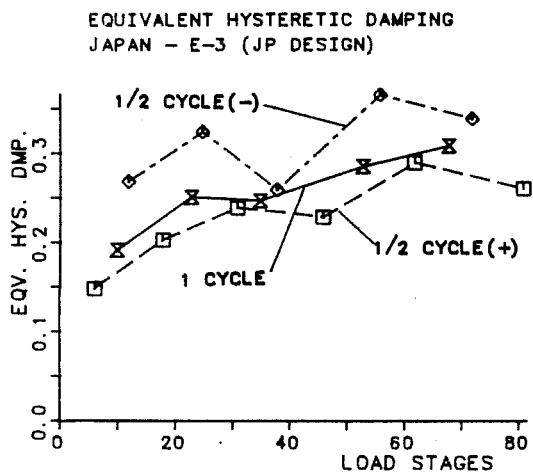


Fig. 7.40 - E-3, I-3 - Japanese Tests Damping History.

components with higher beam reinforcement ratios and components without a slab.

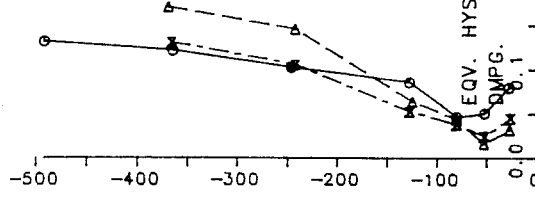
Based on the hysteretic damping response history, it was found that at each excursion to a new peak displacement level, the specimen responded with higher peak damping ratios. At subsequent cycles within the same deformation level, the damping ratio dropped and remained fairly constant. The component response was studied for half-cycles because of T-beam response on the direction of loading. The first peak half-cycle where a "new" displacement level was reached was labeled "cycle 1" and the subsequent cycles at the same deformation level "cycle 2" and "cycle 3."

7.6.1 Exterior Components. The damping response in the US components is shown in Fig. 7.41. It can be seen that when the longitudinal beam was loaded downwards, the damping ratio was lower than when it was loaded in the opposite direction. This was also observed in the Japanese specimens, Fig. 7.42. The US tests subjected to identical load histories showed that during cycles 2 and 3, the damping ratio dropped and stabilized at half the value at the initial peak displacement (cycle 1). However, when the cantilever beam moved upwards, cycle 2 damping ratios were slightly higher than in cycle 1 and then in the third cycle were identical to the first cycle. The Japanese specimens subjected to a more limited loading program showed very high

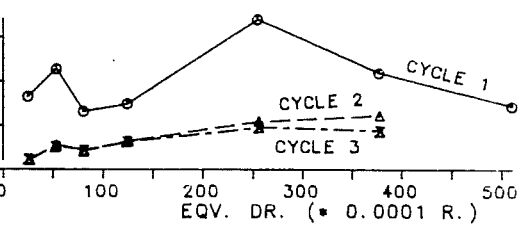
EQUIVALENT HYSTERETIC DAMPING AT PEAK HALF-CYCLES

USJ - 2 : EXTERIOR PROTOTYPE

* W-BEAM UP *

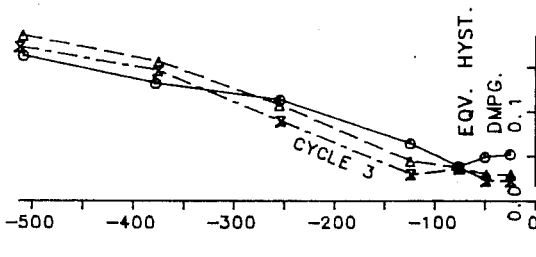


* W-BEAM DOWN *

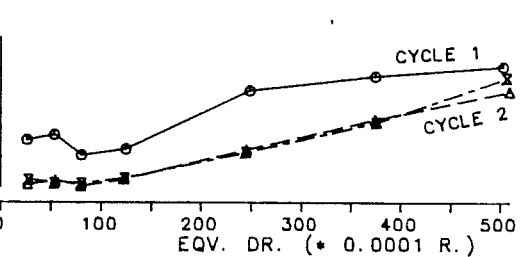


USJ - 4 : EXTERIOR MODIFIED

* W-BEAM UP *

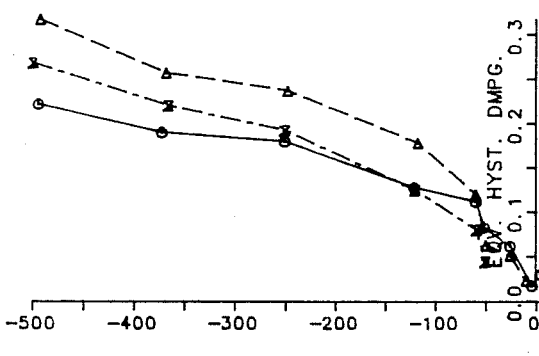


* W-BEAM DOWN *

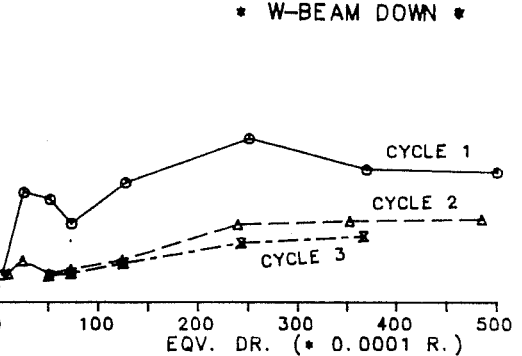


SU - ES : EXTERIOR JOINT W/ SLAB

* W-BEAM UP *

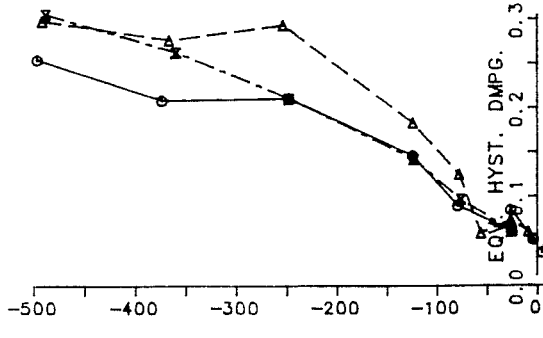


* W-BEAM DOWN *



SU - EJ : EXTERIOR JOINT W/O SLAB

* W-BEAM UP *



* W-BEAM DOWN *

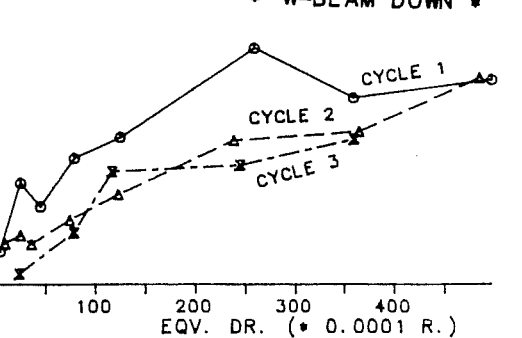
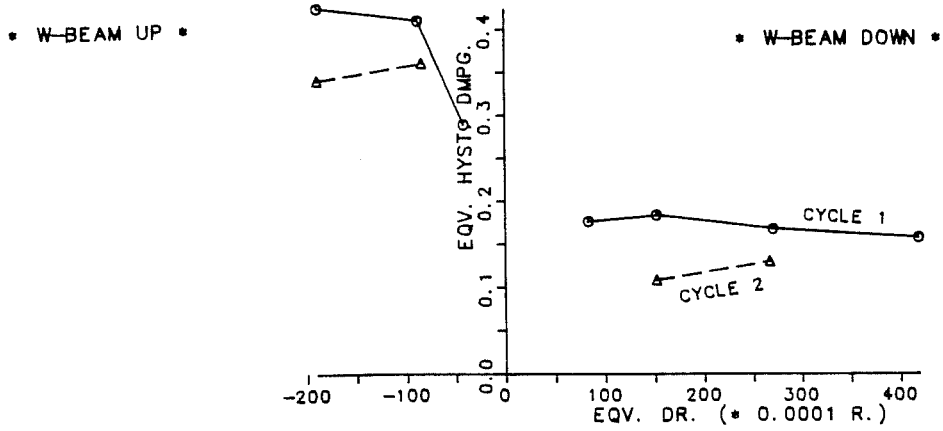


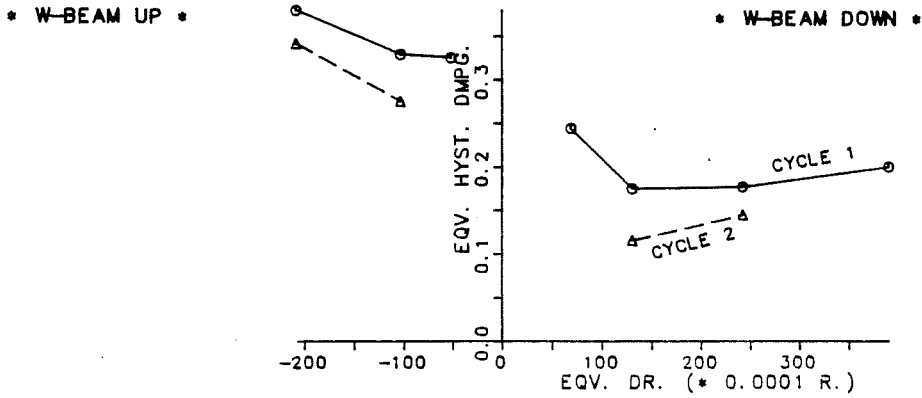
Fig. 7.41 - Us Exterior Tests Damping at Peak Drifts.

EQUIVALENT HYSTERETIC DAMPING AT PEAK HALF-CYCLES

JPN - E1 : EXTERIOR JOINT W/ SLAB (JPN DESIGN)



JPN - E2 : EXTERIOR JOINT W/ SLAB (US DESIGN)



JPN - E3 : EXTERIOR JOINT W/O SLAB (JPN DESIGN)

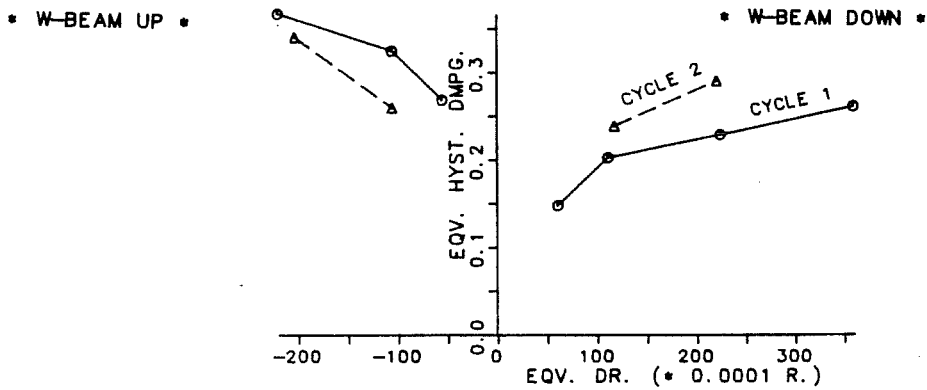


Fig. 7.42 - Japanese Exterior Tests Damping at Peak Drifts.

hysteretic damping ratios; on the order of 35 to 50% at $-1/50$ equivalent drift (beam up). A 20% damping ratio (beam down) was obtained at equivalent drifts of $+1/50$.

The observed lower damping ratios when the beam was loaded down may have resulted from the presence of higher beam shear forces combined with the more unstable behavior of a narrowly compressed beam web (negative moment). In the reversed direction (slab in compression) more stable behavior may be obtained (larger compressed slab width) combined with smaller beam shear forces.

A comparison among all the different tests and the BRI floor Z2 is shown in Figs. 7.43 and 7.44. For the prototype tests it can be observed that at first peak half-cycles (cycle 1): (1) the components damping ratio was smaller than the BRI floor Z2; (2) both UTA (USJ-2) and SU(ES) components showed a more damping when the specimens were subjected to a load-control program up to an equivalent drift of $+1/40$; (3) test JPN(I-1) showed consistently higher damping ratios due to the reduced number of cycles in the loading program; and, (4) test ES showed higher damping ratios than test USJ-2. On the other hand, at the second peak half-cycles (cycle 2), the exterior prototype showed a large decrease in damping for the slab in tension (beam down) as opposed to an increase for the slab in compression (beam up), Fig. 7.43. The other exterior joint tests showed similar

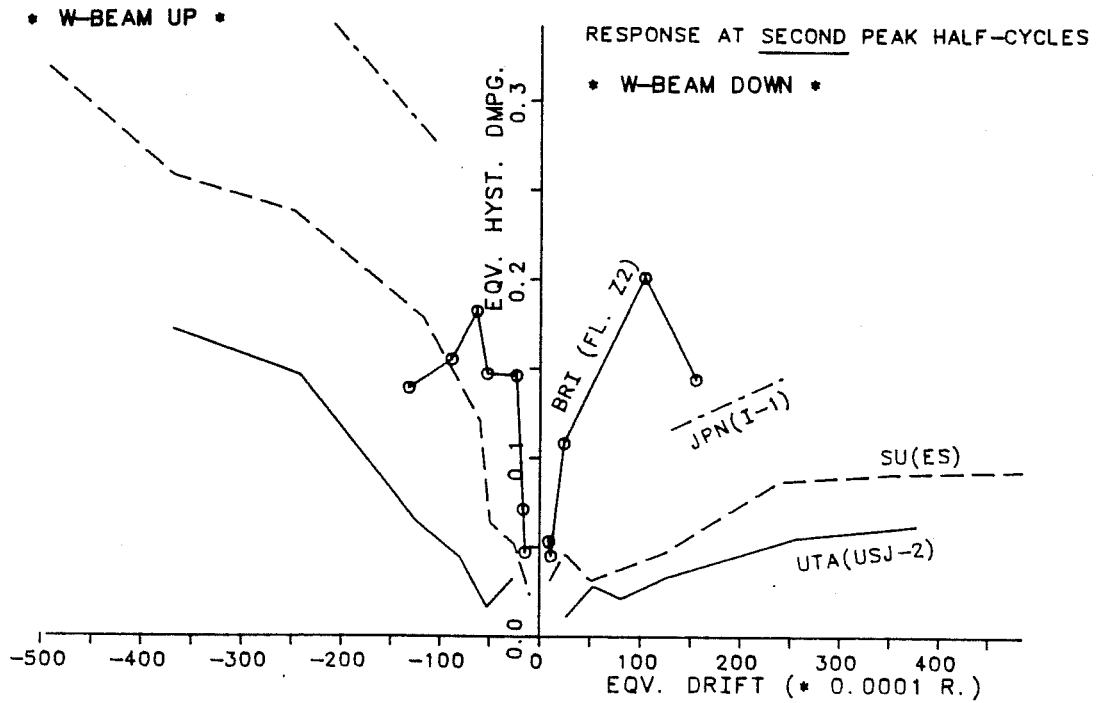
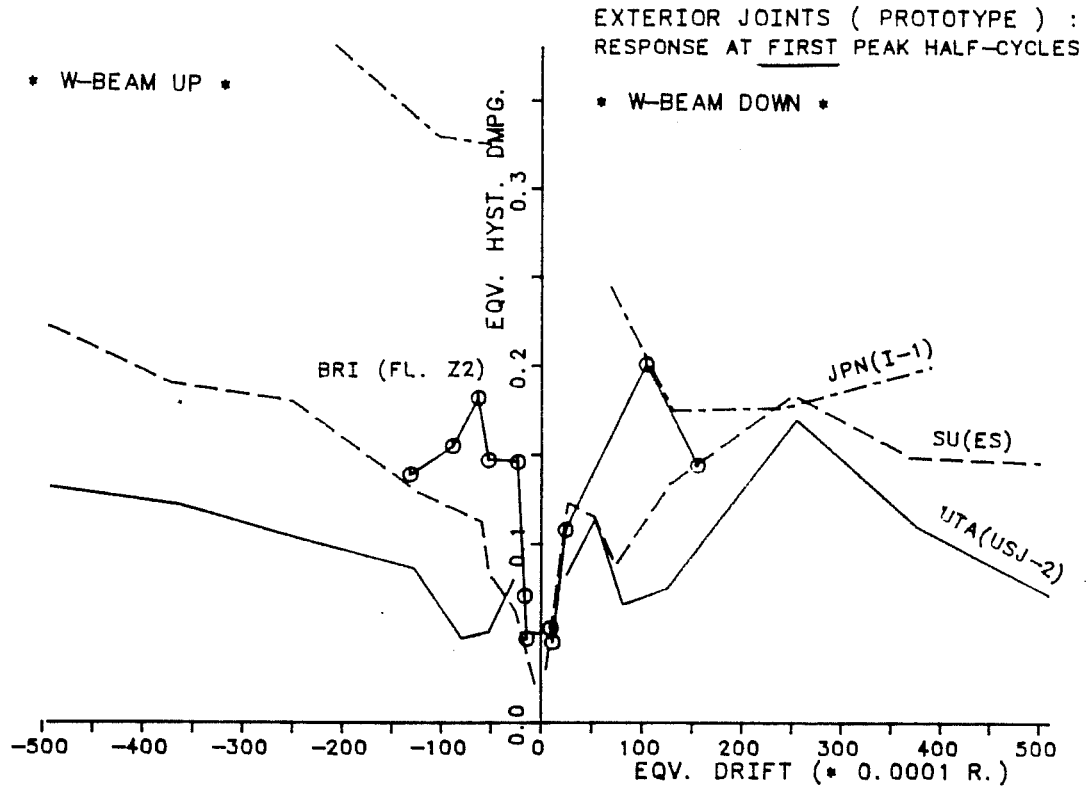


Fig. 7.43 - Exterior Prototype Tests Damping.

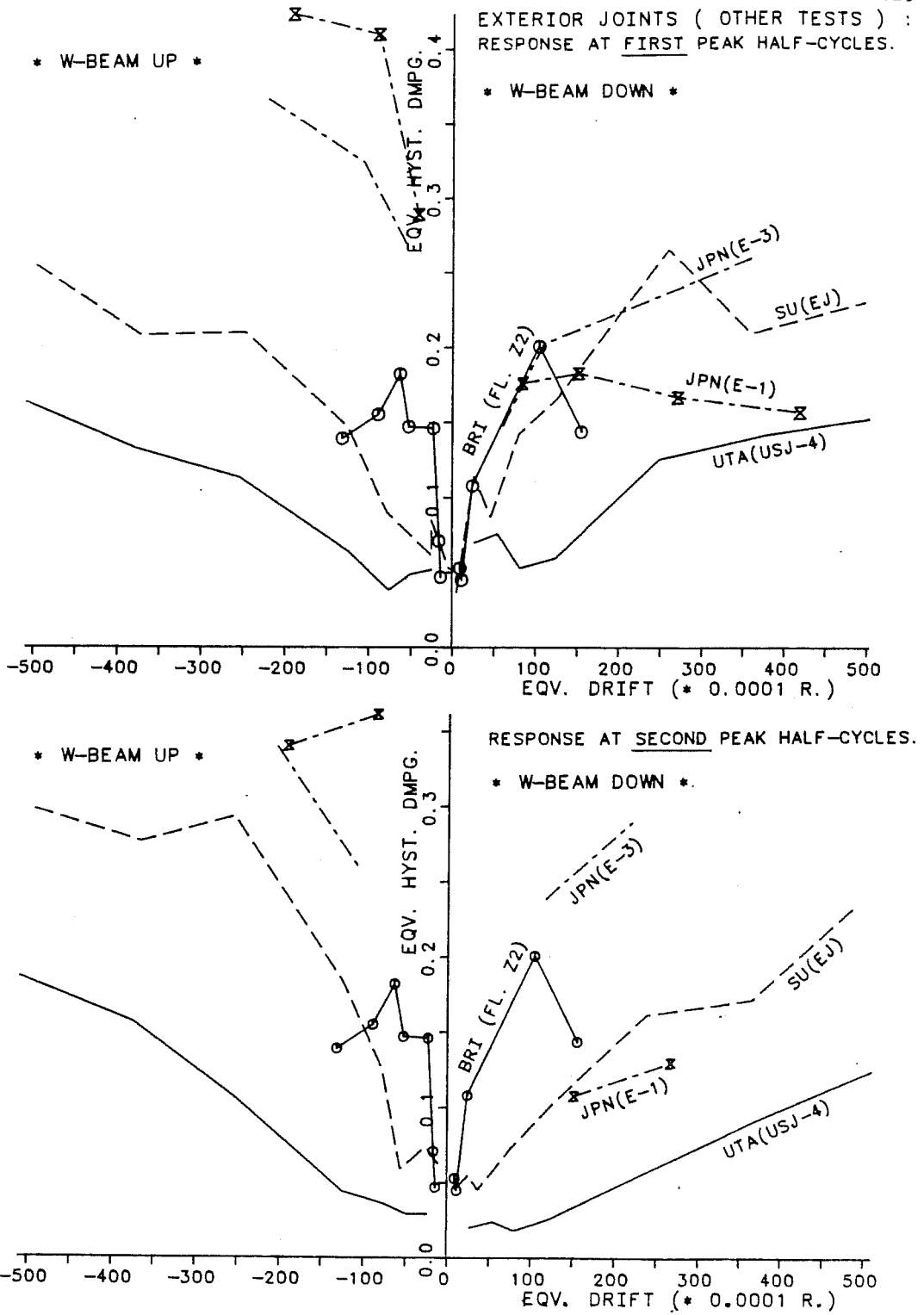


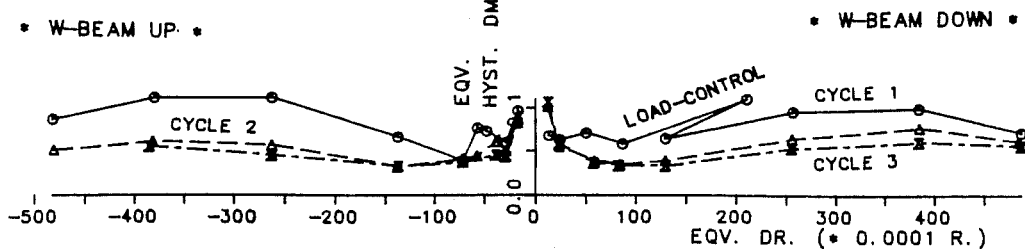
Fig. 7.44 - Other Exterior Tests Damping.

response features as did the prototypes, particularly the decrease in damping ratios from the first to the second peak cycles when the longitudinal beam moved down. An increase in the damping ratio was observed for the reversed case of west-beam up for Specimens UTA (USJ-4) and SU(EJ), Fig. 7.44. The BRI floor Z2 damping ratio was plotted as a reference for both cases.

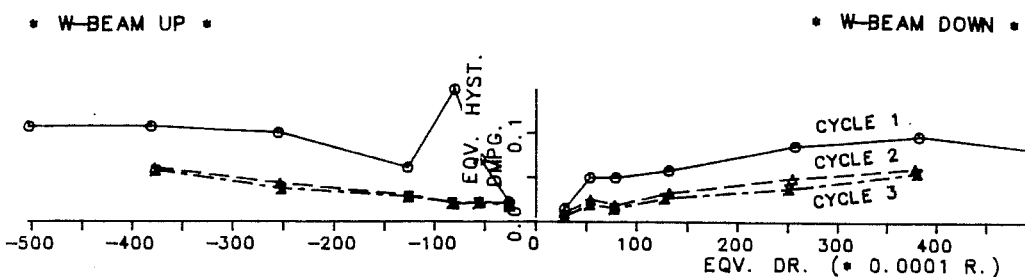
7.6.2 Interior Components. The influence of the load-control testing program as applied in Specimens UTA (USJ-1) and SU(IS, IJ) is shown in Fig. 7.45. The sudden first peak displacement increase near a component equivalent drift (which was computed by averaging both beam tip displacements) of $+1/60$ to $+1/50$ clearly showed that increasing ductility demands had to be met by the component. The higher damping ratio was associated with larger forces. On the other hand, components subjected to a load-control test up to equivalent drifts of $\pm 1/50$ showed higher damping ratios near the origin than at $1/200$ or $1/100$ drifts. This phenomena may imply that this type of loading program was more severe, Fig. 7.45. It was also observed in all interior tests that the second and third cycles showed a smaller (50% less) and more stable damping ratio. The Japanese interior tests were characterized by damping ratios in the order of 20 to 30% as compared with the 10 to 20% observed in the US tests, Fig. 7.46. This was a result of fewer but more severe peak displacements applied to the component.

EQUIVALENT HYSTERETIC DAMPING AT PEAK HALF-CYCLES

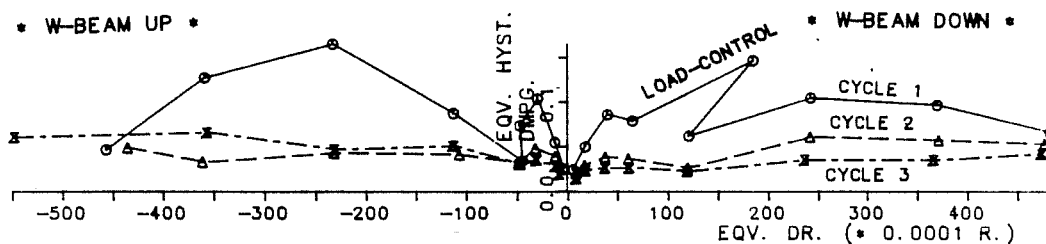
USJ - 1 : INTERIOR PROTOTYPE



USJ - 3 : INTERIOR MODIFIED



SU - IS : INTERIOR JOINT W/ SLAB



SU - IJ : INTERIOR JOINT W/O SLAB

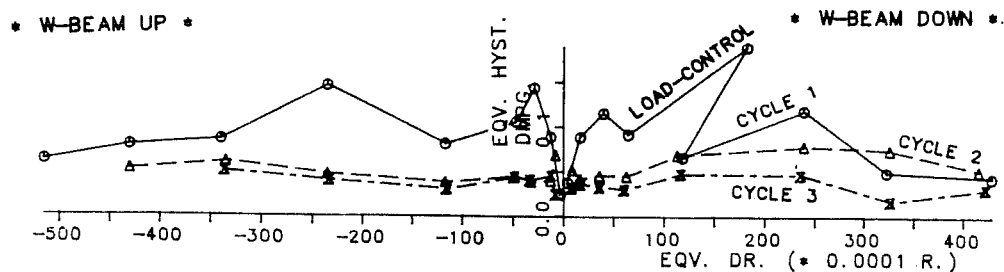


Fig. 7.45 - US Interior Tests Damping Ratio.

A comparative study of damping response among all the prototype tests is depicted in Fig. 7.47. Good agreement is evident between full-scale test USJ-1 and small-scale component IS up to large deformation levels ($\pm 1/20$), at first and second peak drift half-cycles. Approximately symmetric response was obtained for interior specimens as opposed to the unsymmetric response of the exterior tests. The BRI floor Z2 showed higher damping level which may be the result of applying a reduced numbers of load cycles.

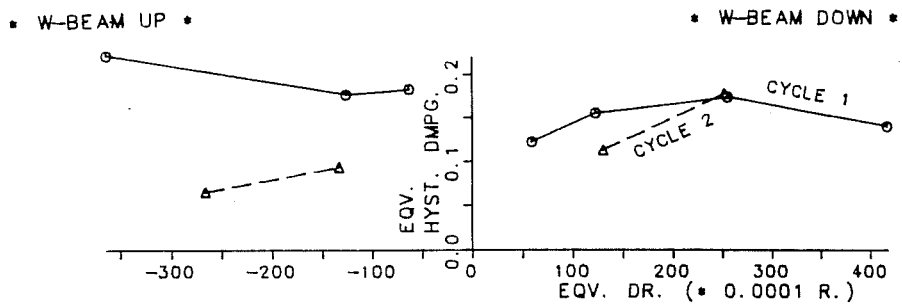
The other interior (Fig. 7.48) tests exhibited a response pattern characterized as follows: (1) higher initial damping ratios (first cycles) followed by a 50% reduction in the subsequent cycles (US tests); (2) higher damping ratios in the Japanese tests; and (3) symmetry in damping response for both drift directions.

7.7 Hysteretic Damping in Component Elements

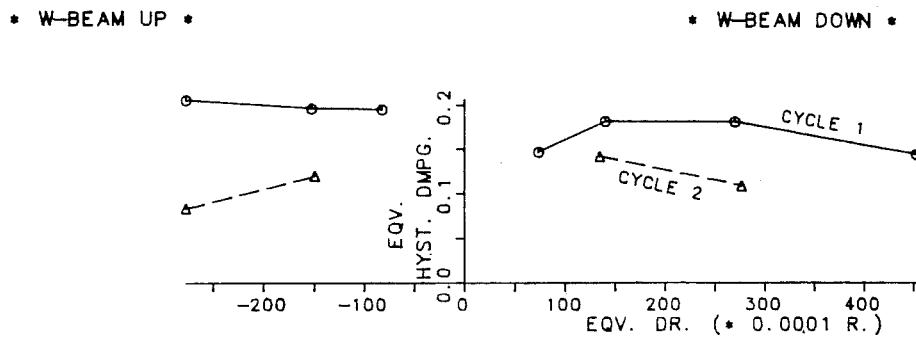
The study of damping in the component elements (beams, joints, columns) is another source of data that can be used to interpret local energy response. It was shown that most of the energy dissipation-absorption was processed in the beam plastic hinge for the exterior components. But in the interior tests, it was observed that hinging in the two longitudinal beams and shear distortion of the joint region were responsible for absorbing

EQUIVALENT HYSTERETIC DAMPING AT PEAK HALF-CYCLES

JPN - I1 : INTERIOR JOINT W/ SLAB (JPN DESIGN)



JPN - I2 : INTERIOR JOINT W/ SLAB (US DESIGN)



JPN - I3 : INTERIOR JOINT W/O SLAB (JPN DESIGN)

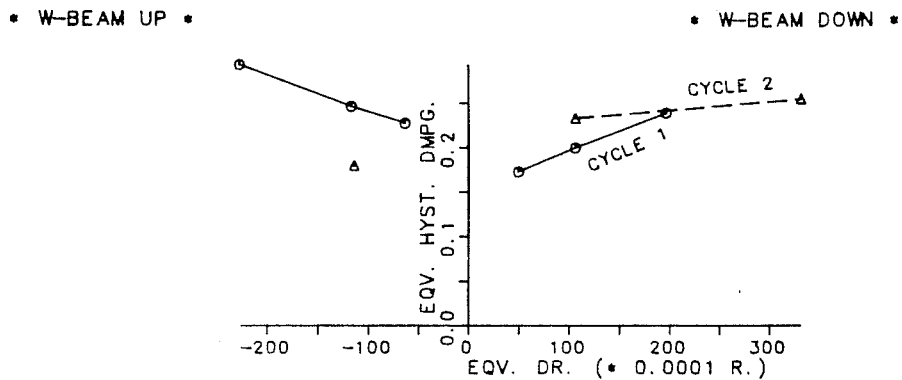
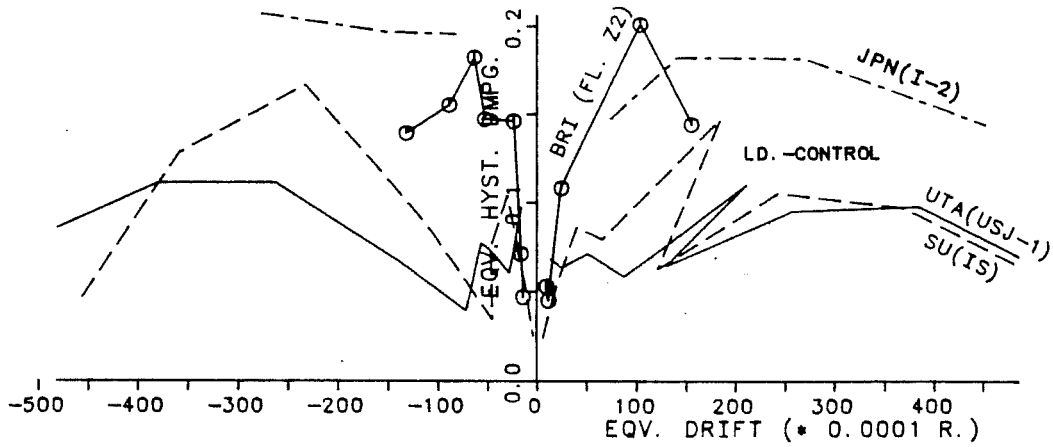


Fig. 7.46 - Japanese Interior Tests Damping Ratio.

INTERIOR JOINTS (PROTOTYPE) :
 RESPONSE AT FIRST PEAK HALF-CYCLES

* W-BEAM UP *

* W-BEAM DOWN *



RESPONSE AT SECOND PEAK HALF-CYCLES

* W-BEAM UP *

* W-BEAM DOWN *

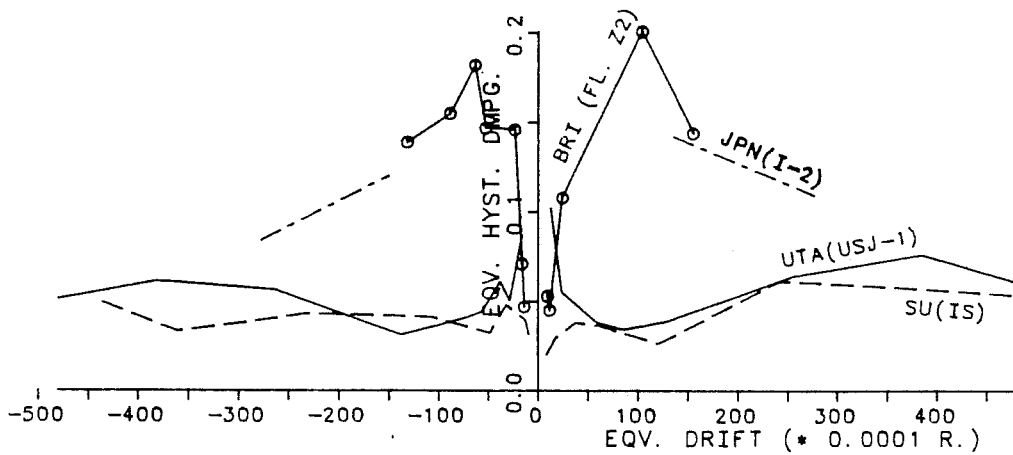
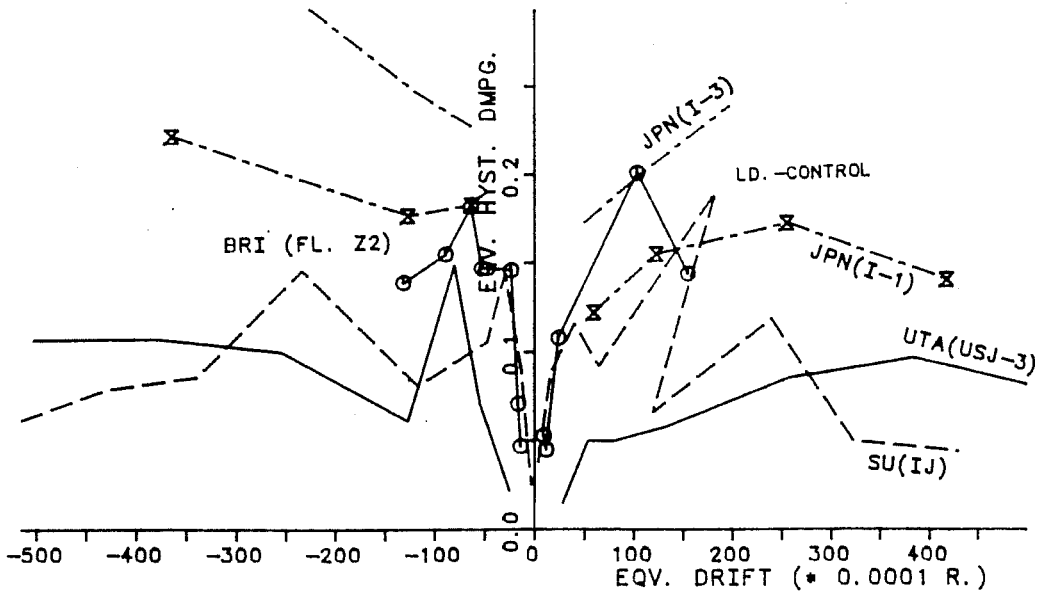


Fig. 7.47 - Interior Prototype Tests Damping Ratio.

INTERIOR JOINTS (OTHER TESTS) :
 RESPONSE AT FIRST PEAK HALF-CYCLES.

* W-BEAM UP *

* W-BEAM DOWN *



RESPONSE AT SECOND PEAK HALF-CYCLES.

* W-BEAM UP *

* W-BEAM DOWN *

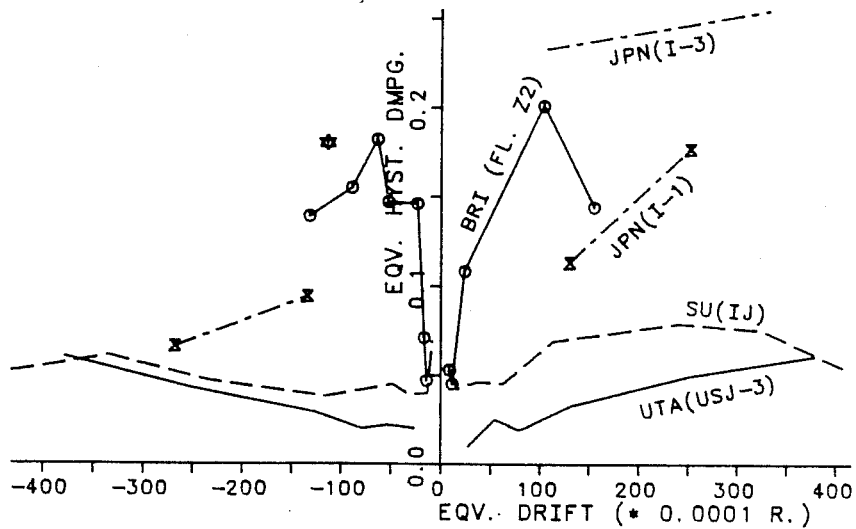


Fig. 7.48 - Other Interior Tests Damping Ratio.

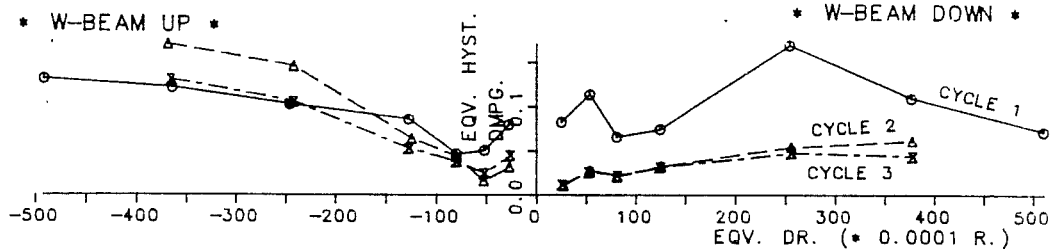
energy. Although deformation data was available for the UTA tests (joint shear distortion) separation of the joint distortion from joint extension was not possible and consequently, only longitudinal beam damping response was analyzed.

7.7.1 Exterior Joint Longitudinal Beam. One of the major damping sources is located in the exterior component longitudinal beam near the column face. Figures 7.49 and 7.50 yield some interesting observations pertaining to the UTA, SU and Japanese exterior components beam damping ratios (BDR): (1) in general the BDR when the slab was in tension was lower than when the slab was in compression; (2) the first incursion into a larger peak drift (cycle 1) usually required larger BDR than the subsequent cycles (cycle 2, 3); (3) the BDR at the second cycle usually showed more stable behavior; and, (4) strong dependence on the loading program was shown by the Japanese exterior tests where a few loading cycles led to larger BDR (slab in compression - beam up).

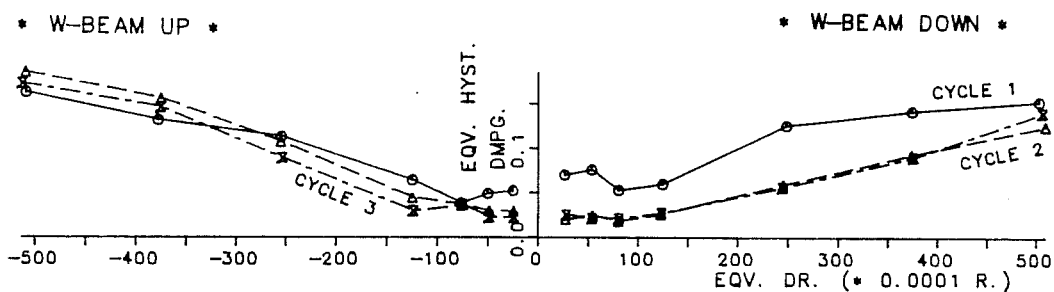
A comparison among all the different component tests and BRI floor Z2 is shown in Figs. 7.51 and 7.52. The prototype components detailed in the same fashion as the equivalent critical regions in level Z2 (BRI) experienced a much broader deformation range. Specimen USJ-2 (UTA) which failed in the anchorage showed consistently lower BDR than any other exterior prototype tests. The BDR at a second peak half-cycle dropped

EQUIVALENT HYSTERETIC DAMPING AT PEAK HALF-CYCLES

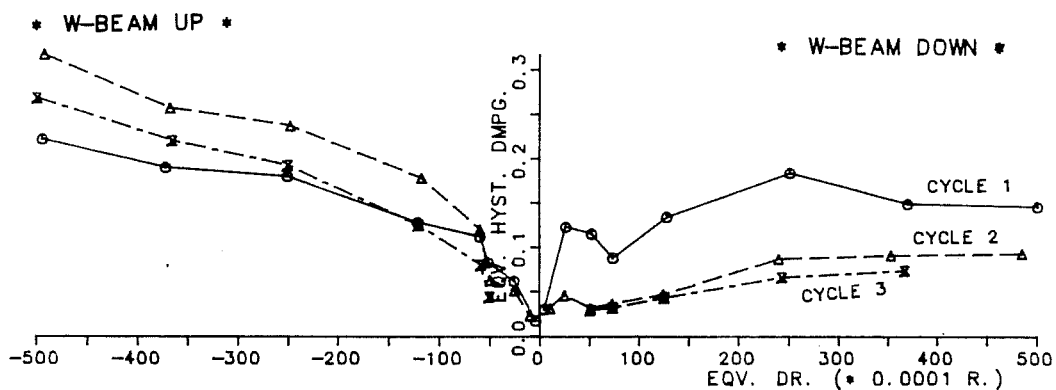
USJ - 2 : EXTERIOR PROTOTYPE



USJ - 4 : EXTERIOR MODIFIED



SU - ES : EXTERIOR JOINT W/ SLAB



SU - EJ : EXTERIOR JOINT W/O SLAB

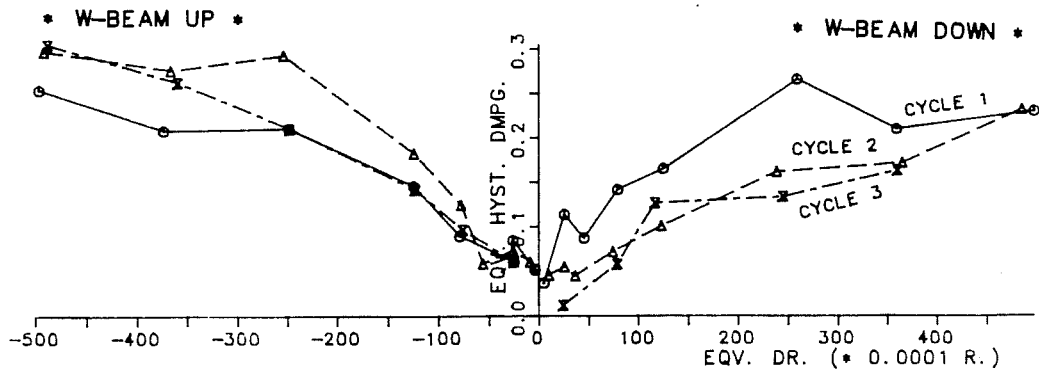
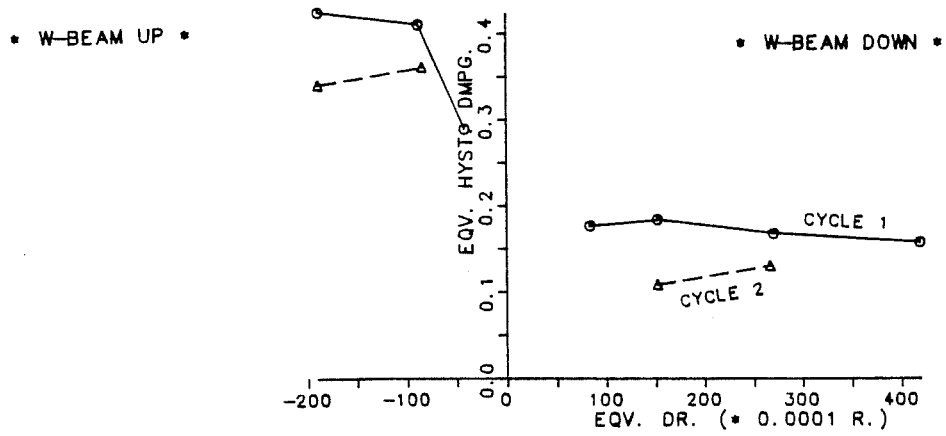


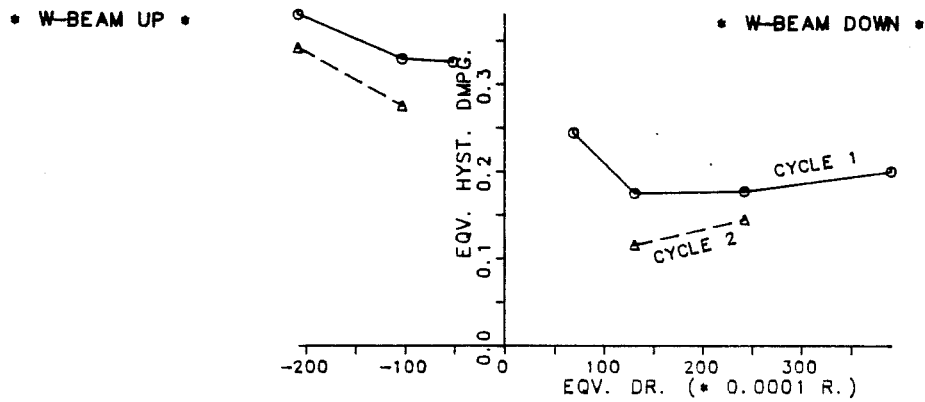
Fig. 7.49 - US West Beam Exterior Tests Damping.

EQUIVALENT HYSTERETIC DAMPING AT PEAK HALF-CYCLES

JPN - E1 : EXTERIOR JOINT W/ SLAB (JPN DESIGN)



JPN - E2 : EXTERIOR JOINT W/ SLAB (US DESIGN)



JPN - E3 : EXTERIOR JOINT W/O SLAB (JPN DESIGN)

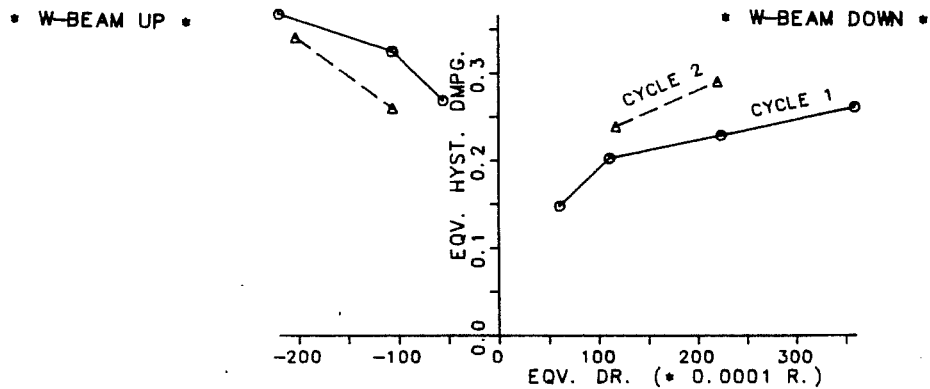


Fig. 7.50 - Japanese West Beam Exterior Tests Damping.

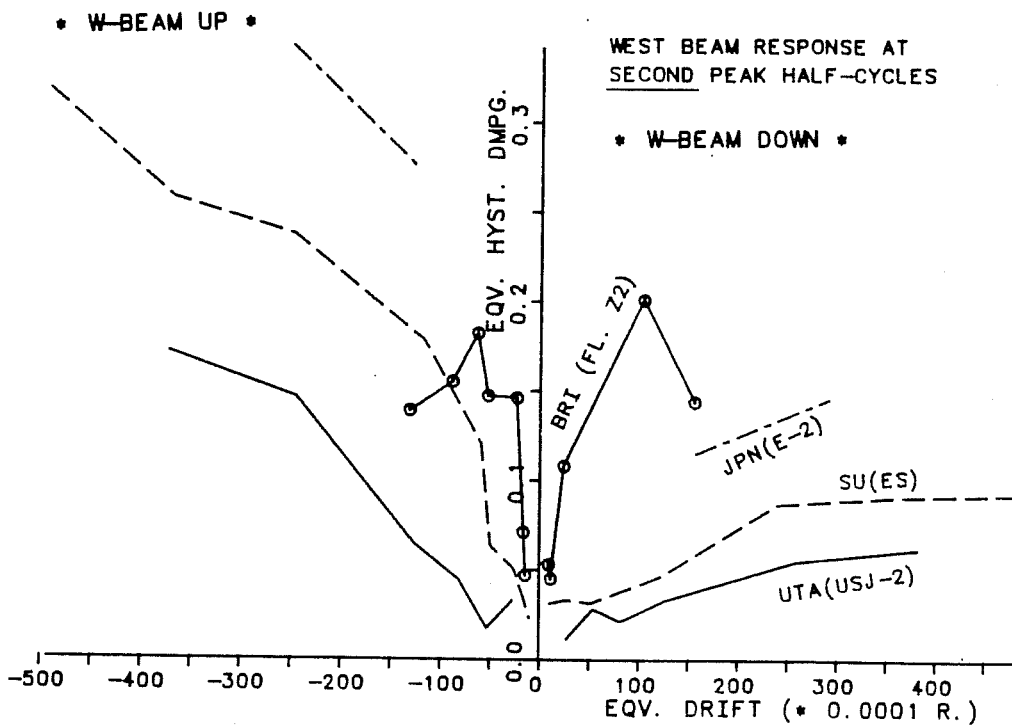
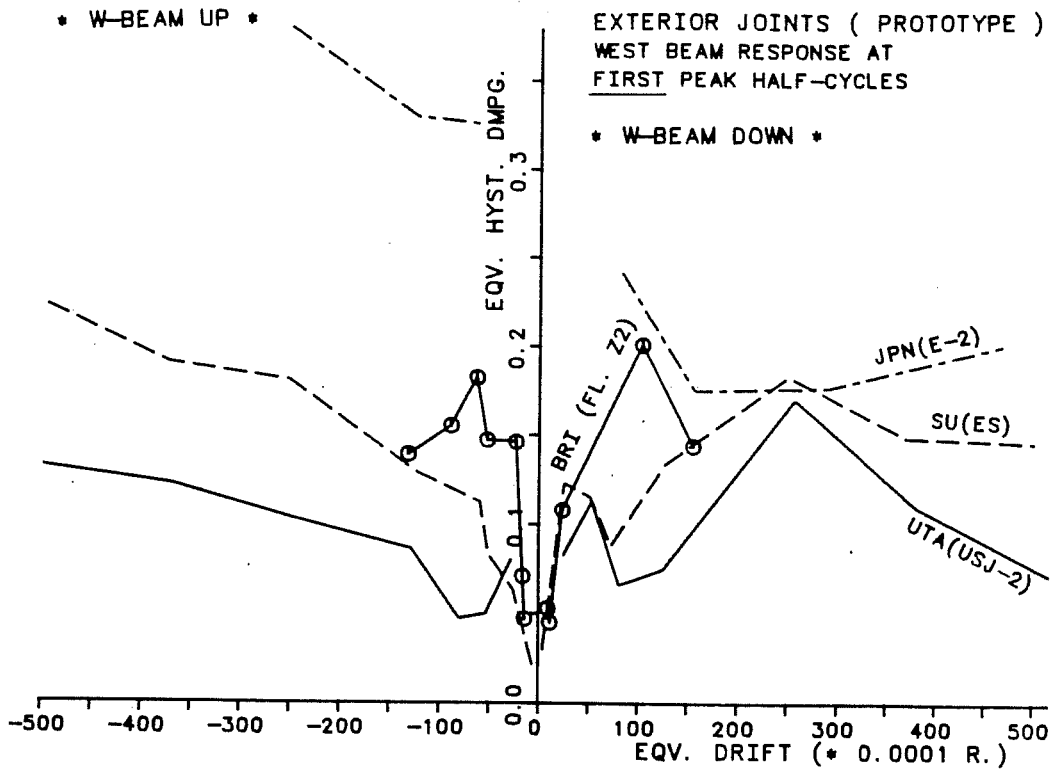


Fig. 7.51 - Exterior Prototype West Beam Damping.

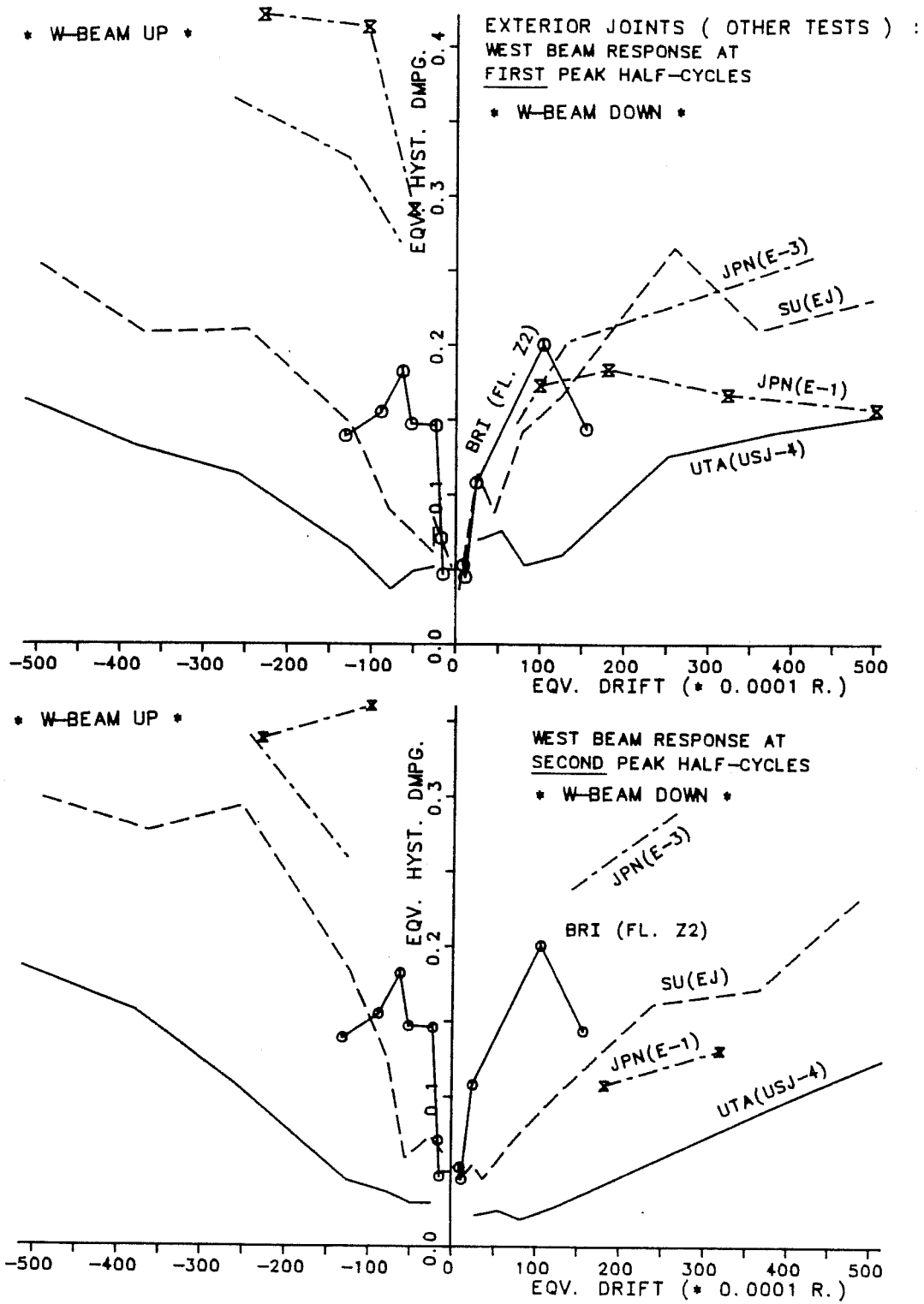


Fig. 7.52 - Other Exterior Tests West Beam Damping.

under positive equivalent drift (beam down) whereas it tended to increase when the beam moved up, Fig. 7.51.

A comparison between level Z2 and the "other" component tests is also shown in Fig. 7.52. The Japanese (E-1) and the UTA (USJ-4) tests showed lower BDR than the other tests without a slab. It also can be observed in the second peak half-cycles that the BDR tended to increase (beam up) or decrease (beam down) compared to the first peak half-cycles results, Fig. 7.51.

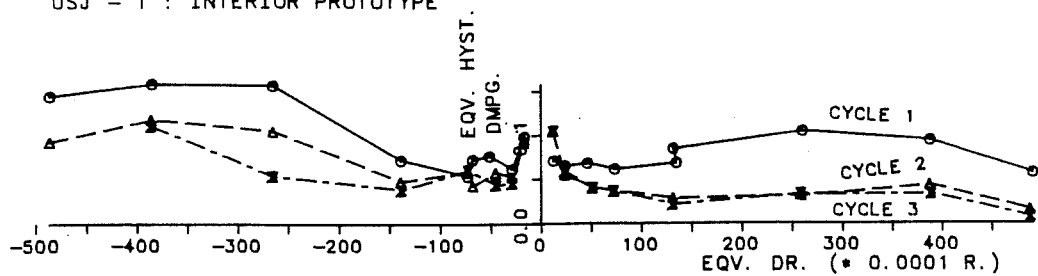
7.7.2 Interior Joint Longitudinal Beam.

7.7.2.1 West Beam. The interior joint response was studied for the west beam separately. The west beam response as shown in Fig. 7.53 revealed several different important features: (1) nearly symmetric response was obtained in either displacement direction; (2) the first incursion into "new" peak displacements usually led to higher BDR (cycle 1); and, (3) the subsequent half-cycles showed lower BDR but they were usually consistent with each other (cycles 2, 3).

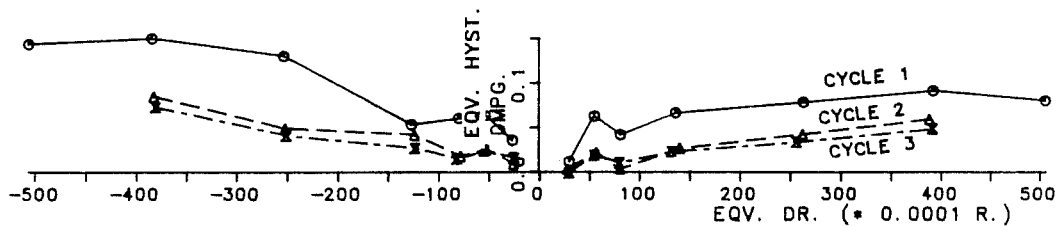
7.7.2.2 East Beam. The east beam response in the UTA (USJ-1) test showed an initial increase in the BDR due to the load-control program, Fig. 7.54. This variation was successfully modeled in the SU component tests that underwent a similar loading program. As shown for the west beam, the second and third peak half-cycles usually developed more stable damping response than the first cycle (E-beam down). When the E-beam

WEST BEAM EQUIVALENT HYSTERETIC DAMPING AT PEAK HALF-CYCLES

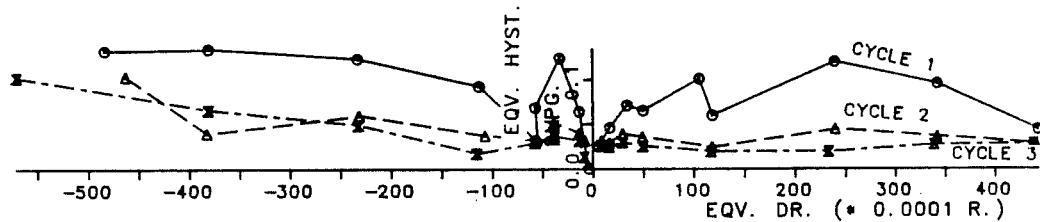
USJ - 1 : INTERIOR PROTOTYPE



USJ - 3 : INTERIOR MODIFIED



SU - IS : INTERIOR JOINT W/ SLAB



SU - IJ : INTERIOR JOINT W/O SLAB

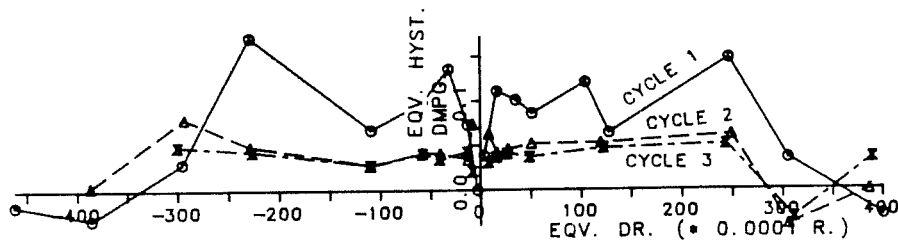


Fig. 7.53 - US Interior Tests West Beam Damping.

EAST BEAM EQUIVALENT HYSTERETIC DAMPING AT PEAK HALF-CYCLES

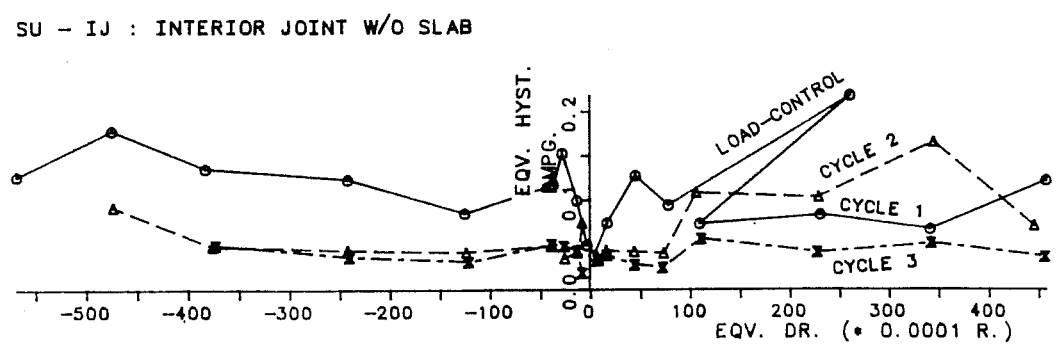
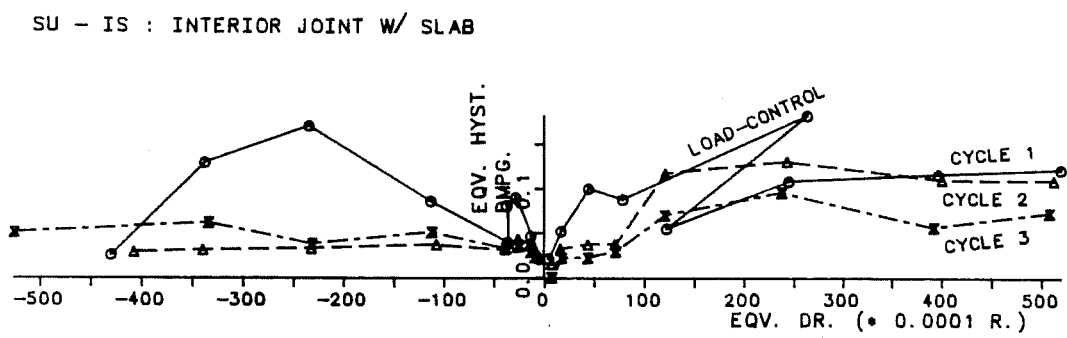
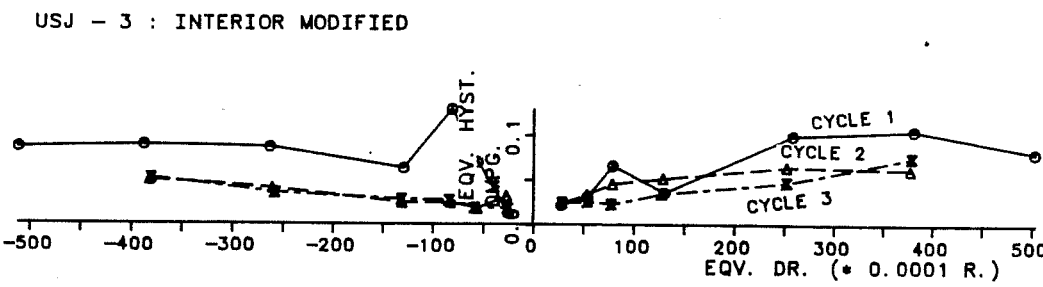
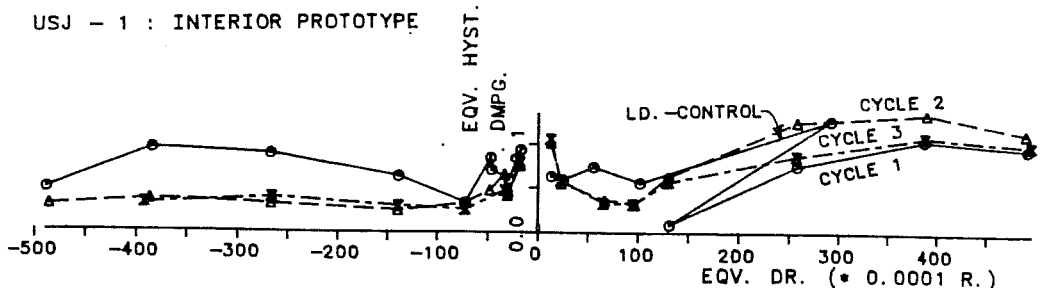


Fig. 7.54 - US Interior Tests East Beam Damping.

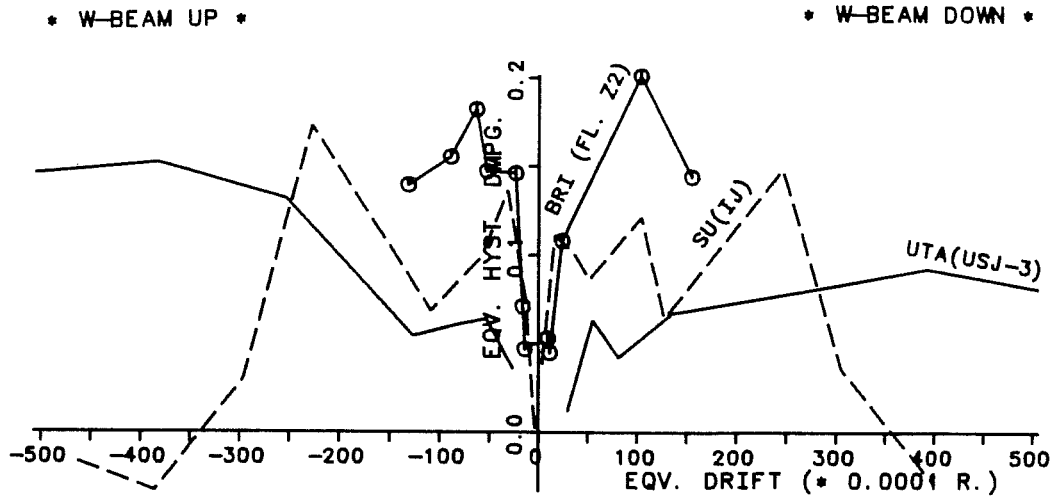
moved up the incursion made at earlier loading stages to a large upward displacement produced a significant drop in the first cycle damping ratio. The cycle 1 damping ratio (beam-up) had its response in the vicinity of the other two cycles (2, 3) for tests USJ-1, IS and IJ. Test USJ-3 that was run on a displacement-control basis showed higher damping ratios in both drift directions as shown in Fig. 7.54.

7.7.2.3 Interior Prototype. The response of all interior tests at first and second peak half-cycles is shown together with BRI floor Z2 response, Figs. 7.55 and 7.56. Although the components response (USJ-1, IS) fell well below the BRI (Z2) response, there was good agreement among the tests over a large deformation range.

7.7.2.4 Other Interior Tests. The absence of a slab in test SU-IJ and increased beam reinforcement ratios in UTA-USJ-3 test showed some peculiar aspects of response, Figs. 7.57 and 7.58. In test IJ, the sudden decrease in the W-beam damping ratio was very marked as compared with the USJ-3 test.

7.7.3 Exterior vs. Interior Joint Longitudinal Beam. Some important conclusions may be drawn based on the results plotted for exterior and interior tests. First, the BDR was generally higher when the slab was in compression as compared to the slab in tension. More stable behavior was obtained after the first incursion to a new peak displacement. The Japanese

INTERIOR JOINTS (OTHER TESTS) :
 WEST BEAM RESPONSE AT
FIRST PEAK HALF-CYCLES



WEST BEAM RESPONSE AT
SECOND PEAK HALF-CYCLES

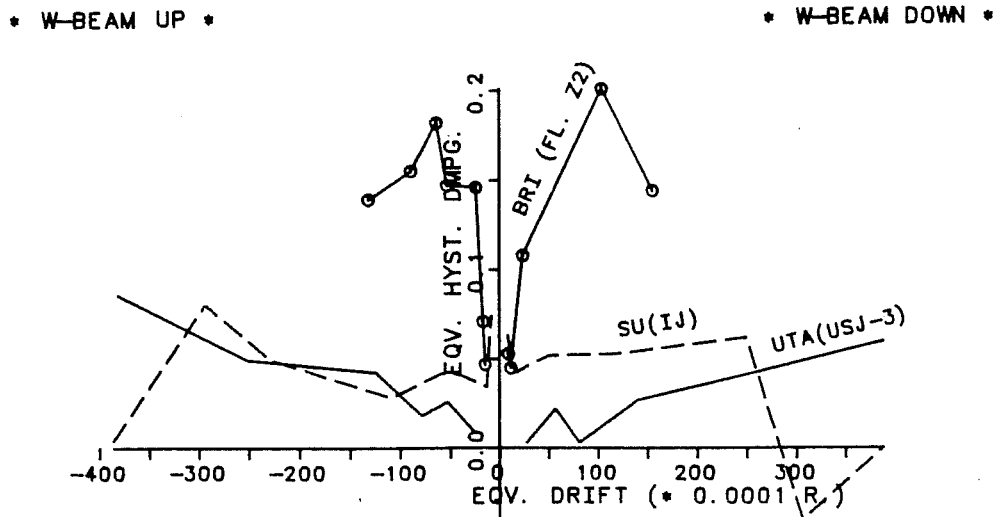


Fig. 7.57 - West Beam Damping in Other Interior Tests.

interior tests could not be used in this comparison due to lack of data. However, the exterior tests showed that with fewer load cycles, the damping ratios may be higher due to the absence of accumulated damage such as may occur in a more comprehensive test. Comparisons between the components and the complete BRI floor system cannot be made because the floor system hysteretic damping included effects from the shear wall, connections, beams, columns which could not be separated.

7.8 Conclusions

The instrumentation used in the critical regions of the UTA specimens proved to be a precious source of information on energy response. The computation of the different types of energy dissipation was based on elementary assumptions subjected to verification "a posteriori". The external work applied to the specimen was computed as one-half the product of the hydraulic jack force times its displacement. The external work was dissipated by component elements such as: (1) longitudinal beam; (2) joint core; and, (3) transverse beam. The components were designed based on the strong column - weak beam concept and it was expected that the beam plastic hinges would provide the main sources of energy dissipation. The remaining energy would be dissipated by the joint region and the transverse beam. As the

columns were "elastic" the amount of energy being dissipated was considered negligible.

From the interpretation of UTA test results it can be shown that: (1) in the exterior components the major source of energy dissipation was the longitudinal beam (~ 90%) with the joint core and the transverse beams playing a limited role in this process; and, (2) in the interior components the major sources of energy dissipation were the longitudinal beams plastic hinges and the joint core distortion under horizontal shearing forces.

The method of strain energy evaluation proved very useful in identifying the anchorage failure in the exterior joint USJ-2. In the exterior joint, the beam dissipated about 10% of the energy dissipated as opposed to the interior joints in which the beams dissipated 45 to 55%. The joint distortion created a "support settlement" for the transverse beam and consequently the transverse beam net twist was very small up to large deformation levels. The SU specimens without a slab clearly showed the influence of the slab on energy response by exhibiting a 1:1 input-dissipated energy response curve throughout the test.

Further studies were performed on the available tests by using a nondimensional parameter that related the energy input to the inelastic response at peak displacements - the equivalent hysteretic damping. This parameter is independent of the test

frequency and was used first to evaluate in the complete specimens and then to evaluate the beam plastic hinge critical region. As the components showed nonsymmetric damping behavior depending on the deformation being applied, two half-cycles were considered - one for the positive drift and another for the negative drift. Furthermore, three consecutive cycles were used to study the effect of loading on hysteretic response. It was found that: (1) in the BRI structure large floor damping ratios (15 to 20%) were obtained up to (1/64) equivalent drift; (2) the Japanese components which were subjected to a more rapid loading program but fewer cycles had much higher damping ratios than the US tests subjected to a larger number of cycles; (3) the first incursion into a new first peak displacement led to higher damping ratios; (4) subsequent cycles at the same displacement magnitude showed a reduction up to 50% in the damping ratio with stabilization in the next cycles; and, (5) damping ratio response strongly depended on the loading history and the specimen cross section characteristics.

The small-scale SU specimens had damping response similar to the identical UTA prototype tests. However, the observed SU first peak cycle damping ratios were higher than in the UTA tests which may imply the difficulties in modeling microconcrete cracking and bond around the wire reinforcement.

On the other hand, at second peak drifts damping ratios tended to drop and stabilize at nearly identical values for both SU and UTA identical tests.

The SU specimen without a slab (IJ) showed that at very large deformation levels the damping ratios dropped. This may suggest that strong losses in stiffness followed by bond deterioration in the joint region were responsible for this behavior.

The assessment of the observed energy response in the BRI floor and in the test components proved to be very valuable in studying their response. A more accurate estimate of the hysteretic load-deflection response was done rather than the simple visual observation of the same loops. The subsequent nondimensional studies done on the components by using the concept of equivalent hysteretic damping also proved to be helpful in establishing a base for comparing all components. The particular aspects of beam hysteretic damping were also studied as they strongly influenced the global component response.

7.9 References

1. ACI Committee 318 - Building Code Requirements for Reinforced Concrete and Commentary. ACI, Detroit, MI, 1983.
2. AIJ - Standard for Structural Calculation of Reinforced Concrete Structures (English version). The Architectural Institute of Japan (AIJ), Tokyo, Japan, 1980.

3. S.F. Borg - Earthquake Engineering - Damage Assessment and Structural Design, J. Wiley & Sons, Chichester, U.K., 1983.
4. E.C. Carvalho and C.S. Oliveira - Manual de Construcao Anti-Sismica (Edificios de Pequeno Porte), Laboratorio Nacional de Engenharia Civil, Lisboa, Portugal, 1985.
5. CEB-FIP - International Recommendations for Structural Concrete (Vol. 1) and Concrete Structures (Vol. II), CEB-FIP, Cement and Concrete Association Edition, London, 1978.
6. R.W. Clough and J. Penzien - Dynamics of Structures, McGraw-Hill Book Co., New York, 1975.
7. W. Corley and J.O. Jirsa - "Equivalent Frame Analysis for Slab Design", ACI Journal, Vol. 67, No. 11, November 1970.
8. D.J. Dowrick - Earthquake Resistant Design - A Manual for Engineers and Architects, J. Wiley & Sons, Chichester, U.K., 1977.
9. T. Hsu - Torsion of Reinforced Concrete, Van Nostrand Reinhold Co., New York, 1984.
10. P. Lampert - "Bruchwiderstand von Stahlbetonbalken unter Torsion und Biegung", Bericht No. 26, Institut fur Baustatik ETH Zurich, 1970.
11. P. Lampert and B. Thürlimann - "Torsionsversuche an Stahlbetonbalken", Bericht No. 6506-2, Institut für Baustatik, ETH Zurich, June 1968.
12. F. Leonhardt and G. Schelling - "Torsionsversuche an Stahlbetonbalken", Heft 239, Deutscher Ausschuss für Stahlbeton, Berlin, 1974.
13. R. Park and T. Paulay - Reinforced Concrete Structures, John Wiley & Sons, New York, 1975.
14. C.F. Richter - Elementary Seismology, Freeman, San Francisco, 1958.
15. M. Seckin - "Inelastic Behavior of Reinforced Concrete Beam - Column Joints Subjected to Slow Load Reversals", M.A. Sc. Thesis, Dept. of Civil Engineering, University of Toronto, Canada, 1974.

16. T. Tassios (Rapporteur) - "Response of Structural Concrete Critical Regions under Large Amplitude Reversed Actions", CEB General Task Group 10, CEB, Bulletin d'Information, No. 161, Paris, August, 1983.
17. H. Umemura and H. Takizawa - Dynamic Response of Reinforced Concrete Buildings, Structural Engineering Documents, No. 2, IABSE, Zurich 1982.
18. M. Wakabayashi - Design of Earthquake Resisting Buildings, McGraw-Hill Book Co., New York, 1986.

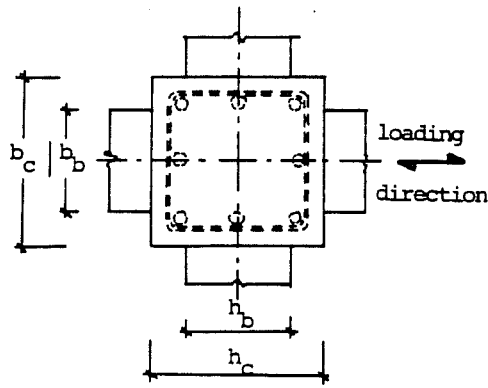
CHAPTER VIII
EVALUATION OF DESIGN CODE REQUIREMENTS

8.1 Introduction

A study of the component testing program would be incomplete without examining the data in comparison with code provisions. For this purpose, design codes used in the US, Japan and New Zealand, are studied. The response of the DMRF connection region under reversed cyclic loads is vital in guaranteeing overall stability. Consequently, the horizontal joint shear, bond and related energy absorption/dissipation characteristics were studied. Near ultimate, the effective slab width actually participating in resisting lateral forces is an important factor in evaluating the DMRF capacity. Therefore, different slab widths were considered in studying the ultimate frame strength.

8.2 Horizontal Joint Shear

8.2.1 Initial Remarks. The component tests provided useful data for evaluating the horizontal shear stress in the joint. The horizontal shear stress was computed using three methods for defining the area of the joint core, Fig. 8.1: ACI 318-83 (1) and the NZS 3101 (17) utilize the largest joint area, followed by ACI-ASCE Committee 352 (2) and AIJ (3). The approach



$$b_j = (b_b + b_c) / 2$$

Standard	Code Equation	Test Value
ACI 318 - 1983	$A_j = b_c \cdot h_c$	$19.68 \times 19.68 = 387.7 \text{ in.}^2$
ACI - ASCE Comm. 352	$A_j = b_j \cdot h_c$	$15.75 \times 19.68 = 310.1 \text{ in.}^2$
NZS 3101 - 1982	$A_j = b_c \cdot h_c$	$19.68 \times 19.68 = 387.7 \text{ in.}^2$
ALJ - SRC 1982	$A_j = b_j \cdot j_c$ $j_c = 7/8 \cdot d_c$	$15.75 \times 15.16 = 238.8 \text{ in.}^2$

Fig. 8.1 - Joint Shear Stress Area.

1. Longitudinal Beam Shear

$$V_{jb} = C_1 + T_2 = \frac{M_1}{d} + \frac{M_2}{d} = (P_1 + P_2) \cdot \frac{l_n}{d}$$

2. Column Shear

$$V_c = \frac{2 M_c}{d} = \frac{M_1 + M_2}{d} = (P_1 + P_2) \cdot \frac{l_n}{h}$$

3. Horizontal Joint Shear

$$V_{jh} = V_{jb} - V_c$$

4. Joint Shear Stress

$$v_{jh} = V_{jh} / A_j$$

5. Normalized Joint Shear Stress

$$v_{jh} = v_{jh} / \sqrt{f'_c} \text{ or,}$$

$$\gamma = \frac{[(\frac{1}{d} - \frac{1}{h}) \cdot (P_1 + P_2) \cdot l_n]}{A_j \cdot \sqrt{f'_c}}$$

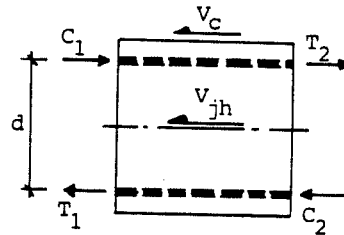
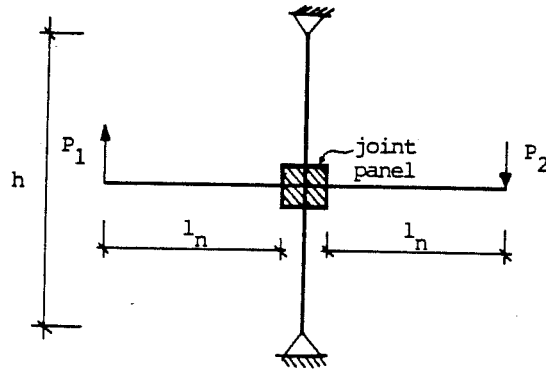


Fig. 8.2 - Component Test Joint Shear Stress.

for evaluating the experimental horizontal joint shear force is shown in Fig. 8.2. The lever arm between beam tensile and compressive forces was assumed to be equal to the distance between the top and bottom longitudinal beam reinforcement.

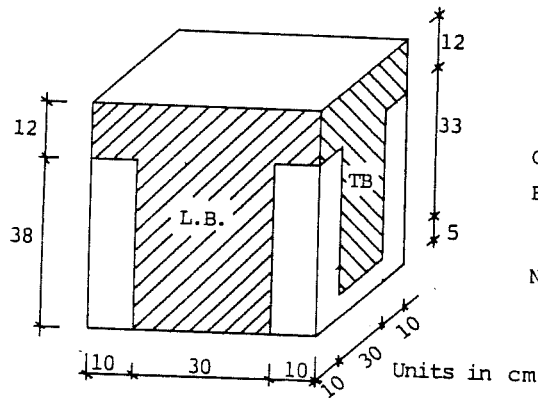
The experimental joint shear stress was compared with Code values. Various procedures based on different philosophies have been proposed to determine the joint shear resistance [ATC-11 (5)]: (1) the beam-shear mechanism (ACI-ASCE Committee 352, 1976; ACI 318, 1977); (2) the compression strut mechanism [Zhang and Jirsa (6); ACI 318-83 (1); ACI-ASCE 352-84 (2)]; and, (3) a combination of compression strut and joint truss mechanisms [AIJ-SRC (4), NZS 3101-82 (7)]

Two basic joint types are currently identified: (1) Type I - for regions of low-seismicity where no significant inelastic deformations may occur and strength requirements are met with nominal reinforcement; and, (2) Type II joints that are expected to undergo load reversals well into the inelastic range. Only Type II joints are considered in this report and the design equations related to the US-Japan tests are summarized in Table 8.1. The Kamimura equation (11) was based on interior components that had joint shear failure and were built without a slab. Kamimura showed that better fit was obtained by reducing the steel participation by 50%, Fig. 8.3. The amount of joint

TABLE 8.1 - DESIGN CODE HORIZONTAL SHEAR STRENGTH.

Standard	ACI 318	ACI-ASCE Comm. 352	NZS 3101-82	AIJ - SRC	Kamimura Eq.
Horizontal Joint Shear Stress, v_{jh} (psi)	$\phi \cdot \gamma \cdot f'_c$ $\phi = 1$ f'_c (psi)	$\phi \cdot \gamma \cdot f'_c$ $\phi = 1$ f'_c (psi)	$v_{cj} + v_{sj}$ $C_j = 1.0 :$ $\sigma_c = \frac{f'_c}{10}$ $v_{ch} = \frac{2/3}{b_c \cdot h_c} \cdot \left(\frac{P_e}{A_g} - \frac{f'_c}{10} \right)$ $\sigma_c < \frac{f'_c}{10}$ $v_{ch} = 0.0$ $v_{sj} = \frac{A_{sh} \cdot f_{yh}}{b_c \cdot h_c}$	$2\psi f'_c + \rho_w f_{yh}$ $f'_c = \min[f'_{c1}, f'_{c2}]$ $f'_{c1} = \left(\frac{f'_c}{66.7} + 107 \right)$ $f'_{c2} = f'_c / 20.$ $\psi = 2$ $\psi = 3$	$\beta v_{ch} + \frac{1}{2} \rho_w \cdot f_{yh}$ $f'_c < 3485 \text{ psi} :$ $v_{ch} = (0.78 - \frac{0.112}{1000} f'_c) \cdot f'_c$ $f'_c = 3485 \text{ psi} :$ $v_{ch} = 1358 \text{ psi}$ $\beta = 2 / 3$ $\beta = 1$
Exterior	$\gamma = 15$	$\gamma = 12$			
Interior	$\gamma = 15$	$\gamma = 15$			

* Verification of Confinement *



L.B. = longitudinal beam ;
 T.B. = transverse beam .
 Confinement Requirements :
 Face Ratio = $\frac{\text{Beam Face Area}}{\text{Column Face Area}} \geq 0.75$
 Note : 1. in. = 2.54 cm.

Components	Column Face	Longitudinal Beam		Transverse Beam	
	Area (cm ²)	Area (cm ²)	Ratio	Area (cm ²)	Ratio
w/ slab	2500	1740	0.70	1570	0.64
w/o slab	2500	1500	0.60	1350	0.54

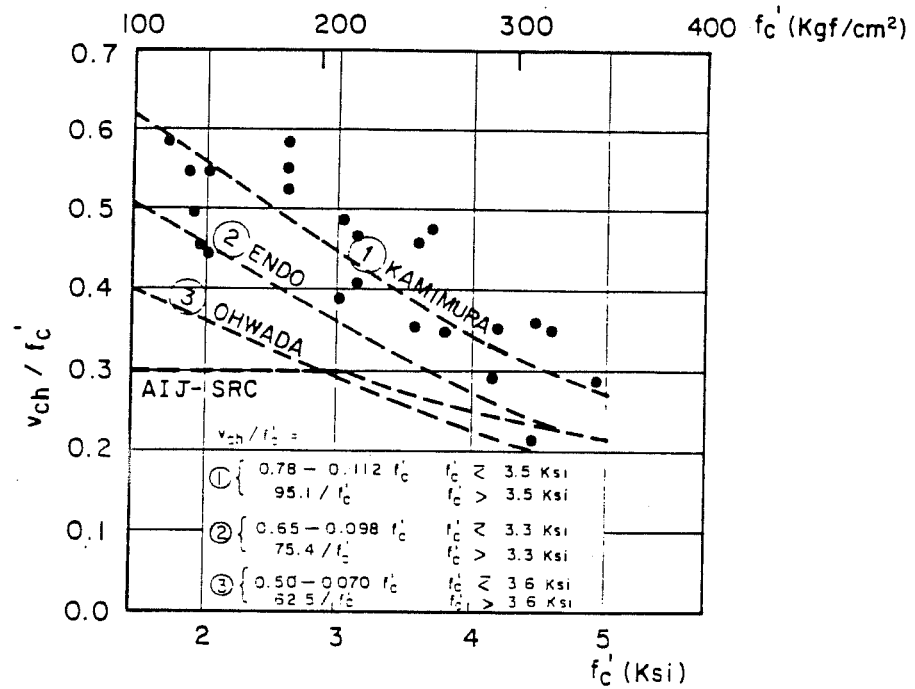


Fig. 8.3 - Joint Shear Stress - Kamimura Equation.

TABLE 8.2 - JOINT CORE REINFORCEMENT DETAILS.

Design Types	USA			Japan	
	Prototype	Modified		Japan	US
Tests	USJ - 1,2 ES,EJ,IS,IJ	USJ - 3	USJ - 4	E - 1,3 I - 1,3	E - 2 I - 2
1. Joint Ties	□ #3 @ 4"	□ #3 @ 4"	□ #3 @ 4" +] #3 @ 4"	□ #4@7"	□ #4 @ 2" + ⊕ #4 @ 2"
ρ_{jw}	(0.28 %)	(0.28%)	(0.42%)	(0.29%)	(0.77%)
2. Longit. Beam					
Top reinf.	3 # 6	5 # 7	5 # 7	3 # 6	3 # 6
ρ_{st}	(0.67 %)	(1.54 %)	(1.54 %)	(0.65 %)	(0.65 %)
Bott. steel	2 # 6	3 # 7	3 # 7	2 # 6	2 # 6
ρ_{sb}	(0.43 %)	(0.88 %)	(0.88 %)	(0.43 %)	(0.43 %)
3. Column					
Main Bars	8 # 7	12 # 8	12 # 8	4#7 + 4#8	4#7 + 4#8
ρ_g	(1.24 %)	(2.45 %)	(2.45 %)	(1.27 %)	(1.27 %)
ρ_t	(0.53 %)	(0.93 %)	(0.93 %)	(0.49 %)	(0.49 %)

reinforcement and the existence of column compression loads is considered in NZS 3101 and AIJ-SRC design equations. Therefore, in Table 8.2 a summary of the joint region reinforcement details is given.

Based on the resistance equations shown in Table 8.1 and on the actual material properties for the different tests ultimate shear stresses were computed and are shown in Table 8.3.

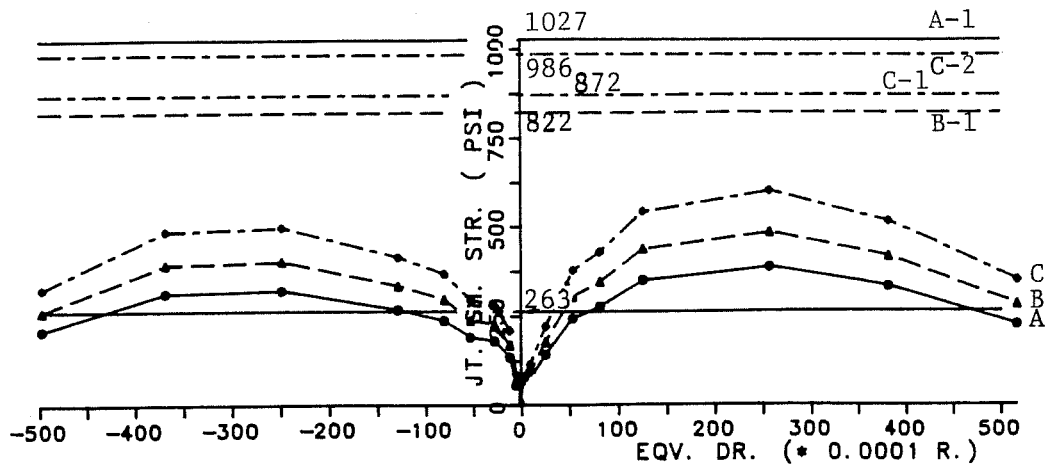
8.2.2 Exterior Joint Shear Stress. The estimated joint shear stress was based on the cross section defined in the current design provisions. The values are shown as horizontal lines in Fig. 8.4. It is likely that the full joint shear capacity in the UTA tests was never fully exploited even at large equivalent drifts. It can be seen that the maximum experimental joint shear stress was below the design value except for USJ-4. In this particular component, the longitudinal beams were heavily reinforced and the joint reinforcement was improved. The maximum joint shear stress was close to that estimated using ACI 318-83 and well above the values proposed by ACI-ASCE 352 and AIJ. Based on energy studies in Chapter VII and on strain readings on the joint reinforcements for USJ-4, longitudinal beam hinging may have occurred before the joint failed in shear. It is shown in Table 8.3, that only USJ-4 had an experimental vs. Code joint stress ratio greater than 1.0 (excluding the NZS data) and the

TABLE 8.3 - EXPERIMENTAL VS. CODE ULTIMATE JOINT SHEAR STRESS.

Standard Joint Stress (psi)	ACI 318-83		NZS 3101-82		ACI-ASCE 352		ALJ - SRC		Kaminura Eq.		Failure Mechanism	
	e.	c.	e.	c.	e.	c.	e.	c.	e.	c.		
Exterior Component	USJ-2	e.	387	0.38	387	1.47	484	0.59	600	0.61	600	Anchorage
		c.	1027		263		822		872		986	
Exterior Component	ES	e.	423	0.37	423	1.25	529	0.58	663	0.66	663	Beam Hinge
		c.	1142		340		914		986		1010	
Exterior Component	E-2	e.	451	0.43	451	0.64	565	0.68	695	0.62	695	Beam Hinge
		c.	1044		702		835		1133		1112	
Exterior Component	USJ-4	e.	935	0.90	935	1.83	1169	1.40	1433	1.35	1433	Beam Hinge
		c.	1045		511		836		1034		1062	
Exterior Component	EJ	e.	233	0.20	233	0.69	291	0.32	364	0.36	364	Beam Hinge
		c.	1142		340		914		986		1010	
Exterior Component	E-1	e.	439	0.42	439	1.19	549	0.66	676	0.69	676	Beam Hinge
		c.	1044		370		835		873		1133	
Exterior Component	E-3	e.	208	0.20	208	0.56	260	0.31	320	0.33	320	Beam Hinge
		c.	1044		370		835		873		982	
Interior Component	USJ-1	e.	845	0.81	845	3.21	1057	1.01	1310	0.91	1310	Beam Hinge
		c.	1046		263		1046		1242		1439	
Interior Component	IS	e.	871	0.77	871	2.56	1089	0.96	1364	0.93	1364	Bar Sliding + Beam Hinge
		c.	1132		340		1132		1365		1463	
Interior Component	I-2	e.	590	0.57	590	0.83	738	0.71	908	0.58	908	Beam Hinge
		c.	1044		714		1044		1492		1565	
Interior Component	USJ-3	e.	1364	1.45	1364	4.01	1706	1.81	2090	1.43	2090	Beam Hinge Joint Shear
		c.	943		340		943		1208		1463	
Interior Component	IJ	e.	392	0.35	392	1.15	490	0.43	614	0.42	614	Bar Slippage + Beam Hinge
		c.	1132		340		1132		1365		1463	
Interior Component	I-1	e.	599	0.57	599	1.57	750	0.72	922	0.64	922	Beam Hinge
		c.	1044		382		1044		1232		1435	
Interior Component	I-3	e.	377	0.36	377	0.99	472	0.45	581	0.41	581	Beam Hinge
		c.	1044		382		1044		1232		1435	

Note : e. = experimental value ; c. = code equation value .

HORIZONTAL JOINT SHEAR STRESS
USJ - 2 : EXTERIOR PROTOTYPE



Code Areas :

A - ACI 318-83 ; NZS 3101-82 ; A = 387.7 in.²
 B - ACI-ASCE 352 ; A = 310.1 in.²
 C - AIJ-SRC ; Kamimura Eq. A = 239.0 in.²

Code Equations :

A-1 : ACI 318-83
 A-2 : NZS 3101-82
 B-1 : ACI-ASCE 352
 C-1 : AIJ-SRC
 C-2 : Kamimura

USJ - 4 : EXTERIOR MODIFIED

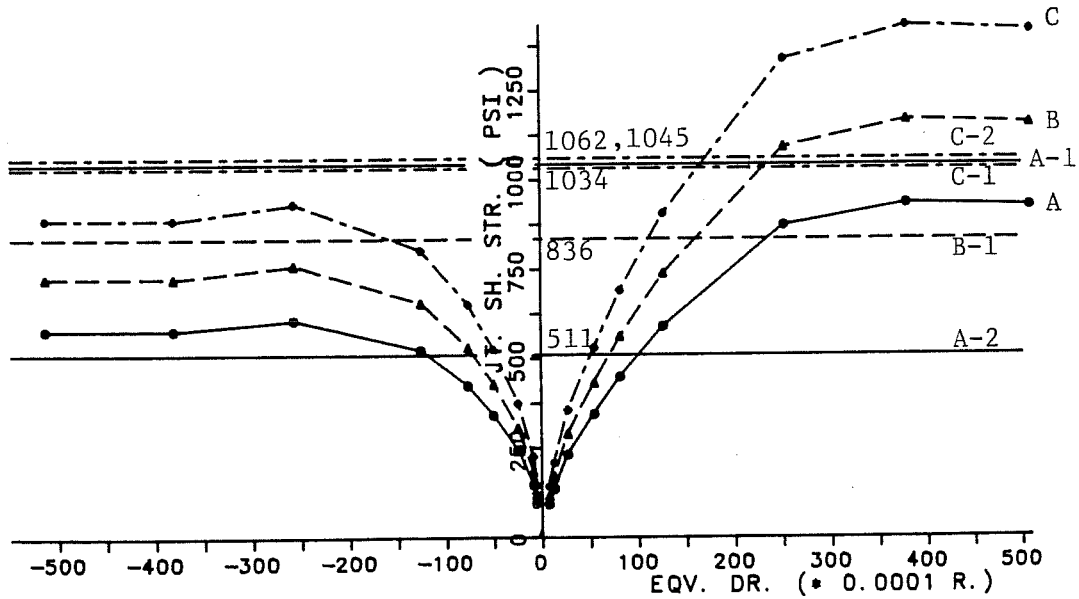


Fig. 8.4 - UTA Exterior Joint Shear Stress.

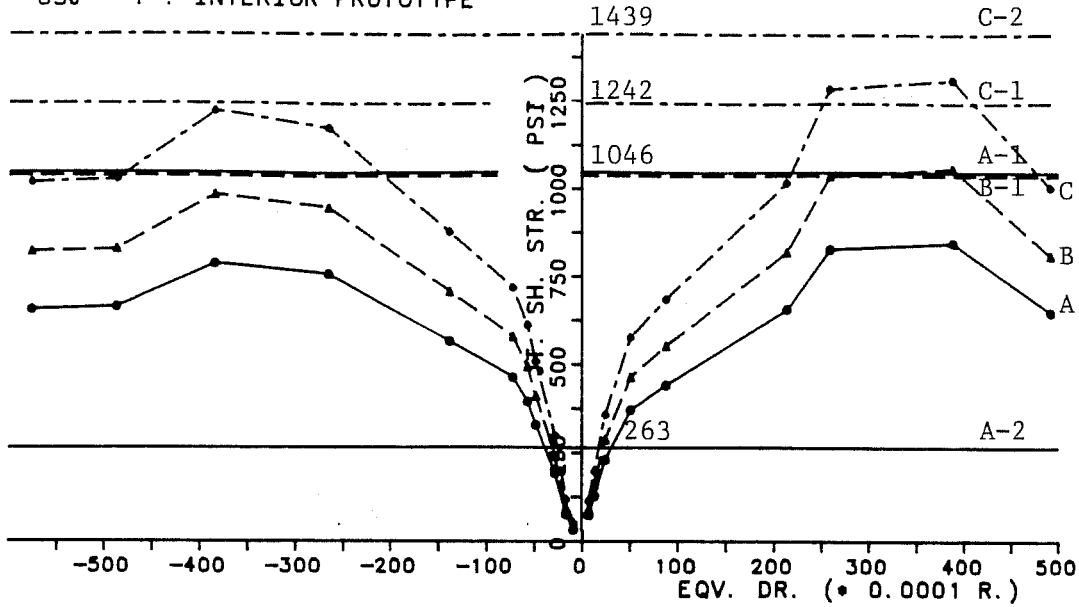
ratios given by ACI-ASCE Committee 352, AIJ-SRC and the Kamimura equation were fairly identical.

8.2.3 Interior Joint Shear Stress. As in the exterior tests, the interior component joint shear stress was computed using on three different joints areas and compared with five design recommendations. From values in Fig. 8.5, test USJ-1 reached values that were at the level of ACI-ASCE 352 and Japanese Code values for joint shear stress. The maximum measured stress was attained at an equivalent drift of $1/50 - 1/33$. The USJ-3 modified test was subjected to very large shear stresses and it may have experienced joint shear failure combined with longitudinal beam hinging at $R = 1/25 - 1/20$ as indicated by strain gauge readings on the joint reinforcement (bars, ties) and the previous chapter energy studies.

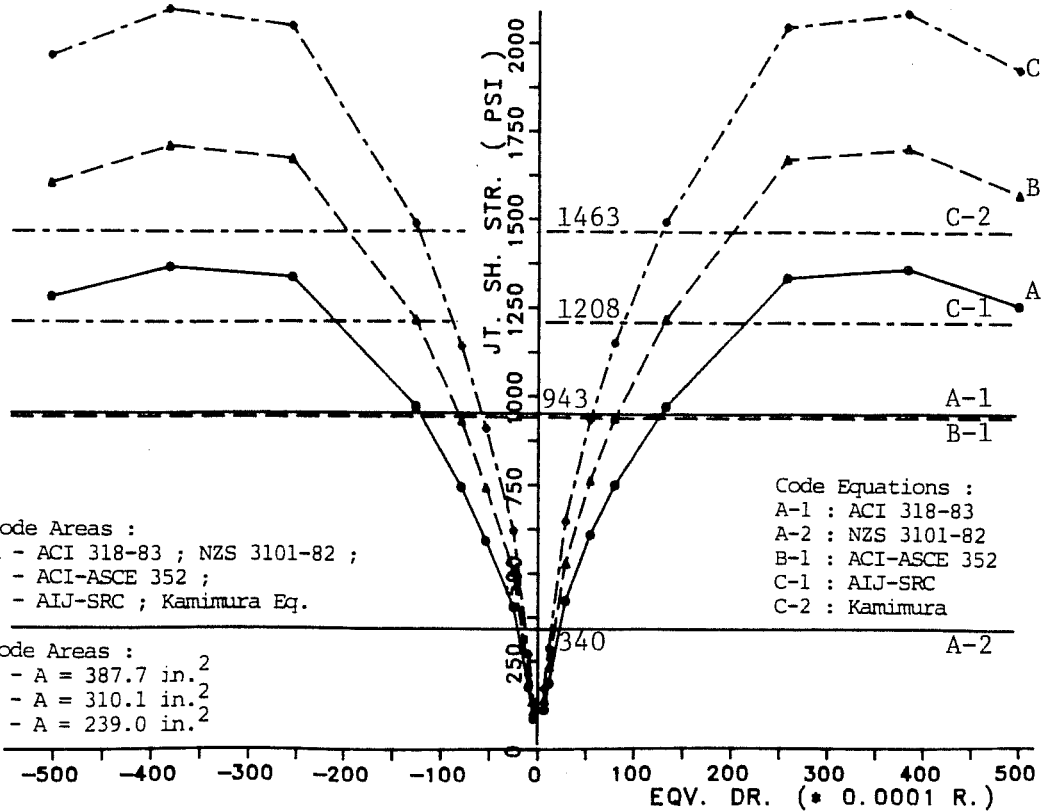
8.3 Normalized Joint Shear Stress

The joint shear stress is often expressed in the ACI 318-83 (1) and ACI-ASCE 352 (2) as a γ -multiplier or in terms of $\sqrt{f'_c}$. The current γ values were suggested by Meinheit and Jirsa (16). However, some differences exist in defining the joint area. Two definitions are followed: (1) the gross area as given by ACI 318-83 and NZS 3101-82 (17); and (2) the reduced area as proposed by ACI-ASCE 352.

HORIZONTAL JOINT SHEAR STRESS
USJ - 1 : INTERIOR PROTOTYPE



USJ - 3 : INTERIOR MODIFIED



Code Areas :
A - ACI 318-83 ; NZS 3101-82 ;
B - ACI-ASCE 352 ;
C - AIJ-SRC ; Kamimura Eq.

Code Equations :
A-1 : ACI 318-83
A-2 : NZS 3101-82
B-1 : ACI-ASCE 352
C-1 : AIJ-SRC
C-2 : Kamimura

Code Areas :
A - A = 387.7 in.²
B - A = 310.1 in.²
C - A = 239.0 in.²

Fig. 8.5 - UTA Interior Joint Shear Stress.

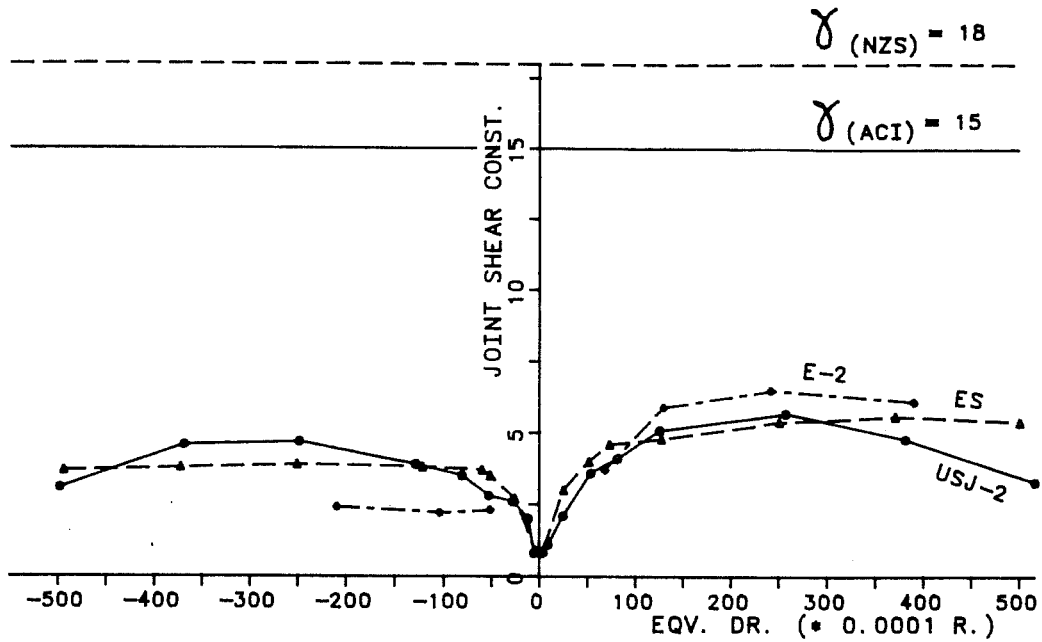
8.3.1 Gross Joint Core Area. The exterior prototypes (USJ-2, ES, E-2) showed similar response over a large deformation range although $\gamma = 5-6$ was well below the values specified for unconfined joints (15 to 18), Fig. 8.6. The modified test USJ-4 reached $\gamma = 15$ at $R = 1/50 - 1/33$. Tests without a slab (EJ, E-3) showed also similar response although the maximum γ was 2.5 - 3.0, Fig. 8.6.

In the interior prototypes (USJ-1, IS, I-2) identical performance was observed over a large deformation range where the maximum $\gamma = 12$ was below the 15-18 design Code values, Fig. 8.7. In the interior modified tests USJ-3, $\gamma = 15$ at $R=1/100$ and reached a maximum value of $\gamma = 22$ at $R=1/40$. The tests without a slab (IJ, I-3) reached maximum values close to $\gamma = 5$, well below Code values.

The interior joints experienced larger joint shear stresses compared with equivalent exterior joints and this fact was not recognized by ACI 318-83 in which only confined or unconfined joints were considered and the component geometry (shape) was disregarded.

8.3.2 Reduced Joint Core Area. The use of the reduced joint core area and the specimen shape factor as proposed by ACI-ASCE 352 resulted in smaller differences between experimental and predicted values.

JOINT SHEAR CONSTANT ($A_j = 387.7 \text{ IN.}^2$)
 EXTERIOR PROTOTYPE COMPONENTS



OTHER EXTERIOR COMPONENTS

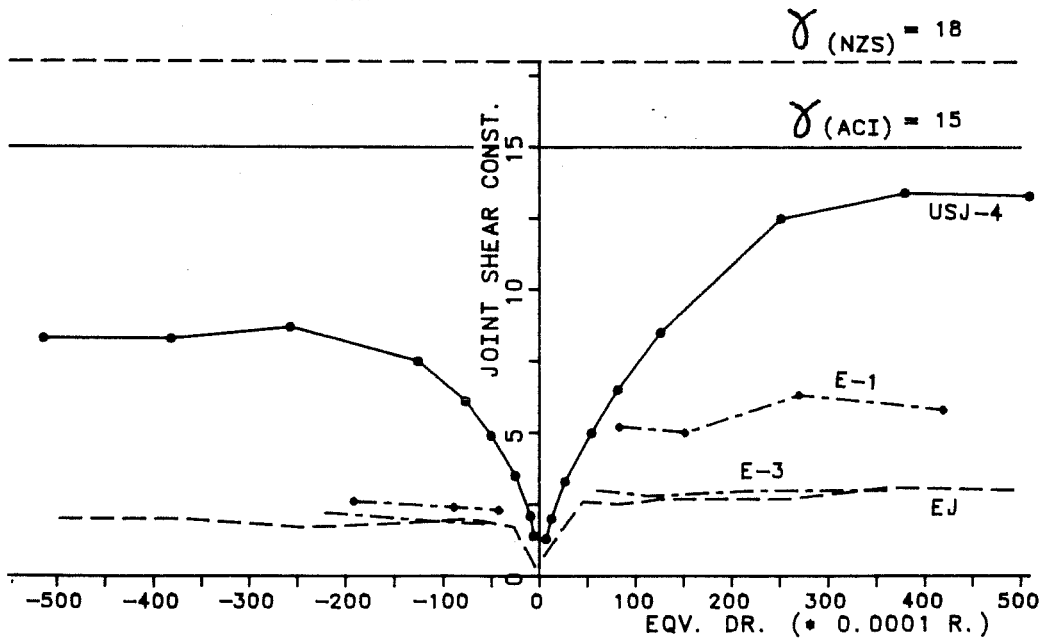
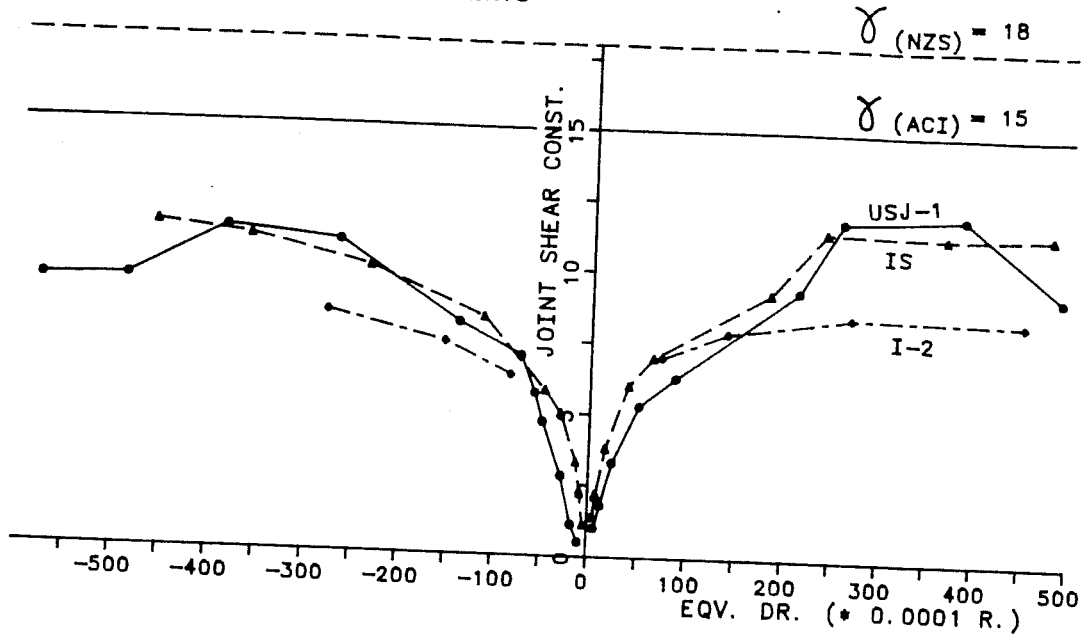


Fig. 8.6 - Gross Area Exterior Joint Multiplier.

JOINT SHEAR CONSTANT ($A_j = 387.7 \text{ IN.}^2$)
 INTERIOR PROTOTYPE COMPONENTS



OTHER INTERIOR COMPONENTS

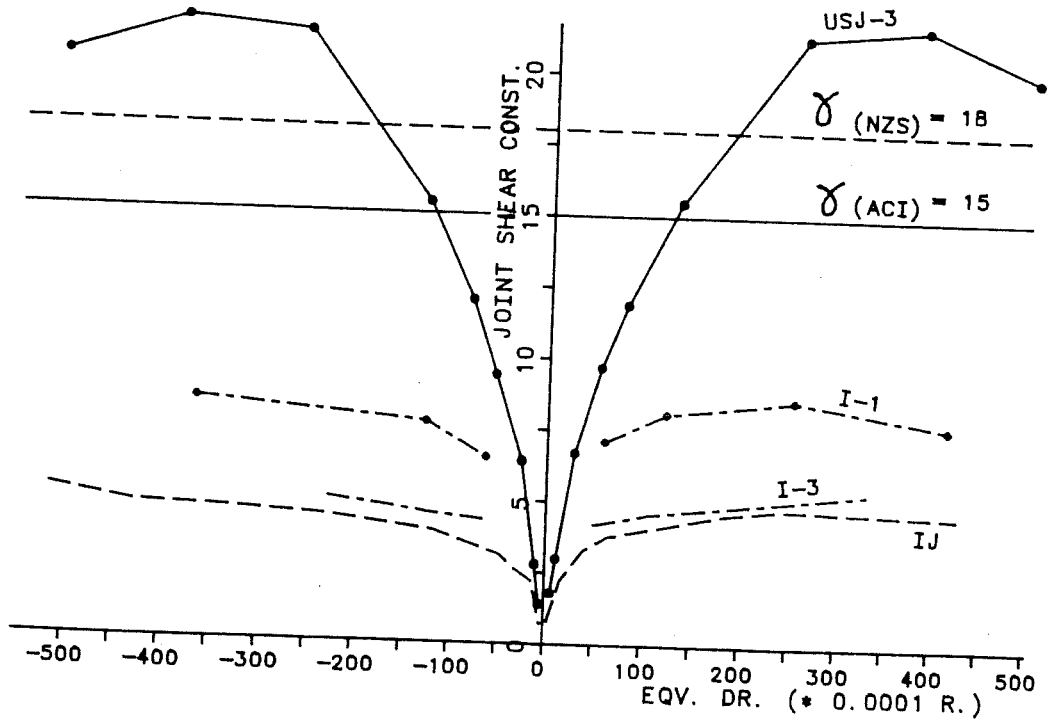


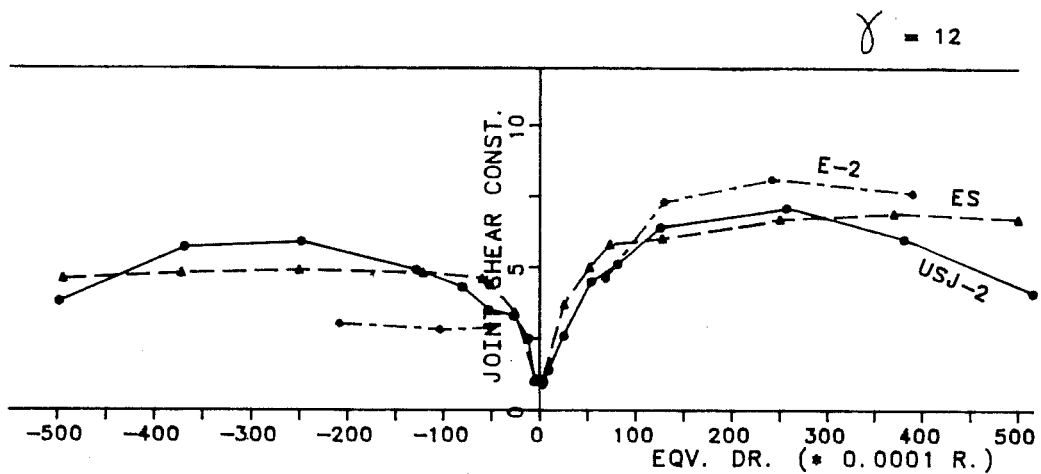
Fig. 8.7 - Gross Area Interior Joint Multiplier.

In the modified exterior test (USJ-4), $\gamma = 12$ was exceeded at $R = 1/60$ and a peak value of 17 was reached at $R = 1/40$. The prototype tests and tests without a slab showed similar response within each group, Fig. 8.8. The interior prototypes (USJ-1, IS) reached $\gamma_{\max} = 15$ at $R = 1/40 - 1/30$, Fig. 8.9. The interior modified test USJ-3 attained $\gamma = 15$ at $R \sim 1/125$ and nearly twice that value at $R \sim 1/40$. By this approach, there is a large reserve in strength and it is likely that joint shear failure occurred at the end of the test. The difference in response between interior and exterior specimens is recognized by ACI-ASCE 352 and clearly shown in Figs. 8.8 and 8.9. The components without a slab did not reach high shear values and were consistently $1/3 - 1/5$ of the design value. Horizontal joint shear stresses became critical only with a slab present.

8.4 Component Tests-Bond Response

The performance of reinforced concrete is dependent on developing bond between steel reinforcement and the surrounding concrete. Bond develops through the participation of adhesion and mechanical bond around the deformed bar surface [Tassios (20)]. The participation of each of the two bond mechanisms depends strongly on the history of the previous loads, bar geometry, concrete strength and casting position, rate of loading and incursion into new displacement/stress levels.

JOINT SHEAR CONSTANT ($A_j = 310.1 \text{ IN.}^2$)
 EXTERIOR PROTOTYPE COMPONENTS



OTHER EXTERIOR COMPONENTS

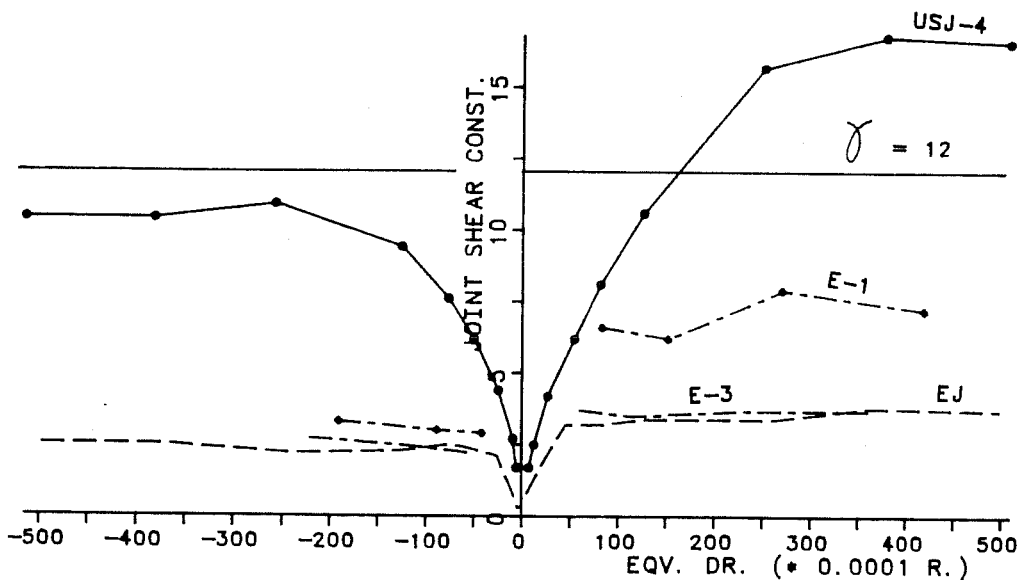
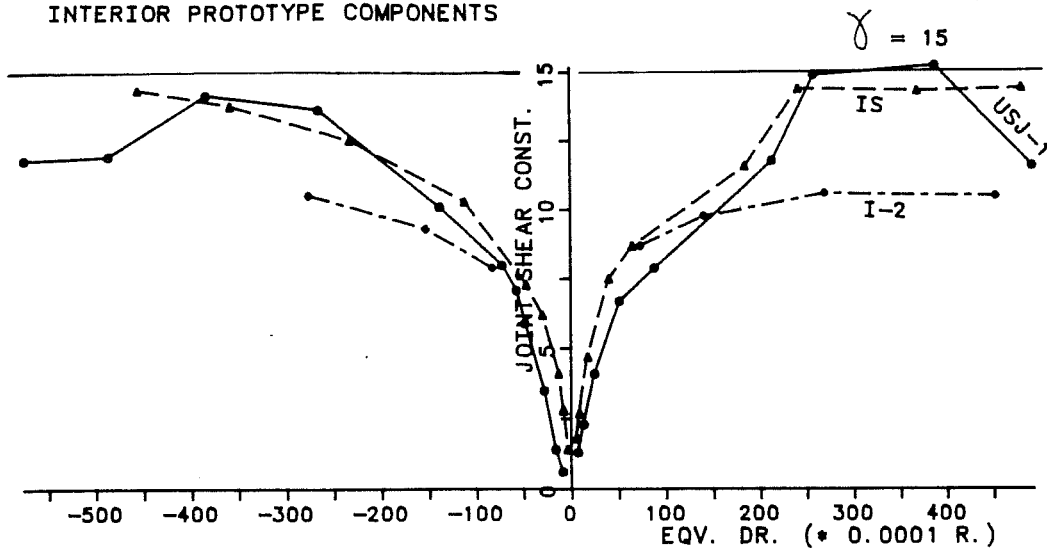


Fig. 8.8 - Reduced Area Exterior Joint Multiplier.

JOINT SHEAR CONSTANT ($A_j = 310.1 \text{ IN.}^2$)
 INTERIOR PROTOTYPE COMPONENTS



OTHER INTERIOR COMPONENTS

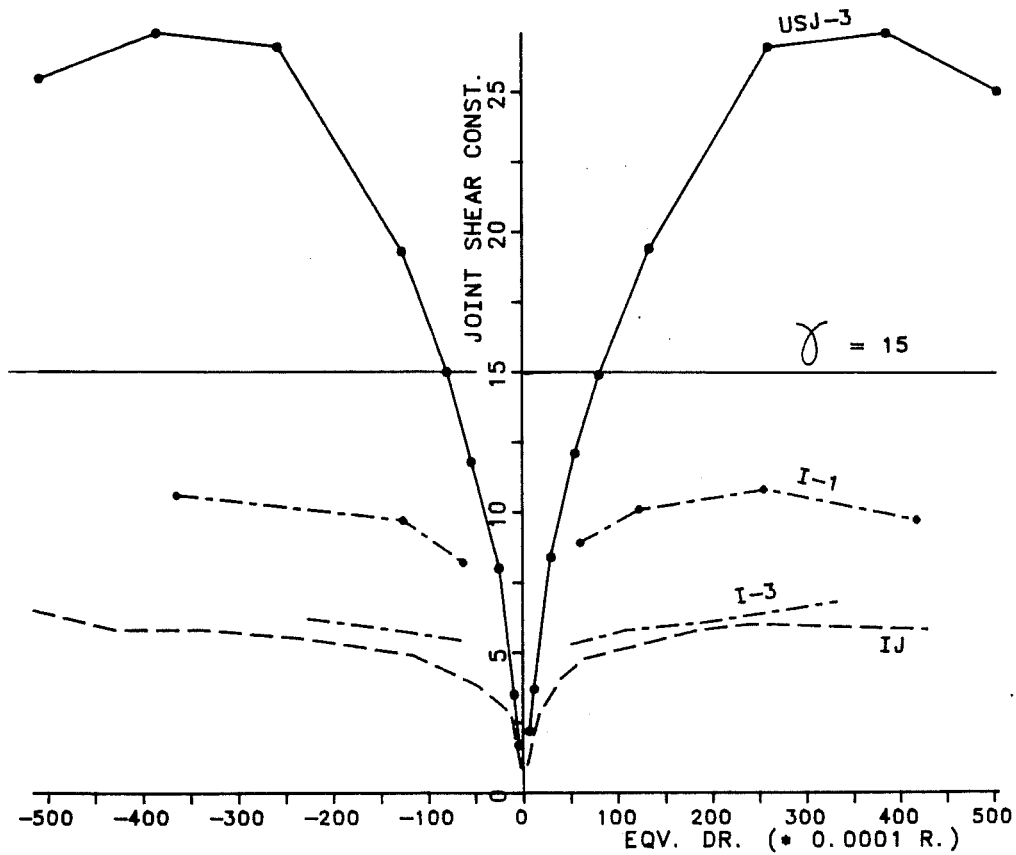


Fig. 8.9 - Reduced Area Interior Joint Multiplier.

In earthquake design of R/C structures particular emphasis is placed on providing recommended development lengths at critical sections, particularly in the beam-column joints. However, current design Code specifications may be too stringent and may lead to very large columns.

Under reversed cyclic loads more severe bond stresses are imposed on the reinforcement. Comparisons between a bond index parameter and the energy response in longitudinal beams are also made.

8.4.1 Development Length. Different development length requirements are currently specified depending on the type of joint being considered (exterior, interior) and are summarized in Table 8.4. Whereas the US Codes make bond depend directly on the concrete and steel strengths, the Japanese Code considers indirectly the concrete through an allowable bond stress (f_{bond}). In the case of temporary loads and connections, this bond stress can be increased twice by a 1.5 factor (1.5×1.5). Current AIJ bond provisions are considered too conservative and Japanese researchers are studying the possibility of implementing an ultimate bond stress $\tau_{\text{ub}} = 15\sqrt{f'_c}$ (psi). In this study only the current Code provisions have been considered.

8.4.1.1 Exterior joints. The recommended anchorage lengths for 90° hooks are shown in Table 8.5. However, it is found that easier interpretation is obtained by plotting the data

TABLE 8.4 - CODE DEVELOPMENT LENGTH.

Standard	Component Top Bars	
	Exterior Joints (90°hook)	Interior Joints
1. ACI 318 - 1983	$\frac{f_y \cdot d_b}{65 \cdot \sqrt{f'_c}} \geq \begin{cases} 8 d_b \\ 6 \text{ in.} \end{cases}$	n/a
2. ACI - ASCE Comm. 352	$\frac{f_y \cdot d_b}{60 \cdot \sqrt{f'_c}} \geq \begin{cases} 8 d_b \\ 6 \text{ in.} \end{cases}$	$\frac{h_c}{d_b} \geq 20$
3. NZS 3101 - 1982	$0.8 \cdot \frac{f_y \cdot d_b}{70 \cdot \sqrt{f'_c}} + \min. [h_c/2, 10d_b] \geq \begin{cases} 8 d_b \\ 6 \text{ in.} \end{cases}$	$\frac{h_c}{d_b} \geq 35$
4. ALJ - RC 1982	$\frac{f_y \cdot d_b}{9 \cdot f_{\text{bond}}} \geq 20 d_b$	$\frac{f_y \cdot d_b}{9 \cdot f_{\text{bond}}} \geq 30 d_b$

TABLE 8.5 - REQUIRED TOP BEAM DEVELOPMENT LENGTH.

$h_c^{\text{provided}} / h_c^{\text{required}} \quad (h_c^{\text{prov.}} = 19.68 \text{ in.})$								
Design Equation	Exterior Joint				Interior Joint			
	USJ-2	USJ-4	ES,EJ	E-1,2,3	USJ-1	USJ-3	IS,IJ	I-1,2,3
ACI 318	1.67	1.19	1.88	1.82
ACI-ASCE 352	1.35	1.00	1.49	1.45	1.31	1.13	1.31	1.31
NZS 3101	1.17	0.92	1.25	1.22	0.75	0.65	0.75	0.75
ALJ-RC 82	1.38	0.88	1.68	1.58	0.88	0.63	0.88	0.88

as shown in Fig. 8.10-a. It should be noted that specimen USJ-2 failed in anchorage. Except for the ACI-ASCE 352 development requirements, the #6 (19mm) longitudinal beam bars did not need column sizes as large as provided and the #7 (22 mm) needed columns very close to the size provided.

8.4.1.2 Interior joints. The development requirements for the interior joints are simply specified in the US equations by a constant factor times the bar size. Only ACI-ASCE 352 column requirements were less than the column depth provided, Fig. 8.10-b.

Based on the experimental data described in the previous chapters it can be inferred that the column depth provided in the joint region for the interior tests was sufficient to allow yielding in the longitudinal beam bars. In the exterior tests, although it seemed that enough column depth had been provided, the failure mode characterized by anchorage pull-out (USJ-2) required more attention to improved detailing and confinement.

8.4.2 Beam Bar Bond Index. Under reversed cyclic loadings the joint regions in strong column - weak beam DMRF frames must be able to sustain the high shears developed through the beams. It is recognized that the complete elimination of bond deterioration in the beam bars is virtually impossible due to the very large yielding beam stresses, Fig. 8.11. However it

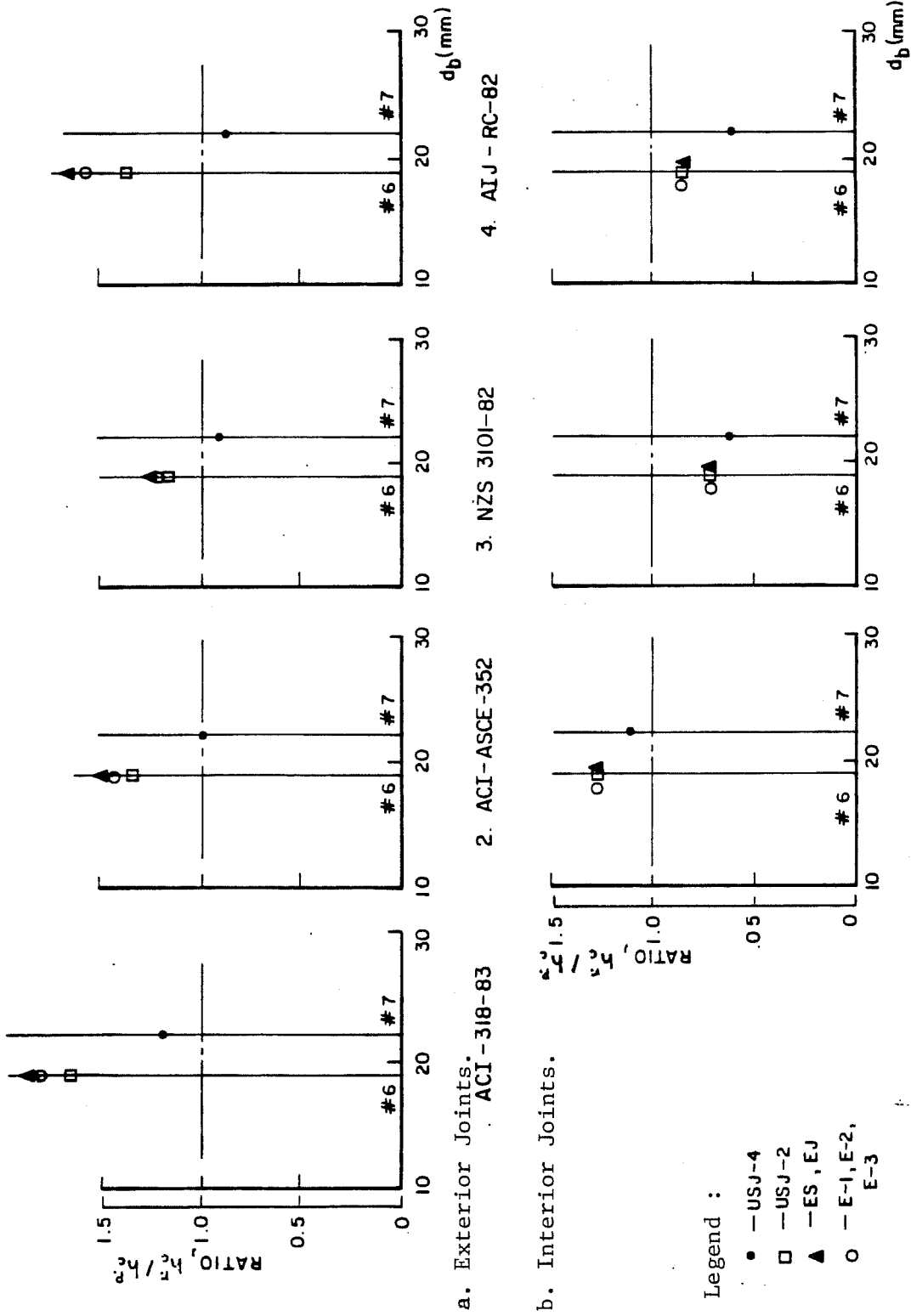


Fig. 8.10 - Column Ratio vs. Top Beam Bar Sizes.

is important that beam bar bond deterioration is delayed up to very large drift levels to avoid: (1) the reduction in energy absorption/dissipation due to beam bar sliding; and (2) the decrease in the joint shear capacity due to alterations in the shear transfer mechanism.

A global evaluation of the bond conditions within the interior joint region was proposed by Otani et al. (19) through a parameter - the beam bar bond index, u_b :

$$u_b = \frac{1}{2} f_y \frac{d_b}{h_e} \quad (8.1)$$

where: f_y = steel yield strength; d_b = beam bar diameter; and, h_e = column depth. The actual bond variation may be different than the assumed tensile and compression yielding of a beam bar at the column faces, Fig. 8.11. The beam bar bond index is not a bond stress, but it gives an indication of the possible bond variation along the interior joint.

The actual column depth and material properties were used in equation 8.1 to compute the experimental bond index ratio for the different tests, Table 8.6. These values are compared with nominal bond ratios (Grade 60 steel) computed with ACI-ASCE 352 and NZS 3101. The Japanese tests have a lower value because of the lower nominal steel yield strength (Grade 50). The interior tests show satisfactory bond index ratios if ACI-ASCE 352

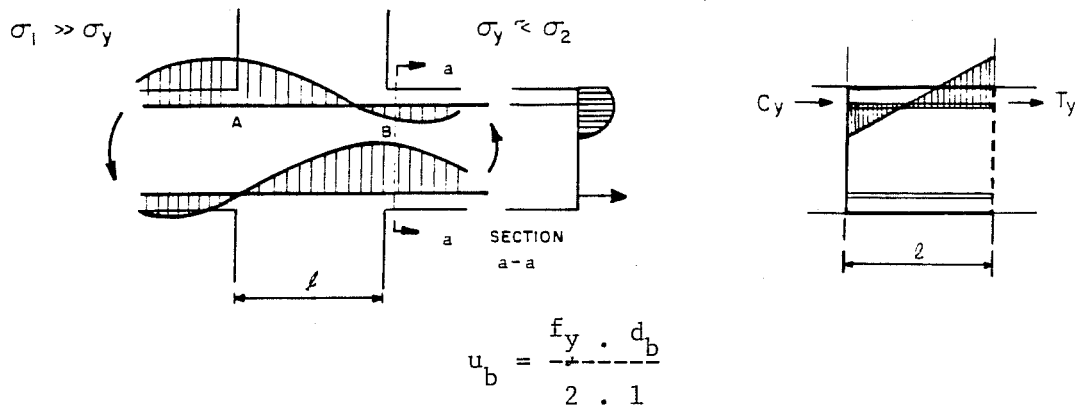


Fig. 8.11 - Interior Joint Bond Index Ratio.

TABLE 8.6 - EXPERIMENTAL VS. NOMINAL BOND INDEX RATIO.

Test Specimens	Univ. Texas at Austin		Stanford University	Japan
	USJ - 1	USJ - 3	IS , IJ	I - 1,2,3
f_y (psi)	61	75	56	53.3
d_b (in.)	.75	.875	.75	.75
h_c (in.)	19.68			
u_b (psi)	1162.	1667.	1107.	1015.
CODE VALUES steel grade	Grade 60			Grade 50
ACI-ASCE Comm. 352	1500.			1250.
NZS 3101 - 1982	857.			714.

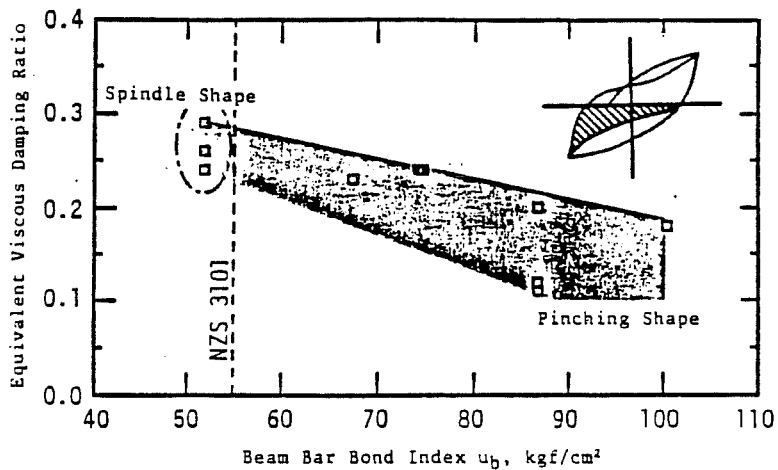


Fig. 8.12 - EHD vs. Beam Bar Bond Index Ratio, [Otani et al.(19)].

equation is used (except in test USJ-3). The NZS 3101 is more conservative and indicates lower limit bond index ratios.

8.4.3 Bond and Hysteretic Response. The top beam bar bond response under reversed cyclic loads can also be assessed through the bond index ratio and the equivalent hysteretic damping (EHD) defined in chapter VII. The longitudinal beam EHD was evaluated in the second cycle peak equivalent drift because it showed more consistent response throughout the tests. The identification of good-spindle shape vs. pinching hysteretic response is important because the whole system behavior is affected by bond performance [Kitayama et al. (12)]. Bond destruction, bar slip, can be easily perceived through the evaluation of the beam EHD for the different component elements (beam, joint panel, column). In the case of a large series of tests conducted in Japan where components were designed for different failure modes (beam hinging, joint shear), the response obtained at an equivalent drift of $R = 1/46$ showed lower damping ratios as the bond index ratio increased, Fig. 8.12.

The U.S. prototype tests that had similar geometries and beams yielding at approximately the same displacement levels shown in Fig. 8.13. The other modified tests (UTA) and tests without a slab (SJ) are also used in the study. Due to the T-beam effect, the response is separated into positive and negative equivalent drifts, R .

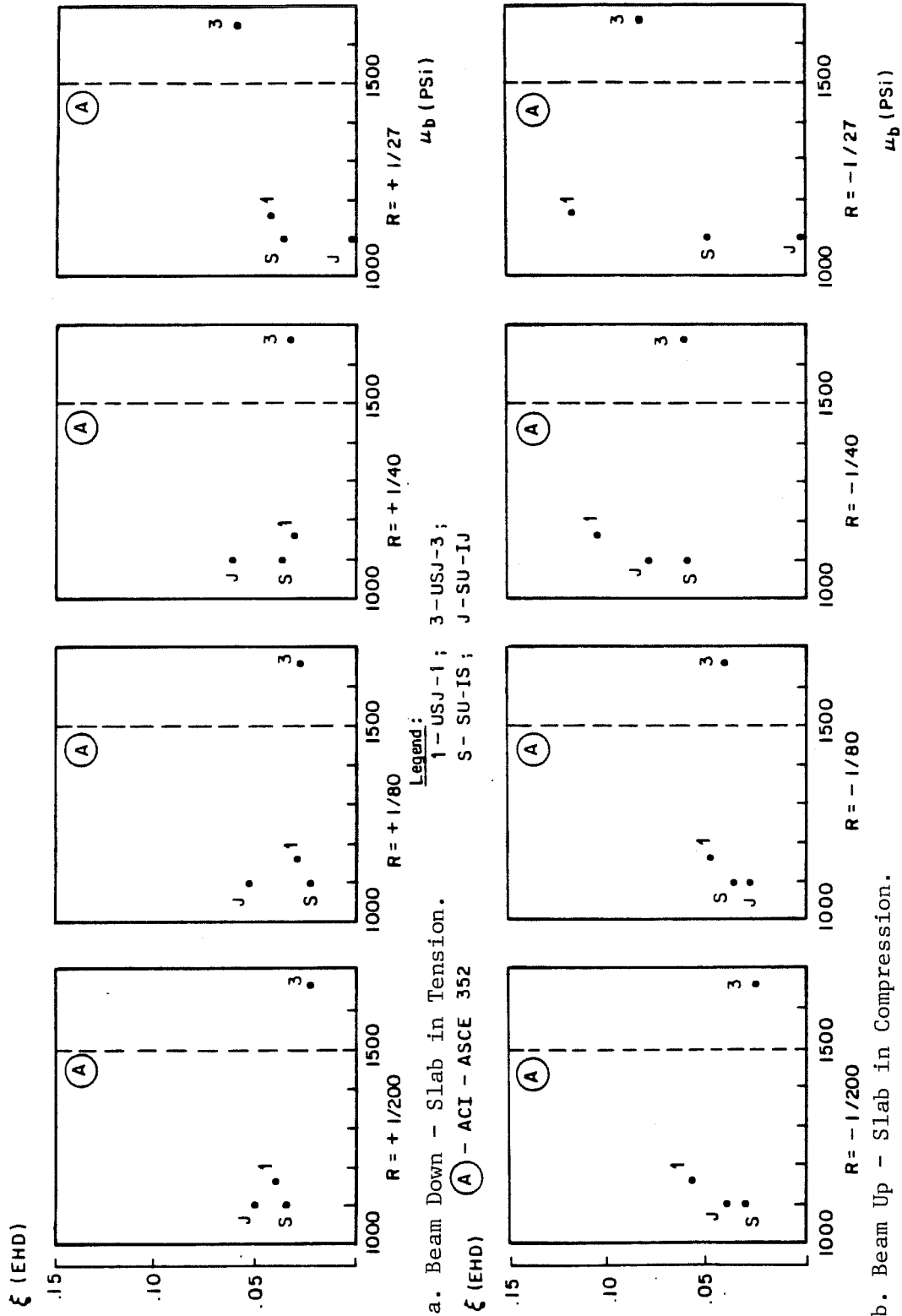


Fig. 8.13 - US Interior Tests Bond Index Ratio Response.

In the interior tests, beam EHD ratios ($\xi = 3$ to 9%) in tension or compression were observed. However, for test SU-IJ at $R = -1/27$ the EHD (ξ) was zero which may indicate large bar sliding in the bottom beam tensioned bars. Otherwise, in the drift range $R = -1/40$ to $+1/27$ increasing EHD (ξ) ratios may indicate that satisfactory bond conditions existed despite the insufficient development lengths by some standards (interior joints only).

8.5 BRI Building - Ultimate Strength Evaluation

8.5.1 Background. Ultimate strength evaluation of structural systems is used in seismic design because of the need to obtain, simply and reliably, the capacity of a structure. Since the early 1914 pioneering studies by the Hungarian Kazinczy, increasing research has been done in the ultimate strength area [Tichy and Rakosnik (21)]. However, it has been observed that although the ultimate capacity can be reached, the level of imposed deformation may be greater than the structure would experience under any reasonable loading conditions. The level of deformations generated by lateral seismic loading of a DMRF creates a characteristic beam plastic hinge pattern which is different from that under gravity loading. The spread and distribution of plastic hinges in the DMRF is closely related to the amount of imposed lateral drift.

The BRI frame provides an excellent opportunity to evaluate ultimate strength based on current design techniques. The experimental base shear will be compared with the calculated base shear. The computed value is determined using: (1) actual material properties; (2) force-deformation characteristics of RC sections, and (3) a failure mechanism based on the recorded member yield strains.

8.5.2 Experimental Evidence.

8.5.2.1 Spread of yielding. At the end of test PSD-4 ($R_{max} = +1/64$), the BRI frame had member yielding in the locations shown in Fig. 8.14-a. The bar strains were recorded when the structure reached a flat load-deflection response implying that the structure had attained its lateral capacity, Fig. 8.14-b. Based on this recorded data, a possible failure mechanism for Frames A, C, and Frame B is proposed, Fig. 8.14-c. The location of plastic hinges in either the beams or the columns depends on: (a) the level of deformation; (b) the amount of slab width working monolithically with the beam (slab acting as a flange on the beam); (c) the previous loading history on the member; and, (d) out of plane three-dimensional effects (wall uplift) transmitted through transverse frames.

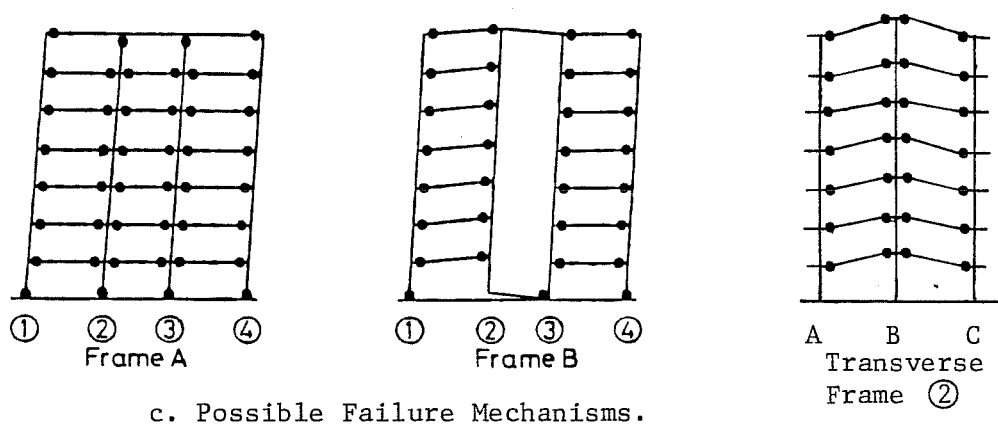
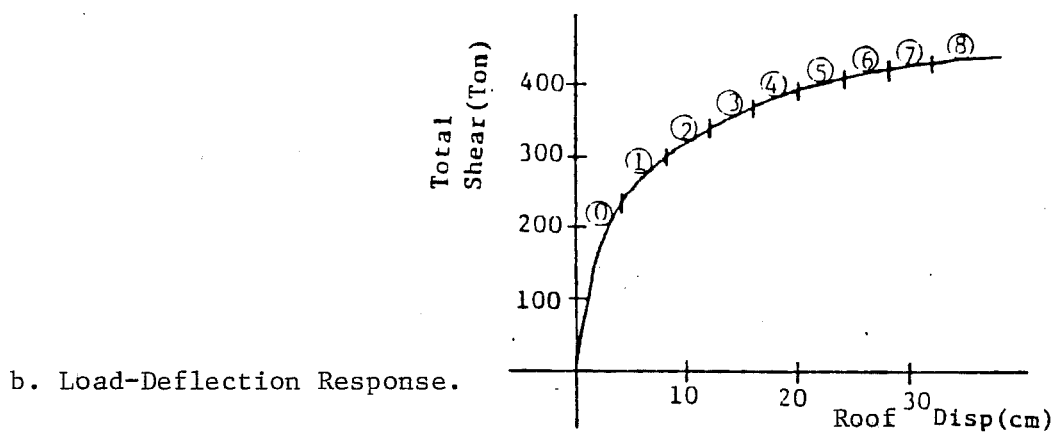
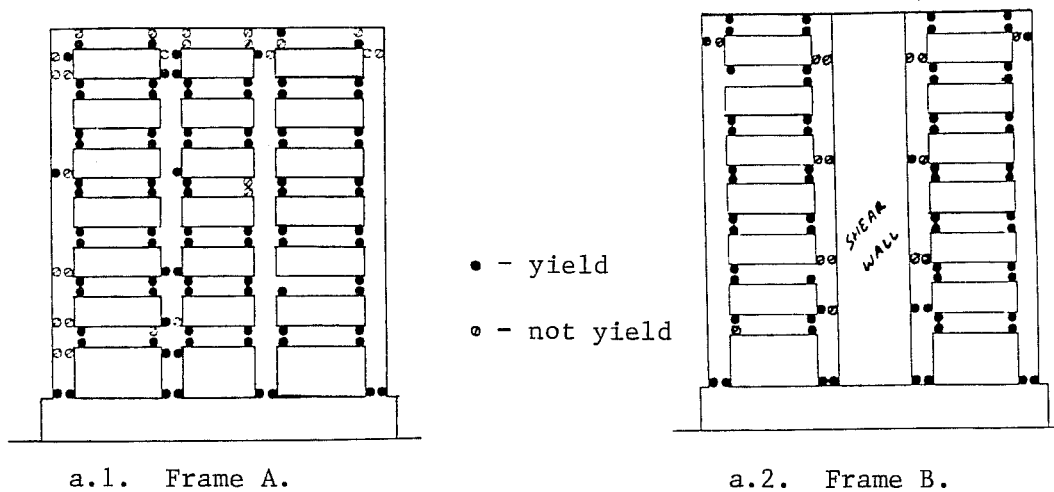
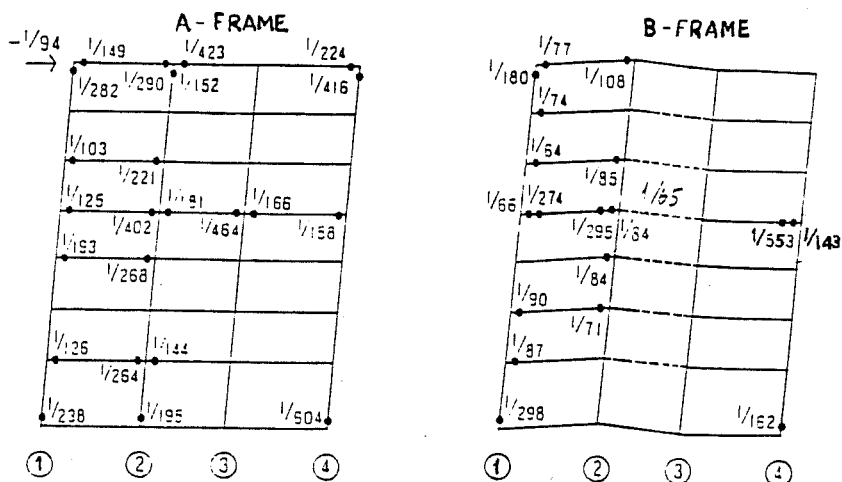


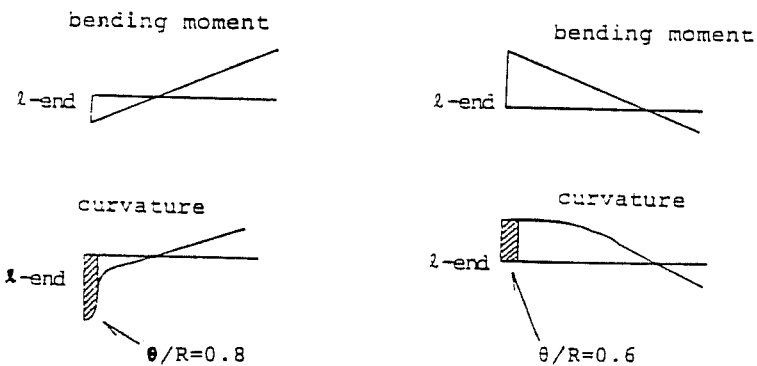
Fig. 8.14 - BRI Building at the End of Test PSD-4.

8.5.2.2 Beam Member Rotation. The member end rotation at the connections was studied by Kurose and Yoshimura (13, 24) for an equivalent drift $R_{\max} = -1/94$ (Test PSD-3), Fig. 8.15-a. All the rotations in Frame A were measured at a distance $d/2$ ($d =$ member effective depth) and are fairly consistent along the height. The beam rotations when the slab was in compression (Frame A/1) were a little smaller than the imposed drift ($-1/94$), whereas when the slab was in tension (Frame A/2) they were less than $1/2$ the imposed drift. This may indicate that there was a difference in the plastic hinge length depending on the loading direction and the role of the slab on T-beam behavior. This was shown by Kurose et al. (13) and is included on Fig. 8.15-b. The beam rotations in Frame B clearly showed the effect of wall uplift between column lines 1 and 2 where the recorded beam rotation was nearly twice the imposed drift. At column line 4, the beam rotation ($-1/114$) taken over a distance d from the column was close to the imposed drift value ($-1/94$), Fig. 8.15-a. The wall boundary column on the tension side extended considerably as lateral deformations were applied, whereas on the compression side the contraction effects on the boundary column were negligible.

The measured member rotations were based on filtered data because the original LVDT information had high noise frequencies, [Kurose et al. (13)]. However, some unfiltered data were also

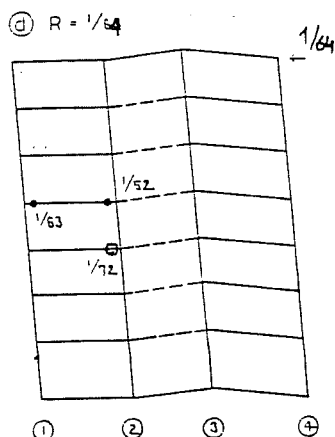
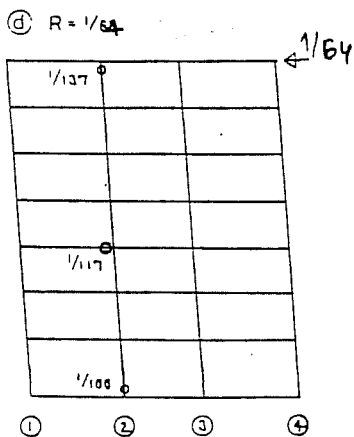


a. BRI Building Member Rotation (PSD-3).



b.1. Slab in Compression

b.2. Slab in Tension.

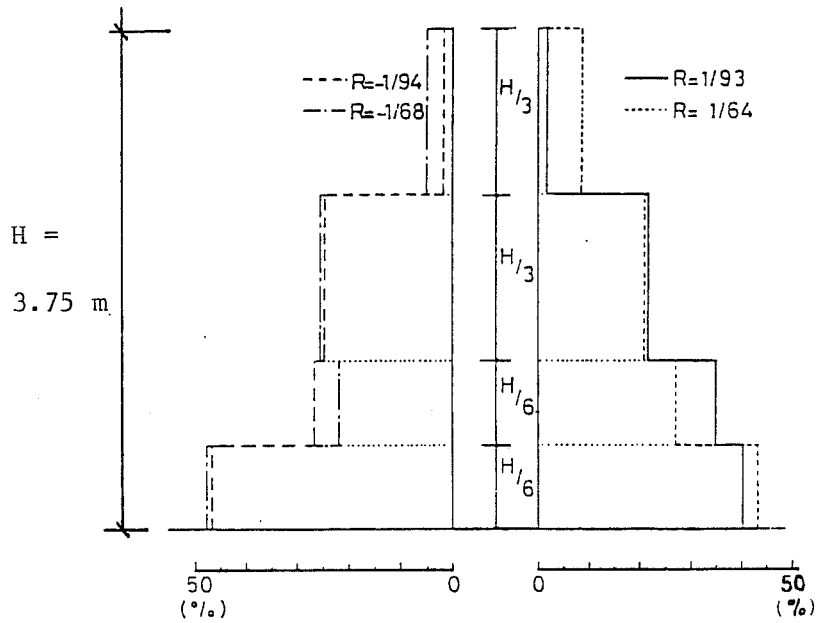


c. BRI Building Member Rotation (PSD-4).

Fig. 8.15 - BRI Building Experimental Member Rotation.

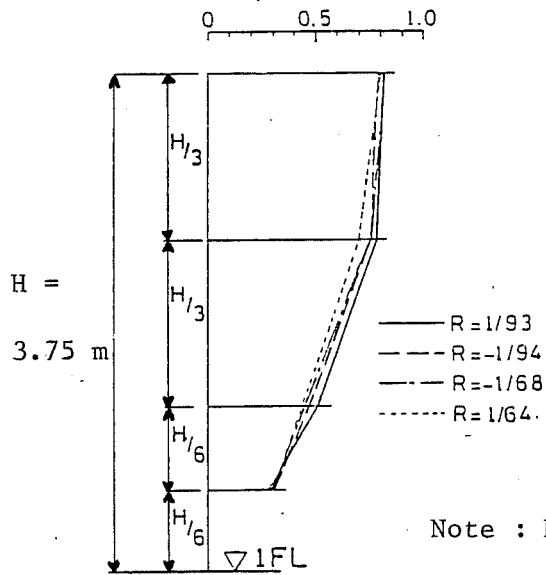
initially reported for a limited number of member rotations, Fig. 8.15-c [Yoshimura (23)]. It is shown that beam rotation at a peak equivalent drift $R = +1/64$ (unfiltered) exhibited the same trends as loading to $R = -1/94$.

8.5.2.3 Shear Wall Deformation. The shear wall response was also studied by Yoshimura et al. (25) at an equivalent drift $R = -1/94$ (PSD 3) and $+1/64$ (PSD4), Fig. 8.16. The measurements showed that initially ($R = -1/94$), most of the wall curvature was limited to the bottom $2/3$ (2.50 m) of the first level Z2. However, at a larger drift ($R = +1/64$) with the spread of yielding and increased damage, the plastic rotation length passed the first floor level (3.75 m). The cracking patterns shown in Appendix A indicate a plastic hinge length L_p of 3.75 - 5.50 m ($0.68 - 1.0 d_w$; $d_w =$ wall depth). The shear wall response has been studied by Hiraishi (9) and the main components of deformation were identified: (1) flexure; (2) shear; and (3) expansion. For the BRI building it was found that [Watabe et al. (22)]: (a) shear deformation may represent 30 to 40% of the total deformation; (b) shear deformation increased with the number of load reversals because of the deterioration in shear resistance; (c) shear wall deformation dominated first storey response ($3.75/5.5 = 0.68 d_w$); and, (d) the shear wall plastic hinge formed at $R = 1/400$, but as R increased, spread of yielding occurred in the vertical wall reinforcement.



Note : Each curvature is normalized with respect to the sum.

a, Curvature Distribution.



Note : Each rotational angle is normalized with drift angle.

b. Rotation Distribution.

Fig. 8.16 - First Floor Shear Wall Deformation.

The expansion effect resulted from extension of the shear wall boundary columns with permanent yield deformations caused by unclosed, debris filled cracks.

8.5.3 BRI Building Ultimate Strength.

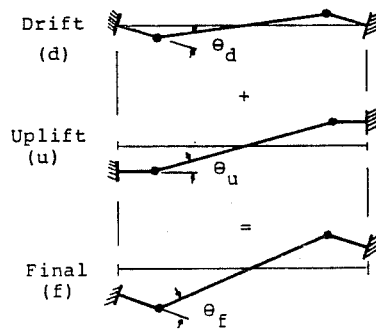
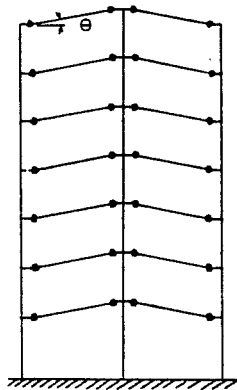
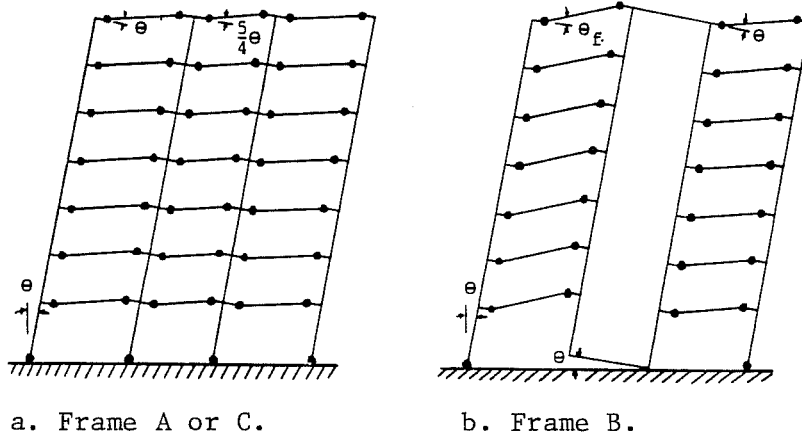
The ultimate capacity of the BRI building was evaluated by using the Upper Bound Theorem for limit analysis. The assumed failure mechanism is shown in Fig. 8.17, under an external lateral force distribution that followed the inverted triangular pattern over the height.

In the virtual work computations, several assumptions were made in regard to the exterior and interior work terms. The exterior work was computed assuming the inverted triangular load distribution. The pseudo-dynamic test of the equivalent SDOF system showed good agreement with the experimental data, indicating that the first mode dominated in both the elastic and inelastic ranges. The total external work, W_e , delivered by the actuators is given by (in inches):

$$W_e = \sum P_i \times \delta_i = 2516 \cdot P_7 \cdot \theta \quad (8.2)$$

with: P_i = horizontal load at level i ; δ_i = horizontal displacement at level i ; P_7 = roof load; and, θ = drift rotation. In terms of the horizontal base shear, V_b , the external work is given by (in inches):

$$W_e = 613 V_b \cdot \theta \quad (8.3)$$



$$\theta_f = \theta_d + \theta_u = \frac{5.25}{5} \cdot \theta + \theta$$

c. Transverse Frame.

d. Uplift Effect.

Fig. 8.17 - Assumed Failure Mode in the BRI Building.

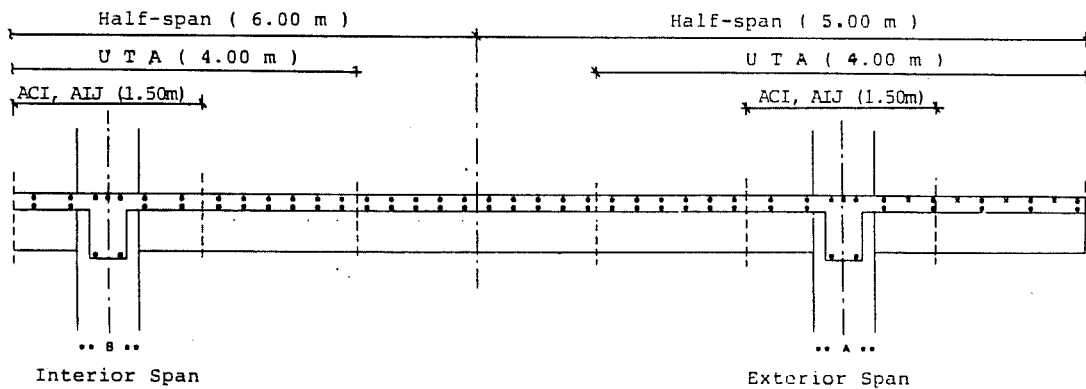


Fig. 8.18 - Effective Slab Width.

The contribution of internal work to the failure mechanism was studied using four different effective slab widths (Fig. 8.18) and was compared with the measured base shear of 433 Tf (954 kips) attained at $R = +1/64$ in test PSD-4 [Okamoto et al. (18)]. The four cases considered are: (1) bare frame-rectangular beam; (2) ACI, AIJ slab width (1.50 m, 59.0 in.); (3) UTA test slab width (4.00 m, 157.5 in.); and, (4) half-span slab width (Frames A, C - 5.00 m (197 in.), Frame B - 6.00 m (236.2 in.). In the shearwall, the plastic hinge was assumed to be located at the column centroid although the actual location was near the shearwall-boundary column interface.

The moment-curvature characteristics of each structural element (shearwall, beam, column) were studied with a computer program - RCCOLA, developed at The University of California at Berkeley and modified at The University of Texas at Austin by Farahany and Klingner (8). In this program the actual material properties were used including steel strain-hardening and concrete confinement effects. The moment-curvature relationships for the different building elements (shearwall, column, longitudinal and transverse beams) are shown in Figs. 8.19 to 8.22. Two important aspects deserve special attention: (1) the T-beam flexural response depends on the loading direction; and, (2) members under combined bending and axial load (shearwall,

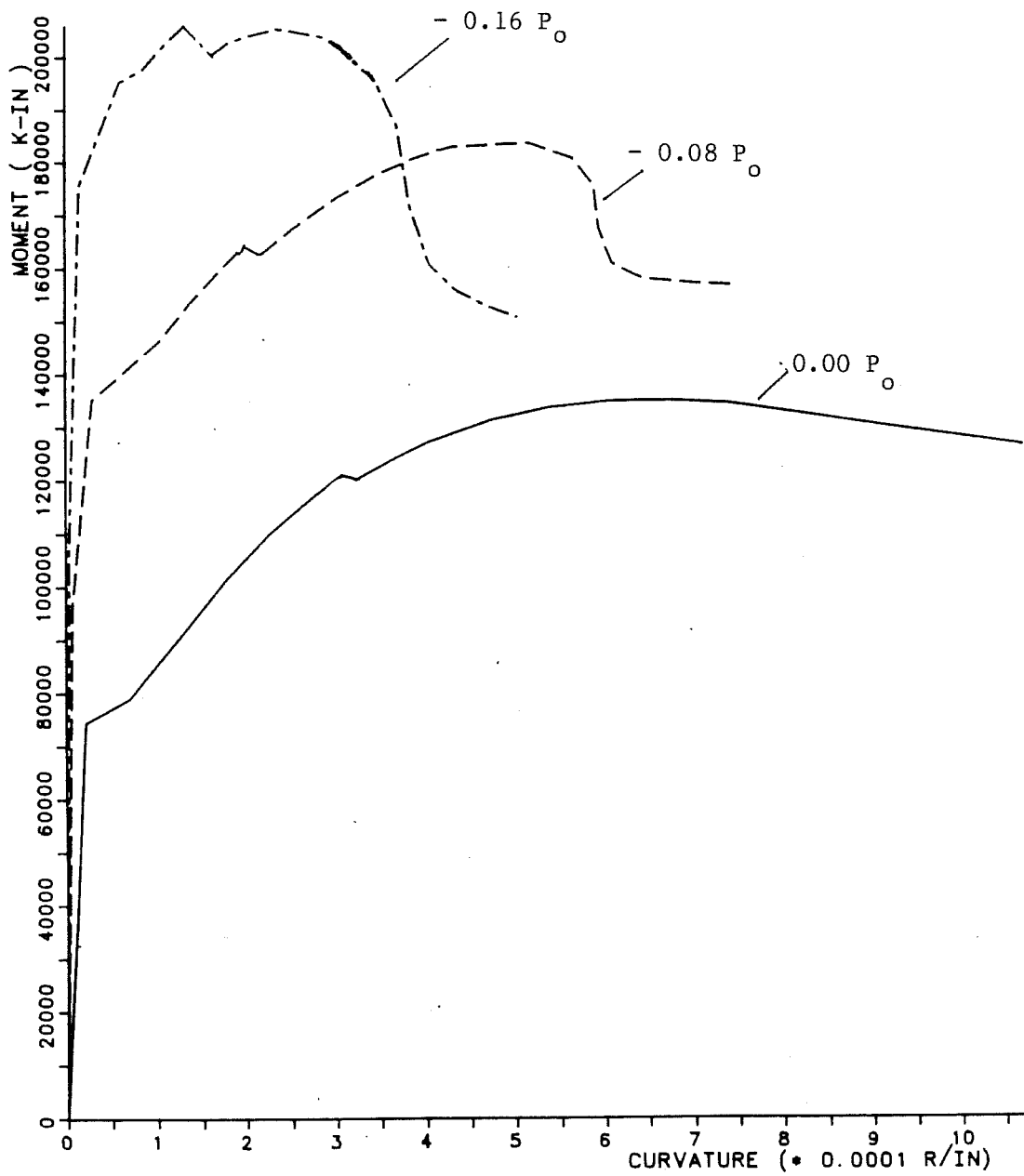


Fig. 8.19 - Shear Wall Moment Curvature.

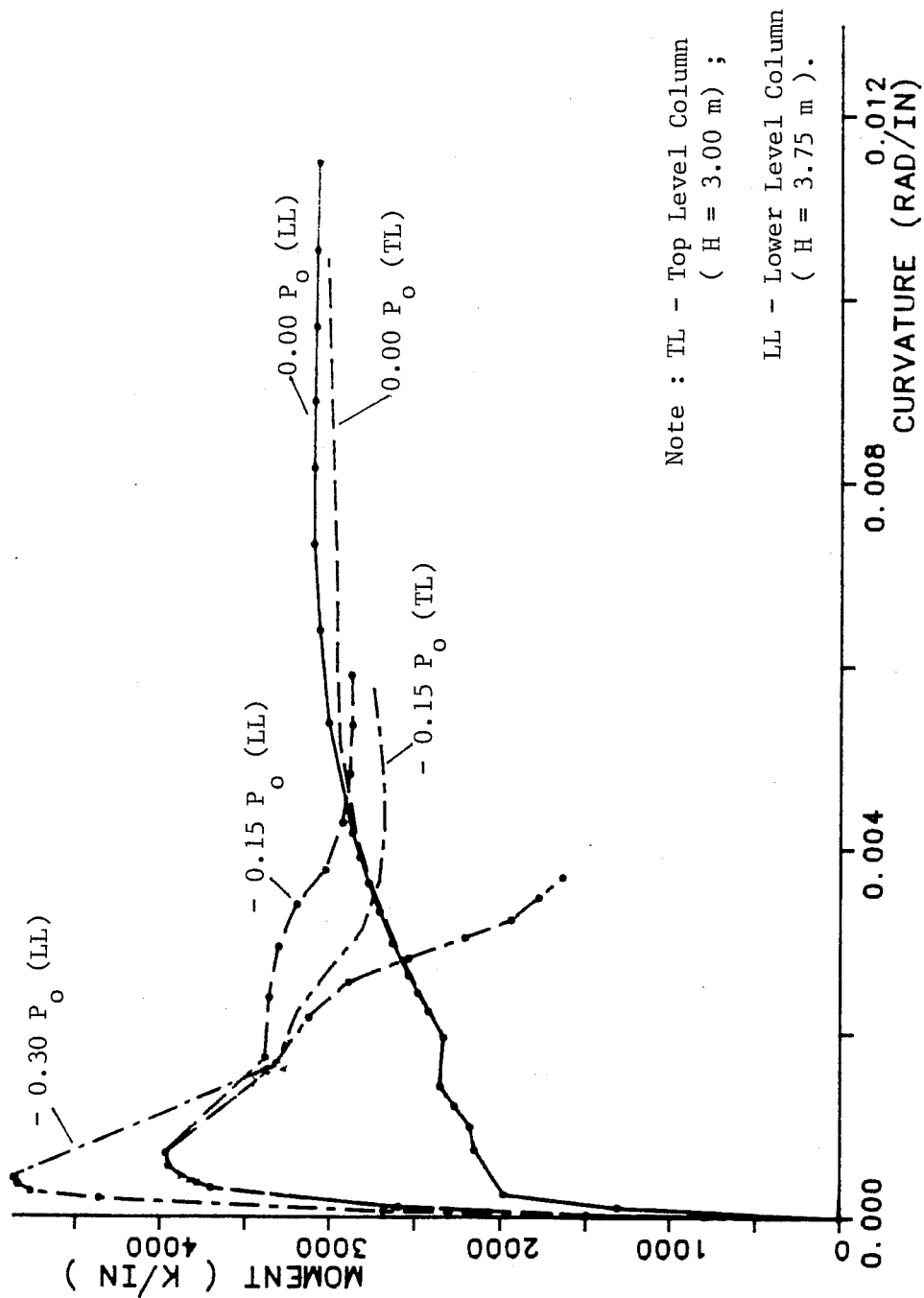
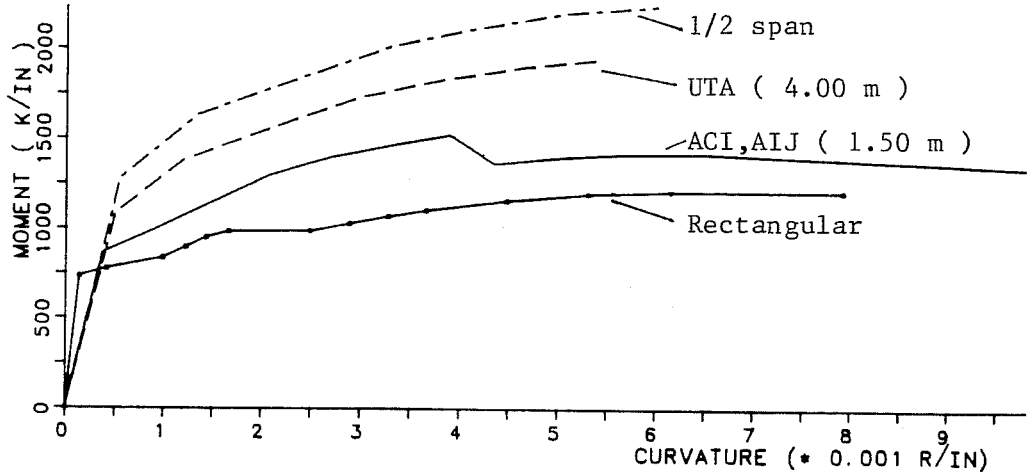
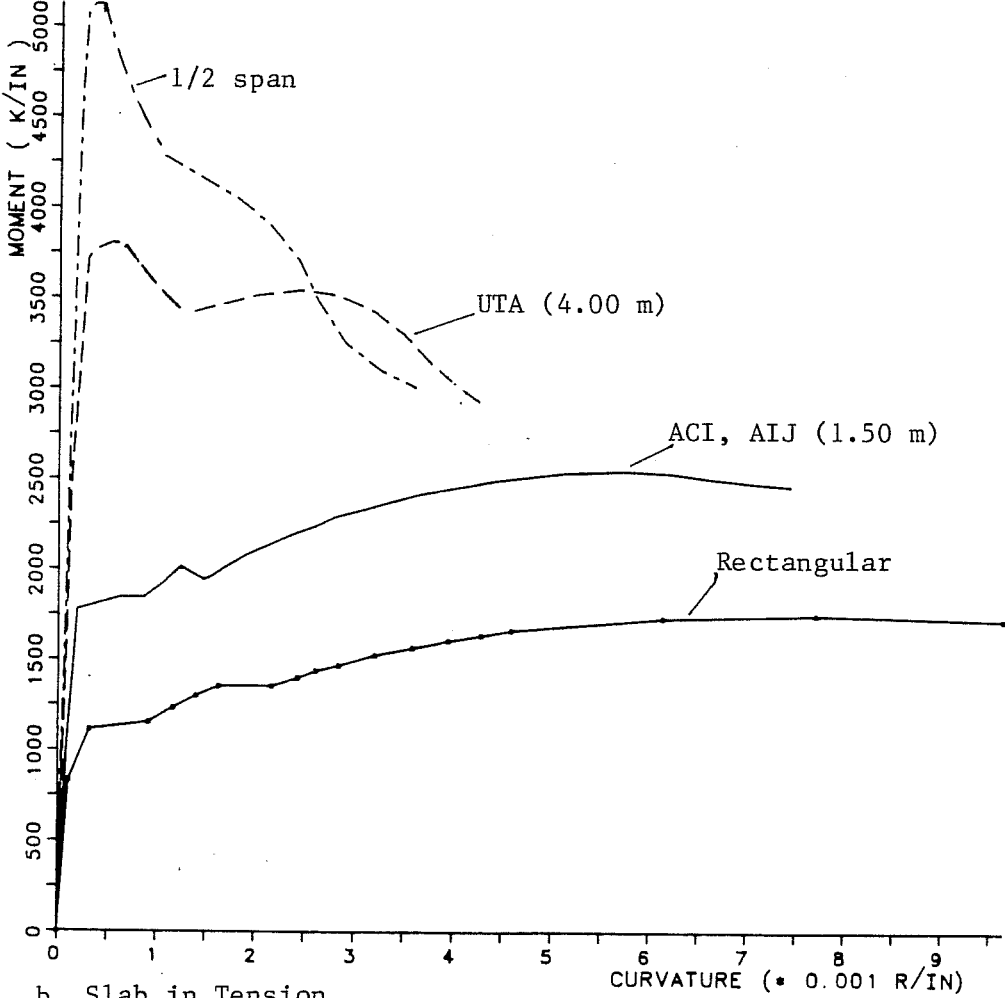


Fig. 8.20 - Column Moment Curvature.

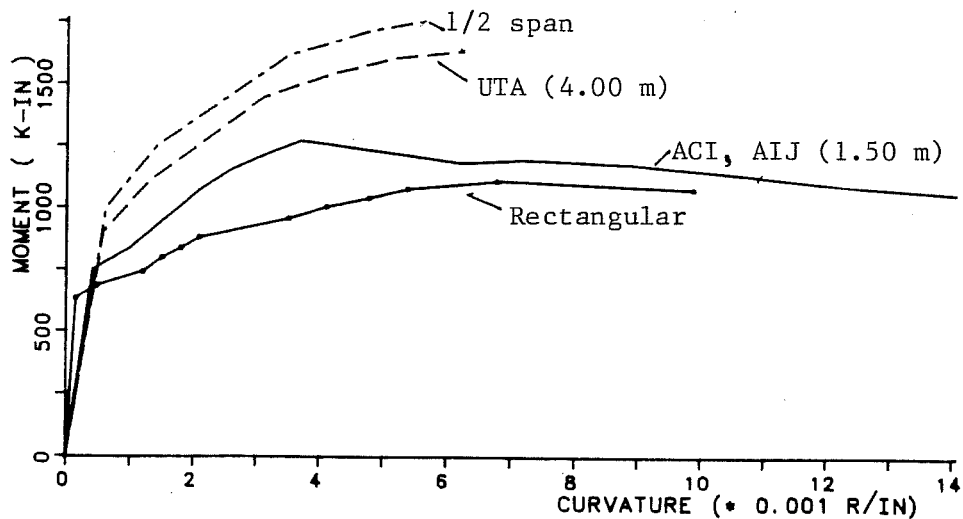


a. Slab in Compression.

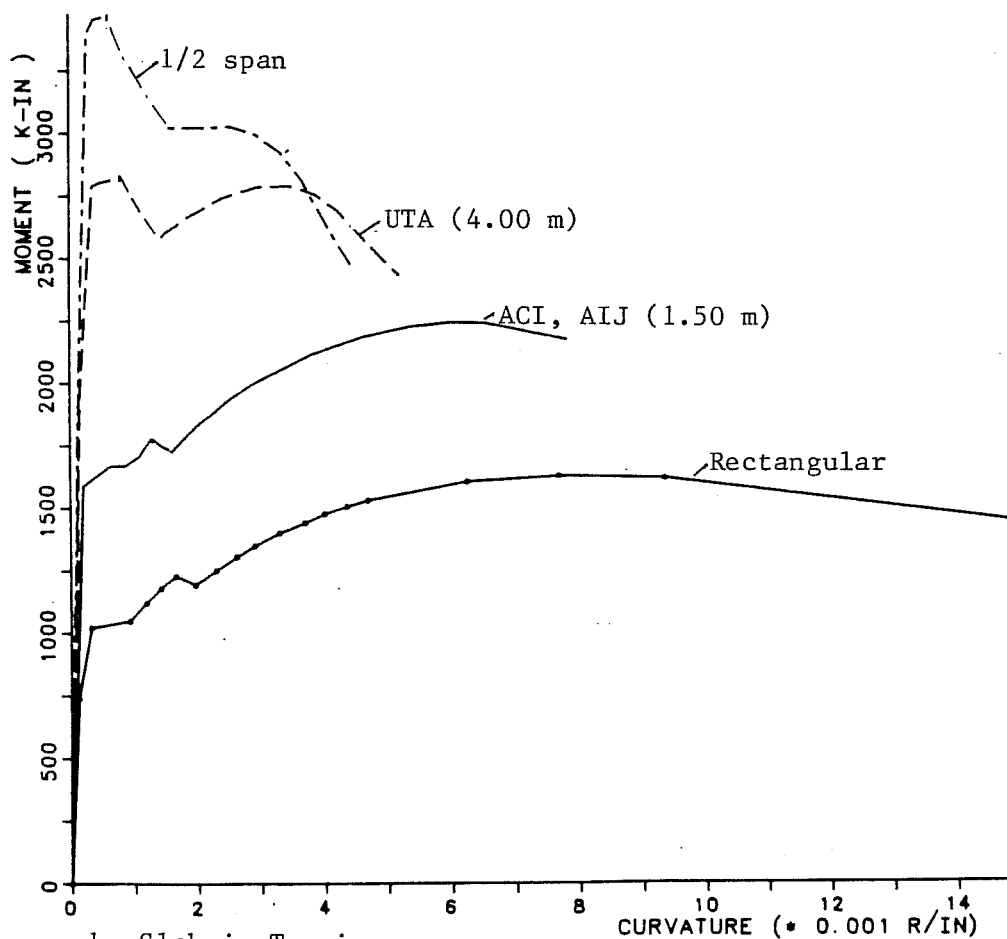


b. Slab in Tension.

Fig. 8.21 - Longitudinal Beam Moment Curvature.



a. Slab in Compression.



b. Slab in Tension.

Fig. 8.22 - Transverse Beam Moment Curvature.

columns) may show increased flexural capacity. The axial load effects result from the gravity load and, in the case of the shear wall, from the "prestressing effect" developed by the transverse beams over the tensioned boundary column. The increase in axial load leads to an increase in the moment capacity (if it is below the balance point) as shown by the interaction P-M diagram, Fig. 8.23. The amount of axial force due to gravity loads has been estimated by Kabeysawa et al. (10) for the different vertical members, Fig. 8.24-a. However, actual measurements in a 1:5-scale model tested at the University of California - Berkeley indicate that some variation between the estimated and actual values may exist, Fig. 8.24-b [Bertero et al. (6)].

With the moment-curvature, it is necessary to evaluate the length of plastic hinge assigned to each member. The average member rotation, θ_{av} , is generally obtained by:

$$\theta_{av} = \phi_{av} \cdot L_p \quad (8.4)$$

where: ϕ_{av} = average curvature over a length L_p ; and L_p = plastic hinge length. The choice of a plastic hinge length is not well defined and different values can be obtained depending on the reference. The shearwall plastic length is indirectly defined in the NZS 3101 (17) by the larger of d or $H/6$, 5.50 m or 3.625 m, in the case of cantilever walls, Fig. 8.25. Based on

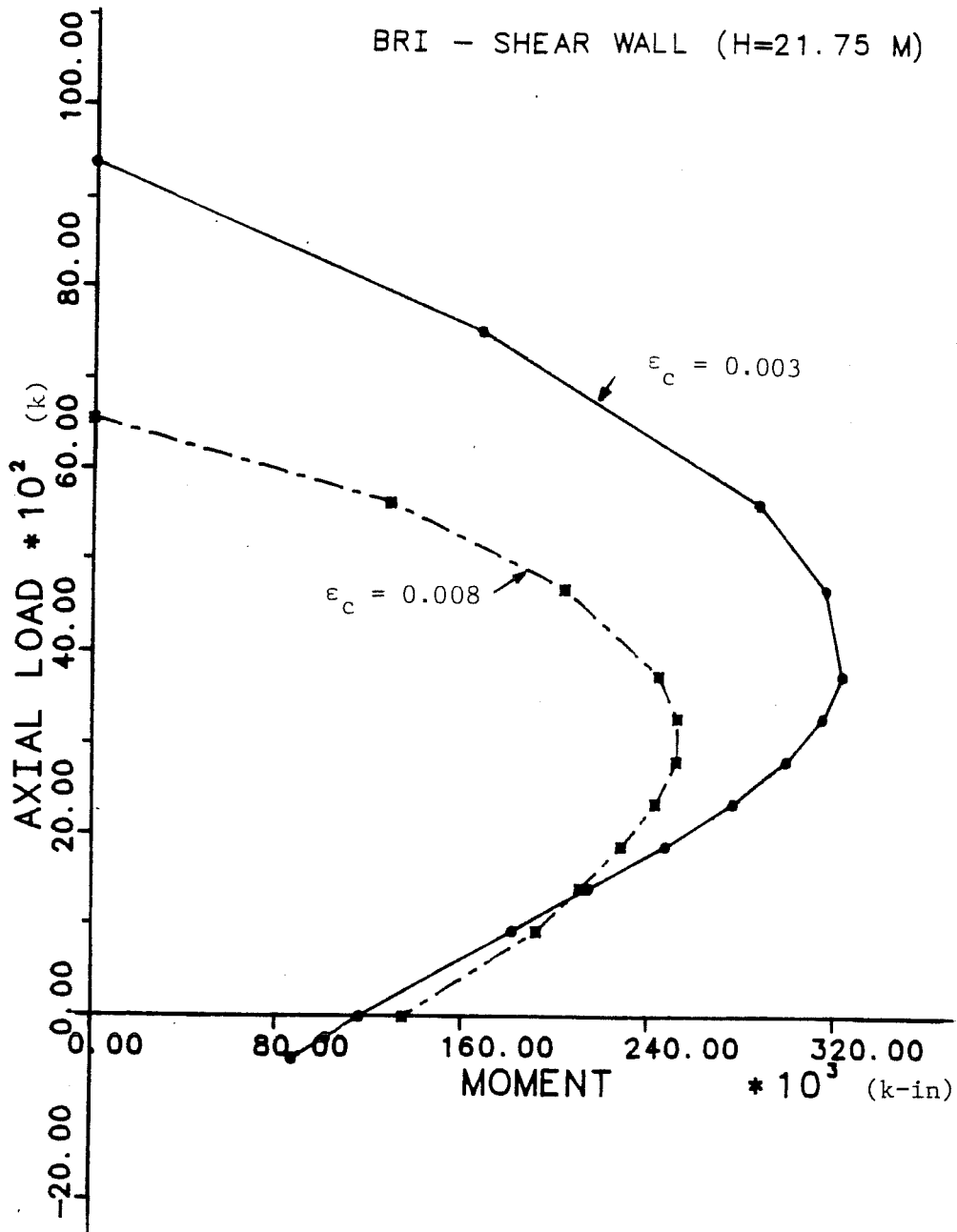
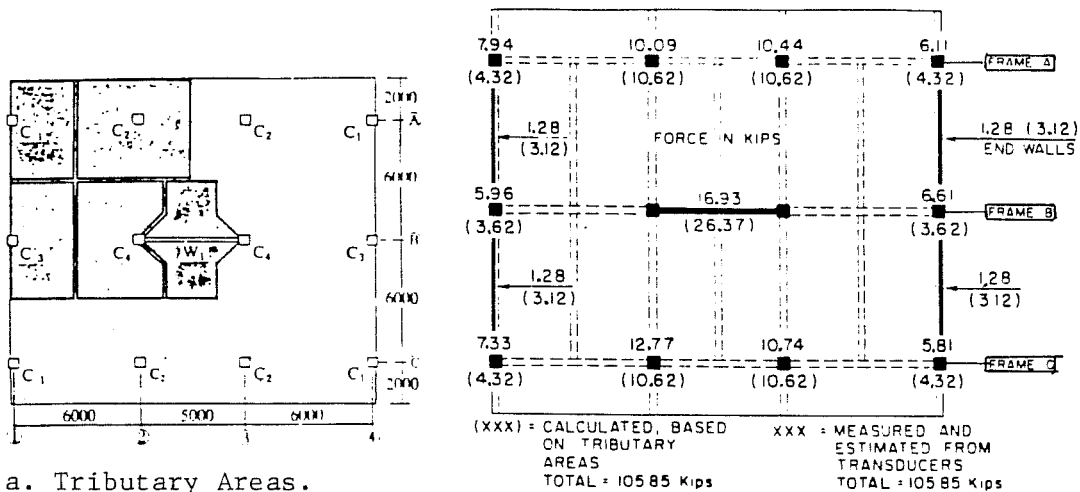


Fig. 8.23 - Shear Wall Interaction Diagram.



VERTICAL MEMBER	TOP FLOOR		BOTTOM FLOOR	
	Load (k)	P / P _C	Load (k)	P / P _C
Column C ₁	18.5	0.01	174.3	0.09
	31.1	0.02	213.5	0.12
	23.9	0.01	242.9	0.14
Shearwall (2C ₄)	-	-	622.6	0.07

b. UCB (1:5) Model.

c. Japanese Column Load Values.

Fig. 8.24 - Gravity Loads in Vertical Members.

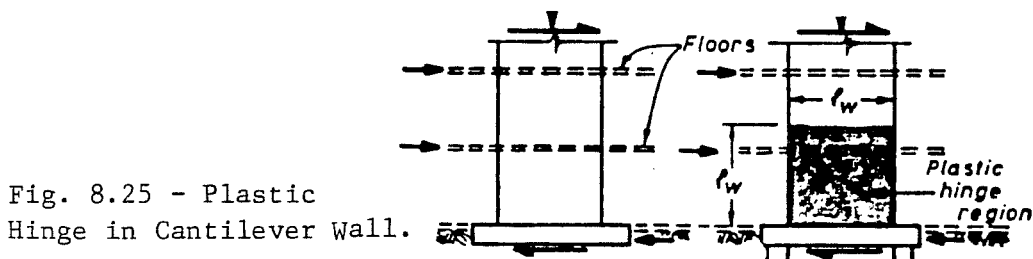


Fig. 8.25 - Plastic Hinge in Cantilever Wall.

TABLE 8.7 - PLASTIC HINGE LENGTH AND CURVATURES.

Member	h (in.)	Corley	Mattock	NZS 3101	Value Used	e* _{avg.}	φ ⁻⁴ _{r/in}
Shearwall	216.5	.53 h	.68 h	h	.68 h	e	1.1
Column	19.7	.62 h	.63 h	-	.62 h	e	12.8
Long. Beam	6.m	.73 h	.75 h	-	.74 h	e	10.7
	5.m	.73 h	.75 h	-	.74 h	1.25 e	13.4
Trv. Beam	17.7	.78 h	.77 h	-	.77 h	e	11.5

* R = 1 / 64 = e_{avg.}

the work of Corley (7) and Mattock (14, 15), a summary of the results, L_p used and average curvature at a drift $R(\theta) = +1/64$ is shown in Table 8.7.

The computation of the internal work, W_i , with beam rotation at $h/2$ (h = member depth) is given by:

$$\begin{aligned} \sum W_i = & 14 [M_t(+)+M_t(-)] \theta + \{M_s\theta + 21[M_i + M_i(-)] \theta\} \\ & + \{26[M_e(+)+M_e(-)]\theta + 12[M_e(+)+M_e(-)]1.25\theta\} \\ & + [10 \cdot M_c(b) + 4 \cdot M_c(t)] \theta \end{aligned} \quad (8.5)$$

where the plastic moments are: M_t = transverse beam, M_s = shear wall; M_i = interior longitudinal beam; M_e = exterior longitudinal beam; M_c = column. The indices between brackets correspond to: (+) = positive moment; (-) = negative moment; (t), (b) = top, bottom of column. In the shearwall moment evaluation, the additional axial load, ΔN , due to uplift is given by:

$$\Delta N = 14[M_t(+)+M_t(-)] / \ln \quad (8.6)$$

The calculated $V_B(\text{cal})$ value is then compared with the experimental value $V_B(\text{exp}) = 954$ kips. The influence of different effective slab widths is clearly shown in Table 8.8. It can be seen that low estimates of the ultimate building lateral strength are obtained if the effective slab width is improperly considered and the assumed location of beam plastic.

TABLE 8.8 - VIRTUAL WORK COMPUTATION.

CASE	Transverse Frame		N (kips)	N (kips)	Frame B		Frames A & C	Columns	W _i	V cal. (kips)	V cal. / V exp.
	W _i	M (k-i)			Shearwall	Beams					
1. Bare Frame	26,600	26,600	122.8	745.	155,000	43,767	84,050	45,440	354,857	579.	0.61
2. ACI,AIJ (1.5m)	36,820	36,820	170.	793.	160,000	64,050	123,000	45,440	429,310	700.	0.73
3. UTA (4.0m)	53,900	53,900	249.	872.	167,000	102,480	196,800	45,440	565,620	923.	0.97
4. Half-Span	63,000	63,000	291.	914.	171,000	123,830	217,300	45,440	620,570	1012.	1.06

TABLE 8.9 - EFFECT OF CONSIDERING DIFFERENT BEAM HINGE LOCATIONS.

Location of Beam Pl. Hinge	Bare Frame	ACI,AIJ (1.5m)	UTA (4.0m)	Half-span
@ Column centerline	0.56	0.67	0.86	0.94
@ Column face	0.58	0.70	0.91	1.00
@ h/2 from col. face	0.61	0.73	0.97	1.06

TABLE 8.10 - MEMBER PARTICIPATION IN ULTIMATE STRENGTH.

Participation (%)	Transv. Frame (uplift)	Frame B		Frames A & C	Columns
		Shearwall	Beams		
1. Bare Frame	7.7	42.3	12.6	24.3	13.1
2. ACI, AIJ	8.6	37.3	14.9	28.7	10.6
3. UTA	9.5	29.5	18.1	34.8	8.0
4. Half-Span	10.2	27.6	20.0	35.0	7.3
Univ. Calif. @ Berkeley	-	66.0	-	-	-

The difference in considering beam hinging at the column axis, column face and at a distance $h/2$ from column face is shown in Table 8.9.

The 1:5 UC-Berkeley model showed higher base shear at an equivalent drift $R = 1/68$, $V_B = 1346$ kips (+40%) that eventually dropped at $R = 1/55$ to $V_B = 1267$ kips. The shearwall participation was estimated to be $0.66V_B$ (at $R = 1/68$) and $0.60V_B$ (at $R = 1/55$) [Bertero et al. (6)]. The contribution of each element/system to the total internal work is shown in Table 8.10 and compared with the 1:5 UC-Berkeley model.

Based on Table 8.10, it can be seen that at a peak equivalent drift $R = +1/64$ the column and transverse beam plastic hinges were responsible for nearly 20% of the total base shear. The shearwall participation decreased from 42% to 28% if increasingly larger amounts of effective slab width are assigned to the beams (from bare frame to half-span widths). If the total slab is considered, Frame B takes nearly 50% of the ultimate base shear, Frame A and C, 20% each, and the transverse frame, 10%.

8.5.4 Comments on the Assumed Failure Mechanism

In the collapse mechanism utilized for the BRI building ultimate strength evaluation, no column plastic hinge formation other than at the foundation and top floor levels was assumed. This choice was based on strain gauge readings made on the actual structure (Fig. 8.14-a). However, it can be seen that a few

Frame A columns showed yielding at the intermediate floors (interior columns). It is felt that this may have resulted from uplift rather than overturning effects. On the other hand overturning moments are more important on the exterior columns. However, in this particular building the stiffening of the spandrel beams by the lightly reinforced eccentrically placed end walls (Fig. 8.26) prevented hinges from forming anywhere but the main beam, even under large negative moments. It is assumed that a more correct failure mechanism could be used where column plastic hinges would have been created once the sum of beam moment capacity would exceed the column capacities, Fig. 8.27. However, this would only apply to interior columns of Frames A and C, from the building midheight up to the top floors, when effective slab widths larger than 4.00m would be considered. As these conditions would only apply to a limited number of hinges it is assumed that the influence on the total internal work would be small.

8.6 Final Observations

The ultimate BRI building strength evaluation was performed on an "ansatz" (educated guess) assumed failure mechanism. The failure mechanism was maintained as the effective slab widths increased, although beam hinges may have been shifted into the columns. Member capacities were estimated by using

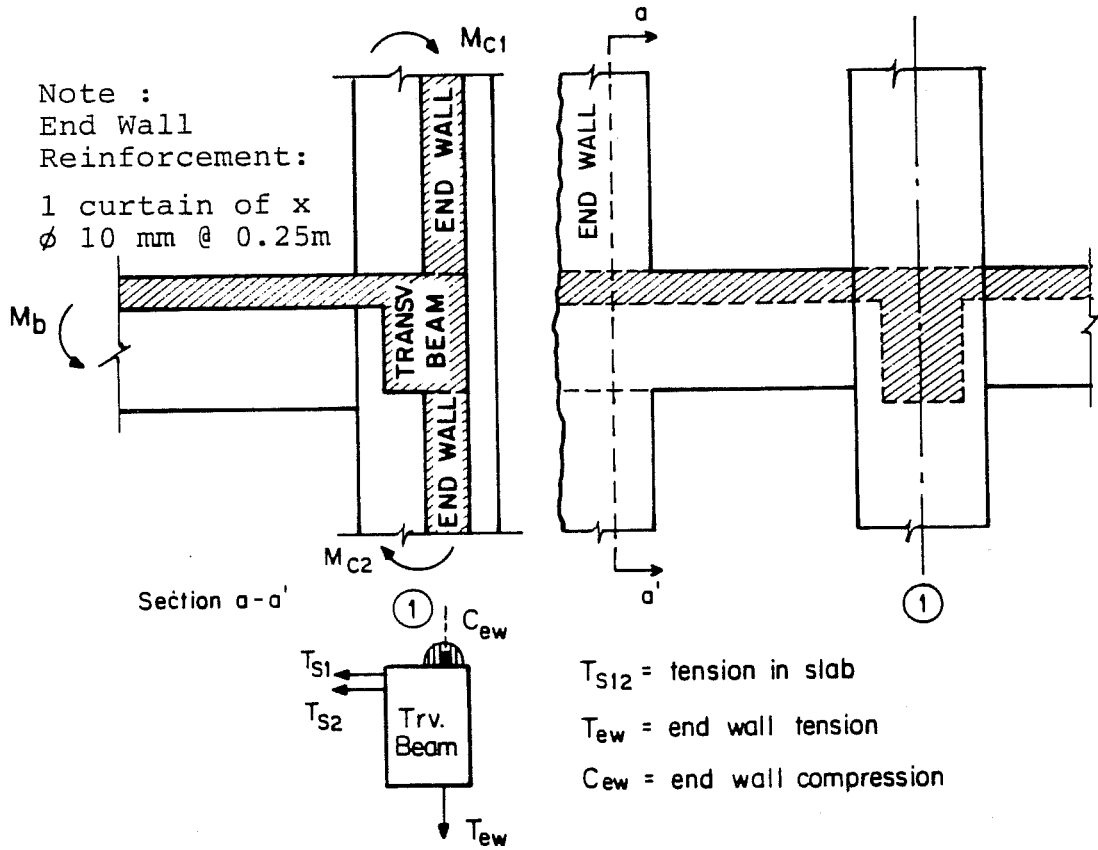


Fig. 8.26 - End Wall Restraint.

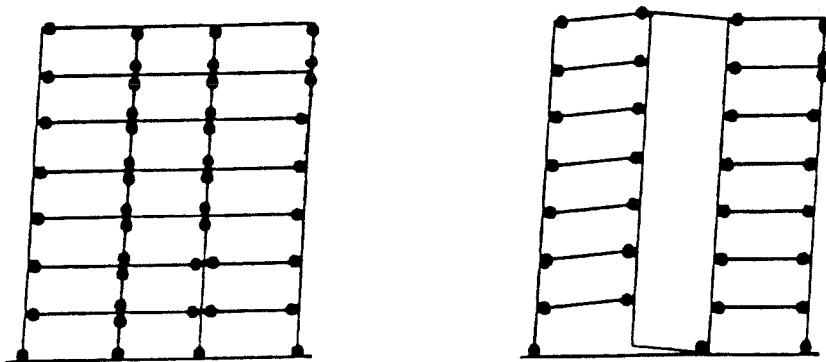


Fig. 8.27 - Failure Mechanism Considering the Whole Slab Width as Effective, [Yoshimura and Kurose (24)].

actual concrete and steel properties, including strain hardening and confinement effects. The plastic hinge lengths were assumed based on current references and member rotations were considered as follows: (a) columns, shearwall - similar to the equivalent lateral drift; and, (b) beams - at a distance $h/2$ from the column face. The uplift effect and the transverse frame restraint was only considered on the shearwall. Overturning effects with axial load variation in the columns were not considered.

At a peak drift $R = +1/64$, the BRI building ultimate moment capacity evaluated with a large effective slab width and with an admissible failure mechanism yielded results that were compared with the measured base shear. A variation in the order of -9 to +6% was observed in the calculated/experimental horizontal base shear value, which is considered satisfactory. By considering the entire slab as effective, the interior dual-system (Frame B) was responsible for 50% of the base shear, the exterior Frames A and C for 20% each, and the transverse frame uplift for 10%.

The component tests were also used in evaluating joint shear capacity and development length requirements based on current Code provisions for seismic design.

The UTA tests with two different beam reinforcement ratios were used in the joint stress evaluation. Although no clear

joint shear failure was obtained in the modified tests, test shear strength greater than the US and Japanese Code values was obtained: (a) exterior joint - -28% (ACI-ASCE 352) to +12% (ACI 318); and, (b) interior joint - -55% (ACI-ASCE 352) to -30% (Kamimura Eq.). The NZS 3101 Code underestimated the actual capacity by -55% (exterior joint) and -75% (interior joint).

An important parameter in joint design is the γ multiplier for $\sqrt{f'_c}$ because of its practicality in estimating joint shear strength. In this study the tests with a slab developed very large shear stresses as opposed to tests without a slab. However, the maximum observed γ -factor (modified UTA tests) was above Code values which may indicate a reserve in joint strength.

The exterior joint development length requirements for #6 and #7 bars were considered satisfactory by current Standards. However, the anchorage failure observed in the USJ-2 test (#6 bar) may indicate the existence of detailing problems. In the interior components the available column size for the #6 and #7 bars was considered sufficient by US standards and by NZ and Japanese requirements.

8.7 References.

1. ACI 318-83 - "Building Code Requirements for Reinforced Concrete and Commentary", American Concrete Institute, Detroit, MI, 1983.

2. ACI-ASCE Committee 352 - "Recommendations for Design of Beam-Column Joints in Monolithic Reinforced Concrete Structures", ACI Journal, May-June, 1985.
3. AIJ-Standard for Structural Calculation of Reinforced Concrete Structures (English ed.), The Architectural Institute of Japan (AIJ), Tokyo, Japan 1980.
4. AIJ-SRC - "Standard for Structural Calculation of Steel Reinforced Concrete", (in Japanese), The AIJ, Tokyo, Japan, November, 1975.
5. ATC 11 - "Seismic Resistance of Reinforced Concrete Shear Walls and Frame Joints: Implications of Recent Research for Design Engineers", Applied Technology Council, Palo Alto, California, 1983.
6. V. Bertero, A. Aktan, F. Channey, R. Sause - US - Japan Cooperative Research Program: Earthquake Simulation Tests and Associated Studies of a 1/5th-Scale Model of a 7-Story R/C Test Structure, Report No. UCB/EERC - 84/05, UC - Berkeley, June 1984.
7. W.G. Corley - "Rotational Capacity of Reinforced Concrete Beams", ASCE, Vol. 92, ST5, October 1966.
8. M. Farahany and R. Klingner - "Computer Analysis of Reinforced Concrete Cross-Sections", unpublished M.Sc. Report, Dept. of Civil Engineering, University of Texas at Austin, December 1983.
9. H. Hiraishi - "Evaluation of Shear and Flexural Deformations of flexural Type Shear Walls", The 4th J.T.C.C., BRI, Tsukuba, Japan, June 1983.
10. T. Kabeyasawa, H. Shioara, S. Otani, H. Aoyama - "Analysis of the Full-Scale Seven-Story Reinforced Concrete Test Structure", Journal of the Faculty of Engineering, Univ. of Tokyo, Japan, Vol. 37, No. 2, 1983.
11. T. Kamimura - "Ultimate Shear Strength of Reinforced Concrete Beam-Column Connections", (in Japanese), Proceedings of the AIJ, Kanto Japan, Sept., 1975.
12. K. Kitayama, S. Otani, H. Aoyama - "Behavior of R/C Three-Beam-Column Connections with Slabs", Dept. of Architecture, University of Tokyo, Japan, April 1986.

13. Y. Kurose and M. Yoshimura - "Method of Data Processing and Behavior of Plastic Hinges", The 3rd Joint Technical Cooperative Coordinating Meeting, BRI, Tsukuba, Japan, July 1982.
14. A.H. Mattock - "Rotational Capacity of Hinging Regions in Reinforced Concrete Beams", Proc. of the International Symposium on Flexural Mechanics of Reinforced Concrete, ACI SP-12, Miami, Nov., 1964.
15. A.H. Mattock - Discussion of W.G. Corley paper: "Rotational Capacity of Reinforced Concrete Beams", Jnl. of the Structural Division, ASCE, ST2, April 1967.
16. D.F. Meinheit and J.O. Jirsa - "The Shear Strength of Reinforced Concrete Beam-Column Joints", Report CESRL 77-1, FSEL, The University of Texas at Austin, 1977.
17. NZS 3101:1982 - "Code of Practice for the Design of Concrete Structures", Part 1 & 2, Standards Association of New Zealand (SANZ), Wellington, New Zealand, 1982.
18. S. Okamoto, S. Nakata, Y. Kitagawa, M. Yoshimura, T. Kaminosono - Report on the Full-Scale Seismic Experiment of a Seven-Story RC Building - US-Japan Cooperative Program, BRI, Tsukuba, Japan, 1982.
19. S. Otani, K. Kitayama, H. Aoyama - "Beam Bar Bond Stress and Behavior of R/C Interior Beam-Column Connections", Second US-NZ-Japan Seminar on Design of R/C Beam-Column Joints, Tokyo, Japan, May 1985.
20. T. Tassios - "Properties of Bond Between Concrete and Steel under Load Cycles Idealizing Seismic Actions," CEB, Bulletin d'Information, No. 131, Paris, 1979.
21. M. Tichy and J. Rakosnik - Plastic Analysis of Concrete Frames (with Particular Reference to Limit States Design), Collet's Publishers, London 1977.
22. M. Watabe, S. Nakata, M. Yoshimura, Y. Kurose - "Analysis of RC Full-Scale Building Test", The 15th Joint Meeting, U.S. Japan Panel on Wind and Seismic Effects, U.J.N.R., Tsukuba, Japan, May 1983.

23. M. Yoshimura - "Measurement of Hinge Rotations", The 2nd J.T.C.C., BRI, Tsukuba, Japan, July 1981.
24. M. Yoshimura and Y. Kurose - "Inelastic Behavior of the Building", Earthquake effects on RC Structures, US - Japan Research, ACI SP-84-7, ACI, MI, 1985.
25. M. Yoshimura, H. Hiraishi, Y. Kurose - "Inelastic Behavior of Shear Wall in R/C 7-Story Building, The 4th J.T.C.C., BRI, Tsukuba, Japan, June 1983.
26. L. Zhang and J.O. Jirsa - "A Study of Shear Behavior of Reinforced Concrete Beam - Column Joints", PMFSEL Report No. 82-1, Univ. of Texas at Austin, Feb. 1982.

CHAPTER IX
SUMMARY AND CONCLUSIONS

9.1 Objective

The main objective of this work was to compare the response of critical slab-beam-column joint regions in a full-scale seven-story building tested at the Building Research Institute (BRI), Tsukuba Science City, Japan, and the response of component test specimens representing these regions. The BRI structure was built following current (1980) construction practices in both Japan and the US. The component test specimens were fabricated with and without slabs and had different reinforcement details. The component tests include: (1) eight half-scale specimens [exterior (3), interior (3), top floor (2)] designed according to the Architectural Institute of Japan (AIJ) provisions and tested at the Building Research Institute (BRI), Japan; (2) four full-scale [exterior (2), interior (2)] specimens designed according to ACI 318-77 provisions tested at the University of Texas at Austin (UTA); and, (3) four small-scale (1:12.5) [exterior (2), interior (2)] specimens tested at Stanford University (SU).

This report was organized as follows: (1) comparisons between the complete BRI building and the components were made; and, (2) comparisons among components of different scale and

geometry were studied. Although current DMRF design methodologies focus on the design of individual members (columns, slabs, beams, joints, footings), the engineer must always consider the behavior of the "gestalt" (unified) structure. Consequently, the US-Japan Cooperative Program provided a unique opportunity to establish a bridge between the critical joint regions (weak links) in a complete DMRF under lateral loads and the isolated components modelled after the same regions.

9.2 Scope

The large amount of information gathered during the US-Japan Cooperative Research Program has been reported during the past years in technical presentations and individual project reports and papers. However, valuable information can be obtained through an in-depth correlation study of the data from the BRI building response and from the component tests.

The approach followed in comparing the building and the components was to study strength/stiffness response and energy criteria (energy absorption/dissipation, hysteretic damping). The fundamental assumption in the comparisons was the concept of an equivalent drift ratio which was defined by considering the deflection at inflection points at column mid-height and beam mid-length. Other variables considered in these studies were:

(1) cracking patterns; (2) member rotations and distortions; and, (3) bar strains and slippage.

9.3 Summary of Behavior - Strength and Stiffness

The total specimen response showed that strong similarities existed at identical deformation levels between the cracking patterns observed both in the BRI building joint regions and in the equivalent component tests with a slab. The existence of a slab in a component led to large ductility demands and cracking in the floor system near the column face (localized hinge) when the slab was in tension (negative moment). Components without a slab showed regularly spaced cracks along the loaded beam (diffused plastic hinge).

The component strength was studied using story shear/story deformation characteristics. A basic difference existed between exterior and interior component strength. In exterior tests with a slab, non-symmetric response diagrams were obtained due to the slab participation under positive (slab in tension) or negative loadings (slab in compression) which controlled the component behavior. In the interior components symmetric load-deformation diagrams were obtained due to the alternating contribution of the slab in tension and compression. The influence of a slab in the interior component strength was clearly shown in the UTA tests where values larger than the 1.5 m

(59 in.) AIJ, ACI Code effective slab width were obtained, although inferior to the value obtained by considering the whole slab (4.0 m) as effective. The observed stiffness degradation in the components was very rapid, up to $\pm 1\%$ equivalent drifts and it tended to stabilize thereafter.

The local response of the critical slab-beam-column connection was dominated by the behavior of the longitudinal beams. The BRI building critical regions at level Z2 were compared with the component beam rotations. In the exterior joint it was found that the measured rotations in the components agreed very well with building values in the negative drift range (slab in compression), but the building was stiffer than the component when the slab was in tension. Furthermore, component beam rotations were concentrated at a distance $d/3$ (6.0 in.) from the column face. In the interior tests, the BRI building beam rotations compared well with the component values, although the Stanford University component test was nearly twice as flexible as the equivalent UTA component at an equivalent drift of 1%. As in the exterior tests, most of the beam rotation in the interior tests was concentrated at a distance $d/3$ from the column face. The maximum ultimate strength in the exterior components was reached at a peak drift of 1 to 2% whereas in the interior tests it was at the 2 to 3% peak drift level. The spread of yielding in slab bars at the critical section across the slab-column

lateral beam interface was similar in the BRI building and in the components.

9.4 Summary of Behavior - Energy Considerations

The extensive instrumentation used in the component tests proved to be very useful in carrying out energy studies. The components were designed using the strong column-weak beam concept and some simplifying assumptions could be made in regard to the test response. It was assumed that the columns would remain elastic and the beams and joint core would be responsible for dissipating energy. Verification of this assumption was obtained by equating the total external work input to the component with the internal work developed by the plastified regions (longitudinal beam, joint core). It was found that two different failure modes characterized the test response, depending on the joint type-exterior or interior. The exterior joint response was dominated in energy terms by the longitudinal beam (approximately 90%). The interior joint response was controlled in nearly equal terms by the two beam plastic hinges (approximately 55%) and by the joint core (approximately 45%). These differences in the component response resulted from the intrinsic nature of the transfer of beam forces to the joint core. The anchorage of beam bars into the joint core dominated the exterior component response. In the interior test, the joint

core was subjected to large horizontal forces which dominated response.

The equivalent hysteretic damping ratio was computed for the floor system in the BRI building and in the component tests. It was found that very large damping ratios were obtained for the building in the order of 15 to 20% at $1/64$ peak drift. On the other hand, the component response showed that damping depended on the loading program, the number of cycles, and the specimen geometry. A more stable damping value was obtained using the second peak equivalent drift. The first excursion to a displacement level resulted in large, highly varying damping ratios. The energy studies also showed the inability of the specimen to dissipate energy when anchorage failure (UTA, USJ-2) or bar sliding (SU, IJ) occurred.

9.5 Design Implications and Conclusions

9.5.1 Slab Participation. The available test results showed the importance of slab participation in the ultimate lateral load resistance of a reinforced concrete building with relatively large transverse beams. It was observed that at small deformation levels, the slab width working effectively with the beam was limited. However, at large deformation levels (large column face rotations) the amount of slab plastification showed a much larger slab width working effectively with the beam. This

larger slab width needs to be considered in design calculations in order to achieve more realistic results. Therefore, it is recommended that although the ACI 318-83 (Sec. 8.10.3) effective slab width may be satisfactory for gravity load calculations, at very large deformations (ultimate conditions) the consideration of the half-distance between adjacent frames would be more appropriate for design calculations.

9.5.2 Shear. The BRI building and the component data were used to examine current design recommendations. It was found that the maximum joint shear obtained in the prototype tests was either below or close to the US and Japanese values. However, there was no visible sign of joint shear failure. Specimens with increased beam flexural capacity exhibited ultimate joint strengths larger than predicted by design codes.

9.5.3 Bond. Beam bar bond was considered satisfactory by the design codes used. However, the response of the exterior components showed that although development length requirements can be easily met, careful detailing to provide adequate confinement around the anchored bar plays a critical role in the test response under reversed cyclic loading.

9.5.4 Ultimate Strength. The BRI building ultimate strength was evaluated by using the Upper Bound Theorem on Limit Analysis and by using the actual material properties including steel strain hardening and concrete confinement. The available

data on the building and on the components proved to be invaluable in defining the admissible failure mechanism. The importance of considering 3-D effects (wall uplift), the location of beam plastic hinges and the amount of slab width being effective with the beam was critical in estimating the horizontal base shear. By considering the whole slab width as effective, the interior Frame B (including the shear wall) was responsible for 50% of the total base shear, the exterior Frames A and C for 20% each, the the transverse Frame 3 for 10% (at peak equivalent drift $R = +1/64$).

9.6 An Overview of the Research Program

In regard to the US-Japan Cooperative Research Program some comments are relevant to these studies. It was found that the timing of the projects resulted in a certain lack of coordination between researchers. The US component tests were performed later than the actual BRI building testing. It is assumed that better instrumentation location and test results could have been obtained if the component test data were used in the designing details and in instrumenting the BRI building.

In regard to the available information, some data were incompletely identified and in some cases not readily available. On the other hand, due to differences in the system of units and specimen scale, many tests were reported on a single system of units and in their reduced scale value.

Therefore it is thought that for future joint research programs the following measures would yield better results: (1) increase the communication links among principal investigators in each country, particularly during the specimen design stage; (2) make available the recorded information in a data bank for each country; and, (3) establish a standard format for recording the data (tapes, diskettes), so that it can be easily accessed and exchanged.

Finally, it is important to observe that the most important information for the engineering profession is at the last phase of the project where comparisons among different tests need to be done. Unfortunately funds are generally exhausted prior to reaching this phase. Consequently, provisions need to be taken so that the information can be utilized by establishing realistic budget estimates.

APPENDIX A

THE BRI BUILDING AND THE COMPONENT TEST DATA

The strain gauge and LVDT data for the BRI building (Level Z2) plotted in this section were graciously made available by Dr. Vahid Sattary-Javid and Prof. James K. Wight (The University of Michigan at Ann Arbor).

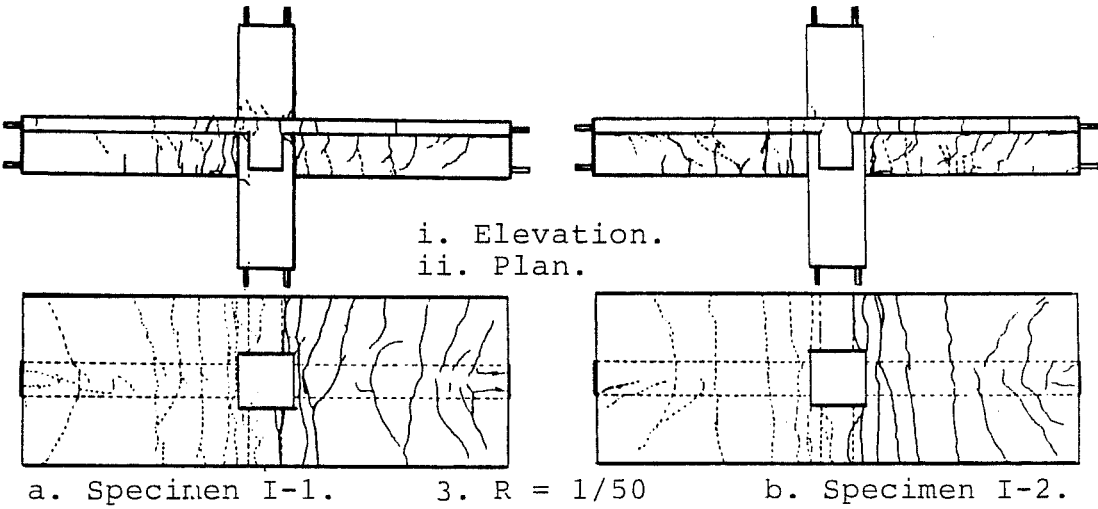
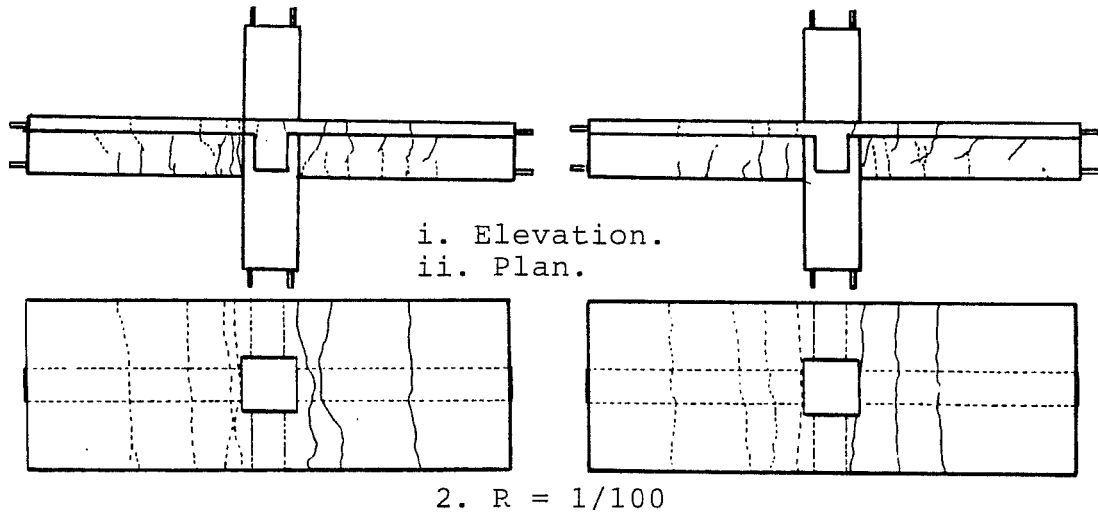
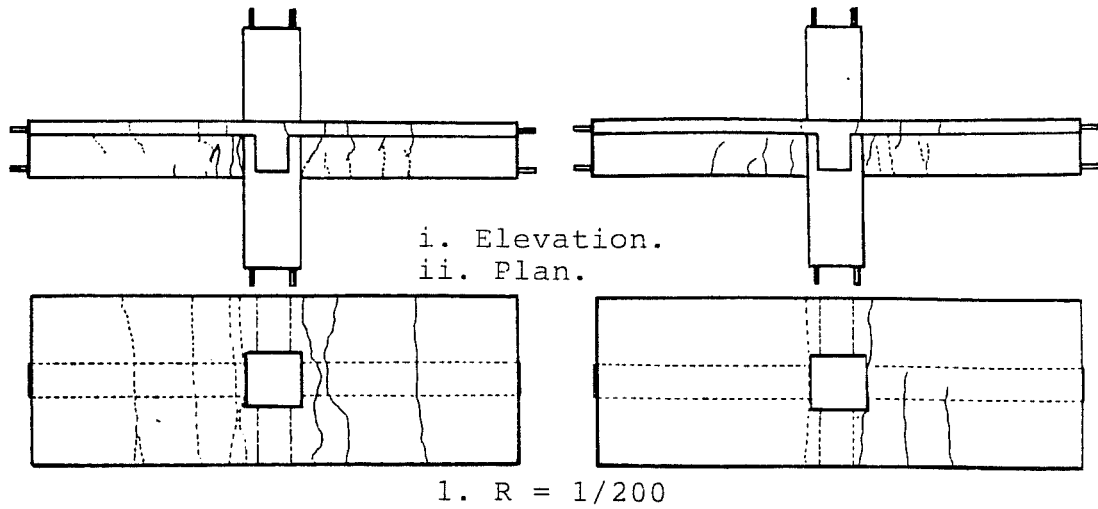
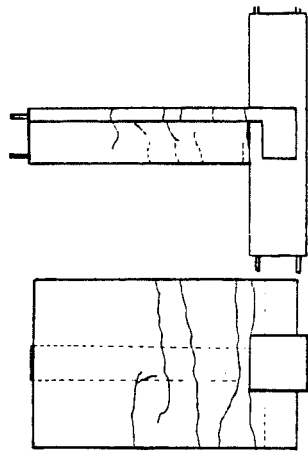


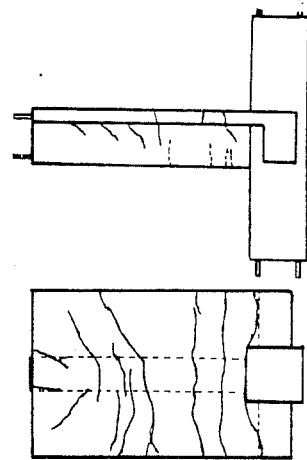
Fig. A.1 - BRI Interior Tests Cracking Patterns.



i. Elevation.

ii. Plan.

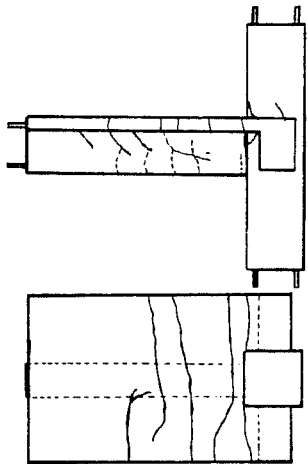
1. R = 1/200



i. Elevation.

ii. Plan.

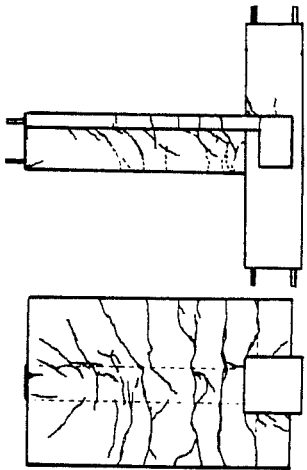
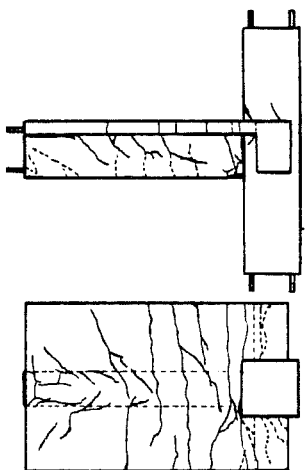
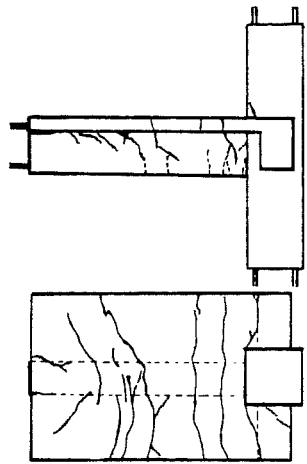
2. R = 1/100



i. Elevation.

ii. Plan.

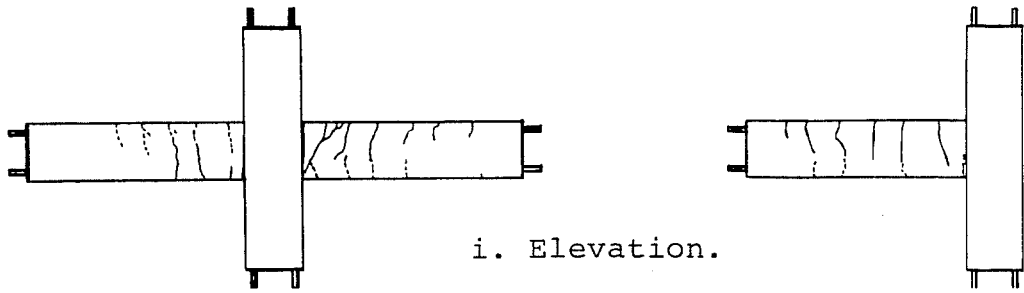
3. R = 1/50



a. Specimen E-1.

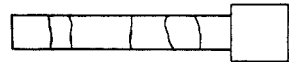
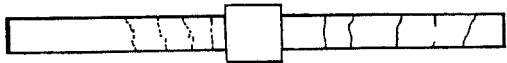
b. Specimen E-2.

Fig. A.2 - BRI Exterior Tests Cracking Patterns.

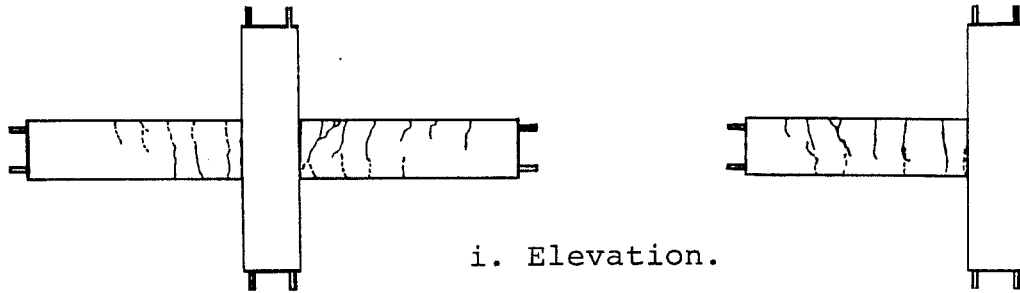


i. Elevation.

ii. Plan.

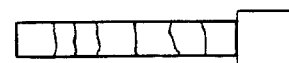
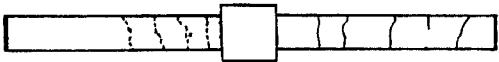


1. $R = 1/200$

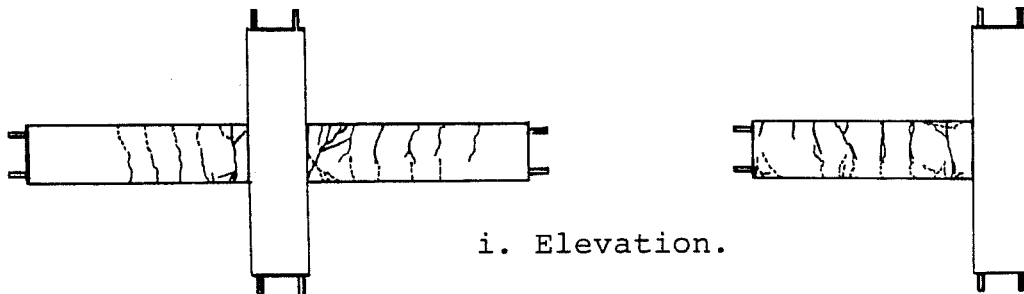


i. Elevation.

ii. Plan.

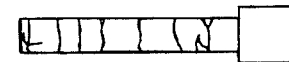


2. $R = 1/100$



i. Elevation.

ii. Plan.

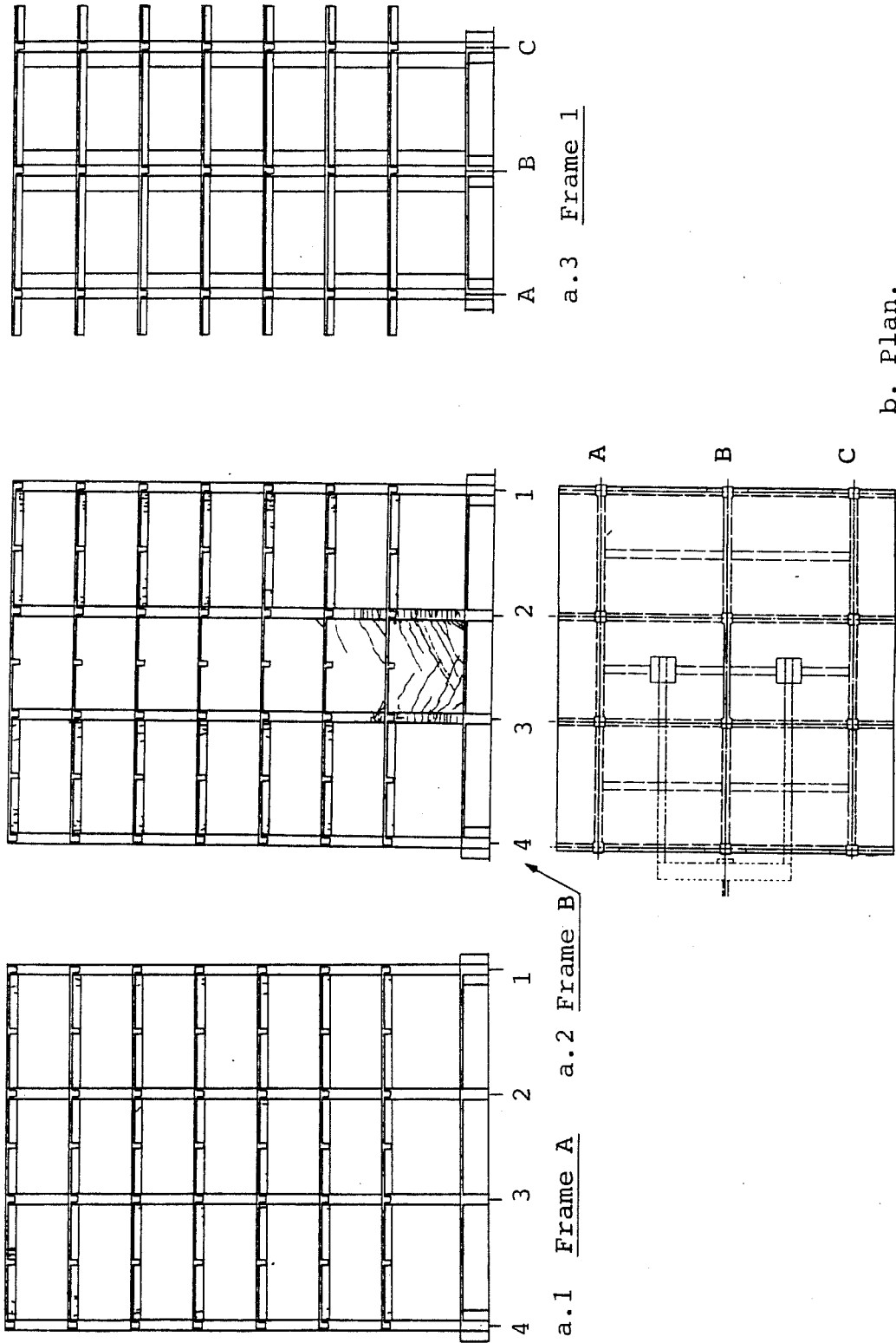


3. $R = 1/50$

a. Specimen I-3.

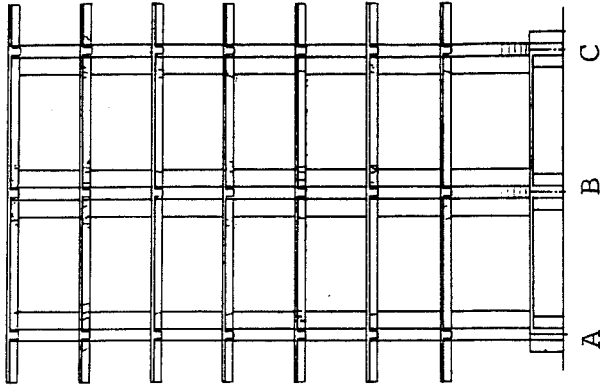
b. Specimen E-3.

Fig. A.3 - BRI Tests without a Slab Cracking Patterns.

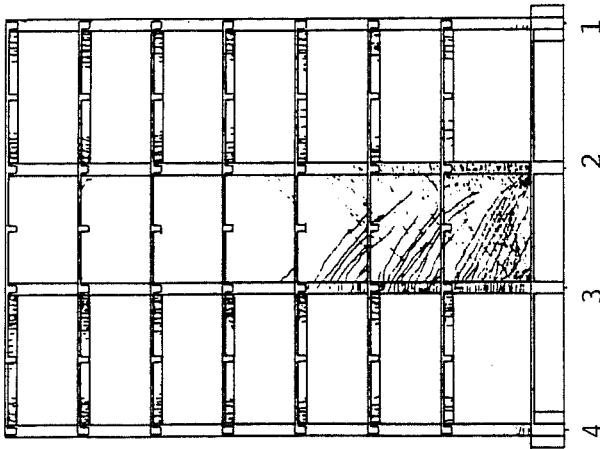


b. Plan.

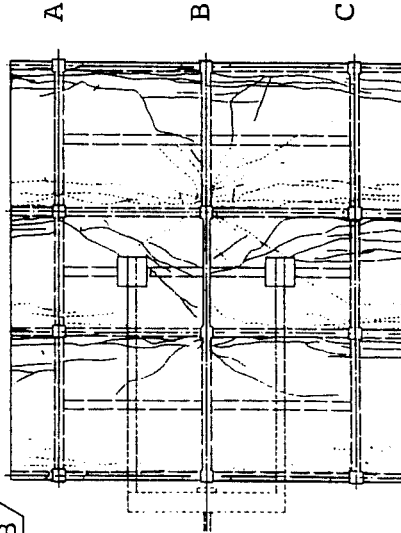
Fig. A.4 - BRI Building Cracking Patterns (PSD 2).



a.3 Frame 1



a.1 Frame A a.2 Frame B



b. Plan.

Fig. A.5 - BRI Building Cracking Patterns (PSD 3).

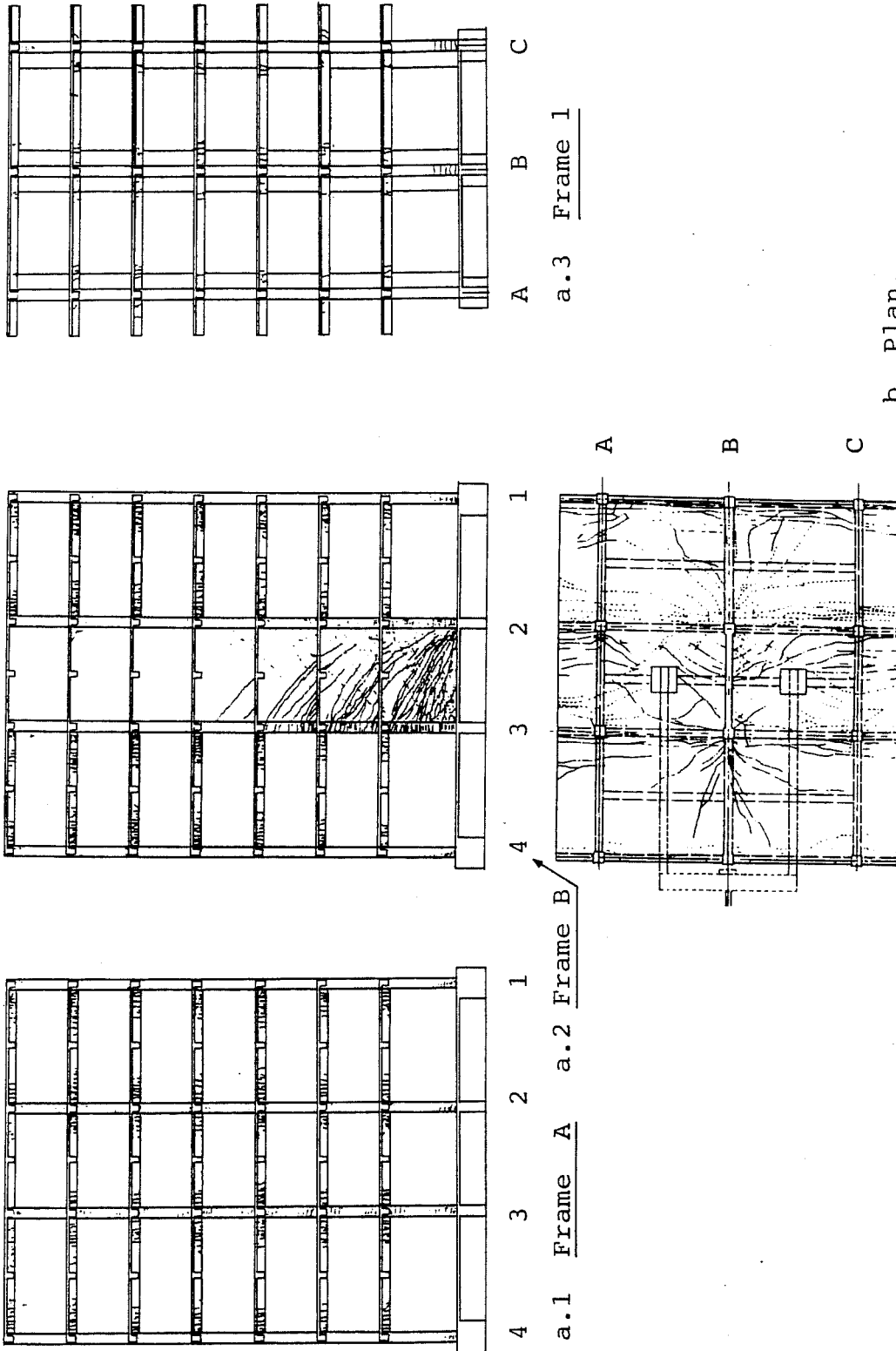


Fig. A.6 - BRI Building Cracking Patterns (PSD 4) .

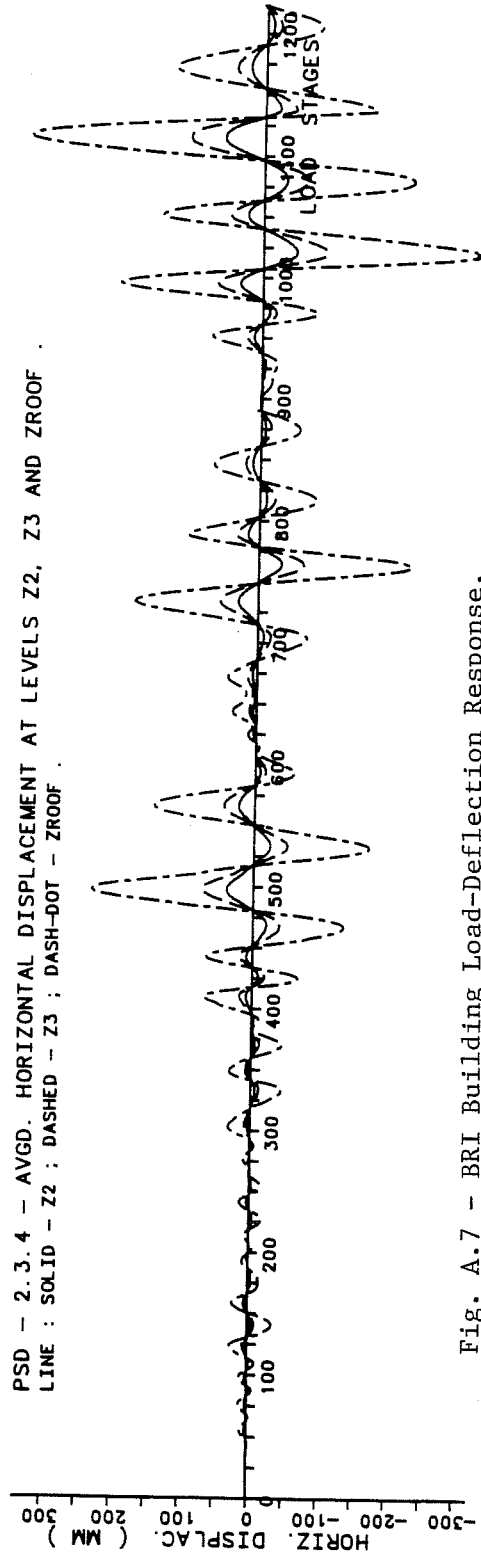
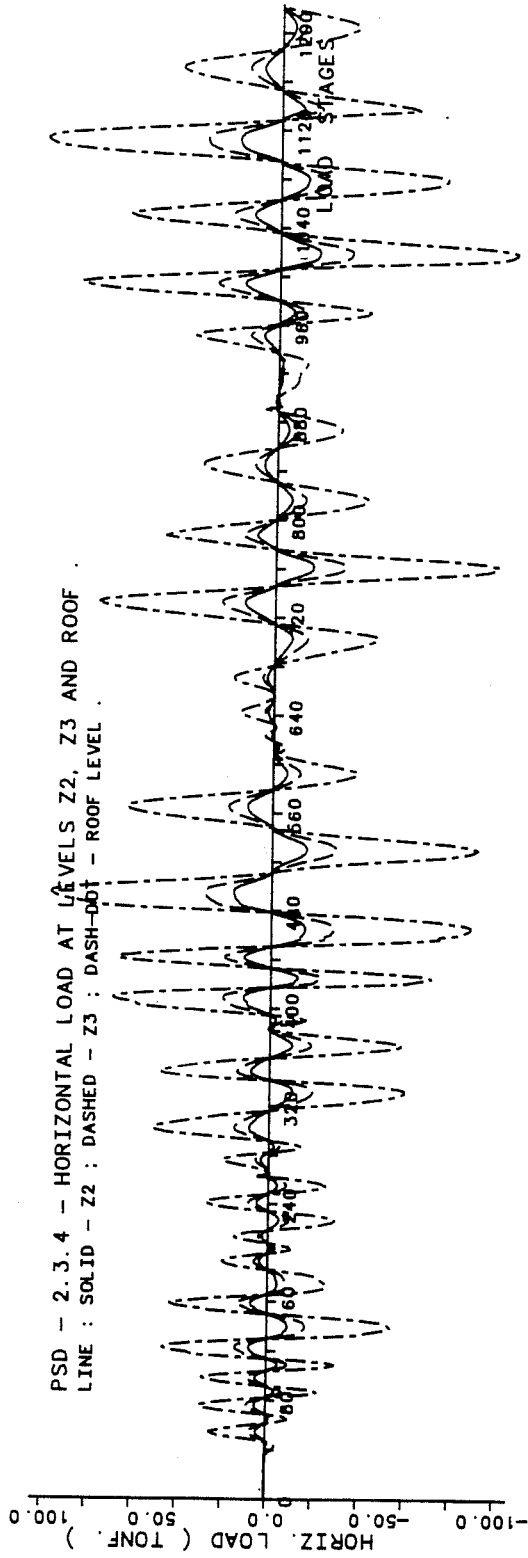


Fig. A.7 - BRI Building Load-Deflection Response.

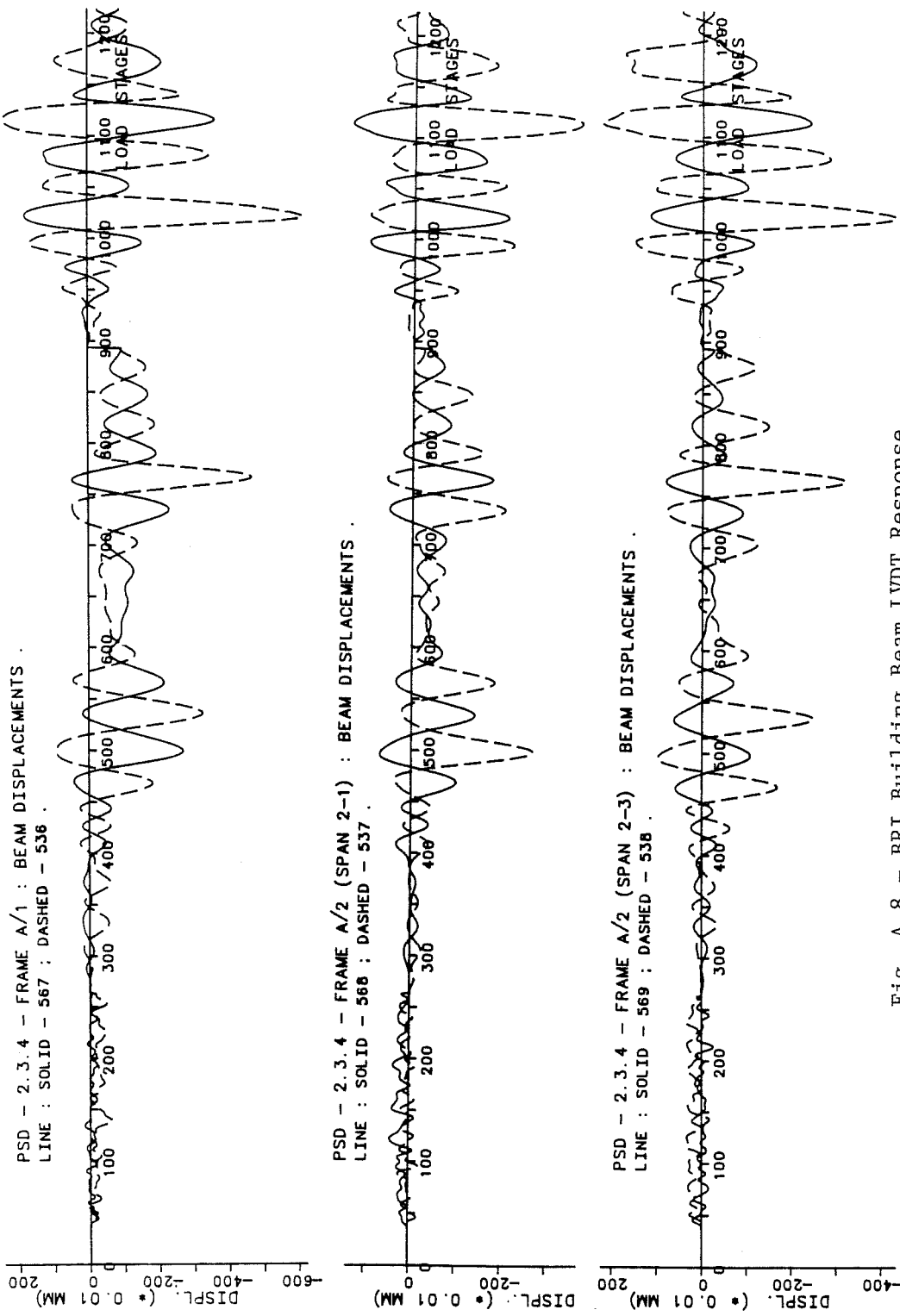


Fig. A.8 - BRI Building Beam LVDT Response.

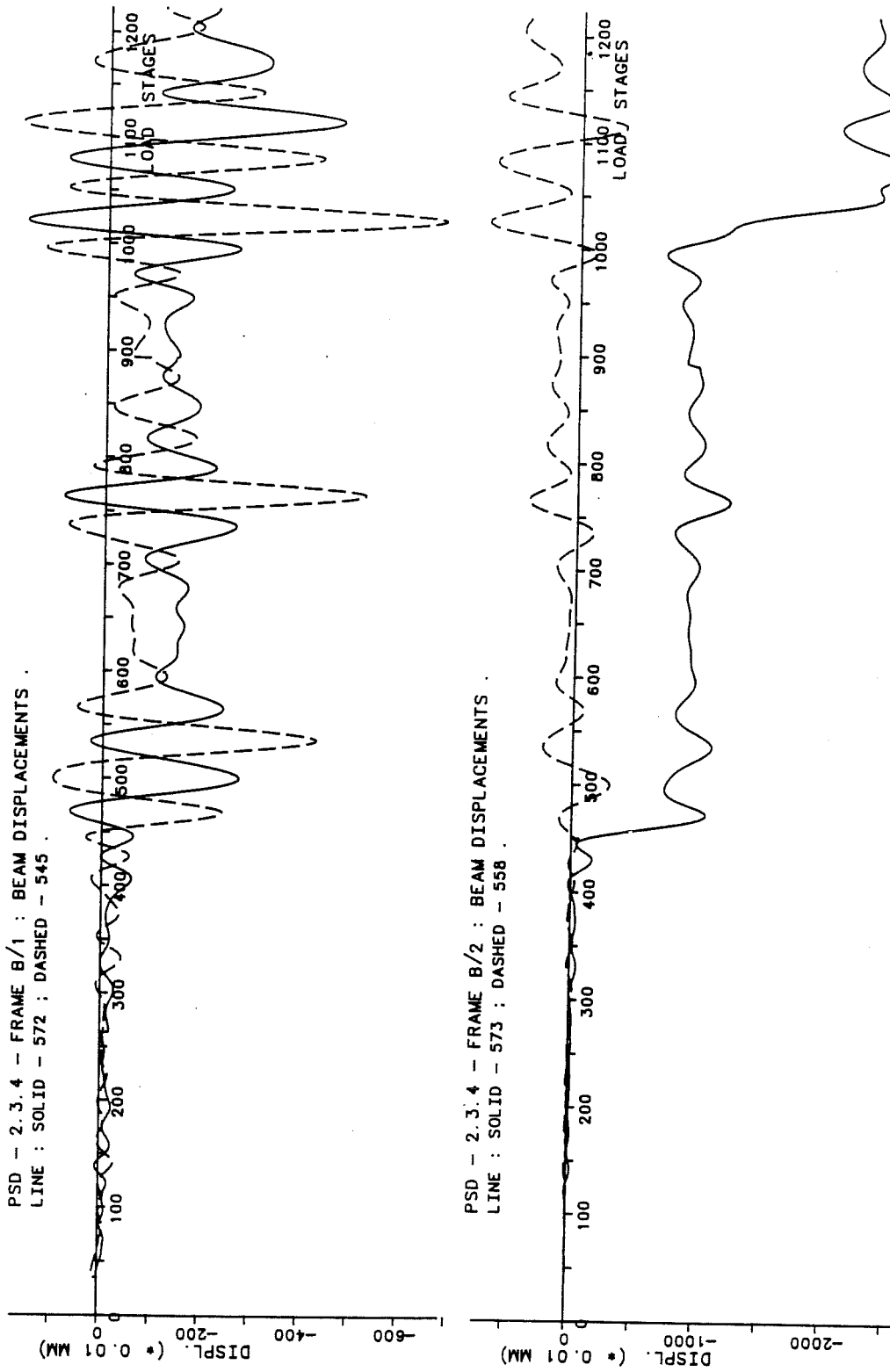


Fig. A.8 (cont.) - BRI Building Beam LVDT Response.

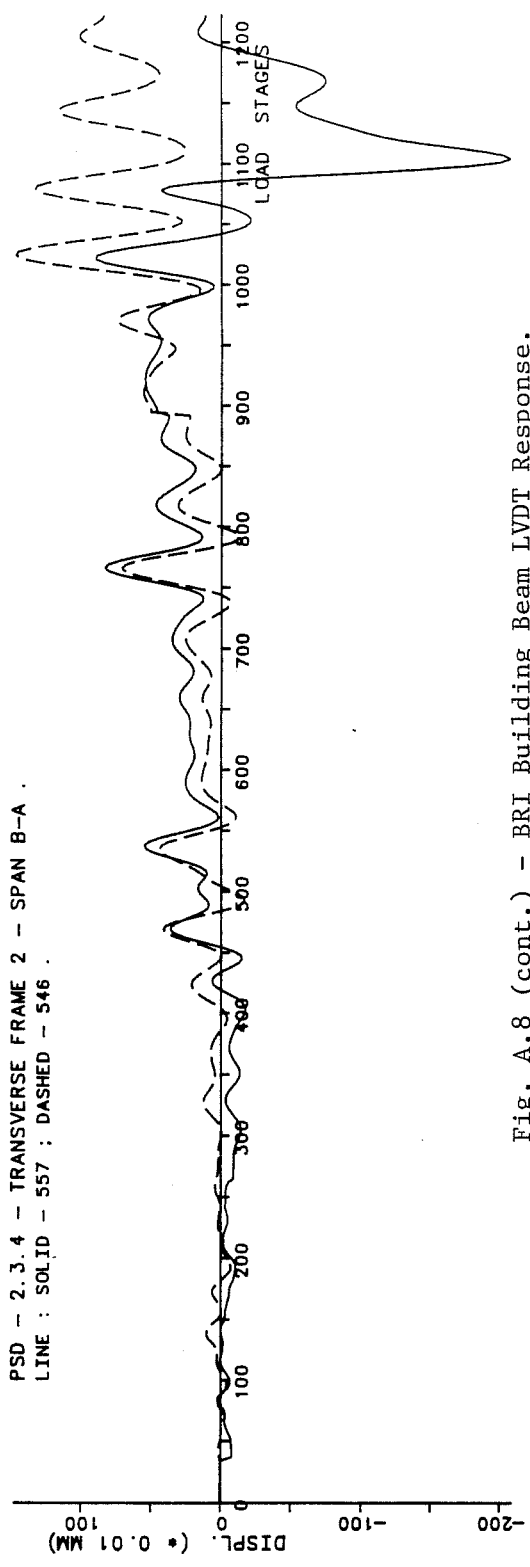
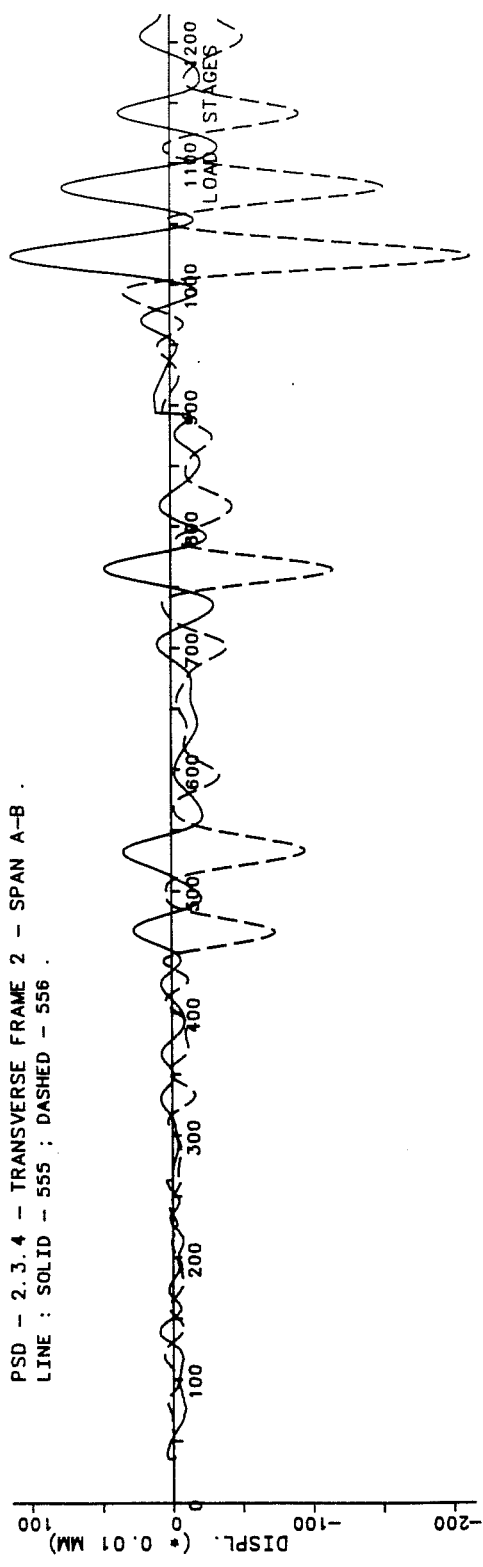


Fig. A.8 (cont.) - BRI Building Beam LVDT Response.

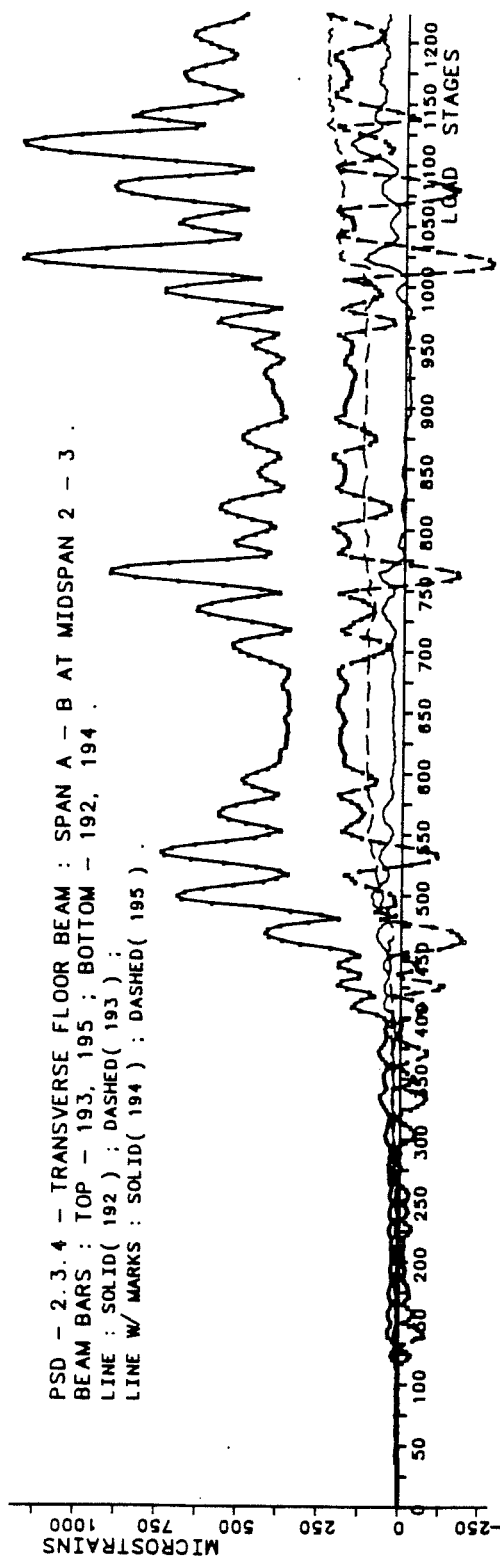
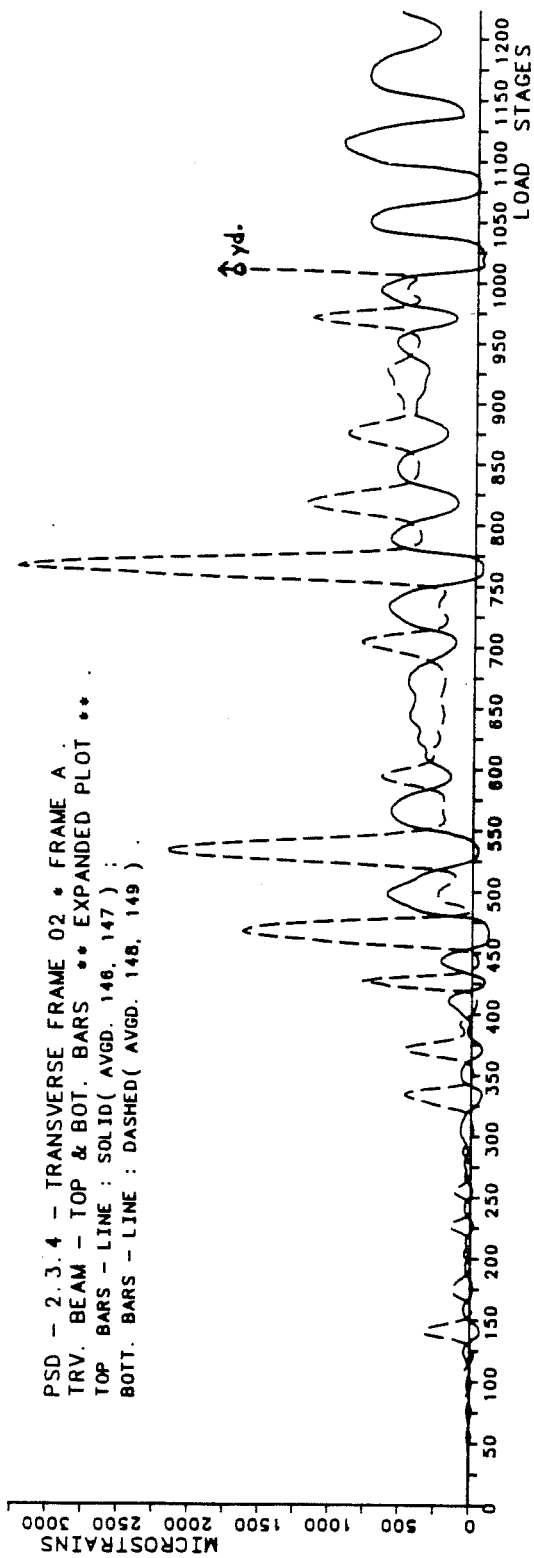


Fig. A.9 - BRI Building Transverse Beam Bar Strains.

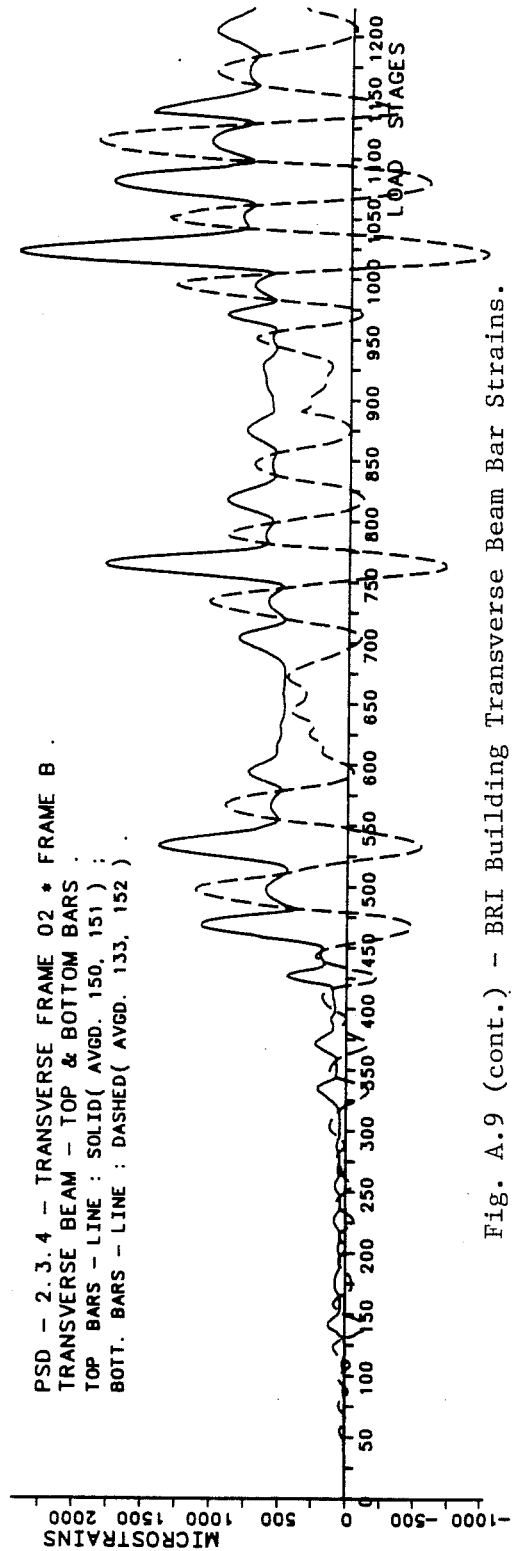
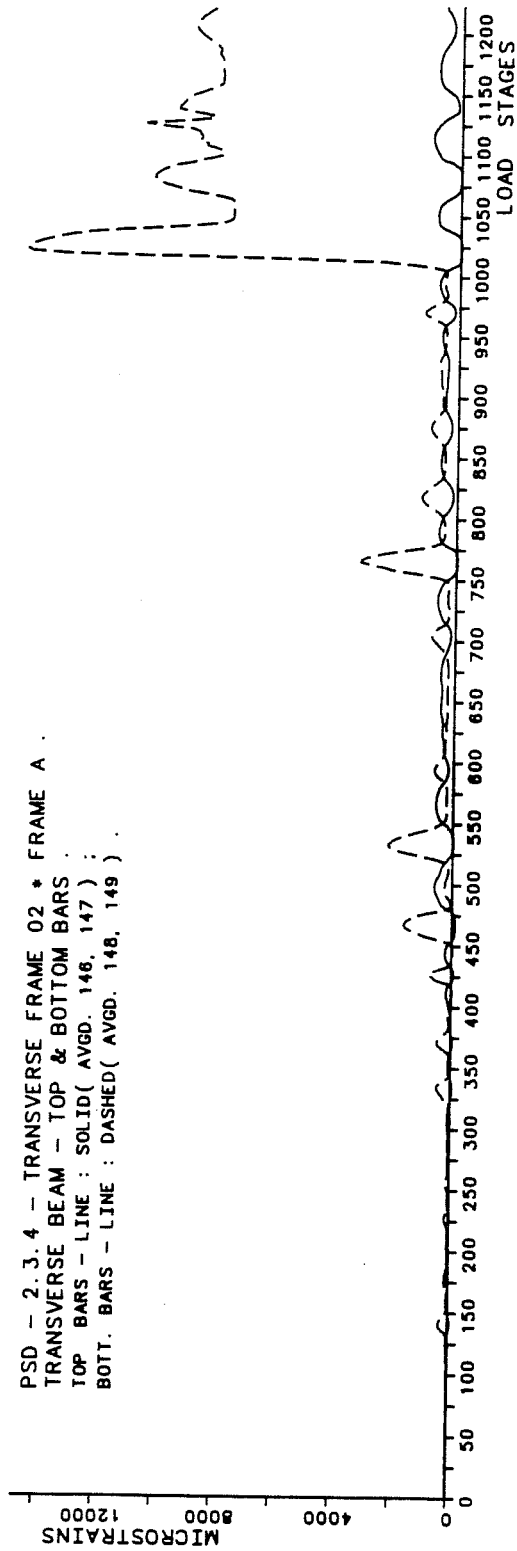


Fig. A.9 (cont.) - BRI Building Transverse Beam Bar Strains.

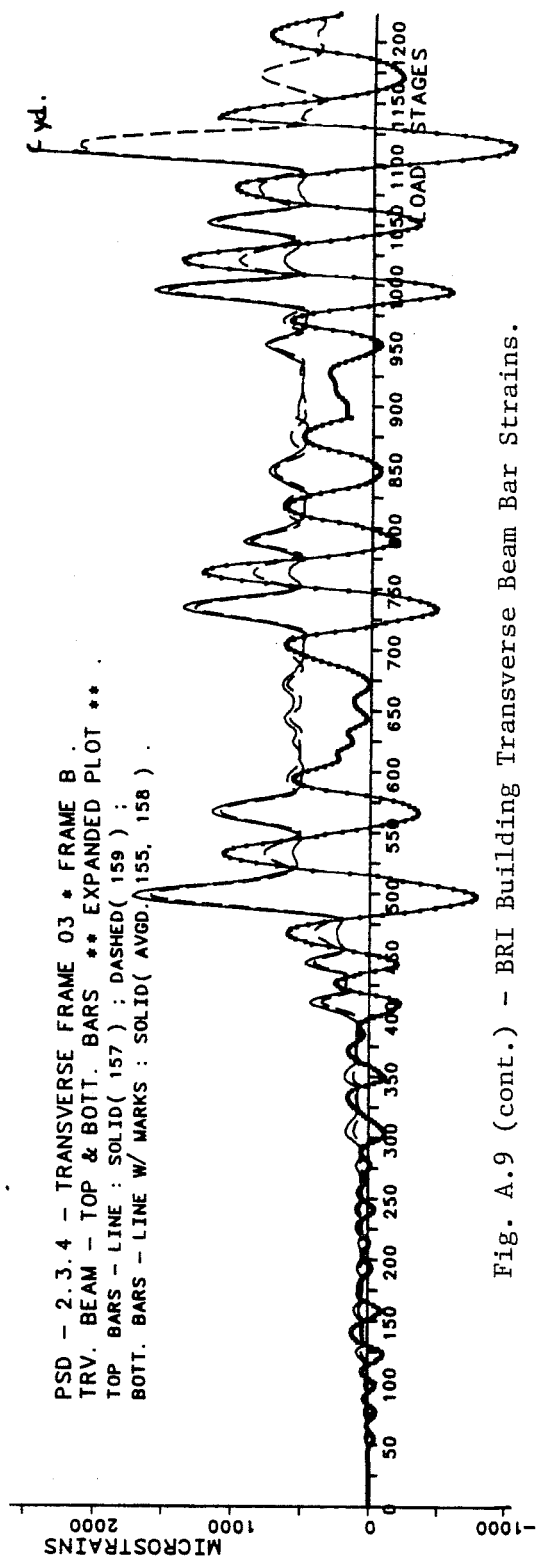
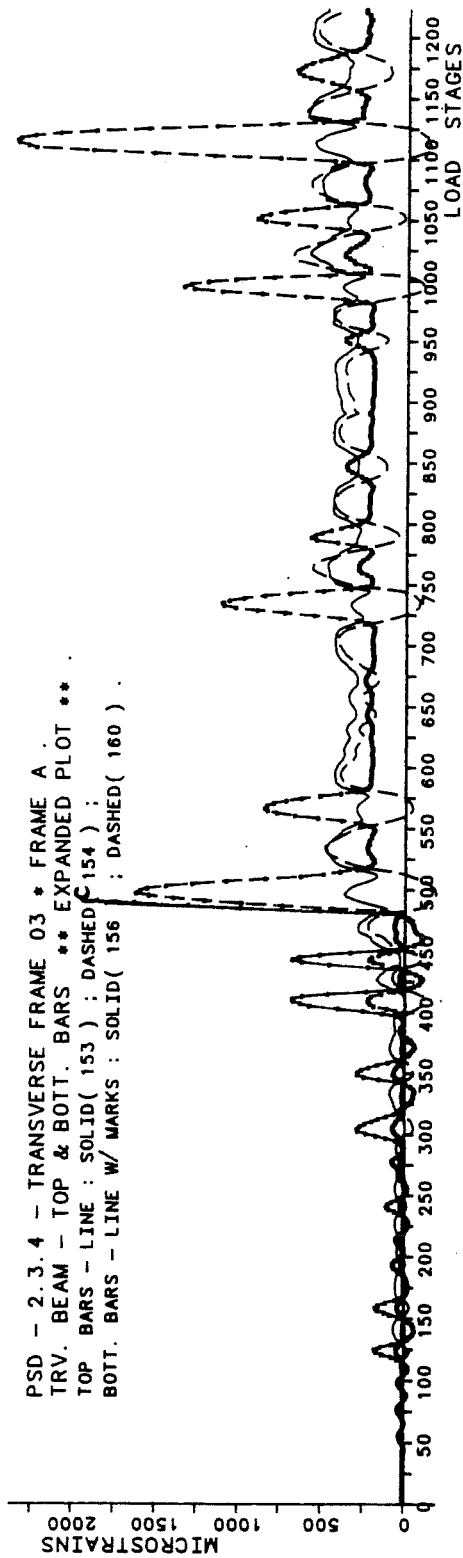


Fig. A.9 (cont.) - BRI Building Transverse Beam Bar Strains.

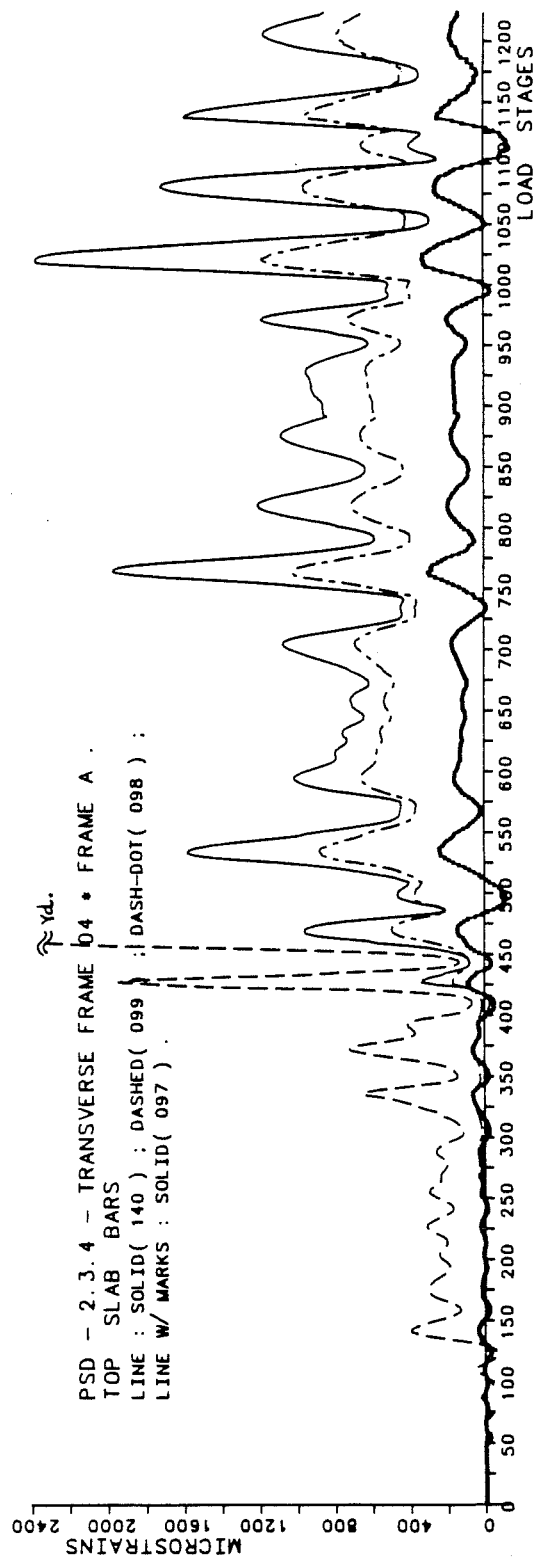
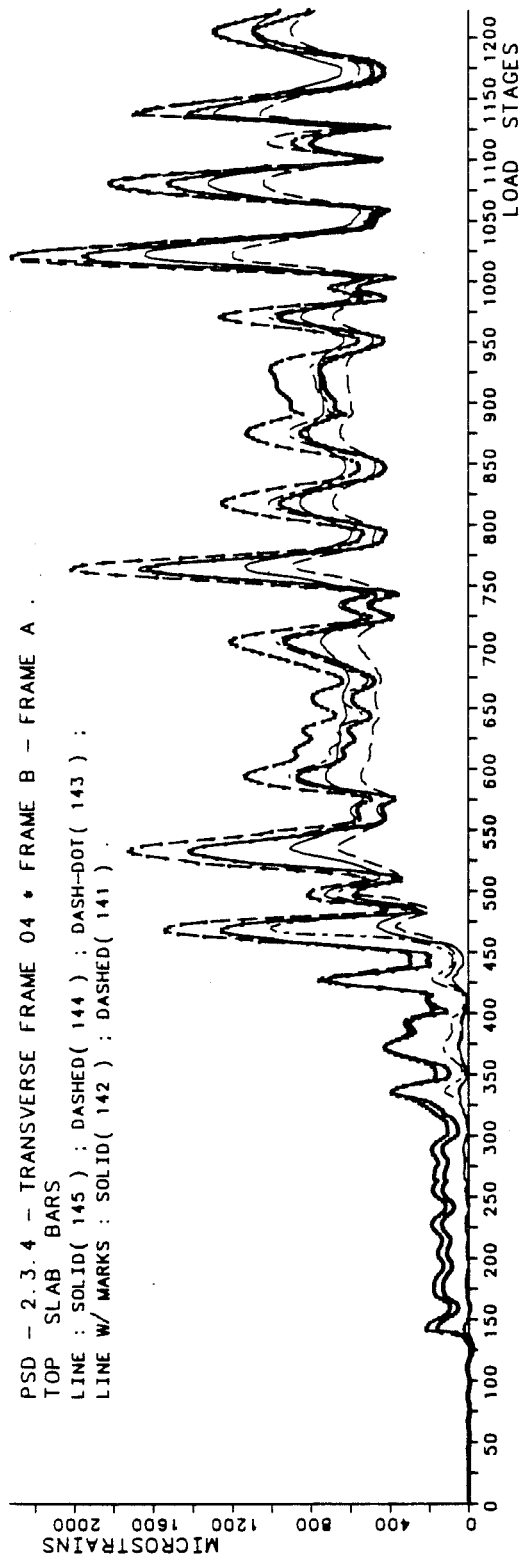


Fig. A.10 - BRI Building Slab Bar Strains.

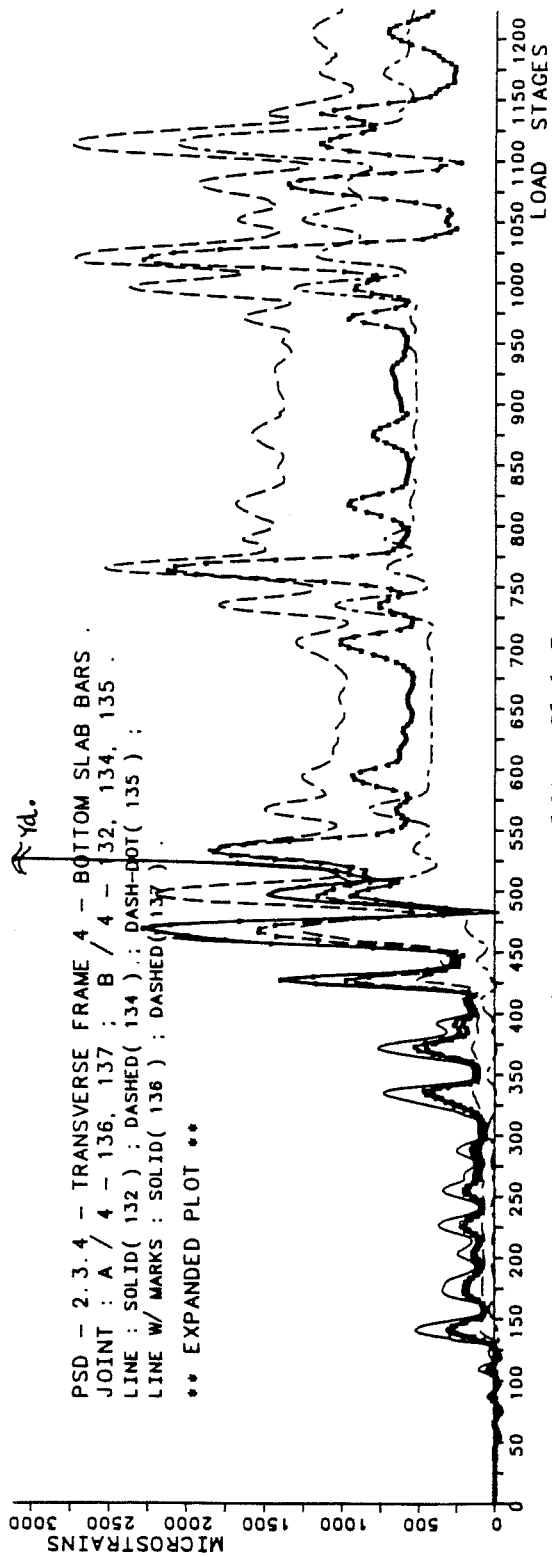
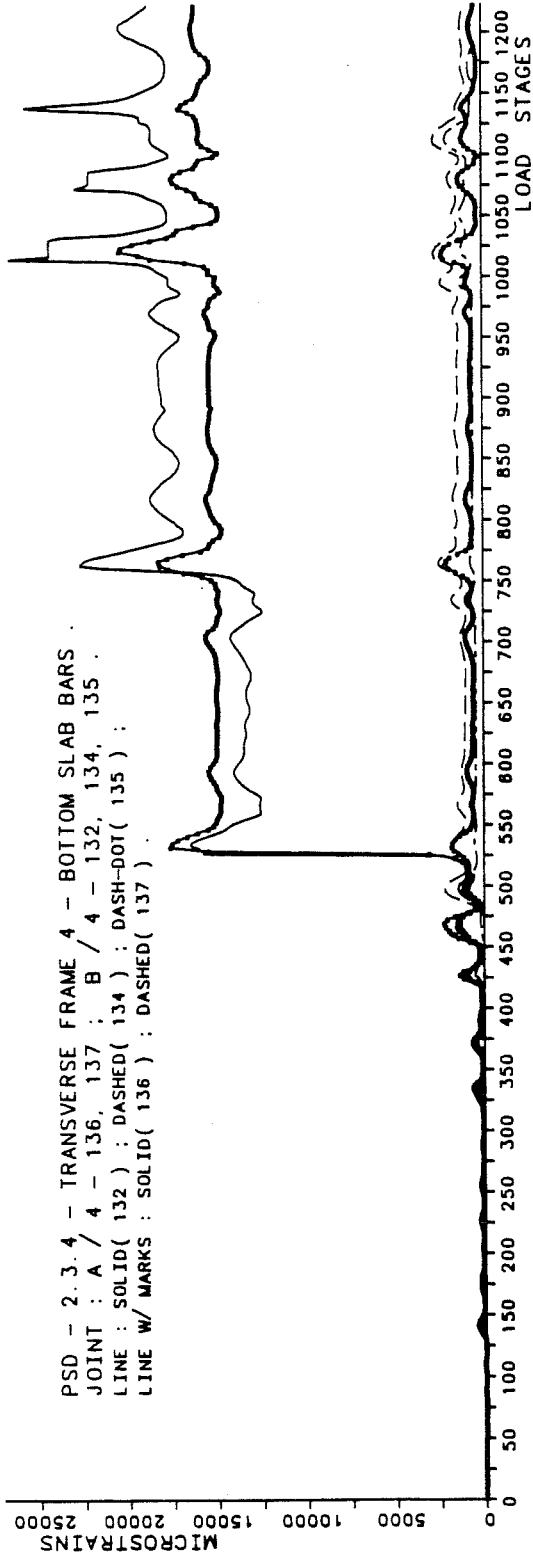


Fig. A.10 (cont.) - BRI Building Slab Bar Strains.

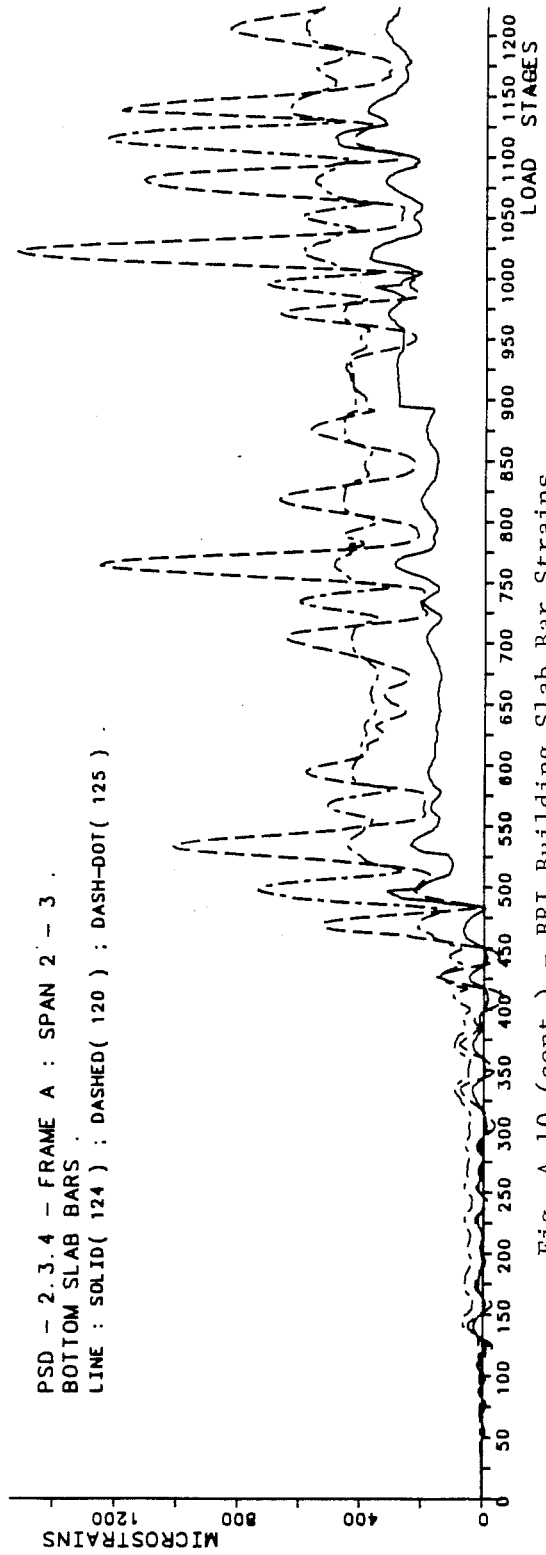
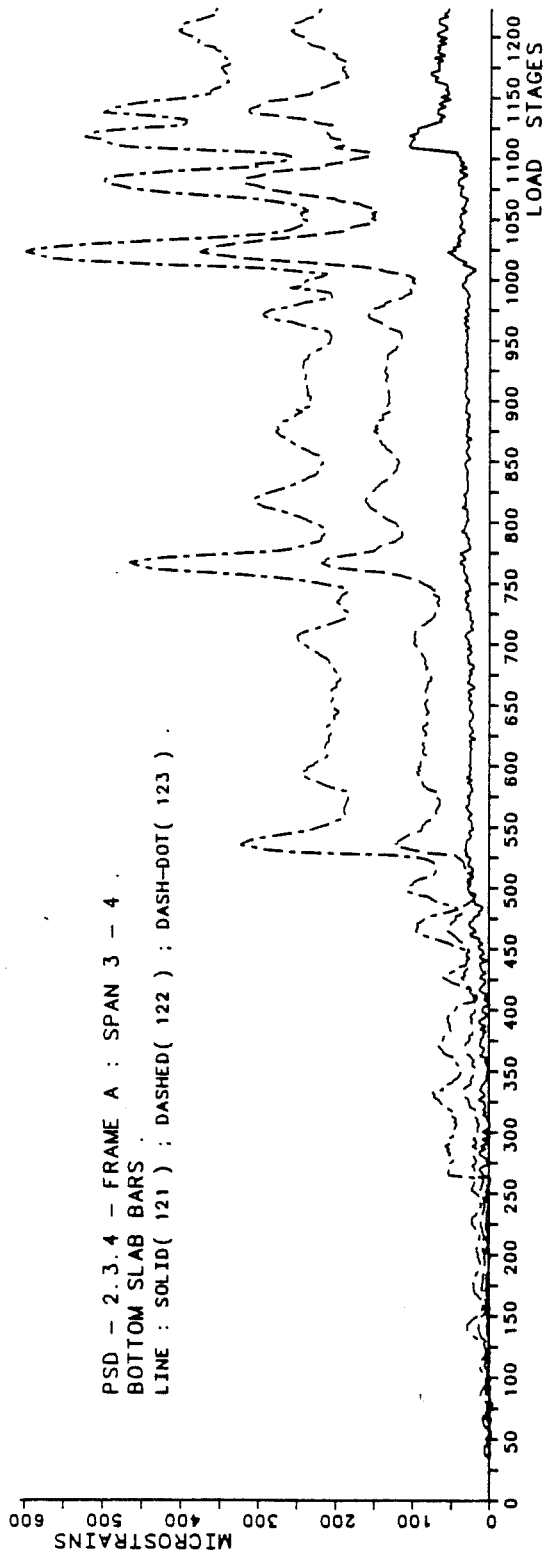


Fig. A.10 (cont.) - BRI Building Slab Bar Strains.

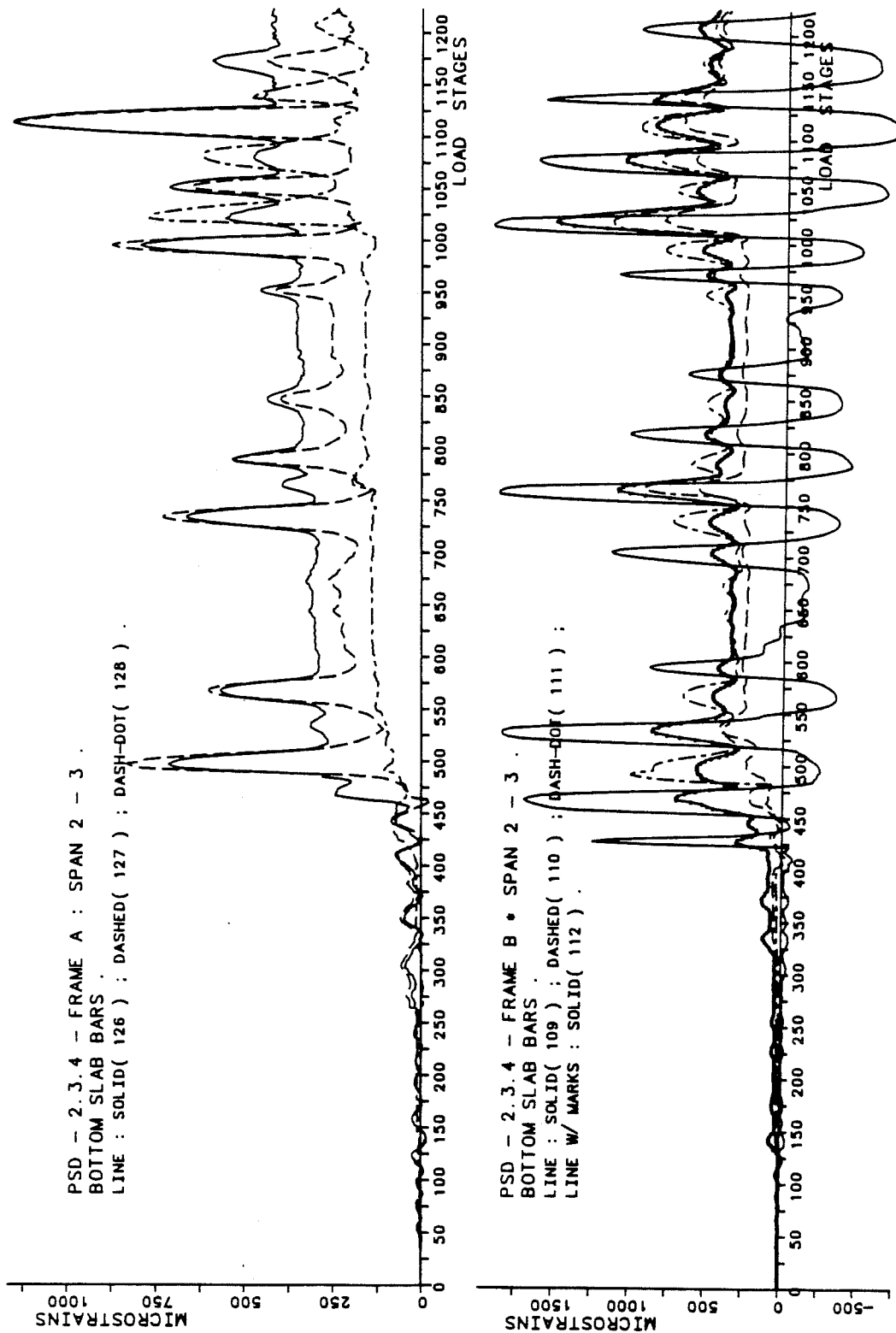


Fig. A.10 (cont.) - BRI Building Slab Bar Strains.

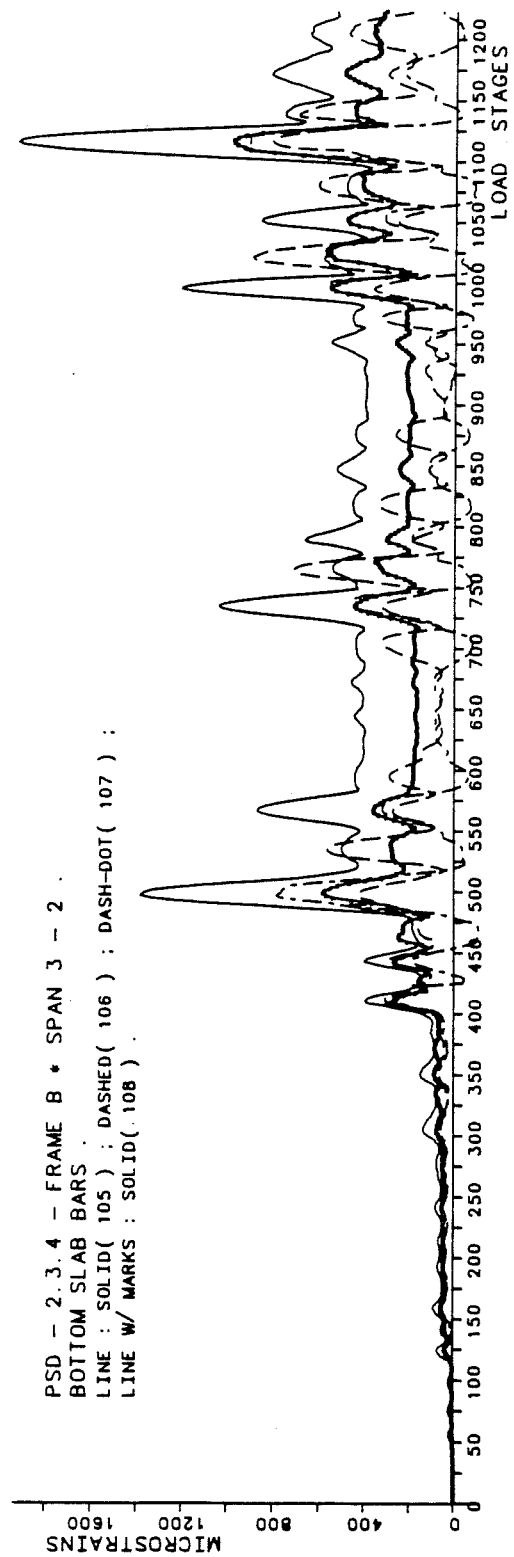
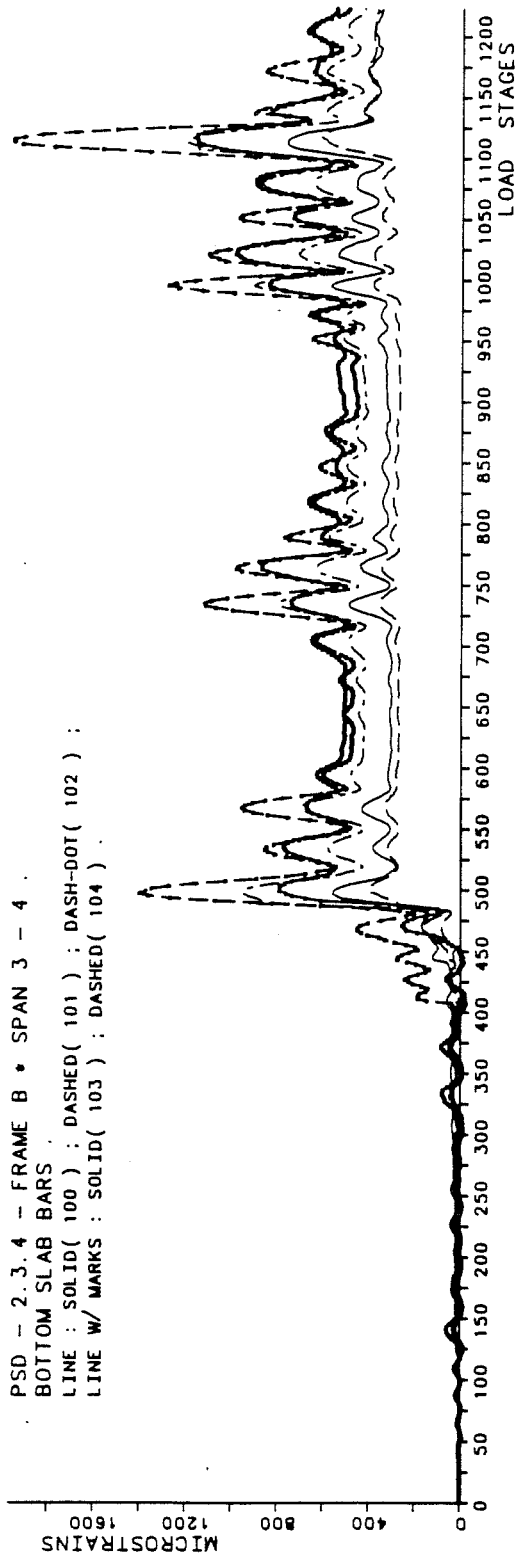


Fig. A.10 (cont.) - BRI Building Slab Bar Strains.

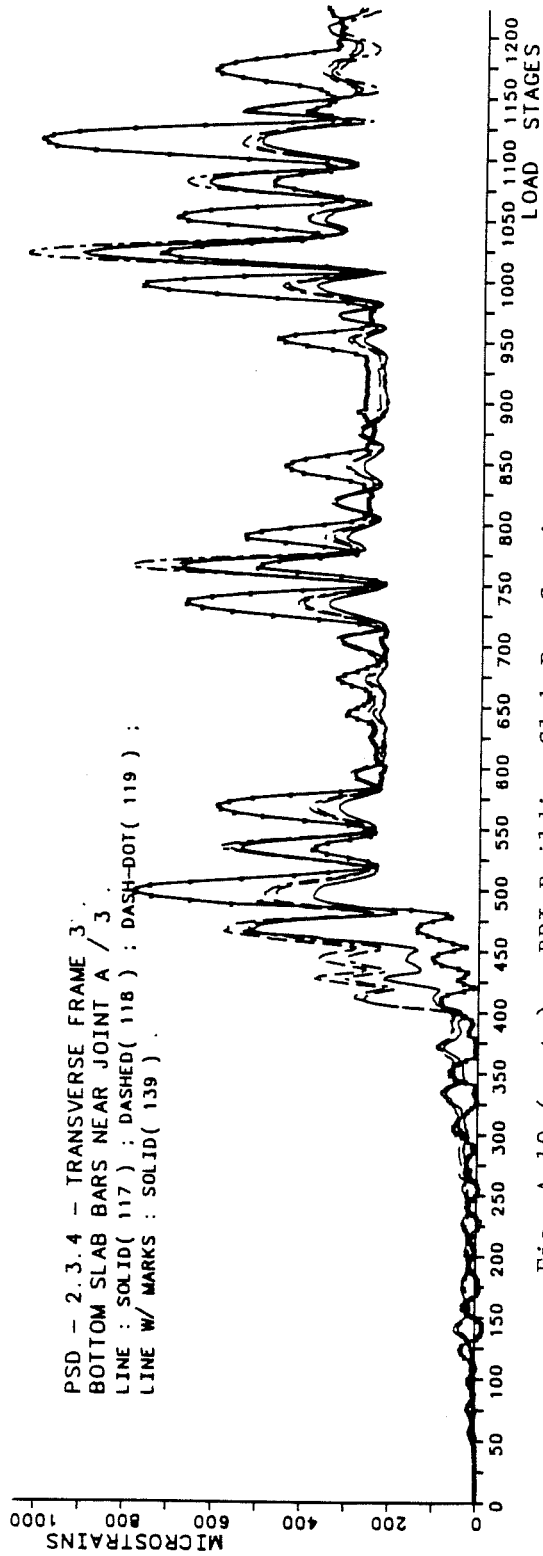
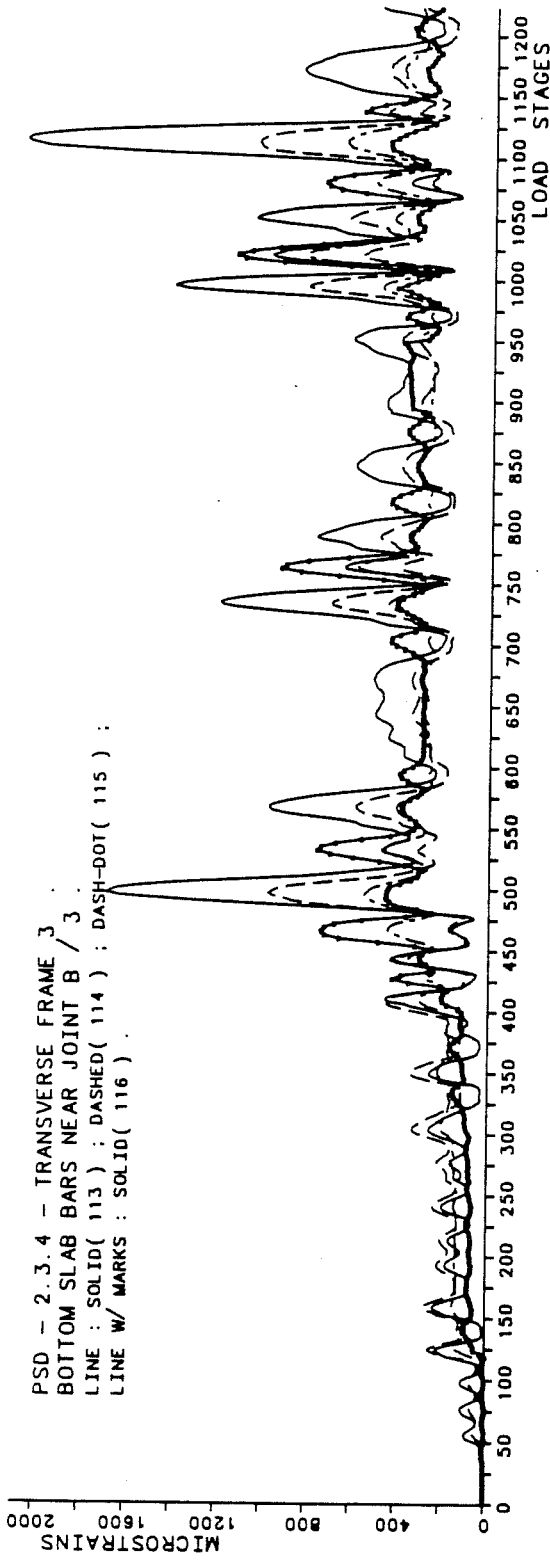


Fig. A.10 (cont.) - BRI Building Slab Bar Strains.

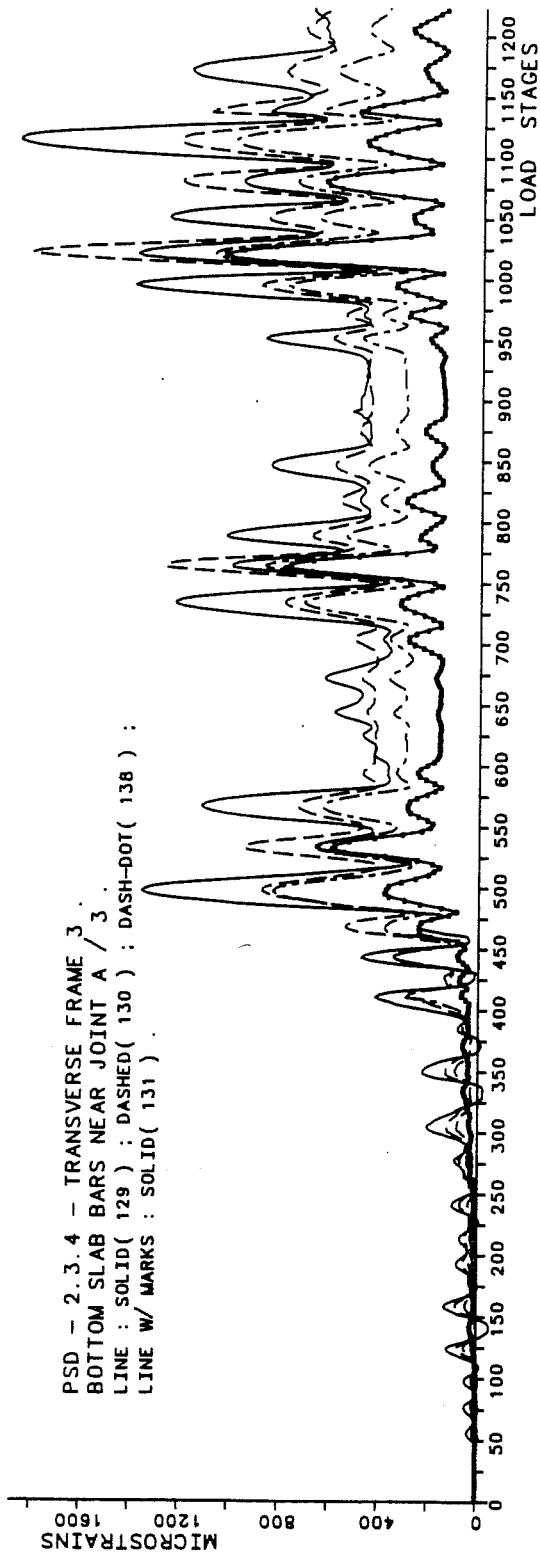


Fig. A.10 (cont.) - BRI Building Slab Bar Strains.

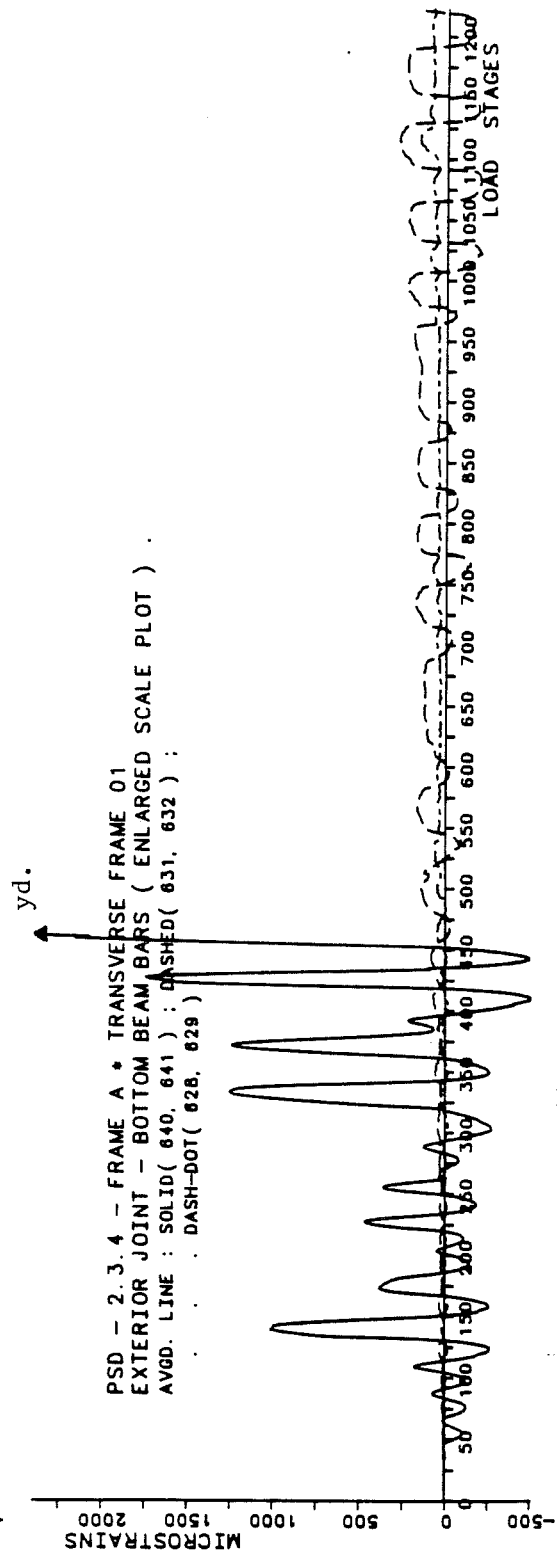
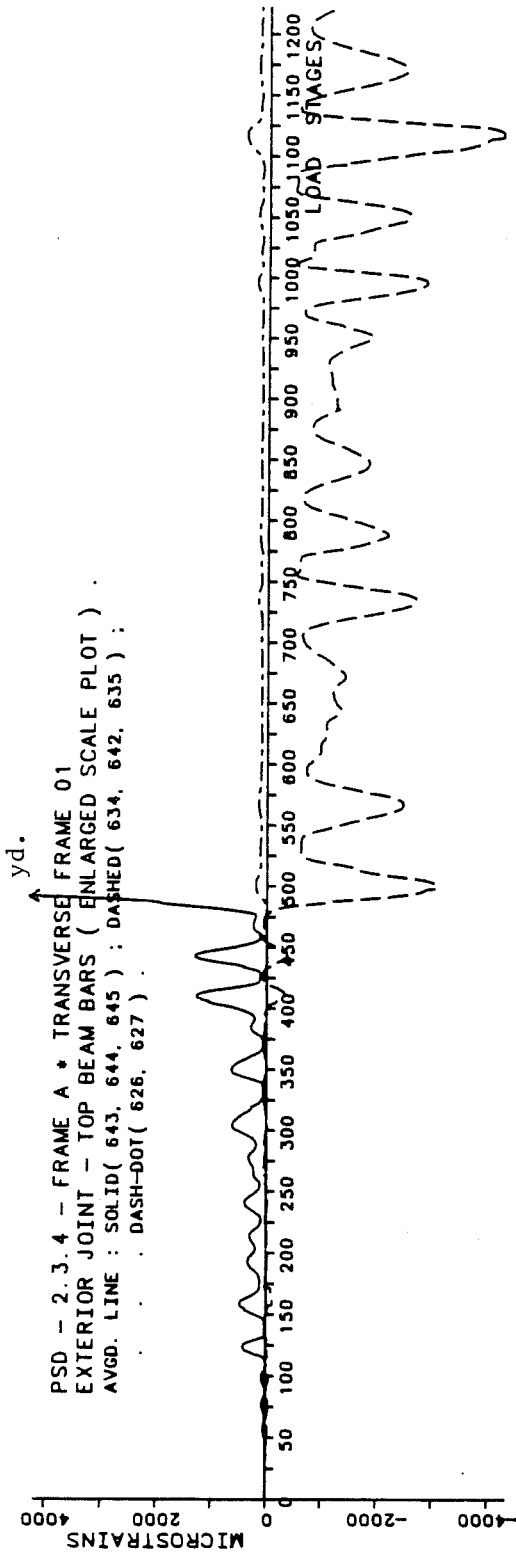


Fig. A.11 - BRI Building Exterior Joint Beam Bar Strains.

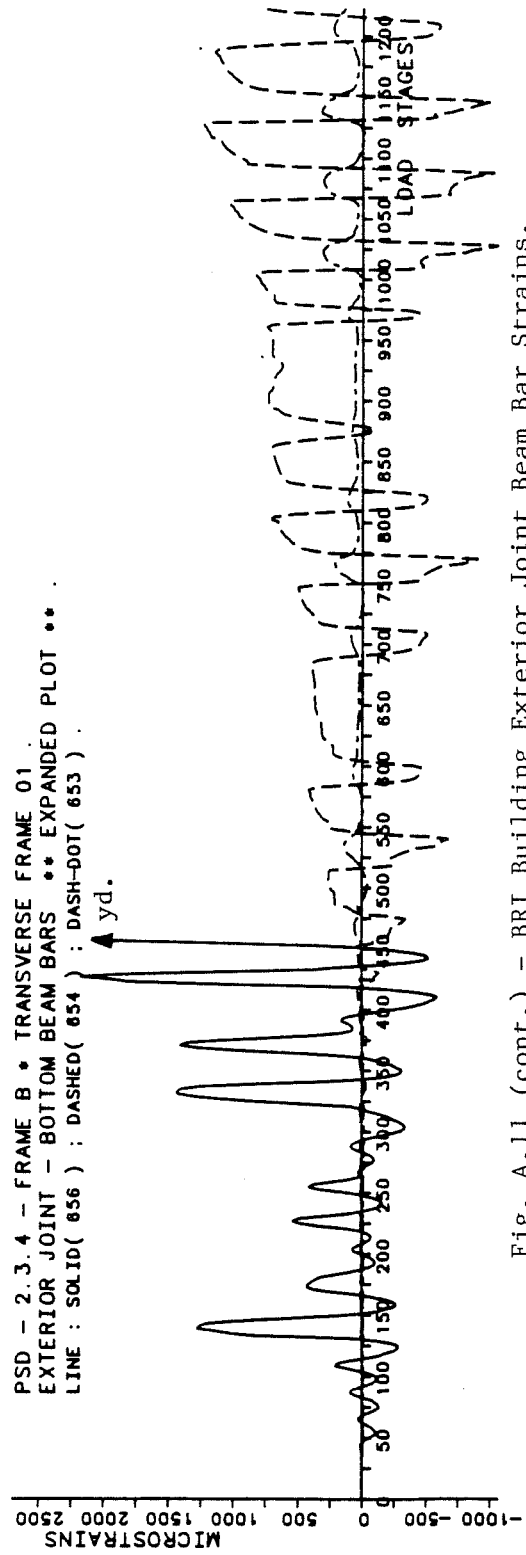
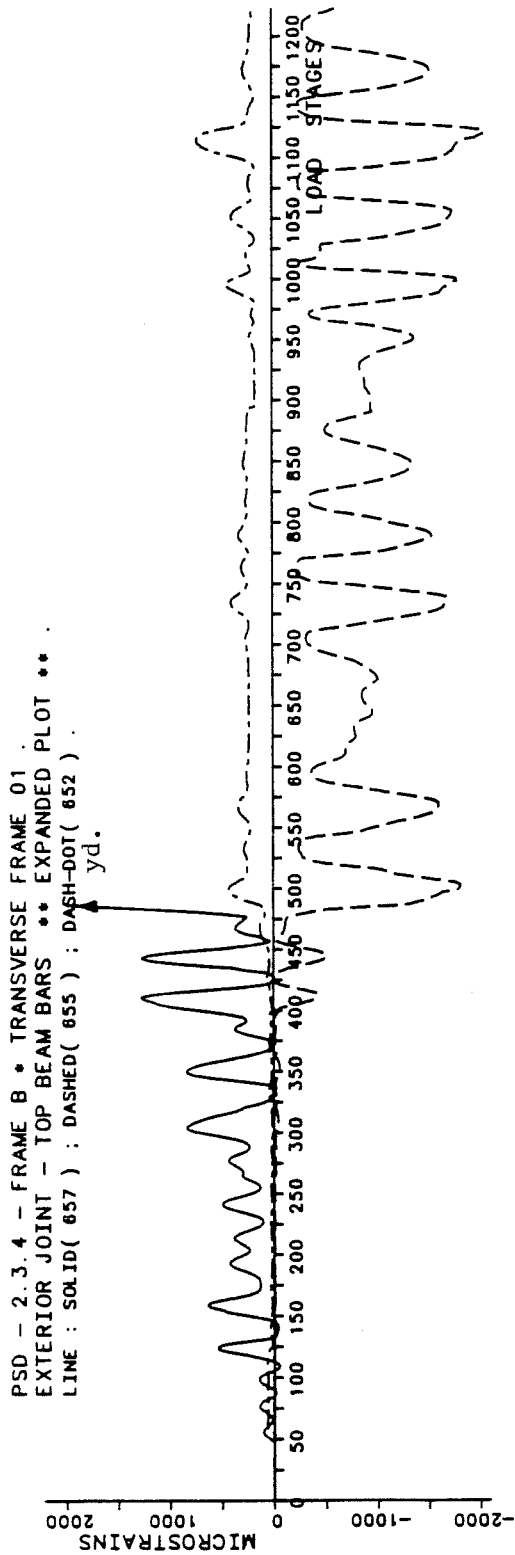


Fig. A.11 (cont.) - BRI Building Exterior Joint Beam Bar Strains.

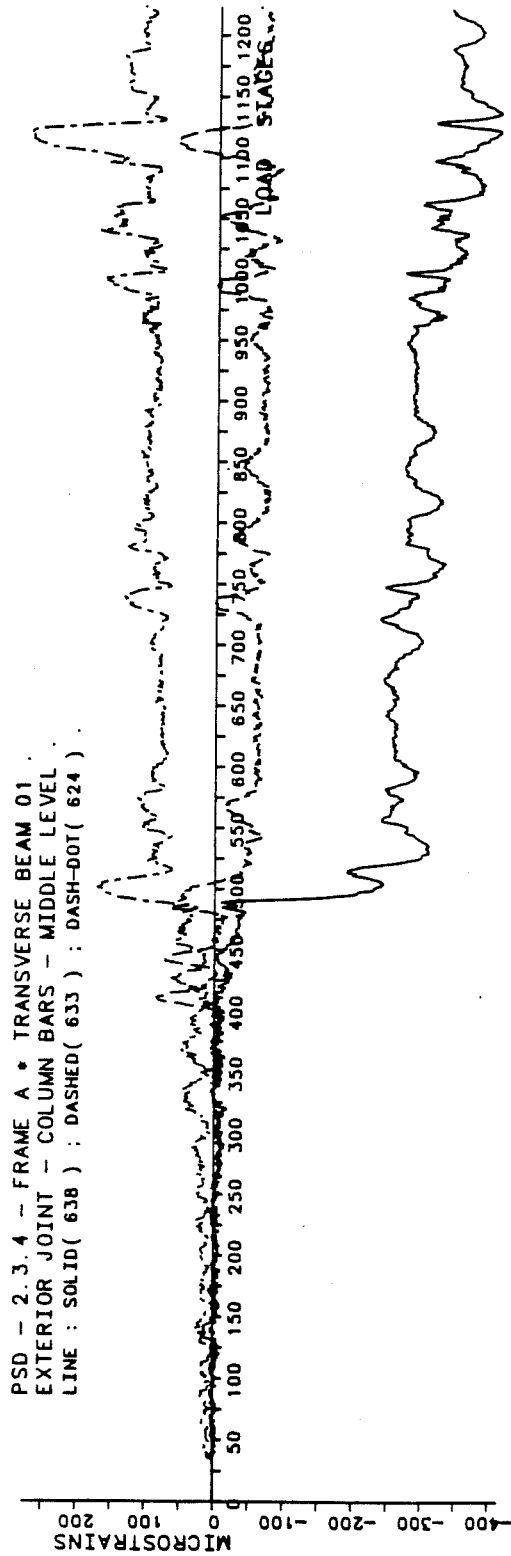
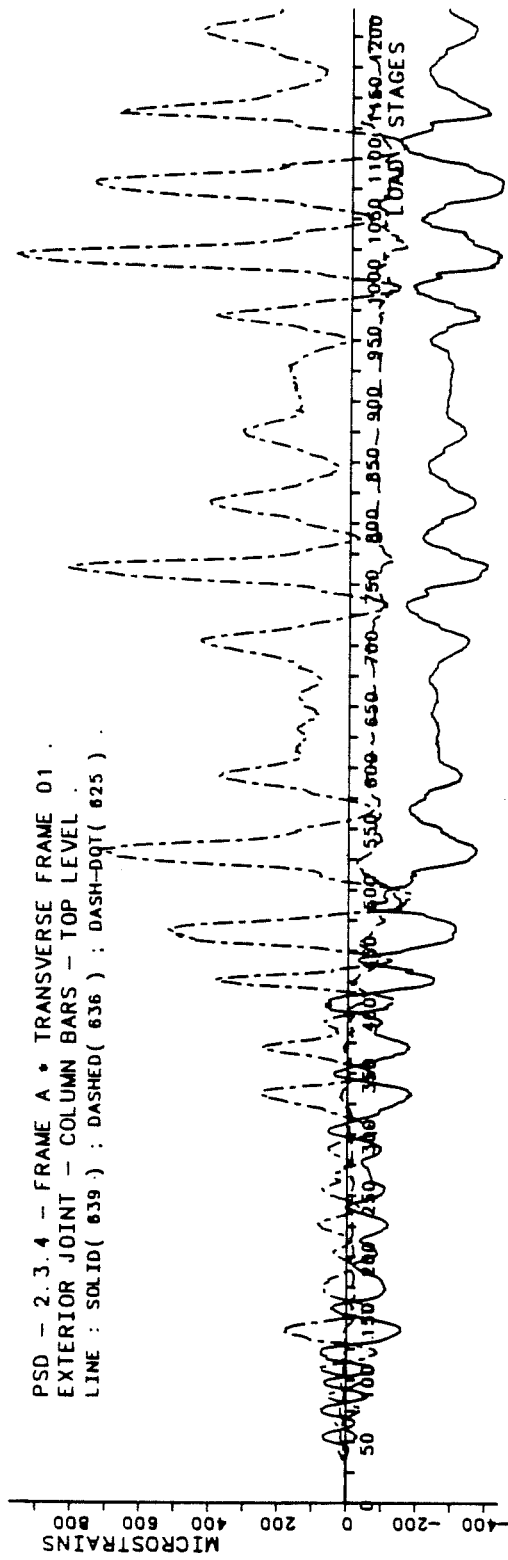


Fig. A.12 - BRI Building Exterior Joint Column Bar Strains.

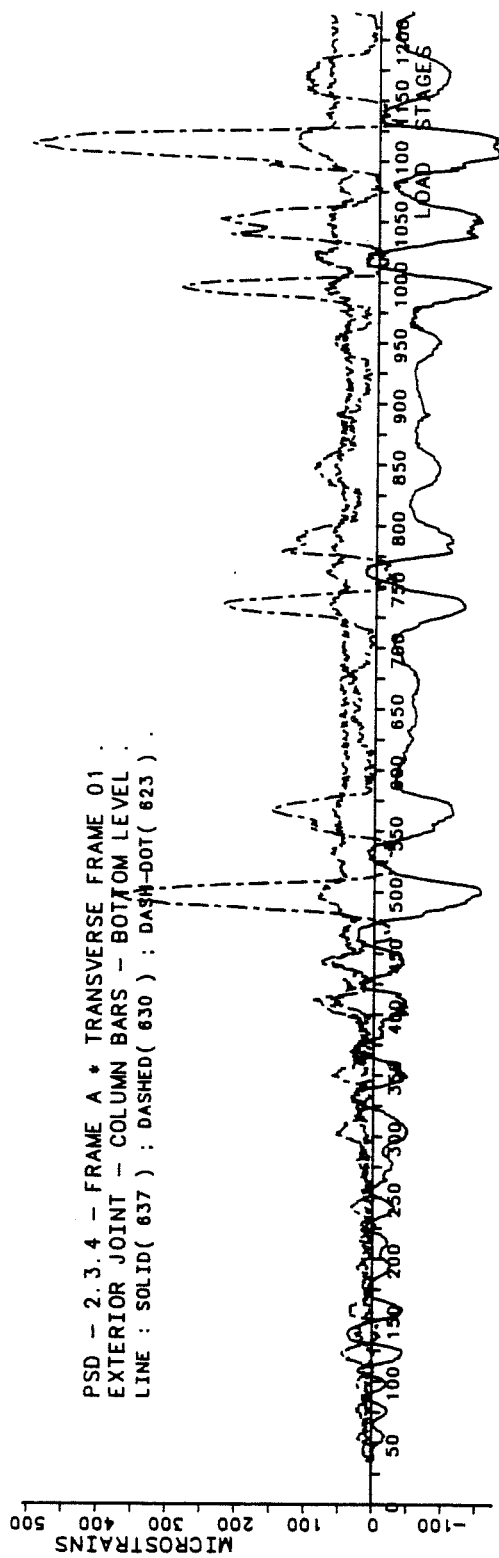


Fig. A.12 (cont.) - BRI Building Exterior Joint Column Bar Strains.

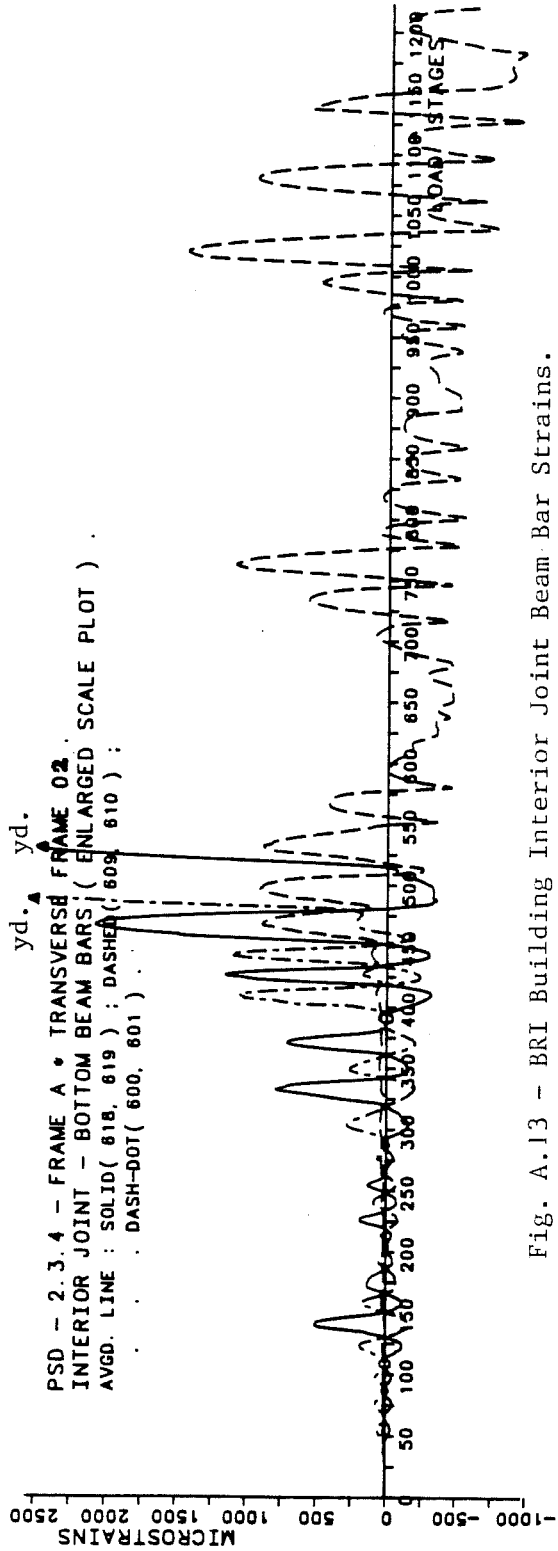
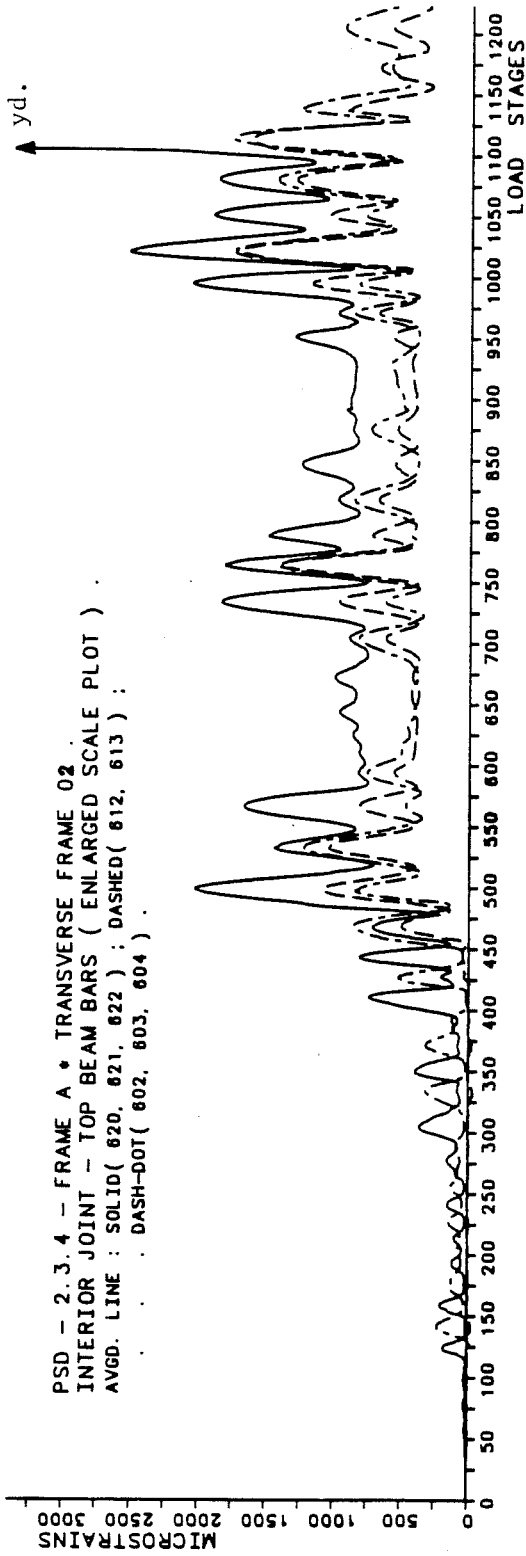


Fig. A.13 - BRI Building Interior Joint Beam Bar Strains.

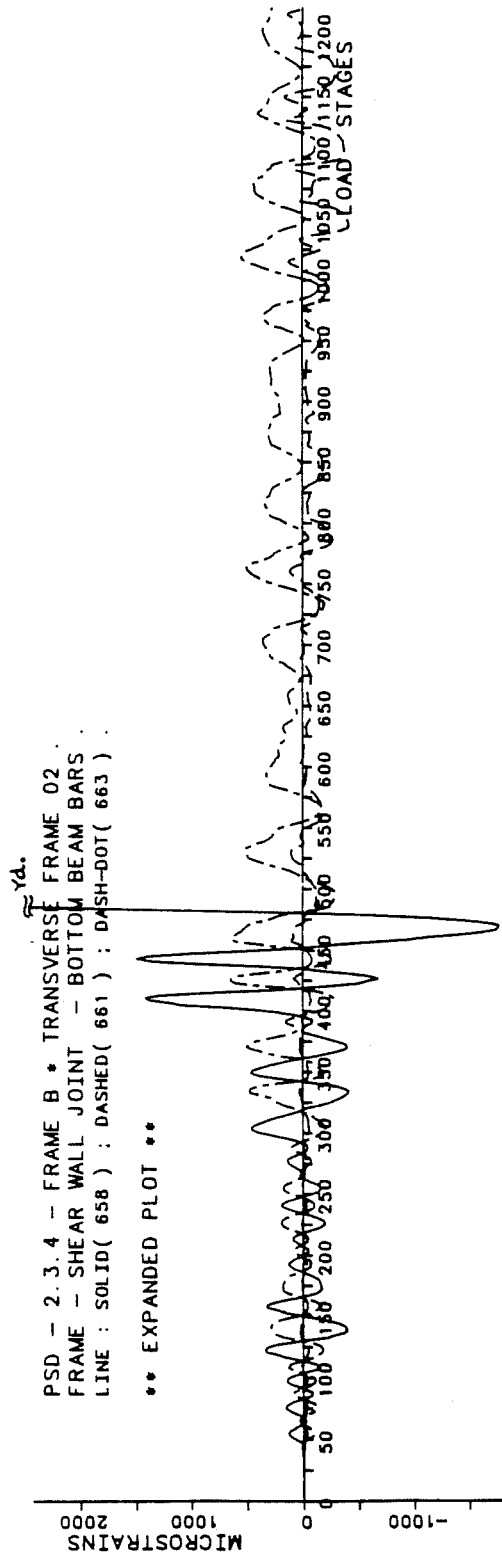
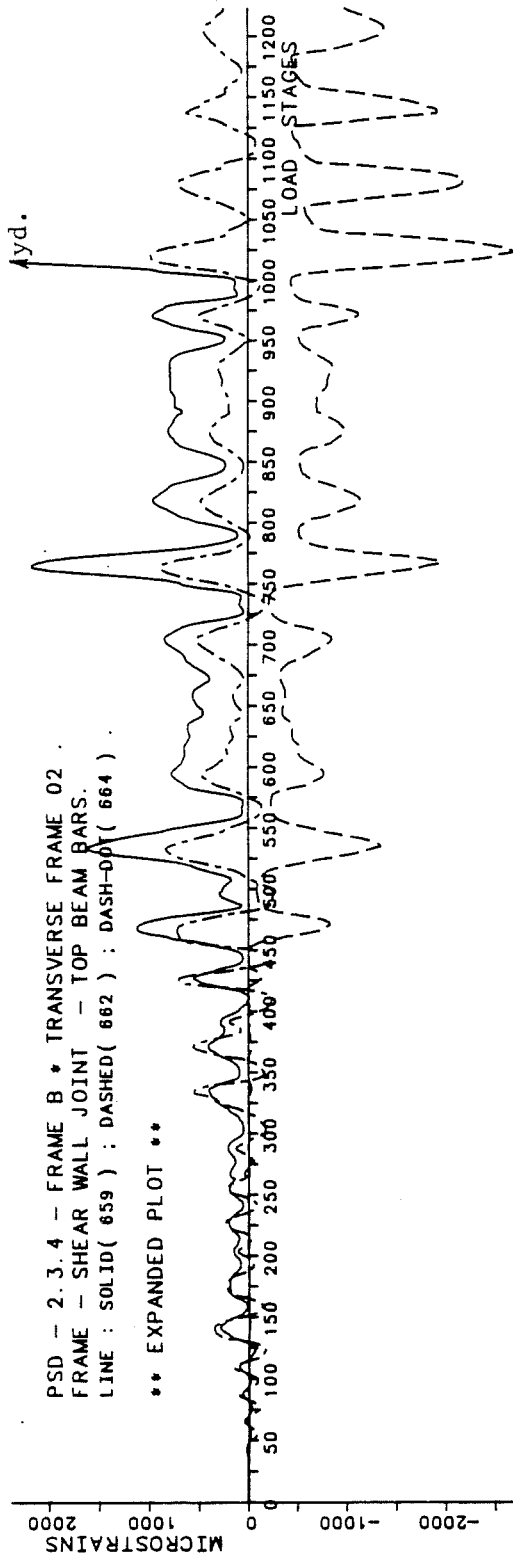


Fig. A.13 (cont.) - BRI Building Interior Joint Beam Bar Strains.

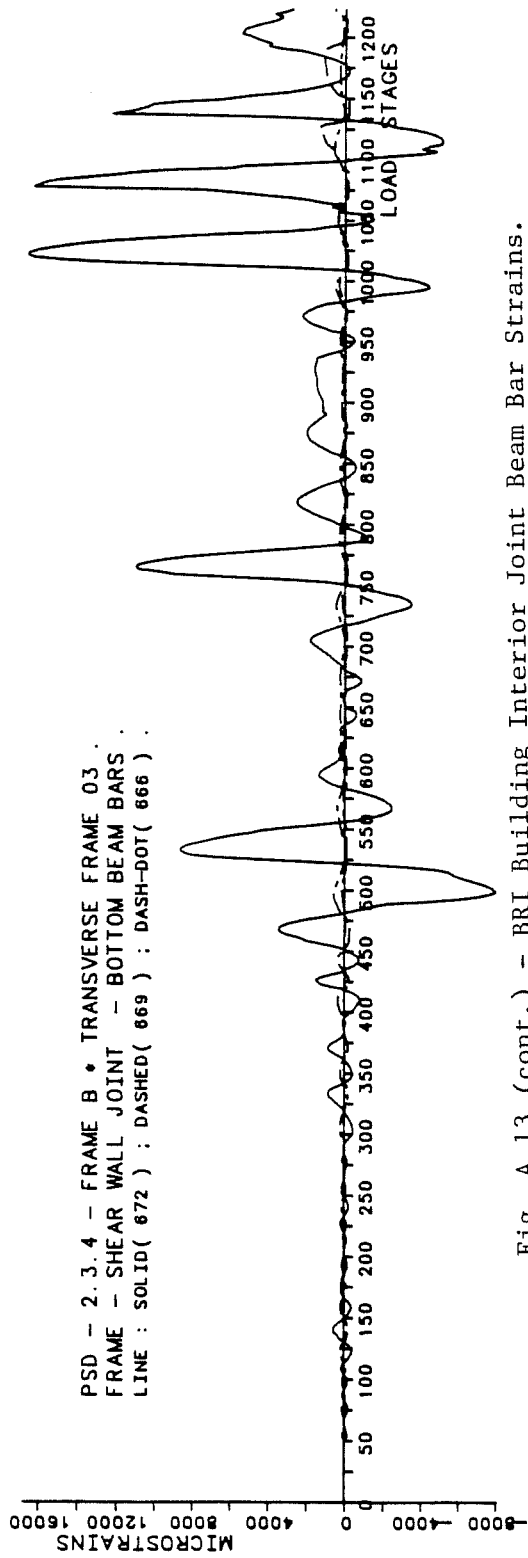
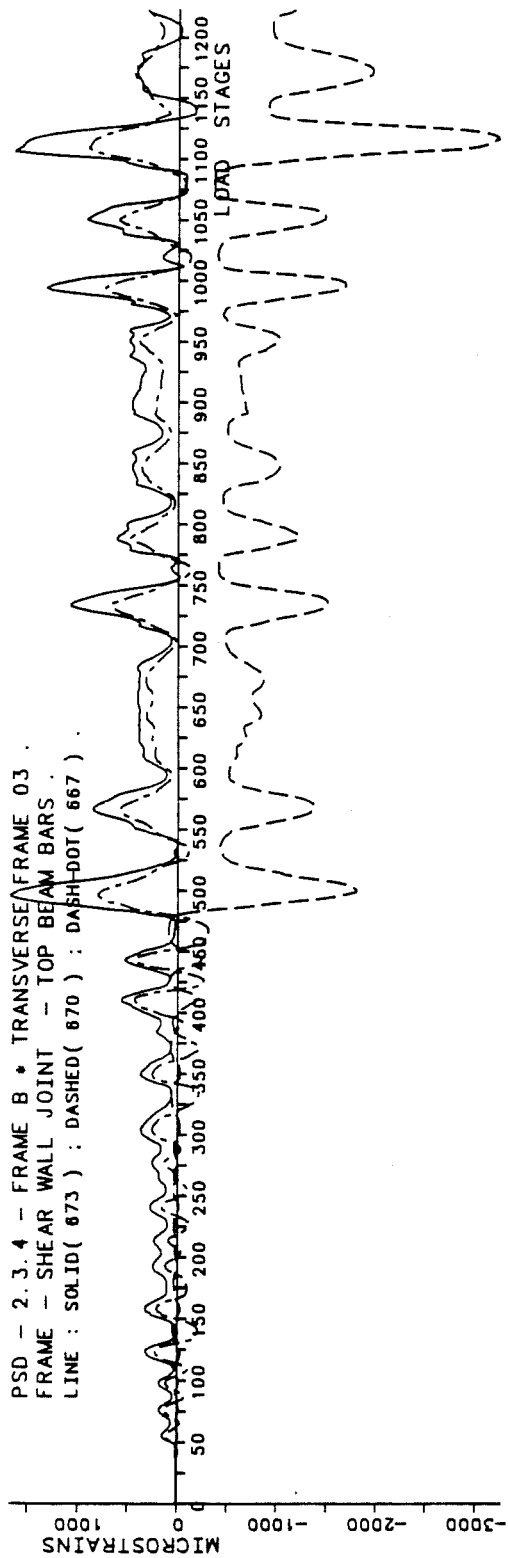


Fig. A.13 (cont.) - BRI Building Interior Joint Beam Bar Strains.

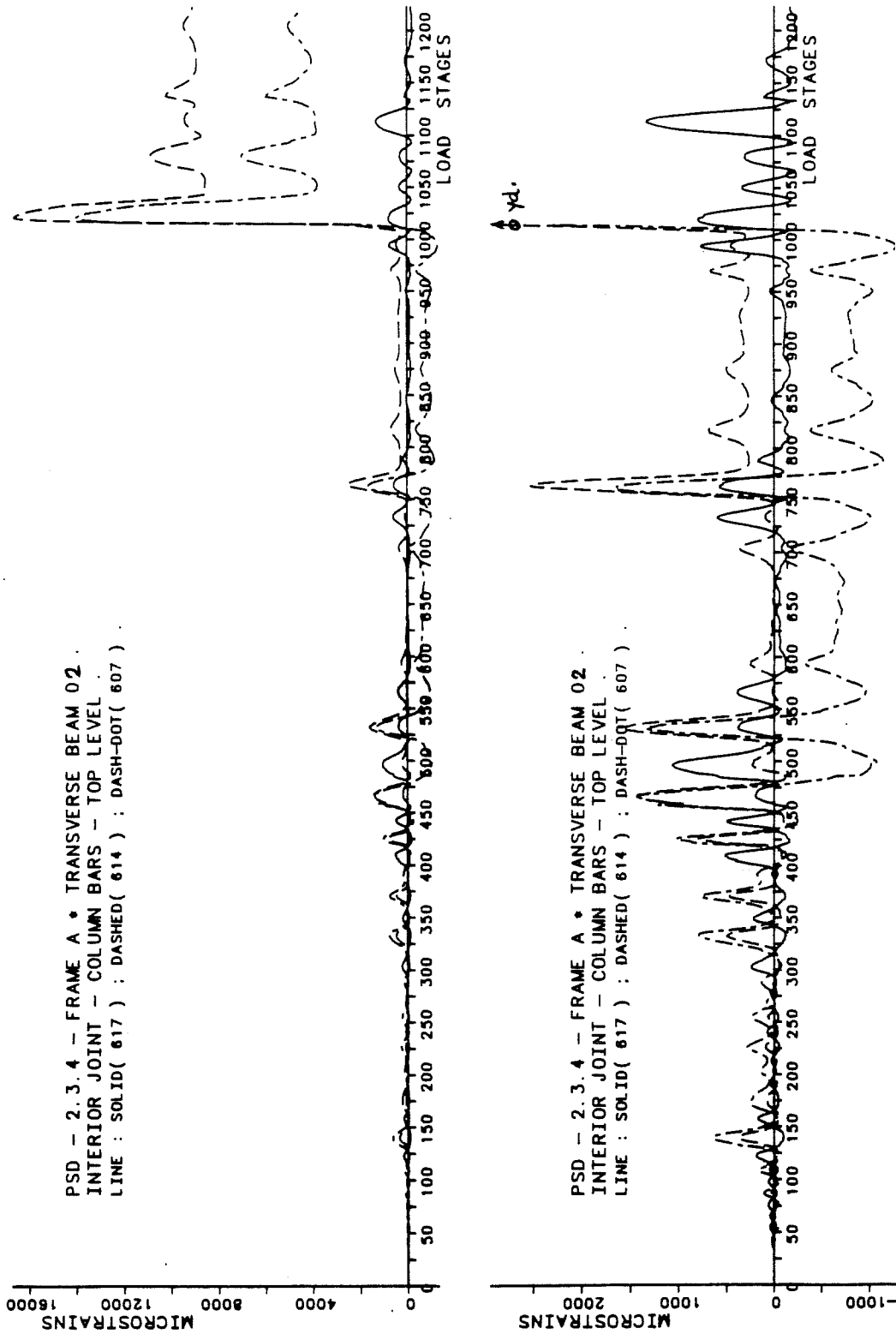


Fig. A.14 - BRI Building Interior Joint Column Bar Strains.

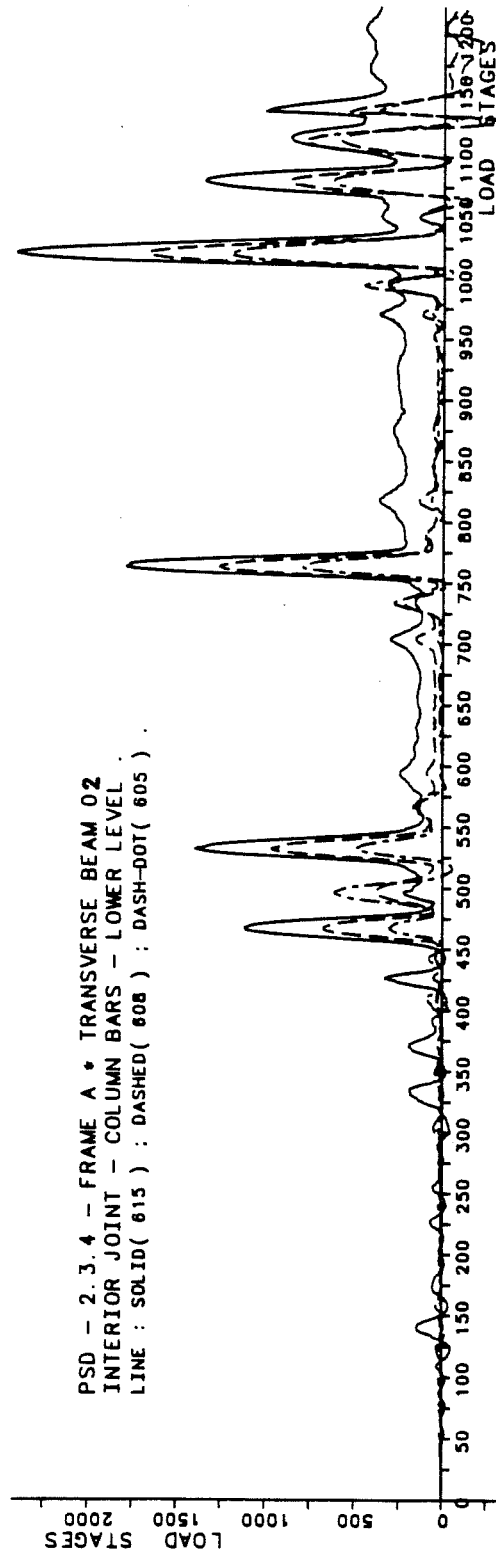
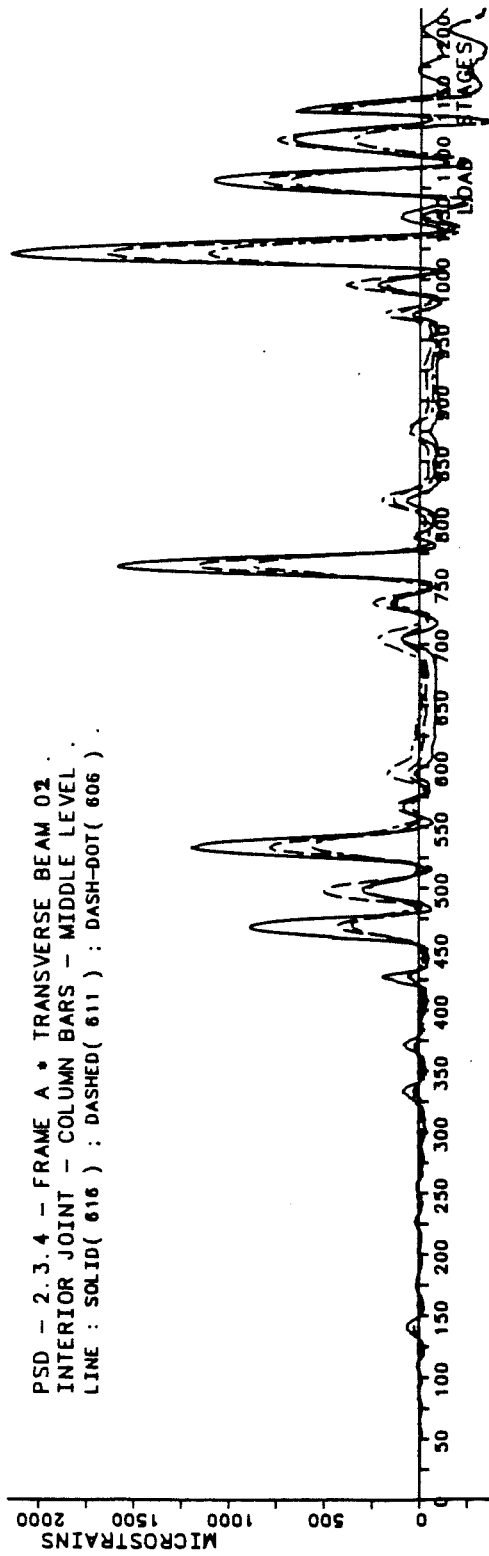


Fig. A.14 (cont.) - BRI Building Interior Joint Column Bar Strains.

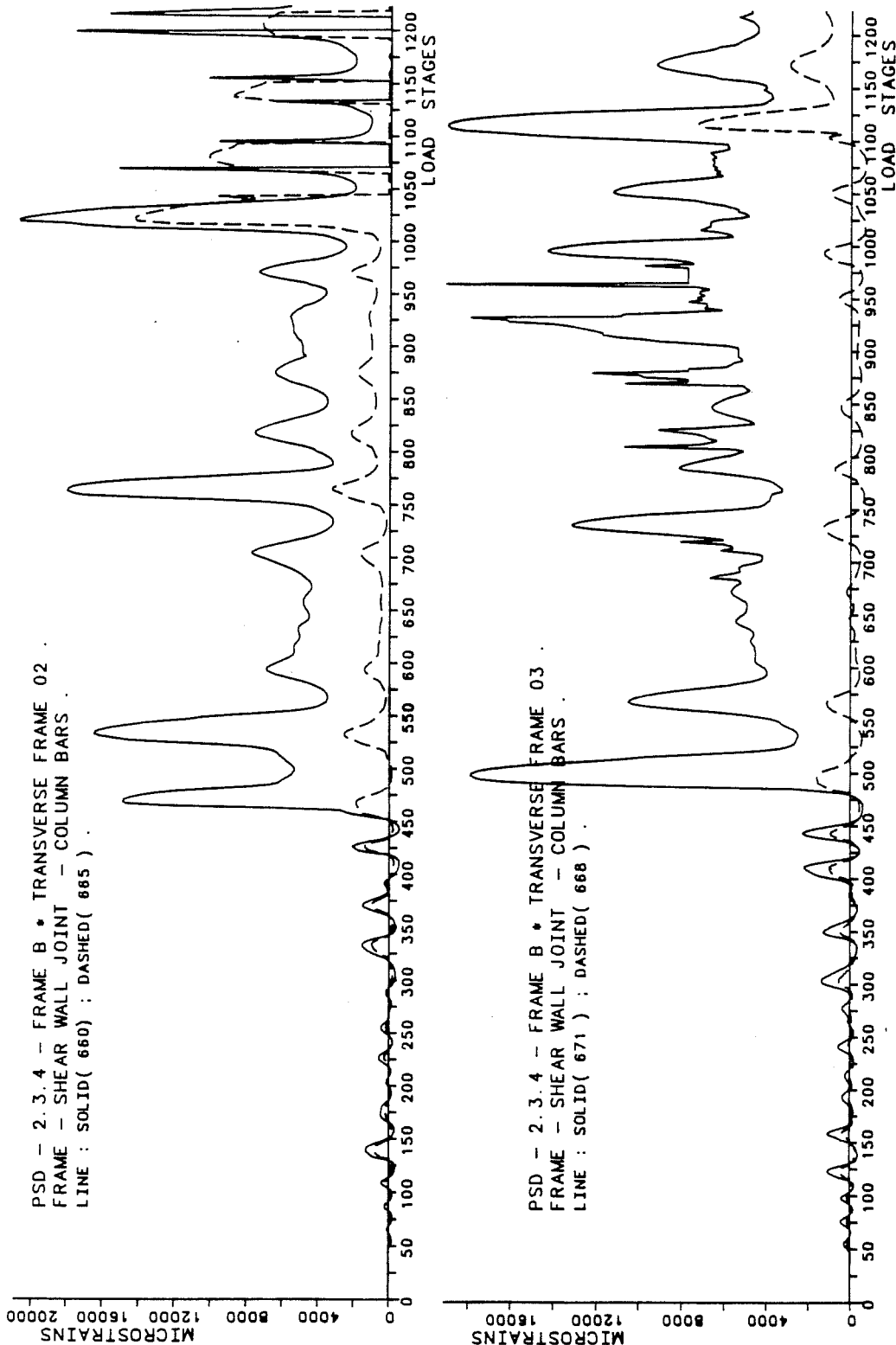


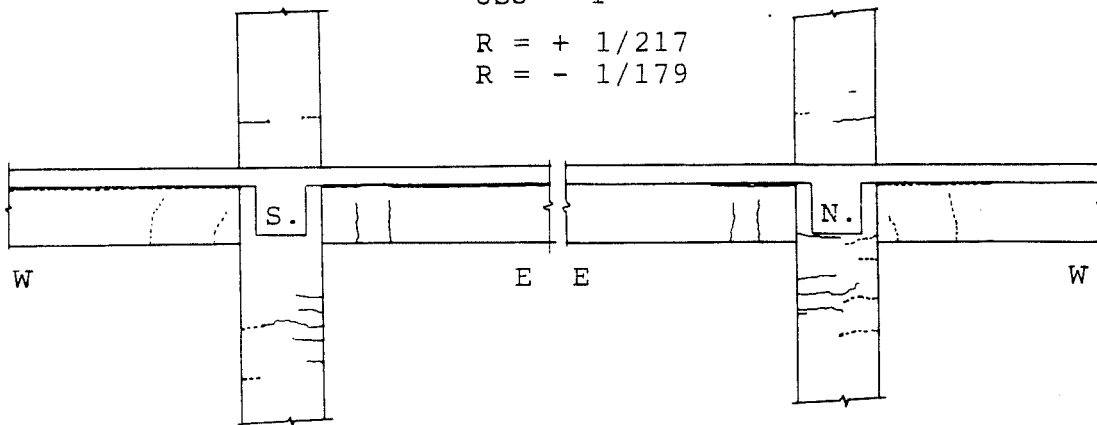
Fig. A.14 (cont.) - BRI Building Interior Joint Column Bar Strains.

APPENDIX B

THE UNIVERSITY OF TEXAS AT AUSTIN COMPONENT TEST DATA

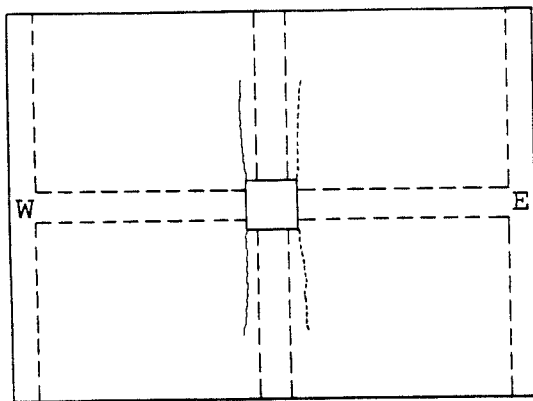
The plotted data provided in this section was once reported forever lost from the Ferguson Structural Engineering Laboratory. However, through the most generous help and encouragement of Drs. Patricia Baker and Phil Kelton - Department of Astronomy - The University of Texas at Austin and the author's endeavour the data was retrieved and stored in the mainframe CDC computer.

USJ - 1
 R = + 1/217
 R = - 1/179

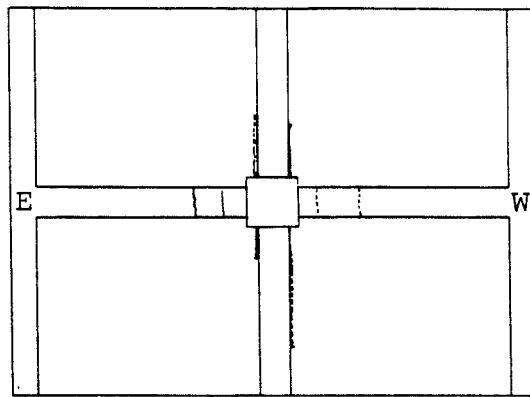


a. South Elevation.

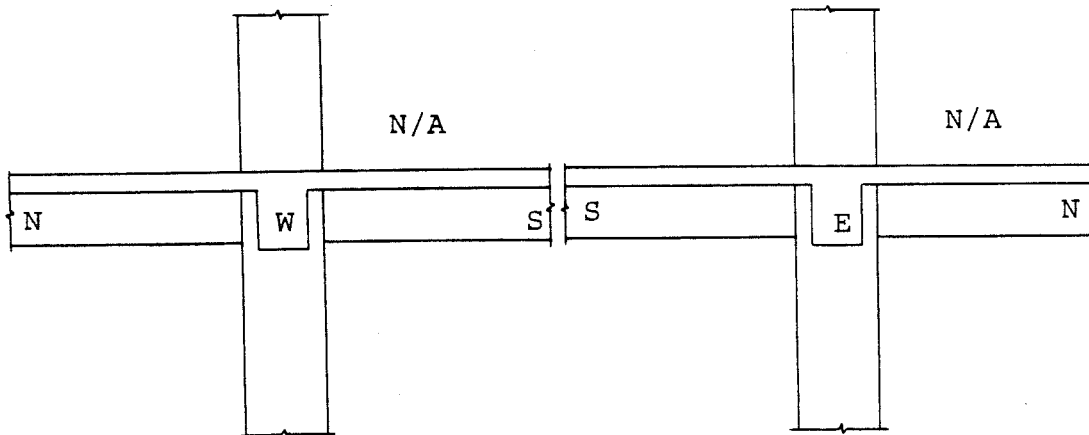
b. North Elevation.



c. Top View.



d. Bottom View.



e. West Elevation.

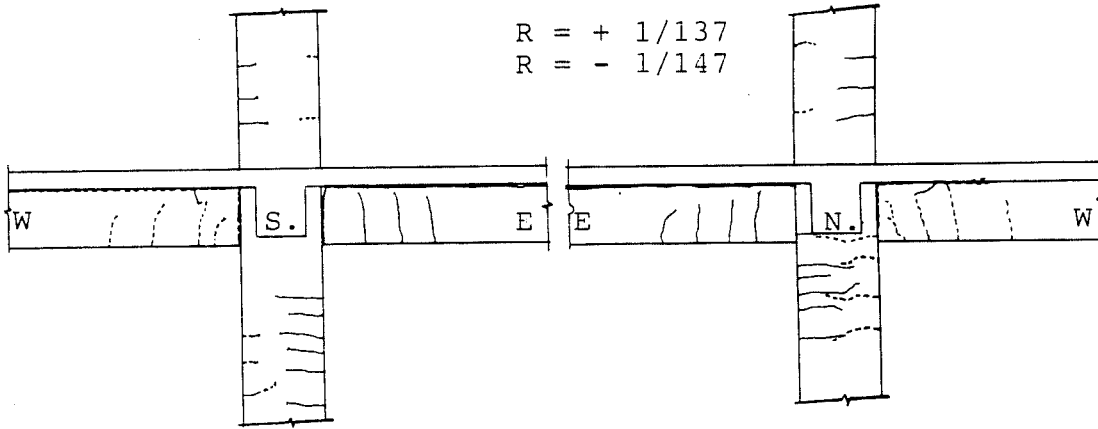
f. East Elevation.

Fig. B.1 - USJ-1 - Cracking Patterns.

USJ - 1

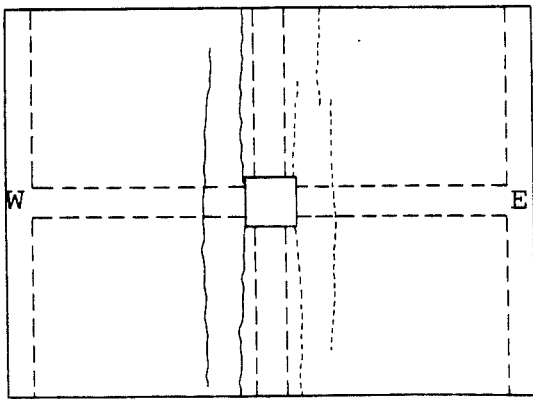
R = + 1/137

R = - 1/147

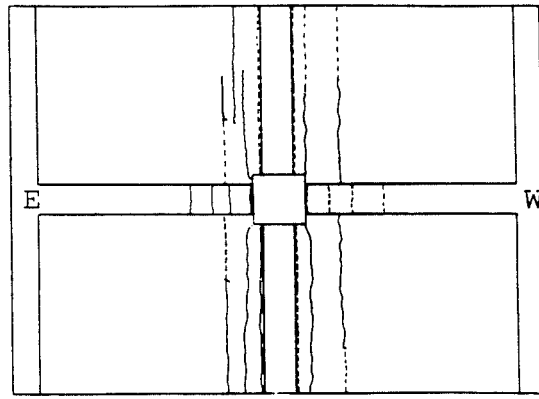


a. South Elevation.

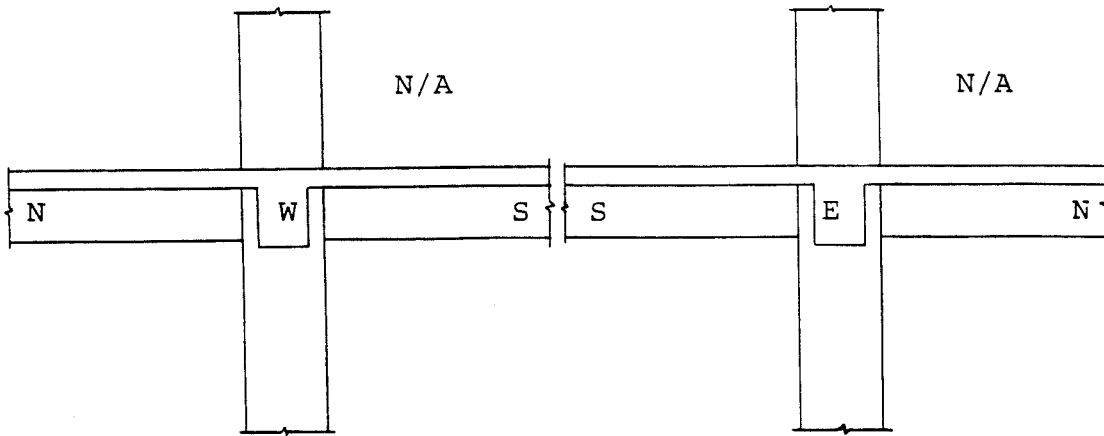
b. North Elevation.



c. Top View.



d. Bottom View.



e. West Elevation.

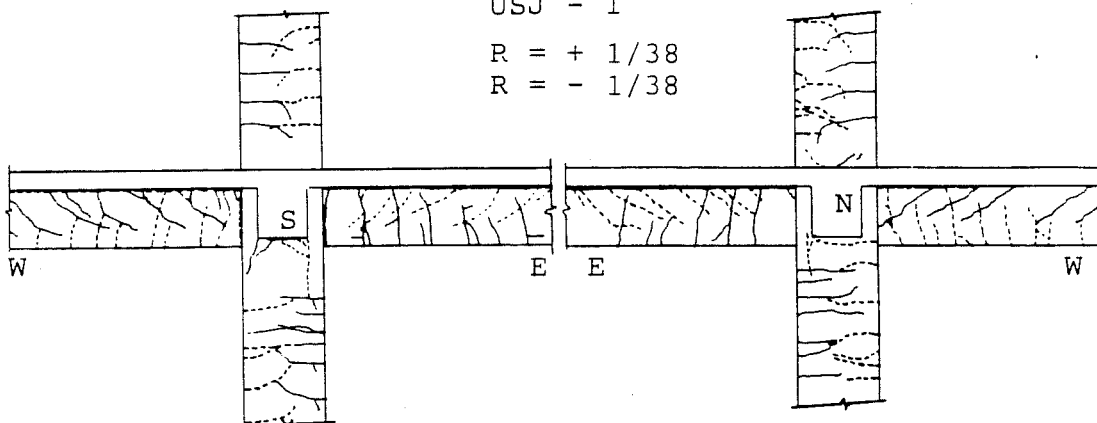
f. East Elevation.

Fig. B.1 (cont.) - USJ-1 - Cracking Patterns.

USJ - 1

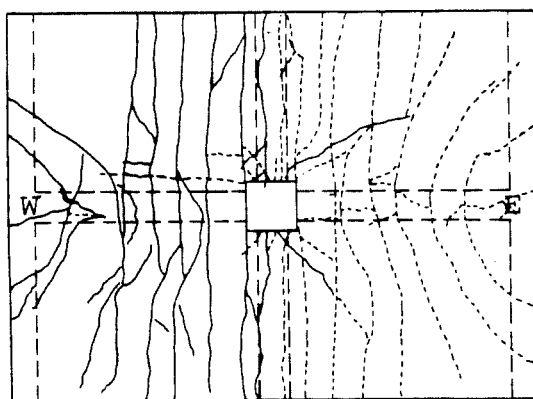
R = + 1/38

R = - 1/38

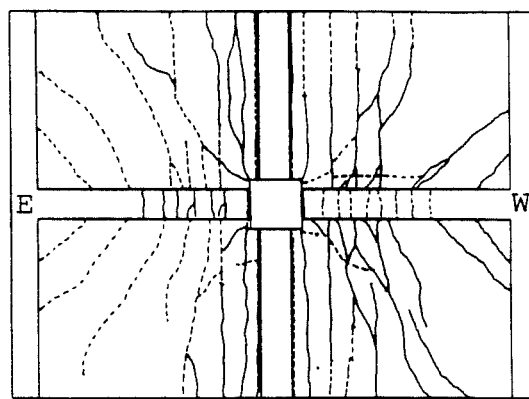


a. South Elevation.

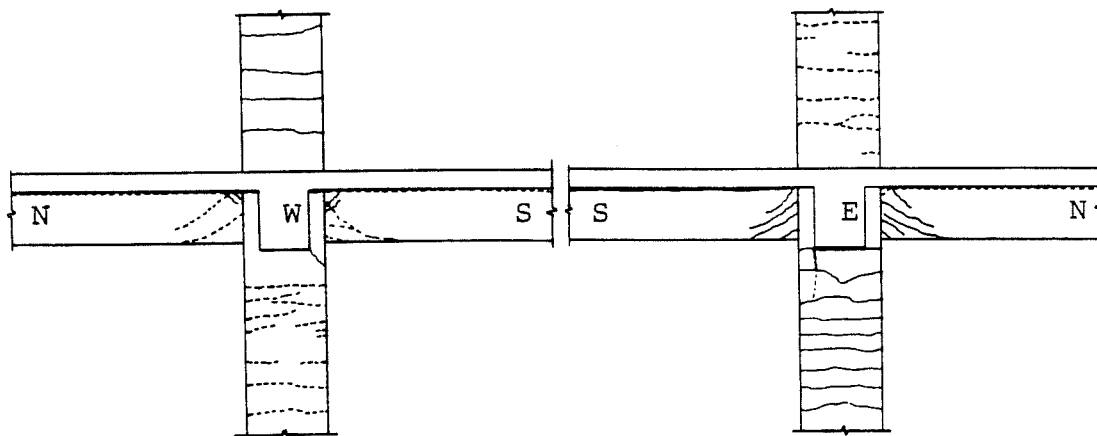
b. North Elevation.



c. Top View.



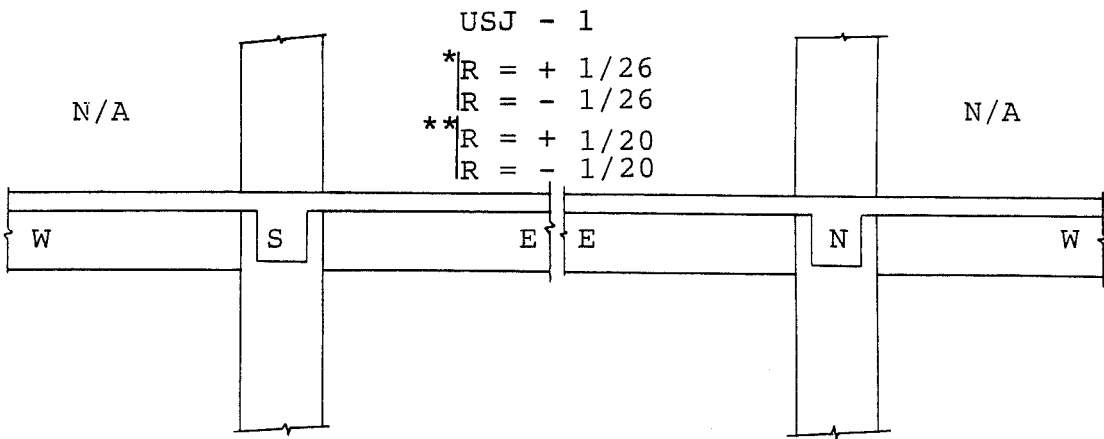
d. Bottom View.



e. West Elevation.

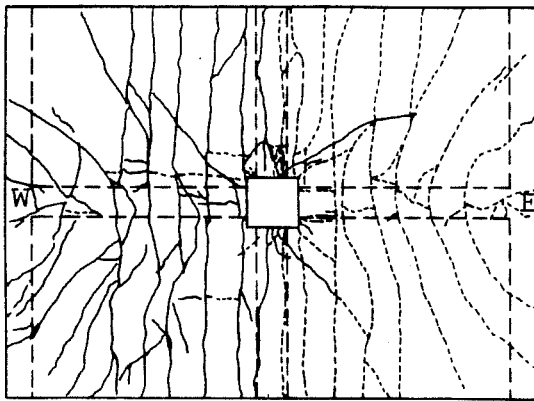
f. East Elevation.

Fig. B.1 (cont.) - USJ-1 - Cracking Patterns.

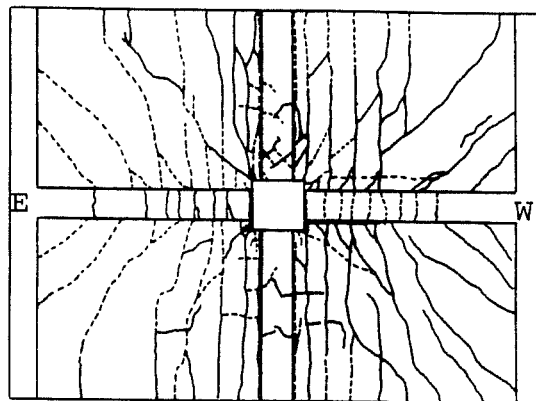


a. South Elevation.

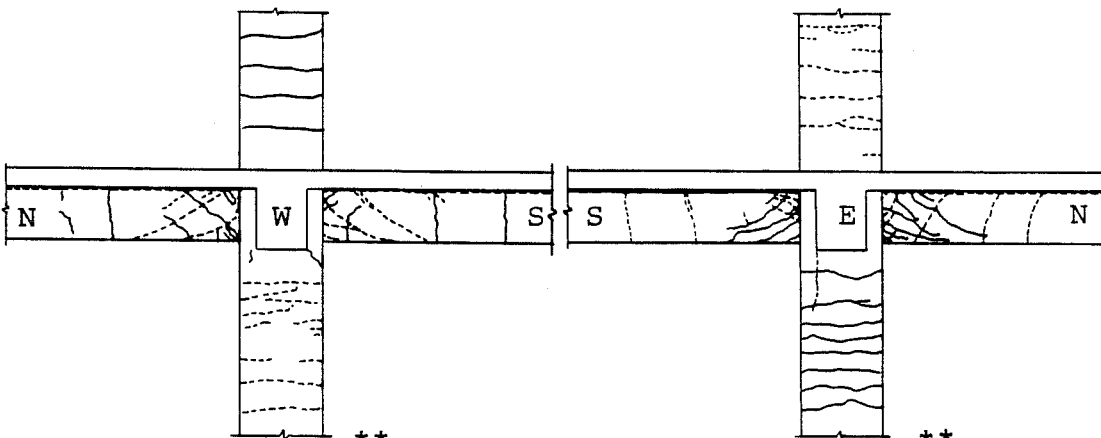
b. North Elevation.



c. Top View*



d. Bottom View*



e. West Elevation.**

f. East Elevation.**

Fig. B.1 (cont.) - USJ-1 - Cracking Patterns.

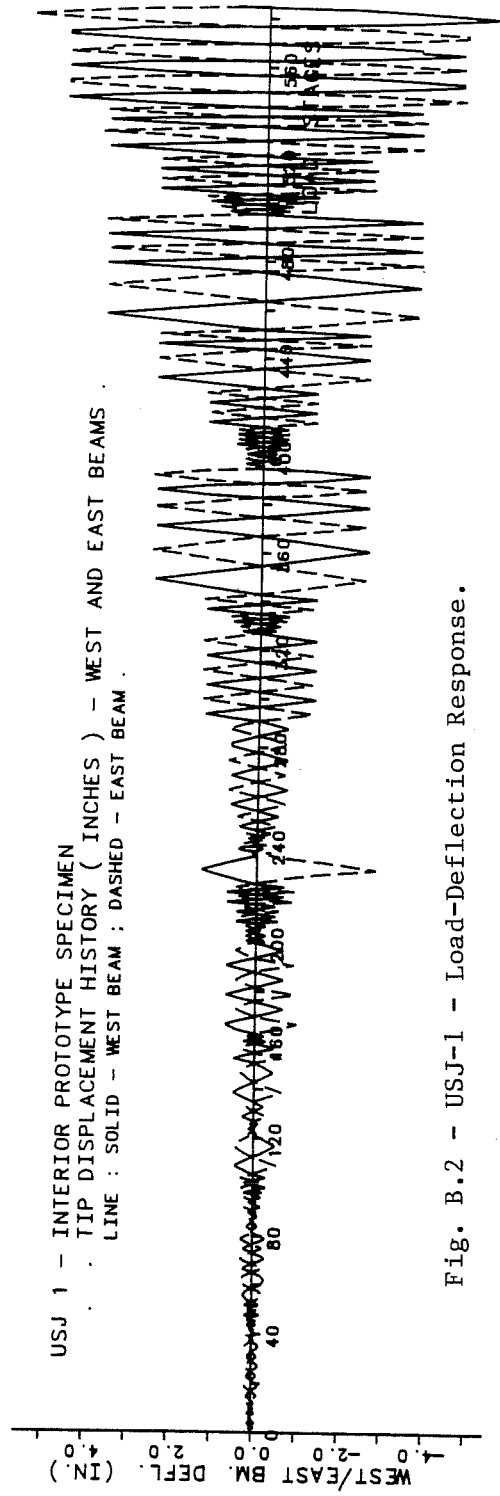
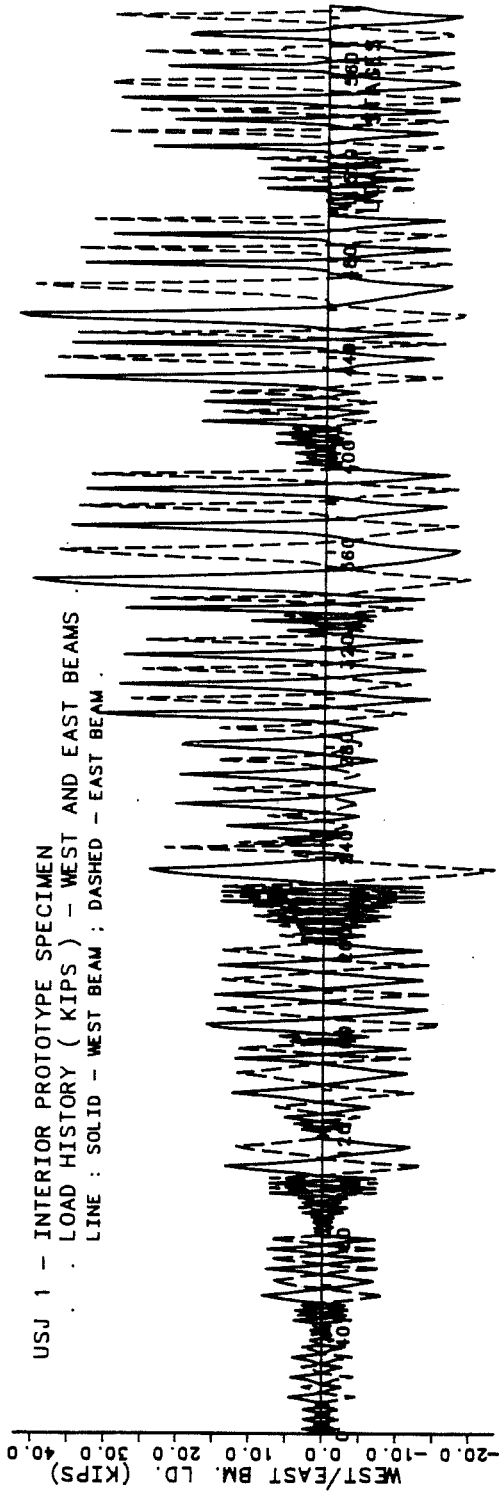


Fig. B.2 - USJ-1 - Load-Deflection Response.

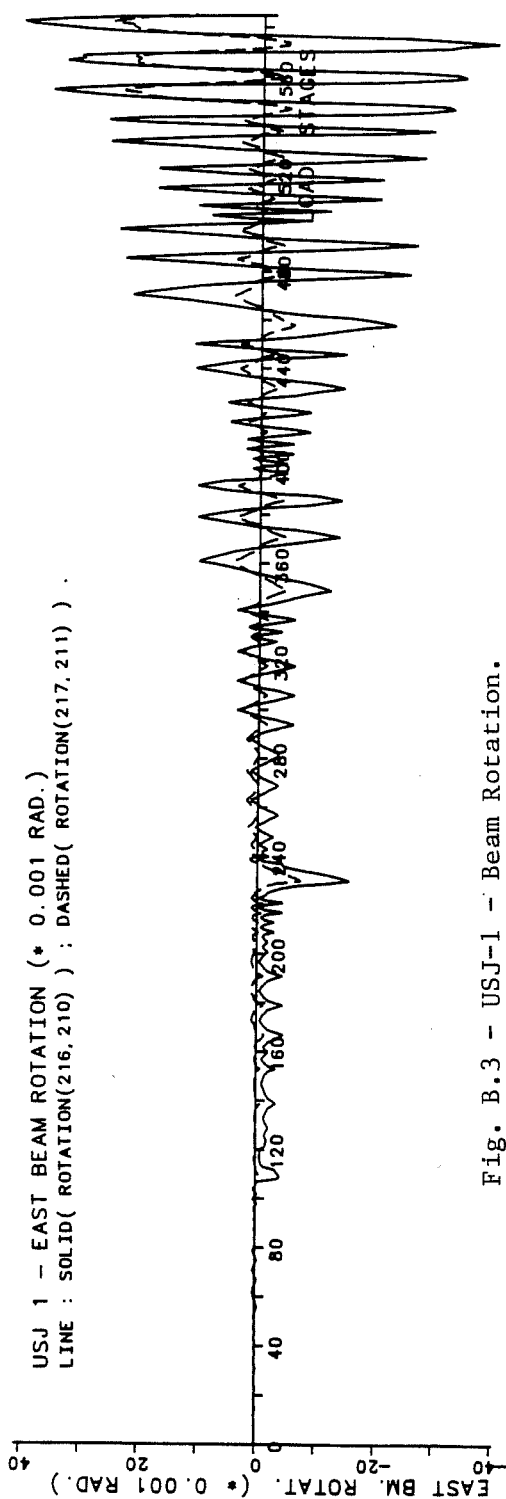
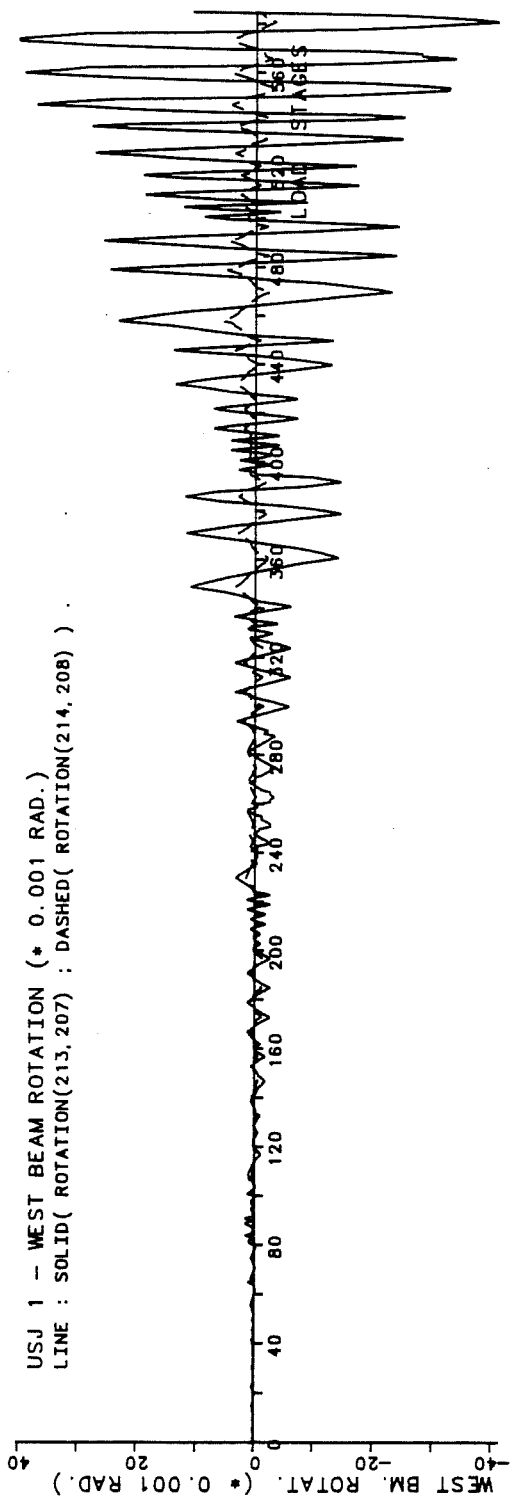


Fig. B.3 - USJ-1 - Beam Rotation.

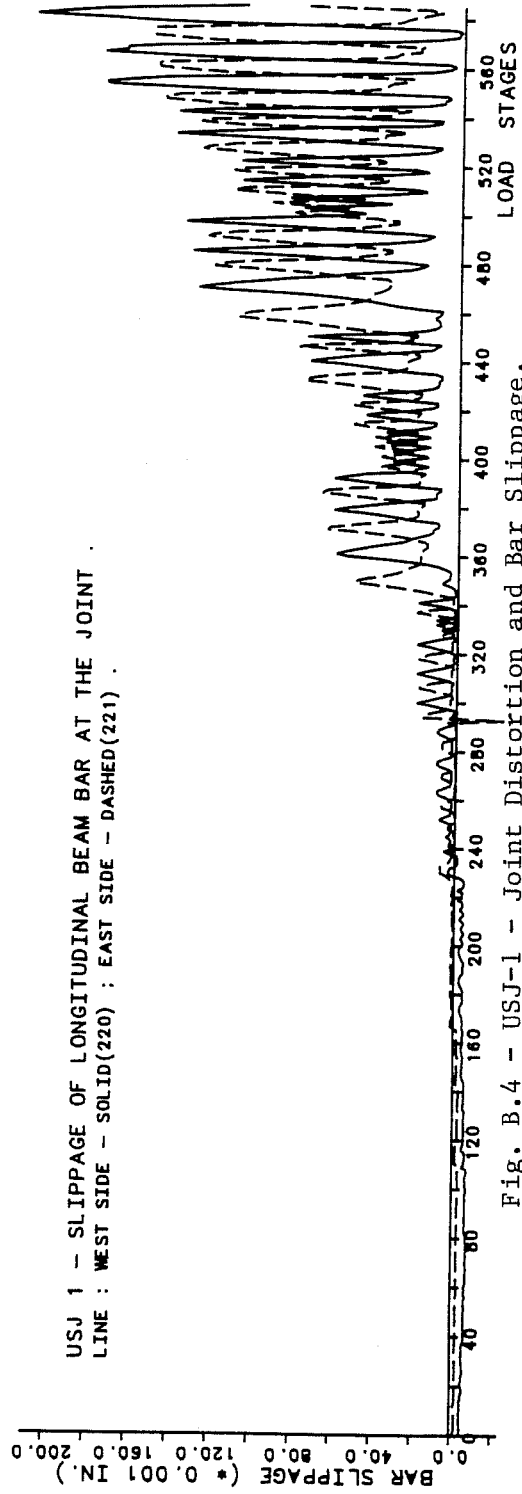
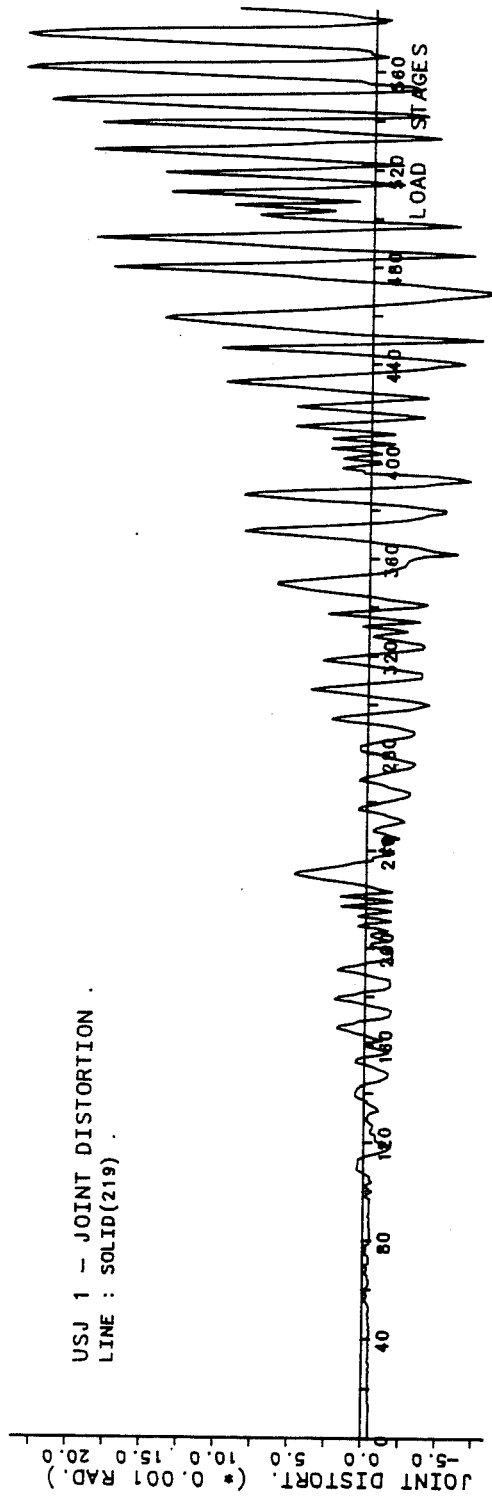


Fig. B.4 - USJ-1 - Joint Distortion and Bar Slippage.

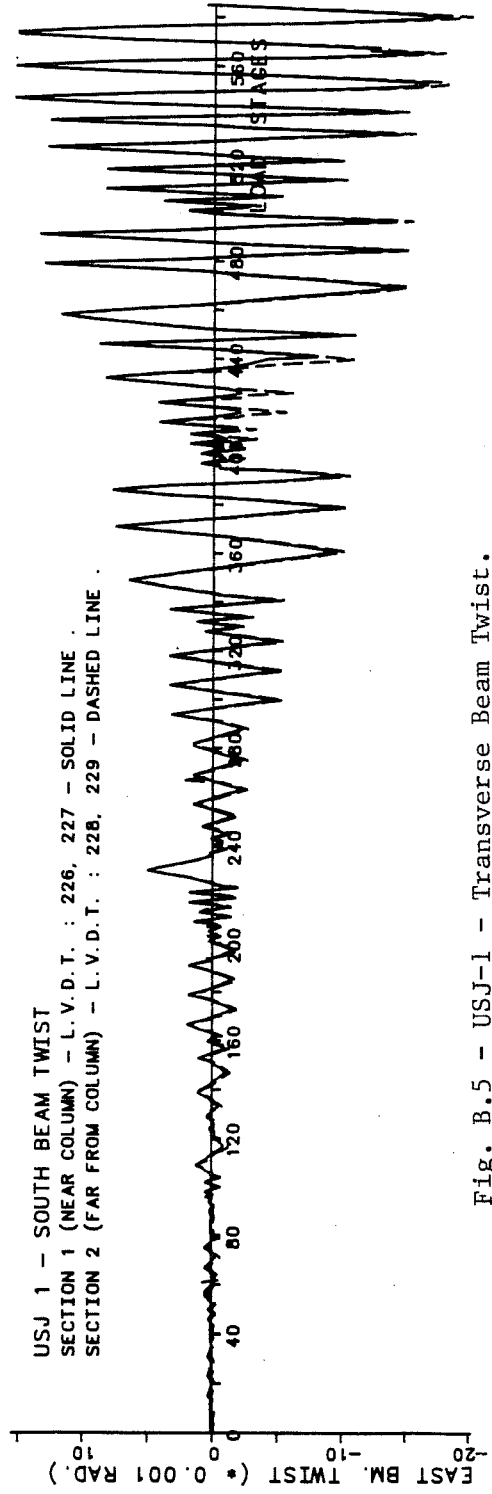
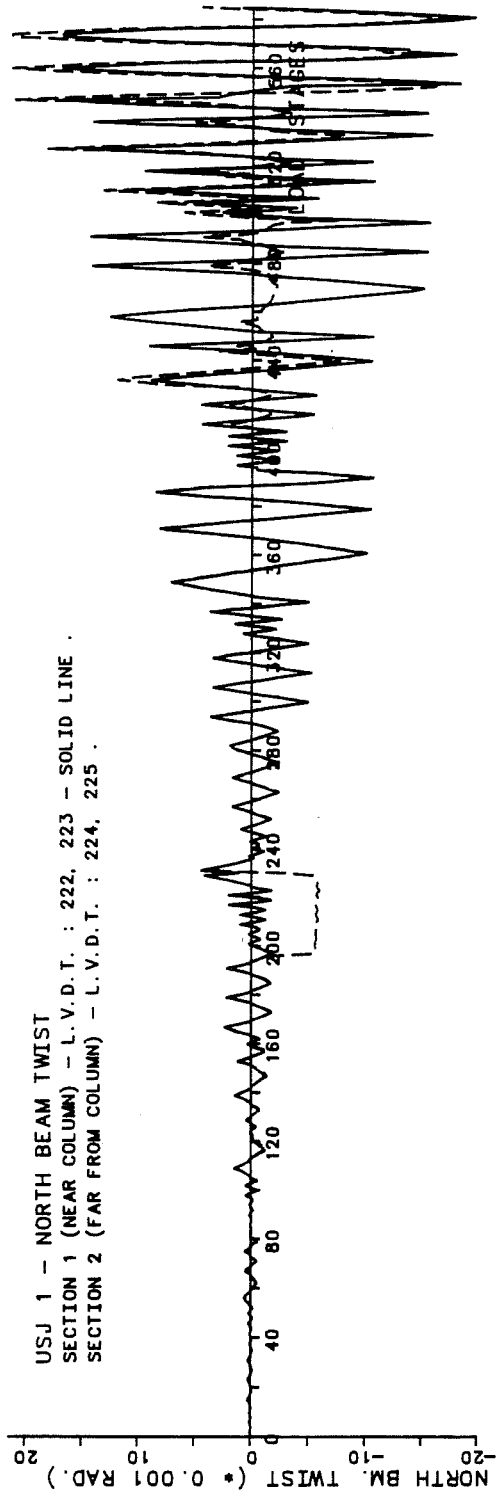


Fig. B.5 - USJ-1 - Transverse Beam Twist.

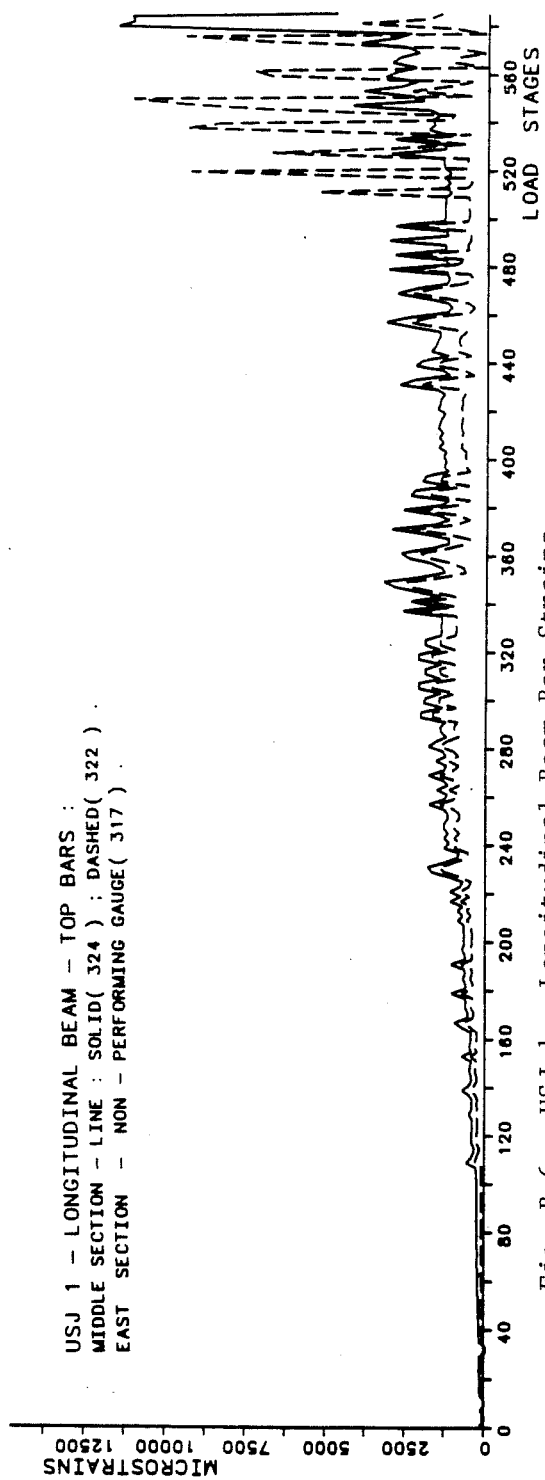
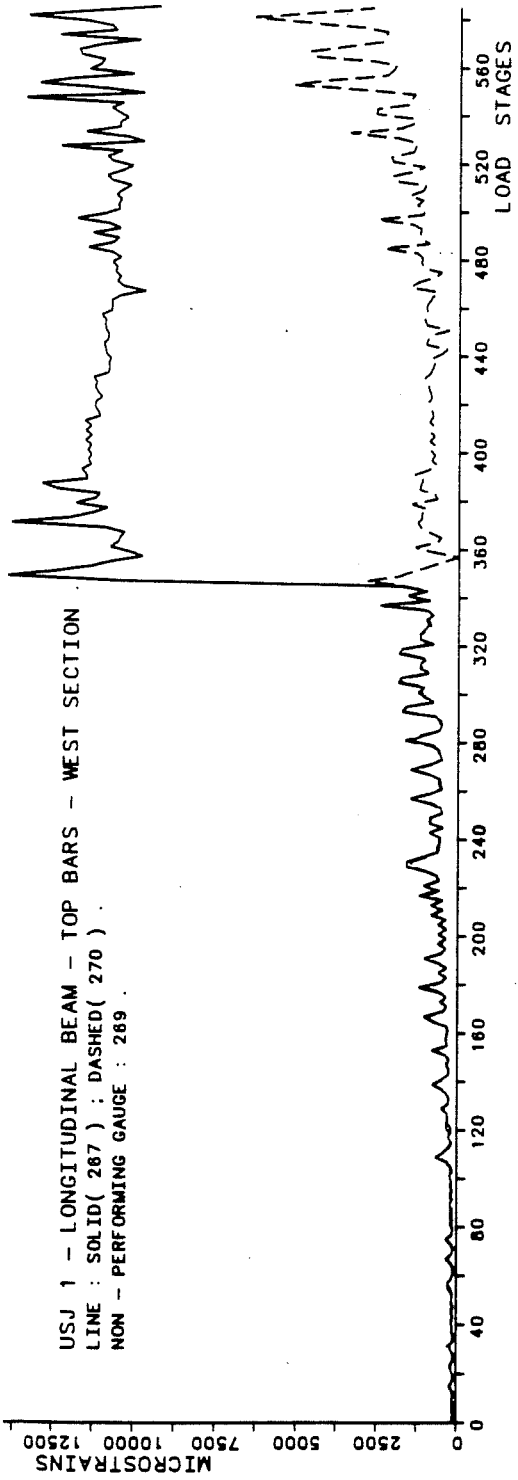


Fig. B.6 - USJ-1 - Longitudinal Beam Bar Strains.

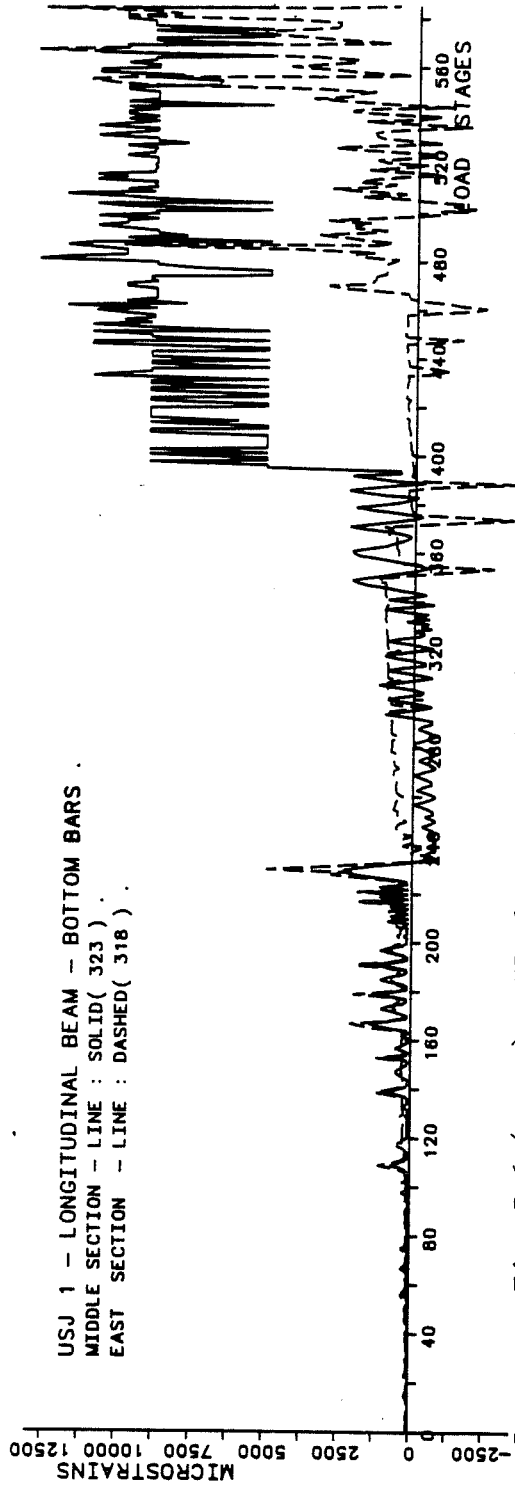
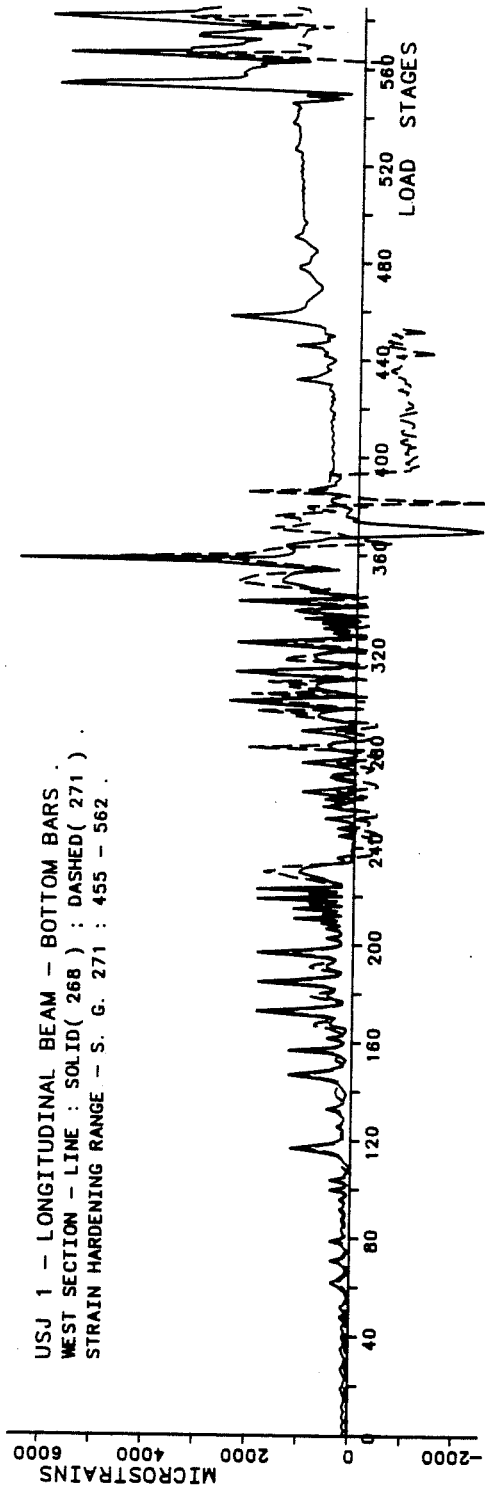


Fig. B.6 (cont.) - USJ-1 - Longitudinal Beam Bar Strains.

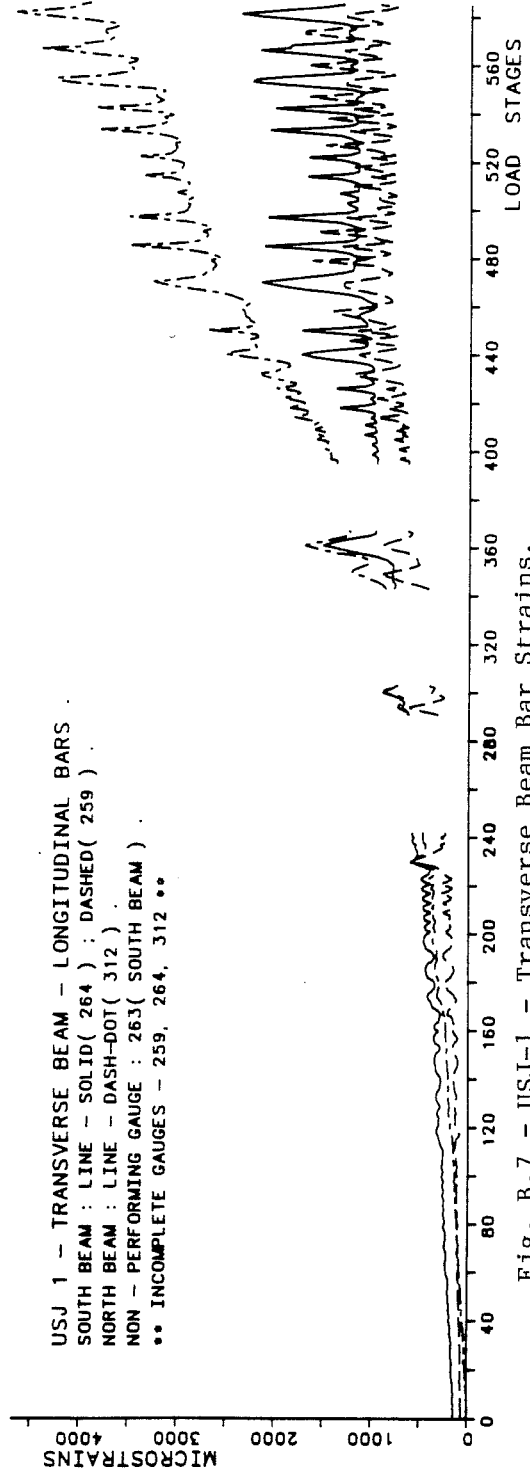
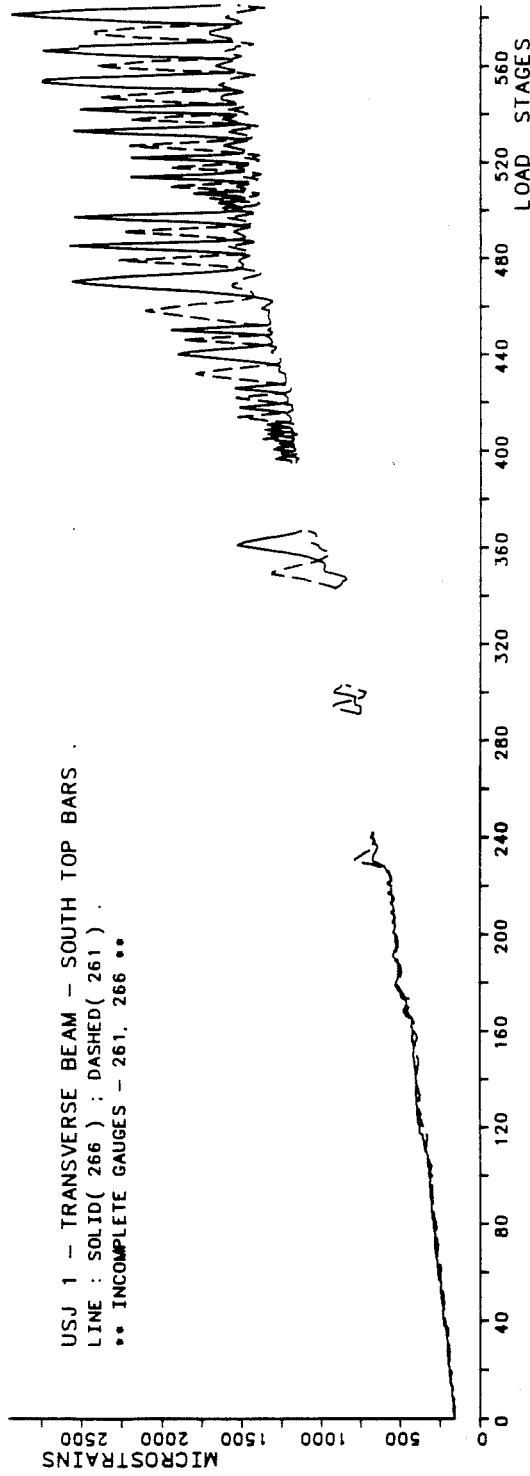


Fig. B.7 - USJ-1 - Transverse Beam Bar Strains.

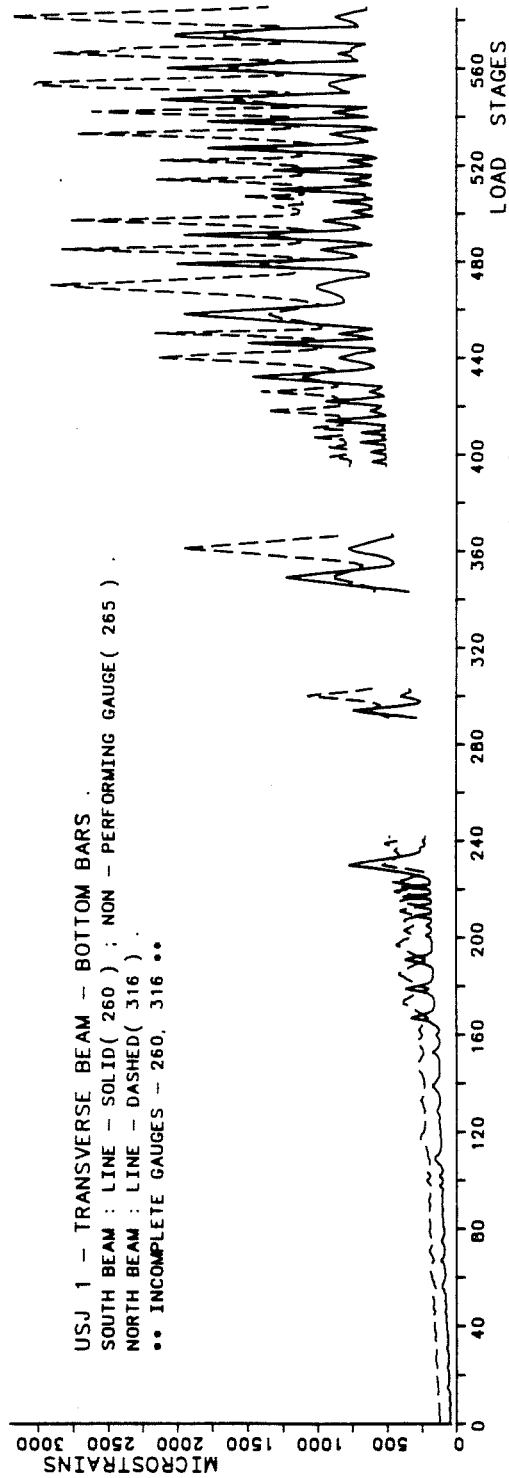
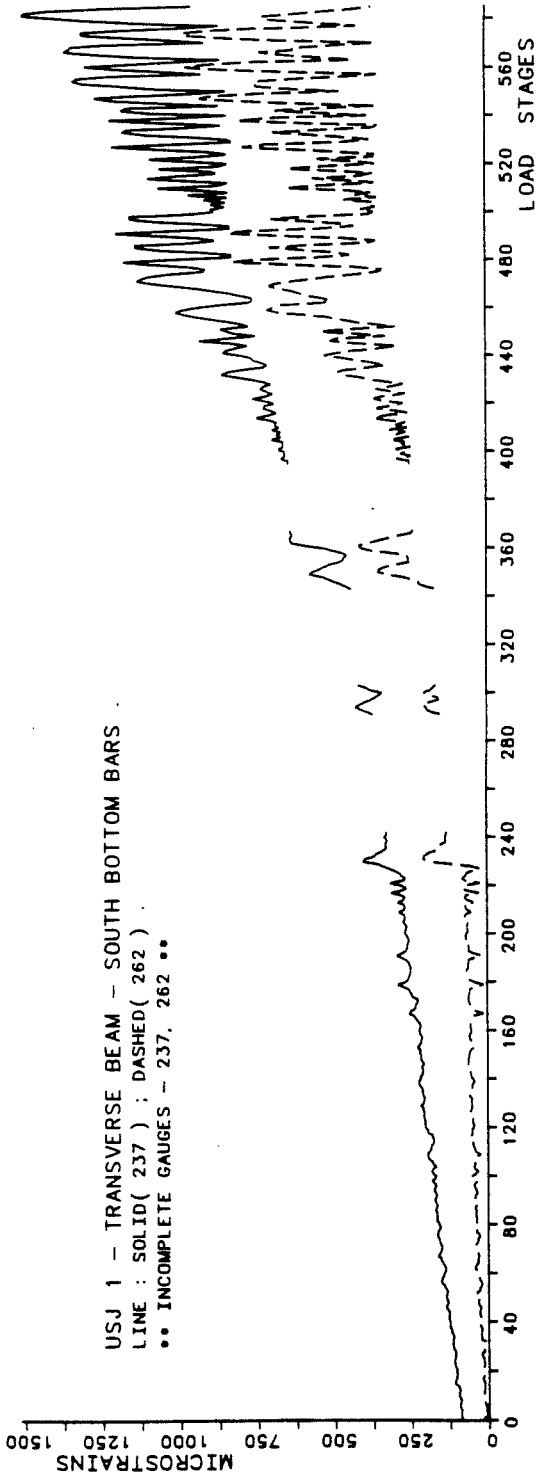


Fig. B.7 (cont.) - USJ-1 - Transverse Beam Bar Strains.

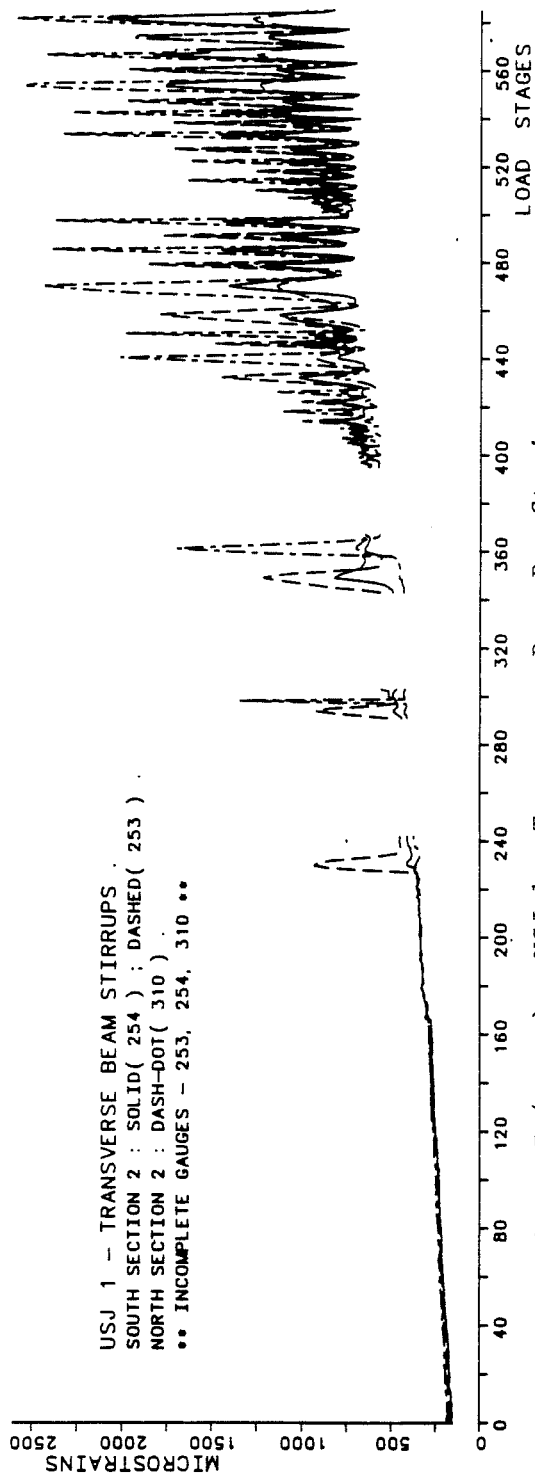
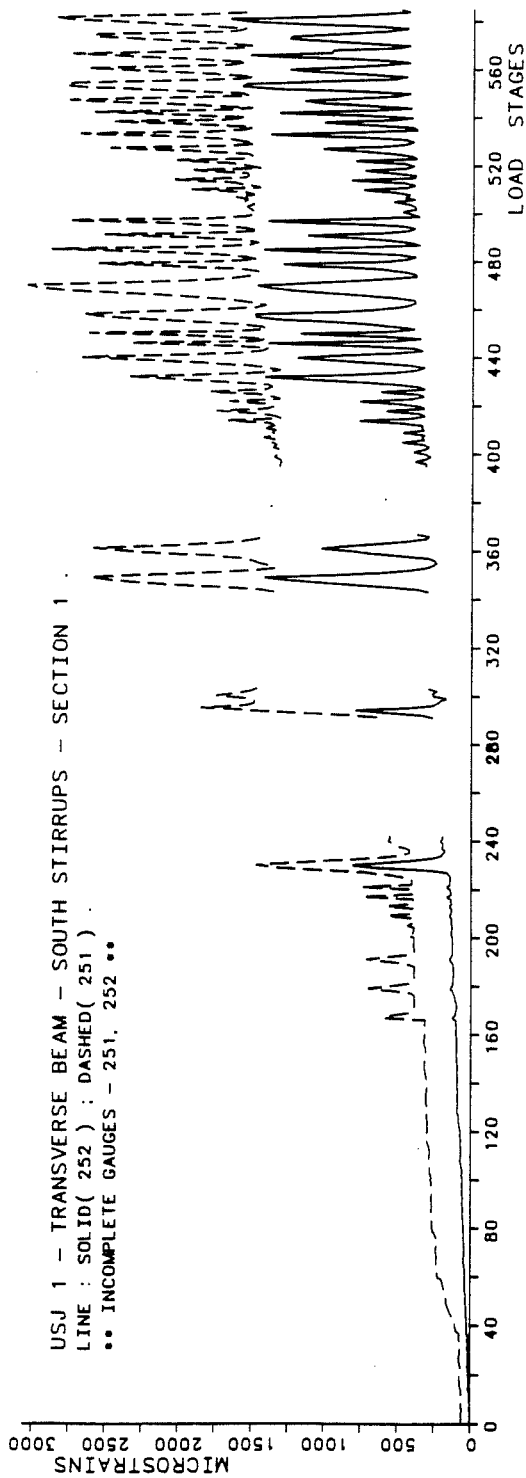


Fig. B.7 (cont.) - USJ-1 - Transverse Beam Bar Strains.

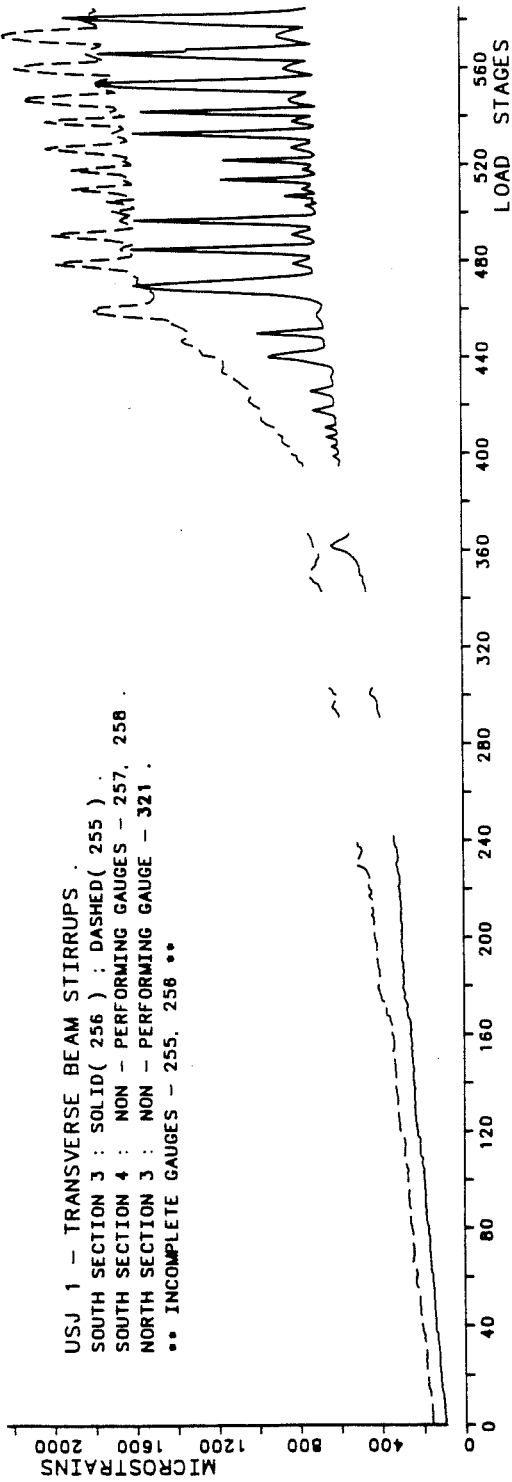


Fig. B.7 (cont.) - Transverse Beam Bar Strains.

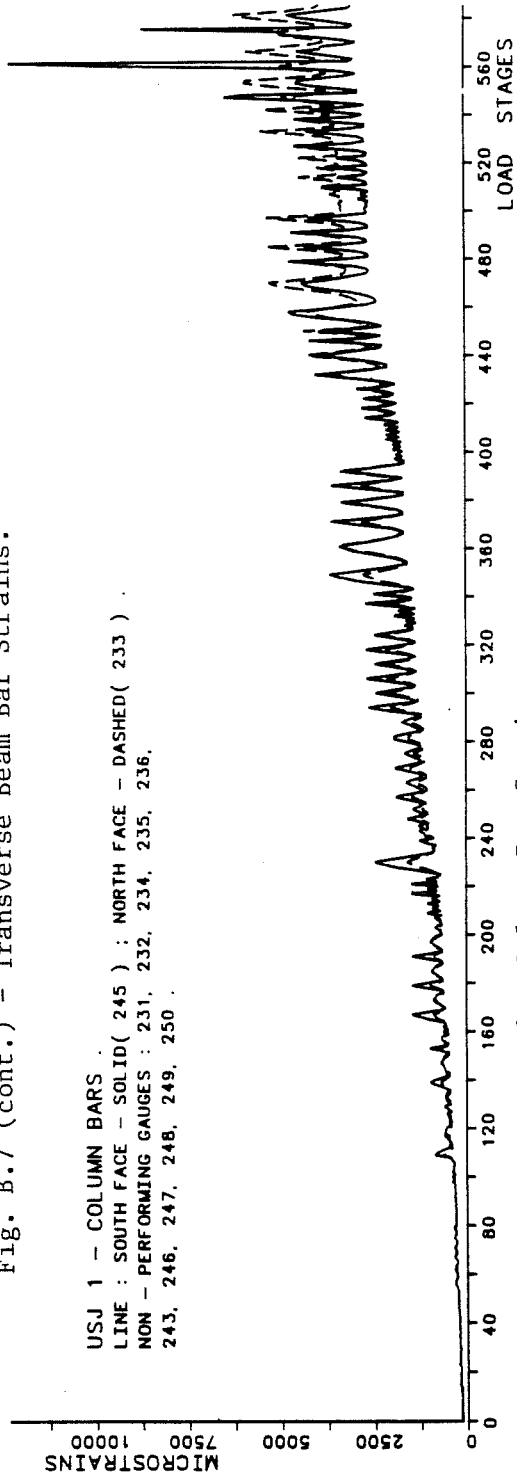


Fig. B.8 - USJ-1 - Column Bar Strains.

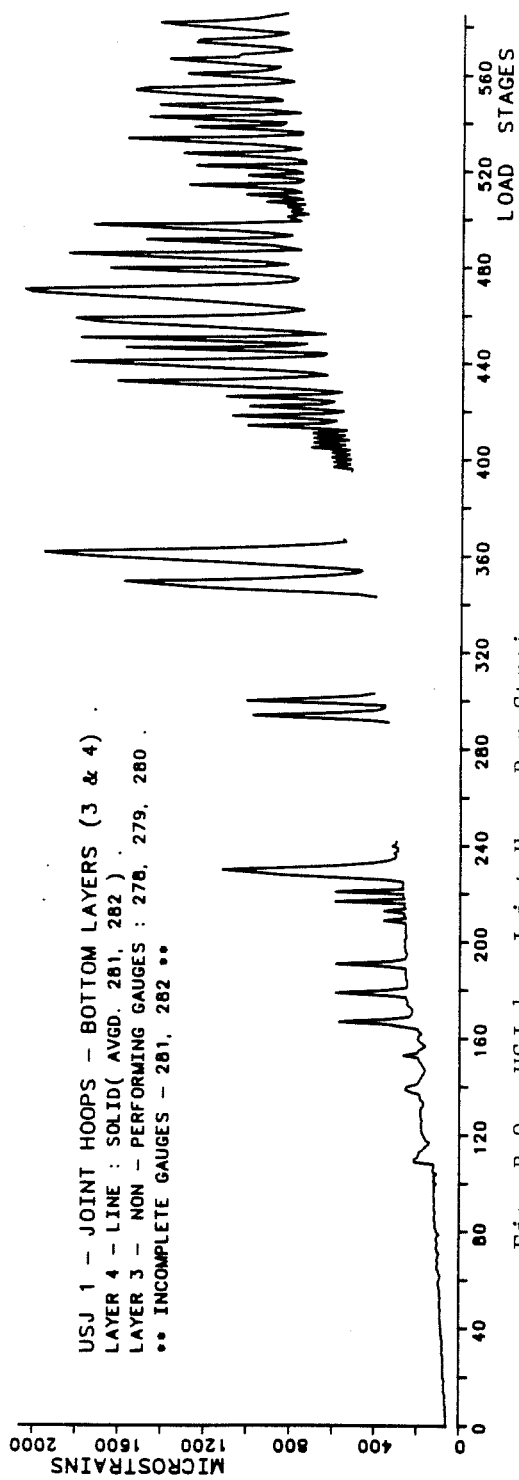
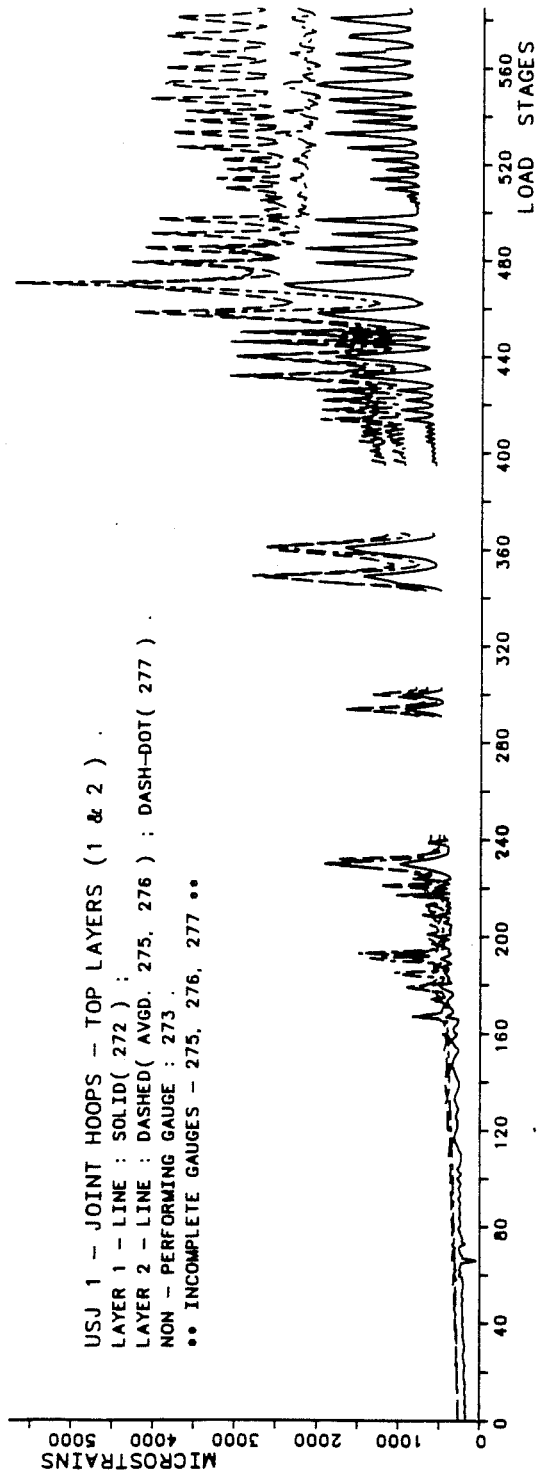


Fig. B.9 - USJ-1 - Joint Hoop Bar Strains.

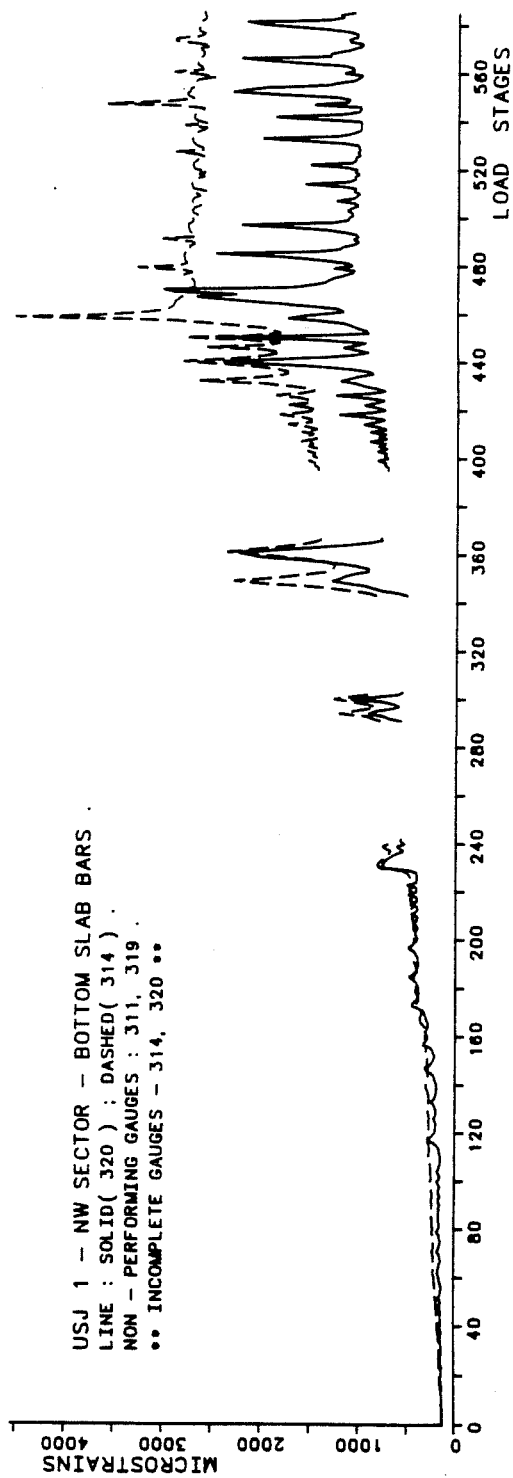
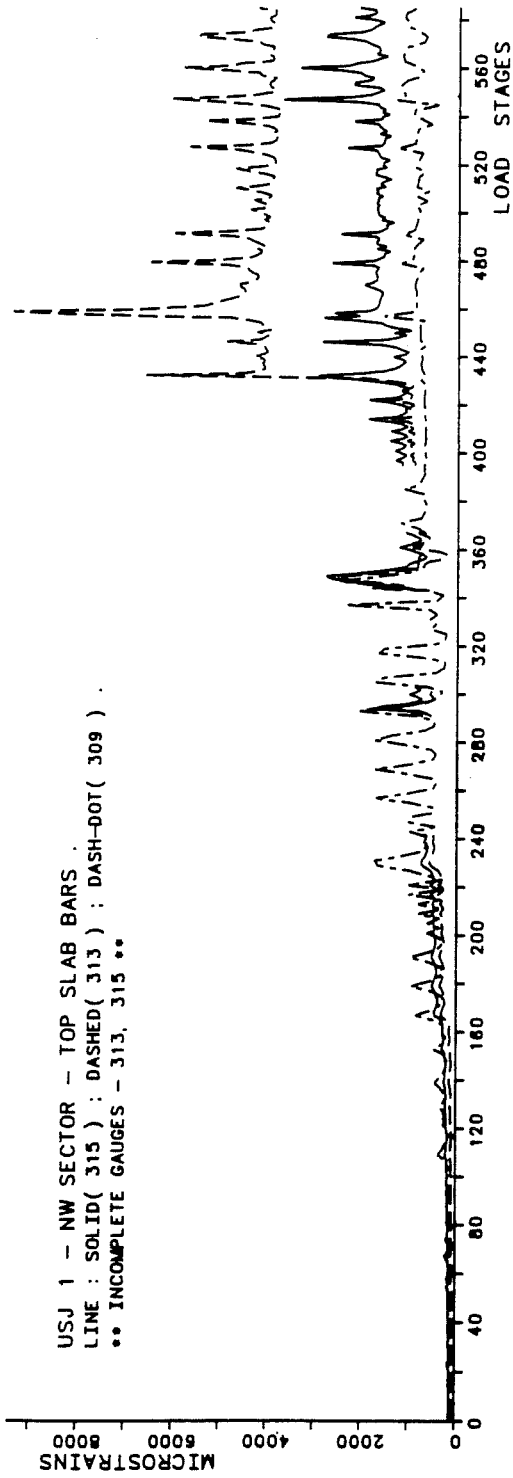


Fig. B.10 - USJ-1 - Slab Bar Strains.

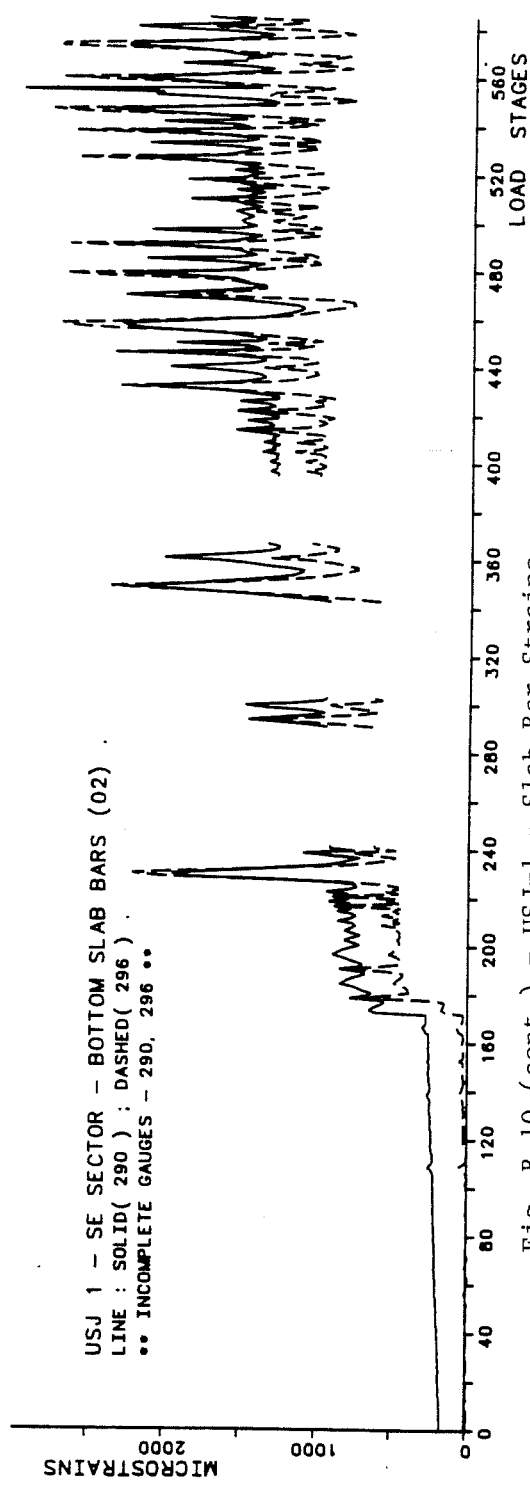
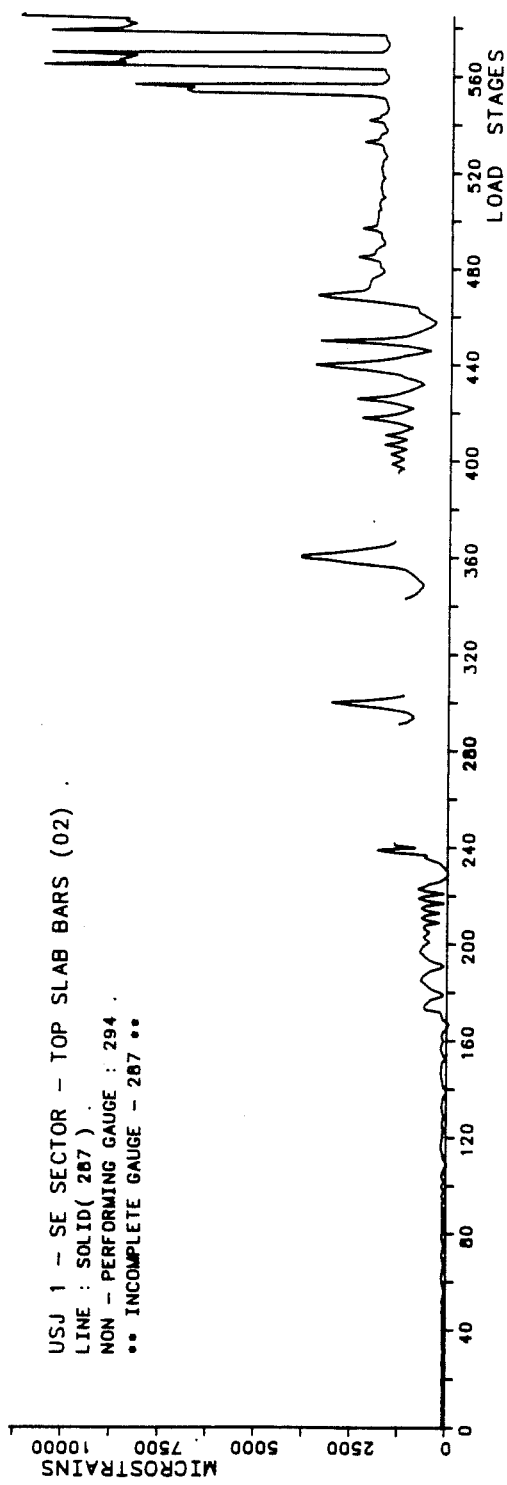


Fig. B.10 (cont.) - USJ-1 - Slab Bar Strains.

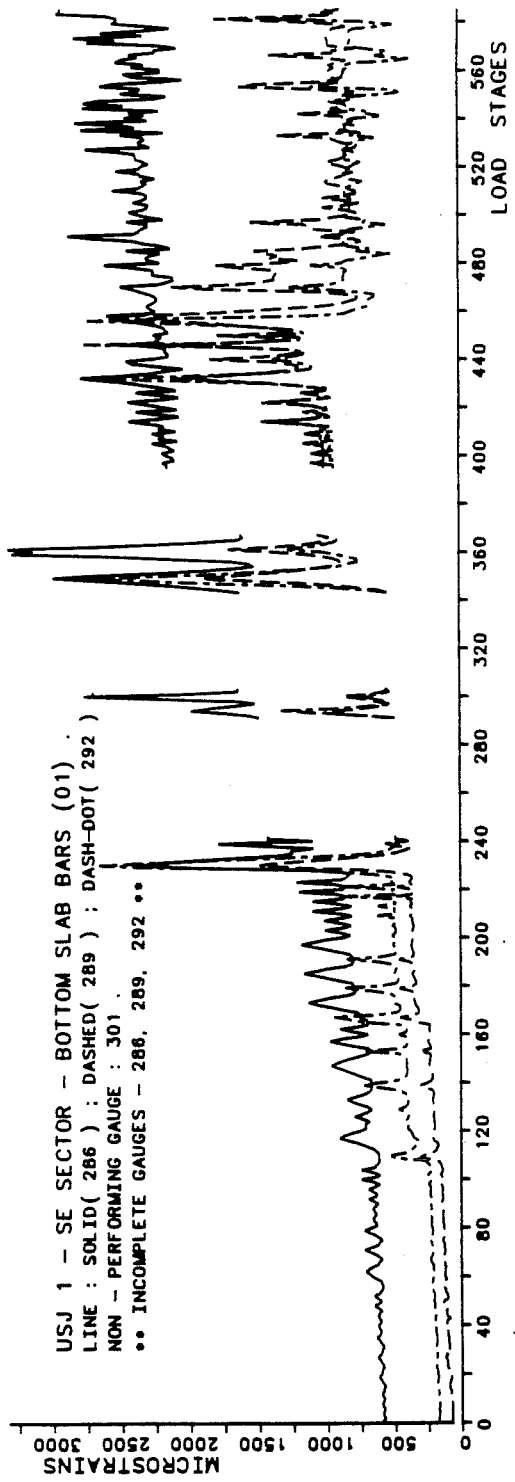
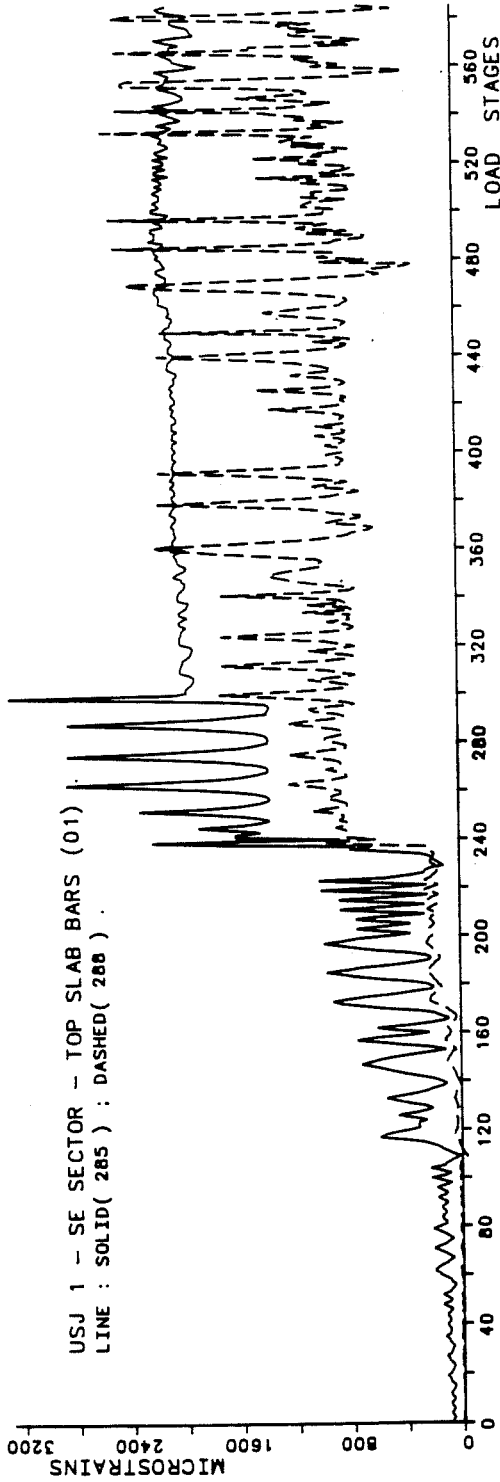


Fig. B.10(cont.) - USJ-1 - Slab Bar Strains

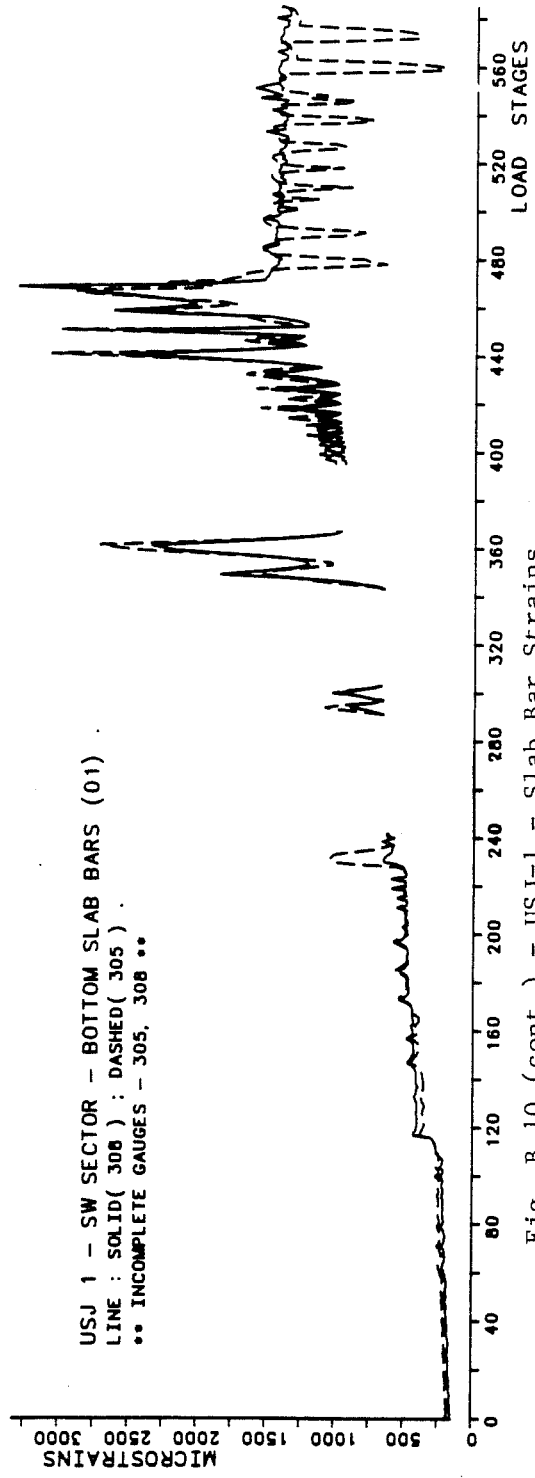
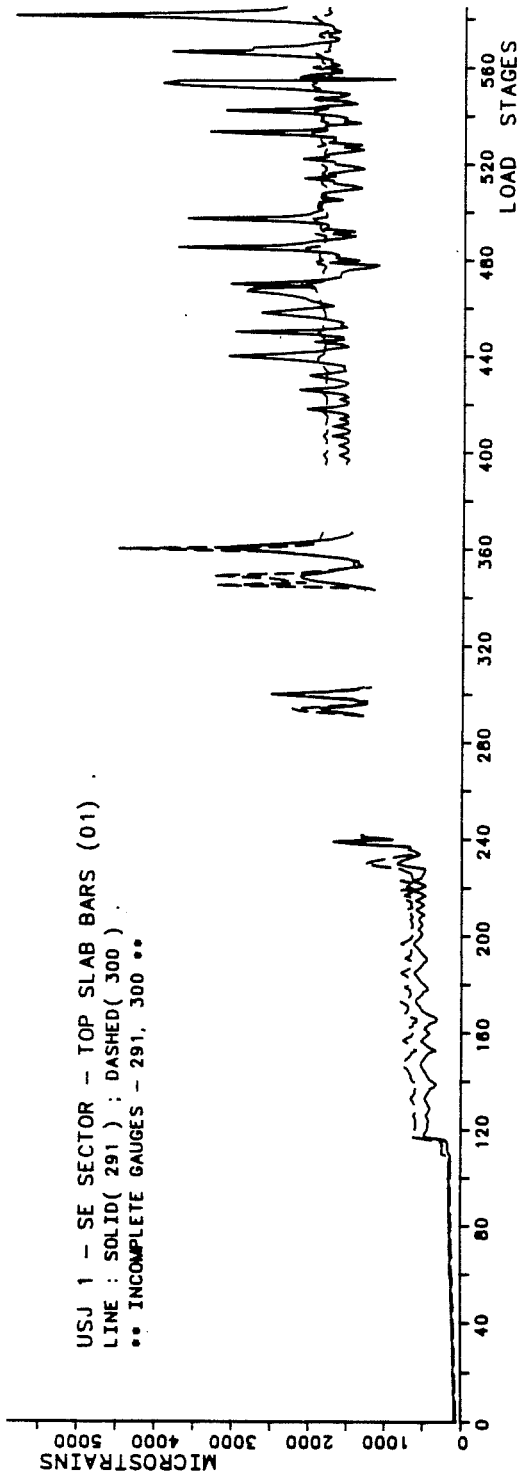


Fig. B.10 (cont.) - USJ-1 - Slab Bar Strains.

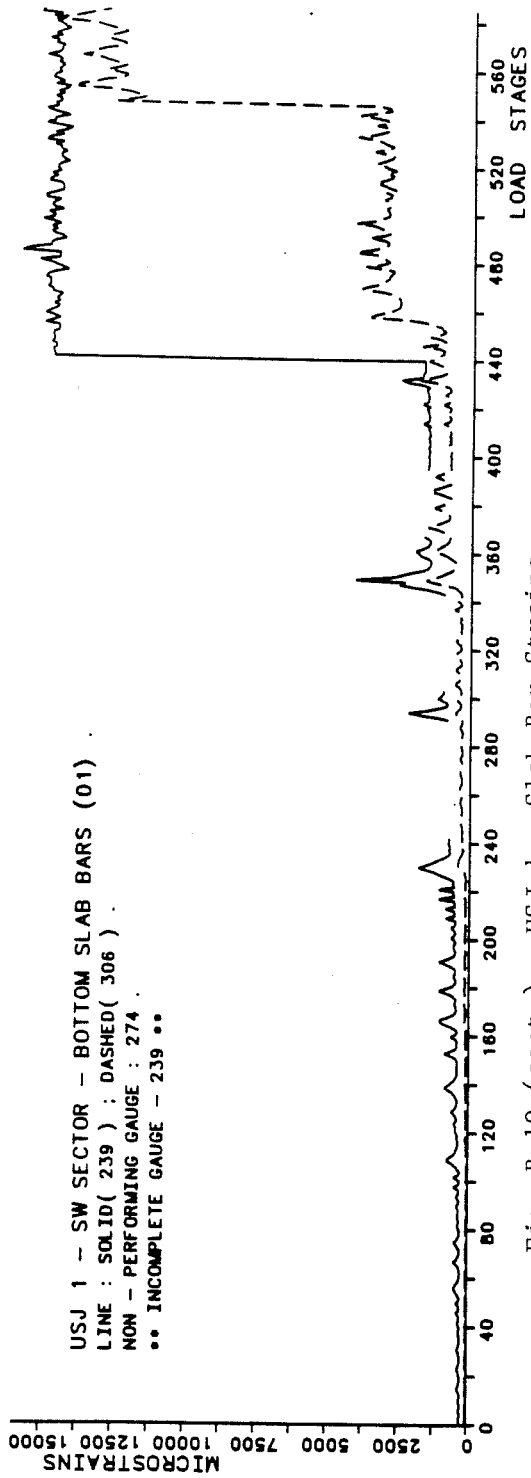
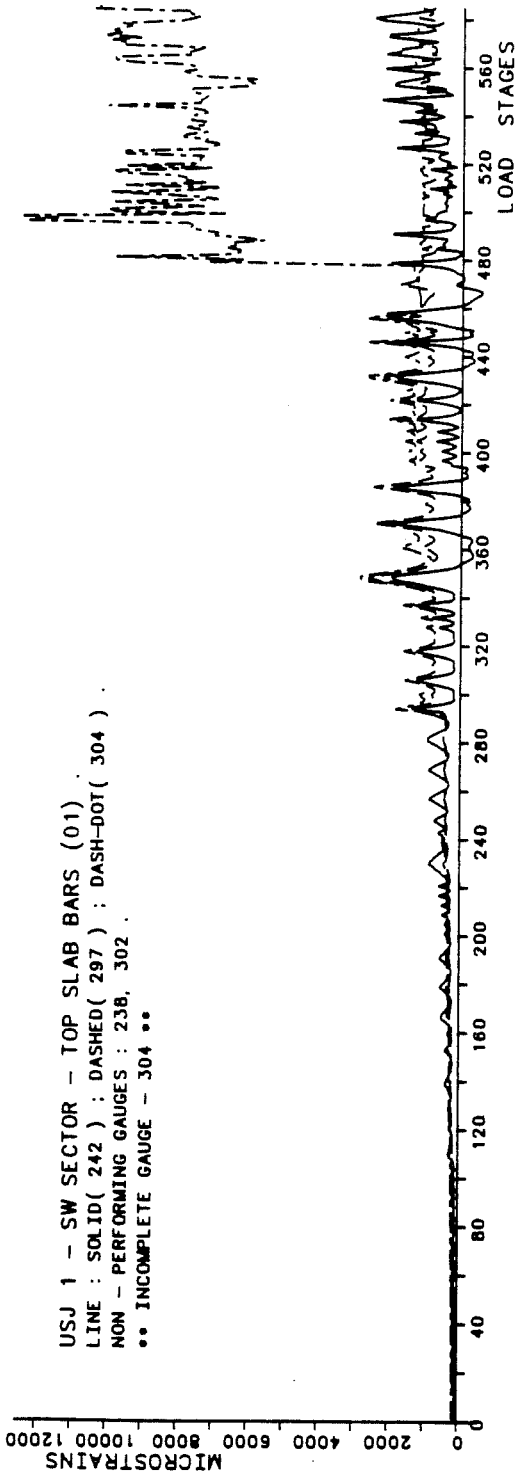


Fig. B.10 (cont.) - USJ-1 - Slab Bar Strains.

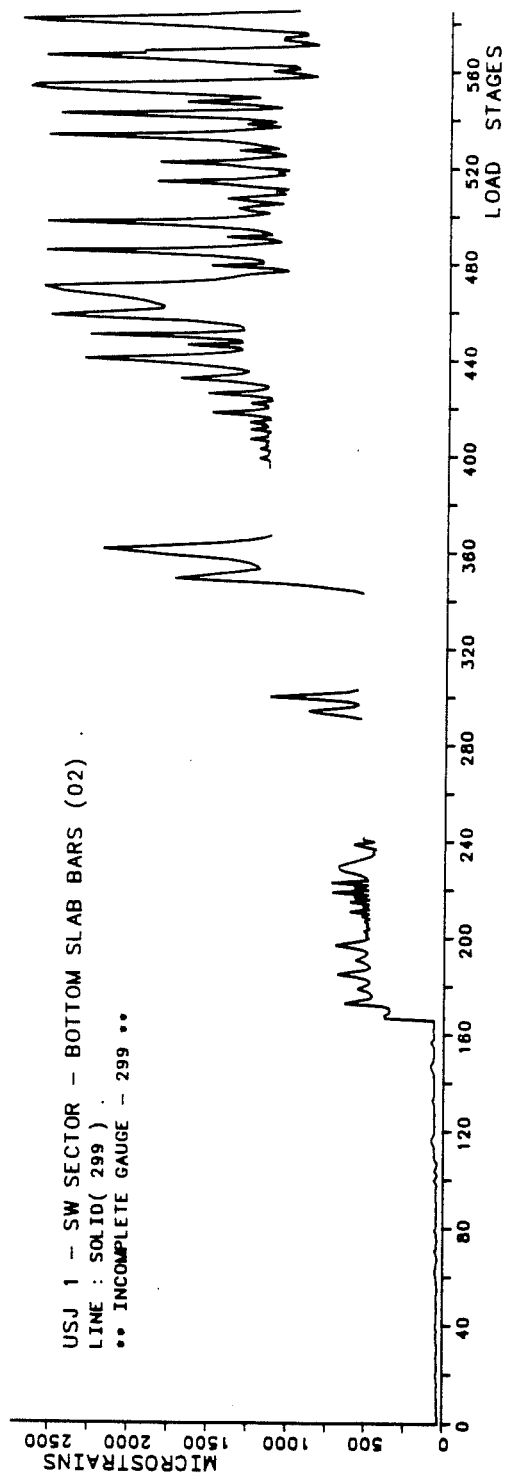
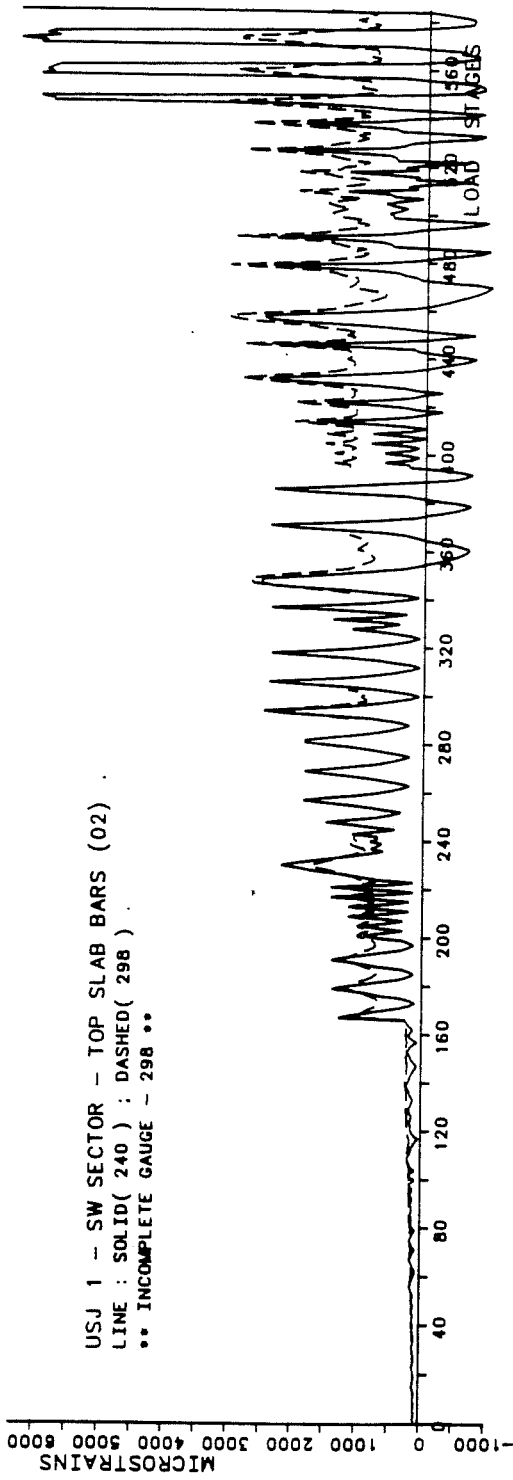
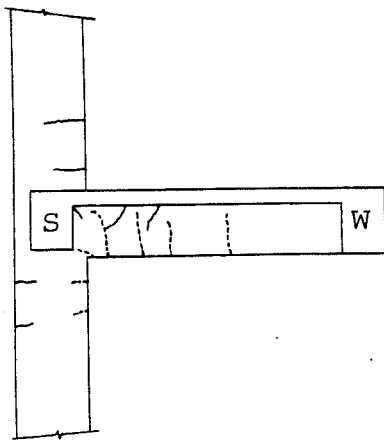


Fig. B.10 (cont.) - USJ-1 - Slab Bar Strains.

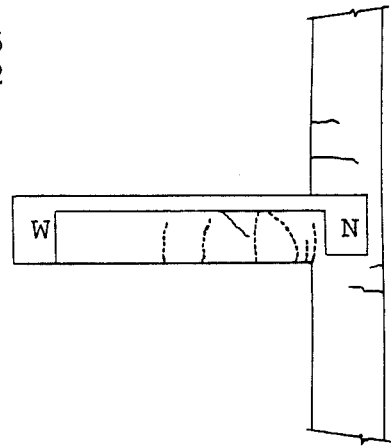
USJ - 2

R = + 1/185

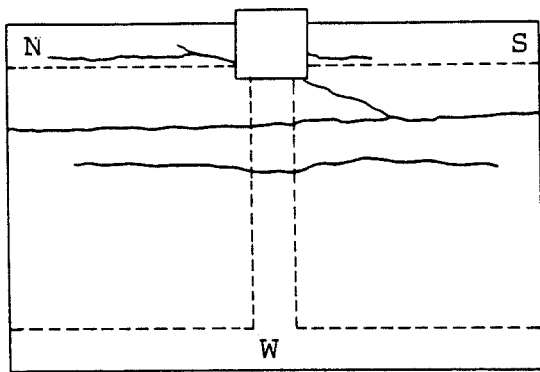
R = - 1/192



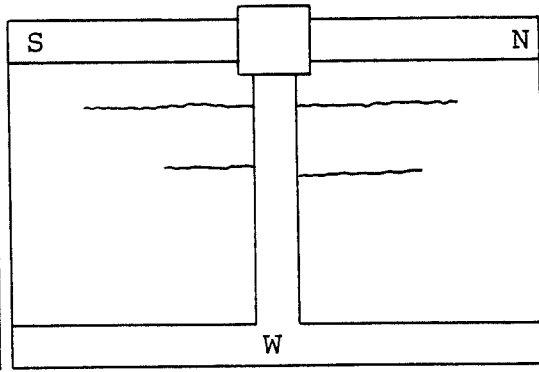
a. South Elevation.



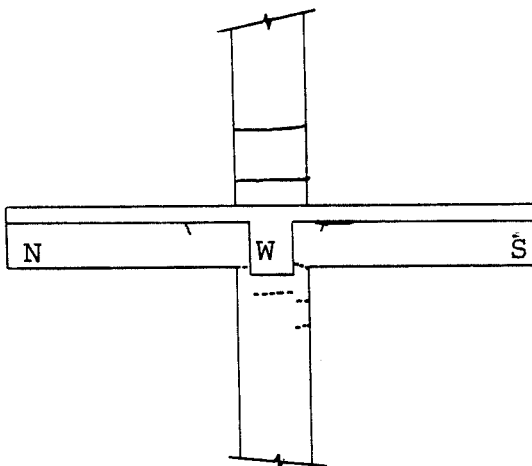
b. North Elevation.



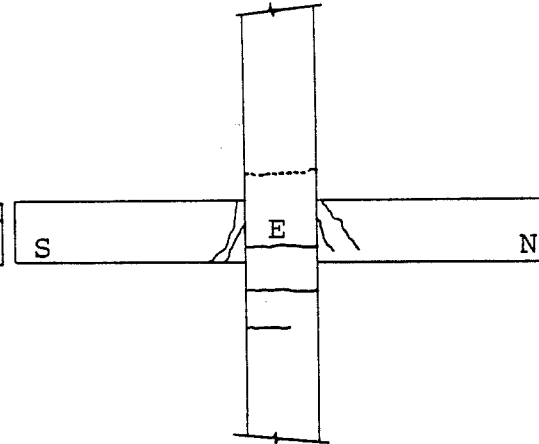
c. Top View.



d. Bottom View.



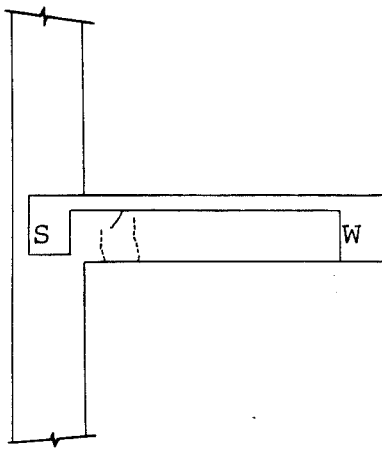
e. West Elevation.



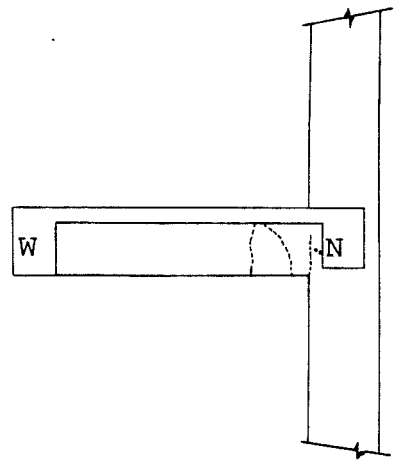
f. East Elevation.

Fig. B.11 (cont.) - USJ-2 - Cracking Patterns.

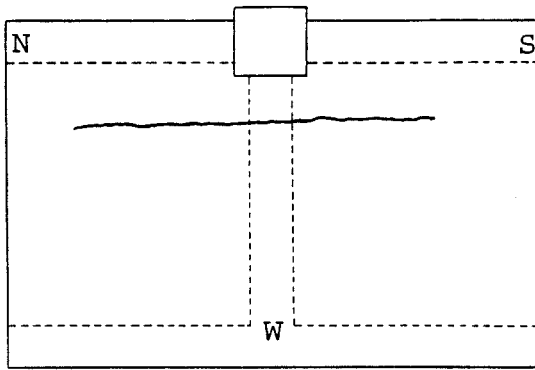
USJ - 2
R = + 1/385
R = - 1/370



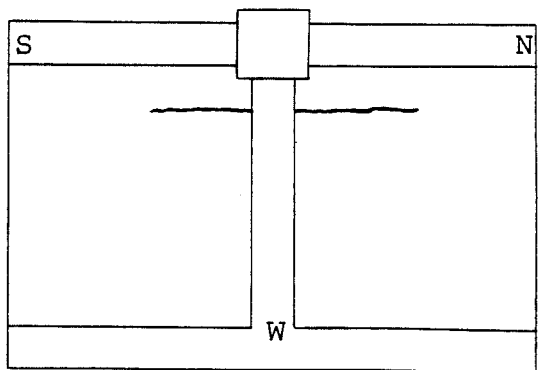
a. South Elevation.



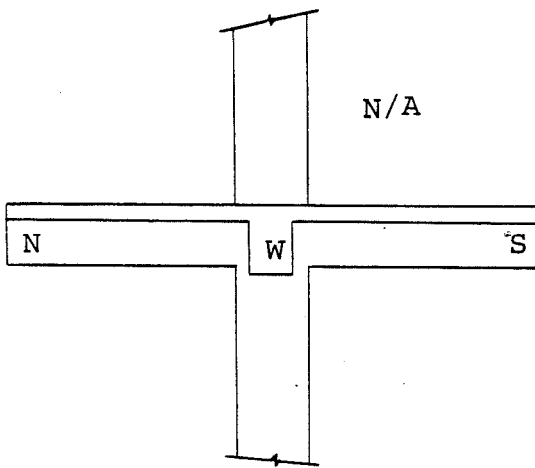
b. North Elevation.



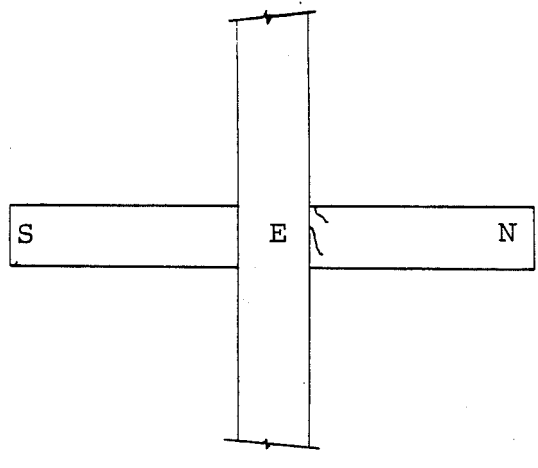
c. Top View.



d. Bottom View.



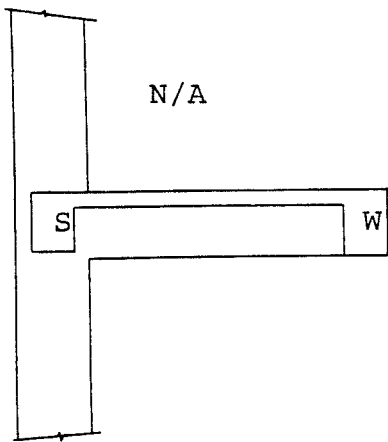
e. West Elevation.



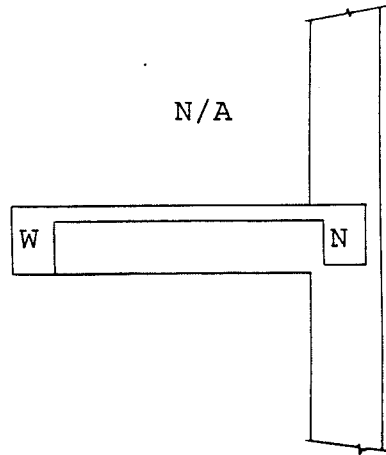
f. East Elevation.

Fig. B.11 - USJ-2 - Cracking Patterns.

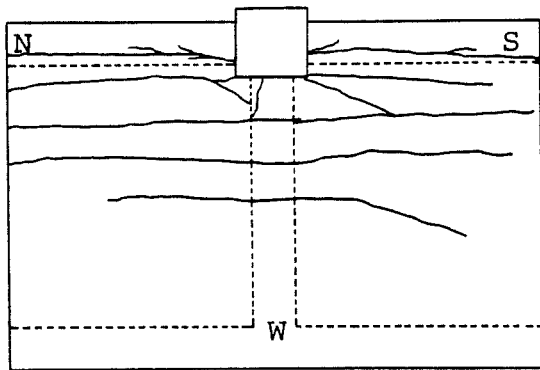
USJ - 2
R = + 1/80
R = - 1/79



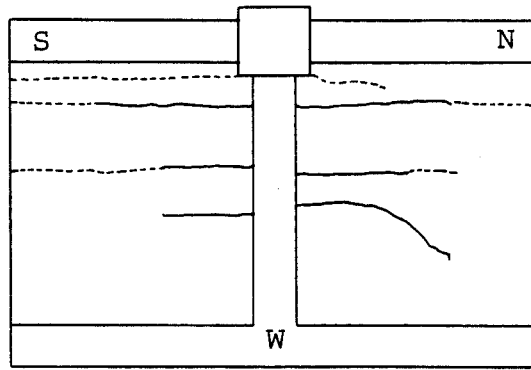
a. South Elevation.



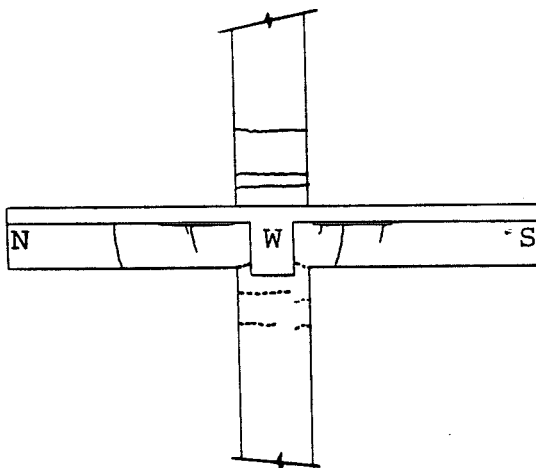
b. North Elevation.



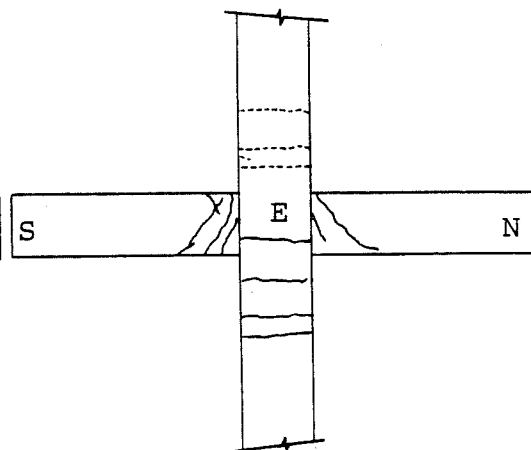
c. Top View.



d. Bottom View.



e. West Elevation.



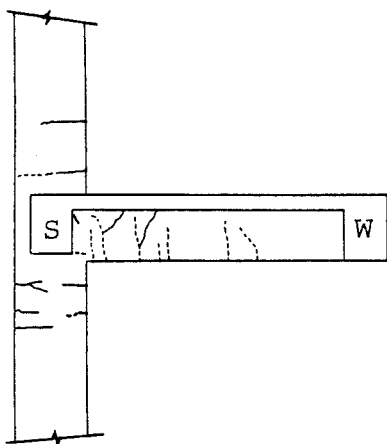
f. East Elevation.

Fig. B.11 (cont.) - USJ-2 - Cracking Patterns.

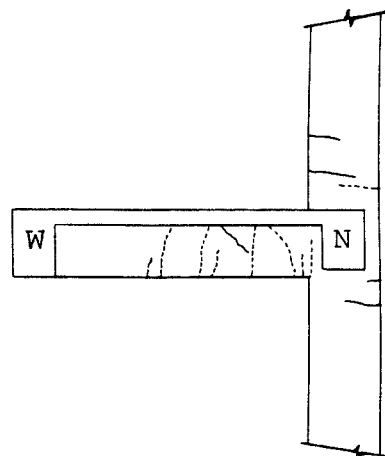
USJ - 2

R = + 1/123

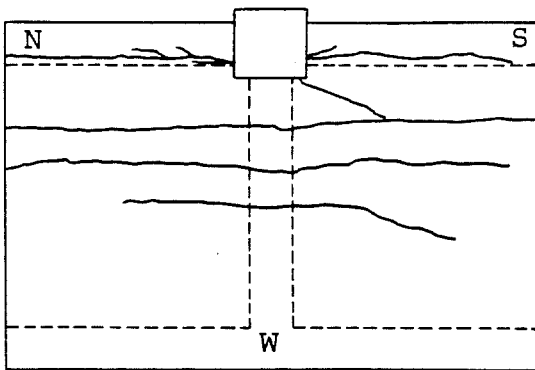
R = - 1/127



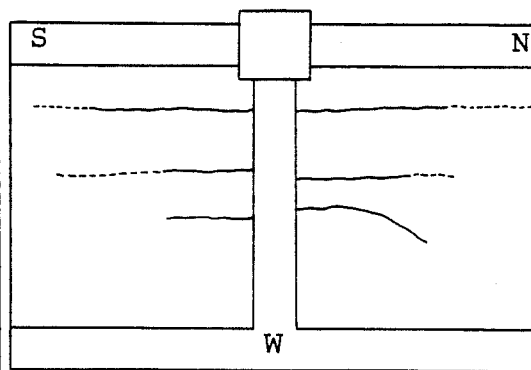
a. South Elevation.



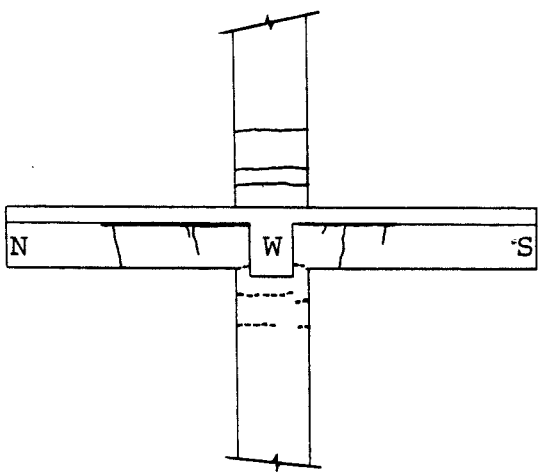
b. North Elevation.



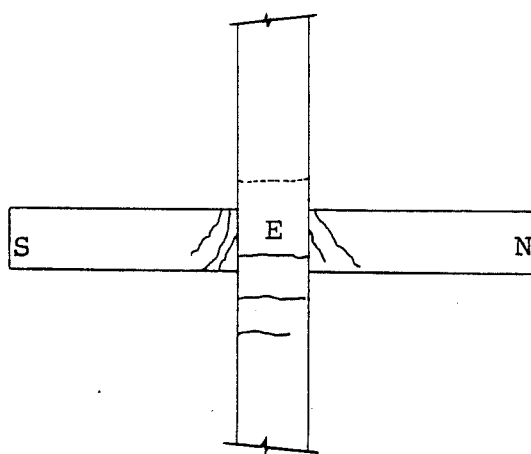
c. Top View.



d. Bottom View.



e. West Elevation.



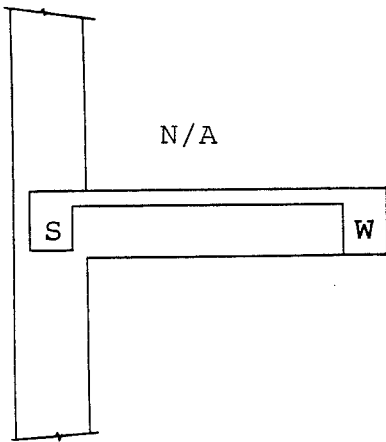
f. East Elevation.

Fig. B.11 (cont.) - USJ-2 - Cracking Patterns.

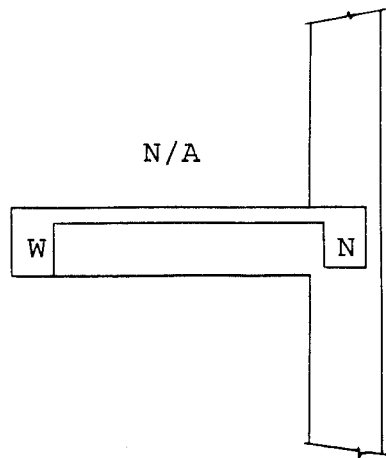
USJ - 2

R = + 1/26

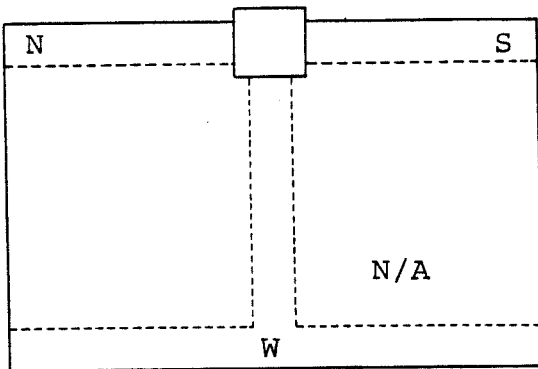
R = - 1/27



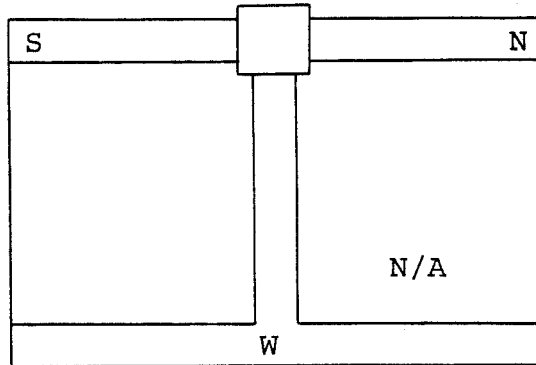
a. South Elevation



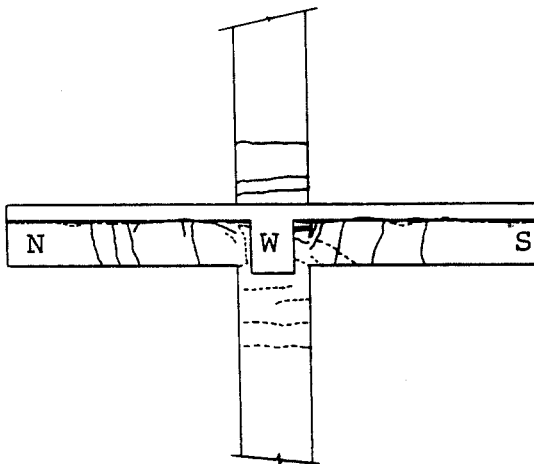
b. North Elevation.



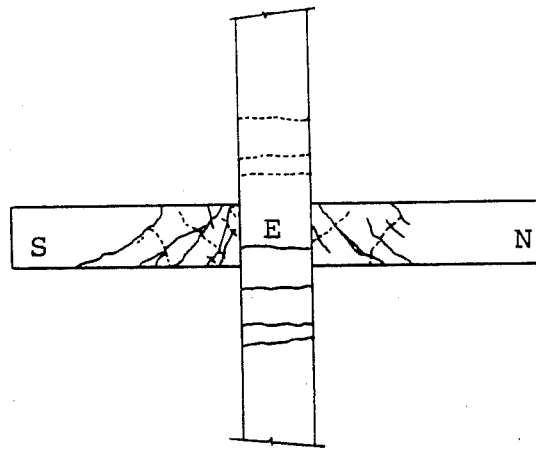
c. Top View.



d. Bottom View.



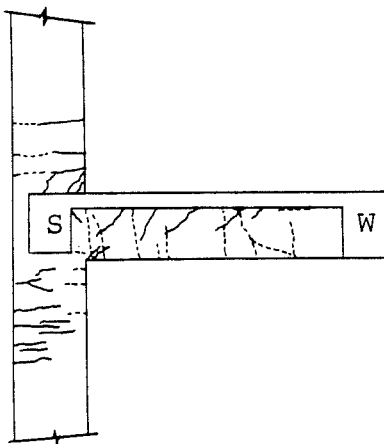
e. West Elevation.



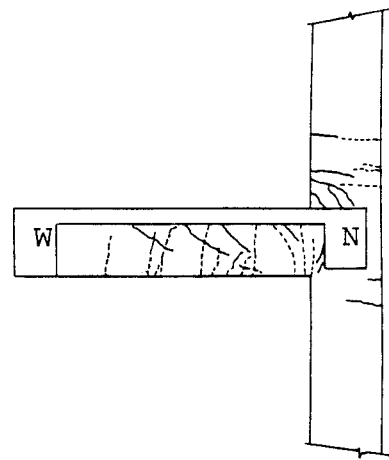
f. East Elevation.

Fig. B.11 (cont.) - USJ-2 - Cracking Patterns.

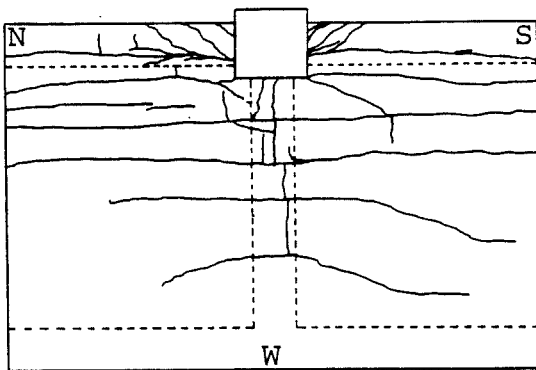
USJ - 2
 R = + 1/39
 R = - 1/41



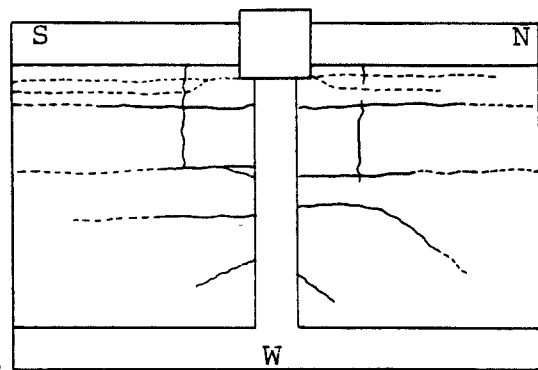
a. South Elevation.



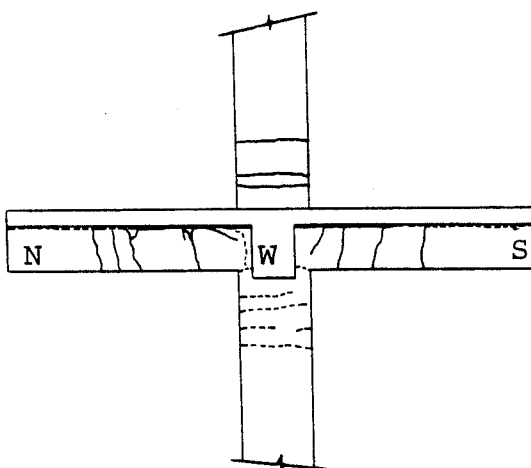
b. North Elevation.



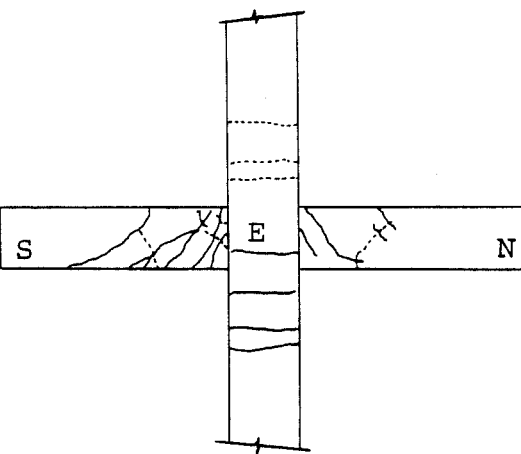
c. Top View.



d. Bottom View.



e. West Elevation



f. East Elevation.

Fig. B.11 (cont.) - USJ-2 - Cracking Patterns.

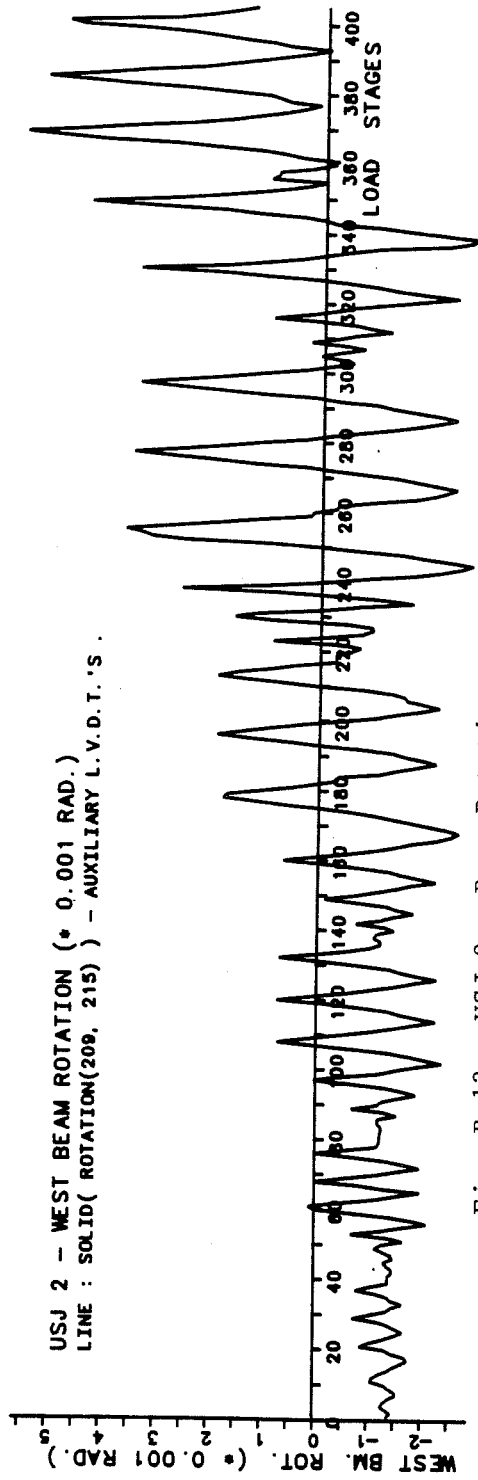
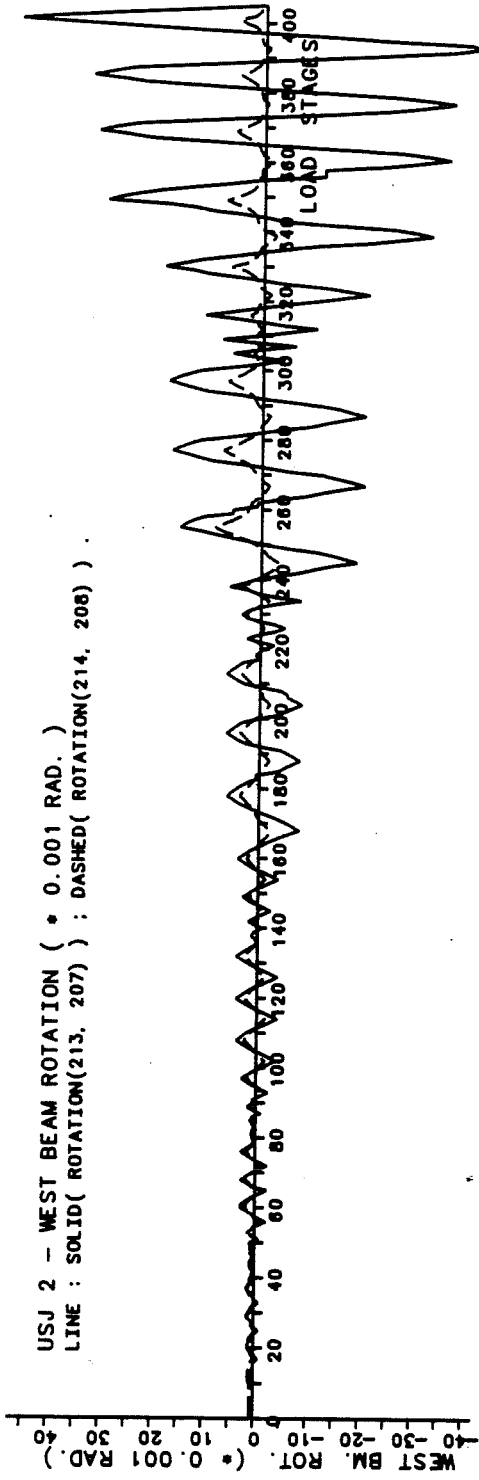


Fig. B.13 - USJ-2 - Beam Rotation.

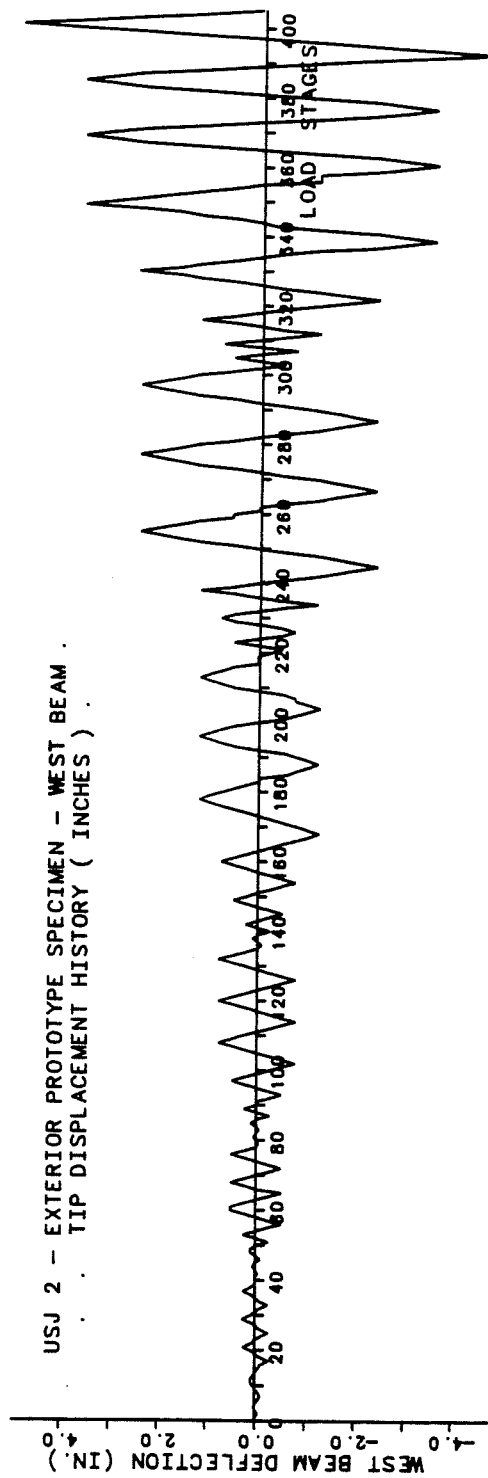
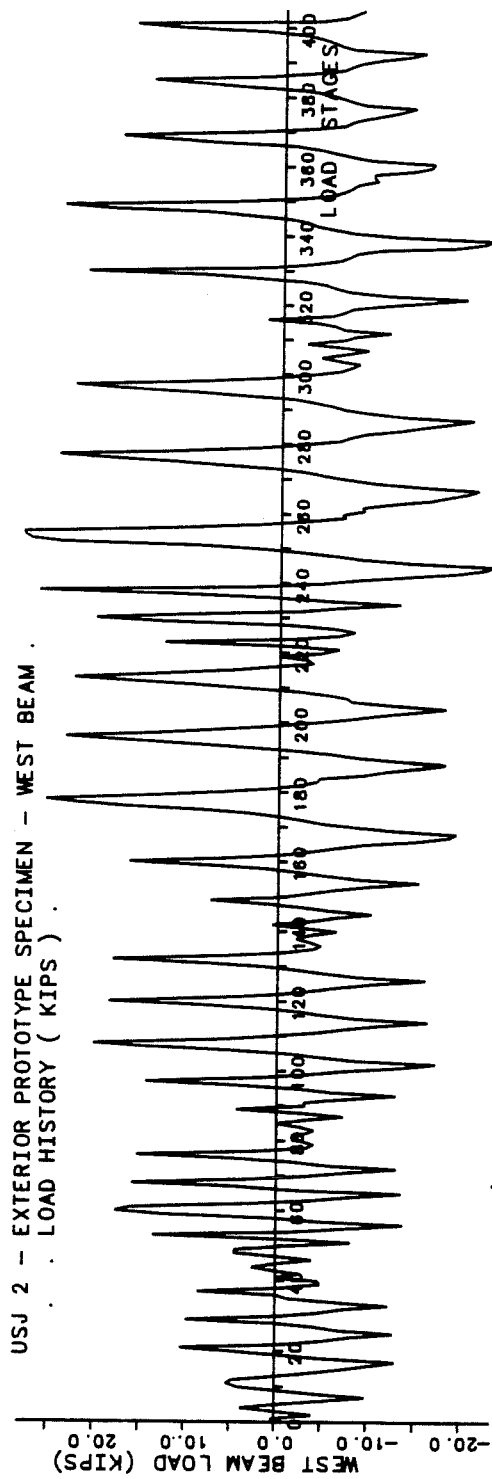


Fig. B.12 - USJ-2 - Load-Deflection Response.

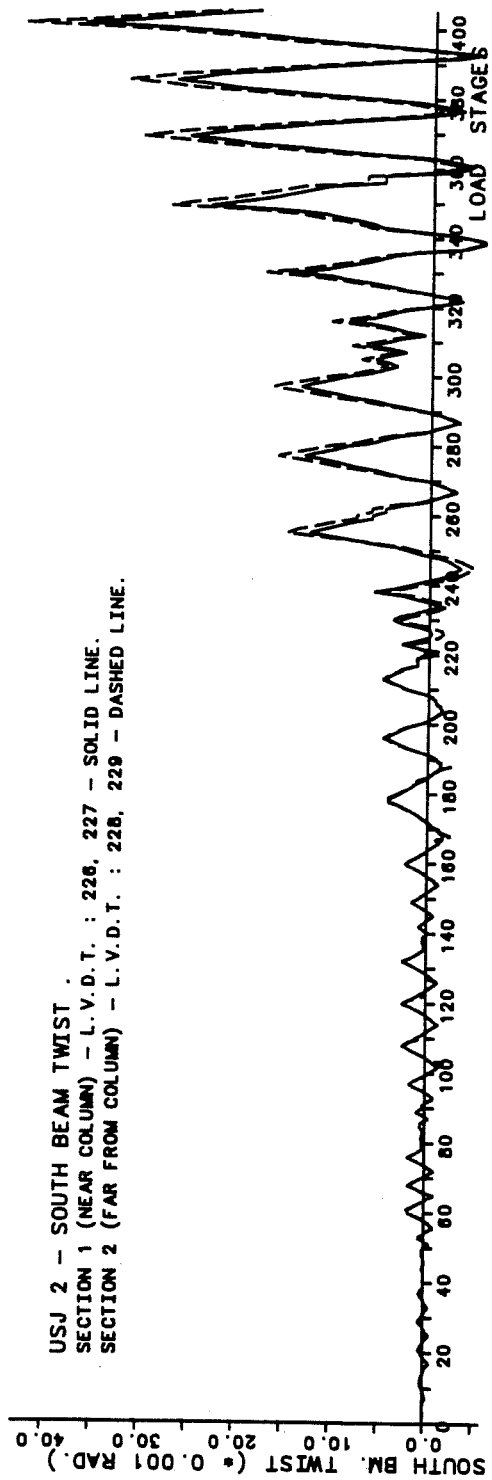
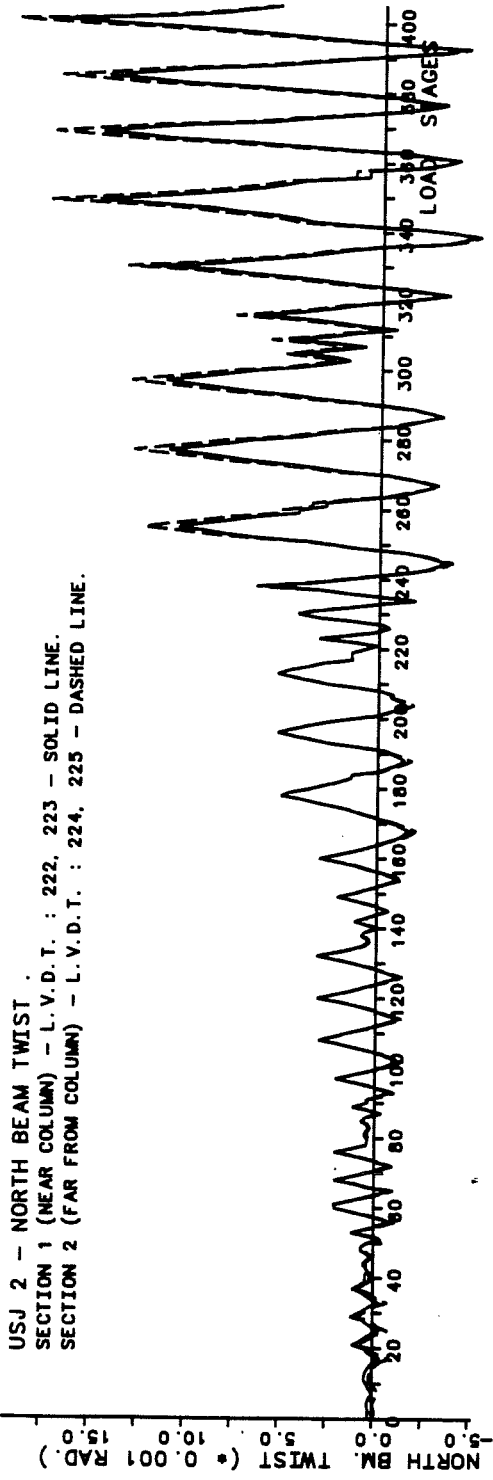


Fig. B.15 - USJ-2 - Transverse Beam Twist.

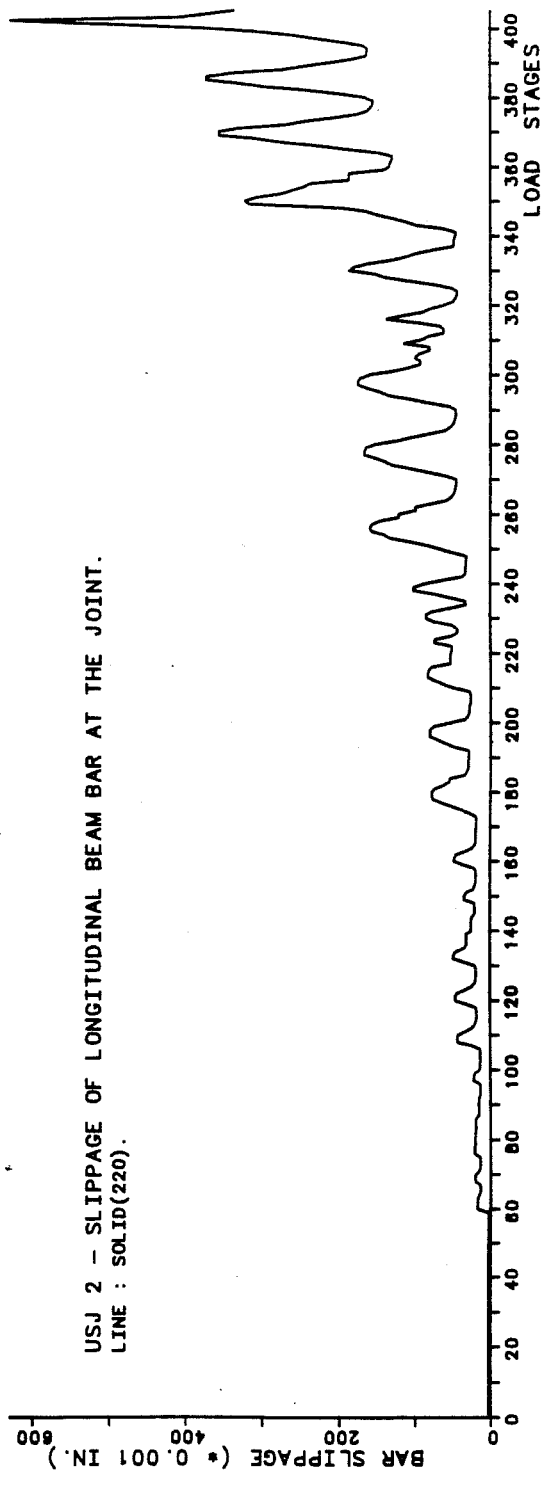
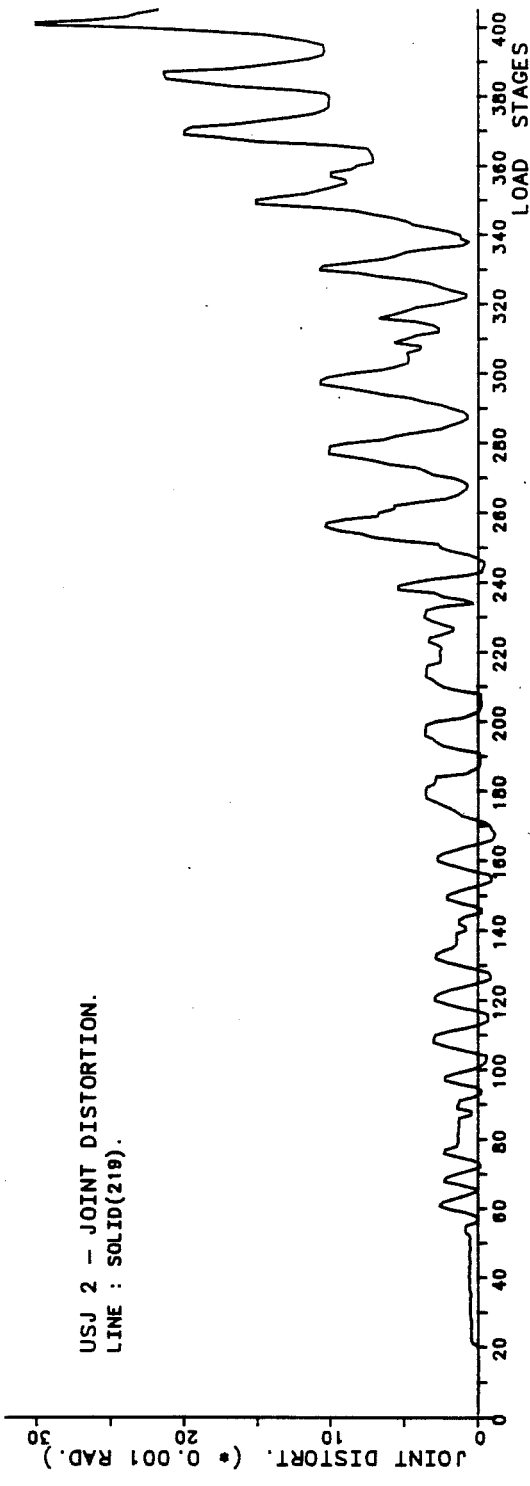


Fig. B.14 - USJ-2 - Joint Distortion and Bar Slippage.

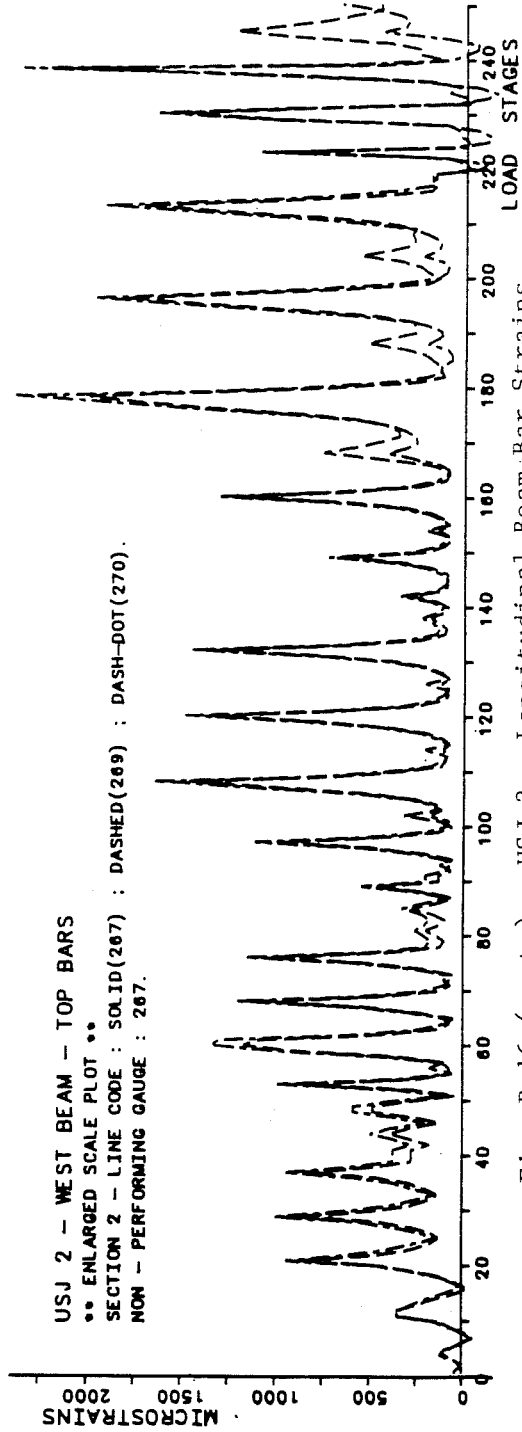
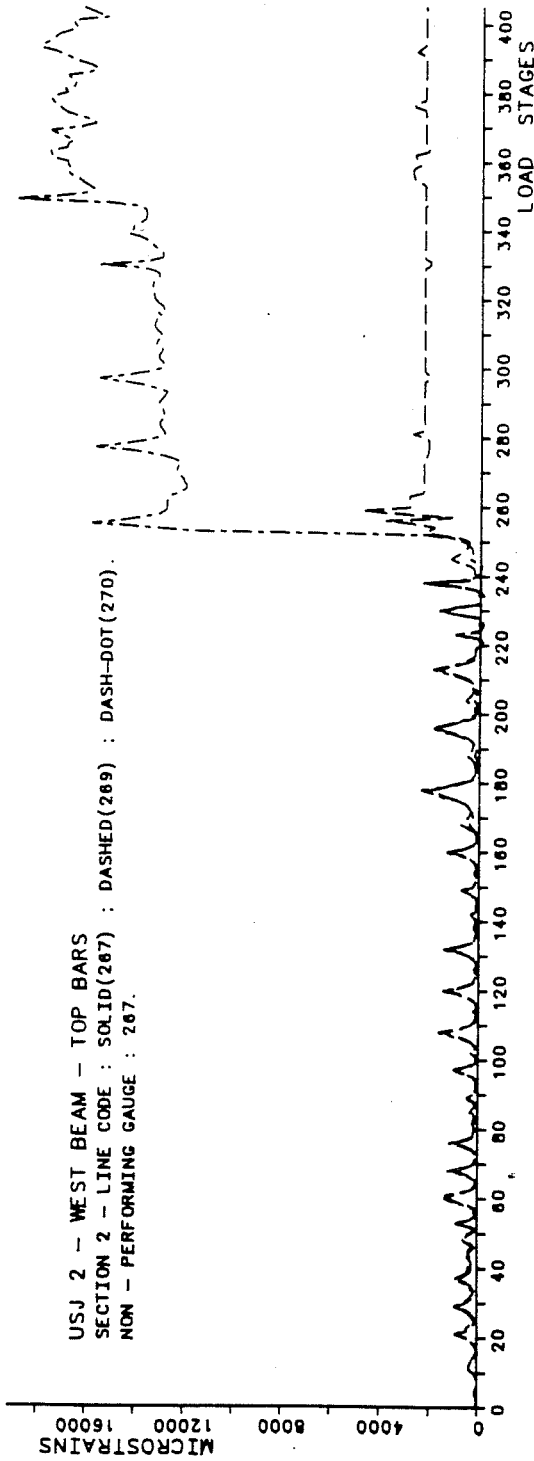


Fig. B.16 (cont.) - USJ-2 - Longitudinal Beam Bar Strains.

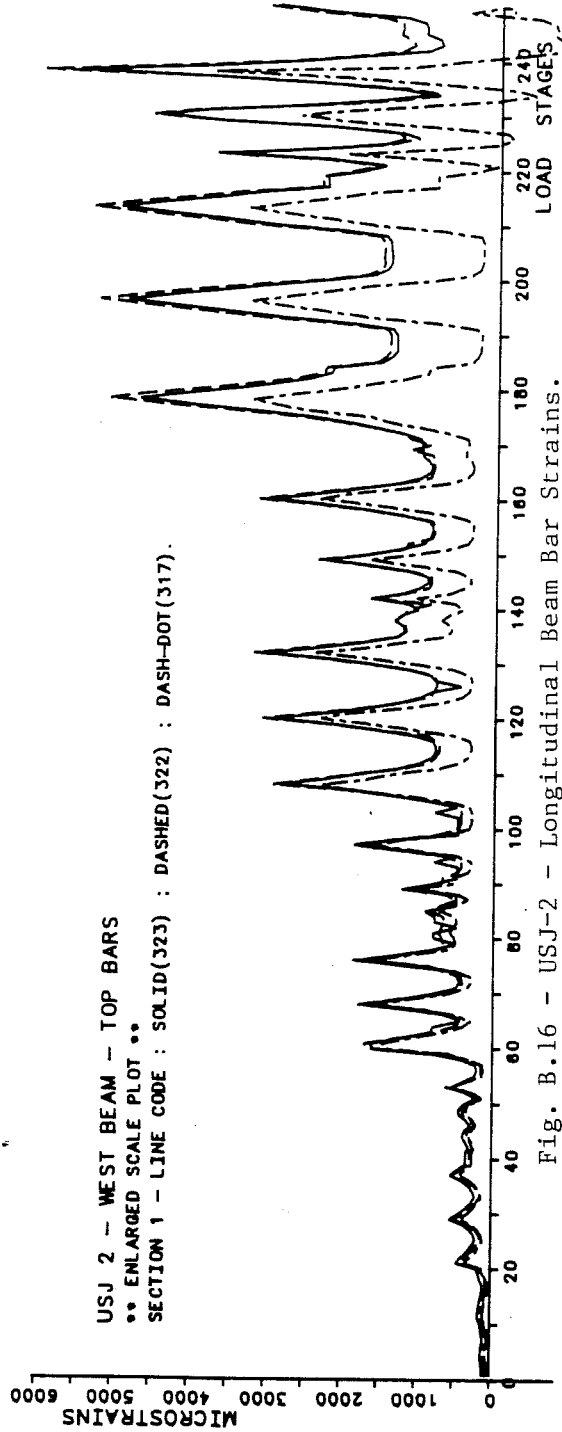
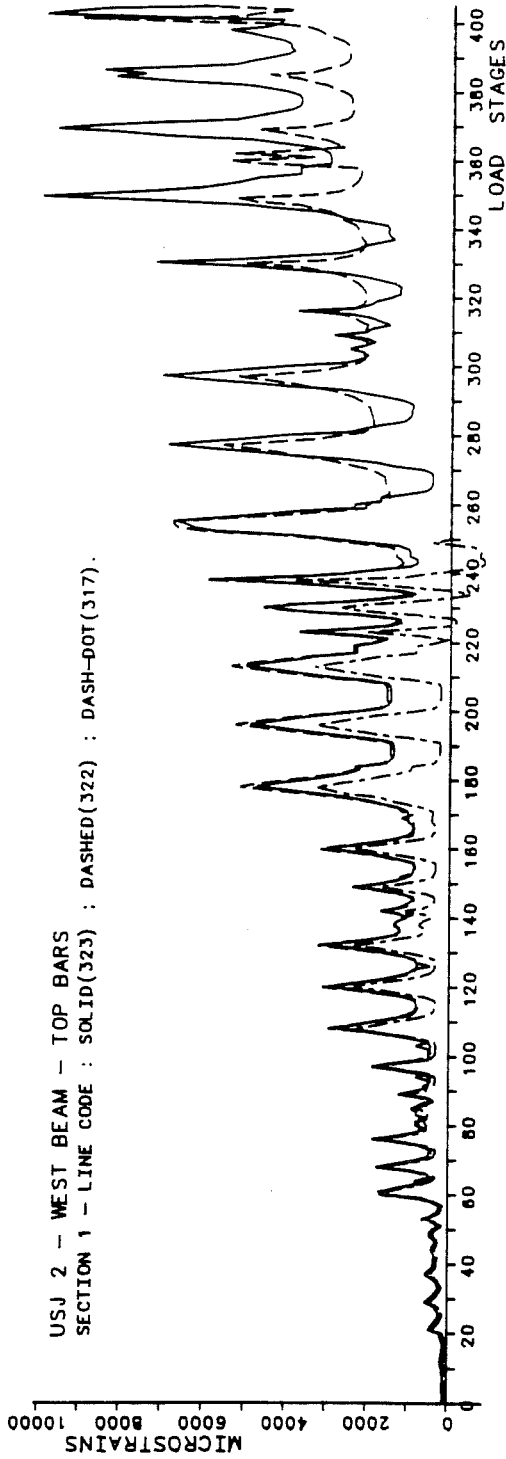


Fig. B.16 - USJ-2 - Longitudinal Beam Bar Strains.

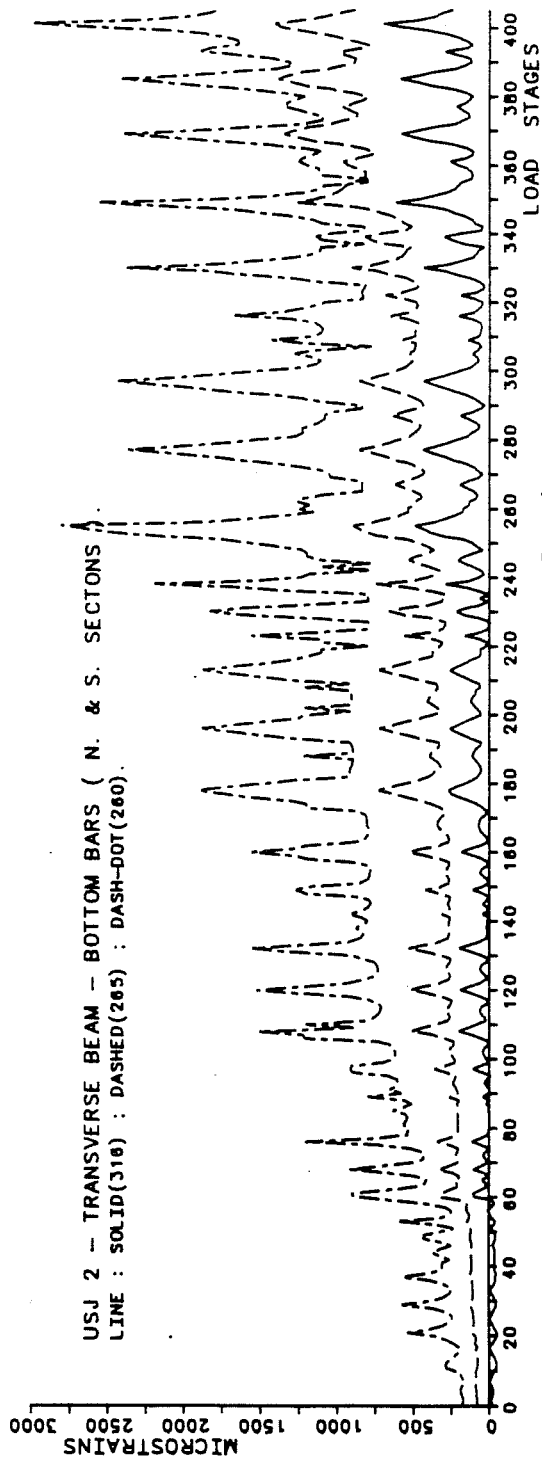
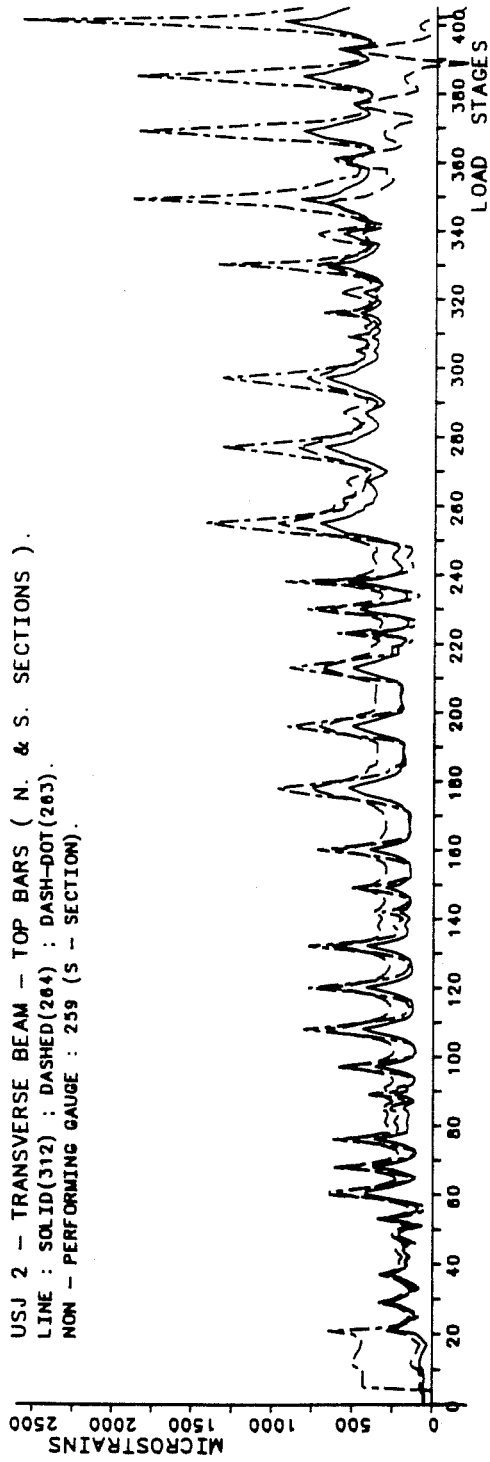


Fig. B.17 - USJ-2 - Transverse Beam Bar Strains.

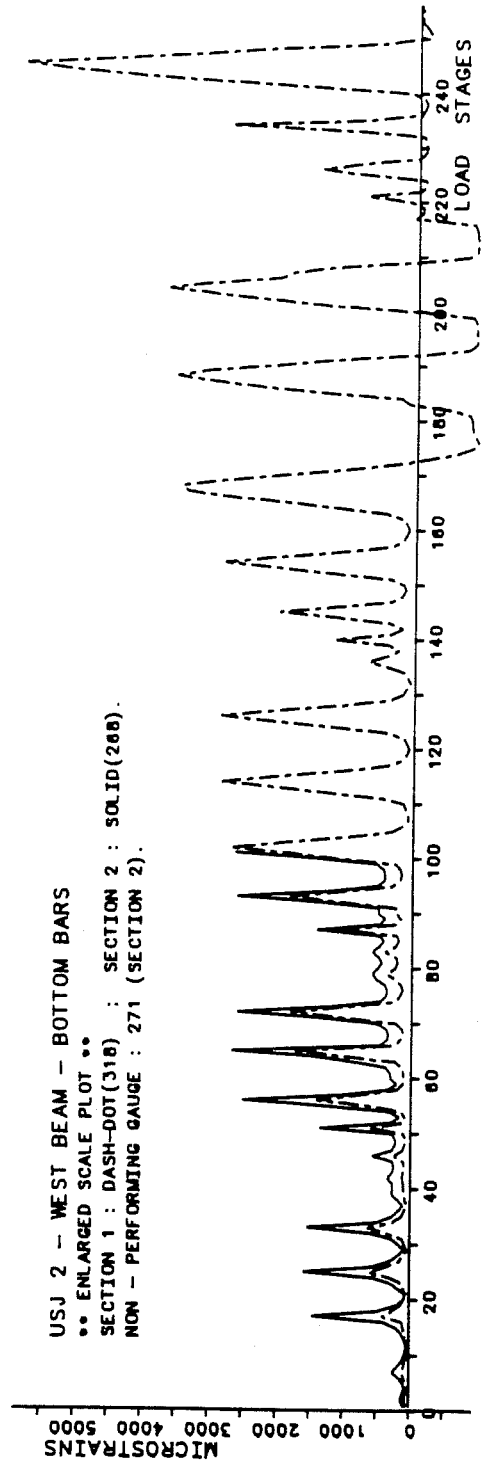
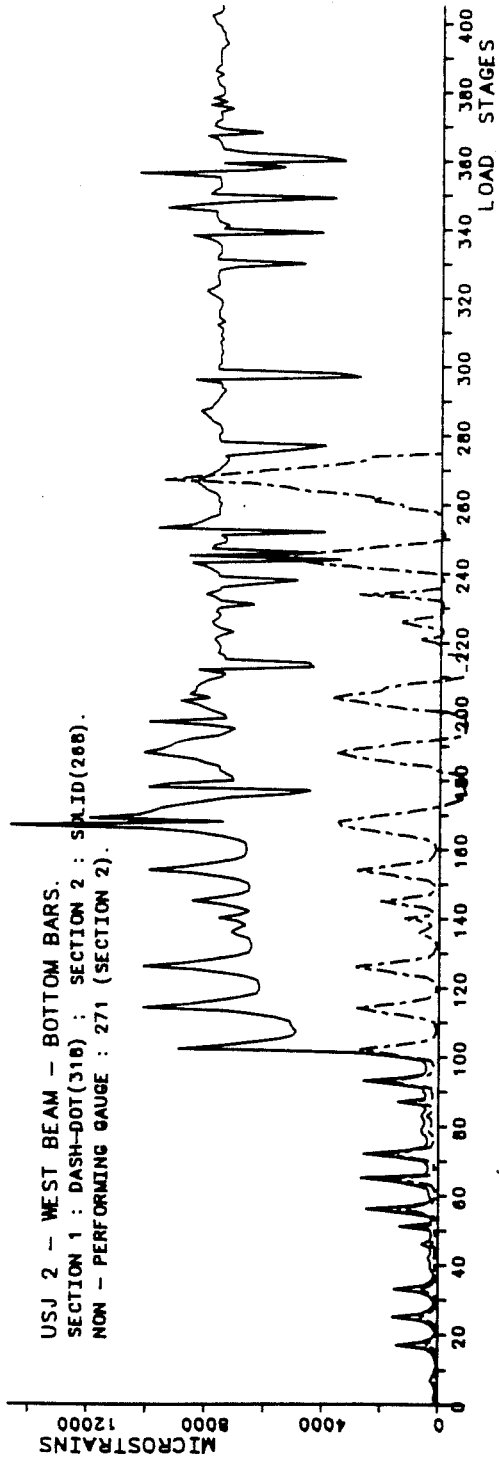


Fig. B.16 (cont.) - Longitudinal Beam Bar Strains.

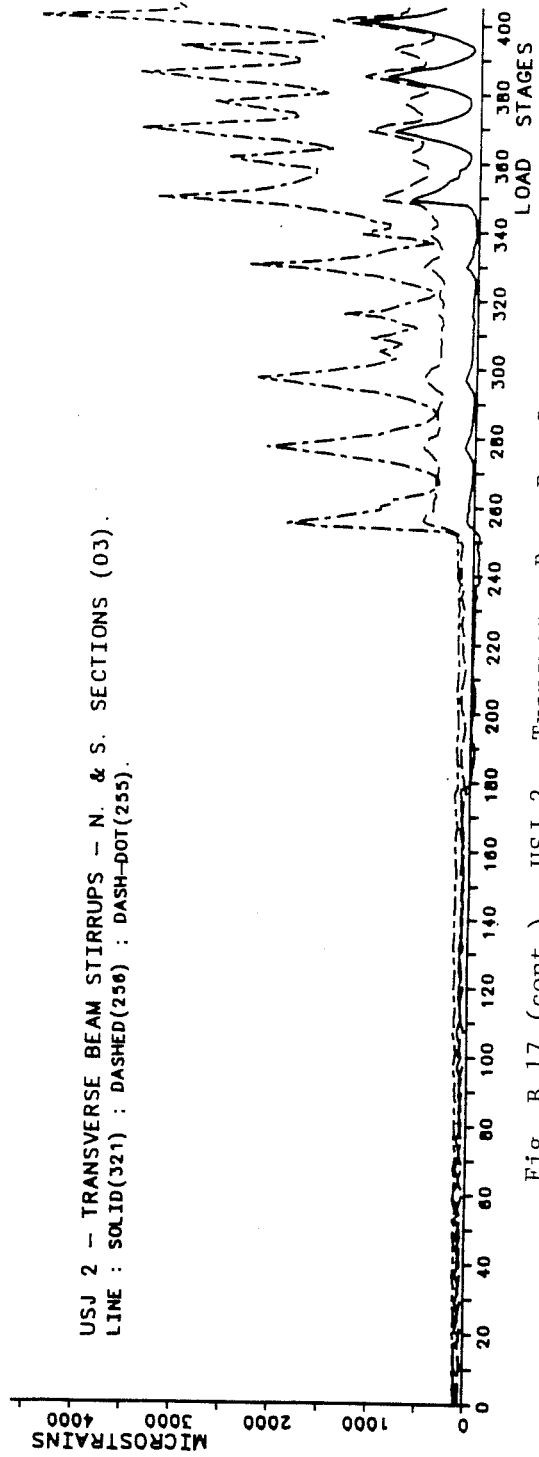
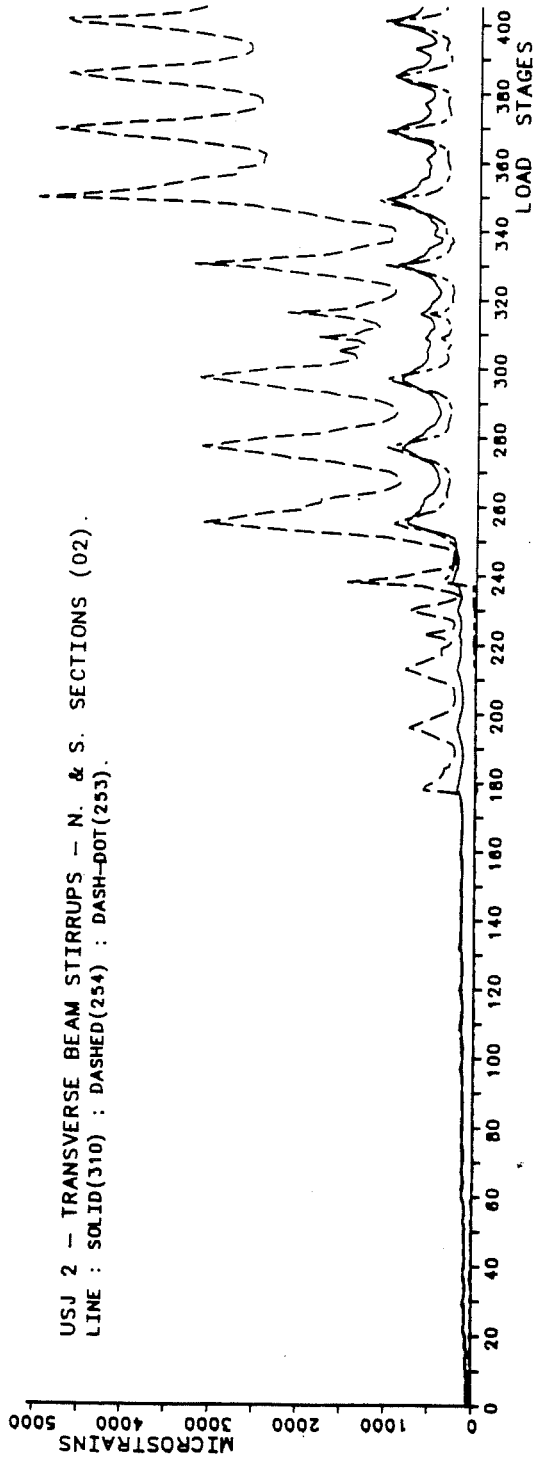


Fig. B.17 (cont.) - USJ-2 - Transverse Beam Bar Strains.

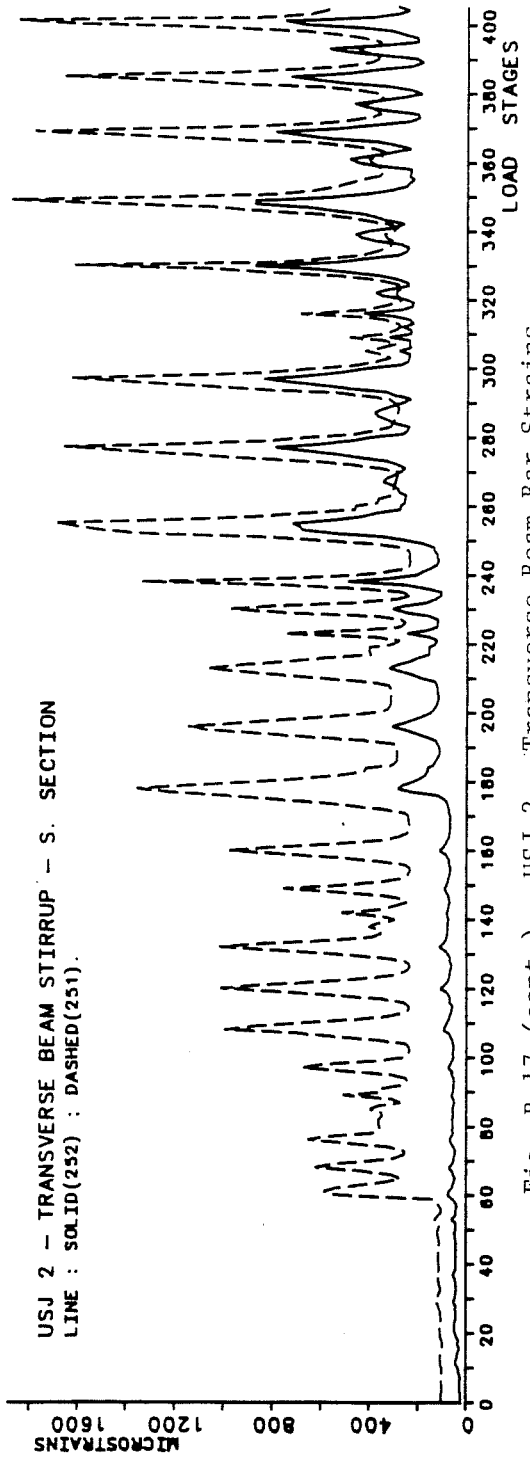
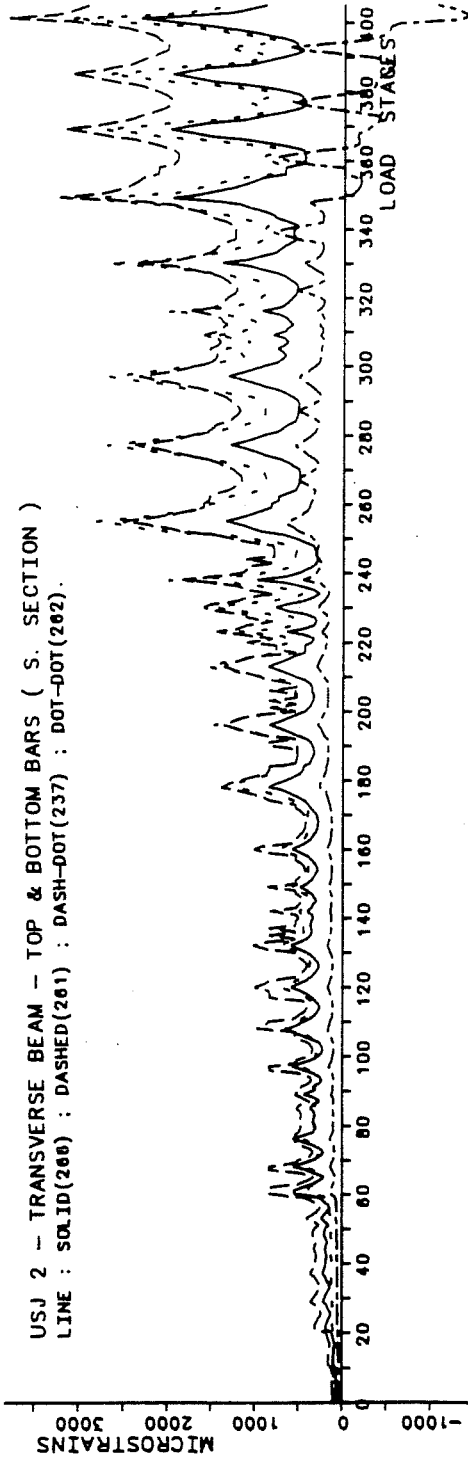


Fig. B.17 (cont.) - USJ-2 - Transverse Beam Bar Strains.

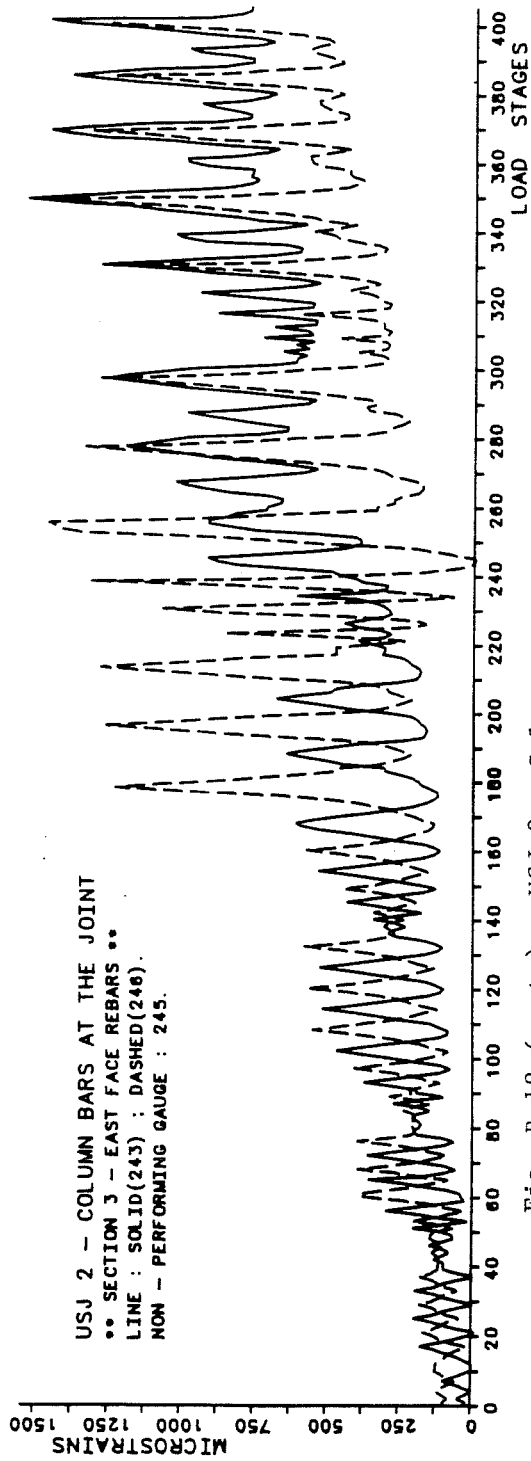
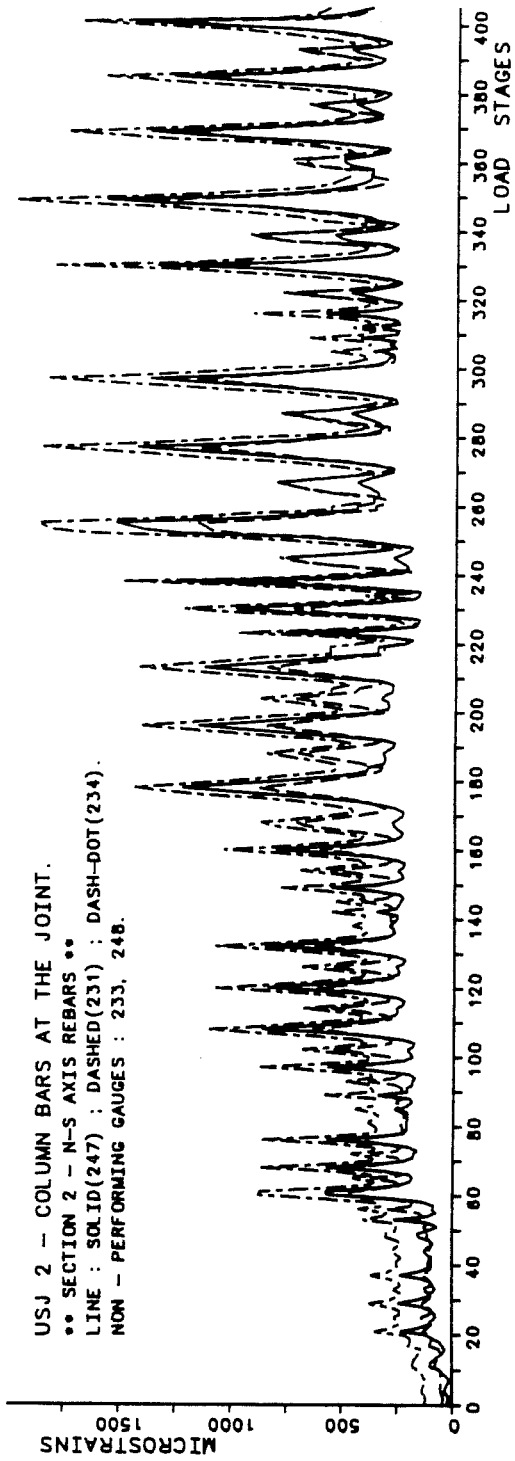
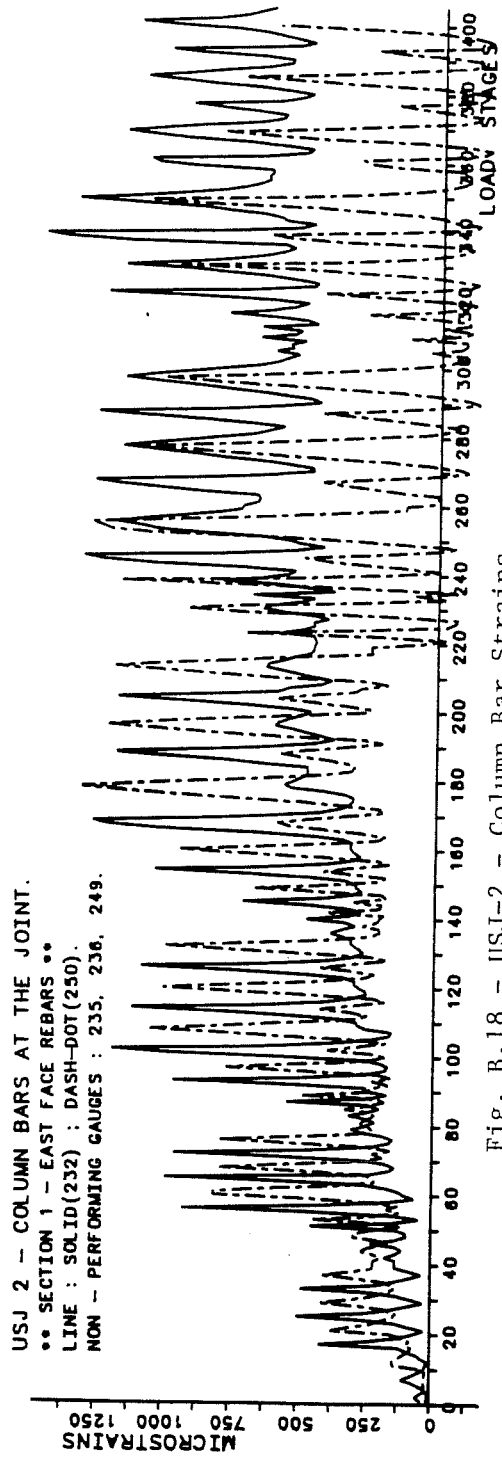
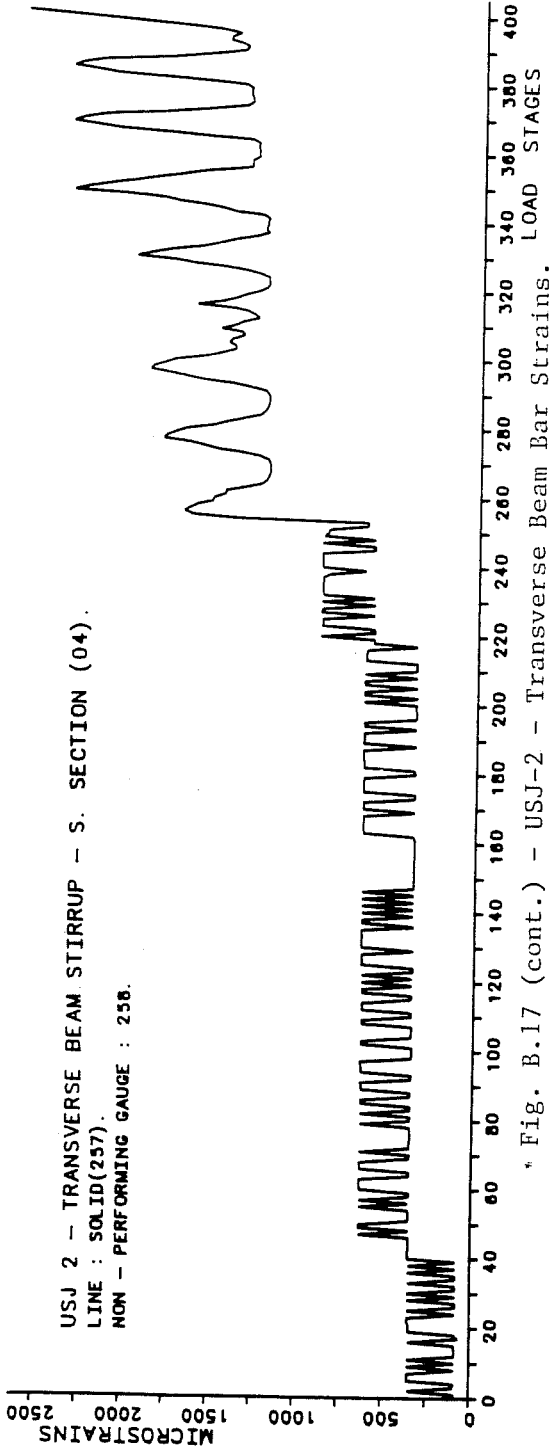


Fig. B.18 (cont.) - USJ-2 - Column Bar Strains.



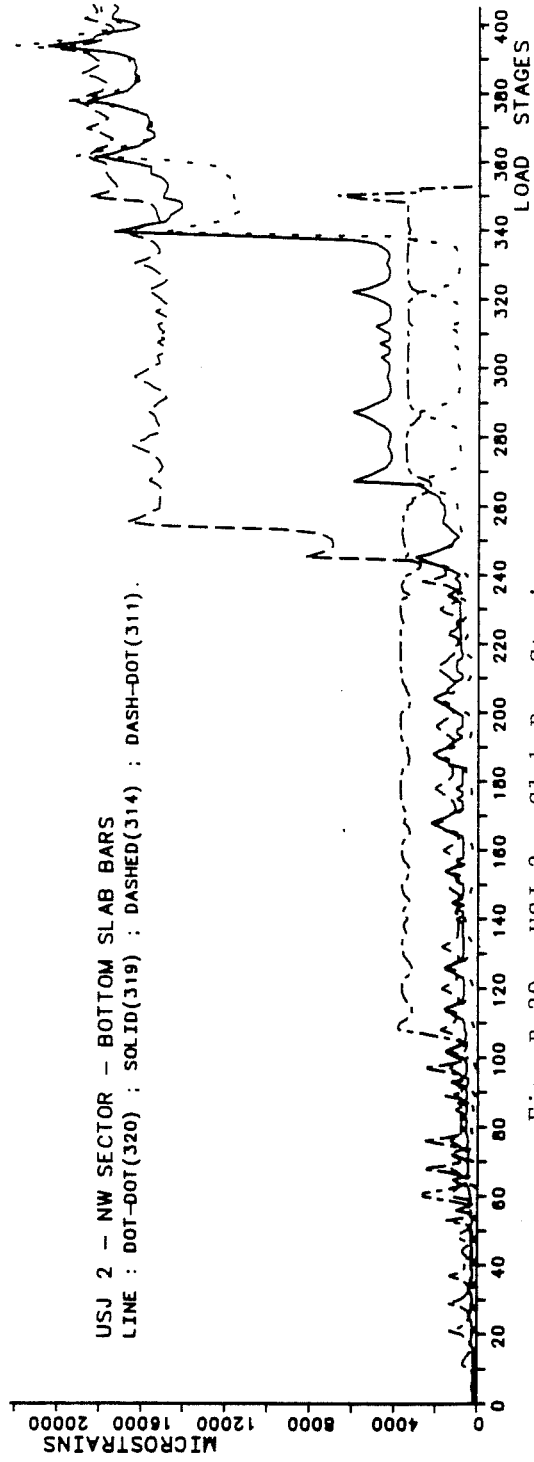
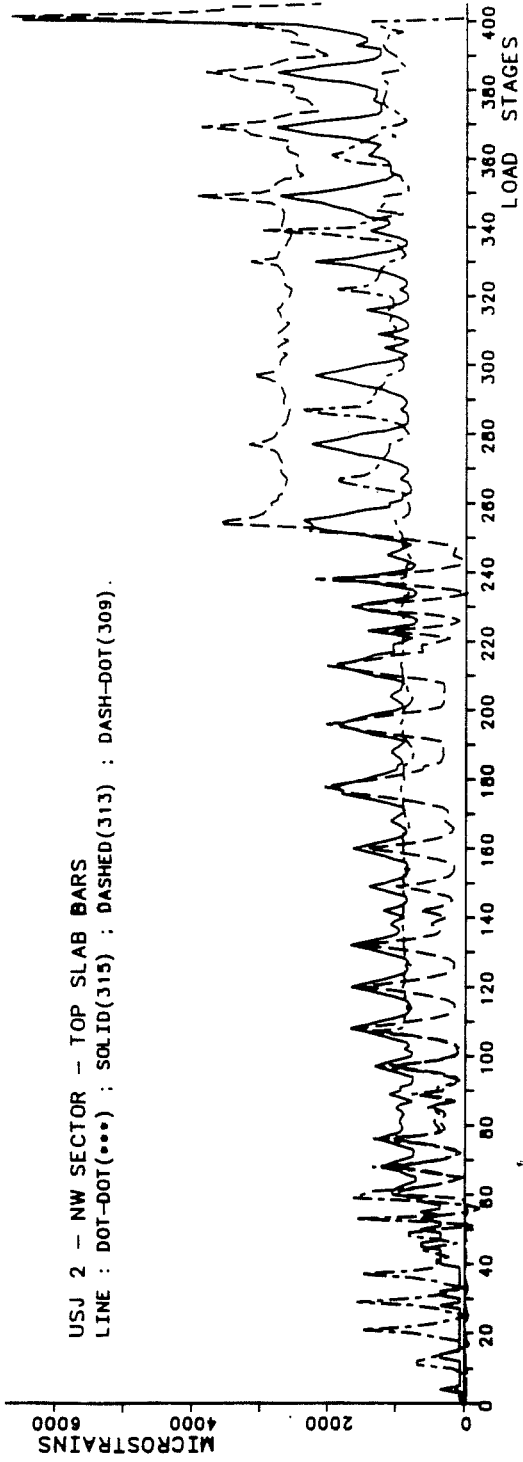


Fig. B.20 - USJ-2 - Slab Bar Strains.

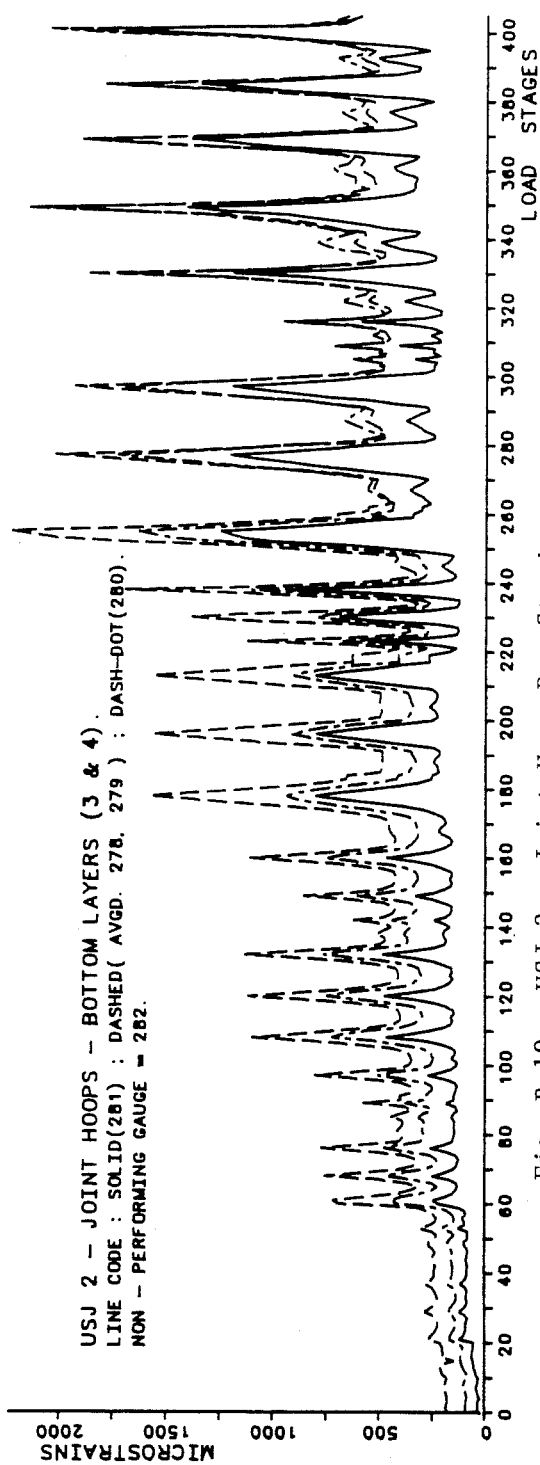
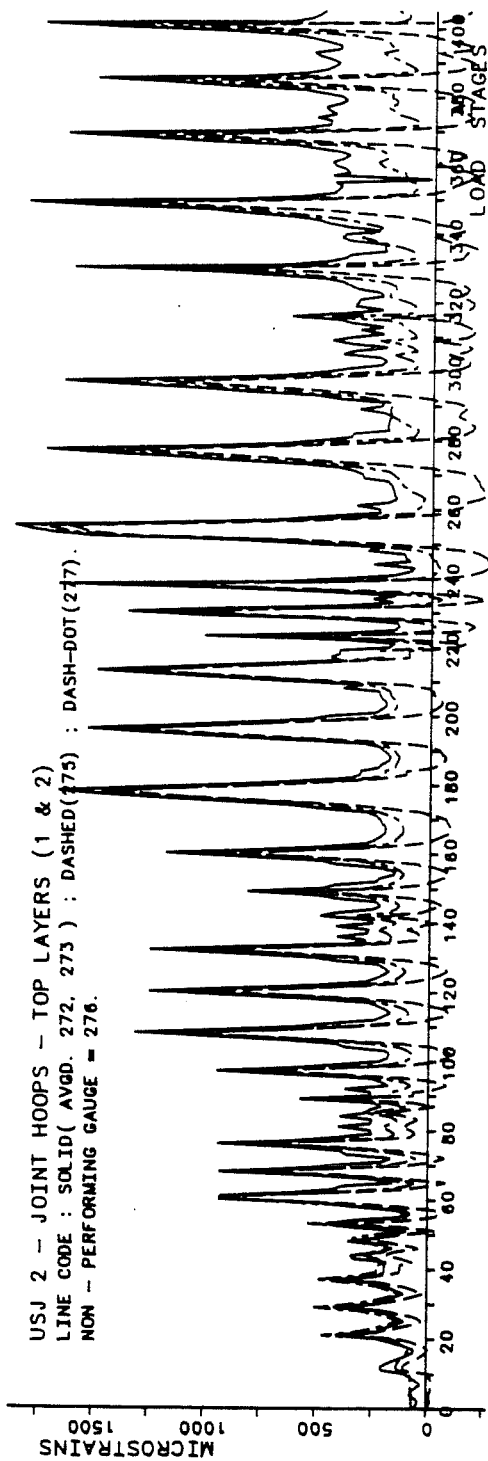


Fig. B.19 - USJ-2 - Joint Hoop Bar Strains.

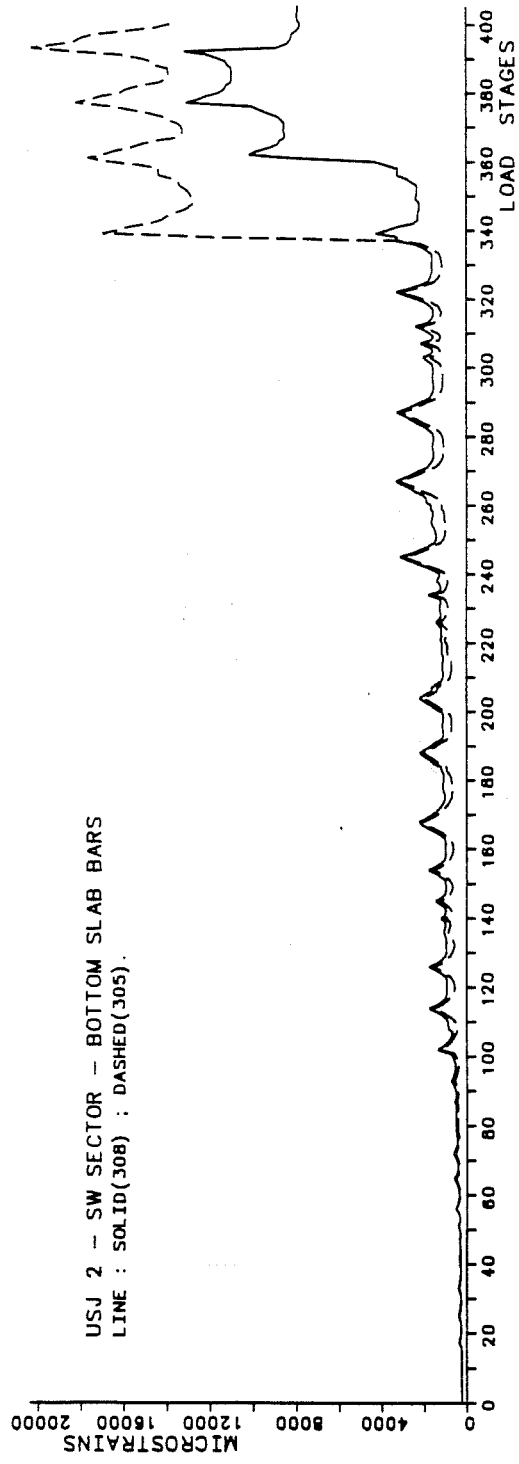
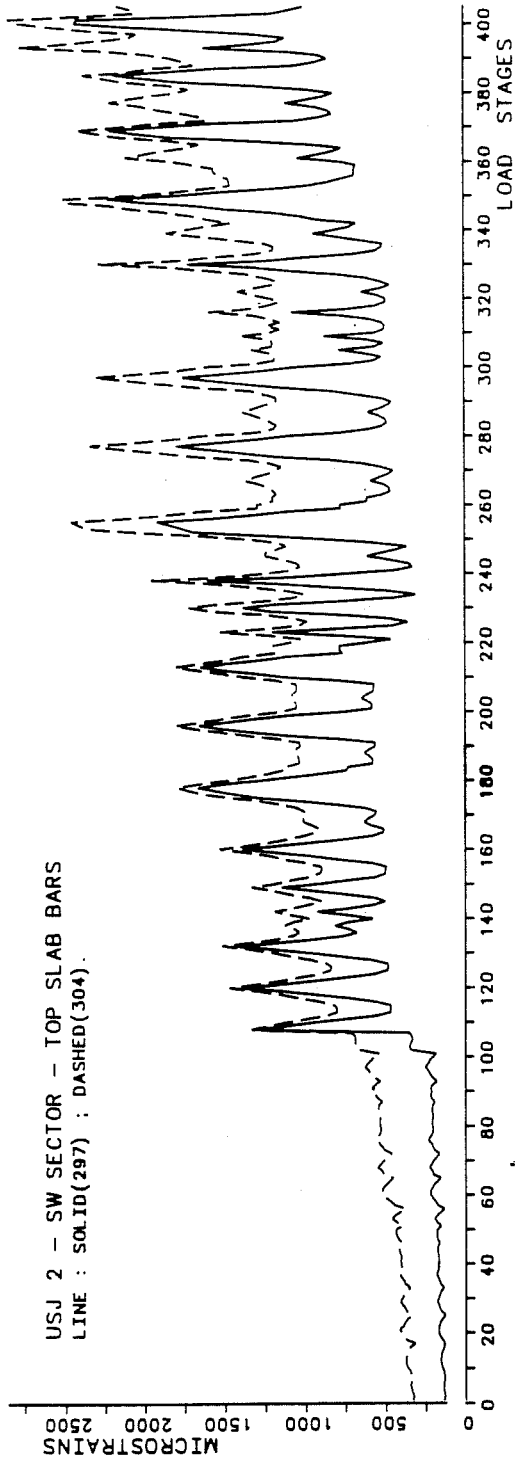


Fig. B.20 (cont.) - USJ-2 - Slab Bar Strains.

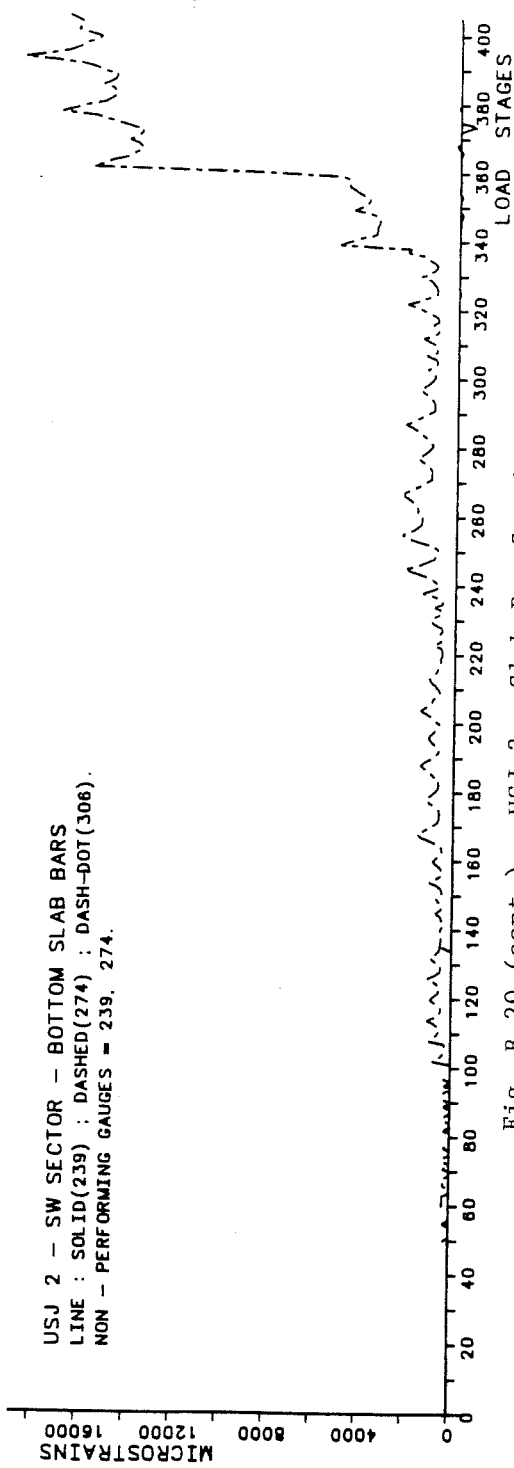
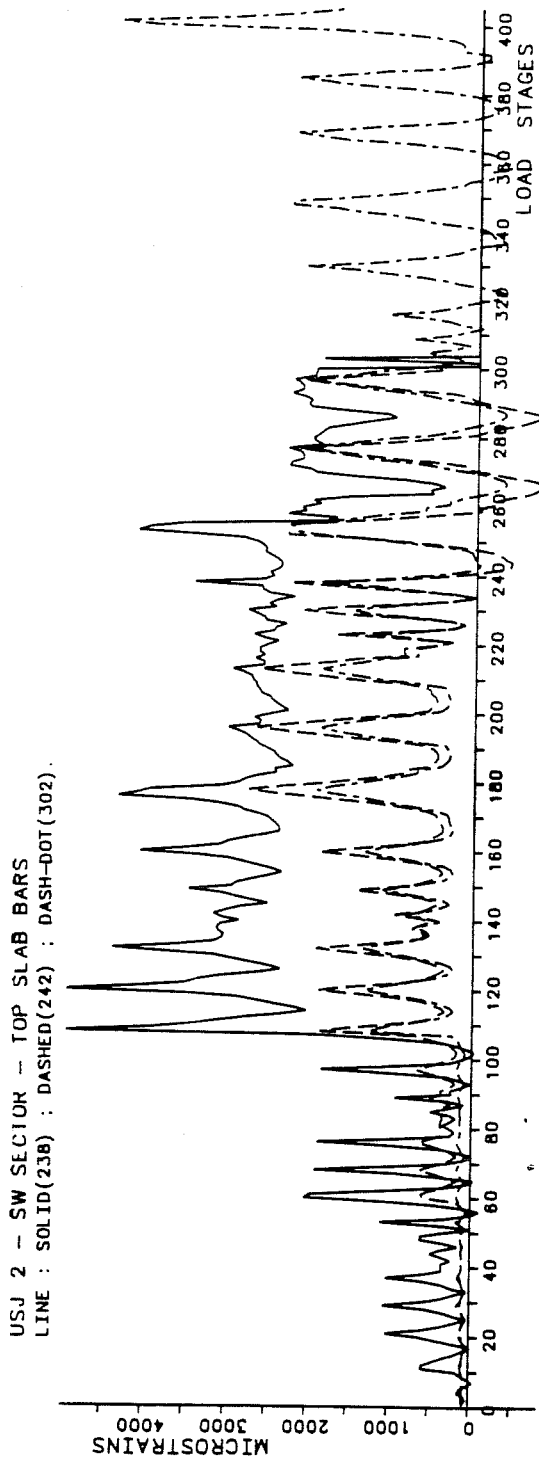


Fig. B.20 (cont.) - USJ-2 - Slab Bar Strains.

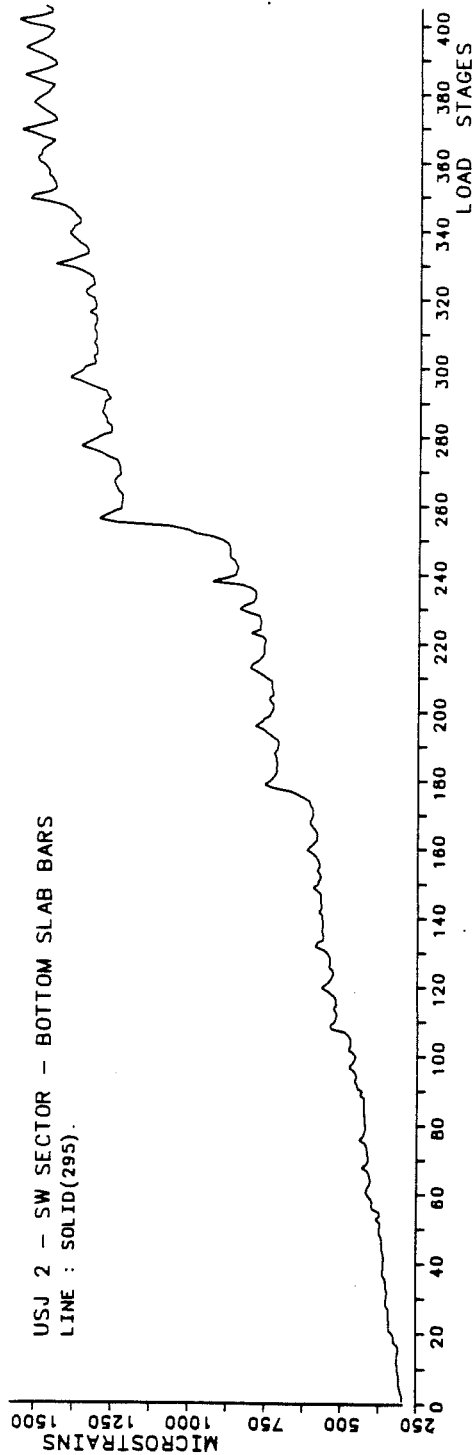
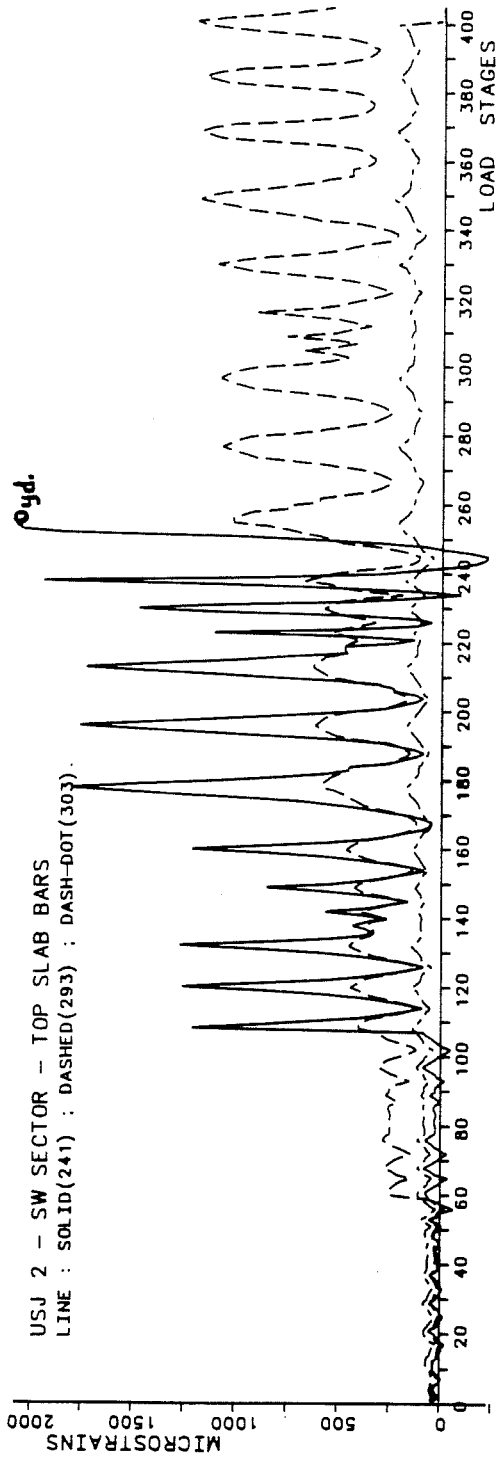


Fig. B.20 (cont.) - USJ-2 - Slab Bar Strains.

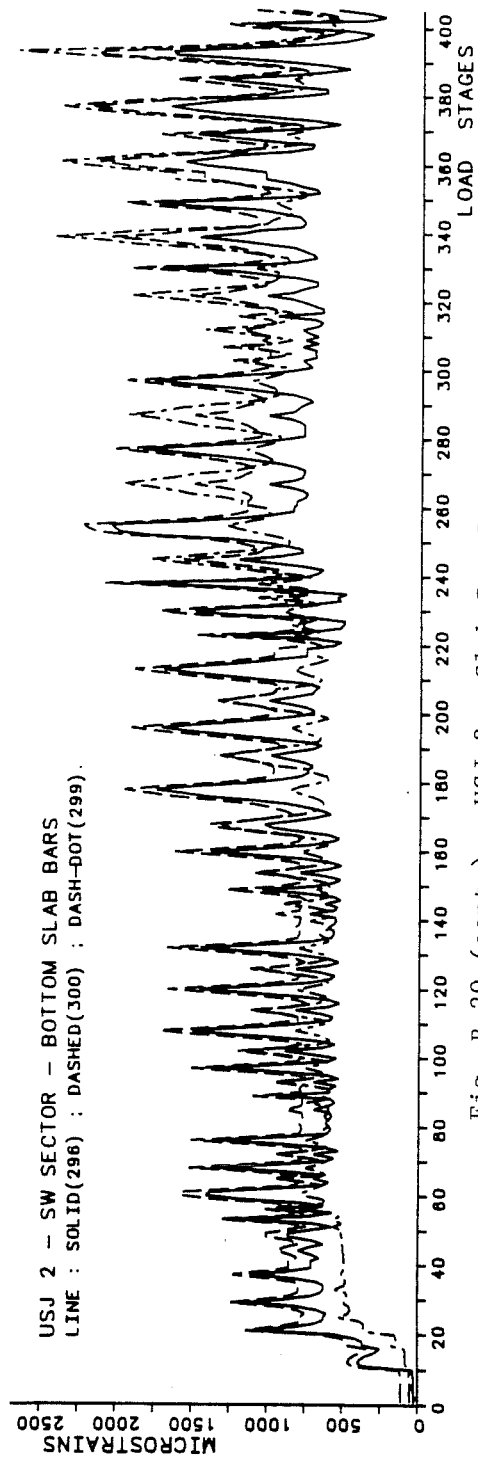
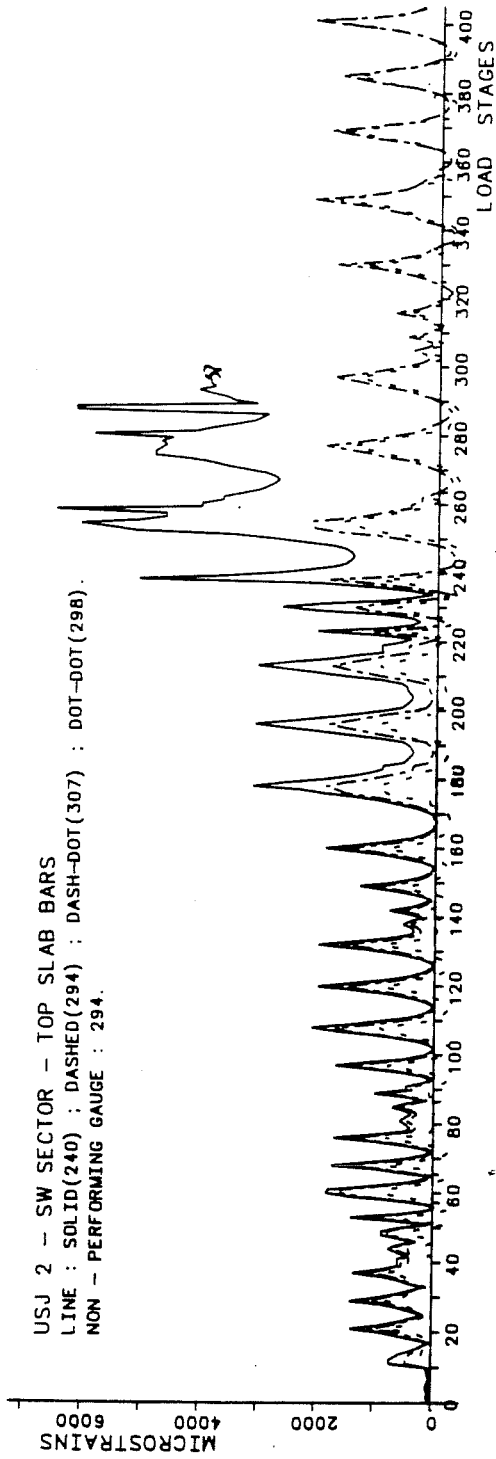


Fig. B.20 (cont.) - USJ-2 - Slab Bar Strains.

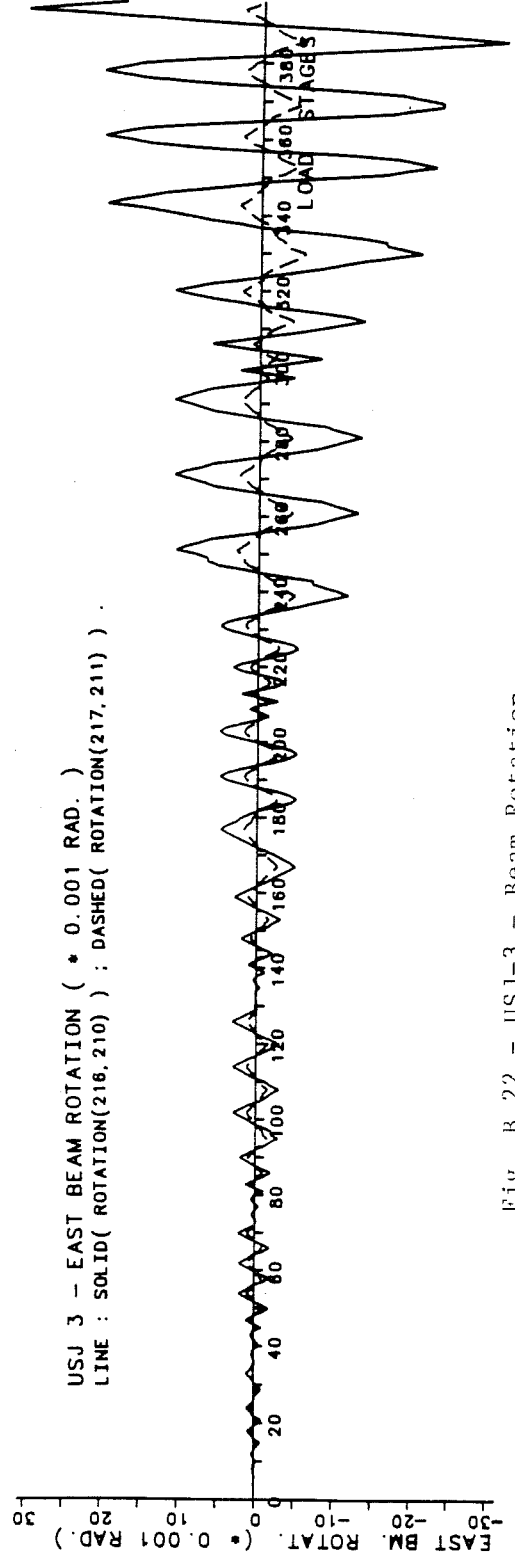
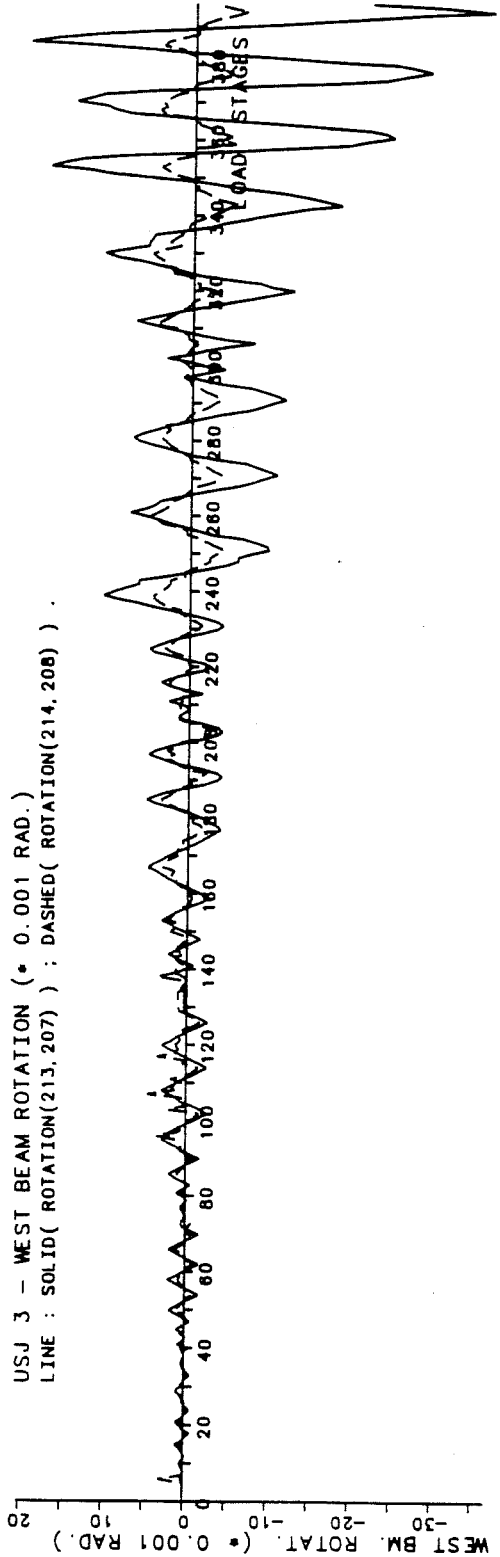


Fig. B.22 - USJ-3 - Beam Rotation.

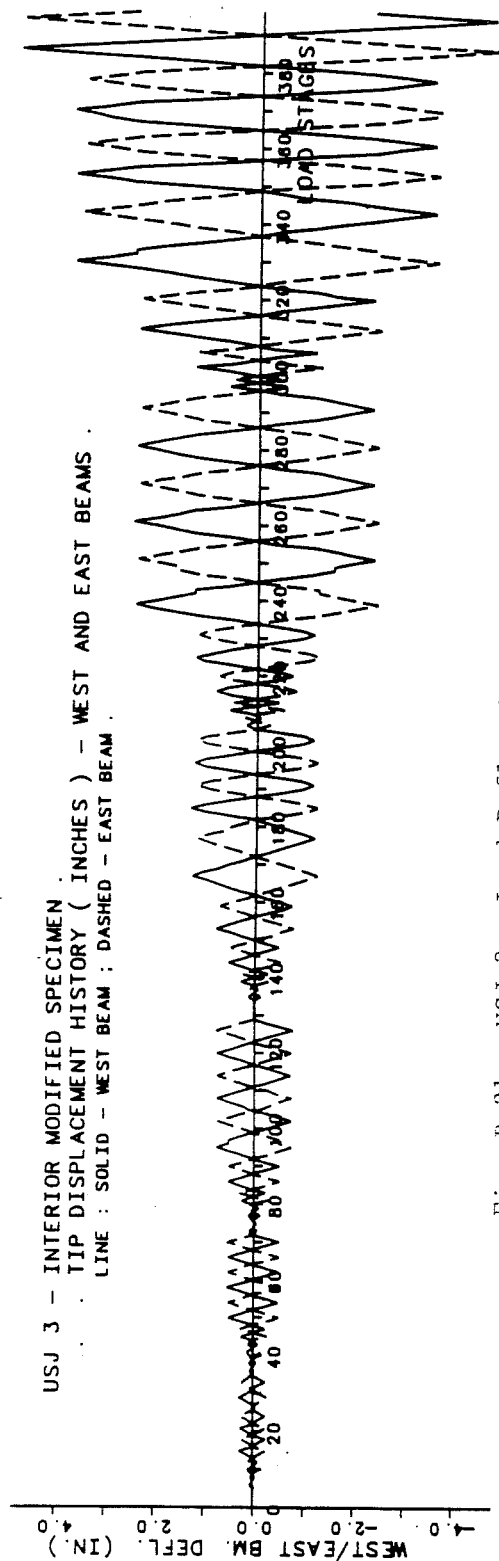
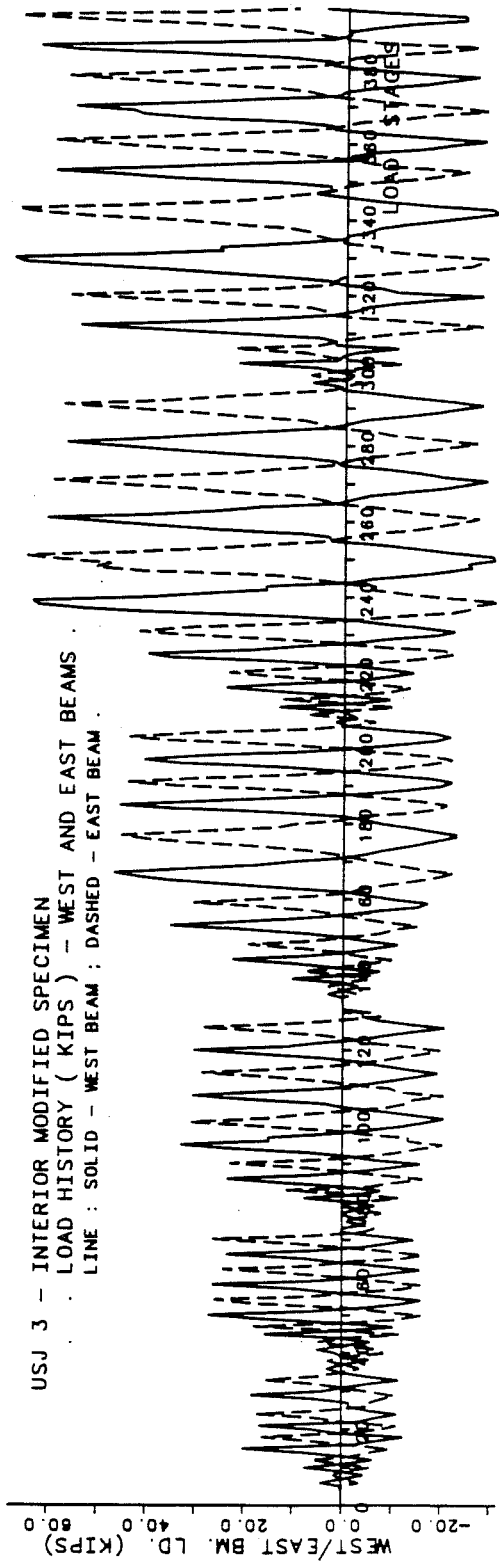


Fig. B.21 - USJ-3 - Load-Deflection Response.

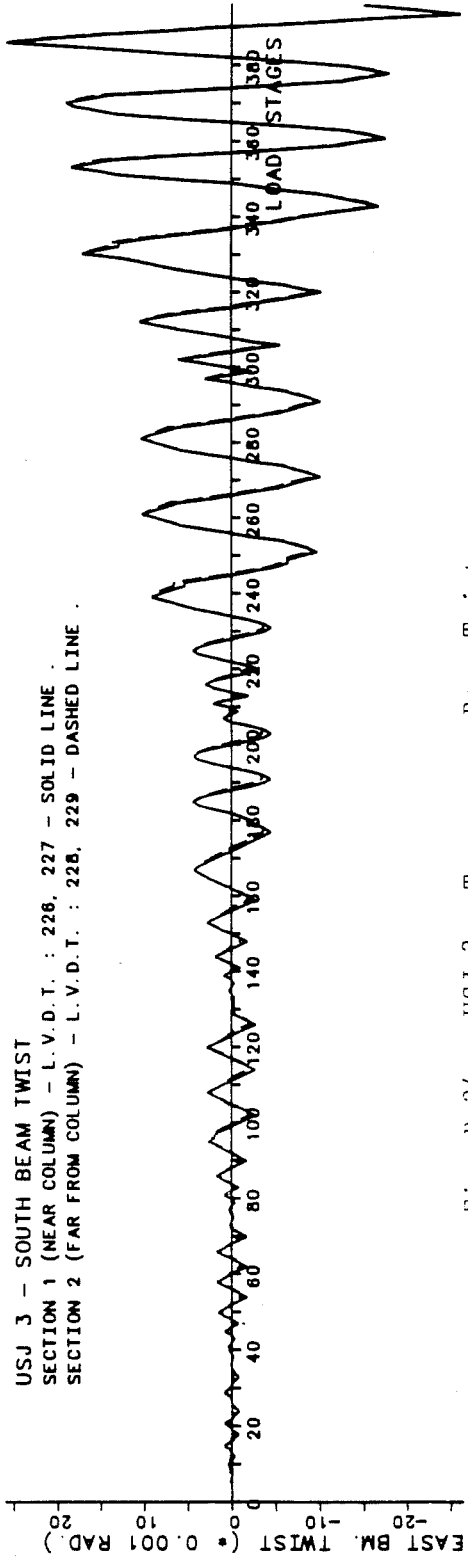
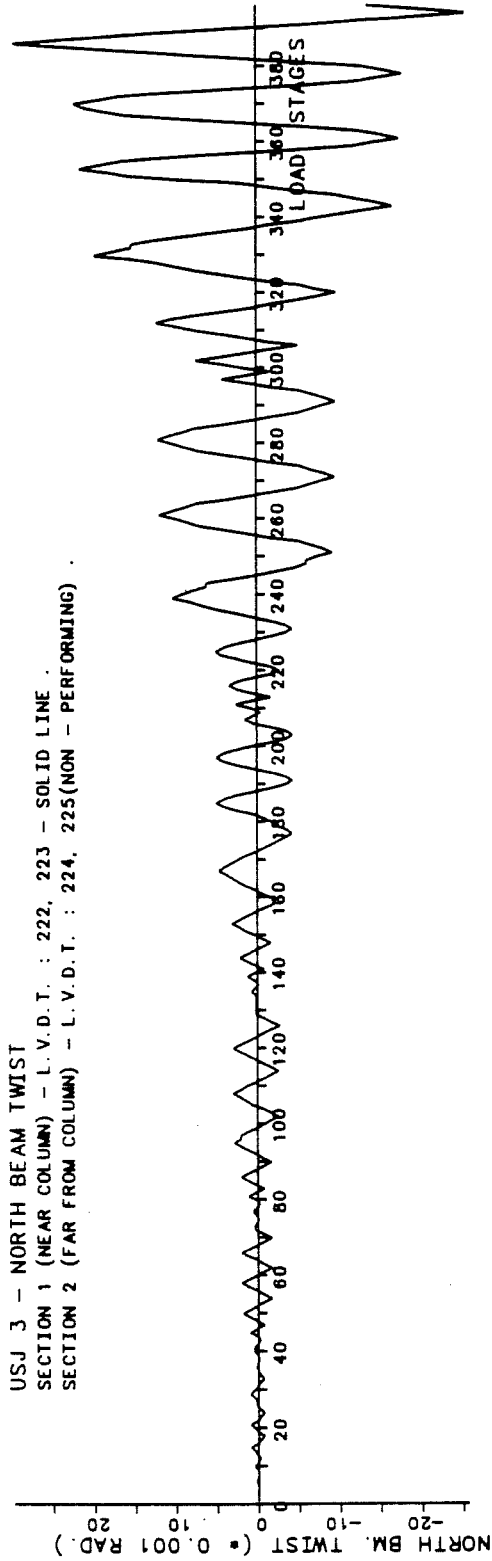


Fig. B.24 - USJ-3 - Transverse Beam Twist.

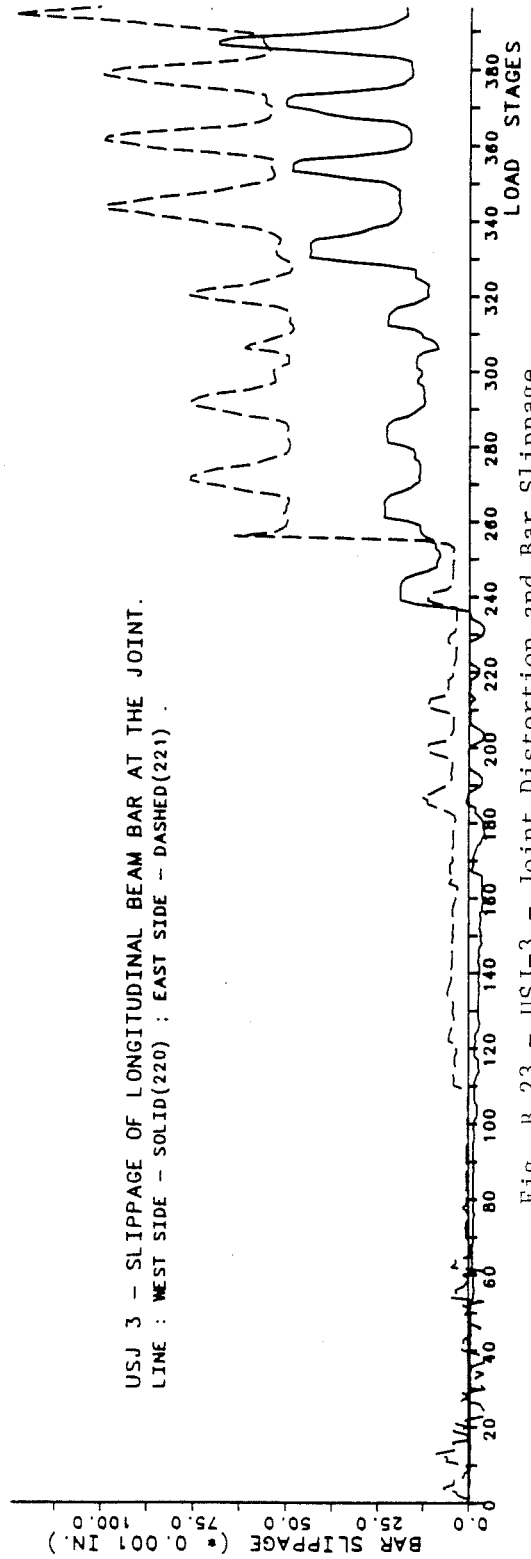
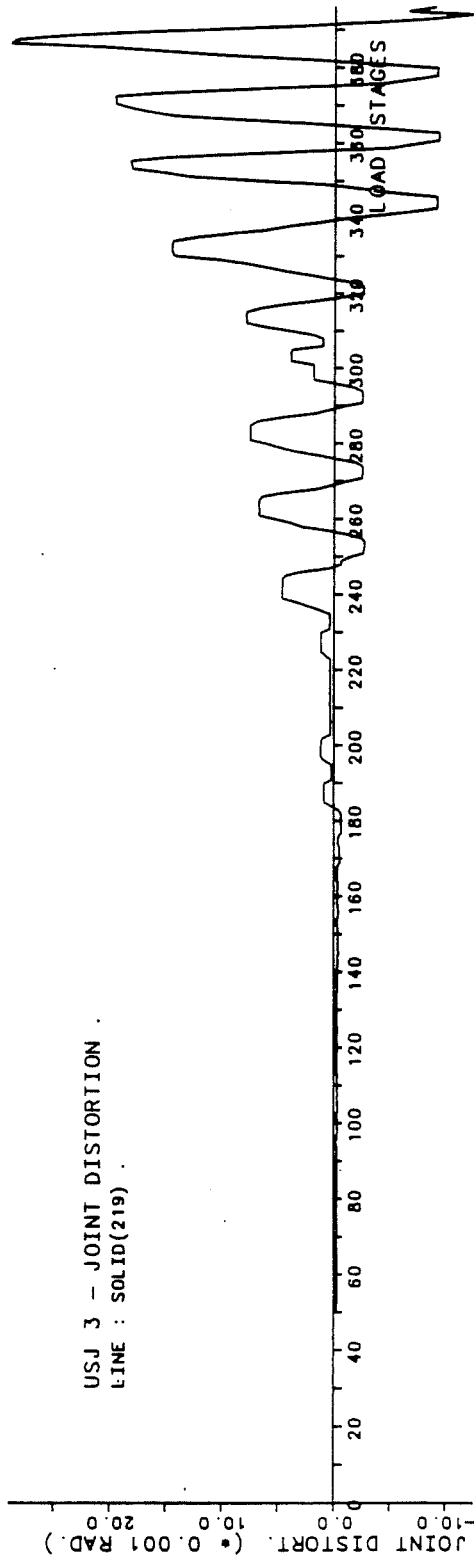


Fig. B.23 - USJ-3 - Joint Distortion and Bar Slippage.

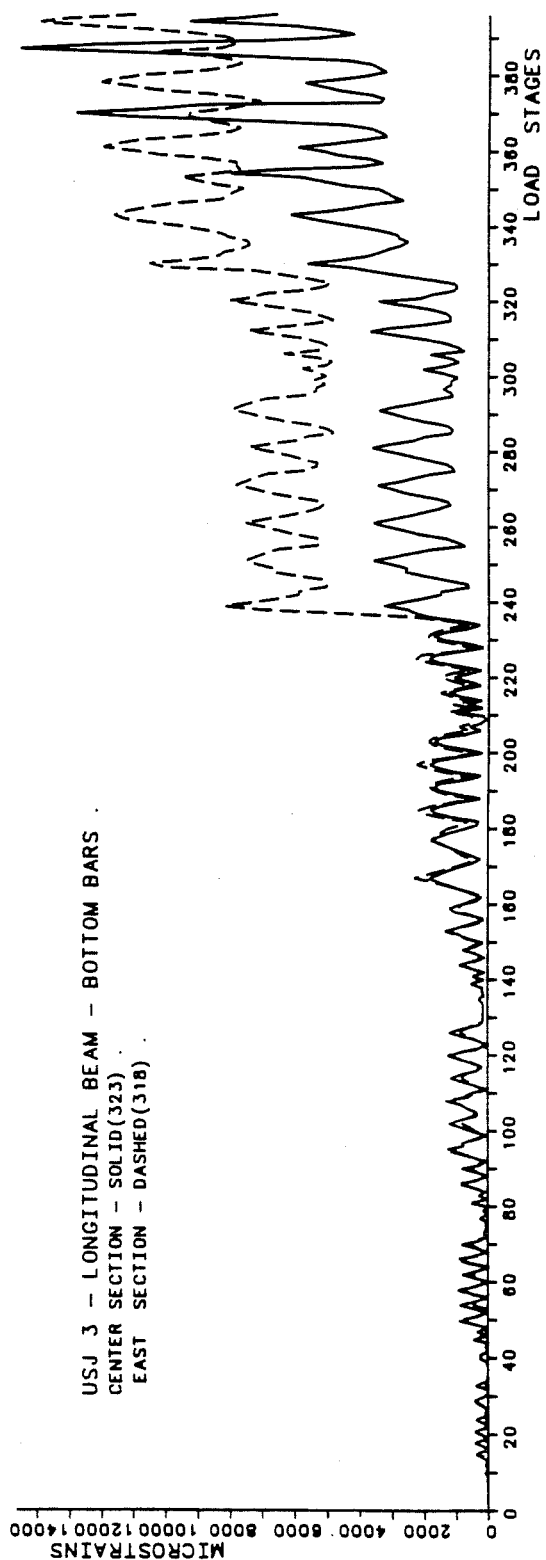
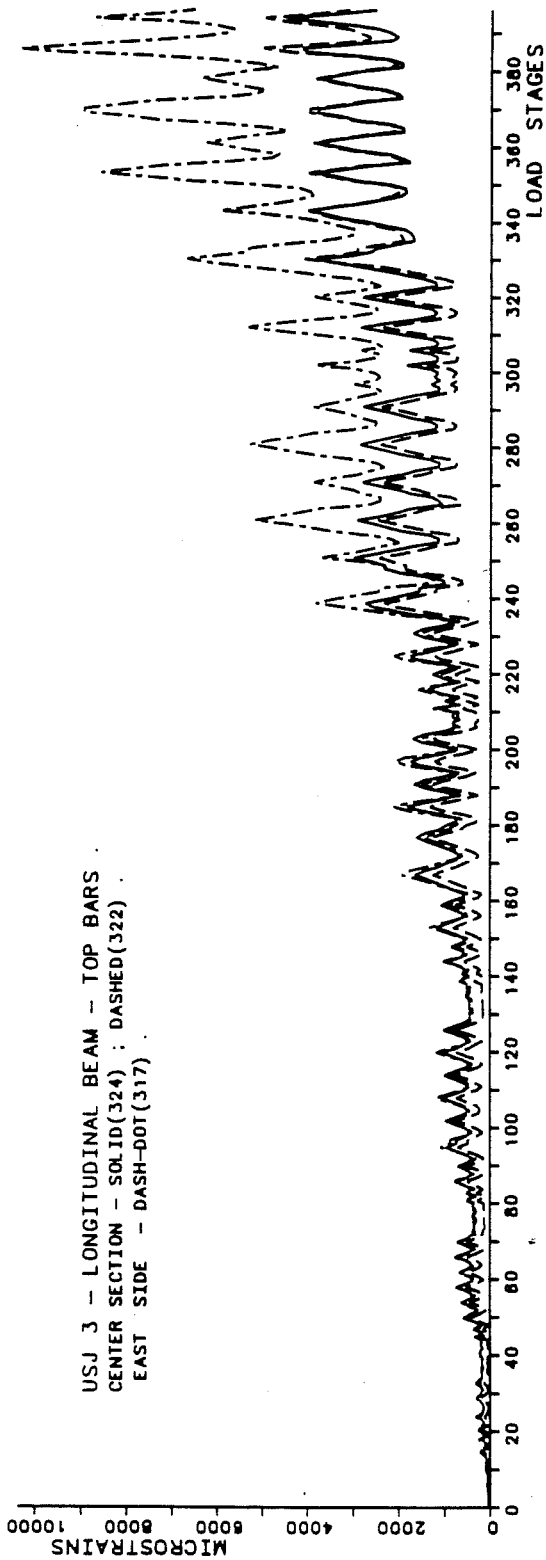


Fig. B.25 (cont.) - USJ-3 - Longitudinal Beam Bar Strains.

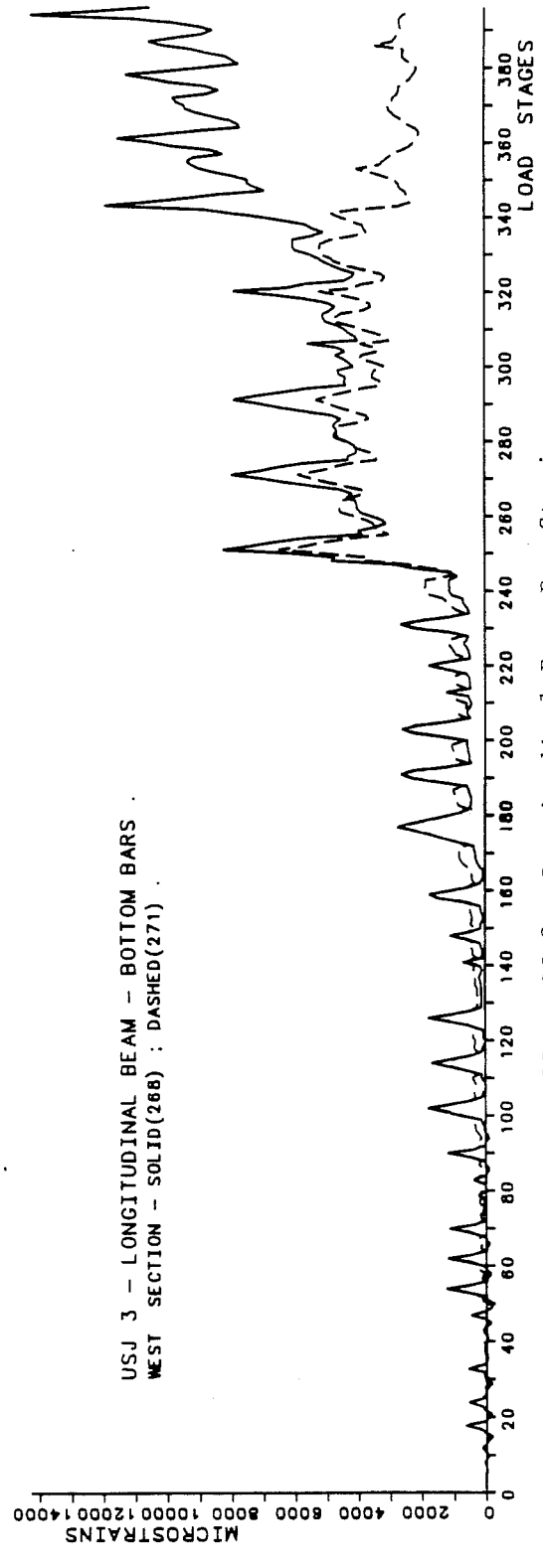
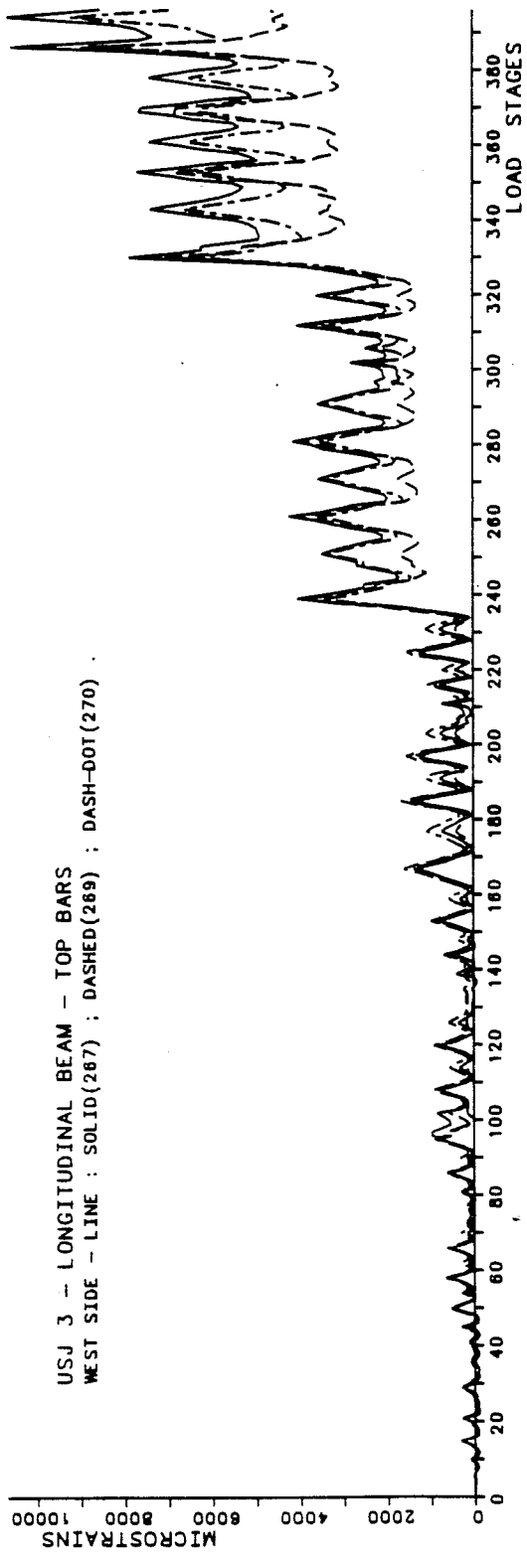


Fig. B.25 - USJ-3 - Longitudinal Beam Bar Strains.

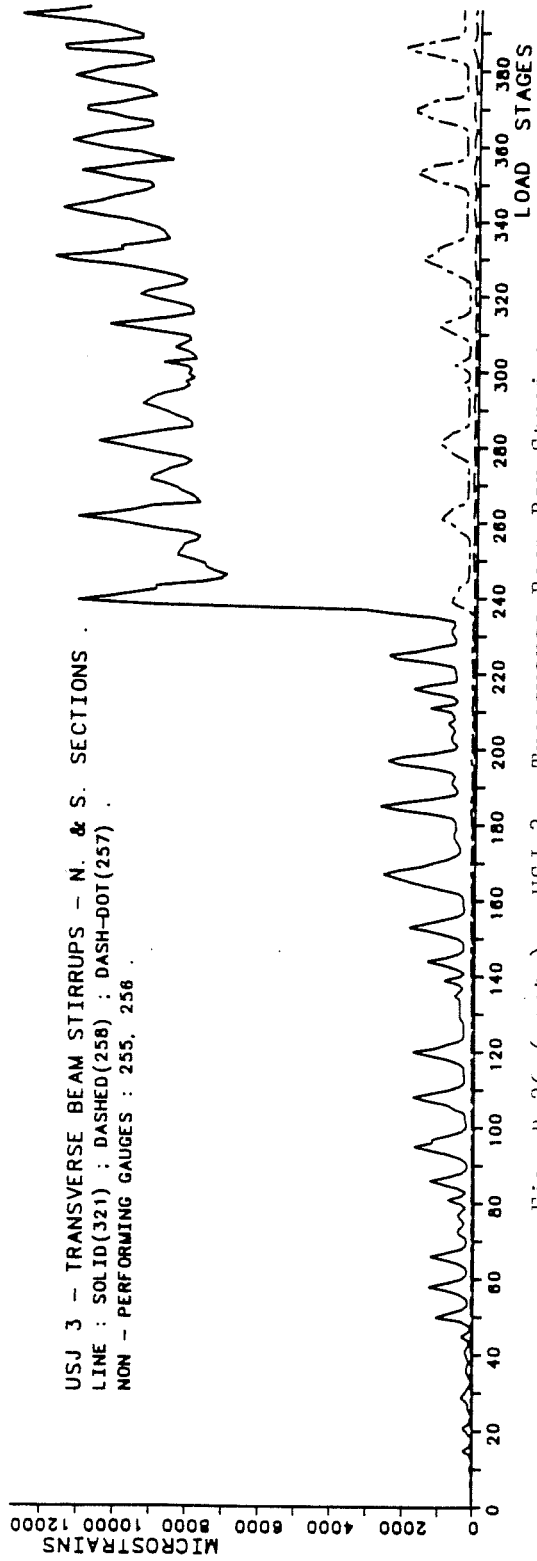
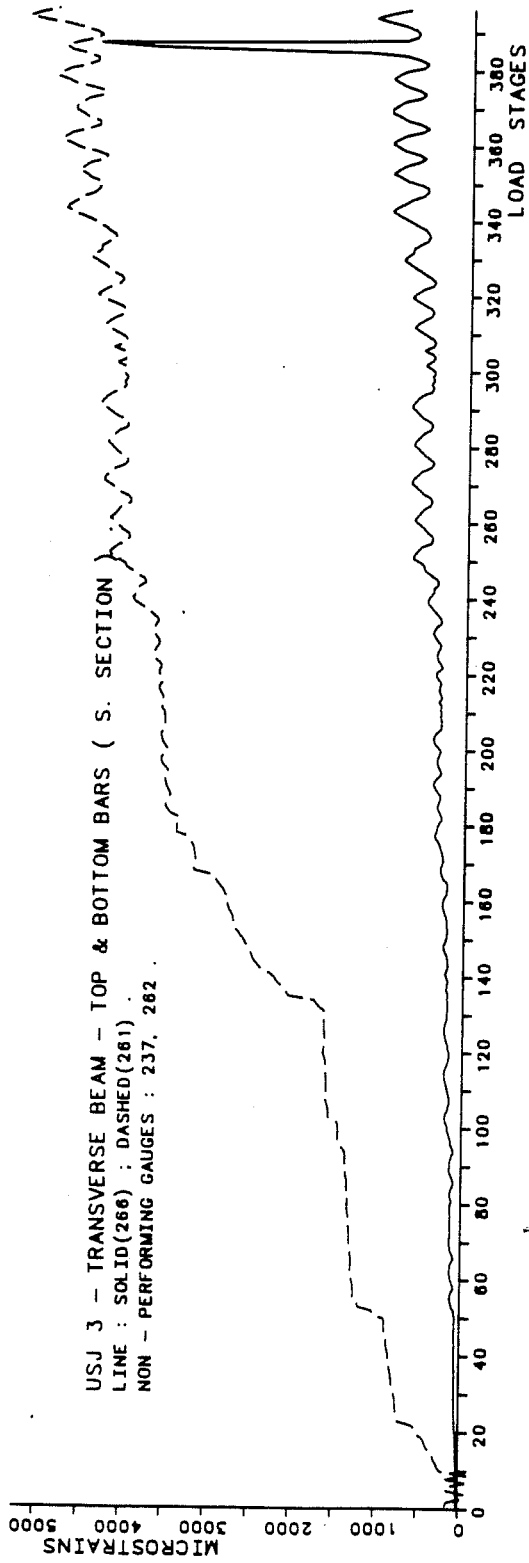


Fig. B.26 (cont.) - USJ-3 - Transverse Beam Bar Strains.

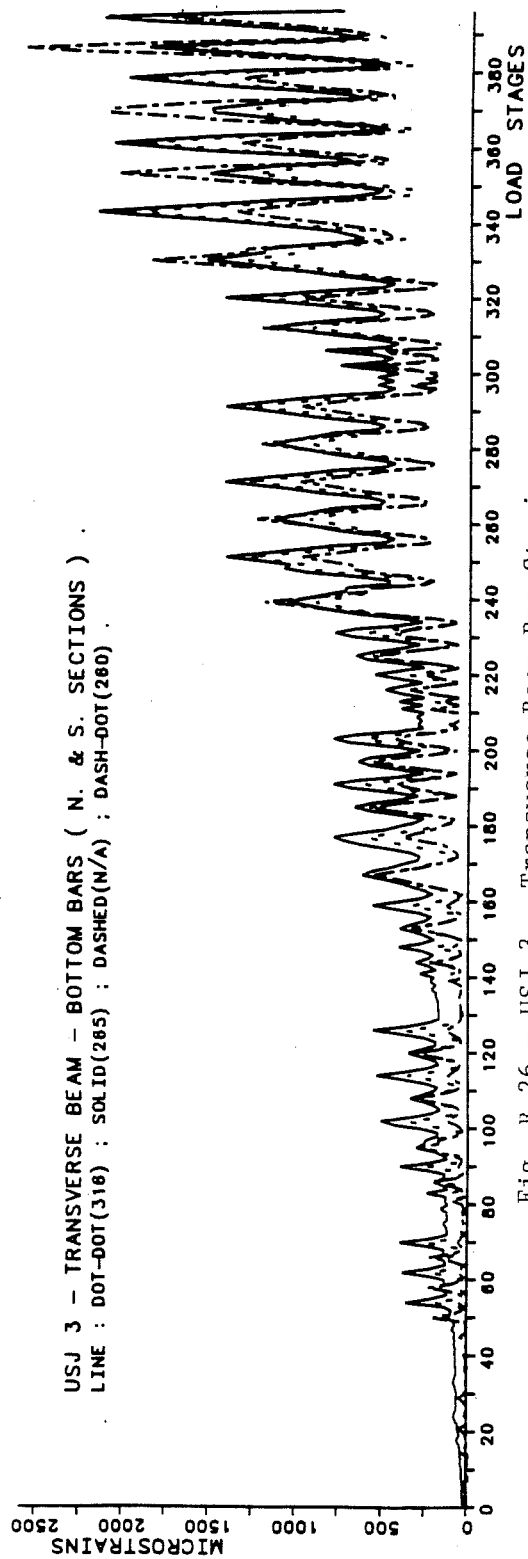
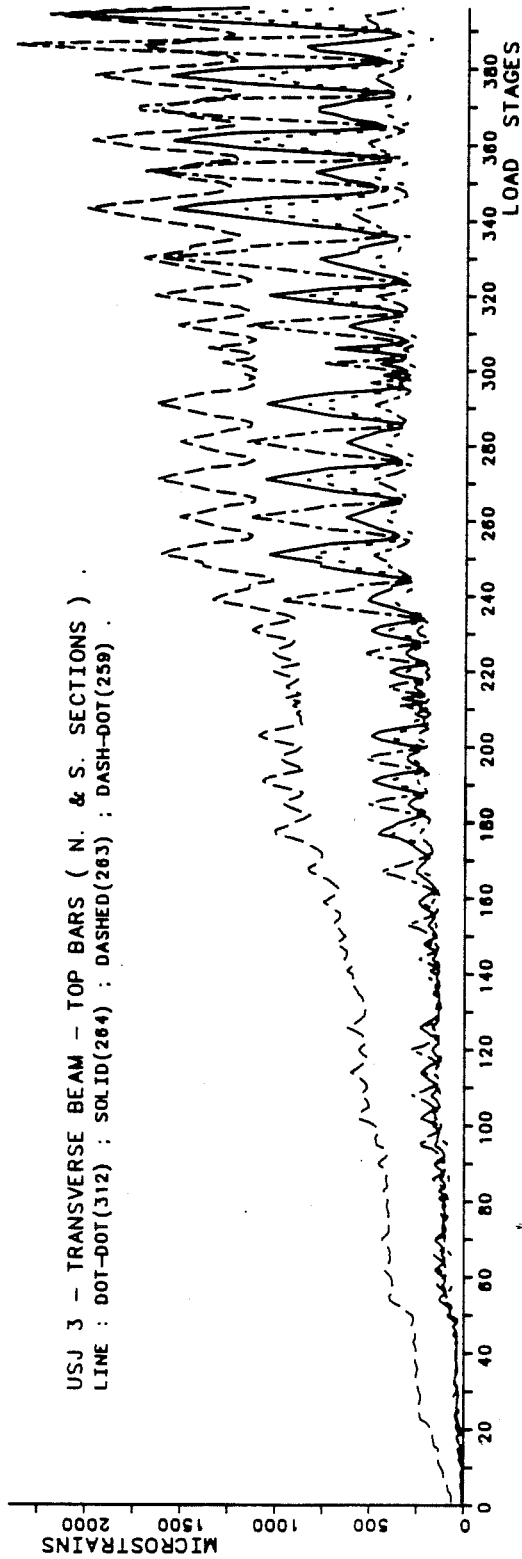


Fig. B.26 - USJ-3 - Transverse Beam Bar Strains.

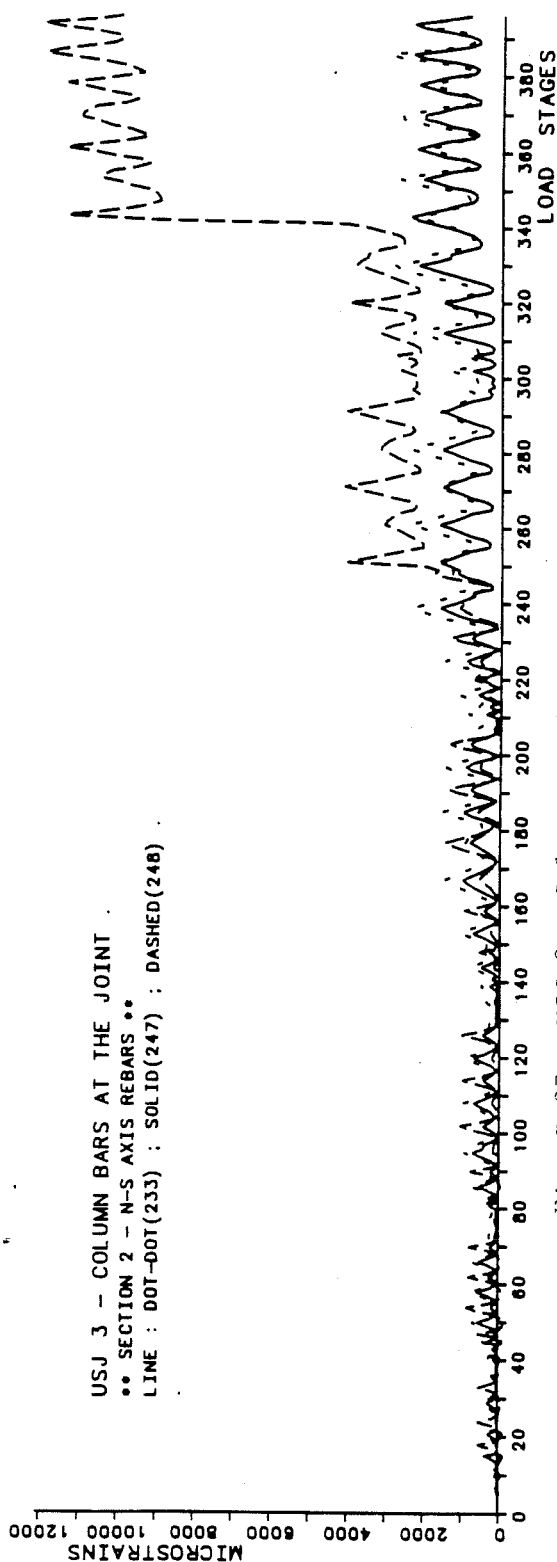
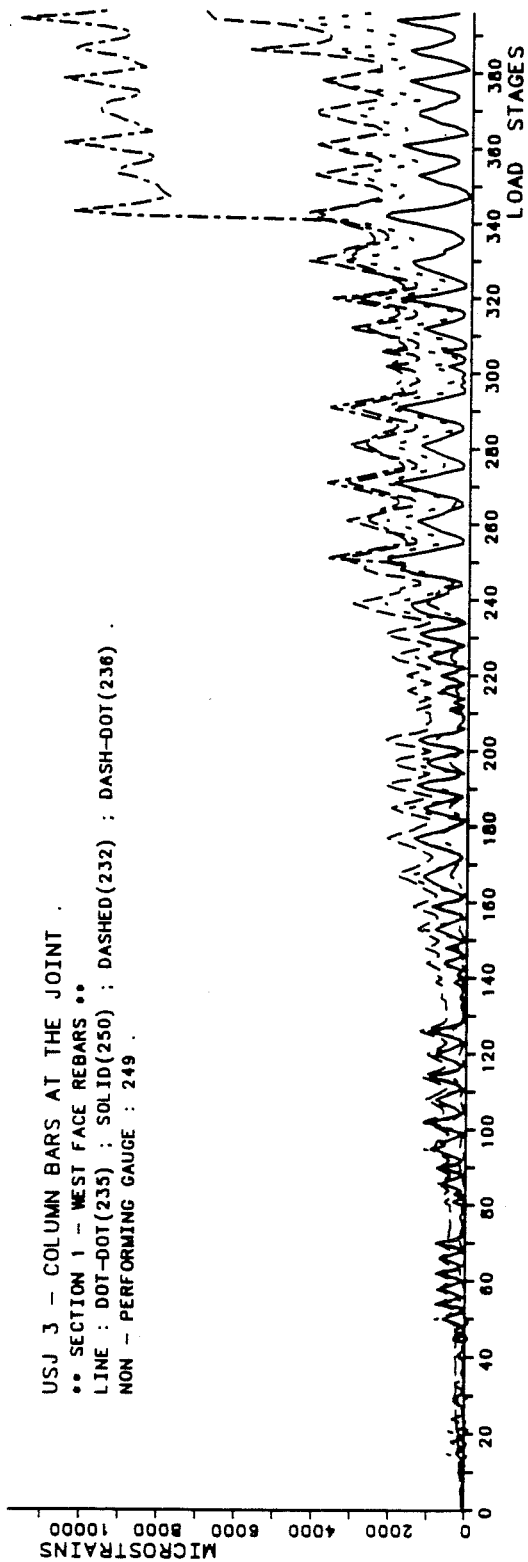


Fig. B.27 - USJ-3 - Column Bar Strains.

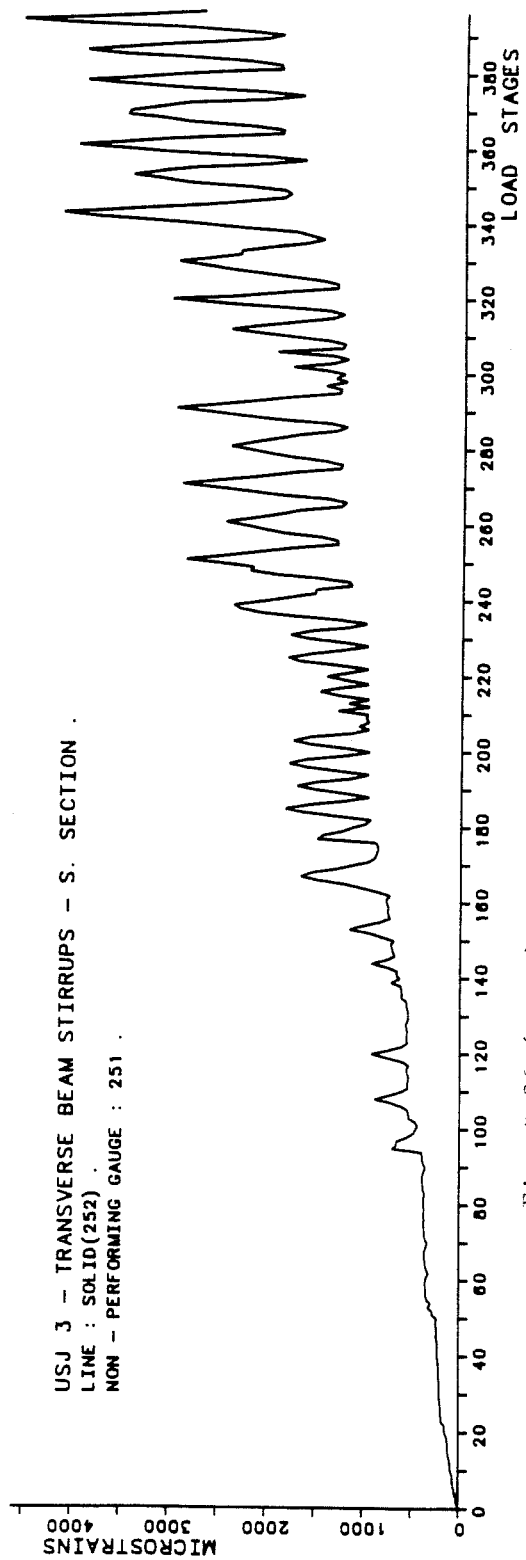
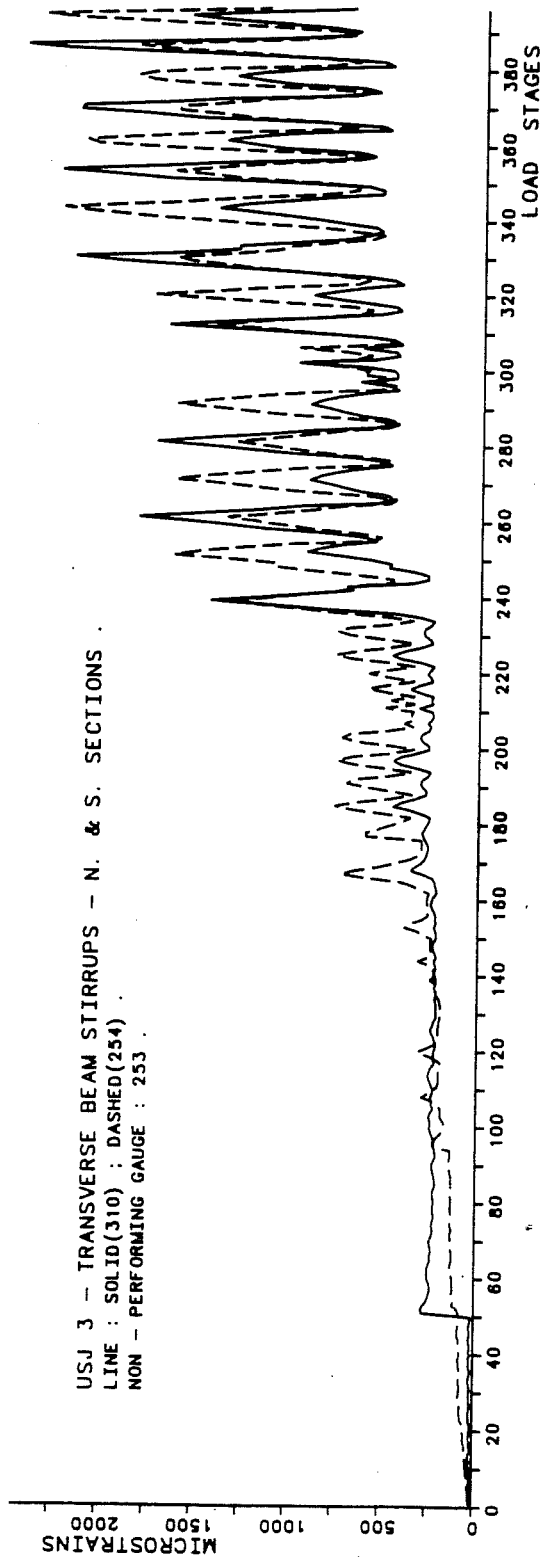


Fig. B.26 (cont.) - USJ-3 - Transverse Beam Bar Strains.

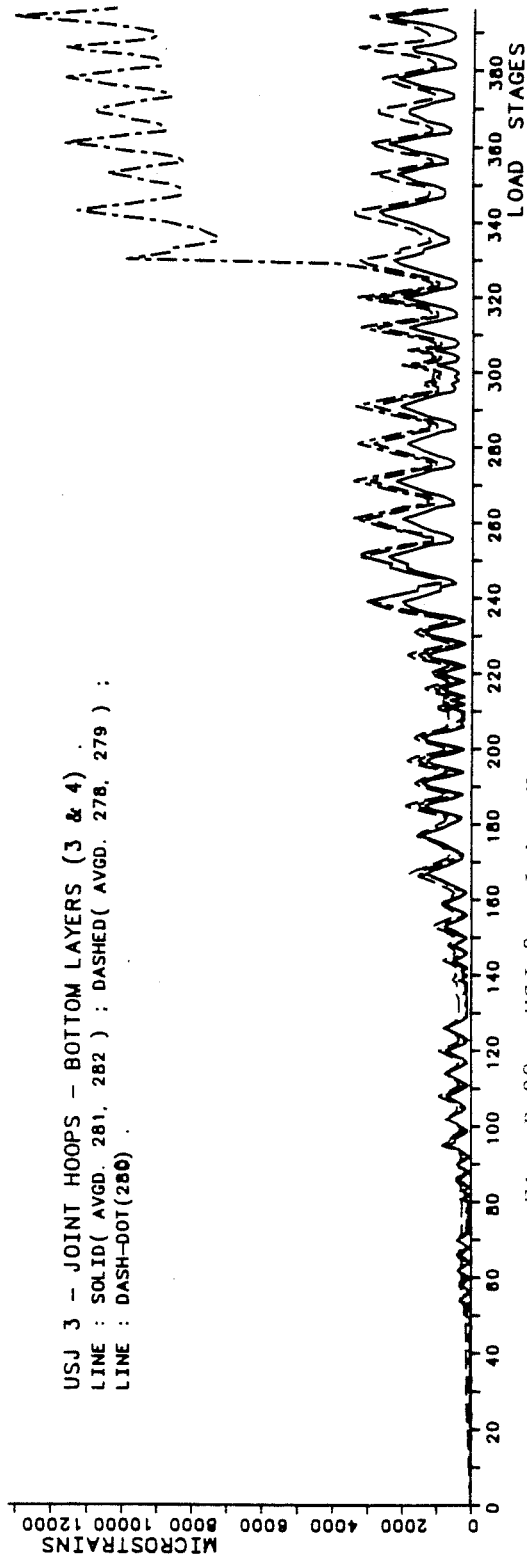
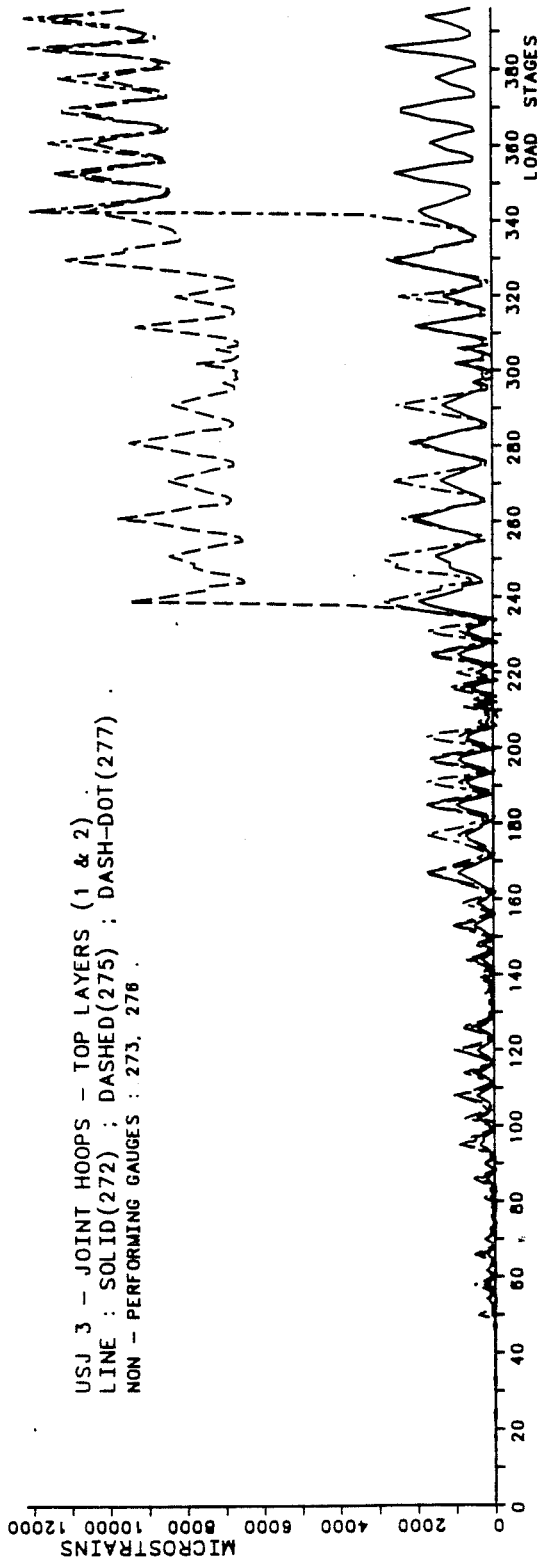


Fig. B.28 - USJ-3 - Joint Hoop Bar Strains.

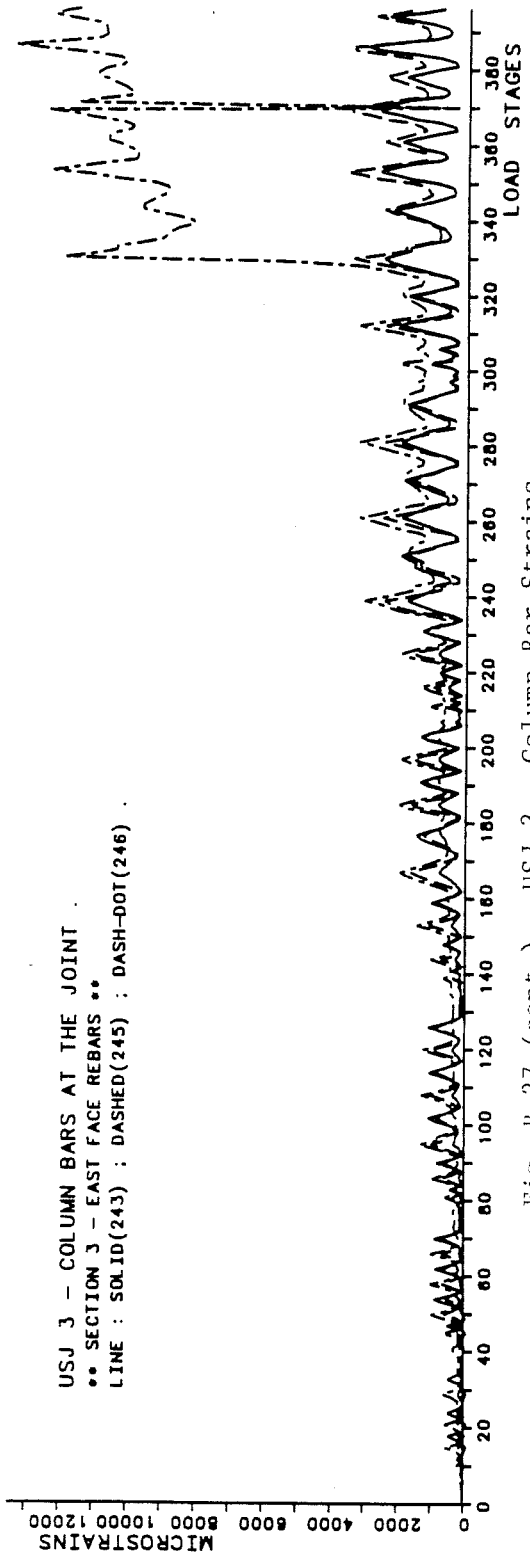
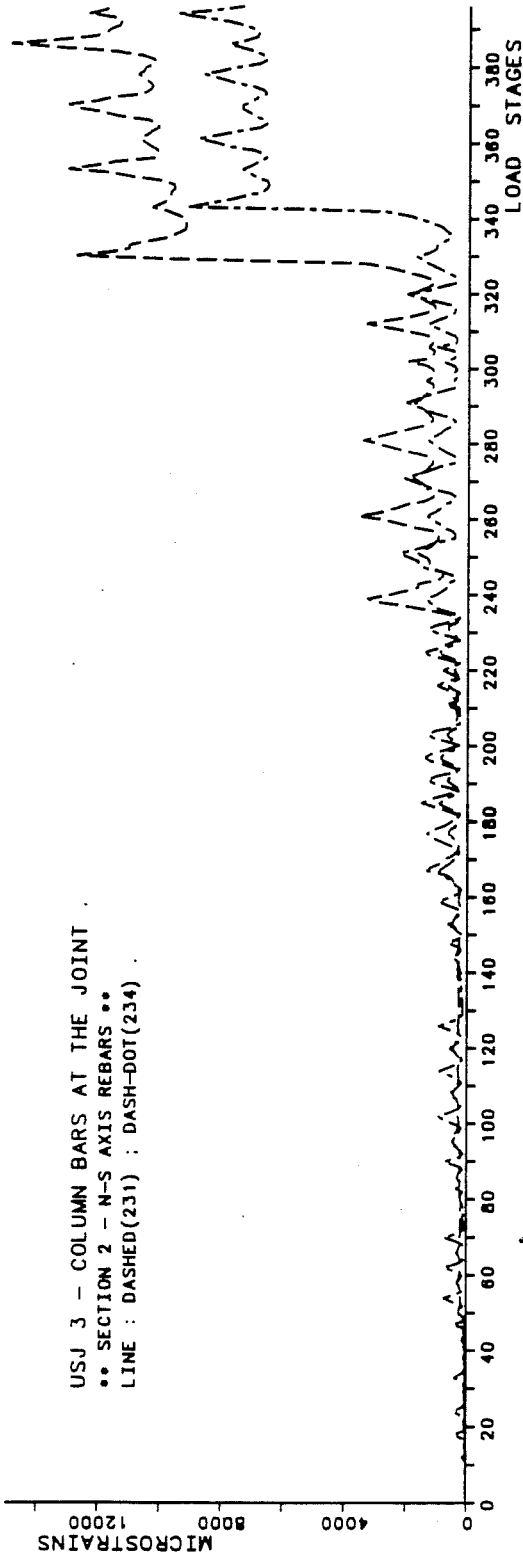


Fig. B.27 (cont.) - USJ-3 - Column Bar Strains.

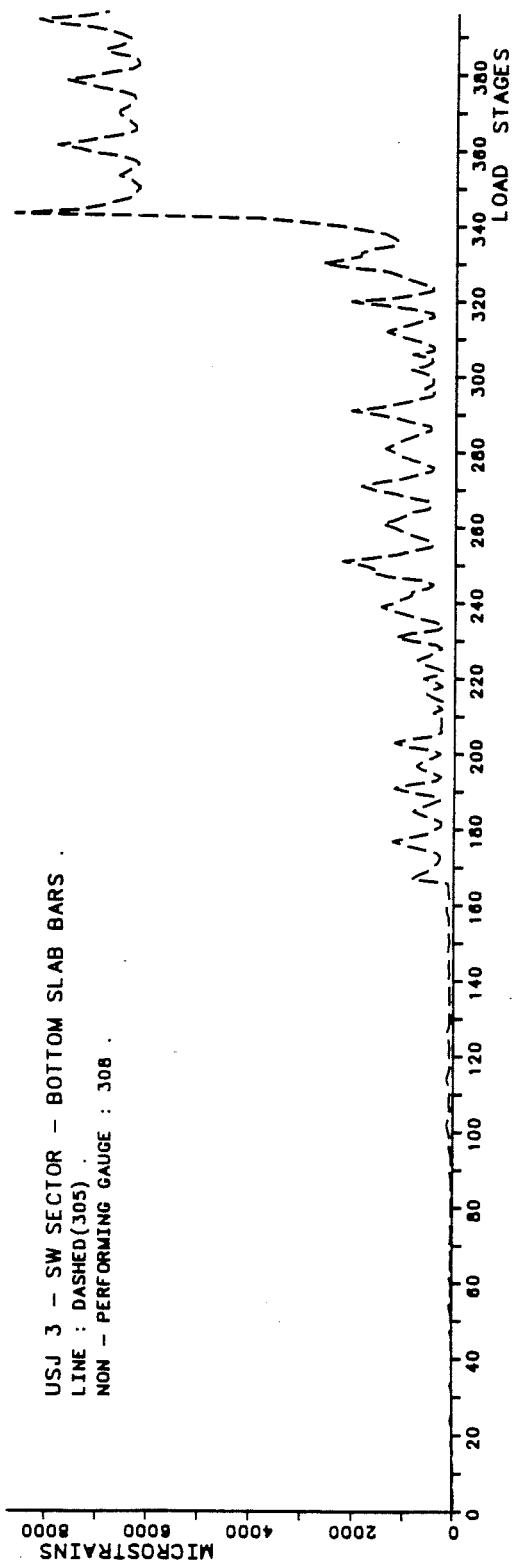
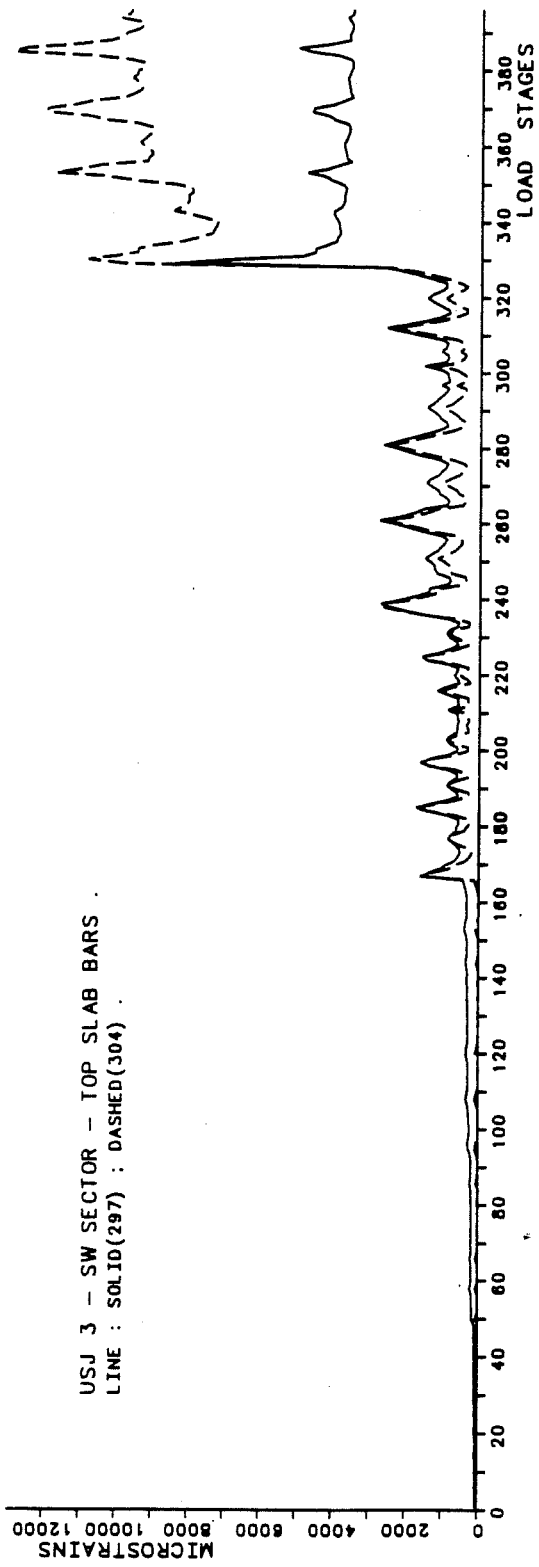


Fig. B.29 (cont.) - USJ-3 - Slab Bar Strains.

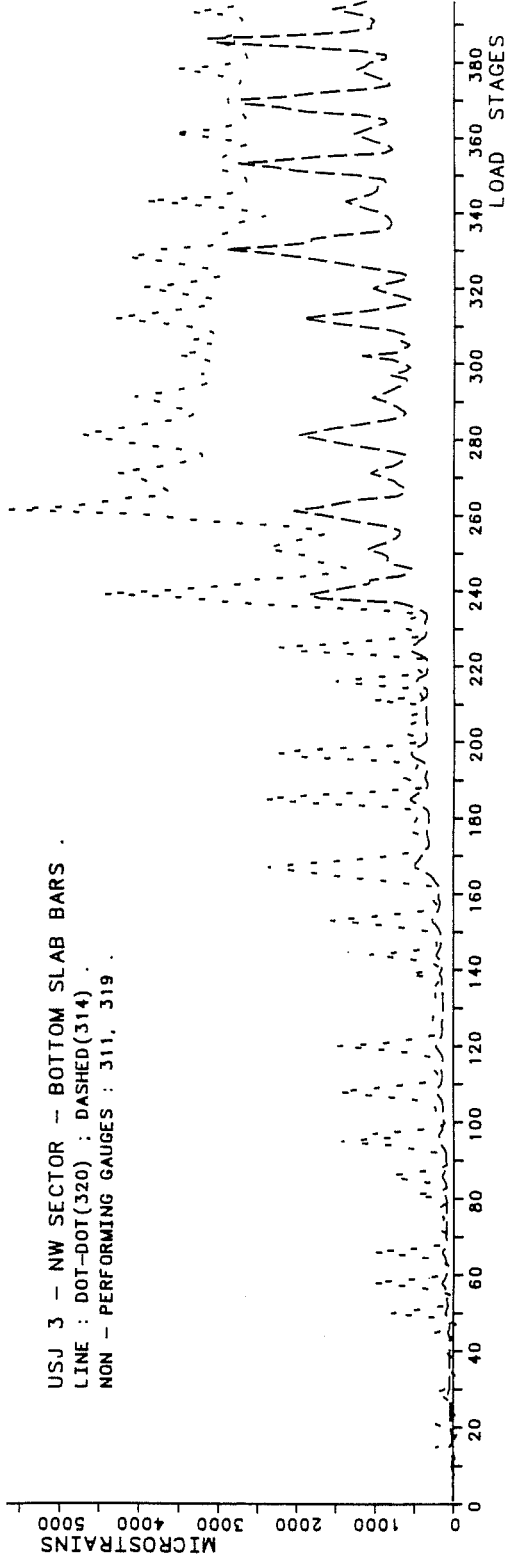
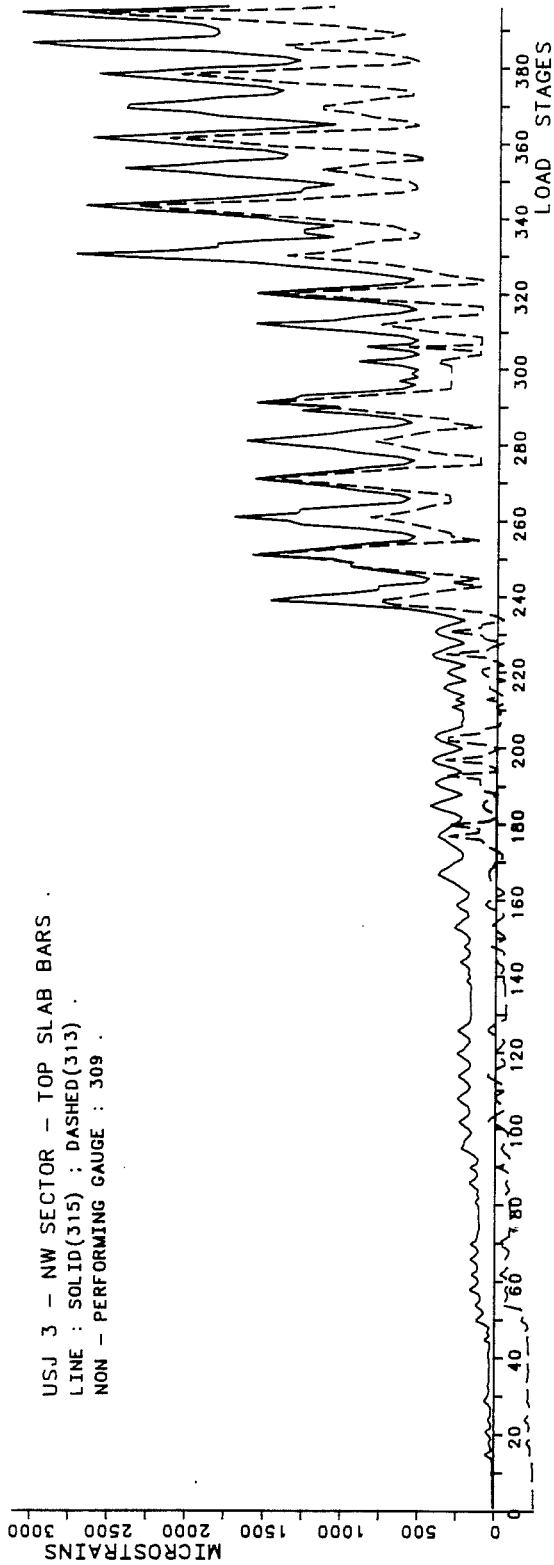


Fig. B.29 - USJ-3 - Slab Bar Strains.

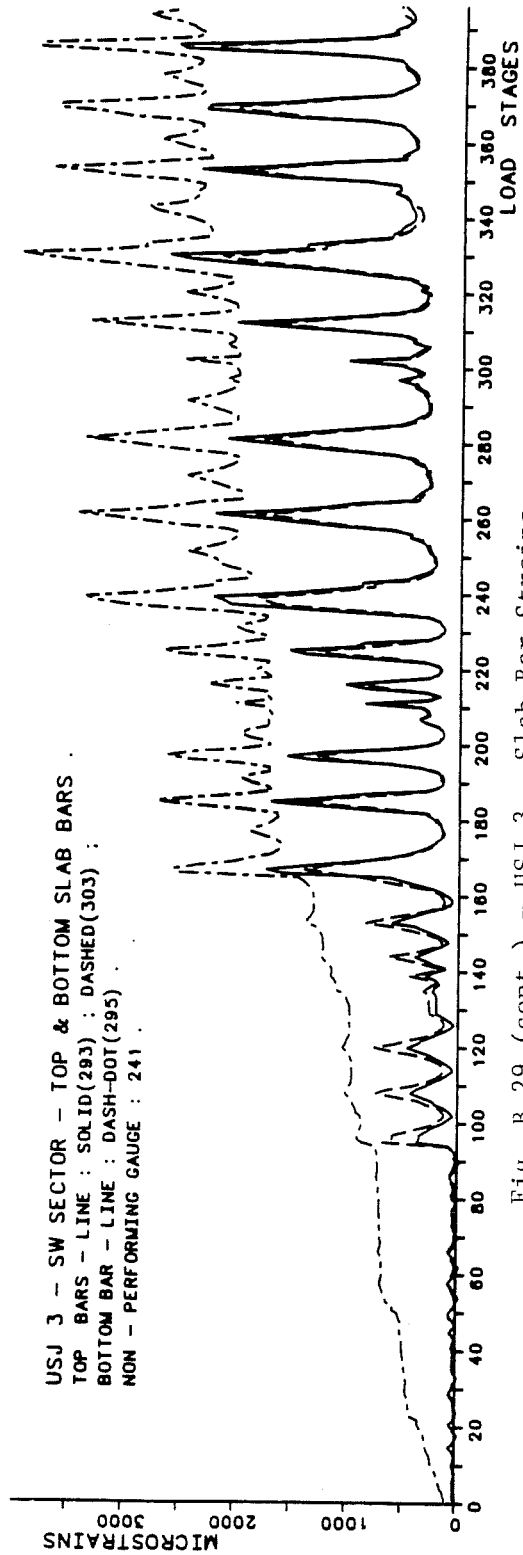
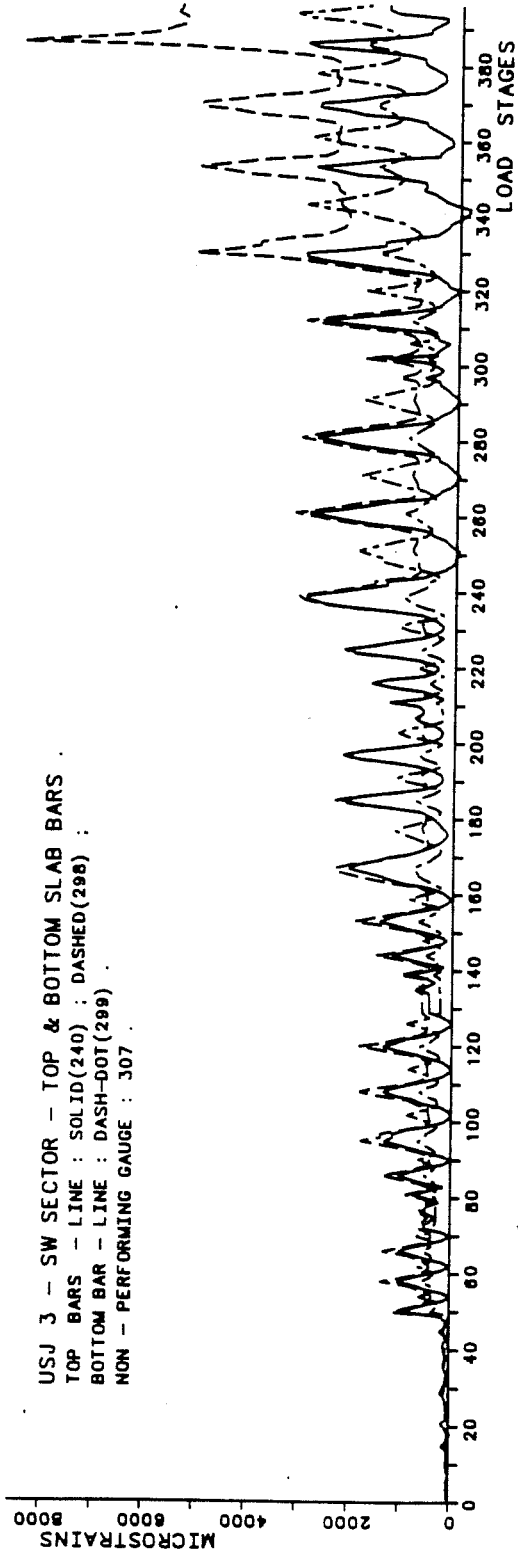


Fig. B.29 (cont.) - USJ-3 - Slab Bar Strains.

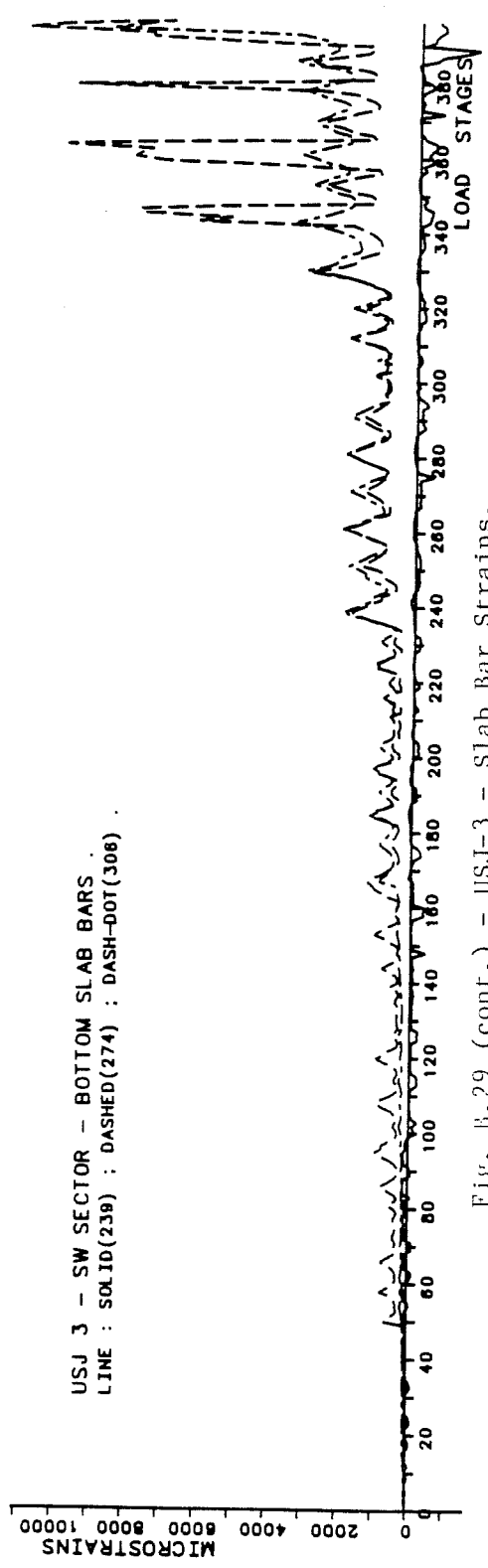
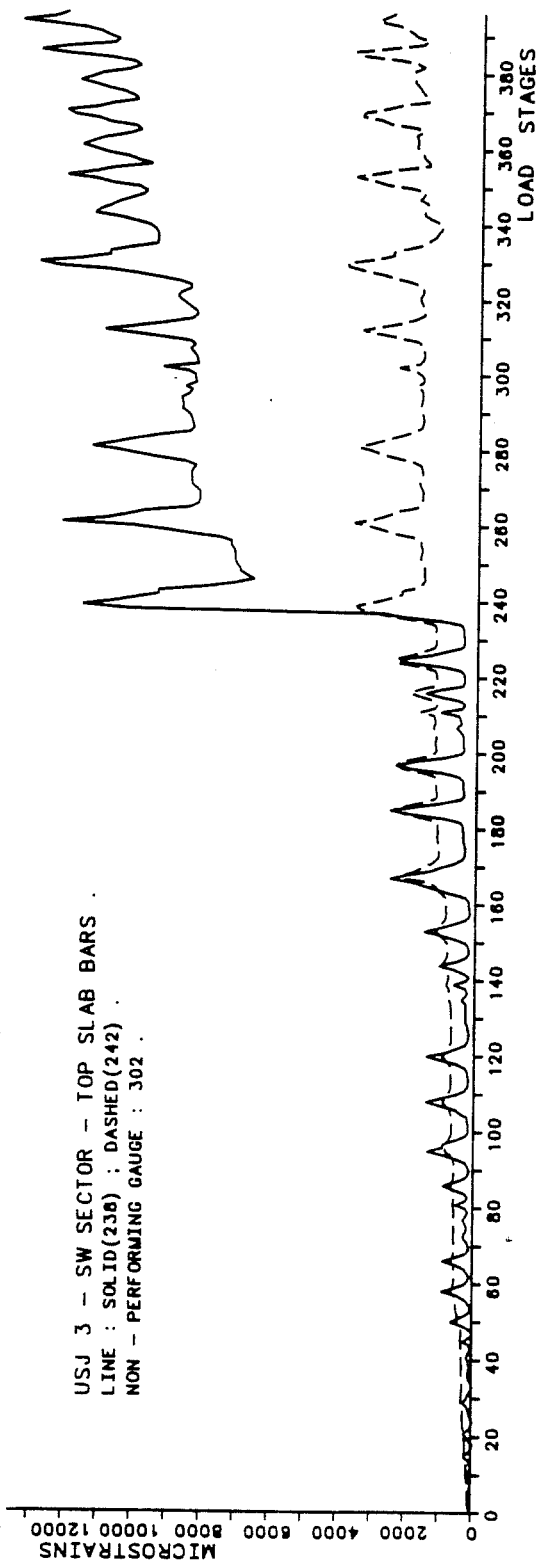


Fig. B.29 (cont.) - USJ-3 - Slab Bar Strains.

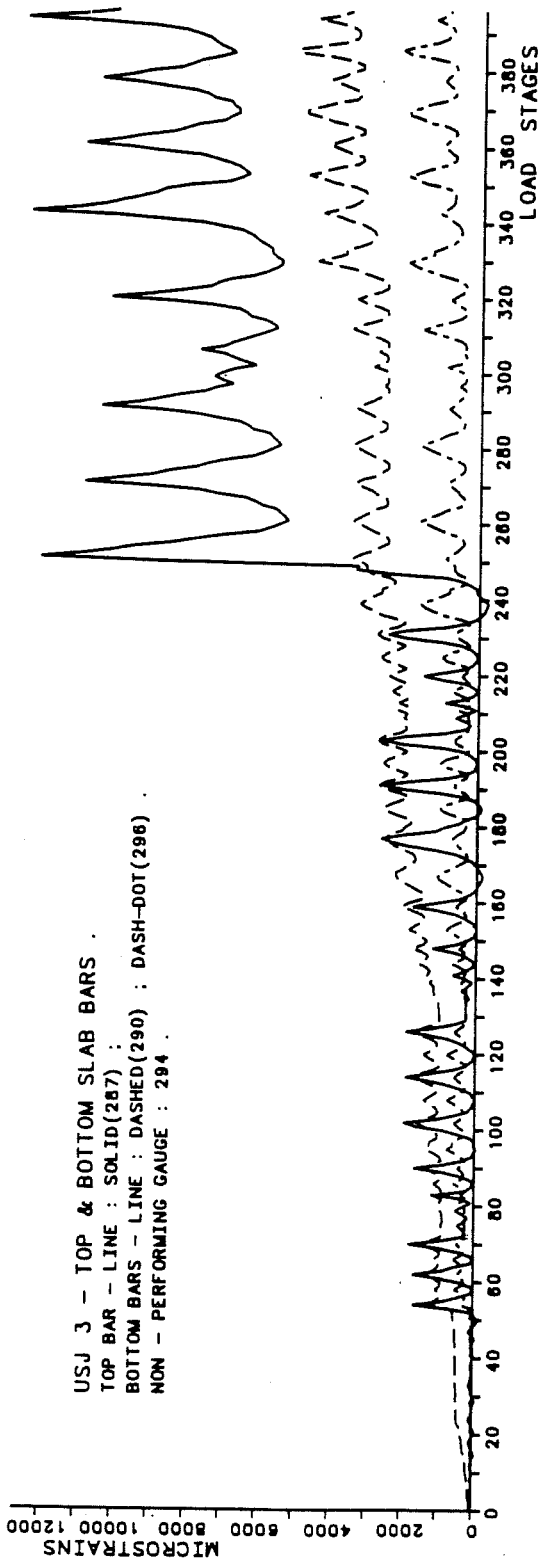


Fig. B.29 (cont.) - USJ-3 - Slab Bar Strains.

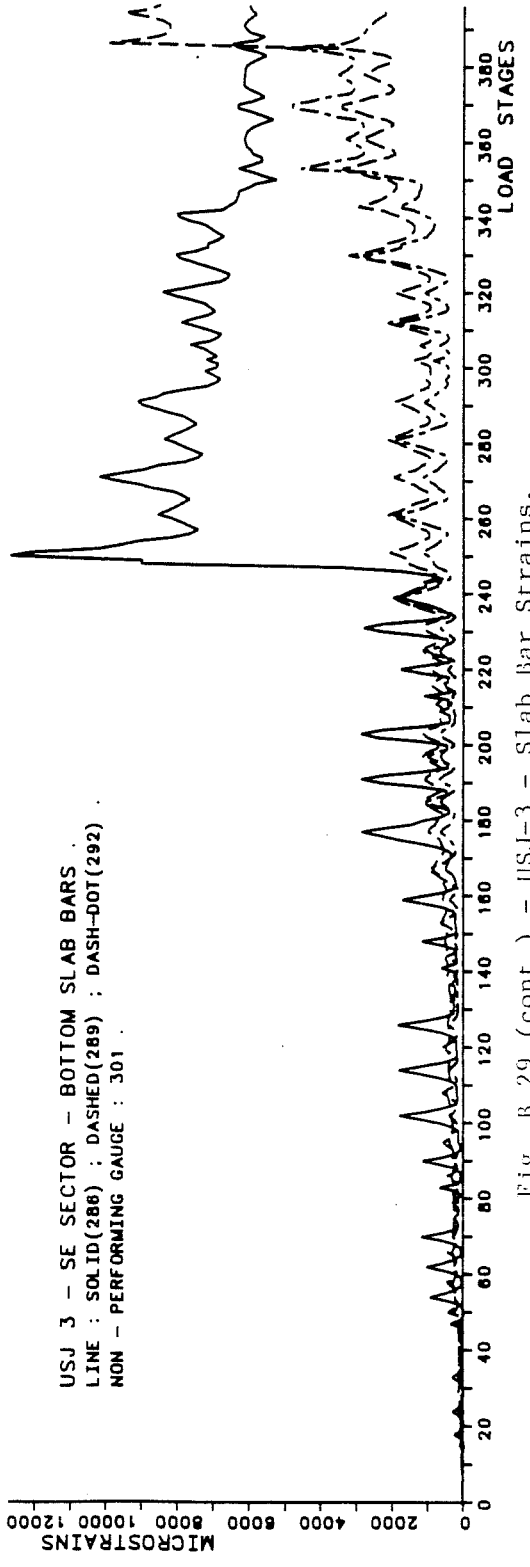
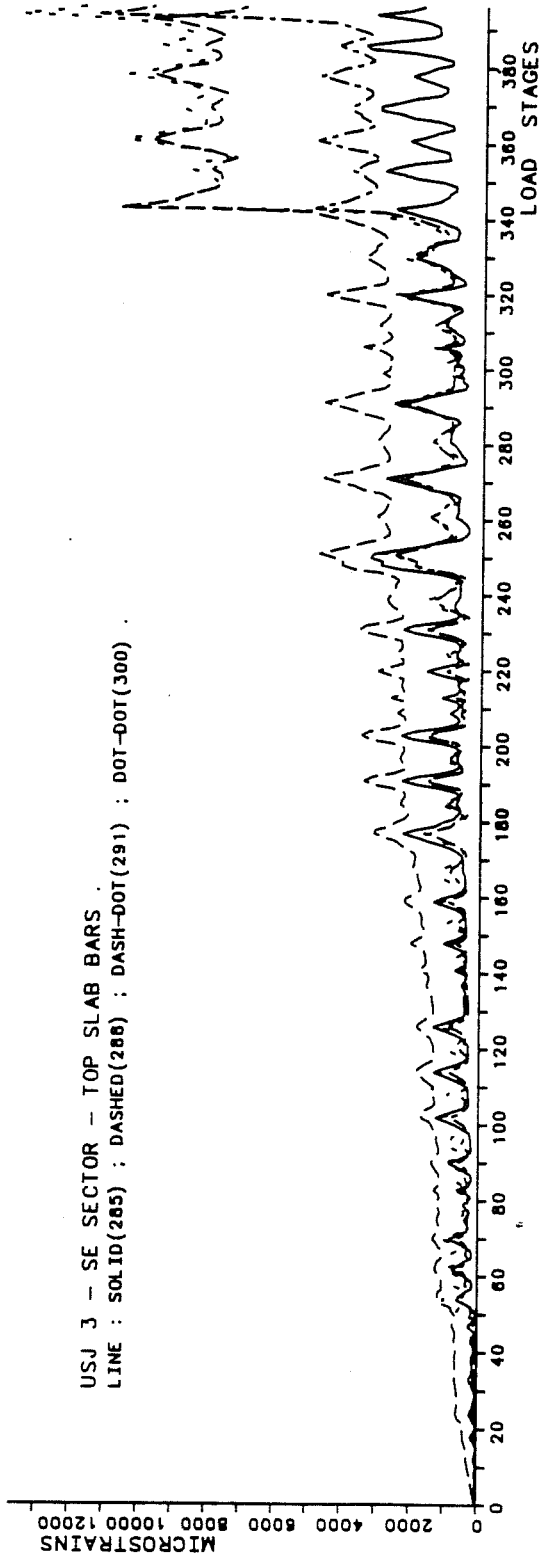


Fig. B.29 (cont.) - USJ-3 - Slab Bar Strains.

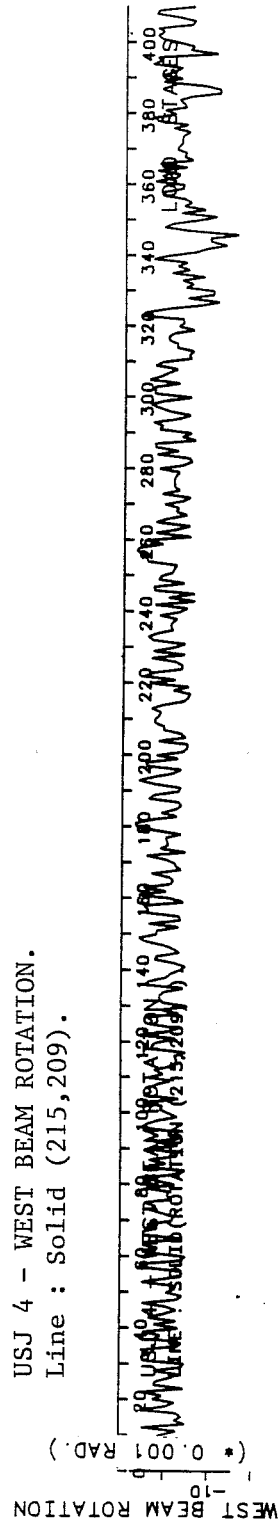
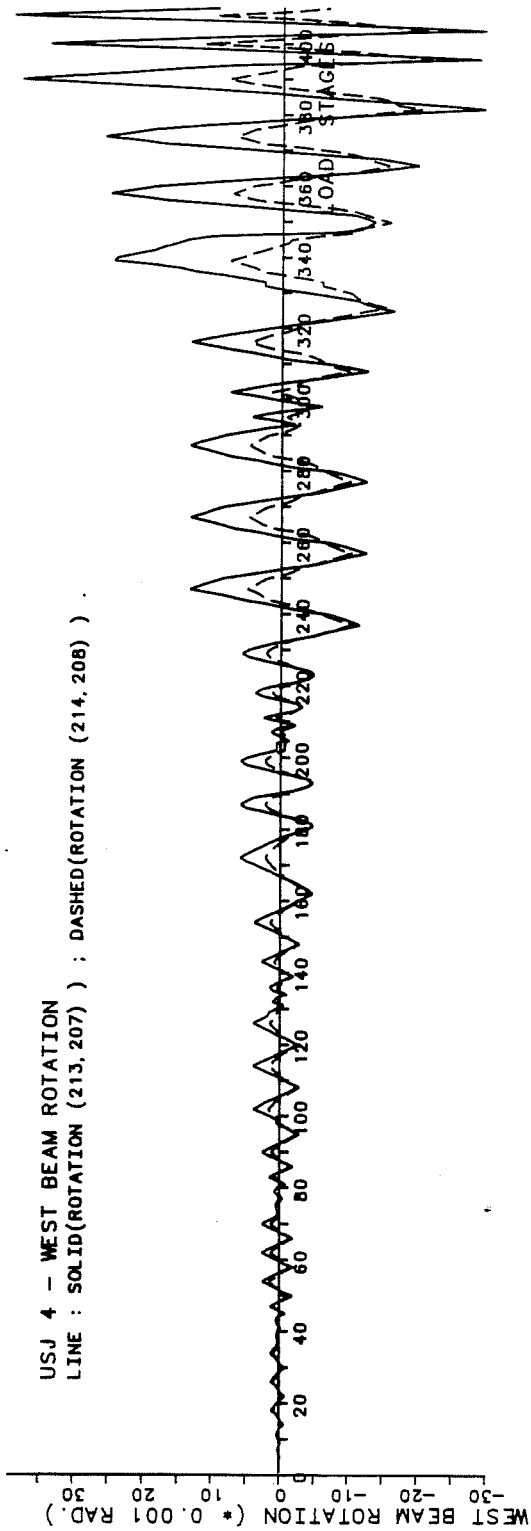


Fig. B.31 - USJ-4 - Beam Rotation.

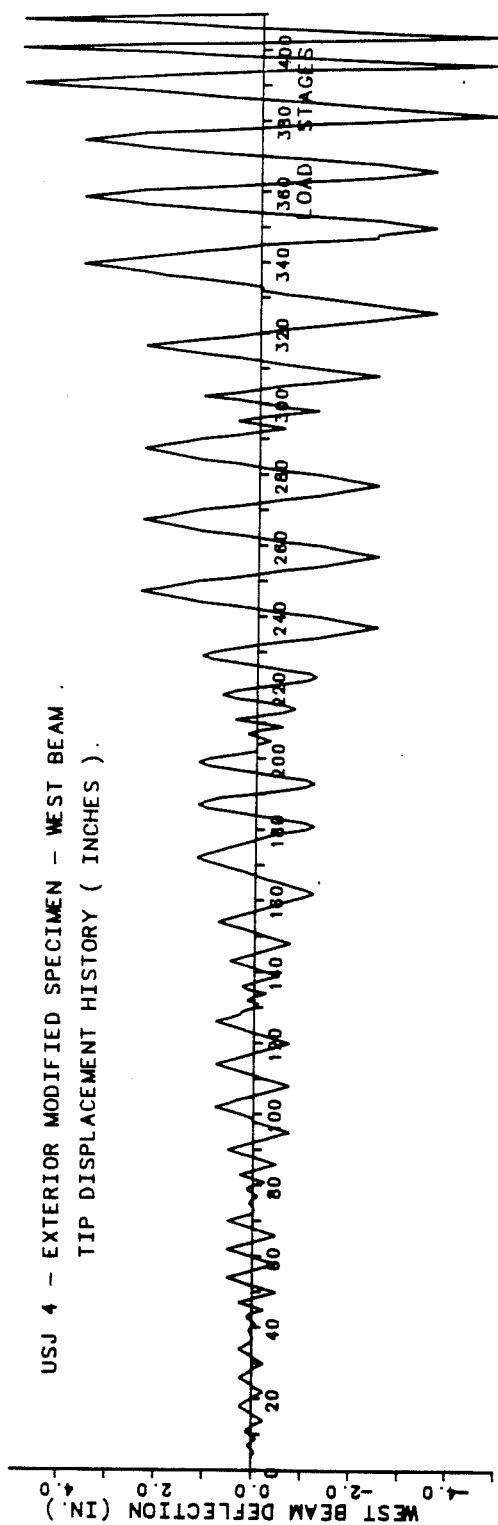
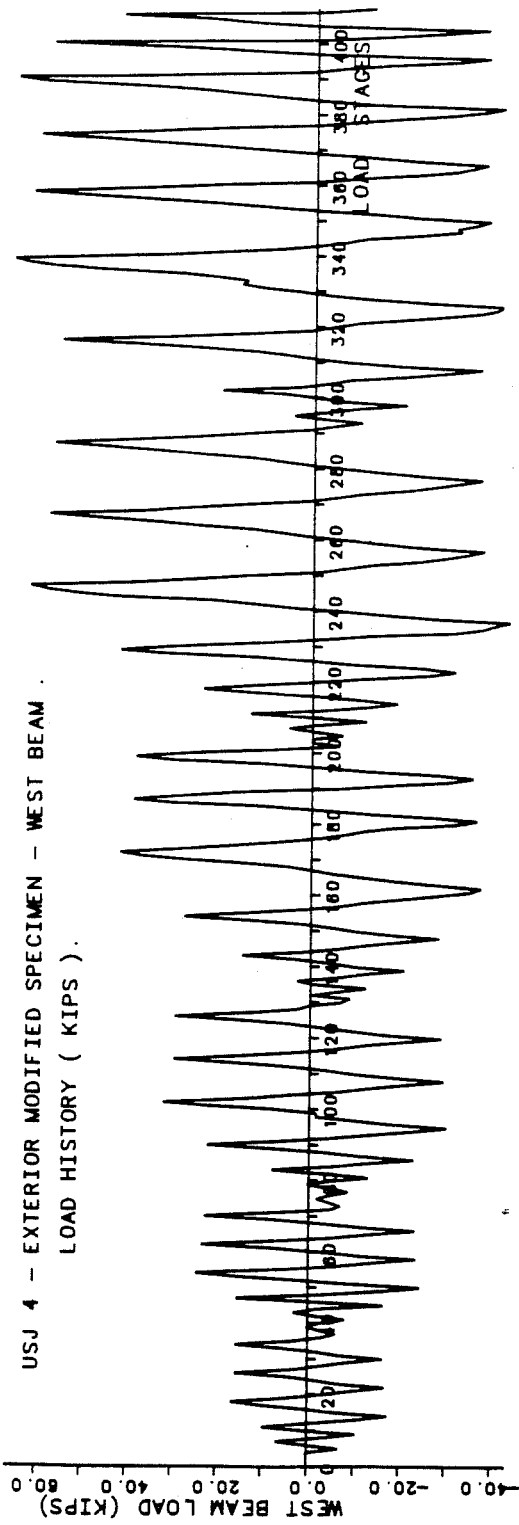


Fig. B.30 - USJ-4 - Load-Deflection Response.

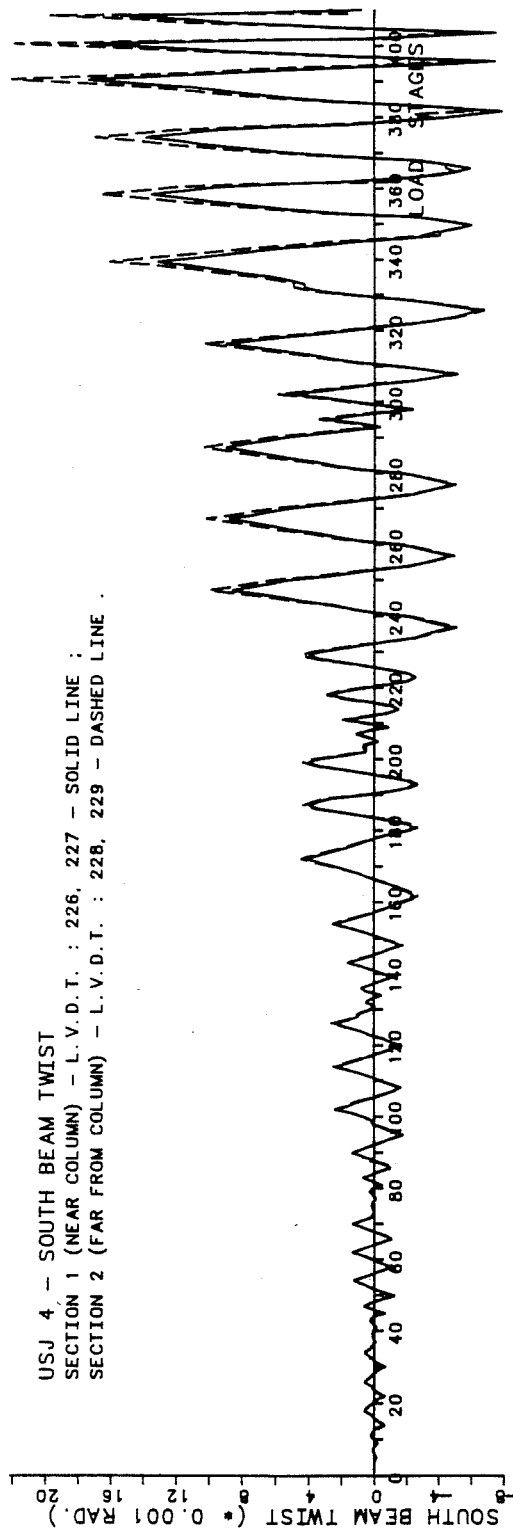
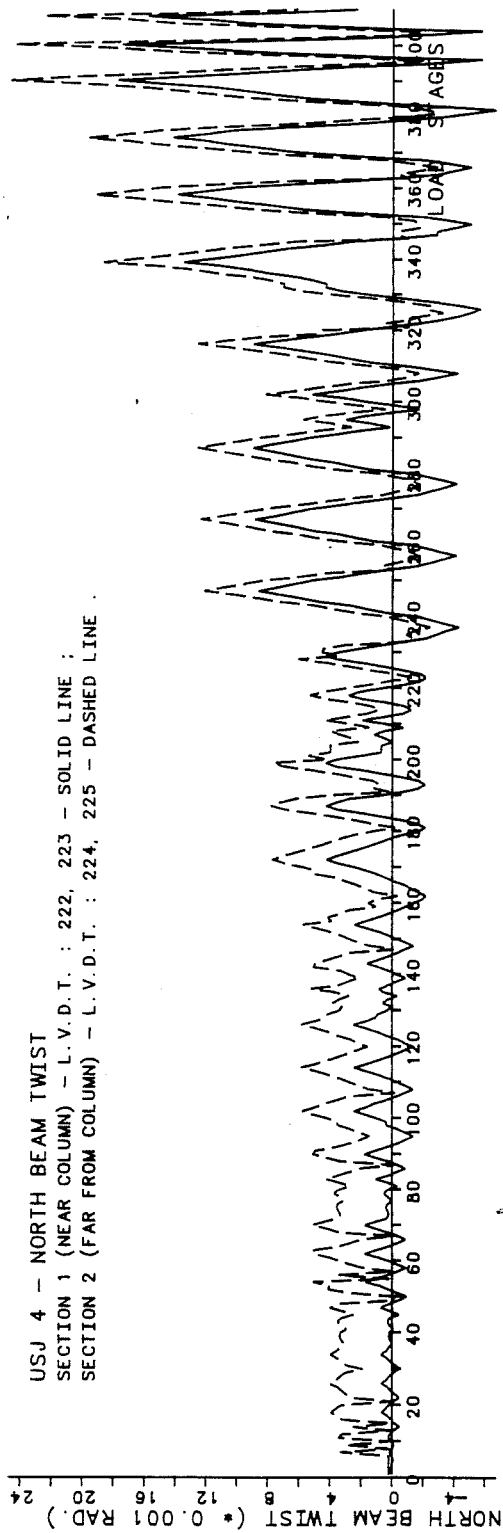


Fig. B.33 - USJ-4 - Transverse Beam Twist.

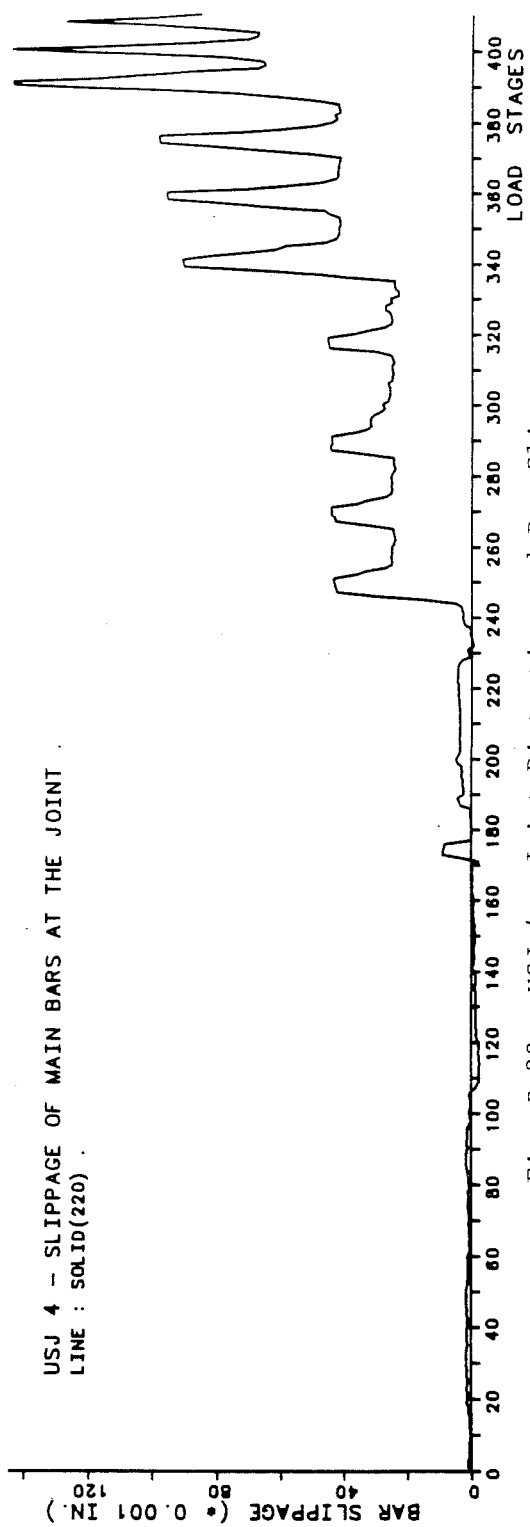
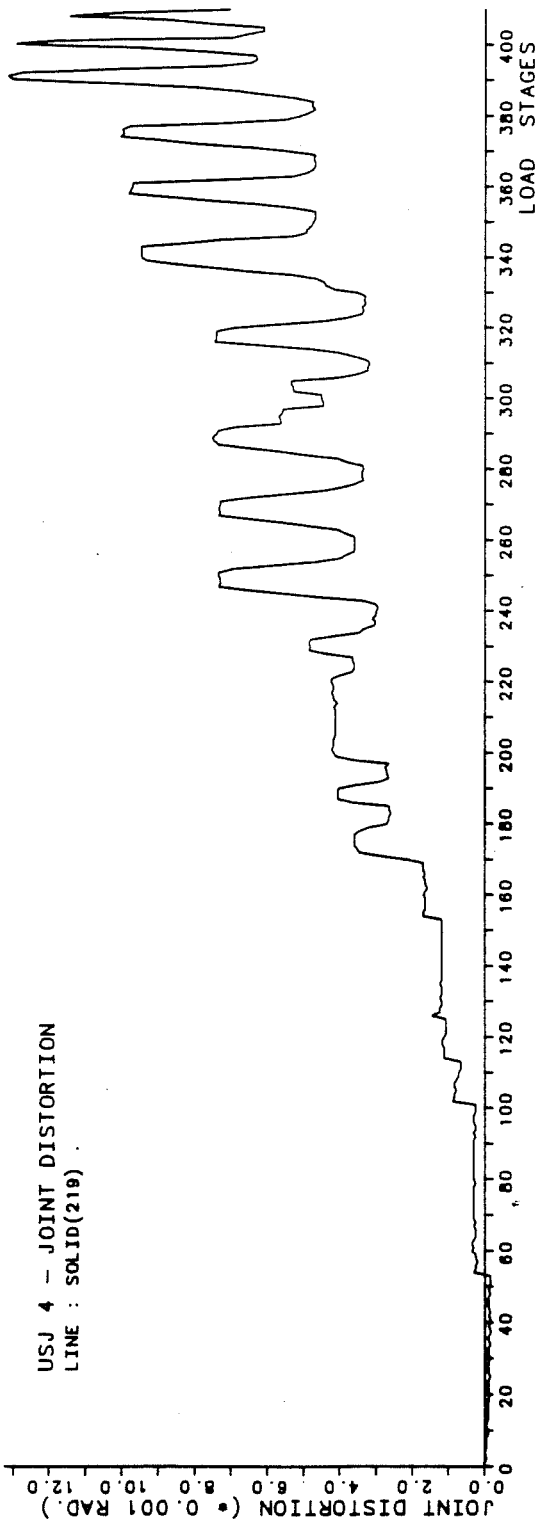


Fig. B.32 - USJ-4 - Joint Distortion and Bar Slippage.

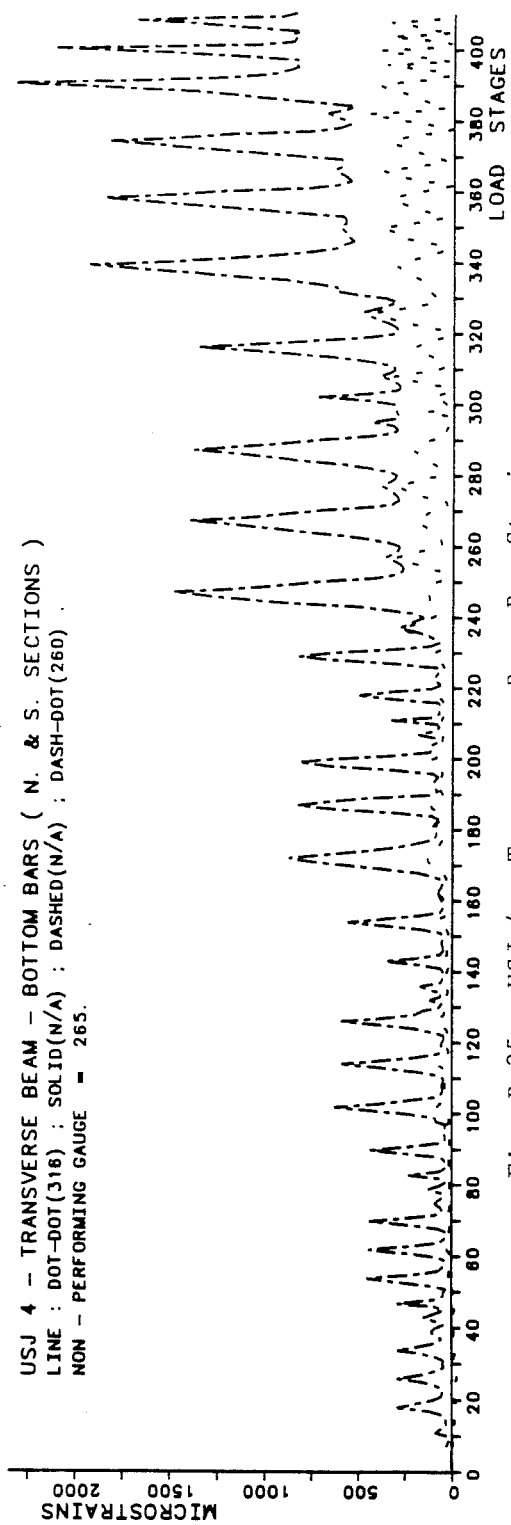
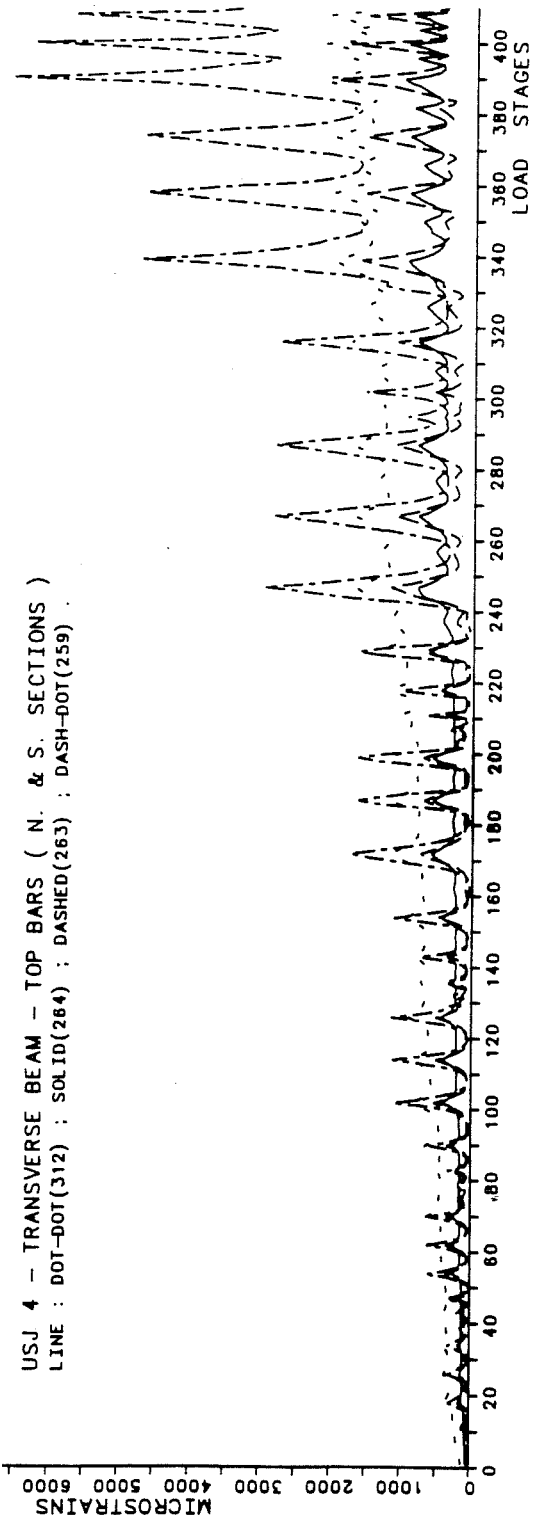


Fig. B.35 - USJ-4 - Transverse Beam Bar Strains.

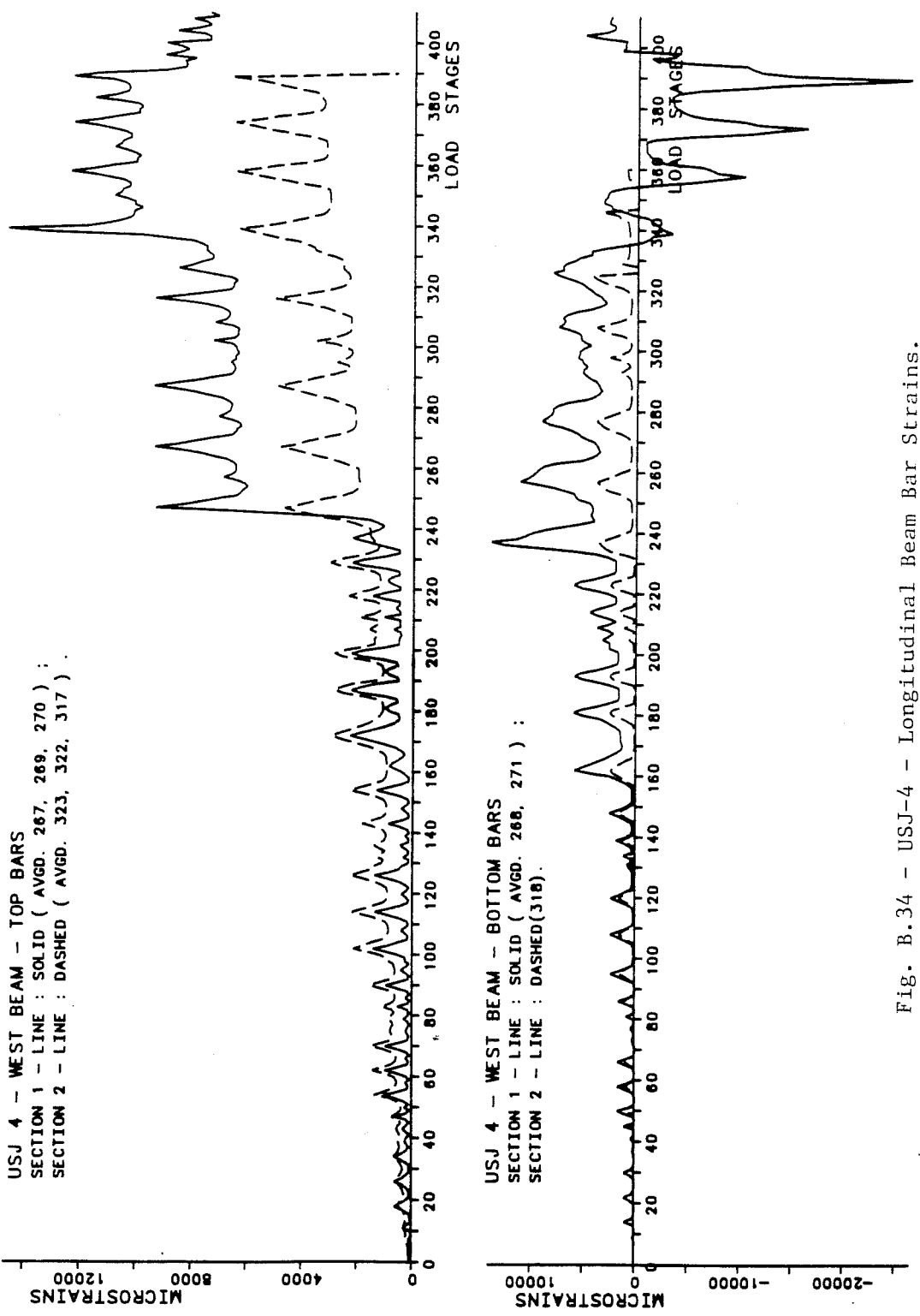


Fig. B.34 - USJ-4 - Longitudinal Beam Bar Strains.

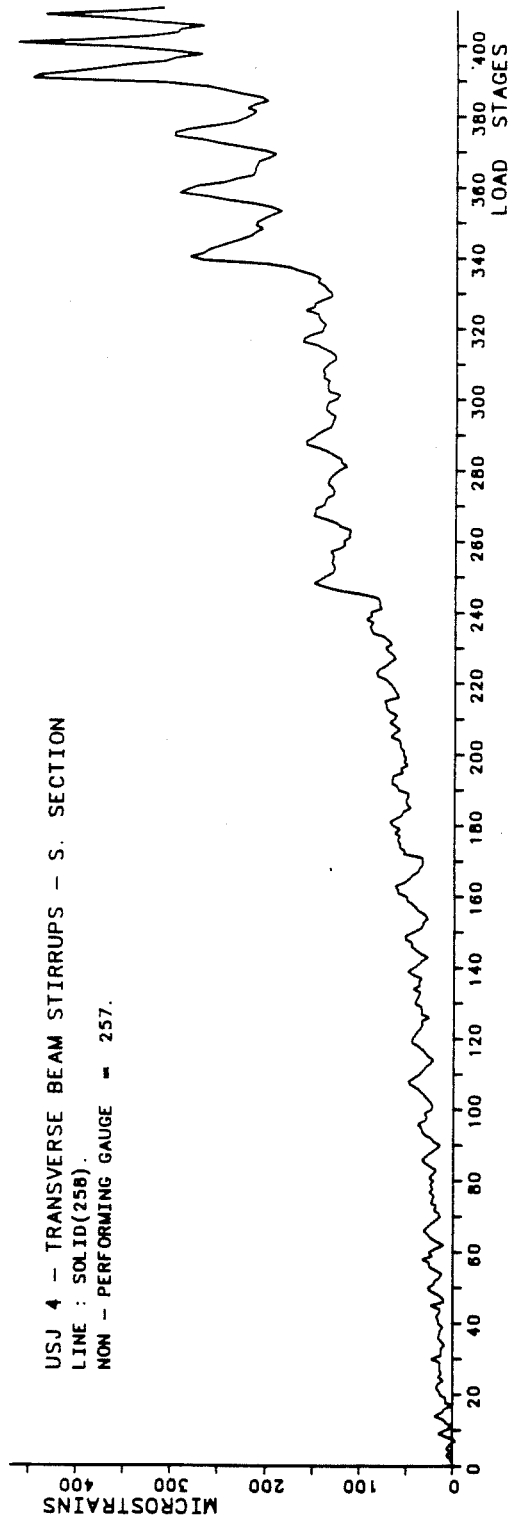
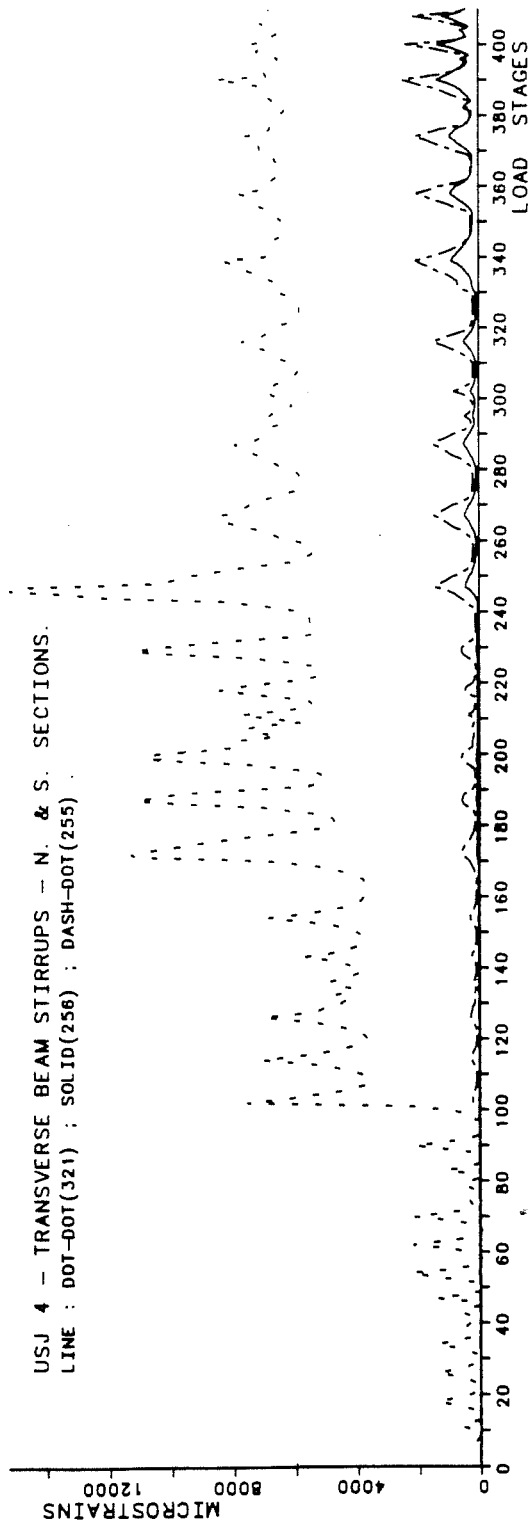


Fig. B.35 (cont.) - USJ-4 - Transverse Beam Bar Strains.

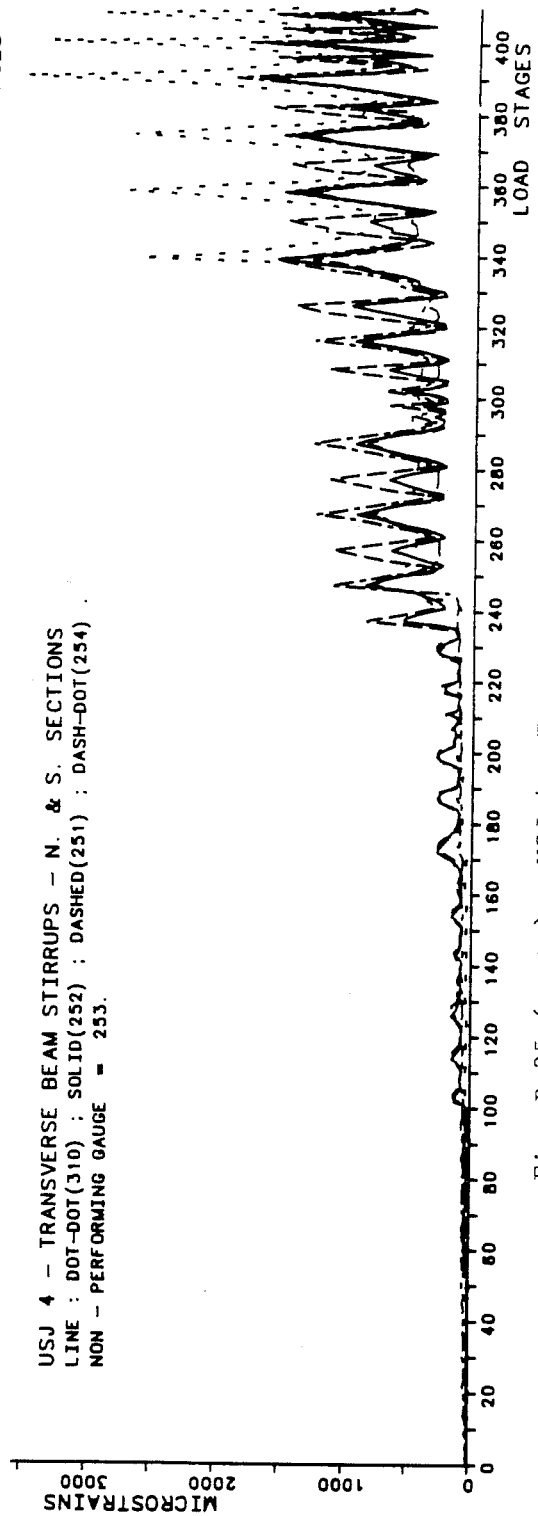
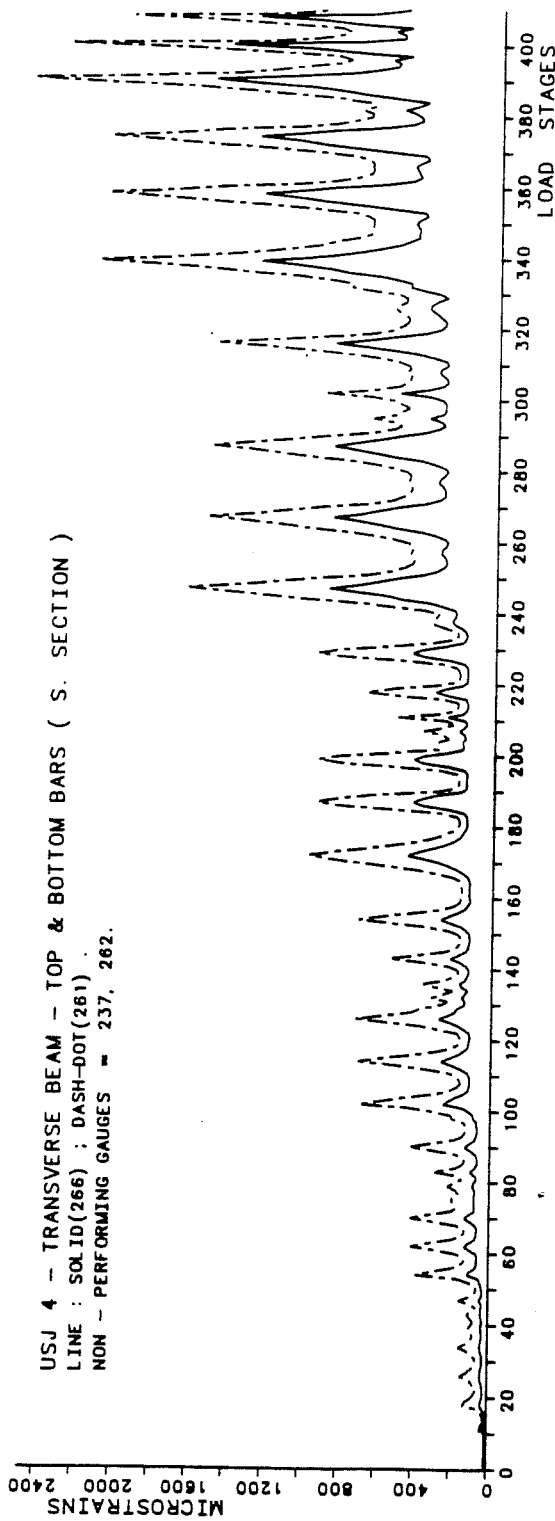


Fig. B.35 (cont.) - USJ-4 - Transverse Beam Bar Strains.

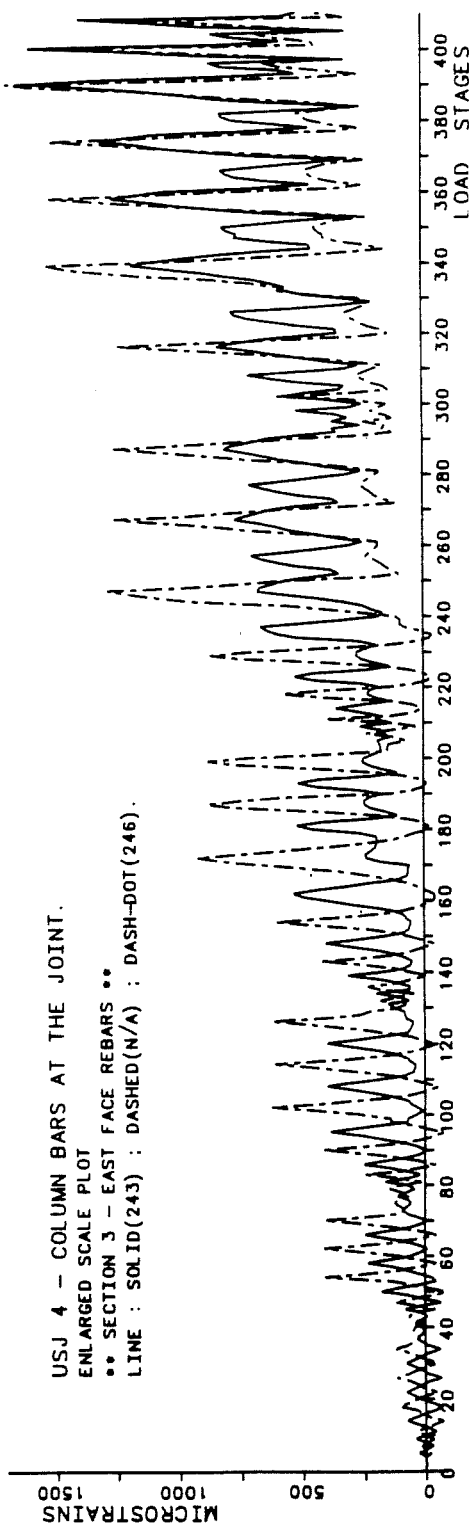
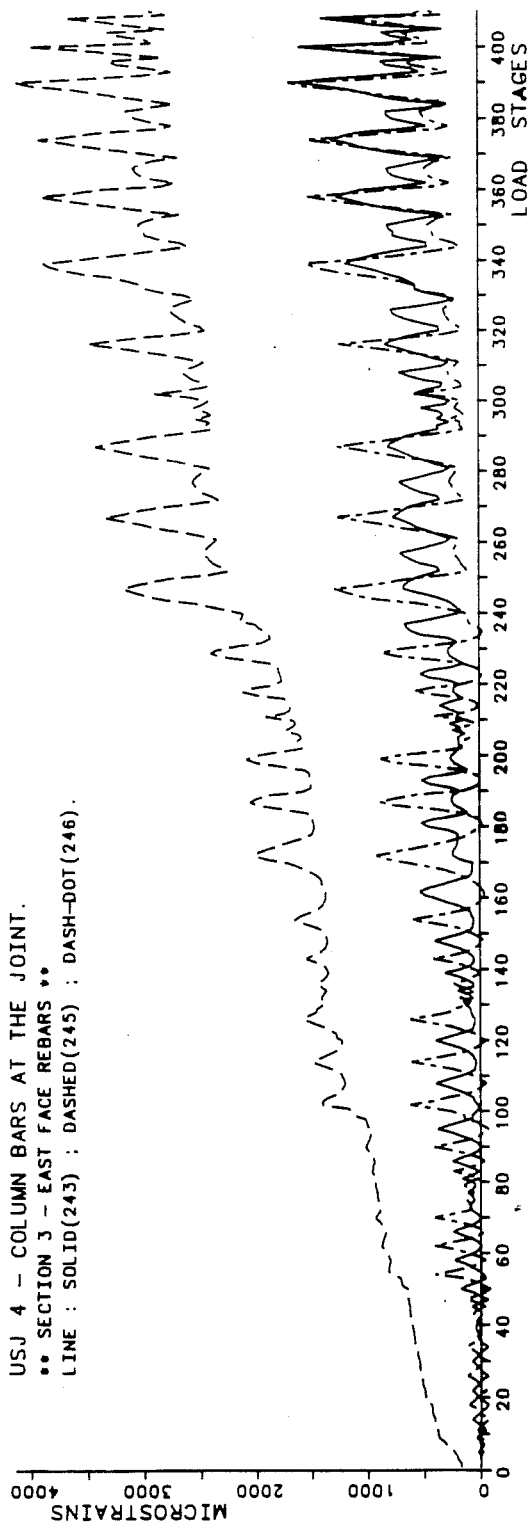


Fig. B.36 (cont.) - USJ-4 - Column Bar Strains.

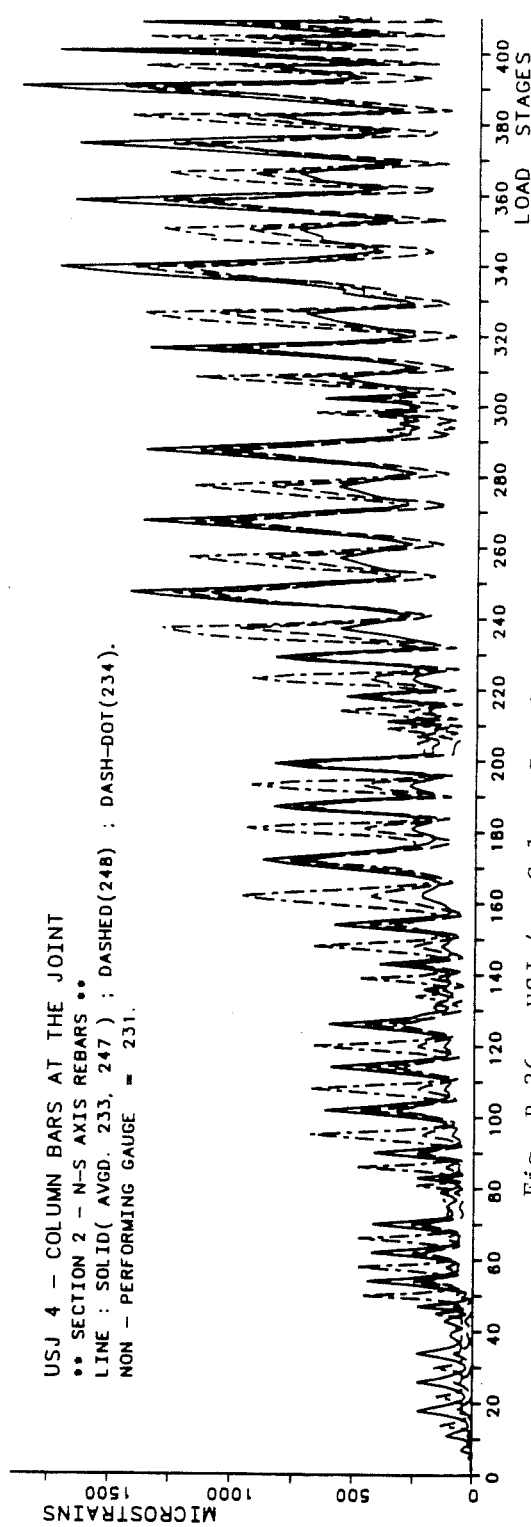
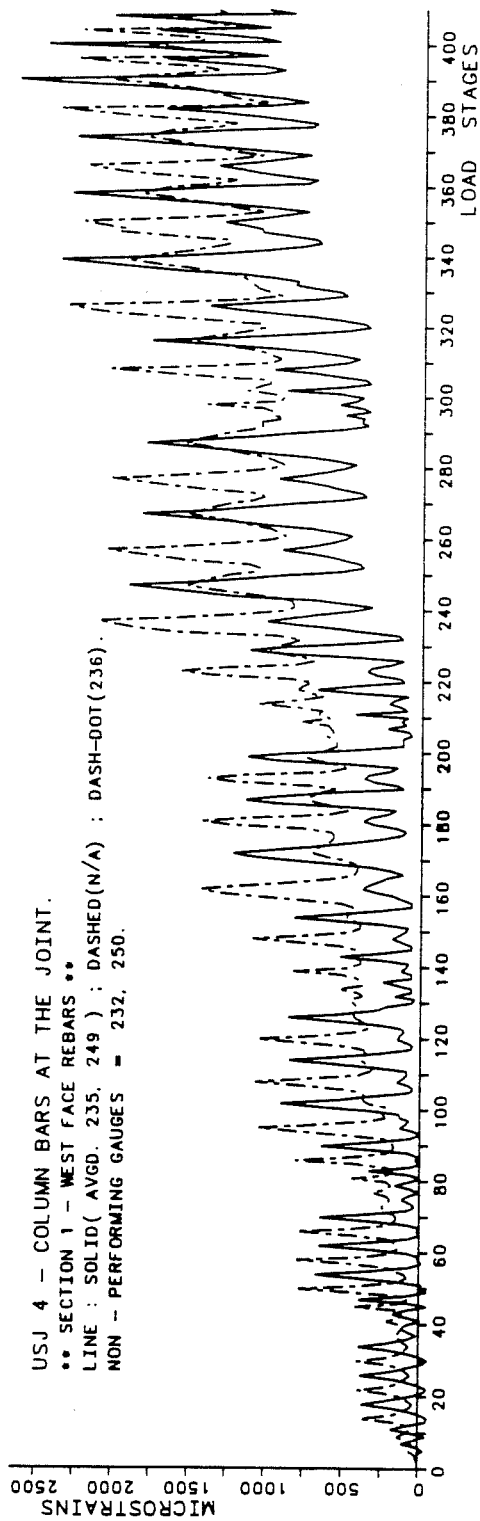


Fig. B.36 - USJ-4 - Column Bar Strains.

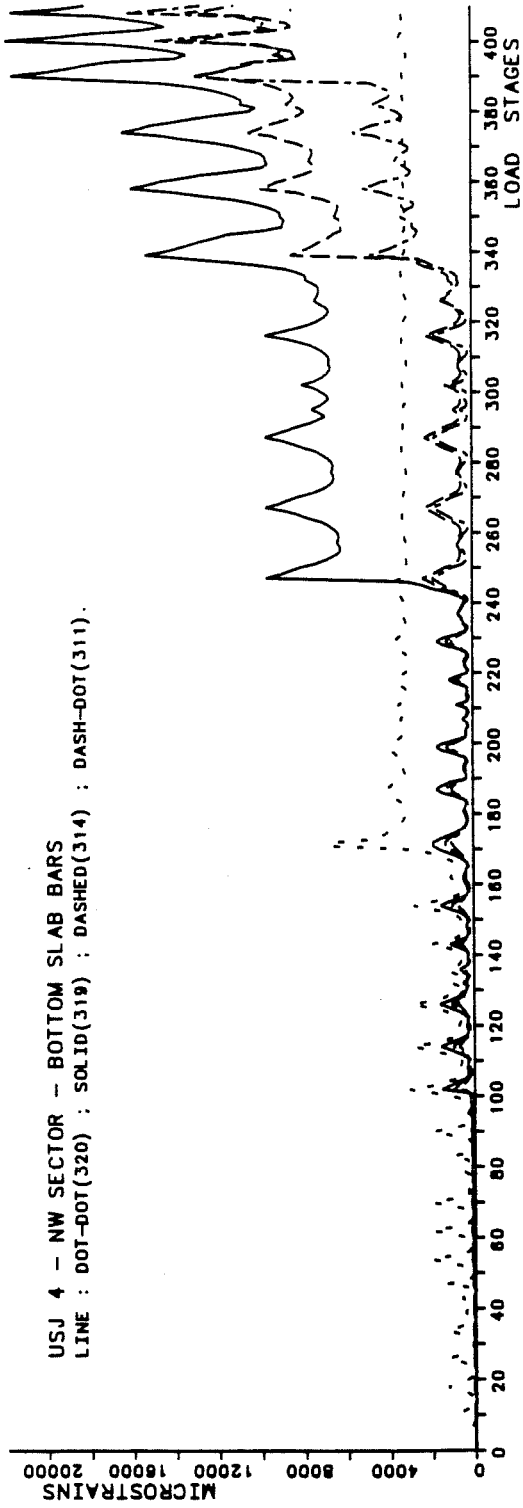
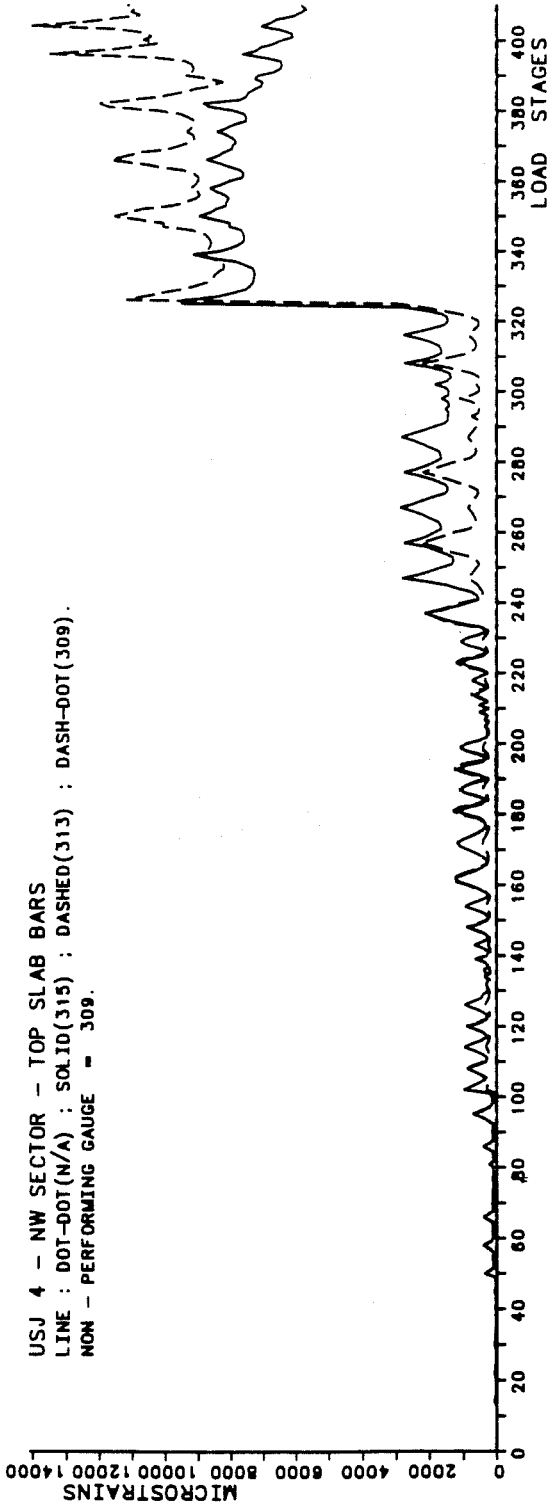


Fig. B.38 - USJ-4 - Slab Bar Strains.

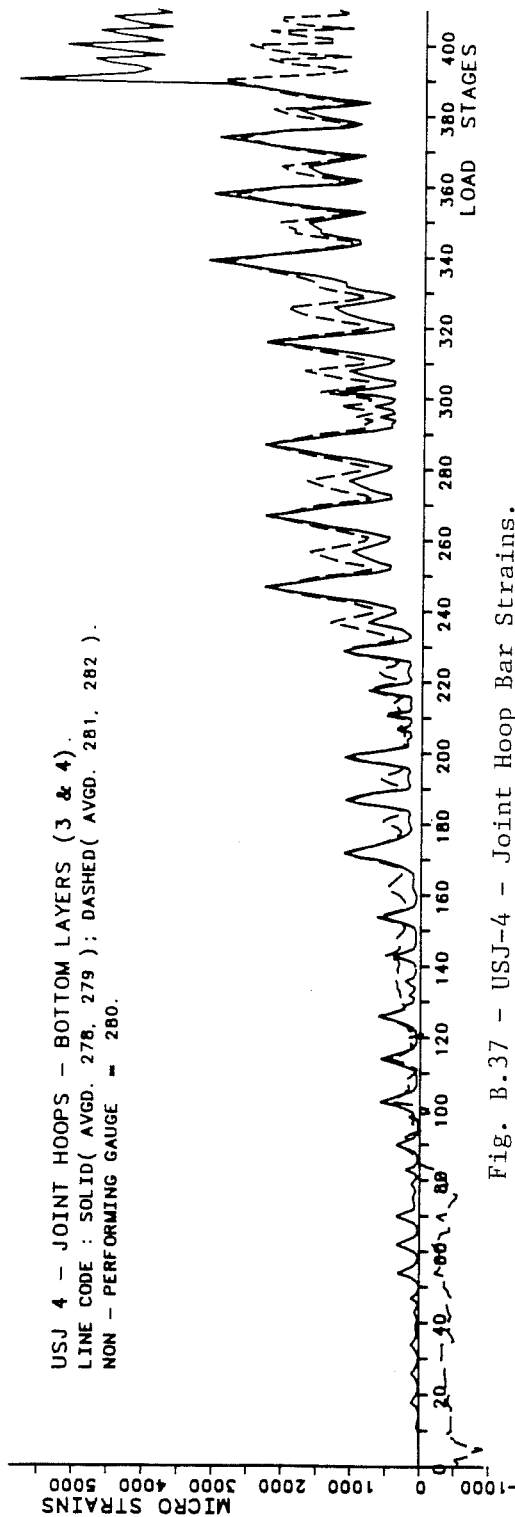
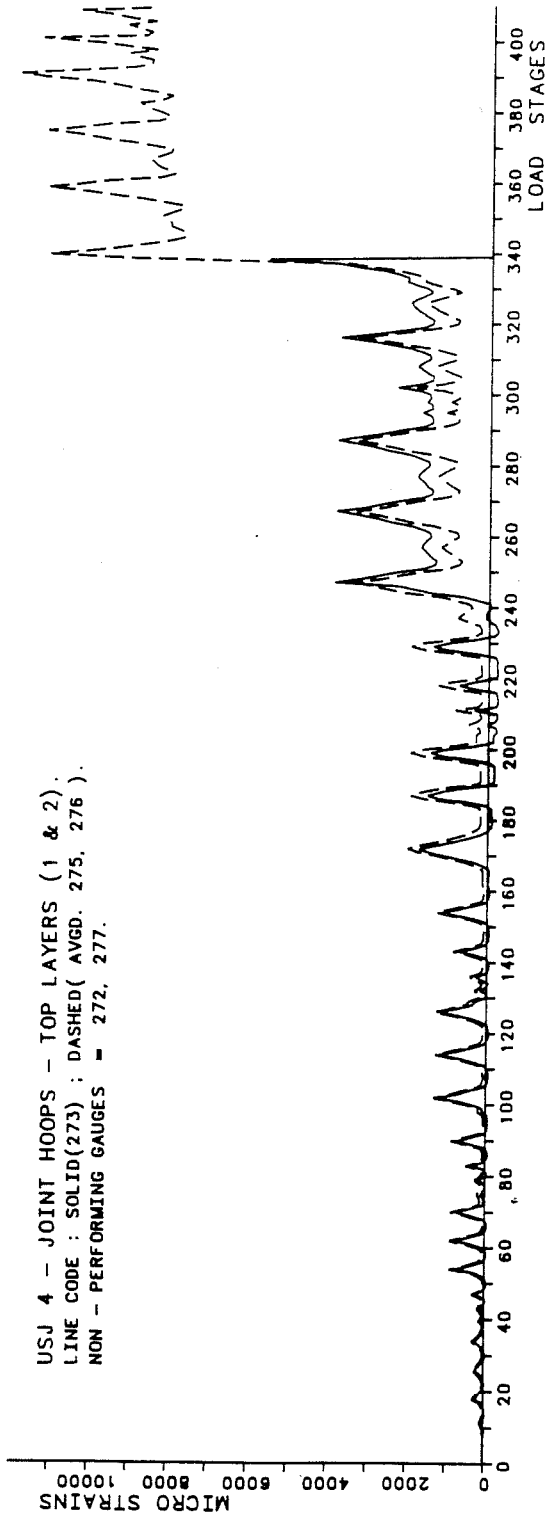


Fig. B.37 - USJ-4 - Joint Hoop Bar Strains.

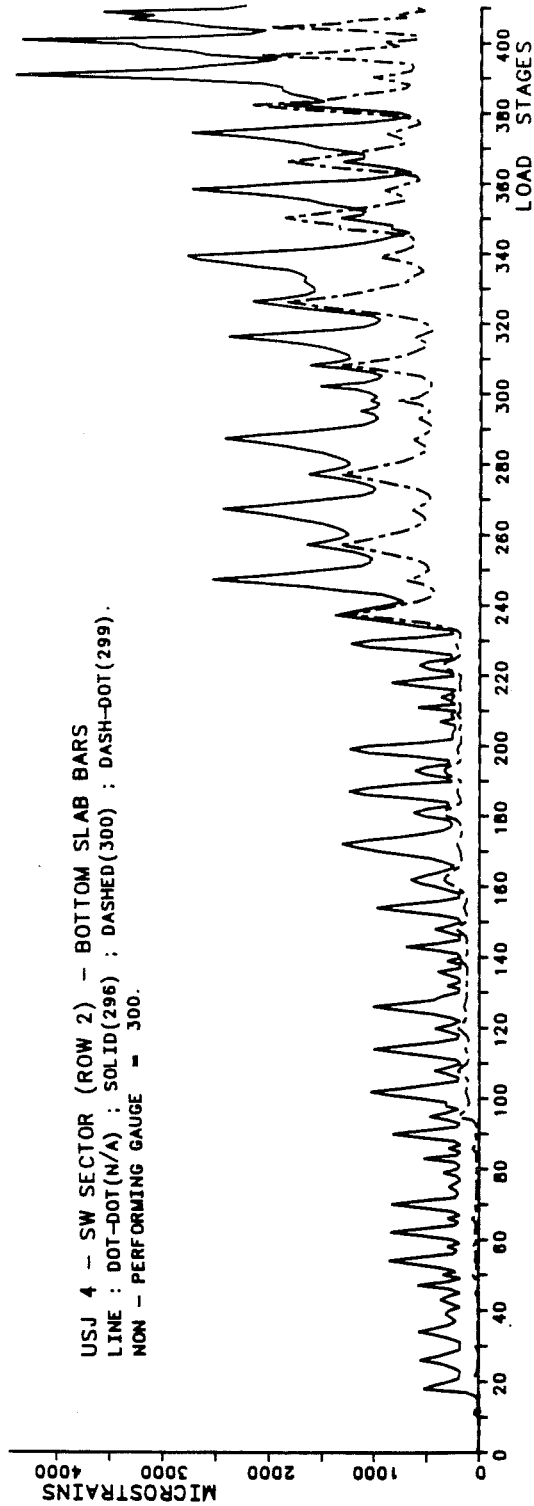
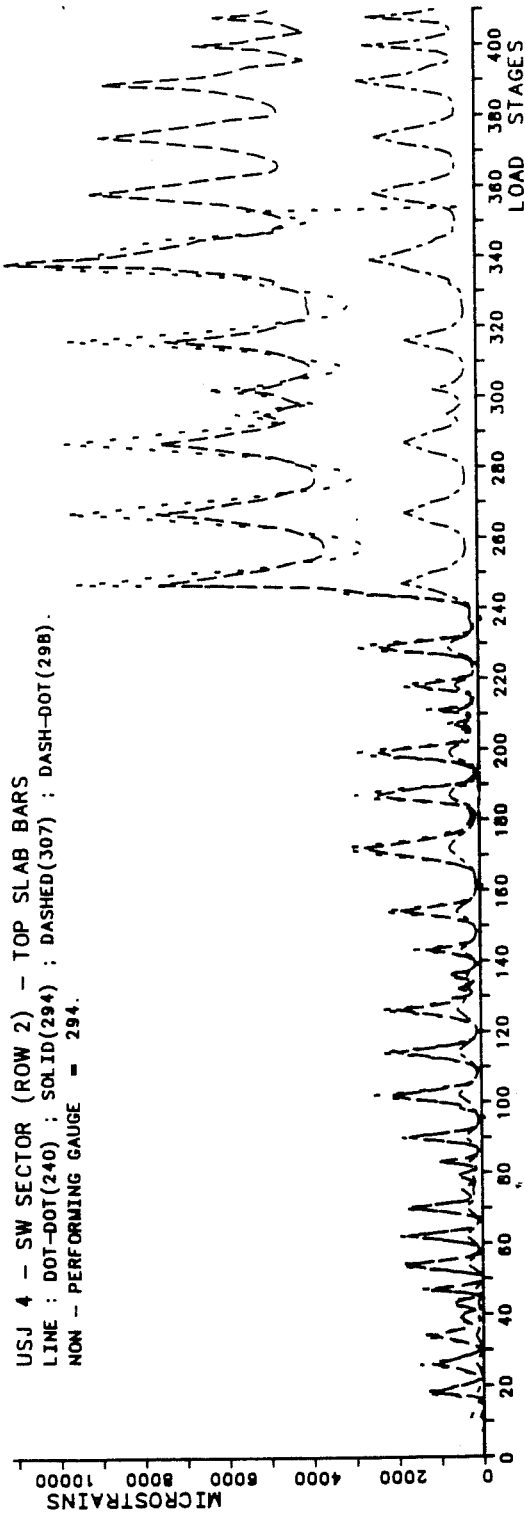


Fig. B.38 (cont.) - USJ-4 - Slab Bar Strains.

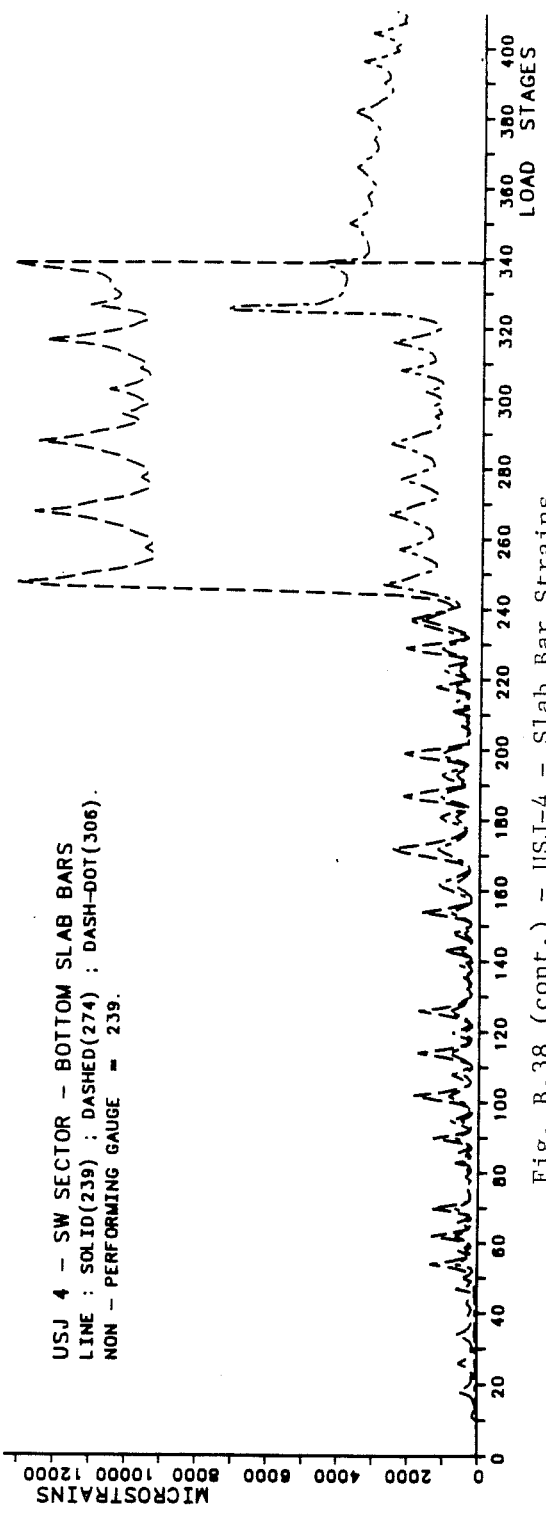
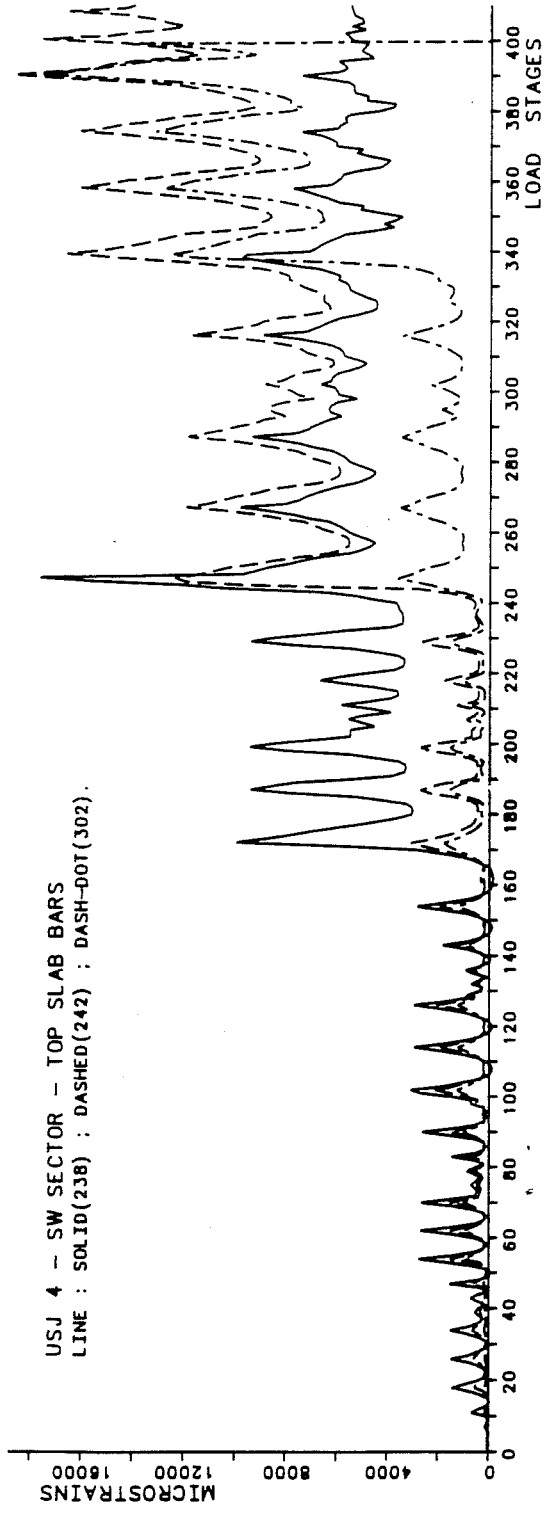


Fig. B.38 (cont.) - USJ-4 - Slab Bar Strains.

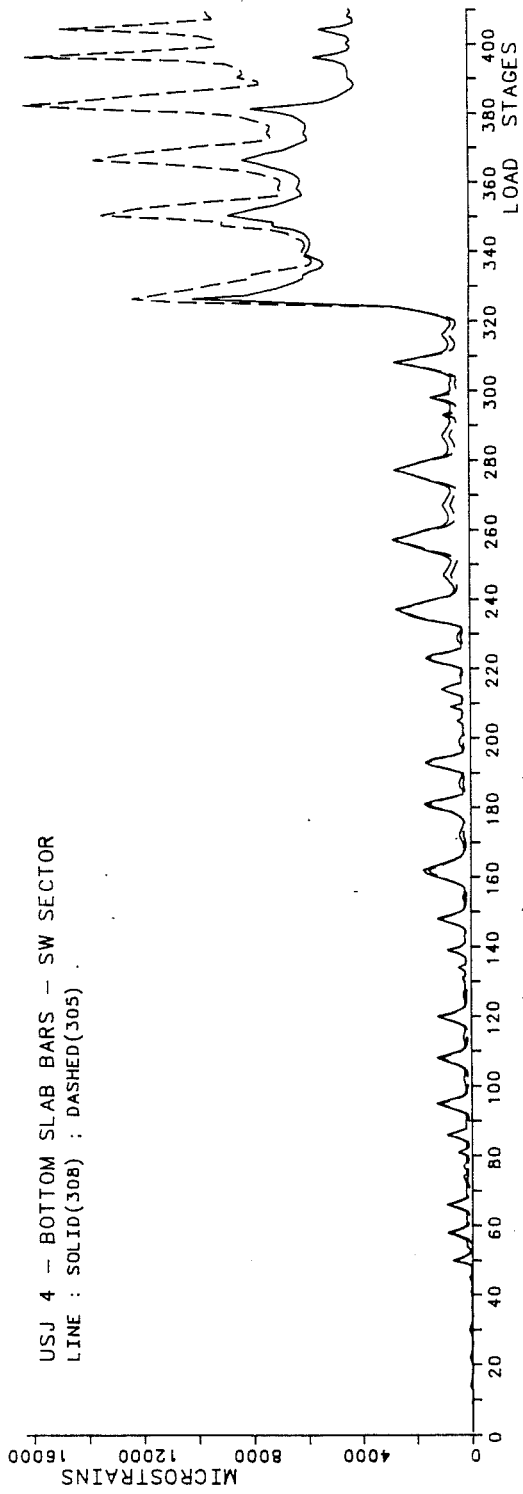
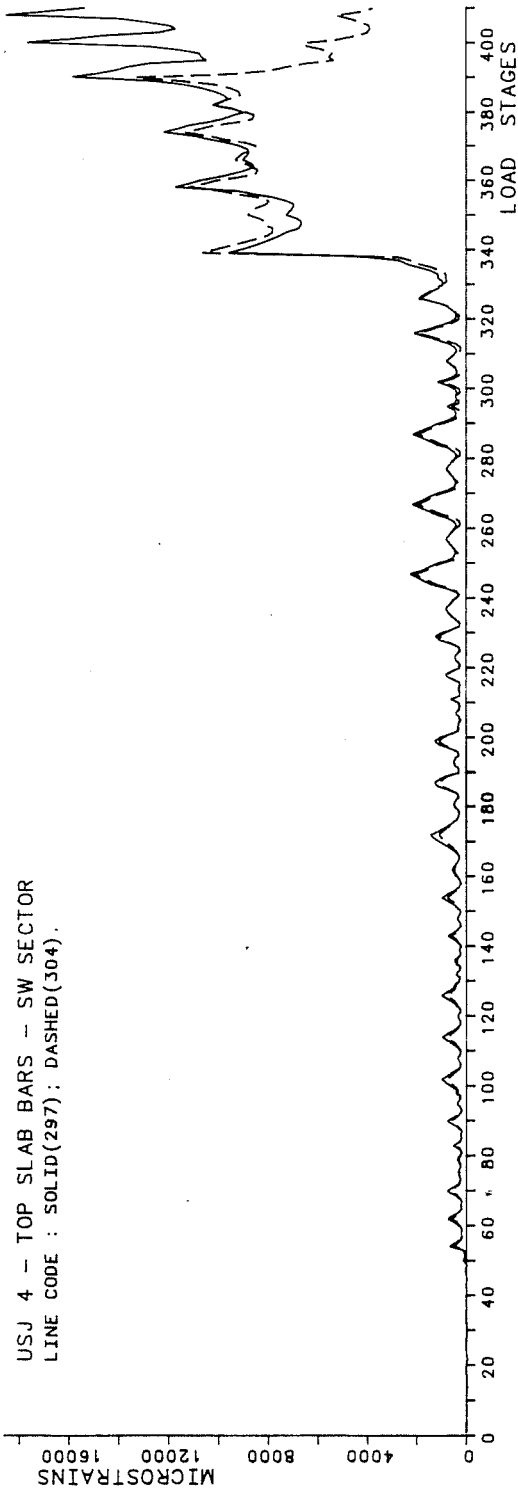


Fig. B.38 (cont.) - USJ-4 - Slab Bar Strains.

APPENDIX C

THE STANFORD UNIVERSITY COMPONENT TEST DATA

In exchange for the UTA component test data, Prof. Benjamin J. Wallace (University of Oklahoma) and Prof. Helmut Krawinkler (Stanford University) graciously made available the small-scale component test data to the author of this study.

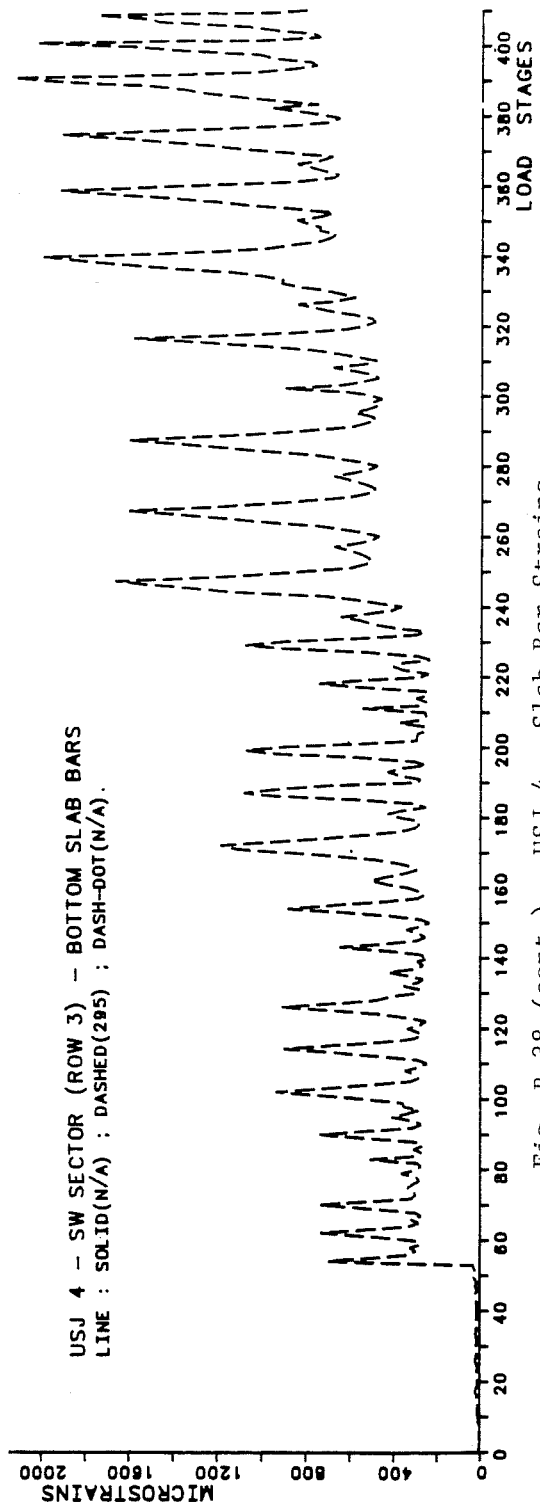
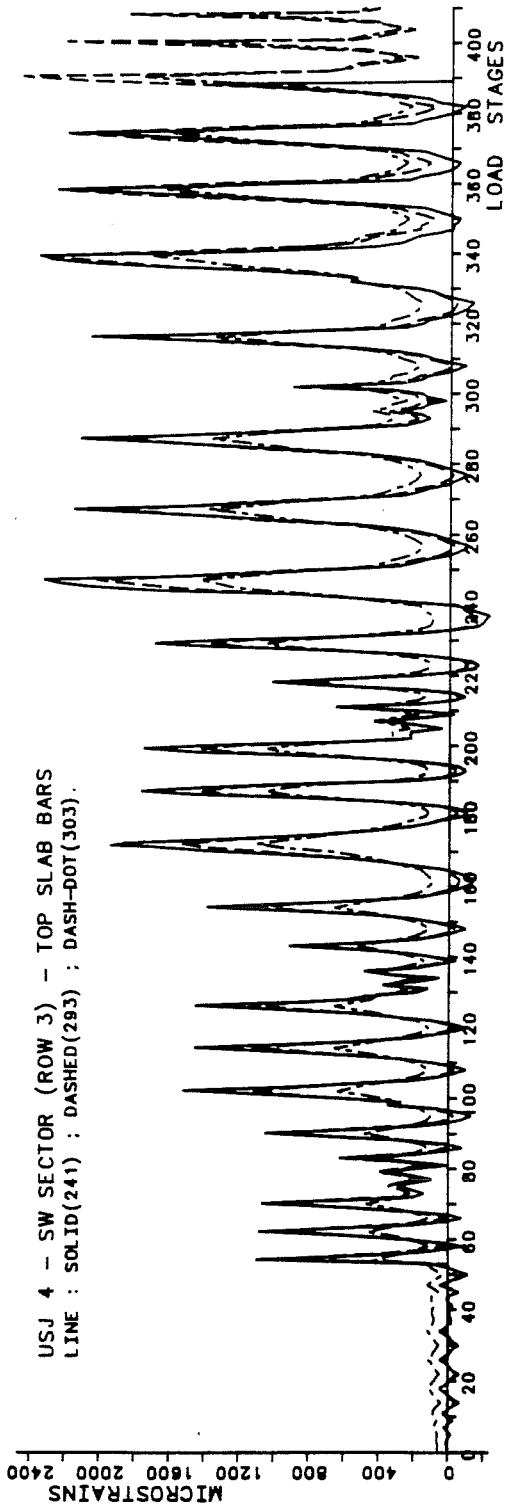
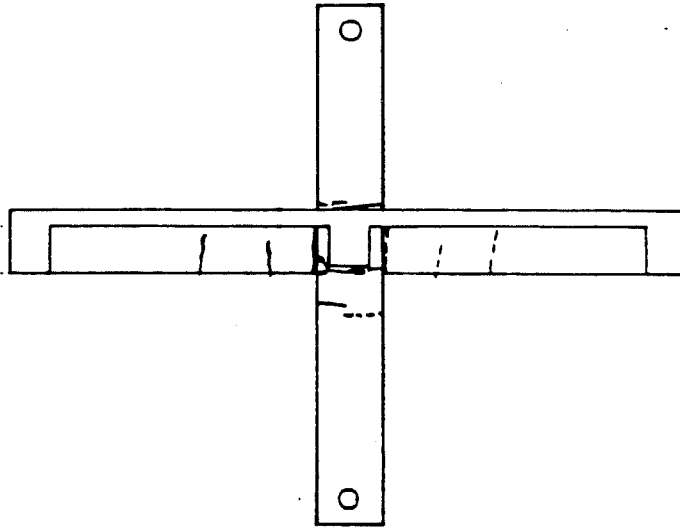
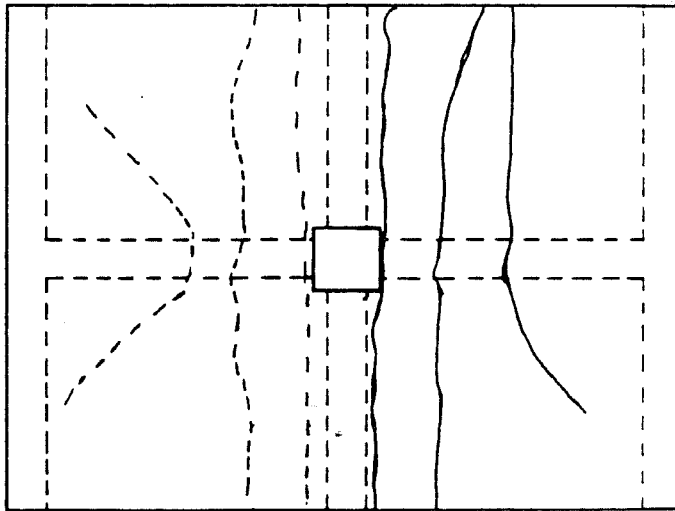


Fig. B.38 (cont.) - USJ-4 - Slab Bar Strains.



a. Elevation.



b. Plan.

Fig. C.1 - SU - IS - Cracking Patterns.

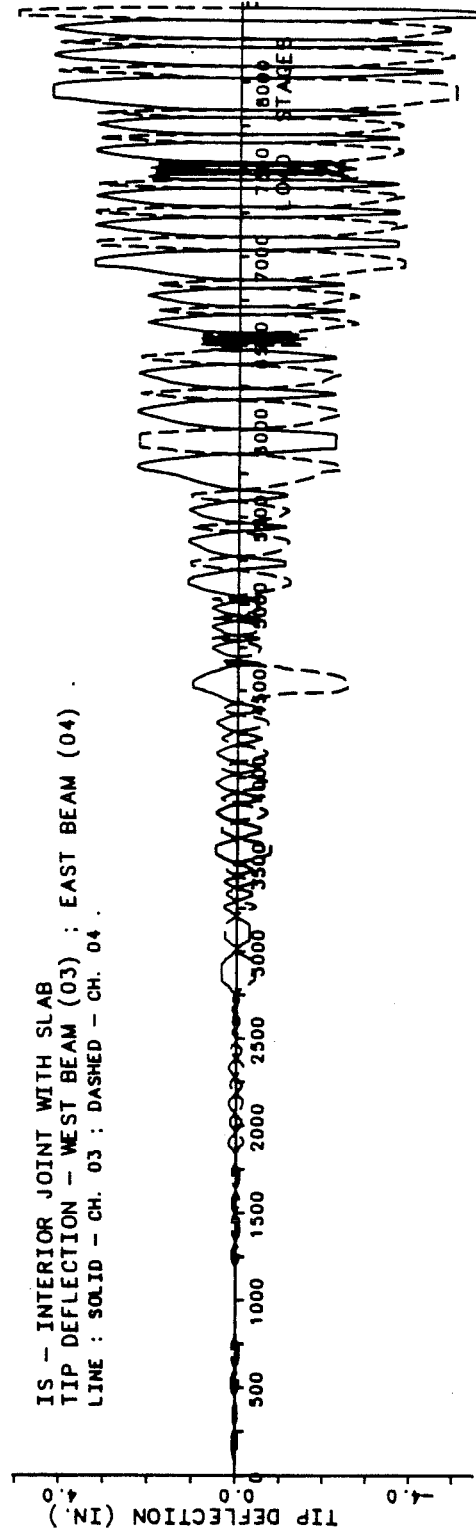
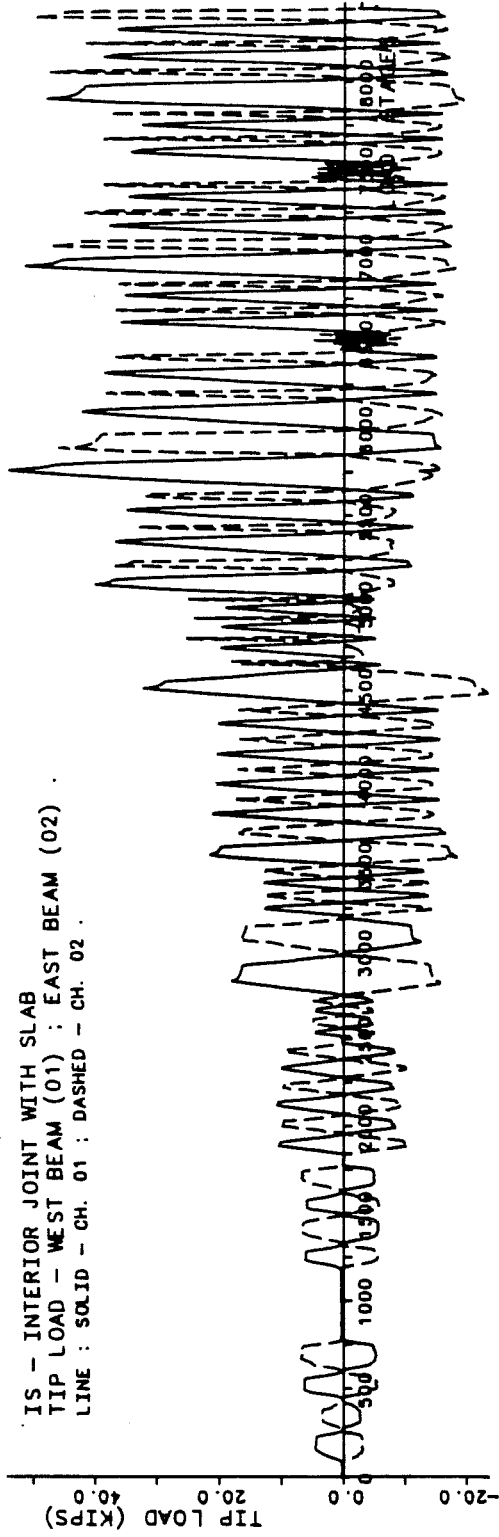


Fig. C.2 - SU - IS - Load-Deflection Response.

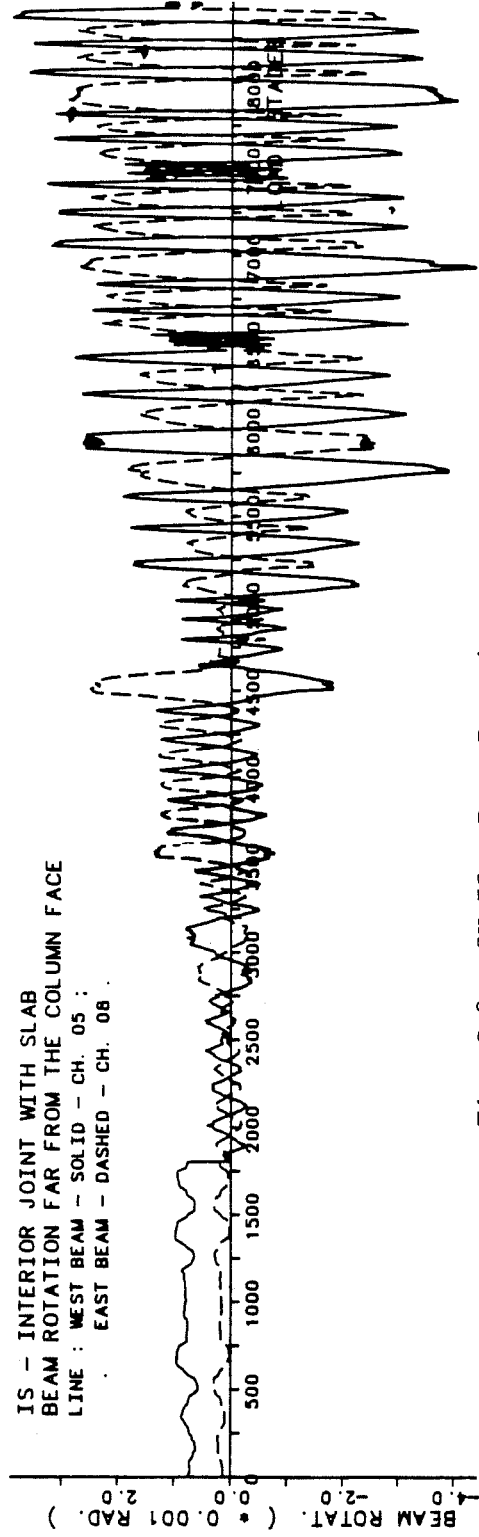
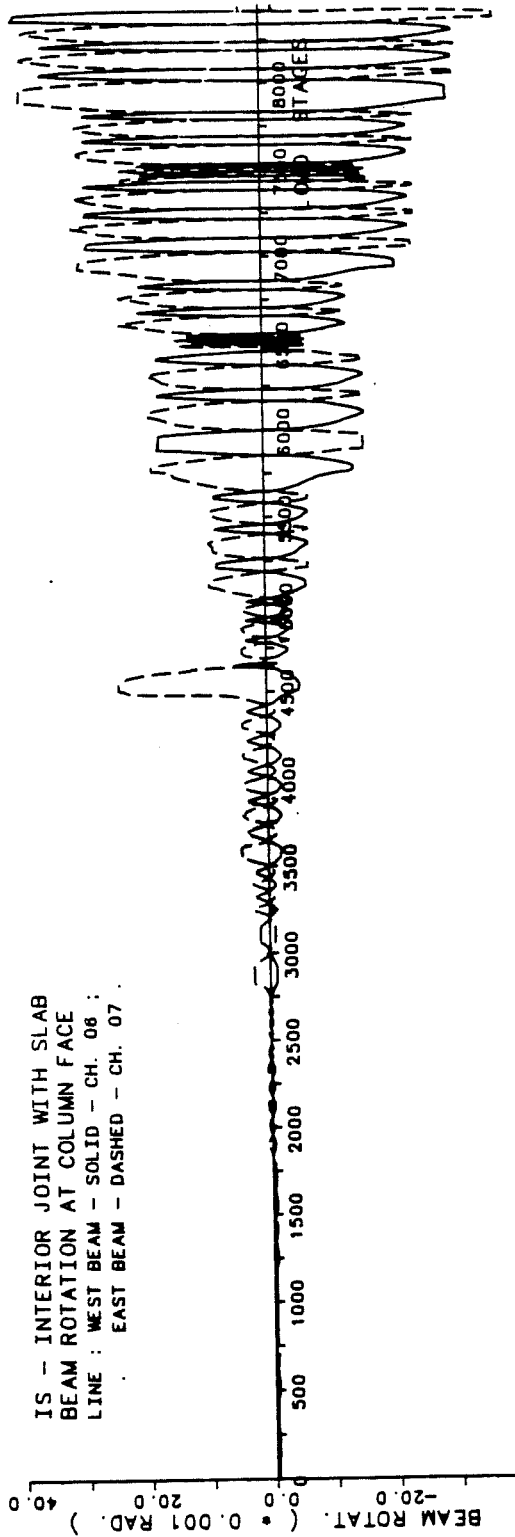


Fig. C.3 - SU-IS - Beam Rotation.

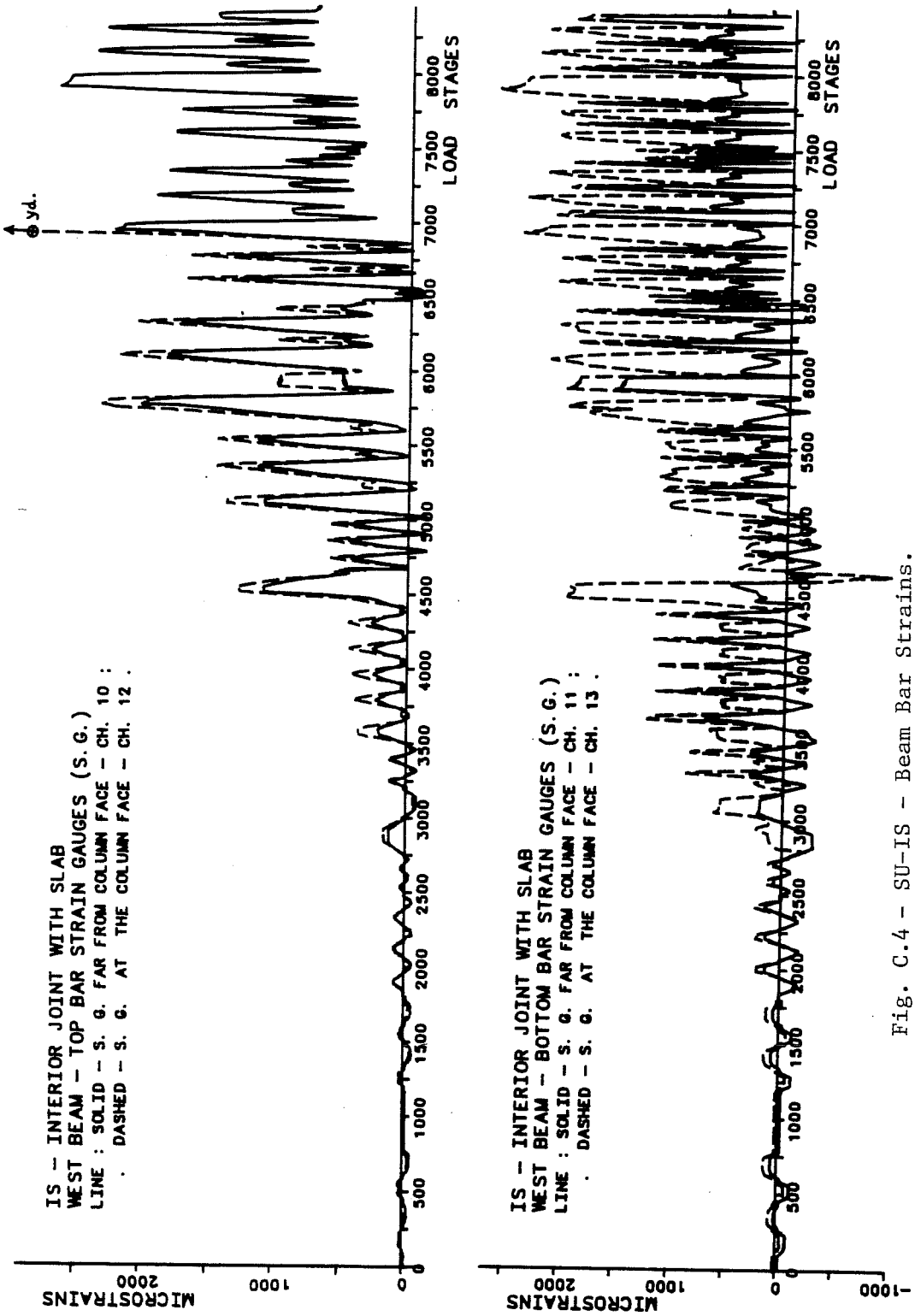


Fig. C.4 - SU-IS - Beam Bar Strains.

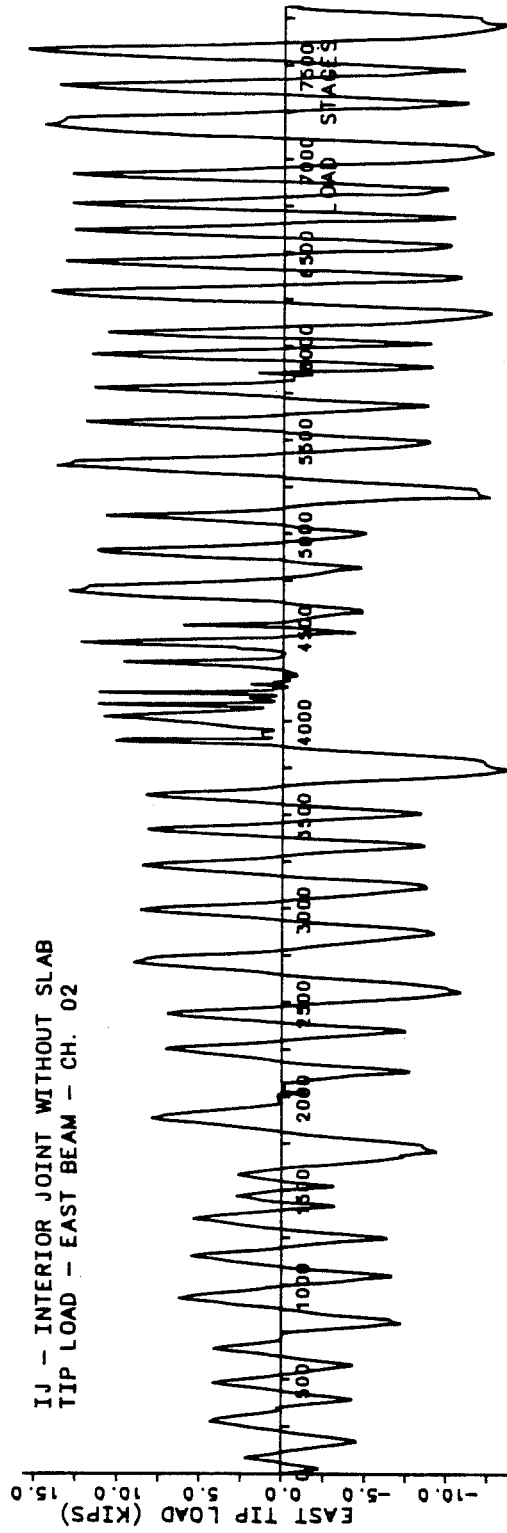
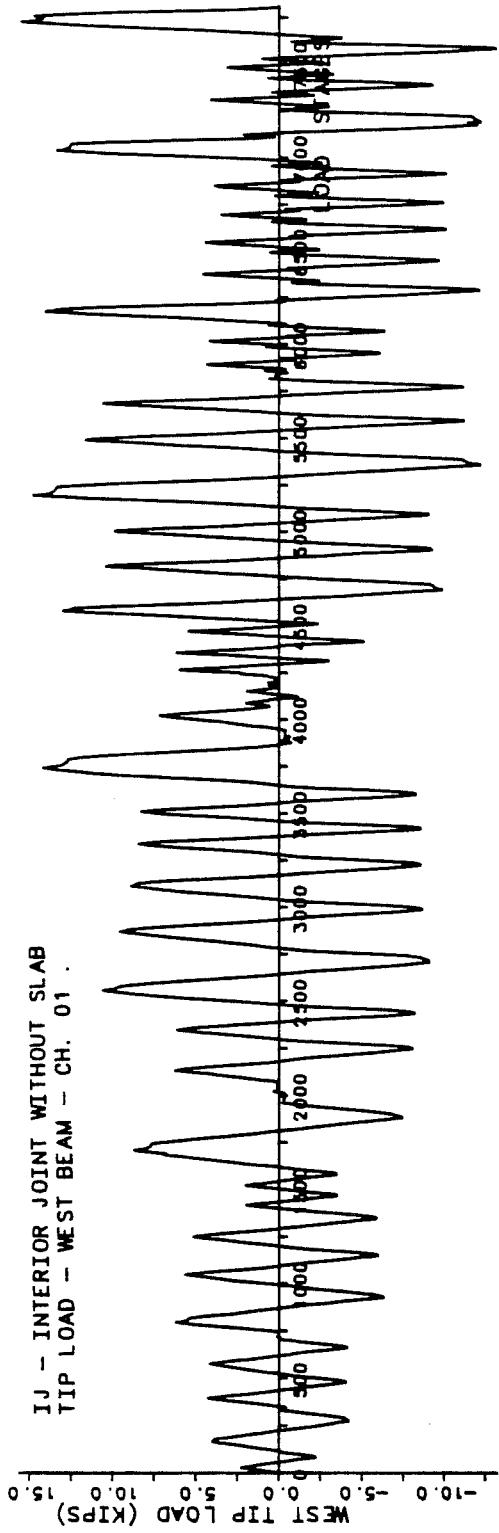


Fig. C.5 - SU-IJ - Load-Deflection Response.

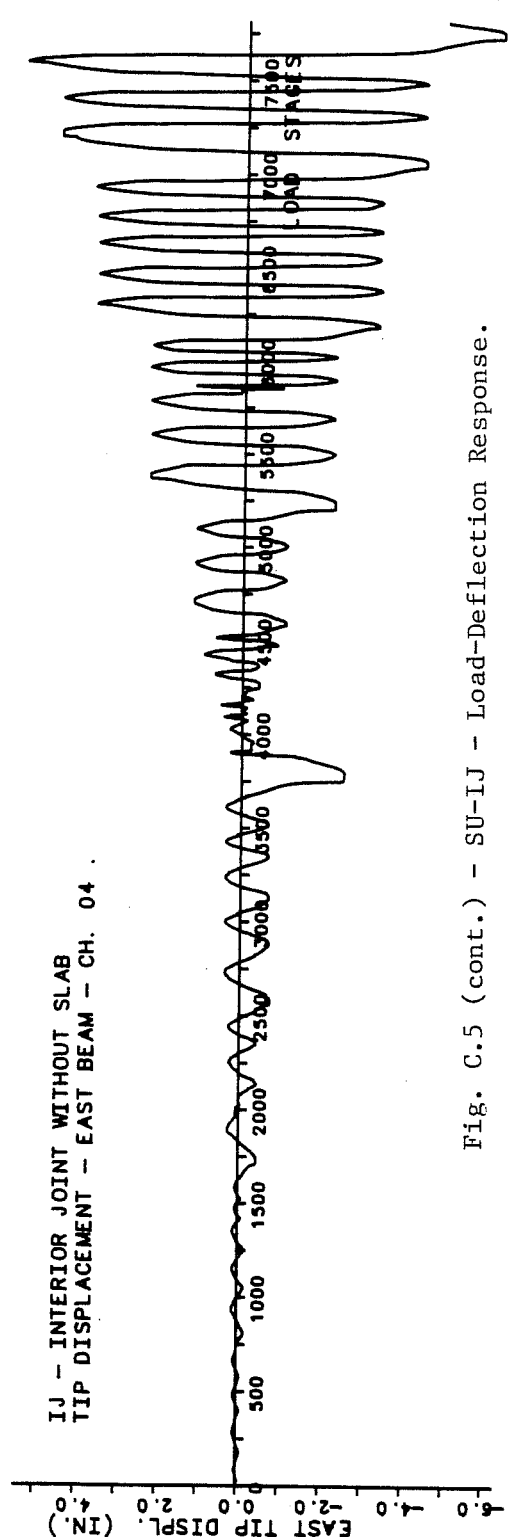
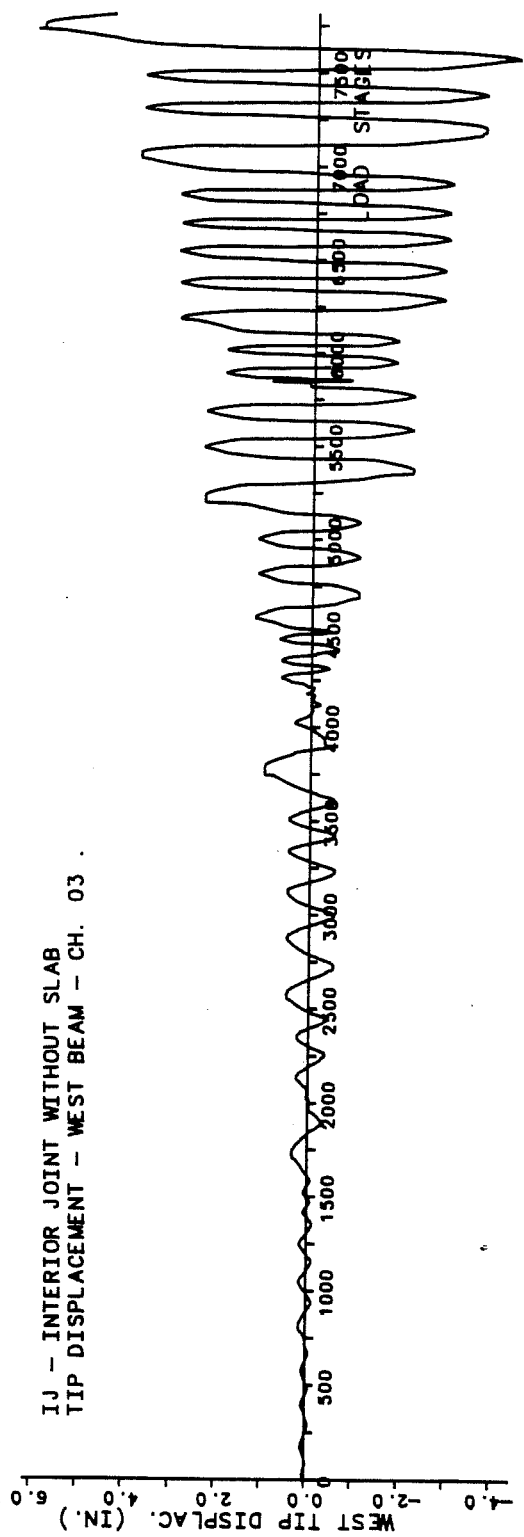


Fig. C.5 (cont.) - SU-IJ - Load-Deflection Response.

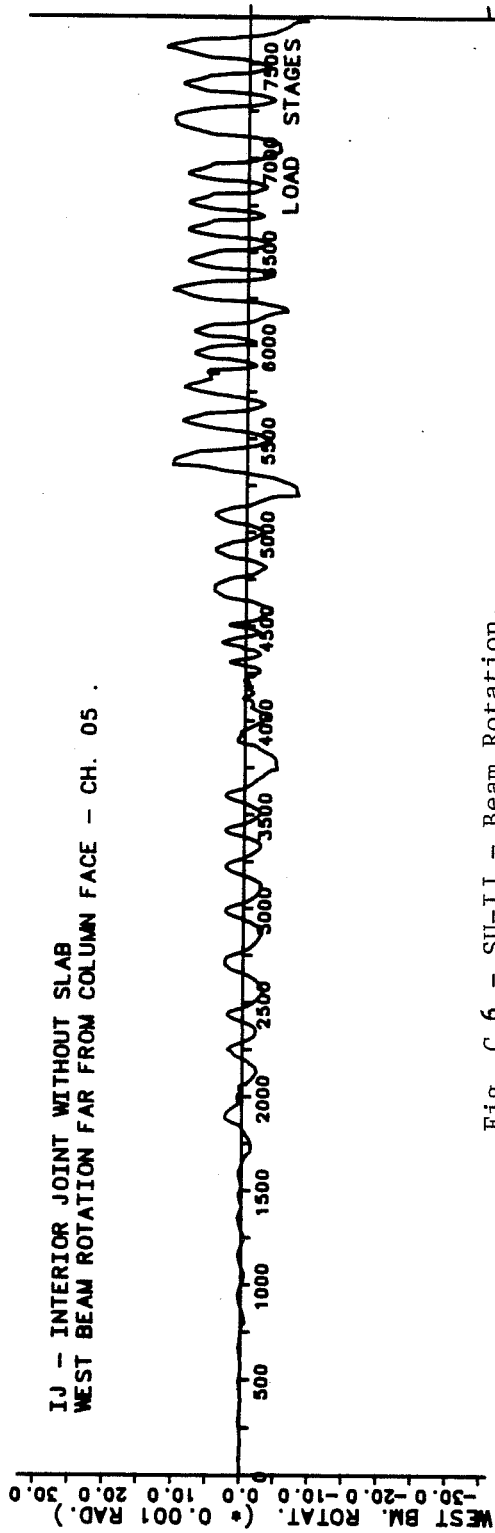
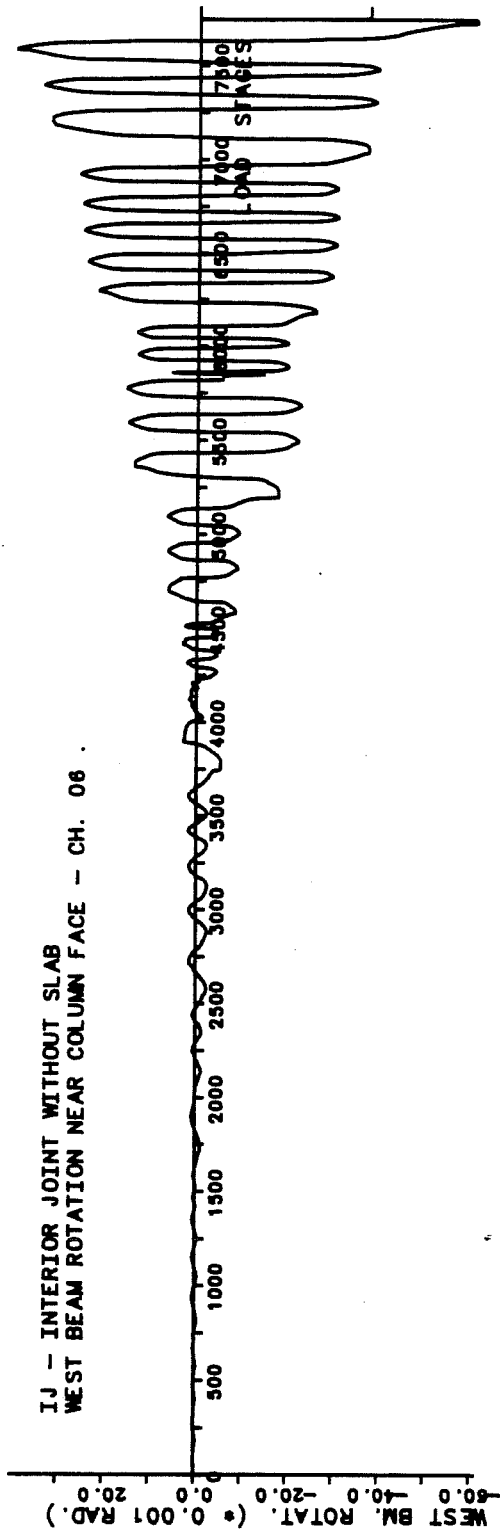


Fig. C.6 - SU-IJ - Beam Rotation.

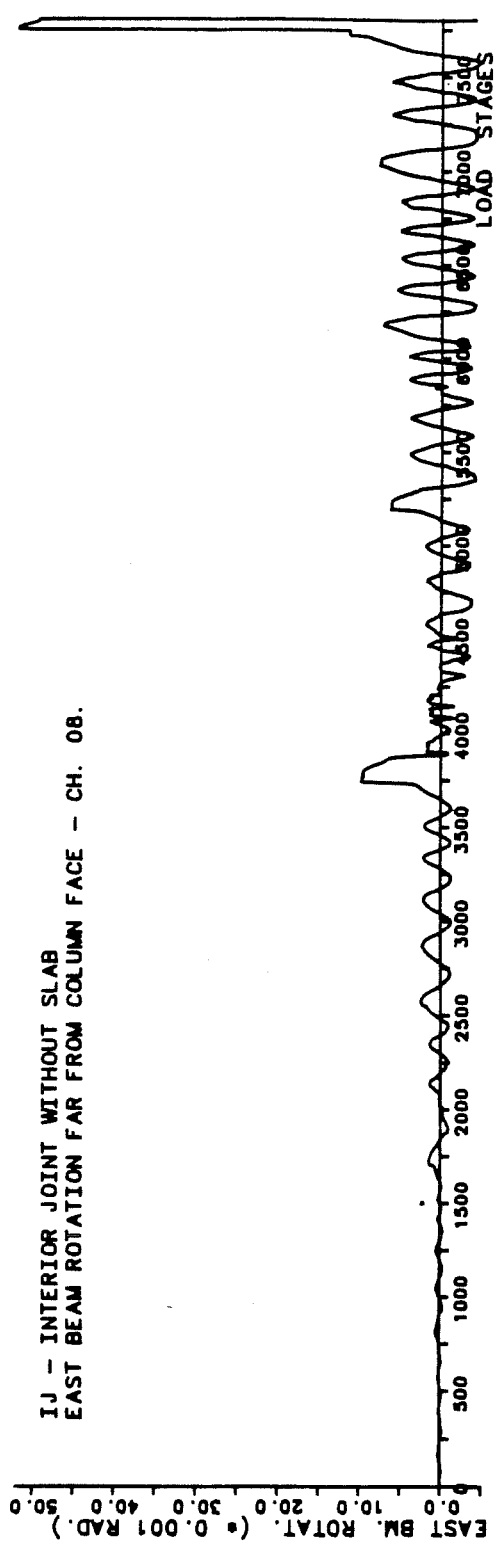


Fig. C.6 (cont.) - SU-IJ - Beam Rotation.

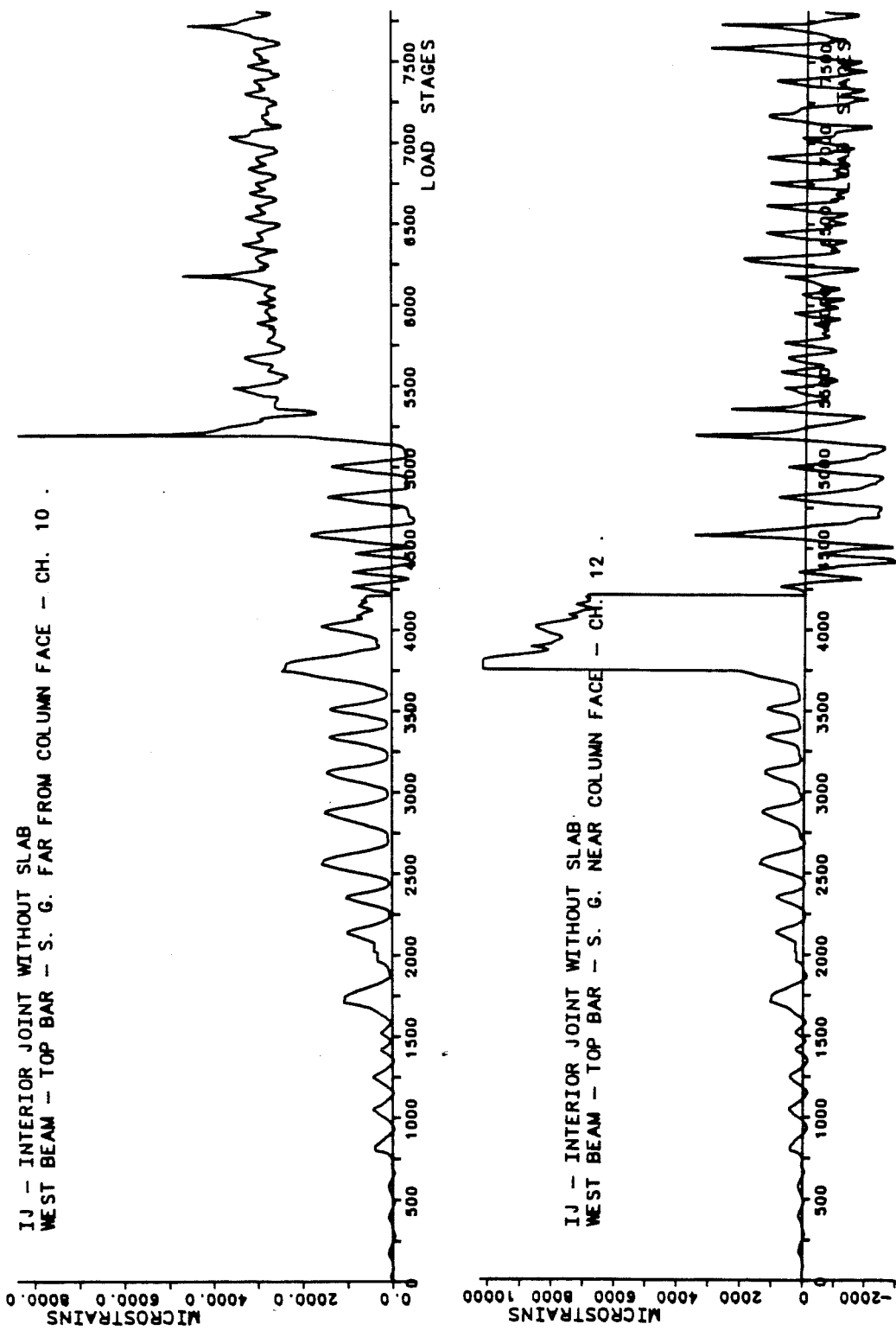


Fig. C.7 - SU-IJ - Beam Bar Strains.

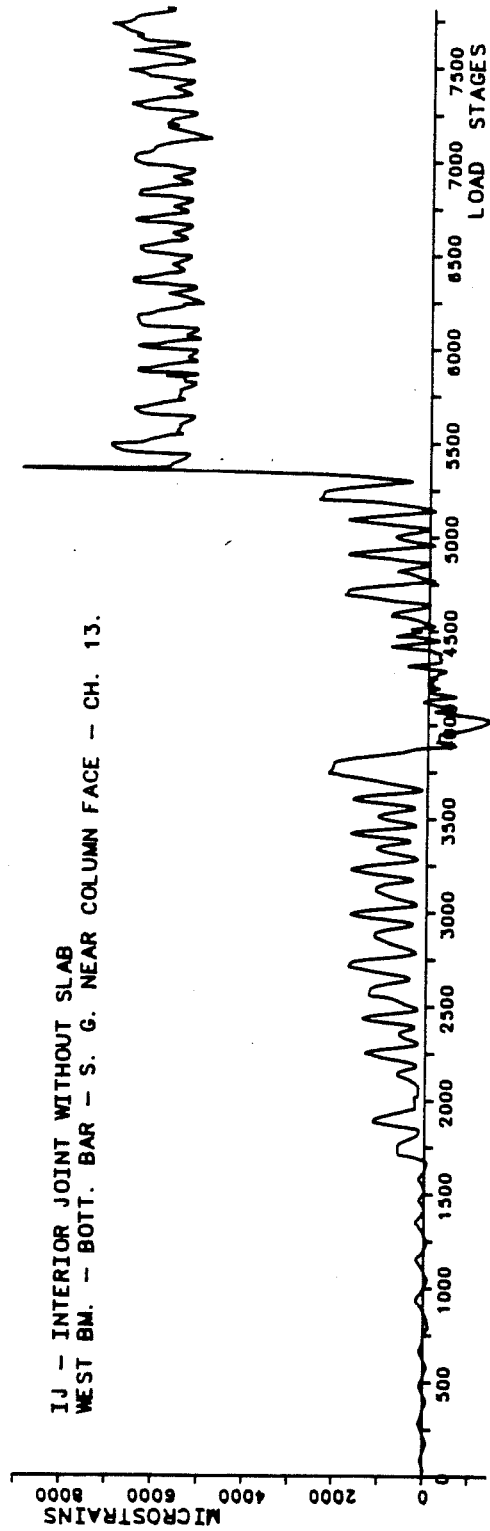
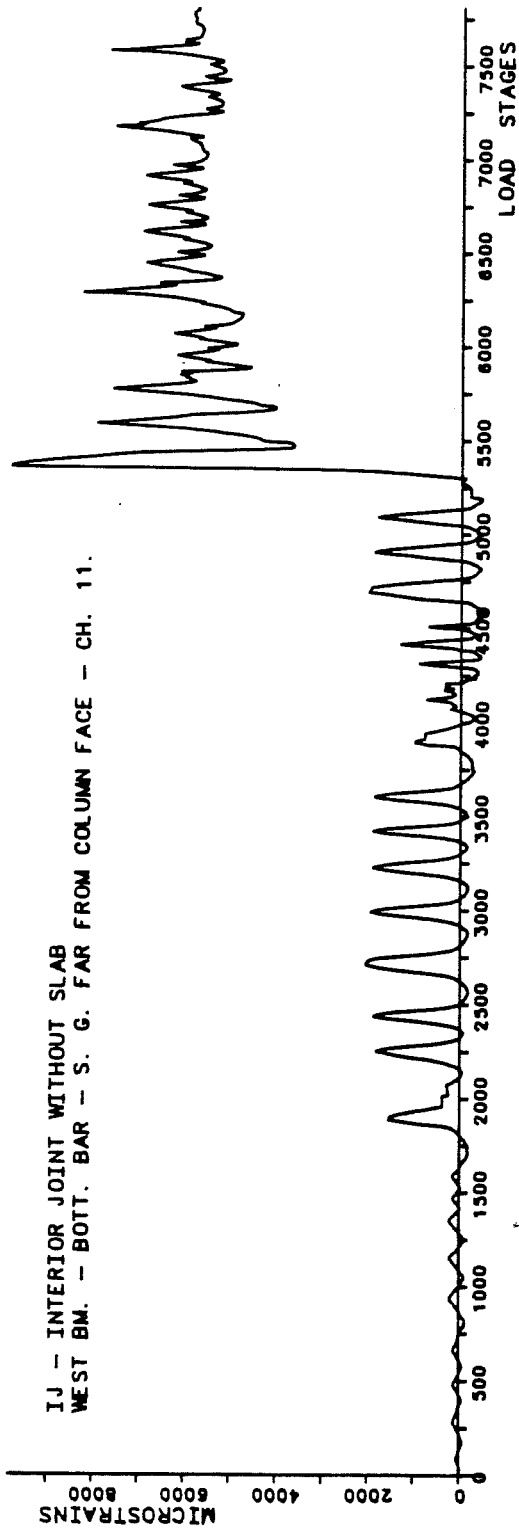


Fig. C.7 (cont.) - SU-IJ - Beam Bar Strains.

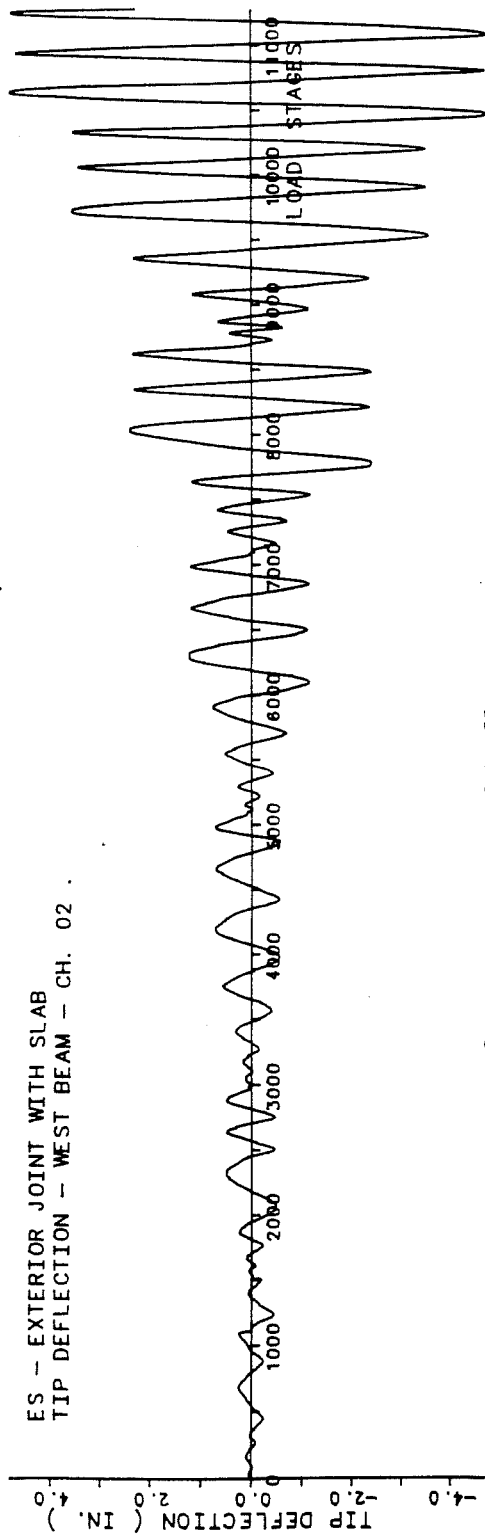
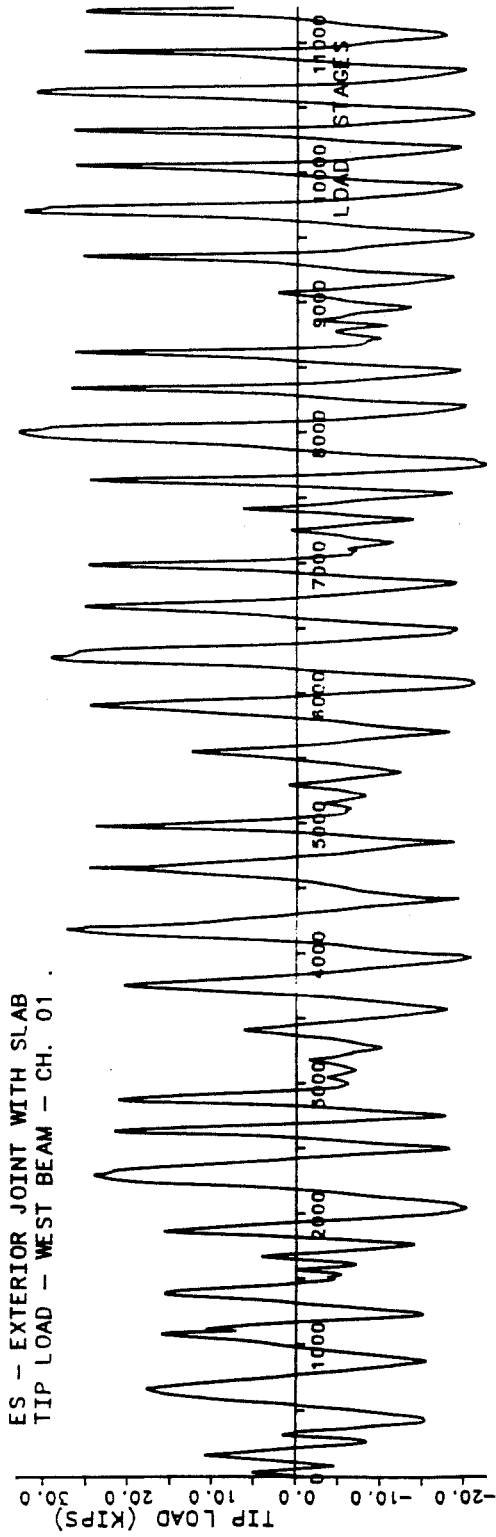


Fig. C.8 - SU-ES - Load-Deflection Response.

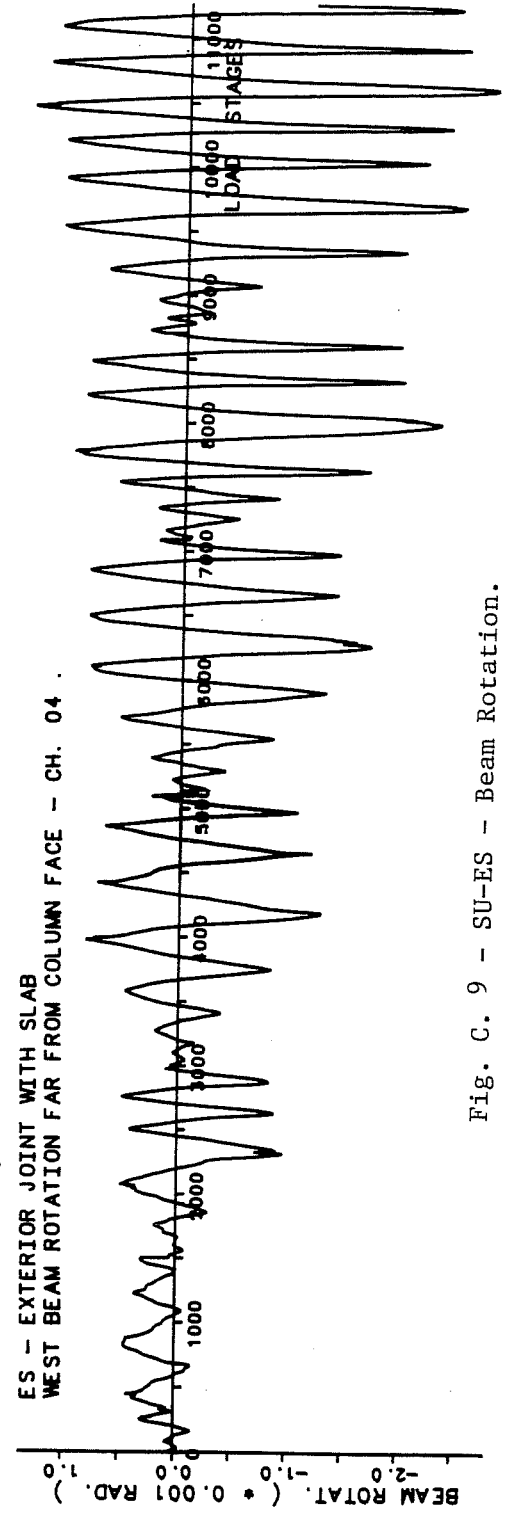
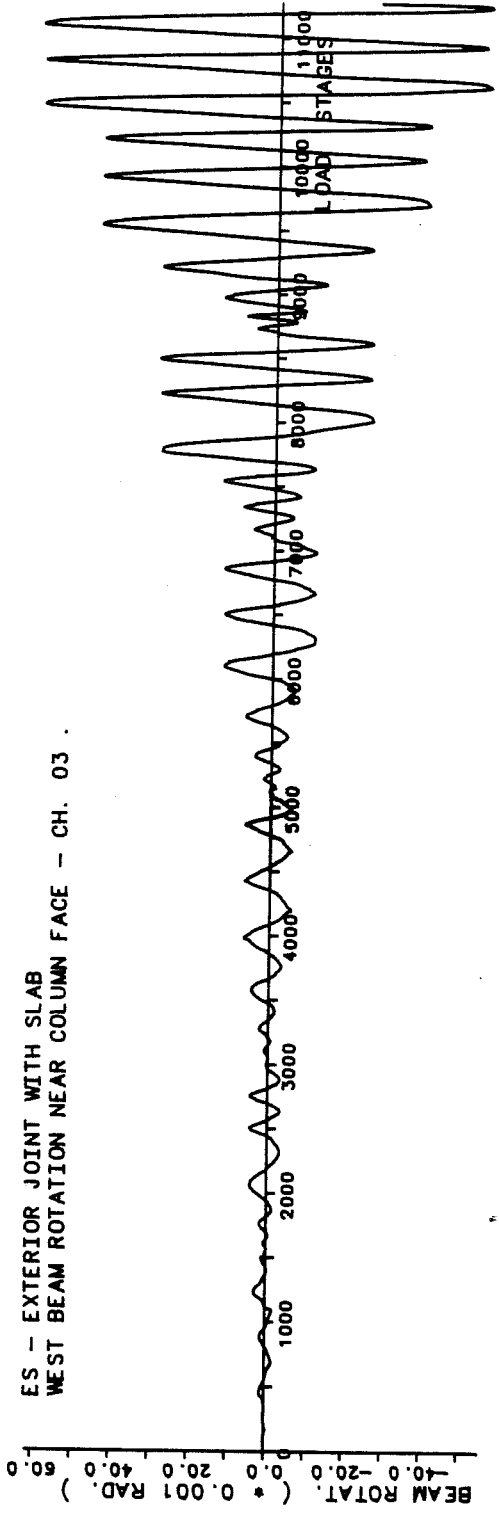


Fig. C. 9 - SU-ES - Beam Rotation.

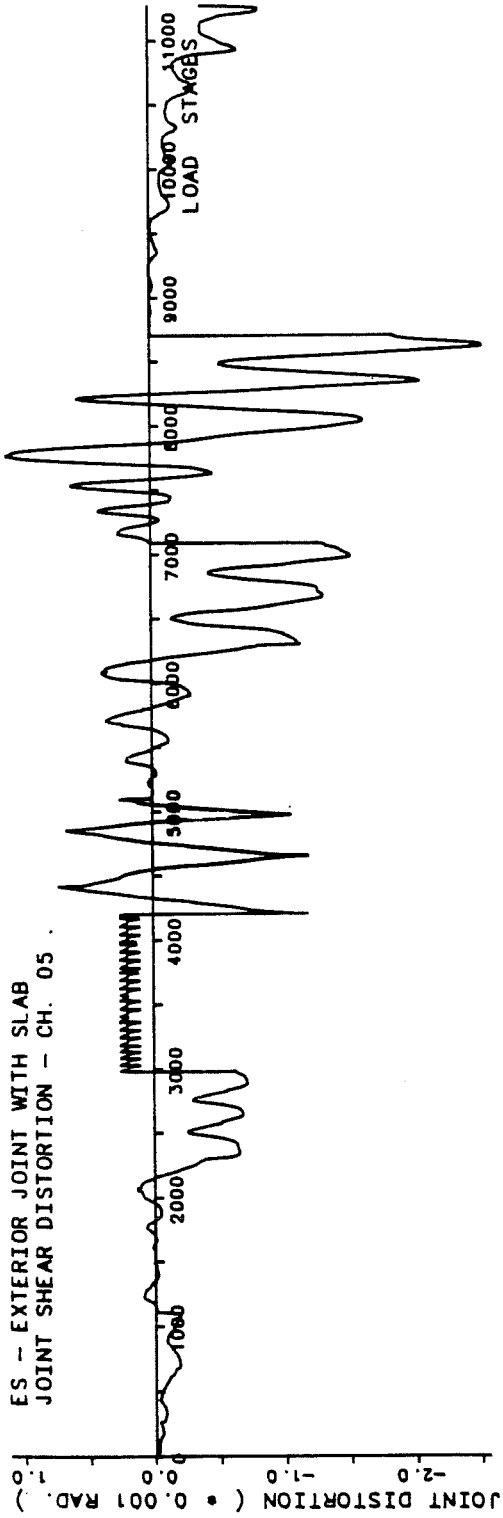


Fig. C.10 - SU-ES - Joint Shear Distortion.

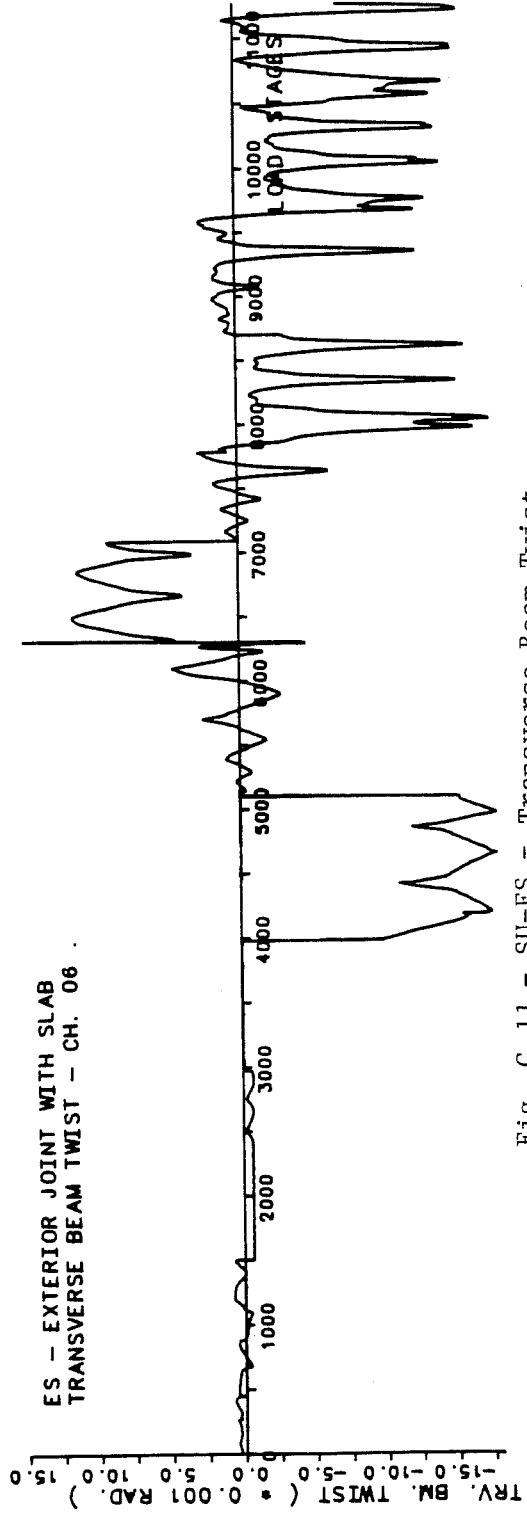


Fig. C.11 - SU-ES - Transverse Beam Twist.

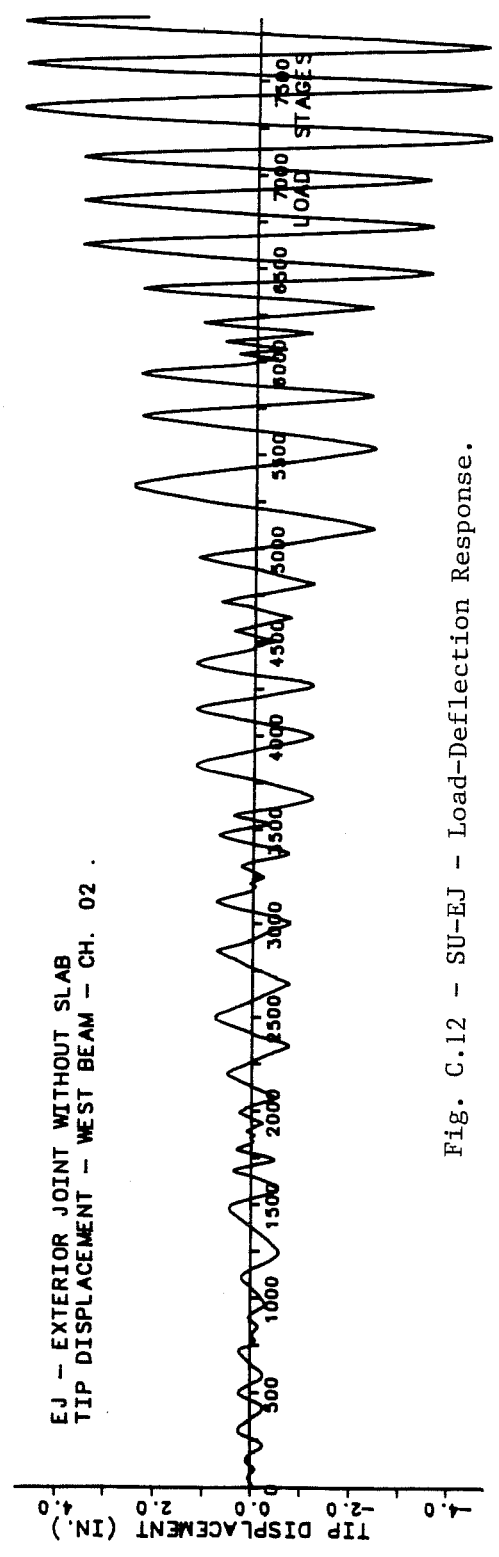
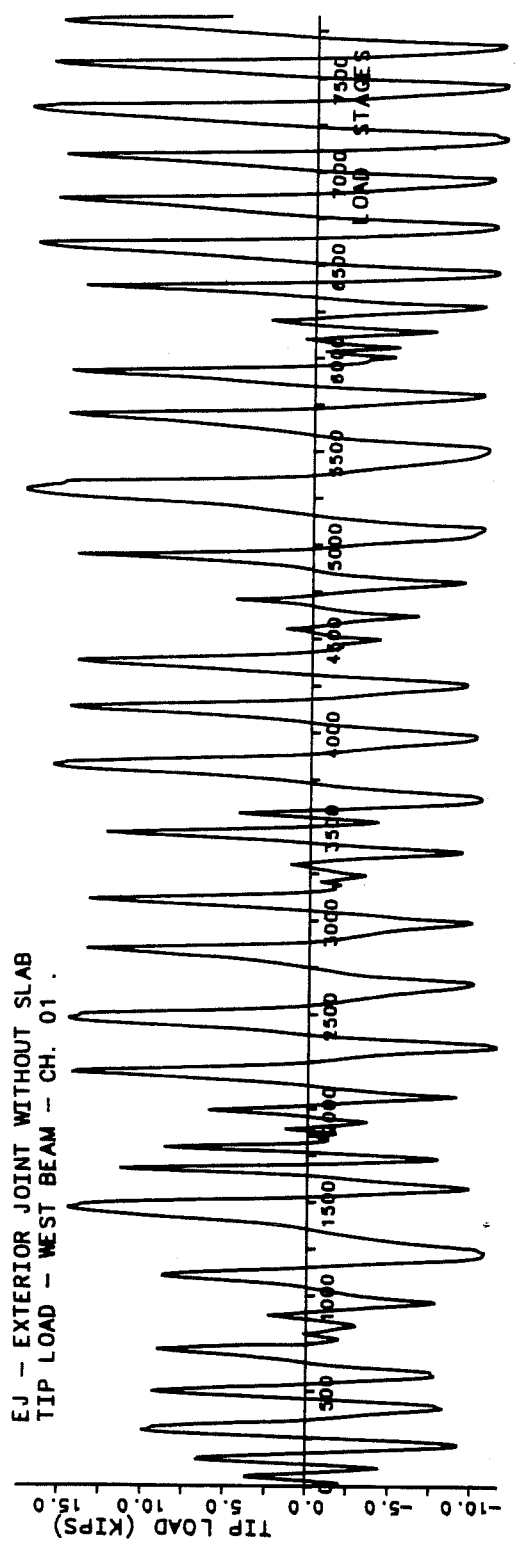


Fig. C.12 - SU-EJ - Load-Deflection Response.

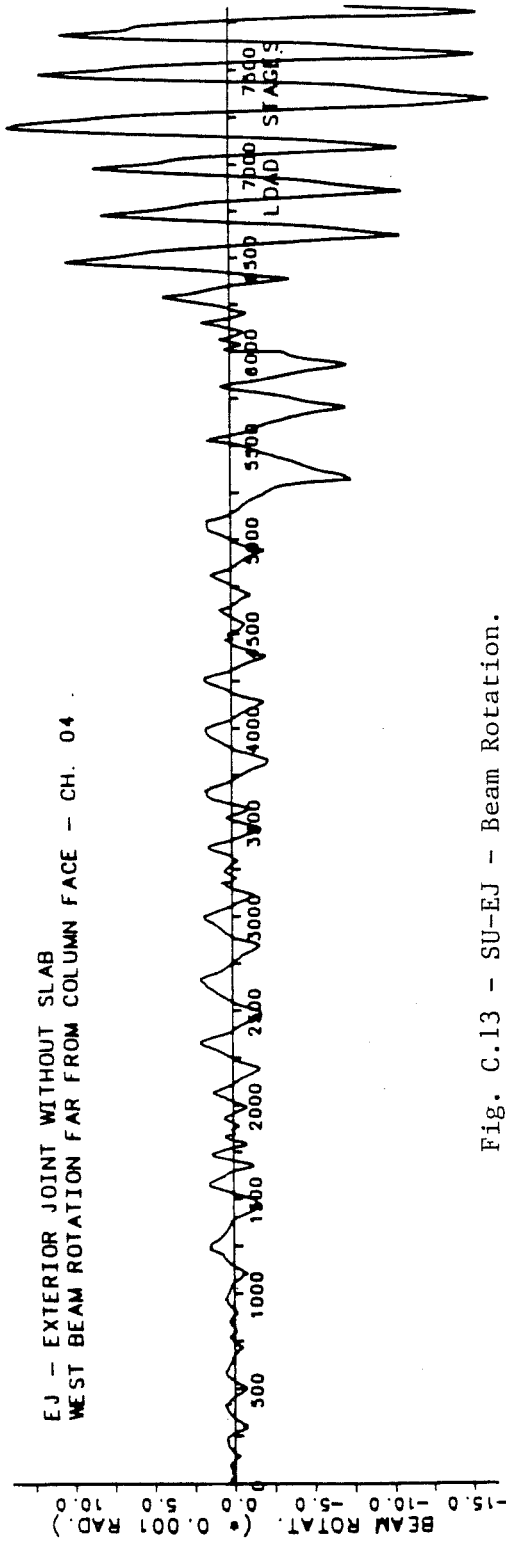
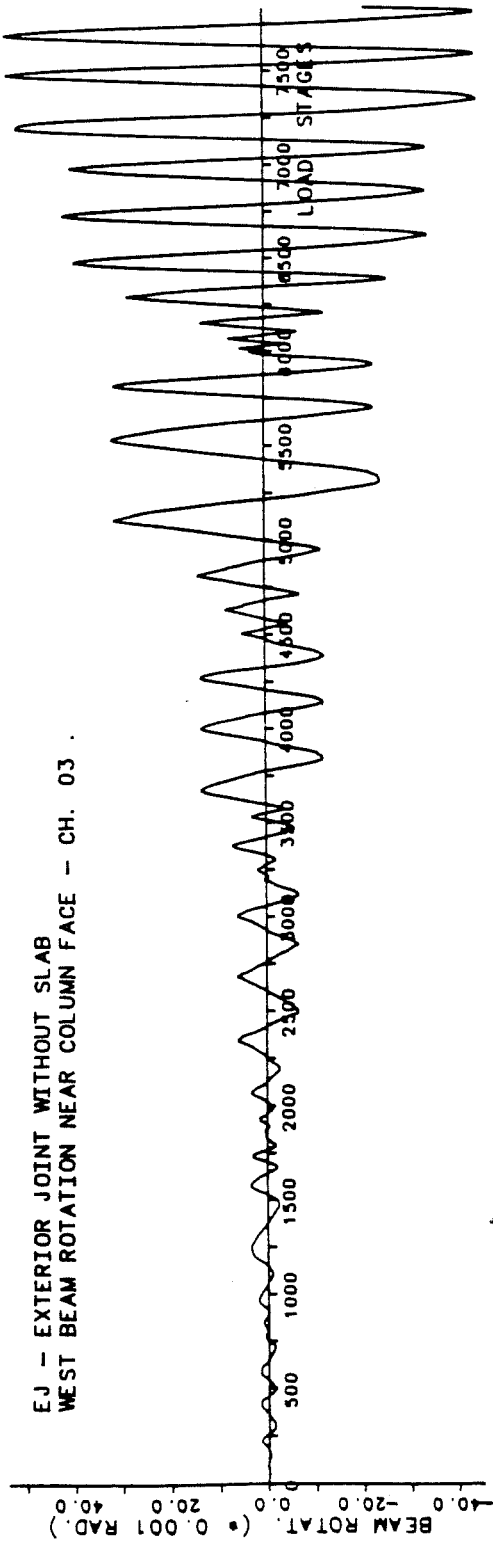


Fig. C.13 - SU-EJ - Beam Rotation.

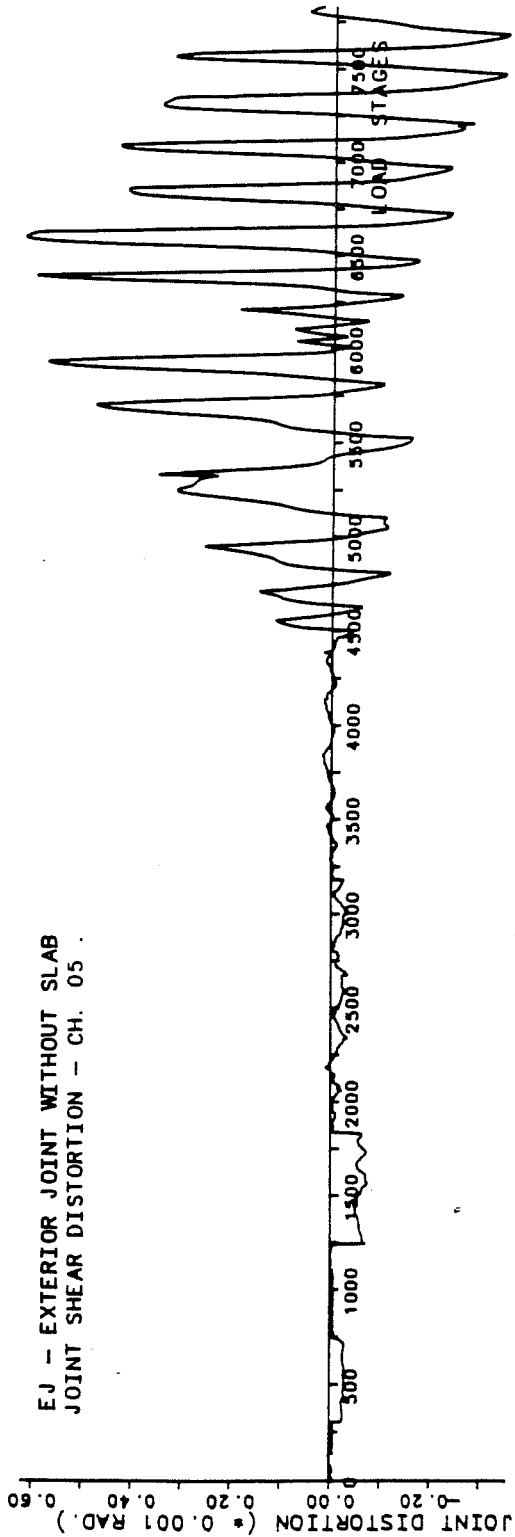


Fig. C.14 - SU-EJ - Joint Distortion.

VITA

Jorge de Novais Teles de Faria Correa Bastos was born in Lourenco Marques, Mocambique, on February 6, 1957, the son of Manuela Armanda Frederico de Novais Leite and Joaquim Telles de Faria Correa Bastos.

In October 1973, he entered the Universidade de Lourenco Marques and in October 1974, he was transferred to the Faculdade de Engenharia - Universidade do Porto, Portugal, where he graduated as Licenciado em Engenharia Civil in June 1978. From 1979-1980 he attended the Graduate Programme in Geotechnique, at The Universidade Nova de Lisboa, where he graduated in July 1980.

In September 1980, he entered the Graduate School of The University of Texas at Austin where he graduated with a Master of Science in Civil Engineering in August 1983. Since Fall 1982, he has been working on his Ph.D. degree in the Department of Civil Engineering - The University of Texas at Austin.

Permanent address: Faculdade de Arquitectura
Largo da Biblioteca Publica
Lisboa, Portugal

This dissertation was typed by Sharon Cunningham.